Plasma Physics Series

The Plasma Boundary of Magnetic Fusion Devices

Peter C Stangeby

University of Toronto Institute for Aerospace Studies

IoP
Institute of Physics Publishing
Bristol and Philadelphia

British Library Cataloguing-in-Publication Data

A catalogue record for this book is available from the British Library.

ISBN 0 7503 0559 2

Library of Congress Cataloging-in-Publication Data are available

Publisher: Nicki Dennis
Production Editor: Simon Laurenson
Production Control: Sarah Plenty
Marketing Executive: Colin Fenton

Published by Institute of Physics Publishing, wholly owned by The Institute of Physics, London

Institute of Physics Publishing, Dirac House, Temple Back, Bristol BS1 6BE, UK

US Office: Institute of Physics Publishing, The Public Ledger Building, Suite 1035, 150 South Independence Mall West, Philadelphia, PA 19106, USA

Typeset in TEX using the IOP Bookmaker Macros
Printed in the UK by J W Arrowsmith Ltd, Bristol

dedicated to

Sharron

Contents

Acknowledgements

It is a pleasure to thank the many people who helped me with this book. The genesis of the book was a mini-course given at JET in 1993 on tokamak edge physics that Günther Janeschitz encouraged me to give during a sabbatical year at JET arranged by the good offices of George Vlases. Ian Hutchinson, prompted by Garry McCracken, provided me a second opportunity to air the material as a graduate half-course given at MIT in 1995. In 1997 Peter Stott, acting on the suggestion of Garry again, asked me to turn the material into a book. Garry has been my mentor in tokamak edge physics since I spent a sabbatical year with him at Culham in 1980/81 and I owe him a great debt as a student, colleague and friend.

To the many friends and colleagues who read sections of the book and provided much valued suggestions, corrections, comments, and—in some cases—new results, my sincere thanks: Tine Baelmans, Jose Boedo, Alex Chankin, Jim Davis, Ralph Dux, David Elder, Michael Endler, Kevin Erents, Wojciech Fundamenski, Gerd Fussmann, Mattias Groth, Houyang Guo, Tony Haasz, Lorne Horton, Ian Hutchinson, Andre Kukushkin, Brian LaBombard, Hans Lingertat, Bruce Lipschultz, Steve Lisgo, Geoff Maddison, Guy Matthews, Garry McCracken, Spencer Pitcher, Gary Porter, Detlev Reiter, Karl-Ulrich Riemann, Tom Rognlien, Mike Schaffer, Peter Stott, Hugh Summers and George Vlases. I also must thank the many other colleagues I have had the privilege of working with in tokamak edge physics—and who will no doubt find much of their own work in this book—all, I hope, properly acknowledged!

To the graduate students at the University of Toronto Institute for Aerospace Studies who worked many of the problems in the book and provided valuable feedback, my thanks: Jasmine El-Khatib, Andrew Pavacic, Patrick Wright—and a special thanks to Peter Schwanke who co-authored the solutions section with me and who scoured the text for typos and worse.

My thanks to the artists in the JET Reprographics Department who produced most of the new figures in the book: Roger Bastow, John Machin and Stuart Morris. A blessing on the dedicated and tolerant typists who worked on the book at JET and the University: Karen Clifford, Win Dillon, Pam Peisley, Nicci Povey, Gail Woolnough—and also my wife Sharron.

Most of all I want to thank Sharron for her unfailing patience and support through the writing of this book—as throughout our 35 years of happy life together.

University of Toronto Institute for Aerospace Studies,
JET, Oxfordshire
and
General Atomics, San Diego
September 1999 Peter Stangeby

Preface

This book is based on a series of lectures 'Elements of edge physics' given at JET in 1993, MIT in 1995 and the University of Toronto in 1998. The lectures were intended as an introduction to the basic ideas about the boundary or scrape-off layer, SOL, of magnetic fusion devices—particularly of tokamaks—for people with a plasma physics education. Concepts about the SOL have largely been developed during the 1980s and 1990s and, as yet, little of this has found its way into plasma texts. The first part of this book was written with the intention of filling this gap.

The book is divided in to three parts. Part I attempts to retain the spirit of the original lecture series, namely that of a quick review of the central ideas about the SOL. This would be appropriate for an introductory course on the subject. Derivations are heuristic and physical intuition is emphasized. The reader should be able to cover this material reasonably quickly, with little need to pause for careful derivations or to consult related texts.

In part I, problems have been included to aid the student. The problems are of two types. The first type is embedded in the text and has the character of a worked example intended to illuminate the point being discussed. The reader is encouraged to include these problems when reading the text, even if deciding not to actually work through the maths. Additional problems appear at the end of each chapter. Solutions, or hints, are included at the end of the book.

Part II provides an introduction to methods of modelling the plasma edge region of magnetically confined plasmas. A number of sophisticated computer codes have been developed during the last two decades to model the edge plasma in all its 2D or 3D glory, including time dependence and employing all the numerical power of modern computational fluid dynamics, CFD, techniques. As in other fields, this effort has resulted in creating what now constitutes a third basic line of attack on our ignorance of the physical world—additional, that is, to the two traditional lines of experiment and theory. The shear complexity of *code modelling*, however, requires that its output be subject to efforts aimed at interpretation and understanding—just as experiments always have required. The need for simpler modelling has been enhanced rather than diminished by the advent of computer code modelling.

Part II of this book is aimed at simple approaches to modelling the plasma

edge—although the rudiments of 2D fluid code modelling are also touched on. Emphasis is therefore placed on 1D models of the edge, which often turn out to provide surprisingly close matches to the output of the sophisticated 2D computer code models. The modelling material of part II has been included for those envisaged readers who probably identify themselves as experimentalists, but with a penchant for interpreting their experimental results—as the best experimentalists always do. It is also for those who want to try to make sense of the output of their sophisticated code—i.e., to interpret code results—as the best code scientists always do. Even 1D modelling enterprises can reach the point that they require recourse to a computer—but simple numerical procedures such as Runge–Kutta quadrature are often adequate. Thus little maths need come between us and the physics in this type of modelling work.

Part III of the book is a collection of essays on currently active research topics in plasma edge physics. The selection of topics is inevitably arbitrary. The coverage is uneven. The topics tend to reflect the personal interests of the author. The sound of hobby-horses may be heard in the land. The material in Part III will undoubtedly date more quickly than that in parts I and II—and in the subsequent, numerous editions of the book, it is anticipated that some of this material may be revised, replaced or repudiated.

A distinction is made between the *plasma edge* and the scrape-off layer: the former includes the SOL, but also extends some distance inboard of the *last closed (magnetic) flux surface, LCFS*, or *separatrix*, into the *main* or *core* plasma. This region just inboard of the SOL is an important one in its own right and warrants separate treatment. Like the SOL, it is not a region of traditional magnetic confinement physics; atomic physics processes are also important. Effects such as the 'transport barrier', involved in H-mode confinement, are a feature of this region. This region is not the subject of this text. We take here the expression 'plasma boundary of a magnetic confinement device' to mean the *scrape-off layer*.

In the early decades of fusion energy research, the SOL was little considered, apparently in the hope that the edge would just sort itself out with little need for intervention or understanding. This hope was misplaced and by the 1980s it had been recognized that certain edge problems were sufficiently serious as to jeopardize the achievement of controlled fusion energy using magnetically confined plasmas. One of the most serious problems is that of high power handling or heat removal which results from the very small plasma-interaction areas characteristic of the SOL. Magnetic fields which are strong enough to provide adequate confinement of the main plasma are simply *too* effective for the SOL, where the characteristic cross-field scale length, i.e. the SOL width, ends up being only about 1 cm. The total exhaust power thus tends to be deposited on a total plasma-wetted area of solid surface of a few m^2 or less—an area far smaller than that which is in principle available, i.e. $\sim$1000 m^2, the internal wall area in a typical reactor design. It is turning out to be a challenge to keep the steady-state heat fluxes incident on the solid surfaces down to $\sim$5 MW m^{-2}, which is about the level briefly experienced by the nose cone of a space vehicle re-entering the

Earth's atmosphere.

In addition to this power-removal problem, impurities generated by plasma–surface interactions (PSI) have been the bane of fusion from the beginning and continue to be a serious problem. Their presence in the central fusion-producing plasma reduces power output by cooling the plasma radiatively and by diluting the hydrogenic fuel. The SOL is both the source and sink for most impurities and is the key to their control in magnetically confined devices. The one impurity that is produced in the core of fusion DT plasmas—helium—must be efficiently removed from the system to avoid poisoning the reaction. Helium removal is also largely a SOL issue.

In principle, all magnetically confined plasmas have scrape-off layers. While this text has been written in the context of tokamaks, much of the material applies directly to other magnetic configurations used in fusion or other applications.

The SOL is a very long and very thin plasma region aligned to the magnetic field $\boldsymbol{B}$. Not surprisingly, SOL modelling draws heavily on 1D, zero-$\boldsymbol{B}$ analysis. In most of the analysis in this book, in fact, $\boldsymbol{B}$ does not explicitly appear. Much of SOL analysis is thus applicable to non-magnetic plasmas, such as those used in plasma process applications, and students in such fields should also find material in this text helpful.

PART 1

AN INTRODUCTION TO THE SUBJECT OF THE PLASMA BOUNDARY

Introduction

Man-made plasmas almost always involve interaction with the solid state, for example, electrodes or the walls of a containing vessel. This *plasma–surface interaction*, PSI, often has profound effects on both the plasma and the solid.

Energetic plasma particles strike the solid surface, dislodging atoms from the lattice in a process called *sputtering*. In time, sputtering can result in substantial *erosion* of the surface. The sputtered atoms enter the plasma where they may be ionized by the impact of plasma electrons. Usually the intended plasma species—hydrogen isotopes in the case of fusion devices—is different from the solid species and sputtering thus results in plasma *contamination*.

Of yet greater importance, the basic properties of the plasma, such as its *density* and *temperature*, are often strongly dependent on the way solid and plasma interact. At the interface between the solid and the plasma, a thin net-charge layer called the *Debye sheath* develops spontaneously. The most important practical consequence of the formation of a sheath is that it mediates the flow of particles and energy out of the plasma to the solid surface. It therefore plays a central role in establishing the temperature, density and other properties of the plasma.

Simple electrical *gas discharges*—such as a fluorescent light—have solid electrodes at each end of a long cylindrical tube, whose wall completes the containment vessel. Air is removed from the vacuum-tight vessel using gas pumps. A gas, of the same species as is intended for the plasma, is then introduced to the vessel at a pressure which is simply related to the intended particle density [ions and electrons per m^3] of the plasma. Once the plasma is formed, the PSI occurring at the electrodes and walls largely controls the properties of the discharge [0.1]. If the discharge is placed inside a magnetic coil which produces a field $\boldsymbol{B}$ aligned with the tube axis, then the radial flow of charged particles to the tube walls can be greatly reduced [0.2] and thus also all aspects of the PSI occurring there. This is the principle of *magnetic confinement* of a plasma. Even for the strongest $\boldsymbol{B}$-fields the outflow of particles and energy can never, however, be reduced to zero and, inevitably, PSI is always involved. The PSI occurring at the end electrodes can be eliminated by bending the cylinder to make a closed, *toroidal* vessel. If a current is required along the toroidal axis, this can be induced by use of a transformer, with the toroidal plasma acting as a single-loop secondary and a coil, made e.g. of copper, acting as the primary. This is involved in such magnetic confinement

devices as *tokamaks* [0.3].

In principle, the $\boldsymbol{B}$-field could be so perfectly aligned as to be tangential at every point of the cylindrical or toroidal vessel wall. In that case, the plasma particles would reach the bounding sheath, and subsequently the vessel walls by purely *radial*, that is by *cross-field*, motion. In practice, such perfect alignment is not possible. Let us consider what happens when there is even a tiny misalignment. The plasma particles are not affected by the $\boldsymbol{B}$-field with regard to their motion along $\boldsymbol{B}$, and they move in this *parallel direction* with very high speeds, typically, of order random thermal speeds. The effect of a strong $\boldsymbol{B}$-field is to reduce the cross-field speed of the charged particles by many orders of magnitude relative to thermal speeds. Thus, if $\boldsymbol{B}$ is not aligned almost perfectly with the vessel walls, the charged particles will reach the sheath and wall by *parallel* motion rather than cross-field motion.

Therefore to understand the most basic aspects of the PSI occurring in a magnetically confined plasma requires analysis of one-dimensional, parallel-to-$\boldsymbol{B}$ motion of charged particles in a system bounded by sheaths at each end. *For this reason*, $\boldsymbol{B}$ *does not explicitly appear in the analysis*, since the magnetic field has no influence on parallel motion of charged particles. This is greatly simplifying. It also means that most of the analysis involved is applicable to non-magnetic plasmas.

Most of the analysis in this book is one dimensional and $\boldsymbol{B}$ *does not appear explicitly*.

In chapter 1, the basic features are presented of the simplest system—namely, the *isothermal* plasma, where temperature is constant along the 1D flow direction. Since the heat conductivity of plasma is usually very high, the isothermal assumption is often a good one.

In chapter 2, the basic properties of the sheath are covered. These give the relation between the plasma temperature and density, on the one hand, and the outflow rates of particles and energy to the sheath and solid surface, on the other.

Chapter 3 reviews the databases required for analysis of PSI. These include, for example, *sputtering yields*, Y, defined as the number of lattice atoms dislodged per impacting particle.

Chapter 4 returns to the simplest, isothermal case of chapter 1—termed the *simple SOL*—covering further aspects of it and also discussing the transition to *the complex SOL*. The region at the edge of a magnetically confined plasma where parallel transport to the surfaces occurs is called the *scrape-off layer*, SOL. The Complex SOL can have a number of important differences with the simple SOL, most importantly the existence of significant *parallel temperature gradients* along the length of the SOL.

Chapter 5 covers the most basic features of the complex SOL. Since this regime is most typically found for geometrical configurations involving *divertors*, this chapter is entitled 'The divertor SOL'. The simple SOL is most typically encountered for geometrical configurations involving *limiters*.

Chapter 6 deals with the production of impurities arising from PSI and the

resulting *transport* or motion of the impurity ions through the plasma.

Chapters 7 and 8 deal briefly with the implications for the boundary plasma of the important tokamak operational mode—the H-mode (high energy confinement)—and of plasma fluctuations, which are believed to be the cause of the otherwise unexplained (anomalous), rapid transport of particles and energy across $\boldsymbol{B}$.

These first eight chapters make up part I of the book constituting an 'Introduction to the subject of the plasma boundary'. Part II provides an introduction to edge modelling, with particular emphasis on 1D models. Part III primarily consists of a collection of essays on current research topics related to the edge.

References

[0.1] von Engel A 1965 *Ionized Gases* 2nd edn (Oxford: Oxford University Press)
[0.2] Franklin R N 1976 *Gas Discharges* (Oxford: Oxford University Press)
[0.3] Wesson J 1997 *Tokamaks* 2nd edn (Oxford: Oxford University Press)

Chapter 1

Simple Analytic Models of the Scrape-Off Layer

1.1 Solid Surfaces Are Sinks for Plasmas

The most basic cause of fluid flow is the presence of a fluid source and a fluid sink. Usually some effort and expense is involved in creating fluid sink action, for example, that achieved with mechanical pumping of gases and liquids. In the case of a plasma fluid, however, implementation of sink action could scarcely be simpler: the presence of a solid surface is sufficient. If charged particles happen to strike a solid surface they tend to stick to it long enough to recombine, figure 1.1.

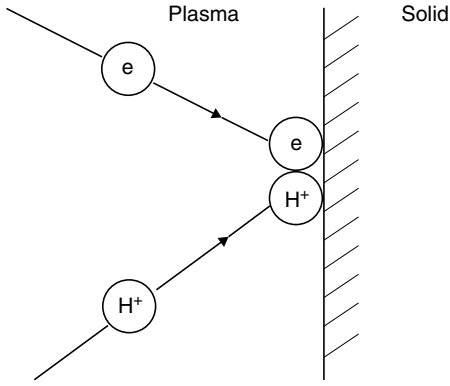

Figure 1.1. Charged particles tend to stick to solid surfaces, which therefore act as *plasma sinks*.

While ions do have a finite probability of back-scattering from a solid surface, section 3.1, they do so mainly as neutrals, picking up electrons from the surface. Electrons also stick to solid surfaces, section 3.2. Thus a solid surface

acts as an effective sink for *plasma*. It is not necessarily a *mass* sink, however, since the particles are subsequently released as *neutrals*.

For solid surfaces which are insulators or are electrically isolated, opposite charges build up on the surfaces exposed to a plasma, quickly leading to *surface recombination*. The resulting neutral atoms generally are not strongly bound to surfaces and are thermally re-emitted back into the plasma where they can be re-ionized, usually by electron impact. A steady-state condition can result, termed *re-cycling*, whereby plasma charged pairs are lost to the surface at the same rate as recombined neutrals re-enter the plasma, figure 1.2. While no external source of particles is then needed, an external source of energy to provide the ionization power is still required.

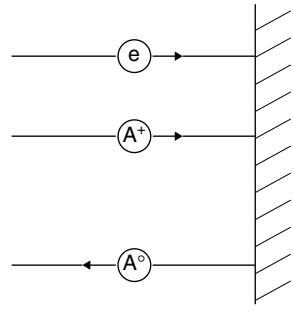

Figure 1.2. Charged particles adsorbed on solid surfaces recombine. The resulting neutral is weakly bound to the surface and desorbs back into the plasma. Thus *particle recycling* occurs and in steady state the plasma *refuels itself*.

The solid surface not only acts as a sink for the plasma, but it is intimately involved in the plasma source mechanism as well. The mean free path of the neutral for ionization may be large compared with the system size, in which case the ionization will occur more or less uniformly throughout the system. In other cases the ionization mean free path is short compared with system size and so the average location of re-ionization—i.e. the plasma source—and the plasma sink can be quite close to each other. In that case, the rest of the available volume then 'back-fills' e.g. by diffusion—much as heat fills a room where a heat source, such as radiator, is usually placed close to a principal heat sink, such as a window.

A solid surface exposed to a plasma initially also acts as a pump in a mass sense, since all but the promptly back-scattered particles are initially retained in or on the solid, section 3.4. Such retention saturates at some level and thereafter a steady-state situation results with the plasma '*refuelling itself*'. At that point any external source of fuelling, such as a gas injection, can be turned off and the plasma density will remain constant, provided no active pumping (cryopumping, etc) is used.

It is evident that the behaviour and properties of a plasma can be dominated by the contact it has with solid surfaces. Given the enormous differences in the

properties of the first (solid) and fourth (plasma) states of matter, this is scarcely surprising. The powerful sink action resulting from plasma–solid contact is the controlling feature of tokamak edge plasma behaviour.

1.2 The Tokamak: An Example of a Low Pressure Gas Discharge Tube

Fluorescent lights and neon signs are familiar examples of low pressure gas discharge tubes. Neutrals are ionized by electron impact more or less uniformly throughout the cylindrical volume. The resulting electron-ion pairs 'fall' radially to the walls, figure 1.3(a), and adhere to the surface until they recombine to form neutrals. Sooner or later the neutrals are released back into the plasma where they are re-ionized. Thus steady-state recycling is established and a constant plasma density results with particles neither being added to nor removed from the system. Power must be provided continuously—via a longitudinal electric field which

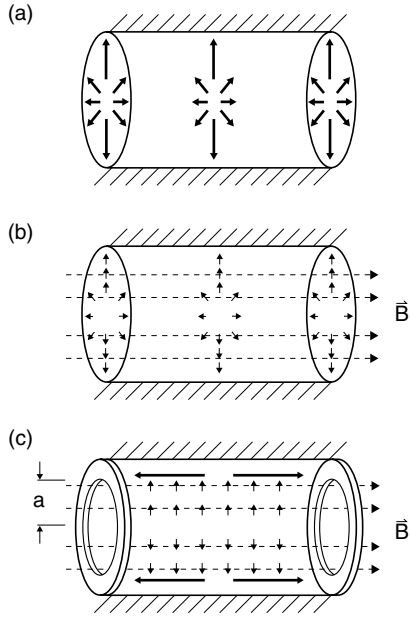

Figure 1.3. Cylindrical gas discharge tubes. (a) Simple cylinder. No magnetic field. Plasma moves radially and rapidly to the cylinder walls. (b) Simple cylinder. With axial magnetic field added. Plasma moves radially but slowly to the cylinder walls. (c) Cylinder with two washer-limiters (poloidal ring limiters) inserted. With magnetic field. Plasma moves radially and slowly out to radius a, followed by rapid motion parallel to $\boldsymbol{B}$ to the sides of the washer-limiters. Plasma does not reach the cylinder walls.

causes ohmic heating of the electrons—in order to provide for the steady loss of power to excitation and ionization of atoms and molecules, etc. Most of the power invested in ionization, excitation, dissociation and elastic collisions ends up as wall heating. A fraction of the input power ends up in photon energy from these light sources—which actually shed more heat than light.

Consider the addition of a longitudinal, i.e. axial, magnetic field, figure 1.3(b). This retards the rate at which electron–ion pairs 'fall' to the walls [1.1]. For a given axial value of plasma density, the loss rate—thus also the recycling rate in steady state—is reduced as the magnitude of $\boldsymbol{B}$ is increased, i.e. the plasma becomes *magnetically confined*. In the simplest geometry of a cylinder without wall protrusions, the net motion of the electron–ion flow, i.e. the *plasma* flow, is purely radial to the walls. An *electrostatic sheath*, the *Debye sheath*, arises just in front of the walls, figure 1.4(a). The sheath is a thin region of net positive space charge. The walls have net negative surface charge.

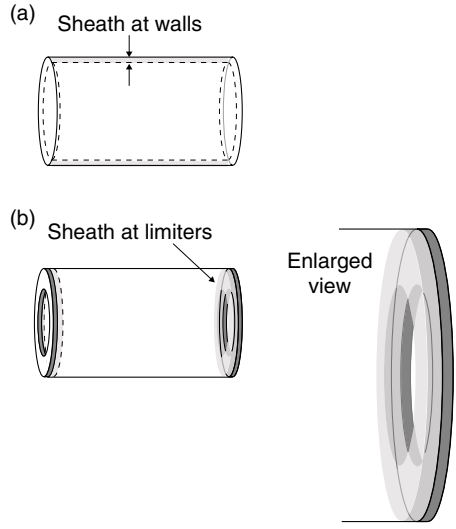

Figure 1.4. Electrostatic sheaths develop in front of the plasma-wetted surfaces: (a) at the walls for the simple cylinder, (b) at the sides of the washer-limiters.

Throughout most of the volume a quasineutral *plasma* resides with electron and ion densities being almost exactly equal to each other at each location. The sheath governs the relation between, on the one hand, the plasma density and temperature, and on the other hand, the fluxes of particles, momentum and energy flowing from the plasma to the walls.

A tokamak is a low pressure gas discharge tube bent into a closed circular shape and with the ohmic current usually induced by transformer action. Often there are protrusions at the walls called *limiters*. Consider a cylindrical tube with

two circular washers (limiters) inserted at two locations along the cylinder length, figure 1.3(c). The outer radius of each washer is equal to the radius of the cylinder; the inner radius a is specifiable.

Charged particles *diffuse* very slowly across magnetic fields, compared with their unrestricted motion along $\boldsymbol{B}$, which tends to be at velocities of order of the sound speed due to the strong sink action. Consider a charged particle originating on axis and diffusing slowly out toward the wall. At the same time it is moving randomly along $\boldsymbol{B}$ at high speeds due to its thermal energy. For an infinitely long cylinder (or for one closed into a torus), this parallel-to-$\boldsymbol{B}$ motion is of no consequence for the fate of this particle—not, that is, until the particle has diffused across radius a. Then this motion will cause its rapid removal from the plasma, by carrying the particle quickly to the sides of the washer-limiter. Thus, in this geometry the loss of particles to the surface sinks involves first a net *radial* motion across the radius of the tube, followed by a *parallel-to-*$\boldsymbol{B}$ motion near the 'edge' of the plasma at radius a. In this geometry the sheath forms on the *sides* of the washer-limiter rather than at the wall, figure 1.4(b). Indeed the plasma no longer extends all the way out to the walls; the loss of particles to the sides of the washer-limiters is so fast that the particles only have time to diffuse a short distance beyond a. The inner radius of the washer, a, thus tends to *limit* the radius of the plasma column to being not much greater than a. Hence the name 'limiter'. The thin, annular plasma region outboard of radius a is called the 'scrape-off layer', SOL.

The wall is thus protected by the limiters from contact with the plasma. One price paid is that the *plasma–surface interaction* is now concentrated on thin *plasma-wetted* areas on each limiter, tending to cause localized over-heating and other problems.

The first and fourth state of matter do not co-exist easily. Plasma erodes solids and the eroded material enters the plasma, degrading its desired properties. Much of the challenge for magnetic confinement fusion is to find a solution that will allow these two mutually irritating states of matter to cohabit a small space. The situation would not be so bad if the area of interaction could be made large, thus diminishing the local intensity of interaction. As we will see, however, a magnetic confinement arrangement that is effective enough to contain the main, fusion producing plasma is *too good* for the SOL, resulting in quite small plasma-wetted areas, and very intense plasma–solid interactions.

It is often the case that systems are strongly influenced—or even controlled—by their boundary conditions. In the early days of magnetic fusion research it was hoped, however, that the edge region 'would take care of itself'. The edge region was not of primary interest to the main thrust of the fusion enterprise, which focuses on the hot central core region where the fusion reaction can occur. It became clear fairly early in fusion research that the edge region was not in fact going to 'take care of itself', but was going to require significant attention. The power balance in early magnetic devices tended to be dominated by radiation from impurities in the plasma which had originated from

the plasma–surface interactions at the edge. The radiative cooling was so strong that core temperatures fell far below that needed to achieve fusion.

It would have been surprising, of course, if magnetic confinement fusion had managed to easily escape serious edge problems. Upon first hearing about the idea of a miniature star in a solid container, the response of most laymen is that this must be impossible due to strong interactions between the radically different states of matter involved. It turns out, unfortunately, that the layman is almost right. Despite great strides, the problems arising from plasma–surface interactions continue to threaten the achievement of a viable fusion reactor based on magnetic confinement. Plasma contamination levels, although much reduced from early days, are still unacceptable. The erosion rates of the solid edge structures are too high for practical reactor designs where the replacement of internal components cannot be frequent.

To make progress, better understanding of the plasma boundary region is necessary. Our understanding is weak and we have many questions. What controls the width of the SOL? How can it be manipulated? How can some of the power reaching the SOL be dispersed before reaching the small, plasma-wetted, solid surfaces? Can the impurity radiation itself be exploited to achieve this, or will that cause such contamination of the core plasma that the fusion reaction will stop there? Can the spatial distribution of the naturally produced impurities be manipulated so that they do more good than harm? Are there benefits to be had from injecting non-intrinsic impurities? What is the connection between the plasma properties of the SOL—its density and temperature—and the fluxes of particles and power to the solid surfaces? How does the plasma move along the SOL to the surface? (It turns out, upon closer inspection, that the simple picture above of free thermal motion along $\boldsymbol{B}$ is inadequate.) What can be achieved by manipulating the geometry of the edge, or by changing the magnetic fields at the edge, or by changing the arrangements of the solid structures? Can the *internal* structures of the SOL be manipulated to advantage? For example, can temperature variations be induced to occur along the length of the SOL, so that at the 'target' (solid) end the temperature is low, while at the 'upstream' end, where most of the coupling to the main plasma occurs, it is hot? Can the SOL plasma be 'intercepted' or 'obstructed' before it reaches the solid surface, perhaps by e–i recombination in the plasma itself, i.e., *volume recombination*, perhaps by frictional slowing of the plasma outflow by neutral gas, i.e. by 'clogging the drain'? Helium produced in the core by DT fusion reactions is an unavoidable impurity; it must be removed at the edge so that it does not poison the fusion reaction; can the edge plasma and solid structures be manipulated and configured to achieve adequate pumping of the helium, using practically achievable pumping arrangements? Solid material eroded into the plasma eventually re-deposits on other edge surfaces; virtually none of the material is actually removed through the vacuum pumps. Will the re-deposited solid surfaces give acceptable performance of the fusion device? Will the tritium become trapped in such re-deposited material (*co-deposited*), resulting in unacceptable radioactive inventories in a reactor?

This list of questions is long but by no means complete.

In order to address these and other questions which will critically affect the demonstration of the scientific, engineering and environmental feasibility of magnetic fusion power, we will need to better understand the plasma boundary. This book addresses these questions and attempts to improve our understanding of the behaviour of the plasma edge.

1.3 Tokamak Magnetic Fields

There are two principal components of a tokamak magnetic field, figure 1.5, the toroidal magnetic field B_ϕ created by external magnetic coils and the poloidal, or self-, magnetic field B_θ created by the toroidal plasma curent I_p induced e.g. by an external transformer.

The resulting $\boldsymbol{B}_{\text{total}}$ is helical, with each magnetic field line lying on one of a nested set of toroidal *flux surfaces*, figure 1.6 [1.2]. Figure 1.7 shows a poloidal cross-section of a tokamak, displaying the characteristic magnetic contours which result from taking a poloidal plane slice through the nested toroidal surfaces.

Magnetic field lines which lie on flux surfaces that never make contact with

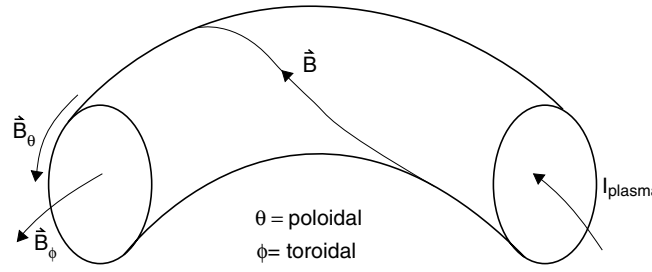

Figure 1.5. The toroidal direction ϕ is the long way round, the poloidal θ the short way. The two principal magnetic fields of a tokamak are $\boldsymbol{B}_\phi$ due to external coils and $\boldsymbol{B}_\theta$ due to the plasma curent I_{plasma} in the ϕ direction. For a tokamak $|B_\phi| \gg |B_\theta|$. Thus $\boldsymbol{B}_{\text{total}} = \boldsymbol{B}_\phi + \boldsymbol{B}_\theta$ is helical and with a shallow pitch angle.

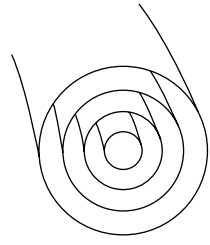

Figure 1.6. Magnetic flux surfaces forming a set of nested toroids.

a solid surface are termed *closed*, while those which pass through a solid surface are termed *open*. A key role is played by the *last closed (magnetic) flux surface*, figure 1.7, LCFS. The LCFS is the last flux surface, going outwards from the *main plasma*, that does not touch a solid surface. Surfaces radially further in are all *closed* while those further out are all *open*.

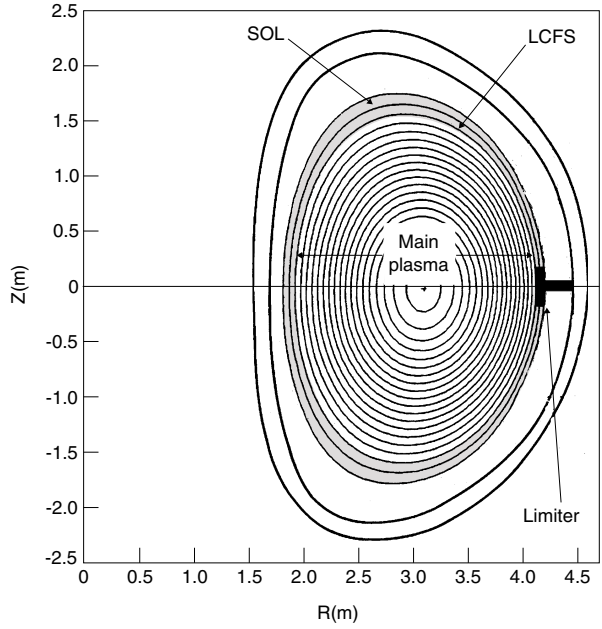

Figure 1.7. For the limiter configuration, the *last closed magnetic flux surface*, LCFS, is defined by the leading edge of the limiter. A JET-size plasma is shown.

Because of the helical pitch of $\boldsymbol{B}_{\text{total}}$, a field line which breaks the poloidal plane at one poloidal location will, on the next toroidal pass around the torus, usually cut that plane at a different poloidal location, figure 1.8.

Although they remain on a given magnetic flux surface, most magnetic field lines never close on themselves, thus eventually mapping out the entire flux surface. A resonance exists if the *safety factor* [1.3]:

$$\boxed{q \approx \frac{r B_\phi}{R B_\theta}} \tag{1.1}$$

takes on rational values for a particular flux surface. Equation (1.1) is the approximation for a large *aspect ratio*, circular cross-section tokamak. Aspect ratio $= R/a$ where R is the major radius of the torus and a is the minor radius of the (circular) LCFS. r is the minor radius of any particular (circular) flux surface. For example, if $q = 4$ for a particular flux surface, then a field line lying on

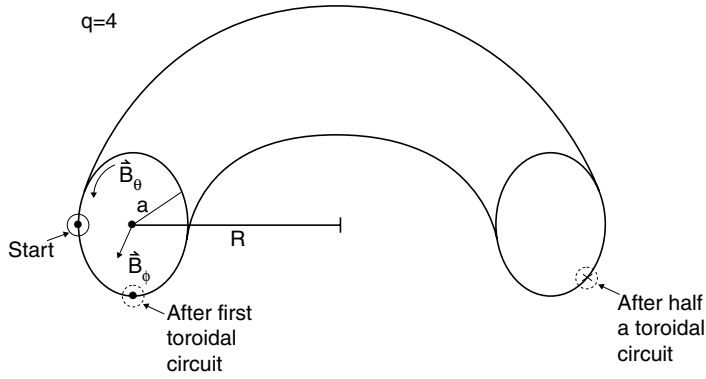

Figure 1.8. The safety factor q, when an integer, is the number of *toroidal* transits required for $\boldsymbol{B}_{\text{total}}$ to make one *poloidal* transit. The example shown is for $q = 4$.

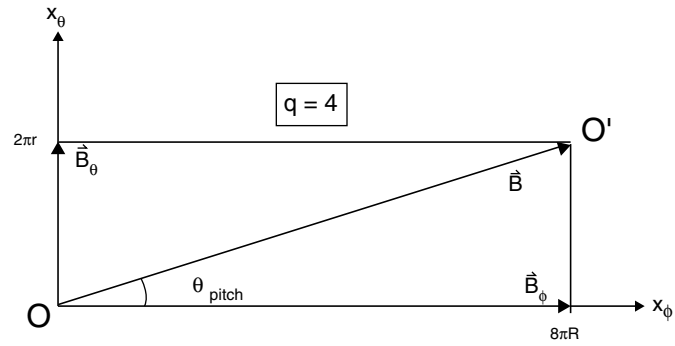

Figure 1.9. A single toroidal flux surface has been cut and flattened. The specific example of $q = 4$ is illustrated, showing that four toroidal transits are required for one poloidal transit.

that surface makes exactly four large (toroidal) transits to complete one short (poloidal) transit, closing exactly on itself. Figure 1.9 shows a $q = 4$ magnetic flux surface which has been cut, opened up and flattened to make a rectangle.

O and O′ represent the same location. Since one has from Ampère's law, approximately:

$$\boxed{B_\theta(a) \approx \frac{\mu_0 I_p}{2\pi a}} \tag{1.2}$$

then q is large for small plasma current and/or large external magnetic field, B_ϕ. One also has the local pitch angle of $\boldsymbol{B}_{\text{total}}$:

$$\boxed{\theta_{\text{pitch}} \approx B_\theta / B_\phi \approx B_\theta / B} \tag{1.3}$$

typically $\theta_{\text{pitch}} \approx 0.1$ since the tokamak magnetic field is primarily toroidal.

In the *main* or *confined plasma*, i.e. inside the LCFS, the principal significance of the safety factor q is that the plasma is magnetohydrodynamically unstable if $q \leq 2$ at the edge (the LCFS) [1.4], and so such operating conditions are usually avoided. In the region outside the LCFS, the role of q is primarily geometrical, as will be shown. It is this necessary avoidance of small values of q at the edge that results in small pitch angles of $\boldsymbol{B}_{\text{total}}$.

1.4 The Scrape-Off Layer, SOL

As noted, the region radially outboard of the LCFS is called the *scrape-off layer*, SOL. Cross-field velocities are of order:

$$v_\perp \simeq D_\perp/\ell_\perp \tag{1.4}$$

where $D_\perp$ is the cross-field diffusion coefficient [$\text{m}^2\ \text{s}^{-1}$] and $\ell_\perp$[m] is the characteristic radial scale length of density. (Fick's law of diffusive motion: $\Gamma = -D\,\text{d}n/\text{d}x$ where Γ is the particle flux density [particles $\text{m}^{-2}\ \text{s}^{-1}$], D is the particle diffusion coefficient and $\text{d}n/\text{d}x \approx n/\ell_\perp$, and with Γ related to an effective cross-field velocity, $v_\perp$, $\Gamma \equiv nv_\perp$, one obtains equation (1.4).) To date, attempts to calculate $D_\perp$ from first principles have been of limited success [1.5]. $D_\perp$ is generally anomalous compared with classical rates and is obtained from experiment; see section 4.3. Values of order 1 $\text{m}^2\ \text{s}^{-1}$ are found empirically [1.5]. The radial density length may be as large as the minor radius, a, which would be the case if the neutrals were all ionized at the very centre, e.g. for deep injection of fuel pellets. More typically $\ell_\perp$ is of the order of the ionization mean free path, mfp, of the recycling neutrals at the edge, $\lambda_{iz}^{\text{neutral}}$. Thus $v_\perp$ may be as slow as $\approx 1\ \text{m}\ \text{s}^{-1}$, while $v_\parallel \approx$ plasma sound speed, c_s, which is typically many orders of magnitude larger. c_s is calculated in section 2.4 to be:

$$\begin{aligned} c_s^2 &= k(T_e + T_i)/(m_e + m_i) \\ \boxed{c_s &\approx [k(T_e + T_i)/m_i]^{1/2}.} \end{aligned} \tag{1.5}$$

For example: for $T_e = T_i = 25$ eV, and D^+ ions, $c_s \approx 5 \times 10^4\ \text{m}\ \text{s}^{-1}$.

It is this enormous difference between $v_\parallel$ and $v_\perp$ that makes the SOL so thin relative to its length.

A great variety of geometries are possible for the solid surfaces which cause the sink actions. They are generally considered to fall into one of the two categories: (a) limiters, (b) divertors.

1.4.1 Limiter SOLs

Conceptually the simplest limiter sink action is achieved by inserting an annulus of solid material—a washer—with inner circular radius a—called a *poloidal limiter*—at one or more toroidal locations, figure 1.10. The magnetic flux surfaces

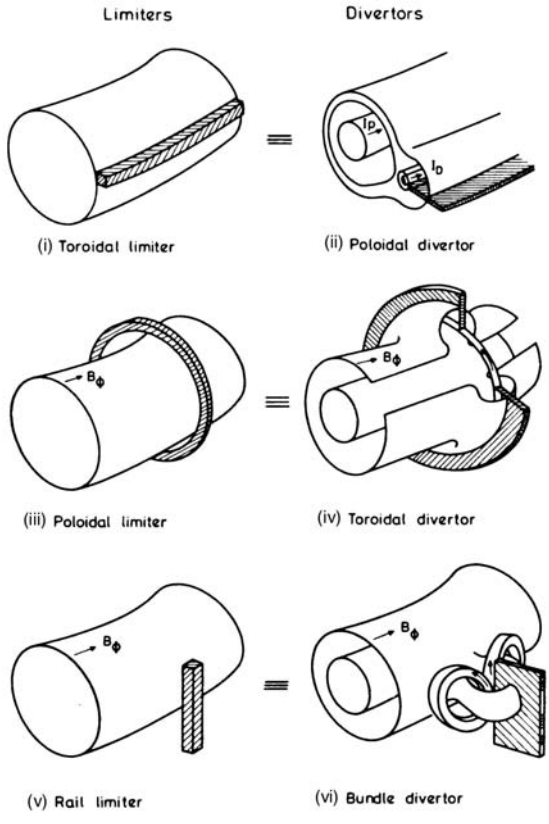

Figure 1.10. Various limiter and divertor configurations [1.37]:

(i) The *toroidal limiter* consists of a toroidally symmetric, protruding structure attached to the wall, mounted at the outside of the vessel, as shown here, or at the bottom, etc.
(ii) The *poloidal divertor* involves a diversion of the poloidal magnetic field near the edge, making for a toroidally symmetric configuration, analogous to the *toroidal limiter.*
(iii) The *poloidal ring limiter*, in the simplest case, is a circular annular plate of inner radius $r = a_{\text{plasma}}$, outer radius $r = a_{\text{wall}}$.
(iv) The *toroidal divertor* involves a diversion of the toroidal magnetic field near the edge, making for a configuration analogous to that of the *poloidal ring limiter*.
(v) The *rail* or *probe limiter* involves insertion of a solid object into the plasma at a specific toroidal and poloidal location.
(vi) The *bundle divertor* involves a non-symmetric diversion of some portion of the toroidal field near the edge, creating a configuration analogous to that of a *rail* or *probe limiter*.

are assumed to be perfectly circular here. The typical parallel-to-$\boldsymbol{B}$ distance that a particle has to travel in the SOL before striking a limiter is

$$L \approx \frac{\pi R}{n} \tag{1.6}$$

where n is the number of poloidal limiters (we have implicitly assumed here a small pitch angle, i.e. a not very small q). L is called the *connection length*, and the distance along $\boldsymbol{B}$ in the SOL between two points of contact with the solid surface is $2L$ [1.6, 1.7]

A *toroidal limiter* can consist simply of a (toroidal) circular rail, projecting inward from, say, the wall at the midplane, figure 1.10. This configuration involves longer L due to the small pitch angle of $\boldsymbol{B}$:

$$\boxed{L \approx \pi R q.} \tag{1.7}$$

Values of L of 100 m or more can result for large tokamaks such as JET. However, due to the very large ratio $v_{\parallel}/v_{\perp}$, the SOL radial width is still only of order 1 cm.

These first two limiter examples involved either toroidal or poloidal symmetry. Limiter sink action can also be achieved by inserting *any* shape of object into the plasma: since almost none of the field lines close on themselves, but eventually map out the entire flux surface they lie on, then most field lines which lie on flux surfaces outside the LCFS will eventually strike the inserted limiter. Cross-field diffusion within poloidal flux surfaces also helps ensure that all points in a SOL are *actually* in contact with a solid surface, i.e. effectively there are no infinite L values in the SOL. A limiter which is small in poloidal and toroidal extent will have a particularly large L.

An important variant of the toroidal limiter is the *wall-limiter* where the plasma simply contacts, say, the inner wall near the midplane. Typically the wall would be fully covered by protective tiles. Wall-limiters enjoy the advantage of particularly large *plasma-wetted areas*, and thus lower power loadings, W m^{-2}, see section 5.6.

1.4.2 Divertor SOLs

For limiter tokamaks the poloidal magnetic field is largely created by I_p and is approximately circular. A *poloidal divertor* configuration can be produced using an external conductor carrying a current I_D in the same direction as I_p, figures 1.10 and 1.11.

In the poloidal plane, the magnetic field lines make a figure-of-eight shape, figure 1.11(b). At some point between the two current centres a null in the poloidal field, and thus a magnetic *X-point*, exists. The magnetic flux surface passing through the X-point is called the magnetic *separatrix*. The flux surfaces inside the separatrix, surrounding the I_p channel, contain the *main* or *confined plasma* within closed flux surfaces. A sink action is achieved simply by introducing a solid plane which cuts through the flux surfaces surrounding the I_D channel, figure 1.11(a): any plasma particles which diffuse across the separatrix of the confined plasma find themselves on open flux surfaces which connect directly to the solid surface, which are called the *divertor targets*, and the particles move rapidly to the target-sinks before diffusing very far cross-field. The separatrix

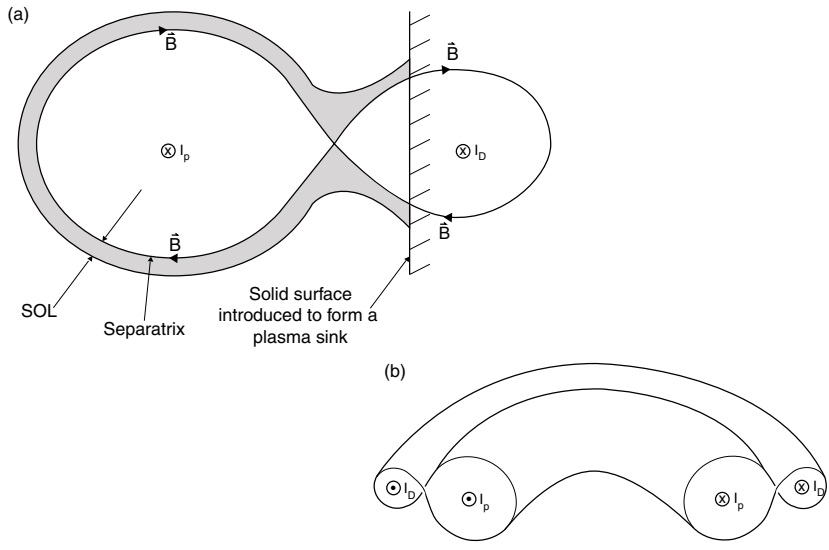

Figure 1.11. The poloidal field $\boldsymbol{B}_\theta^{\text{plasma}}$ created by I_{plasma} is *diverted* by the $\boldsymbol{B}_\theta^{\text{coil}}$ created by a *divertor coil* current I_D, parallel to I_{plasma}, which is carried by a coil internal or external to the vacuum vessel.

is the LCFS. A thin SOL results, just as for the limiter geometry. If the targets are located not too far from the X-point (the case of short 'divertor legs'), then the length of the average SOL field line is approximately the same as for the toroidal limiter geometry, with $L \approx \pi Rq$. There is an important reason to keep the divertor legs short: the entire configuration shown in figure 1.11 lies inside the toroidal field coils; magnetic volume is expensive to produce and only the confined region is hot enough to produce fusion power.

The length of a field line on the separatrix is, in principle, infinite, due to the poloidal field null at the X-point. There is, however, strong *magnetic shear* just near the separatrix with the local values of L varying rapidly with radius. Inevitable field errors effectively prevent infinite L. Further, cross-field transport has the effect of 'shorting' any extremely long field lines by transport on to immediately adjacent, shorter field lines. Typically L is quoted for the magnetic flux surface lying slightly outside the separatrix.

Figure 1.12 shows a close-up of a divertor region, located at the bottom of the vessel. The region below the X-point and inside the separatrix is called the *private plasma*. It contains a thin layer of plasma lying along the two separatrix arms, terminating at the targets. The private plasma is sustained by the transport of plasma particles and power from the main SOL, across the private plasma separatrix.

While the divertor configuration is less efficient in the use of magnetic vol-

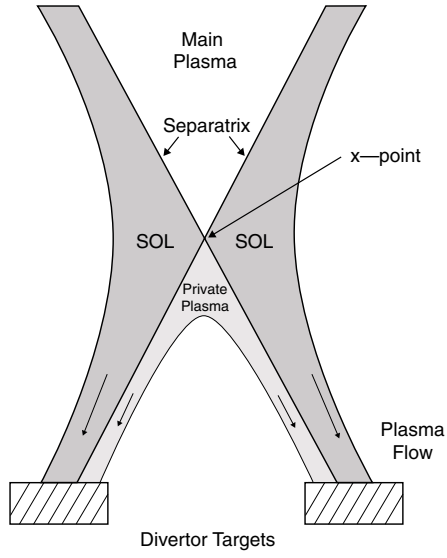

Figure 1.12. The SOL surrounds the main plasma above the X-point and extends to the target. The private plasma receives particles and energy from the SOL by cross-field transport.

ume than the limiter one, there are off-setting advantages. The most important one is the opportunity to move the solid surfaces where the intense plasma surface interactions occur—the divertor targets—away from the confined plasma. Further comparisons of the two configurations are discussed in section 5.1.

The divertor geometry shown in figures 1.11 and 1.12 is termed 'poloidal', because it is the poloidal magnetic field which has been diverted by I_D—it is however *toroidally symmetric*—a sometimes confusing fact. Other magnetic divertor configurations can also be produced [1.8], figure 1.10. The limiter shown in figure 1.10 is termed 'poloidal' because it is poloidally symmetric. The 'toroidal' limiter is termed similarly. The presence of the divertor targets is also seen to *limit* the radial extent of the SOL in the same way as limiters do.

1.5 Characteristic SOL Time

The most used configurations are the poloidal divertor and the toroidal limiter since both can provide (relatively) large *plasma-wetted areas*, the area of solid surface in contact with significant plasma fluxes, section 5.6. For both, one has $L \approx \pi Rq$. Plasma particles which move freely along $\boldsymbol{B}$ in the SOL have velocities of the order of the plasma sound speed, c_s, and so characteristic particle

dwell times in the SOL are

$$\boxed{\tau_{\text{sol}} \simeq L/c_s.} \tag{1.8}$$

Typical edge temperatures are 1–100 eV, section 4.5, thus $c_s \approx 10^4$–10^5 m s^{-1}. For a JET-sized tokamak $R \approx 3$ m; for $q = 4$, then $L \approx 40$ m, resulting in $\tau_{\text{sol}} \approx$ 1 ms. Thus, characteristic SOL dwell times are seen to be very short compared with energy confinement times of the main plasma which, for JET, are of the order of 1 s, section 4.5. This time is also very short compared with the average dwell-time of an ion originating at the centre of the main plasma, i.e. $\sim a^2/D_\perp \sim 1$ s for a JET-size plasma. $\tau_{\text{centre}} \approx a/v_\perp$ with $v_\perp \approx D_\perp/a \therefore \tau_{\text{centre}} \approx a^2/D_\perp$.

1.6 The 1D Fluid Approximation for the SOL Plasma

In analysing plasma behaviour in the SOL, the most common assumption is that the effects of toroidal magnetic curvature can be ignored, except in calculating L. Thus *neo-classical effects* which arise from 'toroidicity' i.e. the non-zero value of a/R [1.9], are ignored in the simplest analysis. In effect, the SOL is 'straightened out', figure 1.13, [1.6, 1.7], and then analysed either two dimensionally or one dimensionally.

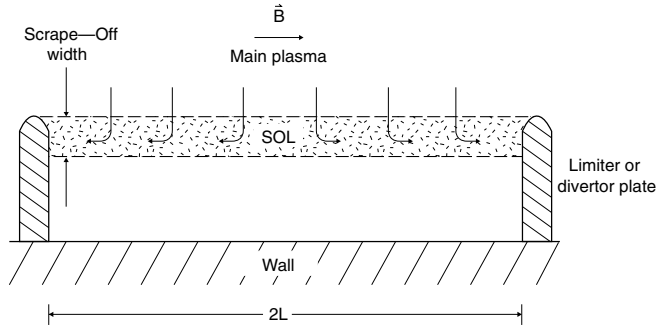

Figure 1.13. The SOL has been straightened out. Energy and particles flow from the main plasma into the SOL by slow cross-field transport, followed by rapid transport parallel to $\boldsymbol{B}$ along the SOL to the targets.

The justification for neglecting neo-classical effects such as banana orbits [1.10] in the SOL is the high level of collisionality that characterizes cold plasmas. The self-collisional mfps are approximately [1.11]:

$$\boxed{\lambda_{ee} \approx \lambda_{ii} \approx \frac{10^{16} T^2}{n_e}} \tag{1.9}$$

λ [m], T [eV] and n_e [m^{-3}] is the number of electrons m^{-3}. In table 1.1 two examples are given comparing λ and L values for a large (JET) and small (Alcator CMOD) tokamak. When $\lambda < L$, the SOL is said to be collisional.

Table 1.1. Representative SOL conditions.

	JET	CMOD
T_e [eV]	50	10
n_e [m^{-3}]	10^{19}	10^{20}
L [m]	40	8
ν_e^*	25	1000
$\lambda_{ee}, \lambda_{ii}$ [m]	2.5	0.01
$\tau_{SOL} = L/c_s$ [ms]	0.6	0.3

ν_e^* [1.31] is the ratio of the electron collision frequency to the electron bounce frequency. The bounce frequency is that at which electrons trapped on banana orbits [1.31] oscillate back and forth between the turning points. When $\nu_e^* \gg 1$ collisionality is too strong to permit the electrons to behave in this 'neo-classical' way.

The degree of collisionality is important for deciding a very basic question: whether a *fluid* analysis of the plasma behaviour is adequate, or a full *kinetic* analysis is required. In kinetic analysis the complete *velocity distribution* of the plasma particles is calculated at every point in space (and time). In fluid analysis one settles for just calculating the *average* quantities at each point in space (and time), e.g. the average (thus 'fluid') velocity. Obviously kinetic analysis is much harder to carry out than fluid analysis, and we want to know when the latter is likely to be good enough. It turns out, section 9.12, that the fluid approximation, as it is called, is likely to be good enough when collisionality is strong. Although, as shown in table 1.1, the SOL may be collisional, the situation can often be marginal. Thus the neglect of neo-classical and also so-called *kinetic effects* [1.12] needs to be re-visited, chapter 26. Nevertheless, the *fluid modelling assumption* is the most common one in SOL analysis. It is known from the analysis of very simple cases—where it is possible to obtain complete *kinetic* solutions and the *complete velocity distributions* are computed—that the results for most quantities of practical interest are not significantly different from those given by simpler *fluid* solutions, chapter 10. Thus, the fluid approximation and the effective 'straightening out' of the SOL in modelling, figure 1.13, appears to be a reasonable first approximation.

For 2D SOL analysis, toroidal symmetry is assumed. The two spatial directions are either (a) radially cross-field and along $\boldsymbol{B}$ or (b) radial and the poloidal projection of the motion along $\boldsymbol{B}$, see figures 1.13, 1.14. The second approach enjoys the advantage that results can be conveniently displayed as poloidal plane plots. Due to the assumed toroidal symmetry, cross-field motion within the poloidal flux surface is ignored, at the first level of analysis. Since the cross-field transport mechanisms are imperfectly understood, in 2D modelling the transport coefficients, such as the cross-field diffusion coefficient, $D_\perp$, are treated as being *anomalous* and are taken from experiment, whenever possible. The parallel (or poloidal-projection) transport is assumed to be classical, i.e.,

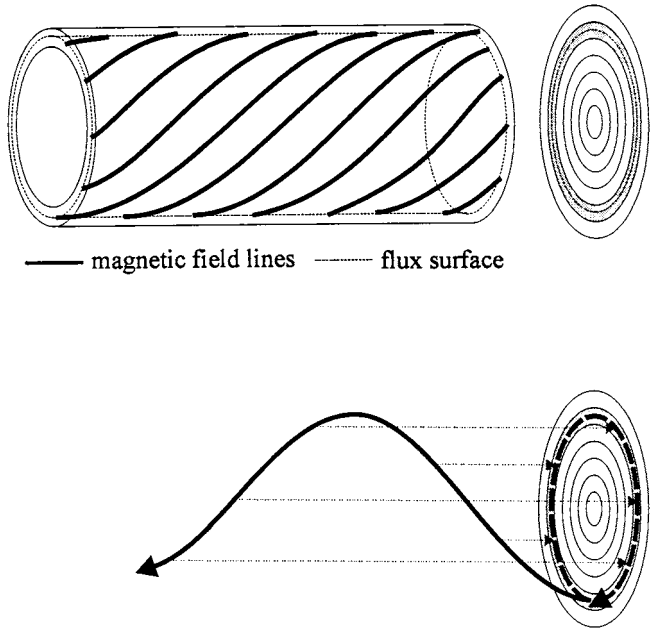

Figure 1.14. The path of a magnetic field line projected onto a poloidal plane. Distances along the field line $s_{\|}$ have corresponding value in the poloidal plane, s_{θ}. Analysis of the plasma behaviour can then be calculated in terms of $s_{\|}$ or s_{θ}.

as if there were no magnetic field. It is usually not possible to carry out any significant 2D modelling analytically and 2D fluid modelling of the SOL now uses sophisticated computer codes [1.13].

It can be difficult to gain insight into SOL behaviour from 2D code modelling, and so the incentive is strong to extract as much as possible from 1D analytic modelling. Such 1D analysis is the principal focus in this book. The cross-field transport of particles and energy are treated as *sources* of particles and energy in the 1D analysis along the field $\boldsymbol{B}$.

1.7 The Simple SOL and Ionization in the Main Plasma

As discussed in section 1.1, hydrogenic neutrals formed by recombination on solid surfaces enter the plasma and are re-ionized in the *fuel recycle process*. Once all solid surfaces are saturated, the plasma density in both the SOL and *main plasma* (the confined plasma on the closed flux surfaces inside the separatrix or LCFS) remains constant, with no new fuelling required unless active pumping is employed. In the simplest situation the neutrals have a sufficiently long ionization mfp that they pass through the SOL and are ionized inside the main plasma. This

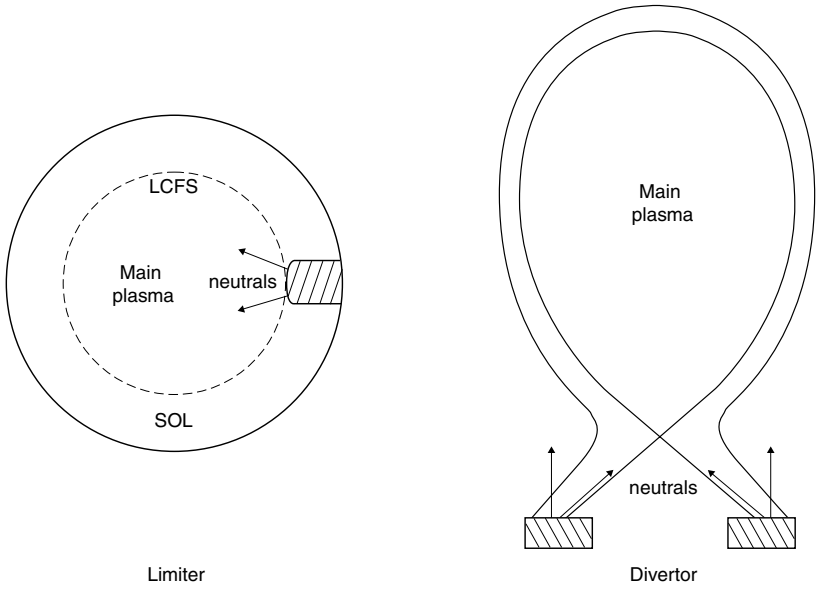

Figure 1.15. Neutral hydrogen recycling from a limiter tends to be ionized inside the LCFS, while hydrogen recycling from divertor targets tends to be ionized in the SOL and private plasma.

has a better chance of happening in limiter configurations—where the recycling surface, the limiter, is in intimate contact with the main plasma—than for divertors where the targets may be remote, see figure 1.15. Ionization in the main plasma results in rapid dispersal of the resulting ions along field lines, so that by the time the ions diffuse across the LCFS into the SOL, all details of the actual 2D spatial distribution of the source have been obliterated, and as far as the SOL is concerned it experiences a source of particles which is distributed more or less uniformly along L. Due to this simplification, such *deep* or *main plasma* ionization of the hydrogenic particles is taken to be an important part of the definition of the *simple SOL* [1.6, 1.7]; [see section 1.8 and chapter 4].

This regime then yields a particularly simple estimate for the SOL radial width λ_{SOL}: the plasma particles diffuse cross-field beyond the LCFS a characteristic diffusion distance of about

$$\lambda_{\mathrm{SOL}} \simeq (D_\perp \tau_{\mathrm{SOL}})^{1/2}$$

$$\boxed{\lambda_{\mathrm{SOL}} = (D_\perp L/c_s)^{1/2}} \tag{1.10}$$

before being removed ($\lambda_{\mathrm{SOL}} \approx v_\perp \tau_{\mathrm{SOL}} \approx (D_\perp/\lambda_{\mathrm{SOL}})\tau_{\mathrm{SOL}}$, thus giving equation (1.10)). For a typical SOL: $D_\perp = 1\ \mathrm{m^2\ s^{-1}}$, $L = 50$ m, $T_{\mathrm{SOL}} = 25$ eV, $c_s = 5\times10^4\ \mathrm{m\ s^{-1}}$, thus $\lambda_{\mathrm{SOL}} \approx$ few cm. One notes how very short a distance this

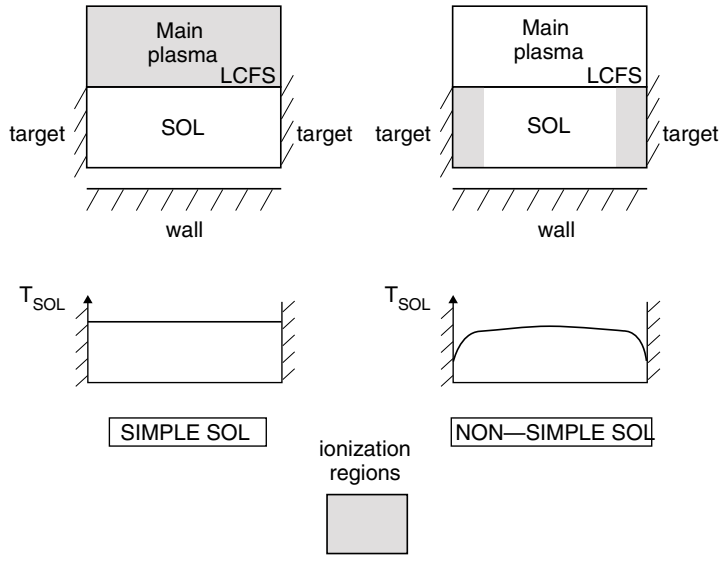

Figure 1.16. For the simple SOL, ionization occurs in the main plasma and the temperature is constant along a given SOL flux tube. For the non-simple SOL, the ionization usually occurs in the SOL and near the targets; also the SOL temperature drops approaching the target, along each SOL flux tube.

is compared with the plasma radius which, for example, for JET is $\approx$ 1 m. Thus the radial extent of the plasma is essentially equal to the location of whichever solid object penetrates most deeply into the plasma. This has the advantage that one can prevent plasma interaction with most of the containing vessel by employing structural components which can be specially designed for the purpose of withstanding intense plasma interaction; at the same time, little of the expensive magnetic volume is tied up. The fusion-producing main plasma can extend almost to the vessel walls, without directly interacting with them. The λ_{SOL} given by equation (1.10) is strictly the plasma *density* scrape-off length. Temperature, pressure, power, etc radial decay lengths will be somewhat different, sections 4.3, 5.5.

It is important to recognize that the expression for λ_{SOL}, equation (1.10), has been obtained for the *simple SOL* assumption that all of the hydrogenic ionization occurs in the main plasma. From the viewpoint of understanding, it is unfortunate that a significant fraction of the ionization often occurs in the SOL near the targets. In that case, equation (1.10) is not valid. Even for the simple SOL, equation (1.10) is only an estimate since T and c_s are not constants but vary radially across the SOL. For the non-simple, i.e., complex, SOL, chapter 4—for example the *conduction-limited* divertor SOL, sections 1.9, 5.3—T and c_s also vary significantly along each flux tube, making equation (1.10) even less appropriate. See figure 1.16.

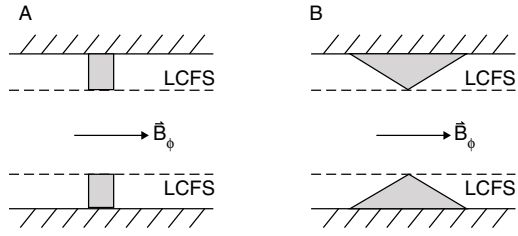

Figure 1.17. The bevel-sided poloidal limiter B has a larger plasma-wetted area than the flat-sided A. Toroidal view.

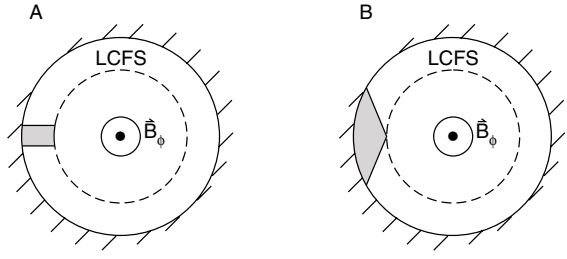

Figure 1.18. The bevel-sided toroidal limiter B has a larger plasma-wetted area that the flat-sided A. View of the poloidal cross-section.

Unfortunately, the small values of λ_{SOL} tend to result in plasma-wetted areas which are very small—and always much smaller than the geometrical surface area of the vessel, all of which could, in principle, be available for plasma heat removal. Mechanisms to increase the effective $D_{\perp}^{\mathrm{SOL}}$ are therefore of interest [1.14–1.17]. For the case of a single, washer (flat sided) poloidal limiter the plasma-wetted area is $A_{\mathrm{wet}} = 2[\pi(a + \lambda_{\mathrm{SOL}})^2 - \pi a^2] \approx 4\pi a \lambda_{\mathrm{SOL}}$. Example: $a = 1$ m, $\lambda_{\mathrm{SOL}} = 1$ cm, $A_{\mathrm{wet}} \approx 0.1$ m^2, which is minuscule compared with the total wall area, $A_{\mathrm{wall}} \approx 2\pi R 2\pi a \approx 100$ m^2 for $R = 3$ m (JET size). One can shape the poloidal limiter so that its surface only gradually increases in minor radius in the toroidal direction, thus increasing A_{wet} substantially—although still not approaching A_{wall}, figure 1.17.

For a single, flat-sided toroidal ring limiter, $A_{\mathrm{wet}} \approx 4\pi R \lambda_{\mathrm{SOL}}$, i.e. larger than for the poloidal limiter. One can also shape a toroidal limiter to be almost tangential to the LCFS, increasing A_{wet} significantly, figure 1.18.

On the TFTR tokamak, the inner wall was employed as a toroidal limiter in this arrangement, giving $A_{\mathrm{wet}} \approx 5$ m^2 [1.18]. Provided the freedom to vary the plasma shape (and LCFS shape) can be sacrificed, then such toroidal wall limiters could in principle have A_{wet} so large as to approach A_{wall}. One would also have to avoid all wall protrusions in the wetted area, requiring careful alignment of the protective tiles in order to avoid hot spots [1.19].

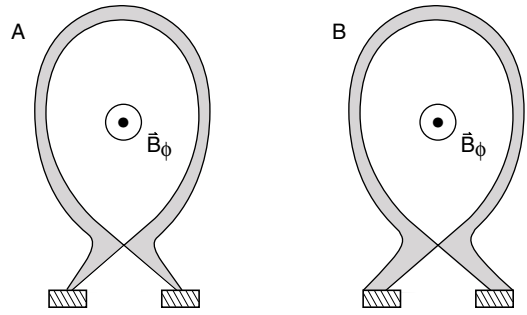

Figure 1.19. The divertor plasma can be spread over a larger target area, case B, compared with case A, by expanding the poloidal field at the targets, i.e., by making B_θ weaker there.

For poloidal divertors, A_{wet} can be increased above $4\pi R\lambda_{\text{SOL}}$ by exploiting the fact that the radial separation of the poloidal magnetic flux surfaces near the target can be increased using external magnetic coils, figure 1.19. This is considered further in section 5.6.

1.8 1D Plasma Flow Along the Simple SOL to a Surface

1.8.1 The Basic Features Reviewed

For clarity, we start by simply stating, without proof, the basic features of 1D flow along the SOL [1.6, 1.7]. In the subsequent section these results are derived.

(1) The plasma fluid flows along the SOL due to the presence of a particle source and sink, the limiter/divertor surfaces. But how does the plasma 'know', at each point along the SOL, that it is supposed to be moving toward the surface? Why isn't the SOL plasma stagnant? Why does it become accelerated up to a non-zero velocity v? What is the *local* force causing this? It is the parallel pressure gradient which is induced in the SOL plasma by the presence of source and sink. See figure 1.20. The *total* pressure is constant along $\boldsymbol{B}$, but the *static* pressure decreases, providing the force: $p_{\text{total}} = p_{\text{static}} + p_{\text{dynamic}}$, where $p_{\text{dynamic}} \equiv mnv^2$; thus as p_{static} drops, the flux of flow momentum, mnv^2, increases, and v increases; see chapter 9.

(2) In the first few μs after the plasma is initiated—that is just after ionization of the *fill* gas in the vacuum vessel and before the recycling and ionization have become established, the electrons, due to their small mass and high mobility, rush ahead of the ions and strike the solid surfaces, charging them up negatively.

(3) From that time on, an electron-repelling potential difference exists between the plasma and the surface, *slowing* the loss rate of the electrons—while, at the same time, *increasing* the ion loss rate. The potential spontaneously

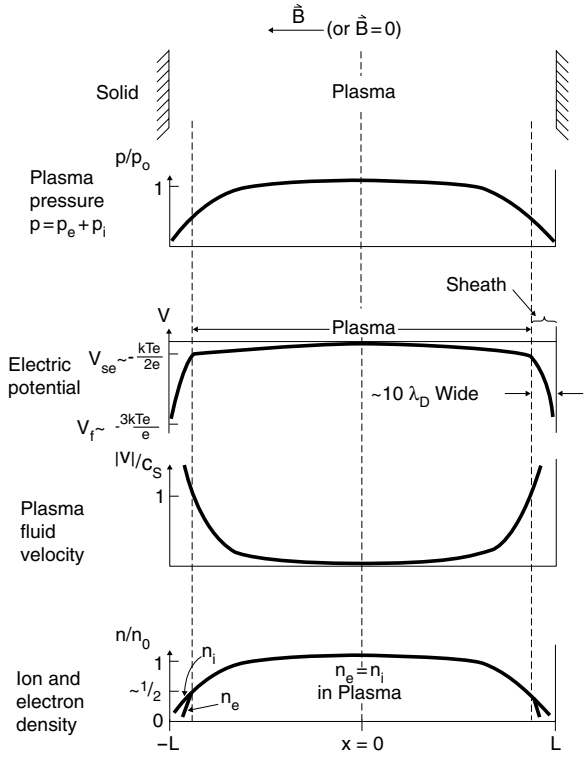

Figure 1.20. Schematic of the variation of plasma pressure, electric potential, plasma velocity and ion/electron densities in the plasma between two semi-infinite planes. The thickness of the sheath is exaggerated for clarity. The total length is $2L$.

adjusts, on an isolated or electrically floating surface, until the loss rates of the two charge species become equal—defined as *ambipolar* plasma transport—i.e. an *ambipolar electric field* arises in the plasma. It will be found that the solid surface will spontaneously charge up to a potential of $V_{\text{wall}} \sim -3kT_e/e$, for a hydrogenic plasma, relative to the *plasma potential*. The plasma is an excellent conductor in the direction along $\boldsymbol{B}$ and can be at almost a constant potential along any given magnetic field line.

(4) Electrostatic potentials on surfaces contacting plasmas are *almost* entirely shielded out within a short distance—regardless of whether the potential arises spontaneously or is applied as an external voltage on an electrode. This phenomenon is termed *Debye shielding* and it occurs over a very short distance of the order of the *Debye length* [1.20]:

$$\boxed{\lambda_{\text{Debye}} = (\varepsilon_0 kT_e/n_e e^2)^{1/2}.} \tag{1.11}$$

Example: $T_e = 20$ eV, $n_e = 10^{19}$ m^{-3}, $\therefore \lambda_{\text{Debye}} \approx 10^{-5}$ m.
This thin region is called the *Debye sheath* and is a region of net positive space charge, existing in a dynamic equilibrium: the ions continue to move through the sheath at high speed. The positive charge density [coulombs m^{-2}], integrated through the sheath thickness, almost equals the negative charge density existing on the solid surface. Thus the rest of the region upstream of the sheath—the essentially neutral plasma itself—is almost completely shielded from the electric field due to the space charge density in the sheath.

(5) The shielding is not perfect, however, and a small electric field $E \approx kT_e/2eL$, penetrates throughout the length of the plasma where the particle source exists. This is called the *pre-sheath electric field* and it acts on the ions in the SOL to help move them toward the target.

(6) The surface sink action causes a depression of the local plasma density creating a parallel density and pressure gradient. The pre-sheath field acts to retard the electrons, which come into a *nearly* perfect parallel momentum, i.e. force, balance between a parallel pressure gradient force pushing the electrons toward the surface, and the retarding electric field force. The electrons thus obey, almost perfectly, a *Boltzmann factor* relation [1.21, 1.22]

$$\boxed{n = n_0 \exp[eV/kT_e].} \tag{1.12}$$

n_0 is the plasma density upstream where the plasma potential is taken to be $V = 0$. As the surface is approached V becomes more negative (the pre-sheath electric field). It is also noted that a parallel ion pressure gradient exists (equal to the electron one if $T_e = T_i$), but this *adds* to the E-force on the ions. There is a direct link between the pressure and potential gradient implied in the Boltzmann relation. Assuming quasineutrality, $n_e = n_i$, and one-dimensional ambipolarity, i.e. $\Gamma_e = \Gamma_i$ where $\Gamma = nv$ is particle flux density, the electron fluid velocity must equal the ion fluid velocity. Thus the electrons cannot actually be in *perfect* force balance along $\boldsymbol{B}$. However, it will be shown that the electron + ion fluid velocity is much less than the electron thermal speed, $\overline{c}_e = (8kT_e/\pi m_e)^{1/2}$, and that the electron force balance is almost exact. The extreme lightness of the electrons requires that they be in nearly perfect force balance, otherwise extremely high electron fluid speeds and currents would occur.

(7) While the ambipolar electric field acts on both the ion fluid and the electron fluid individually, it can exert no force on the *plasma* fluid—which is the sum of the e and i fluids and is therefore (quasi-) neutral. As mentioned in point (1), the only force accelerating the plasma fluid toward the surface is the pressure-gradient force. See figure 1.21.

(8) In the foregoing it has been implicitly assumed that the plasma is isothermal along any given flux tube in the SOL. Since the SOL plasma has very high heat conductivity this can be a good approximation. The effect of parallel

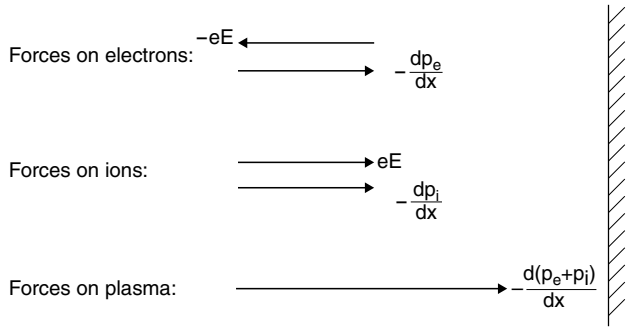

Figure 1.21. The electrons are almost in perfect force balance, while for the ions the electric field force and the ion pressure gradient force are additive (and equal if $T_e = T_i$, the case shown here), accelerating the ions. The force on the plasma is due to the total pressure gradient alone, since an electric field exerts no force on the quasineutral plasma.

T-gradients will be discussed in section 4.10. Here we note that a further element of the definition of the *simple SOL* is that parallel gradients be small. This constitutes the *sheath-limited regime*; see sections 1.9, 9.10. It will be shown that both charge species have a fluid speed which reaches the ion acoustic speed: $c_s = [k(T_e + T_i)/m_i]^{1/2}$ just as the particles enter the sheath, that is $v_{se} = c_s$, where v_{se} is the velocity at the sheath edge.

(9) It will be found that the plasma density drops from n_0 at distance L upstream to $n_{se} = \frac{1}{2}n_0$ at the sheath edge.

1.8.2 Derivations of Results for 1D Plasma Flow in the Simple SOL

1.8.2.1 The 1D Fluid Equations

In this section the fluid particle and momentum conservation equations for an isothermal plasma are derived in an intuitive way. A more systematic derivation is given in chapter 9.

First we show that the particle flux density Γ [particles m^{-2} s^{-1}], is given by $\Gamma = nv$ where v is the bulk or fluid speed (*not to be confused with the individual particle speed which has a component due to random, thermal motion as well as the common fluid speed v of all the particles*). Here we will follow the usual custom: the absence of any subscript on v indicates fluid velocity. If random, thermal or other types of velocity are intended, appropriate subscripts are employed. Consider figure 1.22 where a 'slug' of fluid of cross-sectional area A [m^2] drifts at velocity v past an observer.

In time t [s] a slug of length vt [m] will pass the observer, containing $nvtA$ [particles]. Thus the number of particles per m^2 per s passing the observer is nv, which we define to be Γ.

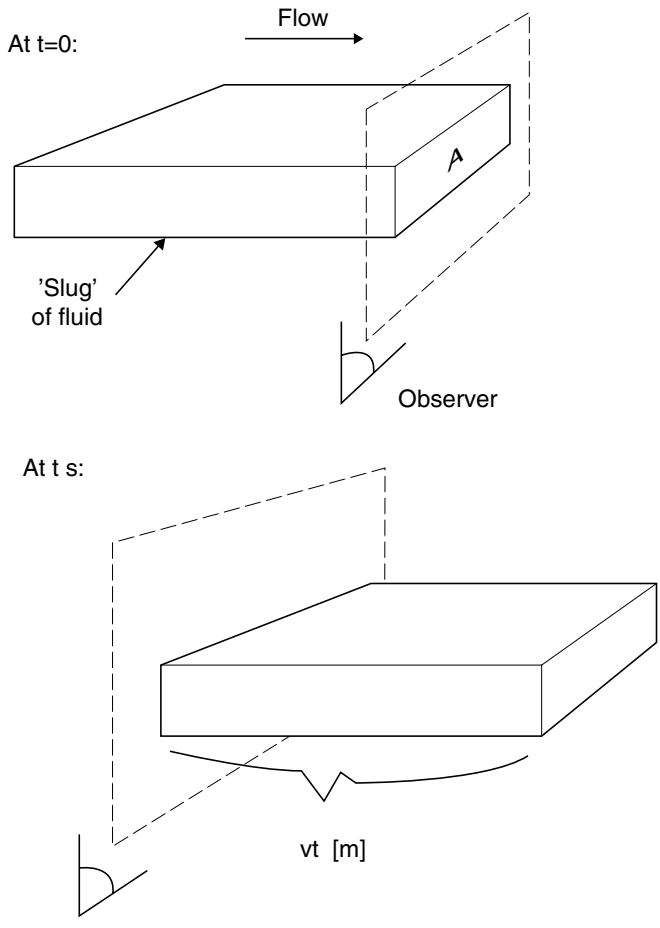

Figure 1.22. Demonstration that $\Gamma = nv$.

Consider next figure 1.23 and the conservation of particles or mass, in 1D for steady state. We must allow that Γ can be a function of x, the distance in the 1D flow direction and that a source of particles—perhaps due to ionization of neutrals—is present of strength S_p [particles m^{-3} s^{-1}]. The net outflow of particles from the volume shown in figure 1.23 is

$$(\Gamma_{\mathrm{out}} - \Gamma_{in})A = \left(\Gamma_{in} + \Delta x \frac{\mathrm{d}\Gamma}{\mathrm{d}x} - \Gamma_{in}\right)A = \Delta x A \frac{\mathrm{d}\Gamma}{\mathrm{d}x} \tag{1.13}$$

which must equal the creation rate in the volume:

$$\Delta x A S_p \tag{1.14}$$

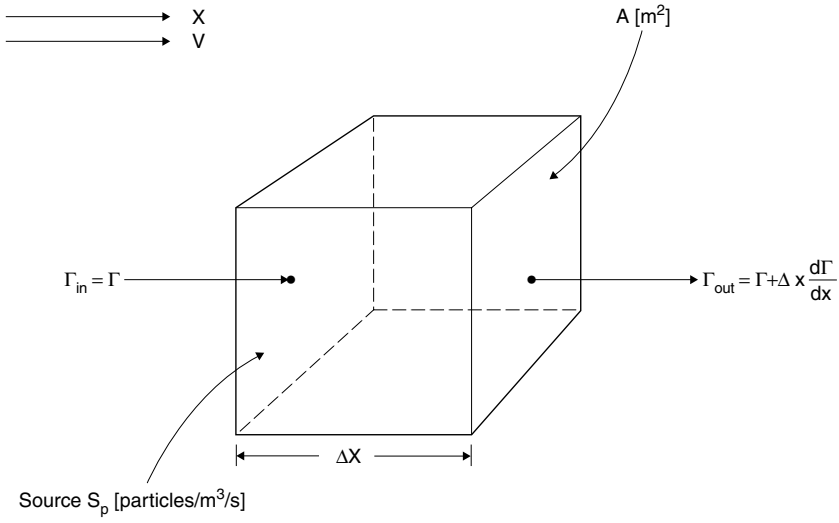

Figure 1.23. Demonstration of the particle conservation equation.

thus giving the particle conservation equation:

$$\boxed{\frac{\mathrm{d}\Gamma}{\mathrm{d}x} = \frac{\mathrm{d}(nv)}{\mathrm{d}x} = S_p.} \tag{1.15}$$

The 1D steady-state, momentum conservation equation can be arrived at from Newton's second law:

$$F = ma = m\frac{\mathrm{d}v}{\mathrm{d}t} = m\frac{\mathrm{d}v}{\mathrm{d}x}\frac{\mathrm{d}x}{\mathrm{d}t} = mv\frac{\mathrm{d}v}{\mathrm{d}x} \tag{1.16}$$

applied to the n particles per m^3, gives

$$nmv\frac{\mathrm{d}v}{\mathrm{d}x} = nF \tag{1.17}$$

and the total force m^{-3}, nF, is due to several contributions:

$$nF = neE - \frac{\mathrm{d}p}{\mathrm{d}x} - nF_{\mathrm{drag}} \tag{1.18}$$

where neE is the parallel E-force exerted on particles of charge $+e$. From figure 1.24 it can be seen that the net pressure force on the particle in the volume shown is:

$$\left[-\left(p + \Delta x\frac{\mathrm{d}p}{\mathrm{d}x}\right) + p\right]A = -\Delta x A\frac{\mathrm{d}p}{\mathrm{d}x} \tag{1.19}$$

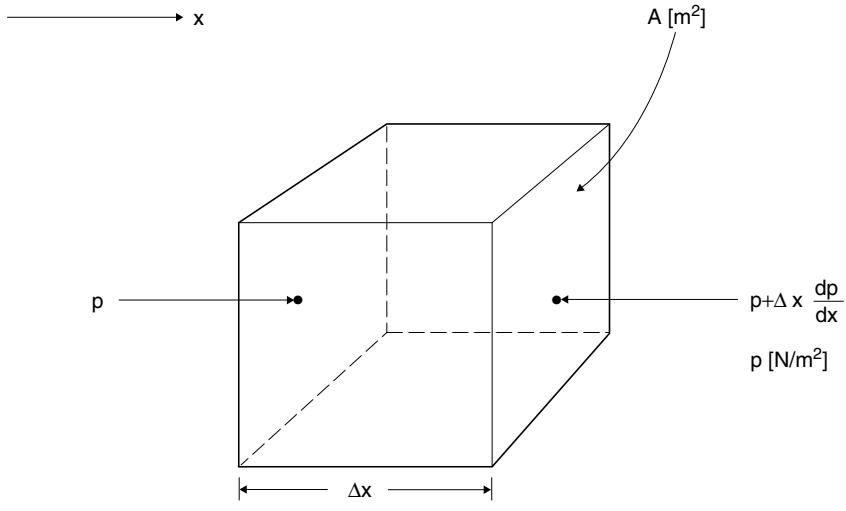

Figure 1.24. Demonstration of the pressure-gradient force.

giving a net p-gradient force on the particles in one m^3 of $-dp/dx$. One notes the minus sign: the force is in the opposite direction to the increasing pressure!

The drag force can include various contributions. There can be viscous drag and drag due to momentum-loss collisions with neutrals, but we start by neglecting such forces here. There is also an *effective* drag in the fluid picture due to the particle source S_p. In the fluid picture all particles at a given location x have the same drift velocity $v(x)$; we assume here, however, that the newly created ions come from non-moving neutrals, and so the momentum required per m^3 per s to bring them instantly up to the local speed, mvS_p, constitutes a local drag force on the fluid. Thus we obtain the 1D, steady-state momentum equation:

$$nmv\frac{dv}{dx} = neE - \frac{dp}{dx} - mvS_p. \tag{1.20}$$

One can proceed further to derive an energy conservation equation but that is not necessary if *isothermal* conditions are assumed, as here. Thus one has two equations, (1.15) and (1.20), in the two unknowns $n(x)$, $v(x)$—i.e., the two dependent variables—in terms of one independent variable x. It may appear that $p(x)$ is a further unknown; however, for the isothermal assumption one has $p(x) = kTn(x)$ with T a *parameter* which has to be found from some *other* considerations. If the isothermal assumption is relaxed then one needs the *energy conservation equation* also. We can also remove E as a dependent variable by using the Boltzmann relation. S_p, m and e must be given.

These two equations will be sufficient to demonstrate the most basic features of plasma flow along the SOL.

1.8.2.2 The Boltzmann Relation for Electrons

Consider the momentum equation for the *electron fluid*:

$$nm_e v\frac{\mathrm{d}v}{\mathrm{d}x} = -neE - \frac{\mathrm{d}p_e}{\mathrm{d}x} - m_e v S_p \tag{1.21}$$

giving approximately:

$$nm_e v\frac{v}{L} \approx -neE - n\frac{kT_e}{L} - m_e v\frac{nv}{L} \tag{1.22}$$

where L is the characteristic parallel length of spatial variations along the SOL and we used also the particle conservation, equation (1.15), $S_p = \mathrm{d}(nv)/\mathrm{d}x \approx nv/L$. Although we have not yet proved that the characteristic drift speed along the SOL is c_s, we appropriate that result here; we will have to confirm consistency at a later point. Thus:

$$nm_e\frac{c_s^2}{L} = -neE - \frac{nkT_e}{L} - \frac{m_e n c_s^2}{L} \tag{1.23}$$

which, taking $T_e = T_i$ becomes approximately

$$n\frac{m_e}{m_i}\frac{2kT}{L} \approx -neE - \frac{nkT}{L} - n\frac{m_e}{m_i}\frac{2kT}{L} \tag{1.24}$$

and thus it is seen that, indeed, the inertia term and the drag term are of the order $m_e/m_i \ll 1$ of the pressure-gradient term. The force balance for electrons is thus between the electric field and $-\mathrm{d}p_e/\mathrm{d}x$, to an excellent approximation, figure 1.21. Inserting $E \equiv -\mathrm{d}V/\mathrm{d}x$ and integrating then gives the Boltzmann factor relation, equation (1.12). It is to be emphasized again that the electrons can satisfy the Boltzmann relation quite closely, yet have a substantial fluid velocity of order $c_\mathrm{s} \ll \overline{c}_e$. A more rigorous derivation of the Boltzmann relation is given in section 2.2.

1.8.2.3 Modelling the Ions

Because the electrons experience a retarding E-field in the SOL, modelling has been seen to be very simple; the Boltzmann factor contains all the electron information. Also, it can be shown (1.22) that the electron velocity distribution remains Maxwellian in a retarding E-field (that is sufficiently strong to limit particle loss from the system), which is a further valuable simplification; the *total* number of electrons m^{-3} merely decreases with increasingly negative V. The ions, on the other hand, are in an accelerating field which substantially disturbs their velocity distribution, which may have been Maxwellian far from the absorbing surface. For the ions it is necessary to retain the terms which could be dropped for the

electrons, last section. We thus have the first two conservation equations for ions:

$$\frac{\mathrm{d}(nv)}{\mathrm{d}x} = S_p \tag{1.25}$$

$$nmv\frac{\mathrm{d}v}{\mathrm{d}x} = -\frac{\mathrm{d}p_i}{\mathrm{d}x} + enE - mvS_p. \tag{1.26}$$

Note that m from now on designates the ion mass, while n, v and S_p need no subscripts to distinguish between electron and ion, since we are assuming here: (a) singly charged ions, (b) $n_e = n_i$, (c) ambipolar outflow, $v_e = v_i$, and (d) ions and electrons produced at the same rates. With the isothermal assumption made here,

$$\frac{\mathrm{d}p_i}{\mathrm{d}x} = kT_i\frac{\mathrm{d}n}{\mathrm{d}x} \tag{1.27}$$

and so, again, there are only two dependent variables—n and v—and a parameter T_i (which has to be established by separate considerations). We can thus achieve the objective of establishing $n(x)$, $v(x)$, $V(x)$. We are able to replace E using the Boltzmann relation for the electrons:

$$enE = -kT_e\frac{\mathrm{d}n}{\mathrm{d}x} \tag{1.28}$$

and so can re-write the *plasma* momentum equation ('plasma' because the electron and ion momentum equations have been combined):

$$nmv\frac{\mathrm{d}v}{\mathrm{d}x} = -mc_s^2\frac{\mathrm{d}n}{\mathrm{d}x} - mvS_p \tag{1.29}$$

where c_s is, strictly, the *isothermal* plasma acoustic speed equation (1.5). (Retaining the m_e-related terms in equation (1.21) and adding the electron and ion momentum equations together, rather than using the Boltzmann relation for the electrons, gives equation (1.29) with $m = m_e + m_i$.) One may note that E does not appear in equation (1.29). The first term on the RHS is the sum of the e and i pressure gradient forces, figure 1.21. It is convenient to define the *plasma Mach number*:

$$M \equiv v/c_s. \tag{1.30}$$

The two equations (1.25), (1.29) can be combined to eliminate $\mathrm{d}n/\mathrm{d}x$ and give a most informative result:

$$\boxed{\frac{\mathrm{d}M}{\mathrm{d}x} = \frac{S_p}{nc_\mathrm{s}}\frac{(1+M^2)}{(1-M^2)}.} \tag{1.31}$$

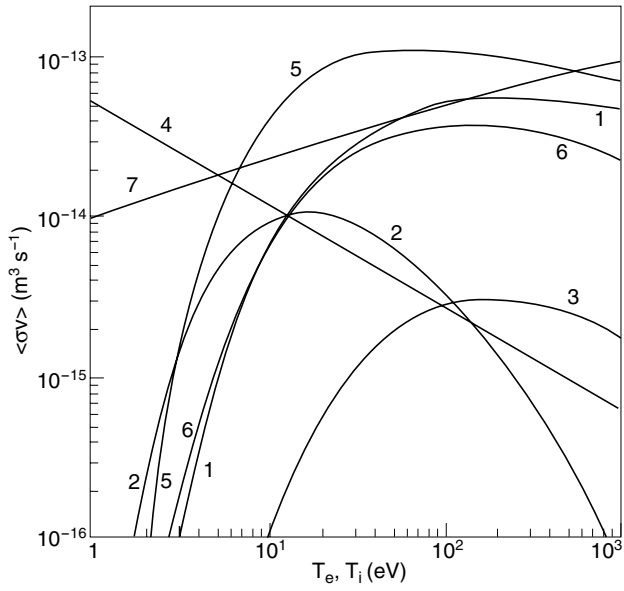

Figure 1.25. The rate coefficients for atomic and molecular hydrogen [1.23]. The numbered reactions are (1): $e + H_2 \rightarrow H_2^+ + 2e$, (2): $e + H_2 \rightarrow 2H^0 + e$, (3): $e + H_2 \rightarrow H^0 + H^+ + 2e$, (4): $e + H_2^+ \rightarrow 2H^0$, (5): $e + H_2^+ \rightarrow H^0 + H^+ + e$, (6): $e + H^0 \rightarrow H^+ + 2e$, and charge exchange (7): $H^0 + H^+ \rightarrow H^+ + H^0$.

1.8.2.4 The Particle Source S_p

The two particle 'source' mechanisms that usually dominate the SOL are: (a) local ionization of neutrals by the plasma electrons, (b) cross-field diffusion. The latter is not a true source of ions in the overall system, but appears as such in 1D analysis.

(a) *Electron ionization.*
Assuming the electrons are Maxwellian, the basic atomic and molecular cross-sections from experiment can be integrated over the velocity distribution (1.25) to give the *rate coefficients* $\overline{\sigma v}(T_e)$ [m^3 s^{-1}], shown in figures 1.25–1.28, [1.23, 1.26]. Thus, for example, the rate of ionization of hydrogen atoms by electron impact, S_{iz} [ionization events m^{-3} s^{-1}], is $S_{iz} = n_e n_H \overline{\sigma v}_{iz}$, where n_H [H atoms m^{-3}] is the atom density and one uses curve (6) in figure 1.25. Figure 1.25 shows $\overline{\sigma v}_{iz}$ values for a number of important processes for hydrogenic neutral atoms and molecules. Figures 1.26–1.28 show $\overline{\sigma v}_{iz}$ for several important plasma impurities. Figures 1.29–1.31 indicate the principal hydrogenic reactions schematically. A certain fraction of the hydrogenic ions recycling from the limiter/divertor targets are promptly back-scattered as neutral atoms with energies which

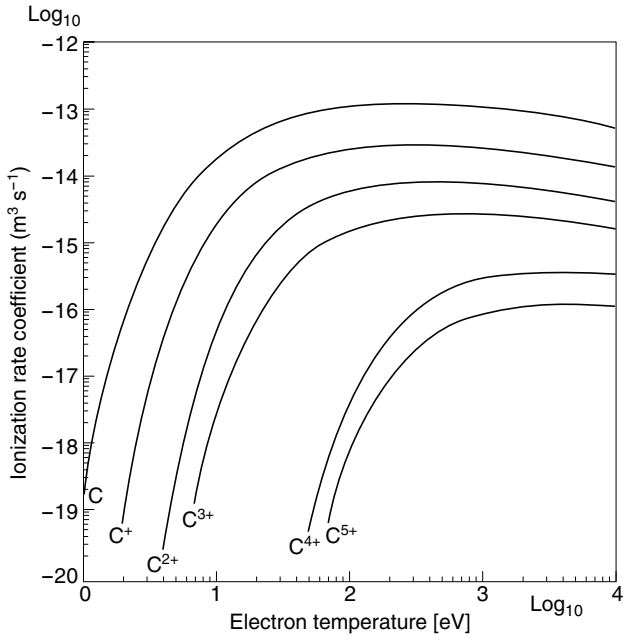

Figure 1.26. Ionization rate coefficients for carbon [1.24].

are an appreciable fraction of the ion impact energy; see section 3.1 and figure 1.29. For these neutrals one uses reaction (6) to calculate $\overline{\sigma v}_{iz}$ in figure 1.25. The other particles recycle as neutral molecules, figure 1.29; some of these will be directly ionized, reaction (1) of figure 1.25, while others will be dissociated into two Franck–Condon atoms by electron impact, reaction (2), with those atoms—of energy about 2 eV [1.26]—becoming ionized, reaction (6), figure 1.30. A most important process for hydrogenic particles is that of *resonant charge exchange*, reaction (7), figure 1.25: the collision of a slow atom entering from the wall and a hot plasma ion results in the creation of a fast atom which, if moving inward, can penetrate deeply into the plasma before ionizing. Indeed, because the resonant charge exchange rate is higher than the ionization rate, this process may be repeated several times resulting, effectively, in a 'neutral accelerator'; figure 1.31. Figure 1.25 indicates that a number of other processes also have to be considered when attempting to model the behaviour of neutral hydrogen in a hydrogenic plasma. The task is a complex one to carry out in detail and for this reason, a number of computer codes have been written over the years to incorporate these and other processes. Currently the most sophisticated treatments are the Monte Carlo codes, DEGAS, EIRENE and NIMBUS [1.13]. The 2D or even 3D

solid-surface configurations and background plasma, including T_e, T_i and n_e as functions of space, are specified as inputs. The recycling neutrals are then launched from the appropriate locations on the limiter/divertor targets where ions arrived, and followed until they are finally ionized—perhaps after a number of wall reflections, charge exchange events, etc.

Impurity particles often enter the plasma as atoms and thus do not usually experience as complex a set of reactions as hydrogen. Even a molecular impurity such as N_2 will not experience the strong charge-exchange process that hydrogen does because the $N + H^+ \rightarrow N^+ + H$ charge-exchange process is not *resonant*, i.e., a potential-energy difference is involved.

The use of sophisticated code modelling of the neutrals is appropriate for coupling to the 2D fluid codes of the SOL [1.13], such as B2, UEDGE, EDGE2D, etc, chapter 13. For our present purposes of simple 1D analytic treatment we will assume for hydrogen the existence of an *effective* ionization rate coefficient $\overline{\sigma v}_{iz}(T_e)$ as an average of reactions (1) and (6) of figure 1.25. The effect of energetic back-scattering and the 'acceleration' process of Franck–Condon dissociation and charge exchange is to make neutral hydrogen penetrate a plasma more deeply before becoming ionized than would be the case if the neutral only had its original thermal velocity, corresponding to the temperature of the solid surface. This can be allowed for, approximately, by assuming that the penetrating neutral velocity

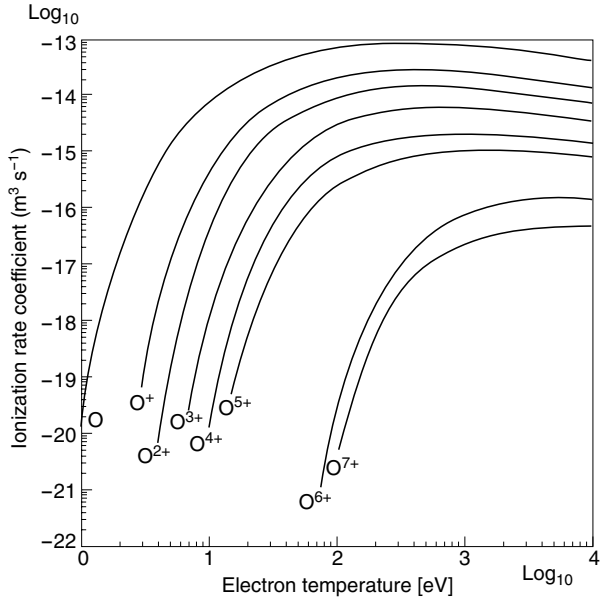

Figure 1.27. Ionization rate coefficients for oxygen [1.24].

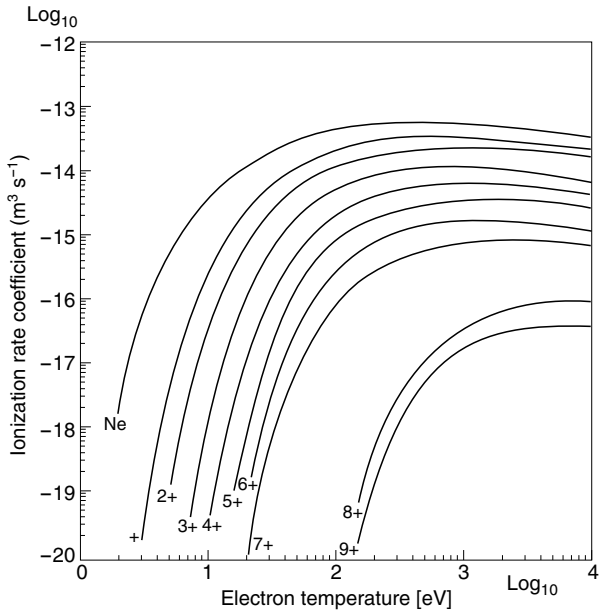

Figure 1.28. Ionization rate coefficients for neon [1.24]. One may note how difficult it is to ionize the He-like ions C^{4+}, O^{6+}, Ne^{8+}.

is greater than the thermal velocity by some specified amount, or using more sophisticated—yet still simple—estimates, see section 4.6.
We then have:

$$S_{p,iz} = nn_n\overline{\sigma v}_{iz}(T_e) \qquad [\text{ion pairs m}^{-3}\ \text{s}^{-1}] \tag{1.32}$$

where n = plasma density (strictly n_e) and n_n = neutral density (some average of atomic and molecular).

(b) *Cross-field diffusive 'source'.*
Consider now the *radial*, cross-field direction r, figure 1.32, and the fact that parallel removal to the solid surface constitutes a particle *sink* for the cross-field particle flux density, $\Gamma_\perp$. Thus, conservation of particles for the r-direction:

$$\frac{\mathrm{d}\Gamma_\perp}{\mathrm{d}r} = S_{p\perp} < 0. \tag{1.33}$$

This cross-field sink gives the parallel source term $S_{p,c\text{-}f}$ we are seeking:

$$S_{p,c\text{-}f} \equiv S_{p\parallel} = -S_{p\perp}. \tag{1.34}$$

Let us assume further that $\Gamma_\perp$ satisfies Fick's law of diffusion:

$$\Gamma_\perp = -D_\perp \frac{\mathrm{d}n}{\mathrm{d}r}. \tag{1.35}$$

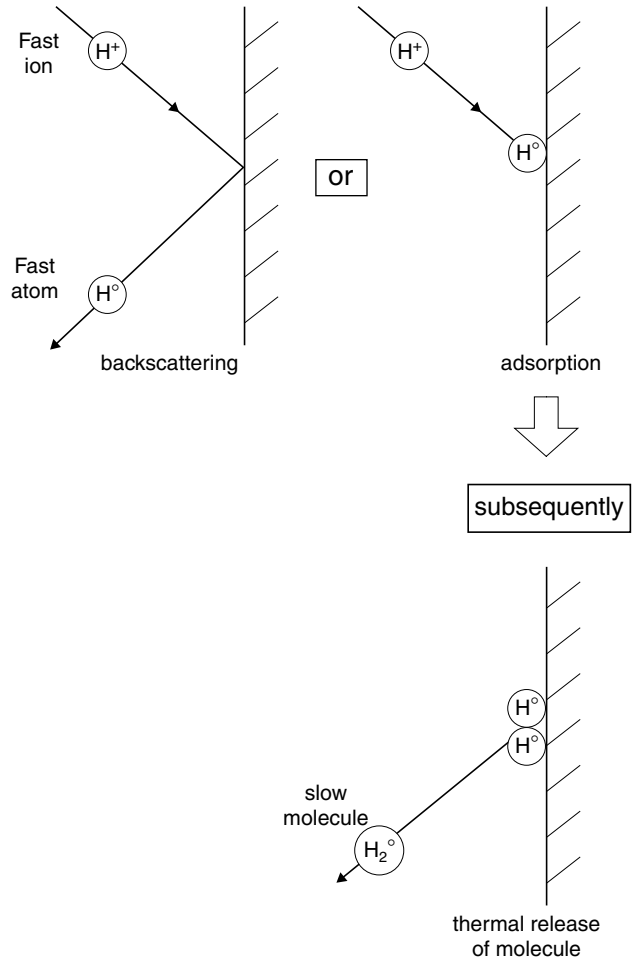

Figure 1.29. Hydrogen atomic ions striking a surface may be energetically back-scattered as a neutral or be adsorbed, subsequently combining with a second atom and thermally desorbing as a molecule.

The plasma density decays radially with characteristic length λ_{SOL}, section 1.6, and so

$$\frac{dn}{dr} \simeq -\frac{n}{\lambda_{SOL}} \qquad \frac{d^2n}{dr^2} \simeq \frac{n}{\lambda_{SOL}^2}. \tag{1.36}$$

Thus:

$$\boxed{S_{p,c\text{-}f} = D_\perp n/\lambda_{SOL}^2.} \tag{1.37}$$

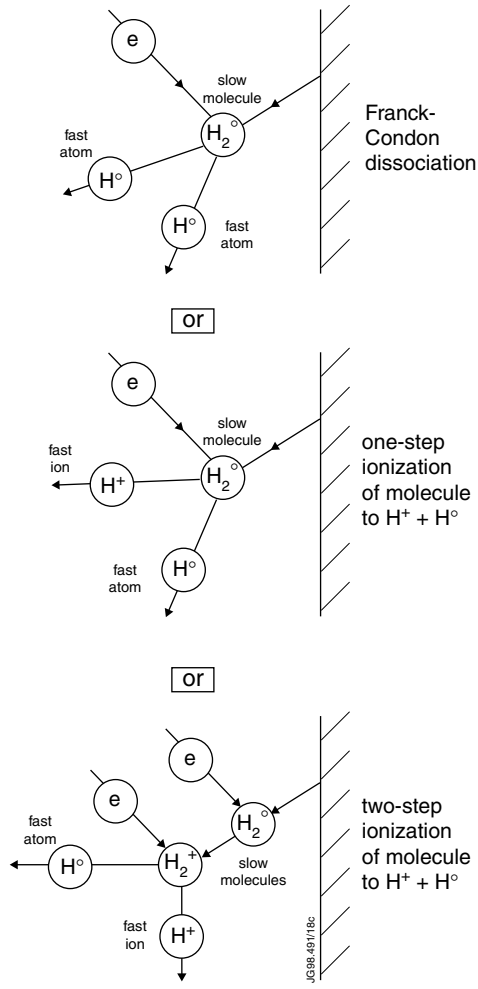

Figure 1.30. A hydrogen molecule struck by an electron may dissociate by the Franck–Condon process, creating two atoms of kinetic energy a few eV, or be ionized in a one-step or two-step process.

One may note that both $S_{p,iz}$ and $S_{p,c\text{-}f}$ vary directly as plasma density, which turns out to be rather convenient for purposes of simple analysis.

1.8.2.5 Sonic Flow of Isothermal Plasma into the Sheath

Returning to equation (1.31) we note that the term S_p/nc_s is intrinsically positive. Thus, assuming from symmetry that the flow at distance L from the surface, i.e. halfway between two surfaces, is stagnant, i.e. $v(0) = M(0) = 0$, then

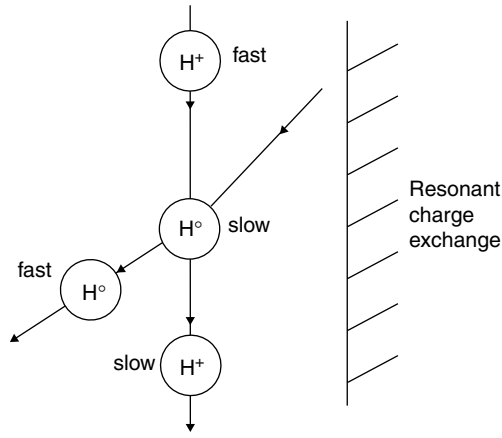

Figure 1.31. A neutral hydrogen atom has a large cross-section for charge exchange with a plasma ion. The neutral can thus, in effect, be strongly accelerated, penetrating deeply into the plasma. In this figure, imagine that $\boldsymbol{B}$ is parallel to the solid surface and that the ions move freely along $\boldsymbol{B}$ while experiencing gyroscopic motion about $\boldsymbol{B}$. If the charge exchange collision occurs at an instant when, as a result of the ion's gyroscopic motion, it happens to be moving away from the wall, then the fast atom created by the charge exchange event will be launched toward the centre of the plasma.

$\mathrm{d}M/\mathrm{d}x > 0$ here, the flow accelerates towards the surfaces—as it must, of course. We note that M cannot exceed unity without introducing an unphysical singularity in the midst of the flow field. We are, however, attracted to the idea that just at the plasma–sheath interface M reaches unity [1.6, 1.7]: this will, indeed, imply infinite gradients for n, v, V at that point—but we know that the sheath, being very thin, is a region where any finite changes in n, v, V will give gradients that are extremely large compared with the ones in the plasma. Thus, to the same degree of approximation that we have employed in treating the plasma as being precisely neutral, we may accept that all gradients become infinite at the plasma–sheath interface.

Alternatively, one need not divide the space filled by the charged particles into the two absolutely distinct regions, i.e. the plasma where $n_e = n_i$ exactly, and the sheath where $n_e < n_i$. Instead, the entire space can be analysed as one region, employing Poisson's equation in order to relate the charge imbalance, $(n_i - n_e)$, to $\mathrm{d}^2V/\mathrm{d}x^2$, i.e. Poisson's equation provides the extra equation when $n_e \neq n_i$. In that case no infinite gradients occur and it is found that at the point where $(n_i - n_e)/n_i$ becomes significant, then $M \approx 1$ [1.27], corresponding in the simpler, two-region analysis, to the plasma–sheath interface. Such an analysis must be numerical, however, and much insight is thereby lost.

It should be noted that we have not proven here that $M = 1$ at the plasma–sheath interface. What has been demonstrated is that M cannot *exceed* 1 in an

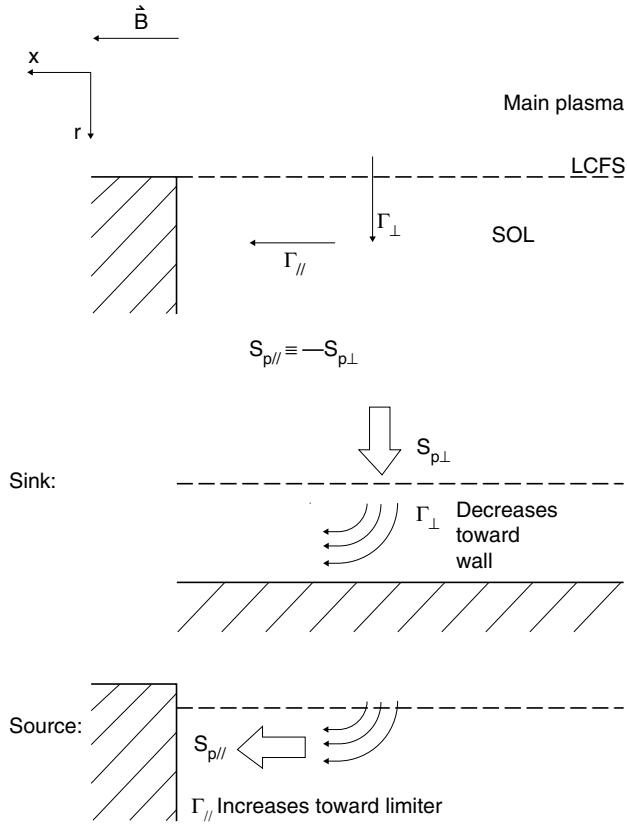

Figure 1.32. Cross-field diffusion into the SOL constitutes an effective particle source in 1D, along-the-SOL modelling.

(isothermal) plasma. At the same time we are receptive to the idea that the flow actually attains sonic speed at the plasma–sheath interface, but this remains to be proven. To do that we will have to carry out an analysis from the *sheath* side, thus obtaining the *Bohm criterion* [1.28], section 2.3. For now, however, we will proceed on the assumption that $M = 1$ at the sheath edge.

We are further inclined toward the idea of sonic flow into the sheath from the general result that a *fluid subject to an uncompensated pressure difference of order* $\Delta p \approx p$ *will 'explode'*, i.e. it is accelerated to a speed of the order of the sound speed in the direction of the pressure-gradient force, figure 1.33. This may be seen by combining the ion and electron momentum equations (1.26) and (1.28) to give for the plasma fluid:

$$nmv\frac{\mathrm{d}v}{\mathrm{d}x} = -\frac{\mathrm{d}p}{\mathrm{d}x} \tag{1.38}$$

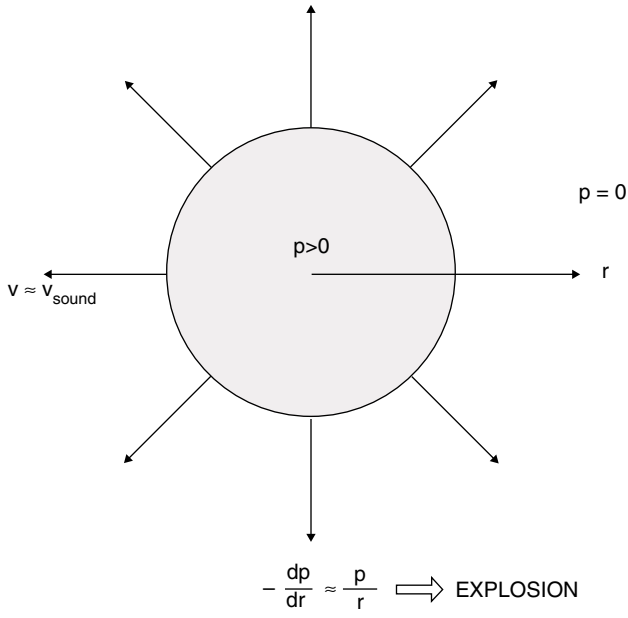

Figure 1.33. An uncompensated pressure-gradient force of magnitude $-\mathrm{d}p/\mathrm{d}r \simeq p/r$ causes a fluid to expand explosively rapidly.

for a freely expanding, no-source, 1D fluid. Here $p \equiv p_e + p_i$. In the direction along $\boldsymbol{B}$ the plasma is subject to no other force than the pressure-gradient force. Since the sheath acts as a perfect sink for the ions, we anticipate intuitively a large Δp along the flow direction, of order p itself. From equation (1.38) we have approximately:

$$nmv^2/L \approx p/L \approx nkT/L \tag{1.39}$$

where L is the gradient scale length and v is a representative velocity. From equation (1.39) one directly obtains the important result that free expansion of a fluid occurs at speed $v \approx (kT/m_i)^{1/2}$, i.e. at the sound speed.

1.8.2.6 The Velocity Distribution Along the SOL

For either $S_{p,iz}$ or $S_{p,c\text{-}f}$ we may set:

$$S_p = Cn \tag{1.40}$$

with C some positive parameter (whose value must be found from some considerations other than the two conservation equations). Thus from equation (1.31) we have

$$\int_0^M \frac{1-M^2}{1+M^2}\mathrm{d}M = \int_0^x \frac{C\mathrm{d}x}{c_s} \tag{1.41}$$

which yields the desired $v(x)$, $M(x)$ as an implicit function:

$$2\tan^{-1} M - M = \frac{Cx}{c_s}. \tag{1.42}$$

We now introduce the *boundary condition*

$$M(L) = 1 \tag{1.43}$$

which is the information, additional to the two conservation equations themselves, needed to constrain C. We have already assumed the upstream boundary condition $M(0) = 0$. (We note that, strictly, we should have used [L-(sheath thickness)] $\approx [L - \lambda_{\text{Debye}}]$ above, but we ignore this tiny correction.) Thus from equation (1.41):

$$\frac{\pi}{2} - 1 = \frac{CL}{c_s}. \tag{1.44}$$

We note that this informs us that the source strength is constrained by the size of the space available, L, and by the plasma temperature (c_s)—or, at least, that all three quantities, C, L, c_s, must satisfy a constraint. Unless this constraint is satisfied the plasma cannot exist in steady state.

(a) *Ionization source*: The constraint gives:

$$\frac{\pi}{2} - 1 = \frac{\overline{\sigma v}_{iz}(T)}{c_s(T)} n_n L. \tag{1.45}$$

Thus, for steady state, the electron temperature is not a free parameter for a locally *self-sustained* plasma (i.e. impact ionization due to the plasma's own electrons), but T_e is a function of the product $n_n L$. This result has been known for almost a century for low pressure gas discharges [1.29], where the degree of ionization is usually very small, and so n_n is simply given by the original gas fill pressure of the discharge tube, while L is replaced by the radius R of the (cylindrical) gas tube, since the sink action is primarily radial to the cylinder walls. Thus a $T_e(p_{\text{gas}}R)$ relation is anticipated theoretically, and is observed experimentally, see figure 1.34 [1.29]. Lowering p_{gas} raises T_e since each electron then 'has to work harder' to maintain particle balance. Decreasing R also forces T_e up since the volume (producing the particles, which is proportional to R^2) is reduced relative to the surface area (sink, which is proportional to R). The gas discharge spontaneously achieves the value of electron temperature required for particle balance, drawing just the necessary power input from the applied longitudinal electric field (this process thus *sets* the value of that field). If some additional external power input were added, the longitudinal field would decrease and/or steady-state conditions would be lost. It is a remarkable fact that it is *particle/momentum* balance—rather than *power* balance—which controls the electron temperature in a locally self-sustained plasma.

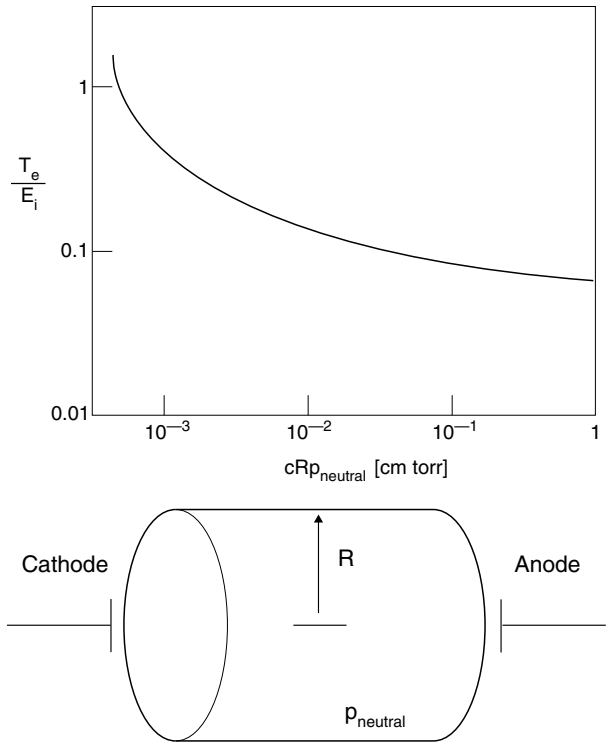

Figure 1.34. For low pressure, non-magnetic electric discharges such as fluorescent lights, T_e is a function of the product $p_{\text{neutral}}R$ where R is the radius of the cylinder and p_{neutral} is the gas pressure, p_{gas}. $E_i \equiv$ ionization potential. Constant c: $\approx 4 \times 10^{-3}$ for He, $\approx 6 \times 10^{-2}$ for Ne, $\approx 4 \times 10^{-2}$ for Ar, $\approx 7 \times 10^{-2}$ for Hg, $\approx 10^{-2}$ for H_2, $\approx 4 \times 10^{-2}$ for N_2 [1.29].

It should also be noted, however, that the foregoing simple picture—where n_n was treated as a fixed, constant, externally controllable parameter—does *not* apply to a tokamak SOL. There, n_n varies spatially by many orders of magnitude, from regions just near the recycling surface, to deep in the core [1.30]. We therefore do *not* conclude, even when ionization within the tokamak SOL is a large part of the 1D flow source, that T_e is fixed, independent of power balance considerations. We return to the matter of including the power balance implication of ionization within the SOL, in section 5.5.

(b) *Cross-field particle source*. The constraint now becomes:

$$\frac{\pi}{2} - 1 = \frac{D_\perp}{\lambda_{\text{SOL}}^2}\frac{L}{c_s} \tag{1.46}$$

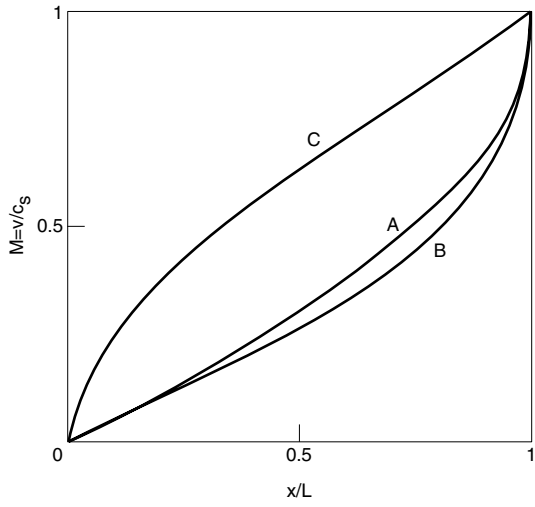

Figure 1.35. Spatial variation of flow Mach number for three models: A: $S_p \propto n_e$; B: $S_p =$ constant; C: $S_p \propto (1 - M^2)/(2M(1 + M^2))$.

i.e.

$$\lambda_{\mathrm{SOL}} \approx \left(\frac{D_\perp L}{c_s}\right)^{1/2} \tag{1.47}$$

We had obtained this result earlier, equation (1.10). That is, the cross-field density gradient is constrained by particle/momentum balance.

For either type of source the spatial variation is the same, equation (1.42), curve A in figure 1.35. One notes that $M(x)$ is not too far from being linear, but it does steepen to an infinite gradient at the sheath edge, $x = L$. This non-linear variation results from assuming $S_p \propto n$; one can show, see problem 1.20, that $n(x)$ does not vary greatly with changes in the form of S_p. One may note that even assuming $S_p =$ constant, curve B in figure 1.35, does not alter the solution very much. One should note that for the '*complex SOL*' where $S_{p,iz}$ is also important, section 1.9 and chapter 5, $n_n(x)$ probably varies strongly, neutral density being much larger near the recycling surface than far upstream. In such cases one anticipates the $M(x)$ would stay small until the ionization region near the plates was reached, where it would rapidly rise to unity, see problem 1.20.

1.8.2.7 Variation of Plasma Density Along the SOL

Algebraic manipulation of the two conservation equations also gives the '*conservative form of the momentum equation*':

$$\frac{\mathrm{d}}{\mathrm{d}x}(p_e + p_i + mnv^2) = 0 \tag{1.48}$$

or:

$$\boxed{p_e + p_i + mnv^2 = \text{ constant.}} \tag{1.49}$$

One should note here that the intuitive argument used in section 1.8.2.1 justifying inclusion of an effective drag term that we employed in what might be called the '*inertial form of the momentum equation*' must now be viewed as somewhat suspect: we do not find such a term in the conservative form, equation (1.49). Why not? The only fully satisfactory answer is to employ a more rigorous derivation of the momentum equation, section 9.4.

For the isothermal assumption, equation (1.49) simplifies to give:

$$\boxed{n(x) = \frac{n_0}{1 + [M(x)]^2}} \tag{1.50}$$

where $n_0 = n(0)$. Note that equation (1.50) is very general since it is completely independent of the particle source S_{p}—including its spatial variation; see also problem 1.20. We know $M(x)$ from equation (1.42), therefore $n(x)$ is also now known. One notes that the variation of plasma density along the SOL is not very great for isothermal conditions, only dropping by a factor of 2 from upstream to the sheath edge.

The particle flux density at the sheath edge, Γ_{se}, is therefore:

$$\boxed{\Gamma_{se} = \tfrac{1}{2} n_0 c_s.} \tag{1.51}$$

1.8.2.8 The Average Dwell-Time in the SOL, τ_{SOL}

While the flow velocity is not constant along the SOL, equation (1.42), a representative value of v is $\sim \frac{1}{2}c_s$, figure 1.35, for the spatially 'well distributed' sources which have been considered here. Thus one estimates $\tau_{\text{SOL}} \approx L/c_{\text{s}}$, equation (1.8). Alternately, we may define τ_{SOL} to be the particle confinement time in the SOL, which is the particle content of the SOL divided by the particle outflux, hence $\tau_{\text{SOL}} = (\overline{n}_{\text{SOL}} L)/(\frac{1}{2} n_0 c_s) \approx L/c_s$, as before.

For a complex SOL it can be the case that the ionization distances are very short and the particle source is concentrated very near the solid surface; the latter way of defining τ_{SOL} will still give $\tau_{\text{SOL}} \approx L/c_s$. In this case, however, flow only exists very near the target and most of the SOL is stagnant. Thus the *average* time in the SOL involves groups of particles with extremely different dwell times in the SOL. Indeed ions having $v \to 0$ have dwell times $\to \infty$! We see again that the result $\lambda_{\text{SOL}} \approx (D_\perp L/c_s)^{1/2}$, Equation (1.10), is not applicable. It also appears that the SOL will extend radially all the way to the wall in these circumstances, assuming that $D_\perp \neq 0$, since many of the particles spend very long times in the SOL. We will return to this matter in chapter 15 on *flow reversal* and chapter 19 on *the relation among* SOL *decay lengths*.

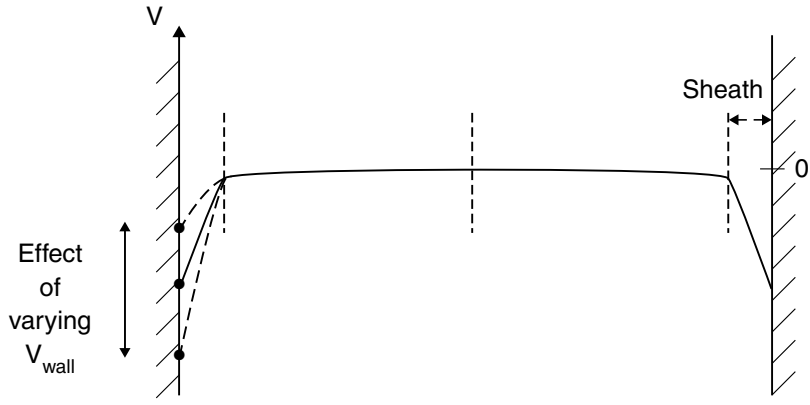

Figure 1.36. Variation of the electric potential on a wall or an electrode is almost entirely 'soaked up' within the thin sheath, leaving the plasma unaffected. Here the potential on the 'far' (right) wall is assumed not to change as the potential of the 'near' (left) wall is varied relative to the plasma potential, which is taken to be $V = 0$ here. See section 2.6 for the case where a potential difference is applied between the two end walls.

1.8.2.9 The Parallel Electric Field in the SOL

We may combine the Boltzmann relation, equation (1.12), with equation (1.50) to eliminate n, obtaining:

$$V(x) = -\frac{kT_e}{e} \ln[1 + (M(x))^2] \tag{1.52}$$

we have $M(x)$ from equation (1.42), thus we know $V(x)$ and $E_\parallel(x)$. This gives the pre-sheath (i.e. the plasma) electric field, figure 1.20. At the sheath edge one has

$$\begin{aligned} V_{se} \equiv V(L) &= \frac{kT_e}{e} \ln 2 \\ &\simeq -0.7\frac{kT_e}{e}. \end{aligned} \tag{1.53}$$

If any larger potential than this is applied externally to a plasma—whether via electrodes connected to a power supply, or the spontaneous surface charging which occurs when the more mobile electrons rush to the walls immediately after initialization of the plasma—then the excess potential is shielded out by the Debye sheath, figure 1.36.

We will show in section 2.6 that the spontaneous wall charging for floating (ambipolar) conditions results in a negative surface potential of $\sim -3kT_e/e$ for hydrogenic plasmas. Therefore, most of the latter potential appears across the sheath, with only $\sim -0.7kT_e/e$ penetrating into the plasma—constituting the

ambipolar electric field required to help move the ions at each point along the SOL to the sink, figure 1.20.

1.8.2.10 Flow With/Without Friction

The above results, for the *simple SOL*, assumed no *true* drag, i.e. no viscous drag and no collisional drag due to neutrals. The rather modest drops of n and V along the SOL given by equations (1.50) and (1.53) then result. When frictional drag, e.g. due to collisions with neutrals, is significant the parallel pressure and potential gradients increase in order still to achieve sonic flow at the sheath edge in the face of such momentum losses, section 10.4, and quite large drops in n and V can then occur within the plasma.

1.8.2.11 The Validity of the Isothermal Fluid Assumption for the SOL

By assuming an isothermal fluid model of the SOL, it has been possible to develop a very simple and entirely analytic prescription for all the major features of the SOL, resulting in quite simple expressions for $n(x)$, $v(x)$, $V(x)$. But how reliable are such results? After all, this model neglects the following real effects, among others:

(a) there is a natural cooling of a flow as it accelerates to the sonic speed;
(b) self-collisional mean free paths can often be $\geq L$, making fluid treatments strictly invalid, section 9.12;
(c) viscous effects have been neglected. (We have already noted in the last section that frictional drag on the plasma due to neutral collisions can certainly have a major effect on the solution and that effect will have to be considered explicitly, section 10.4).

In this section we will show, by comparisons with other solutions; where the foregoing three effects have been allowed for, that these effects do not appreciably alter the results obtained from the isothermal fluid model, and that these results are therefore a good first approximation for the *simple SOL*, section 1.9, chapter 5.

Before proceeding, it should be noted that we are *not* considering here the effect on the SOL solution of the parallel temperature gradients which arise in the SOL due to the finite parallel heat conductivity of the edge plasma. This enormously important regime—the *conduction-limited regime*, section 1.9, which is of particular interest for divertor tokamaks—is dealt with separately, section 5.3. The parallel (ion) temperature gradient being considered here is that caused by the acceleration of the flow, which converts static pressure into dynamic pressure. This is a relatively small effect and of less consequence.

Chapter 10 discusses in detail other 1D plasma solutions where one or more of the following are included:

(a) the fluid approximation is replaced by a kinetic analysis where the complete ion velocity distribution $f_i(x, v)$ is calculated at each location x along the

flow rather than just the average quantities, n, v, p calculated in fluid modelling;

(b) the (ion) isothermal assumption is relaxed and acceleration cooling is allowed for;

(c) the effect of shear viscous drag in the SOL is allowed for (although this is strictly a 2D effect).

Results for the quantities of principal practical importance are given in table 1.2. It can be noted that the differences between these various 1D models are small, and indeed could probably not be measured with existing techniques. See chapter 10 for further discussion. Thus, the simple, isothermal fluid model is an adequate, convenient, analytical tool for describing the behaviour of the *simple SOL*, section 1.9.

1.8.2.12 Is Supersonic Plasma Flow Possible in the SOL?

It should not be concluded from the isothermal fluid model that supersonic plasma flow is actually impossible or even that the gradients of n, v, V, p necessarily have singularities in the plasma solution at the plasma–sheath interface. As will be shown in chapter 14, when temperature varies with x, a smooth transition to supersonic flow *upstream* of the plasma–sheath interface can occur.

Even for the isothermal model one can hypothesize a sufficiently exotic particle source distribution such that singularities do not occur when the flow reaches the sound speed. Consider, for example, the (admittedly rather improbable) source:

$$S_p = \frac{C(1 - M^2)}{2M(1 + M^2)} \tag{1.54}$$

with C some constant. Insertion of this value of S_p in equation (1.31) shows that the singularity is now avoided. This S_p allows for direct integration, giving the result:

$$M(x) = (\exp[(\ln 2)(x/L)] - 1)^{1/2}. \tag{1.55}$$

This solution for $M(x)$is plotted in figure 1.35, curve C, which clearly now has no singularity at $M = 1$. Reaching $M = 1$ as a result of such a source will not cause anything dramatic to happen that would cause us to think that the (quasineutral) plasma solution could not be extended further in space, i.e. that the sheath must start when M reaches unity.

Thus, it is not an absolutely general result—even when the isothermal assumption is made—that analysis of the *plasma* equations will guarantee that the sheath-edge velocity be sonic. In order to establish this critical matter more generally we must examine the *sheath* equations, which is done in the next chapter, resulting in the Bohm criterion.

Table 1.2. Calculated sheath related quantities from various models. $T_e = T_i$.

Quantity	Normal-ization factor	Model							
		1	2	3	4	5	6	7	Ave
1. Plasma density at sheath edge, n_{se}	n_0	0.50	0.40	0.60	0.52	0.50	0.50	0.43	0.51
2. Plasma flow velocity at sheath edge, v_{se}	$(2kT_0/m_i)^{1/2}$	1.00	1.13	0.95	0.90	1.05	1.03	0.88	0.99
3. Normalized potential at sheath edge, η_{se}	kT_0/e	−0.69	−0.72	−0.41	−0.65	−0.69	−0.69	−0.86	−0.67
4. Normalized (floating) wall potential, η_w	kT_0/e	−3.19	−3.08	−2.91	−3.26	−3.13	−3.15	−3.45	−3.17
5. Particle outflux density, Γ_{se}	$n_0(2kT_0/m_i)^{1/2}$	0.50	0.55	0.63	0.47	0.53	0.52	0.38	0.51

Models.

1. Isothermal fluid model, section 10.2 [1.32].
2. Adiabatic fluid model [1.32].
3. Kinetic model of Emmert *et al*., section 10.7 [1.33].
4. Kinetic model of Bissell *et al*., section 10.7[1.34].
5. Fluid, collisionless model, $T_\perp^i \neq T_\parallel^i$, section 10.8 [1.35].
6. Fluid, collisional model, $T_\perp^i = T_\parallel^i$, section 10.9 [1.35].
7. Kinetic model with cross-field viscosity, $\eta_\perp = nmD_\perp$ [1.36].

In order to make a valid comparison, the results of [1.33–1.35] were used for $T_e = T_\perp^i(0) = T_\parallel^i(0) \equiv T_0$, temperature at the symmetry point of the system (e.g., at $x = 0$ of a SOL, figure 1.20), rather than for the examples actually illustrated in [1.35], where $T_\parallel^i(0) < T_\perp^i(0)$; H^+ ions; no secondary electron emission; see chapter 10 for a more complete discussion of these comparisons.

1.9 Comparison of the Simple SOL and the Complex SOL

The most important distinguishing property among SOLs is the existence or absence of a *significant temperature drop along the length of the SOL*. When the plasma is essentially isothermal—along each individual flux tube—the SOL is said to be in the *sheath-limited regime*: the sheath is the only important element in the edge influencing the transport of particles and power from the confined plasma inside the separatrix to the solid surfaces. The acceleration of the flow to sonic speed at the sheath edge can involve a modest drop in temperature, chapter 9, as thermal energy is converted to kinetic energy of flow; however, we will still treat that as an essentially isothermal situation. By contrast, very large parallel temperature gradients can arise in the SOL owing to the *finite heat conductivity* of plasmas and the fact that the heat entering the SOL from the main plasma must traverse a considerable length, of order L, to reach the heat sink at the solid surface. It may seem surprising that classical parallel heat conductivity of a plasma could ever be a constraining factor, but it should be kept in mind that the SOL is much cooler than the core and classical conductivity varies as $T^{5/2}$, a quite strong function; see section 9.6. As will be shown in sections 4.10, 5.3, under a wide range of operating condition—particularly for divertors—the parallel temperature drop can be significant between the upstream location half-way between targets along the SOL, and the sheath edge in front of the target. This is called the *conduction-limited regime* (although the sheath continues to be an important element in this regime). Note that the term 'sheath limited' does *not* imply that T_e drops across the sheath: for both regimes T_e remains effectively constant across the sheath, see section 2.2.

The use of the term 'limited' should not be misunderstood: for magnetic fusion plasmas the power leaving the confined plasma is a *given, fixed* quantity, so far as the SOL is concerned, and the power will reach the solid surfaces regardless of what regime the SOL is in (ignoring direct volumetric power losses from the SOL, such as radiation). It is actually the SOL *plasma density* and *temperature* that are determined or 'limited' by the power entering the SOL, as well as other parameters.

While the presence or absence of a significant parallel temperature gradient is the single most important characteristic distinguishing SOL regimes, other factors, such as the presence or absence of ionization in the SOL, are also important. We thus also define the *simple SOL* as one which is not only in the sheath-limited regime but is characterized by a number of other features which simplify understanding and analysis, such as the absence of local ionization. The presence of such complicating factors is used to define the *complex SOL*, which would usually be in the conduction-limited regime also. More complete definitions of the simple and complex SOLs are given in chapter 4. The distinctions between simple and complex SOLs are summarized in table 1.3.

Table 1.3. The principal distinctions between simple and complex SOLs.

		Simple SOLs	Complex SOLs
1.	Parallel temperature gradients	$\nabla_\parallel T_{e,i} \approx 0$	$\nabla_\parallel T_{e,i} \neq 0$
2.	Thermal coupling of electrons and ions	de-coupled	coupled
3.	Particle source	cross-field transport from the main plasma	ionization within the SOL is important
4.	Volumetric sources and sinks of particles, momentum and energy in the SOL	none	can be important

Problems. Chapter 1

1.1. Find the value of safety factor q and θ_{pitch} at the LCFS for a circular JET-size tokamak: $B_\phi = 3$ T, $I_p = 3$ MA, $R = 3$ m, $a = 1.5$ m. During current 'start-up' and 'ramp-down' I_p changes greatly; consider the effect on $q(a)$.

1.2. Note from equation (1.1) that q is not a constant across the plasma, but depends on r, $q(r)$; $0 \leq r \leq a$. Assume $B_\phi =$ constant. The plasma current concentrates near the centre where the temperature is highest and therefore the electrical conductivity is highest. Find $B_\theta(r)$ assuming a plasma current density j_ϕ [A m^{-2}]:

$$j_\phi(r) = j_0\left[1 - \left(\frac{r}{a}\right)^2\right]^3.$$

Show that $q(a) = 4q(0)$, i.e. the q-value at the edge is four times larger than at the centre. Thus if $q(a) = 2$–3, which gives a stable tokamak, the core of the plasma has $q(0) < 1$, which is unstable. This results in internal disruptions which are observed as sawtooth temporal behaviour of the core temperature: the temperature on the axis builds up over a period of time then crashes down as the central confinement is destroyed, dumping the heat content of the core into the more peripheral regions of the main plasma. In the latter region inverse sawteeth are observed.

1.3. The magnetic field of a poloidal divertor tokamak. Consider two equal and parallel line-currents, I_p: one at $x = +a$ representing the plasma current (which, in reality, is spatially distributed; see problem 1.2) and one at $x = -a$, representing the divertor coil current:

(a) With the aid of the Biot–Savart law, sketch the pattern of $\boldsymbol{B}_\theta(x, y)$, approximately. The location where $\boldsymbol{B}_\theta = 0$ is the 'X-point'; where is it? Where would it be if $I_p(a) = 2I_p(-a)$?

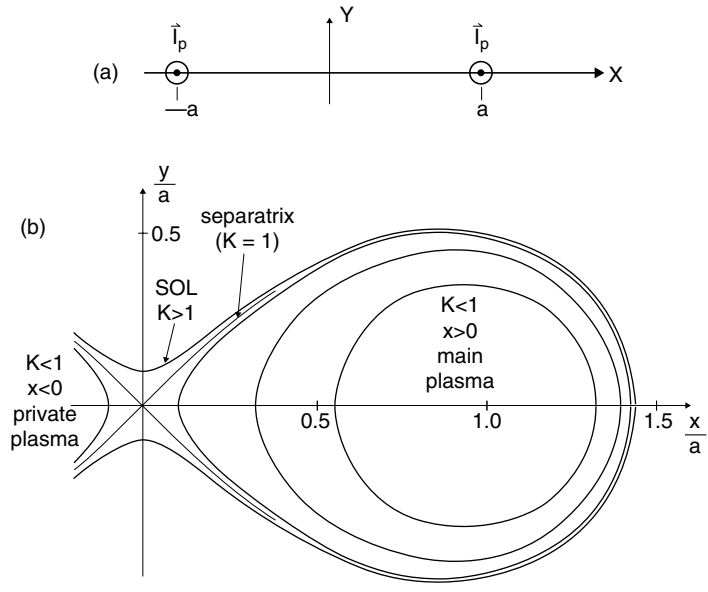

Figure 1.37. Problem 1.3. (a) Two parallel line currents create a poloidal divertor magnetic field. (b) The B_θ-field lines. K is a constant of integration whose value determines the location of the field line. (Figures (a) and (b) not to same scale.)

(b) Find $\boldsymbol{B}_\theta(x, y, I_p, a)$ using the Biot–Savart law.

(c) Thus show the slope of the tangent to $\boldsymbol{B}_\theta$ is:

$$y' \equiv \frac{\mathrm{d}y}{\mathrm{d}x} = \frac{x(a^2 - x^2 - y^2)}{y(a^2 + x^2 + y^2)}.$$

(d) Thus show that the equation of the contours of the B_θ-field lines is:

$$\frac{y}{a} = \pm\left[-\left(\frac{x}{a}\right)^2 - 1 + \left(4\left(\frac{x}{a}\right)^2 + K\right)^{1/2}\right]^{1/2}$$

where K is a different constant on each B_θ-line. Show that $K = 1$ for the separatrix; that the $K < 1$ lines are either the contours in the main plasma, or the contours in the private plasma; and that the $K > 1$ lines are in the SOL; see figure 1.37(b).

(e) Suppose a divertor target is created by inserting a solid plane at $x = 0$, extending in the $\pm y$-directions. (Is there a private plasma in this case? Would there be one if the solid plane were inserted at some location $x < 0$?) Let there be a toroidal magnetic field $\boldsymbol{B}_\phi$, in the same direction as I_p. For flux lines in the SOL, show that the distance $s_\parallel$ measured

along the (total-$\boldsymbol{B}$) line, starting at the target is:

$$s_{\|} = \int_0^x \frac{|\boldsymbol{B}|}{|\boldsymbol{B}_\theta|}(1 + (y')^2)^{1/2}\mathrm{d}x.$$

Is this expression valid all the way to the other target?

(f) Numerical problem: for $a = 2$ m, $I_p = 5$ MA, $B_\phi = 3$ T, $K = 1.1$, find the target-to-target distance, $s_{\|}^{\max}$. Find a simple estimate to compare this numerical value with. What is the value of $s_{\|}^{\max}$ for $K = 1$?

1.4. For a CMOD-size tokamak with $B_\phi = 9$ T, $R = 0.67$ m, $a = 0.22$ m, $I_p = 0.64$ MA, assume in turn:

(i) a limiter configuration consisting of three evenly spaced poloidal rings,
(ii) a single-null poloidal divertor (one X-point, as in figure 1.11).

Assume at the LCFS that $T = 20$ eV and $n_e = 8 \times 10^{19}$ m^{-3}. $D_\perp = 0.5$ m^2 s^{-1}.

(a) Estimate L.
(b) Estimate τ_{SOL} and compare this with the time required for a particle to diffuse from the centre of the main plasma to the LCFS.
(c) Compare τ_{SOL} with the ion–ion collision time, where $\tau_{ii}^{\mathrm{coll}} \approx \lambda_{ii}/v_i^{\mathrm{thermal}}$ and $v^{\mathrm{thermal}} = (8kT/\pi m)^{1/2}$. Is the SOL collisional?
(d) Estimate λ_{SOL}. Estimate the total volume occupied by the SOL and compare this with the volume of the main plasma. For this estimate assume λ_{SOL} remains constant all around the SOL.
(e) What is the plasma-wetted area? Compare it with the total wall area assuming the wall radius is 0.05 m larger than the radius of the LCFS. Find A_{wet} for the poloidal-limiter configuration if the leading edge of the limiter is bevelled at 10° to $\boldsymbol{B}$, as shown in figure 1.38.

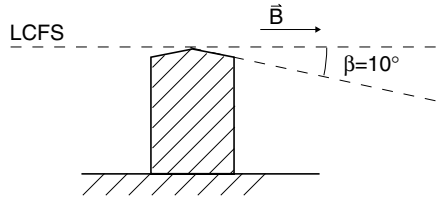

Figure 1.38. Problem 1.4. A beveled leading edge on a limiter distributes the heat load.

(f) For the limiter case it can be reasonable to assume that λ_{SOL} remains constant around the SOL. For the divertor case, as can be seen from figure 1.37(b), there exists an expansion of the separation of the magnetic flux surfaces at the target, relative to the typical value of the separation around most of the main plasma. Thus the value of λ_{SOL} for purposes of

deposition of particles and power on the target (the plasma-wetted area) is increased by a *flux expansion* factor, see section 5.6. Assume here that this factor is 5×. Find A_{wet} for the poloidal divertor configuration.

1.5. For the same parameters as assumed in problem 1.4:

(a) Find λ_{Debye} and compare with L.
(b) Estimate the E-field parallel to $\boldsymbol{B}$ in the SOL plasma.
(c) If at some point in the SOL the electrostatic potential $V = -15$ volts, with the reference potential $V = 0$ at the point where $n = n_0$, find n at that location in terms of n_0.
(d) What is the potential drop along the SOL from the midpoint to the edge of the sheath?
(e) Estimate the pressure gradient force (per particle) on the ions and electrons. Include signs.
(f) At the sheath edge find p_e, p_i [N m^{-2}].

1.6. The particle conservation equation, (1.15), assumes a steady-state. Re-develop this equation to allow for $\partial n/\partial t \neq 0$.

1.7. The momentum conservation equation, (1.20), neglects gravity. Assume gravity acts in the $+x$-direction and re-develop this equation to allow for $g \neq 0$.

1.8. The Boltzmann relation, equation (1.12), is strictly valid only if the electrons have no fluid velocity. Estimate the magnitude of the error involved in using the Boltzmann relation if, in fact, the electron fluid velocity is c_s, the isothermal plasma sound speed. Assume $T_e = T_i$ and that the ions in the plasma are D^+.

1.9. Derive equation (1.31).

1.10. Figure 1.39 is a plot of σ and $\overline{\sigma v}$, as functions of electron energy E (eV) for σ, and of electron temperature T (eV) for $\overline{\sigma v}$, for the ionization of H atoms by electron impact:

$$e + H \rightarrow 2e + H^+.$$

One can estimate $\overline{\sigma v}$ by $\sigma \overline{c}_e$, where $\overline{c}_e \equiv (8kT_e/\pi m_e)^{1/2}$, the thermal electron velocity. When is this likely to provide a good estimate? When not? Explain. Consider specifically the cases for 10, 100 and 1000 eV and comment.

1.11. Collision frequency $\nu_{\text{coll}} \equiv n_f \overline{\sigma v}$ where n_f is the density of 'field' particles that the 'test' particle is colliding with, e.g. electrons in the case of an H-atom test particle entering the plasma. The collisional mean free path of a test particle is $\lambda_{\text{mfp}} = v_t \tau_{coll}$, where v_t = velocity of the test particle and $\tau_{\text{coll}} \equiv \nu_{\text{coll}}^{-1}$.

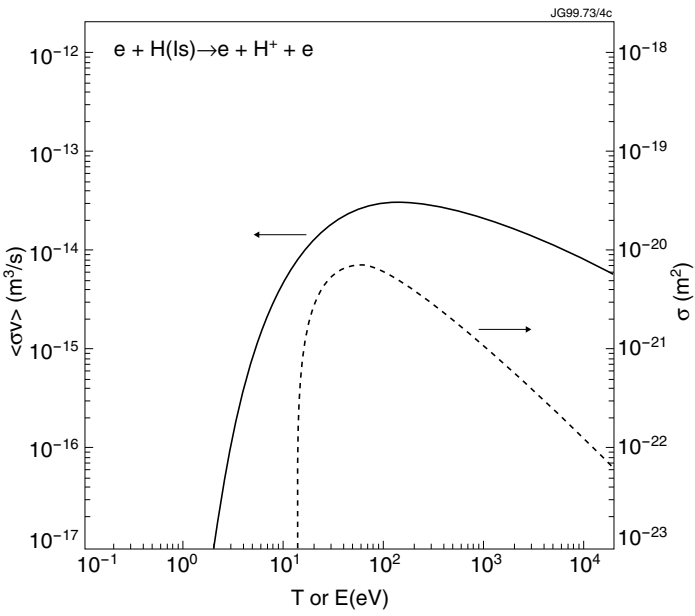

Figure 1.39. Problem 1.10. The electron-impact ionization cross-section and ionization rate for atomic hydrogen [1.26].

(a) Consider a 10 eV H-atom test particle entering a plasma of density 10^{19} m^{-3} and $T_e = T_i =$ (a) 8 eV, (b) 80 eV. Find ν_{coll}, τ_{coll} and λ_{mfp} for (a) ionization by electron impact (b) charge exchange. Compare and comment on the implications.

(b) Consider a 0.2 eV H_2-molecule test particle entering the same plasma, as in (a). Evaluate τ_{coll} and λ_{mfp} for the various processes that the H_2 experiences. Compare and comment.

1.12. At $t = 0$ a carbon atom is injected into a plasma of density 10^{19} m^{-3} and $T =$ (a) 10 eV, (b) 100 eV. If the C particle only stays in the plasma for dwell time 1 ms, a typical value of SOL dwell time, what charge state does the particle spend most time in? Ignore recombination (which, in fact, can be important).

1.13. Consider a radial profile of density in the SOL that is not the usual exponential but rather:

$$n(r) = n_0(1 - ar)\mathrm{e}^{-ar}$$

where $n_0 =$ density at the LCFS and $a = 100$ m^{-1}. For $n_0 = 10^{19}$ m^{-3}, $T = 20$ eV, constant across the SOL, and $D_\perp = 0.3$ m^2 s^{-1}, compare the cross-field particle source, $S_{p,c\text{-}f}$ and the ionization source $S_{p,iz}$ at $r = 0$ and $r = 0.01$ m, assuming $n_H = 10^{18}$ m^{-3}, constant across the SOL.

1.14. It is usually assumed that the plasma speed at the upstream end of the SOL, $x = 0$, is 0. Consider the case when the fluid is already moving at $x = 0$, with Mach number $M(0) = 1/2$. Assume this is caused by a source of ionization at the upstream end of the SOL, i.e. there is some ionization occurring within the SOL. Suppose that otherwise the SOL is supplied by a cross-field source. We want to calculate λ_{SOL} for this case.

(a) Show how equation (1.44) is altered in this case.
(b) Show how eqns. (1.46), (1.47) are altered.
(c) Show as $M(0) \rightarrow 1$, that $\lambda_{SOL} \rightarrow \infty$. Explain physically why this happens.

1.15. Consider a neon light: a cylindrical discharge tube of radius $r = 1$ cm, at pressure 2 torr. What is the electron temperature? Check that equation (1.45) is reasonably consistent with figure 1.34 for He using the fact that $\overline{\sigma v}_{iz} = 10^{-17}$ m^3 s^{-1} for $T_e = 4$ eV. Assume a neutral temperature of 300 K to relate neutral density and pressure.

1.16. Derive equation (1.48).

1.17. Show how the result for the particle flux density at the sheath edge, equation (1.51), would change if $M(0) = \frac{1}{2}$. Explain physically why the density drop along the SOL would disappear as $M(0) \rightarrow 1$.

1.18. Consider a plasma contained between two planes a distance 3 m apart; $n_e = 10^{19}$ m^{-3}, $T = 20$ eV. A transparent planar mesh is inserted at the midplane between the two end surfaces for purposes of applying an electrostatic potential difference across each half of the plasma, as shown in figure 1.40.

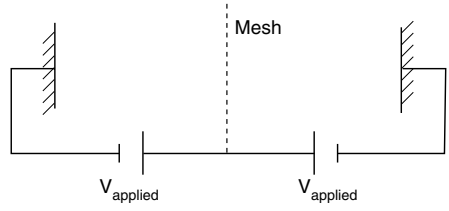

Figure 1.40. Problem 1.18. An electrostatic field applied to a planar plasma between solid electrodes with a central mesh.

For $V_{applied} = 100$ volts, calculate how much voltage drop occurs within the plasma and how much occurs across the sheaths at the end surfaces. For simplicity assume that no sheath develops at the mesh surface. Assume that the polarity is such as to bias the end plates at -100 volts relative to the plasma centre at $V = 0$. Estimate the magnitude of the electric field in the plasma and in the sheath; compare and comment.

1.19. Equation (1.31) shows that $\mathrm{d}M/\mathrm{d}x \to \infty$ as $M \to 1$. For the usual assumptions show that the gradients of n and V also become infinite as $M \to 1$. Show in each case whether the limit is $+\infty$ or $-\infty$. Give a physical interpretation of your findings.

1.20. Consider a one-dimensional, isothermal plasma flow with spatially varying particle source $S_p(x)$. Define a new independent variable y (1.38):

$$y \equiv \int_0^x S_p(x')\mathrm{d}x'.$$

(a) Show that $nv = y$, assuming stagnant upstream conditions.
(b) Show that the momentum equation (1.48) gives $vy + nc_s^2 =$ constant, and find the constant.
(c) Thus show that this gives the result of equation (1.50), $n/n_0 = (1 + M^2)^{-1}$, regardless of the form of $S_p(x)$.
(d) Show that $M(y)$ is also a universal result, independent of the form of $S_p(x)$, and is given by:

$$\frac{y}{c_s n_0} = \frac{M}{1 + M^2}.$$

(e) Evaluate $y(L)$ and thus show that:

$$M(y_n) = y_n^{-1} - [y_n^{-2} - 1]^{1/2}$$

where $y_n \equiv y/y(L)$.
(f) Find $M(x/L)$ and $n(x/L)$ for the case of $y \propto (x/L)^a$ where a is a positive parameter. Plot for $a = \frac{1}{3}$ and $a = 3$. Physically, what situation is indicated when $a \gg 1$? When $a \ll 1$?

1.21. Derive equation (1.55).

References

[1.1] Franklin R N *Gas Discharges* (Oxford: Oxford University Press)
[1.2] Wesson J 1997 *Tokamaks* 2nd edn (Oxford: Oxford University Press) p 108
[1.3] Wesson J 1997 *Tokamaks* 2nd edn (Oxford: Oxford University Press) p 111
[1.4] Wesson J 1997 *Tokamaks* 2nd edn (Oxford: Oxford University Press) p 280
[1.5] Wesson J 1997 *Tokamaks* 2nd edn (Oxford: Oxford University Press) p 186
[1.6] Stangeby P C 1986 *Physics of Plasma–Wall Interactions in Controlled Fusion* ed D E Post and R Behrisch (New York: Plenum) p 41
[1.7] Stangeby P C and McCracken G M 1990 *Nuclear Fusion* **30** 1225
[1.8] Wagner F and Lackner K *Physics of Plasma–Wall Interactions in Controlled Fusion* ed D E Post and R Behrisch (New York: Plenum) p 931
[1.9] Wesson J 1997 *Tokamaks* 2nd edn (Oxford: Oxford University Press) p 145
[1.10] Wesson J 1997 *Tokamaks* 2nd edn (Oxford: Oxford University Press) p 129
[1.11] Wesson J 1997 *Tokamaks* 2nd edn (Oxford: Oxford University Press) p 666.

[1.12] Chodura R *Physics of Plasma–Wall Interactions in Controlled Fusion* ed D E Post and R Behrisch (New York: Plenum) p 99
[1.13] Reiter D 1992 *J. Nucl. Mater* **196–198** 80
[1.14] Grosman A, Ghendrih P, De Michelis C *et al* 1992 *J. Nucl. Mater* **196–198** 59
[1.15] De Grassie J S, Ohyabu N and Brooks N H 1984 *J. Nucl. Mater* **128–129** 266
[1.16] Ghendrih Ph, Grosman A and Capes H 1996 *Plasma Phys. Control. Fusion* **38** 1653
[1.17] Boedo J A, Shoji T, Sakawa Y *et al* 1997 *J. Nucl. Mater* **241–243** 857
[1.18] Pitcher C S, Stangeby P C, Budny R V *et al* 1992 *Nucl. Fusion* **32** 239
[1.19] Ulrickson M 1990 The JET Team and the TFTR Team *J. Nucl. Mater* **176–177** 44
[1.20] Goldston R J and Rutherford P H 1997 *Introduction to Plasma Physics* (Bristol: Institute of Physics Publishing) p 13
[1.21] Goldston R J and Rutherford P H 1997 *Introduction to Plasma Physics* (Bristol: Institute of Physics Publishing) pp 14 and 111
[1.22] Holt E H and Haskell R E 1965 *Foundations of Plasma Dynamics* (New York: Macmillan) p 134
[1.23] Jones E M 1977 *Culham Laboratory Report CLM-R* 175
[1.24] Summers H P 1994 *Atomic Data Analysis Structure (ADAS User Manual)* JET. ADAS figures produced by M O'Mullane
[1.25] Goldston R J and Rutherford P H 1997 *Introduction to Plasma Physics* (Bristol: Institute of Physics Publishing) p 151
[1.26] Janev R K, Langley W D, Evans K Jr and Post D E Jr 1987 *Elementary Processes in Hydrogen-Helium Plasmas* (Berlin: Springer)
[1.27] Self S A 1963 *Phys. Fluids* **6** 1762
[1.28] D Bohm 1949 in *The Characteristics of Electrical Discharges in Magnetic Fields* ed A Guthrie and R K Wakerling (New York: McGraw-Hill) Chap 3
[1.29] von Engel A 1965 *Ionized Gases* (Oxford: Oxford University Press) 2nd edn p 243
[1.30] Ruzic D N, Heifitz D B and Cohen S A 1987 *J. Nucl. Mater* **145–147** 527
[1.31] Wesson J 1997 *Tokamaks* 2nd edn (Oxford: Oxford University Press) p 670
[1.32] Bissell R C, Johnson P C and Stangeby P C 1989 *Phys. Fluids* B **1** 1133
[1.33] Emmert G A, Wieland R M, Mense A T *et al* 1980 *Phys. Fluids* **23** 803
[1.34] Bissell R C and Johnson P C 1987 *Phys. Fluids* **30** 779
[1.35] Scheuer J T and Emmert G A 1990 *Phys. Fluids* B **2** 445
[1.36] Chung K-S and Hutchinson I H 1988 *Phys. Rev.* A **38** 4721
[1.37] McCracken G M and Stott P E 1979 NF **19** 889
[1.38] Thanks to Ian Hutchinson for this suggestion

Chapter 2

The Role and Properties of the Sheath

2.1 The Bohm Criterion. Historical Background

The space within the vessel occupied by the charged particles consists of two regions, Figure 2.1:

(a) the *plasma* which usually fills the vast majority of the available space. The plasma is by definition the region where $n_e = n_i$ (for the case of singly charged ions, otherwise $n_e = \sum_i n_i Z_i$, sum over all ions), i.e. the plasma is electrically *neutral*, or at least $n_e \approx n_i$, i.e. *quasineutrality* holds;
(b) the *sheath* is a region of *net charge*, usually in a thin region adjacent to a solid surface and $n_e < n_i$ in the sheath.

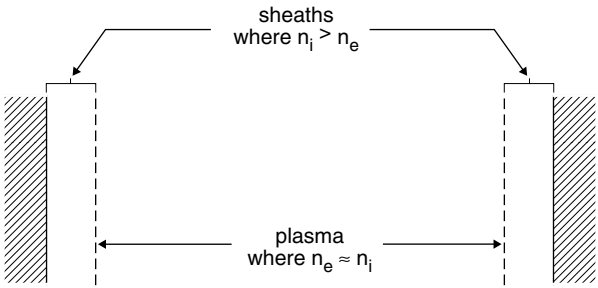

Figure 2.1. The space available to charged particles is divided into the quasineutral *plasma* and the *sheath*, which is characterized by net (positive) space-charge density.

We will later consider the justification of this simplification and will show that it is often an excellent approximation to the actual situation, where in reality no crisp distinction exists between plasma and sheath and no precisely defined sheath edge exists.

When we analysed the *plasma* side and assumed $n_e = n_i$ *precisely*, we found for the simplest assumption—of an *isothermal fluid model with a particle source*

proportional to n—that the plasma fluid velocity could not *exceed* the (isothermal) sound speed, $c_s = [k(T_e + T_i)/m_i]^{1/2}$, without singularities arising, i.e. the plasma solution 'blows up' with $\mathrm{d}v/\mathrm{d}x$, $\mathrm{d}n/\mathrm{d}x$, $\mathrm{d}V/\mathrm{d}x \to \pm\infty$, section 1.8.2.5. Thus we conclude, at least for these assumptions, that:

$$v_{se} \leq c_s \tag{2.1}$$

where the subscript 'se' denotes the sheath edge. By analysing the sheath side of the plasma–sheath interface (plasma–sheath edge), we will now show, following Bohm [2.1], that

$$\boxed{v_{se} \geq c_s.} \tag{2.2}$$

We will thus conclude that the only possibility is:

$$v_{se} = c_s \tag{2.3}$$

at least for the above assumptions. Relation (2.2) is called the *Bohm criterion*. Sometimes, incorrectly, equation (2.3) is called the Bohm criterion, but this is not the most general result.

In the next section we will give a derivation of relation (2.2) for the simple case where $T_i = 0$, following Bohm in that regard. Historically this is an important case and, in fact, gives a more interesting (surprising) result than occurs when $T_e \approx T_i$. Non-magnetic, low pressure discharges—which have been much studied since the 19th century, and which have, in fact, been used to establish a number of the basic findings of modern physics—are characterized by $T_e \gg T_i \approx T_{\text{ambient}}$ [2.2]. This weak energy-coupling between the electrons and ions is due to:

(a) the fact that ohmic heating power, P_{ohmic}, goes preferentially into the lighter charged species; $P_{\text{ohmic}} = \sigma E^2$, where the electrical conductivity $\sigma \propto m^{-1/2}$ [2.3];
(b) energy-transfer collision times between particles of dissimilar mass can be quite long, $\tau_{ei}^{\text{Energy}} = (m_i/m_e)\tau_{ee}^{\text{Energy}}$ [2.4], and longer than the characteristic time for electron energy gain by ohmic heating and energy loss by inelastic, e.g. excitation, collisions and wall collisions (at least at low pressures; in high pressure discharges, e.g. lightning, $T_e \approx T_i$ [2.2]). In magnetically confined discharges $T_e \approx T_i$ can hold due to the much increased loss times to the walls.

For plasmas where $T_e \approx T_i$, it may not be thought too surprising that the ion flow velocity to a (perfectly absorbing) wall would be of the order $(kT/m_i)^{1/2}$ since that is, approximately, the ordinary gas sound speed—and, intuitively, one anticipates that something like sonic velocities would characterize fluid flow into an all-absorbing sink. For plasmas with $T_e \gg T_i$, however, the intuitive expectation that the exit velocity of the ions would be $\approx (kT_i/m_i)^{1/2}$ turns out to be quite wrong. The fact that $v_{\text{exit}}^{\text{ion}} \gg (kT_i/m_i)^{1/2}$ for low pressure discharges had been

established experimentally by the early decades of the 20th century [2.5], but it was not for a long time understood. It was Irving Langmuir, first Nobel Prize Winner in plasma physics—and the originator of the term 'plasma' to describe the fourth state of matter [2.6]—who first showed why the ion exit velocity is related to the *electron* temperature, not the ion temperature (when $T_e \gg T_i$). This was demonstrated in 1929 [2.5] from an analysis of the *plasma* equations (see section 10.6) and was not as definitive as Bohm's 1949 [2.1] analysis which was carried out from the *sheath* side.

We may well ask: 'Why does $v_{\text{exit}}^{\text{ion}}$ have anything to do with T_e?'. The answer lies in the *ambipolar electric field* which spontaneously arises within a plasma which is bounded by electrically isolated, i.e., *electrically floating*, absorbing walls, and because electrons have very high thermal velocities compared with ions. The resulting negative charge on the wall adjusts itself spontaneously to bring about an equal ion and electron loss to the walls, in steady state; figure 2.2. This results in an *electrically floating wall potential* V_w which is sufficient to significantly inhibit the free Maxwellian electron outfluxes. This requires that V_w be of order $-kT_e/e$, and it means, generally, that the changes of electrostatic potential along the plasma, scale as kT_e/e, rather than as kT_i/e, say. The ions experience the same potential changes, but for them an *acceleration* is involved, and hence they gain energy on the scale of kT_e, i.e. $v_{\text{exit}}^{\text{ion}}$ is of the order $(kT_e/m_i)^{1/2}$.

While this plausibility argument correctly gives a rough estimate of $v_{\text{exit}}^{\text{ion}}$—and does correctly identify the ambipolar electric field as the cause—it is too crude to tell us whether this is the velocity at the *plasma–sheath* edge—or the velocity right at the wall. And what if the wall is electrically biased relative to the

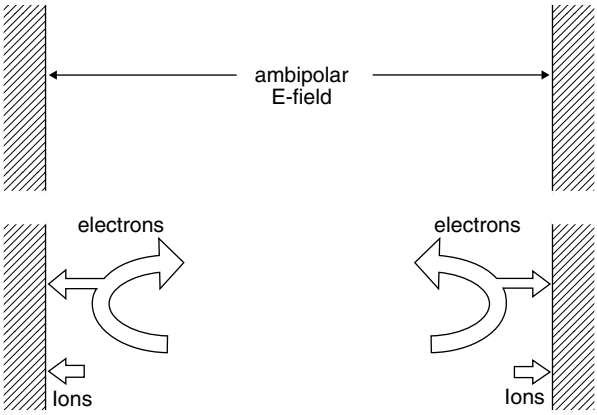

Figure 2.2. If the walls are electrically isolated (floating) an ambipolar electric field spontaneously arises within the plasma and sheath, bringing about zero net outflow of charge to the walls in steady state (1D system). Only a small fraction of the wall-directed electrons reach the wall on the first try, but all of the ions do.

plasma using an external power supply, rather than being allowed to float? (The result turns out to be the same, so long as the surface is not biased so positively as to repel ions, section 2.6.) We will need a more careful treatment in order to proceed further.

2.2 The Maxwellian Velocity Distribution

The sheath is so thin that it is usually collisionless. Many sheath properties are therefore related to Maxwellian fluxes. We will therefore step back for a moment from our development of sheath analysis, for a somewhat extended aside on the properties of Maxwellian distributions.

When a set of identical gas or plasma particles is left alone to interact solely with each other, collisionally—without other forces being present, and with none of the particles being lost from the system, nor new ones introduced—then after a length of time greater than the self-collisional time a *steady state* called *thermodynamic equilibrium* results from this *self-collisionality*—characterized by a *Maxwellian velocity distribution* $f^{\mathrm{Max}}(\boldsymbol{v})$. It can be proven rigorously [2.7] that f^{Max} *must* be of the form:

$$f^{\mathrm{Max}}(v_x, v_y, v_z) = c\exp[-b(1/2)m\{(v_x-a_x)^2+(v_y-a_y)^2+(v_z-a_z)^2\}] \quad (2.4)$$

with no other dependences being possible; a_x, a_y, a_z, b, c are constants whose physical meaning we will identify below, m is the mass of each particle and $f(v_x, v_y, v_z)\mathrm{d}v_x\mathrm{d}v_y\mathrm{d}v_z$ is the number of particles with velocity in [v_x to $v_x+\mathrm{d}v_x$, v_y to $v_y+\mathrm{d}v_y$, v_z to $v_z+\mathrm{d}v_z$]. All velocities are possible, $-\infty < v_{x,y,z} < +\infty$. $\boldsymbol{v} \equiv (v_x, v_y, v_z)$. $\mathrm{d}\boldsymbol{v} \equiv \mathrm{d}v_x\mathrm{d}v_y\mathrm{d}v_z$. Note that at this stage the concept of 'temperature' has not yet appeared, and it still remains for us to *define* 'temperature' and its relation to these, otherwise unknown, constants.

When any of $a_x, a_y, a_z \neq 0$ we have the *drifting Maxwellian distribution*, with *drift* or *mean* velocity $\boldsymbol{v}_{\mathrm{mean}} = (a_x, a_y, a_z)$, as will be shown below. For the moment we take the special case of $\boldsymbol{v}_{\mathrm{mean}} = \boldsymbol{0}$, giving the ordinary Maxwellian distribution.

We may transform to spherical (velocity) coordinates by defining the particle *speed*:

$$w \equiv (v_x^2 + v_y^2 + v_z^2)^{1/2} \quad (2.5)$$

$$0 \leq w < +\infty \quad (2.6)$$

giving

$$f^{\mathrm{Max}}(w)\mathrm{d}w = 4\pi w^2 c\exp[-b(1/2)mw^2]\mathrm{d}w. \quad (2.7)$$

We require that $\int_0^\infty f^{\mathrm{Max}}(w)\mathrm{d}w = n$, the number of particles m^{-3} as a *normalization*. We may use the table of integrals, table 2.1, to then show that the constants b and c are related by:

$$c = n(mb/2\pi)^{3/2}. \quad (2.8)$$

Table 2.1. Some useful integrals.

n	$\int_0^\infty \mathrm{d}x x^n \mathrm{e}^{-\alpha x^2}$	$\int_{-\infty}^\infty \mathrm{d}x x^n \mathrm{e}^{-\alpha x^2}$	$\int_0^\infty \mathrm{d}y y^{\frac{n-1}{2}} \mathrm{e}^{-\alpha y}$
0	$\frac{\pi^{1/2}}{2\alpha^{1/2}}$	$\frac{\pi^{1/2}}{\alpha^{1/2}}$	$\frac{\pi^{1/2}}{\alpha^{1/2}}$
1	$\frac{1}{2\alpha}$	0	$\frac{1}{\alpha}$
2	$\frac{\pi^{1/2}}{4\alpha^{3/2}}$	$\frac{\pi^{1/2}}{2\alpha^{3/2}}$	$\frac{\pi^{1/2}}{2\alpha^{3/2}}$
3	$\frac{1}{2\alpha^2}$	0	$\frac{1}{\alpha^2}$
4	$\frac{3\pi^{1/2}}{8\alpha^{5/2}}$	$\frac{3\pi^{1/2}}{4\alpha^{5/2}}$	$\frac{3\pi^{1/2}}{4\alpha^{5/2}}$
5	$\frac{1}{\alpha^3}$	0	$\frac{2}{\alpha^3}$
6	$\frac{15\pi^{1/2}}{16\alpha^{7/2}}$	$\frac{15\pi^{1/2}}{8\alpha^{7/2}}$	$\frac{15\pi^{1/2}}{8\alpha^{7/2}}$

We may *define* the *temperature* T of a set of gas or plasma particles in a very simple, convenient and physically obvious way as being that quantity which satisfies the definition equation:

$$\tfrac{3}{2}nkT \equiv n\big\langle \tfrac{1}{2}m(v_x^2 + v_y^2 + v_z^2)\big\rangle \equiv \int f(\boldsymbol{v})\big(\tfrac{1}{2}m(v_x^2 + v_y^2 + v_z^2)\big)\mathrm{d}\boldsymbol{v} \qquad (2.9)$$

where k is a constant (the Boltzmann constant) which is required here if we want to render this definition of 'temperature' consistent with the standard, but less physically obvious, definition based on the freezing point of water at atmospheric pressure being 273 K. (If we only ever dealt with monatomic gases or plasmas, where the only random or 'thermal' energy is that associated with the $\boldsymbol{v}$, centre of mass velocities of the particles—then presumably the definition of 'temperature' would simply have been taken to be $\big\langle \frac{1}{2}m(v_x^2 + v_y^2 + v_z^2)\big\rangle$ [joules]. And thus, we might say: 'It's not too hot out today, only 6 maJ', i.e. 16 °C (maJ ≡ milli attojoules)). One apparently could have done without the factor $3/2$ in equation (2.9), just absorbing it into the constant; however, from statistical mechanics it can be shown (2.8) that when other types of thermal energy, 'modes', are also possible—for example rotational and vibrational modes for diatomic molecules—then each energy mode has, on average, $1/2kT$ of energy in equilibrium. The $3/2$ in equation (2.9) is then seen to be due to the three independent velocity components.

Strictly the word 'temperature' should be restricted to cases where f is a Maxwellian (or possibly a drifting one); however, it is not uncommon for equation (2.9) to be used to define the 'temperature' of even non-Maxwellian distributions, a practice we follow here.

Use of table 2.1, then shows that

$$b = 1/kT \tag{2.10}$$

thus

$$c = n(m/2\pi kT)^{3/2}. \tag{2.11}$$

Hence

$$f^{\text{Max}}(w) = n(\beta/\pi)^{3/2} 4\pi w^2 \exp(-\beta w^2) \tag{2.12}$$

where

$$\beta \equiv m/2kT \tag{2.13}$$

also:

$$\boxed{f^{\text{Max}}(\boldsymbol{v}) = n(\beta/\pi)^{3/2} \exp(-\beta(v_x^2 + v_y^2 + v_z^2))} \tag{2.14}$$

or, when $\boldsymbol{v}_{\text{mean}} \neq \mathbf{0}$

$$\boxed{f^{\text{drift Max}}(\boldsymbol{v}) = n(\beta/\pi)^{3/2} \exp[-\beta\{(v_x - a_x)^2 + (v_y - a_y)^2 + (v_z - a_z)^2\}].} \tag{2.15}$$

(It is easily confirmed that none of the foregoing derivations required that $\boldsymbol{v}_{\text{mean}} = \mathbf{0}$.)

Of course, introducing temperature in the preceding way reverses the order in which students usually first encounter Maxwellian distributions where we *start* by assuming that equation (2.14) describes the distribution, with temperature already embedded in the expression. That approach, however, leaves this fundamental quantity—'temperature'—undefined, or at least makes it harder to define.

One can now readily show that

$$\langle v_x \rangle \equiv (1/n) \int_{-\infty}^{\infty} f^{\text{Max}}(\boldsymbol{v}) v_x \mathrm{d}v = a_x \tag{2.16}$$

thus confirming that (a_x, a_y, a_z) is, indeed, the mean drift velocity of the distribution.

It should be emphasized that, strictly, the only velocity distributions possible in complete *thermodynamic equilibrium* are either an ordinary, or a drifting, Maxwellian [2.7].

We also have the *Maxwellian energy distribution*:

$$f^{\text{Max}}(E)\mathrm{d}E = 2\pi^{-1/2}(kT)^{-3/2} n E^{1/2} \mathrm{e}^{-E/kT} \mathrm{d}E \tag{2.17}$$

obtained from

$$E = \tfrac{1}{2} m w^2 \tag{2.18}$$

and

$$\mathrm{d}w = (2/m)^{1/2} \mathrm{d}E/2E^{1/2} \tag{2.19}$$

where $f^{\text{Max}}(E)\mathrm{d}E$ is the number of particles with (thermal) kinetic energy within E to $E + \mathrm{d}E$.

By integrating over v_y and v_z one also obtains the *1D Maxwellian distribution*:

$$f^{\text{1D Max}}(v_x) = n_0(\beta/\pi)^{1/2}\mathrm{e}^{-\beta v_x^2} \qquad -\infty < v_x < +\infty. \tag{2.20}$$

It is straightforward to show that the *average particle speed, or thermal speed*, for the non-drifting Maxwellian is

$$\langle w \rangle \equiv \int_0^\infty w f^{\text{Max}}(w)\mathrm{d}w/n$$
$$\boxed{= (8kT/\pi m)^{1/2} \equiv \bar{c}.} \tag{2.21}$$

Next, we find the *one-way particle flux density* in the x-direction for an ordinary Maxwellian. We note first that the increment of density with velocity (v_x, v_y, v_z) is:

$$\delta n = f(\boldsymbol{v})\mathrm{d}v_x\mathrm{d}v_y\mathrm{d}v_z \tag{2.22}$$

thus the increment of particle flux density in the x-direction is:

$$\delta\Gamma_x = v_x\delta n = v_x f(\boldsymbol{v})\mathrm{d}v_x\mathrm{d}v_y\mathrm{d}v_z. \tag{2.23}$$

Hence

$$\Gamma_x^{\text{Max}} \equiv \int_{v_x=0}^{+\infty} f^{\text{Max}}(\boldsymbol{v})v_x\mathrm{d}v_x \int_{v_y=-\infty}^{+\infty} \mathrm{d}v_y \int_{v_z=-\infty}^{+\infty} \mathrm{d}v_z \tag{2.24}$$

giving:

$$\boxed{\Gamma_x^{\text{max}} = \tfrac{1}{4}n\bar{c}}$$

using table 2.1. Note that the v_x-integral is only over $[0, +\infty)$; the *total* or *net* (both way) particle flux density is zero for an ordinary Maxwellian.

One may note that for a drifting Maxwellian, equation (2.15), there *is* of course a total or net particle flux density in the x-direction:

$$\Gamma_x^{\text{drift Max}} = \int_{v_x=-\infty}^{+\infty} f^{\text{drift Max}}(\boldsymbol{v})v_x\mathrm{d}v_x \int_{-\infty}^{+\infty} \mathrm{d}v_y \int_{-\infty}^{+\infty} \mathrm{d}v_z$$

giving:

$$\boxed{\Gamma_x^{\text{drift Max}} = na_x = n\langle v_x \rangle.} \tag{2.25}$$

One notes, therefore, the important distinction between the one-way particle flux density due to random, *thermal motion* of particles, and the net particle flux density due to average or *fluid* velocity. The integral in equation (2.25) is called the *first moment of the distribution*. Recall the similar-looking result

in section 1.8.2.1, $\Gamma = nv$, figure 1.22. The latter, however, is more general than equation (2.25) which has been obtained for the specific case of a drifting Maxwellian distribution. It is not necessary to assume in fluid modelling that a drifting Maxwellian 'lies behind things', although that can often be a useful picture.

The next 'moment' of the velocity distribution gives the *flux of x-momentum in the x-direction*, which is called the 'pressure' for reasons which will shortly be seen. The increment of x-momentum in the x-direction is the product of the increment of x-directed particle flux density, $\delta\Gamma_x$, multiplied by the x-momentum of each particle, mv_x:

$$mv_x\delta\Gamma_x = (mv_x)v_x f(\boldsymbol{v})\mathrm{d}v_x\mathrm{d}v_y\mathrm{d}v_z. \tag{2.26}$$

This time the integral over dv_x is from $-\infty$ to $+\infty$ because momentum is a *vector* quantity and so the *back*-flux of *backward*-going momentum counts additively with the forward-flux of forward-going momentum. This is perhaps seen more clearly by considering an elemental volume and the flux of mv_x-momentum across the upstream face, for example. Clearly the volume is gaining, i.e. '*importing*', mv_x-momentum due to the part of the distribution for which $v_x > 0$. However, it is also *exporting negative* mv_x-momentum due to the part of the distribution for which $v_x < 0$. The 'export' of negative momentum has the same effect as the 'import' of positive momentum. We may also consider the situation at the perfectly reflecting walls (perfectly reflecting so as not to remove or add energy, i.e. the gas/plasma is in thermal equilibrium with its surroundings): particles can only strike the wall from the one side, thus we now have a v_x-integral only over 0 to $+\infty$; however, the *change* of momentum experienced by the gas/plasma is $2mv_x$ per collision since the reflection is perfect. It is readily shown that the integral of $mv_x\delta\Gamma_x$ from $-\infty$ to $+\infty$ is the same as $2mv_x\delta\Gamma_x$ from 0 to $+\infty$. We also now see why this momentum flux is termed the '*pressure*' since it is equal to the force per unit area exerted on the walls: momentum lost by the gas/plasma equals that gained by the walls. Thus pressure:

$$p = \int_{v_x=-\infty}^{+\infty}(mv_x)v_x f(\boldsymbol{v})\mathrm{d}v_x \int_{v_y=-\infty}^{+\infty}\mathrm{d}v_y \int_{v_z=-\infty}^{+\infty}\mathrm{d}v_z \tag{2.27}$$

and using table 2.1, and for $f = f^{\mathrm{Max}}$, it is readily shown to give the familiar *ideal gas* result:

$$\boxed{p = nkT.} \tag{2.28}$$

We may note that pressure has nothing directly to do with self-collisions.

For an ordinary Maxwellian one obtains the same pressure for the other directions, i.e. the pressure is *isotropic*. For non-Maxwellian distributions one may have different pressures in different directions; also one needs to consider, for example, the x-directed flux of mv_y-momentum, which may integrate to a non-zero value. Then a pressure *tensor*, rather than the foregoing pressure *scalar*, is involved and the pressure is *anisotropic* [2.9].

A further 'moment' of the distribution is the *thermal energy density* 'stored' in each m^3:

$$\boxed{\overline{E} = \tfrac{3}{2}nkT} \tag{2.29}$$

while the *one-way heat flux density* for a Maxwellian is

$$\begin{aligned} q_x^{\text{Max}} &= \int_{v_x=0}^{+\infty} \tfrac{1}{2}m(v_x^2 + v_y^2 + v_z^2)v_x f^{\text{Max}}(\boldsymbol{v})\mathrm{d}v_x \int_{v_y=-\infty}^{+\infty} \mathrm{d}v_y \int_{v_z=-\infty}^{+\infty} \mathrm{d}v_z \\ &= \left(1kT + \tfrac{1}{2}kT + \tfrac{1}{2}kT\right)\tfrac{1}{4}n\overline{c} = 2kT\left(\tfrac{1}{4}n\overline{c}\right) = 2kT\Gamma_x^{\text{Max}} \\ &\boxed{2kT\Gamma_x^{\text{Max}} = q_x^{\text{Max}}.} \end{aligned} \tag{2.30}$$

It may seem surprising that the amount of transported energy is $2kT$ per particle, not just $(3/2)kT$, as it was for the 'stored' energy density. One obtained, in fact, just $(1/2)kT$ from each of the $\mathrm{d}v_y$ and $\mathrm{d}v_z$ integrals in equation (2.30), while it was the v_x-integral that gave $1kT$, for the total of $2kT$. It is the extra weighting given to the higher v_x-particles in the distribution that, through the v_x^3 term in the integral of equation (2.30) (contrasting only v_x^2 in the integral giving equation (2.29)), gives $1kT$, rather than $(1/2)kT$. It will be seen later, section 10.7, that if one wants to *create* particles which will have a Maxwellian distribution, then the energy required to be invested by the source per particle is not $(3/2)kT$, but $2kT$, for this reason.

We may note that the v_x-integral is over 0 to $+\infty$, as it was for equation (2.24), but contrasts with the $-\infty$ to $+\infty$ domain for p, equation (2.27), where a scalar quantity, $\frac{1}{2}m(v_x^2 + v_y^2 + v_z^2)$, was involved. Also note that q_x^{Max} is very close to the standard definition of the *conducted heat flux density* $q_{\text{cond},x}$ which is the same as equation (2.30) except that the v_x-integral is from $-\infty$ to $+\infty$, and any general $f(\boldsymbol{v})$ may be inserted. For $f = f^{\text{Max}}$ then, due to symmetry, one obtains $q_{\text{cond},x} = 0$ (only odd powers of v_x are involved in the integral). In general $f(\boldsymbol{v})$ may be asymmetric, however, and that will then give $q_{\text{cond},x} \neq 0$. Still higher 'moments' can also be evaluated, but we leave the sequence here.

For the *drifting Maxwellian*, equation (2.15), a net, forward power flux does exist. It is readily shown that:

$$q_{x,\text{net}}^{\text{drift Max}} = \left(\tfrac{5}{2}kT + \tfrac{1}{2}ma_x^2\right)na_x$$

$$\boxed{q_{x,\text{net}}^{\text{drift Max}} = \left(\tfrac{5}{2}kT + \tfrac{1}{2}ma_x^2\right)\Gamma_{x,\text{net}}} \tag{2.31}$$

where, as before:

$$\Gamma_{x,\text{net}} = na_x. \tag{2.32}$$

We consider next what happens to a set of particles subject to an external *conservative* force field, such as gravity or an electrostatic force. We will show

that the *distribution remains Maxwellian*, and only the density changes, satisfying a *Boltzmann factor* relation.

That is we will show that the distribution is given by:

$$f(\boldsymbol{v}, x) = n_0(\beta/\pi)^{3/2} \exp[-\beta(v_x^2 + v_y^2 + v_z^2)] \exp[-\Phi(x)/kT] \qquad (2.33)$$

where Boltzmann factor $\equiv \exp[-\Phi(x)/kT]$ and n_0 is the reference value of density at $\Phi = 0$. Thus for an electric potential $\Phi = qV$ the Boltzmann factor is

$$\mathrm{e}^{-qV/kT}$$

where q is the charge on the particle. A '*potential trough*' exists for electrons in regions where V decreases—say in the approach to a negatively charged solid surface—since the electron density decreases as the wall is approached, i.e., for electrons, with charge $-e$, the Boltzmann factor is e^{eV/kT_e}. It is to be noted, however, that *the velocity distribution remains Maxwellian at each point in space and T_e is spatially constant*.

The Boltzmann factor can be demonstrated [2.10] from the steady-state, 1D kinetic equation, section 9.2, which for electrons without any source or sink of particles is:

$$\boxed{v_x \frac{\partial f}{\partial x} + \frac{eE}{m} \frac{\partial f}{\partial v_x} = \left.\frac{\partial f}{\partial t}\right|_{\text{coll}}.} \qquad (2.34)$$

One can show that $f = f^{\text{Max}}\mathrm{e}^{-\Phi/kT}$ satisfies this equation: since $\mathrm{e}^{-\Phi/kT}$ is independent of velocity and since insertion of f^{Max} into $\partial f/\partial t|_{\text{coll}}$ gives zero, then insertion of f will also. It is easy to show that f then satisfies the residual equation.

In practice, there is almost always a source and sink of particles present. The situation that we are most interested in, in edge plasma physics, involves electrons *almost* perfectly trapped in a potential well caused by the presence of negatively charged walls. The trapping, however, is not perfect; indeed for a floating wall the outflow of electrons from the plasma equals the ionic outflow. For the ions, this loss process *strongly* distorts the ion velocity distribution, which is very far from Maxwellian at the sheath edge, section 25.1. The distortion is strong for the ions because there are no backward-going ions at the sheath edge; also, the mean ion velocity is c_s, which is often of the same order as the ion sound (thermal) speed $\overline{c}_i \equiv (8kT_i/\pi m_i)^{1/2}$. While the electrons have the same mean speed as the ions, this is very small compared with $\overline{c}_e$ and the electron distribution may deviate only slightly from Maxwellian. Thus the Boltzmann factor is often an excellent approximation for the electrons—in situations where it would be grossly in error for the ions.

2.3 The Bohm Criterion; $T_i = 0$. Simple Derivation

We return now to the analysis of the sheath, starting with the simplest possible case. Consider the *sheath* where $n_e \neq n_i$. For the electron density we assume

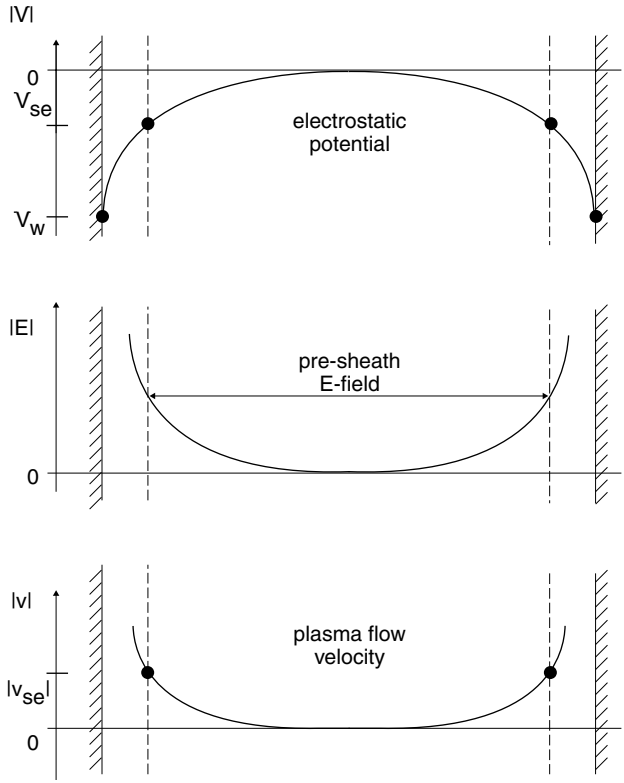

Figure 2.3. The potential drop within the plasma, V_{se}, constitutes the pre-sheath E-field which accelerates the ions to speed v_{se} at the sheath edge (se). We wish to find the values of v_{se} and V_{se}.

that the Boltzmann factor relation [2.10, 2.11] holds, since the electrons find themselves in a *repulsive*, i.e. *confining*, electric field, i.e. an *electrostatic well*, and suffer such slow loss that 'v_e^{loss}' ($\equiv v_{se}$) $\ll \overline{c}_e$. As a result, the electron velocity distribution is approximately Maxwellian, even in the sheath, (see section 2.5), T_e remains constant, and the electron density at each point in the sheath, where the local electrostatic potential is $V(x)$, simply falls off according to a Boltzmann factor:

$$n_e(x) = n_{se} \exp[e(V - V_{se})/kT_e]. \tag{2.35}$$

Note that here we are taking the reference potential to be $V = 0$ at a location in the plasma some distance *upstream* of the sheath edge: the point of the present exercise is to *find* the value of V_{se}, figure 2.3. V_{se} describes the potential drop which occurs *upstream* of the sheath edge, i.e. in the plasma *itself*, i.e. the *pre-sheath electric field*, section 1.8.2.9. We want to know how strong this pre-sheath

potential drop is: for the case of $T_i = 0$ together with the assumption that all the ions originated at a single location upstream of the sheath edge—this is really the same thing as finding the 'plasma exit velocity' v_{se}, since with these assumptions:

$$\tfrac{1}{2}m_i v_{se}^2 = -e\Delta V_{\text{pre-sheath}} = -eV_{se}. \tag{2.36}$$

(Note that in equations (2.35) and (2.36), all $V < 0$.)

In addition to the assumptions that $T_i = 0$ and that all the ions are assumed to start at a *single* location upstream of the sheath edge, with zero velocity, it is assumed that the ions fall *collisionlessly* through a pre-sheath potential drop V_{se}. n_{se} is also unknown, but will cancel out. m_i and T_e are parameters of the system which have to be specified. V is a variable, but will also cancel out.

Next, consider the ions. From energy conservation we have at all points in the sheath and plasma

$$\tfrac{1}{2}m_i v^2 = -eV. \tag{2.37}$$

Equation (2.37) can also be obtained from the ion fluid momentum equation (1.26); momentum and energy conservation give the same result when energy conversion to thermal energy does not occur.

Since the only source of ions is at the upstream source point, particle conservation gives $n_i v =$ constant so that, combining particle and energy conservation:

$$n_i = n_{se}(V_{se}/V)^{1/2}. \tag{2.38}$$

Within the plasma we assume $n_e = n_i$, but in the sheath $n_e < n_i$ and we need an equation to relate n_e, n_i and V. This is given by the *Maxwell equation*:

$$\nabla \cdot \boldsymbol{E} = e(n_i - n_e)/\varepsilon_0 \tag{2.39}$$

which, with $\boldsymbol{E} \equiv -\nabla \boldsymbol{V}$, gives the 1D *Poisson's equation*:

$$\boxed{\frac{\mathrm{d}^2V}{\mathrm{d}x^2} = -\frac{e}{\varepsilon_0}(n_i - n_e)} \tag{2.40}$$

thus

$$\frac{\mathrm{d}^2V}{\mathrm{d}x^2} = -\frac{e}{\varepsilon_0}n_{se}\left[\left(\frac{V_{se}}{V}\right)^{1/2} - \exp[e(V - V_{se})/kT_e]\right]. \tag{2.41}$$

We now focus on the region just inside the sheath and define:

$$\Delta \equiv V_{se} - V (> 0). \tag{2.42}$$

Thus we may expand:

$$\left(\frac{V_{se}}{V}\right)^{1/2} \approx 1 + \frac{1}{2}\frac{\Delta}{V_{se}} = 1 - \frac{1}{2}\frac{\Delta}{|V_{se}|} \tag{2.43}$$

$$\exp[e(V - V_{se})/kT_e] \approx 1 - \frac{e\Delta}{kT_e} \tag{2.44}$$

giving

$$\frac{\mathrm{d}^2\Delta}{\mathrm{d}x^2} \approx \frac{en_{se}\Delta}{\varepsilon_0}\left(\frac{e}{kT_e} - \frac{1}{2|V_{se}|}\right). \tag{2.45}$$

Now, one may recall a basic property of single, second-order differential equations of the form $y'' = ay$: $y(x)$ is non-oscillatory if $a > 0$ and is oscillatory if $a < 0$. Under the assumption that an oscillatory sheath potential, $V(x)$, is unphysical, and, in any case, has never been seen experimentally, we assume that it is therefore necessary that:

$$\frac{e}{kT_e} \geq \frac{1}{2|V_{se}|} \tag{2.46}$$

or

$$m_i v_{se}^2 \geq kT_e \tag{2.47}$$

or

$$\boxed{v_{se} \geq c_s} \tag{2.48}$$

i.e. the *Bohm criterion* for the 'plasma exit velocity'.

We may also note from equation (2.45) that

$$\frac{\Delta}{L_{\text{sheath}}^2} \approx \frac{en\Delta}{\varepsilon_0}\frac{e}{kT_e} \tag{2.49}$$

where L_{sheath} is the characteristic scale length of the sheath, thus

$$L_{\text{sheath}} \approx \left(\frac{\varepsilon_0 kT_e}{e^2 n}\right)^{1/2} \equiv \lambda_{\text{Debye}} \tag{2.50}$$

where λ_{Debye} is the *Debye length*. Example: $T_e = 20$ eV, $n = 10^{19}$ m^{-3}, then $\lambda_{\text{Debye}} = 10^{-5}$ m and one notes how *extremely thin* the sheath is for typical tokamak edge conditions.

We can estimate the actual degree of *charge imbalance* existing in the plasma. We consider the plasma region but do not assume $n_e = n_i$, rather we employ Poisson's equation (2.40), as we just did for the sheath. We must also appropriate the finding of section 1.8.2.9, that the total potential drop within an (isothermal) plasma, i.e. the pre-sheath drop, is $\sim 0.7kT_e/e$, equation (1.53). Thus defining the charge imbalance in the plasma:

$$\alpha \equiv |n_e - n_i|/n_e \tag{2.51}$$

and taking $\mathrm{d}^2V/\mathrm{d}x^2 \approx 0.7kT_e/eL^2$ in the plasma where L is the plasma size, and inserting into Poisson's equation, one finds:

$$\alpha \equiv |n_e - n_i|/n_e \approx \left(\frac{\lambda_{\text{Debye}}}{L}\right)^2. \tag{2.52}$$

Example: $\lambda_{\text{Debye}} = 10^{-5}$ m, $L = 10$ m then the charge imbalance in the plasma is $\approx 10^{-12}$. Thus, plasmas are generally neutral to an extremely high order indeed. The plasma is almost completely shielded by the sheath from external fields such as those arising from wall charges. This electrostatic shielding, called *Debye shielding*, is not perfect, however, and this is manifest by the existence of a non-zero, small, electric field in the plasma, $E_{\text{plasma}} \approx 0.7kT_e/eL$ and non-zero, but extremely small, charge imbalance in the plasma.

While the latter is of no practical consequence, the existence of the pre-sheath or plasma E-field is of critical importance and gives rise to the Bohm criterion. This field is insignificant compared with the sheath electric field, ($E_{\text{sheath}} \approx kT_e/e\lambda_{\text{Debye}} \approx 10^5 E_{\text{plasma}}$), but its role is just as dramatic. We may consider the analogy with a waterfall: the drama of a fall has as much to do with the magnitude of the flow as it has to do with the magnitude of the vertical drop, figure 2.4. The former has nothing to do with the latter, but depends only on the upstream condition including the drop along the river *upstream*. The particle outflow rate of plasma to a solid surface is controlled entirely by the forces in the plasma, not the sheath—i.e. by the conditions upstream of the main drop.

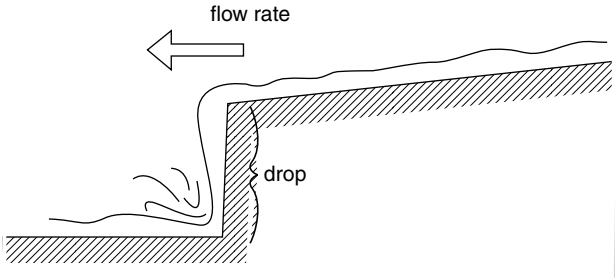

Figure 2.4. Analogy between plasma flow through the potential drop of a sheath and a waterfall. The flow rate over a fall has nothing to do with the magnitude of the drop.

We return to equation (2.35) and the assumption that n_e satisfies the Boltzmann factor. Strictly, this only holds true when the electron population experiences no loss whatsoever, as in the last section. Near the sheath edge one can show that the missing electrons, due to the electron loss to the walls, are only a tiny fraction of the value given by assuming the Boltzmann factor and so the error is slight, section 2.6. Fortunately, the Bohm criterion analysis is only concerned with the region just near the sheath edge. Deeper into the sheath the distortion caused by the missing electrons increases and finally, just at the wall, fully half of the Maxwellian distribution is missing—the backward-going half, figure 2.5. Therefore some error would be involved if one used equation (2.41) to calculate the spatial variation of $V(x)$ all the way through the sheath to the wall—but fortunately there is little practical interest in the details of $V(x)$ in the sheath.

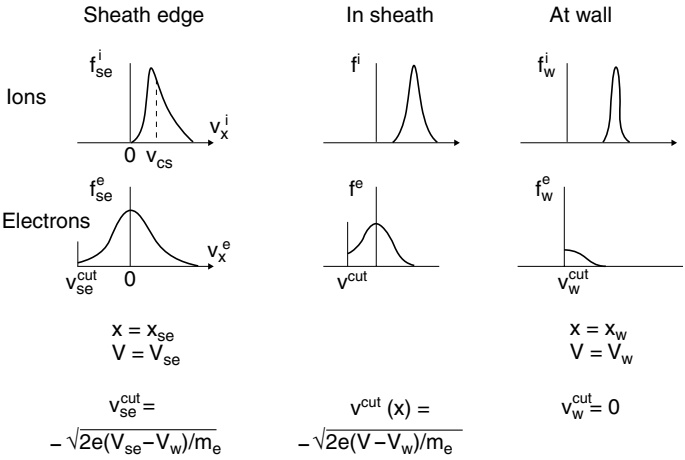

Figure 2.5. The ion and electron velocity distributions at the sheath edge (*se*), at some point part way through the sheath, and at the wall (w). The electron distributions are cut off due to the capture by the wall of the high energy tail of the distribution.

Further, the *magnitude* of the total potential drop to the wall is unaffected.

Why do we make the unnecessary, and somewhat artificial, division of space into the non-neutral sheath and the (quasi-) neutral plasma? Why not just apply Poisson's equation throughout? This has, in fact, been done [2.12, 2.13] and the numerical results support very well the simpler picture of distinct sheath + plasma. Although there is then no precisely definable 'sheath', if one arbitrarily takes the sheath edge to be the location where the charge imbalance exceeds a few per cent, then the sheath thickness is found to be $\sim 10\lambda_{\text{Debye}}$, see figure 2.6 which shows the solutions for $V(x)$, $n_e(x)$, $n_i(x)$, $v_e(x)$ and $v_i(x)$ in the sheath for the case of $T_i = 0$. (The correction to allow for the loss of the electrons absorbed by the wall has also been included here when solving the Poisson equation (2.41) to obtain these results [2.13].) The picture of plasma + sheath is much more informative than purely numerical results, and the loss of absolute precision is rarely of practical importance.

We end this section with a caution: the above derivation is for a case so simple as to be almost artificial:

(a) the particle source is a delta function in space,
(b) the ions are mono-energetic, $T_i = 0$,
(c) there are no collisions.

Relaxation of assumptions (a) and (b) to more realistic ones results in only modest changes to c_s and V_{se}, as in next section, also section 10.6. Ion–ion collisions are not of much importance, but if the ions suffer *momentum-loss collisions to neutrals*, then $|V_{se}|$ can become very large, section 10.4.

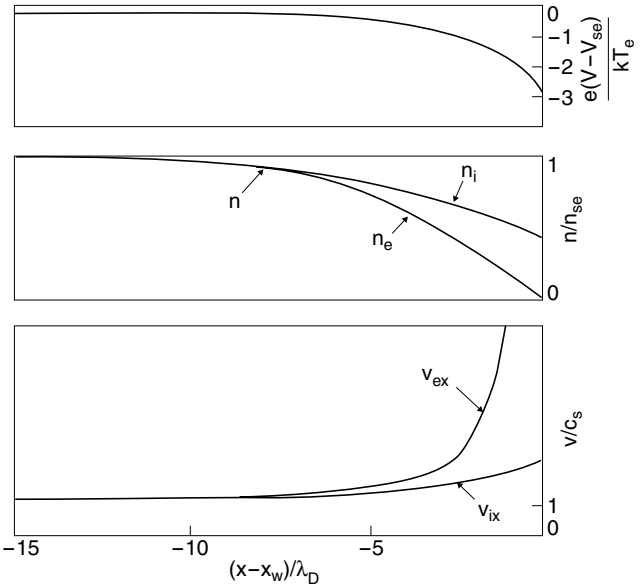

Figure 2.6. Chodura's computed profiles of potential, n_e, n_i and average ion and electron speeds through the sheath [2.13]. Case of $T_i = 0$ H^+ ions. Net space charge becomes significant starting at a distance of about 10 Debye lengths from the wall ($x = x_w$).

2.4 The Bohm Criterion when $T_i \neq 0$

Allowing for $T_i \neq 0$ rather complicates the analysis, but it is nevertheless carried out the same way as in section 2.3. The final result turns out to be expressible in a rather compact way, the *generalized Bohm criterion* [2.14, 2.15]:

$$\boxed{\int_0^\infty \frac{f_{se}^i(v)\mathrm{d}v}{v^2} \leq \frac{m_i}{kT_e}} \tag{2.53}$$

where $f_{se}^i(v)$ is the 1D ion velocity distribution at the sheath edge. For $T_i = 0$ one has mono-velocity ions at each point and the integral in equation (2.53) just gives v_{se}^{-2}, and thus the basic Bohm criterion, equation (2.48).

Next, consider a crude approximation to the situation where $T_i \neq 0$ and let us take $f_{se}^i(v)$ to be the normalized 'top hat' shape, figure 2.7:

$$f_{se}^i(v) = \begin{cases} (2c_i)^{-1} & \text{for } v_{se} - c_i \leq v \leq v_{se} + c_i \\ 0 & \text{otherwise} \end{cases} \tag{2.54}$$

where we define $c_i \equiv (kT_i/m_i)^{1/2}$, essentially the ion thermal speed. Insertion of this distribution into equation (2.53) gives the anticipated result:

$$v_{se} \geq c_s = [(kT_e + kT_i)/m_i]^{1/2}. \tag{2.55a}$$

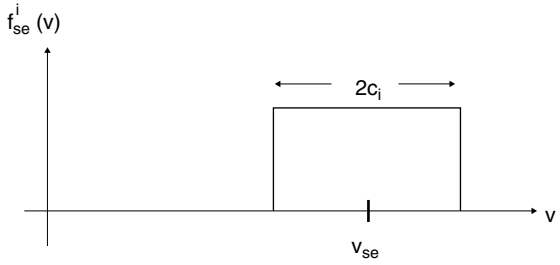

Figure 2.7. A simple 'top hat' approximation to the ion velocity distribution at the sheath edge (*se*). The thermal speed is characterized by $c_i = (kT_i/m_i)^{1/2}$, giving the width of the distribution. The average speed is v_{se}, to be found.

One may note that the $f^i_{se}(v)$ of equation (2.54) has been purposely devised to have no backward-going ions at the sheath edge—a physical necessity since all ions crossing the sheath edge reach the surface and the surface is absorbing. Note also, that if $f^i_{se}(0) \neq 0$, the integral in equation (2.53) will 'blow up', so that even zero-velocity ions are ruled out at the sheath edge, see figure 2.5. Further, one sees from equation (2.53) that the integral is strongly weighted to the slowest ions. Consider the component δn_i of the total n_i that had the value v^i_{se} at the sheath edge. The decrease in the magnitude of δn_i caused by the acceleration in the sheath is larger, the smaller the value of v^i_{se}; $n_i = \sum \delta n_i$ must not drop too fast, specifically not as fast as n_e drops—otherwise there will not be a region of net positive space charge. We thus see why the inequality of equation (2.53) is in the direction shown. This inequality can also be seen to be the same as requiring $n_i > n_e$ just inside the sheath. (Actually, so long as the entrance to the sheath is characterized by the non-oscillatory build-up of either positive or negative net space charge density, the same inequality (2.53) results.)

We can now appreciate why v_{se} must increase with T_i: it is actually due to the ions in the *slow* part of the ion velocity distribution: since they make n_i more susceptible to the acceleration–rarefaction effect, the whole distribution has to be 'shifted up'—i.e. v_{se} increased—in order to 'stiffen up' the ion distribution, i.e. to make the ions less susceptible to the acceleration–rarefaction effect. Any first, intuitive thought that perhaps it is the presence of the high energy tail of the ion distribution which causes v_{se} to go up with T_i, would be incorrect.

Figure 2.5 shows schematically the velocity distributions of ions and electrons at three locations: the sheath edge, part way through the sheath and just at the solid surface. One may note that at the sheath edge there are no backward-going ions since the wall absorbs all ions reaching it. Acceleration of the ions through the sheath tends to narrow the velocity distribution. At the sheath edge there are backward-going electrons; however, the most energetic, forward-going electrons are absorbed by the wall and thus, at the sheath edge, the high energy

backward-going tail of the distribution is missing. Sufficiently far from the wall, electron–electron collisions will replenish this missing part of the distribution, which thus relaxes toward a full Maxwellian. As a historical aside it is appropriate to mention here the so-called *Langmuir paradox*: in the 1920s Langmuir made measurements of the electron distribution in non-magnetic gas discharges and reported that he found that the high energy, backward-going tail was *not* missing, even in circumstances where electron–electron collisions were not frequent enough to have replenished the tail. This gave rise to the apparent paradox. Much speculation arose over subsequent decades to explain this paradox, including a possible role of plasma fluctuations [2.16]; however, it turned out that when more sensitive measurements of the electron distribution were made, that the backward-going tail *was*, in fact, shown to be missing in weakly collisional plasmas [2.17]. If the electron self-collisionality is extremely weak *everywhere* in the plasma, then the high energy tail is not replenished—eventually even in the *forward*-going direction, and a more complicated situation results [2.18]; see section 25.5.

Riemann has written extensively on the Bohm criterion including both comprehensive reviews [2.19, 2.20], as well as much new analysis [2.21–2.30]. In [2.19] Riemann discusses the generalization of the non-zero T_i Bohm criterion, which becomes:

$$v_{se} \geq c_s = [(kT_e + \gamma kT_i)/m_i]^{1/2} \tag{2.55b}$$

with $\gamma = 1$ for isothermal flow, $\gamma = 5/3$ for adiabatic flow with isotropic pressure, section 10.9, and $\gamma = 3$ for 1D adiabatic flow, section 10.8. Riemann points out that the criterion of (2.53)—which he terms the *kinetic form of the Bohm criterion*—is actually only consistent with $\gamma = 3$, since near the sheath edge the plasma flow must become 1D, adiabatic, with no coupling of perpendicular and parallel pressures; also see section 10.8, where the latter concepts are discussed.

2.5 The Particle Flux Density to a Surface

We have now succeeded in achieving one of our major objectives in the analysis of the tokamak edge, namely, the *quantification of the particle sink action caused to a plasma by its contact with a solid surface*: that is we can now relate the particle outflux density, Γ_{se}, from a plasma to a surface, in terms of the plasma properties n and T, equation (1.51):

$$\boxed{\Gamma_{se} = n_{se} v_{se} = n_{se} c_s \approx \tfrac{1}{2} n_0 [k(T_e + T_i)/m_i]^{1/2}.} \tag{2.56}$$

One notes that Γ_{se} [charged particle pairs $\mathrm{m}^{-2}\ \mathrm{s}^{-1}$] has *no* dependence on how large a potential drop exists in the sheath, section 2.3. Usually $(L_{\text{sheath}}/L) \ll 1$ so we neglect the small additional particle source occurring in the sheath and take $\Gamma_{se} = \Gamma_w$, the flux density reaching the actual wall.

2.6 Potential Drop in the Sheath for Floating or Biased Surfaces

We are interested in knowing the potential drop, V_{sf}, that *spontaneously* arises between a plasma and a solid surface in contact with it which is *electrically isolated*, thus *floating*, thus $\Gamma^e_{se} = \Gamma^i_{se}$, assuming a 1D system. *Ambipolar flow* is defined to occur when $\Gamma^e = \Gamma^i$. The quantity V_{sf} is important for determining the ion impact *sputtering* of the solid surface, section 3.3, and the *heat* flux to the solid surface, section 2.8.

We have the ion flux density at the sheath edge, (and reaching the wall):

$$\Gamma_w = \Gamma_{se} = n_{se} c_s. \tag{2.57}$$

For the electrons we invoke the Boltzmann relation equation (2.35), plus the fact that in a retarding (confining) electrostatic field the velocity distribution remains Maxwellian with constant T_e, section 2.2, plus the fact that the one-way, random (thermal) particle flux density for a Maxwellian, section 2.2, is:

$$\Gamma^{\text{Max}} = \frac{1}{4} n \bar{c} = \frac{1}{4} n \left(\frac{8kT_e}{\pi m_e} \right)^{1/2} \tag{2.58}$$

so that the electron flux density reaching the wall is:

$$\Gamma^e_w = \tfrac{1}{4} n_w \bar{c}_e = \tfrac{1}{4} n_{se} \exp[eV_w / kT_e] \bar{c}_e \tag{2.59}$$

where V_w is the potential of the wall relative to the plasma potential at the sheath edge where $V = 0$. For floating conditions the wall sits at 'floating potential' V_{sf}, $V_w = V_{sf} < 0$ ('s' for 'sheath', 'f' for 'floating').

Setting $\Gamma^e_w = \Gamma^i_w$ gives:

$$\boxed{\frac{eV_{sf}}{kT_e} = 0.5 \ln \left[\left(2\pi \frac{m_e}{m_i} \right) \left(1 + \frac{T_i}{T_e} \right) \right].} \tag{2.60}$$

See figure 2.8. One may note that V_{sf} has no dependence on density, since n_{se} has cancelled out. The natural normalization for V_{sf} is kT_e/e. Note that $V_{sf} < 0$, the wall repels electrons, and that its magnitude decreases as T_i increases: for higher T_i, Γ^i_w increases and so the surface now must be less repelling to the electrons to maintain ambipolarity $\Gamma^e_w = \Gamma^i_w$. The voltage drop (absolute magnitude) across the combined pre-sheath and sheath is $\approx -V_{sf} + 0.7kT_e/e$, section 1.8.2.9. For hydrogenic plasmas, $eV_{sf}/kT_e \approx -3$ while for a heavy ion plasma, such as Hg^+, $eV_{sf}/kT_e \approx -6$.

Various extensions of the simple treatment here can be made, including allowing for *secondary electron* production at the solid surface due to electron, ion and photon impact, section 3.2. See section 25.5 which contains a more extended treatment of the topic of this section. The effect of secondary electron emission is

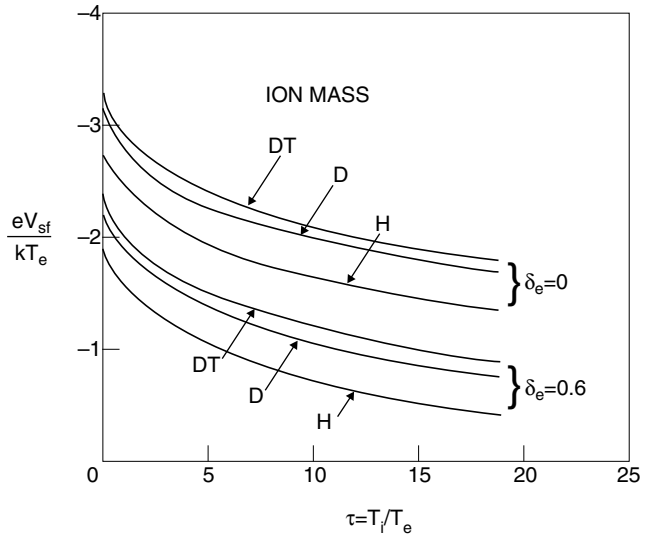

Figure 2.8. The potential drop across the sheath for an electrically floating surface, V_{sf}, as a function of T_i/T_e, for various hydrogenic species ('DT' has mass 2.5 amu). The surface may release secondary electrons due to the plasma electrons striking the surface, section 3.2, which influences V_{sf}, section 25.5, equation (25.31). δ_e is the coefficient of secondary electron emission.

indicated in figure 2.8; it lowers $|V_{sf}|$ since more electrons from the plasma must reach the floating surface when it is releasing electrons back into the plasma.

What if the surface is *not* floating, but has been electrically biased by applying, by external means, a potential difference between the plasma and solid surface, so that $\Gamma_w^e \neq \Gamma_w^i$, i.e. *net current* is drawn through the external circuit? This could be achieved in a 1D system by applying an external power supply to the two solid surfaces at each end, figure 2.9. In this way a net current could be forced to pass through the plasma, and the sheaths at each end, closing through the external circuit.

Regardless of whether the solid is electrically floating or not, Γ_w^i is still given by equation (2.57) (unless very large positive bias voltages are applied, as will be discussed). The change in potential is entirely taken up by changes in the drops in the two sheaths, while the two pre-sheaths, on each side of the mid-point continue to have drops of $\sim -0.7kT_e/e$ (isothermal case). The sheaths continue to provide virtually perfect Debye shielding of the plasma. The Bohm criterion still holds at the sheath edge at each end, since its derivation was based on small Δ/kT_e equation (2.42), i.e. the region of the sheath just at the entrance from the plasma, which is unaffected by the changes at the wall. Also we noted that the analysis from the *plasma* side gave a 'blow up' singularity (gradients of n, V, etc went to

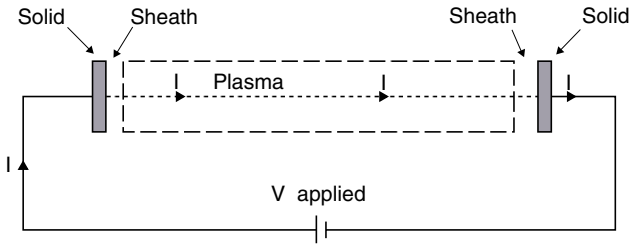

Figure 2.9. An external power supply applies a potential difference between the two (electrically conducting) end walls of a 1D plasma/sheath system, drawing a current. There is either no magnetic field, or $\boldsymbol{B}$ lies along the axial, current direction.

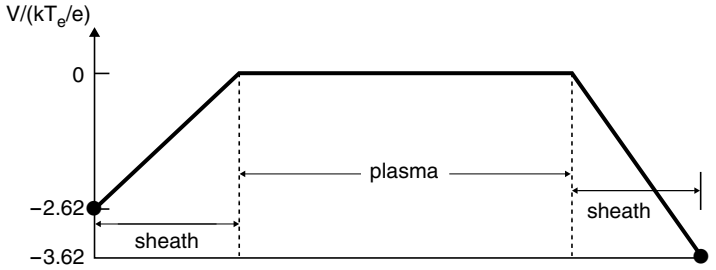

Figure 2.10. Problem 2.1. The potential profile for the case of biasing the right end of the system shown in figure 2.9 by $-1kT_e/e$. Here the plasma potential has been taken as the reference, $V = 0$, and it has been assumed that $V_{sf} = -3kT_e/e$. Pre-sheath potential drops are not shown here for simplicity.

$\pm\infty$), i.e. formation of a sheath edge as soon as V had dropped to $\sim -0.7kT_e/e$ (isothermal case). Thus whenever any voltage drop which is more negative than $\sim -0.7kT_e/e$, is applied across an isothermal, frictionless plasma *all of the excess voltage will develop across the sheaths*.

Consider a symmetrical situation, with floating surfaces at each end, and, say, $V_{sf} = -3kT_e/e$. Next suppose that an external bias is applied to the two end surfaces such that the right end is biased to $-1kT_e/e$, say, relative to the left end surface, figure 2.10. Let the voltage drop across the right, and left, sheaths be V_r, and V_ℓ, respectively. Both pre-sheath voltage drops would remain at $\sim -0.7kT_e/e$ as before (for simplicity these pre-sheaths are not shown in figure 2.10). The electron flux density reaching the right surface will now be

$$\Gamma^e_{rw} = \tfrac{1}{4} n_{se} \overline{c}_e \mathrm{e}^{eV_r/kT_e} \tag{2.61}$$

while

$$\Gamma^i_{rw} = n_{se} c_s = \tfrac{1}{4} n_{se} \overline{c}_e \mathrm{e}^{eV_{sf}/kT_e} \tag{2.62}$$

the same as for $V_{\text{applied}} = 0$. Also $n_{se} = \frac{1}{2}n_0$ (isothermal case) as for $V_{\text{applied}} = 0$. At the left surface:

$$\Gamma^e_{\ell w} = \tfrac{1}{4} n_{se} \overline{c}_e \mathrm{e}^{eV_\ell / kT_e} \tag{2.63}$$

and

$$\Gamma^i_{\ell w} = n_{se} c_s = \tfrac{1}{4} n_{se} \overline{c}_e \mathrm{e}^{eV_{sf}/kT_e} \tag{2.64}$$

by conservation of charge we must have

$$\Gamma^e_{\ell w} + \Gamma^e_{rw} = 2 n_{se} c_s \tag{2.65}$$

and we also have

$$V_r - V_\ell = V_{\text{applied}}. \tag{2.66}$$

Combining equations (2.61)–(2.66):

$$\frac{eV_\ell}{kT_e} = \ln\left[\frac{2\mathrm{e}^{eV_{sf}/kT_e}}{1 + \mathrm{e}^{eV_{\text{applied}}/kT_e}}\right]. \tag{2.67}$$

One also has the net current to the right surface:

$$\begin{aligned} j_r &= \mathrm{e}(\Gamma^i_{rw} - \Gamma^e_{rw}) = -j_\ell && (2.68)\\ &= \tfrac{1}{4} e n_{se} \overline{c}_e (\mathrm{e}^{eV_{sf}/kT_e} - \mathrm{e}^{eV_r/kT_e}) && (2.69)\\ &= \tfrac{1}{4} e n_{se} \overline{c}_e \mathrm{e}^{eV_{sf}/kT_e} (1 - \mathrm{e}^{e(V_r - V_{sf})/kT_e}) && (2.70)\\ &= e n_{se} c_s (1 - \mathrm{e}^{e(V_r - V_{sf})/kT_e}). && (2.71) \end{aligned}$$

Problem 2.1. For $eV_{sf}/kT_e = -3$, and $eV_{\text{applied}}/kT_e = -1$, show that

$$\frac{eV_\ell}{kT_e} = -2.62, \quad \frac{eV_r}{kT_e} = -3.62, \qquad \text{figure 2.10.}$$

Also show that

$$j_r = e n_{se} c_s (1 - \mathrm{e}^{-0.62}) = 0.462 e n_{se} c_s. \tag{2.72}$$

Note that the right surface *receives* a (positive) current $+0.462 e n_{se} c_s$, in this example, while the left surfaces *injects* $+0.462 e n_{se} c_s$ into the plasma—by *receiving* more electrons than ions. There is no *true* electron *emission* from either surface. Fill in the boxes: the right surface receives $\square e n_{se} c_s$ of positive ions plus $\square e n_{se} c_s$ of electrons, and thus receives a positive current of $\square e n_{se} c_s$. The left surface receives $\square e n_{se} c_s$ of positive ions, but also $\square e n_{se} c_s$ of electrons for a net *received* current of $\square e n_{se} c_s$ (i.e. a net *injected* current of $\square e n_{se} c_s$).

It is illuminating to consider what happens if $V_{\text{applied}} \to -\infty$. Then

$$\begin{aligned} V_\ell &\to V_{sf} + \frac{kT_e}{e} \ln 2 \approx -2.3 kT_e/e \\ V_r &\to -\infty \\ j_r &\to e n_{se} c_s. \end{aligned} \tag{2.73}$$

That is, virtually all of V_{applied} is taken up by the right, *electron-repelling* surface, while the left, *electron-attracting* surface *saturates* as to its sheath voltage drop and the current, from left to right, attains the *ion saturation current* level:

$$\boxed{j^i_{\text{sat}} \equiv en_{se}c_s \approx \tfrac{1}{2}en_0c_s.} \tag{2.74}$$

With regard to the distortion caused to the electron distribution by the loss to the wall, it is to be noted that only a small fraction of the electrons in the distribution—only the ones moving toward the target and in the high energy tail of the distribution—are being removed from the distribution. Thus, for the forward-going part of the distribution, the full Maxwellian is present, even at the sheath edge—and this continues to be true even within the sheath, right up to the solid surface. At the sheath edge most of the backward-going electrons are still present since the wall potential is sufficiently repelling of electrons that most are *reflected somewhere within the sheath*. For locations deeper and deeper into the sheath, there are fewer and fewer backward-going electrons at all, until just in front of the solid surface there are no backward-going electrons (assuming that there is no electron emission); see figure 2.5. Thus at the sheath edge the electron density is *almost* the same as if the surface were completely repelling—and the electron density is almost exactly given by the Boltzmann factor. Now *strictly*, at the sheath edge:

$$n_e = n_0 \exp[eV_{se}/kT_e]\left(1 + \int_{E=0}^{-e(V_w - V_{se})} f^{\text{Max}}(E)\mathrm{d}E\right)\Big/ 2 \tag{2.75}$$

where n_0 = electron density halfway between the two walls defining the plasma region, where $V = 0$ is set as reference, V_{se} is the potential at the sheath edge ($\sim -0.7kT_e/e$), and V_w is the floating wall potential ($\sim -3kT_e/e$). The first contribution in equation (2.75) is due to the forward-going electrons, the second (the integral) to the back-going ones. The 'missing' fraction is:

$$\text{fraction} = \frac{\left(\frac{1}{2}\int_{v_x=v_{\text{cutoff}}}^{\infty} \mathrm{e}^{-\beta v_x^2}\mathrm{d}v_x\right)}{\int_{v_x=0}^{\infty} \mathrm{e}^{-\beta v_x^2}\mathrm{d}v_x} \tag{2.76}$$

where

$$\tfrac{1}{2}m(v_{\text{cutoff}})^2 = -e(V_w - V_{se}). \tag{2.77}$$

Thus

$$\text{fraction} = 1 - \text{erf}\left[\left(\frac{-e(V_w - V_{se})}{kT_e}\right)^{1/2}\right] \tag{2.78}$$

where erf is the error function.

Example: $-e(V_w - V_{se}) = 3kT$ gives fraction = 0.0075, a negligible amount.

One might, however, still be concerned that the electron flux density actually reaching the surface might not be given by:

$$\Gamma_{e,\text{wall}} = \tfrac{1}{4} n_{ew} \overline{c}_e = \tfrac{1}{4} n_{se} \overline{c}_e \exp[\mathrm{e}(V_w - V_{se})/kT_e] \tag{2.79}$$

since the electron distribution just at the wall is only a half Maxwellian (forward going). In fact, equation (2.79) is valid since it only depends on the *forward*-going part of the distribution being Maxwellian at constant T_e. Of course, the foregoing assumes that the forward-going part of the distribution has been 'replenished' within the plasma to a Maxwellian form, by some means or other. When collisionality throughout the entire plasma is very weak, this may not be the case and then $\Gamma_{e,\text{wall}}$ can be strongly reduced [2.18].

As noted from table 1.1, the collisionality of the SOL can be marginal and operating conditions exist where the electron self-collisionality is insufficiently strong to ensure that the electrons are Maxwellian. In this situation it may nevertheless *happen* that the SOL electrons are Maxwellian, for example, the case where the electrons entered the SOL primarily by cross-field transport from the main plasma and the electrons happened to be Maxwellian there. The main plasma, however, may also not be strongly collisional and in addition external heating processes can bring about non-Maxwellian distributions of electrons—and ions—in the main plasma. The weakly collisional SOL (the sheath-limited SOL, see sections 1.9, 4.1, 9.10) may therefore be characterized by non-Maxwellian electrons and ions. Such cases are inherently complex since they depend on both the SOL and main plasmas and cannot be analysed purely in terms of SOL processes. The usual working assumption is simply to ignore this possibility, but the fact that the SOL particles are not necessarily Maxwellian in sheath-limited conditions should be kept in mind.

2.7 Langmuir Probes

The results of section 2.6 directly indicate how a Langmuir probe, LP, works. Historically, LPs have been one of the most widely used diagnostic techniques for low temperature plasmas, $T_e \lesssim 100$ eV [2.33], and have also come to be widely used over recent years for SOL measurements [2.34–2.38].

LPs have, in fact, been the 'work horse' of tokamak edge measurements. Most of the basic information about the SOL—plasma density and electron temperature—has been generated by LPs [2.39]. It is therefore appropriate to include a brief discussion of LP interpretation at this point.

LPs are relatively simple and inexpensive diagnostics, robust and compatible with tokamak SOL conditions. They are readily deployable in large arrays built into the edge structures [2.38]—i.e. limiters and divertor targets—or in reciprocating drive mechanisms for probing even to just inside the LCFS [2.38]. When 'built in' they are non-disturbing of the edge plasma. The price paid for these *experimental* advantages is that probe *interpretation* is notoriously difficult. Here

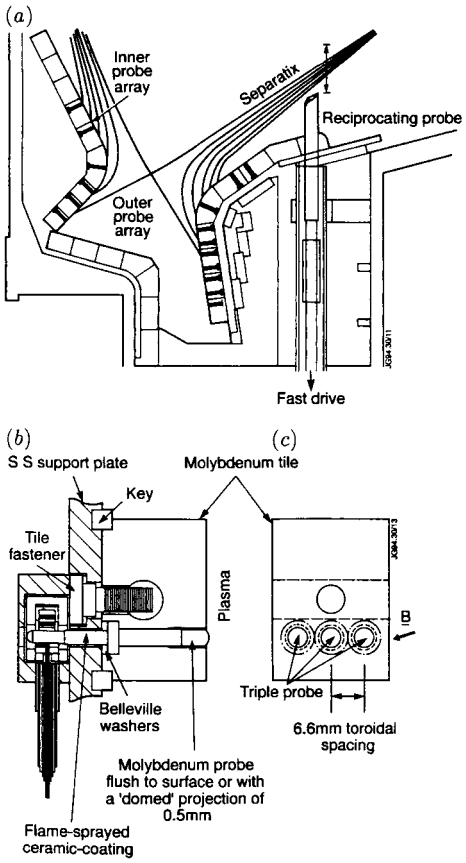

Figure 2.11. (a) Sections through the Alcator C-MOD divertor showing a fast moving (reciprocating) probe and built-in target probe arrays. (b) Side view of target probes and (c) front view showing the toroidal arrangement of built-in triple probes. B LaBombard. Reproduced from [2.38].

we cover only the rudiments of probe theory. For a more detailed discussion see [2.33–2.45].

The simplest geometrical arrangement is the LP built into the divertor target or limiter, figure 2.11. Let us define A_{LP} to be the area of the LP and assume that $\boldsymbol{B}$ is parallel to the normal vector to the probe surface. We also assume that the LP is biased relative to the limiters or divertor plates which are defined as being at 'machine potential'.

The LP current must close through the plasma, returning through the limiter or divertor target surfaces which are in contact with the plasma. In the absence of a B-field, this 'return current' spreads out over the entire area of the solid structure

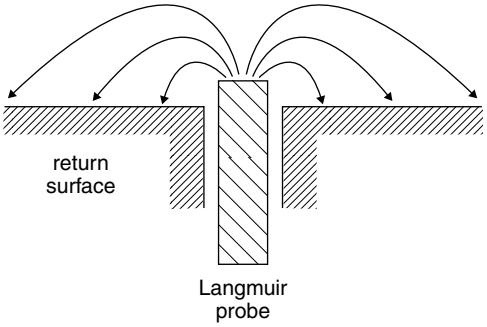

Figure 2.12. Case of no magnetic field and a single Langmuir probe biased relative to the walls. The wall area involved in the return current is typically much larger than the probe area, due to the high electrical conductivity of the plasma.

in contact with the plasma, A_{return}, with $A_{\text{return}} \gg A_{\text{LP}}$, typically, figure 2.12. This, therefore, is not precisely the same geometry as was considered in the last section where the areas receiving current from the plasma and injecting current into the plasma were equal (a 1D system). The situation of $A_{\text{return}} \gg A_{\text{LP}}$ has the important consequence that the potential drop at the 'return sheath', V_{return}, will need to change only very little in order to accommodate even large changes in the current passing through the system. Thus when analysing the I–V characteristic of the LP, $V_{\text{return}} \approx$ constant and it will play no important role; it is merely an *offset*.

In principle the *plasma* resistance will also influence the LP circuit analysis, but usually plasma resistance is too small for this to matter. Thus, the only important element in the LP circuit will usually be the sheath of the LP itself.

We next show that analysis of the LP circuit I–V characteristic can yield measurements of T_e and n_e at the LP. We may take equation (2.71) with $I = jA_{\text{LP}}$ to describe not only the I–V characteristic for the LP sheath, but for the entire LP *internal circuit* which, of course, is all that is experimentally accessible, figure 2.13.

We may assume that such large objects as the limiters/targets will *set* the potential drop between the plasma and the outside world, so that we may take 'machine potential' as the reference for all potentials, $V = 0$ there. In that case the *plasma* will float (rather than vice versa) relative to that reference to a potential of about $+3kT_e/e$ (thus still tending to force electrons to remain in the plasma, of course). Let us take the left side to be the return surface and the right side the LP, figure 2.14; all potentials are now incremented by $|V_{sf}| \sim +3kT_e/e$, hence $V_{\text{LP}} = V_r + 3kT_e/e$ and equation (2.71) gives:

$$\boxed{V_{\text{LP}} = \frac{kT_e}{e} \ln\left(1 - \frac{I_{\text{LP}}}{I^+_{\text{sat},LP}}\right).} \tag{2.80}$$

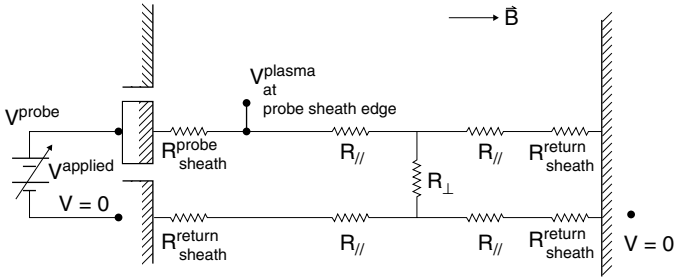

Figure 2.13. Case of non-zero magnetic field and a single Langmuir probe biased relative to the walls. Because of the weak cross-field electrical conductivity of the plasma, the probe circuit can be characterized by substantial 'internal' resistances in the plasma and sheaths, making interpretation of the I–V characteristic difficult.

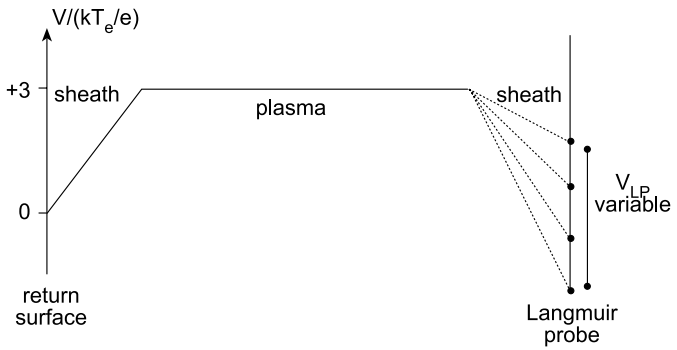

Figure 2.14. Single Langmuir probe for $B = 0$, but now with the main vessel wall (the 'return surface') taken as the reference potential where $V = 0$. The plasma now floats at $\sim +3kT_e/e$ relative to the walls. Changes in voltage applied between probe and vessel walls are taken up almost entirely by the probe sheath.

Therefore a ln plot of I_{LP} against V_{LP} yields a measurement of T_e. Also directly measurable from the I_{LP} against V_{LP} characteristic is the value of $I^+_{\mathrm{sat},LP}$ and since we have:

$$I^+_{\mathrm{sat},LP} \equiv A_{\mathrm{LP}} e n_{se} c_s \tag{2.81}$$

this can yield a measurement of n_{se}, the value near the LP, or $n_0 \approx 2n_{se}$, the density far from the LP. It should be noted that in order to deduce a value of n_{se} or n_0, it is necessary to know the value of c_s. Unfortunately the LP does not provide a measurement of T_i and so some uncertainty is involved here. Sometimes it can be inferred from estimate of equipartition rates, section 4.11, that $T_i \approx T_e$. In any case, since a factor of only $(1 + T_i/T_e)^{1/2}$ is involved the uncertainty can be small.

Strictly, the foregoing applies to a plasma with $\boldsymbol{B} = \boldsymbol{0}$. When $\boldsymbol{B} \neq \boldsymbol{0}$ one needs to consider the fact that the plasma current may have to close by *cross-field current paths* to reach the limiter/target surfaces. Cross-field resistances are not well understood, section 17.5, and it may be that R_{cross} can become a significant element in the circuit [2.40]. The effective resistance of the LP sheath may be defined by

$$R_{LP,\text{sheath}}^{-1} \equiv \frac{\mathrm{d}I_{\text{LP}}}{\mathrm{d}V_{\text{LP}}} \tag{2.82}$$

yielding the estimate

$$R_{LP,\text{sheath}}^{-1} \approx \frac{I_{LP,\text{sat}}^{+}}{V_{sf}} \simeq \frac{e^2 n_{se} c_s A_{\text{LP}}}{kT_e} \tag{2.83}$$

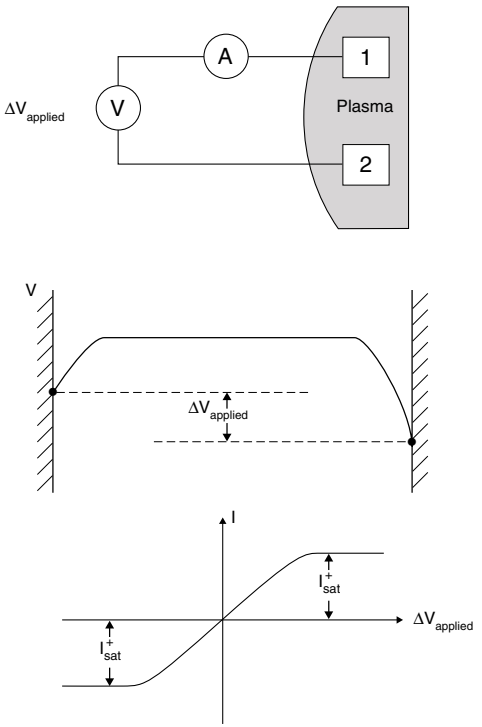

Figure 2.15. Double probe. The entire electrical circuit can be isolated from the vessel (walls). If the two probes have the same collecting area, the I–V characteristic is symmetrical.

Uncertainties about the value of R_{cross} also lead to uncertainties about A_{return} and hence $R_{\text{return sheath}}$ (since the amount by which the return current spreads out

over the limiters/targets—and whether part of the return path involves the limiter/target surface at the *other end* of the flux tube in contact with the LP—depends on the cross-field resistance [2.40]). The standard approach is nevertheless to assume $R_{LP,\text{sheath}} \gg R_{\text{cross}}, R_{\text{return sheath}}$ and to analyse the I–V characteristic as if $\boldsymbol{B} = \boldsymbol{0}$. This assumption appears often to be fairly safe when drawing net *positive* current by the LP, i.e. for $V_{\text{LP}} < V_{sf}$ (i.e. < 0 here), where the maximum current density that can be drawn is $+en_{se}c_s$. In 2D or 3D situations, where the 'return' surface which draws net ion current may be very large, one can draw net electron currents which are substantially larger than $en_{se}c_s$—up to the *electron saturation current* density, j^e_{sat}. For the 1D assumption of section 2.6, by contrast, it would not be possible to draw an electron current to one of the surfaces of more than $-2j^+_{\text{sat}}$, which would occur when the other surface was drawing j^+_{sat}, and no electrons at all; in that case the first surface would draw a net current of $+j^+_{\text{sat}} - 2j^+_{\text{sat}} = -j^+_{\text{sat}}$. The I–V characteristic would be completely *symmetrical*, figure 2.15. This is also the *double-probe characteristic*, since it is what applies also to the arrangement where the 'reference electrode' is changed from being the limiter/targets to being instead a second LP of the same area as the first LP [2.33, 2.35]. (In the derivations of section 2.6 the main aspect of 1D that was actually used was that the two particle-collecting elements, 'probes', had the same area.) The biasing circuit of the double LP, figure 2.15, therefore floats completely separately from 'machine potential', which can have practical advantages (e.g., protection of the probe's power supply from voltage surges, etc). The biasing potential is applied *between* the two probes—just as it was between the two sides of the 1D system of section 2.6. The double LP therefore also yields measurements of T_e and n_e.

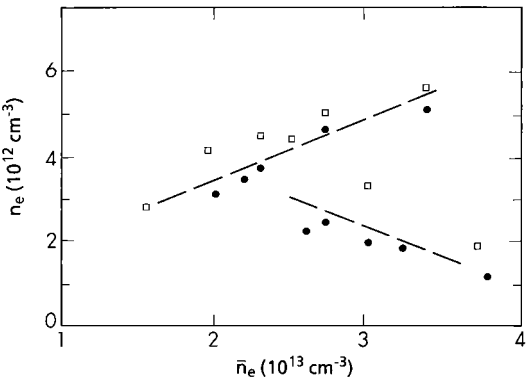

Figure 2.16. Measurements of n_e^{SOL} in the T-10 tokamak by microwave interferometry (□) and Langmuir probes (•) [2.42, 2.39]. Two runs of increasing and decreasing density.

In 2D and 3D geometries—i.e. the usual arrangement of a single LP biased relative to the limiters or targets—equation (2.80) implies that arbitrarily large

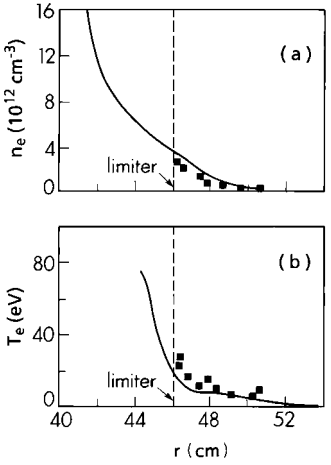

Figure 2.17. Measurements of n_e and T_e in the TEXTOR tokamak using a lithium beam (continuous line) and a Langmuir probe (points) [2.43, 2.39].

(negative) currents of electrons could be drawn to the probe. However, when $V_{\rm LP} \geq V_{\rm plasma} (\approx +3kT_e/e$ if the reference is taken to be the 'machine potential', figure 2.14) one would expect the electron current density to saturate at the random Maxwellian flux density, section 2.2, thus:

$$j^e_{\rm sat} = -\tfrac{1}{4} n e \bar{c}_e \tag{2.84}$$

which is greater in magnitude than $j^+_{\rm sat}$ by the ratio $\approx (m_i/m_e)^{1/2} \approx 60$ for a D^+ plasma. For values of $V_{\rm LP}$ this high (and higher), the currents drawn from the plasma are so large and disturbing that any simple analysis fails. However, it is often found that a more-or-less well defined, if noisy, electron saturation current exists. For $\boldsymbol{B} = \boldsymbol{0}$ plasmas it is indeed found that [2.33]:

$$|j^e_{\rm sat}|/j^+_{\rm sat} \approx (m_i/m_e)^{1/2}. \tag{2.85}$$

However when $\boldsymbol{B} \neq \boldsymbol{0}$ far smaller ratios are usually recorded [2.35]. The reason for this is still not entirely clear, although theories have been advanced starting with Bohm's in the 1940s [2.41]. It does appear that the problem is due to the departure of the net *electron* collecting part of the characteristic from the standard form, equation (2.80)—and is due to $R_{\rm cross}$ and/or $R_{\rm return\ sheath}$ no longer being negligible compared with $R_{LP,\rm sheath}$. Thus, a common practice in tokamaks is to use only the net ion-collecting part of the I–V characteristic to deduce T_e (and, of course, $I^+_{\rm sat}$ and n_e) [2.37, 2.38]. Comparisons with other measuring techniques in tokamaks show that the agreement can be to within a factor of 2 or better, for both T_e and n_e [2.39]. Some comparisons are shown in figures 2.16 [2.42], 2.17, [2.43] and 2.18 [2.44].

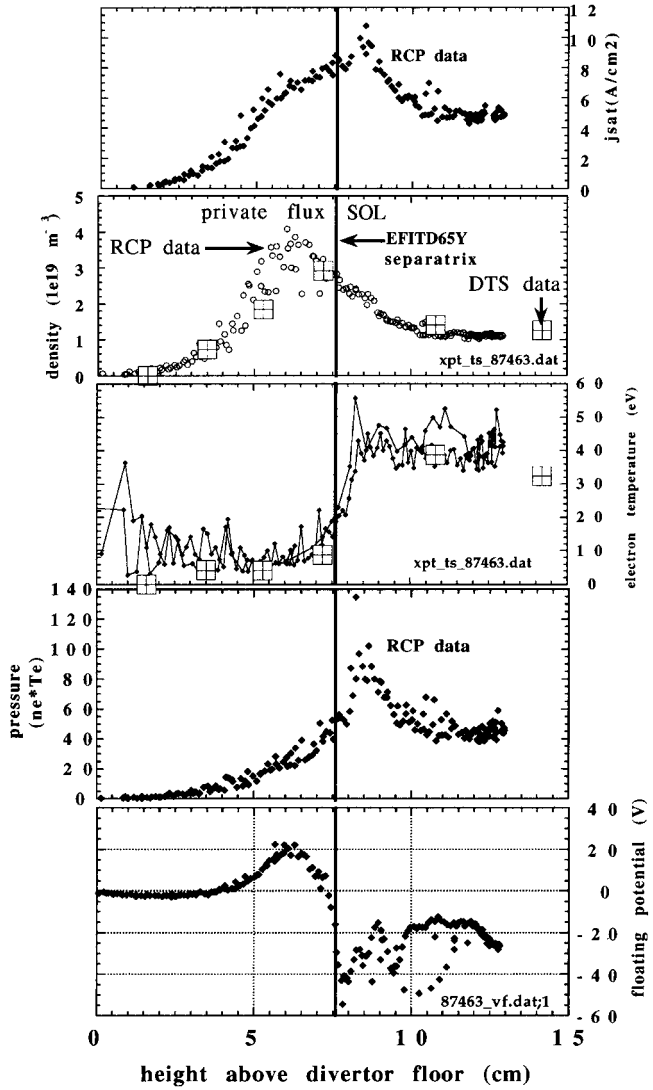

Figure 2.18. Vertical profiles of n_e and T_e made above the divertor target floor in the DIII-D tokamak using Langmuir probes (RCP) and Thomson scattering (DTS) [2.44].

A disadvantage to using only part of the I–V characteristic for net positive current collection is that this means the probe is only sampling the high energy tail of the electron distribution, figure 2.5. If the distribution is non-Maxwellian this can result in erroneous—usually too high [2.45–2.47]—values of T_e being indicated by a standard analysis of the LP I–V characteristic.

2.8 The Sheath Heat Transmission Coefficients. Basic Treatment

The sheath not only constitutes a particle sink for the SOL plasma, but also an energy sink. We wish to relate the electron, q_e, and ion, q_i, power flux densities [W m^{-2}] to the plasma conditions, n and T—similar to our relating of particle out flux density Γ [ions m^{-2} s^{-1}] to n and T. This topic is dealt with in greater detail in section 25.5. Here we present an abbreviated and heuristic treatment.

Consider first the electrons and assume them to be Maxwellian far upstream of the sheath. For a Maxwellian distribution, there is a simple relation between the *one-way* random flux densities of particles Γ, and heat q [W m^{-2}], section 2.2

$$q = 2kT\Gamma. \tag{2.86}$$

(Of course there is no *net* flux of either particles or heat for a Maxwellian distribution.) Right *at* the solid surface (the sheath–solid interface, *ss*), however, the electrons cannot have a perfect Maxwellian distribution, since there are no backward-going electrons there due to the absorption at the surface (and assuming for simplicity no electron reflection or secondary emission), figure 2.5. As to the forward-going electrons at the ss: it can be shown that this will still correspond to a perfect Maxwellian of constant T_e since the electrostatic force is conservative, section 2.2. Thus, the net (also forward-going) electron heat flux density at the ss is

$$q^e_{ss} = 2kT_e\Gamma_{ss} = 2kT_e\Gamma_{se} \tag{2.87}$$

with $\Gamma_{ss} = \Gamma_{se}$ on the assumption that the sheath is so thin that any particle source there is negligible.

Next consider q^e_{se}. At the sheath edge the electron distribution consists of two parts:

(a) the majority of forward-going electrons are too low in energy to surmount the repulsive sheath potential to reach the solid surface, and will be reflected at some point within the sheath, figure 2.2. Therefore there is an equal backward-going set of electrons at the se. Clearly these electrons contribute nothing to q^e_{se} or q^e_{ss} (nor to Γ_{ss}, Γ_{se});

(b) the high energy electrons, those with forward-going kinetic energy of at least $|eV_{sf}|$, will be lost to the solid surface, and there is no corresponding backflow of such electrons at the sheath edge.

The net electron power flow at the sheath edge is therefore

$$q^e_{se} = (2kT_e + |eV_{sf}|)\Gamma_{se} \tag{2.88}$$

since the 'loss electrons' had an energy that was higher at the sheath edge by an amount $|eV_{sf}|$ than at the solid surface.

We thus may note that the sheath acts as an electron 'high energy filter', permitting only the more energetic electrons in the population to escape. The

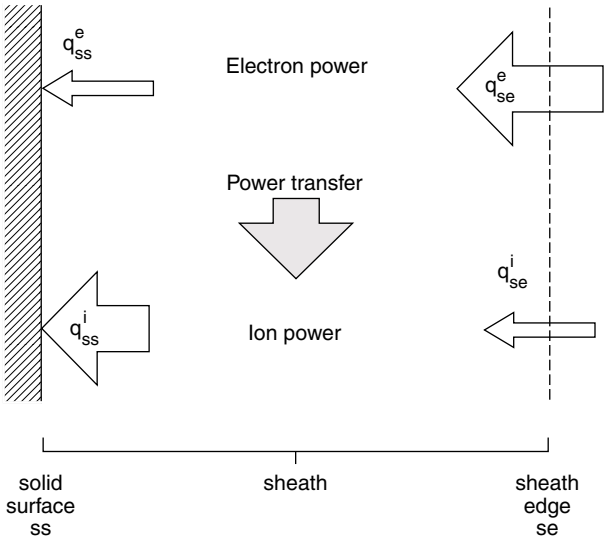

Figure 2.19. The sheath acts as an electron–ion energy-transfer mechanism, transferring energy $|eV_{sf}|$ from the electron to the ion.

sheath therefore constitutes a powerful *cooling* effect on the electrons, i.e. it is not just *power removing*, as it is for the ions, but it is specifically *cooling*, i.e., temperature reducing. (There is not, however, any drop of T_e *across* the sheath. Rather, the temperature of the entire 'reservoir' of plasma electrons in the SOL is reduced.)

It is important to distinguish between the electron power flux *received* by the surface—q^e_{ss}—which is the *surface heating power due to the sheath*—and the power flux *lost* by the plasma electron population—q^e_{se}—which we may call the *electron cooling power due to the sheath*. For purposes of calculating thermal loads on the solid structure, q^e_{ss} is required. For purposes of modelling the behaviour of the plasma electrons, q^e_{se} is required.

Where does the 'missing' electron power go? It is transferred to the ions which are accelerated through the sheath. The motion of ions into the sheath tends constantly to destroy the electrostatic field of the sheath, caused by the net negative charge on the solid surface. The electrons must therefore constantly reinvest energy in the formation of the sheath's electrostatic field, which energy is constantly being transferred to the ions, giving them a larger kinetic energy, by an amount $|eV_{sf}|$, at the ss than they had at the se. The sheath thus also acts as an *e–i energy-transfer mechanism*, transferring energy $|eV_{sf}|$ from electrons to ions for each charged pair lost to the solid, figure 2.19.

In a similar, smaller way the pre-sheath also acts to transfer a further amount $|eV_{\text{pre-sheath}}| \sim 0.7kT_e$ from the electrons to the ions.

It is convenient to define the *electron sheath heat transmission coefficient* γ_e by:

$$\boxed{q^e_{se} \equiv \gamma_e k T_e \Gamma_{se}} \tag{2.89}$$

thus

$$\gamma_e = 2 + |eV_{sf}|/kT_e + |eV_{\text{pre-sheath}}|/kT_e.$$

$$\boxed{\gamma_e \approx 2 + 3 + \tfrac{1}{2} = 5.5.} \tag{2.90}$$

We see that much more heat is removed from the electron population, per electron lost, than we might have naively supposed. We might have supposed $\gamma_e = 1.5$–2, perhaps.

We turn next to the ions which present a more complicated problem than the electrons since they are accelerated by the pre-sheath electric field and so, even if the ion distribution far upstream from the se is Maxwellian, the ion distribution at the se is seriously distorted from the Maxwellian since the ions are not experiencing a net force of zero. There are no backward-going ions *at all* at the se, figure 2.5. Nor is the distribution even a half Maxwellian since there can be no ions with $v = 0$ at the se, section 2.4. Now, if the ion distribution at the se were, in fact, a drifting Maxwellian, drifting with velocity c_s, then we would have:

$$q^i_{se} = \left(\tfrac{5}{2}kT_i + \tfrac{1}{2}m_i c_s^2\right)\Gamma_{se} \tag{2.91}$$

see section 2.2.

Thus

$$q^i_{se} = \tfrac{7}{2}kT\Gamma_{se} \quad \text{if } T_e = T_i \tag{2.92}$$

and

$$\gamma_i = 3.5.$$

Detailed analysis of specific cases where it is possible to calculate the complete ion velocity distribution at the se shows this value of γ_i to be on the high side, with values $\gamma_i \simeq 2$ being more appropriate [2.48]; see section 25.1. Thus $q^i_{se} \cong 2kT_i\Gamma_{se}$ and the ion power flux actually impacting on the solid is correspondingly:

$$\begin{aligned} q^i_{ss} &\approx (2kT_i + |eV_{sf}|)\Gamma_{se} \\ &\approx (2kT_i + 3kT_e)\Gamma_{se} \end{aligned} \tag{2.93}$$

(here we ignore the question of including $|eV_{\text{pre-sheath}}|$ since that is entangled with the problem of establishing the precise value of γ_i).

It is convenient to define the total *sheath heat transmission coefficient* γ by:

$$q_{se} \equiv q^i_{se} + q^e_{se} = \gamma k T_e \Gamma_{se} \tag{2.94}$$

so that:

$$\boxed{\gamma \simeq 7\text{–}8} \tag{2.95}$$

for $T_e = T_i$, comprising $\sim$ 5–6 for the electrons and an estimated $\sim$ 2–3 for the ions. Note that $q_{ss} = q_{se}$, i.e. the power removed from the plasma as a whole, equals the power received by the solid surface. In section 25.5 more complete expressions for γ are derived, allowing for: (i) non-floating solid surface, i.e. electrical bias, i.e. non-ambipolar conditions, (ii) $T_e \neq T_i$, (iii) secondary electron emission and electron reflection, (iv) ion reflection and (v) deposition of the potential energy of atom–atom recombination and e–i recombination on the solid surface.

2.9 Some Basic Consequences of the Existence of the Sheath

(i) The sheath cools the electrons more strongly than the ions, tending to make $T_e < T_i$ in the SOL.

We may consider two different *power channels* or flows *into* the SOL from the main plasma: the electron and ion channels. Each consists of cross-field conduction and convection. (In practice we often only have measurements of the total power into the SOL, P_{in} [W], but for present purposes let us assume that we know the along-the-SOL *parallel power flux density* input for electrons and ions *separately*, figure 2.20.) Suppose $q^e_{\text{in}} = q^i_{\text{in}}$ [W m^{-2}] and that e–i equipartition collisions are negligible so that T_e and T_i may be unequal in the SOL.

In this case

$$q^e_{\text{in}} = q^e_{se}, \quad q^i_{\text{in}} = q^i_{se}$$

so that

$$q^e_{se} = 5.5kT_e\Gamma_{se} = \left(\tfrac{5}{2}kT_i + \tfrac{1}{2}m_i c_s^2\right)\Gamma_{se} = q^i_{se}. \tag{2.96}$$

For simplicity we have assumed the over-estimate of equation (2.91). Equation (2.96) yields

$$T_i/T_e = 5/3.$$

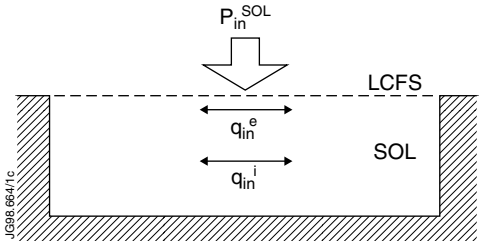

Figure 2.20. In practice, an experimental measurement of the total power entering the SOL from the main plasma, $P^{\text{SOL}}_{\text{in}}$ [W], is all that is available. Here, however, we assume that the parallel power flux densities flowing along the SOL, q [W m^{-2}], are known, and for the ion and electron 'channels' separately.

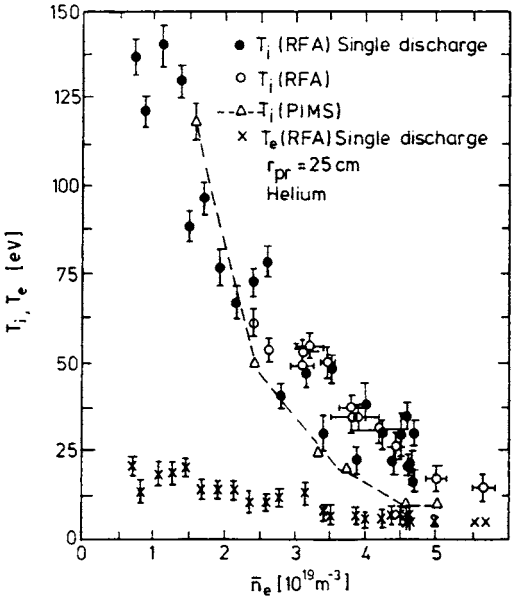

Figure 2.21. Measurements of T_e and T_i made in the DITE SOL using an RFA, retarding field analyser, and a PIMS, plasma ion mass spectrometer [2.49]. T_i^{SOL} can be significantly larger than T_e^{SOL}.

So, we may anticipate $T_i/T_e \gtrsim 2$. Although SOL measurements of T_i are quite sparse, they have been obtained on a few tokamaks using, for example, gridded energy analysers [2.38]. Ratios of $T_i/T_e > 2$ are typical, [2.49–2.53]. Figure 2.21 shows an example of measurements made on the DITE tokamak [2.49], comparing T_e and T_i measured using an RFA, Retarding field analyser, and a PIMS, plasma ion mass spectrometer.

It has to be noted that the tendency of the sheath to force $T_i > T_e$ in the SOL can be offset if $q_{\mathrm{in}}^e > q_{\mathrm{in}}^i$, or if e–i equipartition collisions are effective, section 4.11. Furthermore, volumetric power losses/gains exist in the SOL due to hydrogenic recycle processes, impurity radiation etc. These processes, however, tend to strengthen further the tendency for $T_i > T_e$: the hydrogenic recycle and impurity radiation is almost entirely a cooling action on the electrons. The hydrogenic recycle may, by contrast, actually *heat* the ions: some of the ions are back-scattered from the solid surface, section 3.1, as energetic neutral particles—carrying back into the plasma part of the $|eV_{sf}|$ energy that the ions gained from the electrons via the sheath energy transfer mechanism. When such energetic neutrals are subsequently ionized in the plasma, they constitute a heat source for the plasma ion population. This ion heating is also due to the existence of the sheath, and comes from the electrons.

(ii) Sputtering of the solid is increased due to the presence of the sheath.
For physical sputtering at impact energies $\lesssim$ a few 100 eV, the sputtering yield Y (the number of particles of the solid that are ejected for each impacting particle) is usually a strongly increasing function of the ion impact energy, E_{impact}, section 3.3, and is linearly proportional to the ion particle flux density Γ. When the solid surface is at the plasma potential there is no sheath. In that case, Γ is the one-way Maxwellian value, $\frac{1}{4}n\overline{c}_i$, which is not much different from the value when the sheath is present, $\Gamma \simeq nc_s$, if $T_i \simeq T_e$. On the other hand, $\overline{E}_{\text{impact}}$ is $\simeq 2kT_i$ for no sheath and $\simeq 2kT_i + 3kT_e \approx 5kT$ with sheath. The $3kT_e$ portion is analogous to the energy gained by the water falling through the drop of the waterfall, figure 2.4. Therefore physical sputtering is increased by the presence of a sheath. In fact, the sheath could increase $\overline{E}_{\text{impact}}$ from a value below the sputtering threshold, section 3.3—where there is no sputtering at all (in principle)—to above threshold. The chemical sputtering yields of carbon for hydrogen and oxygen impact, section 3.3, are less dependent on E_{impact}.

(iii) For fixed plasma conditions the sheath reduces the heat flux to the solid surface.
In some (non-fusion) plasma devices, n and T are fixed, for example to meet some external requirements such as photon production in a light source. In that case, the sheath reduces q_{ss}. (It is important to note that this is *not* the situation with the tokamak SOL, which is considered below, (iv).)
For no sheath:

$$q_{ss}^e = 2kT_e \tfrac{1}{4} n\overline{c}_e \tag{2.97}$$

$$q_{ss}^i = 2kT_i \tfrac{1}{4} n\overline{c}_i \tag{2.98}$$

and $q_{ss}^e \gg q_{ss}^i$ since $\overline{c}_e \gg \overline{c}_i$, if $T_i \approx T_e$. With a sheath:

$$q_{ss}^e \simeq 2kT_e \tfrac{1}{4} n \exp(-3)\overline{c}_e \tag{2.99}$$

$$q_{ss}^i \simeq (2kT_i + 3kT_e)\tfrac{1}{2} nc_s. \tag{2.100}$$

Thus: the sheath increases q_{ss}^i approximately twofold while decreasing q_{ss}^e by approximately 20-fold, giving an overall reduction by about an order of magnitude. The sheath serves to protect the solid surface from plasma heat, insulating it.

(iv) For a plasma such as the tokamak edge, where input power is *given*, the resulting plasma n and T are strongly influenced by the presence of a sheath. The sheath properties are the *boundary conditions* for the edge plasma. For the tokamak edge the plasma properties n and T are not directly controlled but are the response to the imposed input power and the imposed plasma content of the tokamak vessel. From (iii) it is clear that, for a given input power and total plasma content, the resulting edge n and T will be quite different with and without a sheath being present at the solid surfaces.

There is usually not much choice in the matter, it should be noted: while portions of the plasma-wetted solid surface can be biased sufficiently to eliminate the sheath, the plasma *on average* must float relative to the solid structure, so sheaths tend to be an unavoidable fact of life when plasmas and solids interact. The real point is that the presence of the sheath very much affects the connection between the independent variables (input power, total plasma particle content) and the dependent variables (the edge density and temperature) and so it is essential to include the *sheath properties as boundary conditions* in modelling the edge plasma.

2.10 The Solid Surface at an Oblique Angle to $\boldsymbol{B}$: The Chodura Sheath

So far we have assumed that the normal to the solid surface is parallel to $\boldsymbol{B}$, which has the result that $\boldsymbol{B}$ does not occur explicitly in the analysis. In tokamaks, because of the small pitch angle, section 1.3, the angle between the surface normal and $\boldsymbol{B}$ can be quite large, for the most natural arrangements of toroidal limiters and poloidal divertors, section 1.4.2. In fact, it is desirable to construct configurations which employ glancing angles between $\boldsymbol{B}$ and the surface—only a degree perhaps—in order to make the deposited heat flux density as small a fraction of the parallel heat flux as possible, section 5.6. In this way the risk of melting and sublimation is reduced.

The *parallel* heat flux density is what we have been considering so far, equations (2.86)–(2.95). Although the latter results were obtained for the *normal sheath*, it will be found that this heat flux along $\boldsymbol{B}$ is little changed for the *oblique sheath*. Let us call this flux density $q_\parallel$ and the actually deposited heat flux $q_{\rm dep}$. Then

$$q_{\rm dep} = q_\parallel \cos\psi \tag{2.101}$$

where ψ is the angle between $\boldsymbol{B}$ and the surface normal; see figure 2.22. For the target plasma conditions $T \approx 25$ eV, $n \approx 10^{20}$ m^{-3}, equation (2.94) gives $q_\parallel > 10^8$ W m^{-2} which is almost two orders of magnitude higher than safe thermal engineering design. Thus values of ψ up to 89° are potentially of interest.

Even if the target surface normal is parallel to the poloidally projected $\boldsymbol{B}$, i.e. $\boldsymbol{B}_\theta$, figure 2.23(a), that still implies a large ψ, $\psi \gtrsim 80°$, simply due to the small pitch angle of the tokamak field, $B_\theta/B_\phi \ll 1$. In order to reduce $q_{\rm dep}$ still further, the divertor target can be tilted within the poloidal plane, figure 2.23(b), so that ψ up to 89° can be achieved. (For a discussion of the limit $\psi \to 90°$, see section 25.2). We wish to know the effect on Γ_{se}, V_{sf} and q_{se} of varying ψ from 0° (normal sheath) to $\sim$ 89° (strongly oblique sheath). The answer turns out to be that the effect is surprisingly small.

Here we present a simplified derivation of the properties of the oblique sheath. Figure 2.22 gives the basic picture, as first identified by Chodura [2.13]. Three regions exist:

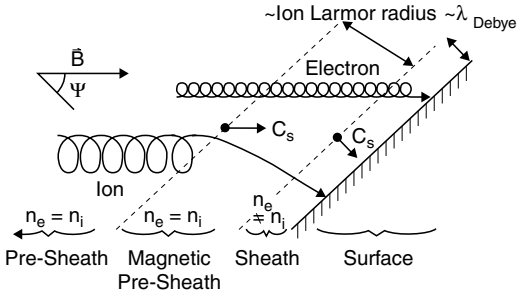

Figure 2.22. Chodura's analysis of the near-surface region for the case of $\boldsymbol{B}$ oblique to the surface [2.13]. A quasineutral magnetic pre-sheath, of thickness a few ion Larmor radii, now arises between the ($\boldsymbol{B} = \boldsymbol{0}$) pre-sheath and the Debye sheath.

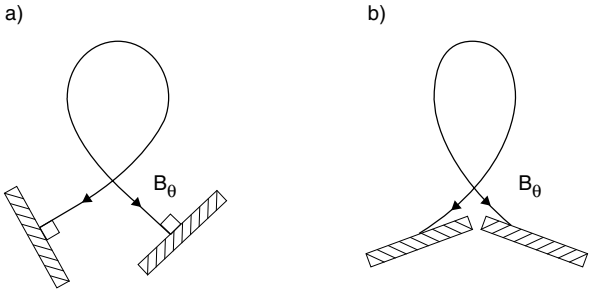

Figure 2.23. The separatrix magnetic field line in the poloidal plane for 'orthogonal' targets (a) and 'non-orthogonal' targets (b).

(1) The usual electrostatic sheath—or *Debye sheath*—where $n_e < n_i$, width a few λ_{Debye}.
(2) The *magnetic pre-sheath*, or *Chodura sheath* which is quasineutral and is of width a few *ion* Larmor radii; $\rho_i = m_i v_\perp / eB \cong m_i c_s / eB$.
(3) The usual *ordinary pre-sheath*, i.e. simply the plasma itself. This is also quasineutral. Characteristic scale lengths are the distance over which the particle source exists, or simply the size of the plasma.

The first and third regions have the same properties as for the normal sheath situation. Just as before, we may ignore the cyclotron motion of the ions and electrons in the pre-sheath/plasma, and only the transport parallel to $\boldsymbol{B}$ is of importance. The Debye sheath is typically so much thinner than an ion Larmor radius that the ion motion in this region is dominated by the E-field, as if the B-field were non-existent. Thus all the properties established in sections 2.3, 2.4 of the Debye sheath—including the Bohm criterion— continue to apply. Therefore the drift velocity at the se of the ions perpendicular to the solid surface must be, at minimum, c_s.

While it is not immediately obvious why it is true, Chodura was able to show that the velocity of the ions along $\boldsymbol{B}$, at the entrance to the Chodura sheath (the magnetic pre-sheath edge, MPSE) is $\geq c_s$. The derivation of this key result is discussed below. This is indeed a critically important result: it means that the plasma upstream of the MPSE—i.e. virtually the entire system—*has no 'knowledge' of whether the plasma flow tube is terminated by a normal sheath or an oblique sheath*. This is the reason why the value of ψ has so little consequence on any aspect of the plasma properties—yet allows us to have the benefits of arranging that $q_{\text{dep}} \ll q_{\parallel}$. (One also has $\Gamma_{\text{dep}} \ll \Gamma_{\parallel}$, of course, but this is of little practical importance since the *total* sputtered flux is not affected; the product of plasma-wetted area and Γ_{dep} is not changed.) Indeed, virtually no information can be communicated back to the plasma from points beyond the MPSE where $v_{\parallel} \geq c_s$, since the usual 'zone of silence' associated with supersonic flow sets in [2.15]. The information cut-off is not total because of the electrons which can convey some information back upstream since $v_{\parallel} \ll \overline{c}_e$; see below.

The function of the Chodura sheath is thus evident: a region of enhanced electric field is required in order to *turn* the sonic/supersonic ion flow from the parallel-to-$\boldsymbol{B}$ direction to the parallel-to-the-surface-normal direction. The electrons, with their much smaller Larmor radius, pass almost straight through both Chodura and Debye sheaths, undeflected.

The particle outflux density from the plasma, for an isothermal plasma is therefore:

$$\Gamma_{\parallel B} = n_{\text{MPSE}} c_s \approx \tfrac{1}{2} n_0 c_s \tag{2.102}$$

i.e. just the same boundary condition as for the normal sheath.

Consider next the floating potential to which the surface charges for ambipolar conditions, V_{sf}. The ions satisfy:

$$\Gamma^i_{\text{dep}} \equiv \Gamma^i_{\perp \text{surface}} = n_{\text{MPSE}} c_s \cos\psi. \tag{2.103}$$

Assuming that the electrons are not deflected at all, then:

$$\Gamma^e_{\parallel B} \approx \tfrac{1}{4} n_{\text{MPSE}} \overline{c}_e \exp[eV_{sf}/kT_e] \tag{2.104}$$

and so

$$\Gamma^e_{\text{dep}} \equiv \Gamma^e_{\perp \text{surface}} = \cos\psi \Gamma^e_{\parallel B}. \tag{2.105}$$

Equating equations (2.103) and (2.105) for the floating surface shows that the $\cos\psi$ term cancels out: *V_{sf} is independent of ψ, to first order*, see figure 2.24.

This total potential drop is distributed between the Debye sheath drop, eV_{DS}, and the Chodura sheath (magnetic pre-sheath) drop, eV_{MPS}:

$$V_{sf} = V_{\text{DS}} + V_{\text{MPS}}. \tag{2.106}$$

The split depends on ψ: the electrons satisfy the Boltzmann relation at all points, to the same high approximation as for the standard sheath, essentially (the

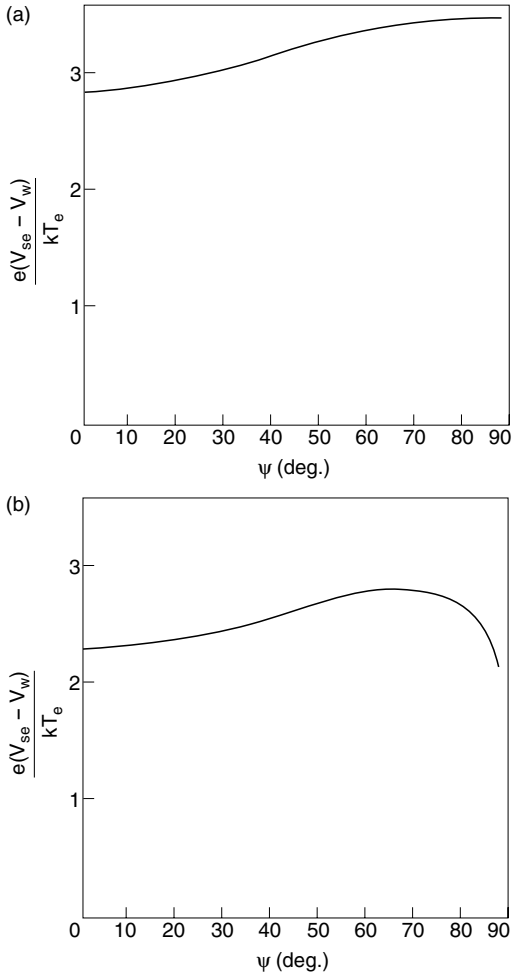

Figure 2.24. To first order the total voltage drop across the magnetic pre-sheath and Debye sheath is independent of angle ψ [2.13]. Electrically floating wall. (a) $T_i = 0$, (b) $T_i = T_e$ H^+ ions.

missing high energy tail is slightly different, see below), thus we take:

$$n_{\mathrm{DSE}} = n_{\mathrm{MPSE}} \exp[eV_{\mathrm{MPS}}/kT_e] \tag{2.107}$$

where n_{DSE}, n_{MPSE} are the densities at the Debye sheath edge (referred to simply as the 'se' previously) and the Chodura sheath edge. For the ions we assume conservation of flux between the two locations:

$$n_{\mathrm{MPSE}} c_s \cos\psi = n_{\mathrm{DSE}} c_s. \tag{2.108}$$

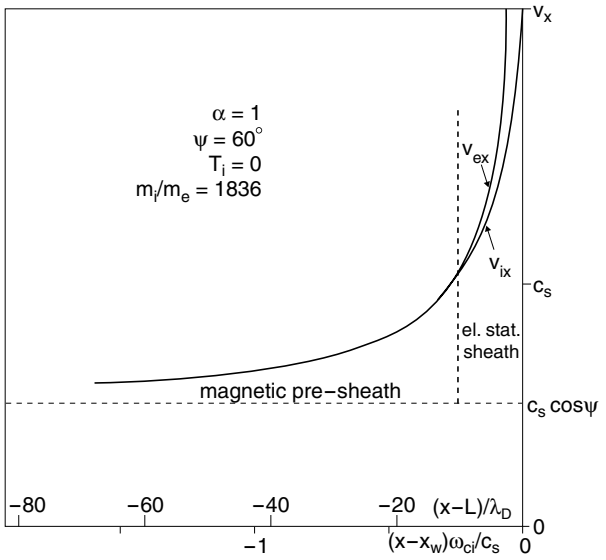

Figure 2.25. The average ion and electron velocities through the magnetic pre-sheath and Debye sheath [2.13] for the specific case of $\psi = 60\,^\circ$, $T_i = 0$, H^+ plasma. The magnetic field strength is specified through the parameter $\propto\equiv \omega_{ce}/\omega_{pe}$, where $\omega_{ce} \equiv eB/m_e$, the electron cyclotron frequency and $\omega_{pe} = (n_e e^2/\varepsilon_0 m_e)^{1/2}$ is the electron-plasma frequency. Here the case of $\alpha = 1$ is illustrated.

Combining (2.107) and (2.108) gives the potential drop across the Chodura sheath as:

$$\boxed{\frac{eV_{\mathrm{MPS}}}{kT_e} = \ln(\cos\psi).} \tag{2.109}$$

Example: $\psi = 80\,^\circ$, $eV_{\mathrm{MPS}}/kT_e = -1.75$, and so if $eV_{sf}/kT_e = -3$ then $eV_{\mathrm{DS}}/kT_e = -1.25$.

In the pre-sheath the E-field is required to overcome ion inertia, while in the Chodura sheath an additional E-force is required to overcome the $\boldsymbol{v} \times \boldsymbol{B}$, Lorenz, force on the ions. As ψ increases $|V_{\mathrm{MPS}}|$increases.

We may estimate the width of the Chodura sheath, L_{MPS}, and thus also the electric field E_{MPS}, as follows: the Lorenz force on the ion, balanced with the E-force, gives:

$$ev_i B \simeq eE_{\mathrm{MPS}} \tag{2.110}$$

with $v_i \simeq c_s$ and $E_{\mathrm{MPS}} \simeq kT_e/eL_{\mathrm{MPS}}$. Thus:

$$\boxed{L_{\mathrm{MPS}} \approx c_s/\omega_{ci} = \rho_i(c_s)} \tag{2.111}$$

that is, L_{MPS} is of the order of the ion Larmor radius ρ_i evaluated for velocity c_s.

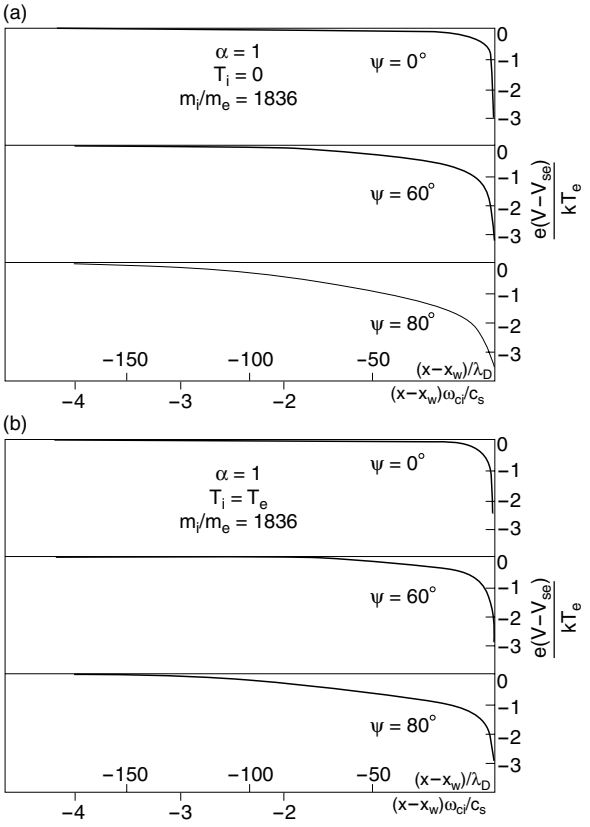

Figure 2.26. The potential drop through the magnetic pre-sheath and Debye sheath for various values of angle ψ and for $T_i = 0$ (a), $T_i = T_e$ (b), for H^+ plasma and $\alpha = 1$, no secondary electron emission for an electrically floating wall.

$\omega_{ci} = eB/m_i$. Chodura's more detailed analysis yields:

$$L_{\mathrm{MPS}} \simeq \sqrt{6}(c_s/\omega_{ci}) \sin\psi. \tag{2.112}$$

Figure 2.25 shows an example of the variation of ion and electron velocities, v_{ix}, v_{ex} through the MPS and the DS, illustrating that the scale length of the MPS is $\rho_i(c_s)$, and that of the DS, λ_{Debye}. One also may note that at the entrance to the MPS (far to the left in figure 2.25) $v_{ex} = c_s \cos\psi$, i.e. $v_{\|B,\mathrm{MPSE}} = c_s$, while at the DSE, $v_{ex} = v_{ix} = c_s$. Figure 2.26 gives examples of the electrostatic potential variation in the MPS and DS, showing that as ψ increases, more of the total potential drop occurs within the MPS (note that the DS is scarcely resolved in this figure).

We return to the derivation of the *Chodura criterion*:

$$\boxed{v_{\parallel B,\mathrm{MPSE}} \geqq c_s.} \tag{2.113}$$

Although the mathematics is more complex due to the presence of a magnetic field, the basic idea is the same as for the derivation of the Bohm criterion, section 2.3: Chodura [2.13], sets up an expression for the potential variation just entering the MPS—equivalent to equation (2.45). Chodura does not assume that quasineutrality holds in the MPS, but employs Poisson's equation, and demonstrates that the MPS is in fact quasineutral. Then, as with the $B = 0$ case, a constraint is found to exist for the ion velocity, in order that the potentials evolve in a non-oscillating way. Chodura formulates the problem in terms of a small time-independent 'disturbance' to the potential of the form $\exp(\mathrm{i}kx)$ and finds a relation between k^2 and $v_{\parallel B,\mathrm{MPSE}}$ (a 'dispersion relation') [2.13]. Only for $k^2 < 0$ will the potential 'disturbance' be non-oscillatory. (We used essentially the same idea in section 2.3). This is found to occur for $v_{\parallel B,\mathrm{MPSE}} \geqq c_s$, equation (2.113). Proceeding differently from Chodura, Riemann [2.27], assumed the MPS to be quasineutral and that the electrons satisfy the Boltzmann relation. He then showed that the existence of a (real) solution requires that relation (2.113) holds—which we may therefore call the Chodura–Riemann condition [2.54].

By treating the electron flow reaching the target in detail, Chodura found that eV_{sf} has a slight dependence on ψ, figure 2.24. As with the normal sheath the electrons would completely conform to the Boltzmann relation right up to the solid surface, were it not for the loss of the high energy tail of the electron distribution, which is absorbed by the surface. For the normal sheath this distortion to the electron distribution has no effect on the electron flux reaching the solid surface, Γ_{ess}, since only the $v_x > 0$ electrons are involved. For an oblique target, the electron absorption involves the v_y and v_z velocity components and the distortion to the electron distribution now effects Γ_{ess} somewhat.

The principal conclusions, however, are that, *to first order, the sink action of the solid surface acting on the plasma, with regard to both particle and power flows, is unaffected by the change from a normal to an oblique target*. Further, *the sheath voltage drop and ion impact energy are unaffected, to first order*.

At this point it is appropriate to return briefly to the topic of Langmuir probes, section 2.7. Probes built into limiters and divertor targets, figure 2.11, have become widely used in tokamaks since about 1990, due to the increasing levels of power and pulse lengths being employed. Fixed probes standing proud of the surface, figure 2.27(a), can suffer over-heating. One approach is to make the probe's collecting surface *almost* flush with the limiter/target surface, figure 2.27(b). The heat flux density received on the probe surface is only slightly higher than at the limiter/target surfaces, while at the same time, the *effective* collection area of the probe, A_{eff}, remains simply defined, namely it is the area of the probe projected perpendicular to $\boldsymbol{B}$. For the reasons just discussed above, the probe analysis can then proceed as if the collecting element were perpendicular

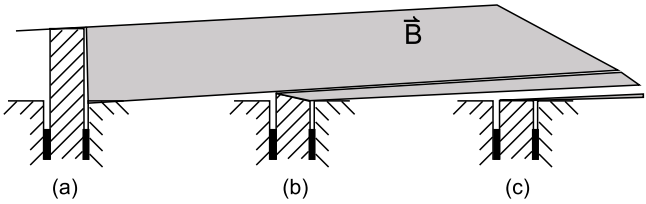

Figure 2.27. Langmuir probes built into divertor targets or limiters may involve highly oblique $\boldsymbol{B}$. The collection area of the probes is that projected perpendicular to $\boldsymbol{B}$.

to $\boldsymbol{B}$, and of area A_{eff} [2.35–2.39]. One would also use the projected area A_{eff} for 'proud' probes, figure 2.27(a).

The most robust built-in probes are *truly* mounted flush to the limiter or divertor target surface, figure 2.27(c). The magnetic field is still oblique to the collecting surface (we do not consider here the case of $\boldsymbol{B}$ perfectly parallel to the surface, which is discussed in section 25.2). In this situation the ion flow to the collecting surface is partly due to parallel-to-$\boldsymbol{B}$ motion, and partly due to cross-field, $\boldsymbol{E} \times \boldsymbol{B}$ drifts (chapter 18 and sections 25.3, 25.4). Riemann and co-workers have provided a simple and convenient analysis of this case [2.55] which is found to be in good agreement with experiment [2.56].

Additional Problems

2.2. Before the role of the pre-sheath in accelerating the ions was understood, it was thought that one could calculate the floating potential of a surface, V_{sf}, by assuming that the electron and ion particle flux densities entering the sheath were simply the one-way Maxwellian fluxes, which are:

$$\Gamma_{e,i}^{\text{Max,one-way}} = \tfrac{1}{4} n_{se} \overline{c}_{e,i}$$
$$\overline{c} \equiv (8kT/\pi m)^{1/2}.$$

Show that this incorrect line of reasoning gives the result:

$$\frac{eV_{sf}}{kT_e} = \frac{1}{2} \ln\left(\frac{m_e}{m_i}\frac{T_i}{T_e}\right).$$

Compare this with the Langmuir–Bohm result, equation (2.60). When is this a good approximation? When poor? Explain physically why this incorrect result gives

$$V_{sf} \to -\infty \text{ when } T_i \to 0.$$

2.3. *The Maxwellian distribution*. It is a general property of systems in equilibrium at temperature T, that the probability of a particle having an energy

E is proportional to $\exp[-E/kT]$. Use this property alone to obtain the Maxwellian distribution for velocities in two dimensions

$$f(v_x, v_y) = n\left(\frac{m}{2\pi kT}\right)\exp\left[-\frac{m}{2kT}(v_x^2 + v_y^2)\right].$$

2.4. Show that for a *three*-dimensional Maxwellian distribution the particle flux density Γ [particles $\mathrm{m}^{-2}\ \mathrm{s}^{-1}$] through any imaginary surface in one direction is $\Gamma = \frac{1}{4}n\overline{c}$ where $\overline{c} = (8kT/\pi m)^{1/2}$ (the net flux, of course is zero). Show that the one-directional energy flow density q [$\mathrm{W\ m}^{-2}$] through the surface is $q = 2kT\Gamma$. Show that the energy density is $\frac{3}{2}nkT$. Explain *physically* why q is greater than the product of Γ and the average energy per particle $3/2kT$.

2.5. Derive equations (2.16), (2.21), (2.28), (2.29), (2.31).

2.6. *Debye shielding*. In order for shielding to occur, i.e., for a plasma to exist (as distinct from simply *ionized gas*) the particle density must be large enough for some particles to exist, on average, in a distance λ_D, the Debye length. Find what conditions this imposes on n and T. Are fusion plasmas likely to satisfy this condition? What about interstellar space where, perhaps, $n = 10^6\ \mathrm{m}^{-3}$, $T = 10^{-2}$ eV?

2.7. Show that $f = f^{\mathrm{Max}}e^{-\Phi/kT}$ satisfies equation (2.34).

2.8. A large voltage is applied to a 1D plasma with $n = 2 \times 10^{18}\ \mathrm{m}^{-3}$ and $T_e = T_i = 15$ eV. The plasma occupies 1 m between the electrodes. Owing to the presence of the neutrals, the ions suffer collisions in responding to the electric field and the result is that a 200 V drop develops within the plasma itself due to friction.

(a) Calculate the charge imbalance in the plasma, i.e., $(n_e - n_i)/n_e$.

(b) The sheath thickness, l_{sh}, is not actually a constant, but it increases with the magnitude of the potential drop across the sheath, ΔV_{sh}. One can make a rough estimate of $l_{sh}(\Delta V_{sh})$ using Poisson's equation together with the crude assumptions that within the sheath $n_e \approx 0$ and $n_i \approx n_0$, constant, i.e. that the electron density decreases *extremely* rapidly compared with the ion density. Assuming that the electric field at the entrance to the sheath can be neglected, show that:

$$l_{sh} \approx \lambda_D(e\Delta V_{sh}/kT_e)^{1/2}.$$

Estimate the sheath thickness here [m], if $\Delta V_{sh} = 150$ volts.

(c) Make less crude approximations to show that one obtains the *Child–Langmuir law* [2.19]:

$$\boxed{l_{sh} \approx \lambda_D(e\Delta V_{sh}/kT_e)^{3/4}.}$$

Hint: see equation (9) of [2.19].

(d) For sufficiently large ΔV_{sh}, the sheath can be made 'visible' as a dark region (due to the relative absence of electrons which cause photon emission by impact with neutrals). Assuming that l_{sh} would need to be at least 1 mm to be seen, how large a sheath voltage drop would be required to make the sheath visible in the above plasma?

2.9. Show that the Bohm criterion, equation (2.48), can also be obtained [2.57] from requiring that:

$$\left.\frac{\mathrm{d}n_i}{\mathrm{d}x}\right|_{se} \geq \left.\frac{\mathrm{d}n_e}{\mathrm{d}x}\right|_{se}$$

that is, as the sheath is entered the electron density decreases as fast as, or faster than, the ion density (note that both gradients are negative).

Hint: $\mathrm{d}n/\mathrm{d}x = (\mathrm{d}n/\mathrm{d}V)(\mathrm{d}V/\mathrm{d}x)$. Give a physical justification for the above assumption.

2.10. The derivation of the Bohm criterion in section 2.3 assumed singly charged ions. Re-derive this criterion assuming a charge of Z on the ions to show that $v_{se} \geq (ZkT_e/m_i)^{1/2}$.

2.11. *Demonstration that in a retarding electric field the electron velocity distribution remains Maxwellian, but the electron density is reduced by the Boltzmann factor.*

(a) Write down the 1D Maxwellian velocity distribution.

(b) Write down the expressions for the conservation of energy and particles. Assume there is no volumetric source or sink of electrons. Let the velocity distribution at any general location be $g(v')$, and at the reference location be $f_{\mathrm{ref}}(v)$, a Maxwellian. From energy conservation:

$$v'^2 = v^2 - 2eV/m_e$$

where the reference potential is taken to be $V = 0$. Argue that particle conservation gives:

$$v'g(v')\mathrm{d}v' = vf_{\mathrm{ref}}(v)\mathrm{d}v.$$

(c) Thus prove the stated result.

2.12. From the generalized Bohm criterion, argue that either $f^i_{se}(v) = 0$ for v below some positive cut-off velocity, or that for small v, $f^i_{se}(v) \propto v^\alpha$, and find the value of α (range). Comment on the significance of your findings.

2.13. Derive equation (2.55*a*).

2.14. (a) For the electrically biased configuration shown in figure 2.9, and analysed in section 2.6, calculate the I–V characteristic, figure 2.15. Assume $n_{se} = 10^{19}$ m^{-3}, $T_e = T_i = 10$ eV, H^+ plasma. Take the

area of each end plate-electrode to be 3×10^{-4} m^2. Plot current I [A] against V_{applied} (V), also the voltage on the left and right plate-electrode, V_ℓ and V_r against V_{applied}. Evaluate the saturation current I^+_{sat} [A].

(b) Prove that

$$\boxed{I/I^+_{\text{sat}} = -\tanh[eV_{\text{applied}}/2kT_e],}$$

the *double-probe characteristic*.

(c) Show how you could analyse the I–V characteristic (pretending that it had been obtained by experiment) to extract measured values of n_e and T_e. Show that there is a simple relation between T_e and $\mathrm{d}I/\mathrm{d}V_{\text{applied}}$, evaluated at $V_{\text{applied}} = 0$. This constitutes a double-probe analysis.

2.15. Derive equation (2.67).

2.16. Repeat problem 2.14(a) but now for a single probe by assuming that the left plate-electrode probe has area 3×10^{-4} m^2 while the right plate-electrode probe has an area much larger. Assume there is no B-field. In order to avoid having to deal with the transition to electron current saturation, just calculate and plot for values of V_{applied} which give net ion current collection. As for problem 2.14(c) find the relation here between T_e and $\mathrm{d}I/\mathrm{d}V_{\text{applied}}$ evaluated at $V_{\text{applied}} = 0$.

2.17. For plasma conditions at the se: $n_e = 10^{19}$ m^3, $T_e = 10$ eV, $T_D = 20$ eV, and assuming an electrically floating surface, calculate:

(a) Γ_{se}, (b) V_{sf}, (c) q^e_{ss}, (d) q^e_{se} (e) q^i_{ss}, (f) q^i_{se} (g) γ and (h) the value of q^e and q^i at a location part way through the Debye sheath, specifically at the location where $V = (1/3)V_{sf}$. Use $V_{se} = 0$.

2.18. For the same plasma as in problem 2.17, find the values of q^i_{ss} and q^e_{ss} if the solid is electrically biased so that there is no potential difference between the plasma and the solid, i.e. no sheath. Compare with the results of the last problem and comment.

2.19. *The Chodura sheath.* Plasma conditions: $n_0 = 10^{19}$ m^{-3}, $T_e = 10$ eV, $T_i = 20$ eV, D^+ plasma, $B = 3$ T. Take $V_{\text{MPSE}} = 0$ and for $\psi = 10\,^\circ, 50\,^\circ, 85\,^\circ$ evaluate:

(a) the ion flux density parallel to $\boldsymbol{B}$ at the MPSE,
(b) the ion flux density perpendicular to the solid surface at the DSE,
(c) the ion flux density received by the solid surface,
(d) the potential at the DSE,
(e) the potential at the solid surface,
(f) the width of the MPS (estimate),
(g) the electric field in the MPS (estimate),
(h) the electric field in the DS (estimate),

(i) the heat flux density parallel to $\boldsymbol{B}$ at the MPSE in the ion 'channel', and in the electron 'channel',
(j) the total heat flux density received by the solid surface.

References

[2.1] Bohm D 1949 *The Characteristics of Electrical Discharges in Magnetic Fields* ed A Guthrie and R K Wakerling (New York: McGraw-Hill) chapter 3
[2.2] von Engel 1965 *Ionized Gases* 2nd edn (Oxford: Oxford University Press) p 264
[2.3] Goldston R J and Rutherford P H 1997*Introduction to Plasma Physics* (Bristol: Institute of Physics Publishing) p 174
[2.4] Goldston R J and Rutherford P H 1997 *Introduction to Plasma Physics* (Bristol: Institute of Physics Publishing) p 177
[2.5] Tonks L and Langmuir I 1929 *Phys. Rev.* **34** 876
[2.6] Goldston R J and Rutherford P H 1997 *Introduction to Plasma Physics* (Bristol: Institute of Physics Publishing) p 1
[2.7] Holt E H and Haskell R E 1965 *Foundations of Plasma Dynamics* (New York: Macmillan) pp 114–135
[2.8] Sears F W 1953 *An Introduction to Thermodynamics, the Kinetic Theory of Gases, and Statistical Mechanics* (Reading, MA: Addison-Wesley) p 244
[2.9] Holt E H and Haskell R E 1965 *Foundations of Plasma Dynamics* (New York: Macmillan) p 168
[2.10] Holt E H and Haskell R E 1965 *Foundations of Plasma Dynamics* (New York: Macmillan) p 134
[2.11] Goldston R J and Rutherford P H 1997 *Introduction to Plasma Physics* (Bristol: Institute of Physics Publishing) pp 14, 111
[2.12] Self S A 1963 *Phys. Fluids* **6** 1762
[2.13] Chodura R 1986 *Physics of Plasma–Wall Interactions in Controlled Fusion* ed D E Post and R Behrisch (New York: Plenum Press) p 99
[2.14] Harrison E R and Thompson W B 1995 *Proc. Phys. Soc*. **72** 2145
[2.15] Allen J E 1976 *J. Phys. D: Appl. Phys*. **9** 2331
[2.16] Gabor D, Ash E A and Dracott E D 1955 *Nature* **176** 916
[2.17] Rayment S W and Twiddy N D 1968 *Proc. R. Soc.* A **340** 87
[2.18] Wang W X, Okamoto M, Nakajima N *et al* 1997 *Nucl. Fusion* **37** 1445
[2.19] Riemann K-U 1991 *J. Phys. D: Appl. Phys*. **24** 493
[2.20] Riemann K-U 1996 *Contrib. Plasma Phys*. **36** S19
[2.21] Riemann K-U 1981 *Phys. Fluids* **24** 2163
[2.22] Riemann K-U 1989 *Phys. Fluids* B **1** 961
[2.23] van den Berg H-P, Riemann K-U and Ecker G 1991 *Phys. Fluids* B **3** 838.
[2.24] Riemann K-U and van den Berg H-P 1991 *Phys. Fluids* B **3** 1300
[2.25] Riemann K-U 1991 *Phys. Fluids* B **3** 3331
[2.26] Riemann K-U 1992 *J. Phys. D: Appl. Phys*. **25** 1432
[2.27] Riemann K-U 1994 *Phys. Plasmas* **1** 552
[2.28] Riemann K-U 1995 *IEEE Trans. Plasma Sci.* **23** 709
[2.29] Schmitz H, Riemann K-U and Daube Th. 1996 *Phys. Plasmas* **3** 2486
[2.30] Riemann K-U 1997 *Phys. Plasmas* **4** 4158

[2.31] Daube Th., Riemann K-U, Schmitz H 1998 *Phys. Plasmas* **5** 117
[2.32] Daube Th. and Riemann K-U 1999 *Phys. Plasmas* **6** 2409
[2.33] Swift J D and Schwar M J 1969 *Electric Probes for Plasma Diagnostics* (London: Elsevier)
[2.34] Chen F F 1965A *Plasma Diagnostic Techniques* ed R H Huddlestone and Leonard S L (London: Academic)
[2.35] Manos D and McCracken G M 1986 *Physics of Plasma–Wall Interactions in Controlled Fusion* ed D E Post and R Behrisch (New York: Plenum Press) p 135
[2.36] Hutchinson I H 1988 *Principles of Plasma Diagnostics* (Cambridge: Cambridge University Press)
[2.37] Stangeby P C 1988 *Plasma Diagnostics* vol 1 ed O Auciello and D (Boston: Academic) p 157
[2.38] Matthews G F 1994 *Plasma Phys. Control. Fusion* **36** 1595
[2.39] Stangeby P C and McCracken G M 1990 *Nucl. Fusion* **30** 1225.
[2.40] Stangeby P C 1995 *Plasma Phys. Control. Fusion* **37** 1337
[2.41] Bohm D 1949 *The Characteristics of Electrical Discharges in Magnetic Fields* ed A Guthrie and R K Wakerling (New York: McGraw-Hill) chapter 2
[2.42] Vasin N L, Vershkov V A, Grashin S A *et al* 1989 *J. Nucl. Mater*. **162–164** 300
[2.43] Pospieszczyk A, Aumayr F, Bay H L *et al* 1989 *J. Nucl. Mater*. **162–164** 574
[2.44] Watkins J G, Moyer R A, Cuthbertson J W *et al* 1997 *J. Nucl. Mater*. **241–243** 645
[2.45] Stangeby P C 1995 *Plasma Phys. Control. Fusion* 37 1031
[2.46] Boedo J A, Porter G D, Schaffer M J *et al* 1998 *Phys. Plasmas* **5** 4305
[2.47] Watkins J G, Batischev O, Boedo J *et al* 1999 *J. Nucl. Mater*. **266–269** 980
[2.48] Stangeby P C 1986 *Physics of Plasma–Wall Interactions in Controlled Fusion* ed D E Post and R Behrisch N.A.T.O. (New York: Plenum Press) p 41
[2.49] Matthews G F, Pitts R A, McCracken G M and Stangeby P C 1991 *Nucl. Fusion* **31** 1495
[2.50] Wan A S, LaBombard B, Lipschultz B and Yang T F 1987 *J. Nucl. Mater*. **145–147** 191
[2.51] Guo H Y, Matthews G F, Davies S J *et al* 1996 *Contrib. Plasma Phys*. **36** S81
[2.52] Pitts R A 1996 *Contrib. Plasma Phys.* **36** S87
[2.53] Erents S K, Breger P, Davies S J *et al* 1997 *J. Nucl. Mater*. **241–243** 433.
[2.54] Stangeby P C 1995 *Phys. Plasmas* **2** 702
[2.55] Daube Th, Riemann K-U and Schmitz H 1998 *Contrib. Plasma Phys.* **38** S 145
[2.56] Wolters W, Daube Th, Riemann K-U and Wiesemann K 1999 *Plasma Phys. Control. Fusion* **41** 721
[2.57] Allen J E and Thonemann P C 1954 *Proc. Phys. Soc*. B **67** 768

Chapter 3

Experimental Databases Relevant to Edge Physics

3.1 Ion and Atom Back-scattering from Surfaces

When ions or atoms strike a solid surface they suffer one of several fates:

(a) they may be directly *back-scattered* or reflected with some fraction of the impact energy E_0 ($\equiv E_{\text{impact}}$ in chapter 2);
(b) they may be implanted in the near surface, where they will become thermally accommodated, and be subsequently released as a *thermal particle*;
(c) as (b) but they remain *trapped* in the solids for some extended period of time.

In this context there are no significant differences between incident atoms and ions. An ion approaching a solid surface extracts an electron as it enters the solid, and so the actual interaction with the solid is the same as for an atom, including any subsequent ionization of the projectile as it collides with the atoms in the solid lattice. Furthermore, when the particle is reflected, the probability that it will do so as a neutral is quite high, irrespective of the charge state of the original projectile, since the velocity of the separation between the reflected particle and the surface is slow compared with typical electron speeds and there is time for an electron to be released from the surface and to neutralize a departing ion. For H^+ impacting on stainless steel, and $E_0 < 1$ keV, less than 10% of the particles are reflected as H^+ or H^-, with $> 90\%$ being H^0 [3.1].

Back-scattering data are expressed in terms of the *particle and energy reflection coefficients* R_N and R_E, which depend on the impacting and substrate species, impact energy E_0, and the angle of incidence α, measured with respect to the surface normal [3.1–3.4]. Acceleration of ions across the Debye sheath tends to make the ions move unidirectionally, normal to the surface, and roughly mono-energetically. When $\boldsymbol{B}$ is oblique to the solid surface, section 2.10, there is a strong 'straightening' effect on the ion trajectories in the Chodura pre-sheath (magnetic pre-sheath), although not enough to achieve normal incidence of the

ions as they strike the solid surface. For practical applications, *surface roughness* rather diminishes the importance of establishing the actual impact angle, and often the normal incidence data are assumed to apply. If the data were experimentally generated, they may well have been obtained for a roughened surface in any case—if not originally rough, then rendered rough on the atomic scale by the bombardment itself. Here we only consider normal incidence data.

The particle reflection coefficient R_N is defined to be the number N of all back-scattered particles divided by the number N_0 of incident particles [3.1]:

$$\boxed{R_N(E_0) = N/N_0.} \tag{3.1}$$

Each back-scattered particle has some particular energy $E < E_0$, spanning a distribution. The energy reflection coefficient R_E is defined as the total energy of the reflected particles divided by the total energy of the incident particles [3.1]:

$$\boxed{R_E(E_0) = \frac{\overline{E}(E_0)N}{E_0 N_0} = \frac{\overline{E}(E_0)}{E_0} R_N(E)} \tag{3.2}$$

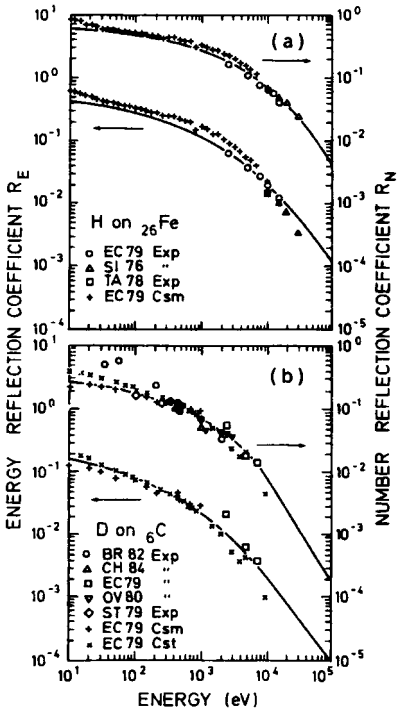

Figure 3.1. Particle (or number) and energy reflection coefficients for (a) H on Fe, and (b) D on C versus the impact energy [3.3].

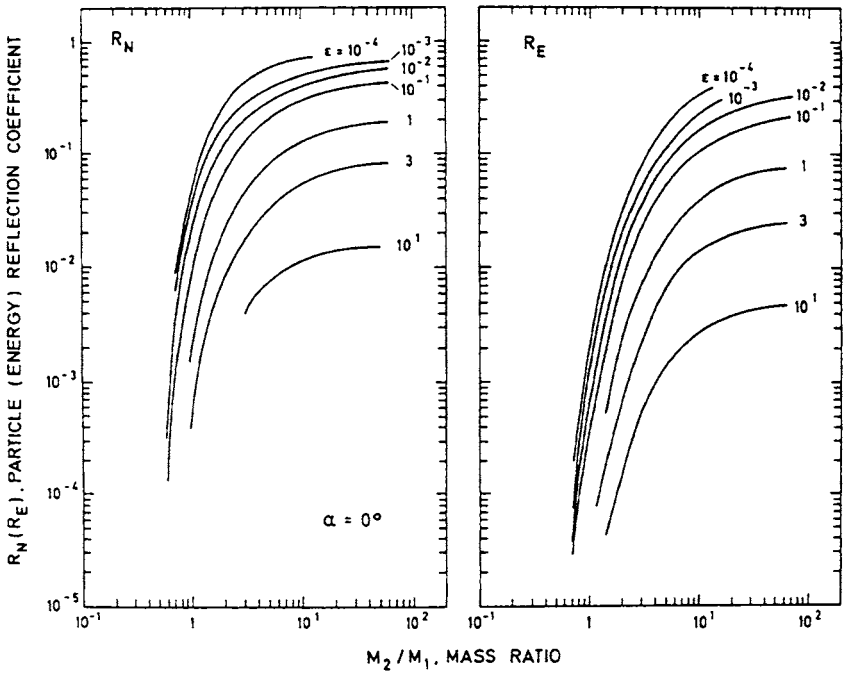

Figure 3.2. Particle and energy reflection coefficients versus mass ratio M_2/M_1, for different reduced energies ε, equation (3.3), at normal incidence [3.3].

where $\overline{E}(E_0)$ is the mean energy of the reflected particles. (Note: R_E is *not* simply defined as $\overline{E}/E_0$.)

Values of R_N, R_E are available in some cases from laboratory measurements. For more extended coverage of projectile and substrate species, R_N and R_E are calculated using computer codes such as TRIM [3.1–3.3]. Examples for H on Fe and D on C are given in figure 3.1 [3.3]. From these examples one may note a number of features:

(1) R_N, R_E drop as E_0 increases. The projectiles bury themselves in the solid more effectively at higher E_0, figure 3.1.
(2) Reflection is more effective the larger the ratio $M_{\text{substrate}}/M_{\text{projectile}}$, where M is atom mass, figure 3.2. Light projectiles reflect from a heavy atom substrate like a ping pong ball hitting a billiard ball.

For other projectile/substrate pairs one may use calculated universal profiles such as figure 3.2 [3.3] where the *reduced energy* ε is defined [3.3]:

$$\varepsilon \equiv 0.032\,534 E_0[\text{eV}] M_2/[(M_1 + M_2) Z_1 Z_2 (Z_1^{2/3} + Z_2^{2/3})^{1/2}]. \qquad (3.3)$$

$M_2 \equiv M_{\text{substrate}}$, $M_1 \equiv M_{\text{projectile}}$ and the Zs are the charges of the bare nuclei. From figure 3.2 it is evident that reflection becomes negligible for $M_2/M_1 \lesssim 0.5$. A number of convenient fitting formulae are available for $R_N(\varepsilon)$ and $R_E(\varepsilon)$ [3.1–3.3, 3.5].

3.2 Particle-Induced Electron Emission

Electrons released from the solid surface into the plasma reduce the (floating) sheath potential drop, and alter the sheath heat transmission coefficient γ, section 25.5, figure 2.8. It has to be noted however, that a low energy electron released from a surface, when $\boldsymbol{B}$ is rather oblique to the surface, has a finite Larmor radius and thus has a good chance of immediately returning to the surface within one Larmor period; see problem 3.2. The *effective* electron emission coefficient for fusion devices is thus sometimes taken to be zero, regardless of the original release rate.

Electrons can be released from solids by impact of electrons, ions, photons, excited neutrals, etc. Here we consider only electron impact which shows peak yields for $E_0 =$ hundreds eV. Peak ion yields occur at $E_0 =$ hundreds of keV, although there are non-negligible yields at hundreds of eV [3.4, 3.6]. Usually electron impact is the most important release process.

The total yield ξ of emitted electrons per primary electron is defined to be:

$$\xi = \delta + \eta. \tag{3.4}$$

δ is due to the true secondary electrons and η represents reflected or back-scattered electrons. While strictly these two contributions cannot be separated, the energy

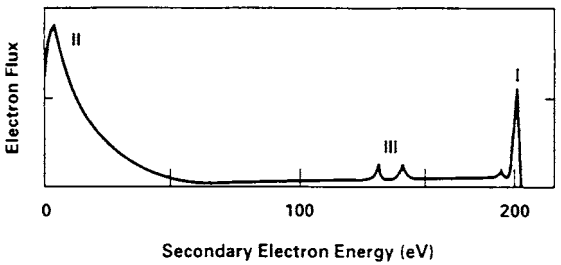

Figure 3.3. Representative energy distribution of electrons emerging from a solid as a result of electron bombardment at a primary energy E (200 eV). Peak I is the main reflected peak with structure at slightly lower energies due to specific energy loss processes. Peak II is the main secondary electron peak. The minor peaks at III are from Auger transitions. The secondary emission coefficient δ includes all electrons ejected at energies below 50 eV. The reflection coefficient η is taken as including all electrons ejected at energies above 50 eV [3.6].

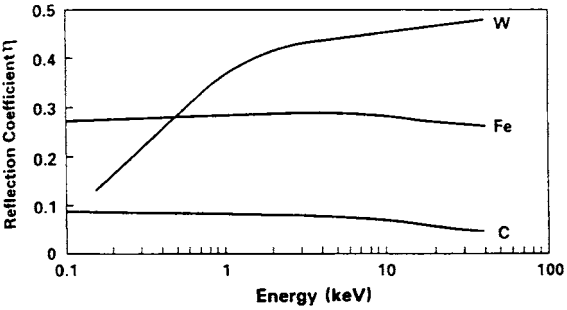

Figure 3.4. Reflection coefficient as a function of incident electron energy for C, Fe and W [3.6].

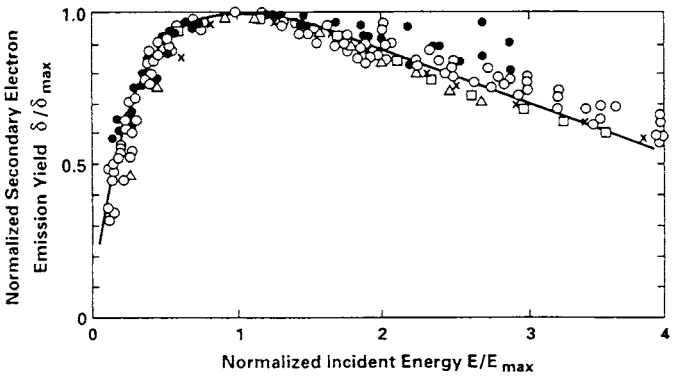

Figure 3.5. Normalized secondary electron emission coefficient $\delta/\delta_{\max}$ as a function of normalized energy $E/E_{\max}$. The circles are data for Li, Mg, Al, Si, Ti, Fe, Cu, Ni, Ga, Ge, Rb, Nb. The other data points are for TaC (×), TiC (Δ) and ZrC (□). The line is the semi-empirical curve, equation (3.5), [3.6].

of the electrons emerging from the solid provides a basis for estimates; see figure 3.3 [3.6]: peak I is due to the back-scattered electrons, peak II to the true secondaries which typically have only a few eV energy (peak III is due to Auger transitions). Figure 3.4 [3.6] gives some example values of η. The form of δ, for many materials, can be approximated by the relation [3.6]

$$\frac{\delta}{\delta_{\max}} = (2.72)^2 \frac{E_0}{E_{\max}} \exp\left[-2\left(\frac{E_0}{E_{\max}}\right)^{1/2}\right] \tag{3.5}$$

where δ has a maximum value of $\delta_{\max}$, when $E = E_{\max}$. Values of $\delta_{\max}$ and $E_{\max}$ for different materials are given in table 3.1 [3.6] and the comparison with data is shown in figure 3.5 [3.6]. For almost all practical purposes the sum ξ is used;

Table 3.1. Maximum of the secondary electron emission yield, δ_{max}, and projectile energy at which it occurs, E_{max}, for selected elemental metals and certain other materials [3.4].

Target	Z	δ_{max}	E_{max}[eV]
Be	4	0.5	200
C (graphite)	6	1.0	300
C (pocographite)	6	0.55	500
Al	13	1.0	300
Ti	22	0.9	280
Fe	26	1.3	400
Ni	28	1.35	550
Mo	42	1.25	375
W	74	1.4	650
TiC		1.0	460
TaC		0.84	270
ZrC		1.25	340
TiN		0.95	350
Stainless steel		1.22	400

Data are for normal incidence.

δ usually dominates over η, so most of the electrons can be taken to be of low energy.

It is worth noting [3.6]: *'δ is very sensitive to surface conditions and topography; it is likely to change significantly during operation of a plasma device. Reliable values of δ can be obtained only by a study of the material in the condition found in the plasma device'*.

3.3 Sputtering

When energetic ions (or neutrals, e.g. from charge exchange occurring in the plasma) strike a solid surface, sufficient momentum can be transferred to an atom in the solid lattice to eject it. This removal via momentum transfer is termed *physical sputtering* and is distinguished from *chemical sputtering*. In chemical sputtering the chemical potential energy of the H atom or ion is involved (the reactivity of the H_2 or O_2 with carbon is negligible in comparison with H^0, H^+, O^0, O^+). This potential energy is available to break C–C lattice bonds, and make C–H bonds, eventually leading to the formation of volatiles such as CH_4 which are released from the surface. Thus, even H atoms with negligible kinetic energy are effective—although the chemical reactivity is greatly enhanced for higher impact energy, section 3.3.2.

Impurities which have been injected into the plasma are ionized but eventually return to strike a solid surface, giving rise to *self-sputtering*. Since momentum transfer between like masses is very effective, this sputtering process can be particularly damaging.

All sputtering processes are characterized by the *sputtering yield*, Y, which is the number of atoms or molecules ejected per impacting particle. Y is dependent on impact energy, E_0, angle of impact α and the two species involved. For physical sputtering Y is either measured, typically employing an ion accelerator, or is calculated using, for example, the TRIM code [3.7–3.10]. Chemical sputtering yields are measured experimentally. Self-sputtering yields often exceed unity, thus indicating the danger of a *runaway self-sputtering cascade*. Physical sputtering yields for H/D/T are generally a few per cent at the maximum. Chemical sputtering yields of C by H are up to a few per cent. The chemical sputtering of C by O has about 100% yield [3.11], indicating the importance of achieving clean vacuum conditions; even if bulk carbon/graphite is not present in the machine, carbon tends to be ubiquitous in vacuum systems, and a nearly steady-state C + O recycling process can occur. Deposition (*gettering*) on surfaces by reactive elements such as Li, Be, B, Ti, etc, to form thin layers which rapidly react with oxygen to form stable oxides, can be used to deal with the stubborn oxygen problem [3.12].

The charge on the incident particle is relevant inasmuch as an ion will be accelerated by the sheath. Once the ion reaches the surface, however, it is neutralized and the yield is the same for ions and atoms of the same energy impacting the surface. The ejected particles are primarily neutral atoms, atom clusters or molecules.

For physical sputtering to occur, enough momentum must be transferred to the lattice atom to overcome the surface binding energy; thus a *threshold energy* E_{th} exists for physical sputtering, below which no sputtering occurs. The value of E_{th} can be estimated simply from known, measured values of the *surface binding energy* E_B—which may be taken as the heat of sublimation; $E_B(\mathrm{Li}) = 1.67$ eV, $E_B(\mathrm{Be}) = 3.38$ eV, $E_B(\mathrm{C}) = 7.4$ eV, $E_B(\mathrm{Fe}) = 4.3$ eV, $E_B(\mathrm{Mo}) = 6.9$ eV, $E_B(\mathrm{W}) = 8.8$ eV for example (3.13). From simple analysis of momentum transfer in a head-on collision between two particles of mass M_1 (projectile) and M_2 (substrate), we know the maximum energy fraction that can be transferred is:

$$\gamma = \frac{4M_1M_2}{(M_1 + M_2)^2}. \tag{3.6}$$

(Note: γ here is not to be confused with the sheath heat transmission coefficient of chapter 2.)

The most common sputtering event for light incident ions involves two collisions between the projectile and lattice atoms: the first collision occurs in the lattice reflecting the projectile back toward the layers nearer the surface; the second collision involves an impact, say on a first-layer atom, from below, ejecting it. Thus, for sputtering due to collisions which are head-on—the most extreme case—one has:

$$\boxed{E_{\mathrm{ejected}} = E_0\gamma(1-\gamma) - E_B.} \tag{3.7}$$

Thus, when $E_0 = E_{th}$, then $E_{\text{ejected}} = 0$ giving:

$$\boxed{E_{th} = \frac{E_B}{\gamma(1-\gamma)}.} \tag{3.8}$$

This provides a good estimate for E_{th}; for example, for H on C, $\gamma = 0.284$, and one obtains from equation (3.8) $E_{th} = 37$ eV, close to the value tabulated in [3.9] of 35 eV. One should, however, use the *fitted* values of E_{th} provided in [3.7–3.10].

Equation (3.8) also indicates the high E_{th} for high Z substrates; for example, H on W, for which $\gamma = 0.0215$, and $E_B = 8.8$ eV, equation (3.8) gives $E_{th} = 418$ eV. One also sees the reduced E_{th} for impurity sputtering; for example, for O on W, for which $\gamma = 0.294$, equation (3.8) gives $E_{th} = 42$ eV.

For substrates such as W, there exists the attractive prospect of having no sputtering at all: if the plasma temperature at the target is low enough then the (floating) sheath potential drop may be low enough that $E_0 < E_{th}$; there will also then be no self-sputtering. This attractive option is compromised, at least to some degree, by:

(a) the fact that the impacting H/D/T ions are not precisely monoenergetic, but there exists a *high energy tail* of their distribution. The sputtering can be dominated by this tail [3.10];
(b) the inevitable presence of light impurities such as C and O which result in impurity sputtering, and subsequently self-sputtering [3.14].

This high Z substrate option (which exploits the fact that generally the higher the Z, the higher E_{th}) nevertheless remains a very important one [3.15].

3.3.1 Physical Sputtering

Convenient formulae have been developed [3.7–3.10, 3.16] for $Y(E_0, \alpha)$ covering many projectile–substrate pairs. As for ion back-scattering, section 3.1, we only cite here the results for normal incidence ions, $\alpha = 0$. While for nearly perfect crystal surfaces Y can change by an order of magnitude with angle, for roughened (practical) surfaces, at glancing angles, there is much less dependence of Y on α [3.9]. In addition—as for ion back-scattering—there exists the 'straightening' effect of the sheaths on the ion trajectories—tending to make the ion impact approach normal incidence. A first approximation allowing for the effects of roughness and non-tangential targets could be simply to double the normal formula for physical sputtering yield [3.17].

Experimentally measured yields for physical sputtering follow the convenient Bohdansky formula fairly well [3.7–3.10]:

$$\boxed{Y(E_0, \alpha = 0) = QS_n(\varepsilon)g(E_{th}/E_0)} \tag{3.9}$$

where Q is called the 'yield factor'. Q depends on the surface binding energy E_B and the projectile and target masses, M_1 and M_2, respectively. The analytic expression for the nuclear stopping cross-section $S_n(\varepsilon)$, which is based on the Thomas–Fermi potential, is given approximately by:

$$S_n(\varepsilon) = \frac{3.441\sqrt{\varepsilon}\ln(\varepsilon + 2.718)}{1 + 6.355\sqrt{\varepsilon} + \varepsilon(6.882\sqrt{\varepsilon} - 1.708)}. \tag{3.10}$$

ε is the reduced energy defined by equation (3.3). $\varepsilon \equiv E_0/E_{\mathrm{TF}}$, where E_{TF} is the Thomas–Fermi energy [3.9]. The function g in equation (3.9) takes into account threshold effects and is given by:

$$g(\delta) = (1 - \delta^{2/3})(1 - \delta)^2 \tag{3.11}$$

with $\delta = E_{th}/E_0$ here (which is *not* the δ of the last section!). Compilations of E_{TF}, E_{th} and Q are given in [3.7–3.10]. Sample values [3.9] are given in table 3.2. One notes from equation (3.11) that indeed $Y \to 0$ for $E_0 \to E_{th}$.

Figure 3.6 gives some examples of yields for normal incidence physical sputtering; these results are from code, TRIMSP [3.10], calculations. Experimental data are typically within a factor of two of code calculations, which is also representative of the data scatter. *This significant uncertainty in the basic data of physical sputtering should always be borne in mind when interpreting tokamak edge experiments. Agreement between modelling and experiment by a factor better than 2 must be fortuitous*. Errors in physical sputtering yields can be very large near the threshold energy due to uncertainties in the threshold value, and the very rapid variations in yield involved there. The uncertainties are usually attributed to variations in surface conditions affecting the binding energy.

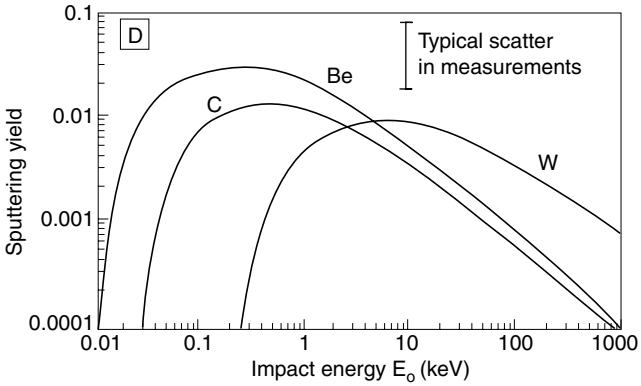

Figure 3.6. Normal incidence physical sputtering yields for D on Be, C and W surfaces, calculated using the TRIMSP code [3.10]. Experimental data are typically within a factor 2 of code calculations, which is also typical of the data scatter.

Table 3.2. Parameters for the physical sputtering yield [3.9].

Target	H	D	T	^{4}He	C	O	self
Beryllium							
E_{th} (eV)	20	9	21	30	40	70	25
E_{TF} (eV)	256	282	308	780	4152	6970	2208
Q (atoms/ion)	0.1	0.3	0.24	0.59	1.6	1.3	1.4
Graphite							
E_{th} (eV)	35	30	30	29	42		42
E_{TF} (eV)	415	447	479	1087	5687	9298	5687
Q (atoms/ion)	0.035	0.10	0.20	0.32	1.5		1.5
Iron							
E_{th} (eV)	64	44	40	33	35		40
E_{TF} (eV)	2544	2589	2634	5514	20 247	29 839	174 096
Q (atoms/ion)	0.042	0.13	0.21	0.44	3.2		13
Molybdenum							
E_{th} (eV)	199	90	70	46	55		64
E_{TF} (eV)	4718	4767	4816	9944	34 183	48 322	533 048
Q (atoms/ion)	0.007	0.023	0.045	0.12	0.93		18
Tungsten							
E_{th} (eV)	443	220	140	110	80	40	65
E_{TF} (eV)	9870	9923	9977	20 373	66 507	91 979	1998 599
Q (atoms/ion)	0.007	0.019	0.038	0.106	0.93	2.2	20

One notes the very rapid drop in Y as $E_0 \rightarrow E_{th}$. Peak yields occur for E_0 in the hundreds to thousands eV, and drop again for very high E_0 where the impacting ions deposit less energy in the surface layers, penetrating deeper into the lattice structure.

3.3.2 Chemical Sputtering of C by H

In fusion devices carbon is much favoured for application as the plasma-facing material used for limiters, divertor targets and walls. Being low Z, it can be tolerated at the level of one per cent or so in the hot core plasma, without resulting in the unacceptably high radiation cooling that a high Z element would cause at such levels. It is also refractory, inexpensive, non-toxic, easy to fabricate, strong (as graphite fibre material), etc. Unfortunately—as has been long known—carbon is susceptible to chemical sputtering by hydrogenic species, to produce CH_4 and higher hydrocarbons.

No threshold (kinetic) energy of impact exists for chemical sputtering, and yields even for sub-eV H^0 are not negligible; the yield of CH_4 for sub-eV H^0 is $\sim 5 \times 10^{-4}$, while the total chemical yield (all hydrocarbons) is $\sim 5 \times 10^{-3}$ at the maximum (substrate) temperature for chemical sputtering [3.18]. The strong dependence on substrate temperature is one of the key signatures of chemical sputtering, see figure 3.7 [3.19] with a peak yield occurring at a substrate temperature which depends on E_0, but generally lying in the region of 700 K. A clear tendency for Y to decrease with decreasing E_0 is evident, figure 3.8 [3.20], but the decrease at low E_0 is not as dramatic near the threshold as for physical sputtering, figure 3.6. One may also note from figure 3.8 that CH_4 is only part—and sometimes a small part—of the total hydrocarbon production.

By comparing figure 3.6 and 3.8, it is evident that chemical sputtering dominates for $E_0 \leq 100$ eV, except at extremely high substrate temperature. For $E_0 \approx$ hundreds eV chemical sputtering yields are comparable to or larger than physical sputtering yields. It is sometimes thought that chemical sputtering can be largely avoided by using room temperature substrates, i.e. by avoiding operation in the $T_s = 700$ K range. While for high $E_0 \sim 200$ eV there is indeed a strong $Y(T_s)$ variation, this is much weaker for the low E_0 of greatest practical interest, and *room temperature chemical sputtering is seen to be significant*, figure 3.7.

Chemical sputtering was originally characterized in the 1970s using accelerators employing rather high particle energies, typically greater than 10 keV, and starting in the 1980s with accelerators operating in the 100–1000 eV range. Ion flux densities were also quite low in these experiments, i.e. less than 10^{20} H^+ m^{-2} s^{-1}, typically. Under these circumstances quite high yields for chemical sputtering are found, for example up to $Y \sim 0.1$ for the peak substrate temperature of $\sim$ 800 K. More recently experiments have been performed at the higher flux densities and lower particle energies appropriate for divertor target operation. With regard to flux dependence, figure 3.9 [3.20], the yields reported for low impact energy span a very wide range. In some cases a significant

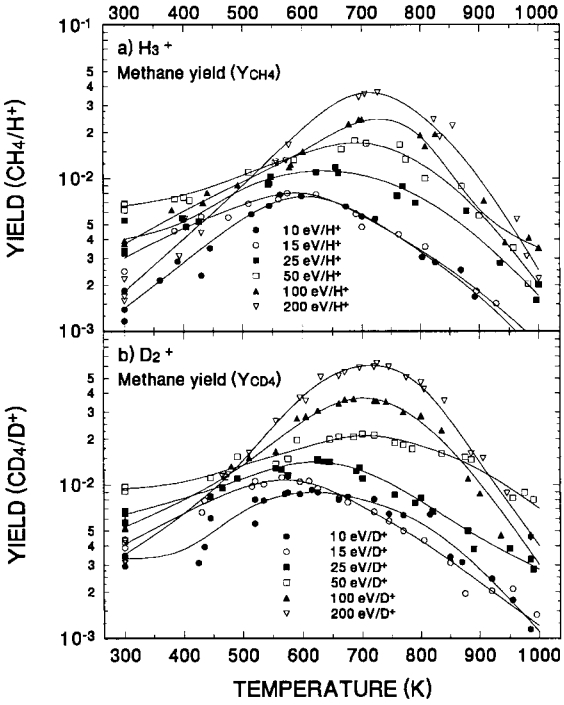

Figure 3.7. Methane yield of pyrolytic graphite as a function of temperature for (a) hydrogen and (b) deuterium impact at 10, 15, 25, 50, 100 and 200 eV/atom. Spline curves are drawn to aid the eye [3.19].

reduction is found, while in others even increases are seen. These measurements cannot be made with accelerators but employ plasma exposure, thus introducing various uncertainties. For example, spectroscopic measurements of C-influx are complicated by the uncertainty of the photon efficiency, section 3.5.1, of C^+ or CD-band light from methane (and other hydrocarbons). It is evident that a yield saturation must set in at some point, but it is still an open question at what flux density this occurs. Nevertheless, there is some grounds for optimism that yields may be reduced at the high flux densities characteristic of target plate exposure in tokamak divertors [3.21]. Wall release of carbon may be a more important cause of core contamination than target release, due to the closer proximity of the wall to the main plasma. Since impacting flux densities are not as high at the wall, this issue (of flux dependence) may not be so critical as is the issue of the yields at low impact energy.

In tokamaks a useful technique for distinguishing the roles of chemical and physical sputtering is to replace deuterium with helium as the fuel, keeping the plasma parameters the same [3.22].

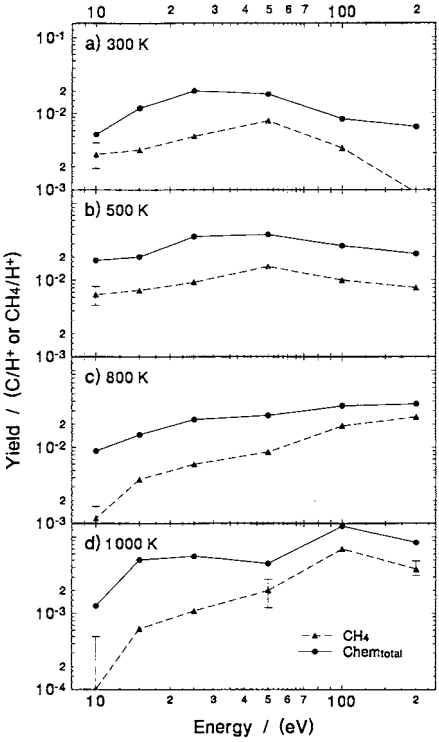

Figure 3.8. Incident energy dependence of the methane yield and the total chemical erosion (i.e., $\mathrm{Chem_{total}} = \mathrm{CH_4} + 2(\mathrm{C_2H_2} + \mathrm{C_2H_4} + \mathrm{C_2H_6}) + 3(\mathrm{C_3H_6} + \mathrm{C_3H_8})$) of graphite due to H^+ impact. The legend in (d) also applies to (a), (b) and (c) [3.20].

The field of chemical sputtering measurements continues to be characterized by variations in reported yields, particularly in the low E_0 range, which is of greatest interest. *Uncertainties are probably greater than for physical sputtering—and are at least a factor of 2*.

It is known, from laboratory experiments done since the early 1980s, that a *synergistic chemical sputtering process* exists [3.23]: when a small flux of energetic H^+ ions, say at 1 keV, is added to a larger flux of sub-eV H^0, the resulting total yield is greatly increased over that due to the H^+ and H^0 fluxes separately. The presence of just one energetic ion to 20 low energy atoms raises the sputtering rate of the atoms to that of the energetic particle. Solid surfaces in tokamaks are exposed to a wide range of impacting energies—often with the most intense fluxes occurring at low energies, but with smaller, high energy components being present also. When assessed separately it may be that neither component gives significant sputtering, in some specific situation—whereas if synergistic sputtering is a real effect in the tokamak environment, then substantial

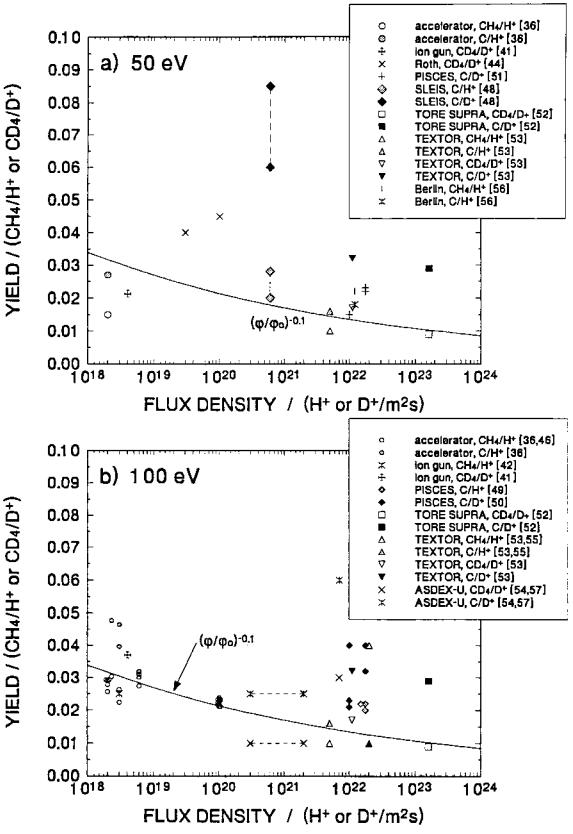

Figure 3.9. Flux dependence data of the chemical erosion of graphite shows very wide variation, making it difficult to identify a trend [3.20]. (See references in [3.20].)

sputtering may actually occur. To date the role in tokamaks of such a synergism appears not to have been addressed.

For recent reviews of chemical sputtering see [3.24, 3.25].

3.3.3 The Energy of Sputtered Neutrals

The depth of penetration of an impurity neutral into the plasma before it is ionized will be shown in section 6.5 to have a strong influence on the resulting impurity density within the plasma, n_z. Impurity penetration depends on the energy with which the neutral is launched from the surface, and also the angular distribution of emission. Since practical surfaces are rough, a cosine angular emission distribution is probably a reasonable approximation. Evaporated and chemically sputtered neutrals have thermal velocities characteristic of the substrate

temperature. Physically sputtered neutrals often obey a Thompson [3.26] velocity and energy distribution to a first approximation [3.7]:

$$\boxed{\frac{\mathrm{d}Y}{\mathrm{d}E_z} \propto \frac{E_z}{(E_z + E_B)^3}} \tag{3.12}$$

where E_z is the energy of the ejected impurity neutral.

This distribution has a maximum at $E_z = 1/2E_B$ and falls off at high energies as E_z^{-2}. Note also, from equation (3.7), that there is a maximum energy $E_Z^{\max}$ which is dependent on the impacting energy:

$$\boxed{E_Z^{\max} = E_0\gamma(1-\gamma) - E_B.} \tag{3.13}$$

For self-sputtering, where like-mass collisions are involved, energy-transfer is quite effective and $E_Z^{\max} \approx E_0$. While a chemically sputtered molecule such as CH_4 is released with thermal energies, its break-up into fragments by electron impact in the plasma effectively accelerates the fragments to ~ 0.5 eV energy by Franck–Condon dissociation [3.27].

3.3.4 Radiation-Enhanced Sublimation, RES

In the early 1980s a new and worrying mechanism for carbon release was discovered in studies using accelerators, radiation-enhanced sublimation, RES [3.28, 3.29], where for substrate temperatures as low as 1200 K, strongly enhanced sublimation occurred under ion impact. It is not clear whether RES occurs in tokamak environments; some studies show clear evidence for it [3.30], others not [3.31]. High incident fluxes are known to reduce RES [3.32].

3.4 Trapping of Hydrogen in Surfaces

The impacting hydrogen particles which are not instantly back-scattered, section 3.1, are trapped in the solid for some period of time—perhaps permanently. When they are released they come off as thermal molecules. The plasma is refuelled by both types of released neutral and the fraction of the incident particles re-cycled thus varies from R_N up to unity (or even, transiently, > 1 since previously trapped hydrogen can be released).

The trapping properties of plasma-facing materials are therefore important for understanding the *fuel recycling* process. A separate reason that trapping is important is the radioactive *tritium inventory* tied up in these components. There are several different trapping mechanisms—at least for carbon—and the type of trapping which is most important for re-cycling differs from those which control inventory.

Initially 100% of the non-back-scattered flux is trapped, when low temperature solid surfaces containing no hydrogen are exposed to energetic hydrogenic

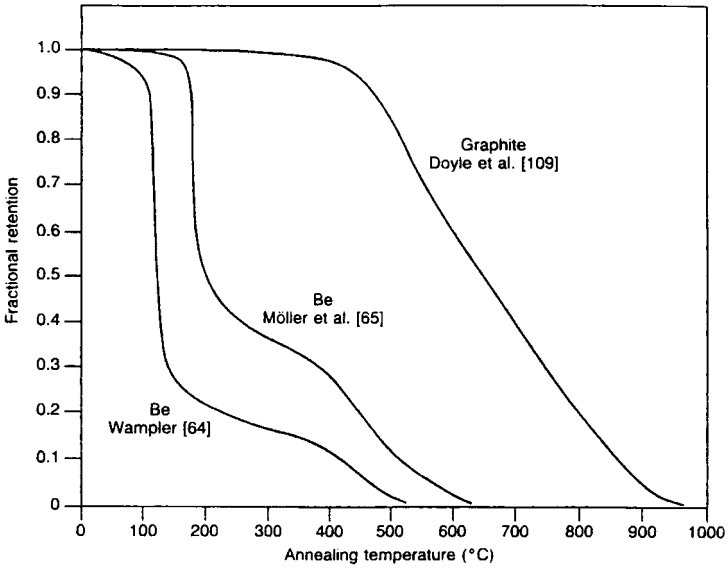

Figure 3.10. Comparison of thermal annealing of Be and C that were implanted with deuterium at room temperature [3.36]. (See references in [3.36].)

bombardment. Above a certain total *fluence* (time integral of the flux), which depends on E_0 and the solid temperature T_s, the retained amount of hydrogen *saturates* and all further incident hydrogen is promptly released as thermal molecules. At room temperature, carbon saturates at a maximum concentration of 0.4–0.5 H/C [3.33]; Be saturates at $\sim$ 0.3 H/Be [3.34–3.36]. The H can be released by then raising the temperature, i.e., by *thermal desorption*, see figure 3.10 [3.36].

Four types of hydrogen retention have been identified as occurring in carbon:

(a) Saturation of the implanted layers. This is primarily what is involved in figure 3.10, and is, in fact, a retention process for all solids.
(b) Co-deposition, an important process for carbon and possibly for other materials, depending on diffusivity and solubility for hydrogen. In co-deposition, hydrogen is buried and trapped by re-depositing carbon.
(c) Absorption on internal porosity.
(d) Transgranular diffusion with trapping, which is important for carbon at high temperatures.

The saturated implant layer retention, (a), dominates re-cycle while the other retention mechanisms—particularly co-deposition—tend to control tritium inventory in carbon; see, for example, [3.37].

Figure 3.11 from [3.34] is a schematic representation of the development of 'local saturation and mixing' [3.38] at low fluence ϕ_0 and multiples of it. The

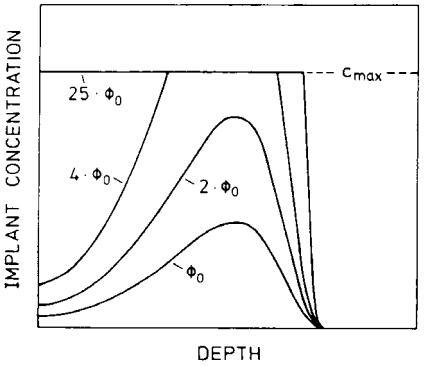

Figure 3.11. Schematic representation of the model of local saturation and mixing, showing depth profiles at low fluence ϕ_0 and multiples of it [3.34].

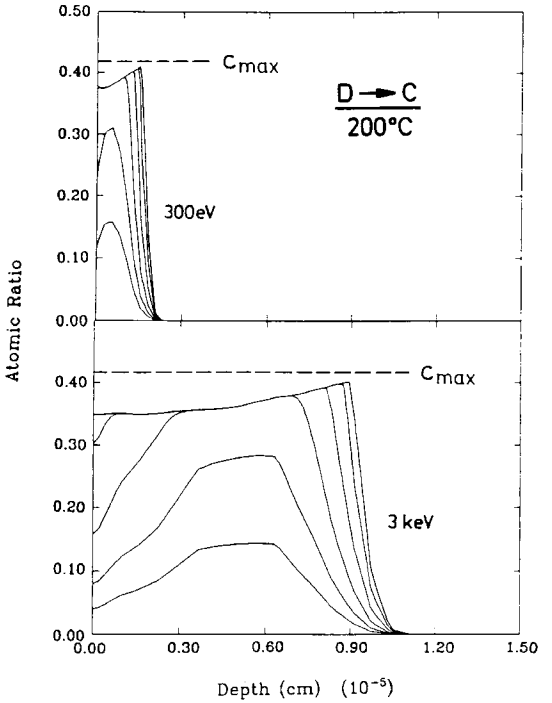

Figure 3.12. Depth profiles obtained from the model calculations at different implantation fluences (range of fluences 1×10^{17} to 2×10^{18} cm^{-2} at 3 keV, 2×10^{16} to 4×10^{17} cm^{-2} at 300 eV). The ion flux is 10^{15} cm^{-2} s^{-1} [3.34].

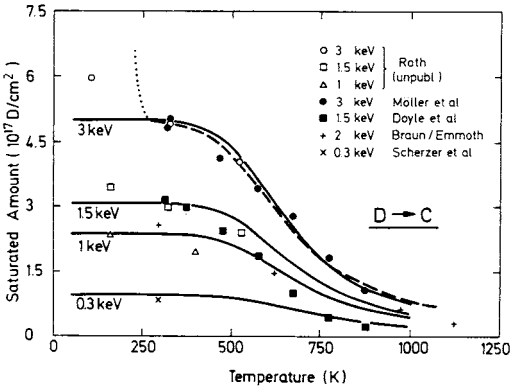

Figure 3.13. Saturated retained amounts of deuterium implanted into graphite as function of temperature and ion energy. Comparison of experimental data and model calculations. Solid lines: analytical approximation, dashed line: numerical result. The calculations were performed for an ion flux of 10^{15} cm^{-2} s^{-1} and a trap concentration of maximum value 0.42; see [3.34] for details.

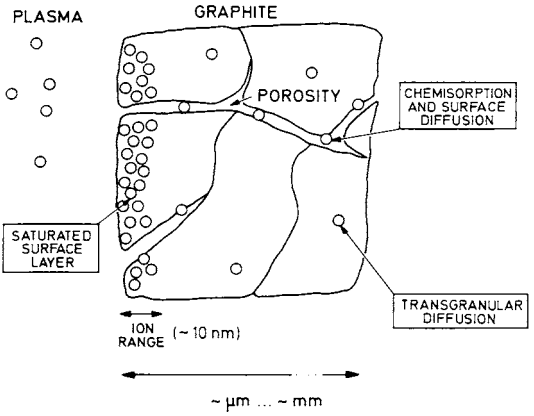

Figure 3.14. Illustration of the main mechanisms for the formation of hydrogen inventory in graphite [3.34].

depth of penetration depends on E_0, figure 3.12 [3.34]. It is believed that when the graphite is *locally* saturated at a point, then all excess hydrogen recombines throughout the implantation zone. The hydrogen diffuses as atoms and molecules (via porosity), mostly to the surface and is released [3.39]. Diffusion into the bulk also occurs; but, since the concentration gradient toward the surface is steeper, most of the particles diffuse to the surface, with the bulk only filling up very

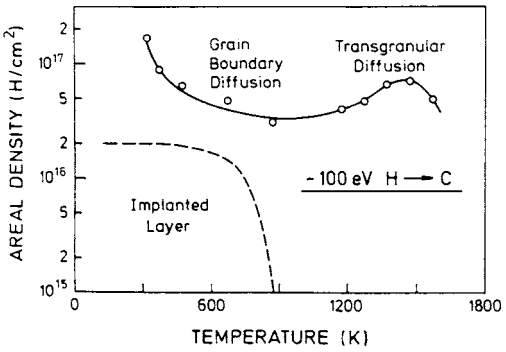

Figure 3.15. Retained amount of 100 eV hydrogen implanted to saturation from a model calculation (dashed line), and due to grain boundary or poroxity diffusion, and transgranular diffusion, from experiment [3.34].

slowly. Diffusion is also enhanced near the surface by the ion bombardment. The retained hydrogen thus saturates at some level, typically of order 10^{21} H m^{-2} in C, figure 3.13 [3.34].

The *diffusivity* of hydrogen is greater in metals such as Be than in graphite [3.36]. Thus, hydrogen thermal desorption occurs at lower temperatures, figure 3.10.

Figure 3.14 [3.34] illustrates types (a), (c) and (d) of retention in graphite. Figure 3.15 [3.34] shows that, for carbon, the two deeper retention mechanisms, (c) grain boundary (porosity) diffusion and (d) transgranular diffusion, dominate over implanted layer retention, so far as inventory is concerned. At the same time, the (c) and (d) mechanisms are slow responding and thus (a) dominates re-cycling.

Co-deposition, type (b), is however, likely to be the most important retention mechanism for tritium inventory in graphite (3.35). Carbon sputtered from the more exposed parts of the limiters and divertor targets tends to deposit on less exposed surfaces, trapping H/D/T to a concentration level of 0.5 or higher as it does. That is, regions of net carbon *re-deposition* build up, which are at the same time *co-deposits* of H/D/T. Since there is no apparent saturation for this process, it appears that virtually unlimited inventories of tritium could build up in this way. Due to the stress at the interface caused by mis-matched thermal expansion, layers of thickness $>\sim 100\ \mu$m tend to flake off due to poor adhesion—but new deposits continue to form. On the other hand, most of this trapped H/D/T is too deep to play a role in re-cycle.

The two retention problems—re-cycle and (tritium) inventory—are thus largely separate, for carbon. Metals with high diffusivity tend not to have a major inventory problem—although there are exceptions such as Ti and Zr in which hydrogen is very soluble.

3.5 Atomic Databases for Ionization, Dissociation and Radiation Rates

In figure 1.25, the reaction rates for some of the most important hydrogen atomic and molecular volume processes are shown. It is evident that considerable complexity is involved in hydrogen re-cycling because (a) much of the release from the surface is as molecules, (b) the charge exchange rate is rather large compared with ionization rates. It is to be noted that the dissociation process, reaction (2) in figure 1.25, yields fast dissociation products, so-called *Franck–Condon neutral atoms* of about 3 eV kinetic energy [3.40], which penetrate more deeply into the plasma than the thermal molecules. A survey of the elementary processes in hydrogen/helium plasmas is provided in [3.40], including the kinetic energy of the product particles.

Extensive reviews of atomic and molecular data for hydrogen, hydrocarbons and atomic impurities are to be found in the series 'Atomic and plasma-materials interaction data for fusion', supplements to the journal *Nuclear Fusion* **2**, 1992; **3**, 1992; **4**, 1993, **6**, 1995. Ongoing literature surveys relevant to atomic and molecular data for fusion are published in the irregular series *International Bulletin on Atomic and Molecular Data for Fusion* published by The International Atomic Energy Agency, Vienna. These data compilations also include data for line and other radiation for hydrogen and impurity atoms and ions.

The most useful form of these data are as *reaction coefficients* $\overline{\sigma v}$ [$m^3\ s^{-1}$], where, for electron-driven reactions, a Maxwellian distribution of the electrons is assumed, and so values of $\overline{\sigma v}(T_e)$ can be tabulated. There may also be a (generally) weaker dependence of $\overline{\sigma v}$ on n_e. Thus, for example the electron-impact ionization rate for hydrogen molecules is:

$$S_{iz} = n_e n_{H_2} \overline{\sigma v}_{iz}^{H_2}(T_e) \qquad [m^{-3}\ s^{-1}] \tag{3.14}$$

where $\overline{\sigma v}_{iz}^{H_2}(T_e)$ is given by plot (1) in figure 1.25.

For purposes of simple calculations and estimates, such single reaction rates can be obtained from these databases. For many applications, however, it is necessary to analyse entire *atomic/molecular systems* i.e. systems of charge stages and the excited states of each charge stage interacting via chains of single reactions. This typically involves so many basic processes that it has to be carried out using a numerical code.

3.5.1 Atomic Databases for Impurities

Recommended ionization rates for impurities are available [3.41, 3.42]. Examples for C, O and Ne are given in figures 1.26–1.28. One may note the relatively small $\overline{\sigma v}_{iz}$ for the He-like (two orbital electrons) charge states. Thus C^{4+}, O^{6+}, Ne^{8+} can be common states in the edge plasma.

Consider first the analysis of an atomic system *without transport*: the plasma is assumed to be infinite in extent and of uniform n_e and T_e. We may consider

as an example, carbon atom and ion populations in a steady state. This implies a balance of ionization and recombination and of excitation and de-excitation in such a plasma, which determines the distribution over the seven charge stages of carbon, and over the various excited states of each charge stage. Further assumptions are often justified, including the following.

(a) The plasma is optically thin, i.e. no radiation trapping.
(b) The *coronal picture* also exists: excitation and ionization are by collisions and de-excitation and recombination involve photon emission. ('Coronal' from the Sun's corona, where n_e is small.) All excited states, including metastable ones, decay *radiatively* on a time scale shorter than any collisional time [3.43], i.e. the electron impact de-excitation time is longer than the radiative decay time. In some analysis, electron impact de-excitation of metastables is included [3.44].
(c) Excitation and ionization is due to electron impact only.
(d) Recombination by photon emission including *two-body* (e and i combine with a photon being released, taking away the potential energy) and *dielectronic* (similar but with two photons released); *three-body* recombination (a second electron takes away the potential energy of recombination) is not included if the equilibrium is a *coronal* one; in some cases charge exchange re-combination is included, requiring that the neutral hydrogen density and temperature be specified.

Then, if the picture is coronal, and the system is in equilibrium, the distribution of the impurity particles amongst the different charge states is purely a function of T_e, with no dependence on n_e [3.45]. Figure 3.16 shows the example of carbon. As can be seen, at any particular value of T_e, most of the carbon is in a single charge state, i.e. the fractional abundance curves are strongly peaked. One may note from this figure that the range of temperatures for C to be in the He-like (C^{4+}) state corresponds to the typical range of SOL temperatures, $T_e \sim$ 10–60 eV.

The ionization–recombination equilibrium in plasmas with realistically high electron density—although this equilibrium may still be *local* and not influenced by *transport*—is not necessarily given by the coronal picture, since at higher n_e, electron-collisional de-excitation competes with spontaneous emission. Three-body recombination, with an electron acting as the third body to take away the recombination energy, ultimately exceeds two-body recombination at high n_e. In that case, the effective excitation, de-excitation, ionization and recombination rates are functions of both T_e and n_e and a charge-state abundance plot such as figure 3.16 is somewhat different for different values of n_e.

The reactions connecting all the charge stages and their excitation states are included in the analysis, and solution of the linear, coupled population equations then gives the equilibrium distribution of carbon in every stage and state, as a function of T_e (and n_e, which goes over to the coronal picture as $n_e \to 0$). At the same time, the self-consistent production of radiated power—the *radiation loss rate* P_{rad}[W m^{-3}] and the *electron cooling rate*, P_{cool}[W m^{-3}], Z_{eff}, the average

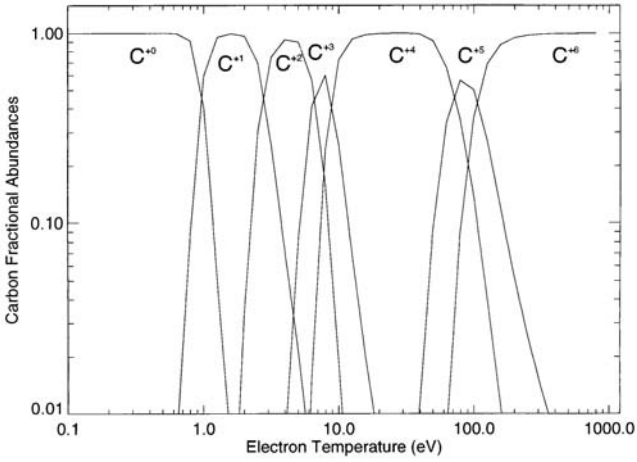

Figure 3.16. The carbon equilibrium ionization state distribution [3.46].

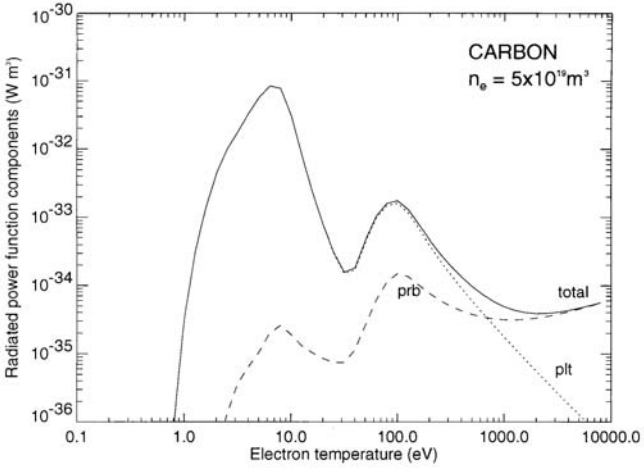

Figure 3.17. The dependence of the radiative loss function on temperature, for carbon, at steady ionization balance (no transport effects) [3.46]. The two dominant contributions are line radiation (plt) and bremsstrahlung radiation (prb).

charge state Z_{avg}, etc are computed.

The *radiation loss rate* P_{rad} is the rate at which energy is lost by radiation, per unit volume, in an optically thin plasma [3.44]. This quantity is experimentally measurable using bolometers. It is to be distinguished from the *electron cooling rate* P_{cool}, which is the rate at which the plasma electrons lose energy by inelastic collisions with ions and atoms; it is not directly measurable; its chief use is in

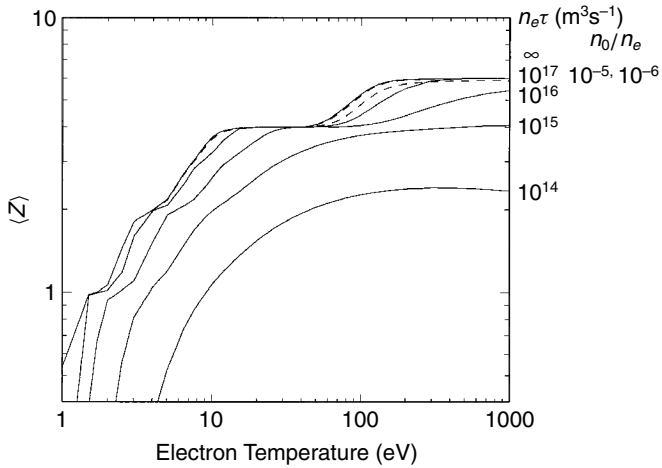

Figure 3.18. The carbon mean ionic charge $\langle Z \rangle$, at various values of $n_e\tau$ (solid lines), and the equilibrium values with neutral hydrogen present (broken line) [3.46]. τ is the dwell time of the impurity in the plasma and thus introduces the effect of *transport*. n_0 is the neutral hydrogen atom density.

modelling the electron power balance. Figure 3.17 [3.46] gives P_r for carbon for coronal equilibrium.

What is actually shown in figure 3.17 is the *normalized* P_{rad}, termed the *radiative loss function or radiative power function*, defined as P_{rad} divided by n_e and by the total (all charge stages) impurity particle density n_z, i.e., $P_{\text{rad}}/n_e n_z$. The (normalized) electron cooling function is defined similarly.

Figure 3.18 [3.46] gives $\langle Z \rangle (T_e)$ for carbon.

The foregoing picture is one in which the *transport* of carbon atoms/ions can be neglected ($\tau = \infty$ in figure 3.18). In real situations, carbon atoms might be sputtered into a plasma of, say, $T_e = 100$ eV. Figures 3.16 and 3.18 indicate that—in *equilibrium*—carbon will be almost completely stripped at 100 eV, existing mainly as C^{6+}. But with impurity transport taken into account this will not be the case, and many low charge states of carbon will exist for a steady inflow of C^0 into 100 eV plasma.

In figure 3.18, τ is the elapsed time since the carbon neutral entered an infinite plasma characterized by uniform values of T_e and n_e. As can be seen, for short times τ, the carbon will be at a lower charge state for a specified T_e, than would be the case in ionization–recombination equilibrium, i.e. for $\tau \to \infty$. The results shown in this figure do, however, assume radiative decay processes only. A separate matter is also indicated by figure 3.18, namely, the effect of neutral hydrogen, which is also important, through the process of charge exchange recombination: the equilibrium ($n_e\tau \to \infty$) value of $\langle Z \rangle$ is shifted downward for even small relative abundances of neutral hydrogen, n_0/n_e. Since low charge

states have more orbital electrons they are more efficient radiators (more line radiation), and the principal consequence of this *non-local equilibrium* is an increase radiated power for a given n_e, T_e, n_z; see below. In order to model these more realistic situations one needs *two* coupled codes: (a) a *transport code* and (b) an *atomic system analysis code*, such as described above. In this approach, the transport code follows the motion of the atoms/ions throughout the spatially varying plasma. It is *not* assumed that the carbon is in coronal or other equilibrium at each point in the plasma—at least not as to the distribution of charge stages. It is, however, assumed that for each individual charge stage, the population of the excited levels of that stage are in collisional–radiative equilibrium at the local T_e and n_e with the ground state population of that particular ionization stage in a quasistatic balance. Sometimes metastables are treated as separate populations.

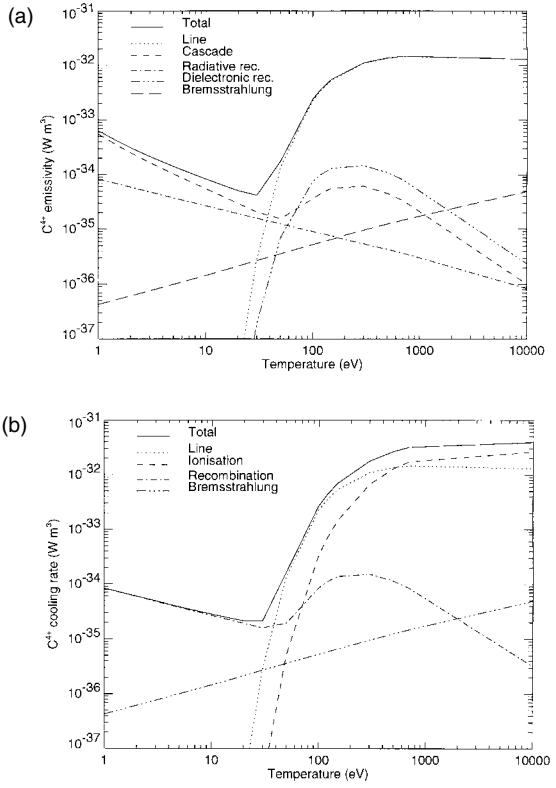

Figure 3.19. (a) The radiative loss coefficients, i.e. the *emissivity*, computed for helium-like carbon as a function of temperature. The various contributions are indicated [3.46]. (b) The cooling coefficient computed for helium-like carbon as a function of temperature. The various contributions are indicated [3.46].

The transport code thus follows, in effect, the transport of ground state (actually total) populations of each charge stage, calculating ionization to the next stage higher and recombination to the stage lower, and using the tabulated $\overline{\sigma v_{iz}}(T_e, n_e)$ and $\overline{\sigma v_{\rm rec}}(T_e, n_e)$ rate coefficients and the local values of T_e, n_e. The atomic systems analysis code is required to provide $P^j_{\rm rad}$ and $P^j_{\rm cool}$ for *each charge stage* j in this approach by provision of the calculated radiative and cooling *coefficients* defined as $P^j_{\rm rad}$ and $P^j_{\rm cool}$ divided by $n_e n^j_z$, where n^j_z is the local density of carbon ions of charge j. These *coefficients* are thus just the single-stage analogues of the *functions* for the total ion population, which are not to be used for transport-influenced equilibrium (so-called 'non-coronal equilibrium').

Figures 3.19(a), (b) [3.46], show the radiative loss coefficient and electron cooling coefficient for C^{4+}. The different contributions are described in the figures.

There is much similarity between $P^j_{\rm rad}$ and $P^j_{\rm cool}$ but differences are also apparent: at low temperature, $P^j_{\rm rad}$ is dominated by radiative cascade and continuum radiation, while $P^j_{\rm cool}$ is dominated by the rate at which recombining electrons lose their kinetic energy. It may seem paradoxical that $P^j_{\rm rad} > P^j_{\rm cool}$; however, it must be kept in mind that figures 3.19(a), (b) do *not* represent a true equilibrium situation: the very existence of C^{4+} at $T_e < 10$ eV implies a non-equilibrium situation, see figure 3.16. The energy to provide the (relatively) large $P^j_{\rm rad}$ at $T_e \leq 10$ eV is drawn from the potential energy *transported* into the local region in the form of C^{4+}, and is not taken from the *local* electron heat content.

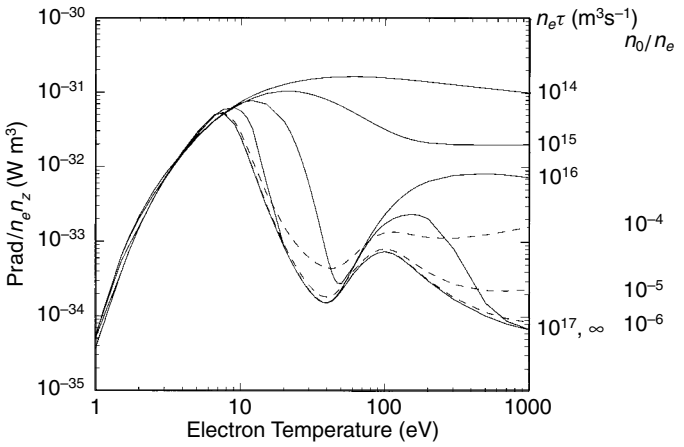

Figure 3.20. The carbon radiation power functions, $P_{\rm rad}/(n_e n_z)$, at various values of $n_e\tau$ (solid lines), i.e. for transport-influenced equilibrium ('non-coronal equilibrium') and the equilibrium functions with neutral hydrogen present (broken lines) [3.46]. Compare with figure 3.17, the equilibrium ('coronal') case ($n_e\tau = \infty$).

As mentioned above, a major consequence of transport-influenced equilibrium ('non-coronal equilibrium') behaviour is an enhanced P_{rad} [3.45]. Figure 3.20 [3.46] shows the radiative loss function for carbon, for finite dwell time in the plasma τ; the results can be generalized by using $n_e\tau$ as the parameter. One may picture a steady inflow of C atoms injected into a plasma of fixed density n_e, temperature T_e, the atoms staying there for time τ [s], then leaving. This radiative loss function may be compared to the equilibirum ('coronal') result of figure 3.17. For very long τ ($n_e > 10^{18}$ m^{-3} s), and no neutral hydrogen (i.e. no charge exchange recombination), the results go over to the 'coronal equilibrium' result. For shorter τ, P_{rad} increases—even by a couple of orders of magnitude—since the carbon exists as strongly radiating low charge stages for much of their dwell time. Increasing neutral hydrogen also raises P_{rad} due to the increased populations of low charge stages, caused by the charge exchange recombination.

The behaviour of impurities in the edge is often reasonably approximated by the scenario just described, namely direct entry of a neutral atom into a fairly hot plasma, with a fairly short dwell time, 1 ms or less. In addition neutral hydrogen densities are highest near the edge. It is thus evident that the transport—i.e. the finite dwell time—of the particles is as important to model as is the atomic system itself. *The transport modelling, in effect, calculates the dwell time* τ.

The foregoing example of carbon is only for illustration and similar atomic system analyses can be performed for other impurities, and also for hydrogen, next section. Various atomic systems analysis codes are available such as ADAS, Atomic Data and Analysis Structure [3.46]. Edge impurity transport is handled in most 2D edge fluid codes and by Monte Carlo impurity codes such as

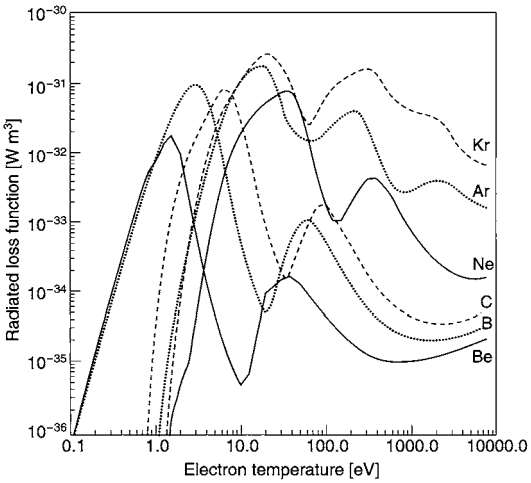

Figure 3.21. Radiative loss functions ('coronal equilibrium') for Be, B, C, Ne, Ar and Kr [3.46].

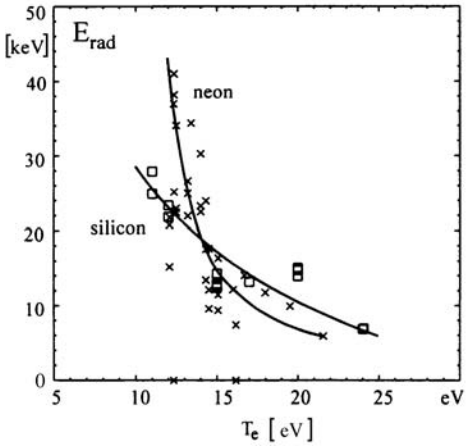

Figure 3.22. Radiation potential versus edge T_e, measured in TEXTOR for neon and silicon [3.55].

DIVIMP [3.47]. The transport of neutral hydrogen is treated by Monte Carlo codes such as EIRENE [3.48], NIMBUS [3.49], DEGAS [3.50], etc, as well as using fluid treatments [3.51].

In figure 3.21 [3.46], the 'coronal equilibrium' radiative loss functions are compared for Be, B, C, Ne, Ar and Kr. The total amount of energy radiated by a single particle during its lifetime in the plasma is defined as the *radiation potential*, $E_{\mathrm{rad,pot},z}$ [eV, keV, J, etc] [3.53, 3.54]. It would greatly simplify modelling if $E_{\mathrm{rad,pot},z}$ were a constant for each element independent of specific plasma conditions and τ_z. Unfortunately, this quantity is not constant although for low Z elements and for typical τ_z-values of $\sim$ ms, $E_{\mathrm{rad,pot},z}$ is typically in the range $\sim$ 1–10 keV. This therefore provides a *rough* guide for relating impurity particle influx rates ϕ_z—whether due to sputtering or artificial injection—and the total radiated power:

$$\boxed{P_{\text{total rad}} = E_{\mathrm{rad,pot},z}\phi_z \text{ [W].}} \tag{3.15}$$

Figure 3.22 gives values of $E_{\mathrm{rad,pot}}$ for Si and Ne measured on TEXTOR [3.55]. Codes such as ADAS can also be employed to generate the extremely useful *photon efficiency* numbers:

$$\boxed{\mathrm{PE}(T_e, n_e) = b_r \langle \sigma v_{\mathrm{exc},lm} \rangle / \langle \sigma v_{iz} \rangle} \tag{3.16}$$

where $\langle \sigma v_{\mathrm{exc},lm} \rangle$ is the excitation rate coefficient for transition from state l to m, giving rise to the subsequent release of a photon of a particular wavelength, and where one takes into account the branching ratio b_r for the particular optical transition; $\langle \sigma v_{iz} \rangle$ is the ionization rate coefficient to the next charge state. When an ion or atom enters a plasma sufficiently hot that it will eventually ionize, then

the number of photons of a particular wavelength that will be released during the lifetime of the particle in that charge state is PE. Thus, by measuring the total number of those photons released, the *particle influx* into that charge state can be deduced. This constitutes *photon influx spectroscopy* [3.56]. If the photons are from neutrals *then a measurement of the original particle influx ϕ_z, e.g. due to sputtering, is obtained*. If the plasma conditions are strongly ionizing and if none of the atoms/ions are transported out of the measurement region—say by redeposition on the solid surface—then one can also obtain redundant, confirmatory measurements of the influx as the ions pass through the various charge states. Influxes into separate ground and metastable states can also be measured.

It is to be noted that sometimes the inverse of PE is quoted in the literature, i.e. ionizations/photon, i.e. *inverse photon efficiencies*.

3.5.2 Atomic Databases for Hydrogen

Figure 1.25 gives the reaction coefficients for *direct* ionization, e.g. an electron strikes a hydrogen atom in the ground state and ionizes it in a *single step*. At low n_e this is the only important electron impact ionization process, but for high n_e, *multi-step* ionization becomes important where ionization from excited states contributes significantly. The same process occurs for impurities and is taken into account, for example, in ADAS, but here we will consider in detail only the case of hydrogen.

The first consequence of multi-step ionization is the obvious one that the *effective* ionization rate $\overline{\sigma v}^{\rm eff}_{iz,{\rm H}}$ increases, figure 3.23 [3.52]. One calculates the ionization rate S_{iz} [ion pairs m^{-3} s^{-1}] for the atoms as $S_{iz} = n_e n_{\rm H} \overline{\sigma v}^{\rm eff}_{iz,{\rm H}}$, where $n_{\rm H}$ is the total atom density, for all excitation states. Thus one can proceed as if

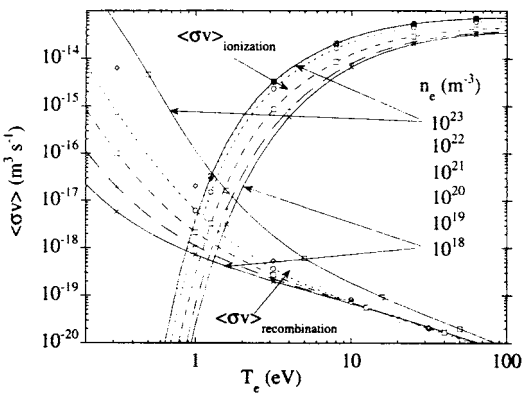

Figure 3.23. $\overline{\sigma v}^{\rm eff}_{iz,{\rm H}}$, $\overline{\sigma v}^{\rm eff}_{{\rm rec},{\rm H}}$, hydrogen ionization and recombination rate coefficients. For no radiation trapping [3.52].

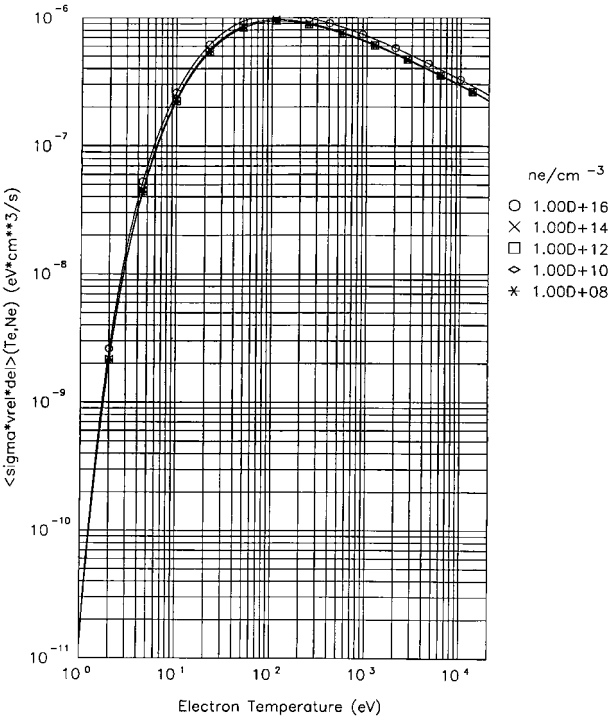

Figure 3.24. $p^{\mathrm{H}}_{\mathrm{cool},iz}$, the hydrogen cooling rate of electrons due to ionization [3.48]. For units [Wm^3], multiply by 1.6×10^{-25}.

all the atoms were in the ground state. One may note from figure 3.23 that for high n_e, say 10^{22} m^{-3}, $\overline{\sigma v}^{\mathrm{eff}}_{iz,\mathrm{H}}$ increases by factors of 2 or more, depending on T_e, compared with low n_e.

Multi-step processes also influence the hydrogenic cooling rate for electrons, $P^{\mathrm{H}}_{\mathrm{cool},iz}$, figure 3.24 [3.48], and the hydrogenic radiation loss rate, $P^{\mathrm{H}}_{\mathrm{rad},iz}$, figure 3.25 [3.52]. The subscript iz indicates power associated with ionizing conditions, to be distinguished from recombining conditions, below. One may note how much $P^{\mathrm{H}}_{\mathrm{rad},iz}$ is reduced for increasing n_e, since radiative de-excitation comes to be replaced by collisional de-excitation. Note also that:

$$\boxed{P^{\mathrm{H}}_{\mathrm{cool},iz} = P^{\mathrm{H}}_{\mathrm{rad},iz} + I_{iz}\overline{\sigma v}^{\mathrm{eff}}_{iz,\mathrm{H}}} \tag{3.17}$$

where $I_{iz} = 13.6$ eV, the ionization potential energy. Equation (3.17) indicates that regardless of how many collisional steps are required to ionize the atom, the non-photon energy 'cost' to the electron population is just I_{iz}, since de-excitation collisions return potential energy to the electrons.

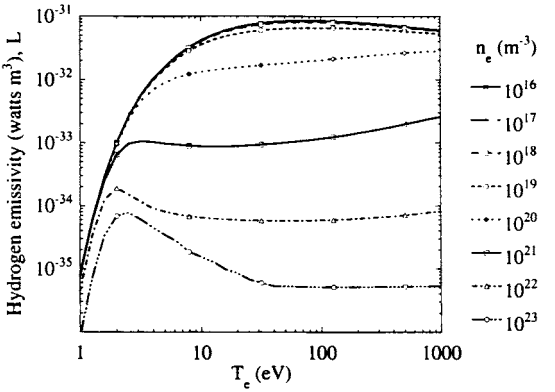

Figure 3.25. $P^{\mathrm{H}}_{\mathrm{rad},iz}$, hydrogen radiation emission rate coefficients due to ionization. For no radiation trapping [3.52].

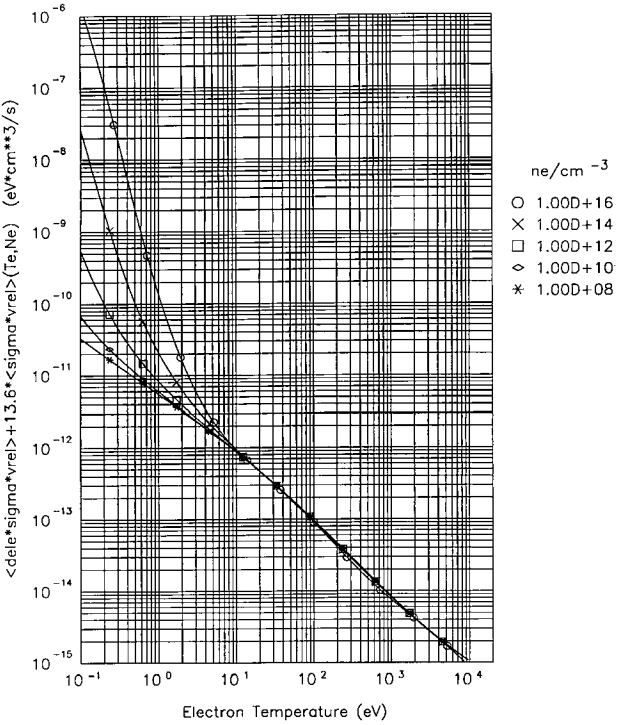

Figure 3.26. $P^{\mathrm{H}}_{\mathrm{rad,rec}}$, the hydrogen radiation rate due to recombination [3.48]. For units [Wm^3], multiply by 1.6×10^{-25}.

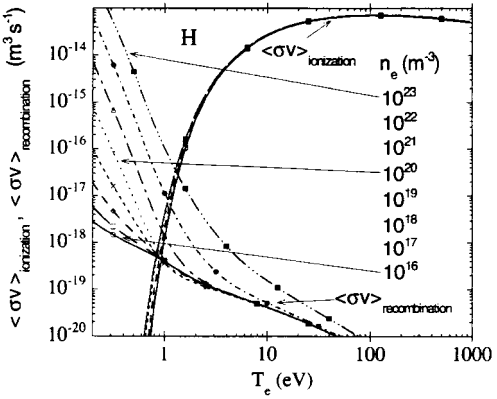

Figure 3.27. $\overline{\sigma v}^{\rm eff}_{iz,{\rm H}}$, $\overline{\sigma v}^{\rm eff}_{{\rm rec,H}}$, hydrogen ionization and recombination rate coefficients with Lyman transitions suppressed [3.52].

At very low temperatures, $T_e < 1$ eV, recombination is more important than ionization, figure 3.23. Again, multi-step processes influence the effective recombination rate $\overline{\sigma v}^{\rm eff}_{{\rm rec,H}}$, causing a dependence on n_e. We are also interested in $P^{\rm H}_{\rm rad,rec}$, figure 3.26 [3.48], and $P^{\rm H}_{\rm cool,rec}$ which can be calculated from:

$$\boxed{P^{\rm H}_{\rm cool,rec} = P^{\rm H}_{\rm rad,rec} - I_{iz}\overline{\sigma v}^{\rm eff}_{\rm rec,H}} \tag{3.18}$$

i.e. the potential energy of recombination *heats* the electrons, at least for three-body, collisional recombination. At low n_e, where radiative two-body recombination dominates, it is readily seen that $P^{\rm H}_{\rm cool,rec} \to 0$, and the ionization energy simply converts to photon energy, leaving the electron population neither heated nor cooled. At high n_e one can also readily show that $P^{\rm H}_{\rm cool,rec} < 0$, i.e. the electrons are *heated* by the (three-body) recombination, with the second electron taking away the energy.

When the plasma is large in size or $n_{\rm H}$ is high, then the resonance Lyman, L_α, photons can be *radiation trapped*. This raises $\overline{\sigma v}^{\rm eff}_{iz,{\rm H}}$; compare figure 3.27 [3.52] and figure 3.23; $\overline{\sigma v}^{\rm eff}_{{\rm rec,H}}$ is also altered, figure 3.27. At the same time, as would be expected, $P^{\rm H}_{{\rm rad},iz}$ decreases; compare figure 3.28 [3.52] and figure 3.25. $P^{\rm H}_{\rm rad,rec}$, not shown, is also altered.

One of the most important photon efficiencies is for the convenient hydrogenic H_α Balmer line at 656.3 nm, since this can be used to deduce hydrogenic influxes. Figure 3.29 [3.57] gives the so-called *Johnson–Hinnov factor* (an inverse photon efficiency). As can be seen there is approximately one H_α photon released for every ten or so entering H atoms (all of which are assumed to ionize). H_α and D_α radiation—i.e. *atomic* line radiation—is also emitted when H_2 or D_2 *molecules* enter a plasma: the process of break-up of the molecule by electron

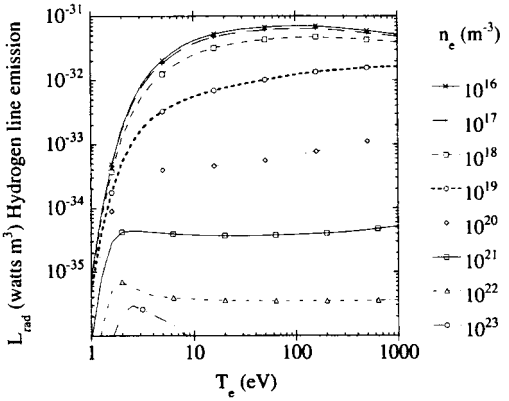

Figure 3.28. $P^{\mathrm{H}}_{\mathrm{rad},iz}$, hydrogen radiation emission rate coefficients, due to ionization and with Lyman transitions suppressed [3.52].

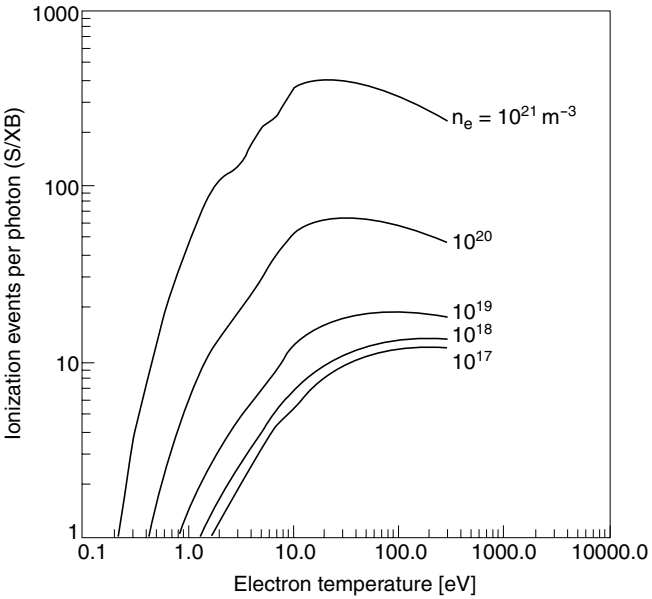

Figure 3.29. The Johnson–Hinnov [3.57] factor: number of ionizations per H_α Balmer photon released [3.46]. Assumes hydrogen enters plasma as atoms.

impact results in the release of such radiation, which therefore has to be considered when interpreting H_α or D_α intensities as a hydrogenic particle influx [3.58]. There are further contributions from dissociation of molecular ions and from negative ions, which are included in the EIRENE code [3.48]. Figure 3.30 [3.46]

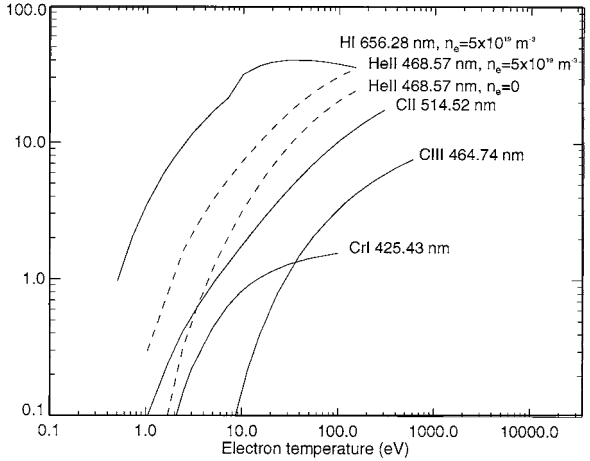

Figure 3.30. Examples of some (inverse) photon efficiencies for ionizing conditions [3.46]. The four lower curves are for low n_e. The two upper curves are for $n_e = 5 \times 10^{19}$ m^{-3}.

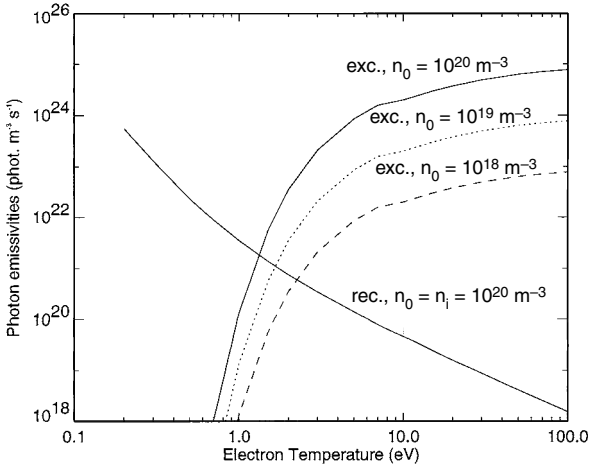

Figure 3.31. The H_α Balmer photon emission rate due to recombination (rec) and ionization (excitation: exc), for the particular value of $n_e = 10^{20}$ m^{-3} and different values of atom density, n_0 [3.46, 3.59].

shows examples of inverse photon efficiencies for a number of impurity lines, as well as for H.

At the very low temperatures, $T_e \lesssim 1$ eV, it can be more appropriate to speak of 'photons per recombination event'. Figure 3.31 [3.59] gives the photon

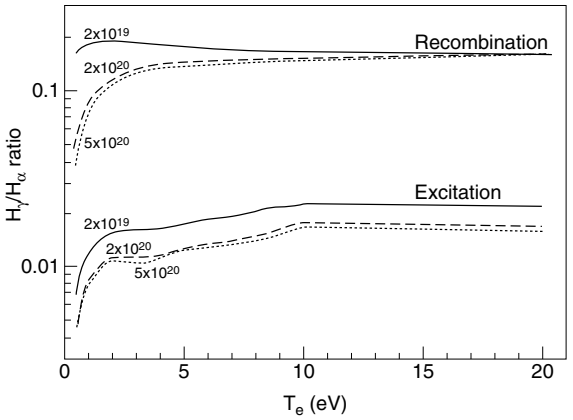

Figure 3.32. The ratio of H_γ/H_α intensities for recombining and ionizing (excitation) conditions [3.46, 3.59]. Note that since ionization is stronger than recombination for $T_e >$ a few eV, figure 3.23, the recombination curves shown here are not of any practical significance for such temperatures. Different values of n_e.

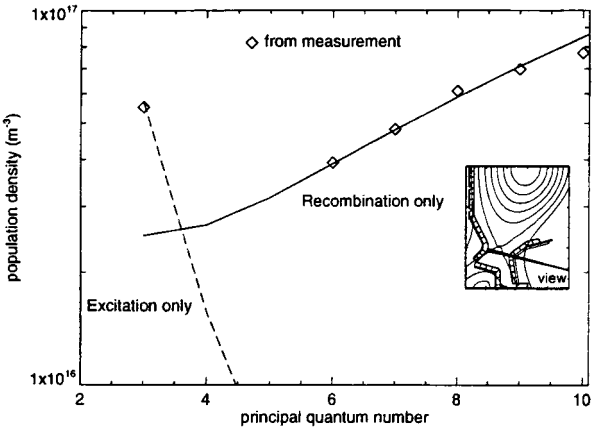

Figure 3.33. Measurements (diamonds) and calculations (lines) of hydrogen excited state population densities for conditions in the C-MOD divertor [3.61].

emissivity [H_α photons m^{-3} s^{-1}] as a function of T_e and n_0 (the atom density) for the specific value of $n_e = 10^{20}$ m^{-3}, as calculated using ADAS. A useful signature of the presence of volume recombination is a substantial increase in the ratio of H_γ/H_α lines, figure 3.32 [3.59, 3.60]. Under recombining conditions the population distribution of excited charge states changes radically; instead of decreasing rapidly with increasing quantum number, the opposite trend occurs,

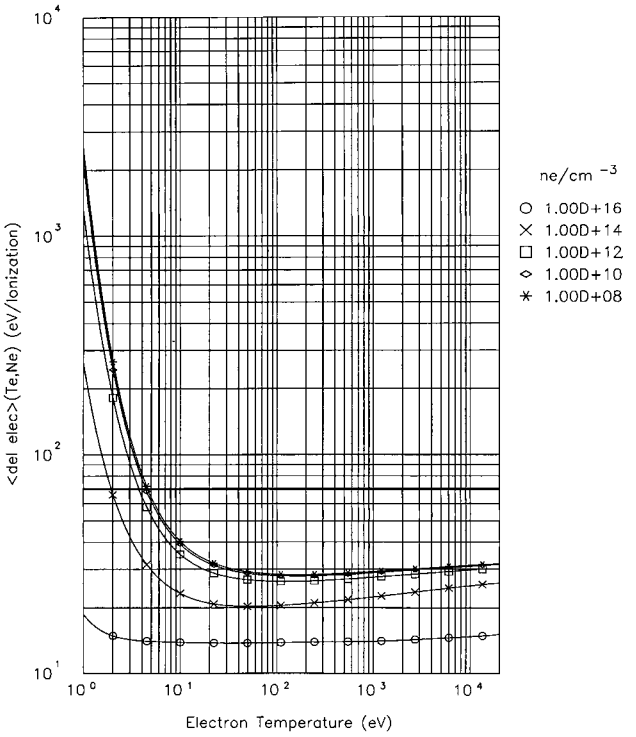

Figure 3.34. The atomic hydrogen electron cooling energy per ionization event, ε [eV/ionization] [3.48]. For $n_e = 10^{14}, 10^{16}, 10^{18}, 10^{20}, 10^{22}$ m^{-3} (the higher the value of n_e the lower the value of ε).

figure 3.33 [3.61]. It is this which causes the large change in the intensity ratio of H_γ/H_α and other line pairs. Clearly the interpretation of line intensities is radically different if the plasma is not in ionizing conditions.

Terry *et al* [3.62] have calculated the number of recombination events per H_γ photon as a function of T_e, which can provide a method of measuring the recombination rate in a plasma. This ratio is rather sensitive, however, to whether or not the plasma is thick enough to absorb (trap) the $Ly_{\alpha,\beta}$ lines.

It is useful to evaluate the electron cooling energy per ionization event for atomic hydrogen, $\varepsilon \equiv P^{\mathrm{H}}_{\mathrm{cool},iz}/\overline{\sigma v}^{\mathrm{eff}}_{iz,\mathrm{H}}$, figure 3.34. At very high n_e, the 'cost' of an ionization event is little more than I_{iz}, while for lower n_e, more energy is invested in photon production. A 'ball-park' figure is $\varepsilon \approx 25$ eV, i.e. about $2I_{iz}$. The very high values of ε at $T <$ a few eV are not of much practical importance in fusion devices where T_e varies spatially and so neutrals will tend simply to pass through regions of low T_e, to be excited and ionized at higher temperatures where ε is smaller.

Problems

3.1. *Particle and energy reflection coefficients*. For the case of normally incident H^+ on Fe, consider how consistent the *specific* normally incident H^+ on Fe, consider how consistent the *specific* experimental data for Fe in figure 3.1(a) are with the *general* forms for R_N and R_E given in figure 3.2. Consider for 10, 10^3 and 10^4 eV H and comment.

3.2. *Prompt re-capture of a secondary electron released from an oblique target*. Suppose the emitted electron has velocity $v_\parallel$ along $\boldsymbol{B}$ and initially the velocity $v_\perp$ perpendicular to $\boldsymbol{B}$ is in the plane shown in figure 3.35. The larmor radius is $r_{Le} = m_e v_\perp / eB$. The Larmor frequency is $\Omega_e = eB/m_e$ [radians s^{-1}]. Find the condition involving Ψ, $v_\perp$, $v_\parallel$ that will allow the electron to escape from the surface without striking the surface again during its first orbit.

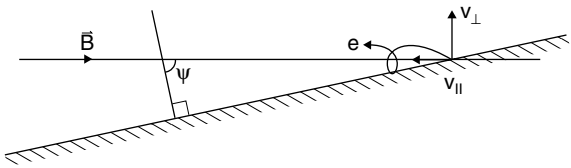

Figure 3.35. For a surface at glancing angle to $\boldsymbol{B}$, an emitted electron may be re-captured during its first Larmor orbit.

Hint: Note that in the figure the *projection* of the orbit onto the plane is shown. For the electron which just escapes, what fraction of its first gyro-orbit has it completed as it just misses striking the solid surface? Show that escape occurs if $v_\parallel \geq f(v_\perp, \Psi)$, i.e. some function of $v_\perp$ and Ψ, and that this result does not depend on the mass of the electron or the magnitude of $\boldsymbol{B}$.

3.3. *Secondary electron emission yield*. Confirm that equation (3.5) for the secondary electron emission yield is consistent with figure 3.5. Compare δ for 100 eV electrons for Be, C, Fe, Mo and W.

3.4. Derive equation (3.6). Draw diagrams to illustrate equation (3.7), showing the energy of each particle at each stage. Consider now a head-on collision of projectile particle M_1 on a substrate particle M_2 in the first lattice layer, and that this M_2 then has a head-on collision with a second M_2 particle in the second lattice layer. Does this result in the back-scatter ejection of the first M_2 particle? If so, at what energy?

3.5. Energy threshold for physical sputtering. *Roughly* estimate E_{th} for D^+ impact on substrates of low, medium, and high Z.

3.6. Show that the *specific* sputtering yields given in figure 3.6 are broadly consistent with the *general* formulae, equation (3.9)–(3.11), for the choice of one of the elements Be, C or W, evaluating for D^+ at $E_{\text{impact}} = 2, 20, 200 \times E_{th}$. How consistent?

3.7. Calculate the rate of carbon removal [atoms m^{-2} s^{-1}] and [kg m^{-2} s^{-1}] due to physical sputtering for a D^+ plasma of $n_e = 10^{19}$ m^{-3}, $T_e = 30$ eV, $T_i = 25$ eV. You will need to calculate the D^+ particle flux density striking the surface and also the floating potential (assume the carbon surface is electrically floating). Assume the D^+ ions are at normal incidence. At what rate will the surface recede [m s^{-1}] and [m/year], assuming no re-deposition of the sputtered particles? Would this erosion rate be acceptable for a high duty-factor reactor?

3.8. Repeat problem 3.7 but for a tungsten surface. Also repeat for W but with the plasma temperatures raised tenfold. Compare C and W with regard to their erosion resistance to plasma contact.

3.9. Repeat problem 3.7 for carbon again, but this time assuming chemical sputtering only. Assume two values of the surface temperature: 300 K, 700 K. Actually, physical and chemical sputtering are additive. Compare these two contributions.

3.10. Repeat problem 3.7 for carbon, including both physical and chemical sputtering, for the surface temperature 300 K, $n_e = 10^{20}$ m^{-3}, $T_e = 2$ eV, $T_i = 2.5$ eV. Such a cold plasma might be expected to cause almost no sputtering, but is this true? Compare the sputtering rate here with that for the hotter plasma of problem 3.9 and comment.

3.11. *The Thompson energy distribution of physically sputtered particles, equation (3.12).* Ignoring the cut-off of the distribution at high energy:

(a) Plot $\mathrm{d}Y/\mathrm{d}E_z$, normalized to unity total yield. What is the normalization factor for equation (3.12)?
(b) Prove that the most probable sputtered energy is $\frac{1}{2}E_B$.
(c) What is the average sputtered energy? Comment on the implications of this result.

3.12. Repeat problem 3.11, but now include the effect of the high energy cut-off and carry out your calculations for the specific case of 100 eV D^+ on C. What is the value of $E_z^{\max}$?

3.13. Repeat problem 3.12 for 100 eV, also 300 eV, D^+ on W. Comment on the comparison with D^+ on C.

3.14. Repeat problem 3.12 for carbon self-sputtering. Compare with the results for D^+ on C and comment.

3.15. *Distribution of the population amongst the different charge states for 'coronal equilibrium'.*

(a) Write down an equation relating the densities in charge states: $j-1$, j, $j+1$ in terms of n_e and of $\overline{\sigma v}_{iz}$ and $\overline{\sigma v}_{\mathrm{rec}}$ for the different transitions that are involved. How does the temperature come into the problem?

(b) For the case of carbon how many such coupled equations are there?

(c) Solution of these coupled equations simultaneously gives the fraction of the total C in the plasma that is in the different charge states, figure 3.16. Solution of the complete set of equations cannot be done analytically; however, by focusing on a narrow T_e-band we may check part of figure 3.16 rather simply. Argue that for 50 eV $\leq T_e \leq$ 90 eV one might expect the density ratio of $n_{\mathrm{C}^{4+}}/n_{\mathrm{C}^{5+}}$ to be approximately:

$$\frac{n_{\mathrm{C}^{4+}}}{n_{\mathrm{C}^{5+}}} \approx \frac{\overline{\sigma v}_{\mathrm{rec}}^{5+}}{\overline{\sigma v}_{iz}^{4+}}.$$

Use the fact that in this temperature range the two-body radiative recombination rate $\overline{\sigma v}_{\mathrm{rec}}^{5+}$ is almost constant, at 9×10^{-19} m^3 s^{-1}; also use values of $\overline{\sigma v}_{iz}^{4+}$ from figure 1.26. Confirm that the density ratios given in figure 3.16 for $n_{\mathrm{C}^{4+}}/n_{\mathrm{C}^{5+}}$ for this range of T_e are approximately in accord with this relation.

(d) The ionization potentials for the charge states of carbon are:

State	C^0	C^+	C^{2+}	C^{3+}	C^{4+}	C^{5+}
I_{iz} [eV]	11	24	48	64	392	490

Why do the charge states become depopulated at values of T_e well below I_{iz}?

3.16. Assuming the coronal picture, find the amount of power radiated by carbon from 1 m^3 of plasma where $n_e = 10^{19}$ m^{-3}, the total carbon density $n_c = 3\times10^{17}$ m^{-3}, and $T_e =$ (a) 5 eV, (b) 50 eV, (c) 5000 eV. Compare and comment on the implications for a fusion reactor.

3.17. Compare the electron radiative loss function P_{rad} for C^{4+}, figure 3.19(a), with the electron cooling function P_{cool}, figure 3.19(b), at high T_e. What is the main cause of the difference between the two functions there? Confirm this difference quantitatively by using figure 1.26 and the data from problem 3.15(d).

3.18. From figure 3.18 it is seen that $\langle Z\rangle$ decreases with decreasing n_e, or decreasing τ, or increasing neutral hydrogen density n_0. Explain physically why these trends exist.

3.19. *'Non-coronal' radiated power.* Carbon atoms are injected continuously into a plasma of uniform temperature and density $n_e = 10^{19}$ m^{-3}. The carbon

experiences ionization and recombination, spending a total time of 10 ms in the plasma before returning to a solid surface where it is re-deposited. The total (all charge states) density of carbon in the plasma is 2×10^{17} m^{-3}. Assume the hydrogen neutral density is negligible. Find the radiated power density associated with the carbon for $T = 5$ eV, 50 eV, 500 eV. Now repeat the calculations assuming a dwell time of 0.1 ms. Compare results and comment on the implications.

3.20. 'Non-coronal' radiation and physical sputtering. A carbon target is exposed to a plasma with $n_e = 10^{19}$ m^{-3}, $T_e = 20$ eV, $T_{D^+} = 30$ eV.

(a) Calculate the impact energy of the ions on the graphite and the physical sputtering yield, assuming normal incidence. Ignore chemical sputtering.
(b) The target is at $\Psi = 85°$ to $\boldsymbol{B}$ and has a plasma-wetted area of 1 m^2, that is the bombarding particles impact over 1 m^2 of actual carbon surface. Calculate the number of D^+ striking the carbon per second, and the number of carbon particles sputtered per second.
(c) Assuming the carbon particles are distributed uniformly throughout the plasma and remain in the plasma for a dwelltime of 10^{-3} s, and the total plasma volume is 5 m^3, find the total impurity density n_c [carbon particles m^{-3}], the total radiated power [W] and the radiation potential $E_{\mathrm{rad,pot},z}$ [eV].

3.21. Consider a simplification of a divertor tokamak with a main plasma of volume 100 m^3, at uniform density of 10^{20} m^{-3} and uniform temperature 1 keV, plus a divertor plasma of volume 1 m^3 also at uniform density 10^{20} m^{-3} but with uniform temperature 5 eV. Either Be, B, C, Ne or Ar is present as an impurity at a density 5% of n_e in each region. Assuming 'coronal' radiation, calculate the total impurity radiation power [W]. Compare the different impurities and the different contributions from the SOL and from the main plasma, commenting on the implications.

3.22. A flux of 10^{23} H atoms per second enters a uniform plasma of 5 m^3 maintained at a constant $n_e = 10^{19}$ m^{-3} and $T_e = T_{H^+} = 20$ eV.

(a) Assuming that all of the atoms become ionized, i.e. none return as atoms to a solid surface, and that no H^+ recombines, calculate the number of Balmer H_α photons that are released per second.
(b) Calculate the recombination rate of H^+ and thus show that this process is indeed unimportant here.
(c) Calculate the average time that the H atoms take before becoming ionized. Suppose that the average loss time of atoms for re-deposition as atoms on a 100%-absorbing solid surface is half this ionization time. What is the number of H_α photons produced per second now? Comment on the implications.

3.23. Repeat problem 3.22, but now assuming $T = 300$ eV, also 2 eV. Comment on the comparisons with $T = 20$ eV.

3.24. A steady flux of 10^{21} C atoms per second enters a uniform plasma of $n_e = 10^{19}$ m^{-3} and $T_e = 30$ eV. Assume that conditions are strongly ionizing such that recombination can be ignored and no C particles re-deposit until they have reached a high stage of ionization. Calculate the total number of photons released at: 514 nm (a CII line) and 464 nm (a CIII line).

3.25. Consider a pure, uniform hydrogen plasma of volume 3 m^3 of $T = 20$ eV and various densities $n_e = 10^{17}, 10^{19}, 10^{21}$ m^{-3}. The average neutral atom density is 5% of n_e. Calculate the total hydrogen radiated power [W] with and without re-absorption of the Lyman transitions. Compare these total radiated powers with the power radiated just in H_α photons (assume no radiation trapping). Comment on your findings.

3.26. We wish to sustain a uniform plasma of volume 1 m^3 at $n_e = 10^{20}$ m^{-3} and $T = 10$ eV by injecting a flux of H atoms ϕ_0 [H^0 s^{-1}]. We also require that the neutral density in the plasma be $n_0 = 10^{20}$ m^{-3}, which we will assume is uniform over the volume. Assuming the hydrogen enters from the walls as 2 eV atoms, how might it be possible to achieve a uniform density, roughly?

(a) Calculate the ionization time of the atoms.
(b) Find the value of ϕ_0 required to result in a neutral density of $n_0 = 10^{20}$ m^{-3}.
(c) Calculate the rate of production of H_α photons [H_α s^{-1}] in two ways, and show they are equal:
  (i) use the Johnson–Hinnov result of figure 3.29;
  (ii) use the results given in figure 3.31.
(d) If the plasma density is to remain constant at $n_e = 10^{20}$ m^{-3}, what must the H^+ loss time be?

3.27. Repeat problem 3.26 but now assume that after an initial filling of the volume with gas and plasma to the level of $n_e = n_0 = 10^{20}$ m^{-3}, the flux ϕ_0 is turned off and assume also that no loss of atoms or ions to the surfaces occurs. A low temperature is now required to support a steady state. What temperature? How many H_α photons are now produced [H_α s^{-1}]? Although no particle influx is required to sustain this steady state, what steady external input is required?

References

[3.1] Eckstein W and Verbeek H 1984 *Nucl. Fusion Special Suppl.* 12
[3.2] Behrisch R and Eckstein W 1986 *Physics of Plasma–Wall Interactions in Controlled Fusion* ed D E Post and R Behrisch (New York: Plenum) p 413

[3.3] Eckstein W 1991 *Suppl. Nucl. Fusion* **1** 17
[3.4] Thomas E W 1984 *Nucl. Fusion Special Suppl.* 94
[3.5] Thomas E W, Janev R K and Smith J 1992 *Nucl. Instrum. Method.* B **69** 427
[3.6] Thomas E W 1991 *Supp. Nucl Fusion* **1** 79
[3.7] Bohdansky J 1984 *Nucl. Fusion Special Suppl.* 61
[3.8] Roth J 1986 *Physics of Plasma–Wall Interactions in Controlled Fusion* ed D E Post and R Behrisch (New York: Plenum) p 351
[3.9] Eckstein W, Bohdansky J and Roth J 1991 *Suppl. Nucl. Fusion* **1** 51
[3.10] Eckstein W, Garcia-Rosales C, Roth J and Ottenberger W 1993 *IPP* 9/82 Max Planck Institute für Plasmaphysik
[3.11] Vietzke E, Tanabe T, Philipps V *et al* 1997 *J. Nucl. Mater.* **145–147** 425
[3.12] Winter J 1990 *J. Nucl. Mater.* **176–177** 14
[3.13] Dasent W E 1970 *Inorganic Energetics* (Harmondsworth: Penguin) p 47
[3.14] Roth J 1990 *J. Nucl. Mater.* **176–177** 132
[3.15] Noda N, Philipps V and Neu R 1997 *J. Nucl. Mater.* **145–147** 227
[3.16] Yamamura Y 1988 *Nucl. Instrum. Method.* B **33** 493
[3.17] Verbeek H, Stober J, Coster D P *et al* 1998 *Nucl. Fusion* **38** 1789
[3.18] Roth J, Vietzke E and Haasz A A 1991 *Suppl. Nucl. Fusion* **1** 63
[3.19] Mech B V 1997 *PhD Thesis* University of Toronto
Mech B V, Haasz A A and Davis J W 1998 *J. Nucl. Mater.* **255** 153
[3.20] Davis J W and Haasz A A 1997 *J. Nucl. Mater.* **241–243** 37
[3.21] Kallenbach A, Bard A, Coster D *et al* 1999 *J. Nucl. Mater.* **266–269** 343; also 1998 *Nucl. Fusion* **38** 1097
[3.22] West W P, Brooks N H, Fenstermacher M E *et al* 1999 *J. Nucl. Mater.* **266–269** 732
[3.23] Vietzke E and Haasz A A 1996 *Physical Processes of the Interaction of Fusion Plasma with Solids* ed W O Hofer and J Roth (Boston: Academic)
[3.24] Roth J 1999 *J. Nucl. Mater.* **266–269** 51
[3.25] Federici G, Anderl R A, Andrew P *et al* 1999 *J. Nucl. Mater.* **266–269** 14
[3.26] Thompson M W 1968 *Phil. Mag.* **18** 377
[3.27] Ehrhardt A B and Langer W D 1987 *PPPL-*2477
[3.28] Roth J, Bohdansky J and Wilson K L 1982 *J. Nucl. Mater.* **111–112** 775
[3.29] Philipps V, Flaskamp K, Vietzke E *et al* 1982 *J. Nucl. Mater.* **111–112** 781
[3.30] Tobin S J, DeMichelis C, Hogan J T *et al* 1998 *Plasma Phys. Control. Fusion* **40** 1335
[3.31] Philipps V, Pospiezczyk A, Schweer B *et al* 1995 *J. Nucl. Mater.* **220–222** 467
[3.32] Philipps V, Vietzke E, Schorn R P and Trinkhaus H 1988 *J. Nucl. Mater.* **155–157** 319
[3.33] Wampler W R, Brice D K and Magee C W 1981 *J. Nucl. Mater.* **102** 304
[3.34] Möller W 1989 *J. Nucl. Mater.* **162–164** 138
[3.35] Causey R A 1989 *J. Nucl. Mater.* **162–164** 151
[3.36] Wilson K L *et al* 1991 *Suppl. Nucl. Fusion* **1** 31
[3.37] Andrew P, Brennan D, Coad J P *et al* 1999 *J. Nucl. Mater.* **266–269** 153
[3.38] Cohen S A and McCracken G M 1979 *J. Nucl. Mater.* **84** 157
[3.39] Chiu S and Haasz A A 1992 *J. Nucl. Mater.* **196–198** 972
[3.40] Janev R K, Langer W D, Evans K Jr and Post D E Jr 1987 *Elementary Processes in Hydrogen–Helium Plasmas* (Berlin: Springer)
[3.41] Bell K L, Gilbody H B, Hughes J G *et al* 1981 *Culham Report* CLM-R216
[3.42] Lennon M A, Bell K L, Gilbody H G *et al* 1986 *Culham Report* CLM-R270

[3.43] Summers H P and McWhirter R W P 1979 *J. Phys. B: At. Mol. Phys.* **12** 2387
[3.44] Bonnin X, Marchand R and Janev R K 1992 *Nucl. Fusion Special Suppl.* **2** 117
[3.45] Carolon P G and Piotrowicz V A 1983 *Plasma Phys*. **25** 1065
[3.46] Summers H P 1994 Atomic Data and Analysis Structure JET. Plots in this chapter produced by M O'Mullane
[3.47] Stangeby P C, Farrell C, Hoskins S and Wood L 1988 *Nucl. Fusion* **28** 1945 and Stangeby P C and Elder J D 1995 *Nucl. Fusion* **35** 1391
[3.48] Reiter D 1992 The EIRENE code Version Jan. 92, User Manual *KFA Juelich Report* JUEL-2599 and *KFA Juelich Report* JUEL-1947 (1984).
[3.49] Cupini E, Matteis A De and Simonini R 1983 EUR XII-324/9 Report
[3.50] Heifetz D B *et al* 1981 A Monte Carlo model of neutral particle transport in diverted plasmas *PPPL*-1843
[3.51] Rognlien T D, Milovich J L, Rensink M E and Porter G D 1992 *J. Nucl. Mater.* **196–198** 347
[3.52] Post D E 1995 *J. Nucl. Mater.* **220–222** 143
[3.53] Pitcher C S, Bures M, de Kock L *et al* 1990 *J. Vac. Sci. Technol.* **A 8** 1760
[3.54] Samm U, Bogen P, Claassen H A *et al* 1990 *J. Nucl. Mater.* **176–177** 273
[3.55] Samm U, Bogen P, Esser G *et al* 1995 *J. Nucl. Mater.* **220–222** 25
[3.56] Behringer K 1987 *J. Nucl. Mater.* **145–147** 145
[3.57] Johnson L C and Hinnov E 1973 *J. Quant. Radiat. Transfer* **13** 333
[3.58] Sawada K, Eriguchi K and Fujimoto T 1993 *J. Appl. Phys.* **73** 8122
[3.59] McCracken G M, Stamp M F, Monk R D *et al* 1998 *Nucl. Fusion* **38** 619
[3.60] Lumma D, Terry J L and Lipschultz B 1997 *Phys. Plasmas* **4** 2555
[3.61] Terry J L, Lipschultz B, Pigarov A Yu *et al* 1998 *Phys. Plasmas* **5** 1759
[3.62] Terry J L, Lipschultz B, Bonnin X *et al* 1999 *J. Nucl. Mater.* **266–269** 30

Chapter 4

The Simple SOL and the Transition to the Complex SOL

4.1 The Simple SOL: The Sheath-Limited Regime

We have defined the simple SOL in chapters 1 and 2 to be characterized by:

(1) T_e and T_i constant along each flux tube (and both species are Maxwellian).
(2) Electrons and ions are thermally de-coupled from each other, i.e. thermal equipartition is weak.
(3) Cross-field transport of particles from the main plasma provides the only particle source in the SOL. No ionization within the SOL.
(4) No volumetric recombination.
(5) No neutral friction.
(6) The sheaths at the limiters or divertor targets are the only particle and heat sinks. No radiative or charge-exchange cooling.

It is assumed that the only source of power is cross-field convection and conduction from the main plasma.

4.2 'Straightening Out' the SOL for Modelling Purposes

In section 1.6, it was noted that plasma collisionality in the SOL is strong enough—due to the low temperature—that the charged particles follow $\boldsymbol{B}$ and neo-classical effects, such as banana orbits, can be ignored. We can thus 'straighten out' the SOL, as in figure 4.1.

The portion of the SOL shown is bounded by the following:

(1) *Opposite-facing solid surfaces at each end.* These could be the two divertor targets at each end of a flux tube which extends all the way around the torus. Or they could be two opposite-facing limiters, or even the back and front side of a *single* poloidal or toroidal limiter.

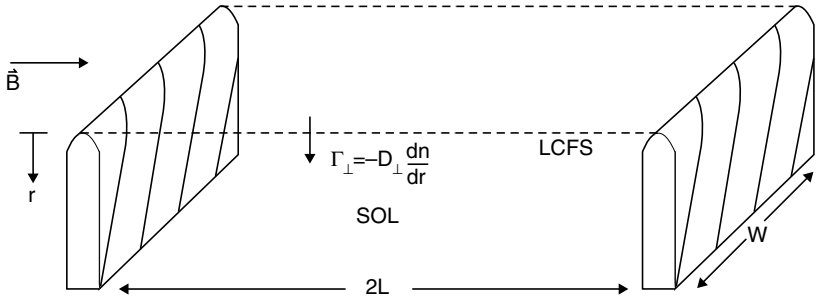

Figure 4.1. The SOL 'straightened out'.

(2) *The last closed flux surface*, LCFS, or separatrix on the top side and the *vessel wall* on the bottom side.
(3) *The two side surfaces* are taken to be separated by width w. One could take w to be a 1 metre portion of the SOL. Note that the w coordinate is perpendicular to both the parallel ($\boldsymbol{B}$) direction and the radial cross-field direction r. Thus w is in the second orthogonal, cross-field direction.

Therefore, if a circular poloidal limiter is involved, section 1.4.1, and if q is very large (so that $\boldsymbol{B}$ is almost purely in the toroidal direction, section 1.3), then w is in the poloidal direction and for $w = 2\pi a$, the poloidal circumference of the limiter, figure 4.1, would represent the *entire* SOL, figure 4.2. For a toroidal limiter or a poloidal divertor, of major radius R, the distance around the machine is $2\pi R$; however, since w is orthogonal to $\boldsymbol{B}$, then $w = 2\pi R B_\theta / B$ gives the effective length orthogonal to $\boldsymbol{B}$ and $\boldsymbol{r}$, figure 4.3. Also recall, from section 2.10, that when $\boldsymbol{B}$ is oblique to the actual solid surface, the plasma does not 'know' this, and the *parallel-to-*$\boldsymbol{B}$ flow is sonic at the Chodura sheath edge. Thus, we must project the actual length of the limiter perpendicular to $\boldsymbol{B}$, i.e. $w = 2\pi R B_\theta / B$ in these cases.

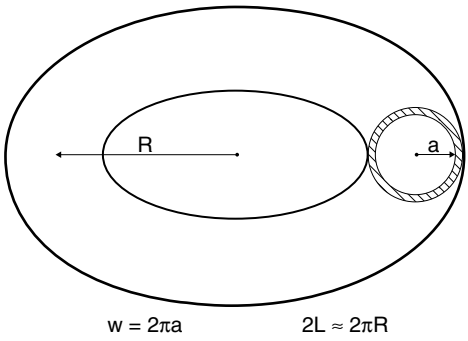

Figure 4.2. A single poloidal ring limiter.

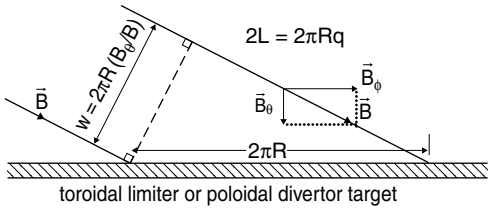

Figure 4.3. For a single toroidal belt limiter the effective width is $w = 2\pi R(B_\theta/B)$.

Although the solid target surfaces in figure 4.1 are shown to be perpendicular to $\boldsymbol{B}$, the actual target surfaces are usually *not* perpendicular to $\boldsymbol{B}$. These surfaces in figure 4.1 are the *effective* surfaces, so far as the sink action on the SOL plasma is concerned: they are the surfaces as *projected* perpendicular to $\boldsymbol{B}$. The Chodura sheath criterion, section 2.10, is most useful in justifying this (further) distortion of the actual geometry: for purposes of analysis the SOL is not only *straightened out*, but it is also turned into a *3D rectangular box*.

Finally, we may note that—for purposes of calculating the heat load received by the solid surfaces—one uses the actual surface area, not the projected one. It is only for purposes of calculating the sink action exerted by the solid surfaces on the SOL plasma that one uses the area projected perpendicular to $\boldsymbol{B}$. Thus, while the plasma does not 'notice' whether the actual solid surface is perpendicular to $\boldsymbol{B}$ or not, the solid certainly does! By making $\boldsymbol{B}$ more glancing, one can reduce surface heating and melting, yet without influencing the plasma itself.

4.3 Relating Density Scrape-Off Length λ_n to $D_\perp^{\mathrm{SOL}}$

For the simple SOL one can derive a relation between the directly measurable quantity λ_n, the characteristic decay length of density in the radial direction, and $D_\perp^{\mathrm{SOL}}$, the cross-field diffusion coefficient in the SOL. Cross-field transport coefficients such as $D_\perp$ can still not be calculated from first principles, but are *anomalous* and have to be extracted, by some means, from experimental data, i.e. they are *empirical*. Clearly knowledge about these coefficients is critical to predicting the confinement properties of magnetic plasmas.

For the simple SOL, where the source of particles for the SOL is entirely due to cross-field transport, it is apparent that a fairly simple relation should exist between the radial density profile $n_e(r)$ and $D_\perp^{\mathrm{SOL}}$. Consider figure 4.1. The total particle out-flow from the confined plasma, crossing the LCFS into the SOL is given by:

$$\phi_\perp = -D_\perp^{\mathrm{SOL}} \frac{\mathrm{d}n}{\mathrm{d}r}\bigg|_{\mathrm{LCFS}} 2Lw \qquad [\text{particles s}^{-1}]. \tag{4.1}$$

We define λ_n to be the characteristic length of radial density decay:

$$\lambda_n \equiv -\left(\frac{1}{n}\frac{\mathrm{d}n}{\mathrm{d}r}\right)^{-1}. \tag{4.2}$$

Thus $\mathrm{d}n/\mathrm{d}r = -n/\lambda_n$ and:

$$\phi_\perp = D_\perp^{\mathrm{SOL}}(n_{\mathrm{LCFS}}/\lambda_n)2Lw. \tag{4.3}$$

The total particle flow to the (two) solid surfaces is:

$$\phi_\parallel = 2w\int_{r=\mathrm{LCFS}}^{\infty} nc_s\mathrm{d}r \tag{4.4}$$

where we have used the Bohm/Chodura sheath criteria, section 2.3. We will approximate the integral in equation (4.4) as the value of nc_s at the LCFS multiplied by λ_n. This result is exact if $c_s(r)$ is constant and if $n(r)$ is actually exponential:

$$n(r) = n_{\mathrm{LCFS}}\mathrm{e}^{-r/\lambda_n} \tag{4.5}$$

which is often found experimentally to hold approximately. Thus we have

$$\phi_\parallel = 2w\frac{1}{2}n_{\mathrm{LCFS}}c_s\lambda_n. \tag{4.6}$$

For the simple SOL there are no other particle sources or sinks, and particle balance, $\phi_\perp = \phi_\parallel$, gives:

$$\lambda_n = (2D_\perp^{\mathrm{SOL}}L/c_s)^{1/2} \tag{4.7}$$

which is almost exactly what was estimated earlier, equation (1.10). The factor $2^{1/2}$ difference results from allowing for the drop in density by a factor 2, along the SOL, as the flow is accelerated to the sound speed. Thus $D_\perp^{\mathrm{SOL}}$ can be evaluated from, for example, Langmuir probe measurements of $n_e(r)$ (for λ_n) and T_{LCFS} (for $c_{s,\mathrm{LCFS}}$)—and using $L = \pi Rq$ for the case of a poloidal divertor geometry. The foregoing ignores the radial variation $c_s(r)$, i.e. of $T(r)$, in equation (4.4). This effect is included in the next section.

Various authors have reported sets of empirical $D_\perp^{\mathrm{SOL}}$ values obtained using equation (4.7). Figure 4.4(a) shows an example from a set of ohmic discharges in JET operated with limiters [4.1].The data for this set shows an inverse dependence on $\overline{n}_e$, the average plasma density in the main plasma. Most reported values of $D_\perp^{\mathrm{SOL}}$ are in the range 0.1 to 10 $\mathrm{m}^2\ \mathrm{s}^{-1}$, but it is still not clear what $D_\perp^{\mathrm{SOL}}$ correlates with. In the 1940s, David Bohm carried out studies on non-toroidal magnetic plasmas, reporting the empirical result [4.2]:

$$\boxed{D_\perp^{\mathrm{Bohm}} \cong 0.06T_e/B} \tag{4.8}$$

with D [$\mathrm{m}^2\ \mathrm{s}^{-1}$], T [eV], B [T]. Such transport is now called *Bohm diffusion*. This expression does give values in the same range as has been found for tokamaks where $B \approx$ 2–10 T and $T_{\mathrm{LCFS}} =$ 10–100 eV are representative, giving $D_\perp^{\mathrm{Bohm}} \sim 0.05$ to $\sim 30\ \mathrm{m}^2\ \mathrm{s}^{-1}$. It is not clear, however, that in tokamaks $D_\perp^{\mathrm{SOL}}$

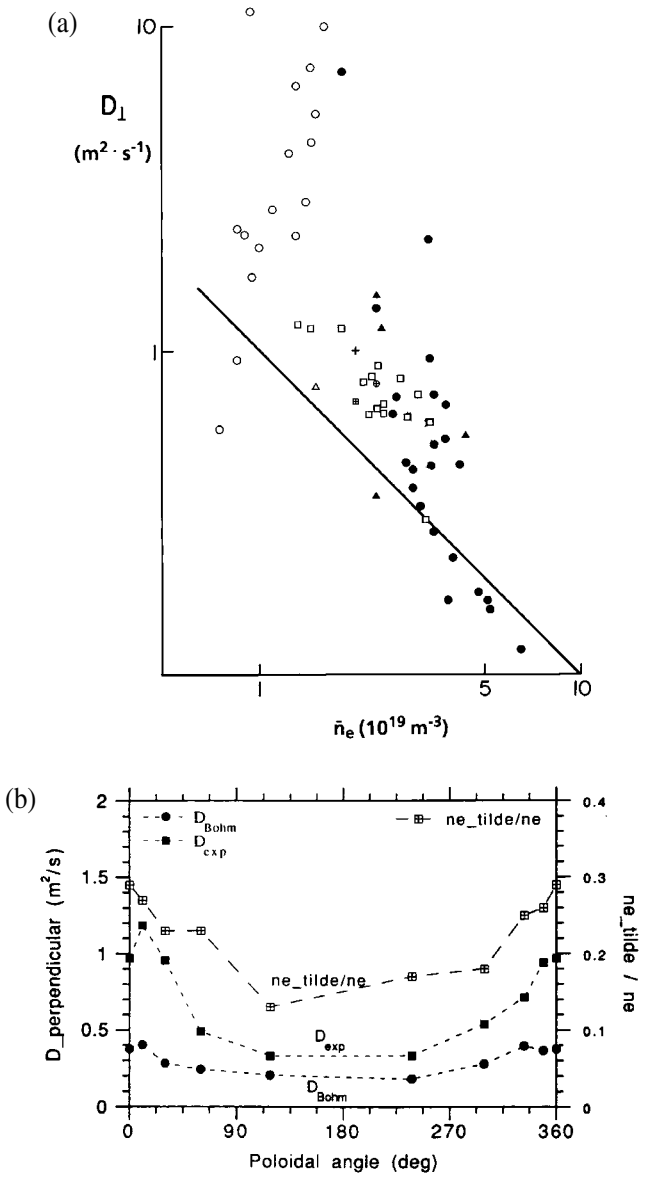

Figure 4.4. (a) Values of $D_\perp^{SOL}$ extracted from measurements of λ_n on JET operated with toroidal limiters, ohmic discharges [4.1]. Langmuir probe data: ○ $I_p = 1$ MA, Δ 2 MA, ▲ 3 MA, □ 4 MA, ● 5 MA. Solid line: $D_\perp = 10^{19}/\bar{n}_e$ [4.1]. (b) Values of $D_\perp^{SOL}$ extracted from measurements of λ_n made on the FTU tokamak operated with a poloidal ring limiter. $\theta = 0$ is the outer mid-plane, and positive direction is upward [4.5]. ne_tilde/ne is the normalized density fluctuation level, see chapter 8.

actually does vary as T_e and as B^{-1}; some studies report behaviour roughly in accord with these dependences [4.3], while others show little or no such correlation [4.4].

Figure 4.4(b) shows values of $D_\perp^{\mathrm{SOL}}$ extracted from measurements of λ_n made on the FTU tokamak, using equation (4.7) [4.5]. FTU employed a poloidal limiter and since $\boldsymbol{B}$ is almost in the toroidal direction, individual SOL flux tubes 'sample' virtually a single poloidal angle. Significant poloidal variations of λ_n can thus exist since, with a poloidal limiter, an individual SOL flux tube does not experience poloidally averaged conditions—as it does for a toroidal limiter. Such poloidal variations were first observed on the Alcator C tokamak [4.6]. The FTU results in figure 4.4(b) indicate a $D_\perp^{\mathrm{SOL}}$ value which tracks $D_\perp^{\mathrm{Bohm}}$ to within an approximately constant factor 2. Fluctuation levels were also found to track $D_\perp^{\mathrm{SOL}}$, supporting the idea that (anomalous) cross-field transport is caused by plasma fluctuations, chapter 8. In any case, the Bohm value comes much closer to matching experiment than does classical cross-field diffusion (based on e–i collisions in a fully ionized plasma) [4.7]:

$$D_\perp^{\mathrm{classical}} = 2\rho_\parallel^{\mathrm{spitzer}} n(kT_e + kT_i)/B^2 \tag{4.9}$$

where $\rho_\parallel^{\mathrm{spitzer}}$ is the classical, parallel electrical resistivity of a fully ionized plasma [4.8].

$$\boxed{\rho_\parallel^{\mathrm{spitzer}} \approx 8 \times 10^{-4}/T_e^{3/2}} \tag{4.10}$$

for T [eV], ρ [ohm m]. For the above range of representative SOL conditions, and $n_{\mathrm{LCFS}} = 10^{19}$–$10^{20}$ m^{-3}, one finds $D_\perp^{\mathrm{classical}} \sim 10^{-6}$ to $\sim 10^{-4}$ [m^2 s^{-1}]. Also one may note that $D_\perp$ classical $\propto B^{-2}$, a much stronger dependence than is measured.

It is clear that $D_\perp^{\mathrm{SOL}}$ is highly anomalous. The value of $D_\perp^{\mathrm{Bohm}}$ may not be a bad first estimate; but, in the absence of measured values for a specific machine under specific operating conditions, there may be nothing to justify anything more than simply taking $D_\perp^{\mathrm{SOL}} \sim 1$ m^2 s^{-1}.

Unfortunately, as noted earlier, some of the reported measurements of $D_\perp^{\mathrm{SOL}}$ have incorrectly applied equation (4.7) to complex SOLs, where local particle sources due to ionization are involved in the particle balance, and this has contributed to the uncertainties in this field.

4.4 Modelling λ_n, λ_{T_e}, λ_{T_i}, etc Simultaneously

The radial decay lengths of T_e and T_i are λ_{T_e}, λ_{T_i}, defined similarly to equation (4.2). Here we will assume exponential decays:

$$n(r) = n_{\mathrm{LCFS}} \exp(-r/\lambda_n) \tag{4.11}$$

$$T_e(r) = T_{e,\mathrm{LCFS}} \exp(-r/\lambda_{T_e}) \tag{4.12}$$

$$T_i(r) = T_{i,\mathrm{LCFS}} \exp(-r/\lambda_{T_i}). \tag{4.13}$$

Other quantities varying across the SOL:

$$p_e(r) = nkT_e \tag{4.14}$$
$$p_i(r) = nkT_i \tag{4.15}$$
$$q_\parallel^e(r) = \tfrac{1}{2}nc_s\gamma_e kT_e \tag{4.16}$$
$$q_\parallel^i(r) = \tfrac{1}{2}nc_s\gamma_i kT_e \tag{4.17}$$

where $p_{e,i}$ are the electron and ion pressures, $q_\parallel^{e,i}$ are the parallel electron and ion power flux densities, $\gamma_{e,i}$ are the electron and ion sheath heat transmission coefficients, section 2.8. (Note the convention of employing T_e in the expression for $q_\parallel^i$; see section 25.5.) Equation (4.16) and (4.17) are actually the expressions for the sheath entrances, but since there are no volumetric power losses in the simple SOL, $q_\parallel$ is constant on each flux tube.

We thus have for the pressure decay lengths:

$$\frac{1}{\lambda_{p_e}} = \frac{1}{\lambda_n} + \frac{1}{\lambda_{T_e}} \quad \text{and} \quad \frac{1}{\lambda_{p_i}} = \frac{1}{\lambda_n} + \frac{1}{\lambda_{T_i}}. \tag{4.18}$$

One would like to also evaluate $\lambda_{q_\parallel}^e, \lambda_{q_\parallel}^i$. However, since $c_s = [k(T_e+T_i)/m_i]^{1/2}$, this does not result in simple expressions, except for special cases. If, for example, e–i equipartition is strong and $T_e = T_i = T$ at each point in the SOL, then one has the simple relations:

$$\frac{1}{\lambda_{q\parallel}^e} = \frac{1}{\lambda_{q\parallel}^i} = \frac{1}{\lambda_n} + \frac{3}{2\lambda_T}. \tag{4.19}$$

Problem 4.1. Prove that equation (4.19) follows from the fact that $q_\parallel \propto nc_sT \propto nT^{3/2}$. Prove the similar relation, equation (4.33). Hint: $\lambda_n \equiv -((1/n)\partial n/\partial r)^{-1}$, etc.

The simple SOL regime, however, is not characterized by strong equipartition. It will be argued below that usually $T_i > T_e$ for the simple SOL, section 2.9. In fact $T_i^{\mathrm{SOL}} > T_e^{\mathrm{SOL}}$ is observed experimentally [4.9, 4.10], although measurements of T_i^{SOL} are sparse. In this case one has approximately the same results as equation (4.19) but with $T \to T_i$. It will also be argued below that for the simple SOL there is a tendency toward $\lambda_{T_i} \to \infty$; in this case one has approximately:

$$\frac{1}{\lambda_{q\parallel}^e} = \frac{1}{\lambda_n} + \frac{1}{\lambda_{T_e}} \quad \text{and} \quad \frac{1}{\lambda_{q\parallel}^i} = \frac{1}{\lambda_n}. \tag{4.20}$$

Applying logic similar to that employed in the last section, but now extending it to cover electron and ion power balances as well, we obtain equations (4.23)–(4.25) below. We assume that both cross-field convection and conduction contribute to

the electron power flow into the SOL. We assume the cross-field conduction to be anomalous and write it in the standard form which, by introducing a factor n, ensures that $\chi_\perp$ and $D_\perp$ have the same units:

$$\boxed{q_\perp^{\text{cond}} \equiv -K_\perp \frac{\mathrm{d}}{\mathrm{d}r} kT \equiv -n\chi_\perp \frac{\mathrm{d}}{\mathrm{d}r} kT \quad [\text{W m}^{-2}].} \tag{4.21}$$

Although $\chi_\perp$ is anomalous we anticipate $\chi_\perp \approx D_\perp$ from analogy with classical transport. The cross-field convection may be taken to be:

$$q_\perp^{\text{conv}} = -\frac{5}{2} kT D_\perp \frac{\mathrm{d}n}{\mathrm{d}r}. \tag{4.22}$$

Then from particle balance:

$$L D_\perp \frac{n_{\text{LCFS}}}{\lambda_n} = \tfrac{1}{2} n_{\text{LCFS}} c_s \lambda_n \tag{4.23}$$

while from electron and ion energy balances:

$$L\left(n_{\text{LCFS}} \chi_\perp^e \frac{kT_{e,\text{LCFS}}}{\lambda_{T_e}} + \frac{5}{2} kT_{e,\text{LCFS}} D_\perp \frac{n_{\text{LCFS}}}{\lambda_n} \right) = \tfrac{1}{2} n_{\text{LCFS}} c_s \gamma_e kT_{e,\text{LCFS}} \lambda_{q\parallel}^e \tag{4.24}$$

$$L\left(\frac{5}{2} kT_{i,\text{LCFS}} D_\perp \frac{n_{\text{LCFS}}}{\lambda_n} \right) = \tfrac{1}{2} n_{\text{LCFS}} c_s \gamma_i kT_{e,\text{LCFS}} \lambda_{q\parallel}^i. \tag{4.25}$$

It will be noted that in equation (4.25), we have made the simplifying assumption that $q_\perp^{\text{cond},i} \ll q_\perp^{\text{conv},i}$ which has therefore been neglected. There is some evidence that in the core plasma cross-field ion conduction can fall to neo-classical levels, while $\chi_\perp^e$ and $D_\perp$ remain anomalously high, although there is currently little information on this for the SOL. This assumption, even if only a rough approximation to the actual situation, gives some important results which appear to correspond approximately to experiment. Since the ion sheath heat transmission coefficient, section 2.8, is approximately $\gamma_i \approx (5/2)T_i/T_e$, we see that each ion entering the SOL from the main plasma brings with it $5/2kT_{i,\text{LCFS}}$ (assuming that only $q_\perp^{\text{conv},i}$ is involved in $q_\perp$), while at the sheath edge $5/2kT_{\text{sheath}}^i$ is removed. Therefore *the ions are not cooled in passing through the SOL*: in this approximation $T_i(r) = T_{\text{LCFS}}$, i.e. $\lambda_{T_i} = \infty$. The ion power flows through the SOL, being lost to the limiter but without ion cooling. We will thus assume further that $T_{i,\text{LCFS}} > T_{e,\text{LCFS}}$ which makes $c_s \approx (kT_{i,\text{LCFS}}/m_i)^{1/2} \approx$ constant across the SOL.

Problem 4.2. With these assumptions, show that equation (4.25) reduces to equation (4.23) which gives the same result for λ_n as before, equation (4.7). Show that

equation (4.24) then gives the relation for λ_{T_e}:

$$\left(1+\frac{\lambda_n}{\lambda_{T_e}}\right)\left(\frac{5}{2}+\frac{\chi_\perp^e}{D_\perp}\frac{\lambda_n}{\lambda_{T_e}}\right)=\gamma_e. \tag{4.26}$$

Thus λ_{T_e}/λ_n is a function of $\chi_\perp^e/D_\perp$.

Problem 4.3. For the example: $\chi_\perp^e/D_\perp = 1$ and $\gamma_e = 5$, section 2.8, show that: $\lambda_{T_e}/\lambda_n = 1.64$, $\lambda_{T_i} = \infty$, $\lambda_{p_e}/\lambda_n = \lambda_{q\parallel}^e/\lambda_n = 0.62$, $\lambda_{p_i}/\lambda_n = \lambda_{q\parallel}^i/\lambda_n = 1$. As $\chi_\perp^e/D_\perp$ increases, λ_{T_e}/λ_n increases; show that for $\chi_\perp^e/D_\perp = 10$, $\lambda_{T_e}/\lambda_n = 5.7$.

While λ_{T_e}/λ_n increases more slowly than $\chi_\perp^e/D_\perp$, show that the ratio $q_\perp^{\mathrm{cond},e}/q_\perp^{\mathrm{conv},e} < 1$, and this ratio only reaches equality as $\chi_\perp^e/D_\perp \to \infty$.

Thus, the electron power entering the SOL is always $\lesssim 5kT_{e,\mathrm{LCFS}}$ per electron, and $T_e(r)$ must decrease radially in order that the average thermal energy of the electrons leaving the SOL, and entering the target sheaths, is less than $T_{e,\mathrm{LCFS}}$. That is, the SOL not only removes electron power, but *cools* the electrons as they pass through the SOL. This creates a tendency for $T_e^{\mathrm{SOL}} < T_i^{\mathrm{SOL}}$, since the ions experience little cooling in the SOL.

The foregoing analysis may be made more general, at the price of increasing the complexity of the analysis, by including $q_\perp^{\mathrm{cond},i} \neq 0$, etc. Also, in equations (4.23)–(4.25) the form of the RHS implies that the cross-field flux densities across the separatrix do not vary along the length of the SOL, although the use of the factor 1/2 on the RHS implies a density drop along the SOL; this small discrepancy can also be roughly corrected for by including a factor of ~ 0.75 on the LHS of these equations, i.e. 'splitting the difference'. Finally, the assumption of the factor 5/2 in equations (4.22) etc. has resulted in convenient simplifications which are somewhat modified if a factor 3/2 is used instead, see chapter 8.

4.5 Relating the Properties of Main and Edge Plasmas

The plasma density and temperature in the confined plasma of a fusion power device must satisfy the Lawson criterion $n_{\mathrm{main}}\tau_E \geq 10^{20}$ m^{-3} s. What plasma conditions in the SOL will correspond to such main plasma conditions? And generally, what are the relations governing the connection between the plasma temperature and density in the confined plasma, and those of the SOL?

This central question can be addressed at several levels of completeness and self-consistency. Here we present an initial treatment which does not treat the combined main plasma + SOL system in a self-consistent way, but takes as *given* either:

(a) the total ion (thus also electron) particle flow rate into the SOL from the main plasma, ϕ_{SOL}^{in} [charged particles s^{-1}] and the total power flow from the main plasma into the SOL, P_{SOL}^{in} [W], or

(b) the particle and energy confinement times of the system, τ_p and τ_E [s]. As shown next, $P^{in}_{\rm SOL}$ and τ_E are simply related. For the simple SOL, which is all that is being considered here, $\phi^{in}_{\rm SOL}$ and τ_p are also simply related.

Since most of the particle and energy content lies inside the LCFS one is tempted to think of $\phi^{in}_{\rm SOL}$, $P^{in}_{\rm SOL}$, τ_p and τ_E as being properties purely pertaining to the *main* plasma. This is reasonable for the energy, since the power input is generally in the main plasma. Particle refuelling, however, is intimately tied up with the SOL and as will be discussed in section 4.6, $\phi^{in}_{\rm SOL}$ and τ_p therefore have as much to do with the SOL as with the main plasma. Nevertheless, for this first treatment we will take $\phi^{in}_{\rm SOL}$, $P^{in}_{\rm SOL}$, τ_p and τ_E as given quantities—independent of the SOL—and will use them to *specify* the particle and power inputs to the (simple) SOL. That is the total particle flow into the SOL is given by either $\phi^{in}_{\rm SOL}$ or τ_p:

$$\phi^{in}_{\rm SOL} = \frac{\overline{n}_{\rm main} V_{\rm main}}{\tau_p} \ [\text{ion pairs s}^{-1}] \tag{4.27}$$

where $\overline{n}_{\rm main}$ is the average plasma density in the main plasma of volume $V_{\rm main} (\approx 2\pi R \pi a^2)$. Ignoring for now radiative losses, the total power entering the SOL from the confined plasma is given by $P^{in}_{\rm SOL}$ or τ_E since:

$$P^{in}_{\rm SOL} = \frac{3\overline{n}_{\rm main} k \overline{T}_{\rm main} V_{\rm main}}{\tau_E} \ [\text{W}] \tag{4.28}$$

where the average ion and electron thermal energy per particle in the main plasma is $\frac{3}{2} k \overline{T}_{\rm main}$. Here $P^{in}_{\rm SOL}$ is measured as the total power into the tokamak, P. τ_E is then calculated from measurements of $\overline{n}_{\rm main}$, $\overline{T}_{\rm main}$, and equation (4.28).

As noted in section 3.5, $\phi^{in}_{\rm SOL}$ can be *inferred* from the intensity of the spectroscopic emission of the recycling hydrogenic atoms, usually the D_α line. This can be interpreted to give a value for the total flux of neutrals entering the plasma, $\phi_{\rm neut}$ [neutrals], all of which are assumed to ionize, i.e. to fuel the plasma, creating ion pairs which eventually enter the (simple) SOL. The particle content, $\overline{n}_{\rm main} V_{\rm main}$ can also be measured, e.g. using interferometry. τ_p is then simply taken to be $\overline{n}_{\rm main} V_{\rm main} / \phi_{\rm neut}$ i.e. $\phi^{in}_{\rm SOL} = \phi_{\rm neut}$ is assumed. Empirical expressions have been published for τ_p for specific machines operating under specific conditions. For example, for JET operated with limiters and for ohmic heating, Cohen *et al* [4.11] reported:

$$\tau_p \approx 1.3 \times 10^{14} R a^2 (\overline{n}_{\rm main})^{-0.8} \tag{4.29}$$

for τ [s], R, a [m], $\overline{n}$ [m^{-3}]. Again, it should be emphasized that an expression such as equation (4.29) for τ_p merely *correlates* τ_p with main plasma conditions—but 'hides' the connection to SOL properties. Thus, as noted, this first approach does not constitute a fundamental analysis.

The foregoing makes it clear that τ_p and τ_E are not basic, measured quantities. Rather they are convenient groupings of the basic, measured quantities:

$\overline{n}_{\text{main}}$, $\overline{T}_{\text{main}}$, V_{main}, ϕ_{neut}, and P. While it is often more convenient to work with τ_p and τ_E than the latter, the origin of τ_p and τ_E should always be kept in mind. It is tempting, but often seriously misleading, to invest these 'confinement times' with meanings suggested by intuition. This is particularly the case for τ_p where it is tempting, but wrong, to think of τ_p as representing the dwell time of most of the particles in the plasma, or that τ_p depends exclusively on $D_\perp$ and the plasma size (minor radius) a. This matter is addressed in the next section. So long as these times are used simply as convenient groupings of other, measured quantities—as done here—then there is no difficulty. It is also emphasized again that the results of this section *only apply to the simple SOL*.

While there are relatively few published correlations for τ_p, such as equation (4.29), by contrast it has always been a high priority in fusion energy research to correlate τ_E with main plasma conditions, machine size, etc. Data fits to the measured τ_E values for most past and present tokamaks are published and updated regularly. An example of such a *scaling expression* is that for L-mode confinement [4.12]:

$$\tau_E^{\text{ITER89-P}} = 0.048 \frac{I_p^{0.85} R^{1.2} a^{0.3} \kappa^{0.5} (\overline{n}_{\text{main}})^{0.1} B^{0.2} A^{0.5}}{P^{0.5}} \tag{4.30}$$

for τ [s]; I_p, the ohmic current [MA]; P, the total power into the tokamak [MW]; $\overline{n}_{\text{main}}$ [10^{20} m^{-3}]; B [T]; $\kappa = b/a$, the plasma elongation (elliptical poloidal cross-section with a the horizontal minor radius, and b the vertical); $A = 1, 2, 3$ for H, D, T. It is to be noted that expressions for τ_E such as equation (4.30) are not calculations from first principles, but empirical fits to measurements. In contrast with τ_p, it does seem plausible that τ_E is largely or entirely governed by main plasma parameters.

We now have the information needed to relate the main and SOL plasmas. Specifically we can now relate the two principal SOL parameters, (n_{LCFS}, T_{LCFS}) to the two main plasma parameters, ($\overline{n}_{\text{main}}$, $\overline{T}_{\text{main}}$), since we have two relations—for particle and power balance. From particle balance:

$$\frac{\overline{n}_{\text{main}} V_{\text{main}}}{\tau_p} = \frac{1}{2} n_{\text{LCFS}} c_{s,\text{LCFS}} A_{\Gamma\parallel} \tag{4.31}$$

where $A_{\Gamma\parallel}$ is the target-wetted area for particle flux, measured $\perp \boldsymbol{B}$:

$$A_{\Gamma\parallel} = \lambda_\Gamma w \tag{4.32}$$

where, following similar reasoning to that used to obtain equation (4.19):

$$\frac{1}{\lambda_\Gamma} = \frac{1}{\lambda_n} + \frac{1}{2\lambda_T} \tag{4.33}$$

and here w is the effective plasma-wetted length of target, see section 4.2:

$$w \cong 4\pi R(B_\theta/B). \tag{4.34}$$

Now allowing for radiative loss, power balance gives:

$$P_{\mathrm{SOL}}^{in} = P - P_{\mathrm{rad,main}} = (1 - P_{\mathrm{rad,main}}/P)\frac{3\overline{n}_{\mathrm{main}}k\overline{T}_{\mathrm{main}}V_{\mathrm{main}}}{\tau_E} \qquad (4.35)$$
$$= (1/2)n_{\mathrm{LCFS}}c_{s,\mathrm{LCFS}}\gamma k T_{\mathrm{LCFS}}A_{q\|}$$

where $A_{q\|}$ is the target plasma-wetted area for power and $A_{q\|} = \lambda_{q\|}w$ with $1/\lambda_{q\|} = 1/\lambda_n + 3/2\lambda_T \cdot \gamma$ is the sheath heat transmission coefficient, section 2.8. We have here allowed for the fact that a significant fraction of P may never reach the SOL, being radiated as photon energy from the main plasma; this fraction will have to be included here as an additional specified input. Here τ_E corresponds to the loss of power by all processes, including radiation. The λ_n, λ_T values can be calculated, section 4.4, although this requires knowledge of $D_\perp^{\mathrm{SOL}}$, $\chi_\perp^{\mathrm{SOL}}$. Since, in reality, any such information probably came from measurements of λ_n and λ_T in the first place, one might as well take λ_n, λ_T as *further empirical input*, like τ_E and τ_p. We now combine equations (4.31) and (4.35), eliminating density, to obtain a relation between main and SOL temperature:

$$\frac{T_{\mathrm{LCFS}}}{\overline{T}_{\mathrm{main}}} = \frac{3}{\gamma}(1 - P_{\mathrm{rad,main}}/P)\frac{\tau_p}{\tau_E}\frac{A_{\Gamma\|}}{A_{q\|}}. \qquad (4.36)$$

For simplicity we take $A_{\Gamma\|} \approx A_{q\|}$ and $\gamma \approx 10$ to obtain

$$\frac{T_{\mathrm{LCFS}}}{\overline{T}_{\mathrm{main}}} \approx 0.15\tau_p/\tau_E \qquad (4.37)$$

where we have also assumed $P_{\mathrm{rad,main}}/P = 0.5$ as an estimate.

Problem 4.4. For a JET example of ohmic heating [4.13], $R = 3$ m, $a = 1.2$ m, $\overline{n}_{\mathrm{main}} = 3 \times 10^{19}$ m^{-3}, $I_p = 3.6$ MA, $P = 2.4$ MW, $B = 3.4$ T, $\kappa = 1.5$, D plasma, show that: $\tau_p \approx 0.15$ [s], $\tau_E \approx 0.71$ [s], (actual measurements for this specific JET shot, No 5507, gave $\tau_E = 0.9$ s). Show that this gives $T_{\mathrm{LCFS}}/\overline{T}_{\mathrm{main}} \approx 0.032$, which compares well with the average of $\overline{T}_{e,\mathrm{main}}$ and $\overline{T}_{i,\mathrm{main}} \approx 2$ keV for this shot, and the measured edge conditions for similar shots, figure 4.5, of $T_{e,\mathrm{LCFS}} \approx 60$ eV, and thus $T_{\mathrm{LCFS}}/\overline{T}_{\mathrm{main}} \approx 0.03$.

One can also combine equations (4.31) and (4.35) to obtain an estimate for T_{LCFS} by itself:

$$kT_{\mathrm{LCFS}} = \frac{\tau_p}{\overline{n}_{\mathrm{main}}V_{\mathrm{main}}}\left(\frac{P - P_{\mathrm{rad,main}}}{\gamma}\right)\frac{A_{\Gamma\|}}{A_{q\|}}. \qquad (4.38)$$

Taking τ_p from equation (4.29), $V_{\mathrm{main}} = 2\pi R\pi a^2\kappa$, $\kappa = 1.5$, $P_{\mathrm{rad,main}}/P = 1/2$, $\gamma = 7$, $A_{\Gamma\|}/A_{q\|} = 1$ gives:

$$T_{\mathrm{LCFS}} = 2 \times 10^{30}(\overline{n}_{\mathrm{main}})^{-1.8}P \qquad (4.39)$$

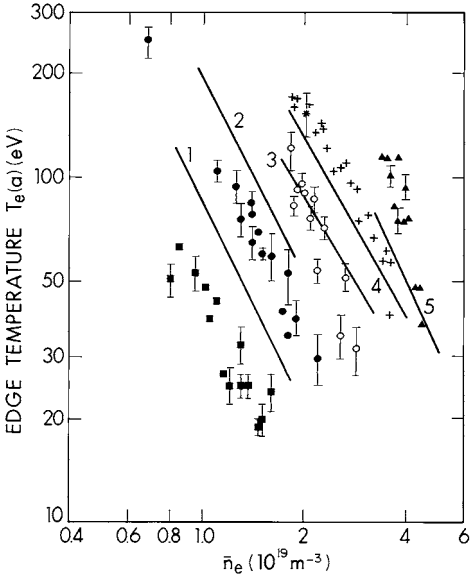

Figure 4.5. Probe results from JET operated with toroidal limiters [4.14]. T_e at the last closed flux surface, LCFS, as a function of the density in the main plasma $\overline{n}_e$, and the plasma current I_p. Ohmic conditions. ■ I_p = 1 MA, B = 2.1 T; ● 2 MA, 2.1 T; ○ 3 MA, 3.4 T; + 4 MA, 3.5 T; ▲ 5 MA, 3.5 T. The solid lines are from equation (4.42) [4.23].

for T [eV], n [m^{-3}], P [W]. One may note from equation (4.39) the tendency for edge temperature to decrease rapidly with increasing density in the main plasma:

$$T_{\mathrm{LCFS}} \propto\sim (\overline{n}_{\mathrm{main}})^{-2} \tag{4.40}$$

and to increase with power reaching the SOL, $T_{\mathrm{LCFS}} \propto P_{\mathrm{SOL}}$. In section 4.6 we will try to explain these dependences in a more self-consistent way.

For JET ohmic discharges P and I_p are experimentally related [4.14]:

$$P = 0.7 \quad I_p^{1.15} \tag{4.41}$$

for P [MW], I_p [MA]. Inserting equation (4.41) into (4.39) finally gives a prediction for T_{LCFS} in terms of tokamak operational parameters:

$$T_{\mathrm{LCFS}} \approx 1.4 \times 10^{36} (\overline{n}_{\mathrm{main}})^{-1.8} I_p^{1.15} \tag{4.42}$$

for T [eV], $\overline{n}$ [m^{-3}], I_p [MA]. Equation (4.42) is compared in figure 4.5 with measurements made on JET using Langmuir probes [4.14]. The reasonable agreement encourages the belief that the controlling phenomena have been at least approximately accounted for.

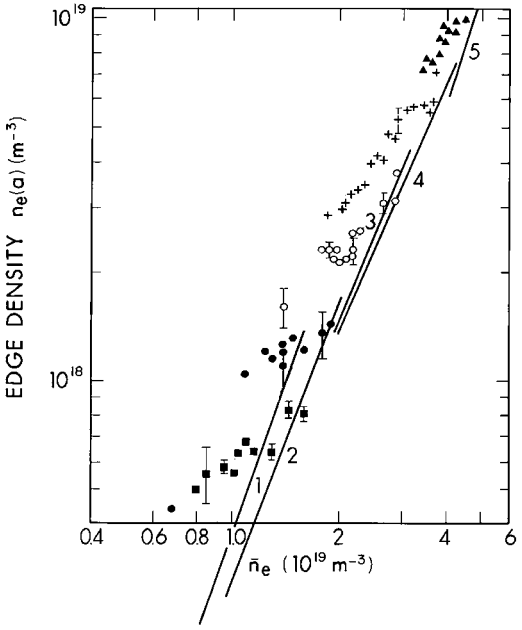

Figure 4.6. As figure 4.5 but for density at the LCFS. Solid lines are from equation (4.45) [4.14, 4.23].

Equation (4.31):

$$n_{\mathrm{LCFS}} = \frac{2\overline{n}_{\mathrm{main}} V_{\mathrm{main}}}{\tau_p A_{\Gamma\parallel} c_{s,\mathrm{LCFS}}} \tag{4.43}$$

can also be combined with equation (4.35) to give an estimate for n_{LCFS}, where now we can use equation (4.42) for T_{LCFS} to calculate $c_{s,\mathrm{LCFS}} = (2kT_{\mathrm{LCFS}}/m_i)^{1/2}$ and equation (4.29) for τ_p. This yields:

$$n_{\mathrm{LCFS}} \propto (\overline{n}_{\mathrm{main}})^{2.7} P^{-1/2} (A_{\Gamma\parallel})^{-1}. \tag{4.44}$$

For JET operated with discrete limiters [4.14, 4.15], one can estimate $A_{\Gamma\parallel}$ roughly as being that for a single continuous toroidal limiter at the outside wall, $R_W \approx 4$ m, $\lambda_\Gamma \approx 10^{-2}$ m and magnetic pitch angle ~ 0.1; thus $A_{\Gamma\parallel} \approx 4\pi R_W \lambda_\Gamma 0.1 \approx 0.1$ m^2. This quantity varies somewhat with $\overline{n}_{\mathrm{main}}$ and I_p but this is ignored here, giving finally for these JET, limiter, ohmic discharges:

$$n_{\mathrm{LCFS}} \approx 1.6 \times 10^{-31} P^{-1/2} (\overline{n}_{\mathrm{main}})^{2.7}. \tag{4.45}$$

n [m^{-3}], P [W] and P is related to I_p by equation (4.41) for these shots. Comparisons with values of n_{LCFS} measured with Langmuir probes are shown in figure 4.6. Again, the reasonable agreement, both as to trend as well as absolute

magnitude, indicates that the controlling processes have been at least approximately accounted for.

Let us recapitulate what we have done in this section. We took as input: $\overline{n}_{\text{main}}$, $\overline{T}_{\text{main}}$, V_{main}, ϕ_{neut}, P, $P_{\text{rad,main}}$, λ_n, λ_T, and $R(B_\theta/B)$, while we obtained as output: T_{LCFS} and n_{LCFS}. Thus, for the simple SOL we have achieved our objective of establishing the dependence of the SOL plasma properties on those of the main plasma. This approach is based directly on measured experimental quantities; we have not used extracted quantities such as $\chi_\perp$ and $D_\perp$. While this approach has its advantages we can reduce the required number of input data if we work with $\chi_\perp^{\text{SOL}}$ and $D_\perp^{\text{SOL}}$. Since the latter anomalous quantities are actually derived from the same basic measured data as already used, this does not lead to anything fundamentally different, but it can be a conceptually more attractive approach. It can also provide valuable insights. We turn to this approach next.

4.6 Particle Confinement Time, τ_p

In section 4.5 we treated τ_p as a given parameter so far as the SOL was concerned. In fact τ_p is very much governed by processes occurring in the SOL and should, therefore, be solved for *consistently* with the rest of the SOL analysis. To do this in a complete way is non-trivial but insight is provided by a simple model, the Engelhardt model [4.16, 4.17], which is described below. This will also serve to bring out the major difference that in principle exists between energy confinement time τ_E, and particle confinement time τ_p.

It is important to note, that in contrast with most of the analysis so far, *the geometry considered in this section is radial*. We will focus on the radial *depth* of the hydrogenic ionization relative to the LCFS. This section is therefore directly relevant to *limiter* operation where ionization tends to occur in the main plasma, figure 4.7. *Divertor* tokamaks are designed to achieve ionization localized within the divertor SOL, near the targets, figure 4.8. To the degree that a divertor achieves that objective, the results of this section are *totally inapplicable*. In practice, divertors may have significant ionization in the main chamber due to neutral 'leakage' out of the divertor or (undesired) plasma contact with the main vessel walls. In that case the results of this section may be applicable to divertor operation also.

Consider a slab geometry, figure 4.9. Two infinite planar walls at $r = \pm a$ define a plasma with $\boldsymbol{B}$ parallel to the walls. (Again note that figure 4.9 is *not* the along-$\boldsymbol{B}$ picture that we have been using almost exclusively up to this point in this book, but is a *cross-field* view.) We assume all heat input occurs at the centre, along $r = 0$, at rate $q_\perp$ [W m^{-2}]. We also assume that the walls are saturated with hydrogen and a steady-state refuelling exists with a uniform neutral influx of Γ^{neutral} [atoms m^{-2} s^{-1}] occurring from each wall. The neutrals are assumed to penetrate a distance λ_{iz} from the walls, all of them being ionized at the precise radial location $r = a - \lambda_{iz}$. In steady state that results in a uniform *ion out-flow* to the wall at flux density $\Gamma_\perp^{\text{ion}} = \Gamma_\perp^{\text{neutral}}$, the *neutral inflow* to the plasma. We take

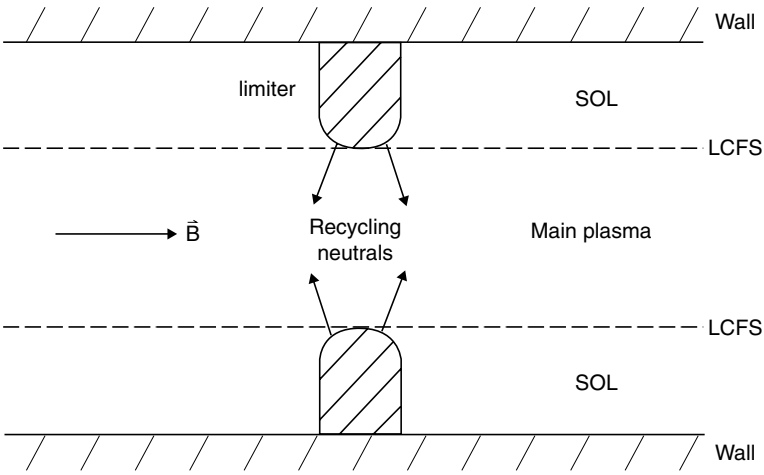

Figure 4.7. For limiters, the recycling hydrogen tends to be ionized in the main plasma.

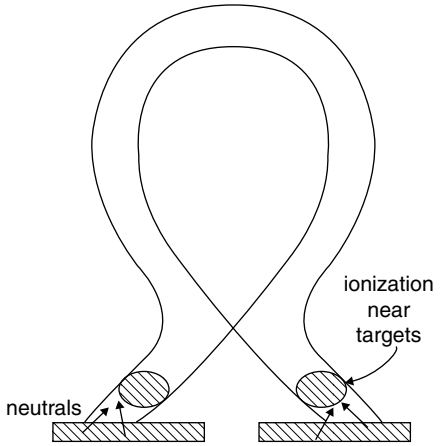

Figure 4.8. For divertors, the recycling hydrogen can be ionized near the targets, outside the main plasma.

simple boundary conditions for plasma density and temperature at the perfectly absorbing walls: $T(a) = n(a) = 0$ (the so-called *'hard' boundary condition*). Note that we have no limiters protruding into the plasma here, thus no SOL and no parallel flows are involved. In this first simple approximation the sink action is *purely radial*. We will include SOL action later. It will be found not to change the basic picture.

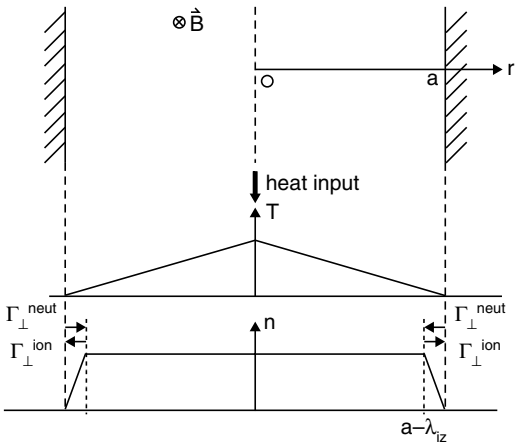

Figure 4.9. Radial profiles of temperature tend to be centrally peaked since power input tends to be central. Radial profiles of plasma density tend to be flat since recycling neutrals tend to be ionized near the edge, i.e., the plasma particle source is near the edge.

4.6.1 The Case with the Hard Boundary Condition

We now show that the $n(r)$ profile is of *plateau shape*, figure 4.9, when only cross-field diffusive transport is involved—which is the most common assumption for magnetic confinement:

$$\boxed{\Gamma_\perp^{\text{ion}} = -D_\perp \frac{\mathrm{d}n}{\mathrm{d}r}.} \tag{4.46}$$

Since neither source nor sink exist inside $r = a - \lambda_{iz}$, then $\Gamma_\perp^{\text{ion}} = 0$ there. Thus:

$$n = n(0), \text{ constant for } 0 < r < a - \lambda_{iz}. \tag{4.47}$$

For $a - \lambda_{iz} < r < a$, the ion flux density is constant and equal to the neutral influx density $\Gamma_\perp^{\text{neutral}}$:

$$-D_\perp \frac{\mathrm{d}n}{\mathrm{d}r} = \Gamma_\perp^{\text{neutral}} \quad \text{for } a - \lambda_{iz} < r < a. \tag{4.48}$$

Together with the boundary conditions $n(a - \lambda_{iz}) = n(0)$ and $n(a) = 0$ this then gives a linear variation of $n(r)$ in this region and:

$$D_\perp \frac{n(0)}{\lambda_{iz}} = \Gamma_\perp^{\text{neutral}}. \tag{4.49}$$

Thus the density profile is given by:

$$\boxed{n(r) = \begin{cases} n(0) = \lambda_{iz}\Gamma_\perp^{\text{neutral}}/D_\perp & 0 < r < a - \lambda_{iz} \\ (n(0)/\lambda_{iz})a(1 - r/a) & a - \lambda_{iz} < r < a \end{cases}} \tag{4.50}$$

i.e. the flat *plateau* profile shown in figure 4.9. For large tokamaks it is likely $\lambda_{iz} \ll a$ and so a very broad, flat density profile is anticipated—and is often observed, approximately.

It may not seem obvious that the $n(r)$ profile will be flat inboard of the ionization, i.e. source, location. It must be kept in mind however, that this is a *steady-state* result. At early times, following plasma start-up, there will be a density peak at $r = a - \lambda_{iz}$ which will 'feed' the central region, 'back-filling it up'; see problem 6.19. In steady state, random particle fluxes will exist in this region, both in and out, but the *net* flux $\Gamma_\perp^{\text{ion}}$ will be zero. Flat profiles are the direct consequence of (a) purely diffusive transport, and (b) source and sink both located close to the outer boundary. (One may consider the analogue of the temperature profile in a room where the source of heat, e.g. radiators, are placed right next to the sinks, the windows.)

We consider next the temperature profile $T(r)$ and the power balance. It is seen that if $q_\perp$ is deposited on axis, $r = 0$, and if it is transported cross-field purely by conduction (certainly there is no convection for $0 < r < a - \lambda_{iz}$ since $\Gamma_\perp^{\text{ion}} = 0$), then:

$$\boxed{q_\perp = -n(0)\chi_\perp \frac{\mathrm{d}kT}{\mathrm{d}r}} \tag{4.51}$$

and a *triangular* $T(r)$ profile results, figure 4.9.

$$kT(r) = \frac{aq_\perp}{n(0)\chi_\perp}(1 - r/a). \tag{4.52}$$

One notes what an important difference the source location makes to profiles.

We can now calculate τ_p and τ_E. We take the volume in slab geometry to be that of depth a and area 1 m^2, thus:

$$\tau_p \approx \frac{n(0)a}{\Gamma_\perp^{\text{neutral}}}$$

$$\boxed{\tau_p \approx \frac{\lambda_{iz}a}{D_\perp}} \tag{4.53}$$

where we assume $\lambda_{iz} \ll a$ so that $n(r) \approx n(0)$ for all $0 < r < a$ and used equation (4.49). JET-size example: $a = 1.5$ m, $\lambda_{iz} = 0.1$ m, $D_\perp = 1$ m^2 s^{-1}, thus $\tau_p \simeq 0.15$ s.

To calculate τ_E, we may note that $\overline{T} = T(0)/2$, thus:

$$\tau_E \approx 3/2n(0)kT(0)a/q_\perp$$

$$\boxed{\tau_E \approx a^2/\chi_\perp.} \tag{4.54}$$

For the same JET-size example and $\chi_\perp = 2$ m^2 s^{-1}: $\tau_E \simeq 1$ s.

Equations (4.53) and (4.54) indicate why τ_p and τ_E are, in principle, very different: the source locations are usually very different. Even if $D_\perp \simeq \chi_\perp$, these two times are in principle quite different. This means that, while $\chi_\perp$ and τ_E just represent the same information (for a given machine size)—$D_\perp$ and τ_p on the other hand actually contain different information and the one is *not* equivalent to the other. This state of affairs is unsatisfactory to some people who take the view: 'But the way *you* have defined τ_p really makes it dependent on 'edge confinement', not just core confinement'—as if *you* had any choice in how to define 'confinement time'! There really *is* no choice, since 'confinement time' is understood in all fields of science and engineering to mean (total content) ÷ (total source or loss rate) in steady state. The thought behind such comments, however, is understandable: some people would prefer τ_p to directly and purely indicate $D_\perp$, just as τ_E indicates $\chi_\perp$ directly. They would prefer it if $\tau_E/\tau_p = D_\perp/\chi_\perp$ so that this ratio would tell us directly about the relative ability of the magnetic field to confine particles and energy.

While complicated redefinitions of τ_p can be formulated in order to achieve a direct, simple relation between τ_p and $D_\perp$, this is probably inadvisable as it can result in creating more confusion. It is recommended that the classical definition of τ_p just be accepted and that *other* times be defined to deal with this matter. If neutrals are injected right to the axis before ionizing, e.g. by pellets, then $\lambda_{iz} \to a$, and $\tau_p \to\sim a^2/D_\perp$. One would also expect total particle content to show a *decay time*, $\tau_{\text{decay}} \simeq a^2/D_\perp$ following the termination of the source. One expects the initial *filling-up time* of the density profile resulting from edge fuelling to also take about this time. τ_p itself is not only a function of the *system* parameters, a and $D_\perp$, but also of the *source location*, here λ_{iz}.

We turn now to the point that $\tau_p (\approx a\lambda_{iz}/D_\perp)$, is largely a function of edge rather than *central* plasma processes:

(a) λ_{iz}, the penetration distance of the neutrals before ionizing is dependent on edge n_e and T_e:

$$\boxed{\lambda_{iz} = v_n/(n_e \overline{\sigma v_{iz}}(T_e))} \tag{4.55}$$

assuming all the neutrals have velocity v_n inward.

(b) If $D_\perp$ varies radially, it is only the average value of $D_\perp$ in the region, $a - \lambda_i < r < a$, that influences τ_p. The values of $D_\perp$ radially further in will effect the filling-up time, τ_{decay}, but not τ_p, which is a steady-state quantity.

An important benefit that results from sticking with the classical definition of τ_p is that both total content and total source rate are measurable—and their ratio is τ_p. The content can be measured from the $n_e(r)$ profiles using, for example, interferometry. The source can be measured in one of two ways:

(a) Target Langmuir probes provide values of I_{sat}^+, i.e. the particle flux density striking the targets which when measured over the entire targets, and integrated, gives the total charged particle outflow, assuming negligible volume recombination.

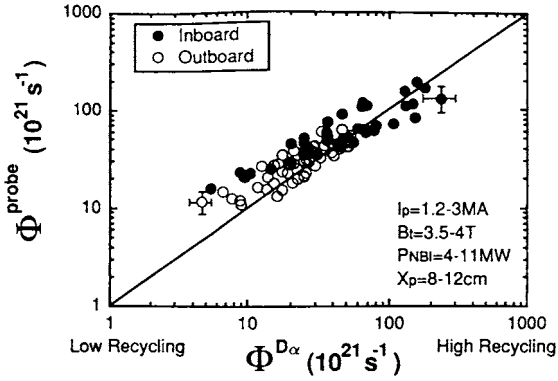

Figure 4.10. Comparisons between the deuterium influx by ionization, $\Phi^{D\alpha}$, measured spectroscopically, and the outflux, Φ^{probe}, measured on JT-60 [4.19]. The results for inner and outer divertor regions are represented by closed and open circles, respectively. Agreement between these two methods of measuring steady-state particle source strengths is to within a factor of about 2.

(b) Each neutral hydrogen entering the plasma emits about 0.1 D_α photon before becoming ionized, section 3.5. Thus by measuring the total D_α intensity the total fuelling rate can be deduced.

These two methods have been compared and found to agree generally [4.18]. Figure 4.10 [4.19], shows total hydrogenic fluxes measured in these two ways on the JT60-U divertor for a range of operating conditions. The agreement between the two methods is to within a factor of two or better. Further improvement might be achieved by (a) allowing for the contribution of molecule-related D_α radiation, (b) allowing for the spatial distribution of n_e and T_e throughout the D_α-emitting region, as it effects the photon efficiency, (c) including the contributions of impurities to the probe I_{sat}^+ measurements, etc. Figure 4.11 gives some τ_p measurements for several tokamaks using the two methods of measuring the fuelling rate. The tendency is for τ_p to decrease with increasing n_e and with decreasing machine size although the dependence on n_e is not always strong, as for example on TEXTOR [4.20].

We will now attempt to explain these basic aspects of τ_p using the Engelhardt model [4.16, 4.17]. We estimate λ_{iz} using equation (4.55), that is assuming that the neutral inward velocity can be estimated using a single, characteristic speed v_n. In reality, hydrogenic penetration of a plasma is complicated with various atomic, molecular and charge-exchange processes being involved, section 3.5. The NIMBUS Monte Carlo neutral hydrogen code, which includes all such processes, has been used [4.21] to analyse a variety of JET limiter discharges. It was found that the ionization depth could be well approximated for that situation by assuming $v_n \simeq 3 \times 10^4$ m s^{-1} and using $n_e = \frac{1}{2}\overline{n}_e$ in equation (4.55)

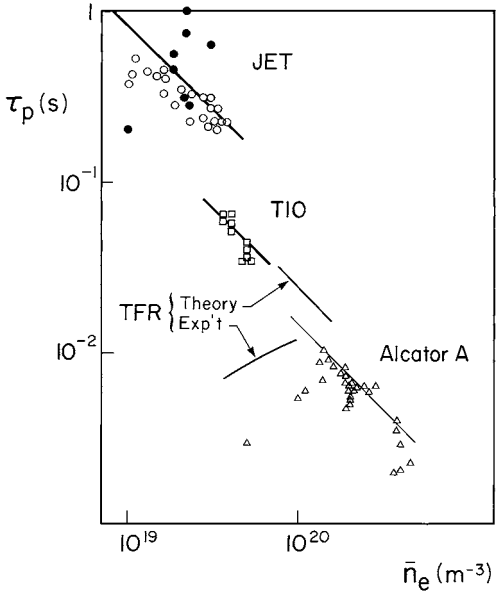

Figure 4.11. Particle confinement time. The straight lines are from $\tau_p \approx 3 \times 10^{18}\, a/(D_\perp \overline{n}_e)$ (see discussion in [4.23, 4.43]) where values of $D_\perp$ were extracted from measurements of λ_n.

with $\overline{\sigma v}_{iz} \simeq 3 \times 10^{-14}$ m^3 s^{-1}. ($\overline{n}_e$ is essentially the main plasma density, in $0 < r < a - \lambda_{iz}$.) This neutral velocity is that which $\sim$ 10 eV D atoms would have and thus indicates that some 'acceleration' by charge-exchange processes has occurred. This value cannot be taken as being universally valid but may be reasonably reliable for limiter geometry. We consider other estimates below. The use of $n_e = \frac{1}{2}\overline{n}_e$ in calculating λ_{iz} is reasonable since $n_e(r)$ rises linearly in the ionization zone from a low value to $\sim \overline{n}_e$. The use of $\overline{\sigma v}_{iz} \simeq 3 \times 10^{-14}$ m^3 s^{-1} is reasonable since this is a close approximation to the hydrogenic ionization rate for 20 eV $\leq T_e \leq$ 500 eV, figure 1.39. We thus obtain for the total neutral influx and ion outflux for the tokamak:

$$\phi = \Gamma_\perp^{\text{neutral}} A_{\text{plasma}} \tag{4.56}$$

where $A_{\text{plasma}} \simeq 2\pi R 2\pi a \kappa^{1/2}$.

Combining equations (4.49), (4.55), (4.56):

$$\boxed{\phi = \frac{\overline{\sigma v_{iz}} D_\perp A_{\text{plasma}} \overline{n}_e^2}{2 v_n}.} \tag{4.57}$$

Note that total flux $\phi \propto \overline{n}_e^2$.

Problem 4.5. For the JET-size example of $A_{\text{plasma}} \simeq 200$ m^2, $D_\perp = 1$ m^2 s^{-1}, show that $\phi \simeq 10^{-16}\overline{n}_e^2$, so that for $\overline{n}_e = 2 \times 10^{19}$ m^{-3}, show that $\phi \simeq 4 \times 10^{22}$ s^{-1} ≈ 1000 torr litre s^{-1}.

It may be noted that this *recycling* source strength is much larger than most external fuelling rates, e.g. from a gas-puffing valve. We also have:

$$\boxed{\tau_p \simeq \frac{a v_n}{D_\perp \overline{n}_e \overline{\sigma v}_{iz}}.} \tag{4.58}$$

The numerical factor 3×10^{18} used in figure 4.11 allows for some inward 'pinch', see below.

Problem 4.6. Derive equation (4.58).

We may note that $\tau_p \propto \overline{n}_e^{-1}$, which is about as seen, often, for limiter tokamaks, figure 4.11. Also recall from section 4.5 equation (4.29), the empirical relation found for JET limiter, ohmic shots: we may compare with the theoretical relation equation (4.58) for $a = 1.2$ m, $\overline{n}_e = 2 \times 10^{19}$ m^{-3}, $D_\perp = 0.5$ m^2 s^{-1}, figure 4.4(a), which gives $\tau_p = 0.12$ s. This is not too far off the $\tau_p = 0.20$ s from equation (4.29) for $R = 3$ m. Note also from equation (4.58) the prediction that $\tau_p \underset{\sim}{\propto} a$ which is also about as seen experimentally, figure 4.11.

Superficially, equation (4.55) for λ_{iz} seems to imply that only the ionization process influences the depth that the neutral hydrogen penetrates before ionizing. The value of $v_n \simeq 3 \times 10^4$ m s^{-1} extracted from the NIMBUS analysis [4.21] however, is far greater than the thermal velocity of molecules—thus indicating the contributions principally of:

(a) prompt back-scattering of energetic D^+ as D^0, section 3.1;
(b) production of 2–4 eV Frank–Condon atoms by electron-impact disassociation of molecules, section 3.5;
(c) charge-exchange collisions between $\sim$ eV D^0 and hotter D^+, section 3.5.

Other analytic expressions have been produced for the *penetration depth*, λ_{pen}, where we have defined the latter term to distinguish it from λ_{iz}, equation (4.55). For example Alexander *et al* define [4.22]:

$$\lambda_{\text{pen}} = (\sigma_{\text{eff}} n)^{-1} \tag{4.59}$$

where σ_{eff} is an effective cross-section combining the effects of ionization and charge exchange:

$$\sigma_{\text{eff}} \equiv (\overline{\sigma v}_{iz}(\overline{\sigma v}_{iz} + \overline{\sigma v}_{cx}))^{1/2}/(kT/m_{\text{atom}})^{1/2}. \tag{4.60}$$

Problem 4.7. Show using figure 1.25 that the value of σ_{eff} is approximately constant for $10 \lesssim T \lesssim 1000$ eV, at $\sim 3 \times 10^{-19}$ m^2 [4.22].

Similar expressions have been used by other authors, see references in [4.23].

4.6.2 The Case with the Soft Boundary Condition

We now relax the 'hard' boundary condition, $n(a) = 0$ (which may be appropriate when the wall itself constitutes the sink rather than limiters, section 25.2), to the assumption of $n(a) = n_{\mathrm{LCFS}} \neq 0$, which corresponds to a limiter-with-SOL sink, i.e. the *'soft' boundary condition*.

Consider the *first case* where ionization occurs inside the main plasma. Then within $a - \lambda_{iz} < r < a$

$$\Gamma_{\perp}^{\mathrm{ion}} = D_{\perp}(\overline{n}_e - n_{\mathrm{LCFS}})/\lambda_{iz} \tag{4.61}$$

and at the LCFS the flow into the SOL is:

$$\Gamma_{\perp}^{\mathrm{ion}} = D_{\perp} n_{\mathrm{LCFS}}/\lambda_n^{\mathrm{SOL}}. \tag{4.62}$$

We may note that the strength of the SOL sink action for particles is given by $\lambda_n^{\mathrm{SOL}} \approx (D_{\perp}\tau_{\mathrm{SOL}})^{1/2} \sim (D_{\perp}L/c_s)^{1/2}$, section 4.3: the stronger the sink action, the shorter is τ_{SOL}, thus also λ_n^{SOL}; for a given $\Gamma_{\perp}$ neutral ($= \Gamma_{\perp}^{\mathrm{ion}}$ ion in steady state), equation (4.62) shows that n_{LCFS} also goes down.

By combining equations (4.61) and (4.62), we thus obtain a simple expression relating n_{LCFS} to $\overline{n}_e$

$$\boxed{\frac{n_{\mathrm{LCFS}}}{\overline{n}_e} = \lambda_n^{\mathrm{SOL}}/(\lambda_{iz} + \lambda_n^{\mathrm{SOL}})} \tag{4.63}$$

which for $n_{\mathrm{LCFS}} \ll \overline{n}_e$ gives:

$$\frac{n_{\mathrm{LCFS}}}{\overline{n}_e} \simeq \frac{\lambda_n^{\mathrm{SOL}}}{\lambda_{iz}}. \tag{4.64}$$

Thus also:

$$\boxed{n_{\mathrm{LCFS}} \simeq \frac{\lambda_n^{\mathrm{SOL}} \overline{\sigma v}_{iz} \overline{n}_e^2}{2v_n}} \tag{4.65}$$

and

$$\boxed{\overline{n}_e = (\lambda_{iz} + \lambda_n^{\mathrm{SOL}})\Gamma_{\perp}^{\mathrm{neutral}}/D_{\perp}.} \tag{4.66}$$

Note that equation (4.65) predicts that $n_{\mathrm{LCFS}} \propto (\overline{n}_e)^2$, which has been seen experimentally on JET approximately, figure 4.6. Note that relaxation from the hard boundary condition has increased $\overline{n}_e$ by the factor $(\lambda_{iz} + \lambda_n^{\mathrm{SOL}})$, equation (4.66), compared with just λ_{iz}, see equation (4.50). τ_p, equation (4.53), also now has λ_{iz} replaced by $(\lambda_{iz} + \lambda_n^{\mathrm{SOL}})$.

Consider now a *second case*: for sufficiently high edge density the ionization location will no longer be in the main plasma, but will be in the SOL, at

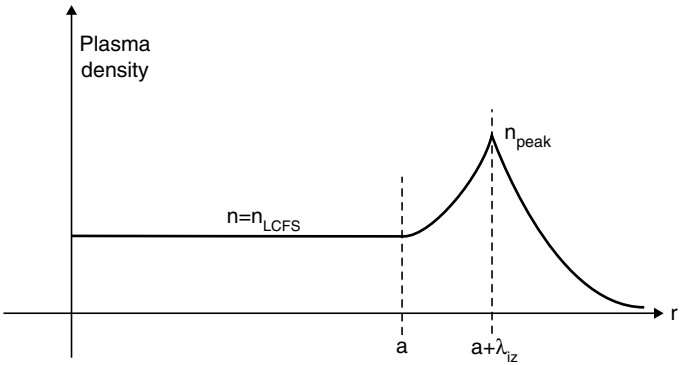

Figure 4.12. Radial profile of plasma density. For sufficiently high edge density, ionization of the recycling neutrals tends to occur within the SOL, leading to a density peak outboard of the LCFS, assuming transport is diffusive. The limiter edge, LCFS, is at $r = a$.

$r = a + \lambda_{iz}$. The analysis in this case yields the profile shown in figure 4.12, given by:

$$n(r) = \begin{cases} n_{\mathrm{LCFS}} & \text{for } r < a \\ \frac{1}{2} n_{\mathrm{LCFS}} [\exp((a-r)/\lambda_n^{\mathrm{SOL}}) + \exp((r-a)/\lambda_n^{\mathrm{SOL}})] & \text{for } a < r < a + \lambda_{iz} \\ n(a+\lambda_{iz}) \exp[-(r-a-\lambda_{iz})/\lambda_n^{\mathrm{SOL}}] & \text{for } r > a + \lambda_{iz} \end{cases} \tag{4.67}$$

where:

$$\boxed{\overline{n}_e = n_{\mathrm{LCFS}} = \frac{\Gamma_\perp^{\mathrm{neutral}} \lambda_n^{\mathrm{SOL}}}{D_\perp} \exp(-\lambda_{iz}/\lambda_n^{\mathrm{SOL}})} \tag{4.68}$$

and a density peak exists in the SOL at $r = a + \lambda_{iz}$ of magnitude:

$$n_{\mathrm{peak}} = n(a + \lambda_{iz}) = \frac{\Gamma_\perp^{\mathrm{neutral}} \lambda_n^{\mathrm{SOL}}}{2 D_\perp} [1 + \exp(-2\lambda_{iz}/\lambda_n^{\mathrm{SOL}})]. \tag{4.69}$$

Note from equation (4.68) that as the ionization location moves further outboard of the LCFS, the density in the main plasma, $\overline{n} = n_{\mathrm{LCFS}}$, drops, exponentially.

This case of a *SOL-ionization* source brings out the important phenomenon of *plasma fuelling* of the main plasma—as distinct from the *neutral fuelling* which occurs when neutrals penetrate inside the main plasma. For a SOL-ionization source, it is to be noted that the *entire* main plasma fills up, i.e. is 'fuelled', by *charged particles* diffusing (or otherwise being transported) across the magnetic field. Fuelling of the main plasma then is by *plasma* transport, not *neutral* transport.

The foregoing *pure-diffusion* transport can be extended to allow for the effect of an *inward pinch*, which adds radial convective transport of plasma to the diffusion, i.e. an inward drift velocity. Sometimes $n(r)$ is observed in experiments to be peaked—and not flat as is implied by the combination of pure diffusion plus an ionization source near the edge. In that case an anomalous inward pinch velocity may be hypothesized to exist, perhaps of the form $v_{in} = SD_\perp r/a^2$, where S is an adjustable numerical factor. Provided S is not extremely large then v_{in} is small compared with the effective diffusive velocity at the edge, $v_{D\perp,\text{eff}} \simeq D_\perp/\lambda_{iz}$, since λ_{iz} is short, and so the effect of v_{in} is simply to add a Gaussian $n(r)$ profile on top of the 'density plateau' which is associated with pure diffusion:

$$n(r) = n_{\text{plateau}} \exp[0.5S(1 - r^2/a^2)] \tag{4.70}$$

where n_{plateau} is given by $n(0)$ of equation (4.50) (the hard BC), or $\overline{n}_e$ of equation (4.66) (the soft BC and ionization in the main plasma) or n_{LCFS} of equation (4.67) (soft BC and ionization in the SOL). Thus if $S = 2$, for example, then a modest density *peaking factor* of $n(0)/n_{\text{plateau}} = \text{e}^1 \approx 2.7$ results. This increases the average plasma density to:

$$\overline{n}/n_{\text{plateau}} \equiv f(S) \equiv 2(\text{e}^{S/2} - 1)/S. \tag{4.71}$$

Problem 4.8. Prove that, including a pinch, τ_p, equation (4.58), should be multiplied by f^2 while particle flux ϕ, equation (4.57), should be divided by f^2.

At this point it is useful to return to the issue of defining τ_p. Sometimes, in an attempt to come up with a re-defined τ_p that will be exclusively a function of processes in the main plasma, some authors have defined a τ_p based on the content of the main plasma, and the ionization rate of neutrals occurring inside of the LCFS. The latter quantity can be calculated using a neutral hydrogen code such as DEGAS, NIMBUS, etc. They then define this to be 'the core particle confinement time'. This is probably inadvisable since the fuelling of the main plasma may be due to ionization outboard of the LCFS. Consider a mixed case where the ionization is partly in the SOL, partly in the main plasma—the usual situation, in fact. Assume for simplicity that the actual spatial distribution can be approximated by two sources, one inside the LCFS at a distance $\lambda_{iz}^{\text{main}}$, one outside the LCFS at a distance $\lambda_{iz}^{\text{SOL}}$. From the foregoing we have the two confinement times for these two sources:

$$\tau_p^{\text{main } iz} = (\lambda_{iz}^{\text{main}} + \lambda_n^{\text{SOL}})a/D_\perp \tag{4.72}$$

$$\tau_p^{\text{SOL } iz} = \exp(-\lambda_{iz}^{\text{SOL}}/\lambda_n^{\text{SOL}})a\lambda_n^{\text{SOL}} D_\perp \tag{4.73}$$

where equation (4.72) can be derived from equation (4.64) and equation (4.73) from equation (4.68). These two times are the same for $\lambda_{iz}^{\text{SOL}} = \lambda_{iz}^{\text{main}} = 0$, of course. Total particle content N [particles m^{-2}] for slab geometry:

$$N \approx a\overline{n}_e = \Gamma^{\text{main } iz}\tau_p^{\text{main } iz} + \Gamma^{\text{SOL } iz}\tau_p^{\text{SOL } iz} \text{ [m}^{-2}\text{]}. \tag{4.74}$$

Problem 4.9. For the example $a = 1.2$ m, $\lambda_n^{\rm SOL} = \lambda_{iz}^{\rm SOL} = \lambda_{iz}^{\rm main} = 10^{-2}$ m, $D_\perp = 1$ m^2 s^{-1}, $\overline{n}_e = 3 \times 10^{19}$ m^{-3}, and $\Gamma^{{\rm main}\ iz}/\Gamma^{{\rm SOL}\ iz} = 10^{-1}$, i.e. taking most of the ionization to be in the SOL, show that: $\tau_p^{{\rm SOL}\ iz} = 4.4$ ms, $\tau_p^{{\rm main}\ iz} = 24$ ms, $\Gamma^{{\rm main}\ iz} = 5.3 \times 10^{20}$ m^{-2} s^{-1}, the content N due to $\Gamma^{{\rm SOL}\ iz}$ is 2.3×10^{19} m^{-2} and that due to $\Gamma^{{\rm main}\ iz}$ is 1.3×10^{19} m^{-2}, i.e. the content is due primarily to the SOL ionization. If one were to re-define τ_p to be $N/\Gamma^{{\rm main}\ iz}$, show that this would give 68 ms, which is clearly misleading and not a useful number.

It is also questionable whether it is useful to define a 'SOL shielding factor', as is sometimes also done. One might define this to be the fraction of the neutrals which are ionized inboard of the LCFS, i.e. 'shielding factor' $\equiv \Gamma^{{\rm main}\ iz}/\Gamma^{{\rm total}\ iz}$. One might then draw the erroneous conclusion that it is only those neutrals which fuel the main plasma. As noted, this would be wrong since it ignores plasma fuelling. Furthermore, this approach also would imply that it is only the ratio $\Gamma^{{\rm main}\ iz}/\Gamma^{{\rm total}\ iz}$ that matters—whereas the actual *depth* inside the LCFS where the ionization occurs, $\lambda_{iz}^{\rm main}$, is also critical, equations (4.72), (4.74).

Problem 4.10. For the same values of a and $\lambda_n^{\rm SOL}$ as in problem 4.9, show that if one were to approximate the situation by assuming (a) that only $\Gamma^{{\rm main}\ iz}(= 5.3 \times 10^{20}$ m^{-2} s$^{-1})$ matters, and (b) $\lambda_{iz}^{\rm main} \simeq 0$, then one would obtain $\tau_p^{{\rm main}\ iz} = 12$ ms and $N = 6.4 \times 10^{18}$ m^{-2} which is a poor approximation to the actual $N = 3.6 \times 10^{19}$ m^{-2}.

It is clear that it is as important to estimate $\lambda_{iz}^{\rm main}$ reliably as it is to estimate any so-called 'shielding factor', such as $\Gamma^{{\rm main}\ iz}/\Gamma^{{\rm total}\ iz}$. Actually there is no need to attempt to define 'shielding factors', 'fuelling efficiencies', etc., since the quantitative capability of any specific source to fuel the plasma is *entirely* expressed by the *value of* τ_p *for that source*.

The foregoing strictures against the concept of a shielding factor are directed solely at the matter of understanding the relation between fuelling, τ_p and $n_e(r)$ profiles. A separate issue is the presence of neutrals and ionization in the main plasma, and the attainment of H-mode confinement [4.24], see chapter 7, which have sometimes been found to be anti-correlated [4.25]. For such studies the concept of a shielding factor can be useful.

The simple analysis in this section is based on 1D *radial* transport, either ignoring parallel transport, or treating it using a single parameter, $\lambda_n^{\rm SOL}$, for the soft boundary condition case. Thus 2D or 3D effects are largely ignored. For ionization inside the LCFS, even if it occurs in a 2D or 3D localized way, since parallel transport is so much faster than perpendicular transport, then *effectively* the ionization occurs uniformly (poloidally/toroidally) and a 1D radial transport

analysis is a good approximation, so far as the region inside the LCFS is concerned. The particles then enter the SOL uniformly along the length and so our 1D, along-$\boldsymbol{B}$ analysis provides a good estimate for $\tau_{\rm SOL}$ and thus $\lambda_n^{\rm SOL}$. Thus, although the SOL is inherently 2D (at least) the 1D radial approximation employed above—where the parallel loss to the targets is simply replaced with an effective and localized sink, $n(r)/\tau_{\rm SOL}$—should often be reasonable.

Consider next, the case of a limiter but with most of the ionization occurring in the SOL. Inevitably this will not occur uniformly along the length of the SOL but will be strongest near the limiter—and may perhaps be highly localized there. So long as the SOL is approximately isothermal, however, it does not significantly affect the SOL average dwell time, $\tau_{\rm SOL}$, whether the ion particle source is distributed uniformly along the SOL, or is entirely near the limiter. In either case the flow velocity at the sheath reaches c_s, while the density at the sheath edge, n, is half the far-upstream density, n_{up}, equation (1.50) (t for target, $n_t = n_{se}$, se for sheath edge). The only difference is the spatial distribution of $n(s_\parallel)$ along the SOL: when the source is close to the sheath, most of the drop occurs very near the target, rather than occurring in a somewhat more extended region; see problem 1.20. Since $\tau_{\rm SOL}$ is the total content of the SOL flux tube divided by the sheath outflux, the spatial distribution of the source along $\boldsymbol{B}$ is of little importance. Thus, the sink rate of the SOL, $\sim n/\tau_{\rm SOL}$, remains about as before. It would also give a first approximation to take $\lambda_{iz}^{\rm SOL}$ in equations (4.73), etc to be the average radial location of the ionization, even though it is not actually uniform along $\boldsymbol{B}$.

Turning to the divertor SOL: when there are no significant parallel T-gradients the results should be the same as for the limiter case just considered even if ionization is primarily outside the LCFS and near the targets. When significant T-variations are present, however, the simple estimate for $\tau_{\rm SOL}$ fails since (a) $n(s_\parallel)$-variations are now significant, making the calculation of the SOL content complicated, and (b) the out flux rate to the targets is a function of particular values of n and T in the SOL, namely n_t and T_t. Therefore $\lambda_n^{\rm SOL}$ should not be estimated from $(L_c D_\perp/c_s)^{1/2}$ and τ_p is not reliably given by the expressions derived in this section.

4.6.3 The Global Recycling Coefficient

So far we have only considered the case where the solid surfaces are hydrogen saturated and so $\phi_\perp^{\rm ion} = \phi_\perp^{\rm neutral}$, and the latter is just the total flux spontaneously released from the saturated surfaces. Such a situation will exist for long pulse fusion reactors. It can also occur for present day shorter pulse, devices, especially when operated at elevated surface temperatures where saturation sets in more quickly. Otherwise one often has $\phi_\perp^{\rm ion} > \phi_\perp^{\rm neutral}$ (the opposite inequality can also occur temporarily, for example, when previously deposited hydrogen is 'degassed'), and the only way to achieve a constant $\overline{n}_e$ is by external fuelling, e.g. with a gas valve, pellets or neutral beam injection. In addition to this *wall pumping* effect, there may be *active pumping* due, for example to a cryo pump.

For either type of pumping we define the *global recycling coefficient* $\overline{R}$ by:

$$\boxed{\phi_{\perp}^{\text{recycle neutral}} = \overline{R}\phi_{\perp}^{\text{ion}}.} \tag{4.75}$$

Thus, if one turns off all external fuelling, $\overline{n}_e$ will decay with a *measured* decay time τ_p^*:

$$\frac{\overline{n}_e \text{ volume}}{\tau_p^*} = -\frac{\text{d}(\overline{n}_e \text{ volume})}{\text{d}t}. \tag{4.76}$$

We have that:

$$\frac{\text{d}}{\text{d}t}(\overline{n}_e \text{ volume}) = \phi_{\perp}^{\text{recycle neutral}} - \phi_{\perp}^{\text{ion}} = \overline{R}\phi_{\perp}^{\text{ion}} - \phi_{\perp}^{\text{ion}} \tag{4.77}$$

and since

$$\overline{n}_e \text{ volume}/\tau_p = \phi_{\perp}^{\text{ion}} \tag{4.78}$$

we obtain:

$$\boxed{\tau_p^* = \frac{\tau_p}{1 - \overline{R}}.} \tag{4.79}$$

Note that as $\overline{R} \to 1$, $\tau_p^* \to \infty$ and there is no decay, i.e. 100% recycling. Also as $\overline{R} \to 0$, $\tau_p^* \to \tau_p$, which corresponds to very powerful pumping and zero recycling.

(Actually, as $\overline{R} \to 0$, the observed decay time would not actually drop to a value as low as τ_p: equation (4.79) was developed assuming a quasi steady state where, at all times, the $n_e(r)$ profile is in *radial equilibrium* with the recycling source. This requires that any changes occur on a time scale longer than what one might term the 'radial equilibration time', $\tau_{\text{r.eq.}} \approx a^2/D_{\perp}$. The observed decay time cannot fall below $\tau_{\text{r.eq.}}$, which is generally longer than $\tau_p \approx a\lambda_{iz}/D_{\perp}$.)

It is not practical to calculate $\overline{R}$ from basic data since so many surfaces, with very different plasma exposures and levels of saturation, are involved, but it can be found from measured τ_p^* and τ_p values. Figure 4.13 shows an example of $\overline{n}_e(t)$ for TFTR operated with a hydrogen-saturated limiter [4.26]. The external gas puff was turned off at $t = 1.5$ s, and, as can be seen, $\overline{n}_e(t)$ hardly decayed at all, indicating $\tau_p^* \gtrsim 10$ s. The carbon walls of TFTR were then depleted of hydrogen using extensive helium conditioning discharges resulting in hydrogen discharges with $\tau_p \simeq 0.15$ s, which is presumably approaching $\tau_{\text{r.eq.}}$. Since without conditioning, $\tau_p^* \gg \tau_p$, it is evident that present day tokamaks usually operate with $\overline{R}$ close to unity. This also implies that normally in steady state $\phi^{\text{neutral fuel}} \ll \phi_{\perp}^{\text{neutral recycle}}$. That is, tokamaks are usually largely *self-fuelled* and the external fuelling can be ignored for most purposes as a small effect.

The walls—particularly carbon walls—nevertheless constitute pumps for hydrogen and it can sometimes be necessary (in contrast with figure 4.13) to employ a constant $\phi^{\text{neutral fuel}}$ in order to achieve a constant $\overline{n}_e$. The pumping capacity

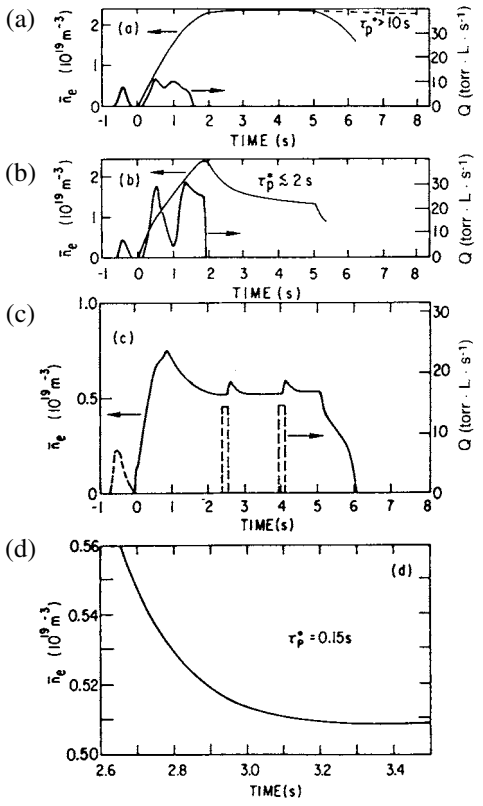

Figure 4.13. Measurements of τ_p^* on TFTR [4.26]. Going from (a) to (d), the carbon walls were depleted more and more completely of hydrogen by helium conditioning discharges.

of tokamak carbon walls has been determined experimentally to be in the range of 100 to 1000 times the plasma content [4.27–4.29], indicating that wall pumping may be effective for up to 1000 particle confinement times—or more, if co-deposition trapping of hydrogen is significant, section 3.4. Sophisticated models have been developed to explain transient wall pumping effects [4.30] and have been successfully used to explain observations in Tore Supra where the plasma contact with graphite surfaces was moved to induce transient wall pumping effects [4.31].

4.7 The Simple versus Complex SOL

In sections 1.9 and 4.1, the distinctions between the simple and complex SOL were introduced. For the complex SOL we must allow for the possibilities of:

(1) parallel gradients of temperature;
(2) ionization of the re-cycling neutral hydrogen within the SOL; volume power loss due to radiation—both hydrogenic and impurity—and to charge-exchange neutrals;
(3) momentum loss by the plasma flow to neutral hydrogen;
(4) volume recombination if T drops below a few eV;
(5) collisional transfer of energy between electrons and ions.

Many other complicating effects could also be included, such as viscous drag, the loss of particles, momentum and energy from the SOL into the private plasma, etc. As already noted, section 4.4, the level of electron–ion thermal coupling or *equipartition* is a moderately complicating effect.

Limiter SOLs are often simple. Divertor SOLs are often complex. A discussion of the reasons for this will be returned to later. While the complex SOL is harder to understand and analyse than the simple SOL, for practical reasons it is most advantageous to operate a tokamak employing a complex SOL. The following discussion of the reasons for this is mainly pertinent to the divertor SOL [4.32].

(1) Large T-gradients along the SOL mean that the plasma in actual contact with the solid divertor targets can be cool—reducing sputtering—while at the upstream end of the SOL, the edge plasma contacting the confined plasma can be hot. It was seen in the last section that in the absence of parallel temperature gradients (the simple SOL), the only way to have a very low value of T_{LCFS} is to employ high values of $\overline{n}_{\mathrm{main}}$, for a given P, equation (4.39). This may cause instability of the main plasma which is subject to an upper *density limit* [4.33]. Further, it seems plausible that the higher the temperature of the edge plasma—which constitutes the boundary of the main plasma—the better will be the energy confinement of the main plasma. Certainly it is known that the high temperature just *inside* the separatrix is associated with good energy confinement [4.34], although the relation of plasma conditions on each side of the LCFS is not well understood.
(2) When ionization of the recycling neutrals occurs in the main plasma—the simple SOL—the resulting outflow of plasma particles into the SOL occurs more-or-less uniformly along the length of the SOL. This gives significant parallel plasma flow—and hence *parallel heat convection*—all along the length of the SOL. This convection means that the parallel *conduction* carries less of the power flow along the SOL than it would otherwise—*thus decreasing the parallel drop in* T. This, as noted, is not desirable. By contrast, when ionization mean free paths are short, ionization occurs mainly in the SOL–and it will also generally occur mainly close to the source of the recycling neutrals, i.e. to the targets. Thus, the role of heat convection is reduced on average, and the temperature drop associated with conduction is greater.
(3) Volume power losses are desirable since they tend to deposit power in a very diffuse way over a substantial portion of the total wall area. By contrast,

the power deposited on the target by electron and ion impact occurs in a comparatively small area—the 'plasma-wetted' area—potentially causing over-heating and melting.

(4) When the plasma temperature near the targets is low, a further benefit results: the recycling neutrals can cause neutral frictional drag on the plasma flow to the targets before they are ionized. This obstruction to the outflow reduces its magnitude for fixed upstream conditions ('plugged drain effect'), i.e. the intensity of recycle is reduced, i.e. particle confinement (for the entire system, SOL plus main plasma) increases, chapter 16. This then also reduces the concentrated particle power deposition on the targets. This *neutral cushion* protects the target.

(5) If the plasma temperature at the targets drops still further, to $\lesssim 1$ eV, then another benefit arises: volume recombination becomes strong [4.35], replacing the sink action of the solid target, with a *gaseous target*. Erosion and heating of the target is then further reduced. This scenario—as well as the neutral cushion one—generally requires that volume power loss processes remove most of the power that entered the SOL before it reaches the targets.

4.8 Comparison of High Recycling, Strongly Radiating and Detached Regimes

As the plasma temperature near the divertor targets, T_t, is reduced further and further, a sequence of progressively more attractive complex SOLs is achieved. At the high values of n_t involved, the ionization occurs close to the targets. In section 5.2 the means of forcing T_t down are considered. Here are briefly described the consequences of low T_t.

(1) *The high recycling regime*. It is a remarkable, and perhaps surprising, fact that as T_t drops, the particle flux to the targets, ϕ_t, *increases*, section 5.2. One's first thought is perhaps that the plasma outflow ϕ_t ought to be more constrained, somehow. We are tempted to feel that it must be 'constrained to match the particle source'. It has to be remembered, however, that when the solid surfaces become fully saturated with hydrogen, section 3.4, a steady-state recycle refuelling sets in: no external source of fuel is then required—and the *plasma sustains itself, so far as particles are concerned*. Thus the plasma (ion) outflow, ϕ_t^+ is *automatically* matched to the neutral inflow rate, ϕ^0_{recycle}—at whatever level is consistent with the *other* balances, i.e. those of pressure and power. Thus the low T_t regime will also be a high recycling regime, high ϕ_t.

The high rate of recycling is in itself of no obvious advantage. The chief *practical* point about the 'high recycling regime' is that T_t is low, thus also the sputtering yield is low. Unless the volume power losses change, all the power still reaches the targets, so the over-heating problem is not affected (although the SOL width may increase, lowering peak power loads).

Table 4.1. Fraction of ionization occurring with the SOL of limiter tokamaks (using multi-dimensional neutral codes)[a].

Tokamak	Refs	Code	$\overline{n}_e$ (10^{19}m^{-3})	n_{LCFS} (10^{18}m^{-3})	Ionization fraction in SOL(%)
PLT (rail limiters)	Ruzic *et al* [4.39]	DEGAS	5.5	5	31
DITE (poloidal limiter)	Maddison *et al* [4.40]	DEGAS	2 2	5 2	14 7
JET (eight rail limiters)	Simonini *et al* [4.41]	NIMBUS	1.4 1.6 2.1 2.1 2.6 3.25 1.79 2.6 3.05 3.63 3.95	1.2 1.7 2.2 2.2 3.0 4.1 2.8 4.0 5.5 7.5 10	21 26 30 25 25 24 28 30 31 31 36
T-10	Pigarov and Vershkov [4.42]	TNG	2.6 (1.8)	4.5 (14.4)	43 63

[a] For ohmic heating; the two values in brackets are for ECH, electron cyclotron heating.

The terms 'conduction-limited regime', section 1.9, and 'high recycling regime' are often used interchangeably since the practical point is the achievement of low T_t. A further practical advantage is that for constant plasma pressure, n_t is large. This tends also to give large neutral densities near the divertor which aids pumping.

(2) *The strongly radiating regime*. There is no precise transition from the high recycling to the strongly radiating regime, since as the intensity of the hydrogenic recycle increases, the associated strong radiative losses also increase, section 3.5. Thus, in fact, the high recycling regime already enjoys, partially, the benefits of this regime. As T_e decreases, the amount of radiative energy loss per recycling hydrogen increases, figure 3.34 (although note that ε includes I_{iz} and this potential energy still ends up being deposited on the targets). This occurs primarily because at lower T_e more excitations occur before ionization. At very low T, below a few eV, recombination contributes to the radiated power. In addition, the *impurity* radiation has to be considered. For low Z elements, the radiation function is largest at very low T_e, figure 3.21. Thus, for progressively lower T_t, an attractive *strongly radiating regime* can be achieved. If the radiating zone is close to the targets

then the radiative heat load on the targets can be significant, however.

(3) *The detached regime*. For the lowest T_t, as already noted in section 4.7, both neutral frictional drag and volume recombination may become strong, resulting in the detached divertor state with significantly reduced n_t, T_t and Γ_t, chapter 16, which further reduces target sputtering and heating.

These attractive SOL regimes are easier to achieve with divertors than with limiters. The recycling surface of a limiter is in direct contact with the main plasma, see figure 4.7, and it is unavoidable that a significant fraction of the ionization of the recycled neutrals will occur in the main plasma. By contrast, in the divertor configuration, the targets may be located so remotely from the main plasma that the ionization can occur virtually entirely in the SOL near the targets, figure 4.8. This avoidance of significant ionization in the main plasma is a pre-requisite for achievement of the complex SOL, and thus for the attractive regimes described above.

Table 4.1 gives code-calculated results for the location of the hydrogen recycle ionization for a number of *limiter* tokamaks. As can be seen, typically most of the ionization does not occur in the SOL. At the highest value of $n_{\mathrm{LCFS}} > 10^{19}$ m^{-3}, this starts to change—but for limiter tokamaks such edge densities are untypically high, see figure 4.6. By contrast, most of the hydrogen is normally ionized in the SOL for divertor tokamaks—except at low $\overline{n}_e$.

4.9 The Effects of Ionization within the SOL

As already noted, the most important consequence of ionization within the SOL is the tendency to produce the high recycling/conduction-limited regime, section 4.8. Here we consider further effects: (a) the influence on the radial density profile $n_e(r)$, and (b) the influence on the plasma flow pattern within the SOL. These phenomena are closely connected.

We start with an idealized scenario where the plasma flow pattern is *not* significantly altered. For each neutral ionized in the main plasma, let there be $(F_R - 1)$ ionizations within the SOL, uniformly distributed along L. (This uniformity is unphysical, of course, and constitutes the essence of the idealization involved here.) Thus $1 \leq F_R < \infty$. The total source of particles for the SOL is now given approximately by:

$$\phi^+ \approx 2LwD_\perp^{\mathrm{SOL}} \frac{n_{\mathrm{LCFS}}}{\lambda_n} + 2(F_R - 1)LwD_\perp^{\mathrm{SOL}} \frac{n_{\mathrm{LCFS}}}{\lambda_n} \tag{4.80}$$

where the first contribution is the cross-field 'source' from the main plasma, as in section 4.3, and the second contribution is the local ionization source within the SOL. As in section 4.3 this source is equated to the target sink strength of $n_{\mathrm{LCFS}} c_{\mathrm{s,LCFS}} \lambda_n w$, which then gives the new expression for λ_n:

$$\lambda_n = (2LD_\perp^{\mathrm{SOL}} F_R / c_s)^{1/2}. \tag{4.81}$$

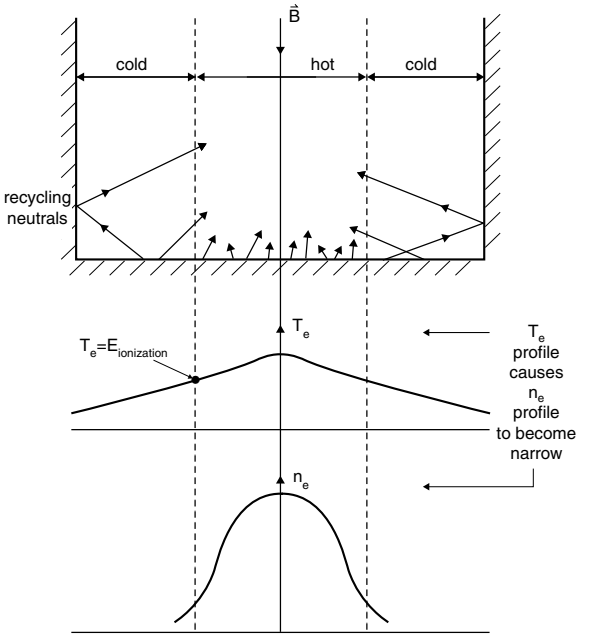

Figure 4.14. A schematic representation of one leg of a deep slot divertor with the separatrix along the centre line. The temperature tends to peak near the separatrix due to the power inflow from the main plasma, which then tends to cause the ionization to occur near the separatrix, and peaking of n_e there.

We may note that the effect of SOL ionization—in this idealized scenario—is to broaden the SOL: as the SOL becomes more and more 'self-sustained' the density gradient, which is needed to draw plasma from the main plasma, can gradually disappear and the SOL plasma would eventually extend indefinitely radially!

The first point to be drawn from the foregoing is that it is not valid to use the now-familiar expression relating λ_n and $D_\perp^{\mathrm{SOL}}$, equation (4.7), when ionization within the SOL is significant.

In the idealized scenario, $T_e(r)$ would still decay radially since the SOL is only self-sustained in a *particle* sense (not in a *power* sense) and a radial T-gradient is always needed to conduct power into the SOL. As T_e drops, then at some radius the plasma will become too cold to ionize neutrals which will just pass through such regions to reach more ionizing regions further in. Thus the $T_e(r)$-profile will always tend to control the $n_e(r)$-profile, even when SOL ionization totally dominates particle balance.

As a first step toward developing a less idealized scenario we consider figure 4.14, which could represent one leg of a deep slot divertor. The centre line is the separatrix, the right side is the SOL and the left side is the private plasma.

Power balance largely controls the $T_e(r)$-profile, which we will therefore take as being fixed, and then consider how the $n_e(r)$-profile would evolve in response to this $T_e(r)$-profile. However wide $n_e(r)$ might have been initially, it will quickly narrow down to the region where $T_e \geq I_{iz}$, the ionization potential energy. Any neutrals recycling from the target further out could only ionize within the hotter region near the separatrix. That creates plasma primarily in the hot region (with some diffusion on to the colder flux tubes). At the same time the neutrals recycling from the target in the hotter zone tend to ionize within the hotter zone.

This scenario is still idealized since it ignores the large-scale recirculation patterns of plasma flow, including *flow reversal*, which are implicit in this scenario. We return to this effect in chapter 15. It is sufficient to note here that when ionization in the SOL becomes significant, the power and particle balances become entangled and simple expressions for λ_n such as equation (4.7) become invalid. The situation seems to be so complicated that one's first thought is that no simple relations of any sort are possible for λ_n here. In chapter 21, it will be shown that some simple relations may nevertheless tend to occur between λ_n and λ_T even in situations where SOL ionization dominates.

4.10 Parallel Temperature Gradients Along the SOL

4.10.1 Calculating $T(s_\parallel)$

For strong parallel T-gradients to form in the SOL, it is generally necessary (although not sufficient) that parallel heat conduction dominate over parallel heat convection. Parallel heat convection density $q_{\parallel\text{conv}}$ [W m^{-2}] for the plasma (electrons plus ions combined) is, section 9.9, equation (9.65):

$$\boxed{q_{\parallel\text{conv}} = (5kT + 1/2m_i v_\parallel^2)\Gamma_\parallel} \tag{4.82}$$

assuming $T_e = T_i$. The classical (Spitzer) parallel heat conduction density $q_{\parallel\text{cond}}$ [W m^{-2}] is, section 9.6:

$$\boxed{q_{\parallel\text{cond}} = -\kappa_0 T^{5/2} \frac{\mathrm{d}T}{\mathrm{d}s_\parallel}} \tag{4.83}$$

for each species separately, using T_e or T_i in equation (4.83), where the thermal conductivity $K_\parallel = \kappa_0 T^{5/2}$, equation (9.46). For a pure hydrogenic plasma, the coefficients κ_0 for electrons and ions are $\kappa_{0e} \simeq 2000$, $\kappa_{0i} \approx 60$, for q [W m^{-2}], T [eV], $\mathrm{d}T/\mathrm{d}s_\parallel$ [eV m^{-1}]. Thus usually $q^e_{\parallel\text{cond}} \gg q^i_{\parallel\text{cond}}$ and so, if electrons and ions are thermally well coupled, electron conduction is used to approximate the transport of the total conducted power.

It is important to note the very strong dependence of the heat conduction coefficient $K_\parallel$ on T, $K_\parallel \propto T^{5/2}$. This turns out to result in a number of useful simplifications. It means that the upstream temperature is a very robust quantity,

depending very little on the power in the flux tube, $q_\parallel$, and indeed on all other parameters. Even a large change in $q_\parallel$ can be accommodated by a small change in T since the dependence of $K_\parallel$ on T is so strong. To within a factor of 3, $T^{up}_{e,\mathrm{LCFS}} \simeq 100$ eV, for divertor tokamaks, usually.

A critical factor influencing the formation of parallel T-gradients is *the ratio of heat flux to particle flux density*. Let us consider two extreme cases, figure 4.15:

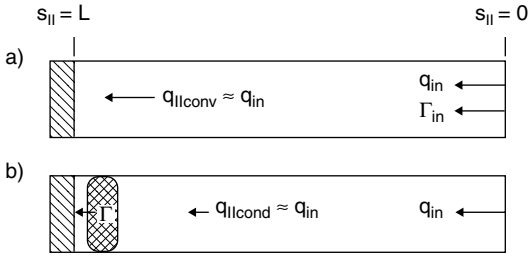

Figure 4.15. Two extreme scenarios of divertor SOL behaviour regarding particle source: (a) with ionization in the main plasma and thus particle inflow more or less at the upstream end; (b) the high recycling regime with most of the ionization occurring near the targets, in the SOL.

(a) All the particles and all the power enter at the top end of the flux tube, figure 4.15(a). The parallel flow will then be at about the sound speed all along the length, section 9.10, hence $q_{\parallel\mathrm{conv}}$ will carry $\approx 6k\overline{T}$ per ion pair. Since the sheath only removes $\sim 7kT_t$ per ion pair, sections 2.8, 25.5, there will be little variation of T along the flux tube, provided also that any volumetric power loss is not too large. This is the *sheath-limited regime*.

(b) All the power enters at the top end, but all the particle source is immediately in front of the targets, i.e. the high recycling regime, figure 4.15(b). This would result from power being purely conducted out of the main plasma, with $q^{\mathrm{LCFS}}_{\perp\mathrm{conv}}$ being negligible. In this case $q_{\parallel\mathrm{cond}}$ will have to carry all the heat, and a large value of $\mathrm{d}T/\mathrm{d}s_\parallel$ may be required, depending on the magnitude of $q_\parallel$ and $\kappa_0 T^{5/2}$. This is the *conduction-limited regime*.

Let us consider this latter extreme case then where $q_{\parallel\mathrm{cond}}$ dominates. The heat enters the SOL from the main plasma with some specific spatial distribution. It turns out that the resulting $T(s_\parallel)$ profile is remarkably insensitive to the details of this spatial distribution. We consider two virtually opposite extremes of the heat input distribution, figure 4.16:

(a) All of P_{SOL} enters at the upper end and is conducted without loss for length L to the target where it is removed via the sheath, figure 4.16(a).

(b) P_{SOL} enters uniformly over length L, figure 4.16(b).

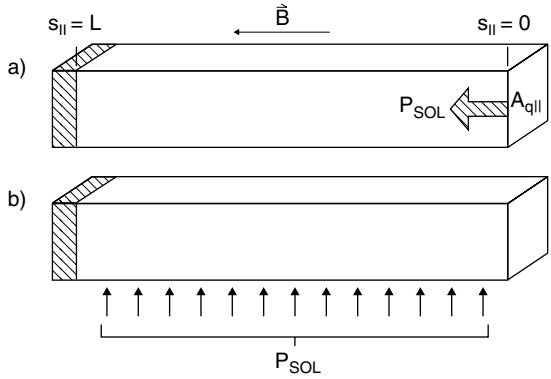

Figure 4.16. Two extreme scenarios of divertor SOL behaviour regarding power source, P_{SOL}: (a) P_{SOL} enters at upstream end; (b) P_{SOL} enters uniformly along the length of the SOL.

For case (a) we have:

$$q_{\parallel\mathrm{cond}} = (P_{\mathrm{SOL}}/A_{q\parallel}) = -\kappa_0 T^{5/2}\frac{\mathrm{d}T}{\mathrm{d}s_\parallel} \tag{4.84}$$

where $A_{q\parallel}$ is the total cross-sectional area of the SOL for power flow; see section 5.7. $A_{q\parallel}$ is thus perpendicular to the parallel flow direction, i.e. is perpendicular to $\boldsymbol{B}$. Here we measure $s_\parallel$ toward the target, from $s_\parallel = 0$ at the upper end. Equation (4.84) is readily integrated to give $T(s_\parallel)$ in terms of either T_u, the temperature at the upstream end, or T_t, the target temperature:

$$\boxed{T(s_\parallel) = \left[T_u^{7/2} - \frac{7}{2}\frac{(P_{\mathrm{SOL}}/A_{q\parallel})s_\parallel}{\kappa_0}\right]^{2/7}} \tag{4.85}$$

also:

$$\boxed{T(s_\parallel) = \left[T_t^{7/2} + \frac{7}{2}\frac{(P_{\mathrm{SOL}}/A_{q\parallel})(L - s_\parallel)}{\kappa_0}\right]^{2/7}}. \tag{4.86}$$

We are most interested in the situation where there is a significant temperature drop along the SOL, i.e. $T_u \gg T_t$. Now, because of the large exponent involved for T_t in equation (4.86), then if T is *even slightly* above T_t, one can neglect this term, resulting in the important simplification:

$$\boxed{T_u \simeq \left(\frac{7}{2}\frac{(P_{\mathrm{SOL}}/A_{q\parallel})L}{\kappa_0}\right)^{2/7}}. \tag{4.87}$$

Next for *case (b)*, where P_{SOL} enters uniformly along L, figure 4.16(b):

$$\frac{\mathrm{d}}{\mathrm{d}s_\parallel}(q_{\parallel\mathrm{cond}}) = \frac{(P_{\mathrm{SOL}}/A_{q\parallel})}{L} \tag{4.88}$$

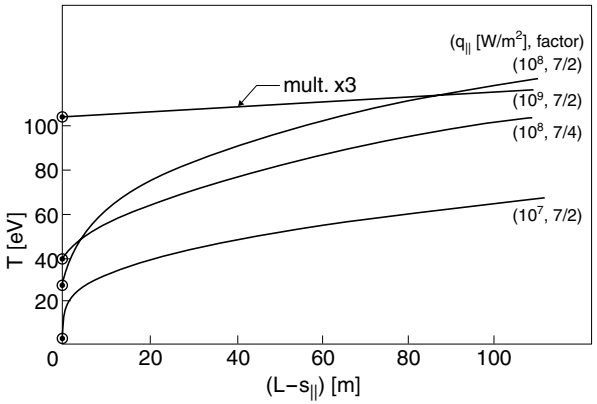

Figure 4.17. Some examples of the spatial distribution of temperature along the SOL, $T(s_\parallel)$, assuming parallel (electron) heat conduction only. $L = 100$ m. For factor $= 7/2$, $P_{\rm SOL}$ enters at upstream end. For factor $= 7/4$, $P_{\rm SOL}$ enters uniformly along length. $q_\parallel \equiv (P_{\rm SOL}/A_{q\parallel})$. (See problems 4.11.)

which gives:

$$\boxed{T(s_\parallel) = \left[T_u^{7/2} - \frac{7}{4}\frac{(P_{\rm SOL}/A_{q\parallel})}{L}\frac{s_\parallel^2}{\kappa_0}\right]^{2/7}} \tag{4.89}$$

and also:

$$\boxed{T(s_\parallel) = \left[T_t^{7/2} + \frac{7}{4}\frac{(P_{\rm SOL}/A_{q\parallel})}{L}\frac{(s_\parallel - L)^2}{\kappa_0}\right]^{2/7}.} \tag{4.90}$$

As for case (a), we are most interested in the situation where $T_u > T_t$, hence:

$$\boxed{T_u \simeq \left(\frac{7}{4}\frac{(P_{\rm SOL}/A_{q\parallel})L}{\kappa_0}\right)^{2/7}.} \tag{4.91}$$

It is clear that these extremely different (in fact, essentially opposite) assumptions concerning the spatial distribution of the entering $P_{\rm SOL}$ have almost no effect on the upstream temperature T_u: the difference between equations (4.87) and (4.91) is only a factor of $(1/2)^{2/7} \approx 0.82$, i.e. 18%. This is a direct consequence of the very strong temperature dependence of parallel heat conduction: a very small change in T can accommodate large changes in the magnitude or distribution of $P_{\rm SOL}$. Indeed, it can be seen that T_u is remarkably insensitive to virtually *all* parameter variations, as noted earlier.

In figure 4.17 several examples of $T(s_\parallel)$ are given. It has been assumed here that the sheath is the only heat sink, i.e. there are no volumetric power losses such as $P_{\rm rad}$, thus from section 2.8:

$$(P_{\rm SOL}/A_{q\parallel}) = \gamma k T_t n_t c_{st}. \tag{4.92}$$

We also assumed simple pressure balance with $M_u = 0$ and $M_t = 1$, thus, see section 9.9:

$$n_u T_u = 2 n_t T_t. \tag{4.93}$$

If we assume P_{SOL} enters at the upper end then we have from equation (4.85):

$$T_t = \left[T_u^{7/2} - \frac{7}{2} \frac{(P_{\mathrm{SOL}}/A_{q\|})L}{\kappa_0} \right]^{2/7}. \tag{4.94}$$

Problem 4.11. Take as specified parameters: $n_u = 3 \times 10^{19}$ m^{-3}, $L = 100$ m, $\kappa_0 = 2000$, $\gamma = 7$, D^+ ions and sample values of $(P_{\mathrm{SOL}}/A_{q\|}) = 10^7$, 10^8, 10^9 W m^{-2}. Combine equations (4.85), (4.92), (4.93), eliminating T_t, n_t, T_u and obtain the relation for $T(s_\|)$ plotted in figure 4.17. For the 10^8 W m^{-2} case also replace equation (4.85) with equation (4.89) (and the equivalent to equation (4.94)) in order to illustrate the effect of P_{SOL} entering uniformly along L.

A number of important features of the conduction-limited regime are illustrated by figure 4.17:

(1) A sufficiently *small* (!) power flux density, $(P_{\mathrm{SOL}}/A_{q\|})$, is required in order to achieve a large T-gradient, not a *large* one as might be one's first thought. When $(P_{\mathrm{SOL}}/A_{q\|})$ is large then T becomes large, making the heat conductivity, $-\kappa_0 T^{5/2}$, *very* large—and so a small $\mathrm{d}T/\mathrm{d}s_\|$ is then adequate to transport even a large $(P_{\mathrm{SOL}}/A_{q\|})$. This result is perhaps counter-intuitive because of our familiarity with non-plasma heat conductivity which is approximately temperature-independent. For very high $(P_{\mathrm{SOL}}/A_{q\|})$, in fact, the SOL becomes almost isothermal along each field line.

(2) When temperature drops are significant, i.e. $T_u/T_t \gg 1$, then most of the drop occurs near the target and most of the flux tube is, again $\sim$ isothermal for most practical purposes.

(3) T_u is far less dependent on P_{SOL} than is T_t, see problem 4.12.

Problem 4.12. The table below gives examples of temperature changes along the SOL for conduction-controlled heat transport. Assume the same conditions as in problem 4.11. Confirm the numbers in the table.

Case	$(P_{\mathrm{SOL}}/A_{q\|})$ [W m^{-2}]	P_{SOL} distribution	T_u [eV]	T_t [eV]	Estimated T_u [eV] equation (4.87) or (4.91)
1	10^7	In at top	61	1	61
2	10^8	"	117	27	117
3	10^9	"	342	317	226
4	10^8	Uniform	97	39	96

One may note that the $T_t = 1$ eV value for the low power case is not realistic since volumetric power losses would be important, section 3.5.

---

(4) The spatial distribution of input power along the separatrix to the SOL is not very important.
(5) The estimates for T_u from equations (4.87) and (4.91) are poor for $T_u/T_t \lesssim 1.1$, as would be expected (last column of table, above).

4.10.2 Criteria for Existence of Parallel Temperature Gradients

We turn next to establishing criteria for *the existence of substantial temperature gradients in the conduction-limited SOL*. We define the *temperature-gradient factor* f_T:

$$f_T \equiv T_u/T_t. \tag{4.95}$$

One also has the *density-gradient factor* $f_n \equiv n_u/n_t = 2/f_T$. For P_{SOL} entering at the top, we combine equations (4.92) and (4.94) which gives f_T in terms of the lumped parameter $n_t L/T_t^2$:

$$\boxed{\frac{n_t L}{T_t^2} = C_1(f_T^{7/2} - 1)} \tag{4.96}$$

n [m^{-3}], L [m], T [eV], and where:

$$C_1 \equiv \frac{2\kappa_0}{7\gamma e c_{s0}}. \tag{4.97}$$

Problem 4.13. Derive equations (4.96) and (4.97).

The factor $\frac{2}{7}$ in equations (4.97) is replaced by $\frac{4}{7}$ when P_{SOL} enters uniformly; $e = 1.6 \times 10^{-19}$ [J eV^{-1}]; c_{s0} = sound speed for $T = 1$ eV. The relation between T_u/T_t and $n_t L/T_t^2$ is illustrated in figure 4.18 for D^+ ions, $T_e = T_i$, $c_{s0} = 9788$ m s^{-1}, $\gamma = 7$, $\kappa_0 = 2000$. We thus have the criteria:

(a) for negligible T-gradient, specifically for $T_u < 1.5T_t$:

$$\frac{n_t L}{T_t^2} \lesssim 10^{17} \tag{4.98}$$

n [m^{-3}], L [m], T [eV];
(b) for significant T-gradient, specifically for $T_u > 3T_t$:

$$\frac{n_t L}{T_t^2} \gtrsim 10^{18}. \tag{4.99}$$

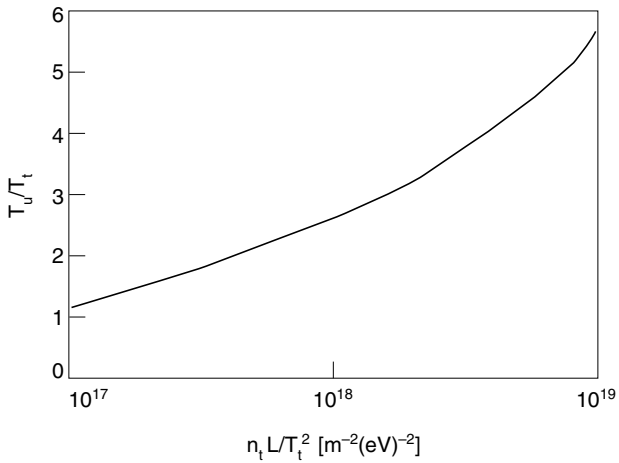

Figure 4.18. Predicted relation between T_u/T_t and the collision parameter evaluated for *target* plasma conditions. For D^+ plasma, with $T_e = T_i$, $\gamma = 7$ and all power carried by parallel electron heat conduction. P_{SOL} entering at the upstream end.

Since target conditions are not necessarily known *a priori* it is useful to find the equivalent criteria expressed in terms of n_u, L, T_u. This can be obtained by combining the same operations as before, now adding pressure balance, equation (4.93), giving:

$$\boxed{\frac{n_u L}{T_u^2} = C_2 f_T^{1/2}(1 - f_T^{-7/2})} \tag{4.100}$$

where

$$C_2 \equiv \frac{4}{7}\frac{\kappa_0}{\gamma e c_{s0}}. \tag{4.101}$$

This applies when P_{SOL} enters at the top; the factor 4/7 in equation (4.101) is replaced by 8/7 if P_{SOL} enters uniformly. For $\kappa_0 = 2000$, $\gamma = 7$, $c_{s0} = 9.79 \times 10^3$ m s^{-1} (for D^+): $C_2 = 1.04 \times 10^{17}$. This relation is illustrated in figure 4.19 for the same parameters as for figure 4.18. Comparison of these two figures illustrates again that target conditions are much more variable than upstream ones. When expressed in terms of the latter the transition from negligible temperature gradient to substantial gradient occurs for small changes in the lumped upstream parameter $n_u L/T_u^2$: for negligible T-gradient, specifically for $T_u \leq 1.5T_t$:

$$n_u L/T_u^2 \lesssim 1 \times 10^{17} \tag{4.102}$$

n [m^{-3}], L [m], T [eV]. For significant T-gradient, specifically for $T_u > 3T_t$:

$$n_u L/T_u^2 \gtrsim 1.5 \times 10^{17}. \tag{4.103}$$

Clearly these criteria correspond to measures of *SOL collisionality*. The electron and ion self-collisionality lengths, section 1.6, are:

$$\lambda_{ee} \approx 10^{16} T_e^2/n \qquad \lambda_{ii} \approx 10^{16} T_i^2/n \tag{4.104}$$

for n [m^{-3}], T [eV], λ [m]. It can be useful to define *SOL collisionality parameters* based on *upstream* plasma values:

$$\boxed{\nu^*_{\mathrm{SOL},e} \equiv L/\lambda_{ee} \approx 10^{-16} n_u L/T_{eu}^2 \quad \nu^*_{\mathrm{SOL},i} \equiv L/\lambda_{ii} \approx 10^{-16} n_u L/T_{iu}^2} \tag{4.105}$$

and when

$$T_e = T_i \quad \text{then} \quad \nu^*_{\mathrm{SOL}} \equiv L/\lambda_{ee\,ii} \approx 10^{-16} n_u L/T_u^2. \tag{4.106}$$

Thus equation (4.102) states that T-gradients are small when:

$$\nu^*_{\mathrm{SOL}} \lesssim 10 \tag{4.107}$$

while equation (4.103) states that they are significant when:

$$\nu^*_{\mathrm{SOL}} \gtrsim 15. \tag{4.108}$$

Also, from equation (4.100) we have that $f_T(\nu^*_{\mathrm{SOL}})$ is given by the solution of:

$$10^{16} \nu^*_{\mathrm{SOL}} \approx C_2 f_T^{1/2} (1 - f_T^{-7/2}). \tag{4.109}$$

See figure 4.19.

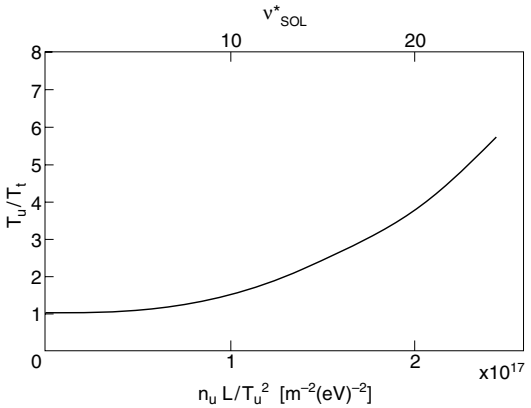

Figure 4.19. As figure 4.18 but plotted against the collision parameter evaluated at the *upstream* plasma conditions.

Problem 4.14. Usually n_u and T_u are not considered to be the independent parameters characterizing the SOL, but more typically n_u and P_{SOL}—or here $(P_{\mathrm{SOL}}/A_{q\|})$—are taken to be the independent parameters; T_u is then a dependent variable. It is therefore useful to have the above criteria expressed in terms of n_u and $(P_{\mathrm{SOL}}/A_{q\|})$. This is achieved using the same set of equations as for the $n_u L/T_u^2$ criteria. Show that this gives:

$$\frac{(P_{\mathrm{SOL}}/A_{q\|})}{n_u^{7/4}L^{3/4}} = C_3 f_T^{-7/8}(1 - f_T^{-7/2})^{-3/4} \tag{4.110}$$

$(P_{\mathrm{SOL}}/A_{q\|})$ [W m^{-2}], n [m^{-3}], L [m], where

$$C_3 \equiv \left(\frac{7}{2\kappa_0}\right)^{3/4}\left(\frac{e\gamma c_{s0}}{2}\right)^{7/4}. \tag{4.111}$$

Show that this holds for P_{SOL} entering at the top and that the factor 7/2 in equation (4.111) is changed to 7/4 if P_{SOL} enters uniformly. Show that this gives the criteria:

(a) for negligible T-gradient, specifically for $T_u \leq 1.5T_t$

$$\frac{(P_{\mathrm{SOL}}/A_{q\|})}{n_u^{7/4}L^{3/4}} \gtrsim 10^{-27} \tag{4.112}$$

for $(P_{\mathrm{SOL}}/A_{q\|})$ [W m^{-2}], n [m^{-3}], L [m].

(b) for significant T-gradient, specifically for $T_u \geq 3T_t$:

$$\frac{(P_{\mathrm{SOL}}/A_{q\|})}{n_u^{7/4}L^{3/4}} \lesssim 4 \times 10^{-28}. \tag{4.113}$$

Note again that $(P_{\mathrm{SOL}}/A_{q\|})$ must not be *too large* if one wants to achieve a significant temperature drop.

When there is in fact no significant T-gradient, then equations (4.92) and (4.93) give the relation between the constant T and the independent parameters $(P_{\mathrm{SOL}}/A_{q\|})$ and n_u:

$$T = \left(\frac{2(P_{\mathrm{SOL}}/A_{q\|})}{n_u e\gamma c_{s0}}\right)^{2/3}. \tag{4.114}$$

Example : D^+ ions, $T_e = T_i$, $c_{s0} = 9788$ m s^{-1}, $\gamma = 7$:

$$T = 3.2 \times 10^9\left(\frac{(P_{\mathrm{SOL}}/A_{q\|})}{n_u}\right)^{2/3} \tag{4.115}$$

T [eV], $(P_{\mathrm{SOL}}/A_{q\|})$ [W m^{-2}], n [m^{-3}]. One notes from equation (4.115), that $T \propto n_u^{-2/3}$, indicating an 'energy dilution' effect.

These considerations lead naturally into divertor SOL analysis, chapter 5, where these matters are considered further.

4.11 Parallel Temperature Gradients in the Context of Electron–Ion Equipartition

4.11.1 An Initial Estimate of the Role of Equipartition in the SOL

Because of their very different masses, ions and electrons have a tendency to thermally de-couple, $T_e \neq T_i$. For sufficiently strong collisionality, however, $T_i \rightarrow T_e$. In general the two temperatures relax toward each other according to:

$$\frac{\mathrm{d}T_i}{\mathrm{d}t} = \frac{T_e - T_i}{\tau_{eq}} \tag{4.116}$$

where τ_{eq} is the *temperature equilibration time* [4.36]:

$$\boxed{\tau_{eq} = \frac{3\pi(2\pi)^{1/2}\varepsilon_0^2 m_i T_e^{3/2}}{n_e Z^2 e^4 m_e^{1/2} \ln\Lambda}} \tag{4.117}$$

$$\approx 4.2 \times 10^{13} T_e^{3/2}/n_e \equiv C_{eq} T_e^{3/2}/n_e \tag{4.118}$$

for τ [s], n_e [m^{-3}], T [eV] and D^+ ions and we have defined $C_{eq} \equiv 4.2 \times 10^{13}$. One may note that, as with all charge-particle collision times, τ_{eq} decreases for low temperatures, i.e. as collisionality increases. Thus, even though τ_{SOL} is short, of order ms, τ_{eq} may be short enough in the cool edge to bring about $T_e \sim T_i$.

We now attempt a first estimate for a criterion which will indicate when collisionality would be strong enough to force $T_i \rightarrow T_e$. We will make what seems like an innocent assumption, namely that the SOL is *isothermal* along its length. We will show in the next section that this is, in fact, an unlikely combination, i.e. an isothermal SOL with $T_e \sim T_i$. We proceed, however, with this assumption for now and, by combining equation (4.117) with equation (4.28) and equation (4.92), estimate the SOL energy confinement time τ_E^{SOL} as:

$$\begin{aligned}\tau_E^{\mathrm{SOL}} &\simeq \frac{3 n_{\mathrm{LCFS}} k T_{\mathrm{LCFS}} L}{\gamma k T_{\mathrm{LCFS}} n_{\mathrm{LCFS}} c_{s,\mathrm{LCFS}}} \\ &\simeq 3L/\gamma c_s. \end{aligned} \tag{4.119}$$

We anticipate $T_i \rightarrow T_e$ will tend to occur when $\tau_{eq} \ll \tau_E^{\mathrm{SOL}}$ which gives

$$\frac{n_{\mathrm{LCFS}} L}{T_{\mathrm{LCFS}}^2} \gg 10^{18} \qquad \text{i.e. } \nu^*_{\mathrm{SOL}} \gg 100 \tag{4.120}$$

n [m^{-3}], L [m], T [eV], D^+ ions, $\gamma = 7$.

We note that the criteria of equation (4.120) regarding equipartition involves the same *collisionality parameter* as appeared in the criteria of equations (4.102) and (4.103) regarding the existence of significant parallel T-gradients. It is thus appropriate to define four SOL types, A–D:

	No T-gradient	Significant T-gradient
$T_e = T_i$	Type A	Type B
$T_e \neq T_i$	Type C	Type D

4.11.2 Case A. $T_e = T_i$. No T-Gradient

Equation (4.102) states that there will be negligible gradient when $\nu^*_{\mathrm{SOL}} \lesssim 10$. Equation (4.120), however, requires that $\nu^*_{\mathrm{SOL}} \gg 100$ in order for $T_e \approx T_i$. We conclude therefore that *case A is unlikely to exist*. This is the reason why the simple SOL was defined to have negligible gradients and to be characterized by thermally de-coupled electrons and ions. From the viewpoint of mere mathematical convenience, the assumption that $T_e = T_i$ would have been still simpler, but it is not realistic. As discussed in section 4.4, case A is not impossible, however.

4.11.3 Case B. $T_e = T_i$. Significant T-Gradients Exist (Very Strong Collisionality)

Equation (4.103) states that significant T-gradients exist when $\nu^*_{\mathrm{SOL}} \gtrsim 15$. We now wish to compare this with the criterion that $T_e \approx T_i$. We cannot use equation (4.120), however, since this assumed no T-variation along the SOL. We need, therefore, to derive the equivalent expression to equation (4.120) for the case where T varies. This is a more complicated situation, and we have to consider the upstream and target ends separately.

Consider the upstream end where we have seen that when equilibration collisions were ignored, there is a tendency for $T_{iu} > T_{eu}$, section 4.4. We anticipate that this tendency will be overcome and that $T_{eu} \to T_{iu}$ when $q^{up}_{eq} \gg q_{\parallel,i,u}$ where q^{up}_{eq} [W m^{-2}] is the integrated equipartition power transfer occurring above the X-point. We will generally assume that the X-point-to-target distance is small compared with the total connection length of the SOL. Assuming that the ion power is conducted rather than convected, then:

$$q_{\parallel,i,u} \simeq \frac{4}{7}\kappa_{0i} T_{iu}^{7/2}/L. \tag{4.121}$$

Also:

$$q^{up}_{eq} \simeq \int_0^L \frac{3}{2}\frac{n_e(kT_{iu} - kT_{eu})\mathrm{d}s_\parallel}{\tau_{eq}}. \tag{4.122}$$

We take $T_{iu} \leq 1.3T_{eu}$ as indicative of approximate temperature equality and using equations (4.118), (4.121), (4.122) obtain the criterion for $T_{eu} \simeq T_{iu}$:

$$\frac{n_u L}{T_{iu}^{5/4} T_{eu}^{3/4}} \simeq \frac{n_u L}{T_u^2} \gg\sim 1.5 \times 10^{17} \tag{4.123}$$

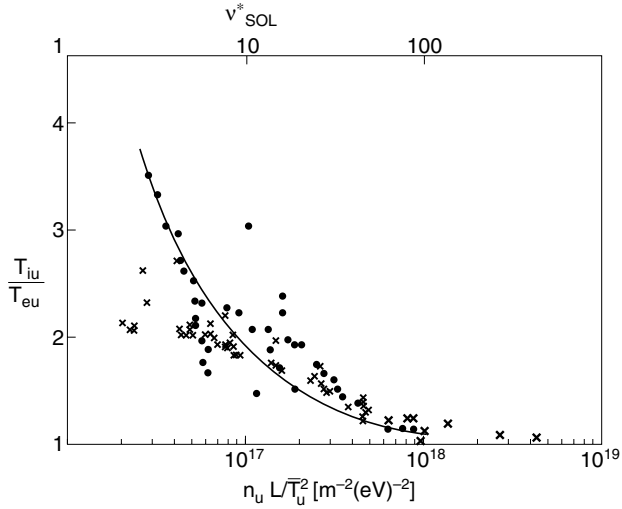

Figure 4.20. Code results for T_{iu}/T_{eu} against the (upstream) collisionality parameter. • from the EDGE2D code for CMOD cases [4.37]. × from onion-skin modelling [4.44] for JET cases. The solid line is only to aid the eye. For $\nu^*_{\rm SOL} \gtrsim 50$, $T_{iu} \approx T_{eu}$.

n [m^{-3}], L [m], T [eV] i.e. $\nu^*_{\rm SOL} \gg\sim 15$.

There are very few measurements of T_{iu}; however 2D fluid edge codes calculate T_{eu} and T_{iu}, allowing for equipartition. In figure 4.20 are shown examples of T_{iu}/T_{eu} against $n_u L/\overline{T}_u^2$ and against $\nu^*_{\rm SOL}$ calculated using the EDGE2D code [4.37], for an Alcator C-MOD geometry and assuming various values of n_u from 3.4×10^{19} to 9.6×10^{19} m^{-3}. Also shown are results from the application of an 'onion-skin method', OSM, code, chapter 12 [4.44], applied to JET geometry and covering a range of plasma conditions. As can be seen, the transition to $T_{eu} \approx T_{iu}$ does not actually occur until $\nu^*_{\rm SOL}$ increases above $\sim$ 50. These code results confirm that T_{eu} and T_{iu} do differ by less than a factor of 2 for $\nu^*_{\rm SOL} \geq 15$; however, for most people 'temperature equality' tends to mean a quite small difference, $\leq 25\%$, perhaps. We will therefore adjust this first estimate, equation (4.123), to take these numerical results into account, so that the criterion for $T_{eu} \simeq T_{iu}$ is altered to:

$$\frac{n_u L}{T_{iu}^{5/4} T_{eu}^{3/4}} \simeq \frac{n_u L}{T_u^2} \gg 5 \times 10^{17} \tag{4.124}$$

i.e.

$$\nu^*_{\rm SOL} \gg 50.$$

The JET results are re-plotted in figure 4.21 with the correlation parameter now being $[(P_{{\rm SOL},i}/P_{{\rm SOL},e})/\nu^*_{\rm SOL}]^{2/7}$. Although the theoretical basis for such a

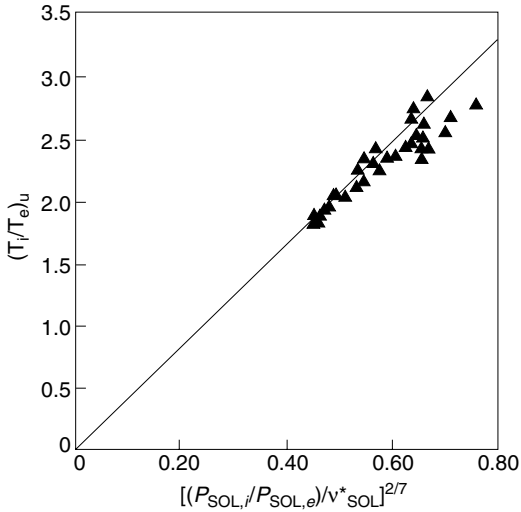

Figure 4.21. Values of T_{iu}/T_{eu} computed using an onion-skin method, OSM, code, applied to JET geometry for a range of conditions [4.44]. Evidently the upstream temperature ratio correlates well with $[(P_{SOL,i}/P_{SOL,e})/\nu^*_{SOL}]^{2/7}$, although the reason for this is not entirely clear. The solid line is simply to guide the eye.

correlation is not entirely clear, it results in a reduction of the scatter and thus may indicate a useful predictive relation.

The criterion for significant T-gradients, equation (4.103), is similar to equation (4.124), but is less demanding, therefore case B corresponds to:

$$\frac{n_u L}{T_u^2} \geq 5 \times 10^{17} \qquad \text{i.e. } \nu^*_{SOL} \gtrsim 50. \tag{4.125}$$

Problem 4.15. In terms of $(P_{SOL}/A_{q\|})$ and n_u, show that criterion (4.125) becomes:

$$\frac{(P_{SOL}/A_{q\|})}{n_u^{7/4} L^{3/4}} \lesssim 1.2 \times 10^{-28} \tag{4.126}$$

$(P_{SOL}/A_{q\|})$ [W m^{-2}], n [m^{-3}], L [m]. Note again that this strongly collisional regime requires that P_{SOL} be not *too* high. Show that for the example $(P_{SOL}/A_{q\|}) = 10^8$ W m^{-2}, $n_u = 5 \times 10^{19}$ m^{-3}, $L = 80$ m satisfies (4.126).

4.11.4 Case C. $T_e \neq T_i$. No Significant T-Gradients. Weak Collisionality (*The Simple SOL*)

Clearly case C occurs for the opposite conditions to case B, i.e. for very weak collisionality. It thus *corresponds to the simple SOL.*

In section 4.9 we derived the $\nu^*_{\rm SOL}$ criterion for the existence of T-gradients, however we assumed $T_e = T_i$. The alterations to equations (4.100), (4.101) to allow for the separate treatment of de-coupled electrons and ions are straightforward and give for $T_u/T_t \leq 1.5$:

$$n_u L/T^2_{eu} \lesssim 1.5 \times 10^{17} \qquad \text{i.e.} \quad \nu^*_{{\rm SOL},e} \lesssim 15 \tag{4.127}$$

$$n_u L/T^2_{iu} \lesssim 10^{16} \qquad \text{i.e.} \quad \nu^*_{{\rm SOL},i} \lesssim 1 \tag{4.128}$$

n [m^{-3}], L [m], T [eV], D^+ ions.

All the analysis to date has implicitly assumed short mean free paths compared with any relevant scale length, such as parallel T-gradient lengths, or L, etc. When this is not true then, strictly, *kinetic analysis* is required, in which the *details* of the particle velocity distributions are calculated. At a minimum, *kinetic corrections* should be introduced to the foregoing *collisional theory*, chapter 26. We appropriate here one specific finding of kinetic analysis concerning heat conductivity: it is the high velocity particles which contribute most to the heat conductivity. The typical hot particle dominating conduction has random velocity $v_{\rm hot} \sim 3$–$5v_{th}$ [4.38], where th indicates the thermal, or typical particles in the distribution, and so it has a much longer mean free path, $\lambda_{\rm hot} \sim 20\lambda_{th}$, chapter 26. Therefore for the electrons the transition to conduction-limited behaviour and the formation of T_e-gradients happens to coincide with $L/\lambda^{\rm hot}_{ee} \simeq 1$ and criterion equation (4.127) may be a valid criterion. For ions, however, the transition given by equation (4.128) would imply that $L/\lambda^{\rm hot}_{ii} \ll 1$, and so this criterion is probably too severe; it may be that when kinetic effects are taken into account for ions, the transition occurs for nL/T_i^2 higher than 10^{16}, e.g. at lower T_{iu}.

Problem 4.16. Show that one can put criteria (4.127), (4.128) into forms involving $(P_{\rm SOL}/A_{q\|e})$, $(P_{\rm SOL}/A_{q\|i})$ and n:

$$\frac{(P_{{\rm SOL},e}/A_{q\|})}{n_u^{7/4}L^{3/4}} \gtrsim 10^{-27} \tag{4.129}$$

$$\frac{(P_{{\rm SOL},i}/A_{q\|})}{n_u^{7/4}L^{3/4}} \gtrsim 3 \times 10^{-27}. \tag{4.130}$$

Assume, for simplicity, $P_{{\rm SOL},e} = P_{{\rm SOL},i}$ and also assume $T_i \gg T_e$ in calculating c_s and the power flows along isothermal SOLs to the target. Show that for an ITER-size example: $(P_{\rm SOL}/A_{q\|}) = 10^9$ W m^{-2}, $L = 100$ m, $n_u = 4 \times 10^{19}$ m^{-3}, makes this ratio $\sim 1.6 \times 10^{-27}$, and so this case would apply. There would be a major practical problem at the targets where the very high temperature would result in strong sputtering. One solution would be to raise the density.

From the last section it is clear that if the criterion for $\nabla_\| T \approx 0$ is satisfied, equations (4.127), (4.128), then the criterion for thermal de-coupling, $T_e \neq T_i$, is likely to be satisfied, equation (4.125). We return to the latter issue in section 4.11.6.

4.11.5 Case D. $T_e \neq T_i$. Significant Temperature Gradients Exist. Intermediate Collisionality

Adapting equation (4.100) for separate electrons and ions we obtain the criteria for significant T_e- and T_i-gradients (specifically for T_{eu}/T_{et}, $T_{iu}/T_{it} \geq 3$):

$$\frac{n_u L}{T_{eu}^2} \gtrsim 2.5 \times 10^{17} \qquad \text{i.e. } \nu^*_{\text{SOL},e} \gtrsim 25 \tag{4.131}$$

$$\frac{n_u L}{T_{iu}^2} \gtrsim 1.8 \times 10^{16} \qquad \text{i.e. } \nu^*_{\text{SOL},i} \gtrsim 1.8. \tag{4.132}$$

The actual *threshold* for this case is given, of course, by equations (4.127), (4.128) which correspond to T_{eu}/T_{et}, $T_{iu}/T_{it} \geq 1.5$.

$T_{iu} \neq T_{eu}$ requires the opposite of equation (4.124), namely:

$$\frac{n_u L}{T_{iu}^{5/4} T_{eu}^{3/4}} \leq 5 \times 10^{17}. \tag{4.133}$$

Problem 4.17. Show that the equivalent criteria in terms of power are:

$$\frac{(P_{\text{SOL},e}/A_{q\parallel})}{n_u^{7/4} L^{3/4}} \lesssim 0.4 \times 10^{-27} \tag{4.134}$$

$$\frac{(P_{\text{SOL},i}/A_{q\parallel})}{n_u^{7/4} L^{3/4}} \lesssim 10^{-27} \tag{4.135}$$

$$\frac{(P_{\text{SOL},e}/A_{q\parallel})^{5/8} (P_{\text{SOL},i}/A_{q\parallel})^{3/8}}{n_u^{7/4} L^{3/4}} \gg 10^{-29}. \tag{4.136}$$

There thus exists this *intermediate* level of collisionality which allows $T_{iu} \neq T_{eu}$ to exist simultaneously with parallel T-gradients: roughly speaking (i.e. ignoring the distinction between T_e and T_i) the window for this regime of intermediate collisionality is

$$15 \lesssim \nu^*_{\text{SOL}} \lesssim 50 \tag{4.137}$$

where we have pushed the lower limit down to 15 to avoid having a gap.

4.11.6 Equipartition near the Target

When T-gradients are significant then T_t is low, n_t is high and so collisionality near the target is generally quite high. One can construct criteria for identifying when $T_{et} \simeq T_{it}$, similar to the foregoing ones for T_{eu}, T_{iu}. However, still stronger assumptions have to be made to keep the analysis simple. At low T_t, radiative cooling and other volumetric power loss or gain processes become important and the relevant comparison is no longer merely between q_{eq} and $q_\parallel$.

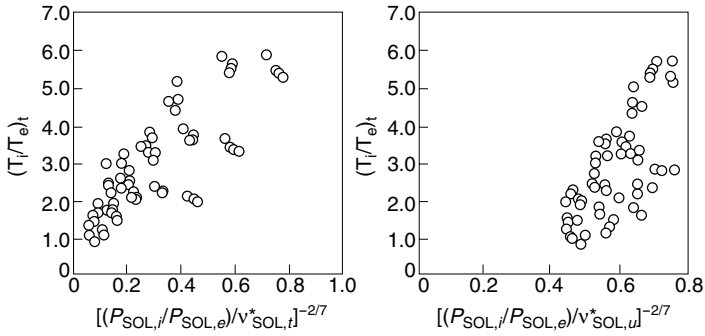

Figure 4.22. Values of T_{it}/T_{et} calculated for a variety of cases using an onion-skin method code [4.44]. The power input to the electrons and ions was varied. Equipartition and volumetric (hydrogen recycle) losses were included. The trends are broadly as might be expected, but no attempt has been made here to model this behaviour with an analytic expression.

We turn therefore to computer codes for an indication of trends. Figure 4.22 presents results from an onion-skin model code [4.44], chapter 12, for the ratio of T_{it}/T_{et} for the same cases as figure 4.21. Equipartition and volumetric power losses associated with recycling were included in the code. Various ratios of input power into the ion and electron 'channels' were assumed as input. Again a correlation parameter based on the ratio $P_{SOL,i}/P_{SOL,e}$ and on ν^*_{SOL}—defined now either for upstream, figure 4.22(b), or target, figure 4.22(a), conditions—has been used. Not surprisingly the correlation with target ν^*_{SOL} is clearer than for the upstream ν^*_{SOL}, although neither correlation for T_{it}/T_{et} is as clear as for T_{iu}/T_{eu}, figure 4.21. Target conditions are evidently more 'volatile' than upstream ones, a matter we return to in chapter 5.

Although it is not safe to make strong generalizations based on such information, it may be reasonable to conclude that for weak collisionality, $\nu^*_{SOL,e} \lesssim 10$, T_{it} and T_{et} can be rather de-coupled; for intermediate collisionality T_{it} may tend to lie above T_{et} at the weaker collisionality end, going over to $T_{et} \approx T_{it}$ for strong collisionality, $\nu^*_{SOL,e} \gtrsim 50$.

4.11.7 Caveats Concerning Criteria for Equipartition and Existence of *T*-Gradients

The criteria developed in the last two sections are merely a *first approximation* and for some cases may not even provide a very good first estimate:

(a) The entire analysis is based purely on parallel heat *conduction*, ignoring heat *convection*. This can be particularly serious for ions since their conductivity is poor. Inclusion of convection as a correction factor reduces the transition values of ν^*_{SOL} calculated in the last two sections, and, of course, when parallel convection dominates the parallel heat transport, then as pointed out

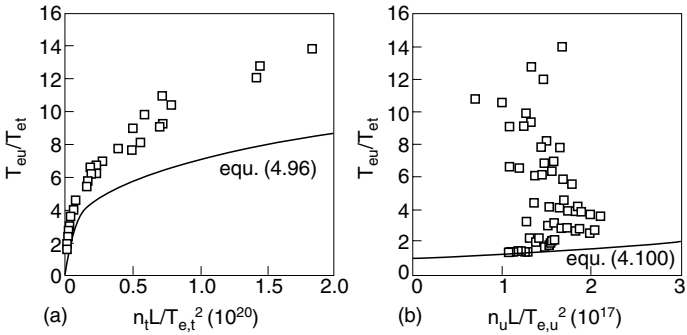

Figure 4.23. T_{eu}/T_{et} as calculated using an OSM code [4.44], including various complicating effects such as convection, equipartition and volumetric loss processes, for a variety of conditions, JET geometry. Figure 4.23(a) shows the correlation with *target* ν^*_{SOL}, and as can be seen the effect of the complicating processes is not major; compare with Figure 4.18. By contrast, these same complicating processes have a major effect when the correlation with *upstream* ν^*_{SOL} is employed; compare figures 4.23(b) and 4.19.

in section 4.10.1, this results in nearly isothermal conditions regardless of whether the foregoing *conduction*-based criteria are satisfied or not.

(b) The targets have been assumed to be the only heat sinks. Volumetric losses and transport loss into the private plasma can be important. Such processes can cause reduction of T_t, even when no significant T-gradient related to *finite heat conduction* exists. In section 5.4, equations (5.33), (5.34), it is shown that volumetric losses of power and momentum can substantially alter the criteria for the existence of parallel temperature gradients.

(c) Other volumetric sources and sinks have also been neglected, such as recombination and ion–neutral friction. Since these processes are important at low temperature, the criteria developed become inapplicable when $T_t \leq 5$ eV.

As an indication of the effects of including such complicating effects as convection and volumetric loss processes, the same OSM code results of figure 4.21 [4.44], are plotted in figure 4.23: figure 4.23(a) is to be compared with figure 4.18, figure 4.23(b) with figure 4.19. As can be seen, based on *target* ν^*_{SOL}, the T_u/T_t ratio is roughly the same when complicating effects are included, figure 4.23(a), as for pure conduction, figure 4.18. By contrast, the same complicating factors have a much more disturbing effect when estimates are based on *upstream* ν^*_{SOL}, compare figure 4.23(b) and figure 4.19. When using upstream ν^*_{SOL} one is, in effect, attempting to predict the target conditions, and these results again make it evident that *upstream conditions are more 'robust' than the 'volatile' conditions near the target*, an important effect we will return to in chapter 5. It is also clear that a simple picture based on parallel electron heat conduction alone is not always a reliable guide.

The criteria derived in this chapter are therefore only a rough guide.

4.11.8 Overview of the Criteria for Equipartition and T-Gradients. SOL Collisionality

Based on upstream ν^*_{SOL}:

(1) For $\nu^*_{\mathrm{SOL},e} \lesssim 10$ one tends to have the *simple SOL* with:
   (a) $\nabla_\parallel T_{e,i} \approx 0$.
   (b) $T_i > T_e$, or even $T_i \gg T_e$.

(2) For $10 \lesssim \nu^*_{\mathrm{SOL},e} \lesssim 50$ one has a regime of *intermediate collisionality* where:
   (a) $\nabla_\parallel T_e$ is significant.
   (b) $\nabla_\parallel T_i$ may or may not be significant.
   (c) $T_{iu} > T_{eu}$.
   (d) $T_{it} > T_{et}$ for the weaker collisionality end of the regime and $T_{it} \approx T_{et}$ for the stronger collisionality end.

(3) For $\nu^*_{\mathrm{SOL},e} \gtrsim 50$ one enters the *strong collisionality* regime where:
   (a) $T_e(s_\parallel) \approx T_i(s_\parallel)$.
   (b) $\nabla_\parallel T$ is significant.

This picture is summarized in figure 4.24.

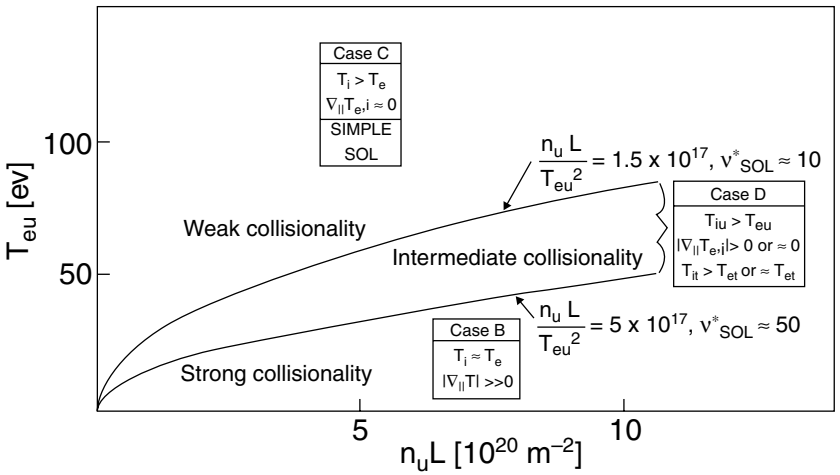

Figure 4.24. The different collisionality regimes, section 4.11, regarding (a) the tendency to temperature equality $T_e \approx T_i$ and (b) the presence of parallel T-gradients.

Additional Problems

4.18. As a check on our picture of SOL geometry, we can calculate the volume of the SOL in two different ways. The first way is to multiply the surface area

of the plasma, $A_p = 2\pi r 2\pi R$, for a circular 'cylindrical tokamak' of length R, by the SOL thickness λ, giving $V_{\rm SOL} = 2\pi r 2\pi R\lambda$. Next consider the specific case of a thin toroidal belt limiter at the outside midplane, figure 4.3, and the 'unfolded' SOL:

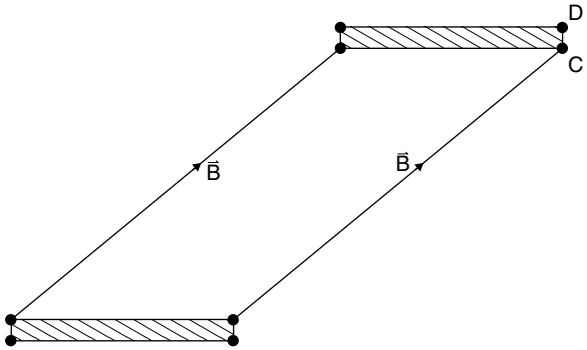

Figure 4.25. The shaded regions represent the belt limiter, i.e. it appears twice in this representation.

(a) Each point marked appears at four different locations in this picture. Mark the other three C points and D points.
(b) Mark the length L, the pitch angle $\theta_{\rm pitch}$, and the width w (see figure 4.3) on figure 4.25.
(c) Calculate $V_{\rm SOL}$ a second way based on w and L, confirming the first calculation.
(d) Argue that figure 4.25 could be altered to a rectangular shape of sides L and w without changing the plasma behaviour. Are the original, and the altered configurations equivalent so far as the *limiter* is concerned, i.e. are the particle and heat fluxes it receives per unit area of solid surface affected?

4.19. (a) For the simple SOL and assuming $T_e = T_i$, find the relation between the ratio of radial decay lengths of pressure and of parallel heat flux density and the ratio of radial decay lengths of density and temperature.
(b) What is the relation if $T_e = \frac{1}{2}T_i$ at all points?

4.20. *Calculating the dependence of λ_n and λ_T on $D_\perp$ and $\chi_\perp$ for the case of $T_e(r) = T_i(r)$ across the SOL.* (Although e–i thermal collisional coupling (equipartition) is associated with the existence of the complex SOL, even for a weakly collisional SOL it can happen by coincidence that $T_e \sim T_i$. Little is known experimentally or theoretically about the split in power, between ions and electrons, entering the SOL—and, by coincidence, it could happen that the ratio $P_{in,i}/P_{in,e} \approx \gamma_i/\gamma_e$ which would then result in $T_e \approx T_i$

when $\nabla_\parallel T = 0$.) Repeat the analysis of section 4.4, now including $c_s = (2kT(r)/m_i)^{\frac{1}{2}}$ and neglecting, as before, $q_\perp^{\text{cond},i}$.

(a) show that one obtains:

$$\lambda_n^2 = \frac{2LD_\perp}{c_{s,\text{LCFS}}}\left(1 + \frac{\lambda_n}{2\lambda_T}\right)$$
$$\left(5 + \frac{\lambda_n}{\lambda_T}\frac{\chi_\perp}{D_\perp}\right)\left(1 + \frac{3\lambda_n}{2\lambda_T}\right) = \gamma\left(1 + \frac{\lambda_n}{2\lambda_T}\right).$$

(b) Assuming $T_{\text{LCFS}} = 40$ eV, $L = 40$ m, $\gamma = 8.5$ and $\chi_\perp/D_\perp = 2$, D^+ plasma, find the expected ratio λ_n/λ_T.

(c) Suppose that instead of using the above expression for λ_n, one had used the simple relation between $D_\perp$ and λ_n, equation (4.7). How large would the error be in the value of $D_\perp$ extracted from a measured value of λ_n?

(d) Continuing on from (b), and further, supposing that the measured value of λ_n is 1 cm. What is the extracted value of $D_\perp$? Assuming that, in fact, $\chi_\perp/D_\perp = 2$, what should the measured value of λ_T be?

(e) If the measured value of λ_T is found, in fact, not to be this expected value (based on the *assumed* ratio $\chi_\perp/D_\perp = 2$) then the implication is that this is *not* the correct ratio. Find $D_\perp$ and $\chi_\perp$ if the *measured* decay lengths are $\lambda_n = 1$ cm, $\lambda_T = 3$ cm. (In reality, of course, one does not know the values of $D_\perp$ and $\chi_\perp$ in advance and so one has to work from the *measured* values of λ_n and λ_T in order to *extract* the values of $D_\perp$ and $\chi_\perp$.)

4.21. *Relating plasma properties of the main plasma and the (simple) SOL plasma for the ohmic, start-up phase of a large, circular tokamak with a toroidal belt limiter at the outside midplane*. Assume: D^+, $R = 6$ m, $a = 3$ m, $I_p = 15$ MA, $B_\phi = 5$ T.

(a) Although L-mode and ohmic confinement times differ, take equation (4.30) to give an estimate for here. Assume $\overline{n}_{\text{main}} = 5 \times 10^{19}$ m^{-3}. In order to calculate the input power P assume a *loop voltage* of 1 volt, i.e. the transformer induces an emf of 1 volt per turn in the secondary, i.e. the tokamak plasma. Find P and show that $\tau_E = 2.7$ s.

(b) Find the volume of the plasma and show that $\overline{T}_{\text{main}} = 1580$ eV. Calculate the loop voltage from the plasma resistivity, assuming the radius of the current channel is a; comment on what you find.

(c) Assume that $P_{\text{rad,main}}/P = 0.3$ and that $A_{\Gamma\parallel}/A_{q\parallel} = 1$. Show that $T_{\text{LCFS}} \approx 200$ eV

(d) Calculate the magnetic pitch angle and safety factor q at the limiter radius. Approximate the tokamak as a straight cylinder of length $2\pi R$.

Show that $B_\theta/B = 0.2 \approx \theta_{\text{pitch}}$, $q(a) = 2.5$. Find the connection length.

(e) Assume $\lambda_n = \lambda_T = 3$ cm. Find λ_Γ and show that $A_{\Gamma\parallel} = 0.4$ m^2. Assuming that at the LCFS $T_e = T_i$ show that $n_{\text{LCFS}} \approx 1.5 \times 10^{18}$ m^{-3}.

(f) Show that the parallel heat flux density at the leading edge of the limiter is ≈ 25 MW m^{-2}. What is the *deposited* heat flux density actually experienced by the limiter, assuming it is flat sided, see figure 1.18(A)? How would you suggest the limiter be designed to make the deposited heat flux density lower?

(g) Would you anticipate a reasonably long operating life for such a 'start-up limiter' made, for example, of graphite? Estimate the plasma operational time that would cause the loss of 1 cm of C thickness at the leading edge of the limiter, assuming that no re-deposition occurs at that location.

4.22. Develop equations (4.85) to (4.91). How small does the ratio T_t/T_u have to be in order for the approximations of equations (4.87) and (4.91) to give the value of upstream temperature T_u correct to within 3%?

4.23. Develop the equivalent to equation (4.89) assuming that the power enters the SOL uniformly over $0 \leq s_\parallel \leq L_x$, where L_x is the distance from upstream to the X-point, with $L_x/L = 0.8$. Assume no power loss or gain in $L_x \leq s_\parallel \leq L$. The target is at $s_\parallel = L$.

4.24. Repeat problem 4.23, but now assume that 15% of the total power which entered the SOL above the X-point, is lost uniformly by cross-field transport to the private plasma over $L_x \leq s_\parallel \leq L$.

4.25. For the sample conditions used in figure 4.17, plot the equivalent curves obtained in problems 4.23, 4.24. Add your numbers to the table of problem 4.12. Compare and comment.

4.26. For the four examples shown in figure 4.17 show that the various criteria for the existence, or non-existence, of significant parallel T-gradients are consistent with the results of this figure, i.e. the criteria based on: (a) target plasma conditions, (b) upstream plasma conditions, (c) ν^*_{SOL}, (d) $(P_{\text{SOL}}/A_{q\parallel})$. How good is equation (4.114) at estimating the (average) temperature in the SOL?

4.27. Derive equations (4.123) and (4.126).

4.28. Derive equations (4.127) and (4.128).

4.29. (a) Show that the values of the constants C_1, equation (4.97), C_2, equation (4.101), C_3, equation (4.111), for the conditions assumed in section 4.10.2 are as given in the table below.

(b) In order to evaluate the temperature gradient factors for the case where electrons and ions are thermally de-coupled, f_{T_e}, f_{T_i}, these constants

have to be re-computed appropriately. Show that for D^+ the values for the two different assumptions about the spatial distribution of power entering the SOL (uniformly or all in at the top) are as given in the following table:

		C_1	C_2	C_3
1.	T_e & T_i coupled. P_{SOL} in at top.	5.21×10^{16}	1.04×10^{17}	9.4×10^{-28}
2.	T_e & T_i coupled. P_{SOL} enters uniformly.	1.04×10^{17}	2.1×10^{17}	5.6×10^{-28}
3.	T_e & T_i de-coupled. P_{SOL} in at top.	$C_{1e} = 7.3 \times 10^{16}$ $C_{1i} = 5.5 \times 10^{15}$	$C_{2e} = 1.5 \times 10^{17}$ $C_{2i} = 1.1 \times 10^{16}$	$C_{3e} = 5.2 \times 10^{-28}$ $C_{3i} = 1.5 \times 10^{-27}$
4.	T_e & T_i de-coupled. P_{SOL} enters uniformly	$C_{1e} = 1.5 \times 10^{17}$ $C_{1i} = 1.09 \times 10^{16}$	$C_{2e} = 2.9 \times 10^{17}$ $C_{2i} = 2.2 \times 10^{16}$	$C_{3e} = 3.1 \times 10^{-28}$ $C_{3i} = 8.7 \times 10^{-28}$

4.30. *The effect on the radial density profile given by equation (4.66) of a wall located radially outside the LCFS*: assume that a limiter defines a LCFS 'radius' a in slab geometry and that radially further out at radius a_w, a wall exists and that the hard boundary condition holds there, $n(a_w) = 0$. Ionization inside the LCFS. Prove that $n(0)$ is then given by

$$n(0) = \frac{\Gamma_\perp^{\mathrm{neutral}}}{D_\perp}[\lambda_{iz} + \lambda_n^{\mathrm{SOL}} \tanh[(a_w - a)/\lambda_n^{\mathrm{SOL}}]]$$

and thus show that this gives equation (4.66) when $(a_w - a) \gg \lambda_n^{\mathrm{SOL}}$.

You may find it useful to proceed as follows:

(a) For the region $a < r < a_w$ argue that $n(r)$ must satisfy:

$$\frac{\mathrm{d}}{\mathrm{d}r}\left(-D_\perp \frac{\mathrm{d}n}{\mathrm{d}r}\right) = -\frac{n}{\tau_\parallel}$$

where $\tau_\parallel = L/c_s$. See section 1.8.2.4.

(b) Prove that the general solution to this differential equation is:

$$n(r) = A \exp[-(r - a)/\lambda_n^{\mathrm{SOL}}] + B \exp[(r - a)/\lambda_n^{\mathrm{SOL}}]$$

where A, B are unknown constants to be evaluated from boundary conditions and where $\lambda_n^{\mathrm{SOL}} \equiv [L D_\perp / c_s]^{1/2}$.

(c) Argue that the boundary conditions include:

$$\Gamma_\perp^{\mathrm{neutral}} = -D_\perp \left.\frac{\mathrm{d}n}{\mathrm{d}r}\right|_{r=a}$$

and thus obtain the above result.

4.31. *Objective: to show that the radial density profile, n(r), equation (4.50) that was calculated for planar slab geometry can be a good approximation for cylindrical geometry.*

(a) For cylindrical geometry show that the radial density profile satisfies:

$$\frac{\mathrm{d}n}{\mathrm{d}r} = -\frac{1}{rD_\perp}\int_0^r r'S'(r')\mathrm{d}r'$$

where S is the ionization source rate [ions $\mathrm{m}^{-3}\ \mathrm{s}^{-1}$].

(b) Assume that $S(r)$ is a delta-function source located at $r = a - \lambda_{iz}$. Take the neutral particle influx rate to be $2\pi a\Gamma_\perp^{\mathrm{neutral}}$ [ions per m length of cylinder per s]. Show that the radial density profile is given by:

$$n(r) = \begin{cases} n(a-\lambda_{iz}) & 0 < r < a - \lambda_{iz} \\ n(a-\lambda_{iz}) - \frac{a\Gamma_\perp^{\mathrm{neutral}}}{D_\perp}\ln(r/a-\lambda_{iz}) & a-\lambda_{iz} < r < a. \end{cases}$$

One notes that, as for slab geometry, $n(r)$ is flat inside the source radius.

(c) For λ_{iz} small compared with a—which is common for large plasmas—and assuming the 'hard' boundary condition, $n(a) = 0$, show that $n(r)$ becomes the same as for slab geometry, equation (4.50).

4.32. (a) Derive equation (4.67). You will need to make the assumption that a 'hard' boundary condition still applies, but now at the location of a wall at $r = a_w > a, n(a_w) = 0$. In order to obtain equation (4.67) you will need to assume that $a_w \gg a$.

(b) Start with the general case, i.e. do not assume that $(a_w - a) \gg \lambda_n^{\mathrm{SOL}}$, and by using the hints in problem 4.30 show that:

$$n(0) = n_{\mathrm{LCFS}} = \frac{\Gamma_\perp^{\mathrm{neutral}}\lambda_n^{\mathrm{SOL}}}{D_\perp}\frac{\sinh[(a_w - a + \lambda_{iz})/\lambda_n^{\mathrm{SOL}}]}{\cosh[(a_w - a)/\lambda_n^{\mathrm{SOL}}]}.$$

(c) Finally, assume $(a_w - a) \gg \lambda_n^{\mathrm{SOL}}$.

4.33. *The density profile for a spatially distributed source of ionization [4.17].* Assume slab geometry and that neutrals enter from the edge with constant inward velocity v_n. Take the wall to be far outside the LCFS, $(a_w - a) \gg \lambda_n^{\mathrm{SOL}}$. Assume that the neutral influx is attenuated by the ionization process so that the neutral density and flux density vary as:

$$\Gamma_\perp^{\mathrm{neutral}} \propto n_n \propto \mathrm{e}^{-y/\ell_{iz}}$$

where y is measured inward starting at radial location $r = a + \Delta$, with Δ being a specified parameter of the problem. ℓ_{iz} is the distance over which

the ionization occurs, a specified parameter. We want to allow for $\Delta > 0$ or $\Delta < 0$, i.e., for the ionization to start at a location, either inboard or outboard of the LCFS, and to extend inward. Show that

$$n(0) = \frac{\ell_{iz}\Gamma_{\perp}^{\text{neutral}}}{D_{\perp}} \mathrm{e}^{-\Delta/\lambda_n^{\text{SOL}}} \left[\frac{\mathrm{e}^{\Delta/\lambda_n^{\text{SOL}}(1-\lambda_n^{\text{SOL}}/\ell_{iz})} - (\lambda_n^{\text{SOL}}/\ell_{iz})^2}{1 - \lambda_n^{\text{SOL}}/\ell_{iz}} \right].$$

Thus, for $\ell_{iz} \to 0$ show that the result goes to that of equation (4.68).

4.34. Derive equations (4.70), (4.71).

4.35. Along the same lines as the example following equation (4.74), find $\overline{n}_e$ for the case of $a = 0.5$ m, $\lambda_n^{\text{SOL}} = 2$ cm, $\lambda_{iz}^{\text{SOL}} = 2$ cm, $\lambda_{iz}^{\text{main}} = 1$ cm, $D_{\perp} = 0.3\ \text{m}^{-2}\ \text{s}^{-1}$, $\Gamma^{\text{main}\ iz} = 10^{21}\ \text{m}^{-2}\ \text{s}^{-1}$ and $\Gamma^{\text{main}\ iz}/\Gamma^{\text{SOL}\ iz} = 0.2$. Also find $\tau_p^{\text{SOL}\ iz}$, $\tau_p^{\text{main}\ iz}$ and the contribution to the total plasma content due to the two ionization locations.

References

[4.1] Stangeby P C, Tagle J A, Erents S K *et* al 1988 *Plasma Phys. and Control. Fusion* **30** 1787

[4.2] Bohm D 1949 *The Characteristics of Electrical Discharges in Magnetic Fields* ed A Guthrie and R K Wakerling (New York: McGraw-Hill) chapter 2

[4.3] Lipschultz B, Becker H and Bonoli P *et al* 1989 *J. Nucl. Mater.* **162–164** 793

[4.4] Wootton A J, Tsui H Y W and Prager S 1992 *Plasma Phys. and Control. Fusion* **34** 2023

[4.5] Ridolfini V P, Zagorski R, Crisanti F *et al* 1995 *J. Nucl. Mater.* **220–222** 218

[4.6] LaBombard B and Lipschultz B 1987 *Nucl. Fusion* **27** 81

[4.7] Goldston R J and Rutherford P H 1997 *Introduction to Plasma Physics* (Bristol: Institute of Physics Publishing) p 196

[4.8] Goldston R J and Rutherford P H 1997 *Introduction to Plasma Physics* (Bristol: Institute of Physics Publishing) p 174

[4.9] Guo H Y *et al* 1996 *Contrib. Plasma Phys*. **36** S81

[4.10] Pitts R A 1996 *Contrib. Plasma Phys*. **36** S87

[4.11] Cohen S A, Ehrenberg J, Jones T T C *et al* 1987 *Plasma Phys. and Control. Fusion* **29** 1205

[4.12] Wesson J 1997 *Tokamaks* 2nd edn (Oxford: Oxford University Press) p 177

[4.13] Bickerton R J, Alladio F, Bartlett D V *et al* 1986 *Plasma Phys. and Control. Fusion* **28** 55

[4.14] Erents S K, Tagle J A, McCracken G M *et al* 1988 *Nucl. Fusion* **28** 1209

[4.15] Erents S K, Tagle J A, McCracken G M *et al* 1986 *Nucl. Fusion* **26** 1591

[4.16] Engelhardt W and Feneberg W 1978 *J. Nucl. Mater.* **76–77** 518

[4.17] Engelhardt W, Becker G, Behringer K *et al* 1982 *J. Nucl. Mater.* **111–112** 337

[4.18] Loarte A, Monk R D, Martin-Solis J T *et al* 1998 *Nucl. Fusion* **38** 331

[4.19] Asakura N, Shimizu K, Hosogane N *et al* 1995 *Nucl. Fusion* **35** 381

[4.20] Gray D S, Boedo J A, Baelmans M *et al* 1998 *Nucl. Fusion* **38** 1585

[4.21] Simonini R, Spence J and Stangeby P C 1991 *Plasma Phys. and Control. Fusion* **33** 653
[4.22] Alexander K F, Guenther K, Hintze W *et al* 1986 *Nucl. Fusion* **26** 1575
[4.23] Stangeby P C and McCracken G M 1990 *Nucl. Fusion* **30** 1225
[4.24] Wesson J 1997 *Tokamaks* 2nd edn (Oxford: Oxford University Press) p 179
[4.25] Kaye S M, Bell M G, Bol K *et al J. Nucl. Mater.* **121** 1984 115
[4.26] Dylla H F, LaMarche P H, Ulrickson M *et al* 1987 *Nucl. Fusion* **27** 1221
[4.27] Bosch H-S, Coster D, Dux R *et al* 1997 *Plasma Phys. and Control. Fusion* **39** 1771
[4.28] Maingi R, Jackson G L, Wade M R *et al* 1996 *Nucl. Fusion* **36** 245
[4.29] Grisolia C, Ghendrih Ph, Pegourie B and Grosman A 1992 *J. Nucl. Mater.* **196–198** 281
[4.30] Sugihara M, Federici G, Grisolia C *et al* 1999 *J. Nucl. Mater.* **266–269** 691
[4.31] Mioduszewski P K, Hogan J T, Owen L W *et al* 1995 *J. Nucl. Mater.* **220–222** 91
[4.32] Vlases G C 1993 *Plasma Phys. and Control. Fusion* **35** B67
[4.33] Wesson J, 1997 *Tokamaks* 2nd edn (Oxford: Oxford University Press) p 351
[4.34] ASDEX Team 1989 *Nucl. Fusion* **29** 1959
[4.35] Massey H S W and Gilbody H B 1974 *Electronic and Ionic Impact Phenomena* vol IV (Oxford: Oxford University Press) p 2129
[4.36] Goldston R J and Rutherford P H 1997 *Introduction to Plasma Physics* (Bristol: Institute of Physics Publishing) p 179
[4.37] Loarte A private communication
[4.38] Chodura R 1992 *Contrib. Plasma Phys.* **32** 219
[4.39] Ruzic D N, Heifetz D B and Cohen S A 1987 *J. Nucl. Mater.* **145–147** 527
[4.40] Maddison G P, Allen J, Fielding S J *et al* 1987 *J. Nucl. Mater.* **145–147** 534
[4.41] Simonini R, Spence J, Stangeby P C 1988 *Contrib. Plasma Phys.* **28** 459
[4.42] Pigarov A and Vershkov V 1988 private communication
[4.43] Stangeby P C 1987 *J. Nucl. Mater.* **145–147** 105
[4.44] Fundamenski W 1999 *PhD Thesis* University of Toronto Institute for Aerospace Studies

Chapter 5

The Divertor SOL

5.1 Why use Divertors Rather than Limiters?

A number of issues are involved in the decision of whether to use a divertor or limiter. This is a large question. This introduction to the Divertor SOL only touches on the main issues involved. We will find that two of the most important benefits of divertors are improved energy confinement (the H-mode, H for high energy confinement, chapter 7) and better He pumping.

The original motivation for introducing divertors into magnetic confinement devices was to reduce the impurity content of the main plasma; see review [5.1]. The first few items on the list below therefore pertain to impurities. One can model impurity behaviour on the basis of three steps, chapter [6]: (i) production, (ii) transport within the edge, (iii) transport within the main plasma. Production of impurities is largely due to sputtering—physical and chemical, section 3.3—by ion and atom impact on limiters, divertor targets and walls. To a first approximation it is appropriate to treat impurity ion transport within the main plasma as 1D, radial. By some point not very far into the main plasma, any poloidal/toroidal variations in impurity density caused by the localization of edge impurity production are 'washed out' by the rapidity of parallel-to-$\boldsymbol{B}$ transport. Indeed, when the impurity neutrals are all ionized well outside the separatrix, it may be that the impurity density will be approximately constant all along the separatrix, at least from X-point to X-point. In that case 'edge transport' would refer to the impurity motion—both as neutrals and ions—from the sites of production, to the separatrix, so that 'edge transport' and 'SOL transport' would be synonymous. In the case of limiters one would include the location of the plasma lying inside the LCFS to a depth of the impurity ionization, λ_{iz}^{z}, in the category of 'edge transport', figure 5.1.

In the following we consider the differences between limiters and divertors with regard to impurity: (i) production, (ii) edge transport.

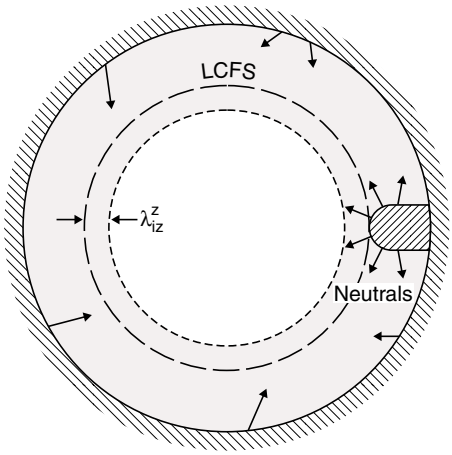

Figure 5.1. The region designated as involving 'edge transport' extends to a distance λ_{iz}, the ionization depth, inside the LCFS.

5.1.1 Production of Impurities by Ion Impact

The location of plasma contact with solid surfaces is usually the strongest source of impurity production, due to physical and chemical sputtering by ion impact, section 3.3. Sputtering yields are minimized when the plasma temperature at the sheath is minimized. Limiter tokamaks almost always operate in the sheath-limited regime, section 1.9, with little temperature variation existing along the LCFS. Therefore rather high plasma temperatures can exist at the sheath, at the *strike point*, i.e. where the LCFS strikes the limiter, up to $\sim$ 100 eV, figure 4.5. Divertor tokamaks can be operated in the conduction-limited regime, section 1.9; while the 'upstream' temperature along the LCFS or separatrix may be high, $\gtrsim$ 100 eV, at the sheath temperatures of only a few eV may exist, thus minimizing sputtering. In principle, it might be possible to arrange for the *upstream* temperature to be very low—using either a limiter or divertor tokamak; this, however, requires low power into the SOL and/or very high SOL density, which is often not consistent with desired conditions in the main plasma. It seems likely that the hottest possible periphery of the confined plasma, combined with the coldest possible plasma in contact with the solid surfaces, is an ideal to be aimed for. This is more readily achieved using divertor configurations than using limiters.

The divertor targets can be located at an arbitrarily large distance (along $\boldsymbol{B}$) from the last point where the SOL separatrix flux tube had contact with the hot confined plasma—i.e. at the X-point—by arranging for the divertor to be as 'deep' as wanted. The largest parallel T-drop occurs between the X-point and the targets, which is the last point along the SOL where heat can enter the flux tube.

5.1.2 Impurity Production by Neutral Impact on Walls

Charge-exchange collisions and Franck–Condon processes result in bombardment of targets and walls by neutrals over a wide range of energies. The neutral flux is most intense at very low energy, a few eV, but with some neutrals having energy equal to the hottest ions in the core plasma. Neutral flux densities are largest at/on the limiters and divertor targets—i.e. where the recycling occurs—but finite fluxes exist over the entire inner walls of the vessel to some degree, figure 5.2. It is thus likely that the temperature of the ions involved in the average *cx* collision event is lower for the divertor case than for limiters—so that total sputtering may also be less. That is not guaranteed however, since the magnitude of the recycling—perhaps surprisingly—increases as the plasma temperature in the divertor is reduced, section 5.2, and all associated fluxes, including *cx* neutral fluxes are also increased.

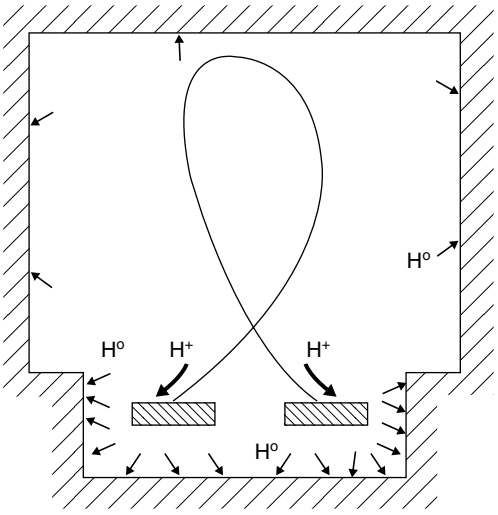

Figure 5.2. Due to recycling at the divertor targets, neutral hydrogenic bombardment of the walls near the target, and also the targets themselves, can be intense. Neutral fluxes, at lower intensities, also strike the distant walls.

In any event, this region of most intense *cx* flux may not be the critical region so far as contamination is concerned, as discussed next.

5.1.3 Transport of Impurities to the Main Plasma

5.1.3.1 Impurities Produced by Ion Impact

The limiter is in intimate contact with the main plasma and its leading edge—which is the site of the most intense ion bombardment—actually *defines* the LCFS

and the edge of the main plasma, figure 5.1. It is therefore not possible to do a great deal to prevent the transport of impurities into the main plasma. Of course, the actual *depth* at which the impurity neutrals are ionized inboard of the LCFS has a major effect on the impurity content of the main plasma, i.e. the impurity confinement time τ_z; see sections 4.6, 6.4, regarding the Engelhardt model, which may be applied to impurities as well as hydrogen.

The shorter the ionization depth, λ_{iz}^{z}, the smaller is τ_z; see equation (4.53). Thus the higher $n_{e,\mathrm{LCFS}}$, $T_{e,\mathrm{LCFS}}$ are, the lower will be τ_z. Unfortunately, such an intense plasma at the LCFS increases impurity production, and so the net effect can actually be an increase in impurity content of the main plasma when $n_{e,\mathrm{LCFS}}$ and $T_{e,\mathrm{LCFS}}$ are increased.

The divertor targets may be located at arbitrarily large distances from the main plasma, reducing or entirely eliminating the penetration to the main plasma of impurity neutrals from the targets. One must still consider transport as ions, along the SOL, then cross-field across the separatrix, section 6.5; however, it is clear that, in principle, the divertor configuration provides opportunities which are not available to limiters for reducing impurity transport to the main plasma of ion-sputtered particles. In practice, this ideal is sometimes compromised and direct plasma (ion) contact with the parts of the main vessel walls—i.e. outside the divertor itself—may be an important impurity source. That is, the wall clearance is not always large enough to ensure that 100% of the plasma–solid contact is at the divertor targets.

5.1.3.2 Impurities Produced by Neutral Impact

The largest part of neutral impact sputtering occurs at/near the limiters or divertor targets and the same considerations as in 5.1.3.1 hold. Unfortunately, the relatively weak part of this source, located some distance from the ion-impact regions, may be an important contributor to the impurity content of the main plasma [5.1]. As is discussed in section 6.5, the sink action exerted by the SOL on such remote sources can be weak, making the τ_z of such contributions long, i.e. their *efficiency of contamination* can be very high. It is not clear what differences exist between limiter and divertor tokamaks in this regard.

5.1.4 Removal of the Helium Impurity, Pumping

While edge impurity production can, at least in principle, be avoided, helium is unavoidably produced as a contaminant in DT fusion. It must be removed to avoid unacceptable fuel dilution [5.2, 5.3]. Since this impurity is uniquely created in the centre of the plasma, its initial confinement time is particularly long, $\tau_{\mathrm{He}}^{\mathrm{primary}} \approx a^2/D_\perp$, section 4.6. When it reaches the edge it must be pumped with good efficiency since, unlike C, etc, it naturally recycles. Indeed, even with efficient removal by active pumping, it is probable that the helium *recycling* source will exceed the *primary* (DT fusion) source. Even though the recycle He confinement

time $\tau_{He}^{recycle} < \tau_{He}^{primary}$, the contribution to the total He content of the plasma can be dominated by the recycle source, see section 6.7.

One needs, therefore, to be able to pump away a reasonably large fraction of the recycling He atoms, before they re-ionize. When using a limiter, the simplest approach is to locate active pumps at the walls near the limiters. This was done on TFTR (Tokamak Fusion Test Reactor) [5.4] (although for the purpose of pumping hydrogen, not helium) using Zr–Al getter panels mounted on the walls; however, the removal rate was poor due to the substantial re-ionization within the SOL and main plasma, i.e. the neutral pressure at the walls is generally very low. The *pumped limiter*, figure 5.3, involves a pump duct opening very near the leading edge of the limiter, and thus the LCFS, and so a significant fraction of the total ionic outflux from the plasma is neutralized on the target plate within the pumped-limiter duct. This allows a reasonable fraction of the recycling neutrals to be transported into the pump itself and removed, without re-ionizing. One drawback of the pumped limiter is that of *sharp leading edges* in regions of intense heat fluxes with attendant risks of melting.

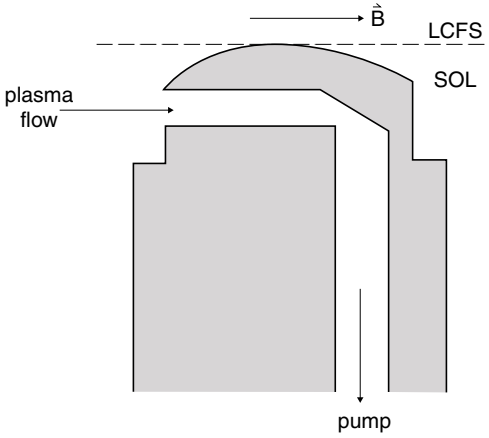

Figure 5.3. Schematic diagram of a pumped limiter.

The divertor configuration rather naturally allows the divertor plasma leg to be 'stuffed' into the pump opening, figure 5.4, while at the same time employing exclusively surfaces which are nearly tangential to $\boldsymbol{B}$. This can result in strong *compression* and the achievement of quite high neutral pressures in the pump entrance; on CMOD pressures $\gtrsim$ 100 mtorr (hydrogen) have been achieved—orders of magnitude higher than pressures at the main vessel walls [5.5]—implying that He could also be effectively pumped. This makes possible efficient and compact pumping systems which can minimize the recycle He source.

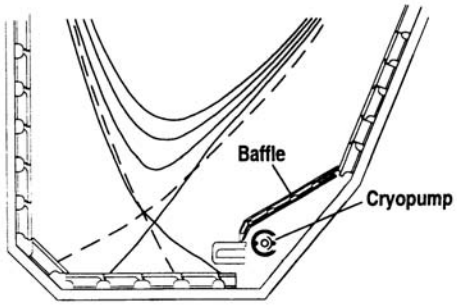

Figure 5.4. Schematic diagram of the lower divertor of DIII-D showing the location of the baffle plate and cryocondensation pump. Also shown are two magnetic equilibria with the outer strike point (OSP) close to the pumping plenum entrance (solid lines) and with the OSP far away from the entrance (dashed lines) [5.64].

5.1.5 Removal of Hydrogen, Pumping

It is advantageous to employ various processes in tokamaks which have the consequence of adding to the DT fuelling, even if that was not the primary purpose. For example, neutral beam injection used to heat the plasma also fuels it. Pellet fuelling of the centre of the main plasma is used to achieve peaked radial profiles which give improved fusion performance. It may be useful to puff additional hydrogen into the SOL, far from the targets, so as to set up SOL plasma flows to 'flush' impurities out of the SOL. All such fuelling processes can change the main plasma density $\bar{n}_e$, causing it to deviate from the value specified by other considerations, for example, the Lawson criterion or the avoidance of density limits. It is therefore desirable to be able to *de-couple fuelling and density control*. This requires active pumps for hydrogen.

This problem thus amounts to essentially the same one as for helium and the divertor again has an important advantage over the limiter. Although much of the original motivation for introducing the divertor was for control of impurities produced by sputtering, it may be that the superior pumping of the divertor configuration for hydrogen—and even more for helium—is a more important advantage.

5.1.6 Efficient Use of Magnetic Volume

The volume within the toroidal-field magnets is very expensive and ideally as much of it as possible should be filled with hot, D–T-burning plasma. The limiter configuration comes closer to this ideal than the divertor. Very 'deep' divertors, i.e. with long X-point-to-target distances, are particularly inefficient by this measure.

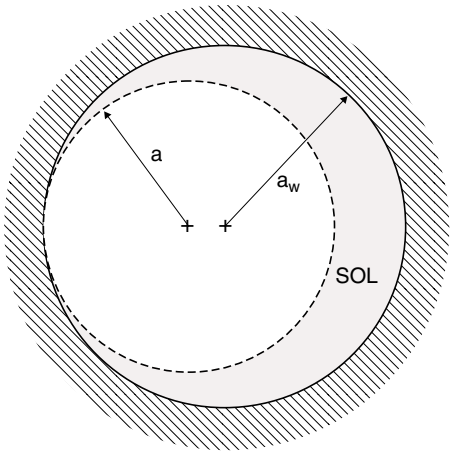

Figure 5.5. Poloidal cross-section of a wall-limiter geometry characterized by a large plasma-wetted area.

5.1.7 Size of Plasma-Wetted Area

A limiter-controlled tokamak can involve plasma-wetted areas spanning a large range. At one extreme, a single fistlike 'probe limiter', extending only a few cm in the toroidal and poloidal directions, can be inserted to define the LCFS. The plasma-wetted area, where the ions and electrons strike, would then only be a few tens of cm^2, assuming a λ_{SOL} of a few cm. Unless the total power is small, or the pulse is short, the power flux density onto such a limiter would be so high as to destroy it quickly. Multiple limiters can be inserted, however, increasing the plasma-wetted area. A very large increase of area can be achieved by carefully shaping, say, the inner wall of the vessel so that it has almost the same curvature as the magnetic flux surfaces, figure 5.5. On TFTR and TORE-SUPRA this has resulted in the achievement of very large plasma-wetted areas of $\sim$ 1–10 m^2 [5.6, 5.7]. In principle, this approach could be pushed to the limit where the shape of the entire vessel wall was made to conform almost precisely to that of the magnetic flux surfaces—causing the entire interior wall to become plasma wetted, $\sim$ 100 m^2 for a JET-size tokamak. Such an arrangement would be at the cost of the loss of operational flexibility in terms of magnetic shape of the plasma. The required precise positioning of the plasma would be difficult. The engineering of the protective tiles so as to avoid exposed edges would be demanding, particularly because λ_{SOL} would become very short. Nevertheless, the limiter approach does, in principle, permit the achievement of very large plasma-wetted areas, and thus a wide dispersal of the power deposition over the solid structure.

The poloidal divertor configuration can also include arrangements where the target surface is made almost parallel to $\boldsymbol{B}$, thus maximizing the plasma-wetted

area. Nevertheless, it is evident that the area theoretically available cannot approach that available to wall limiters—unless the volume occupied by the divertor approaches that occupied by the main plasma.

This problem of power dispersal in the divertor is a serious one for reactors, see sections 5.6, 5.7.

5.1.8 Opportunity for Power Removal by Volumetric Loss Processes

As noted under 5.1.7, it is problematical to achieve removal of all the plasma power by charged particle impact through target sheaths. The power densities tend to be unacceptably high for reactor conditions. Power reaching the edge can also be dissipated by volumetric processes, principally (a) radiation (hydrogenic and impurity) and (b) charge-exchange neutral hydrogen fluxes. The great advantage of these processes is that the power can be deposited over larger areas, rather than being restricted to the small plasma-wetted (sheath) areas.

Some hydrogenic radiation always occurs as part of the recycling process. For the sheath-limited regime, however, the recycle source is not as great as for the conduction-limited regime, section 5.2, and this favours divertors. Impurity radiation also occurs naturally, but is enhanced at low T_e, section 3.5—at least for low Z elements which tend to be favoured for edge structures: at the high temperatures in the centre of the main plasma, low Z elements have the opposite property—they radiate little (they are fully ionized and therefore do not line radiate; also bremsstrahlung radiation is proportional to Z^2, thus low). This also favours divertors, which can achieve low T_e near the targets.

One may also increase radiation by puffing impurities such as N or Ne, etc into the vessel, chapters 22–24. In principle this is risky since the benefits (power dispersal) may be offset by fuel dilution and cooling of the core. At first glance the divertor might have the advantage here since it is conceivable that the injected impurities could be largely confined to the divertor volume, section 6.5, radiating much of the power away there, while leaving the main plasma relatively uncontaminated. It is not clear that such efficient *divertor retention of impurities* has been achieved to date and when adequate radiative cooling is achieved by impurity injection, the contamination of the main plasma may be too high for reactor operation [5.8]. It is also important that as much of the divertor volume as possible be filled with radiating plasma, but the radiation region can become localized, forming MARFEs (multifaceted asymmetric radiation from the edge) chapter 22, thus making the utility of a 'deep' divertor questionable [5.9].

While the limiter configuration would appear to be at a disadvantage compared with divertors in this respect, neon injection into the TEXTOR limiter discharges gave about as good a performance as divertors in terms of high P_{rad} together with a low Z_{eff} [5.10]. In this case the impurity radiating layer extends well inside the LCFS, so a strong link to the central impurity level may be a problem, although the TEXTOR experiments have achieved low central impurity levels, chapter 23.

Substantial charge-exchange cooling would not be acceptable if it occurred in the main vessel:

(a) The resulting impurity production through *cx* sputtering is particularly effective at contaminating the main plasma, see 5.1.3.2 above.
(b) The achievement of H-mode energy confinement has been negatively correlated with neutral hydrogen levels in the main vessel in some cases, [5.11, 5.12] (although not in others [5.9, 5.13]).

This favours the divertor where charge-exchange cooling can be restricted to the divertor volume. For limiters it is not possible to avoid the presence of recycling neutrals in the main vessel.

5.1.9 Achievement of Plasma Detachment

Limiter detachment can be achieved by injecting neon to create a *radiating mantle* at or inside the LCFS, thus reducing T_{LCFS} to extremely low levels—effectively detaching the plasma from the limiters [5.10]—at least so far as power flow is concerned, chapter 23. As noted under 5.1.8, however, substantial contamination of the main plasma may be a concern.

Divertor detachment also occurs with both target density and temperature, n_t and T_t, dropping to low levels [5.14]. This can be achieved by impurity injection and radiative cooling, but it can also be achieved simply by raising $\bar{n}_e$: for the conduction-limited regime this can reduce T_t to low levels, section 5.2. At sufficiently low T_t *volume recombination* and *ion–neutral frictional drag on the parallel plasma flow* become important, also reducing n_t, and thereby 'detaching the plasma from the targets', chapter 16.

Detached plasma regimes are attractive for reactors since erosion and melting of edge structure are reduced. Both configurations show promise in this regard.

5.1.10 Energy Confinement

Improved energy confinement modes, typically H-modes, chapter 7, were first achieved in divertor tokamaks. While the H-mode has subsequently also been achieved in limiter tokamaks, it is more difficult to achieve and the increase in τ_E is less. This is undoubtedly one of the main reasons that divertors are favoured currently.

5.1.11 Conclusions

Many factors are involved in choosing between limiters and divertors. With regard to most of the issues understanding continues to evolve. While the balance of consideration presently favours divertors it is likely that limiters will continue to find application and could regain their previous widespread use.

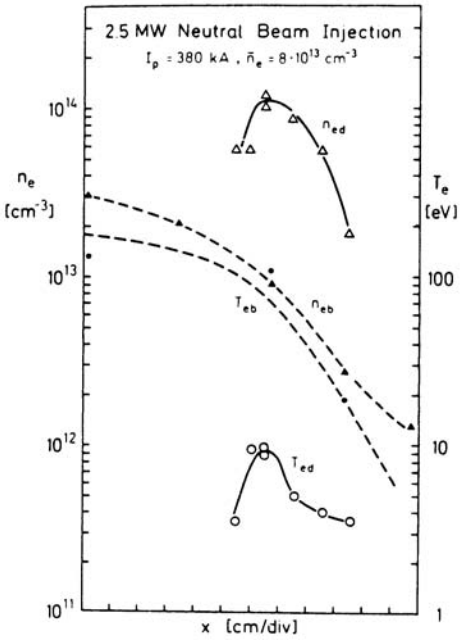

Figure 5.6. ASDEX: radial profiles of electron temperature and density at two characteristic positions along the SOL, namely in the torus midplane (upstream) ('n_{eb}, T_{eb}') and in the divertor chamber (target) ('n_{ed}, T_{ed}'), for a beam heated discharge ($P_{\mathrm{NI}} = 2.5$ MW). The midplane values are measured by laser scattering; the divertor data are obtained from a Langmuir probe [5.15].

5.2 The Basic Two-Point Model of the Divertor SOL

One of the principal objectives of using a divertor is to achieve a large temperature drop along the length of the SOL, with the plasma temperature at the target end, T_t, being low, e.g. $\lesssim 10$ eV. ASDEX was one of the earliest divertor tokamaks to demonstrate this; in figure 5.6 are shown measurements of the electron temperature at the target, $T_{et}(x)$, ('d' = 't') where x is measured across the SOL, and also for the upstream temperature, $T_{eu}(x)$ ('b' = 'u') [5.15], demonstrating that this objective can be achieved. One also notes that the plasma densities behave inversely, i.e. $n_{eu} < n_{et}$, $T_{eu} > T_{et}$.

We describe in this section the basic two-point model of the divertor SOL [5.16–5.20] in order to model results such as those in figure 5.6. The *two points* referred to are:

(a) The upstream, 'u', location which can be taken to be half-way between targets, figure 5.7. We will see later that there is little change if the mid-plane is used instead for 'u'. Here we assume a single-null, i.e.

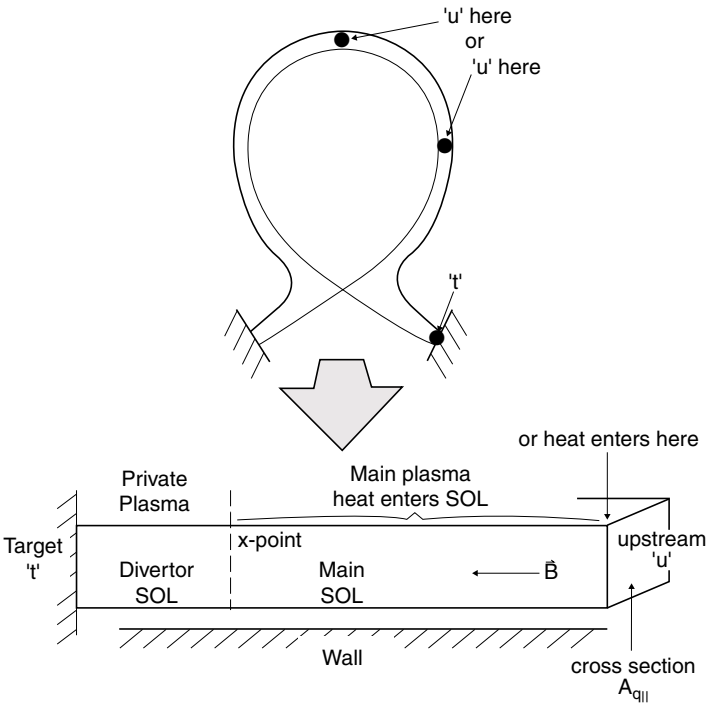

Figure 5.7. For purposes of simple modelling, the divertor SOL is 'straightened out'. Since (calculated) parallel gradients are usually small at locations far from the targets, the precise location chosen to represent the 'upstream' point is not critical.

single-X-point, poloidal divertor geometry, with targets at the top or bottom of the vessel.

(b) The target, 't'. As usual for SOL analysis, we then 'straighten out' the SOL for conceptual purposes, figure 5.7.

The reason that the model is called 'two point' is that one makes no attempt to model $T_e(s_\|)$, etc, i.e. the temperature as a function of parallel distance $s_\|$ along the SOL. Rather, one is content with the lesser objective of simply relating T_{eu} and T_{et}, etc, or, generally, upstream and target conditions. This is therefore the simplest divertor model. It is sometimes called the '0D' (zero-dimensional) divertor model.

The principal assumptions for the *basic* two-point model are now described.

(1) *Particle balance*. It is assumed that neutrals recycling from the targets are all ionized in a thin layer immediately in front of the target. Further, a neutral which resulted from an ion impacting the target while travelling along a particular magnetic field line is assumed to be re-ionized on that same field

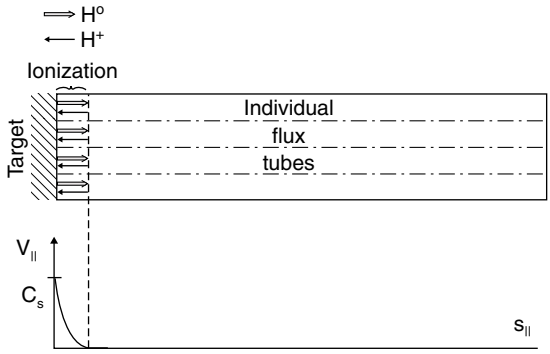

Figure 5.8. In the conceptually simplest situation, the neutrals recycling from each element of target surface are entirely ionized within the flux tube terminated by that element. As a result particle balance occurs for each flux tube individually and there is no flow reversal, chapter 15. The ionization region may also exist very near the target, resulting in stagnant plasma conditions over most of the length of the SOL.

line figure 5.8. In steady state, therefore, each flux tube has its own, highly localized particle balance with the same particles just recycling over and over, spending part of their time as ions and part of their time as neutrals. The only parallel plasma flow is in a very thin layer between the ionization point and the target. There is no parallel flow, therefore, throughout essentially all of the SOL, while in this very thin layer the flow velocity increases from zero—at the start of the ionization zone—up to the sheath entrance speed. The latter is taken to be the sound speed, section 2.3. There is no cross-field particle flow—either as neutrals or ions. There is therefore also no *flow reversal*, chapter 15. The particle balance is purely one dimensional. There is no volume recombination, the target being the only particle sink.

(2) *Pressure balance*. It is assumed that there is no friction between the plasma flow in the thin ionization region and the target and no viscous effects. Thus throughout the entire length of each SOL flux tube, section 9.11:

$$p + nmv^2 = \text{constant}. \tag{5.1}$$

$T_e = T_i$ is assumed, thus the plasma (*static*) pressure p:

$$p = nkT_e + nkT_i = 2nkT. \tag{5.2}$$

The *dynamic* pressure is $p_{\text{dyn}} \equiv mnv^2$. The *total* pressure is $p + p_{\text{dyn}}$. The entire length of the flux tube from 'u' down to the start of the thin ionization zone is characterized by $v = 0$, while at the target, $v_t = c_{st} = (2kT_t/m_i)^{1/2}$, section 2.3. Thus, we have the relation between upstream and target total pressures:

$$n_t(2kT_t + mv_t^2) = 2n_u kT_u \tag{5.3}$$

i.e.

$$2n_t T_t = n_u T_u. \tag{5.4}$$

(3) *Power balance*. Since $v = 0$ over almost the entire length L of the flux tube, parallel heat convection is absent and the parallel power flux density $q_\parallel$[W m^{-2}] is carried by conduction. If it is assumed that $q_\parallel$ entered entirely at the upstream end, and was removed at the target, distance L downstream, then from section 4.10:

$$T_u^{7/2} = T_t^{7/2} + \frac{7}{2} q_\parallel \frac{L}{\kappa_{0e}} \tag{5.5}$$

where the electron parallel conductivity coefficient κ_{0e} is used, assuming electrons and ions are thermally coupled, and neglecting parallel ion heat conductivity as comparatively small, section 9.6. It has been assumed that there are no volumetric power sources or sinks in the flux tube. In principle there is a temperature change across the ionization zone, but, as this is taken to be a very thin region, this is ignored and thus T_t in equation (5.5) is the temperature at the target sheath edge. Thus we also have for $q_\parallel$, section 2.8:

$$q_\parallel = q_t = \gamma n_t k T_t c_{st} \tag{5.6}$$

where q_t is the heat flux density entering the sheath, γ is the sheath heat transmission coefficient, $\gamma \approx 7$.

Summing up, we thus have three equations in the three *unknowns*, n_t, T_t, T_u of the **two-point model**:

$$\boxed{\begin{aligned} 2n_t T_t &= n_u T_u && (5.4)\\ T_u^{7/2} &= T_t^{7/2} + \frac{7}{2}\frac{q_\parallel L}{\kappa_{0e}} && (5.5)\\ q_\parallel &= \gamma n_t k T_t c_{st} && (5.6) \end{aligned}}$$

with n_u and $q_\parallel$ as specified *control parameters*, i.e., the independent variables; L, γ and κ_{0e} are specified constants of the problem.

We have not yet addressed explicitly the question of what *radial portion* of the SOL is involved here. In the crudest model we ignore radial variations of n_u, T_u, n_t, T_t, etc across the SOL or take the values to be radially averaged ones. In a more refined approach we apply equations (5.4)–(5.6) to individual *flux tubes* within the SOL. The concept of flux tubes is considered further in chapter 12. Here we take it that the SOL can be sub-divided radially into long, narrow regions, aligned with $\boldsymbol{B}$, of constant cross-sectional area, along which the plasma flows to the targets.

It seems natural to treat n_u and $q_\parallel$ as the *control parameters*. The two principal 'control knobs' available to tokamak operators are the input power P_{in} [W] and the main plasma density $\bar{n}_e$. In the simplest scenario where all solid surfaces

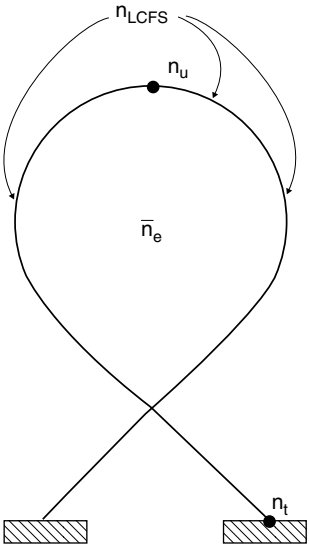

Figure 5.9. Relating the upstream density, n_u, of 1D parallel-to-$\boldsymbol{B}$ analysis, and the n_{LCFS} of 1D radial analysis. The separatrix constitutes the last closed flux surface, LCFS.

would remain 100% hydrogen saturated from the very start of the discharge, and no pumping of any form existed, $\bar{n}_e$ would simply be given by the number of gas atoms in the original gas-fill of the vessel—an externally controlled quantity. The existence of non-saturated surfaces, of hydrogen-releasing surfaces and of active pumping complicates control of $\bar{n}_e$, but in principle $\bar{n}_e$ is a controllable quantity. The relation between $\bar{n}_e$ and n_{LCFS} was discussed in section 4.6. for the limiter case. Assuming all ionization occurs in the SOL—which is the assumption here—and assuming only diffusive radial transport in the main plasma, then $\bar{n}_e = n_{\mathrm{LCFS}}$. The presence of an inward drift velocity ('pinch') v_{in} in the main plasma alters the ratio $n_{\mathrm{LCFS}}/\bar{n}_e$, section 4.6, but for purposes of *edge* analysis, we may treat n_{LCFS} as being just as much controlled or imposed as is $\bar{n}_e$.

We next ask: what is the relation between the 'n_{LCFS}' of the 1D *radial* analysis of section 4.6 (the Engelhardt model) and the 'n_u' here, which is part of a 1D *parallel-to-*$\boldsymbol{B}$ model (figure 5.9)? Let us assume here that we are using the crude approach where n_u, etc represent radially averaged values. This still leaves an apparent problem, however: n is not constant with distance $s_\parallel$ along the SOL, raising the question of which location along the SOL to take as the one to equate to the density n_{LCFS}. It would certainly be questionable to equate n_{LCFS} and n_u if it turned out that $n(s_\parallel)$ varied greatly along the flux tube from X-point to upstream end—i.e. the interface with the main plasma. Fortunately, a key feature of the conduction-controlled SOL saves the day: we have seen in figure 4.17 that $T(s_\parallel)$ varies little except rather near the target, and so is nearly constant above

the X-point. We also have from equation (5.1) that $p(s_\parallel)$ is constant, therefore $n(s_\parallel)$ is also, approximately. (For the sheath-limited regime $n(s_\parallel)$ is also nearly constant, of course.) Therefore, we may with little error equate $n_{\rm LCFS}$ and n_u. In the refined approach we equate $n_{\rm LCFS}$ to $n_u^{\rm sep}$, the upstream density on the *separatrix* flux tube, i.e. the first sub-layer of the SOL just outside the separatrix. Thus, we may treat n_u as being almost as directly controllable a quantity as $\bar{n}_e$—at least for purposes of *edge* analysis.

Of course, just as for limiters, some of the ionization may occur inside the LCFS and so we do not expect that $n_{\rm LCFS}$ is actually *equal* to $\bar{n}_e$. Inward pinches and other radial transport effects such as *H-mode transport barriers*, chapter 7, occurring just inside the LCFS also influence the $n_{\rm LCFS}/\bar{n}_e$, i.e. $n_u/\bar{n}_e$, ratio, chapter 19. These effects occur in the main plasma, not the SOL, and therefore we will treat $n_{\rm LCFS}/\bar{n}_e$ as a *SOL input parameter*, to be taken from experiment, ideally.

We will show shortly that target conditions—n_t, T_t, etc—turn out to be strongly dependent on n_u. Unfortunately $n_u^{\rm sep}$ is not regularly measured on most tokamaks. Measuring $n_u^{\rm sep}$, or inferring it from other measurements, is often difficult. On the other hand, $\bar{n}_e$ is always measured. It is therefore of great practical importance to establish the relation between $n_u^{\rm sep}$ and $\bar{n}_e$. For cases where it has been possible to measure or infer $n_u^{\rm sep}$, data have been collected on this important ratio, $n_u^{\rm sep}/\bar{n}_e$, see chapter 19. Here, we treat n_u or $n_u^{\rm sep}$ as a SOL control variable, equivalent to $\bar{n}_e$.

We turn next to $q_\parallel$. This, unfortunately, is not given directly by the controllable quantity P_{in}. These quantities have different units: $q_\parallel$ [W m^{-2}], P_{in} [W]. In order to relate $q_\parallel$ and the *power entering the SOL*, $P_{\rm SOL} \equiv P_{in} - P_{\rm main,rad}$, where $P_{\rm main,rad}$ is the power radiated from the main plasma, we have to know $A_{q_\parallel}$, figure 4.16, and thus the *power width* in the SOL. We return to this matter in section 5.7. For now we assume that $q_\parallel$, like P_{in}, is an externally controllable variable.

From a mathematical viewpoint, of course, one can choose any three of the quantities in equations (5.4)–(5.6) as being the unknowns, treating the other quantities as independent variables or parameters. (For purposes of generating solutions, this in fact is often useful.) We now proceed to obtain n_t, T_t, T_u in terms of n_u and $q_\parallel$.

(1) *Upstream temperature* T_u. We have seen earlier, section 4.10, the useful simplification that occurs when even a slight T-drop exists, sufficient to make $T_t^{7/2} \ll T_u^{7/2}$, and thus from equations (4.87), (5.5):

$$\boxed{T_u \simeq \left(\frac{7}{2}\frac{q_\parallel L}{\kappa_{0e}}\right)^{2/7}} \tag{5.7}$$

T [eV], $q_\parallel$ [W m^{-2}], L [m].$\kappa_{0e} \simeq 2000$, section 9.6. Equation (5.7) assumes all the power enters at the 'top end'. For power entering along the length L,

the factor $7/2 \rightarrow 7/4$, equation (4.91). There are a number of important implications of equation (5.7):

(a) T_u is not a function of n_u. It is a remarkable feature of fully ionized plasmas that neither electrical conductivity nor heat conductivity depend on the number of carriers, i.e. on n_e—something which is quite foreign to our ordinary experience of material properties. It is this which makes T_u independent of n_u.

(b) T_u is quite insensitive to $q_\parallel$. Indeed T_u is quite insensitive to *all parameters*. This is the consequence of the fact that the heat conductivity $K_\parallel$ of a fully ionized plasma is such a strong function of temperature, $K_\parallel \propto T^{5/2}$, section 9.6. By changing T a small amount, $T^{5/2}$ changes a lot, and this can accommodate large changes in other factors. This leads to a relation between $q_\parallel$ and $\nabla_\parallel T$ which is the opposite of our ordinary experience, see section 5.3.

(2) *Target temperature* T_t. Combine equations (5.4) and (5.6) to obtain:

$$\boxed{T_t = \frac{m_i}{2e}\frac{4q_\parallel^2}{\gamma^2 e^2 n_u^2 T_u^2}} \tag{5.8}$$

T [eV], m_i [kg], $q_\parallel$ [W m^{-2}], n [m^{-3}], $e = 1.6 \times 10^{19}$. It may be noted that equation (5.8) is actually more general than is needed here, since it holds regardless of how $q_\parallel$ is transported from 'u' to 't': it holds *whether parallel convection is present or not*, since it only assumes pressure and power conservation. Equation (5.8) is not, however, directly usable since the unknown T_u also appears on the RHS. This can be eliminated using equation (5.7) to yield:

$$\boxed{T_t = \frac{m_i}{2e}\frac{4q_\parallel^2\left(\frac{7}{2}\frac{q_\parallel L}{\kappa_{0e}}\right)^{-4/7}}{\gamma^2 e^2 n_u^2}} \tag{5.9}$$

i.e.

$$T_t \propto q_\parallel^{10/7}/L^{4/7}n_u^2. \tag{5.10}$$

This expression for T_t, equation (5.9), is of course only for the case where parallel heat transport is conductive. Now we want T_t to be as low as possible; we may note:

(a) T_t increases faster than linearly with $q_\parallel$, unfortunately.

(b) T_t decreases with increasing length of the SOL, but the effect is rather weak and this is probably not a practical way to reduce T_t, target sputtering, etc.

(c) Fortunately T_t is a strong function of upstream density, $T_t \propto n_u^{-2}$ and this is the most direct way to drive down divertor temperature—i.e. operate the tokamak at higher $\bar{n}_e$. Fortunately, high $\bar{n}_e$ is also required for

high fusion power. The importance of knowing the relation between $\bar{n}_e$ and n_u, chapter 19, is also evident—but *presumably* $\bar{n}_e$ and n_u increase together. For reactor operation it is necessary that density limits on $\bar{n}_e$ not be so low as to make n_u too low, with unacceptably high T_t resulting.

Note that $T_t \propto n_u^{-2}$ is a rather strong form of *dilution cooling*. From equation (5.8), which is general and does not assume that a large T-drop necessarily exists, we see that for negligible drop, $T_u \sim T_t$ and one has $T \propto n^{-2/3}$, a much weaker dilution cooling effect. The key is, again, the fact that T_u is virtually a constant for the conduction-limited regime. Thus, this powerful dilution cooling can also be traced back to the fact that $K_\parallel \propto T^{5/2}$.

(3) *Target density* n_t. From equations (5.4), (5.7), (5.9):

$$\boxed{n_t = \frac{n_u^3}{q_\parallel^2}\left(\frac{7}{2}\frac{q_\parallel L}{\kappa_{0e}}\right)^{6/7}\frac{\gamma^2 e^3}{4m_i}} \tag{5.11}$$

$$n_t \propto n_u^3 q_\parallel^{-8/7} L^{6/7}. \tag{5.12}$$

One notes that n_t is a particularly strong function of n_u, $n_t \propto n_u^3$.

(4) *Particle flux density* Γ_t. *Recycling rate*. The particle flux density onto the target Γ_t [ion pairs m^{-2} s^{-1}] is given by $\Gamma_t = q_\parallel/\gamma e T_t$, thus from equation (5.9):

$$\boxed{\Gamma_t = \frac{n_u^2}{q_\parallel}\left(\frac{7}{2}\frac{q_\parallel L}{\kappa_{0e}}\right)^{4/7}\frac{\gamma e^2}{2m_i}} \tag{5.13}$$

$$\Gamma_t \propto n_u^2 q_\parallel^{-3/7} L^{4/7}. \tag{5.14}$$

($e = 1.6 \times 10^{-19}$ C enters these expressions since T is in [eV] in equation 5.7.) One may note the strong dependence of Γ_t on n_u. Thus the Langmuir probe I_{sat}^+ for probes at the target are also expected to show a variation like $I_{\text{sat}}^+ \propto \bar{n}_e^2$ in this regime (again, assuming that n_u and $\bar{n}_e$ are tightly linked, see chapter 19). The total intensity of the recycling flux at the targets ϕ_{recycle} is equal to the product of $(B_\theta/B)_t \Gamma_t$ and the effective wetted area of target, A_{wet}. One thus also anticipates $\phi_{\text{recycle}} \propto \bar{n}_e^2$. Since particle confinement time $\tau_p = \bar{n}_e \times \text{volume}/\phi_{\text{recycle}}$, $\tau_p \propto \bar{n}_e^{-1}$, which was also seen approximately for limiters, although for quite different reasons, equation (4.58). One notes again, as in section 4.6, that particle confinement time is *not* purely a property of the confined plasma, e.g. of $D_\perp^{\text{main}}$, but is also very sensitive to the details of what happens in the SOL. Since the ionization is assumed to occur in a thin layer in front of the targets, the main plasma is 100% *ion fuelled*: no ionization of neutrals occurs inside the separatrix. The entire SOL (above the thin ionization layer) plus the main plasma are all 'back-filled' by particles from the recycling zone right at the targets. Since the latter regions are *self-sustained* in a particle sense (neutral inflow = ion

outflow) the recycle can operate at *any* level of intensity—so long as this is consistent with conservation of momentum and power along the flux tubes, i.e. equation (5.13) has to be satisfied, i.e. $\phi_{\text{recycle}} \propto \bar{n}_e^2$. *Otherwise there is no constraint on the intensity of* ϕ_{recycle}—an initially surprising fact. It is not correct to assume similarity between power and particle balance in this regard, since the power input is a *specified* boundary condition of the system. Taking $\bar{n}_e = n_u$ for simplicity, then the particle confinement time, τ_p, is approximately:

$$\tau_p = \frac{q_\parallel}{n_u(\frac{7}{2}q_\parallel L/\kappa_{0e})^{4/7}} \frac{2m_i}{\gamma e^2} \frac{\text{volume}}{A_{\text{wet}}(B_\theta/B)_t}. \tag{5.15}$$

As noted $\tau_p \propto n_u^{-1}$, thus approximately $\tau_p \propto \bar{n}_e^{-1}$, as for the limiter case, equation (4.58). It is clear that this is coincidental since, unlike equation (4.58), equation (5.15) has *no* dependence on $D_\perp^{\text{main}}$; also there now appears a new dependence, namely on power, $\tau_p \propto q_\parallel^{3/7}$. It is noteworthy that in this scenario τ_p *has no dependence at all on the cross-field transport in the main plasma*. As discussed in section 4.6, energy and particle confinement are not necessarily related in any way—which is perhaps surprising.

Problem 5.1. One may also note how small τ_p is in this regime: show for a JET-size example, $q_\parallel = 10^8$ W m^{-2}, $n_u = 3 \times 10^{19}$ m^{-3}, $L = 50$ m, $\gamma = 7$, volume $= 100$ m^3, $A_{\text{wet}} = 1$ m^2, $(B_\theta/B)_t = 0.02$, D$^+$plasma, that $\tau_p = 70$ ms.

It is noteworthy that the recycle flux, ϕ_{recycle} and Γ_t, have no important or significant relationship with other particle fluxes, for example, the net particle ion flux entering the SOL from the main plasma, ϕ_{LCFS}^+: in the present scenario in fact, $\phi_{\text{LCFS}}^+ = 0$. It is therefore not useful or informative to define a quantity such as the 'particle flux amplification, or multiplication factor' $R \equiv \phi_{\text{recycle}}/\phi_{\text{LCFS}}^+ \equiv \Gamma_t/\Gamma_u$, although this is sometimes done [5.21]. While this does give the result $kT_t = q_\parallel/\gamma\Gamma_u R$, implying that one needs to raise R in order to reduce T_t—i.e. one needs to achieve a 'high recycling' divertor with large R—this reasoning is based on the incorrect assumption that it is Γ_u or ϕ_{LCFS}^+ that are given, rather than n_u or $\bar{n}_e$. As discussed in section 4.10.1, *the reason that high recycling is important is that it allows conduction to transport most of the power, making possible large* $\nabla_\parallel T$, *and low* T_t.

Since there is a finite amount of energy radiated for each recycle event, section 3.5, this also means that by raising $\bar{n}_e$, hydrogenic radiation losses can be substantially increased.

(5) *Sputtering production*. We have seen generally that the sputtered flux density Γ_{sput}:

$$\Gamma_{\text{sput}} = Y\Gamma_t \tag{5.16}$$

where Y is the sputtering yield, section 3.3. Targets are usually operated in the regime where Y is an increasing function of impact energy, hence of T_t. Since $T_t \propto n_u^{-2}$ while $\Gamma_t \propto n_u^2$ it is not immediately clear whether increasing $\bar{n}_e$ and n_u will increase or decrease sputtering. For physical sputtering, Y can be a strong function of T_t, $Y \propto T_t^m$, with $m = 2$ or more. In that case Γ_{sput} will decrease with increasing $\bar{n}_e$. For chemical sputtering of carbon by hydrogen, section 3.3.2, the dependence of Y on impact energy can be weak, depending on the carbon substrate temperature. When $Y(T_t)$ varies more weakly than linearly, the Γ_{sput} will increase with increasing $\bar{n}_e$. Chemical sputtering is therefore a potential problem for this regime.

Before leaving this section we return to the assumption that the ionization region is very thin: since L enters the expressions for T_t, n_t, etc only relatively weakly, this assumption turns out not to be critical. Consider, for example, the effect on T_t. Let all the ionization occur at distance L_1 upstream from the target. Starting at that point, parallel heat convection will be quite strong and, since $q_{\parallel\text{conv}} \approx 6kT\Gamma$ for sonic flow, section 9.10, this transport process by itself could carry all of $q_\parallel (= q_t \approx 7kT_t\Gamma_t)$ at a value of T slightly above T_t. Thus, from the 'ionization front' to the target, T will be almost constant at approximately the target value, T_t, i.e. strong convection flattens any parallel temperature variation. We now apply the foregoing two-point model to the region from $s_\parallel = L_1$ to L, and so obtain the same results as before, provided L_1 is not too large a fraction of L. For example, for $L_1/L = 0.2$, T_t is raised by only a factor $(0.8)^{-4/7} \approx 1.14$.

5.3 The Conduction-Limited Regime. The High Recycling Regime

As discussed in section 1.9, the *conduction-limited regime* CLR is characterized by significant parallel T-drops due to the finite value of heat conductivity. The *high-recycling regime* HRR is a term inspired by the observation, last section, that $\phi_{\text{recycle}} \propto \bar{n}_e^2$ in the CLR. The two regimes are therefore almost coincident, with the HRR lying toward the higher $\bar{n}_e$ end of the CLR. The use of 'high' raises the obvious question: high compared with what? Certainly if one kept $q_\parallel$, L, etc fixed and raised $\bar{n}_e$, n_u, then the divertor would evolve from the sheath-limited regime, SLR (which is also the low recycling regime, LRR) to the CLR/HRR and in doing so ϕ_{recycle} would rise. But something *stronger* is intended here by the expression 'high': namely, one goes from a *linear* increase of ϕ_{recycle} with $\bar{n}_e$ to a *quadratic* (or even stronger) dependence. The increased T-drop 'causes' the increased ϕ_{recycle} through the conservation of momentum and power. More correctly one should say that large ϕ_{recycle} and low T_t are *associated* because of momentum and power conservation.

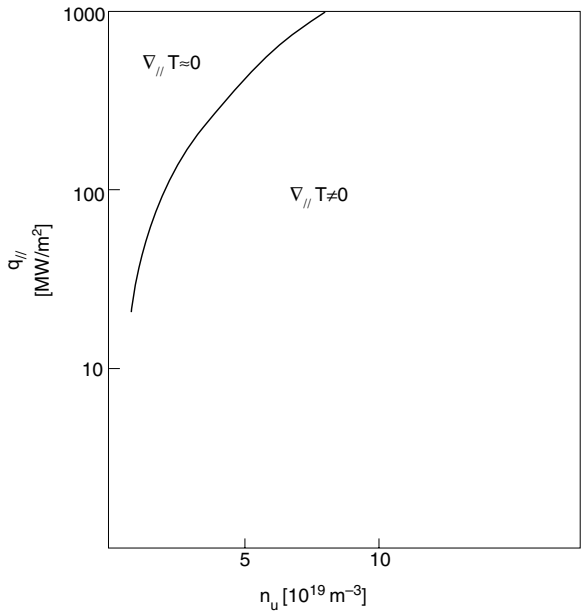

Figure 5.10. For the case of all parallel power carried by (electron) heat conduction, significant parallel temperature gradients only arise when the heat flux density $q_\parallel$ is not *too* high—i.e., the opposite of ordinary experience. Case of $L = 100$ m, D^+ plasma, $\gamma = 7$.

The criteria for the transition to these attractive regimes are therefore quite important, see section 4.11. In figure 5.10 we plot the criteria based on $q_\parallel$, n_u and L from equation (4.110), for the example of $L = 100$ m. Again, we note that if $q_\parallel$ is too *high* then the T-drop will be negligible.

It may be considered that the achievement of a satisfactory temperature distribution within the SOL requires something more than just a large T-drop. For example, if $T_u/T_t = 1000$ eV/100 eV one would still be concerned about the large value of T_t and the problem of sputtering, while if $T_u/T_t = 10$ eV/1 eV one might be concerned about such a low temperature being present at the boundary of the confined plasma. Let us require, therefore, that the following criteria be satisfied simultaneously: (i) $T_u \gg T_t$, (ii) $T_u \geq 100$ eV, (iii) $T_t \leq 10$ eV. Using equations (5.7) and (5.9) this requires that just the two following criteria be satisfied in fact:

$$\underset{(\text{for } T_u \geq 100 \text{ eV})}{5.7 \times 10^9 L^{-1}} \leq q_\parallel \leq \underset{(\text{for } T_t \leq 10 \text{ eV})}{3.2 \times 10^{-21} n_u^{7/5} L^{2/5}} \tag{5.17}$$

q [W m^{-2}], L [m], n [m^{-3}]. Equation (5.17) used the factor 7/4 in equation (5.7) for T_u, equation (4.91), i.e. power input is assumed to be constant along the length L.

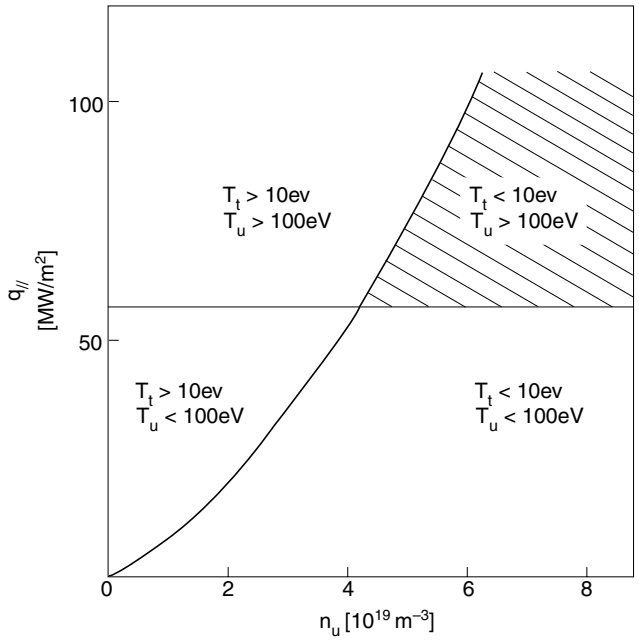

Figure 5.11. For pure parallel (electron) heat conduction, the four temperature regimes. For $L = 100$ m, D^+ plasma, $\gamma = 7$.

The preferred regime is shaded in figure 5.11 for the example of $L = 100$ m, D^+ ions, $\gamma = 7$. What is required is a high enough value of n_u together with a value of $q_\parallel$ which is not so low as to cause $T_u < 100$ eV, nor so high as to cause $T_t > 10$ eV. It may be appreciated that these are demanding criteria and it may not be possible for reactors to satisfy them.

Problem 5.2. Consider the example of an ITER-size tokamak where the SOL cross-section area for carrying the power, $A_{q_\parallel}$, may be only of order ~ 1 m^2 or less, section 5.7. For $P_{\rm SOL} = 10^8$ W, then $q_\parallel \approx 10^8$ W m^{-2}. Show that achievement of $T_t < 10$ eV for $L \simeq 100$ m would require $n_u > 6 \times 10^{19}$ m^{-3}, which might correspond to $\bar{n}_e$-levels above the density limit of the main plasma. Show that the achievement of a significant T-drop, however, would require only $n_u > 2.5 \times 10^{19}$ m^{-3}, figure 5.10. If $n_u = 3.5 \times 10^{19}$ m^{-3}, for example, then show that $T_u \sim 120$ eV, $T_t \simeq 20$ eV.

5.4 Extensions to the Basic Two-Point Model. 'Corrections'

The basic model can readily be extended to provide estimates for the effect of including various processes which were excluded originally.

Volumetric power losses due to radiation and charge exchange loss, $q_{\text{rad}}^{\text{SOL}}$, q_{cx}^{SOL} [W m^{-2}] can be included by introducing a *power loss factor* f_{power}:

$$q_{\text{rad}}^{\text{SOL}} + q_{cx}^{\text{SOL}} \equiv f_{\text{power}} q_{\parallel}. \tag{5.18}$$

Thus

$$(1 - f_{\text{power}}) q_{\parallel} = q_t = \gamma k T_t n_t c_{st} \tag{5.19}$$

and so the power equation (5.6) is only modified slightly. At the end of section 5.2 it was argued that the ionization zone need not be vanishingly thin, and that so long as the ionization zone does not occupy a large fraction of the total SOL length L, the effect on n_t, T_t, etc is small. A similar argument holds with regard to the spatial distribution of $q_{\text{rad}}^{\text{SOL}}$, q_{cx}^{SOL}: so long as these losses occur primarily below the X- point one can simply use $(1 - f_{\text{power}})q_{\parallel}$ in place of $q_{\parallel}$ in the expressions for n_t, T_t, etc, with little error.

The plasma flow toward the target may experience *momentum loss* due to the frictional collisions with neutrals, viscous forces and volume recombination. We define a *momentum loss factor* f_{mom}:

$$p_t \equiv f_{\text{mom}} \tfrac{1}{2} p_u \tag{5.20}$$

that is:

$$2 n_t T_t \equiv f_{\text{mom}} n_u T_u. \tag{5.21}$$

As earlier, it is assumed that $M_t = 1$.

In general, parallel heat convection plays some role even if parallel conduction dominates. The tendency is for convection to reduce T-gradients. The T-gradient is largely due to the fraction of the parallel power carried by conduction. It is therefore useful to introduce a *conduction factor* f_{cond}:

$$q_{\parallel\text{cond}} \equiv f_{\text{cond}} q_{\parallel}. \tag{5.22}$$

Thus equation (5.5) becomes

$$T_u^{7/2} = T_t^{7/2} + \frac{7}{2} \frac{f_{\text{cond}} q_{\parallel} L}{\kappa_{0e}}. \tag{5.23}$$

Note that one does not, however, insert the f_{power} factor into equation (5.23) since it is assumed that the volumetric power losses occur below the X-point. Thus over most of SOL length L, the conduction equation (5.23) applies: $q_{\parallel}$ supplies both the volumetric and target power losses at essentially the same distance from the upstream end. It is implied in equation (5.23), however, that the convection occurs approximately uniformly over length L. At the end of section 5.2 we considered the effect of convection becoming strong just near the target and showed that this had no large effect.

The effects of these *correction factors* on the basic two-point model are considered next.

(1) *Upstream temperature* T_u. Assuming T_u is at least slightly greater than T_t then:

$$T_u \simeq \left(\frac{7}{2}\frac{f_{\text{cond}} q_{\parallel} L}{\kappa_{0e}}\right)^{2/7} \tag{5.24}$$

$$T_u \propto f_{\text{cond}}^{2/7}. \tag{5.25}$$

Neither momentum loss nor volumetric power loss affects T_u, and the effect of upstream convection, making $f_{\text{cond}} < 1$, is very small. As before, T_u is insensitive to almost all factors. One notes, nevertheless, that upstream convection does tend to reduce T_u.

(2) *Target temperature* T_t. It is readily shown that the original result of equation (5.9) is to be multiplied by a factor such that:

$$T_t \propto \frac{(1 - f_{\text{power}})^2}{f_{\text{mom}}^2 f_{\text{cond}}^{4/7}}. \tag{5.26}$$

One notes that volumetric power loss *strongly* decreases T_t while momentum loss strongly *increases* T_t: the latter is perhaps not intuitively obvious. The effect of upstream convection is not strong but tends to *raise* T_t. The cooling effect of volumetric power losses is intuitively obvious, although the strength of the effect is possibly not. It should be noted that some power loss processes, e.g. due to charge exchange, would be accompanied by momentum loss, i.e. ion–neutral collisional friction. Whether the net result will be a reduction or an increase in T_t is not immediately clear and will depend on the details of the processes involved. Since the tendency for volumetric loss processes to become important can be strongly dependant on T_t—generally increasing as T_t drops—the overall balance may be complicated, chapter 16.

(3) *Upstream/downstream T-ratio*. T_u/T_t. From the above:

$$T_u/T_t \propto \frac{f_{\text{cond}}^{6/7} f_{\text{mom}}^2}{(1 - f_{\text{power}})^2}. \tag{5.27}$$

One notes, as earlier, the effect of convection is to reduce/eliminate parallel temperature gradients.

(4) *Target density* n_t. It is readily shown that:

$$n_t \propto \frac{f_{\text{mom}}^3 f_{\text{cond}}^{6/7}}{(1 - f_{\text{power}})^2}. \tag{5.28}$$

The effect on target density of momentum loss by the plasma flow is quite dramatic, involving a cubic relation. The influence of volumetric power loss is also quite strong. The role of upstream convection is significant. Since some volumetric processes, such as recombination, are strongly dependent

on n as well as T, and since power and momentum losses influence n_t oppositely, the overall balance can be made more complex.

(5) *Target particle flux density* Γ_t. Recycle intensity. One can show that:

$$\Gamma_t \propto \frac{f_{\text{mom}}^2 f_{\text{cond}}^{4/7}}{1 - f_{\text{power}}}. \tag{5.29}$$

Momentum loss quite strongly suppresses fluxes to the target ('plugged drain' effect) and hence, in steady state, the total recycling source; this probably plays an important role in divertor detachment, chapter 16. Power loss has the opposite influence on Γ_t, but is weaker. Since hydrogenic volumetric power losses are proportional to Γ_t, a positive feedback effect can result.

(6) *Sputtering production*. Let us assume that sputtering yield $Y \propto T_t^m$ with m a parameter. Then, the sputtering flux $\phi_z \propto Y\Gamma_t$ is:

$$\phi_z \propto \frac{q_\parallel^{\frac{10}{7}m-\frac{3}{7}}}{L^{\frac{4}{7}(m-1)} n_u^{2(m-1)}} \frac{(1 - f_{\text{power}})^{2m-1}}{f_{\text{mom}}^{2(m-1)} f_{\text{cond}}^{\frac{4}{7}m-\frac{2}{7}}}. \tag{5.30}$$

Physical sputtering yield can be strongly dependent on impact energy. For example, assuming $m = 2$:

$$\phi_z^{\text{phys}} \propto \frac{q_\parallel^{\frac{17}{7}}}{L^{\frac{4}{7}} n_u^2} \frac{(1 - f_{\text{power}})^2}{f_{\text{mom}}^2 f_{\text{cond}}^{6/7}}. \tag{5.31}$$

Thus, it would be advantageous to (a) decrease the power into the SOL (thus $q_\parallel$), (b) raise the volumetric power loss, (c) raise the upstream density and (d) minimize momentum loss.

Chemical sputtering yields are rather insensitive to impact energy for some conditions, section 3.3. Assuming for example $m = 0$:

$$\phi_z^{\text{chem}} \propto \frac{n_u^2 L^{4/7}}{q_\parallel^{3/7}} \frac{f_{\text{mom}}^2 f_{\text{cond}}^{2/7}}{(1 - f_{\text{power}})}. \tag{5.32}$$

One may note that all the things one would do to decrease physical sputtering would increase chemical sputtering—for these m-values at least. It is essential, therefore, to establish which type of sputtering is more important to know how to control it.

(7) *Criteria for existence of large parallel* T*-gradients*. The prescriptions of section 4.10 for existence of a significant T-gradient, $T_u \geq 3T_t$ specifically, equations (4.103) and (4.113), are now changed to:

$$\frac{n_u L}{T_u^2} \geq 1.5 \times 10^{17} \frac{(1 - f_{\text{power}})}{f_{\text{mom}} f_{\text{cond}}} \tag{5.33}$$

$$\frac{q_\parallel}{n_u^{7/4} L^{3/4}} \leq 4 \times 10^{-28} \frac{f_{\text{mom}}^{7/4} f_{\text{cond}}^{3/4}}{(1 - f_{\text{power}})^{7/4}}. \tag{5.34}$$

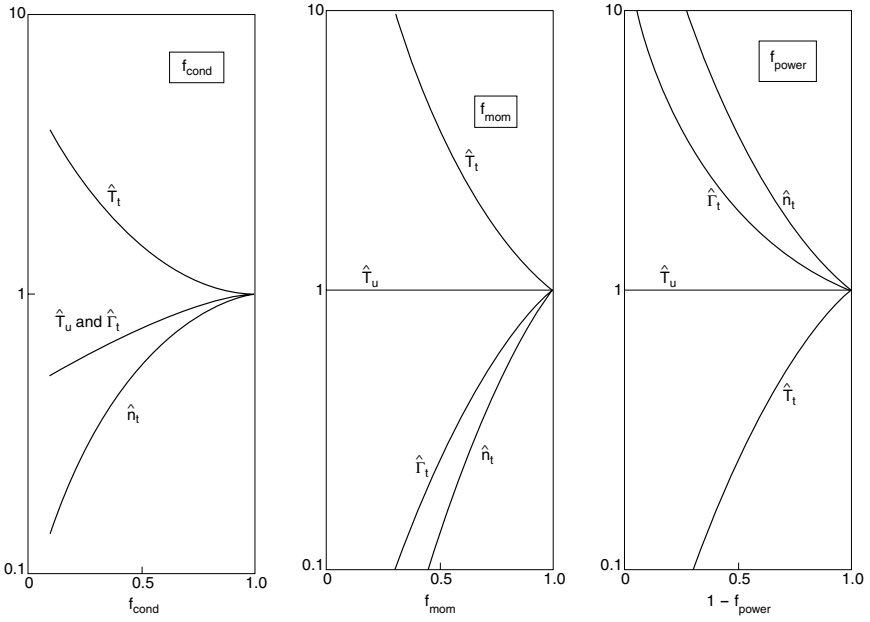

Figure 5.12. The effect of the two-point model 'correction factors', $f_{\rm cond}$, $f_{\rm mom}$, $f_{\rm power}$. The 'hats' indicate values normalized to values for $f_{\rm cond} = f_{\rm mom} = 1 - f_{\rm power} = 1$. The effect on T_t of increasing momentum loss (decreasing $f_{\rm mom}$), for example, is for T_t to rise.

As is intuitively obvious, volumetric power losses make it easier to achieve significant T-drops: this can be achieved at lower $n_u L$, and higher T_u and $q_\parallel$ than without power losses. Perhaps less intuitively, momentum loss makes it harder to achieve large T-drops.

(8) *Criteria to achieve $T_t < 10$ eV and $T_u > 100$ eV simultaneously.* The criteria of equation (5.17) now become:

$$\underset{\text{(for } T_u \geq 100 \text{ eV)}}{\frac{5.7 \times 10^9}{L f_{\rm cond}^{2/7}}} \lesssim q_\parallel \lesssim \underset{\text{(for } T_t \leq 10 \text{ eV)}}{\frac{3.2 \times 10^{-21} n_u^{7/5} L^{2/5} f_{\rm mom}^{7/5} f_{\rm cond}^{2/5}}{(1 - f_{\rm power})^{7/5}}} \tag{5.35}$$

The effect is mainly on T_t: volumetric power loss eases the constraint on $q_\parallel$ (higher $q_\parallel$ is allowed).

Problem 5.3. For the same conditions as in problem 5.2, $q_\parallel = 10^8$ W m^{-2}, $L =$ 100 m, then if $f_{\rm power} = 1/2$, show that a density of $n_u \geq 4 \times 10^{19}$ m^{-3} would be adequate to ensure $T_t \leq 10$ eV, compared with $n_u > 6 \times 10^{19}$ m^{-3} if $f_{\rm power} = 0$.

A number of these SOL variables are plotted in figure 5.12 as functions of $f_{\rm cond}$, $f_{\rm mom}$ and $f_{\rm power}$, to bring out how insensitive to these correction factors the upstream quantities are, and, by contrast, how extremely sensitive all of the target quantities are.

5.5 Including the Hydrogen Recycle Loss Energy in the Two-Point Model

In the case of the electron power sink caused by the hydrogenic recycle process, it is possible to formulate an explicit treatment, rather than use just the general form, $f_{\rm power}$, equation (5.18). If it can be assumed that all of the neutral hydrogen recycling from the target is excited and ionized near the target in a plasma at temperature and density T_t and n_t, then the energy lost by the electrons due to each recycled neutral ε [eV] is readily available, figure 3.34. Although ε is a function of (T_e, n_e), we will take $\varepsilon = 25$ eV, constant, here for illustration. Note that we use the value of ε corresponding to the *cooling rate*, $P_{\rm cool}$, rather than the *radiation loss rate*, $P_{\rm rad}$, section 3.5: the former includes, for example, the energy of ionization, I_{iz}, which is excluded from the latter. While this energy—unlike the photon energy lost by excitation—does remain in the plasma, it does so as *potential* energy, and for the purpose of calculating n, T, etc this energy has 'disappeared' just as effectively as has the photon energy. When calculating the power flux actually deposited on the target, of course, this *potential energy flow* density, $I_{iz}\Gamma_t$, has to be added to the *kinetic/thermal power flux density* $\gamma k T_t \Gamma_t$; one should also include the atom–atom recombination energy in the potential energy flow. Note that the direct cooling effect of the target on the plasma is still $\gamma k T_t \Gamma_t$.

As before we assume that the region of recycle power loss is below the X-point. Thus: the power flux density into the recycle region supplies $e\varepsilon\Gamma_t$ as well as the sheath power flow:

$$q_\parallel = e\varepsilon\Gamma_t + q_t = e\varepsilon\Gamma_t + \gamma k T_t \Gamma_t = \gamma\left(1 + \frac{\varepsilon/\gamma}{T_t}\right) k T_t \Gamma_t. \tag{5.36}$$

The other equations of the two-point model remain unchanged, equations (5.4) and (5.5), with equation (5.36) replacing equation (5.6): the latter two differ only by the factor $(1 + (\varepsilon/\gamma)/T_t)$.

(1) *Upstream temperature* T_u. This is unchanged, equation (5.7).
(2) *Target temperature* T_t. Equation (5.8) is now multiplied by the factor $(1 + (\varepsilon/\gamma)/T_t)^{-2}$. Let us define the '*upstream forcing function*' F_u from equation (5.8):

$$F_u \equiv \frac{m_i}{2e}\frac{4q_\parallel^2}{\gamma^2 e^2 n_u^2 T_u^2}. \tag{5.37}$$

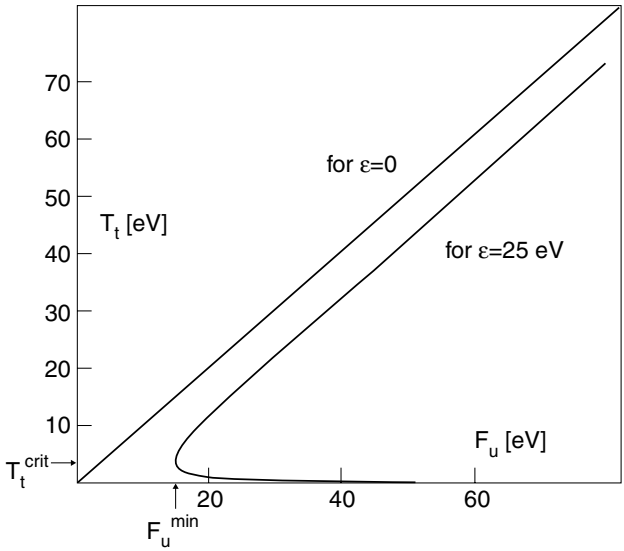

Figure 5.13. Two-point model including hydrogen recycling loss. The dependence of T_t on F_u, the upstream forcing function, equation (5.37).

Whenever T_u is even slightly larger than T_t, then:

$$F_u \simeq \frac{m_i}{2e}\frac{4q_\parallel^2}{\gamma^2 e^2 n_u^2}\left(\frac{7}{2}\frac{q_\parallel L}{\kappa_{0e}}\right)^{-4/7}. \tag{5.38}$$

Note that F_u depends on the *standard control parameters* only: $q_\parallel$, n_u and L. Conveniently F_u has units [eV] (in fact $F_u = T_t(\varepsilon = 0)$). We thus have when $\varepsilon \neq 0$:

$$T_t = F_u\left(1 + \frac{\varepsilon/\gamma}{T_t}\right)^{-2}. \tag{5.39}$$

F [eV], T [eV], $\varepsilon/\gamma = 25/7 = 3.57$ here.

Equation (5.39) thus provides the implicit functional relation $T_t(F_u)$, i.e. the dependence of T_t on the upstream conditions, represented by the lumped parameter F_u; see figure 5.13. We see a number of important results in this figure.

(a) At high temperature, T_t is lowered by an amount $2\varepsilon/\gamma \sim 7$ eV compared with the case when $\varepsilon = 0$. The reduction is greater at low $T_t \leq 15$ eV.

(b) The upstream forcing function cannot be reduced below a certain minimum value $F_u^{\min} = 4\varepsilon/\gamma \approx 14.3$ eV, at which point $T_t = T_t^{\text{crit}} = \varepsilon/\gamma \approx 3.57$ eV.

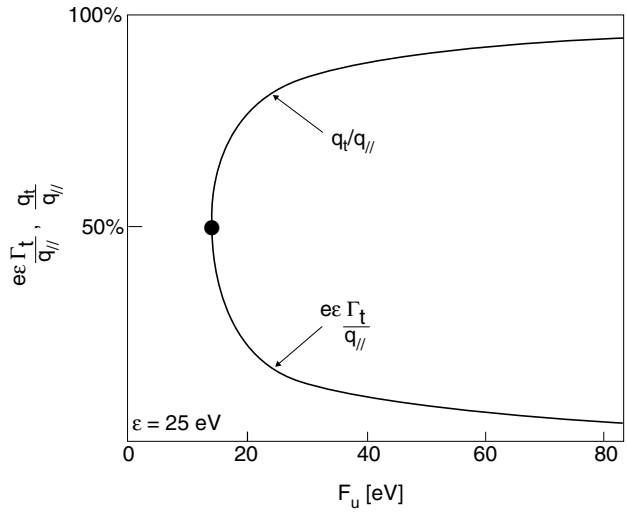

Figure 5.14. Two-point model including hydrogen recycling loss. The fraction of the entering power flux density which reaches the target, $q_t/q_\parallel$, and the fraction that is lost in hydrogen recycling processes, $e\varepsilon\Gamma_t/q_\parallel$, as functions of the upstream forcing function F_u.

(c) For any $F_u > F_u^{\min}$, there are *two branches* to the solution: a *high temperature branch* with $T_t > T_t^{\text{crit}}$, and a *low temperature branch*, with $T_t < T_t^{\text{crit}}$, i.e. a *bifurcation* exists. We show below that the lower branch solution is *unstable* and therefore will not actually occur.

What happens if $q_\parallel$ is lowered further, or n_u raised further, forcing F_u to fall below $4\varepsilon/\gamma$? Then, either:

(a) a non-steady-state occurs, or
(b) other physical processes neglected in this simple model come into play, e.g., power transfer to neutrals, volume recombination, etc. Thus, $F_u^{\min}$ and T_t^{crit} strictly should not be thought of as absolute limits, but represent *the limits of the regime* in which only the simple physical processes so far considered are the controlling ones.

It is illuminating to consider the power split. See figure 5.14 which gives $e\varepsilon\Gamma_t/q_\parallel$ and $q_t/q_\parallel$ as functions of F_u. The sum of the two is unity, of course. Figure 5.14 can be taken to represent this situation for the high temperature branch, in which case the upper curve gives $q_t/q_\parallel$ and the lower curve gives $e\varepsilon\Gamma_t/q_\parallel$. At the critical $F_u^{\min}$, the two fractions are equal, $1/2$. Alternatively, this figure represents the low temperature branch, in which case the upper curve is $e\varepsilon\Gamma_t/q_\parallel$, the lower $q_t/q_\parallel$. With regard to the *deposited* power: estimating $I_{iz} \approx e\varepsilon/2$ then the deposited power is never less than 75% of the input power $q_\parallel$, at least for the assumptions made here.

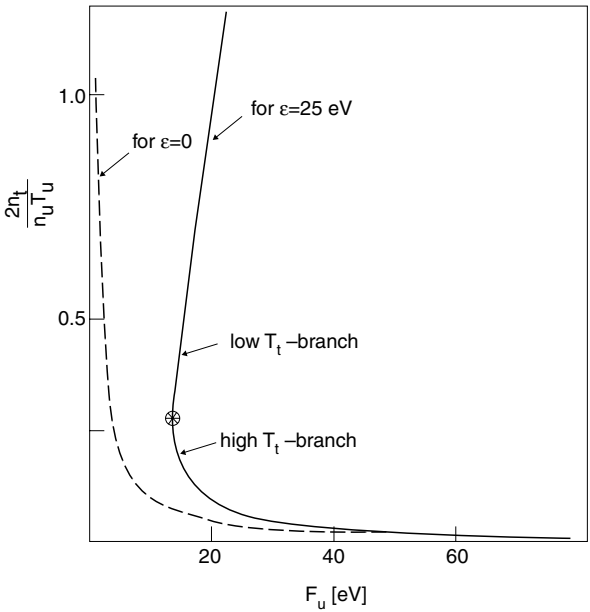

Figure 5.15. Two-point model including hydrogen recycling loss. Target density (normalized) as a function of the upstream forcing function, F_u.

One may note that the effect of including ε is perhaps stronger than might be thought at first. For example, $T_t(\varepsilon = 0) = 15$ eV is reduced to $T_t \approx 5$ eV by including $\varepsilon = 25$ eV. One might have thought—since at $T_t = 15$ eV, there is ~ 105 eV carried into the target per ion pair, while only ~ 25 eV is consumed by recycle processes—that therefore the correction should be modest. Note, however, that the appropriate comparison has to be made at the *altered* temperature, here ~ 5 eV, where only ~ 35 eV is carried per ion pair into the sheath. Thus f_{power}, equation (5.18), is $(1 - f_{\text{power}}) \approx 35/(35 + 25) \approx 0.58$, and so according to equation (5.26) one expects T_t to be reduced by $\sim 0.58^2 \sim 0.34$, i.e. to ~ 5 eV from 15 eV. One notes again, therefore, *how sensitive target conditions are to almost all parameter variations*.

(3) *Target density n_t.* The target density can be represented in a 'normalized' way which shows that it is solely dependent on upstream quantities:

$$\frac{n_t}{\frac{1}{2}n_u T_u} = (1 + (\varepsilon/\gamma)/T_t)^2/F_u. \tag{5.40}$$

See figure 5.15. For a specified F_u, the corrections at low T_t are very large. Note, however, that if instead T_t is taken to be specified then n_t is unchanged since $\frac{1}{2}n_u T_u = n_t T_t$.

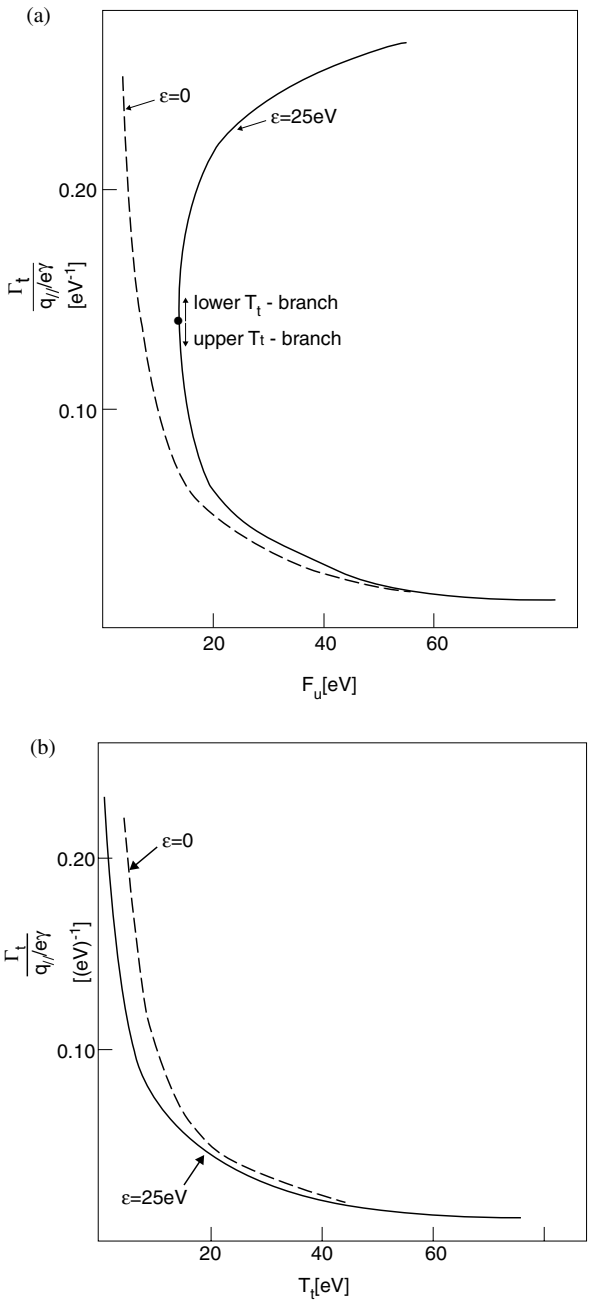

Figure 5.16. (a) Two-point model including hydrogen recycling loss. The (normalized) particle flux density to the target as a function of the upstream forcing function, F_u. (b) As (a), but as a function of target temperature T_t.

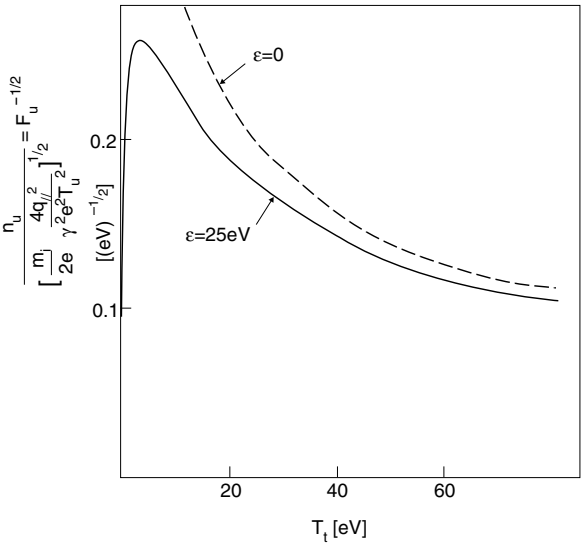

Figure 5.17. Two-point model including hydrogen recycling loss. Upstream (normalized) density against target temperature, T_t, showing that there is a maximum upstream density for a stable, steady-state solution.

(4) *Particle flux density* Γ_t. *Recycling rate*. We now have an expression for 'normalized' Γ_t, i.e. expressed so as to depend solely on upstream parameters:

$$\frac{\Gamma_t}{q_\parallel/\gamma e} = \left(1 + \frac{\varepsilon/\gamma}{T_t}\right)/F_u. \tag{5.41}$$

See figure 5.16(a) plotted against F_u and figure 5.16(b) plotted against T_t. One notes from figure 5.16(b) the standard pattern that the intensity of recycling, Γ_t, *increases* rapidly as T_t falls—a simple and direct consequence of the conservation of momentum and power, as already noted. This basic pattern is not essentially changed by including ε. While, from equations (5.39) and (5.41) $q_t \propto T_t\Gamma_t \propto (1+(\varepsilon/\gamma)/T_t)^{-1} \to 0$, as $T_t \to 0$, on the one hand, on the other hand, $e\varepsilon\Gamma_t$ goes on increasing as T_t drops. This is the reason why a minimum $q_\parallel$ exists, i.e. a $F_u^{\min}$ exists, figure 5.13: enough power must be 'reserved' to supply $e\varepsilon\Gamma_t$. On the other hand, if $\varepsilon = 0$, then $q_\parallel$ may be lowered to 0, with T_t then going to 0 also.

It is illuminating to re-plot figure 5.13 as $F_u^{-1/2}$ against T_t which for fixed $q_\parallel$ and L is effectively a plot of n_u against T_t, see figure 5.17. Again one notes the high T_t and low T_t branches. Now it is apparent that a *maximum* n_u *exists*:

$$n_u^{\max} = \frac{q_\parallel}{T_u}\left(\frac{m_i}{2e^3\varepsilon\gamma}\right)^{1/2}. \tag{5.42}$$

Problem 5.4. For the example $q_\parallel = 10^8$ W m^{-2}, $T_u = 150$ eV, D$^+$, $\varepsilon = 25$ eV, $\gamma = 7$ show that $n_u^{\max} = 3.2 \times 10^{19}$ m^{-3}.

It has been proposed that this may be a cause of the density limit of tokamaks [5.19, 5.22] (assuming also the existence of a close connection between n_u and $\bar{n}$ in the main plasma, chapter 19). Any higher n_u would reduce F_u below $F_u^{\min}$, resulting in either non-steady-state behaviour or the onset of physical processes not considered in this simple model.

In order to include the effect of friction we combine the formulations of this section with the f_{mom}-factor of section 5.4 to obtain expressions for the (normalized) $q_\parallel$ and Γ_t in terms of the normalized T_t:

$$\hat{q}_\parallel = [f_{\text{mom}}^2 \hat{T}_t (1 + (\hat{T}_t)^{-1})^2]^{7/10} \tag{5.43}$$

$$\hat{\Gamma}_t = \hat{q}_\parallel^{-3/7} f_{\text{mom}}^2 (1 + (\hat{T}_t)^{-1}) \tag{5.44}$$

where we define:

$$\hat{\Gamma}_t = \Gamma_t / (C(e\varepsilon C)^{-3/10}) \tag{5.45}$$

$$\hat{q}_\parallel = q_\parallel / (e\varepsilon C)^{7/10} \tag{5.46}$$

$$C \equiv e^2 \gamma n_u^2 \left(\frac{7L}{2\kappa_0} \right)^{4/7} / 2m_i \tag{5.47}$$

$$\hat{T}_t = T_t / (\varepsilon / \gamma). \tag{5.48}$$

For illustration, let us assume that momentum loss increases as T_t decreases, according to the arbitrary, but convenient prescription:

$$f_{\text{mom}} = \begin{cases} \hat{T}_t / 3 & \text{for } \hat{T}_t \leq 3 \\ 1 & \text{for } \hat{T}_t > 3. \end{cases} \tag{5.49}$$

One can then calculate $\hat{\Gamma}_t(\hat{q}_\parallel)$, figure 5.18, which shows that 'starving the SOL for power', i.e. reducing $q_\parallel$ for fixed L, n_u, etc, will then also drive down the particle flux to the target. This only happens, however, when a momentum-loss process is also present, $f_{\text{mom}} < 1$. Figure 5.18 includes the result for $f_{\text{mom}} = 1$, showing that in that case there is no drop in Γ_t as $q_\parallel$ is reduced. This effect is apparently a feature of divertor detachment, chapter 16. The foregoing simple assumptions still give a monotonic dependence of Γ_t on n_u, for fixed $q_\parallel$; if ε is also assumed to increase with decreasing T_t, however, then a non-monotonic $\Gamma_t(n_u)$ results.

It is illuminating to consider how the equilibrium values of T_t may be found by using a *graphical* method, since this will also demonstrate that the *lower branch solutions are unstable*, and therefore will not actually occur.

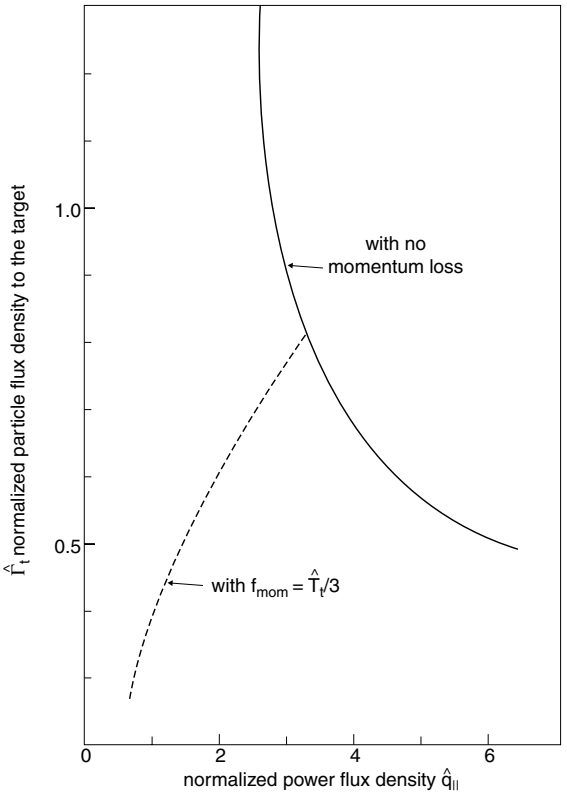

Figure 5.18. Two-point model including hydrogen recycling loss. The (normalized) particle flux density to the target increases with decreasing power flux into the SOL, unless momentum loss also occurs. Illustrated for a specific momentum-loss assumption, equation (5.49).

Problem 5.5. This is best illustrated by considering a concrete example: $q_{\|} = 120$ MW m^{-2}, $L = 50$ m, $n_u = 5 \times 10^{19}$ m^{-3}, D$^+$plasma. Show that this gives $T_u = 101$ eV, $F_u = 18.7$ eV. Show that from figure 5.13 we therefore anticipate a high temperature solution at $T_t \approx 10$ eV and a low temperature solution at $T_t \approx 1$ eV. One has enough information to also calculate $e\varepsilon\Gamma_t$ and q_t individually as functions of T_t; confirm that these are as given in figure 5.19. The only possible (equilibrium) solutions, of course, occur when the sum $e\varepsilon\Gamma_t + q_t$ equals the input $q_{\|}$. Show from figure 5.19 that this does indeed occur for $T_t \approx 10$ eV and ≈ 1 eV.

Now consider the system existing at the high temperature solution and that a positive perturbation to T_t occurs. This will temporarily increase the total power loss rate, $e\varepsilon\Gamma_t + q_t$, above the input $q_{\|}$, which is actually physically

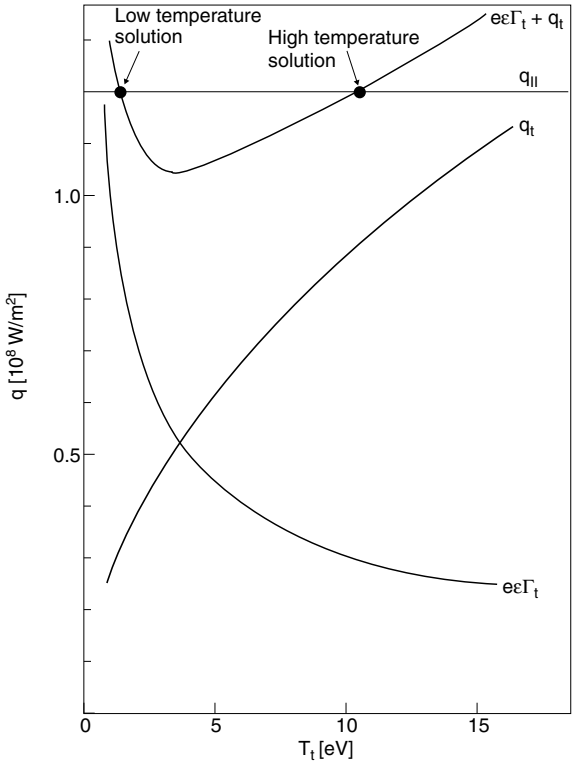

Figure 5.19. Two-point model including hydrogen recycling loss. Graphical procedure to find the two solutions that can exist for a given power input $q_{\parallel}$. The low temperature solution is unstable.

possible since—in a time-dependent situation—heat can be drawn from the divertor plasma by it *cooling down*. The high temperature solution is therefore *stable*. A negative temperature perturbation to the high temperature solution also experiences natural self-stabilization. By contrast, the low temperature solution is unstable: a negative temperature excursion *increases* the power loss, thus cooling the plasma further, and the situation runs away as a result of this positive feedback.

5.6 The Plasma-Wetted Area of Limiters and Divertors. The Parallel Flux Area of the SOL

It is important to distinguish between A_{wet}, the plasma-wetted area of the limiters and divertor targets, and $A_{\parallel}^{\text{SOL}}$, the cross-sectional area of the SOL perpendicular to $\boldsymbol{B}$, that defines the parallel heat flux density in the SOL (as well as other parallel flux densities). See figure 5.20(A).

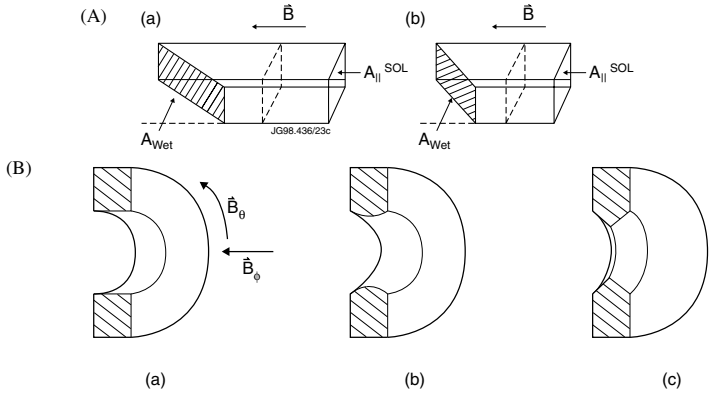

Figure 5.20. (A) For both (a) and (b) $A_{\parallel}^{\mathrm{SOL}}$ is the same but (a) has larger A_{wet}. (B) Poloidal ring limiters: (a) flat sided, (b) rounded, (c) bevelled. For (b) and (c) the plasma-wetted area is greater than for (a), thus better distributing the power load.

We start by considering a case of such artificial simplicity that in fact $A_{\mathrm{wet}} = A_{\parallel}^{\mathrm{SOL}}$: a tokamak of circular cross-section in the cylindrical approximation (i.e. the torus is 'unwound' to make a cylinder and no toroidal corrections are made) with a single poloidal flat-plate ring limiter and $q = \infty$, i.e. $B_\theta = 0$. The magnetic field lines strike the sides of the limiter at 90°. Then $A_{\mathrm{wet}} = A_{\parallel}^{\mathrm{SOL}} = 4\pi a\lambda$ where λ is the SOL scrape-off length; for $\lambda = \lambda_{q_\parallel}$ the areas are for power deposition, $A_{q_\parallel}$, while with λ_Γ they are for particle deposition, $A_{\Gamma\parallel}$, etc. Now for this same configuration, let q be finite so that the field lines strike the sides of the target at angle $\alpha = \tan^{-1}(B_\theta/B_\phi)$, figure 5.20(B(a)). Recall from section 2.10 that the plasma is not 'aware' of whether a SOL flux tube is terminated by a solid surface which is orthogonal to $\boldsymbol{B}$, or is at some finite angle. Thus, while A_{wet} remains as before, $A_{\parallel}^{\mathrm{SOL}}$ is now the *projected* area of A_{wet} perpendicular to $\boldsymbol{B}$, $A_{\parallel}^{\mathrm{SOL}} = 4\pi a\lambda\cos\alpha$. Of course, if B_θ/B_ϕ is small, as is usual, then $\cos\alpha \sim 1$ and this is not an important correction. Thus, for poloidal flat-plate ring limiters, $A_{\mathrm{wet}} \approx A_{\parallel}^{\mathrm{SOL}}$.

It is desirable, however, to spread the heat load over as large an area of solid surface as possible, i.e. to increase A_{wet}. Rather than use a flat plate for the poloidal ring limiter, one may *round* it, or *bevel* it, figure 5.20(B(b),(c)), so as to increase A_{wet}. For a bevel angle β, figure 1.38, A_{wet} is thus increased by the factor $(\sin\beta)^{-1}$, which could be made very large. Note, however that $A_{\parallel}^{\mathrm{SOL}}$ *is unchanged*.

Consider next a toroidal flat-plate ring limiter located at the outside of the torus at radius R_L. Now if $q = \infty$ there is no limiter action, but for q finite, all parts of the SOL contact this limiter. Thus $A_{\mathrm{wet}} = 4\pi R_L\lambda$ while $A_{\parallel}^{\mathrm{SOL}} = 4\pi R_L\lambda(B_\theta/B_\phi)$, figure 5.21. We may check these formulae by calculating the SOL volume two ways: $V_{\mathrm{SOL}} = \pi a A_{\mathrm{wet}} = L A_{\parallel}^{\mathrm{SOL}} = 2\pi a 2\pi R\lambda$. Let us now

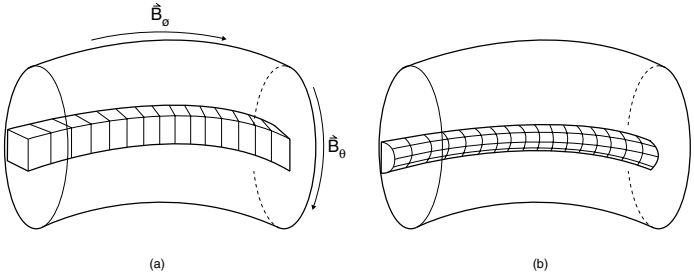

Figure 5.21. Toroidal ring limiters: (a) flat-sided, (b) rounded. The latter has increased plasma-wetted area.

bevel the toroidal limiter, which also increases A_{wet} by the factor $(\sin\beta)^{-1}$ but leaves $A_{\parallel}^{\text{SOL}}$ unchanged. On JET such 'toroidal belt limiters' [5.23] achieved plasma-wetted areas of more than 1 m^2.

Consider next the *wall limiter* where the inner wall, for example, may be shaped to match the curvature of the flux surfaces closely, figure 5.5. Consider the simple case of the inner wall being a straight vertical cylinder of major radius R_s, figure 5.22. Let a be the radius of the magnetic flux surface which is tangential to the inner wall at the mid-plane, i.e. a is the minor radius of the plasma since this point of contact with the inner wall defines the LCFS. The flux surface of radius $a+\lambda$ cuts the inner wall at $z \approx \pm(2a\lambda)^{1/2}$, thus making $A_{\text{wet}} = 2(2a\lambda)^{1/2}2\pi R_s$. For all toroidally symmetrical limiters or divertor targets, the value of $A_{\parallel}^{\text{SOL}}$ is essentially the same, here $A_{\parallel}^{\text{SOL}} \approx 4\pi R_s\lambda(B_\theta/B)$. When the inner wall has a compound curvature, with radius in the poloidal plane $a_w \gtrsim a$ then the foregoing expression for A_{wet} is changed somewhat, figure 5.5. Inner wall limiters on JET and TFTR achieved quite large values of $A_{\text{wet}} \approx 5$ m^2 [5.6].

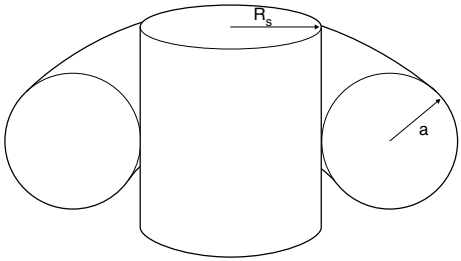

Figure 5.22. An (inner) wall limiter can have particularly large plasma-wetted area.

It should be noted that the flux densities actually *deposited* on limiters with curved surfaces (and the wall limiter even without double curvature) do not fall off in a simple exponential way, even if the parallel flux density decays strictly

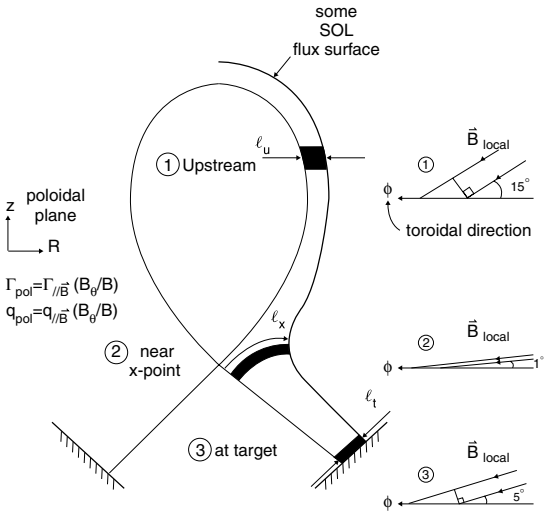

Figure 5.23. Poloidal cross-section of the SOL magnetics for a poloidal divertor. The cross-sectional *shape* of a magnetic flux bundle, in black, changes greatly following the flux line from upstream to X-point to target. The cross-sectional *area* of the flux bundle, however, changes much less and it is often assumed to be constant.

exponentially. If fluxes reach the surface purely as the result of parallel motion, then the deposited flux density at the LCFS for a curved limiter must be zero since the solid surface at that point is exactly tangential to $\boldsymbol{B}$. In experiments, however, fluxes are observed to be incident at such locations. This matter is discussed further in section 25.2.

We now turn to the poloidal divertor—with a toroidally symmetrical target system. The variation of B_θ/B along SOL flux tubes is so great that it is necessary to account for it, even for first estimates. For example, at the outside mid-plane, B_θ/B might be $1/3$ or even larger, while near the X-point, $B_\theta/B \rightarrow 0$; it then increases back to perhaps $\sim 1/10$ at the targets. The total magnetic field strength varies much less, $B \propto R^{-1}$ [5.24], and so the cross-sectional area $A_\parallel^{\mathrm{SOL}}$ of any specific SOL flux tube, i.e. magnetic flux bundle, does not vary too greatly along the SOL, $A_\parallel^{\mathrm{SOL}} \propto B^{-1} \propto R$. The greatest variation in $A_\parallel^{\mathrm{SOL}}$ is from inside to outside mid-plane, a factor of ~ 2 for JET, for example, where $a/R \sim 1/3$. For simple modelling of the SOL, however, one considers one half of the SOL, and so the variation of $A_\parallel^{\mathrm{SOL}}$ is small. Here we ignore such variation.

What *does* change very substantially, however, is the cross-sectional *shape* of the flux tube for different locations along the SOL. Let us picture a flux tube with square cross-section at the outside midplane, figure 5.23. We take $B_\theta/B \approx 1/4$ for illustration. By the time this tube has reached the X-point region, it has become wide and thin in cross-section: the poloidal flux surfaces have become

well separated due to the weak B_θ near the X-point, so in order that $A_\parallel^{\mathrm{SOL}}$ may remain approximately constant, the cross-sectional shape has become wide and thin. Right on the separatrix $B/B_\theta \to \infty$ at the X-point, in principle, but a few mm out, a value of 20 might be representative. By the point where the flux tube reaches the target, then perhaps $B_\theta/B \sim 1/10$ and so the cross-sectional area is less elongated and thin than near the X-point, but more so than at the mid-plane. (What is not shown in figure 5.23 is the effect of *magnetic shear*: since L decreases across the SOL, an initially square cross-sectional shape does not remain even rectangular, but it experiences a shear distortion into a parallelogram, approximately; $A_\parallel^{\mathrm{SOL}}$, however, still remains approximately constant.)

We thus have that the width of the flux tube in the poloidal plane, ℓ, measured 'radially', varies as:

$$\ell(B_\theta/B) \approx \text{constant} \tag{5.50}$$

since the width (in the orthogonal direction, within the poloidal plane) varies as B/B_θ and we are taking $A_\parallel^{\mathrm{SOL}} = \text{constant}$. Thus:

$$\boxed{A_\parallel^{\mathrm{SOL}} \approx 4\pi R\lambda_u(B_\theta/B)_u \approx 4\pi R\lambda_t(B_\theta/B)_t.} \tag{5.51}$$

We can then define the *flux expansion* as:

$$\boxed{\text{flux expansion} \equiv \frac{\ell_t}{\ell_u} \equiv \frac{\lambda_t}{\lambda_u} \simeq \frac{(B_\theta/B)_u}{(B_\theta/B)_t}.} \tag{5.52}$$

Thus, if the targets are orthogonal to the flux surfaces as projected in the poloidal plane (which means, of course, that they are already rather oblique to $\boldsymbol{B}$ because $|B_\phi| \gg |B_\theta|$, typically), then A_{wet} is greater than $A_\parallel^{\mathrm{SOL}}$ by the factor (B_θ/B) since:

$$A_{\mathrm{wet}} \approx 4\pi R \cdot \lambda_t. \tag{5.53}$$

For the above example, this would make $A_{\mathrm{wet}}/A_\parallel^{\mathrm{SOL}} \approx 10$. In order to further A_{wet} increase, the targets may be slanted at an oblique angle β relative even to the flux surfaces as projected in the poloidal plane, figure 5.24, thus reducing the angle between $\boldsymbol{B}$ and the tangent to the target surface to $\lesssim 1°$, and increasing the ratio of $A_{\mathrm{wet}}/A_\parallel^{\mathrm{SOL}}$ to perhaps 100. There are practical limitations to proceeding further, however, related to divertor target tile edges.

In order to accommodate thermal expansion of the target structure, the target is usually constructed of separate tiles. This also facilitates target installation and replacement. At small glancing angles of $\boldsymbol{B}$ the exposed tile edges will receive a large part of the total heat flux, figure 5.25(a). This heat is deposited on a small area and can result in damage. In order to protect the tile edges, the tiles can be tilted slightly so that each tile shields the edge of the next one, figure 5.25(b). This, however, reduces operational flexibility of the tokamak since the tilt angle is only ideal for one particular value of the magnetic pitch at the target, $(B_\theta/B)_t$. For larger $(B_\theta/B)_t$ the tile edges are again exposed, while

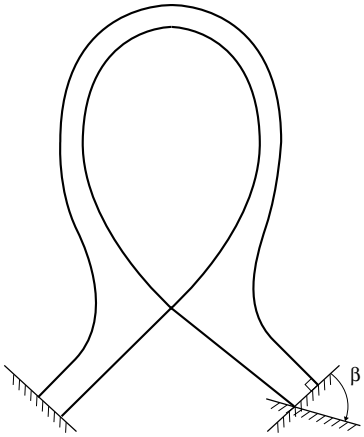

Figure 5.24. Non-orthogonal divertor targets increase the plasma-wetted area. The poloidal projection of the magnetic field is all that is seen in this figure, thus it is not apparent that $\boldsymbol{B}$ is already at a shallow angle to the surface, even for $\beta = 0$. Increasing β makes the angle of incidence yet smaller.

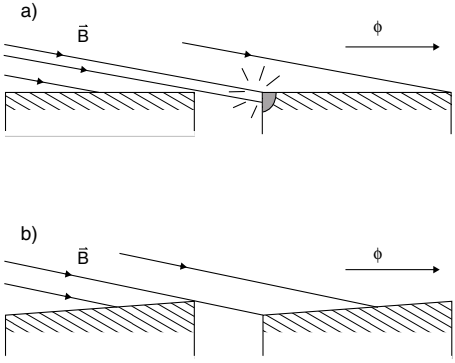

Figure 5.25. By employing a 'ski-slope' design of the target tiles, (b), over-heating of exposed tile corners can be avoided, (a). ϕ is the toroidal direction.

for smaller $(B_\theta/B)_t$, shadows are created on the tile front faces, which reduces $A_{\rm wet}$ and thus necessarily raises q_t on the loaded surfaces. Also operation of the tokamak with reversed direction of B_ϕ or I_ϕ is not possible, reducing operational flexibility.

Large increases in $A_{\rm wet}/A_\parallel^{\rm SOL}$ are possibly necessary since $q_\parallel$ can exceed 10^9 W m^{-2} for reactor conditions. Limitations of heat-transfer technology make heat removal at levels above $\sim$ 5 MW m^{-2} problematical. (For comparison, the heat flux for the interior of a rocket nozzle is about 1 MW m^{-2} and for a missile

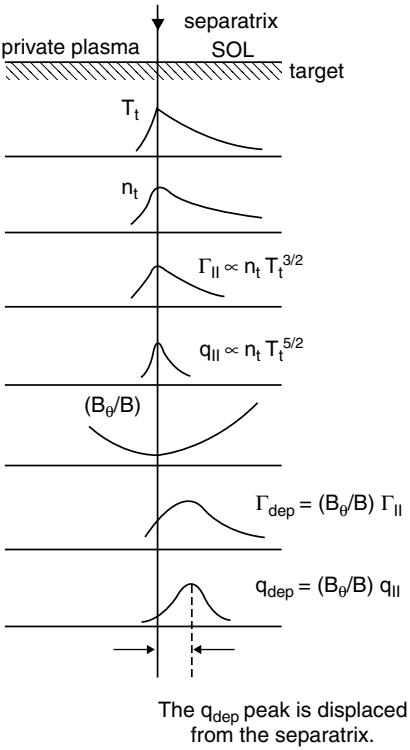

Figure 5.26. Even if *parallel* particle, $\Gamma_\parallel$, and heat, $q_\parallel$, fluxes peak at the separatrix, the *deposited* fluxes, $\Gamma_{\rm dep}$, $q_{\rm dep}$, may not do so due to strong variation of B_θ/B across the target. The latter occurs, for example, when the X-point-to-target distance is short [5.25].

nose cone during ballistic re-entry it is about 4 MW m^{-2}.) Assuming the example $R = 8$ m, that $\lambda_{qu} = 5 \times 10^{-3}$ m, $\lambda_{qt} = 5 \times 10^{-2}$ m, and $\lambda_{q_{\rm deposited}} = 0.5$ m, then $A_{\rm wet} \approx 50$ m^2, which for $P_{\rm SOL} = 150$ MW gives a tolerable $q_{\rm deposited} = 3$ MW m^{-2}.

Because $\Gamma_{\rm deposited}/\Gamma_\parallel = q_{\rm deposited}/q_\parallel \approx B_\theta/B$ (for the case of orthogonal targets), deposited flux densities do not necessarily peak at the separatrix, even if the parallel flux densities do [5.25]. For a 'deep divertor' with the targets far from the X-point, $B_\theta/B \approx$ constant with distance d_t across the target. For a 'shallow divertor', however, i.e. the X-point very close to the targets, B_θ/B is a strongly varying function of d_t, being small near the strike point and rising further out. When this variation is stronger than the radially decaying parallel flux densities, then the deposited flux densities peak at some distance away from the separatrix (strike point), figure 5.26.

5.7 Expressions for the Power Scrape-Off Width, etc

5.7.1 Introduction

The power scrape-off width $\lambda_{q_\parallel}$ is perhaps the most important parameter of the edge plasma. All our prescriptions thus far have been expressed in terms of $q_\parallel$. We wish to use $P_{\rm SOL}$, instead, since this is much closer to being a true control variable. That requires relating $\lambda_{q_\parallel}$ to the control variables, n_u, $P_{\rm SOL}$, L, and to $\chi_\perp$, etc. Assuming that $P_{\rm SOL}$ [W] enters the SOL entirely via perpendicular conduction then:

$$\boxed{P_{\rm SOL} \approx A_\perp n_u \chi_\perp k T_u / \lambda_{T_u}} \tag{5.54}$$

where $K_\perp \equiv n_u \chi_\perp$ is the anomalous heat conduction coefficient; $A_\perp$ is the surface area of the LCFS from X-point to X-point; $A_\perp \simeq 2\pi R 2\pi a \kappa^{1/2}$, where κ is the plasma elongation, $\kappa = b/a$. (Elliptic poloidal shape with $a =$ horizontal minor radius, and $b =$ vertical; hereafter the κ is absorbed into a, converting it into an effective minor radius.) It has been assumed that $q_{\perp\rm cond}$ occurs uniformly over area $A_\perp$. It should be noted that now n_u designates $n_u^{\rm sep}$ specifically, and *not* some radially averaged density—which was one of the possible interpretations of the two-point model expressed in terms of $q_\parallel$, section 5.2. *Throughout the present section, n_u generally means $n_u^{\rm sep}$.*

Equation (5.54) identifies a problem: if $A_\perp$, n_u, $\chi_\perp$, T_u, are fixed, then as $P_{\rm SOL}$ is raised, λ_{T_u} decreases. From equation (5.7) we have the important relation between power decay length and temperature decay length for the conduction-limited regime:

$$\boxed{\lambda_{q_\parallel} = \tfrac{2}{7}\lambda_T.} \tag{5.55}$$

Thus $\lambda_{q_\parallel}$ will also decrease as $P_{\rm SOL}$ increases and we have $q_\parallel \propto P_{\rm SOL}/\lambda_{q_\parallel} \propto P_{\rm SOL}/\lambda_{T_u} \propto P_{\rm SOL}^2$, i.e. *$q_\parallel$ will grow even faster than $P_{\rm SOL}$*. This is clearly a concern. We note, however, that n_u, $\chi_\perp$ and T_u are not necessarily constant and in the following we will take that into consideration. Nevertheless, the final conclusion is that there is a tendency for $q_\parallel$ to increase at least as fast as $P_{\rm SOL}$.

5.7.2 Case of Negligible Parallel T-Gradient

We start by considering the case of weak parallel gradients . Then instead of equation (5.55), we have, section 4.4:

$$\lambda_{q_\parallel} = \left(\lambda_n^{-1} + \tfrac{3}{2}\lambda_T^{-1}\right)^{-1}. \tag{5.56}$$

For simplicity take $\lambda_n \sim \lambda_T$, thus:

$$\lambda_{q_\parallel} \simeq \tfrac{2}{5}\lambda_T. \tag{5.57}$$

We also have:

$$P_{\mathrm{SOL}} = \tfrac{1}{2}\gamma n c_s k T A_{\|q}^{\mathrm{SOL}} \tag{5.58}$$

$$A_{\|q}^{\mathrm{SOL}} = 4\pi R \lambda_{q_\|} (B_\theta / B)_u \tag{5.59}$$

which when combined with equations (5.54) and (5.57) gives:

$$\lambda_{q_\|} = \frac{\left(\frac{2}{5} n \chi_\perp e A_\perp\right)^{3/5}}{P_{\mathrm{SOL}}^{1/5} [(2e/m_i)^{1/2} \gamma e n 2\pi R (B_\theta / B)_u]^{2/5}}. \tag{5.60}$$

One can then express $q_\|$ similarly, using equation (5.59), and also the deposited power flux density q_{dep}, using the flux expansion and $\cos\beta$. For the case of negligible T-gradients, the decrease of $\lambda_{q_\|}$ with increasing P_{SOL} is fortunately quite weak. Indeed the dependence of $\lambda_{q_\|}$ on all parameters is rather weak. Of course, it must be kept in mind that $\chi_\perp$ is anomalous and may turn out to be correlated with P_{SOL} or other variables. One can also extract the temperature from these same equations:

$$T = (2P_{\mathrm{SOL}}/(2e/m_i)^{1/2} \gamma n e 4\pi R (B_\theta / B)_u \lambda_{q_\|})^{2/3}. \tag{5.61}$$

One notes, as earlier, equation (4.114), that the 'dilution cooling' effect, $T \propto n^{-2/3}$, is much weaker than for the case with T-gradients, where $T_t \propto n_u^{-2}$, equation (5.10). The 'dilution cooling' is also weaker than was found for the limiter case, section 4.5, equation (4.39), where $T \propto \bar{n}^{-2}$ was also found; there, although there were also no T-gradients, the fact that the ionization occurred inside the LCFS caused a fortuitous similarity with the case of a divertor with T-gradients.

Problem 5.6. For the JET-size example $P_{\mathrm{SOL}} = 10$ MW, $n_u = 10^{19}$ m^{-3}, $\chi_\perp = 2$ m^2 s^{-1}, $A_\perp = 200$ m^2, $R = 3$ m, $(B_\theta/B)_u = 0.3$, D$^+$ plasma, show that $\lambda_{q_\|} \approx 5$ mm, $A_{q_\|}^{\mathrm{SOL}} \approx 0.06$ m^2, $T_u \simeq 200$ eV, $q_\| \approx 170$ MW m^{-2}.

This would clearly be an unsatisfactory divertor characterized by both sputtering and melting problems. One notes the unfortunate tendency for $\lambda_{q_\|}$ to be very small. It is disappointing that a large device, with such a huge area potentially available for power removal, $A_\perp \approx 200$ m^2, only utilizes such a tiny area: even multiplying $A_{q_\|}^{\mathrm{SOL}}$ by the flux expansion, and by a further factor allowing for non-orthogonal targets, still tends to result in $A_{\mathrm{wet}} \leq 1$ m^2.

5.7.3 Case of Significant Parallel T-Gradient

We turn now to the case of greatest practical interest, that of significant temperature gradients along the SOL, [5.16–5.20]. One can formulate an expression for $\lambda_{q_\|}$ in various equivalent ways.

(a) *First method*. From the general behaviour of diffusive transport:

$$\lambda_{q_\parallel} \approx (\chi_\perp \tau_E^{\mathrm{SOL}})^{1/2}. \tag{5.62}$$

We estimate τ_E^{SOL} from:

$$3\overline{nkT}_{\mathrm{SOL}} V_{\mathrm{SOL}}/\tau_E^{\mathrm{SOL}} = P_{\mathrm{SOL}} \tag{5.63}$$

with:

$$V_{\mathrm{SOL}} = L A_\parallel^{\mathrm{SOL}}. \tag{5.64}$$

From pressure balance:

$$\overline{nkT}_{\mathrm{SOL}} \approx n_u k T_u. \tag{5.65}$$

Thus:

$$\lambda_{q_\parallel} \approx (3\chi_\perp n_u k T_u L A_{q_\parallel}^{\mathrm{SOL}}/P_{\mathrm{SOL}})^{1/2} \tag{5.66}$$

and we may use

$$T_u \simeq \left(\frac{7}{2}\frac{P_{\mathrm{SOL}}}{A_{q_\parallel}^{\mathrm{SOL}}}\frac{L}{\kappa_{0e}}\right)^{2/7} \tag{5.67}$$

to eliminate T_u from equation (5.66). We can also eliminate $A_{q_\parallel}^{\mathrm{SOL}}$ using equation (5.59). This gives an expression for $\lambda_{q_\parallel}(n_u, \chi_\perp, P_{\mathrm{SOL}}, L, R, (B_\theta/B)_u)$, see below.

(b) *Second method*. From power conservation we have

$$\frac{\mathrm{d}q_\perp}{\mathrm{d}s_\perp} \simeq -\frac{\mathrm{d}q_\parallel}{\mathrm{d}s_\parallel} \tag{5.68}$$

and with $q_\perp = -K_\perp \mathrm{d}T/\mathrm{d}s_\perp$, $q_\parallel = -K_\parallel \mathrm{d}T/\mathrm{d}s_\parallel$ one has:

$$\lambda_{q_\parallel} \simeq (K_\perp/K_\parallel)^{1/2} L. \tag{5.69}$$

Using

$$K_\perp = e n_u \chi_\perp \tag{5.70}$$

for T [eV], and

$$K_\parallel = \kappa_{0e} T_u^{5/2} \tag{5.71}$$

one finds essentially the same expression as equation (5.66). Note also the useful approximate result from equation (5.69):

$$\boxed{\lambda_{q_\parallel} \simeq (e n_u \chi_\perp/\kappa_{0e} T_u^{5/2})^{1/2} L.} \tag{5.72}$$

(c) *Third method*. We combine equation (5.7):

$$T_u \simeq \left(\frac{7}{2}\frac{P_{\mathrm{SOL}}}{A_{q_\parallel}^{\mathrm{SOL}}}\frac{L}{\kappa_0}\right)^{2/7} \tag{5.73}$$

with the relation for decay lengths derived from this:

$$\lambda_{q_\parallel} = \tfrac{2}{7}\lambda_{T_u}. \tag{5.74}$$

and:

$$A^{\mathrm{SOL}}_{q_\parallel} = 4\pi R\lambda_{q_\parallel}(B_\theta/B)_u \tag{5.75}$$

also:

$$P_{\mathrm{SOL}} = n_u \chi^{\mathrm{SOL}}_\perp k T_u A_\perp/\lambda_{T_u}. \tag{5.76}$$

Note that we are taking a *single* location along the separatrix—i.e. the 'upstream' point—as being representative of the perpendicular power flux density for the *entire* LCFS area $A_\perp$. Although one could choose point 'u' to be half way from target to target, it is more standard to take 'u' as being at the midplane. Since there is little variation of $T(s_\parallel)$, etc along the upper length of the flux tube, see figure 4.17, there is little error in doing this. The reason for favouring the midplane is that the magnetic flux surfaces are generally closest together there and, thus, if $\chi^{\mathrm{SOL}}_\perp$ is spatially constant, this is where most of the power enters the SOL. It would therefore be a good choice for 'u' when assuming all power enters at the 'upstream end' (and one would then simply take the region from the midplane to the top to be at essentially constant T and n). Sometimes, however, it is hypothesized that the (anomalous) $\chi^{\mathrm{SOL}}_\perp$ varies proportionately to the separation of the flux surfaces in the poloidal plane, i.e. $\chi^{\mathrm{SOL}}_\perp \propto B_\theta$. In that case, power enters virtually uniformly along the separatrix, X-point to X-point, and the choice of midplane as the representative location is as good as any. One would be better to use equation (4.91) in place of equation (5.7) in that case, but the effect is clearly small.

In proceeding to combine equations (5.7), (5.74) and (5.75) we need to make a decision about whether or not to attempt to relate $(B_\theta/B)_u$ to L. If we make the *circular tokamak* assumption then we may use:

$$q \approx \frac{a}{R}\frac{B}{B_\theta} \tag{1.1}$$

and

$$L \approx \pi R q \tag{1.7}$$

to replace $(B/B_\theta)_u$ with either L or q, the *safety factor* (note: q is *not* the power flux density here!). This makes for more convenient expressions and such formulae are given below for $\lambda_{q_\parallel}$, etc. Unfortunately, for the typical divertor geometry this can introduce substantial errors, particularly for $q_\parallel$ and for the target region quantities such as T_t, etc. Generally $(B_\theta/B)_u$ is substantially larger than the circular tokamak expressions would imply $((B_\theta/B)^{\mathrm{circular}}_u = a\pi/L)$ and this can significantly underestimate the size of $A^{\mathrm{SOL}}_{q_\parallel}$. It is better therefore to retain both L and $(B_\theta/B)_u$, which can be

obtained from magnetics calculations for each tokamak discharge of interest. In the following therefore we list three alternative expressions for each quantity such as $\lambda_{q\|}$, namely, in terms of (a) q, (b) L or (c) L and $(B_\theta/B)_u$. The last one is preferred.

For ***power decay length*** $\boldsymbol{\lambda_{q\|}}$:

(a)

$$\lambda_{q\|} = \left(\frac{7}{8}\right)^{2/9}\left(\frac{8\pi^2}{7}\right)^{7/9}(en_u^{\rm sep}\chi_\perp^{\rm SOL})^{7/9}P_{\rm SOL}^{-5/9}\kappa_0^{-2/9}q^{4/9}Ra^{5/9} \qquad (5.77)$$

(b)

$$\lambda_{q\|} = \left(\frac{8\pi^2}{7}\right)^{5/9}(en_u^{\rm sep}\chi_\perp^{\rm SOL})^{7/9}P_{\rm SOL}^{-5/9}\kappa_0^{-2/9}L^{4/9}(aR)^{5/9} \qquad (5.78)$$

(c)

$$\lambda_{q\|} = \frac{8^{5/9}\pi^{4/3}}{7^{5/9}}(en_u^{\rm sep}\chi_\perp^{\rm SOL})^{7/9}P_{\rm SOL}^{-5/9}\kappa_0^{-2/9}L^{2/9}(B_\theta/B)_u^{-2/9}a^{7/9}R^{5/9}. \qquad (5.79)$$

As an example: equation (5.77) is obtained by (i) combining (5.73) and (5.76) to eliminate T_u, (ii) using (5.74) to convert λ_{T_u} to $\lambda_{q\|}$, (iii) using $A_\perp = 2\pi R 2\pi a$, $L = \pi Rq$, and $(B_\theta/B)_u = a\pi/L$. It is readily shown that these results are essentially the same as from the first two methods. The expressions can be applied separately to electrons and ions, or combined when equipartition is strong.

Problem 5.7. For a JET-size example: $P_{\rm SOL}^e = 5$ MW, $n_u = 2\times10^{19}$ m^{-3}, $\chi_\perp^{\rm SOL} = 4$ m^2 s^{-1}, $R = 3$ m, $L = 50$ m, $a = 1.5$ m, $(B_\theta/B)_u = 0.3$, use the (c) formulation to show that: $\lambda_{q\|e} = 10$ mm, $A_{q\|e}^{\rm SOL} = 0.11$ m^2, $q_{\|e} = 44$ MW m^{-2}. Using the results of section 4.10.2 show that one would therefore anticipate that this SOL would have a significant T_e-gradient.

Next use the (b) formulation to show that $\lambda_{q\|e} = 13$ mm, $A_{q\|e}^{\rm SOL} = 0.046$ m^2, $q_{\|e} = 110$ MW m^{-2}. Note how much smaller $A_{q\|e}^{\rm SOL}$ is with formulation (b). (It is necessary consistently to replace $(B_\theta/B)_u$ with $a\pi/L$ in all expressions, including that for $A_{q\|e}^{\rm SOL}$ which becomes $A_{q\|e}^{\rm SOL} = 4\pi^2 aR\lambda_{q\|e}/L$.) Show that using the (b) formulation that one would *not* expect to find a significant T_e-gradient. Comment.

Note: These expressions for $\lambda_{q\|e}$—and the ones below for T_u, $q_{\|e}$, T_t, etc—are for a *single-null* divertor where $P_{\rm SOL}$, the total power into the SOL, goes equally to the two targets.

Problem 5.8. For analysis of each divertor leg *separately*, for a single-null divertor $P_{\rm SOL}$ is re-defined to be the power input to the one leg; argue that one also changes to: $A_\perp = \frac{1}{2}2\pi a 2\pi R$ and $A^{\rm SOL}_{q\parallel} = 2\pi R\lambda_{q_\parallel}(B_\theta/B)_u$; argue that one still uses $L \approx \pi Rq$ and $(B_\theta/B)^{\rm circular}_u = a\pi/L$.

For analysis of each divertor leg *separately*, for a *double-null* divertor, $P_{\rm SOL}$ is also re-defined to be the power input to one leg; argue that one then also uses: $L \approx \frac{1}{2}\pi Rq$, $(B_\theta/B)^{\rm circular}_u = a\pi/2L$, $A^{\rm SOL}_{q\parallel} = 2\pi R\lambda_{q_\parallel}(B_\theta/B)_u$ and $A_\perp = \frac{1}{4}2\pi a 2\pi R$.

The expressions for $\lambda_{q_\parallel}$, T_u, etc are then re-calculated in a straightforward way and only the numerical factors change. Find the numerical factors for the two cases for equation (5.77). These considerations also apply to the case of negligible parallel T-gradients, section 5.7.2.

A number of observations may be made about these key expressions for the power width. First, however, it is important to note that since $\chi^{\rm SOL}_\perp$ is anomalous, it may well be correlated with n_u, $P_{\rm SOL}$, etc, and so these expressions should *not* be taken to guarantee, for example, that $\lambda_q \propto n_u^{7/9}$, etc. However *if* $\chi^{\rm SOL}_\perp$ is a constant then a number of important conclusions follow:

(1) $\lambda_q \propto P_{\rm SOL}^{-5/9}$. This is unfortunate, as it means that the power flux density will increase even faster than the SOL power itself. This may be a rather robust dependence since it is due to the simple and basic point already made in the discussion following equation (5.54), namely that the principal way the SOL handles extra power is by reducing λ_T.

(2) $\lambda_q \propto L^{4/9}$, so it is helpful to increase connection lengths. The dependence is about the same as for the simple SOL, section 4.3, where $\lambda \propto L^{1/2}$.

(3) If electrons and ions are thermally de-coupled upstream—a common situation, section 4.11—then we may apply these relations to them separately. Unfortunately, little is known about the power split entering the SOL, but if $P^e_{\rm SOL} \approx P^i_{\rm SOL}$, and if $\chi^{{\rm SOL}e}_\perp \approx \chi^{{\rm SOL}i}_\perp$ then $\lambda_{q\parallel e}/\lambda_{q\parallel i} \approx (\kappa_{0i}/\kappa_{0e})^{-2/9} \approx (60/2000)^{-2/9} \approx 2.2$. That is, the ion power may be less concentrated than the electron power. This may be one explanation of the experimental observation that power profiles are not always single exponentials.

(4) With regard to the comparison of tokamaks of different sizes: for the same $P_{\rm SOL}$, 'bigger is better', i.e. λ_q is bigger; specifically $\lambda_q \propto Ra^{5/9}$. However, it is presumably also the case that $P_{\rm SOL} \propto$ volume $\propto Ra^2$ in which case $\lambda_q \propto R^{4/9}a^{-5/9}$, and so size would have little effect.

(5) Increasing density is helpful, $\lambda_q \propto n_u^{7/9}$; however, the above caveat is noted: $\chi^{\rm SOL}_\perp$ may itself depend on n_u. One usually wants the highest possible n_u, $\bar{n}_e$ in order to increase fusion power.

(6) From measurements of $\lambda_{T_u}\left(= \frac{7}{2}\lambda_{qu}\right)$ it is possible, in principle, to extract $\chi^{\rm SOL}_\perp$ from experimental data using the above expressions, or proceeding equivalently, chapters 20, 21.

In section 5.2 we obtained expressions for T_u, T_t, etc, but in terms of $q_\parallel$ rather than the true control variable $P_{\rm SOL}$. Now that we have λ_q in terms of $P_{\rm SOL}$, we may express T_u, etc on the same basis.

It is to be noted that, just as n_u represents $n_u^{\rm sep}$ here, so the following expressions for T_u, $q_{\parallel u}$, T_t, n_t, Γ_t represent values *at the separatrix*. In the simplest situations these are also the *peak* values in the SOL.

(1) ***Upstream temperature T_u.***

(a)
$$T_u = \left(\left(\frac{7}{8\pi}\right)^2 \frac{P_{\rm SOL}^2 q^2}{e n_u^{\rm sep} \chi_\perp^{\rm SOL} \kappa_0 a^2}\right)^{2/9} \tag{5.80}$$

(b)
$$T_u = \left(\left(\frac{7}{8\pi^2}\right)^2 \frac{P_{\rm SOL}^2 L^2}{e n_u^{\rm sep} \chi_\perp^{\rm SOL} \kappa_0 a^2 R^2}\right)^{2/9} \tag{5.81}$$

(c)
$$T_u = \left(\left(\frac{7^2}{8^2\pi^3}\right) \frac{P_{\rm SOL}^2 L}{e n_u^{\rm sep} \chi_\perp^{\rm SOL} \kappa_0 a R^2 (B_\theta/B)_u}\right)^{2/9}. \tag{5.82}$$

As before, T_u is weakly dependant on all variables.

Problem 5.9. For the same JET-size example as above show $T_u = 76$ eV from equation (5.82).

---

(2) ***Parallel power flux density $q_\parallel$.***

(a)
$$q_\parallel = 7^{5/9} 8^{-11/9} \pi^{-23/9} \left(\frac{P_{\rm SOL}^2}{e n_u^{\rm sep} \chi_\perp^{\rm SOL}}\right)^{7/9} \frac{q^{5/9} \kappa_0^{2/9}}{a^{14/9} R} \tag{5.83}$$

(b)
$$q_\parallel = 7^{5/9} 8^{-11/9} \pi^{-28/9} \left(\frac{P_{\rm SOL}^2}{e n_u^{\rm sep} \chi_\perp^{\rm SOL}}\right)^{7/9} \frac{L^{5/9} \kappa_0^{2/9}}{(aR)^{14/9}} \tag{5.84}$$

(c)
$$q_\parallel = 7^{5/9} 8^{-11/9} \pi^{-7/3} \left(\frac{P_{\rm SOL}^2}{e n_u^{\rm sep} \chi_\perp^{\rm SOL}}\right)^{7/9} \frac{\kappa_0^{2/9}}{L^{2/9} (B_\theta/B)_u^{7/9} R^{14/9} a^{7/9}}. \tag{5.85}$$

The leading numerical factors above are: 0.0125, 0.006 59, 0.0161. The same JET-size example gives 44 MW m^{-2} from equation (5.85). We note that $q_\parallel \propto\sim P_{\rm SOL}^{3/2}$ which shows, unfortunately, that the power flux density does tend to increase faster than the SOL power itself (assuming $\chi_\perp^{\rm SOL}$ constant). Roughly $q_\parallel \propto (n_u \chi_\perp^{\rm SOL})^{-1}$, so that increasing density is helpful,

as also is increased cross-field transport, $\chi_\perp^{\rm SOL}$. Also $q_\parallel \propto\sim L^{1/2}$, so that longer connection lengths are helpful. As to dependence on machine size, assuming $P_{\rm SOL} \propto Ra^2$, then $q_\parallel \propto R^{5/9}a^{14/9} \propto (\text{size})^2$, approximately, which is unfortunate.

(3) ***The power flux density deposited on the target***. The power flux density deposited on the target, assuming no volumetric power losses in the SOL and no heat transport from the SOL into the private plasma, is:

$$q_{\rm dep} = P_{\rm SOL}/A_{\rm wet} = \cos\beta \frac{(B_\theta/B)_t}{(B_\theta/B)_u}(B_\theta/B)_u q_\parallel. \tag{5.86}$$

where we have included the $\cos\beta$ factor to allow for a possible tilt of the targets relative to $\boldsymbol{B}_\theta$ ('non-orthogonal targets'), figure 5.24. One also notes that $q_{\rm dep}$ is increased relative to $q_\parallel$ by the inverse of the flux expansion, equation (5.52). Thus:

(a)

$$q_{\rm dep} = \cos\beta \frac{(B_\theta/B)_t}{(B_\theta/B)_u} 7^{5/9}8^{-11/9}\pi^{-23/9}\left(\frac{P_{\rm SOL}^2}{en_u^{\rm sep}\chi_\perp^{\rm SOL}}\right)^{7/9}\frac{\kappa_0^{2/9}}{q^{4/9}a^{5/9}R^2} \tag{5.87}$$

(b)

$$q_{\rm dep} = \cos\beta \frac{(B_\theta/B)_t}{(B_\theta/B)_u} 7^{5/9}8^{-11/9}\pi^{-26/9}\left(\frac{P_{\rm SOL}^2}{en_u^{\rm sep}\chi_\perp^{\rm SOL}}\right)^{7/9}\frac{\kappa_0^{2/9}}{L^{4/9}a^{5/9}R^{14/9}} \tag{5.88}$$

(c)

$$q_{\rm dep} = \cos\beta \frac{(B_\theta/B)_t}{(B_\theta/B)_u} 7^{5/9}8^{-11/9}\pi^{-7/3}\left(\frac{P_{\rm SOL}^2}{en_u^{\rm sep}\chi_\perp^{\rm SOL}}\right)^{7/9} \times \frac{\kappa_0^{2/9}(B_\theta/B)_u^{2/9}}{L^{2/9}R^{14/9}a^{7/9}}. \tag{5.89}$$

The leading numerical factors above are: 1.25×10^{-2}, 9.65×10^{-3}, 1.61×10^{-2}.

Problem 5.10. For the same JET-size example, and also assuming a flux expansion of 10, $\cos\beta = 1$ and $(B_\theta/B)_u = 1/4$ show for the (c) formulation that $q_{\rm dep}/q_\parallel = 0.025$ and $q_{\rm dep} = 1.1$ MW m^{-2}.

---

(4) ***Target temperature T_t***.

(a)

$$T_t = 2 \times 7^{2/9}8^{-14/9}\pi^{-38/9}\left(\frac{m_i}{\gamma^2 e^{37/9}}\right)\frac{P_{\rm SOL}^{20/9}q^{2/9}\kappa_0^{8/9}}{(n_u^{\rm sep})^{28/9}(\chi_\perp^{\rm SOL})^{10/9}a^{20/9}R^2} \tag{5.90}$$

(b)

$$T_t = 2 \times 7^{2/9} 8^{-14/9} \pi^{-40/9} \left(\frac{m_i}{\gamma^2 e^{37/9}} \right) \frac{P_{\rm SOL}^{20/9} L^{2/9} \kappa_0^{8/9}}{(n_u^{\rm sep})^{28/9} (\chi_\perp^{\rm SOL})^{10/9} (aR)^{20/9}} \tag{5.91}$$

(c)

$$T_t = 2 \times 7^{2/9} 8^{-14/9} \pi^{-10/3} \left(\frac{m_i}{\gamma^2 e^{37/9}} \right) \times \frac{P_{\rm SOL}^{20/9} \kappa_0^{8/9}}{(n_u^{\rm sep})^{28/9} (\chi_\perp^{\rm SOL})^{10/9} L^{8/9} (B_\theta / B)_u^{10/9} a^{10/9} R^{20/9}} \tag{5.92}$$

The leading numerical factors above are: 9.66×10^{-4}, 7.49×10^{-4}, 2.67×10^{-3}.

Problem 5.11. For the same example as above show for the (c) formulation that $T_t = 28$ eV for D^+ ions and $\gamma = 7$. Next use the (b) formulations to calculate T_u and T_t, thus showing that, as anticipated in problem 5.7, this formulation would predict very little T_e-variation along the SOL for these plasma conditions.

To a good approximation:

$$T_t \propto P_{\rm SOL}^2 / n_u^3 \tag{5.93}$$

and one may note that T_t is even more sensitive to control parameters when the effect on the power width is included; compare this to equation (5.10) which gave $T_t \propto q_\parallel^{10/7} / n_u^2$. One notes that it is particularly effective to raise the upstream density in order to reduce T_t and thus also target sputtering.

(4) ***Target density n_t.***

(a)

$$n_t = 2^{4/3} 7^{2/9} \pi^{34/9} \left(\frac{\gamma^2 e^{35/9}}{m_i} \right) \frac{(n_u^{\rm sep})^{35/9} q^{2/9} a^{16/9} (\chi_\perp^{\rm SOL})^{8/9} R^2}{P_{\rm SOL}^{16/9} \kappa_0^{10/9}} \tag{5.94}$$

(b)

$$n_t = 2^{4/3} 7^{2/9} \pi^{32/9} \left(\frac{\gamma^2 e^{35/9}}{m_i} \right) \frac{(n_u^{\rm sep})^{35/9} L^{2/9} (aR)^{16/9} (\chi_\perp^{\rm SOL})^{8/9}}{P_{\rm SOL}^{16/9} \kappa_0^{10/9}} \tag{5.95}$$

(c)

$$n_t = 2^{4/3} 7^{2/9} \pi^{8/3} \left(\frac{\gamma^2 e^{35/9}}{m_i} \right) \times \frac{(n_u^{\rm sep})^{35/9} L^{10/9} a^{8/9} R^{16/9} (\chi_\perp^{\rm SOL})^{8/9} (B_\theta / B)_u^{8/9}}{P_{\rm SOL}^{16/9} \kappa_0^{10/9}}. \tag{5.96}$$

The leading numerical factors above are: 293.3, 227.4, 82.2.

Problem 5.12. For the same example as above for the (c) formulation show that $n_t = 2.7 \times 10^{19}$ m^{-3} and confirm this answer using pressure balance directly.

Approximately,

$$n_t \propto n_u^4 / P_{\mathrm{SOL}}^{3/2} \tag{5.97}$$

and thus the target density is even more sensitive to the control parameters than T_t. The sensitivity has also increased compared with the result neglecting the variation in $\lambda_{q\parallel}$; compare equation (5.97) with equation (5.12) where $n_t \propto n_u^3 / q_\parallel^{8/7}$.

(6) ***Target particle flux density Γ_t. Recycle intensity.***

(a)

$$\Gamma_t = 7^{1/3}\pi^{5/3}\left(\frac{\gamma e^{7/3}}{m_i}\right)\frac{(n_u^{\mathrm{sep}})^{7/3} q^{1/3} a^{2/3} (\chi_\perp^{\mathrm{SOL}})^{1/3} R}{P_{\mathrm{SOL}}^{2/3}\kappa_0^{2/3}} \tag{5.98}$$

(b)

$$\Gamma_t = 7^{1/3}\pi^{4/3}\left(\frac{\gamma e^{7/3}}{m_i}\right)\frac{(n_u^{\mathrm{sep}})^{7/3} L^{1/3} (aR)^{2/3} (\chi_\perp^{\mathrm{SOL}})^{1/3}}{P_{\mathrm{SOL}}^{2/3}\kappa_0^{2/3}} \tag{5.99}$$

(c)

$$\Gamma_t = 7^{1/3}\pi\left(\frac{\gamma e^{7/3}}{m_i}\right)\left(\frac{(n_u^{\mathrm{sep}})^7 L^2 a R^2 \chi_\perp^{\mathrm{SOL}} (B_\theta/B)_u}{P_{\mathrm{SOL}}^2 \kappa_0^2}\right)^{1/3}. \tag{5.100}$$

Problem 5.13. For the above example use the (c) formulation to show that $\Gamma_t = 1.4 \times 10^{24}$ ion pairs m^{-2} s^{-1} and confirm the answer using the value of sound speed calculated for T_t from problem 5.11.

Approximately:

$$\Gamma_t \propto n_u^2 \tag{5.101}$$

which is about the same relation as when the variation of $\lambda_{q_\parallel}$ was not included, equation (5.14).

One may introduce, as in section 5.4, the same *correction factors*, f_{power} equation (5.18), f_{mom}, equation (5.20), and f_{cond}, equation (5.23). This introduces slightly different correction multiplying factors than found earlier when variations of $\lambda_{q_\parallel}$ were not included:

Quantity	Allowing for $\lambda_{q_\parallel}$ variation	Neglecting $\lambda_{q_\parallel}$ variation
$\lambda_{q_\parallel}$	$(f_{\rm cond})^{2/9}$	—
T_u	$(f_{\rm cond})^{2/9}$	$(f_{\rm cond})^{2/7}$
$q_\parallel, q_{\rm dep}$	$(f_{\rm cond})^{-2/9}$	—
T_t	$\dfrac{(1-f_{\rm power})^2}{f_{\rm mom}^2 f_{\rm cond}^{8/9}}$	$\dfrac{(1-f_{\rm power})^2}{f_{\rm mom}^2 f_{\rm cond}^{4/7}}$
n_t	$\dfrac{f_{\rm mom}^3 f_{\rm cond}^{10/9}}{(1-f_{\rm power})^2}$	$\dfrac{f_{\rm mom}^3 f_{\rm cond}^{6/7}}{(1-f_{\rm power})^2}$
Γ_t	$\dfrac{f_{\rm mom}^2 f_{\rm cond}^{2/3}}{(1-f_{\rm power})}$	$\dfrac{f_{\rm mom}^2 f_{\rm cond}^{4/7}}{(1-f_{\rm power})}$
T_u/T_t	$\dfrac{f_{\rm mom}^2 f_{\rm cond}^{10/9}}{(1-f_{\rm power})^2}$	$\dfrac{f_{\rm mom}^2 f_{\rm cond}^{6/7}}{(1-f_{\rm power})^2}$

The upstream quantities $\lambda_{q_\parallel}$, T_u, $q_\parallel$ remain robust while the target quantities are even more sensitive than before. The power width is perhaps the most critical edge quantity, owing to its great practical impact, and therefore its insensitivity to virtually all factors warrants further discussion. Note from equations (5.77) to (5.79) that $\lambda_{q_\parallel}$ depends only on *upstream* quantities—and is independent of the *volatility* which is characteristic of target quantities—as indicated by the foregoing table. The power width *entering* the divertor—even if volumetric losses are strong—is thus also robust, although in this case the power *reaching* the actual target is no longer a robust quantity. One positive consequence of this robustness is a useful simplification for our understanding of divertor behaviour. A serious negative consequence, that it is difficult to do anything about the power width, which given its tendency to being thin, is a major concern.

It may seem not only unfortunate but surprising that $\lambda_{q_\parallel}$ cannot be influenced by manipulation of target conditions, for example through the secondary electron emission coefficient of the target—which does influence power widths for the simple SOL, the sheath-limited regime: see equation (5.60) which indicates that $\lambda_{q_\parallel}$ is sensitive to the sheath transmission coefficient γ, which in turn is sensitive to secondary electron emission. Certainly we are free to write the power balance equation:

$$A_\perp n_u k T_u \chi_\perp / \lambda \approx 4\pi R \lambda \gamma (B/B_\theta)_t n k T_t c_{st} \tag{5.102}$$

where for simplicity we ignore here the fact that 'λ' on the RHS is λ_{T_u}, while 'λ' on the LHS is $\lambda_{q_\parallel}^{\rm target}$. Together with pressure balance, $n_u T_u = 2 n_t T_t$, this gives [5.20]:

$$\lambda_{q_\parallel} \propto \left(\frac{2 A_\perp \chi_\perp}{\gamma c_{st} 4\pi R} \right)^{1/2}. \tag{5.103}$$

From this equation it *appears* that $\lambda_{q_\parallel}$ is sensitive to target quantities, specifically γ, c_{st}. This is not true however, since it is *also* necessary to satisfy:

$$\tfrac{2}{7}T_u^{7/2}\kappa_0/L \approx \gamma n_t k T_t c_{st} \tag{5.104}$$

$$= \gamma c_{st}\tfrac{1}{2}n_u k T_u. \tag{5.105}$$

Since T_u, κ_0, L and n_u are essentially fixed, then so must be the product γc_{st}, and thus from equation (5.103) it is evident that one cannot influence $\lambda_{q_\parallel}$ by changing γ.

We thus see that in the conduction-limited regime, the sheath is indeed not a limiting factor—at least so far as the *upstream* quantities $q_\parallel$, $\lambda_{q_\parallel}$, T_u are concerned, and the sheath heat coefficient γ therefore does not appear in the expressions for these quantities. For *target* quantities, T_t, n_t, etc, the sheath does play a role and γ appears in the expressions for these quantities.

In section 4.11.3 we showed that significant T-drops occur ($T_u/T_t \geq 3$) when:

$$q_\parallel \leq 1.3 \times 10^{-28} n_u^{7/4} L^{3/4}. \tag{5.106}$$

The corresponding expression in terms of the true control valuable $P_{\rm SOL}$ is obtained by combining this equation with equation (5.82):

$$P_{\rm SOL} \leq 4.4 \times 10^{-27} n_u^{13/8} L^{5/8} [(B_\theta/B)_u R^2 a \chi_\perp^{\rm SOL}]^{1/2} \tag{5.107}$$

for P [MW], n [$\rm m^{-3}$], χ [$\rm m^2\,s^{-1}$], a, R, L [m]. The previous JET example gives 4.7 MW and recall that for the assumed $P_{\rm SOL}^e = 5$ MW it was found that $T_u/T_t = 76\ {\rm eV}/28\ {\rm eV} \approx 3$. Equation (5.107) was calculated using $\kappa_{0e} = 2000$; the numerical coefficient in equation (5.107) varies as $\kappa_0^{-1/7}$, thus making it slightly larger for ions.

When the $f_{\rm power}$ and the other corrections are included, then a multiplying factor:

$$\frac{f_{\rm mom}^{7/4} f_{\rm cond}^{35/36}}{(1 - f_{\rm power})^{7/4}} \approx \frac{f_{\rm mom}^2 f_{\rm cond}}{(1 - f_{\rm power})^2} \tag{5.108}$$

appears on the RHS of equation (5.107).

Volumetric power loss can be quite effective at changing the SOL from being sheath limited, $\nabla_\parallel T \sim 0$, over to one having a large T-drop, thus reducing problems at the target.

Problem 5.14. Consider an ITER-size example: $n_u = 3 \times 10^{19}$ $\rm m^{-3}$, $P_{\rm SOL}^e = 100$ MW, $\chi_\perp = 4\ \rm m^2\,s^{-1}$, $R = 8$ m, $a = 3$ m, $L = 100$ m, $(B_\theta/B)_u = 0.3$. Applying equation (5.107) show that $P_{\rm SOL}^e$ must be 53 MW for a significant T-drop to exist, so this SOL will be characterized by $\nabla_\parallel T \sim 0$. Next use equation (5.61) to show that $T_e \approx 150$ eV. Clearly sputtering will be extremely strong since ion impact energies will be of order 1 keV. Show that $q_{\parallel e} \approx 300\ \rm MW\ m^{-2}$ so that the angle between $\boldsymbol{B}$ and the target surface will have to be quite glancing, $\lesssim 1^\circ$, to avoid deposited heat loads exceeding 5 $\rm MW\ m^{-2}$.

We may conclude that the situation in problem 5.14 is probably not a practical divertor solution. One solution would be to raise the density. Let us also consider a different solution, namely one that includes volumetric power loss, say, $f_{\text{power}} = 2/3$; we will keep $f_{\text{cond}} = f_{\text{mom}} = 1$.

Problem 5.15. Use equation (5.108) to show that now values of P^e_{SOL} up to $\approx$ 350 MW will still give a large T-drop. Therefore, for the same example as in problem 5.14, except now with $f_{\text{power}} = 2/3$, use equation (5.79) to show that $\lambda_{q\|u} = 8.9$ mm, equation (5.82) to show that $T_{ue} = 170$ eV, and equation (5.92) to show that $T_{te} = 20$ eV, a much lower value and one which will reduce sputtering considerably. Show that the parallel electron power flux density reaching the target is 125 MW m^{-2}, which will make power removal more practical.

We see from problem 5.15 the benefits of removing two-thirds of the SOL power by volumetric processes. We must, however, also consider how feasible it is actually to remove such a large fraction of the power. It will probably be necessary to exploit impurity radiation in order to achieve $f_{\text{power}} = 2/3$, i.e. 67 MW of total volumetric power loss.

Problem 5.16. Consider the hydrogenic recycle radiative loss, say $\varepsilon^{\text{rad}}_{\text{recycle}} = 25$ eV/recycling neutral, section 3.5. For the last example show that the target particle flux density is $\Gamma_t = 5.6 \times 10^{24}$ m^{-2} s^{-1}, and taking $A_{\|\Gamma} \approx A_{\|q}$ as an (under-) estimate, show that the total recycling flux becomes $\phi_{\text{recycle}} = 1.5 \times 10^{24}$ s^{-1}. Thus show that the recycle radiative loss $= \varepsilon^{\text{rad}}_{\text{recycle}}\phi_{\text{recycle}} = 6$ MW. There will also be charge-exchange neutral losses: let us suppose there is one cx neutral deposition event per recycling neutral. Show that this gives a power loss of $\approx \frac{3}{2}kT_e\phi_{\text{recycle}} = 7$ MW here.

The total power radiated by impurities, section 3.5: $P_{\text{rad},z} = E_{\text{rad pot},z}\phi_z$ where the total impurity influx rate, $\phi_z = \overline{Y}\phi_{\text{recycle}}$ and $\overline{Y}$ is the average yield at the target. For illustration, take $\overline{Y} = 0.03$ and $E_{\text{rad pot},z} = 5$ keV per sputtered particle. Show that this gives $P_{\text{rad}} \sim 40$ MW. This is of the order required. Show, however that this erosion rate for carbon targets corresponds to about 10 cm/year, neglecting re-deposition, and assuming the target is tilted to the field lines such that $A_{\text{wet}}/A_{\|} \sim 100$. It is also a concern that the resulting contamination level of the main plasma may be unacceptably high.

5.8 SOL Collisionality and the Different Divertor Regimes

In the conduction-limited regime the temperature ratio, T_u/T_t, is a simple function of the collisionality parameter, ν^*_{SOL}. One can combine equations (4.91),

(4.105), (5.4), and (5.19) to obtain:

$$\boxed{\frac{T_u}{T_t} = \left(\frac{7e\gamma}{8\times 10^{-16}\kappa_0(m_i/2e)^{1/2}}\right)^2\left(\frac{\nu^*_{\rm SOL}}{1-f_{\rm power}}\right)^2}$$

$$\approx 2.3\times 10^{-3}\left(\frac{\nu^*_{\rm SOL}}{1-f_{\rm power}}\right)^2 \tag{5.109}$$

where $e = 1.6\times 10^{-19}$, $\kappa_0 = 2000$, $\gamma = 8$, $m_i = 2\times 1.67\times 10^{-27}$ were used in equation (5.109) and $\nu^*_{\rm SOL}$ is given by equation (4.106).

The definition of the transition from the conduction-limited to the sheath-limited (constant T along flux tube) regimes is somewhat arbitrary, but let us take the transition to occur at:

$$T_u/T_t \approx 1.5. \tag{5.110}$$

Thus, taking $f_{\rm power} \approx 1/2$ as representative, one arrives at the collisionality criterion for the transition:

$$\boxed{\nu^*_{\rm SOL}|_{\rm cond\leftrightarrow sh} \approx 10} \tag{5.111}$$

This then gives also:

$$T_u|_{\rm cond\leftrightarrow sh} \approx 3.2\times 10^{-9}(n_u L)^{1/2}. \tag{5.112}$$

Next we consider the transition from the conduction-limited regime to the detached regime. The properties of the detached divertor are discussed in more detail in chapter 16. Here we will simply assume that detachment sets in when T_t has been reduced to a few eV, at which point the principal physical processes governing detachment—ion-neutral friction and volume recombination—become important. This criterion only involves T_t, not T_u, and so strictly we cannot use the convenient relation between T_u/T_t and $\nu^*_{\rm SOL}$, equation (5.109), to obtain a simple quantitative criterion equivalent to equations (5.111) and (5.112). We may recall, however, that T_u is rather insensitive to all control parameters and for a first approximation we may simply take T_u to be 100 eV, fixed. We will also arbitrarily take $T_t = 1.5$ eV to be indicative of a low enough temperature for detachment to set in. Thus we insert the ratio $T_u/T_t = 100/1.5$ into equation (5.109) (although otherwise T_u is left free of course) to obtain the criterion for transition from the conduction-limited regime to the detached regime:

$$\boxed{\nu^*_{\rm SOL}|_{\rm cond\leftrightarrow det} \approx 85} \tag{5.113}$$

and thus

$$T_u|_{\rm cond\leftrightarrow det} \approx 1.1\times 10^{-9}(n_u L)^{1/2}. \tag{5.114}$$

The obvious benefit of this approximate treatment is that both transitions, equations (5.112) and (5.114), occur along straight lines on a T_u–$(n_u L)^{1/2}$ plot; see figure 5.27. One can also then say that, to within a factor of $\approx \pm 50\%$:

$$T_u \approx 2\times 10^{-9}(n_u L)^{1/2} \tag{5.115}$$

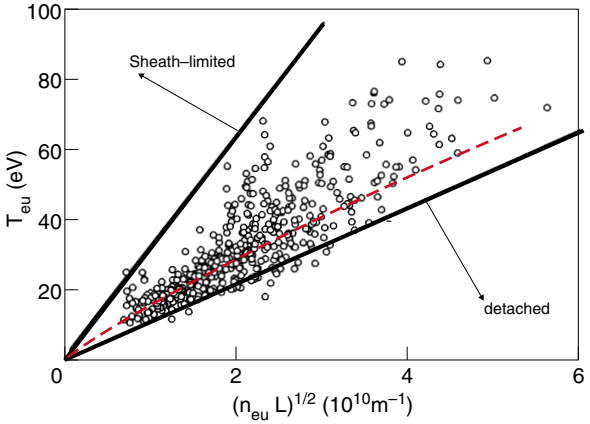

Figure 5.27. Values of upstream electron temperature T_{eu} on JET as a function of $(n_{eu}L)$ [5.26]. The values of T_{eu} and n_{eu} were calculated using onion-skin method analysis, chapter 12, based on target Langmuir probe measurements. The solid lines are from equations (5.112) and (5.114). The JET discharges had been pre-selected, before the OSM analysis, as ones which were known not to be detached. JET tends not to run in the sheath-limited regime, except perhaps in so-called 'hot ion H-mode' shots, where low values of $\bar{n}_e$ are employed, together with strong beam heating, in order to maximize fusion power output [5.65]. Such shots are likely to be low recycling/sheath limited, and had also been excluded from the original data set. The remaining JET shots might therefore have been expected to be conduction limited, which is seen in fact to be consistent with the predictions of equations (5.112) and (5.114). The dashed line is equation (21.13), chapter 21.

is representative of upstream plasma conditions in the conduction-limited regime.

It is perhaps surprising that T_u and n_u are so closely related in the conduction-limited regime, but this has been reported for some tokamaks [5.26], figure 5.27.

It is not necessary to use the assumption that $T_u = 100$ eV, fixed, although the quantitative criterion is then no longer expressible purely in terms of ν^*_{SOL}. We may combine equations (5.7) and (5.8) with the same assumption as before that detachment sets in at $T_t = 1.5$ eV to obtain:

$$T_u|_{\text{cond}\leftrightarrow\text{det}} = 1.7 \times 10^{-7}(n_u L)^{2/5} \tag{5.116}$$

where the same values of the constants were used as before. One may note that the constant in equation (5.116) only depends on T_t as $T_t^{1/5}$, and so the precise choice of T_t to represent the transition to detachment is not critical.

It is also useful to obtain a criterion for this transition in terms of the power

entering the SOL. Combining as before equations (5.7) and (5.8) and using the same constants as before gives:

$$T_u|_{\text{cond}\leftrightarrow\text{det}} = 3.6 \times 10^{-21} n_u^{7/5} L^{2/5} \tag{5.117}$$

$q_\parallel$ [W m^{-2}], n_u [m^{-3}], L [m]. The numerical factor in equation (5.117) depends on the choice of T_t as $T_t^{7/10}$.

Problem 5.17. For $n_u = 3 \times 10^{19}$ m^{-3}, $L = 50$ m show that $q_\parallel|_{\text{cond}\leftrightarrow\text{det}} = 3.2 \times 10^7$ W m^{-2}.

It is more useful to express this criterion in terms of P_{SOL}, rather than $q_\parallel$. We now use equation (5.91) inserting $T_t = 1.5$ eV to give the transition:

$$n_u|_{\text{cond}\leftrightarrow\text{det}} = 4.2 \times 10^{15} \frac{P_{\text{SOL}}^{5/7} L^{1/14} (1 - f_{\text{power}})^{9/14}}{\chi_\perp^{5/14} (aR)^{5/7}} \tag{5.118}$$

n [m^{-3}], P [W], L [m], χ [m^2 s^{-1}], a [m], R [m], and where the same constants were used as before. The numerical factor in equation (5.118) only depends on the choice of T_t as $T_t^{-9/28}$, and is thus not critical. The dependence on $\chi_\perp$ in equation (5.118) is rather weak and we will use $\chi_\perp = 0.3$ m s^{-1} for an estimate here. The dependence on L, thus on safety factor q, is particularly weak and we will use $L = 50$ m for an estimate. The dependence on volumetric power loss in the divertor, f_{power}, is more significant, but for a rough estimate we may take $f_{\text{power}} = 1/2$, fixed, as before. Thus:

$$n_u|_{\text{cond}\leftrightarrow\text{det}} = 5.5 \times 10^{15} (P_{\text{SOL}}/aR)^{5/7}. \tag{5.119}$$

Problem 5.18. For a JET-size example, $P_{\text{SOL}} = 1$ MW, $a = 1.5$ m, $R = 3$ m, show that $n_u|_{\text{cond}\leftrightarrow\text{det}} = 3.6 \times 10^{19}$ m^{-3}. Find the transition for a CMOD-size example: $P_{\text{SOL}} = 0.5$ MW, $a = 0.25$ m, $R = 0.6$ m.

Equations (5.118), (5.119) indicate that $n_u|_{\text{cond}\leftrightarrow\text{det}} \propto q_\perp^{5/7}$, where $q_\perp$ is the power flux density into the SOL. As noted above, the dependence on f_{power}, equation (5.118), is non-negligible, $9/14 \approx 0.64$, and in reality variations in this parameter with n_u and P_{SOL} would probably weaken the dependence of $n_u|_{\text{cond}\leftrightarrow\text{det}}$ on $q_\perp$. The foregoing should therefore only be considered as crude estimates.

If we make the further crude simplification that $n_u \approx \bar{n}_e$, see however chapter 19, then equation (5.119) provides an estimate for the onset of detachment in terms of the main control parameters of a tokamak, $\bar{n}_e$ and power input.

5.9 Divertor Asymmetries

It is important to achieve as large a plasma-wetted area as possible, section 5.6, and to distribute the power load as evenly as possible over this area. Divertor

asymmetries are therefore a concern. An early disappointment was the discovery that double-null divertors essentially use only the two outer targets for power loading; see review [5.1]. This appears to be largely due to two geometrical factors:

(a) A torus has a larger area over its outer half than over its inner half and if the power outflow density across the separatrix is uniform, the outside SOL will receive more power than the inside.
(b) The magnetic flux surfaces on the outboard side are usually compressed with respect to the inboard-side due to the Shafranov shift [5.27] and if the cross-field heat flux is proportional to radial gradients, the outboard side is further favoured.

Asymmetries in target power loading are much smaller for single-null divertors—typically of order 2X, favouring the outside—presumably due to the fact that the SOL then strongly connects the inside and outside and because parallel transport is so rapid. The fluctuation levels are different in the inner and outer SOLs [5.1] presumably indicating that the cross-field transport coefficients vary poloidally. That would also contribute to the strong inside/outside asymmetries observed for double-null divertors, but would be smoothed out for single-null divertors.

Even for single-null divertors some asymmetry persists and typically:

$$\begin{aligned} T_{\text{inner}} &< T_{\text{outer}} \\ n_{\text{inner}} &> n_{\text{outer}} \\ P_{\text{inner}}^{\text{rad}} &> P_{\text{outer}}^{\text{rad}} \\ P_{\text{inner}}^{\text{target}} &< P_{\text{outer}}^{\text{target}} . \end{aligned} \tag{5.120}$$

As $\bar{n}_e$ is raised the inner divertor tends to enter the conduction-limited regime before the outer divertor and then tends to detach before the outer does.

It is conceivable that these asymmetries are due to an asymmetry in the *total* power reaching each divertor leg, $P_{\text{div}}^{\text{total}}$:

$$P_{\text{div}}^{\text{total}} \equiv P_{\text{div}}^{\text{rad}} + P_{\text{div}}^{\text{target}} . \tag{5.121}$$

It may be that the power enters the SOL primarily near the outside midplane due to strong fluctuations there associated with 'bad curvature' [5.28]. Thus the distance from source to sink is shorter for the outside target, apparently implying $P_{\text{outer}}^{\text{total}} > P_{\text{inner}}^{\text{total}}$. Careful measurements of $P_{\text{div}}^{\text{rad}}$ and $P_{\text{div}}^{\text{target}}$ on JT60-U [5.29], however, showed not much asymmetry in $P_{\text{div}}^{\text{total}}$, figure 5.28. There is not even a very significant dependence in the JT60-U results on the direction of the toroidal magnetic field, which might have been expected to have some effect via *drifts*, chapter 18. See [5.1] for further references on in/out asymmetries in divertor tokamaks. Similar near-balance in $P_{\text{div}}^{\text{total}}$ (in : out $\sim$ 1 : 1.3) was reported on DIII-D [5.30]. The picture is not, however, totally consistent, with substantial asymmetries in $P_{\text{div}}^{\text{total}}$, favouring the inside, being reported on JET [5.31].

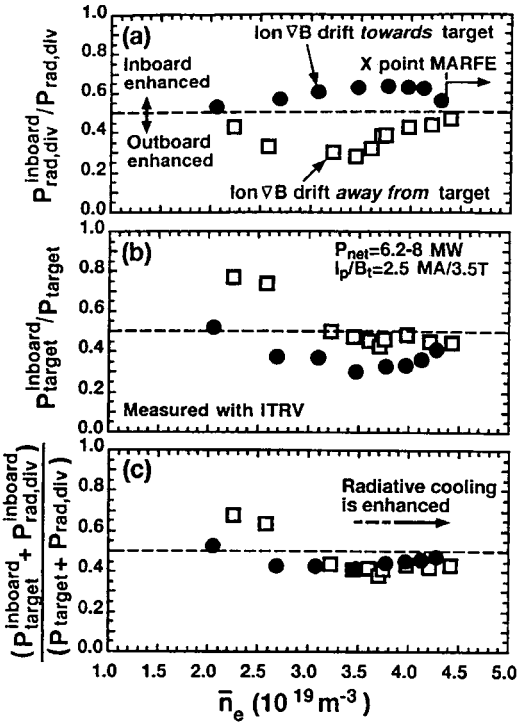

Figure 5.28. Data from JT-60U for the inner divertor share of the radiated power, deposited power and the sum of the two as a function of density for the two field directions for L-mode discharges [5.29].

It is not clear at this time what the underlying cause is of these asymmetries in single-null divertors. It may well be, however, that some small, hard to identify factor acts as a *trigger* for a strong, positive *feedback* effect: if for some reason the level of $P_{\rm div}^{\rm rad}$ should increase then $T_{\rm div}$ will drop, and through pressure balance, $n_{\rm div}$ will rise. Hydrogenic and low Z impurity radiation increases in efficiency with decreasing T_e, section 3.5, and increases in absolute intensity with increasing n_e. Thus a positive feedback results, further raising $P_{\rm div}^{\rm rad}$ and n_t while reducing $P_{\rm div}^{\rm target}$ and T_t, etc. The feedback would be further strengthened by the great sensitivity of n_t and T_t in the conduction-limited regime as discussed in section 5.4:

$$T_t \propto (1 - f_{\rm power})^2,\ n_t \propto (1 - f_{\rm power})^{-2}. \tag{5.122}$$

A number of effects have been proposed as possible asymmetry triggers, including thermoelectric current instabilities [5.32–5.34], gyro-orbit effects [5.35], etc.

5.10 The Effect of Divertor Geometry

The volume devoted to the divertor involves a reduction of the volume available for the main, fusion-producing plasma within the expensive toroidal magnets. It is therefore important to optimize the geometry of the magnetic field and the solid structures within the divertor, so as to maximize the dispersal of the exhaust power, while minimizing structural erosion and leakage of impurities and hydrogenic neutrals to the main plasma. It is also desirable to compress the helium impurity produced as DT fusion ash, in the divertor to facilitate efficient removal at the pumps.

In the 1990s, substantial variations of divertor geometry were evaluated on JET [5.9, 5.13, 5.36–5.38]; ASDEX-U [5.39–5.42]; JT-60 [5.43–5.45]; DIII-D [5.46, 5.47]; CMOD [5.48–5.50]; JFT-2M [5.51]. This topic is a complex, multi-faceted one that we cannot examine further here. Broadly, it is found that changes to divertor geometry tend not to have large effects on the main plasma properties, but can result in significant changes to the way the divertor itself performs, primarily with regard to the neutral pressure near the divertor, where a pump is most naturally located. Given the major cost implications of this issue, it will remain an evolving focus of tokamak research.

5.11 The Ergodic Divertor

As was pointed out in chapter 1, magnetic confinement is actually *too* good at the plasma edge, making scrape-off layers thinner than is desirable for good spatial distribution of the power exiting the plasma and depositing on the solid structure. It would therefore be advantageous if one could engineer an 'edge *deconfined* volume' [5.52], i.e. a region localized at the edge where the magnetic confinement is significantly degraded. Such an approach—termed the *ergodic divertor*—was proposed by Feneberg in 1977 [5.53–5.55], involving creation of a layer in the plasma by applying an harmonic perturbation to the tokamak magnetic equilibrium using special magnetic coils. This introduces *ergodicity* to the magnetic field at the edge and a *stochatization* of the edge plasma. A chain of magnetic islands is created near the edge. When overlapping of the islands occurs, stochasticity of the field lines is generated. Particles can thus move across the *equilibrium* (unperturbed) magnetic field because of what is, in fact, motion along the actual, local magnetic field. The result is effective cross-field transport coefficients, which are much enhanced over the usual anomalous ones. On TORE SUPRA, $\chi_{\perp}^{\text{eff}}$ values exceeded 10 $\text{m}^2\ \text{s}^{-1}$ over the perturbed edge region, exceeding 100 $\text{m}^2\ \text{s}^{-1}$ at its outer boundary [5.52].

The result of such enhanced cross-field transport can be significant flattening of radial profiles. Figure 5.29 shows an example of the flattening of the $T_e(r)$ profile on the TEXT tokamak with/without an ergodic magnetic limiter [5.56].

One of the original, explicit motivations for the creation of ergodic layers,

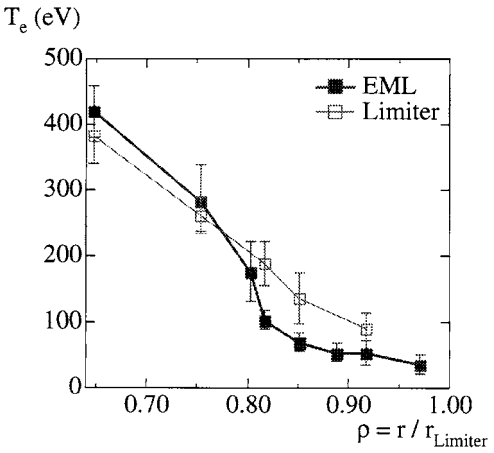

Figure 5.29. Edge temperature profile in the TEXT tokamak in the limiter and ergodic magnetic limiter (EML) configurations [5.56].

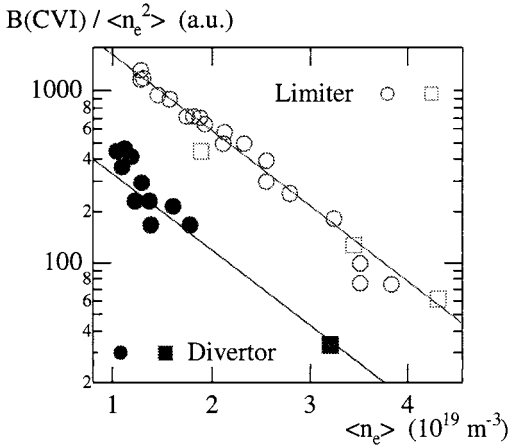

Figure 5.30. TORE SUPRA. Carbon content of the bulk plasma in limiter and ergodic configuration as a function of $\langle n_e \rangle$. The squares are for shots with pellet injection [5.57].

and enhanced radial transport, was the reduction of impurity levels in the main plasma [5.54]. As found in section 4.6 central density levels are inversely proportional to $D_\perp$ (in section 4.6 this was demonstrated for the hydrogenic plasma, but the arguments apply equally to impurities, section 6.4.1). Indeed, such reductions have been found experimentally, see figure 5.30 [5.57], which shows a reduction of the carbon content in TORE SUPRA. The explanation of such reductions, however, may be more complex than originally thought [5.52].

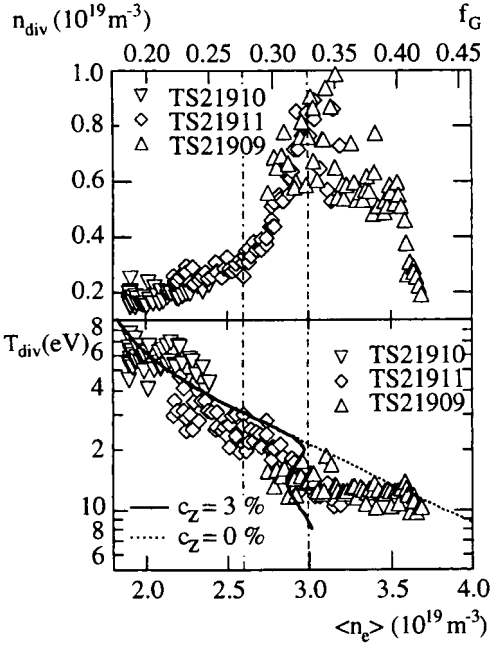

Figure 5.31. TORE SUPRA. Experimental evidence of divertor density regimes achieved with the ergodic divertor when $\langle n_e \rangle$ is increased [5.62, 5.63]. Parameter f_G is the value of $\langle n_e \rangle$ as a function of the Greenwald density limit, section 22.1. For $f_G < 28\%$, $n_{\rm div}$ is in the linear regime with detachment setting in at $f_G \sim 33\%$. The lines in lower figure, for $T_{\rm div}$, are from a 1D model which assumed different impurity fractions, c_z.

Another principal motivation for use of ergodic layers was the wider dispersal of exhaust power over the solid edge structures, i.e. larger plasma-wetted areas. It turns out that the heat flux deposition resulting from ergodic layers is not homogeneous, as might have been expected from original thinking, largely because a non-stochastic, laminar layer (classical SOL) exists near the solid structures, with the stochastic layer existing radially further in [5.58–5.60]. The large volume of the ergodic region gives particularly high levels of radiative cooling of the edge [5.61].

The same three regions as observed with standard divertors—sheath limited, conduction limited and detached—have been found on TORE SUPRA, figure 5.31, [5.62, 5.63]. At low density $n_{\rm div}$ varies linearly with $\bar{n}_e$, then at high density, a more rapid variation is found, $n_{\rm div} \propto\sim (\bar{n}_e)^3$, finally resulting in detachment, i.e. a drop in $n_{\rm div}$, chapter 16 [5.63].

The ergodic divertor thus involves much of the same physics as standard (X-point) divertors, but with possibilities for larger divertor plasma volumes and increased operational flexibility.

Additional Problems

5.19. Derive equation (5.13).

5.20. (a) *Basic two-point model.* Use equation (5.7) for T_u and equation (5.9) for T_t to confirm the results shown in figure 4.17; $n_u = 3 \times 10^{19}$ m^{-3}, $L = 100$ m, $\kappa_0 = 2000$, $\gamma = 7$, D^+ ions.

(b) For the examples shown in figure 4.17 use the two-point model to find n_t, Γ_t and the average impact energy of D^+ ions on the targets.

(c) Assuming a plasma volume of 1000 m^3, a plasma-wetted area of 10 m^2 and $(B_\theta/B) = 0.03$ at the target, estimate the total recycling flux and the particle confinement time. Take the average plasma density to be approximated by n_u.

(d) For the above assumptions, and assuming a carbon target, use the sputtering yields of section 3.3 to estimate physical and chemical sputtering rates. Assume the carbon temperature is 600 K. If the average impurity density in the plasma is 3×10^{17} m^{-3}, estimate the impurity ion confinement time.

5.21. Use the basic two-point model to calculate how large a value of n_u would be required to result in negligible sputtering of tungsten targets. Assume $P_{SOL} = 10^8$ W, $A_{q_\parallel} = 0.3$ m^2, $L = 100$ m, $\kappa_0 = 2000$, $\gamma = 7$, D^+-ions. The sputtering yield for D^+ on W is given in figure 3.6.

5.22. *The effect of raising n_u on $\phi_{recycle}$, τ_p and H_α production.* Use the basic two-point model with the assumptions $q_\parallel = 10^8$ W m^{-2}, $L = 50$ m, $\kappa_0 = 2000$, $\gamma = 7$, D^+-ions, $A_{wet} = 0.5$ m^2, $V_{plasma} = 100$ m^3, (B_θ/B) at the target of 0.02, to calculate $\phi_{recycle}$, τ_p and the H_α production rate as a function of n_u. Plot your results for a range of n_u. For the sheath-limited regime use equation (4.115), etc. Use figure 3.29 for H_α production rates. Compare your $\tau_p(n_u)$ plot with figure 4.11 and comment.

5.23. Plot the equivalent of figure 5.10 for $L = 50$ m, for 10 m. Discuss the effect of changing L.

5.24. Plot the equivalent of figure 5.11 for $L = 50$ m, for 10 m. Discuss the effect of changing L.

5.25. Derive equations (5.27), (5.28).

5.26. Derive equations (5.17), (5.35).

5.27. *Extended two-point model, section 5.4.* In a tokamak, the upstream density was raised in two steps, from $n_u = 4 \times 10^{19}$ m^{-3} to 5×10^{19} m^{-3}, then to 6×10^{19} m^{-3}, with all other control parameters held fixed. It was observed that at the lowest density 35% of P_{SOL} was radiated in the SOL, increasing to 45%, then 65% as n_u was raised. At the two lowest densities, probe

measurements upstream and at the targets showed $p_u = 2p_t$, but when n_u was increased to 6×10^{19} m^{-3}, the plasma *detached*, chapter 16, and the target pressured plunged, $p_t \to 0.1 p_u$. Predict the relative variation of the target recycle flux $\phi_{\text{recycle}}^{\text{target}}$ as n_u was changed.

5.28. *Including the hydrogen recycle loss energy in the two-point model, section 5.5.* Assume $P_{\text{SOL}} = 10^7$ W, $A_{q_\parallel} = 0.1$ m^2, $L = 70$ m, H^+ ions, $\gamma = 8$, $\kappa_{0e} = 2000$, $\varepsilon = 32$ eV. Find as a function of n_u, from 10^{19} m^{-3} up to $n_u^{\max}$: F_u, T_t, n_t, Γ_t, q_t. What is the value of $n_u^{\max}$? Assuming that half of ε is due to radiation, find the maximum radiation loss fraction. Assume friction to be absent.

5.29. Calculate the total plasma-wetted area for a double-null poloidal divertor configuration, assuming $R = 3$ m, $a = 1$ m, $\lambda_u = 10^{-2}$ m, $(B_\theta/B)_u = 0.3$, $(B_\theta/B)_t = 0.03$, and with non-orthogonal divertor targets at an oblique angle $\beta = 60°$ relative to the local poloidal field (figure 5.24). What is the angle between $\boldsymbol{B}$ and the target surface?

5.30. *Inner wall limiter.* For the geometry of figures 5.5, 5.22, derive the result that $A_{\text{wet}} \approx 4\pi R_s (2a\lambda)^{1/2}$.

5.31. (a) *Power scrape-off widths.* For the example of $P_{\text{SOL}} = 2$ MW, $n_u^{\text{sep}} = 3 \times 10^{19}$ m^{-3}, $L = 50$ m, $(B_\theta/B)_u = 0.3$, $a = 1$ m, $R = 3$ m, $\chi_\perp^{\text{SOL}} = 1$ m^2 s^{-1}, D^+plasma, $\gamma = 7$, find $\lambda_{q_\parallel}$ for a single-null poloidal divertor.

(b) Find $A_{q_\parallel}$ and $q_\parallel$, assuming orthogonal targets.

(c) Find T_u and use equation (5.72) as a *rough* check of the value of $\lambda_{q_\parallel}$ found in part (a).

(d) Find the peak deposited heat flux density, assuming $(B_\theta/B)_t = 0.02$ and $\beta = 70°$.

(e) Find T_t, n_t and Γ_t.

(f) Find the value of $P_{\text{rad}}^{\text{SOL}}$ required to lower T_t to 4 eV.

5.32. Show that equation (5.66) gives essentially the same result for $\lambda_{q_\parallel}$ as equation (5.78).

5.33. Derive equation (5.109).

5.34. Derive equation (5.118).

References

[5.1] Pitcher C S and Stangeby P C 1997 *Plasma Phys. Control. Fusion* **39** 779
[5.2] Reiter D, Wolf G H and Kever H 1990 *Nucl. Fusion* **30** 2141
[5.3] Behrisch R and Prozesky V 1990 *Nucl. Fusion* **30** 2166

[5.4] Dylla H F and the TFTR Team 1987 *J. Nucl. Mater.* **145–147** 48
[5.5] Niemczewski A, Hutchinson I H, LaBombard B *et al* 1997 *Nucl. Fusion* **37** 151
[5.6] Pitcher C S, Stangeby P C, Bell M G *et al* 1992 *J. Nucl. Mater.* **196–198** 241
[5.7] Guilhem D, Hogan J, Aniel T *et al* 1999 *J. Nucl. Mater.* **266–269** 272
[5.8] Matthews G F, Allen S, Asakura N *et al* 1997 *J. Nucl. Mater.* **241–243** 450
[5.9] Vlases G C, Horton L D, Matthews G F *et al* 1999 *J. Nucl. Mater.* **266–269** 160
[5.10] Messiaen A M, Ongena J, Samm U *et al* 1996 *Nucl. Fusion* **36** 39
[5.11] Stambaugh R D, Wolfe S M, Hawryluk R J *et al* 1990 *Phys. Fluids* B **2** 2941
[5.12] Groebner R J 1993 *Phys. Fluids* B **5** 2343
[5.13] Horton L D, Vlases G C, Andrew P *et al* 1999 *Nucl. Fusion* **39** 1
[5.14] Matthews G F 1995 *J. Nucl. Mater.* **220** 104
[5.15] Keilhacker M, Becker G, Behringer K *et al* 1982 *Plasma Physics and Controlled Nuclear Fusion Research* (Vienna: IAEA) Vol III p 183
[5.16] Hobbs G D and Wesson J A 1966 *Culham Report* CLM-R61
[5.17] Keilhacker M, Lackner K, Behringer K *et al* 1982 *Phys. Scri.* **T2/2** 443
[5.18] Mahdavi A M, DeBoo J C, Hsieh C L *et al* 1981 *Phys. Rev. Lett.* **47** 1602
[5.19] Lackner K, Chodura R, Kaufmann M *et al* 1984 *Plasma Phys. Control. Fusion* **26** 105
[5.20] Harbour P J 1984 *Nucl. Fusion* **24** 1211; Harrison M F A, Harbour P J, Hotston E S 1983 *Nucl. Technol. Fusion* **3** 432
[5.21] Post D E, Langer W D and Petravic M 1984 *J. Nucl. Mater.* **121** 171; Post D E and Lackner K 1986 *Physics of Plasma-Wall Interactions in Controlled Fusion* ed D E Post and R Behrisch (New York: Plenum) p 627
[5.22] Borrass K 1991 *Nucl. Fusion* **31** 1035
[5.23] Stott P E 1989 *J. Nucl. Mater.* **162–164** 3
[5.24] Wesson J 1997 *Tokamaks* 2nd edn (Oxford: Oxford University Press) p 106
[5.25] Loarte A and Harbour P J 1992 *Nucl. Fusion* **32** 681
[5.26] Erents S K, Stangeby P C and LaBombard B *Nucl. Fusion* at press
[5.27] Wesson J 1997 *Tokamaks* 2nd edn (Oxford: Oxford University Press) p 119
[5.28] Vershkov V A and Chankin A V 1989 *Sov. J. Plasma Phys.* **15** 371
[5.29] Asakura N, Hosogane H, Tsuji-iio S *et al* 1996 *Nucl. Fusion* **36** 795
[5.30] Leonard A W, Lasnier C J, Cuthbertson J W *et al* 1995 *J. Nucl. Mater.* **220–222** 325; Lasnier C J, Hill D N, Petrie T W *et al* 1998 *Nucl. Fusion* **38** 1225
[5.31] Chankin A V, Campbell D J, Clement S *et al* 1996 *Plasma Phys. Control. Fusion* **38** 1579
[5.32] Staebler G M 1996 *Nucl. Fusion* **36** 1437
[5.33] LaBombard B, Goetz J A, Hutchinson I H *et al* 1997 *J. Nucl. Mater.* **241–243** 149
[5.34] Hayashi N, Takizuka T, Hatagama A *et al* 1999 *J. Nucl. Mater.* **266–269** 526
[5.35] Shimada M and Ohkawa T 1999 *J. Nucl. Mater.* **266–269** 906
[5.36] Matthews G F, Balet B, Cordey J G *et al* 1999 *Nucl. Fusion* **39** 19
[5.37] McCracken G M, Barnsley R, Guo H Y *et al* 1999 *Nucl. Fusion* **39** 41
[5.38] Monk R D and the JET Team 1999 *Nucl. Fusion* **39** 1751
[5.39] Bosch H-S, Fuchs J C, Gafert J *et al* 1999 *Plasma Phys. Control. Fusion* A **41** 401
[5.40] Schneider R, Bosch H-S, Coster D *et al* 1999 *J. Nucl. Mater.* **266–269** 175
[5.41] Schweinzer J, Sandmann W, Haas G *et al* 1999 *J. Nucl. Mater.* **266–269** 934
[5.42] Coster D P, Borrass K, Schneider R *et al* 1999 *J. Nucl. Mater.* **266–269** 804
[5.43] Asakura N, Sakurai S, Hosogane N *et al* 1998 *17th IAEA Fusion Energy Conf. (Yokohama 1998)*

[5.44] Hosogane N, Tamai H, Higashijima S *et al* 1999 *J. Nucl. Mater.* **266–269** 296
[5.45] Asakura N, Hosogane N, Itami K *et al* 1999 *J. Nucl. Mater.* **266–269** 182
[5.46] Allen S L, Fenstermacher M E, Greenfield C M *et al* 1999 *J. Nucl. Mater.* **266–269** 168
[5.47] Wolf N S, Porter G D, Hill D N and Allen S L 1999 *J. Nucl. Mater.* **266–269** 739
[5.48] Lipschultz B *et al* 1996 *IAEA* F1-CN-64/A4-5
[5.49] Lipschultz B, Goetz J A, Hutchinson I H *et al Proc. 22nd EPS Conf. on Controlled Fusion and Plasma Physics (Bournemouth, 1995)* vol 19C, part III p 325
[5.50] Pitcher C S, Goetz J A, and LaBombard B *et al Proc. 26th EPS Conf. on Controlled Fusion and Plasma Physics (Maastricht, 1999)*
[5.51] Ogawa H, Miura Y, Fukumoto N *et al* 1999 *J. Nucl. Mater.* **266–269** 623
[5.52] Grosman A 1999 *Plasma Phys. Control. Fusion* **41** A185
[5.53] Feneberg W *Proc. 8th EPS Conf. on Controlled Fusion and Plasma Research (Prague, 1977)* vol 1, p 4
[5.54] Engelhardt W and Feneberg W 1978 *J. Nucl. Mater.* **76–77** 518
[5.55] Feneberg W and Wolf G H 1981 *Nucl. Fusion* **21** 669
[5.56] Evans T E, DeGrassie J S, Jackson G L *et al* 1987 *J. Nucl. Mater.* **145–147** 812
[5.57] Monier-Garbet P *et al* 1993 *Plasma Physics and Controlled Nuclear Fusion Research* vol 1 (Vienna: IAEA) p 317
[5.58] Ghendrih Ph and Grosman A 1997 *J. Nucl. Mater.* **241–243** 517
[5.59] Nguyen F, Ghendrih Ph and Grosman A 1997 *Nucl. Fusion* **37** 743
[5.60] Grosman A, Ghendrih Ph, Capes H *et al* 1998 *Control. Plasma Phys.* **38** 82
[5.61] Monier-Garbet P, DeMichelis C, Ghendrih Ph *et al* 1999 *J. Nucl. Mater.* **266–269** 611
[5.62] Meslin B, Loarer T, Ghendrih Ph and Grosman A 1999 *J. Nucl. Mater.* **266–269** 318
[5.63] Ghendrih Ph, Grosman A, Gunn J *et al* 1999 *J. Nucl. Mater.* **266–269** 189
[5.64] Wade M R, Hogan J T, Hillis D L *et al* 1995 *J. Nucl. Mater.* **220–222** 178
[5.65] Guo H Y, Balet B, Conway G *et al* 1999 *J. Nucl. Mater.* **266–269** 825

Chapter 6

Plasma Impurities

6.1 Introduction: Harmful and Beneficial Effects of Impurities

Ideally, DT fusion would involve the presence of only hydrogenic species in the plasma. Plasma impurities, however, are unavoidable. At a minimum, He ash from the DT fusion reactions will be present. Plasma-surface interactions are also inevitable, resulting in the release into the plasma of atoms and molecules from the solid structural components by evaporation, sputtering, etc.

Plasma impurities have both harmful and helpful consequences. The principal harmful consequence is cooling of the main plasma, an effect which historically limited progress toward the high central temperatures needed for fusion [6.1, 6.2]. In the magnetic fusion devices of the 1950s, the combination of (a) poor vacuum conditions—including the lack of baking, (b) the use of medium Z, non-refractory structural materials such as steel in contact with the plasma and (c) imperfect magnetic field geometry resulted in impurity radiation accounting for almost all the energy loss from the central regions of the main plasma. The heat insulating effect of the magnetic field was thus sabotaged. During the 1960s and early 1970s the impurity problem was considerably improved by introduction of ultra-high vacuum technology, control of stray magnetic fields and the use of refractory materials such as tungsten and molybdenum for the limiters. Starting in the mid-1970s, low Z materials were largely used for limiters and divertor target plates, particularly the refractory, carbon. Gettering with low Z materials such as Li, Be, and B [6.3] is used regularly on many devices to control the stubborn problem of oxygen contamination.

The *radiation power function*, section 3.5, varies greatly amongst elements, see figure 6.1. That fractional impurity level which results in radiation power equal to 50% of the alpha-heating power is shown in figure 6.2. Such impurity levels would make ignition impossible, ruling out practical fusion reactors. Clearly it is much more damaging to have high Z elements present in the core, than low Z ones. Figure 6.1 brings out a second critical difference between low Z and

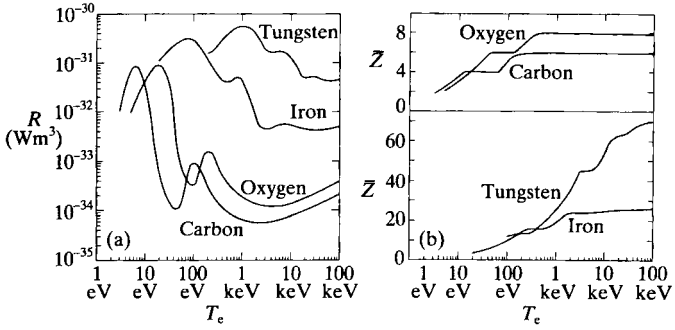

Figure 6.1. (a) The radiation loss or power function R (defined as L in section 3.5) and (b) the mean charge $\overline{Z}$ as functions of T_e for C, O, Fe and W [6.5].

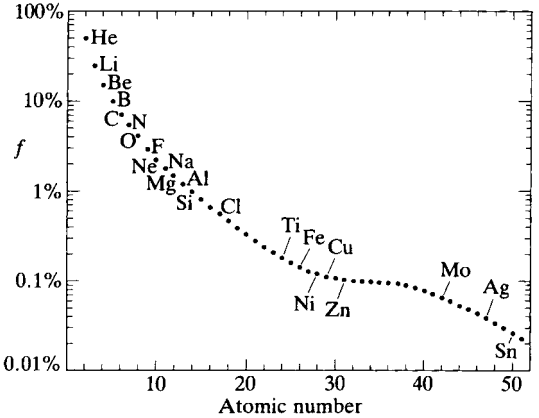

Figure 6.2. Fractional impurity level which produces a radiation power equal to half of the alpha-heating power [6.5].

high Z impurities, regarding their radiative properties: low Z elements become completely stripped of their orbital electrons at relatively low temperatures, $T_e \leq$ 1 keV; this results in a drastic fall of the radiation power function to the low residual level given by bremsstrahlung radiation. The high Z elements, however, retain some orbital electrons even at the high temperatures of the core plasma and their line radiation continues to make them efficient radiators. Fortunately, the intrinsic impurity helium can be tolerated more than other impurities. Nevertheless a maximum level of about 10% is acceptable for a reactor-like device [6.4].

Impurities present in the fusion core of the plasma are also harmful because of *fuel dilution*. The total plasma pressure, for a given field strength B, is limited by MHD instabilities; the plasma β ($\equiv \sum_i n_i k T_i / (B^2/2\mu_0)$ summed over

electrons and all ion species cannot exceed the Troyon beta limit [6.6]:

$$\beta_{\max}[\%] = \frac{2.8 I_p}{aB} \tag{6.1}$$

I_p [MA], B [T], a [m]. The electrons released by the impurities can 'use up' a lot of this permitted maximum plasma pressure even for impurity fractions which are rather low. One cannot just 'overwhelm' the impurity content with more fuel particles.

Problem 6.1. For the example of carbon and $n_{C^{6+}}/n_e = 4\%$, show that $n_{\mathrm{DT}}/n_e = 0.76$ and $Z_{\mathrm{eff}} = 2.2$ and that, for fixed n_e and T, the fusion power is reduced by a factor $(0.76)^2 = 0.58$, i.e. almost half. Such a degradation of performance would be equivalent to the loss of the improvement of τ_E by two times, i.e. what is obtained in H-modes, chapter 7, and is therefore unacceptable.

Low Z impurities radiate rather near the edge of the main plasma, where T_e is low enough that the ions are not fully stripped. This is potentially very advantageous, as will be discussed. It is also potentially harmful. Sufficiently strong radiation in the periphery of the confined plasma can reduce the electrical conductivity so much that the tokamak current profile contracts leading to an increased destabilizing current gradient inside the $q = 2$ surface [6.7]. This then results in a disruption of the current. This is effectively a type of density limit disruption since the impurity radiative power is proportional to the product $n_e n_z$.

Density limits are also often preceded by the formation of MARFEs, (multifaceted asymmetric radiation from the edge), see chapter 22, which are also characterized by strong, low Z impurity radiation near the edge. In contrast with the first-described case involving the $q = 2$ surface, MARFEs involve poloidally localized radiation, typically at the inner wall or the X-point.

Unless impurity levels are kept below a critical level, there is the risk of a *sputtering run-away catastrophe*. While the normal incidence ion yields of hydrogenic species on all substrates are less than unity, *self-sputtering yields* often exceed unity [6.8]. Since most sputtered neutrals become ionized within the plasma they can return to the solid surfaces as multiply charged ions and be accelerated by the sheath potential drop to very large impact energies. (Fortunately, this would cool the edge plasma due to impurity radiation, giving a negative feed-back effect and reducing the risk of catastrophe.)

Plasma impurities are not all bad news and we consider next their *beneficial* effects. As already mentioned, the greatest benefit of impurities is volumetric power loss, so long as it occurs either in the SOL or near the periphery of the main plasma, and does not compromise the energy confinement of the magnetic device: after all, 100% of the heat must be lost at the edge one way or another. Such disposal of the exhaust power is greatly preferable to the intense, highly localized power deposition by particle impact on the very small plasma-wetted areas, $\sim$1 m^2, that tend to characterize magnetically confined devices, section 5.6.

The photons can distribute the exhaust power over most of the very large wall area—hundreds of m^2 for a reactor-like device. Furthermore, photons do not cause sputtering. It is almost certainly essential that reactor-like devices dispose of a substantial portion of the exhaust power through SOL radiation—and with much of it as impurity radiation. Experimentally, it has been demonstrated in most divertor tokamaks that by injecting impurity gases such as N, the radiated power can exceed 50% of the input power [6.9–6.17].

Peripheral radiation by impurities in the *main plasma* also shows considerable promise. This was first proposed in the 1970s [6.18, 6.19], and called the *cold plasma mantle*. An early successful demonstration of peripheral radiation was on TFTR [6.20]. On TEXTOR [6.10] neon puffing has been used to radiate 85% of the input power in plasmas attached to the limiters, see chapter 23.

Because hydrogenic species have only one orbital electron, which they quickly lose in even a cool plasma, the *spectroscopic diagnostic* possibilities are much less than for impurity species. Even if impurities were not naturally present in magnetic confinement plasmas, they would be injected for diagnostic purposes. Atomic beams of impurity atoms have been injected into plasmas in order to make core measurements of q-profiles [6.21] and to make edge measurements of n_e and T_e [6.22]. High Z beams are used to measure the electric potential within the core plasma and also fluctuations [6.23]. The Doppler shift of impurity radiation can be used to infer rotational velocities of the hydrogenic plasma, while impurity line widths provide measurements of local temperature, assuming equilibration, $T_z = T_i$ (background). Injection of impurities in short bursts, by laser blow-off or brief gas puffs, is used to deduce the transport coefficients in the main plasma. In the SOL the 2D spatial distribution of impurities provides a multitude of opportunities for inferring the properties of the SOL 'background plasma', section 6.6.

The plasma impurity story is also an important one to understand because of the information it can provide about the erosion of the solid structure. In experimental devices this is not a problem, but for reactors with their long duty cycles it will be a major concern. Even for experimental devices, the erosion problem is important when tritium is used: the eroded material, when it re-deposits, traps H/D/T and this *re-deposition trapping*—or *co-deposition*—is the principal removal mechanism of H/D/T when carbon structures are used, section 3.4.

Therefore, if magnetic fusion cannot live without impurities, it will have to learn how to live with them. Impurities are not an extraneous detail but an intrinsic part of the fusion story. We must therefore understand how they enter plasmas, how they behave while they are there, and how they are removed.

6.2 The Three Principal Links in the Impurity Chain

In the simplest case the source and sink of impurities are the same, namely the limiters or divertor targets. Impurity neutrals are released at these solid surfaces,

typically by sputtering or evaporation. Most neutrals enter the plasma and are ionized. Most impurity ions promptly return to the solid surface but some are transported further into the plasma and some reach as far as the centre of the main plasma. All ions, however, eventually return to the limiters or targets, in this simplest case, i.e. to these particle sinks. Let us consider the impurity chain of processes connecting the source of impurities at the limiter/targets to the impurity density at the centre of the main plasma. This chain may be considered to consist of three principal links, see figure 6.3:

(1) the source;
(2) edge transport;
(3) transport in the main plasma.

Taking each of these links in turn:

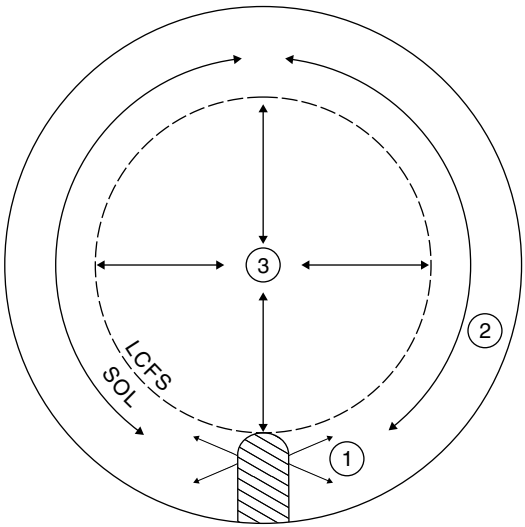

Figure 6.3. The three principal links in the impurity chain: (1) the source, (2) edge transport, (3) transport in the main plasma.

6.2.1 The Source

Section 3.3 describes the principal source of *intrinsic* impurities—sputtering. Unusually, other processes can also release impurities from edge structures [6.2].

Ideally, the only plasma contact is with the limiters or divertor targets. In practice this is not always achieved and ion-impact sputtering can occur on the walls and on the structure at the entrance to the divertor. Even if there is no plasma–wall contact, charge-exchange neutrals bombard all edge surfaces, including walls. The largest component of such neutral fluxes is too low in energy to

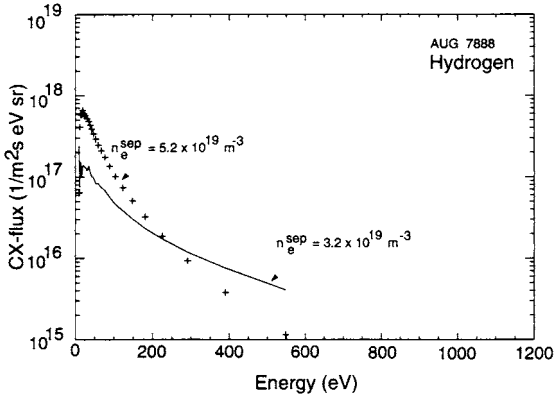

Figure 6.4. Neutral hydrogen flux spectrum measured at the walls of the ASDEX-U tokamak using the LENA diagnostic, for two different separatrix densities [6.24].

cause physical sputtering, but it causes chemical sputtering where carbon is used, section 3.3.2. Figure 6.4 shows the measured flux of neutral hydrogen reaching the outside wall of ASDEX-U, near the midplane [6.24]; the most probable energy is ∼25 eV; the spectrum shifts to lower energies as the plasma density is increased, since the charge-exchange neutrals then come from regions closer to the edge of the plasma.

For *recycling* impurities (i.e. naturally gaseous ones), either the intrinsic He, or injected ones such as Ne, the source remains at the limiters or targets. Here, however, one is interested in an additional link, namely that coupling the *ionic* population in the SOL—say next to the divertor target plates—and impurity *neutral* density or pressure in a pumping duct adjacent to that edge plasma region, section 6.7. Understanding and modelling this link requires solution of a *neutral* transport problem.

In section 6.3, we consider measurements of impurity sources in tokamaks. In section 6.7, we briefly consider the special helium impurity case. In chapter 27, the general case of recycling impurities is taken up.

6.2.2 Edge Transport

For impurity (or hydrogenic) transport purposes we may define the 'edge' as follows.

(a) When ionization of neutrals occurs entirely outside the LCFS, then 'edge transport' is considered to be that which occurs outside the LCFS.
(b) If the ionization of the neutrals extends inside the LCFS some distance λ_{iz} then 'edge transport' is considered to be that which occurs outside radius $r = a - \lambda_{iz}$, figure 5.1.

In either case the impurity transport inboard of the edge region—i.e. the transport in the main plasma—can usually be taken to be a 1D (radial) ion transport problem. Even if all the neutrals were ionized at a single toroidal and poloidal location at some point radially inboard of the LCFS, parallel transport is generally so much faster than cross-field transport that the impurities will have become uniformly distributed toroidally/poloidally before they have moved radially very far from the ionization radius. For the case of ionization entirely outside the LCFS, there can be spatial variation of impurity density along the LCFS itself, but at radial locations even slightly inside the main plasma, the spatial distribution will be uniform.

In the simplest picture, the behaviour of impurities is modelled using the quasi-1D Engelhardt model, as applied in section 4.6 to hydrogen. This model applies equally to impurities and is not repeated here. Generally, however, ion impurity transport in the edge is 2D, or even 3D. Also, in edge transport one must consider both *neutral* and *ionic* transport. Edge impurity transport is usually inherently more complex than transport in the main plasma—since the latter can often be taken to be 1D radial.

6.2.3 Transport in the Main Plasma

The 1D radial transport in the main plasma is usually described by:

$$\Gamma_\perp = -D_\perp \frac{\mathrm{d}n}{\mathrm{d}r} - v_{\mathrm{pinch}} n \tag{6.2}$$

where $\Gamma_\perp$ is the (generally outward) perpendicular flux density of hydrogenic or impurity species of density n. The cross-field transport coefficients, $D_\perp$ and v_{pinch} ($\equiv v_{in}$, inward drift velocity) are not yet calculable from first principles; they are *anomalous*, with typical values of the cross-field diffusion coefficient, $D_\perp \sim$ 0.1–1 $\mathrm{m^2\ s^{-1}}$, and the pinch velocity, $v_{\mathrm{pinch}} \sim 10\ \mathrm{m\ s^{-1}}$ [6.25]. Experimentally measured values of $D_\perp$, v_{pinch} are often found to vary radially.

If $v_{\mathrm{pinch}} = 0$ inboard of the edge region, as defined above, then in steady state n is radially constant, whether $D_\perp$ is radially constant or not, figure 4.9. That is, the density throughout the main plasma is entirely given by the source and by the edge transport. Even when $v_{\mathrm{pinch}} \neq 0$, the radial density profile may still be rather simply related to the edge density, section 6.4.1.

6.3 Measuring the Impurity Source

To start at the beginning, the first and principal quantity that must be measured in order to understand impurity behaviour in a fusion plasma is the impurity source(s). One needs to know:

- the impurity species;
- the locations of all significant sources—walls, limiters, RF wave antennas, divertor plates, etc;
- the absolute magnitude of the influxes;
- the location of first (neutral) ionization.

Until the 1980s, such impurity measurements were rarely made in tokamaks, and spectroscopic impurity studies focused on the central plasma to measure impurity levels there. Such impurity information is essential, but it provides only limited information on the cause of the impurity problem and little indication of how to solve it. First on ASDEX and then on JET, Behringer [6.26], developed the technique of measuring impurity influxes on the basis of *visible wavelength emission spectroscopy*; this powerful technique is now used on most magnetic confinement devices. The method involved absolute measurement of the photon intensity I_{ph} [photons m^{-2} s^{-1} $sterad^{-1}$] of specific lines of C I, C II,..., O I, O II,...Cr I, etc, in the immediate vicinity of the sources. The particle influx of impurities $\Gamma_{in,z}$ [particles m^{-2} s^{-1}] is then given by:

$$\boxed{\Gamma_{in,z} = 4\pi I_{ph}/\mathrm{PE}} \tag{6.3}$$

where $\mathrm{PE}(n_e, T_e)$ is the *photon efficiency*, section 3.5, equation (3.16). The units of PE are discussed below. Examples of calculated photon efficiencies, given in figure 3.30 (which actually gives inverse PEs), emphasize the importance of knowing the local electron temperature in the emission zone. The technique can require sophisticated corrections when densities of atoms in the metastable state are comparable to ground state densities; for Be I, for example, 50–70% of the population can be in metastable states [6.27]. Table 6.1 gives examples of measured influxes of Be, Cr, Ti, D and O from both walls and limiters in the ISX-B tokamak [6.27] using Be limiters. It is noted that the limiters are, not surprisingly, the main source of Be influx, although the walls are significantly contaminated by Be, causing some influx; the influx from the wall increased by more than an order of magnitude after the limiters suffered melting, indicating that a large fraction of the wall was covered by Be. It may also be noted that the ratio $\Phi_{in}^{\mathrm{Be}}/\Phi_{in}^{D} \sim 7 \times 10^{-4}$ for the limiters corresponds to the physical sputtering yield for BeO at 40 eV D^+ impact [6.27], (Φ in [particles s^{-1}]). The wall is seen to be the dominant source of oxygen—a stubborn contaminant which can enter vacuum systems by many routes.

The particle influxes given in table 6.1 were calculated assuming a constant $T_e = 30$ eV for the photon efficiencies, a value estimated to be characteristic of the plasma conditions in the emission region. One may obtain such estimates from Langmuir probe measurements of T_e at, say, the LCFS near a limiter, or at the separatrix 'strike point' on a divertor target. Unfortunately n_e and T_e can vary rapidly in space near impurity sources making it difficult or impossible to come up with a meaningful single temperature on which to base the photon efficiency.

Table 6.1. Integrated fluxes from the wall and limiter[a] on ISX [6.27].

Conditions	Ion	Φ_w (s^{-1})	Φ_L (s^{-1})	Φ_w/Φ_L	Time point in discharge (ms)
Before melting of Be (115 kA)	Be I	1.6×10^{17}	1.1×10^{18}	0.14	280
	Cr I (a^7S)	1.2×10^{19}	1.7×10^{18}	6.9	280
	Ti II (a^4F)	4.7×10^{18}	4.7×10^{17}	10.0	280
	Ti II (a^2F)	2.0×10^{18}	1.6×10^{17}	12.8	280
	D I	5.0×10^{21}	1.5×10^{21}	3.3	280
	O II			19.0	280
Melting sequence (150 kA)	Be I	2.9×10^{18}	1.2×10^{19}	0.25	150
	Cr I	1.1×10^{19}	3.6×10^{17}	32.0	150
	Be I	5.0×10^{18}	1.3×10^{20}	0.04	340
	Cr I	7.3×10^{18}	3.2×10^{17}	24.0	340
After fluence test (115 kA)	Be I	4.5×10^{18}	1.39×10^{19}	0.3	150
	Cr I	5.5×10^{18}	8.3×10^{17}	6.6	150
	Be I	3.3×10^{18}	7.2×10^{19}	0.05	290
	Cr I	3.9×10^{18}	4.6×10^{17}	8.4	290

[a] The electron temperature is assumed to be 30 eV.

This is one reason to employ an *impurity code*, section 6.6, in order to deal with such spatial complexity.

When the line emission is from the neutral state, then equation (6.3) can be used to deduce the impurity particle source rate, assuming:

(a) that the plasma is sufficiently strongly ionizing that it is opaque to neutrals, i.e. that 100% of all neutrals are, in fact, ionized without redepositing first on a solid surface: one notes that, strictly, equation (6.3) does not give the *entry* rate of neutrals but rather their *loss* rate to the singly ionized state. The implicit assumption in any simple, direct use of equation (6.3) is that the entry rate equals the (ionization) loss rate. The idea behind the PE-based approach is that both the excitation and the ionization rate vary as the product $n_e n_z$ and so the number of photons emitted before a neutral or ion is ionized depends only on the ratio $\overline{\sigma v_{\rm exc}}/\overline{\sigma v_{iz}} x (\equiv$ PE, essentially). This ratio is mainly dependent on the value of T_e in the region involved, and hence if T_e is known then the theoretical value of this ratio can be used, together with a measurement of I_{ph} to deduce the value of Γ_{in}—all assuming strongly ionizing conditions. One thus sees that the units of PE are [number of excitations per ionization] or [photons/ionization] or [photons per entering particle].

(b) The plasma is hot enough that ionization totally dominates over recombination, so that there is 'once-through traffic'. For $T_e >$ a few eV this is a good assumption for neutrals, but under cold, e.g. detached, divertor conditions, chapter 16, this assumption may not hold.

Equation (6.3) can also be applied to higher ionization stages, if the above mentioned assumptions hold also for the higher stages—thus providing confirmatory measurements of the source rate. It is less and less likely, however, that these assumptions do continue to hold as one proceeds to higher ionization stages:

(a) plasma forces on the ions, section 6.5, can result in the low ionization stage particles being lost back to the limiters/targets, i.e. re-deposition, before they can ionize to the next stage;
(b) recombination becomes more probable for higher ionization stages.

It is necessary to employ an impurity source/transport code to deal with such complicating effects, section 6.6.

It is equally important to know the average location of ionization of the neutral impurities. As illustrated by the 1D radial case of the Engelhardt model, next section, the depth of ionization relative to the LCFS, i.e. λ_{iz}, is just as important as the source rate in setting the impurity density in the main plasma, n_z. As for PE, one can use simple estimates of the depth of penetration of the neutral impurities using information on n_e and T_e near the source.

Problem 6.2. Consider the example of physical sputtering of C by D^+ ions and assume a uniform plasma temperature of 20 eV over the entire plasma-wetted area. Take the impact energy to be $E^{\text{impact}} = 2kT_i + 3kT_e$, section 2.9, $E_{\text{impact}} = 100$ eV; show that for a Thompson energy distribution of the physically sputtered neutrals one obtains a most probable C^0 energy of $E_{C^0}^{m.p.} = \frac{1}{2}E_B \approx 3.7$ eV, with a maximum energy $E_{C^0}^{\max} \approx 18$ eV; this gives an average neutral energy of $\overline{E}_{C^0} \approx 10$ eV, section 3.3.3. Sputtered energies can sometimes be rather low; for the example $T = 10$ eV, H^+ on C, show that $E_{C^0}^{\max} \approx 3$ eV; this gives $\overline{E}_{C^0} \approx 1$ eV. One can then estimate the penetration distance from $\lambda_{iz} = v_0/(n_e\overline{\sigma v}_{iz})$. For the example: $E_{C^0} = 10$ eV ($\therefore v_0 = 8900$ m s^{-1}), $n_e = 10^{19}$ m^{-3}, $T_e = 20$ eV show that $\lambda_{iz} = 0.019$ m, using figure 1.26 for $\overline{\sigma v}_{iz}$.

In reality a number of complications occur:

(a) Plasma temperature generally varies substantially across the plasma-wetted surface. Thus the yield, E_{impact} and $\overline{E}_{Z^0}$ vary greatly in space.
(b) n_e and T_e generally vary significantly in the plasma region where the neutrals are ionized, making the simple estimate, $\lambda_{iz} = v_0/(n_e\overline{\sigma v}_{iz})$, of uncertain validity.
(c) The use of a single energy, $\overline{E}_{Z^0}$, or velocity to characterize the sputtered neutrals does not always adequately account for the effects of the energy/velocity spectrum involved.
(d) Self-sputtering will also be present, generally, introducing a second set of spatially varying $\overline{E}_{Z^0}$, etc.

Again, it is necessary to employ an impurity source and transport code to deal with such complications, i.e. to perform the 'book keeping'.

While the measurements of the influx of impurity atoms and ions, where PE values are often available, can be relatively straightforward, the PE values for molecular species, such as the fragments of CH_4, are harder to establish [6.28, 6.29]. On TEXTOR, Philipps has demonstrated using 'sniffer probes' [6.30, 6.31], that the production rates of volatiles such as CH_4 can be measured by mass spectroscopy, providing an alternative approach.

6.4 Models for 1D Radial Transport

6.4.1 The Engelhardt Model

In principle, impurity generation need not be damaging to tokamak operation. If the impurities are ionized near the source and return to it directly, then there is no net erosion and the main plasma is not contaminated. That such situations can exist is indicated in figure 6.5 [6.26]. For JET discharge 6574, the carbon limiter, contaminated with Cr, became hot late in the discharge and Cr evaporated from it, as shown by the Cr I signal directly from the limiter; however, virtually no Cr (Cr XXII) was seen in the centre of the plasma. By contrast, shot 7536—a more conventional case evidently characterized by physical sputtering only—showed low (Cr I) influx throughout, but relatively high central levels (Cr XXII). The qualitative explanation is that the slow evaporated atoms were ionized in the SOL near the limiter, where they were subject to drag and electrostatic forces associated with the SOL plasma flow to the limiter, section 6.5, and promptly returned to the surface. The faster sputtered atoms, by contrast, penetrated the plasma to greater distances where the limiter directed forces were weak or absent, and the resulting ions had a greater probability of reaching the core plasma before eventually returning to the edge, figure 6.6.

We now attempt a quantitative description of these processes. First, we briefly consider the overall impurity transport picture of the tokamak. Impurity transport within the *main* plasma, section 6.2.3, has been a much studied subject in fusion research and will not be dealt with in any detail here. Such studies are based either on natural impurities or on injected ones, e.g. from laser ablation. These studies generally take up the story starting at a point fairly far into the plasma radially and with the impurity already highly stripped of electrons, i.e. the complex processes near the edge and in the SOL are essentially ignored, and the intensity and radial location of successive rings of the different ionization stages are measured and modelled. Such studies provide information on $D_\perp$ and v_{pinch} for the main plasma. In some circumstances, a very high v_{pinch} is measured, associated theoretically with neo-classical impurity transport [6.32], and experimentally with impurity accumulation, non-steady-state conditions and even radiation collapse—a *radiative catastrophe*. Often, however, v_{pinch} is found to be low and the transport is dominated by diffusion with $D_\perp^{\text{imp}} \approx D_\perp^{\text{fuel}} =$

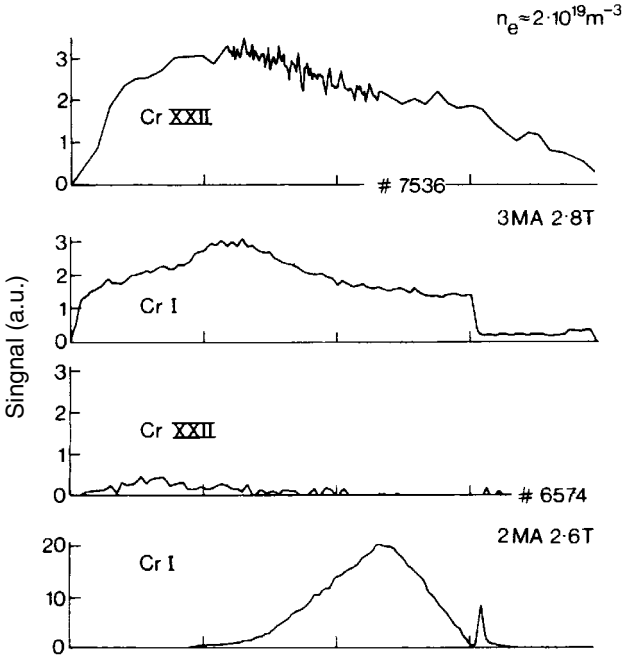

Figure 6.5. JET limiter: intensities of Cr I ($\propto$ chromium influx) and Cr XXII ($\propto$ Cr density in the main plasma) for cases of hypothesized sputtered Cr (top pair) and hypothesized evaporated Cr (bottom pair) [6.26].

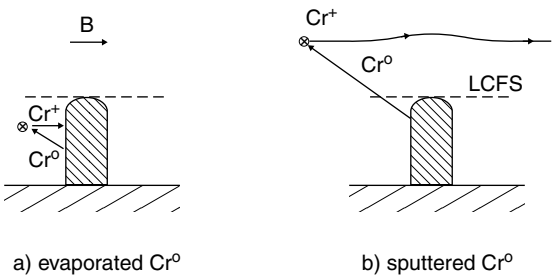

Figure 6.6. (a) Slow neutrals, e.g. from evaporation, can be ionized within the SOL and promptly returned to the limiter by the plasma flow while (b) fast neutrals, e.g., from sputtering, may be ionized in the *main* plasma. The latter may have a long dwell time in the plasma, efficiently contaminating it.

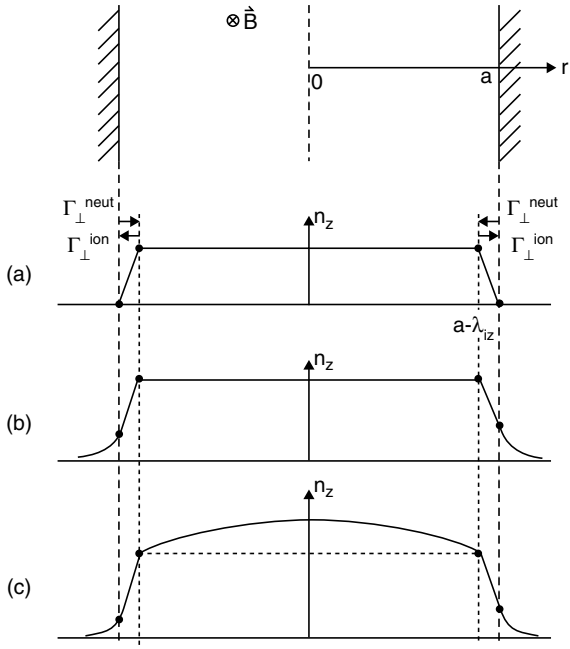

Figure 6.7. Engelhardt model of radial profiles of impurity density $n_z(r)$: (a) (cross-field) diffusion, no inward pinch, and 'hard' boundary condition, (b) as (a) but soft boundary condition, i.e. a SOL is present. (c) As (b) but with inward pinch also. Central density $n_z(0)$ increases as (a) → (b) → (c).

1 m^2 s^{-1} and $v_{\text{pinch}} \approx D_\perp r/a^2$, or less [6.32]. Whatever the form of the central transport, however, the boundary conditions are always, in a sense, controlling—and it is therefore critical to understand the latter in order to deal with the ultimate question of relating the central impurity density $\hat{n}_z$ to the neutral impurity influx Φ_{in}^0 [neutrals s^{-1}]. For the case of low v_{pinch}, this relation appears, in principle, to be quite simple and dominated by conditions near the edge; the conditions within a few centimetres of the LCFS set the level of $\hat{n}_z$, with little dependence on processes elsewhere in the plasma—a remarkable situation.

We consider the work of Engelhardt and Feneberg [6.33, 6.34], which provides a simple and useful model for relating central impurity levels to edge conditions. The same model was applied in section 4.6 to the fuel species. Consider figure 6.7. Over a plasma surface area A_p, a uniform, radial neutral influx density of impurities Φ_{in}^0/A_p is assumed; Φ_{in}^0 in [particles s^{-1}]. All the neutrals are assumed to be ionized at a distance λ_{iz}^0 inside the LCFS.

Assuming perpendicular transport to be governed purely by diffusion, the resulting impurity ion density profile is very simple: a linear (in slab geometry) decay to a level $n_z(a)$ at the LCFS and a profile inside $r = a - \lambda_{iz}^0$ which gradually

'back-fills' up to a constant value in reaching steady state. One thus has, for the hard boundary condition:

$$\Phi_{in}^{0}/A_p = \Gamma_{\text{out}}^{+} \approx D_\perp \hat{n}_z/\lambda_{iz}^{0}. \tag{6.4}$$

Using the 'soft' boundary condition as discussed in section 4.6, equation (4.61):

$$\Gamma_{\text{out}}^{+} = D_\perp(\hat{n}_z - n_z(a))/\lambda_{iz}^{0} = D_\perp \frac{n_z(a)}{\lambda_{\text{SOL}}} \tag{6.5}$$

where λ_{SOL} is the characteristic decay length of impurities in the SOL. Thus,

$$\boxed{\hat{n}_z = \frac{\Phi_{in}^{0}(\lambda_{iz}^{0} + \lambda_{\text{SOL}})}{D_\perp A_p}} \tag{6.6}$$

and the edge plasma properties are seen to play yet a further role. The effect of going from the hard boundary condition to the soft one is that $\hat{n}_z$ is raised, all else being equal; compare figures 6.7(a) and (b). If ionization is in the SOL, $\lambda_{iz}^{0} < 0$, then it can be shown, section 4.6, that:

$$\boxed{\hat{n}_z = \Phi_{in}^{0}\lambda_{\text{SOL}} \exp(\lambda_{iz}^{0}/\lambda_{\text{SOL}})/D_\perp A_p} \tag{6.7}$$

i.e. essentially equation (4.68).

Problem 6.3. These simple models can give reasonably correct predictions. Consider, for example, a typical limiter JET case where carbon sputtered from the limiter governs Φ_{in}^{0}. Spectroscopic measurements (C II, C III light) of influx (also approximately confirmed by sputtering calculations based on the Langmuir probe measurements of the JET SOL properties) give Φ_{in}^{0}/Φ of the order 10^{-1}, where Φ is the hydrogenic flux and Φ_{in}^{0} is of the order of 10^{21} s^{-1}. Take $D_\perp^{\text{SOL}} \sim 0.5$ m^{2}s^{-1} and $A_p \approx 200$ m^2. From Langmuir probe measurements, one measures or calculates $\lambda_{in}^{0} \approx \lambda_{\text{SOL}} \approx 2$ cm. These values of $D_\perp$ and $\lambda_{\text{SOL}}(\lambda_n)$ are for the D^+ plasma, but are presumably also roughly indicative of impurity behaviour. Insert these values into equation (6.6) to show that $\hat{n}_e \approx 4 \times 10^{17}$ m^{-3}, i.e. a few per cent of $\overline{n}_e$, which is, in fact, of the order of the central carbon levels measured in JET and other tokamaks, chapter 24.

As in the case of the fuel ions, a number of further refinements to the simple model can be readily incorporated. A weak, anomalous pinch $v_{\text{pinch}} \approx 2SD_\perp r/a^2$ (with the pure-number parameter $S \approx 1$), often appears to be necessary to 'explain', i.e. replicate, slightly peaked $n_z(r)$ profiles. In steady state there is no *net* radial motion and a balance exists between convective inflow due to v_{pinch} and diffusive outflow driven by the density gradient associated with the peaked profile. For a pinch of this form, the flat part of the profile is simply multiplied

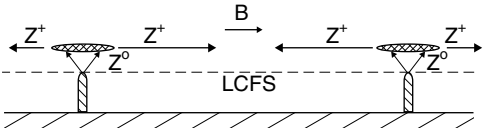

Figure 6.8. For ionization in the main plasma, the ion source can be effectively uniform along $\boldsymbol{B}$ because parallel transport is so much faster than perpendicular transport—even if the actual ionization was localized near the limiters.

by a factor $\exp[S(1-r^2/a^2)]$, figure 6.7(c). For stronger pinches the plasma may never attain a steady state, since the impurity accumulation can cause sufficiently high radiation levels in the core to disrupt the discharge. Assuming, however, that a steady state is reached, edge processes may still establish a 'base level', given by equation (6.6) or (6.7), on which the inward convection builds the central impurity density profile. This would require that the diffusive velocity at the edge, $D_\perp/\lambda_{iz}^0$, exceed local convective velocities, which should usually be satisfied considering the small value of λ_{iz}^0.

These expressions for $\hat{n}_z$ are valid strictly only for a toroidally/poloidally uniform influx of impurity neutrals, for example, a uniform wall source. Most impurity sources are highly localized, e.g. from limiter sputtering. Real wall sources are also typically quite non-uniform. One thus might think that these 1D model results would be unrealistic. In many situations, however, a 1D model is likely to be a good first approximation:

(a) When $\lambda_{iz}^0 > 0$, i.e. ionization is inside the LCFS, parallel transport is so rapid compared with radial transport that a local source is an effectively uniform one, figure 6.8. Thus the above estimate of core carbon density for a JET limiter source can be reasonably accurate.

(b) Most wall sources, even if not uniform, and even if $\lambda_{iz}^0 < 0$, will result in ionization not concentrated too closely to the limiter/divertor-target sink. Thus parallel transport can again achieve reasonably uniform dispersal of the ions before they are lost to the sink. In that case equation (6.7) can again be a reasonable approximation.

Problem 6.4. For a limiter or divertor-target source, with $\lambda_{iz}^0 < 0$, e.g. figure 6.6(a), a 1D radial model may not be applicable. Nevertheless, it is noteworthy that equation (6.7) for $\lambda_{iz}^0 < 0$ already gives a smaller $\hat{n}_z$ than equation (6.6) for $\lambda_{iz}^0 > 0$; show that the ratio of central densities for an example of $\lambda_{iz}^0 = \pm\lambda_{SOL}$ is ~5, while for $\lambda_{iz}^0 = \pm 2\lambda_{SOL}$ it is ~22.

As indicated by the JET Cr results shown in figure 6.5, however, yet larger ratios have to be explained. This cannot be achieved with a purely 1D radial model, since the ionization of the evaporated Cr is so close to the limiter that it

is *not* effectively uniform. Such situations require the use of an impurity-source-plus-transport code, and we will return to this discussion in section 6.6.

Following Tokar [6.35], the Engelhardt model can also be used to estimate the impurity total radiated power $P_z^{\rm rad}$—due to line, bremsstrahlung, etc radiation—when the impurity particle source is effectively uniform, typically for $\lambda_{iz}^0 > 0$, and the impurity radiation is in a uniform 'radiating mantle' inside the LCFS. Let us also approximate equation (6.6) using:

$$\hat{n}_z = \frac{\Phi_{in}^0 \lambda_{iz}^0}{D_\perp A_p} \tag{6.8}$$

i.e. taking the hard boundary condition of $n_z(a) \approx 0$, section 4.6. We also use:

$$\lambda_{iz}^0 = \frac{v_0}{n_e \overline{\sigma v}_{iz}^0} \tag{6.9}$$

where, for simplicity, we will take n_e constant in the main plasma, and $\overline{\sigma v}_{iz}^0$ is the ionization rate for the impurity neutrals.

We have that the *radiation loss rate*, section 3.5, due to impurities $P_{r,z}$[W m^{-3}]:

$$P_{r,z} = n_e n_z L_z \tag{6.10}$$

where L_z is the *radiative loss function*, section 3.5, and n_e and n_z are the values in the radiating volume and are taken as constants here, $n_z = \hat{n}_z$, equation (6.8). Thus the total impurity radiation power, $P_{{\rm rad},z}$ [W]:

$$P_{{\rm rad},z} = n_e n_z L_z V_{\rm rad} \tag{6.11}$$

where $V_{\rm rad}$ is the radiating volume. The latter is taken to be a uniform layer of thickness $\delta_{\rm rad}$, and of area equal to that of the LCFS, i.e. the radiation is in *a thin mantle* at/near the LCFS. We may estimate $\delta_{\rm rad}$ by:

$$\delta_{\rm rad} \approx (D_\perp \tau_{\rm rad})^{1/2} \tag{6.12}$$

where $\tau_{\rm rad}$ is the time it takes for the impurity ion to be ionized to a sufficiently high charge-state that its value of L_z drops significantly; this occurs when the ions are reduced to the He-like state with two orbital electrons. Thus:

$$\tau_{\rm rad} \approx (n_e \overline{\sigma v}_{iz}^*)^{-1} \tag{6.13}$$

where $\overline{\sigma v}_{iz}^*$ is the ionization rate of the Li-like state, figures 1.26–1.28. Combining equations (6.8)–(6.13) then gives:

$$P_{{\rm rad},z} = \frac{v_0 L_z}{\overline{\sigma v}_{iz}^0 (n_e D_\perp \overline{\sigma v}_{iz}^*)^{1/2}} \Phi_{in}^0. \tag{6.14}$$

We also have from equation (3.15) that:

$$P_{{\rm rad},z} = E_{{\rm rad,pot}} \Phi_{in}^0 \tag{6.15}$$

where $E_{\mathrm{rad,pot}}$ is the *radiation potential*. Thus $E_{\mathrm{rad,pot}}$ and L_z are related:

$$E_{\mathrm{rad,pot}} = \frac{v_0}{\overline{\sigma v}^*_{iz}(n_e D_\perp \overline{\sigma v}^*_{iz})^{1/2}} L_z. \tag{6.16}$$

Problem 6.5. Use equation (6.16) to estimate $E_{\mathrm{rad,pot}}$ for a carbon example. Assume $T_e = 30$ eV, $n_e = 10^{19}$ m^{-3}, $D_\perp = 1$ m^2 s^{-1}, $v_0 = 10^4$ m s^{-1} From figure 1.26 find $\overline{\sigma v}^0_{iz}$ and $\overline{\sigma v}^*_{iz} = \overline{\sigma v}^{3+}_{iz}$ and from figure 3.19 find L_z (assume a value for non-coronal radiation, i.e. a short dwell time τ). Show that this gives $E_{\mathrm{rad,pot}} =$ a few keV per entering atom.

The result from problem 6.5 is comparable to the values for the low Z impurities Si and Ne which have been measured on TEXTOR, figure 3.22, and is much larger, of course, than for hydrogen, ~25 eV, figure 3.34. This type of estimate, however, can only be rough. As can be seen from figures 1.26–1.28, $\overline{\sigma v}^*_{iz}$ varies extremely rapidly with T_e; and figure 3.20 shows that L_z also varies extremely rapidly with T_e and τ; from simple estimates one is uncertain about what values of T_e and τ to assume; an impurity source/transport code is needed for more reliable estimates.

6.4.2 The Controlling Role of Edge Processes in Impurity Behaviour

It is remarkable, and perhaps surprising, that the impurity 'story' is largely one of edge processes. First, the source of impurities—for intrinsic ones—is entirely due to processes occurring at the edge. Even for He, whose *original* source is in the core, the *recycling* He source dominates the total He source unless the He pumping is very strong, and so even in this case the source depends on edge processes. As to the edge transport link, this is obviously entirely dependent on the properties of the edge plasma. Regarding the third link in the chain, transport in the main plasma: in the simplest case of $v_{\mathrm{pinch}} = 0$, and for steady-state conditions, the entire impurity content of the plasma is simply given by the density of impurity ions at the edge of the main plasma—regardless of the value, or variation, of $D_\perp(r)$ in the main plasma.

The value of $D_\perp$ used in equations (6.6) and (6.7) is $D_\perp^{\mathrm{edge}}$, the average value of $D_\perp$ outboard of the ionization radius. Thus, in this case, the impurity density throughout the main plasma—which is of size $a \sim$ several metres perhaps—is entirely governed by processes occurring in the edge—typically in a region of radial extent a few cm only.

6.4.3 The Questionable Concept of 'Impurity Screening'

We have an intuitive sense that the edge plasma can be seen as having a greater or lesser 'impurity screening' effect on the main plasma. While this concept may

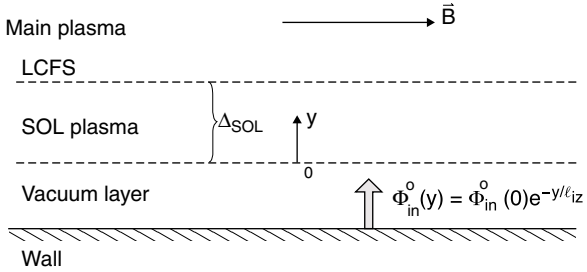

Figure 6.9. A uniform wall influx of impurities, $\Phi_{in}^{0}(0)$, is attenuated with characteristic (radial) decay length l_{iz}, starting at the 'outer edge' of the SOL, $y = 0$.

be intuitively satisfactory, it turns out to be somewhat difficult to give it a precise quantitative definition and the utility of this concept is questionable.

A simple and common definition of 'screening efficiency' is the fraction η_{screen} of the neutrals which are ionized within the SOL. The screening concept appears to be based on the erroneous idea that only the neutrals ionized inside the LCFS contribute to $\hat{n}_z$. Thus for a wall source of impurities one might define η_{screen}:

$$\eta_{\text{screen}} = 1 - \exp(-\Delta_{\text{SOL}}/l_{iz}^{0}) \tag{6.17}$$

where Δ_{SOL} is the total thickness of the SOL and l_{iz}^{0} is the (radial) attenuation length of the impurity neutrals as they are ionized while entering the SOL from the wall, figure 6.9. It is reasonable to estimate Δ_{SOL} as being $\approx \lambda_{\text{SOL}}$. On the other hand, λ_{iz}^{0} and l_{iz}^{0} differ: λ_{iz}^{0} represents the *single* radial location, relative to the LCFS, where *all* of the ionization is taken to occur; on the other hand, l_{iz}^{0} is an *attenuation length*, implying a *radially distributed* ionization source. Let us for illustration, however, consider the case of $\lambda_{\text{SOL}}/l_{iz}^{0} \gg 1$, i.e. all the ionization occurs right at the edge of the SOL, i.e. $\lambda_{iz}^{0} = -\lambda_{\text{SOL}}$. While one then has $\eta_{\text{screen}} = 1$, apparently implying negligible contamination of the main plasma, equation (6.7) gives a significant impurity level, $\hat{n}_z \approx 0.37\Phi_{in}^{0}\lambda_{\text{SOL}}/D_{\perp}A_p$. Even for more penetrating neutrals, so long as all of the ionization occurs in the SOL, any simple definition of 'screening' would still give $\eta_{\text{screen}} = 1$.

'Screening' concepts make too great a distinction between neutrals which are ionized just inside and just outside the LCFS; in fact, a source of neutrals ionized just inside the LCFS results in virtually the same value of $\hat{n}_z$ as a source of neutrals ionized just outside the LCFS! (Compare equations (6.6) and (6.7).) This, of course, is the same point that was made in section 4.6 with regard to the concept of a 'SOL shielding factor' as applied to the hydrogenic species. For both impurities and hydrogen it is important to recognize that the main plasma can just as well be fuelled/contaminated by *ion fuelling* as by *neutral fuelling*. Indeed, it may well be that the neutrals, whether hydrogen or impurities, may all be ionized in 'a remote corner' of the 2D or 3D system—typically near a divertor

target plate—with all the rest of the plasma being fuelled by the parallel, and perpendicular transport of *ions*.

Clearly the modelling of such situations is difficult or impossible to do analytically and impurity source/transport codes are required. We do not deal with that topic until section 6.6; but, we wish to consider here the basis for defining a meaningful measure akin to the questionable η_{screen}. We will define an *impurity reduction factor* f^z_{rdn}:

$$f^z_{\text{rdn}} \equiv \hat{n}_z / \hat{n}^{\text{ref}}_z \tag{6.18}$$

where $\hat{n}^{\text{ref}}_z$ is the value calculated from the *analytic* formulae of equations (6.6) or (6.7) (which assumes uniform neutral influx) and $\hat{n}_z$ is the *code-calculated* value for the actual (spatially localized) source; the same values of Φ^0_{in}, $D_\perp$, A_p are assumed in each case. Note that with such a definition, f^z_{rdn} is essentially insensitive to the value of v_{pinch}, since it will affect $\hat{n}_z$ and $\hat{n}^{\text{ref}}_z$ virtually equally. The DIVIMP impurity transport code, section 6.6, was used to generate sample values of f^z_{rdn}. For example, for $T_{\text{LCFS}} = 25$ eV, $n_{\text{LCFS}} = 8 \times 10^{18}$ m^{-3}, $\lambda_n = \lambda_T = \infty$, $D_\perp = 1$ m^{2}s^{-1}, $v_{\text{pinch}} = 0$, $a = 1.2$ m, $L = 40$ m. A value of $f^z_{\text{rdn}} = 0.013$ was obtained for a source of carbon neutrals that are all ionized at a point at a depth of 1 cm outside the LCFS and 2 cm along $\boldsymbol{B}$, away from a flat-sided limiter; $\hat{n}^{\text{ref}}_z$ was then calculated for $\lambda^0_{iz} = -1$ cm and $\lambda_{\text{SOL}} = (D_\perp L/c_s)^{1/2}$ in equation (6.7). This shows that such a localized source would be only 1.3% as effective as a uniformly distributed source, both located at the same distance outside the LCFS. This is thus an approximation to the JET evaporative Cr cases described in section 6.4.1, figure 6.5. The f^z_{rdn} value has to be calculated using a code for each case of interest (e.g. for limiter sources: $T_{\text{LCFS}}, n_{\text{LCFS}}, \lambda_n, \lambda_T, D_\perp, v_{\text{pinch}}, L$, limiter shape, impurity species, ionization source location). One may eliminate the source location as a required input by calculating instead the spatial distribution of neutral ionization using a code. It is then appropriate to change the definition of $\hat{n}^{\text{ref}}_z$ since the ionization does not all occur at one radius. An arbitrary but convenient re-definition of $\hat{n}^{\text{ref}}_z$ is that value which would hold if all the ionization occurred uniformly along the LCFS:

$$\hat{n}^{\text{ref}}_z = \Phi^0_{in} \lambda_{\text{SOL}} / D_\perp A_p \tag{6.19}$$

with

$$\lambda_{\text{SOL}} = (L D_\perp / c_{sa})^{1/2} \tag{6.20}$$

c_{sa} = value of sound speed at LCFS; now values of $f^z_{\text{rdn}} < 1$ correspond to sources located deep in the SOL, near a limiter; values of $f^z_{\text{rdn}} > 1$ correspond to sources deep in the main plasma.

As with the hydrogenic species there is no need to attempt to define 'screening factors', etc, since the confinement time, here τ_z, for each specific impurity source, *entirely* expresses the quantitative capability of that source to contaminate the plasma.

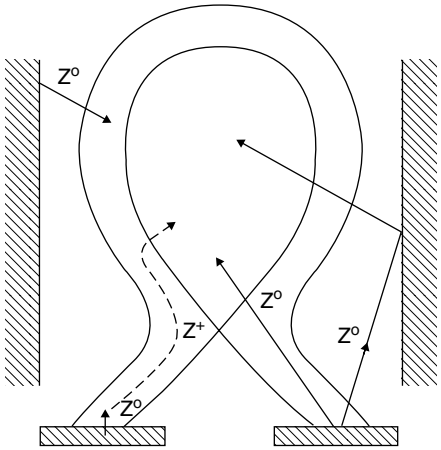

Figure 6.10. Impurities can reach the main plasma by neutral transport, or ion transport, or by a combination.

6.5 Impurity Transport Parallel to *B* in the SOL

6.5.1 Introduction

The original motivation for employing a divertor, in magnetically confined plasma devices, was to suppress the level of edge-produced impurity ions in the main plasma. It seems plausible that if the location of the most intense plasma–surface interaction is made more remote from the confined plasma, then core contamination will be reduced for a given impurity production rate. This would certainly be true if the impurity particles were only transported from their release point to the confined plasma as *neutrals*: a limiter is, by definition, in intimate physical contact with the confined plasma since its inner tip defines the last closed flux surface. Thus some of the neutral impurity particles sputtered, evaporated, etc., from the limiter tip always penetrate the confined plasma before being ionized. By removing the divertor targets some distance from the confined plasma it should be possible to prevent virtually all target-released neutrals from penetrating to the confined plasma before ionizing. As already noted, we must also consider the possibility that the impurity will be transported as an *ion* from its point of ionization along the scrape-off layer (SOL) flux tubes—to the periphery of the confined plasma where, by cross-field transport, it will gain entry to the main plasma, figure 6.10. Even if the impurity can travel only a short distance as a neutral from the target before being ionized, it is possible that leakage as an ion may be very effective. For divertors this SOL parallel transport aspect of edge impurity transport is almost always a critical link in the impurity chain connecting the sources to the impurity density in the core plasma—i.e. the *divertor leakage* or *divertor retention* problem.

This parallel transport aspect of divertor impurity behaviour is the focus of the present section. It is only the first step in answering the larger question of whether a divertor can be expected to be an effective means of impurity control in a tokamak. In order to answer the larger question one also has to consider:

(a) Such leakage as depends strongly on transport as neutrals, for example, volatile impurities such as noble gases released at the target. Such volatiles can make multiple bounces off solid surfaces to reach the main plasma, figure 6.10.
(b) Wall-released impurities; these could be released by energetic charge exchange neutral hydrogen bombardment of the walls or by chemical sputtering, etc, figure 6.10; the released material may include, not just the original wall covering, but material from the targets which migrated by successive sputtering steps along the walls.
(c) The core-produced impurity, helium.

It is appropriate to make some comments on these last three processes by way of putting the present section in context. Divertor retention of volatiles such as helium, neon and argon is an important impurity problem. Unfortunately, there are a number of different routes by which impurities could reach the confined plasma in such cases, and it is not straightforward to assess the relative importance for each route: (a) the original puff location is generally not right at the target plate and the core contamination is probably strongly dependent on puff location; (b) some of these gases can be strongly recycling and the secondary source, associated with recycling at the targets, can quickly become much stronger than the primary (puff) source. Furthermore, the recycling coefficient is not necessarily spatially or temporally constant.

It is beyond the scope of the present section to consider the case of strongly recycling impurities that traverse a large part of the distance from the target to the main plasma in the neutral state, perhaps via multiple wall reflections. We will, however, consider the final step of such a process, namely, starting at the point where the neutral is finally ionized—typically at some appreciable distance from the target. This will be termed the 'deep injection' case.

Here then we take the impurity ion to be injected at a specified and arbitrary distance from the target, either shallow or deep.

6.5.2 Defining the 'Simple One-Dimensional Case' for Modelling Impurity Retention by Divertors

We define the simplest possible case that will still contain the most basic elements of a divertor as they pertain to the retention/leakage of impurities:

(a) We start with the particle as an ion at some specified distance from the target and assume that the impurity ions can move only along ***B***, i.e. we are only considering a *1D picture*. The definition of 'leakage' is based either on

the fraction of the injected ions that leak past a specified upstream point (corresponding to the target-to-X-point distance, for example) or on the ratio of impurity density far upstream to the impurity density near the target. The background plasma, here taken as D^+/e, is assumed to flow towards the target at all points, or to be stagnant. Thus, flow reversal of the background plasma, chapter 15, is not allowed, although in reality such two-dimensional (2D) behaviour may be an important leakage mechanism. The 1D plasma background is taken as specified, and not directly altered by the impurities.

(b) Impurity–impurity collisions are not included.
(c) Diamagnetic and $\boldsymbol{E} \times \boldsymbol{B}$ drifts, chapter 18, are not included.
(d) Steady state is assumed.
(e) The ionization state is taken to be frozen, typically as C^{4+} ions, with ionization/recombination turned off.
(f) The impurity ion is taken to be everywhere in thermal equilibrium with the deuterons or other background ion, $T_z = T_D$.

6.5.3 The Parallel Forces on Impurity Ions

We will start with the physically plausible assumption that the force on an individual impurity ion of mass m_z and charge Z in the direction parallel to $\boldsymbol{B}$ can be represented by:

$$F_z = -\frac{1}{n_z}\frac{\mathrm{d}p_z}{\mathrm{d}s} + m_z\frac{(v_i - v_z)}{\tau_s} + ZeE + \alpha_e\frac{\mathrm{d}(kT_e)}{\mathrm{d}s} + \beta_i\frac{\mathrm{d}(kT_i)}{\mathrm{d}s} + \sim \qquad (6.21)$$

where s is distance measured in the parallel direction from the target in the upstream direction; the subscript i indicates the background ion species, e.g. D^+. Equation (6.21) can be derived from first principles. We do not attempt that here, but start with a heuristic demonstration, in the same spirit as was used for the fluid equations of chapter 1. We consider each of the terms in equation (6.21):

(1) FPG $\equiv -(1/n_z)(\mathrm{d}p_z/\mathrm{d}s)$ is the *impurity pressure gradient force*. It has the same heuristic explanation as in section 1.8.2.1, figure 1.24. A more basic derivation is given in chapter 9, equation (9.14). One thus sees that equation (6.21) constitutes a prescription for following individual particle behaviour, based on a *fluid* description.
(2) FF $\equiv m_z(v_i - v_z)/\tau_s$ is the *friction force* on the impurity ions moving with fluid parallel velocity v_z exerted by the background ions moving with fluid parallel velocity $v_i \cdot \tau_s$ is the stopping time, discussed below. In this heuristic approach one takes this term simply as a physically plausible hypothesis. Below we will substantiate this hypothesis from more basic considerations.
(3) FE $\equiv ZeE$ is the straightforward, and fundamental *electrostatic force* exerted by the parallel electric field E in the SOL.
(4) FeG $\equiv \alpha_e(\mathrm{d}(kT_e)/\mathrm{d}s)$ is the *electron temperature gradient force*, where α_e is a coefficient of order Z^2.

(5) FiG $\equiv \beta_i(\mathrm{d}(kT_i)/\mathrm{d}s)$ is the *ion temperature gradient force*, where β_i is a coefficient, also of order Z^2.

These last two forces are not as intuitively obvious as the others. Their origin lies in a fundamental aspect of the Coulomb interaction that occurs between charged particles: the cross-section for momentum transfer decreases strongly with the relative speed of the colliding particles. As a result the collision frequency has a—perhaps surprising—inverse dependence on temperature, see section 9.4:

$$\nu_{ez}^{\mathrm{mom}} \approx \frac{Cn_zZ^2}{m_e^{1/2}T_e^{3/2}} \tag{6.22}$$

$$\nu_{iz}^{\mathrm{mom}} \approx \frac{Cn_zZ^2}{m_i^{1/2}T_i^{3/2}} \tag{6.23}$$

where C = a constant. Therefore the electrons and background ions that strike the impurity ion from the cold side impart more momentum to it than do the particles striking it from the hot side. The result is forces that push the impurity up the temperature gradients, $\mathrm{d}T_{e,i}/\mathrm{d}s$. We may estimate the dependences and magnitudes of these forces from the following simple model, illustrating for the case of FeG.

The electrons striking the virtually stationary impurity ions at s_0 from the left (cold) side, had experienced their last collision with another electron at $s_0 - \lambda_{ee}$, while those from the right (hot) side had done so at $s_0 + \lambda_{ee}$. Thus the impacting cold electrons have temperature $T_{0e} - \lambda_{ee}(\mathrm{d}T_e/\mathrm{d}s)$, and the hot ones, $T_{0e} + \lambda_{ee}(\mathrm{d}T_e/\mathrm{d}s)$. Therefore the net forward (to the right) force on the n_z impurity ions per m^3 at location s_0 is approximately:

$$F_{ez} \approx m_e\overline{c}_e n_e\,[\nu_{ez}^{\mathrm{mom}}(s_0 - \lambda_{ee}) - \nu_{ez}^{\mathrm{mom}}(s_0 + \lambda_{ee})] \quad [\mathrm{N\,m^{-3}}] \tag{6.24}$$

i.e., ν_{ez}^{mom} is evaluated at the two locations. Expanding and assuming $\lambda_{ee}(\mathrm{d}T_e/\mathrm{d}s)/T_e \ll 1$ (i.e., assuming temperature gradient lengths are larger than λ_{ee}), then:

$$F_{ez} \approx m_e\overline{c}_e n_e \nu_{\mathrm{ezo}}^{\mathrm{mom}} \frac{1}{kT_e}\frac{\mathrm{d}(kT_e)}{\mathrm{d}s}\lambda_{ee}. \tag{6.25}$$

Noting that $\lambda_{ee} \approx \overline{c}_e/\nu_{ee}^{\mathrm{mom}}$ and taking equation (6.22) to give ν_{ee}^{mom} approximately when $Z = 1$, one obtains:

$$F_{ez} \approx n_z Z^2 \frac{\mathrm{d}(kT_e)}{\mathrm{d}s}. \tag{6.26}$$

The force F_{iz} is derived similarly. We thus see that the FiG, FeG forces on each impurity ion are as shown in equation (6.21) and with the coefficients α_e, β_i each being of order Z^2. More refined treatments have been carried out [6.36–6.38]

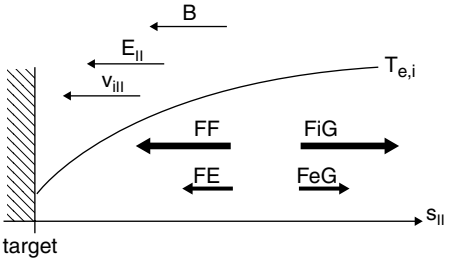

Figure 6.11. The principal parallel forces acting on impurity ions in the SOL. The friction, FF, and electrostatic, FE, forces are usually toward the target while the electron- and ion-temperature gradient forces, FeG, FiG, are usually away. Typically |FF| > |FE|, |FiG| > |FeG|.

giving:

$$\alpha_e = 0.71Z^2 \tag{6.27}$$

$$\beta_i = \frac{3(\mu + 5\sqrt{2}Z^2(1.1\mu^{5/2} - 0.35\mu^{3/2}) - 1)}{2.6 - 2\mu + 5.4\mu^2} \tag{6.28}$$

where

$$\mu \equiv m_z/(m_z + m_i). \tag{6.29}$$

For $\mu \to 1$, $\beta_i \to 2.6Z^2$.

Therefore FiG tends to be more important than FeG. This tendency is reinforced by the fact that ion heat conductivity is weaker than electron conductivity, which tends to make $\mathrm{d}T_i/\mathrm{d}s > \mathrm{d}T_e/\mathrm{d}s$. It is important to remember that FeG and FiG are, in fact, *due to collisions* since this fact is no longer obvious after the cancellation of the similar collision term involved in λ_{ee} and ν_{ez}^{mom}, equation (6.25).

Other forces, such as due to viscosity (forces dependent on velocity gradients), etc, may also be important, but usually the above forces are thought to be the controlling ones.

In principle each of the above forces can be in either direction—toward or away from the target. However, in the simplest case the hydrogenic flow is directed toward the target at all points, i.e. we assume no flow reversal and thus FF is generally toward the target, i.e. it tends to *suppress* divertor leakage. This is usually the principal parallel force acting on the impurities to make the SOL act all along its length as an *impurity sink*, see figure 6.11.

The parallel temperature gradient is usually positive, $\mathrm{d}T/\mathrm{d}s > 0$, and so FeG and FiG push the impurity ions in the upstream direction, toward higher T, i.e. they tend to *increase* divertor leakage. It is readily shown that usually FiG > FeG. Thus the force 'competition' tends to be between FF and FiG. Typically FE is in the same direction as FF but weaker.

It will be seen that FF weakens as plasma temperature increases, while FiG strengthens. Thus the basic expectation is that divertor leakage will increase as the divertor plasma temperature is raised. There thus exists this further practical reason to achieve low divertor temperatures. The impurity pressure-gradient force generally acts in both directions, away from the location where the ions are created by neutral ionization. The pressure-gradient force can be interpreted on an individual ion basis as *parallel diffusion* (although *self*-collisions need not be involved). Consider the simple case when (a) the only forces are the impurity pressure gradient force and the force of friction with a stagnant plasma, i.e. $v_i = 0 = E = \mathrm{d}T_e/\mathrm{d}s = \mathrm{d}T_i/\mathrm{d}s$, (b) collisionality is strong enough that the ion inertial term, $m_z(\mathrm{d}v_z/\mathrm{d}t)$, can be neglected, the ions are in force balance, i.e. $F_{\mathrm{total}} = 0$ and (c) $T_z = T_i$, constant in space. One can rearrange equation (6.21) to give:

$$\Gamma_z \equiv n_z v_z = -\frac{\tau_s k T_z}{m_z}\frac{\mathrm{d}n_z}{\mathrm{d}s} \equiv -D_{\parallel}\frac{\mathrm{d}n_z}{\mathrm{d}s} \tag{6.30}$$

where we have defined a *parallel diffusion coefficient*:

$$D_{\parallel} \equiv \tau_s k T_z/m_z \equiv \tau_s v_{\mathrm{th}}^2 \tag{6.31}$$

where v_{th} is the thermal velocity of the impurity ion:

$$v_{th} \equiv (kT_z/m_z)^{1/2}. \tag{6.32}$$

Let us now take a second look at equation (6.21) and try to justify it from a more fundamental viewpoint. Consider an impurity ion moving with parallel velocity v_z. What could cause v_z to change in time? The most important effects are a parallel electric field E and collisions with electrons and ions. All of the terms in equation (6.21) are due to these effects. In a time Δt, one expects v_z to change by amount $\Delta v_z = ZeE\Delta t/m_z$ just due to the electric field. To this we need to add the Δv_z resulting from collisions with electrons and ions. All three of the forces, FPG, FF and FiG, are largely due to a single process: collisions with ions. Ion collisions tend to dominate over electron collisions due to the fact that $m_i \gg m_e$; only FeG is due to electron–impurity collisions.

Let us focus, therefore, on the effect of ion collisions and try to improve on our initial, purely heuristic approach. The collision rates between charged particles (Coulomb interaction) have been calculated from first principles by Spitzer [6.39] who formulated the problem in terms of the changes of *velocity* caused by collisions, rather than changes of *spatial location*. Thus, the *slowing down rate of velocity* (in the parallel, i.e. 'forward', direction defined by the initial velocity) is calculated, also the *diffusion of velocity* in the parallel direction. (The velocity diffusion in the perpendicular direction is also calculated, but here we will not consider this further since it relates, in the present case, to the gyroscopic motion of the impurity ions as their guiding centre moves along $\boldsymbol{B}$—an effect which is not of first importance.) It is readily shown from Spitzer's analysis that the slowing down process relates to τ_s and governs FF while the

parallel velocity diffusion relates to a different collisional coefficient and governs FPG. By establishing this correspondence between our heuristic development of equation (6.21), and Spitzer's analysis, we can directly put two of the terms, FF and FPG, on a more fundamental basis. (For the moment, however, we will continue to carry along the heuristic forms of FeG, FiG.)

We may consider the change in parallel velocity Δv_z of a particle at each small time step Δt which can be written following Spitzer:

$$\Delta v_z = \langle \Delta w_\parallel \rangle \Delta t + [\langle (\Delta w_\parallel)^2 \rangle \Delta t]^{\frac{1}{2}} r_G + \left(\frac{ZeE}{m_z} + \frac{\alpha_e}{m_z} \left(\frac{\mathrm{d}(kT_e)}{\mathrm{d}s} \right) + \frac{\beta_i}{m_z} \left(\frac{\mathrm{d}(kT_i)}{\mathrm{d}s} \right) + \sim \right) \Delta t \tag{6.33}$$

where the collisional information calculated by Spitzer is entirely contained in the *Spitzer collisional coefficients* $\langle \Delta w_\parallel \rangle$ and $\langle (\Delta w_\parallel)^2 \rangle$ which, despite appearances, are two quite different functions of n_i, T_i, m_i, m_z, T_z. Clearly they give the changes in v_z due to collisions. The Spitzer coefficients include the effect of both small angle and large angle Coulomb collisions between the impurity and background ion species. Owing to the small mass of the electrons, they do not contribute significantly to these terms. r_G is a number drawn randomly from a Gaussian distribution with average value $\langle r_G^2 \rangle = 1$.

We will now extract from Spitzer's expressions simpler, more intuitive expressions to use in modelling impurity behaviour. This will also allow us to relate FF and FPG to the Spitzer collision coefficients. Allowing for the average velocity of v_i of the plasma background it is readily shown that one can re-write Spitzer's results to give:

$$\langle \Delta w_\parallel \rangle \equiv (v_i - v_z)/\tau_s \tag{6.34}$$

where the value of τ_s is extracted from Spitzer's results, his table 5.2; for simplicity we may use Spitzer's tabulated value for $x \equiv \ell_f w \equiv v/(2kT_i/m_i)^{1/2} \ll 1$ (x and $\ell_f w$ are the symbols used by Spitzer) which gives:

$$\boxed{\tau_s = \frac{1.47 \times 10^{13} m_z T_i (T_i/m_i)^{1/2}}{(1 + m_i/m_z) n_i Z^2 \ln \Lambda}} \tag{6.35}$$

τ [s], T [eV], m [amu], n [m^{-3}] and for convenience, we take the Coulomb logarithm $\ln \Lambda = 15$, constant. Clearly this gives the friction force, FF. Turning next to the impurity pressure gradient force, FPG, and its equivalent, parallel diffusion, we can also rewrite from Spitzer:

$$\boxed{[\langle (\Delta w_\parallel)^2 \rangle \Delta t]^{1/2} \equiv \left(\frac{kT_z}{m_z} \right)^{1/2} \left(\frac{2\Delta t}{\tau_\parallel} \right)^{1/2} = v_{th} \left(\frac{2\Delta t}{\tau_\parallel} \right)^{1/2}} \tag{6.36}$$

where we have defined a *parallel collisional diffusion time* $\tau_\parallel$:

$$\boxed{\tau_\parallel = \frac{1.47 \times 10^{13} m_z T_z (T_i/m_i)^{1/2}}{n_i Z^2 \ln \Lambda}} \tag{6.37}$$

τ [s], T [eV], m [amu], n [m^{-3}]. While it is convenient to use this representation for parallel diffusion and while it does make this process appear to depend on T_z, through the T_z in equation (6.36), it should be noted that the parallel diffusive steps (in velocity space) do not actually depend on T_z (for the assumption here of $m_z \gg m_i$): $v_{th} \propto T_z^{1/2}$, however $\tau_\parallel \propto T_z$, also, and therefore a cancellation results in equation (6.36).

We now replace τ_s with $\tau_\parallel$ in equation (6.31) to obtain an improved expression for the spatial diffusion coefficient $D_\parallel$:

$$\boxed{D_\parallel = v_{th}^2 \tau_\parallel.} \tag{6.38}$$

Interestingly, comparisons of velocity and spatial diffusion—using equation (6.38) for the latter—give very similar results [6.40], except for cases where mean free paths are long compared with the problem scale length.

Finally we return to FeG and FiG. If it is really the case that FiG is also due to ion collisions, then why is this force not automatically covered by the Spitzer coefficients $\langle \Delta w_\parallel \rangle$ and $\langle (\Delta w_\parallel^2) \rangle$, as FPG and FF were? Why do we continue to include the heuristic form of FiG and FeG in equation (6.33)? The reason is that Spitzer assumed a constant temperature in his analysis. In the analysis of [6.36–6.38], however, the Spitzer approach was extended to include the effect of a temperature gradient and the average effect on an ensemble of impurity ions—i.e., the *fluid* forces—were calculated. We have appropriated these convenient fluid expressions, dividing by n_z, to obtain *estimates* for the forces on individual impurity ions. These expressions are strictly appropriate only for *fluid* analysis of impurity behaviour. For analysis which involves following the *specific* velocity of *individual* particles, as in Monte Carlo analysis, these expressions are only approximately valid since they do not include the effect of the specific velocity of the impurity ion. Recently Reiser *et al* [6.41] have extended the Spitzer approach to include the effect of an ion temperature gradient, and casting the results in a form which is appropriate for following individual particles, allowing for their *specific* velocity at each instant; thus one would replace the Spitzer coefficients in equation (6.33) with Reiser's coefficients, and drop the heuristic/fluid FiG expression (the FeG term would remain, however).

6.5.4 A Simple 1D Fluid Model of Impurity Leakage from a Divertor

6.5.4.1 Introduction

The Engelhardt model provides a simple and useful picture of the 1D *radial* behaviour of impurities, section 6.4. It would be useful to have an equivalent model

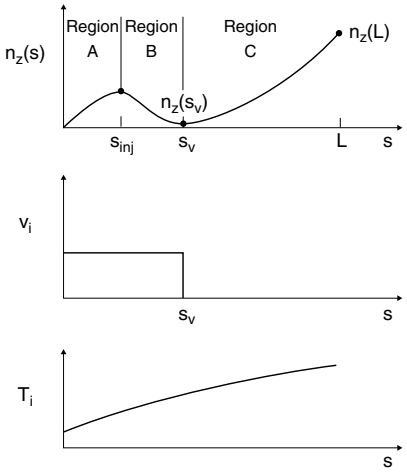

Figure 6.12. General impurity density profile along ***B*** allowing for friction, temperature gradient forces, parallel diffusion, etc. For simplicity we consider the (background) plasma flow velocity to be a step function.

for the 1D *parallel* impurity behaviour in the SOL, particularly for a divertor. We outline such a model here. As with the Engelhardt model it will be necessary to make strong assumptions, for example, that all the neutrals are ionized at a single location—which here will be at some distance $s_{\rm inj}$ ('inj' for 'injection') upstream from the target.

It is useful to consider three regions, figure 6.12:

(a) Region A, closest to the target, $0 \leq s \leq s_{\rm inj}$ will be termed the 'plateau' or 'prompt-loss region'.

(b) Further upstream, region B, will be termed the 'impurity density decay' region, $s_{\rm inj} \leq s \leq s_v$ where s_v is defined as the limit of the hydrogenic recycle region, and thus will be taken, in this simple picture, to be the region over which v_i is non-zero.

(c) Yet further upstream, $s_v \leq s \leq L$, is region C, the 'impurity build-up' or 'trap' region. Since flow reversal, etc is assumed to be absent, then $v_i = 0$, for $s_v \leq s \leq L$. Here FF ≈ 0 and FiG is unopposed, thus causing a build-up of impurity density, i.e. an 'impurity trap'. It is necessary to emphasize the *assumption* made here that $v_i = 0$ for $s \geq s_v$. In reality significant flow may well exist over much or all of $0 \geq s \leq L$, perhaps due to flow reversal, chapter 15, or drift effects, chapter 18, but for this first, simple treatment we assume such flows to be absent.

It is from this upstream SOL reservoir of impurities that particles diffuse into the main plasma. *Our principal object therefore is to relate the upstream impurity density to the impurity injection rate* $\Gamma_{\parallel}^{in}$ *and to the parallel forces in the SOL.*

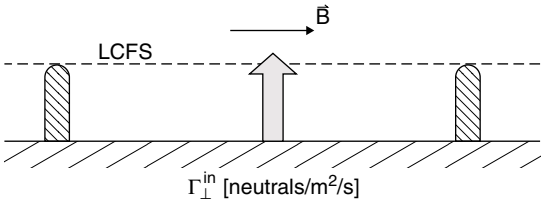

Figure 6.13. The Engelhardt model is used to analyse *radial* profiles, and one needs to specify $\Gamma_\perp^{in}$.

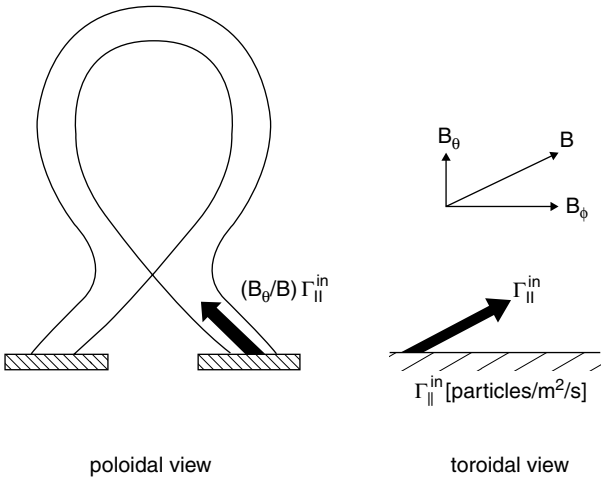

Figure 6.14. For analysis of *parallel* impurity profiles one needs to specify $\Gamma_\parallel^{in}$.

$\Gamma_\parallel^{in}$ [particles m^{-2} s^{-1}] is to be understood in a geometrically different way than was used in the Engelhardt radial model, where Φ_0^{in} [particles s^{-1}], section 6.4, could be written $\Gamma_\perp^{in} A_p$, i.e. as an influx in the *radial* direction, where $\Gamma_\perp^{in}$ is in particles per s per m^2 of total plasma surface area, $A_p = 2\pi a 2\pi R$, figure 6.13. By contrast, $\Gamma_\parallel^{in}$ is the injection rate of impurity ions per second per square metre of area perpendicular to the plasma flow or parallel direction, figure 6.14. Thus, if Φ_0^{in} represents the total influx of impurities for the entire tokamak then:

$$\Phi_0^{in} = \Gamma_\parallel^{in} A_\parallel^{\mathrm{SOL}} \tag{6.39}$$

see sections 5.6 for the precise definition of $A_\parallel^{\mathrm{SOL}}$. In reality of course, $\Gamma_\parallel^{in}$ is unlikely to be a constant across the SOL. Here, however, we simply take $\Gamma_\parallel^{in}$ as a control parameter of the problem. We can estimate $\Gamma_\parallel^{in}$ for the case of a source due to target sputtering characterized by yield Y, i.e. $\Phi_0^{in} = Y\Phi_i^{\mathrm{out}}$. Since

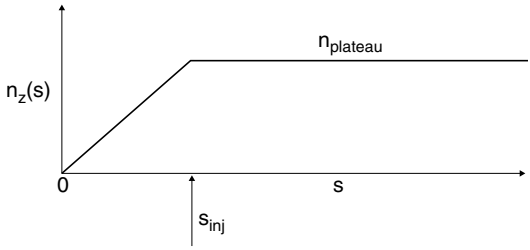

Figure 6.15. In the absence of parallel forces on the impurity, with only parallel diffusion acting, a parallel density profile results which is the analogue of the radial profile given by the Engelhardt model (for perpendicular diffusion with no inward pinch).

$\Phi_i^{\text{out}}/A_\parallel^{\text{SOL}} = \Gamma_{it}$, i.e. the particle flux density of the background ions striking the target, then:

$$\Gamma_\parallel^{in} = Y\Gamma_{it}. \tag{6.40}$$

This result is only approximate since Γ_{it} varies across the target and the impurities sputtered from one part of the target are not necessarily ionized on the same flux tube.

6.5.4.2 Region A: The Plateau or Prompt-Loss Region

Let us start with the simplest situation of $v_i = 0 = E = \mathrm{d}T_e/\mathrm{d}s = \mathrm{d}T_i/\mathrm{d}s$. Assuming all the impurity ions are injected at location s_{inj}, then in steady state the impurity density profile of $n_z(s)$ will be the simple one shown in figure 6.15, with a 'plateau' density

$$n_z(s_{\text{inj}}) \equiv n_p \approx s_{\text{inj}}\Gamma_\parallel^{in}/D_\parallel. \tag{6.41}$$

A symmetry or reflection point is assumed to exist at $s = L > s_{\text{inj}}$, where L is the connection length, section 1.4.2.

Problem 6.6. The result in equation (6.41) is approximate since the density just in front of the target, $n_z(0)$, has been assumed to be negligible compared with n_p; argue that in fact, $n_z(0) \approx \Gamma_\parallel^{in}/v_{\text{th}}$. By considering some example conditions, however, show that often $v_{th} \gg v_{\text{diff}}$, where

$$v_{\text{diff}} \equiv D_\parallel/s_{\text{inj}}. \tag{6.42}$$

We used $v_{\text{diff}} = v_{th}^2\tau_s/s_{\text{inj}} = v_{\text{th}}(\lambda_{\text{mfp}}/s_{\text{inj}})$ here, where

$$\lambda_{\text{mfp}} \equiv v_{th}\tau_s. \tag{6.43}$$

Note that since we take $T_z = T_i$ in this first treatment, therefore $\tau_s \approx \tau_\parallel$. Thus argue that when the mean free path for collisions between impurity and plasma ions λ_{mfp} is much less than s_{inj} one can neglect $n_z(0)$ compared to n_p.

Since $\tau_s \propto T_i^{3/2}/n_i Z^2$, $D_\parallel \propto T_i^{5/2}$ and so $n_p \propto T_i^{-5/2}$. For this case $n_p = n_u$, the upstream density, i.e. the density adjacent to the main plasma, this density directly gives the leakage to the main plasma. Thus, the leakage will actually *decrease* strongly with increasing T, which is the opposite of expectations (and also, one should emphasize, the opposite of more realistic situations, as considered below). This result is not very physical, and therefore should not be considered further.

For the collisionless extreme, $\lambda_{\text{mfp}}/s_{\text{inj}} \gg 1$, we expect that $n_p \approx \Gamma_\parallel^{in}/v_{th}$ which gives a weaker, but still inverse temperature dependence, $n_z(L) \propto T^{-1/2}$.

Consider next the case where the force of friction, FF, dominates all other forces and also assume strong collisionality so that the acceleration (inertia) can be neglected. In this case one has $v_z \to v_i$ and thus $n_p \approx \Gamma_\parallel^{in}/v_i$.

When the ion temperature force, FiG is dominant, with strong collisonality and $v_i = 0$, then one has, from equation (6.21)

$$v_z \approx v_{T_i} \equiv \beta_i \tau_s (\mathrm{d}(kT_i)/\mathrm{d}s)/m_z. \tag{6.44}$$

(For T in [eV], rather than [degrees], replace k with $e = 1.6 \times 10^{-19}$ C.) One therefore expects for the general case that approximately

$$n_p \approx \Gamma_\parallel^{in}/v_{th} \qquad \text{for } \lambda_{\text{mfp}} \gg s_{\text{inj}} \tag{6.45}$$

$$n_p \approx \Gamma_\parallel^{in}/v_{\text{prompt loss}} \qquad \text{for } \lambda_{\text{mfp}} \ll s_{\text{inj}} \tag{6.46}$$

where

$$v_{\text{prompt loss}} = v_{\text{diff}} - (v_i + v_E - v_{T_i} - v_{T_e}) \tag{6.47}$$

with

$$v_E \equiv \tau_s Z e E/m_z \tag{6.48}$$

and

$$v_{T_e} \equiv \alpha_e \tau_s (\mathrm{d}(kT_e)/\mathrm{d}s)/m_z. \tag{6.49}$$

Note the negative sign applied to equation (6.47): our convention here is that the positive direction is away from the target. Equation (6.47) is directly derived from equation (6.21) by neglecting inertia, assuming $T =$ constant, and approximating $-\mathrm{d}n_z/\mathrm{d}s$ by n_z/s_{inj}. The expression is only approximate since $T_i =$ constant was used to estimate v_{diff}, but clearly that cannot be assumed when calculating v_{T_i}. The signs in equation (6.47) assume the usual situation where FF and the electric force, FE, are towards the target, while FiG and FeG are away from the target. As earlier noted, it often turns out to be the case that |FF| > |FE| and |FiG| > |FeG|, so that in the following FE and FeG are usually neglected for simplicity. (It is not always true that |FF| > |FE|, of course: for weakly collisional cases FF $\to$ 0 while FE remains finite.)

The existence of a density 'plateau' extending from s_{inj} to L, figure 6.15, assumes $v_i = \mathrm{d}T_i/\mathrm{d}s = 0$ in the region upstream of s_{inj}. If, in fact, |FF| < |FiG| in this latter region, then there will not be any density plateau, but rather the

density will build up, implying truly *catastrophic* leakage to the main plasma. Clearly, then, a necessary (but, as will be shown, not sufficient) criterion for the avoidance of leakage is that |FF| > |FiG| in the region upstream of the injection point. This is the basis of the leakage criteria given by Neuhauser *et al* [6.42] and by Krasheninnikov *et al* [6.43].

Problem 6.7. The *Neuhauser criterion* to avoid leakage is that

$$\boxed{|M_i| > \lambda_{ii}/\lambda_T} \tag{6.50}$$

where $M_i \equiv$ Mach number of the 'background', e.g. deuterium, plasma flow, $\lambda_{ii} \equiv$ the mean free path for collisions between deuterium ions and λ_T is the characteristic scale length for variations of T_i along s. One has FF $\approx M_i c_s m_z/\tau_s$ where $c_s \equiv$ background plasma acoustic speed and

$$\text{FiG} = e\beta_i T_i/\lambda_T \approx eZ^2 T_i/\lambda_T. \tag{6.51}$$

With $\lambda_{ii} \approx c_s\tau_{ii}$ ($\overline{c}_i \approx c_s$ for $T_i = T_e$) and $\tau_{ii}/\tau_s \approx m_i Z^2/m_z$ show that requiring |FF| > |FiG| is the same as equation (6.50).

Problem 6.8. The *Krasheninnikov criterion* to avoid leakage is that

$$\boxed{|q_\parallel^{i,\text{conv}}| > |q_\parallel^{i,\text{cond}}|} \tag{6.52}$$

where $q_\parallel^{i,\text{conv}}$ and $q_\parallel^{i,\text{cond}}$ are the parallel ion heat flux densities along s carried by convection and conduction, respectively. Neglecting, for simplicity, the convected flow energy of $\frac{1}{2}m_i v_i^2 n_i v_i$ one has $q_\parallel^{i,\text{conv}} = \frac{5}{2}n_i v_i k T_i$ while $q_{\parallel i,\text{cond}} = -\kappa_{i0} T_i^{5/2}(\mathrm{d}T_i/\mathrm{d}s)$, where $\kappa_{i0} \approx 60$ for T_i [eV], $\mathrm{d}T_i/\mathrm{d}s$ [eV m^{-1}], q [W m^{-2}]. Show that requiring |FF| > |FiG| is the same as equation (6.52).

In the following we focus on the case where |FF| > |FiG| just upstream of $s = s_{\text{inj}}$ since it will turn out that even when this necessary condition is satisfied, leakage may nevertheless occur. We also note that when |FF| > |FiG|, then generally there is not a density *plateau* at $s = s_{\text{inj}}$, but rather a density *peak* occurs, constituting a base level from which there is catastrophic leakage to the main plasma. We will therefore call region A, $0 \leq s \leq s_{\text{inj}}$, the 'prompt-loss region' and $n_p \equiv n_z(s_{\text{inj}})$ will refer to this 'prompt-loss' or near-target impurity density. The definition of *efficient divertor retention* or *low divertor leakage* will then be that $n_u/n_p \ll 1$, where n_u is the impurity density upstream, say at the X-point, where the SOL first comes into contact with the confined plasma. For the background plasma one often has $n_{iu}/n_{ip} \ll 1$ (owing to the tendency for $T_{iu}/T_{ip} \gg 1$ and also assuming pressure balance holds) but simple pressure

balance does not apply to the impurity species. One may note that the question of what constitutes *acceptable* divertor leakage, is a larger question, of course; that also depends on the charge, Z, of the impurity element and the absolute impurity production rate $\Gamma_{\parallel}^{in}$, as well as the *consequences* of a specific absolute level of n_z existing in the main plasma.

6.5.4.3 *Region B: The Impurity Density Decay Region*

To recapitulate, we consider $n(s)$ profiles such as those shown in figure 6.12, consisting of three regions:

(a) Region A, the prompt-loss region, $0 \leq s \leq s_{\text{inj}}$, characterized by a density n_p typically near $s = s_{\text{inj}}$.

(b) Region B is defined by $s_{\text{inj}} \leq s \leq s_v$, where $v_i \neq 0$ but $v_i \rightarrow 0$ at $s = s_v$. We assume that |FF| > |FiG|, hence that this is a region where $n_z(s)$ decays. The characteristic scale length along s for v_i, i.e. the value of s_v, is given by the spatial distribution of the ionization of the deuterium (or other background) neutrals recycling from the plate. To calculate this precisely requires sophisticated neutral codes such as DEGAS, EIRENE or NIMBUS. Vlases and Simonini [6.44], guided by NIMBUS code results for JET geometries, have obtained the approximation:

$$s_v \approx 0.25/(n_e \times 10^{-20}) \text{ [m]} \tag{6.53}$$

where n_e is the plasma density near the target. (Note that s_v is measured along $\boldsymbol{B}$, and not in the poloidal direction.)

(c) Region C where we will assume $v_i = 0$ and FiG is only opposed by (back-) diffusion in this impurity build-up region. Region C spans $s_v \leq s \leq L$.

The principal objective is to evaluate Γ_{leak}, the forward flux of impurities at s_v, and also n_u/n_p. In steady state, of course, the forward and backward fluxes at s_v are equal.

Region B is a stagnant zone for impurities since it is upstream of both the source (s_{inj}) and the sink (at $s = 0$), thus $v_z = F_{\text{total}} = 0$ here. (Other sources of impurities, e.g. He produced in the main plasma as ash from DT fusion, have to be analysed differently.) Assuming $T_z = T_i$, one can then integrate equation (6.21) to obtain the result [6.44–6.46]:

$$\boxed{n_z(s) = n_p \exp[\text{FFf}(s) + \text{FEf}(s) + \text{FeGf}(s) + \text{FiGf}(s)]} \tag{6.54}$$

where the 'f' refers to 'factor' and

$$\text{FFf}(s) \equiv \int_{s_{\text{inj}}}^{s} \frac{m_z v_i(s')}{kT_i \tau_s} \mathrm{d}s' \tag{6.55}$$

$$\text{FEf}(s) \equiv \int_{s_{\text{inj}}}^{s} \frac{ZeE(s')}{kT_i} \mathrm{d}s' = -\int_{V_{\text{inj}}}^{V} \frac{Ze}{kT_i} \mathrm{d}V' \tag{6.56}$$

$$\mathrm{FiGf}(s) \equiv \int_{s_{\mathrm{inj}}}^{s} \frac{(\beta_i - 1)(\mathrm{d}(kT_i)/\mathrm{d}s')}{kT_i}\mathrm{d}s' = (\beta_i - 1)\ln[T_i(s)/T_i(s_{\mathrm{inj}})] \tag{6.57}$$

(the -1 in $\beta_i - 1$ comes from the T_i dependence of the impurity pressure gradient force); finally

$$\mathrm{FeGf}(s) \equiv \int_{s_{\mathrm{inj}}}^{s} \frac{\alpha_e \mathrm{d}(kT_e)/\mathrm{d}s'}{kT_i}\mathrm{d}s'. \tag{6.58}$$

In cases where the variation of T_i is small over $s_{\mathrm{inj}} \leq s \leq s_v$ one can ignore the variations of $T_i(s)$ and $\tau_s(s)$, making the evaluation of $\mathrm{FFf}(s)$, $\mathrm{FEf}(s)$ and $\mathrm{FeGf}(s)$ much simpler. (Note that $kT_i\tau_s \propto T_i^{5/2}$. Since these factors appear in an exponential, small corrections to them can be important. For some cases one then has to allow for this variation in the integral, but this is straightforward. Of course, one cannot neglect T_i-variations in FiG since this force depends directly on the gradient of T_i.) Let us take the case where this correction is unimportant; we adopt also the convenient assumption that $v_i(s) = v_{it}$, a constant over $0 \leq s \leq s_v$; $v_{it} < 0$ since flow is assumed to be toward the target. The subscript 't' indicates target values. Then for $s < s_v$:

$$\mathrm{FFf}(s) \approx \frac{m_z v_{it} s}{kT_i\tau_s} = \frac{v_{it}}{D_\parallel}s \equiv -\frac{s}{\lambda_\parallel} \tag{6.59}$$

where we have also assumed that $s, s_v \gg s_{\mathrm{inj}}$ and defined $\lambda_\parallel \equiv -D_\parallel/v_{it}$. Therefore, if we ignore the other forces we find that $n_z(s)$ decays with characteristic length $\lambda_\parallel$, which is directly related to the prescription of Roth *et al* [6.47] that to avoid leakage one needs a short $\lambda_\parallel$, and thus low temperature (since $D_\parallel \propto T^{5/2}$, then $\lambda_\parallel \propto T^2$). Generally, however, one should include at least FiG, since β_i can be quite large, for example, about 32 for C^{4+} in D^+, and so even a weak T_i-gradient can influence the density decay length in region B, λ_{decay}. Nevertheless, $\lambda_\parallel$ gives a first estimate of λ_{decay}.

Thus, an impurity density minimum occurs at s_v, figure 6.12:

$$n_z(s_v) \approx n_p \exp[\mathrm{FFf}(s_v) + \mathrm{FiGf}(s_v)] \tag{6.60}$$

from which a build-up can then occur in region C.

When the variation of T_i in the denominators of equations (6.55)–(6.58) can be ignored, then it is useful to define an *impurity potential*:

$$V_z \equiv -\int F_z \mathrm{d}s. \tag{6.61}$$

Then:

$$n_z(s) = \exp[V_Z/kT_i] \tag{6.62}$$

i.e. a Boltzmann factor relation.

6.5.4.4 *Region C: Impurity Density Build-Up or Trap Region*

In regions C, equation (6.54) applies again with $n_z(s_v)$ replacing n_p. While one could combine regions B and C there are good reasons not to do this, as discussed below.

Neglecting diffusion, leakage of impurities past point s_v is given by the flux density

$$\Gamma_{\text{leak}} = v_{T_i} n_z(s_v) \tag{6.63}$$

neglecting v_{T_e}; in equilibrium, diffusion gives an equal leakage back out of the trap located upstream of s_v, i.e. region C. The density maximum in region C generally occurs at $s = L$ and *can be of enormous magnitude* since $|\text{FiGf}(L)|$ can be much larger than $|\text{FFf}(L)|(= |\text{FFf}(s_v)|)$, and the difference in these factors appears in an exponential. It turns out that this result, fortunately, is an *artificial and physically unrealistic* one. It is the consequence of assuming a strictly 1D system, where the ions can only move along $\boldsymbol{B}$, i.e. along s. It can readily be shown that even very small cross-field losses will stop such an impurity build-up from occurring [6.42]. We can define the *parallel de-trapping time* (based on loss of ions, by diffusion, from the trap region back past s_v in steady state) by:

$$\tau_{\parallel}^{\text{de-trap}} = \frac{N_{\text{trap}}}{A_{\parallel}^{\text{SOL}} \Gamma_{\text{leak}}} \approx \frac{\overline{n}_{\text{trap}} L}{\Gamma_{\text{leak}}} \tag{6.64}$$

where $\overline{n}_{\text{trap}}$ is the average impurity density in the trap, $\overline{n}_{\text{trap}} \approx n_u$ and N_{trap} is the total trap particle content. This time may be much more than 1 s. Consider, however, the effect of a competitive loss mechanism, say, cross-field transport into the private plasma or out to the periphery of the SOL, which will take $\tau_{\perp} \sim 10^{-3}$ to 10^{-2} s (for $D_{\perp} \approx 1$ m^2 s^{-1} and cross-field distances of the order of centimetres). While there exists little understanding of how impurity ions behave in these peripheral regions of the edge plasma, these may be regions of weak collisionality and we will assume that ions which reach such flux tubes move along **B** to reach solid surfaces in impurity thermal transit times, i.e. milliseconds. That is we assume that an impurity trap does *not* exist on peripheral flux tubes; it is therefore to be noted that *this is a critical hypothesis*. Proceeding then:

$$\tau_{\text{de-trap}}^{\text{actual}} = [(\tau_{\parallel}^{\text{de-trap}})^{-1} + \tau_{\perp}^{-1}]^{-1}$$

and so $\tau_{\text{de-trap}}^{\text{actual}} \approx \tau_{\perp}$. Thus, the actual value of $\overline{n}_{\text{trap}}$ is

$$\overline{n}_{\text{trap}} = \Gamma_{\text{leak}} \tau_{\perp} / L = n_z(s_v) v_{T_i} \tau_{\perp} / L \tag{6.65}$$

$$\boxed{\overline{n}_{\text{trap}} = \frac{\Gamma_{\parallel}^{in}}{v_{\text{prompt loss}}} \left(\frac{n_z(s_v)}{n_p} \right) v_{T_i} \frac{\tau_{\perp}}{L}} \tag{6.66}$$

where $v_{\text{prompt loss}}$ is given by equation (6.47), $n_z(s_v)/n_p$ is given by equation (6.60), v_{T_i} is given by equation (6.44) and equation (6.46) has

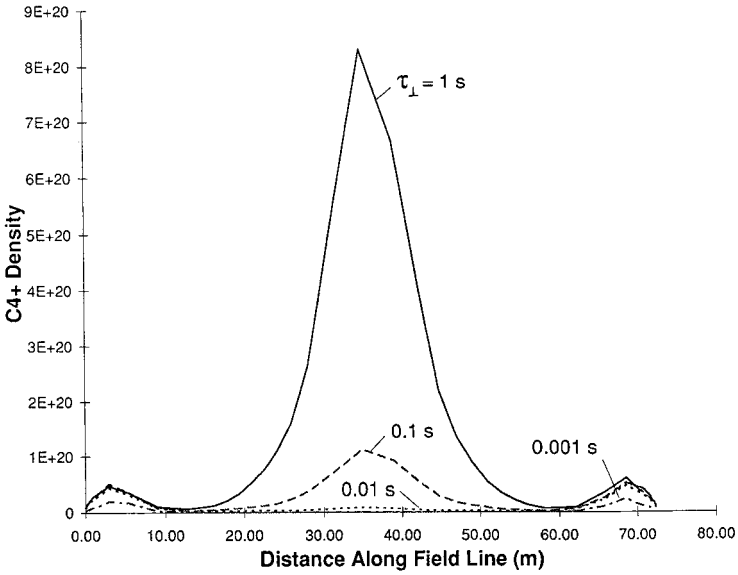

Figure 6.16. Calculated C^{4+} profiles using DIVIMP for a 'deep injection' case: $\Gamma_{\parallel}^{in} = 1.73 \times 10^{23} [C^{4+} m^{-2} s^{-1}]$, $n_e = 10^{19}$ m^{-3}, $T_t = 50$ eV, $s_{inj} = 5$ m, $s_v = 10.85$ m, $M_D = 0.1$, $f_{cond} = 1$ (discussed in section 6.5.5.1) and various values of $\tau_\perp$. Evidently, only for $\tau_\perp \leq 10$ ms is divertor retention good for this value of T_t, and for these parameters [6.40].

also been used assuming $\lambda_{mfp} \ll s_{inj}$. Thus, fortunately $\overline{n}_{trap}/n_p$ can be much less than unity, i.e. divertor retention of impurities can be much better than is indicated by a strictly 1D analysis. One may note from equation (6.65) the usefulness in being able to calculate the one-way leakage rate at s_v, Γ_{leak}, since together with an estimate of $\tau_\perp$ this gives the result of chief interest, namely the value of $\overline{n}_{trap}$. Figure 6.16 shows the effect of $\tau_\perp \neq \infty$.

Although the original objective here was to develop a *one*-dimensional model for impurity behaviour, we see that if we stick strictly to 1D impurity transport the departure from reality can be enormous. One must, therefore, include at least this one particular 2D effect, which, fortunately, requires only the foregoing simple correction. This correction is, however, only *conceptually* simple since we now need to know how actually to evaluate $\tau_\perp$. We return to this below.

It is thus seen that the larger the value of $D_\perp$ (i.e. the *smaller* the value of $\tau_\perp$), the *smaller* will be $\overline{n}_{trap}$ and thus, in steady state, the smaller will be the impurity content of the main plasma. This, possibly counter-intuitive, conclusion is strictly dependent on the assumption that the impurity content of the main plasma does indeed reach steady-state equilibrium with the upstream impurity density in the

SOL, $\overline{n}_{\text{trap}}$. In other circumstances, such as ELMing discharges (ELM = edge localized modes) where the main plasma is periodically purged of impurities, chapter 7, there will be offsetting dependences on $D_\perp$: large values of $D_\perp$ will, as before, carry impurities more effectively across the SOL into the (assumed) sink at the far periphery of the SOL, lowering $\overline{n}_{\text{trap}}$; however, large values of $D_\perp$ will rapidly replenish the impurity content of the main plasma between ELMs, perhaps increasing the time-averaged impurity content there. The analysis of such time dependent situations is not undertaken here.

It is unfortunate that our ability accurately to calculate the impurity density in the main plasma, n_z^{main}, which is given essentially by the value of $\overline{n}_{\text{trap}}$, is directly dependent on $\tau_\perp$, equation (6.66), *since we do not know very much about this quantity*. It may depend on the properties of the 'far periphery' of the SOL, which is a poorly understood region. For modelling the background plasma as well as the impurities, it is generally found that the boundary conditions at the periphery of the SOL influence solutions—and this remains an important issue in all edge modelling, calling for attention. While our ability accurately to calculate n_z^{main} is poor, fortunately it turns out that we can more reliably estimate the divertor plasma conditions n_t and T_t, which correspond to efficient divertor retention. The reason for this is that the leakage probability is a strong function of n_t and T_t, and so the precise value chosen for $\tau_\perp$ is not greatly important for *this* purpose. We may also roughly bracket the value of $\tau_\perp$:

(a) on the short side, by the time required for an ion to move at the hydrogenic sound speed a distance along the SOL to the target, about 1 ms typically;
(b) on the long side, by the time required for an ion to cross-field diffuse out to the walls, a distance of about $\Delta r \approx 0.1$ m, typically; $\Delta r \approx (D_\perp \tau_\perp)^{1/2}$, which for $D_\perp \approx 1\ \text{m}^2\ \text{s}^{-1}$ gives about 10 ms.

We may thus estimate $10^{-3}\ \text{s} \lesssim \tau_\perp \lesssim 10^{-2}\ \text{s}$.

6.5.5 Estimating Divertor Leakage

6.5.5.1 The Case of Ionization of Impurities Near the Target

We may now use equation (6.66) to calculate the divertor leakage Γ_{leak} and the impurity density upstream in the SOL, $\overline{n}_{\text{trap}}$. We will consider two cases:

(a) Near-target 'injection' of impurities, i.e. the ionization of impurities occurs near the target. This would be the typical situation for sputtering of non-recycling impurities from the targets, e.g. C. For such cases we will assume particularly simple approximations for the integrals in equations (6.55)–(6.58).
(b) 'Deep injection', considered in section 6.5.5.3.

We will assume that the parallel force balance is between the FF and FiG forces. Because an exponential is involved, the $n_z(s_v)/n_p$ factor, equation (6.54),

can be the most sensitive one, and we start by considering it. For 'shallow injection' we will assume that the integrand in equation (6.55) can be taken as constant and be evaluated for the target values. Thus:

$$\mathrm{FFf}(s_v) = -\frac{m_z \overline{M}_i c_{st} \Delta s}{k T_t \tau_{st}} \tag{6.67}$$

where $\overline{M}_i$ = the (absolute magnitude of) Mach number of the background plasma averaged over $s_{\mathrm{inj}} \leq s \leq s_v$, $\overline{M}_i = |v_i|/c_{st}$.

$$\Delta s \equiv s_v - s_{\mathrm{inj}}. \tag{6.68}$$

One also then has:

$$\mathrm{FFf}(s_v) = -\overline{M}_i \Delta s / \lambda_{\parallel t} \tag{6.69}$$

where

$$\lambda_{\parallel t} \equiv \frac{k T_t \tau_{st}}{m_z c_{st}} \tag{6.70}$$

i.e. the value of the *Roth–Fussmann friction length*, $\lambda_\parallel$, equation (6.59), evaluated for conditions at the target. Subscript t for target. For T_t in [eV], rather than [degrees], replace k in equation (6.70) with e.

To evaluate $\mathrm{FiGf}(s_v)$, equation (6.57), we will assume for simplicity and illustration a constant temperature gradient exists over $s_{\mathrm{inj}} \leq s \leq s_v$ of the value just at the target. (In reality the gradient right at the target differs from that upstream, e.g. at s_v.) Thus:

$$T_i(s) = T_i(s_{\mathrm{inj}}) + (s - s_{\mathrm{inj}}) T_t' \tag{6.71}$$

where the derivative T_t' can be evaluated from the heat conduction equation

$$-\kappa_0 T_t^{5/2} T_t' = f_{\mathrm{cond}} q_t. \tag{6.72}$$

Here it is assumed that over the region $s_{\mathrm{inj}} \leq s \leq s_v$ a fraction f_{cond} of the total parallel power flux density $q_\parallel$ is carried by conduction, $f_{\mathrm{cond}} \leq 1$. The target power flux density:

$$q_t = -\gamma n_t c_{st} k T_t. \tag{6.73}$$

For T_t in [eV], rather than [degrees], replace k with e. The effect of volumetric power loss, e.g. radiation, in $s_{\mathrm{inj}} \leq s \leq s_v$ is to increase $|q_\parallel|$ and thus T_t'. In an approximate way we can allow for this quantitatively by using values f_{cond} greater than unity. Thus we are interested in values of this generalized parameter, in the range $0.1 \leq f_{\mathrm{cond}} \leq 10$, roughly.

From equation (6.57) we have:

$$\mathrm{FiGf}(s_v) = \ln\left(1 + \Delta s \frac{T_t'}{T_t}\right)^{\beta_i - 1}. \tag{6.74}$$

By combining equations (6.71)–(6.74):

$$\mathrm{FiGf}(s_v) = \ln\left(1 + \frac{\Delta s f_{\mathrm{cond}} e\gamma n_t \hat{c}_{st}}{\kappa_0 T_t^2}\right)^{\beta_i - 1} \tag{6.75}$$

where

$$c_{st} \equiv \hat{c}_{st} T_t^{1/2} \tag{6.76}$$

T [eV]; e appears in equation (6.75) because T is in [eV] here. Thus for D^+ -plasma, and $T_e = T_i, \hat{c}_{st} = 9788\ \mathrm{m\,s^{-1}}$. Equation (6.75) is convenient and informative. It emphasizes the powerful effect of the FiG force on impurity leakage since $(\beta_i - 1)$ is often a very large number; for example, for C^{4+}, $\beta_i = 32.8$. Thus even a modest temperature gradient can result in strong leakage.

Unfortunately, this formulation does not lend itself very well to a direct comparison of the effects of the FiG force and the FF force. In order to do that we will employ the approximations that $\ln(1 + x) \simeq x$ for x small, which then gives:

$$\mathrm{FiGf}(s_v) \simeq \frac{(\beta_i - 1)\Delta s f_{\mathrm{cond}} \gamma e n_t \hat{c}_{st}}{\kappa_0 T_t^2} \tag{6.77}$$

T in [eV]. In the following we will sometimes be considering situations where the condition of this approximation is not well satisfied and, strictly, equation (6.75) should be used.

Comparison of equations (6.67) and (6.77) show, perhaps surprisingly, that the ratio of these two terms is independent of almost all the parameters of the problem, and specifically is independent of n_t, T_t and Δs. The ratio is also approximately independent of the impurity species—of m_z and Z. Both terms vary simply as:

$$\Delta s n_t Z^2 / T_t^2. \tag{6.78}$$

For a D^+ plasma, with $\gamma = 7$, $\kappa_0 = 2000$, $\ln \Lambda = 15$, $\beta_i \approx 2.6Z^2$, one finds:

$$\frac{\mathrm{FiGf}(s_v)}{\mathrm{FFf}(s_v)} \simeq -0.1 \frac{f_{\mathrm{cond}}}{\overline{M}_i}. \tag{6.79}$$

Assuming $\overline{M}_i$ of the order of $\frac{1}{2}$, within $s_{\mathrm{inj}} \leq s \leq s_v$, and f_{cond} of the order of 1, then one sees that fortunately the FF force is stronger than the FiG force, tending to lead to effective divertor retention. Ratios of $f_{\mathrm{cond}}/\overline{M}_i$ are conceivable, nevertheless, which would violate this. In addition, even when $\mathrm{FiGf}(s_v)$ can be neglected compared with $\mathrm{FFf}(s_v)$, the absolute magnitude of Γ_{leak} and $\overline{n}_{\mathrm{trap}}$ may not actually be *acceptable*, as discussed below.

We may therefore use:

$$\frac{n_z(s_v)}{n_p} = \exp\left[-\frac{\overline{M}_i \Delta s}{\lambda_{\|t}}\left(1 - 0.1\frac{f_{\mathrm{cond}}}{\overline{M}_i}\right)\right]. \tag{6.80}$$

Problem 6.9. Consider the example of C^{4+}, $n_t = 10^{19}$ m^{-3}, $T_t = 50$ eV, $\Delta s = 1$ m, $\overline{M}_i = f_{\rm cond} = 1$, D^+ plasma and show that this gives $\tau_{st} = 16$ μs, $\lambda_{\|t} = 0.09$ m, $n_z(s_v)/n_p = e^{-9.8} = 5.7 \times 10^{-5}$, i.e. the divertor retention is quite efficient (although we must also evaluate the other terms in equation (6.66)).

We may note that:

$$\frac{n_z(s_v)}{n_p} \propto \exp[-\Delta s n_t Z^2/T_t^2] \tag{6.81}$$

and so this ratio is very sensitive to the control parameters of the problem.

Problem 6.10. Show that changing T_t to 25 eV and 100 eV in the above changes $n_z(s_v)/n_p$ to $(5.7 \times 10^{-5})^4 \sim 10^{-17}$ and $(5.7 \times 10^{-5})^{1/4} \approx 0.1$, respectively, i.e. quite enormous changes.

The onset of divertor leakage is a particularly strong function of the plasma temperature in the divertor [6.44]. One also notes the following.

(a) The more extended is the ionization zone of the background plasma, i.e. the larger is s_v, then the greater is the divertor retention:

$$n_z(s_v)/n_p \propto \exp[-(s_v - s_{\rm inj})].$$

(b) The closer to each other are the ionization zones of the impurity and the background species, the greater the leakage.

(c) The higher the divertor plasma density, the lower the leakage: $n_z(s_v)/n_p \propto e^{-n_t}$.

(d) The higher the charge state, the less the divertor leakage: $n_z(s_v)/n_p \propto e^{-Z^2}$. One should note, however that the impurities tend to ionize rather quickly in typical SOL conditions, up to the He-like state, and so estimates of leakage should be made for such charge states. Hence the choice of C^{4+} used here.

We turn next to the other terms in equation (6.66), starting with $\Gamma_\|^{in}/v_{\rm prompt\ loss}$. The first step is to establish whether $\lambda_{\rm mfp}$ is greater than or less than $s_{\rm inj}$, equations (6.45)–(6.47), for the particular case of interest. For illustration here we will assume $\lambda_{\rm mfp} < s_{\rm inj}$. Next we may note that the ratio v_{T_i}/v_i in the prompt-loss region is essentially the same ratio as ${\rm FiGf}(s_v)/{\rm FFf}(s_v)$, equation (6.79), friction dominates and so here we will take $v_{\rm prompt\ loss} \simeq c_{st}$. Hence:

$$\Gamma_\|^{in}/v_{\rm prompt\ loss} = \Gamma_\|^{in}/c_{st}. \tag{6.82}$$

Next we evaluate the v_{T_i} term in equation (6.66). Using equation (6.72) and now neglecting the $f_{\rm cond}$ term as having a small effect here, also using $|q_t| \sim 2\kappa_0 T_u^{7/2}/7L$, one obtains:

$$v_{T_i} = \frac{2}{7}\beta_i \left(\frac{\lambda_{\|t}}{L}\right)\left(\frac{T_u}{T_t}\right)^{7/2} c_{st}. \tag{6.83}$$

Thus the *normalized leakage rate* $\hat{\Gamma}_{\rm leak}$ is:

$$\hat{\Gamma}_{\rm leak} = \frac{\Gamma_{\rm leak}}{\Gamma_{\parallel}^{in}} = \frac{2}{7}\beta_i \left(\frac{T_u}{T_t}\right)^{7/2} \left(\frac{\lambda_{\parallel t}}{L} {\rm e}^{-\Delta s/\lambda_{\parallel t}}\right) \tag{6.84}$$

where for simplicity we have neglected the contribution of FiG to $n_z(s_v)/n_p$, equation (6.80), and taken $\overline{M}_i = 1$.

From equation (6.84) one may note:

(1) The term dependent on the Roth–Fussmann length $\lambda_{\parallel t}$ tends to dominate leakage through the exponential, which is the same point as made earlier regarding $n_z(s_v)/n_p$.
(2) Leakage increases strongly with temperature variation along the SOL, $(T_u/T_t)^{7/2} \gg 1$, all else being equal. It should be noted, however, that the highly collisional conditions required to *achieve* large T_u/T_t in the first place, section 4.11, will tend to make the $\lambda_{\parallel t}$ term strongly suppressing of leakage, i.e. $\lambda_{\parallel t}$ small.

We will therefore take it that *efficient divertor retention*, i.e. $\hat{\Gamma}_{\rm leak} \ll 1$, will be given by:

$$\Delta s/\lambda_{\parallel t} \gtrsim 10. \tag{6.85}$$

It is readily shown using equations (6.36) and (6.70) that the Roth–Fussmann length:

$$\lambda_{\parallel t} = 6.8 \times 10^{15} T_t^2/n_t Z^2 \tag{6.86}$$

λ [m], T [eV], n [m^{-3}] where $\ln \Lambda = 15$, D^+ plasma and $m_i/m_z \to 0$ have been used. Combining equations (6.85) and (6.86) we thus obtain the critical divertor temperature above which the divertor will start to leak, $T_t^{\rm leak}$:

$$T_t^{\rm leak} \simeq 3.8 \times 10^{-9} Z (n_t \Delta s)^{1/2}. \tag{6.87}$$

Thus, for the case of carbon where we will assume $Z = 4$ and taking $\Delta s = 1$ m for illustration:

$$T_t^{\rm leak} \simeq 1.5 \times 10^{-8} n_t^{1/2}. \tag{6.88}$$

So, for $n_t = 10^{20}$ m^{-3}, $T_t^{\rm leak} \simeq 150$ eV while for $n_t = 10^{19}$ m^{-3}, $T_t^{\rm leak} \approx 50$ eV.

One may note that these are rather high temperatures for a divertor—so high as to cause unacceptable sputtering in the first place. That is, the *source* of impurities would already be unacceptably strong, without even considering impurity *transport*. It thus appears that *divertors are unlikely to leak for near-target sources*. Of course, such complications as flow reversal have not been included here so the result merely indicates a *strong tendency* for divertors to efficiently retain particles released by near-target sources.

Problem 6.11. For the example of $T_u/T_t = 10$, $C^{4+}(\beta_i = 32.8)$, $L = 50$ m, $\Delta s = 1$ m, $\Delta s/\lambda_{\|t} = 10$ show that $\hat{\Gamma}_{\text{leak}} = 2.7 \times 10^{-3}$, i.e. the divertor retention is indeed efficient. Suppose further that $n_t = 10^{19}$ m^{-3}, $T_t = 50$ eV and that the sputtering yield $Y = 0.03$. Show from equation (6.42), that $\Gamma_{\|}^{in} = 2.1 \times 10^{22}$ [m^{-2} s^{-1}]. Thus show that $\Gamma_{\text{leak}} = 5.7 \times 10^{19}$ [m^{-2} s^{-1}]. If we assume $\tau_{\perp} = 10^{-2}$ s then from equation (6.66), show that $\overline{n}_{\text{trap}} = 1.1 \times 10^{16}$ [m^{-3}], which would be a quite tolerable carbon density in the main plasma.

Before leaving this section, we consider the neglect of FeG compared with FiG, and of FE compared with FF. One has FeG/FiG $\simeq$ (0.71/2.6) (T_e'/T_i') and since equipartition tends to hold near the targets, then FeG/FiG $\simeq \frac{1}{4}$. Also FE/FF $\simeq ZeE/(m_z c_{st}/\tau_{st})$ and assuming $E \simeq kT_e/eL$, then FE/FF $\simeq Z\lambda_{\|t}/L$, which is small here.

6.5.5.2 *Estimates of Hydrogenic and Impurity Ionization Lengths*

As equation (6.87) makes evident, divertor retention of impurities depends predominantly on $\Delta s \equiv s_v - s_{\text{inj}}$, i.e. on achieving a region of significant hydrogenic flow velocity that extends as far as possible upstream of the point where the impurities are ionized. (It is generally not sufficient to have high flow velocity merely *at* the impurity ionisation point.) Fortunately, even natural hydrogenic recycling tends to result in $s_v > s_{\text{inj}}$ for most impurities. For 'deep injection' cases, for example, recycling gases such as neon, special efforts may be required to increase s_v, for example, strong hydrogenic pumping at the target region, combined with gas puffing of hydrogen far upstream.

Table 6.2. Ionization distances for deuterium, s_v, calculated using the NIMBUS code. The 'perpendicular' distances, i.e. in the poloidal plane, are shorter by the factor B_θ/B, i.e. about 10× shorter.

n_e (m^{-3})	T_e (eV)	T_i (eV)	s_v (m)
10^{19}	10	10	3.0
10^{19}	100	10	0.93
10^{19}	10	100	2.3
10^{19}	100	100	1.1
10^{20}	10	10	0.061
10^{20}	100	10	0.026
10^{20}	10	100	0.22
10^{20}	100	100	0.049

For present purposes we only seek an estimate of s_v for natural recycling. Fortunately, T_t^{leak} depends only on the square root of Δs.

Hydrogenic neutral penetration into a plasma, allowing for the effect of charge exchange, can be roughly estimated using equation (4.55) for the penetration length. This penetration distance is essentially in the poloidal plane, and so allowing for a typical magnetic pitch of $B_\theta/B = 0.1$, one obtains the estimate:

$$s_v \approx \frac{0.3}{10^{-20} n_e} \tag{6.89}$$

s_v [m], n_e [m^{-3}], which is very close to the estimate given by Vlases and Simonini [6.44], equation (6.53).

The foregoing neglects ionization of molecular hydrogen and so the NIMBUS code was used to generate more realistic estimates for a particular JET grid [6.40] and assuming a range of plasma conditions—various n_e, T_e and T_i, (spatially constant). The value of s_v was taken here to be given by:

$$s_v = \int_0^L \Gamma_i(s)\mathrm{d}s/\,\Gamma_i(0) \tag{6.90}$$

where $\Gamma_i(s)$ is the deuterium ion flux density given by $n_i(s)v_i(s)$, calculated along the separatrix flux tube, using the ionization source directly from NIMBUS. The results are shown in table 6.2. As can be seen the approximation of equation (6.89) is within a factor of 2 for $n_e = 10^{19}$ m^{-3} but is somewhat high for $n_e = 10^{20}$ m^{-3}. We will therefore take equation (6.89) only as a guide for estimating s_v. For example, the situation will be different for $T \lesssim 10$ eV, where detached divertor operation is approached.

Turning next to the impurities, we will take carbon physically sputtered by D^+ as an example. Suppose the energy of the sputtered carbon is ≈ 10 eV, thus $v_C \approx 10^4$ m s^{-1}. Suppose the plasma background is $T_e = 50$eV, $n_e = 10^{19}$ m^{-3}, then the (poloidal) ionization distance is $\sim$1 cm, and so $s_{\mathrm{inj}} \approx 0.1$ m (distance along ***B***). The DIVIMP code, section 6.6.4, was used to refine this estimate, for the same particular JET grid [6.40] and with $T_e = T_{\mathrm{D}+} = 50$ eV and $n_e = 10^{19}$ m^{-3}, constant in space. The average sputtering energy was calculated to be 12.5 eV and the average $\overline{s}_{\mathrm{inj}}$ was found to be 0.11 m, in close agreement with the simple estimate. A spatially varying plasma background was also used, with T decreasing from 50 eV, on the separatrix, to 14 eV at 4 cm out into the SOL (at the target), and n_e decreasing from 10^{19} to 10^{18} m^{-3}. The average carbon energy was calculated to be 9.9 eV and the value of $\overline{s}_{\mathrm{inj}} = 0.24$ m, averaged over all the SOL flux tubes. It thus appears that simple estimates for s_{inj} will be adequate for present purposes. Neutrals released by self-sputtering will be somewhat more penetrating.

From equations (6.81) and (6.85) we have the prediction that $\hat{\Gamma}_{\mathrm{leak}} \propto \exp[\Delta s n_t Z^2/T_t^2]$. This theoretical relation, including the factors that give the absolute magnitude, is shown in figures 6.17 and 6.18, solid lines. The conduction-controlled expression given in the next section was used to provide $T(s)$ with $f_{\mathrm{cond}} = 1$. Also assumed: C^{4+}, $v_i = -0.1c_{st}$ (figure 6.17) or $-c_{st}$ (figure 6.18)

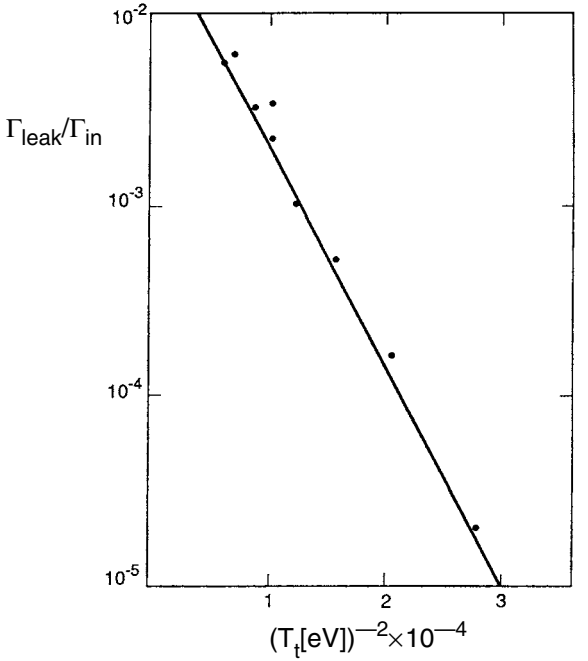

Figure 6.17. Points show DIVIMP calculated values of $\Gamma_{\text{leak}}/\Gamma_{in}$, as a function of T_t. Highly collisional case, $\lambda_{\text{mfp}} \leq 0.1$ m. The solid line shows the result from equation (6.80). $n_e = 10^{20}$ m^{-3}, $s_{\text{inj}} = 0.15$ m, $s_v = 1.2$ m, $\overline{M}_i = 0.1$, $f_{\text{cond}} = 1$, C^{4+} [6.40].

and $s_v = 1.2$ m. The injection was quite 'shallow', i.e. near the target: $s_{\text{inj}} = 0.15$ m. For figure 6.17, $n_e = 10^{20}$ m^{-3}, corresponding to $\lambda_{\text{mfp}} \lesssim 0.1$ m, i.e. strongly collisional conditions. For figure 6.18, $n_e = 10^{19}$ m^{-3}, $\lambda_{\text{mfp}} \leq 1$ m, i.e. a marginally collisional case. The points in both figures are from DIVIMP code results, section 6.6.4, showing that the simple analytic model does best for strongly collisional conditions, as expected. For weak or marginal collisionality the quasi-kinetic Monte Carlo approach should be more reliable. Leakage is again seen to be slight unless T_t is high, $\gtrsim 100$ eV.

We can therefore conclude that for physically sputtered impurities, such as carbon (and even more so for heavier elements), s_{inj} is small compared with s_v. For chemically sputtered carbon, or evaporated atoms, one will have an even more extreme situation, $s_{\text{inj}} \ll s_v$. Back-scattered helium, on the other hand, can have $s_{\text{inj}} \gtrsim s_v$; consider the example of a 50 eV He^0 atom entering a plasma with $T_e = 50$ eV and $n_e = 10^{19}$ m^{-3}, giving a (poloidal) ionization distance of ~0.3 m, and thus an s_{inj} perhaps 10 times larger, which is comparable to s_v. *The ability of a divertor to retain He is thus a concern*, section 6.7. Studies on CMOD [6.48],

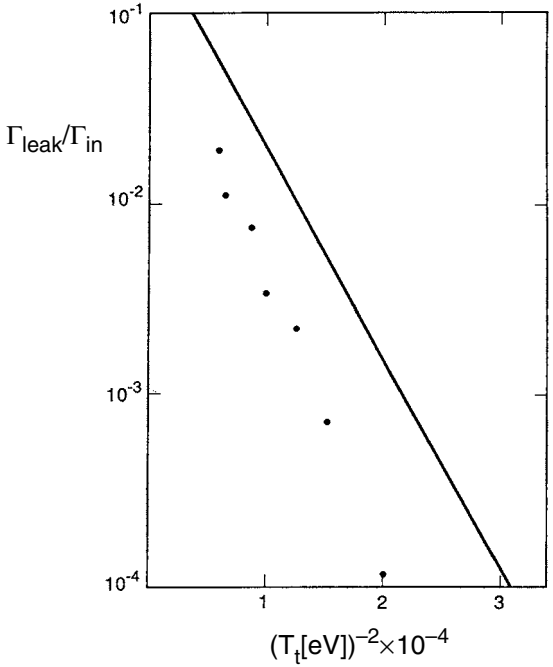

Figure 6.18. As figure 6.17 but for case with $n_e = 10^{19}$ m^{-3}, $\overline{M}_i = 1$. For this marginally collisional case, where $\lambda_{mfp} \approx 1$ m, the agreement with equation (6.80) (solid line) is less good. The simple fluid model overestimates the leakage [6.40].

comparing the divertor retention of He, Ne, A and Kr, show a strong correlation with the ionization distance, s_{inj}, He being rather poorly, and Kr rather strongly, retained. The energy reflection coefficient, R_E, of He is much higher than that of Ne, making the recycling He neutrals particularly penetrating [6.49].

6.5.5.3 The Case of Ionisation of Impurities Far from the Target

For 'deep injection' of impurities the ionization of the impurities occurs in the SOL, but rather far from the target. This would sometimes be the case for recycling impurities such as He and Ne which, by multiple reflections from side walls, could penetrate deeply into the SOL before ionizing, figure 6.10. This would also apply to sputtering of non-recycling impurities by charge-exchange neutral hydrogen atoms striking side wall surfaces, figure 5.2. Such sources extend around the entire vessel, but are strongest near the targets, and it may be that these sources, although weaker in strength than the target sources, leak so much more effectively that they dominate N_z^{main}. In this case less simple approximations have to be used for the integrals in equations (6.55)–(6.58).

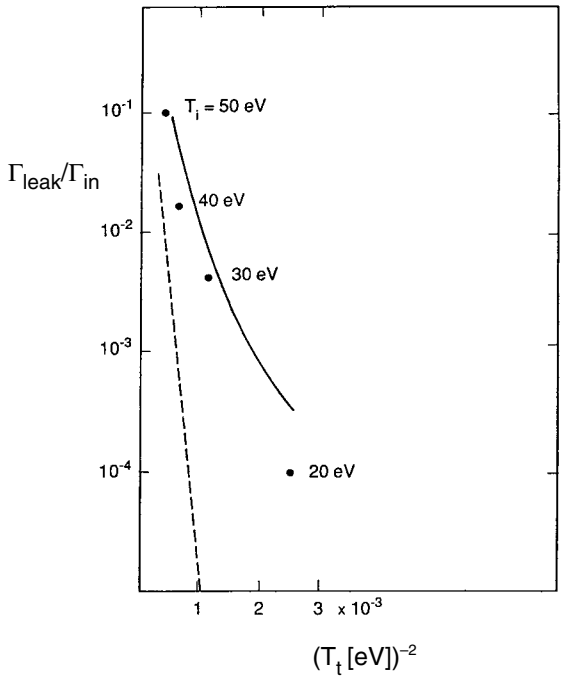

Figure 6.19. Calculated $\Gamma_{\rm leak}/\Gamma_{in}$, using DIVIMP for a 'deep injection' case (points). The solid curve is for the simple fluid model allowing for the spatial variation of $kT_D\tau_s$ in the friction force integral, equation (6.55); the dashed line neglects that variation. $n_e = 10^{19}$ m^{-3}, $s_{\rm inj} = 5$ m, $s_v = 10$ m, $\overline{M}_i = 0.1$, $f_{\rm cond} = 1$, C^{4+} [6.40].

For entry of impurities into the SOL upstream of s_v obviously leakage to the main plasma will be extremely high (neglecting flow reversal, etc). Even for entry below s_v, M_i may be rather small, which would make convection small also, hence $f_{\rm cond} \approx 1$. While we cannot use the 'shallow injection' results of section 6.5.5.1 directly here, equation (6.80) still indicates the trend: for $M_i \lesssim 0.1$ and $f_{\rm cond} \approx 1$, divertor leakage will be catastrophic, even for $s_v > s_{\rm inj}$.

For 'shallow injection' we could approximate the integrals in equations (6.55)–(6.58) by evaluating the integrands at the target values. Now we must allow for the variation of the integrands, which can be quite substantial: $kT_i\tau_s$, for example, varies as $T_i^{5/2}$. We therefore need to have a more detailed model of the plasma background and the variations of $v_i(s)$, $T_i(s)$, etc. For example one might assume that $T(s)$ satisfies a modified conduction equation, chapter 5.4:

$$T(s)/T_t = \left(1 + \frac{7 f_{\rm cond}|q_\parallel|s}{\kappa_0 T_t^{7/2}}\right)^{2/7}. \tag{6.91}$$

One might then obtain $n_i(s)$ from the assumption of pressure balance, based on a specified value of n_t and assuming $M_t = -1$. For simplicity assume $\overline{M}_i$ equal to a specified constant value for purposes of evaluating FFf(s). Inserting such variations into equations (6.55)–(6.58) is a straightforward algebraic exercise and the details are left to the reader. For illustration, see figure 6.19 which shows Γ_{leak} against T_t for the specific case: $T(s)$ from equation (6.91) with $f_{\text{cond}} = 1$, $n_t = 10^{19}$ m^{-3}, $s_{\text{inj}} = 5$ m, $s_v = 10$ m, $v_i = -0.1c_{st}$ (constant). The solid line in figure 6.19 allows for the s-dependence of the integrands in FFf(s_v), FiGf(s_v), while the dashed lines took them to be constant at the target values, as for 'shallow injection'. As can be seen, the prediction of the latter modelling that $\hat{\Gamma}_{\text{leak}} \propto \mathrm{e}^{-\mathrm{T}_t^{-2}}$ is now somewhat modified, and the absolute level changes substantially: the 'deep injection model' predicts much more leakage for a given set of parameters than does the 'shallow injection model'. (The solid points in figure 6.19 are from DIVIMP code modelling, section 6.6.4.)

Since the parameters characterizing deeply injected impurities are, already, indicative of more efficient leakage, it is clear that any deep sources are likely to be particularly important at contributing to the impurity content of the main plasma.

6.6 Edge Impurity Source/Transport Codes

6.6.1 Why Have Codes?

Why are we interested in developing and using edge impurity codes? We should be realistic about expectations. One could play the devil's advocate, and make the argument that there are so many *basic* uncertainties involved that one might as well stick with crude analytic models. Without doubt the list of basic uncertainties is a sobering one:

(1) The scatter in the basic accelerator-generated sputtering yields *under the best circumstances* is a factor of 2, section 3.3. Further uncertainty is involved with regard to dependence on the bombarding flux density, surface roughness, sputtering properties of re-deposited material, the angular and velocity distributions of emitted particles, etc.

(2) The boundary conditions for impurities at the outer edge of the SOL are virtually unknown, but may control the dwell time of impurities in the SOL, upstream of the frictional zone near the targets, section 6.5.5.1, thus controlling the relation between the impurity source and n_z^{main}, i.e. the problem of estimating $\tau_\perp$.

(3) There are very few data and also limited understanding of flow reversal, chapter 15, which could strongly influence parallel transport of impurities in the SOL since it involves FF and FiG being reinforcing rather than opposing forces.

(4) Understanding of $\boldsymbol{E} \times \boldsymbol{B}$ and other drifts, chapter 18, is still emerging.

(5) The temperature-gradient forces are essentially theoretical concepts and little direct experimental confirmation has been obtained of their existence and magnitude.
(6) The upstream SOL is only weakly collisional, making all simple theoretical evaluations of FF, FiG, etc strictly invalid. In addition, the existence of the background parallel temperature gradient itself is theoretically questionable—due to the weak collisionality; it is also impractical to measure it directly since the temperature differences involved are so small, and the problem of identifying a specific SOL flux tube at different poloidal/toroidal locations is very difficult. It is therefore not proven that the upstream SOL impurity trap actually exists.
(7) $D_{\perp}^{\mathrm{SOL}}$ and $v_{\mathrm{pinch}}^{\mathrm{SOL}}$ for impurities are essentially unknown. They may vary substantially throughout the SOL given that n and T vary so greatly.

It would not be difficult to add to this list. Unfortunately a computer code can do nothing to help with most of these problems. As with all code results, however, the computer output often has the superficial appearance of authority and reliability, and there is the risk of being misled and of gaining false confidence. *One needs to be constantly reminded of the truth about codes*: '*Rubbish in. Rubbish out*'.

On the other hand, to abandon edge impurity source/transport codes would involve ignoring the obvious fact that a great deal of straightforward 'book keeping' is called for if one does not want to *add* to the problems we already have. It is clearly not helpful, for example, to ignore the fact that n and T vary across plasma-wetted surfaces, and to simply calculate sputtering yields, photon efficiencies, penetration depths, etc. for the values of n and T at, say, the LCFS. Yet, to take such variations into account within analytic formulations would be impractical. *Clearly codes are ideally suited to handle such book-keeping tasks. This, then is their main function*. They *cannot* reduce the basic—and substantial—uncertainties implicit in modelling edge impurity behaviour, but they can help us make the best use of the information that we have.

6.6.2 Interpreting Edge Impurity Measurements Using Codes

We therefore have good reason to employ edge impurity codes even if only to carry out *purely predicative* studies, e.g. of n_z^{core} for a future ITER-like machine or reactor. The capability of codes to handle detailed book keeping is even more valuable for *interpretative* studies, where one may have a large amount of experimental data concerning the impurities, throughout the SOL and main plasma. Such experimental measures are themselves typically rich in detail. For example, one may have measurements of the absolute intensity of some particular C II line, say, as a function of poloidal angle across the divertor region, made with fine spatial resolution; an example is shown in figure 6.20 [6.50]. It is clear that no analytic interpretive procedure can really do justice to such detailed information.

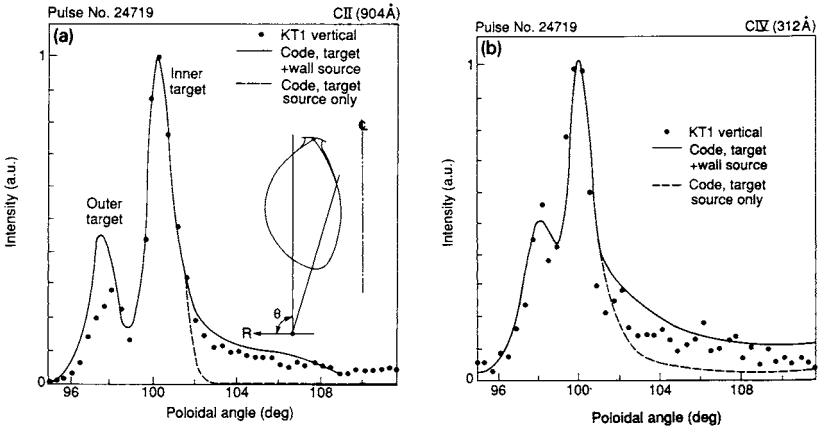

Figure 6.20. VUV poloidal profiles of (a) C II and (b) C IV obtained with the KT1 vertical viewing system, looking into the JET divertor [6.50]. DIVIMP code results.

Previously, spectroscopic measurements were largely confined to the main plasma, but recently it has become common on all tokamaks to have increasingly detailed measurements made of the edge including:

(1) Spatially resolved, absolutely calibrated measurements of various hydrogenic lines, almost always H_α but with many other lines often, including ones in the UV.
(2) Similar measurements for most of the charge states of the low Z impurities, particularly for C.
(3) Sometimes impurity ion temperatures and drift velocities are measured from Doppler widths and shifts [6.51].

It may well be that the quantities we are *ultimately* interested in modelling, explaining and predicting are such 'bottom line' quantities as n_z^{core} and $P_{z,\text{rad}}$. Because of the many uncertainties involved in the chain of processes leading to these quantities, however, our ability to do so is rather modest. It is therefore most helpful when we have as many *intermediate* impurity measurements as possible, for example, the spatial distributions of line intensities of C I, C II, C III, etc, throughout the edge region. This allows us, in effect, to *isolate* sub-components for the overall impurity behaviour, and to study and try to understand each part separately. For example, if modelling of the lowest charge state lines, e.g. of C I and C II, is successful, then we may be confident that we have understood the *source* mechanism. In another situation, there may be a problem in sorting out the source, but perhaps the modelling can succeed in matching the progression through middle charge states, e.g. the relation between the C III, C IV, C V, etc; in such a situation we would have some confidence that we understood the SOL *transport* part of the chain.

The most practical way of confronting detailed experimental measurements of edge impurities in such a way as to extract the underlying physics—i.e. to perform *interpretative* studies—is by the use of impurity source/transport codes.

With regard to the *source* aspect of the impurity chain: codes include the effect of the spatial variation of n and T across the plasma-wetted surfaces—which govern the spatial variation of impacting flux density and energy, and thus the sputtering production rate. If the yield is dependent on the substrate temperate—e.g. chemical sputtering of C by H—then the code can include that effect. The angular and velocity distribution of the sputtered neutrals is often incorporated. Self-sputtering can be included—although that then brings transport into the picture.

With regard to modelling the specific line emissions, the spatial variations of n_e and T_e are allowed for in the code as they set the photon efficiency, section 3.5. The code calculates the local density of each charge state of the impurity which, together with information on the local n_e and T_e, gives the calculated local emissivity which can be compared with experimental measurement. Sometimes a sufficiently comprehensive set of lines of sight are used to produce the experimental data, that a *tomographical reconstruction* can be performed on the data to produce a 2D (in the poloidal plane) set of experimental emission contours, which can then be compared with the code. This is not actually necessary, however, since every line of sight used in the experiment can be *simulated* by the code to produce a calculated signal which can be *directly* compared with the raw (i.e. not deconvolved) light-of-sight measurement. Since deconvolution of data always degrades the experimental information to some degree, it is usually preferable to make direct comparisons. In some situations a 3D comparison of experiment and code may be involved.

The *transport* aspect of the problem requires that the code allow for 2D motion of the impurity particles (neutrals and ions)—typically done within the poloidal plane. Toroidal symmetry is usually assumed, but in some cases 3D motion is allowed for. The 'radial' cross-field transport is usually assumed to be anomalous, with the values of $D_\perp$, and v_{pinch} if required, taken to have assigned values. The parallel transport is assumed to be classical, section 6.5.3. The parallel transport may be followed in the actual parallel-to-$\boldsymbol{B}$ direction, with final results for impurity density, etc then being projected onto the poloidal plane for further analysis or for display. Alternatively, the parallel motion of the particles may be followed as motion projected onto the poloidal plane, with $v_{\text{pol}} = (B_\theta/B)v_\parallel$, where (B_θ/B) is the local value input to the code; see figure 6.21.

There are many unknowns governing the impurity sources and transport. In some cases these uncertainties translate directly into individual *adjustable parameters* in the code. $D_\perp$ is such an example. By adjusting these parameters until a fit with the experimental data is achieved, one indirectly deduces the values of such parameters. In other cases, it is not a simple matter of a single parameter characterizing an unknown aspect of impurity behaviour—but rather one is trying to decide between different *scenarios*. Again, however, the basic idea is that

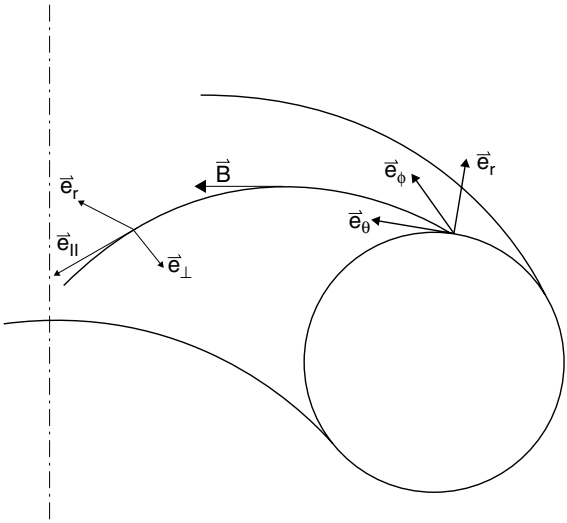

Figure 6.21. Two different orthogonal coordinate systems for toroidal geometry.

if/when a good match is obtained with the measurements then one assumes that the correct scenario has been identified.

The *uniqueness* of the solution that one finds in this way can be questioned. While it is not possible to prove the uniqueness of a solution mathematically, it is intuitively clear that the more data that can be successfully matched simultaneously by the code, the greater will be one's confidence that the correct physics has been identified. Such edge impurity interpretative studies thus require a reasonably comprehensive set of measurements with which to confront the code output.

Since the impurity behaviour depends so greatly on the plasma background it is important that the code simultaneously confront as much of the *background plasma data* as possible also. At a minimum this should include:

(1) Spatially resolved absolute intensity measurements of hydrogenic line radiation—at the very least H_α. This provides information on the intensity of the bombarding hydrogenic flux.
(2) Langmuir probe measurements of T_e and I_{sat}^+ should be made at as many locations as possible. At a minimum these should be made across the plasma-wetted surfaces, using built-in probes, figure 2.11. It is also very valuable to have fast reciprocating probes deployed at upstream locations to provide radial scans of $T_e(r)$ and $I_{sat}^+(r)$ there (fast so as to avoid over-heating when used to probe deeply).
(3) Pressure gauges provide hydrogenic pressure measurements at various locations around the vessel.

Other hydrogenic data may be available such as H_γ/H_α ratios, which are sensitive to the presence of very cold, recombining regions, section 3.5. On some devices Thompson scattering systems provide 2D measurements of n_e and T_e in the divertor plasma. Line-of-sight measurements of n_e may be available from interferometry. T_i-measuring probes are sometimes employed, etc.

It is therefore important that the interpretive code not only model the impurity behaviour, but the hydrogenic background as well. The latter is needed to calculate the parallel transport of impurities, their progress through the successive ionization stages including the effect of recombination, the thermalization of the impurities, etc. At the same time the code can produce simulated signals of the hydrogenic diagnostics for comparison with experiment.

6.6.3 Edge Fluid Impurity Codes

The edge plasma can be modelled as a set of fluids, at a minimum including separate electron and hydrogenic-ion fluids. To study impurity behaviour, *multi-fluid* modelling is carried out, where an additional fluid is included for each charge state of the impurity. Fluid models of the edge are the subject of part II of this book and will not be discussed further here. See chapter 13.

6.6.4 Monte Carlo Impurity Codes

In the Monte Carlo, MC, approach to edge impurity modelling individual impurity particles are followed in time as they move in 2D or 3D within a *given* or *specified* 'plasma background', where the 2D or 3D spatial distribution of n_e, T_e, T_i, $v_\parallel$, n_H, T_H, etc have been provided as *input* to the MC code. Each particle is followed from its creation point as a neutral, for example due to sputtering from some point on the divertor target. The particle is followed as it ionizes to higher and higher charge states, perhaps also experiencing recombination, until it strikes a solid surface—the targets or walls—where, in the simplest case, it will be assumed to just re-deposit, figure 6.22.

A new neutral will then be launched and followed similarly. When enough particles have been launched and followed to give acceptably good statistics—typically a few thousand particles—then the results are averaged to give as output:

(a) The 2D or 3D spatial distribution of each charge state density n_j [particles m^{-3}].
(b) The erosion, re-deposition and net erosion rates for all solid surfaces [particles m^{-2} s^{-1}].
(c) The leakage rate, in [particles s^{-1}] or [particles s^{-1} m^{-1} toroidally], of impurities across any specified surface within the plasma, for example the LCFS. Since in steady state the flux of particles across many internal surfaces is zero, with equal fluxes existing in each direction, the leakage rate across the LCFS is taken to be the *one-way* flux.

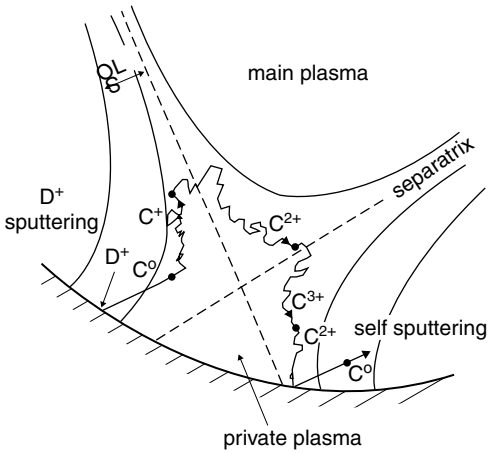

Figure 6.22. Monte Carlo impurity codes, such as DIVIMP, follow individual particles starting as sputtered neutrals which move freely across $\boldsymbol{B}$, subject only to ionizing collisions with electrons and momentum-transfer collisions with background ions and neutrals. Once ionized, the parallel and cross-field transport of the ion are followed. The ion eventually returns to a solid surface where it re-deposits, causing self-sputtering.

(d) By drawing on an atomic database such as ADAS to provide photon efficiencies, section 3.5, the intensity of various spectroscopic lines can be calculated in [photons m^{-3} s^{-1} $sterad^{-1}$]. In order to compare with a line-of-sight (LOS) measurement the viewing coordinates of the diagnostic, its angle of view and acceptance angle of photon collection are input to the code so that a computed code value for the LOS signal is generated for comparison with measurement.

(e) The 2D or 3D distribution of the total impurity radiation $P_{\rm rad}$ [W m^{-3}], also broken down by charge state, and by line, bremsstrahlung, recombination, etc contributions.

(f) The 2D or 3D distribution of $Z_{\rm eff}$ and of the fuel dilution, $n_{\rm DT}/n_e$.

(g) The 2D or 3D distribution of the temperature of each impurity ionization stage. One of the advantages of the MC approach compared with the fluid approach is that it is not computationally very costly to follow the temperature of each charge state separately. The LOS, intensity-weighted average T_z for each charge state can be calculated for comparison with a LOS Doppler-width measurement.

(h) The 2D or 3D distribution of $v_\parallel$ for each charge state can be processed, similarly weighted as for the temperature.

(i) The relative contributions to the impurity content of the main plasma due to the different sputtering mechanisms, source locations, etc. Also the fraction of the production of each source type and location that enters the main plasma.

(j) The average impurity dwell time in the SOL, the main plasma, etc.
(k) The energy and charge state distribution of the impurity ions for each element of solid surface they deposit on; such information is needed for calculation of self-sputtering.
(l) Since it is necessary to run a coupled hydrogenic neutral code such as EIRENE anyway, e.g. to find n_{H}, it is convenient also to output the calculated 2D/3D distributions of hydrogenic atomic and molecular densities, the intensities of the various hydrogenic lines (including LOS simulations), etc.

With regard to the launching of the sputtered neutral, the spatial distribution across the targets of the sputtering source is first calculated from the input information about the variation of n_e, T_e and T_i across the targets and the sputtering yield. The source is then normalized by the total, integrated production rate per metre toroidally. The location for the launch of an impurity neutral is then selected in a Monte Carlo way from this normalized distribution: let the fraction of the total sputtering that occurs on a target element j be f_j where $\sum_{j=1}^{n} f_j = 1$, and there are n target elements. Draw a random number ξ, uniform on [0,1]. Suppose ξ falls in $\sum_{j=1}^{k-1} f_j < \xi < \sum_{j=1}^{k-1} f_j + f_k$, then the neutral is launched from target element k. As to the angle and velocity of the sputtering neutral, this is similarly selected in a Monte Carlo way from specified angular, e.g. cosine and velocity, e.g. Thompson, distributions, section 3.3.

Each sputtering mechanism—physical and chemical—is treated this way. The wall and target sources due to charge exchange sputtering are also calculated using as input the flux and energy of impacting hydrogenic neutrals calculated by e.g. EIRENE. Each neutral is then followed in 2D/3D until it is ionized. In the simplest treatment the neutral is assumed to move in a straight line until ionized. The neutral is followed in time, using time steps Δt which are smaller than all collisional times, including the ionization time:

$$\tau_{iz} \equiv (n_e \overline{\sigma v}_{iz}^{0})^{-1} \tag{6.92}$$

with '0' indicating the neutral. At each time step a random number ξ, uniform on [0,1], is drawn and if $0 < \xi < \Delta t/\tau_{iz}$, then ionization is deemed to have occurred at that time step, otherwise the trajectory is continued. The effect of scattering collisions, both neutral–neutral and neutral–ion, can be included by, for example, changing the trajectory direction $\pm 90°$ (randomly chosen) whenever at a particular time step a random number ξ, uniform on [0,1], falls within $0 < \xi < \Delta t/\tau_{\mathrm{scat}}$, where:

$$\tau_{\mathrm{scat}}^{-1} = n_i \overline{\sigma v}_{in}^{\mathrm{scat}} + n_n \overline{\sigma v}_{nn}^{\mathrm{scat}} \tag{6.93}$$

and $\overline{\sigma v}_{in}^{\mathrm{scat}}$, $\overline{\sigma v}_{nn}^{\mathrm{scat}}$ are the 90°-scattering rates for striking ions and neutrals respectively.

When a neutral becomes ionized, the singly charged ion is then followed in its 2D motion parallel and perpendicular to $\boldsymbol{B}$. The parallel motion was described

in section 6.5. At each time step Δt the cross-field location r is changed by:

$$\Delta r = \pm(2D_{\perp}\Delta t)^{1/2} - v_{\text{pinch}}\Delta t \tag{6.94}$$

with the $\pm$ chosen randomly. Equation (6.94) is appropriate for rectangular geometry only. For circular, or more complicated 'grid' geometries it is necessary to make appropriate corrections to equation (6.94) to avoid artificial drifts.

The plasma background values of n_e, T_e, $v_{\parallel}$, $E_{\parallel}$, etc must all be provided as functions of $(s_{\parallel}, s_{\perp})$, i.e. for each grid cell, as input to the MC code. Two methods for generating such information:

(a) 'onion-skin' method, OSM, modelling can be used, chapter 12.
(b) A 2D fluid edge code can be used, chapter 13.

Since in the Monte Carlo method the particles are followed, not just in space, but in *time*, this method lends itself to the analysis of time-evolving situations where the background plasma and/or impurity source are changing in time. The most common applications, however, are to steady-state situations. How, then, to compute the steady-state 2D spatial distributions of the different charge states from the basic MC output? Consider a slice of the tokamak which is 1 metre in toroidal extent. The volume of each cell in the grid is thus numerically equal to the cell area in the poloidal plane. Say N particles in total are launched in a MC run. Let each cell be divided into 'bins', one for each charge state. Define $\hat{C}(m, n, Z, t)$ to be the number of particles of charge Z, in grid cell number (m, n) at time t s after the particle was sputtered. One obtains $\hat{C}$ by launching all N particles and dividing the count in each cell bin by N, to obtain an average value. The total number of particles sputtered during the time interval of length dt at the time t s before $t = 0$ is $\phi_z^{in}\mathrm{d}t$ where ϕ_z^{in} is the number of particles sputtered per second per metre toroidally. The total, un-normalized number in the cell bin is therefore $\hat{C}(m, n, Z, t)\phi_z^{in}\mathrm{d}t$ and the grand total, integrating (time running backwards) from $t = 0$ to ∞ is the steady-state impurity number of charge Z in cell (m, n):

$$n(m, n, Z) = \phi_z^{in}\int_{t=0}^{\infty}\hat{C}(m, n, Z, t)\mathrm{d}t. \tag{6.95}$$

One therefore does not need actually to calculate the specific time dependence of $\hat{C}(m, n, Z, t)$ if only the steady-state density is required since it is sufficient simply to increment the count in each cell bin at each Δt step by an amount $1\ \Delta t$, dividing the final total by N, i.e. 'integration on the fly'.

To handle ionization and recombination of a particle in charge state j, a random number ξ, uniform on [0,1], is drawn at each time step Δt. If $0 < \xi < \Delta t/\tau_{ch}$ then a 'change of state' is deemed to have occurred, where:

$$(\tau_{ch})^{-1} = n_e\overline{\sigma v}_{iz}^{j} + n_e\overline{\sigma v}_{\text{eirec}}^{j} + n_H\overline{\sigma v}_{\text{cxrec}}^{j}. \tag{6.96}$$

If an 'event' occurs, a second random number is drawn and if $0 < \xi < \tau_{ch} n_e \overline{\sigma v}^j_{iz}$, then the change is deemed to be ionization to state $j + 1$, etc.

In the simplest case it is assumed that any impurity ion reaching a solid surface re-deposits and that particular particle history is terminated. Other options are:

(a) In order to allow for self-sputtering, the value of E_{impact} is calculated and the self-sputtering yield $Y_{ss} < 1$ is used to launch a new neutral of assigned weight $Y_{ss} < 1$ (the particles originally sputtered by background ion impact are assigned weight unity). This particle is followed as before and when it returns to a solid surface this self-sputtering cascade continues, but now with the launch of a particle of weight given by the product $Y_{ss1} Y_{ss2}$. This is continued until the particle weight becomes negligibly small.

(b) A recycling impurity such as He involves the launch of a new particle with weight $R_{\text{recycle}} \leq 1$, an assigned value. The appropriate fractions that are energetically back-scattered and thermally released can be allowed for. If $R_{\text{recycle}} = 1$ for *all* surfaces bounding the system then the code-run will never terminate, obviously, and it is necessary to allow for some or all of the bounding surfaces to act as *pumps*, with $R_{\text{recycle}} < 1$.

In reality, the impurity ions do not instantly thermalize with the background ions, but have a finite thermalization time given by the Spitzer energy transfer time:

$$\boxed{\tau_T \equiv \frac{0.71 \times 10^{13} m_z T_i (T_i/m_i)^{1/2}}{n_i Z^2 \ln \Lambda}} \tag{6.97}$$

τ [s], m [amu], T [eV], n [m^{-3}]. Thus the simplest way to follow the evolution of T_z is to increment it at each time step Δt using the formula:

$$\Delta T_z^f = (T_i - T_z^f) \Delta t / \tau_T \tag{6.98}$$

where the superscript f indicates that the temperature has been calculated from this formula. Since the *velocity diffusion* is also calculated, equation (6.33), one can separately confirm that this formula is valid; the mean value of the random kinetic energy is, after all, simply related to the temperature—at least in conditions where the collisionality is strong enough to ensure the existence of a Maxwellian distribution. These expectations have been confirmed [6.40].

Conditions may well not be sufficiently collisional to ensure the existence of Maxwellian distributions, particularly for short lived, low charge states. In that case, it is strictly incorrect to use equation (6.98) to calculate T_z, and the average random thermal energy, i.e. the *effective* T_z, should be computed directly from the dispersion of parallel velocity, see below.

The most basic mode of employing a Monte Carlo code is the *non-feedback* mode, where the plasma background solution is kept fixed, and the MC code is run once for this background. In *feedback* mode the MC code is coupled iteratively to the code calculating the plasma background.

Monte Carlo impurity codes include pioneering work by Sengoku *et al* [6.52], followed by a number of other codes including REDEP [6.53], ZTRANS [6.54], DIVIMP [6.55], IMPMC [6.56], BBQ [6.57] and MCI [6.58].

In some Monte Carlo codes both the gyroscopic and parallel motion of the ions are followed. A rather complete formulation has been provided by Reiser *et al* [6.41] who have also calculated collisional terms which combine FPG, FF and FiG. Since all of these forces are the result of collisions, it is most natural to treat them in a combined way.

In its most basic mode of operation, a Monte Carlo impurity code employs the *trace impurity approximation*. This is sometimes taken to indicate that FPG, the impurity pressure gradient force, is therefore neglected. This is incorrect. As was shown in section 6.5.3, inclusion of parallel diffusion in a MC code incorporates this important force. The impurity ions diffuse via collisions with the hydrogenic ions. What is neglected in the trace impurity approximation is the effect of impurity–impurity collisions—on all the parallel forces. Strictly therefore the trace approximation is invalid once the Z–Z collision frequency exceeds the Z–i collision frequency. This turns out to be an overly strict criterion, however, because the corrections for impurity–impurity collisions affect the opposing forces on the impurity approximately equally.

The two most important forces in the impurity parallel force balance are usually FF and FiG, section 6.5.3. We have that FF $\propto (\tau_s^{z-i})^{-1}$, equation (6.21), (the stopping time for impurity ions striking background ions), thus FF $\propto n_i$, equation (6.35). Therefore, compared with a pure plasma, FF is reduced by a factor (n_i/n_e) for a given n_e. The correction for FiG follows the simple derivation of FeG in chapter 9, equations (9.25)–(9.27), with appropriate substitutions, including the replacement of λ_{ee} by the thermalization mean free path λ_E for background ions in the presence of both background ions and impurity ions. It is then readily shown that FiG is reduced by a factor $\approx (1+(m_i/m_z)(n_z/n_i)Z^2)^{-1}$. Example: C^{4+} in D^+ with $n_c^{4+}/n_e = 0.1$. Then $Z_{\text{eff}}^{\text{SOL}} = 2.2$ and if the core n_c^{6+}/n_e is also 0.1, then $Z_{\text{eff}}^{\text{core}} = 4.0$, and so this is certainly a strongly contaminated plasma. One finds $n_i/n_e = 0.6$, so FF is reduced by a factor of 0.6. The FiG correction factor is 0.69, i.e. about the same. Thus, the force balance between FF and FiG is almost unchanged, even for this high level of impurity content. It can thus be expected that the trace impurity approximation will hold up fairly well even when impurity levels are higher than trace ones.

The foregoing considerations concerning the trace assumption only pertain to the *parallel force balance*. Impurity *radiation* can strongly influence the plasma properties, particularly the temperature. Inclusion of the latter effect should therefore be the first correction made to improve a trace analysis.

It is useful to compare fluid and Monte Carlo edge impurity codes, which may be done under the following categories.

6.6.4.1 Self-consistency

Multi-fluid 2D edge codes automatically treat the hydrogenic and impurity components in a self-consistent way. Thus, for example, the impurity transport is strongly influenced by the n_e, T_e, T_i, $v_\parallel$, etc of the hydrogenic plasma; conversely, the resulting $P_{\mathrm{rad},z}$ can strongly influence the hydrogenic temperature, etc. In the most basic mode of operation, Monte Carlo impurity treatments, employing for example a 2D fluid code to compute the 'plasma background', do not include such coupling. For predictive work the multi-fluid approach is therefore superior. The strongest linkage between the hydrogenic and impurity species is usually via $P_{\mathrm{rad},z}$ so this is the most important element to include in an iterative, feedback coupling of a fluid 'plasma background' code and a Monte Carlo impurity code.

6.6.4.2 Trace Versus Non-Trace Impurity Levels

As already discussed, the Monte Carlo approach probably retains validity up to higher levels of n_z/n_i than would be indicated by simple comparisons of collision times, i.e. it extends into the regime of non-trace impurity levels. Nevertheless, for particularly strongly contaminated plasmas it is necessary to employ either a multi-fluid code, or a coupled fluid/MC code where all three of the conservation equations for the fluid analysis are updated iteratively to include the impurity contributions. The latter have not been developed to date.

6.6.4.3 Input of Experimental Data and 'Onion-Skin' Method Modelling

Uncertainties are substantial even regarding the modelling of the hydrogenic edge plasma. Uncertainties are therefore compounded when one attempts to model edge impurity behaviour since a kind of 'uncertainty-squared' effect arises. For interpretative work, therefore, it is desirable to take as input in the analysis, as much experimental data as possible about the hydrogenic plasma, so as to be obliged to calculate as little as possible, i.e. about the impurities. Ideally, one would take the 2D distributions of n_e, T_e, T_i, $v_\parallel$, $E_\parallel$ from measurement, in which case the *only* quantities remaining to be computed would be the impurity ones. This would then permit focusing specifically on impurity behaviour, and should greatly aid in its elucidation. Unfortunately such complete experimental descriptions of the hydrogenic edge plasma are not presently available. What are usually available are Langmuir probe data across the targets, from which it is possible to carry out onion-skin method, OSM, analysis of the edge plasma, see chapter 12. This may be supplemented by other hydrogenic-plasma-related data, e.g. spatial distributions of H_α intensity, 2D Thompson scattering measurements of n_e and T_e, etc. Thus an OSM can be constructed which, although also dependent on theoretical concepts, is strongly based on experimental data.

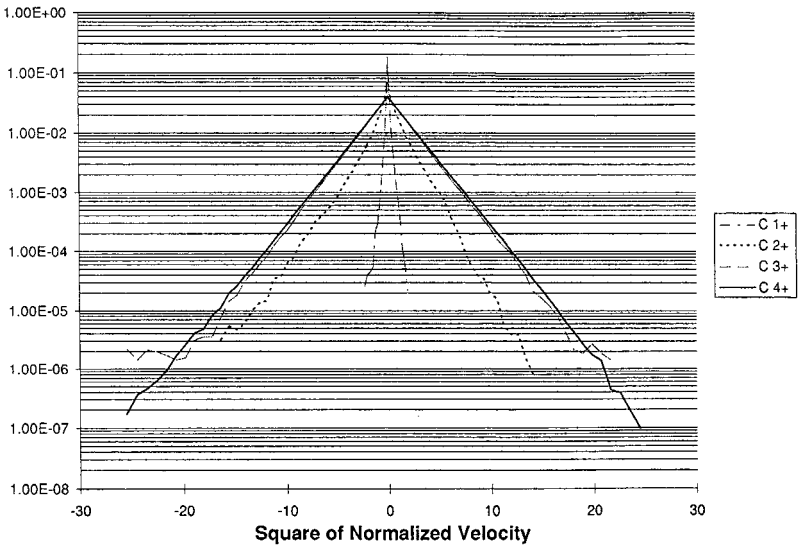

Figure 6.23. Velocity distributions of different charge states for 1 eV C^+ ions injected into a plasma of $T_e = T_D = 50$ eV, $n_e = 10^{19}$ m^{-3} and allowed to thermalize and ionize. The finite thermalization of the lower charge states is evident. It is also clear that the lower charge states are less fully Maxwellianized, particularly the high energy tails. Calculated using the DIVIMP code [6.40]. The horizontal scale is in units of kT_D/m_C. Thus if the carbon ions are fully thermalized to the D^+, their distribution would vary as $\exp(-m_C v^2/2kT_D)$, which is approximately the case for the C^{4+}.

The combination of experimental data input, an OSM, plus a Monte Carlo impurity code is therefore a useful one for interpretive studies,

6.6.4.4 Finite Thermalization of the Impurity Ions

In edge multi-fluid modelling it is considered to be computationally too costly to include a separate energy equation for each ion species and charge state, and it is assumed that all ions share a common (local) temperature. Further it is implicitly assumed that the ion velocity/energy distributions are Maxwellian. Near the targets impurity ion transit times can be shorter than thermalization times, τ_T, equation (6.97), and these assumptions become invalid. Monte Carlo codes include, at negligible computational cost, the separate tracking of the temperature of each species and charge state, and if the velocity distributions are non-Maxwellian, this is automatically allowed for as well. An example of the finite thermalization process is shown in figure 6.23. The DIVIMP code was used to calculate the velocity distributions of the different charge states of carbon. C^+ ions were injected into an infinite D^+ plasma with $T_D = T_e = 50$ eV, $n_e = 10^{19}$ m^{-3}.

The initial temperature of the C^+ was 1 eV. The ions were removed at 100 ms after injection. The finite thermalization of the lower charge states is evident. It is also clear that the lower charge states are less fully Maxwellianized, particularly the high energy tails. For C^{4+} the Maxwellianization time is ~20 ms and thus the C^{4+} distribution is expected to be almost perfectly Maxwellian, as is seen to be the case in the DIVIMP results.

6.6.4.5 *Finite Mean-Free-Path Effects*

All fluid models implicitly assume strong collisionality, short collisional mean free paths, see section 9.12. The edge plasma is, in fact, often of marginal collisionality and a variety of 'kinetic corrections' can be required to try to extend the validity of fluid models, chapter 26. By contrast Monte Carlo modelling is quasi-kinetic and all variations of mean free path are automatically allowed for (at least for the impurities themselves). As was already noted regarding figure 6.18, Monte Carlo and fluid results can diverge significantly even for marginally collisional conditions.

6.6.4.6 *Modelling Recycling Neutrals*

Recycling neutrals such as He, Ne, etc move as neutrals around the periphery of the plasma—in the 'vacuum' region—as well as doing so as ions within the plasma. The modelling of these two quite different types of transport is difficult/impossible to do using a fluid code, and a Monte Carlo code is usually used to track the neutrals, in combination with a fluid code for the ions. Alternatively, the Monte Carlo code can directly track impurity particles through both regions.

6.6.4.7 *Computational Time*

Convergence of 2D multi-fluid codes is typically slow and computationally expensive. Convergence is not involved in MC modelling and computational times are usually short.

6.7 Helium and Pumping

He is the one completely unavoidable impurity for DT fusion and the requirement to remove it efficiently motivates much edge design. Failure to remove the He from the plasma adequately will cause the DT fusion process to poison itself. One of the primary purposes of a divertor is to compress the neutral gas—including He—as much as possible, in some region of the edge, in order that it can be removed through small ducts to compact pumps.

The He production rate is directly given by the DT fusion power and it can be shown [6.59, 6.60], that in order to achieve a stationary and ignited burning

DT plasma it is necessary that:

$$\boxed{\tau_\alpha^*/\tau_E \leq 10} \tag{6.99}$$

where τ_α^* is the *global alpha particle confinement time* and τ_E is the energy confinement time. That is, the particle confinement time must not be *too good*.

See [6.61] for a further assessment of He removal requirements.

The global confinement time τ_α^* is experimentally determined by turning the original alpha source off and observing the time decay of the total alpha particle content of the plasma, N_α:

$$\mathrm{d}N_\alpha/\mathrm{d}t = -N_\alpha/\tau_\alpha^*. \tag{6.100}$$

We employ a simplified form of the analysis of Reiter *et al* [6.59] in the following. The relation of τ_α^* to $D_\perp$ is complex because two populations of alpha particle are present in the plasma:

(a) The first generation alphas which were born in the central plasma and have not yet reached the wall. Let their content be $N_{\alpha 1}$ and their mean dwell time in the plasma be $\tau_{\alpha 1}$.
(b) He which has *recycled* from the wall and re-entered the plasma; total content $N_{\alpha 2}$ and mean dwell time $\tau_{\alpha 2}$.

If $v_{\mathrm{pinch}} = 0$ then $\tau_{\alpha 1} \simeq a^2/D_\perp$ since the first generation alphas must diffuse across most of the plasma radius. $\tau_{\alpha 2} \ll \tau_{\alpha 1}$ since the recycled He particles are ionized rather near the edge. For the Engelhardt model, section 6.4, one would anticipate $\tau_{\alpha 2} \approx a\lambda_{iz}^0/D_\perp$ where λ_{iz}^0 is the ionization depth inboard of the LCFS. For a high density divertor the latter expression is unlikely to be applicable, but the point remains that $\tau_{\alpha 1}$ is likely to be much larger than $\tau_{\alpha 2}$. Clearly τ_α^* is a weighted average of $\tau_{\alpha 1}$ and $\tau_{\alpha 2}$, with the weight set by the strength of the two sources. While a pump can do nothing to influence $\tau_{\alpha 1}$, it does reduce $\tau_{\alpha 2}$, and thus also reduces τ_α^*, to the degree that the pumping is effective. We wish to relate τ_α^* to the pumping. $\mathrm{d}N_{\alpha 1}(t)$ satisfies:

$$\frac{\mathrm{d}N_{\alpha 1}(t)}{\mathrm{d}t} = -\frac{N_{\alpha 1}}{\tau_{\alpha 1}} + \frac{N_D N_T \overline{\sigma v}_F}{V} \tag{6.101}$$

where N_D, N_T are the total content of the plasma of volume V and $\overline{\sigma v}_F$ is the average fusion reaction rate in V. If the fusion reaction ceases at $t = 0$ then:

$$N_{\alpha 1}(t) = (\tau_{\alpha 1} N_D N_T \overline{\sigma v}_F / V)\mathrm{e}^{-t/\tau_{\alpha 1}}. \tag{6.102}$$

With regard to the recycling population, we will assume that a fraction R_{eff}, the *effective recycling coefficient*, of the fluxes leaving the plasma, ϕ_{out}, re-enters the plasma. Thus

$$\phi_{\mathrm{out}} = \frac{N_{\alpha 2}(t)}{\tau_{\alpha 2}} + \frac{N_{\alpha 1}(t)}{\tau_{\alpha 1}} \tag{6.103}$$

$$\frac{\mathrm{d}N_{\alpha 2}(t)}{\mathrm{d}t} = -\frac{N_{\alpha 2}(t)}{\tau_{\alpha 2}} + R_{\mathrm{eff}}\left(\frac{N_{\alpha 2}(t)}{\tau_{\alpha 2}} + \frac{N_{\alpha 1}(t)}{\tau_{\alpha 1}}\right). \tag{6.104}$$

R_{eff} is not a simple surface reflection coefficient since it implicitly contains information about the pumping. Thus in steady state (at $t \leq 0$):

$$N_{\alpha 1} = \tau_{\alpha 1} N_D N_T \overline{\sigma v}_F / V. \tag{6.105}$$

$$N_{\alpha 2} = \frac{R_{\text{eff}}}{1 - R_{\text{eff}}} \frac{\tau_{\alpha 2}}{\tau_{\alpha 1}} N_{\alpha 1} \tag{6.106}$$

$$N_\alpha \equiv N_{\alpha 1} + N_{\alpha 2} = (N_D N_T \overline{\sigma v}_F / V)\left(\tau_{\alpha 1} + \frac{R_{\text{eff}}}{1 - R_{\text{eff}}} \tau_{\alpha 2}\right). \tag{6.107}$$

The time-dependent solution [6.59] gives:

$$\boxed{\tau_\alpha^* = \tau_{\alpha 1} + \frac{R_{\text{eff}}}{1 - R_{\text{eff}}} \tau_{\alpha 2}.} \tag{6.108}$$

A number of important consequences of equation (6.108) may be noted:

(a) If the recycling is too strong, $R_{\text{eff}} \to 1$, then it will not be possible to achieve the low value of τ_α^* required, equation (6.99).
(b) In steady-state reactor-like conditions, where the walls are fully saturated with hydrogen, the only way to make $R_{\text{eff}} < 1$ is with *active pumping*.
(c) There is no benefit, however, in installing so much pumping as to make $R_{\text{eff}} \tau_{\alpha 2} / (1 - R_{\text{eff}}) \ll \tau_{\alpha 1}$.

We wish to now relate R_{eff} to the properties of the pump, ε_p, by defining:

$$\phi_{\text{pump}} \equiv \varepsilon_p \phi_{\text{out}}. \tag{6.109}$$

We may analyse ε_p by defining the 'collection efficiency' of the pump, $\varepsilon_{\text{coll}}$:

$$\phi_{\text{coll}} \equiv \varepsilon_{\text{coll}} \phi_{\text{out}}. \tag{6.110}$$

ϕ_{coll} is the flux striking the pump opening. $\varepsilon_{\text{coll}}$ is the fraction of the wall area that is effectively occupied by the pump opening. Not all neutrals entering the pump opening will actually be removed by the pump, as some will return to the main vessel. One thus defines the 'removal efficiency' of the pump, ε_{rem}, by

$$\phi_{\text{pump}} \equiv \varepsilon_{\text{rem}} \phi_{\text{coll}}. \tag{6.111}$$

Thus

$$\varepsilon_p = \varepsilon_{\text{rem}} \varepsilon_{\text{coll}}. \tag{6.112}$$

From the above result we have the following:

$$R_{\text{eff}} = 1 - \varepsilon_p = 1 - \varepsilon_{\text{rem}} \varepsilon_{\text{coll}}. \tag{6.113}$$

One wants as large a pump opening as possible, as large an $\varepsilon_{\text{coll}}$ as possible. If the neutrals struck the entire wall surface uniformly in a reactor over a wall

area $\sim 10^3$ m^2, then it would probably be impractical to have $\varepsilon_{\rm coll}$ as large as even 10^{-2}. This, therefore, is the motivation for the use of divertors and pumped limiters, where by concentrating the $\phi_{\rm out}$ in a small space, it is practical to raise $\varepsilon_{\rm coll}$, perhaps to the order of 10^{-1}. It is also advantageous to *direct* the neutrals into the pump opening, thus decreasing the probability the neutrals will return, i.e. raising $\varepsilon_{\rm rem}$. This, therefore, is the advantage of divertor designs, figure 5.2, where the plasma flow and resulting neutral flow can be channelled into the pump opening.

Most of the foregoing analysis applies equally well to the fuel species, where a central source of particles may exist due to neutral beam injection or pellet injection. Effective pumping of fuel particles is then necessary in order to achieve control of the plasma density.

Clearly it would also be helpful if the He were *enriched* in the divertor. The *helium enrichment factor* $\eta_{\rm He}^{\rm enrich}$ is defined [6.62, 6.63]:

$$\boxed{\eta_{\rm He}^{\rm enrich} \equiv \frac{n_{\rm He}^{\rm pump}/2n_{\rm H_2}^{\rm pump}}{n_{\rm He}^{\rm main}/n_{\rm H}^{\rm main}}} \tag{6.114}$$

where $n_{\rm He}^{\rm pump}$ ($n_{\rm H_2}^{\rm pump}$) are the He (H_2) gas densities at the edge of the plasma, near the pumps, and $n_{\rm He}^{\rm main}$ is the He-ion density in the main plasma where the average plasma density is $n_{\rm H}^{\rm main}$ (we neglect plasma dilution due to He here, $n_e \approx n_{\rm H}$). Unfortunately, virtually all experiments to date have shown $\eta^{\rm enrich}$ somewhat *less* than unity, i.e. a modest *re-enrichment*; see the review in [6.64]. Presumably this is due to the fact that $\rm He^0$ is hard to ionize ($\overline{\sigma v}_{iz}^0$ is small) and some of the He ions recycling at the target does so as energetically back-scattered neutrals—thus penetrating more deeply into the plasma than does the recycling hydrogen. As was shown in section 6.5.5, when impurities ionize further from the target than the hydrogen does, divertor leakage of impurities is increased.

As with all impurities, there are a number of links in the chain that connects the 'two ends'—in this case $n_{\rm He}^{\rm main}$ and $n_{\rm He}^{\rm pump}$. It is useful to bring this out by defining a number of *concentrations*:

$$C_{\rm main} \equiv n_{\rm He}^{\rm main}/n_{\rm H}^{\rm main} \tag{6.115}$$

$$C_{\rm pump} \equiv n_{\rm He}^{\rm pump}/2n_{\rm H_2}^{\rm pump} \tag{6.116}$$

$$C_{\rm SOL} \equiv n_{\rm He}^{\rm SOL}/n_{\rm H}^{\rm SOL} \tag{6.117}$$

$$C_{\rm div} \equiv n_{\rm He}^{\rm div}/n_{\rm H}^{\rm div}. \tag{6.118}$$

Note: SOL indicates the upstream end of the SOL, adjacent to the main plasma; div indicates the region next to the target. Note: $C_{\rm main}$, $C_{\rm SOL}$, $C_{\rm div}$, are ratios of *ion* densities; $C_{\rm pump}$ is a ratio of *neutral* densities. Thus:

$$\eta^{\rm enrich} \equiv C_{\rm pump}/C_{\rm main} \tag{6.119}$$

and by extension we may define:

$$\eta^{\text{enrich}}_{\text{SOL/main}} \equiv C_{\text{SOL}}/C_{\text{main}} \tag{6.120}$$

$$\eta^{\text{enrich}}_{\text{div/SOL}} \equiv C_{\text{div}}/C_{\text{SOL}} \tag{6.121}$$

$$\eta^{\text{enrich}}_{\text{pump/div}} \equiv C_{\text{pump}}/C_{\text{div}} \tag{6.122}$$

so that:

$$\eta^{\text{enrich}} = \eta^{\text{enrich}}_{\text{SOL/main}}\eta^{\text{enrich}}_{\text{div/SOL}}\eta^{\text{enrich}}_{\text{pump/div}}. \tag{6.123}$$

These latter definitions emphasize the fact that there are three links in the transport chain, figure 6.3:

(1) radial (ionic) transport in the main plasma;
(2) parallel (ionic) transport along the SOL;
(3) neutral transport from the divertor plasma into the pump.

The transport coefficients $D_\perp$ and v_{pinch} in the main plasma have been measured on a number of tokamaks and do not differ significantly from the hydrogenic coefficients [6.65]. Thus, $\eta^{\text{enrich}}_{\text{SOL/main}}$ appears to be reasonably well understood. Parallel impurity transport in the SOL was discussed in section 6.5.5 and is still very much an evolving field; $\eta^{\text{enrich}}_{\text{div/SOL}}$ is thus less well in hand.

The quantity $\eta^{\text{enrich}}_{\text{pump/div}}$ depends on the coupling of plasma in the divertor fan and the neutral gas density outside the fan. This coupling is not simple even for the hydrogenic species itself. On DIII-D it is possible to adjust the location of the outside strike point so as to be able to 'stuff' the divertor plasma leg into the opening of the cryo-pump—to an adjustable degree, figure 5.4 [6.66]. For attached discharges, i.e. at relatively low density, this resulted in large variations in the hydrogen pumping rate, varying up to fivefold between the extremes of positioning. By contrast, for partially detached conditions, i.e. at higher plasma density, the variation of pumping rate with positioning was rather slight. The difference was attributed to the short ionization length of the neutrals at high density, and the tendency of neutrals to be 'trapped' or pumped by the plasma itself. Changes in the geometry of the divertor structural components can significantly influence the pumping [6.67, 6.68].

Other more complicated effects also appear to be involved—again, even for hydrogen—as now briefly described. Fielding reported results from DITE bundle divertor [6.69] that the H_2 outside the divertor plasma fan was impeded in penetrating the plasma due to the 'backwash' of energetic Franck–Condon and charge-exchange neutrals emanating from the plasma fan, in high pressure/density operation. In this finding it was concluded that neutral–neutral collisions strongly influenced the coupling between the particle population within the divertor plasma fan, and the neutral density just outside the fan. Allen *et al* reported apparently related difficulties in explaining D_α measurement on DIII-D [6.70]. Haas and co-workers [6.71, 6.72] reported a similar effect, but in this case it was attributed to H^2–H^+ elastic back-scattering collisions acting to impede the coupling of the

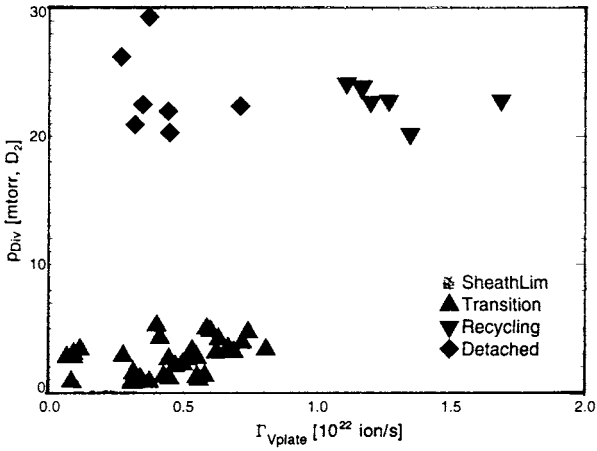

Figure 6.24. CMOD divertor neutral pressure plotted as a function of the integrated ion flux striking the vertical target plates (inner and outer) below the divertor nose (entrance). The outer strike point is on the vertical target and the divertor pressure is measured with a capacitance gauge [6.73].

two populations. Niemczewski *et al* [6.73] reported on a similar effect in CMOD with code-computed neutral densities near the divertor plasma fan being an order of magnitude below experimental values. Figure 6.24 shows divertor neutral pressure on CMOD against the integrated ion flux to the targets for the different regimes: sheath limited, 'transitional', 'recycling' (i.e. conduction limited) and detached. For the latter two regimes the divertor pressure is particularly high, evidently due to H_2–H^0 and H_2–H^+ collisions.

It seems likely that the coupling between He ions in the divertor fan, and the He gas density outside the fan, will be influenced by similar processes; understanding of $\eta^{\text{enrich}}_{\text{pump/div}}$ is thus still evolving. Elucidation of the complex processes involved—whether just for the hydrogen behaviour alone, or for He in hydrogen—requires use of sophisticated neutral codes such as EIRENE, incorporating all of the complicated atomic and molecular collisional processes implied by the observations described in the previous paragraphs [6.74], including neutral–neutral collisions.

Since η^{enrich} is of the order of unity, our interest then focuses on achieving the highest possible hydrogenic gas densities in the divertor adjacent to the plasma legs. Since the earliest divertors were operated it has been observed that the neutral pressure in the divertor was considerably higher than in the region in the main vessel just outside the plasma, i.e. a strong *divertor compression* was achieved [6.75, 6.76]. In the high density CMOD tokamak [6.73], particularly high divertor pressures—greater than 150 mtorr [6.48]—and high compression ratios—up to 100—have been achieved, figure 6.25. Such high gas pressures in

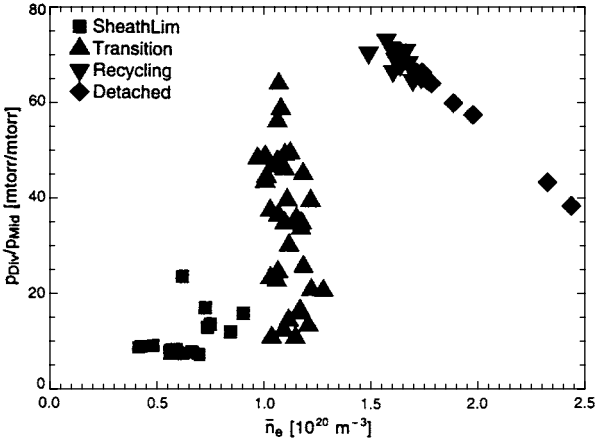

Figure 6.25. CMOD. Compression ratio (divertor to midplane neutral pressure) dependence on core plasma density $\overline{n}_e$, showing the SOL plasma transport regimes with different symbols. The outer strike point is on the vertical target, and the divertor pressure is measured with a capacitance gauge [6.73].

the divertor are valuable for efficient removal of He—and are also of value for controlling the hydrogen itself: it can be advantageous to fuel the plasma using neutral beam injection or pellets, in which case equal outflows of particles must be pumped to achieve steady state. The achievement of high compression, to the degree this involves low pressures in the main vessel, may be advantageous as this has been correlated with achievement of H-mode confinement in some studies [6.77], although not in others [6.78].

6.8 Erosion and Redeposition of Solid Structures at the Plasma Edge

Plasma-surface interactions are generally mutually harmful to both of the states of matter involved. The plasma becomes contaminated with particles released from the solid structures at the edge, degrading plasma performance (for the most part). At the same time, the solid structures are eroded, a process which eventually degrades their functionality. In present experimental devices the total exposure time of the edge structures to plasma is generally too short to result in very significant erosion and the emphasis to date has therefore primarily been on the effect of impurities on the plasma. This situation will change as fusion development proceeds to more reactor-like operation.

The study of plasma erosion in fusion devices is already well established, with the pioneering work of J. N. Brooks dating back to the early 1980s. It is

evident that this aspect of 'impurity' behaviour is more complex and challenging that the plasma-contamination processes which constitute but the first step in the *net* erosion process. Virtually all of the solid material released into the plasma will eventually *redeposit* on some part of the edge structure—and it is the *net deposition* which is of principal interest. Therefore in order to unravel the full erosion/redeposition story it is necessary to unravel all of the impurity production and transport processes—including the processes involving the *return* of the impurity particles to the edge structures.

We do not attempt here to analyse or review the studies carried out in this field of increasing importance, but refer the reader to the work of Brooks [6.53, 6.79–6.85], Naujoks [6.86–6.89] and others [6.90–6.97].

Additional Problems

6.12. *Variation of collisionality of different charge states.* Assume a uniform plasma of $n_e = 10^{19}$ m^{-3} and values of $T_e = T_{D^+} = T_C = 10$ eV, also 100 eV. Calculate the dwell time in each charge state, also the collision times τ_s, and τ_T. What do you conclude about the collisionality of the different charge states? Repeat for $n_e = 10^{18}$ m^{-3}, $n_e = 10^{20}$ m^{-3}.

6.13. Consider a point source of 5 eV C^{3+} ions at a location in the SOL where $T_e = 30$ eV, $T_{D^+} = 100$ eV and $n_e = 10^{19}$ m^{-3}. The plasma background is stationary.

(a) How long is τ_{iz}, the time for the C^{3+} to become ionized to C^{4+}, i.e. its 'lifetime' in this charge state?
(b) How far will a 5 eV C^{3+} ion, with its velocity purely along $\boldsymbol{B}$, travel before a momentum-loss collision with the background plasma? How much time will that take? Will such a collision actually occur within the lifetime of the C^{3+} ion?
(c) What is the thermalization time of the C^{3+}? What would the temperature of the C^{3+} be at $t = \tau_T, 2\tau_T, 3\tau_T$? Will the C^{3+} actually have time to reach this temperature? Show that the average temperature of the C^{3+} over its lifetime is 87 eV.
(d) In part (b) we considered some aspects of the dispersal of the C^{3+} ions along $\boldsymbol{B}$ during their lifetime. How long would it be before the C^{3+} experienced a (parallel) diffusion collision? Estimate this time by assuming a value for the C^{3+} temperature equal to the time-average value of T_z over the C^{3+} lifetime, $\overline{T}_z$. Calculate $D_\parallel$, also assuming this T_z-value, equation (6.38). Estimate the diffusive spread of the C^{3+} ions along $\boldsymbol{B}$. Compare this with the distance that a 5 eV and a 100 eV C^{3+} would travel collisionlessly in its lifetime; compare also with the momentum-loss mean free path calculated in part (b); comment.
(e) What do you think of the suggestion that the dispersal of the ions in

the parallel direction due to diffusion collisions, $\Delta s_{\parallel}^{\text{diff}}$, can be estimated by calculating the distance that an ion would travel collisionlessly with a parallel velocity corresponding to $\overline{T}_z$, i.e. $\Delta s_{\parallel}^{th}$? Find the latter quantity here and compare with $\Delta s_{\parallel}^{\text{diff}}$. Comment. Show that generally $\Delta s_{\parallel}^{th}/\Delta s_{\parallel}^{\text{diff}} = (\tau_{iz}/2\tau_{\parallel})^{1/2}$ and comment on the implications.

(f) Assume that the cross-field diffusion coefficient is $D_{\perp} = 0.5\ \text{m}^2\text{s}^{-1}$. Estimate the diffusive spread of the C^{3+} cross-field. Compare with the parallel diffusive spread and comment.

6.14. Repeat problem 6.13 for $n_e =$ (a) $10^{18}\ \text{m}^{-3}$, (b) $10^{20}\ \text{m}^{-3}$.

6.15. *Parallel transport of impurity ions in the presence of friction and an electric field.*

Consider an impurity ion of charge Z and mass m_z located at s_0 at time $t = 0$, with parallel velocity v_{z0}. The plasma background has a flow velocity v_i and and a parallel electric field E is present. Show that the location of this ion at time t, $s(t)$, and its parallel velocity, $v_z(t)$, are given by:

$$\boxed{s(t) = s_0 + \left(\frac{Z_e \tau_s}{m_z}\right) E[t - \tau_s(1 - \mathrm{e}^{-t/\tau_s})] + v_i t + \tau_s(v_{z0} - v_i)(1 - \mathrm{e}^{-t/\tau_s})}$$

$$\boxed{v_z(t) = \left(\frac{Ze\tau_s}{m_z}\right) E(1 - \mathrm{e}^{-t/\tau_s}) + v_i + (v_{z0} - v_i)\mathrm{e}^{-t/\tau_s}.}$$

6.16. Consider the same situation as in Problem 6.13, but now with $v_i \neq 0$, $E \neq 0$. For the values of v_i and E take those of a simple, isothermal pre-sheath plasma as described in sections 1.8.2.6–1.8.2.9.

(a) If the plasma background Mach number is 0.5 at the injection point, show that the location of the injection is $s = 0.252L$, where s is measured from the target. What is the value of v_i [m s^{-1}]? What is the sign?

(b) By differentiating equation (1.52) show that:

$$E = -(\pi - 2)\frac{kT_e}{eL}\frac{M}{1 - M^2}$$

Assuming $L = 100$ m, show that the value of E at the injection location is $-0.23\ \text{V m}^{-1}$.

(c) Make a first estimate of the shape of the 'C^{3+} cloud', by calculating the distance the C^{3+} travels in the two parallel directions (with and against the flow) in its lifetime, neglecting parallel diffusion effects. Neglect the spatial variation of M and E, taking their values at the injection point for purposes of this estimate. Assume initial velocities corresponding

to 5 eV, moving upstream or downstream. Which has more effect, the electric field or friction? Compare these distances with the distances that the ion would have travelled at the plasma background velocity, and comment.

(d) On the basis of part (c) you might be tempted to conclude that the C^{3+} ion 'cloud' would span between these two limiting locations. But taking parallel diffusion into account shows that this is not realistic. Using the results of problem 6.13(d) together with those of 6.16(c), estimate the central location of the C^{3+} ion 'cloud', and its spread along $\boldsymbol{B}$.

6.17. Repeat problem 6.16 for $n_e =$ (a) 10^{18} m^{-3}, (b) 10^{20} m^{-3}.

6.18. (a) For $\hat{n}_z^{\text{ref}}$ defined by equation (6.19) show that for a uniform wall source that:

$$f_{\text{rdn}}^z = \begin{cases} 1 + \lambda_{iz}^0/\lambda_{\text{SOL}}, & \lambda_{iz}^0 \geq 0 \\ \mathrm{e}^{\lambda_{iz}^0/\lambda_{\text{SOL}}}, & \lambda_{iz}^0 \leq 0. \end{cases}$$

Plot $f_{\text{rdn}}^z(\lambda_{iz}^0/\lambda_{\text{SOL}})$ for $-3 \leq \lambda_{iz}^0/\lambda_{\text{SOL}} \leq +3$.

(b) Consider next a limiter source of impurity neutrals, ionized at rather small distances, along $\boldsymbol{B}$, from the limiter. For ionization inside the LCFS, $\lambda_{iz}^0 > 0$, assume that the impurities have become distributed uniformly along $\boldsymbol{B}$ by the time they have diffused out to the LCFS. Will the above formula for f_{rdn}^z apply for such a source?

(c) As in part (b), but now consider the case of impurities ionized in the SOL, $\lambda_{iz}^0 < 0$. Assume: (a) that the ionization occurs at distance L_{iz}, along $\boldsymbol{B}$, from the limiter, (b) that the impurities are so strongly coupled by friction to the background plasma that they are convected at the plasma flow speed back to the limiter and (c) that, over length L_{iz}, the plasma is moving at the sound speed. Although, in reality, the impurity ions will not be distributed uniformly along the length of the SOL, make the crude approximation that they are, but that their dwell time in the SOL is reduced to L_{iz}/c_{sa}. By considering the derivation of equation (4.68) argue that one can use equation (6.7) to calculate $\hat{n}_z$, but now using $\lambda_{\text{SOL}}^{\text{eff}} \equiv (L_{iz} D_\perp / c_{sa})^{1/2}$ in place of λ_{SOL}. Thus show that:

$$f_{\text{rdn}}^z = (L_{iz}/L)^{1/2} \mathrm{e}^{\lambda_{iz}^0/\lambda_{\text{SOL}}^{\text{eff}}}.$$

For the example of $L = 10$ m, $L_{iz} = 0.1$ m, $D_\perp = 0.5$ m^2 s^{-1}, $T_a = 25$ eV, D^+ ions, $\lambda_{iz}^0 = -5 \times 10^{-3}$ m, show that $f_{\text{rdn}}^z = 6.7 \times 10^{-4}$. Consider figure 6.5 and comment.

6.19. *Time-dependent evolution of a radial density profile.* Consider the case of slab geometry and a 'hard' boundary condition at $x = 0$ and $2a$, figure 6.26.

The neutrals are all ionized at $x = \lambda_{iz}$ and $2a - \lambda_{iz}$. Consider two increments of particles, $\Gamma_0 \delta t$ [particles m^{-2}], launched at time $t = 0$. We will follow

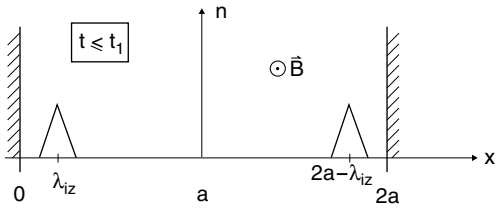

Figure 6.26. Two equal particle sources are located at distance λ_{iz} from each wall in a slab geometry configuration. $t < t_1$.

the evolution of the particles starting at $x = \lambda_{iz}$; the other increment behaves in a symmetric way. We will approximate the particle spatial distribution by a *triangular* profile of half-base width equal to $2\sqrt{2D_\perp t}$. Justify this approximation to a diffusion profile by considering the actual Gaussian shape which is calculated from classical physics [6.98].

Assume that no particles will be lost until time t_1, where:

$$2\sqrt{2D_\perp t_1} = \lambda_{iz}. \tag{6.124}$$

For $0 \leq t \leq t_1$ the centre of the triangle remains at $x = \lambda_{iz}$. For $t > t_1$ the inside edge of the triangle continues to advance toward the far wall as $2\sqrt{2D_\perp t}$, while the outside edge remains fixed thereafter at $x = 0$. The triangle is assumed to remain symmetrical, however, so the location of the peak of the distribution moves inward for $t > t_1$, figure 6.27.

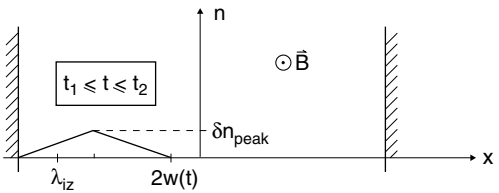

Figure 6.27. Approximate behaviour of a density profile evolving in time due to diffusion, $t_1 \leq t \leq t_2$. Only the density due to the left source of figure 6.26 is shown.

At $t = t_2$ the leading edge of the triangle reaches the opposite wall. Let the location of the leading edge be $2w(t)$, thus:

$$2w(t) = 2\sqrt{2D_\perp t} + \lambda_{iz}. \tag{6.125}$$

The total content of the increment is $\delta C(t)$:

$$\delta C(t) = w(t)\delta n_{\text{peak}} \tag{6.126}$$

where δn_{peak} is the peak density for the increment.

(a) For $t < t_1$ argue that:

$$\delta C(t) = \Gamma_0 \mathrm{d}t, \quad \text{constant.} \tag{6.127}$$

(b) For $t_1 < t < t_2$ argue that:

$$\frac{\mathrm{d}}{\mathrm{d}t}[\delta C(t)] = \frac{-D_\perp \delta n_{\text{peak}}}{w}. \tag{6.128}$$

(c) For $t > t_2$ argue that:

$$\frac{\mathrm{d}}{\mathrm{d}t}[\delta C(t)] = -\frac{-2D_\perp \delta n_{\text{peak}}}{w}. \tag{6.129}$$

(d) Thus show that:

$$\delta n_{\text{peak}}(t) = \begin{cases} \Gamma_0 \delta t / 2\sqrt{2D_\perp t} & \text{for } t \le t_1 \\ \Gamma_0 \delta t \lambda_{iz} \mathrm{e}^{0.5-\lambda_{iz}/2\mathrm{w}}/w^2 & \text{for } t_1 \le t \le t_2. \end{cases} \tag{6.130}$$

(e) Define a normalized time $\hat{t} \equiv t/t_1$. Calculate and plot $\delta C(\hat{t})/(\Gamma_0 \delta t)$.

(f) Find the values of $\delta n(t_2)$ and $\delta C(t_2)$. Why is it reasonable to take these quantities to be approximately zero?

(g) Assume now that a continuous influx of neutrals occurs at a constant rate Γ_0 [neutrals $\mathrm{m}^{-2}\ \mathrm{s}^{-1}$], and that this can be approximated as a series of increments of particle addition, in amounts $\Gamma_0 \delta t$ [particles m^{-2}] occurring every δt seconds. Argue that the total content of the plasma at time t after the start of the influx is:

$$C(t) = \int_0^t \delta C(t) = \int_0^t w(t) \delta n_{\text{peak}}(t) \tag{6.131}$$

and thus use equation (6.130) to show that for $\lambda_{iz}/a \ll 1$:

$$C(t) \approx \frac{\Gamma_0 \lambda_{iz} a}{D_\perp} \tag{6.132}$$

i.e., the same result as we would obtain from the steady-state Engelhardt model, section 6.4.1, allowing for the contribution from the source at $x = 2a - \lambda_{iz}$. Hint: Show that the exponential factor in equation (6.130) differs very little from unity.

6.20. Continue with the analysis of problem 6.19:

(a) Consider the *distribution of particle confinement times*, $\mathrm{d}f/\mathrm{d}\tau_p$, where $(\mathrm{d}f/\mathrm{d}\tau_p)\mathrm{d}\tau_p$, is the fraction of the ions which have a dwell time in the plasma between τ_p and $\tau_p + \mathrm{d}\tau_p$. Argue that:

$$\frac{\mathrm{d}f(\tau_p)}{\mathrm{d}\tau_p} = \frac{1}{\Gamma_0 \delta t} \frac{\mathrm{d}(\delta C(t))}{\mathrm{d}t} \tag{6.133}$$

and thus show that for $t_1 < t < t_2$:

$$\boxed{\frac{\mathrm{d}f}{\mathrm{d}\tau_p} = \frac{D_\perp \lambda_{iz} \mathrm{e}^{0.5-\lambda_{iz}/2u}}{u^3}} \tag{6.134}$$

where $u \equiv (2D_\perp \tau_p)^{1/2} + \lambda_{iz}/2$.

(b) For the specific case of $\lambda_{iz} = 0.02$ m, $a = 1$ m, $D_\perp = 0.5$ m^2 s^{-1} plot $\mathrm{d}f(\tau_p)/\mathrm{d}\tau_p$ against τ_p.

(c) The average particle dwell time, usually just written as τ_p, is:

$$\overline{\tau}_p = \int_{\tau_p^{\min}}^{\infty} \tau_p \frac{\mathrm{d}f}{\mathrm{d}\tau_p} \mathrm{d}\tau_p. \tag{6.135}$$

Find $\tau_p^{\min}$. Show for $\lambda_{iz} \ll a$ that:

$$\overline{\tau}_p \approx a\lambda_{iz}/2D_\perp$$

which was also obtained from the steady-state Engelhardt model, section 6.4.1.

Mark $\overline{\tau}_p$ on your plot from part (b). Note that $\overline{\tau}_p$ is dominated by the few ions which stay in the plasma for a long time, while most of the ions spend only a time much shorter than $\overline{\tau}_p$ in the plasma. For the example of part (b) find the fraction of the particles which have $\tau_p > \overline{\tau}_p$.

6.21. Repeat problems 6.19 and 6.20, now allowing, in an approximate way, for 'soft' boundary conditions at the walls, as follows: now assume that no particles are lost until t_1 where: $2\sqrt{2D_\perp t_1} = \lambda_{iz} + \lambda_{\mathrm{SOL}}$. Replace $w(t)$ by: $2w(t) = 2\sqrt{2D_\perp t} + \lambda_{iz} + \lambda_{\mathrm{SOL}}$. Otherwise proceed as before. Show that the expressions of problems 6.19 and 6.20 are merely altered by changing $\lambda_{iz} \to \lambda_{iz} + \lambda_{\mathrm{SOL}}$. Illustrate for the same specific example as in problem 6.20, now assuming also $\lambda_{\mathrm{SOL}} = 0.02$ m.

6.22. *A localized impurity source.* Consider an elaboration on problem 6.20 where the ionization is localized in the direction along $\boldsymbol{B}$: let the coordinate be y parallel to $\boldsymbol{B}$, figure 6.28.

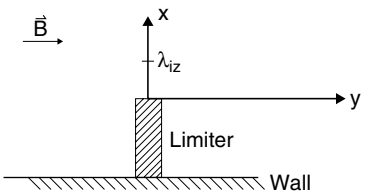

Figure 6.28. A point source of impurities at $(x, y) = (\lambda_{iz}, 0)$ in a rectangular system.

The situation approximates that of sputtering from a limiter with the ionization occurring at $(x, y) = (\lambda_{iz}, 0)$. Crudely approximate the motion of the impurity ions along y as involving an expansion of the fronts of the impurity 'cloud' in the y-direction, with speed $\pm v_\parallel$, where $v_\parallel$ is a specified parameter here. Thus the one-sided y-extent of the 'cloud' is $y(t) = v_\parallel t$. Argue that it would be reasonable to then define

$$\lambda_{\mathrm{SOL}}(t) \equiv \frac{y(t)}{L}\lambda_{\mathrm{SOL}}^{\infty} = \frac{v_\parallel t \lambda_{\mathrm{SOL}}^{\infty}}{L}.$$

where $\lambda_{\mathrm{SOL}}^{\infty}$ is the usual, specified value and L is the connection length. Repeat problem 6.21 assuming $L = 30$ m and $v_\parallel = 10^4$ m s^{-1}. Experiment with the effect of changing λ_{iz}, L, $v_\parallel$, $D_\perp$; how does $\overline{\tau}_p$ depend on these parameters, roughly?

6.23. The lifetime of a particular charge state of an impurity atom or ion depends on the local electron density and temperature since this sets the time for ionization to the next charge state. Thus, if the elapsed time in a charge state can be observed—for example, by monitoring the line radiation specific to that charge state—then it may be possible to infer the local values of n_e and T_e. In a steady-state situation it might be possible to infer n_e and T_e from the spatial extent of particular charge states—say parallel to $\boldsymbol{B}$—if the velocity of expansion of the charge state 'clouds' is known. The latter can be a non-trivial task to calculate, see for example, problems 6.13–6.15; however, for illustration let us assume that the impurities travel along $\boldsymbol{B}$ with velocity corresponding to 15 eV.

(a) For $n_e = 10^{19}$ m^{-3} confirm, using figure 1.26 the results for the ionization mean free paths for the carbon examples in figure 6.29.
(b) Using the information in this figure, suggest a diagnostic method for estimating the local value of n_e, in the absence of any information about T_e.
(c) Similarly, how might one base a diagnostic method on this information that would permit a measurement of T_e, lacking any information on n_e?

6.24. Extract the expression (6.35) for the stopping time from Spitzer's results [6.39]. Discuss the effect on τ_s when $v/(2kT_i/m_i)^{1/2}$ is not very small.

6.25. Extract the expressions in equations (6.36), (6.37) for parallel diffusion from Spitzer's results [6.39].

6.26. Calculate $D_\parallel$, equation (6.38), for C^{4+} ions in a D^+ plasma background with $n_e = 10^{19}$ m^{-3}, $T_{D+} = T_{C^{4+}} = 40$ eV. Compare with typical values of $D_\perp$ and comment on the implications.

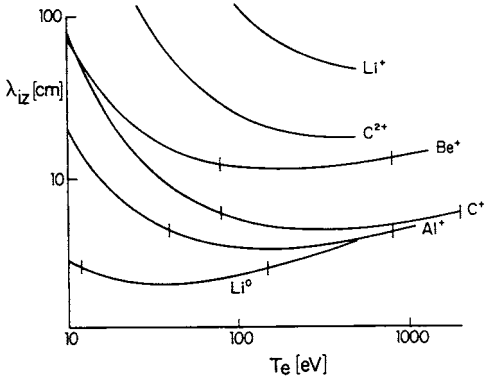

Figure 6.29. Mean free path for ionization λ_{iz} for particles moving with 15 eV kinetic energy as a function of T_e; $n_e = 10^{19}$ m^{-3}. For certain species, such as Li^0, λ_{iz} is essentially constant over a wide range of T_e. The vertical bars indicate the T_e range over which λ_{iz} varies by less than $\pm 10\%$ [6.99].

6.27. Consider a C^{4+} ion in the process of thermalizing with a D^+ plasma, $n_e = 10^{19}$ m^{-3}, $T_{D+} = 40$ eV.

(a) When $T_z = 2$ eV find how much the parallel velocity v_z will change, on average, in a time interval of 0.3 μs, as a result of parallel diffusive conditions. Calculate how much T_z changes in this time interval, using the temperature formula equation (6.98). Compare this with the change in kinetic energy associated with the change in v_z.
(b) Carry out the same calculations when $T_z = 30$ eV.
(c) Comment on the connection between parallel velocity diffusive collisions and thermalizing collisions.

6.28. *The plateau or prompt-loss region, section 6.5.4.2.* Figure 6.30 shows the C^{4+} peak density, n_p, calculated using the DIVIMP code (points) and the simple fluid model (line), equation (6.46) for the case: $T_z = T_{D^+} = 10$ eV, $dT/ds = 1.38$ eV m^{-1}, $E = 0$, $n_e = 10^{19}$ m^{-3}, C^{4+} injected at $s_{inj} = 0.15$ m, $\Gamma_{\|}^{in} = 1.73 \times 10^{23}$ [C^{4+} m^{-2} s^{-1}], and a range of values of v_i ($\equiv v_B$); negative values indicate flow toward the target).

(a) Confirm that this is a highly collisional case by comparing λ_{mfp} with other relevant distances.
(b) Calculate each of the velocities in equation (6.47), compare and comment.
(c) Thus confirm the simple fluid model result in the figure.

6.29. Figure 6.31 shows a similar result to that of problem 6.28, but for: $n_e = 10^{20}$ m^{-3}, various $T_z = T_{D^+}$, $v_i = -0.1c_s$, $s_{inj} = 0.15$ m, $E = 0$, $\Gamma_{\|}^{in} =$

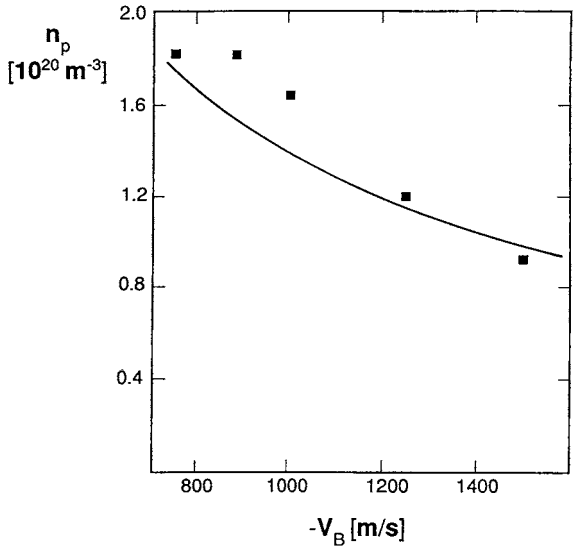

Figure 6.30. Impurity density peak value near the target n_p: comparison of the values from equation (6.46) (solid line) and the results (squares) from the DIVIMP code, for conditions: $T_D(0) = 10$ eV, $\mathrm{d}T_D/\mathrm{d}s = 1.38$ eV m^{-1}, $n_e = 10^{19}$ m^{-3}, $\overline{s}_{\mathrm{inj}} = 0.15$ m, $s_v = 1.2$ m and various values of the background deuterium velocity, $v_B \equiv v_D$. $\Gamma_{\parallel}^{in} = 1.73 \times 10^{23}$ [C^{4+} m^{-2}s^{-1}]. This is a highly collisional case, $\lambda_{\mathrm{mfp}} \approx 1$ cm [6.40].

1.73×10^{23} [C^{4+} m^{-2} s^{-1}]. In this case the temperature gradient is assumed to be given by modified conduction, equation (6.91) with $f_{\mathrm{cond}} = 0.1$; the gradient is evaluated at $s = 0$. Also assumed: $\gamma = 7$, $\kappa_0 = 2000$. The points in the figure are from DIVIMP code runs; the dashed line is the simple analytic result of equation (6.45) for weak collisionality, while the solid line is the simple fluid result of equation (6.46).

(a) Find the approximate temperature, dividing the weak and strong collisionality regimes.
(b) Calculate $(\mathrm{d}T/\mathrm{d}s)_t$; calculate the different velocities involved in estimating n_p and confirm the results shown in this figure.

6.30. *The Neuhauser criterion for divertor retention.* It is clear that for all of the flow velocities shown in figure 6.30 there is good divertor retention in the prompt-loss region itself. For $v_B = -800$ m s^{-1} what is M_i? λ_{ii}? λ_T? $\lambda_T \equiv (1/T)(\mathrm{d}T/\mathrm{d}s)^{-1}$. Show that the Neuhauser criterion is satisfied, equation (6.50). At what velocity v_B would this criterion predict the onset of leakage? Compare with the detailed calculation as in problem 6.28; comment.

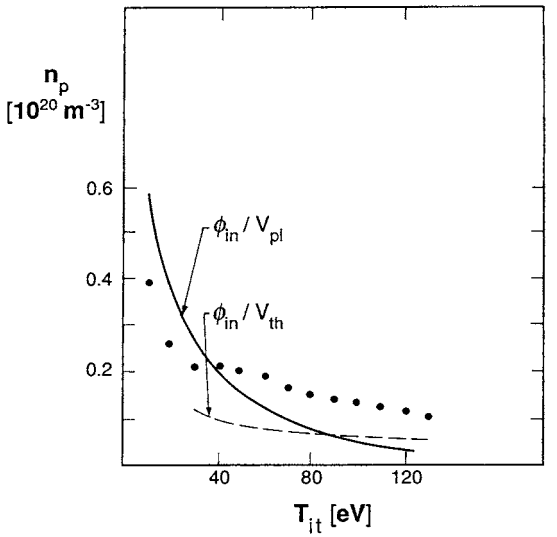

Figure 6.31. Plateau density, n_p. For conditions: $n_e = 10^{20}$ m^{-3}, $\bar{s}_{\rm inj} = 0.15$ m, $s_v = 1.2$ m, $M = 0.1$, $f_{\rm cond} = 0.1$, temperature gradient from equation (6.91) with $f_{\rm cond} = 0.1$ evaluated at $s_\parallel = 0$, and various values of T_{it}. $\Gamma_\parallel^{in} = 1.73 \times 10^{23}$ [C^{4+} m^{-2}s^{-1}]. The solid line results from the simple fluid theory, assuming high collisionality assumption, $n_p = \phi_{in}/v_{\rm th}$; the points show DIVIMP results. For $T_{it} = 110$ eV, $\lambda_{\rm mfp} \approx \bar{s}_{\rm inj}$, thus one expects the results to approach ϕ_{in}/v_{pl} for low T_{it} and $\phi_{in}/v_{\rm th}$ for high T_{it}, approximately as seen [6.40].

6.31. *The Krashninnkov criterion for divertor retention.* For $v_B = -800$ m s^{-1} in figure 6.30, calculate $q_\parallel^{i,\rm conv}$ and $q_\parallel^{i,\rm cond}$, confirming that the Krashenninikov criterion, equation (6.52), is satisfied. At what value of v_B do you predict the onset of leakage using this criterion?

6.32. Derive equations (6.54)–(6.58).

6.33. *Roth–Fussmann impurity density decay.* Figure 6.32 shows results for a density decay region where only parallel diffusion and friction are operating, $E = {\rm d}T/{\rm d}s = 0$, a situation corresponding to Roth–Fussmann density decay, equation (6.59). Conditions: $\Gamma_\parallel^{in} = 1.73 \times 10^{23}$ [C^{4+}m^{-2}s^{-1}], $s_{\rm inj} = 0.15$ m. The points are for different DIVIMP runs:

(i) diamonds: $n_e = 10^{19}$ m^{-3}, $T_{\rm D^+} = 10$ eV, $v_D = -112$ m s^{-1};
(ii) squares: $n_e = 10^{19}$ m^{-3}, $T_{\rm D^+} = 100$ eV, $v_D = -3.55 \times 10^4$ m s^{-1};
(iii) triangles: $n_e = 10^{18}$ m^{-3}, $T_{\rm D^+} = 100$ eV, $v_D = -3.55 \times 10^5$ m s^{-1}.

(a) For each of the three cases evaluate $\lambda_{\rm mfp}$.

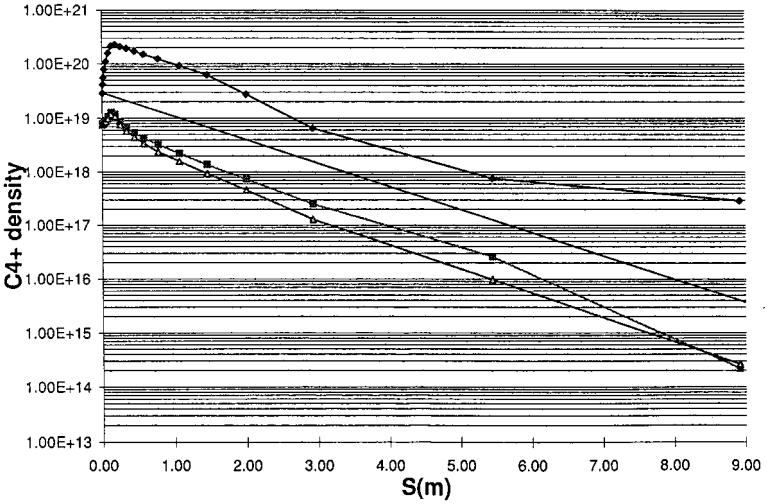

Figure 6.32. Density decay region. The only forces are friction due to D^+ flow at specified velocity, and parallel diffusion. DIVIMP results for various plasma densities, temperature and D^+ flow velocities. These plasma conditions were chosen so as to give the same value of $\lambda_\parallel^{\mathrm{SFT}} \equiv D_\parallel / v_D = 1$ m here; such a slope is shown as the line without points. Clearly the simple fluid model is approximately satisfied for both highly collisional and highly collisionless regimes for region B, the density decay region. Here $\overline{s}_{\mathrm{inj}} = 0.15$ m, which causes the peak at $s \approx 0.15$ m [6.40].

(b) For each of the three cases evaluate $\lambda_\parallel$ and confirm that the line without points in the figure gives the Roth–Fussmann result, i.e., confirm $\lambda_\parallel$ is the same for each of the above cases.

6.34. *Effect of the degree of collisionality on Roth–Fussmann density decay.* It is clear from figure 6.32 that even when $\lambda_{\mathrm{mpf}} \gg \lambda_\parallel$, the density decay follows the Roth–Fussmann prediction, a surprising result since the derivation of equation (6.59) is based on a fluid treatment. Explain this absence of a dependence on collisionality as follows.

(a) Consider an ion launched from $s = 0$ with initial velocity $v_0 > 0$. Integrate the momentum equation to show that the distance s_t that the ion will travel upstream against the D^+ flow before being stopped and turned around by friction is:

$$s_t = \tau_s[|v_i| \ln(1 - v_0/|v_i|) + v_0]. \tag{6.136}$$

Argue that this result is valid for *all* degrees of collisionality.

(b) Consider that there is a *distribution* of launch velocities, with v_0 being the average value. Divide the various velocities in the above equation by $\overline{v}_0$, define $v_r \equiv v_0/\overline{v}_0$, $\lambda_{\rm mfp} \equiv \overline{v}_0/\tau_s$, $\overline{v}_0 \equiv (kT/m)^{1/2}$, $D_\parallel \equiv kT\tau_s/m$, and show that:

$$s_t = \lambda_{\rm mfp}\left[|v_r| - \frac{\lambda_{\rm mfp}}{\lambda_\parallel}\ln\left(1 + |v_r|\frac{\lambda_\parallel}{\lambda_{\rm mfp}}\right)\right].$$

(c) Consider the collisionless limit, $\lambda_{\rm mfp}/\lambda_\parallel \to \infty$ and show that:

$$s_t \to \frac{\lambda_\parallel}{2}v_r^2.$$

(d) Note that the number of ions in a Maxwellian distribution with velocity v is proportional to $\exp(-mv^2/2kT)$ and use this to argue that the number of ions reaching s_t is proportional to $\exp(-x/\lambda_\parallel)$, i.e., the Roth–Fussmann result holds even for weak collisionality.

6.35. *Calculation of* $\overline{n}_{\rm trap}$. Use equation (6.66) to confirm, approximately, the DIVIMP results given in figure 6.33. The results given in this figure correspond to the same conditions as figure 6.31, problem 6.29, explicitly for $T_{\rm D^+} = 100$ eV and $s_v = 1.2$ m. We therefore read from figure 6.31 that $n_p = \Gamma_\parallel^{in}/v_{\rm prompt\ loss} \approx 10^{19}{\rm m}^{-3}$, also seen in figure 6.33.

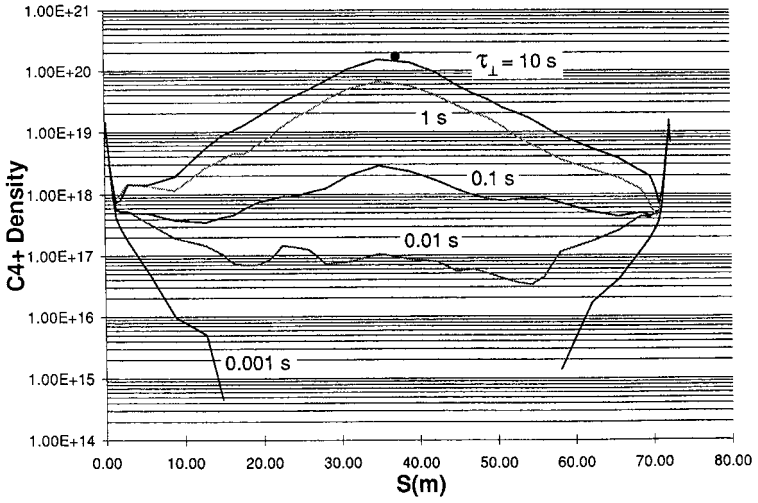

Figure 6.33. Calculated $n(s)$ profiles of C^{4+} using DIVIMP for plasma conditions, $T_t = 100$ eV, $\overline{s}_{\rm inj} = 0.15$ m, $s_v = 1.2$ m, and for various values of $\tau_\perp$. $\Gamma_\parallel^{in} = 1.73 \times 10^{23}$ [C^{4+} m^{-2}s^{-1}]. The point is calculated from the simple fluid model for $\tau_\perp = \infty$. Clearly divertor leakage is catastrophic unless $\tau_\perp \leq 100$ ms [6.40].

(a) Calculate $n_z(s_v)/n_p$ using equation (6.60). Use equation (6.91) to demonstrate that FiGf(s_v) is negligible; this is not surprising at such a high temperature, section 4.10.2. Calculate FFf(s_v) from equation (6.55), approximating the integrand as constant, evaluated at the target values. Thus show that $n_z(s_v)/n_p \approx 0.05$, approximately, as seen in the DIVIMP results of figure 6.33 (corresponding to the initial density decrease seen in front of the target on this large-scale plot).
(b) Use equation (6.72) to estimate v_{T_i}, evaluated at the target. Will the value be very different at s_v? Thus show $v_{T_i} \approx 600$ m s^{-1}.
(c) Thus confirm that the DIVIMP results in figure 6.33 for $\overline{n}_{\text{trap}}$ are roughly given by equation (6.66).

6.36. Confirm that the solid lines shown in figures 6.17 and 6.18 are given by the simple fluid model.

6.37. Confirm that the solid line shown in figure 6.19 is given by the simple fluid model. It is necessary here to allow for the variability of the integrand in equations (6.55)–(6.58).

References

[6.1] Wesson J 1997*Tokamaks* 2nd edn (Oxford: Oxford University Press) p 534
[6.2] McCracken G M and Stott P E 1979 *Nucl. Fusion* **19** 889
[6.3] Winter J 1990 *J. Nucl. Mater.* **176–177** 14.
[6.4] Parker R, Janeschitz G, Pacher H D *et al* 1997 *J. Nucl. Mater.* **241–243** 1
[6.5] Wesson J 1997 *Tokamaks* 2nd edn (Oxford: Oxford University Press) pp 209–210
[6.6] Wesson J 1997 *Tokamaks* 2nd edn (Oxford: Oxford University Press) p 323
[6.7] Wesson J 1997 *Tokamaks* 2nd edn (Oxford: Oxford University Press) p 353
[6.8] Eckstein W, Bohdansky J and Roth J 1991 *Suppl. Nucl. Fusion* **1** 51
[6.9] Matthews G F, Allen S, Asakura N *et al* 1997 *J. Nucl. Mater.* **241–243** 450
[6.10] Samm U, Bertshinger G, Bogen P *et al* 1993 *Plasma Phys. Control. Fusion* B **35** 167
[6.11] Matthews G F, Balet B, Cordey J G *et al* 1999 *Nucl. Fusion* **39** 19
[6.12] Allen S L, Bozek A S, Brooks N H *et al* 1995 *Plasma Phys. Control. Fusion* A **37** 191
[6.13] Itami K and the JT-60 Team 1995 *Plasma Phys. Control. Fusion* A **37** 255
[6.14] Lipschultz B, Goetz J A, LaBombard B *et al* 1997 *J. Nucl. Mater.* **241–243** 771
[6.15] Matthews G F and the JET Team, 1995 *Plasma Phys. Control. Fusion* **37** A227
[6.16] Neuhauser J, Alexander M, Becker G *et al* 1995 *Plasma Phys. Control. Fusion* A **37** 37
[6.17] Matthews G F 1995 *J. Nucl. Mater.* **220–222** 104
[6.18] Gibson A and Watkins M L 1977 *Proc. 8th EPS* vol I p 31
[6.19] Lackner K and Neuhauser J 1981 *Proc. IAEA Tech Comm. Meeting on Divertors and Impurity Control (Garching 1981)* ed M Keilhacker and U Daybelge (Vienna: IAEA) p 58
[6.20] Bush C E, Schivell J, Strachan J D *et al* 1990 *J. Nucl. Mater.* **176–177** 786

[6.21] Wesson J 1997 *Tokamaks* 2nd edn (Oxford: Oxford University Press) p 526
[6.22] Pospiesczyk A, Aumayr F, Bay H L *et al* 1989 *J. Nucl. Mater.* **162–164** 574
[6.23] Wesson J 1997 *Tokamaks* 2nd edn (Oxford: Oxford University Press) p 522
[6.24] Verbeek H, Stober J, Coster D P *et al* 1998 *Nucl. Fusion* **38** 1789
[6.25] Wesson J 1997 *Tokamaks* 2nd edn (Oxford: Oxford University Press) p 186
[6.26] Behringer K 1987 *J. Nucl. Mater.* **145–147** 145
[6.27] Isler R C, Behringer K, Kållne E *et al* 1985 *Nucl. Fusion* **25** 1635
[6.28] Behringer K 1990 *J. Nucl. Mater.* **176–177** 606
[6.29] Naujoks D, Coster D, Kastelewicz H and Schneider R 1999 **266–269** 360
[6.30] Philipps V, Vietzke E and Erdweg M 1989 *J. Nucl. Mater.* **162–164** 550
[6.31] Philipps V, Pospieszczyk A, Esser H G *et al* 1997 *J. Nucl. Mater.* **241–243** 105
[6.32] Wesson J 1997 *Tokamaks* 2nd edn (Oxford: Oxford University Press) p 203
[6.33] Engelhardt W and Feneberg W 1978 *J. Nucl. Mater.* **76–77** 518
[6.34] Engelhardt W, Becker G, Behringer K *et al* 1982 *J. Nucl. Mater.* **111–112** 337
[6.35] Tokar M Z 1994 *Nucl. Fusion* **34** 853
[6.36] Braginskii S I 1965 *Reviews of Plasma Physics* vol 1, ed M A Leontovich (New York: Consultants Bureau) p 205
[6.37] Rutherford P H 1974 *Phys. Fluids* **17** 1782
[6.38] Chapman S 1958 *Proc. Phys. Soc.* **72** 353
[6.39] Spitzer L 1962 *Physics of Fully Ionized Gases* 2nd edn (New York: Wiley) p 120
[6.40] Stangeby P C and Elder J D 1995 *Nucl. Fusion* **35** 1391
[6.41] Reiser R, Reiter D and Tokar M Z 1998 *Nucl. Fusion* **38** 165
[6.42] Neuhauser J, Schneider W, Wunderlich R and Lackner K 1984 *Nucl. Fusion* **24** 39
[6.43] Krashenninikov S I, Kukushkin A S and Soboleva T K 1991 *Nucl. Fusion* **31** 1455
[6.44] Vlases G C and Simonini R 1991 *Controlled Fusion and Plasma Physics (Proc. 18th Eur. Conf. (Berlin, 1991)* vol 15C Part III (Geneva: EPS) p 221
[6.45] Igitkhanov Yu L 1988 *Contrib. Plasma Phys.* **28** 477
[6.46] Zagorski R and Romanelli F 1994 *Contrib. Plasma Phys.* **34** 331
[6.47] Roth J, Krieger K and Fussmann G 1992 *Nucl. Fusion* **32** 1835
[6.48] Goetz J A, Lipschultz B, Pitcher C S *et al* 1999 *J. Nucl. Mater.* **266–269** 354
[6.49] Hillis D L, Hogan J, von Hellermann M *et al* 1999 *J. Nucl. Mater.* **266–269** 1084
[6.50] Matthews G F, Stangeby P C, Elder J D *et al* 1992 *J. Nucl. Mater.* **196–198** 374
[6.51] Isler R C, Brooks N H, West W P *et al* 1999 *Phys. Plasmas* **6** 541
[6.52] Sengoku S, Azumi M, Matsumoto Y *et al* 1979 *Nucl. Fusion* **19** 1327
[6.53] Brooks J N 1983 *Nucl. Technol. Fusion* **4** 33
[6.54] Brooks J N 1987 *J. Nucl. Mater.* **145–147** 837
[6.55] Stangeby P C, Farrell C, Hoskins S *et al* 1988 *Nucl. Fusion* **28** 1945
[6.56] Shimizu K, Kubo H, Takizuka T *et al* 1995 *J. Nucl. Mater.* **220–222** 410
[6.57] Hogan J *et al Proc. 16th IAEA Int. Conf. on Plasma Phys. and Controlled Fusion Research (Montreal, 1996)* vol 2 p 625
[6.58] Evans T E, Finkenthal D F, Fenstermacher M E *et al* 1999 *J. Nucl. Mater.* **266–269** 1034
[6.59] Reiter D, Wolf G H and Kever H 1990 *Nucl. Fusion* **30** 2141
[6.60] Behrisch R and Prozesky V 1990 *Nucl. Fusion* **30** 2166
[6.61] Gray D S, Boedo J A and Conn R W 1997 *Nucl Fusion* **37** 1437
[6.62] Shimada M, Nagami M, Ioki K *et al* 1981 *Phys. Rev. Lett.* **47** 796
[6.63] De Boo J C, Brooks N H, DeGrassie J S *et al* 1982 *Nucl. Fusion* **22** 572
[6.64] Pitcher C S and Stangeby P C 1997 *Plasma Phys. Control. Fusion* **39** 779

[6.65] Hogan J 1997 *J. Nucl. Mater.* 197 **241–243** 68
[6.66] Petrie T W, Maingi R, Allen S L *et al* 1997 *Nucl. Fusion* **37** 643
[6.67] Horton L D, Vlases G C, Andrews P *et al* 1999 *Nucl. Fusion* **39** 1
[6.68] Bosch H-S, Fuchs J C, Gafert J *et al* 1999 *Plasma Phys. Control. Fusion* A **41** 401
[6.69] Fielding S J, Johnson P C and Guilhem D 1984 *J. Nucl. Mater.* **128–129** 390
[6.70] Allen S L, Resink M E, Hill D N *et al* 1989 *J. Nucl. Mater.* **162–164** 80
[6.71] Haas G, Bachmann P, Duchs D *et al* 1992 *J. Nucl. Mater.* **196–198** 481
[6.72] Bachmann P, Reiter D *et al* 1995 *Contrib. Plasma Phys.* **35** 45
[6.73] Niemczewski A, Hutchinson I H, La Bombard B *et al* 1997 *Nucl. Fusion* **37** 151
[6.74] Reiter D EIRENE-1999 private communication
[6.75] Keilhacker M, Lackner K *et al* 1982 *J. Nucl. Mater.* **111–112** 370
[6.76] Shimada M, Nagami M, Ioki K *et al* 1982 *J. Nucl. Mater.* **111–112** 362
[6.77] Kaye S M, Bell M G, Bol K *et al* 1984 *J. Nucl. Mater.* **121** 115
[6.78] Vlasas G C, Horton L D, Matthews G F *et al* 1999 *J. Nucl. Mater.* **266–269** 160
[6.79] Brooks J N 1993 *Atomic and Plasma–Material Interaction Processes in Controlled Thermonuclear Fusion* ed R K Janev and H W Darwin (Amsterdam: Elsevier) p 403
[6.80] Brooks J N 1990 *Fusion Technol.* **18** 239
[6.81] Brooks J N 1990 *Phys. Fluids* B **2** 1858
[6.82] Brooks J N, Brice D K, DeWald A B and McGrath R T 1989 *J. Nucl. Mater.* **162–164** 363
[6.83] Hua T Q and Brooks J N 1992 *J. Nucl. Mater.* **196–198** 514
[6.84] Brooks J N and Whyte D G 1999 *Nucl. Fusion* **39** 525
[6.85] Brooks J N, Alman D, Federici G *et al* 1999 *J. Nucl. Mater.* **266–269** 58
[6.86] Naujoks D, Roth J, Krieger K *et al* 1994 *J. Nucl. Mater.* **210** 43
[6.87] Naujoks D, Behrisch R, Coad J P *et al* 1993 *Nucl. Fusion* **33** 581
[6.88] Naujoks D, Asmussen K, Bessenrodt-Weberpals M *et al* 1996 *Nucl. Fusion* **36** 671
[6.89] Naujoks D 1997 *Nucl. Fusion* **37** 1193
[6.90] Guo H Y, Coad J P, Davies S J *et al* 1997 *J. Nucl. Mater.* **241–243** 385
[6.91] Kreiger K, Roth J, Annen A *et al* 1997 *J. Nucl. Mater.* **241–243** 684
[6.92] Kreiger K, Maier H, Neu R, 1999 *J. Nucl. Mater.* **266–269** 207
[6.93] Philipps V *et al* 1997 *J. Nucl. Mater.* **241–243** 105
[6.94] Stangeby P C and Farrell C 1988 *Contrib. Plasma Phys.* **28** 495
[6.95] Whyte D G, Bastasz R, Brooks J N *et al* 1999 *J. Nucl. Mater.* **266–269** 67
[6.96] Wampler W R, LaBombard B, Lipschultz B *et al* 1999 *J. Nucl. Mater.* **266–269** 217
[6.97] Apicella M L, Maddaluno G, Ridolfini V P *et al* 1999 *J. Nucl. Mater.* **266–269** 429
[6.98] Jost W 1952 *Diffusion in Solids, Liquids and Gases* (New York: Academic Press) p 16
[6.99] Stangeby P C and Elder J D 1991 *Plasma Phys. Control. Fusion* **33** 1435

Chapter 7

The H-Mode and ELMs

In order to increase core plasma temperatures to the levels needed for fusion to occur strongly, *auxiliary heating*—i.e. additional to *ohmic heating*—is often employed, for example using energetic particle beams or RF waves. Disappointingly, the energy confinement time τ_E of the tokamak plasma is found to decrease with applied power P, thus partially off-setting the effect of the additional heating. In the most basic operating mode, called the *L-mode* ('L' for low confinement), the measured τ_E for a large number of tokamaks is found to be well fitted by an expression termed the ITER89-P *confinement time* [7.1], see equation (4.30).

Fortunately a number of *improved confinement modes* have subsequently been discovered, one of the first and most important being the *H-mode* ('H' for high confinement), first reported on the divertor tokamak ASDEX in 1982 [7.2] and since observed on most tokamaks. When the P is raised above some *threshold power* an $L \rightarrow H$ *transition* suddenly occurs and τ_E approximately doubles in magnitude, albeit still showing an inverse dependence on P. Data from a large number of tokamaks are found to be well fitted by an expression termed the ITER 97H-P(Y) *energy confinement* time [4.3]:

$$\tau^{\text{ITER97H-P(Y)}} = 0.029 \frac{I^{0.90} R^{2.03} \kappa^{0.92} (\overline{n}/10^{20})^{0.40} B^{0.20} A^{0.20} \varepsilon^{0.19}}{P^{0.66}}. \qquad (7.1)$$

(This is the value for H mode discharges which have ELMs, see below.) $\kappa \equiv b/a$, $\varepsilon \equiv a/R$, $a \equiv$ horizontal minor radius. $b \equiv$ vertical minor radius. τ[s], I[MA], P [MW], B is the toroidal magnetic field [T], $A = 1, 2, 3$ for H, D, T. One also defines an *H factor* relating the measured τ_E to τ_E^L given, say by equation (4.30):

$$\boxed{H \equiv \tau_E/\tau_E^L} \qquad (7.2)$$

Typically $H \approx 2$ for H-mode plasmas. H modes are more commonly observed in divertor tokamaks but have also been achieved with limiters.

Figure 7.1 shows the central electron temperature measured on ASDEX during an H-mode, compared with the level in a comparable L-mode [7.2]. The

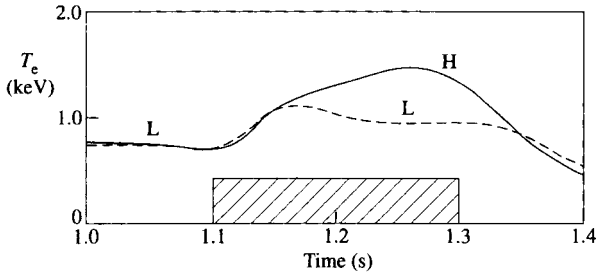

Figure 7.1. *ASDEX*. Time dependence of central electron temperature for L- and H-mode discharges. The neutral injection heating phase is indicated by the hatched time interval [7.2].

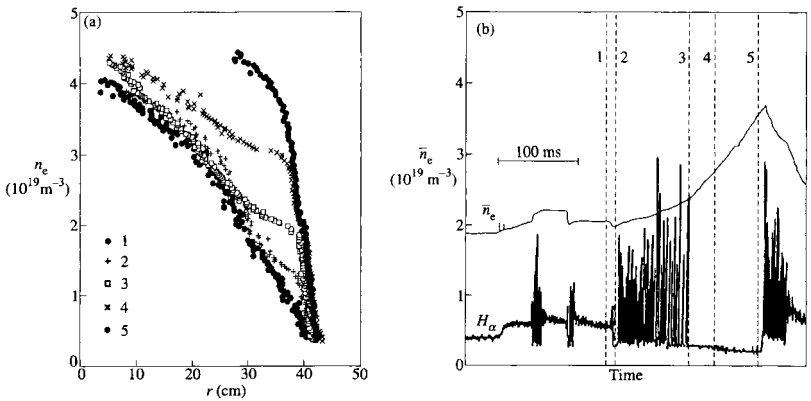

Figure 7.2. Sequence of density profiles measured on ASDEX through and following an L–H transition. The profiles in (a) are at the times shown in (b), which gives the time dependence of $\overline{n}_e$ and the H_α signal [7.19].

central density also increases. It was subsequently established by spatially well resolved measurements of $n_e(r)$ and $T_e(r)$ that the improved particle and energy confinement occurs primarily just inside the separatrix where very steep density and temperature gradients arise. Figure 7.2(a) shows the time evolution of $n_e(r)$ in ASDEX at the $L \rightarrow H$ transition. Thus *temperature and density edge pedestals* are observed, which are ascribed to an *edge transport barrier*. The underlying cause of the $L \rightarrow H$ transition and of this transport barrier is still being sought [7.3–7.6]. The role of neutral hydrogen particles in the dynamics of enhanced confinement is examined in [7.7]. See also [7.8–7.10].

Usually the most readily observed feature of the $L \rightarrow H$ transition is a more-or-less sudden drop in the H_α signal observed at the targets, see location 2 in figure 7.2(b), indicating an increase in the particle confinement: a reduction

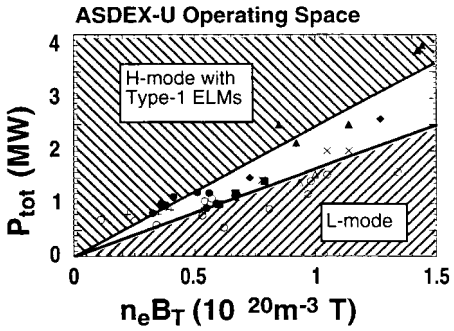

Figure 7.3. Operating space for obtaining H mode and different kinds of ELM in ASDEX-U. Space between shaded regions is ELM-free and type 3 ELM region. ○ ohmic, △ L mode, ● ohmic H-mode, ♦ ELM free, + dither, × type 3, ■ ICRH, ▲ type 1 [7.6,7.12].

in the hydrogen ion out-flow from the main plasma into the SOL, thence to the targets, results in a reduction in the neutral hydrogen recycling at the target, and thus also the H_α signal there—within the SOL particle transit time, of the order of ms.

A universal expression for the $L \rightarrow H$ threshold power has not yet been established, although such have been identified for individual tokamaks. Figure 7.3 shows that on ASDEX-U, the required power scales as $n_e B_T$ [7.6] and more specifically:

$$P_{\text{sep}}/A_{\text{sep}} = 0.044 n_e B_T. \tag{7.3}$$

P [MW], A [m^2], n_e [10^{20} m^{-3}], B [T], and where A_{sep} is the surface area of the separatrix surface, $2\pi R 2\pi a\kappa^{1/2}$. It appears that the controlling parameter is the power flux density actually crossing the separatrix, $P_{\text{sep}}/A_{\text{sep}}$, rather than the total power into the tokamak.

A dramatic effect usually characterizing the H-mode are temporal features called *ELMs, edge localized modes*. These are most readily observed as H_α spikes, figure 7.2(b), clearly indicating that ELMs involve periodic expulsion of particles (and it turns out, of energy also) from the confined plasma into the SOL. It is thus also evident that ELMs act to limit the enhanced confinement associated with the H-mode. This can be seen, for example, in the behaviour of the $\overline{n}_e(t)$, the temporal rise of which during the H-mode is stopped at each ELM burst, figure 7.4. Spatially and temporally resolved measurements of $n_e(r,t)$, $T_e(r,t)$ at the edge show that the ELM acts to suddenly eject into the SOL particles and energy that had built up in the pedestals, figure 7.5. The ejection occurs in $\sim 10^{-4}$ s typically; the power—particularly that conducted by the electrons—is transferred more rapidly than the particles.

Although many of the consequences of ELMs are deleterious, as will be

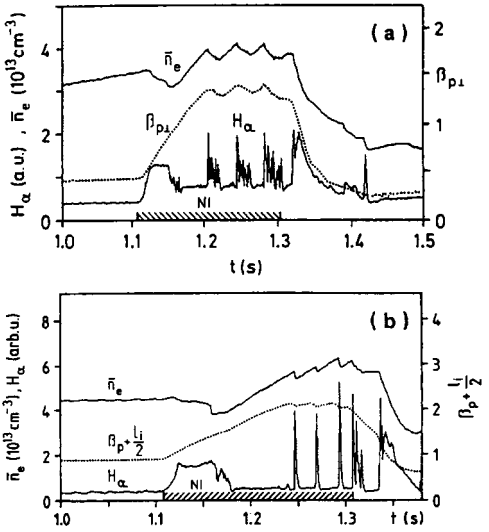

Figure 7.4. H_α emission showing ELM activity during H-modes with neutral injection in ASDEX, (a) with continuous bursts, and (b) with separated large ELMs. The figure also shows the response of the electron density [7.11].

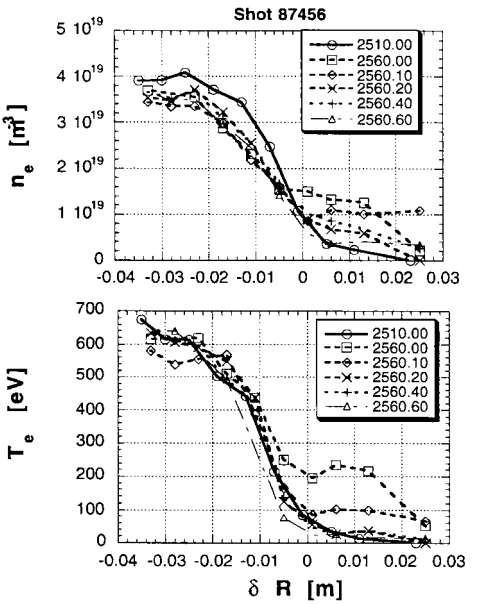

Figure 7.5. Radial profiles of electron density and temperature before (2510 ms) and during type 1 ELMs in DIII-D starting at 2559.9 ms [7.12].

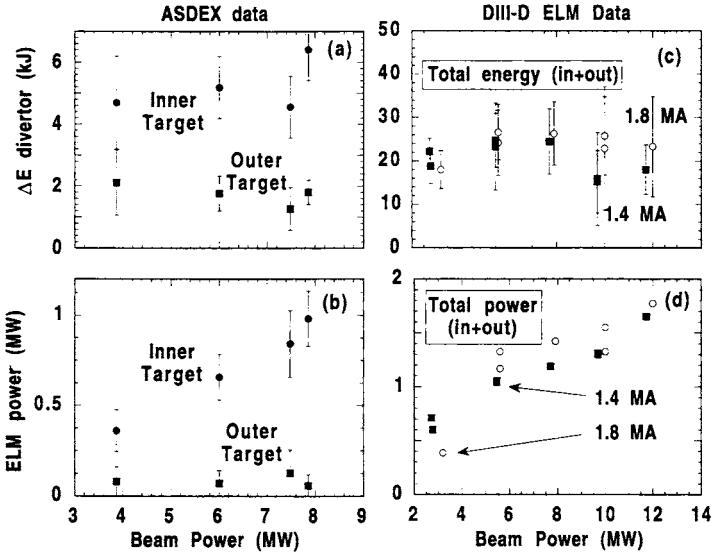

Figure 7.6. Power scaling of energy loss per ELM and time-averaged power due to type 1 ELMs in ASDEX-U and DIII-D [7.12].

discussed, they are probably necessary in order to control *impurity accumulation* in the core which tends to occur in those H-modes which are (un-typically) ELM free—and are thus *stationary* [7.11]: with regard to particles, ELMs free H-mode confinement can be *too* good. The *non-stationary* characteristic of ELM H-modes is important for impurity control of the main plasma.

ELMs have been categorized into three types [7.12]:

(1) *Type 1. Giant ELMs*. When heating power is well above the $L \rightarrow H$ threshold, $\geq$ 20%, relatively isolated, low frequency, 1–100 Hz, large amplitude ELMs occur, as in figure 7.4(b). These *giant ELMs* can eject up to 10% of the stored energy in the main plasma in each ELM, $\Delta E/E \lesssim 10\%$. The time-averaged contribution to the energy confinement is nevertheless modest, 10–20%. The frequency of type 1 ELMs increases with heating power, which is part of their defining properties. On ASDEX-U and DIII-D [7.12] the energy loss per type 1 ELM is approximately constant, independent of beam power, figure 7.6. Thus the ELM power loss (averaged through the ELMs) increases linearly with beam power, remaining a constant fraction of the beam power: 15% and 2% at the inner and outer targets respectively on ASDEX-U. It is a general finding that the ELM power goes preferentially to the inside target of a single-null divertor, but the reason is not known.

(2) *Type 2. Grassy ELMs*. These are observed in highly shaped plasmas and are relatively uncommon. The energy loss per ELM is quite small, $\Delta E/E \ll$

0.01 and does not pose practical problems.

(3) *Type 3 ELMs*. Type 3 ELMs occur for heating powers just above the $L \rightarrow H$ threshold, within $\leq$ 20% of it. The frequency is higher than for type 1, 0.1–1 kHz with amplitude $\Delta E/E \sim 1\%$. Frequency falls with increase of heating power—the opposite trend to type 1 ELMs, and is, in fact, the basis of defining type 3 ELMs.

The pattern of ELM behaviour on ASDEX-U is indicated in figure 7.3. It is evident from figure 7.5 that ELMs have a major effect on the SOL. Type 1 ELMs produce a loss of up to $\Delta N = 10$–15% of the total particle content of the main plasma [7.12], and the time-averaged loss rate, $f\Delta N$, matches the initial density rise $\mathrm{d}N/\mathrm{d}t$, thus indicating that it is the ELMs that bring about time-averaged steady-state particle balance. The effect of the type 1 ELM can be simulated in models by a jump in the cross-field transport coefficients by an order of magnitude. The SOL plasma density profile thus also broadens considerably and can cause plasma–wall contact and sputtering; see figure 7.7. Although the ELM itself (i.e., the underlying MHD event) lasts only $\lesssim 10^{-4}$ s, the particle parallel transport time and recycling/ionization time can be long enough that the SOL density profile remains enhanced—both in magnitude and width—even between ELMs. Figure 7.8 shows such an example. Parallel heat transport along the SOL, however, is more rapid and in the between-ELM periods the temperatures are typically low, figure 7.8.

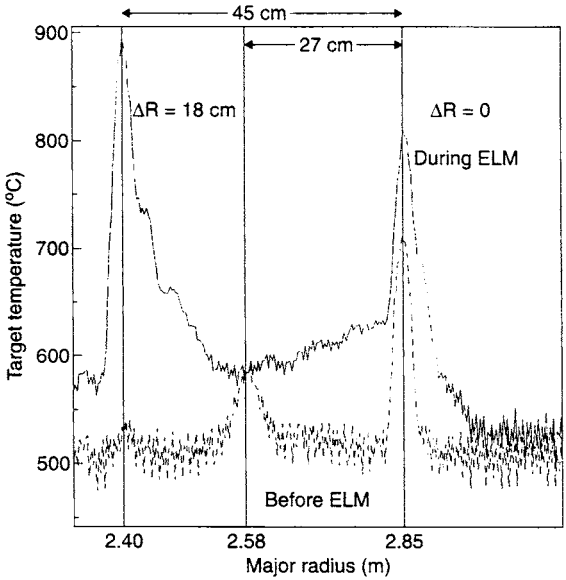

Figure 7.7. JET. Surface temperature distribution on the divertor target plate before and during an ELM (shot 35273) [7.13].

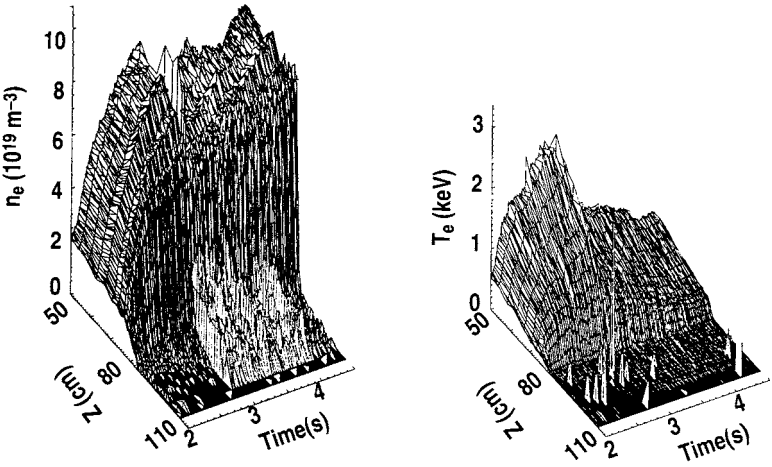

Figure 7.8. Midplane Thomson scattering data in DIII-D showing a broader density SOL after the onset of rapid ELMs at 3 s. The electron temperature in the SOL is largely unaffected in the time-average sense. The separatrix is at 80 cm [7.12].

The most serious consequence of giant ELMs is the high peak heat loads which can cause melt damage of the targets. Peak loads range up to 10 times the time-averaged level, and values up to 10^8 W m^{-2} have been measured [7.12], see figure 7.9. During the ELM, n_e and T_e near the targets increase significantly, figure 7.10. The resulting increase in target sputtering can dominate the time-averaged impurity production from the targets.

Various methods of controlling ELMs have been tested [7.12]. Injection of a radiating gas such as neon can reduce the power flow through the separatrix to a level near the $L \rightarrow H$ threshold, thus changing the ELMs from the damaging type 1 to the benign type 3.

The evolution of a tokamak discharge involving the H-mode is usefully displayed using the *edge operating diagram* [7.13]. An example from JET is shown in figure 7.11 [7.8], where the T_e and n_e are measured just inside the separatrix, at the top of the 'pedestals'. The gas fuelling is increased, and the $L \rightarrow H$ transition occurs (circles), followed by a period of small, transition ELMs (squares). An ELM-free period ensues with the edge pressure rising to a critical value, precipitating large ELMs which cause both T_e and n_e to drop. The discharge is then reheated and refueled to this pressure, or pressure-gradient, limit and cyclical behaviour sets in.

Gas addition increases the maximum n_e (reached just before the ELM crash), reducing the maximum T_e, but such that the maximum pressure remains about constant (diamonds). The ELM frequency increases with fuelling rate. At very high gas rates, the T_e is driven so low that the plasma falls below the H-mode threshold and reverts to the L-mode. See also [7.14–7.17].

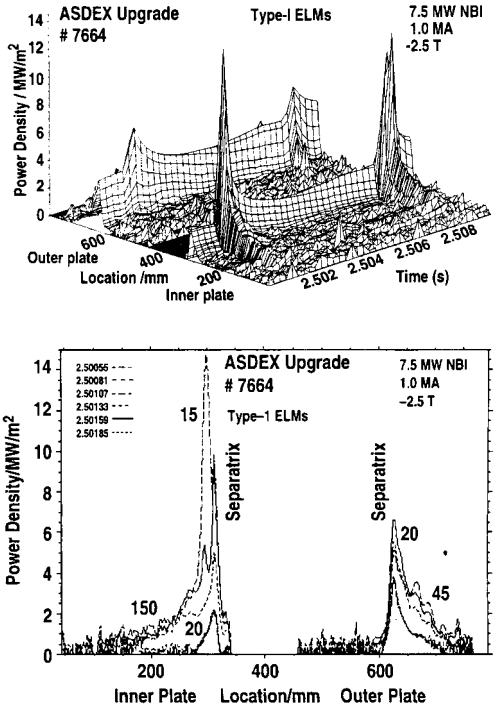

Figure 7.9. Divertor heat flux profiles during ELMs in ASDEX-U as measured by an infrared line array detector. Top: 3D isometric plot showing temporal evolution. Bottom: radial profiles at selected times showing fall-off lengths in mm [7.6, 7.12].

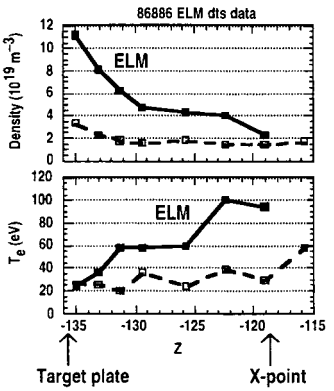

Figure 7.10. Vertical profiles of density and temperature along the outer divertor leg in DIII-D as measured by Thomson scattering. Dashed—quiescent H-mode between ELMs, solid—during a type 1 ELM [7.12].

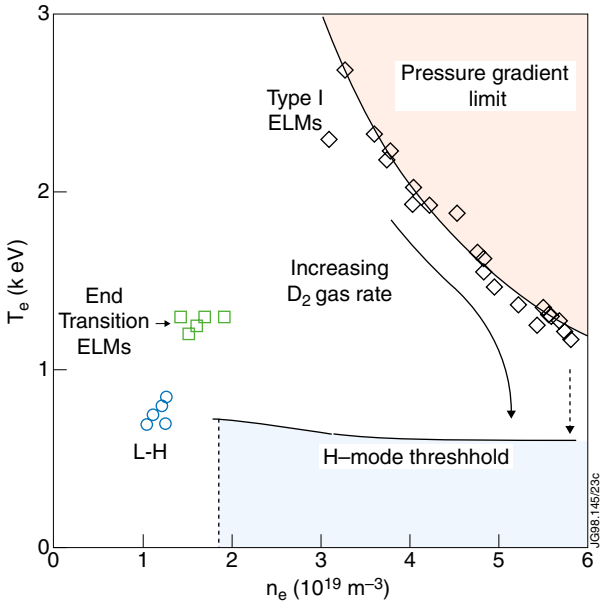

Figure 7.11. JET. Plot of edge electron temperature versus edge electron density for a series of vertical target ELM H-modes with varying rates of gas fuelling. The temperature and density values at the pressure gradient limit (diamonds) are representative of values at the top of the edge pedestal taken just prior to an ELM. The edge electron temperature and density at the L–H transition (circles) and at the end of the period of transition ELMs (squares) are shown for comparison. At the highest gas fuelling rates, the edge electron pressure begins to deviate from the curve of approximately constant pressure (the dashed arrow). In a few cases, transitions back to L-mode have been observed; here the curve for the H-mode threshold is schematic [7.8].

Understanding of all aspects of H-modes, including ELMs, is still evolving. It is clearly important to establish how to scale ELMs to future large devices [7.18].

References

[7.1] Cordey J G 1997 *Plasma Phys. Control. Fusion* **39** B115
[7.2] Wagner F, Becker G, Behringer K *et al* 1982 *Phys. Rev. Lett.* **49** 1408
[7.3] Zohm H 1996 *Plasma Phys. Control. Fusion* **38** 105
[7.4] Connor J W 1998 *Plasma Phys. Control. Fusion* **40** 191
[7.5] 1996 *Papers of the 5th IAEA Technical Committee Meeting/US–Japan Workshop on H-Mode Physics, Plasma Physics and Controlled Fusion* vol 38

[7.6] Ryter F, Buchl K, Fuchs C *et al* 1994 *Plasma Phys. Control. Fusion* **36** (Supplement 7A) A99
[7.7] Itoh S-I, Itoh K and Fukuyama A 1995 *J. Nucl. Mater.* **220–222** 117
[7.8] Horton L D, Vlases G C, Andrew P *et al* 1999 *Nucl. Fusion* **39** 1
[7.9] Kaufmann M *et al* 1997 *Fusion Energy 1996, Proc. 16th Int. Conf. (Montreal, 1996)* vol 1 (Vienna: IAEA) p 79
[7.10] Saibene G, Campbell D J, Horton L D *et al* 1997 *J. Nucl. Mater.* **241–243** 476
[7.11] ASDEX Team 1989 *Nucl. Fusion* **29** 1959
[7.12] Hill D N 1997 *J. Nucl. Mater.* **241–243** 182
[7.13] Lingertat J, Tabasso A, Ali-Arshad S *et al* 1997 *J. Nucl. Mater.* **241–243** 402
[7.14] Suttrop W, Mertens V, Murmann H *et al* 1999 *J. Nucl. Mater.* **266–269** 118
[7.15] Lingertat J, Bhatnagar V, Conway G D *et al* 1999 *J. Nucl. Mater.* **266–269** 124
[7.16] Osborne T H, Burrell K H, Groebner R J *et al* 1999 *J. Nucl. Mater.* **266–269** 131
[7.17] Owen L W, Carreras B A, Maingi R *et al* 1999 *J. Nucl. Mater.* **266–269** 890
[7.18] Leonard A W, Herrmann A, Itami K *et al* 1999 *J. Nucl. Mater.* **266–269** 109
[7.19] Wagner F *et al* 1991 *Plasma Physics and Controlled Nuclear Fusion Research. Proc. 13th Int. Conf.* (*Washington, 1990*) vol 1 (Vienna: IAEA) p 277

Chapter 8

Fluctuations in the Edge Plasma

Cross-field transport of particles and energy generally occurs at rates considerably faster than can be accounted for by classical collisional effects, and it is widely believed that such *anomalous transport* is due to fine-scale fluctuations, that is cross-field transport is *turbulence induced* [8.1].

A fluctuating poloidal electric field, $\tilde{E}_\theta$, will result in a fluctuating $\tilde{E}_\theta \times B_\phi$ radial drift velocity, $\tilde{v}_r = \tilde{E}_\theta / B_\phi$, chapter 18; more precisely, it is the component of $\tilde{E}$ perpendicular to the total magnetic field which results in $\tilde{v}_r$. If the density n is non-fluctuating, then no net (time-averaged) radial drift flux occurs. If, however, there is a fluctuating component of the density, $\tilde{n}$, and if the relative phase between $\tilde{n}$ and $\tilde{E}_\theta$ fluctuations is such that $\tilde{n}$ is positive when $\tilde{v}_r$ is also, and negative when $\tilde{v}_r$ is also, then a net time-average outward radial particle flux density, Γ_r^{ES}, results. Thus:

$$\boxed{\Gamma_r^{\mathrm{ES}} = \frac{1}{B_\phi} \langle \tilde{n} \tilde{E}_\theta \rangle} \tag{8.1}$$

where $\langle \cdots \rangle$ indicates an average over time. The superscript 'ES' designates electrostatic, to distinguish this type of turbulence-induced transport from the type involving fluctuating magnetic fields, $\tilde{B}$, see below.

In the edge plasma it is possible to measure $\tilde{n}$, $\tilde{E}_\theta$ and their time correlations using Langmuir probes [8.2–8.6]. In the simplest method of interpretation the measured fluctuating signal $\tilde{I}_{\mathrm{sat}}^+$ is taken to give $\tilde{n}$, i.e. $\tilde{I}_{\mathrm{sat}}^+ / \overline{I}_{\mathrm{sat}}^+ = \tilde{n}/\overline{n}$ is assumed. That is, the influence of any temperature fluctuations—which would affect the sound speed c_s, and thus break the simple relation between $\tilde{I}_{\mathrm{sat}}^+$ and $\tilde{n}$—is ignored. The probe is also used to measure the fluctuating floating potential $\tilde{V}_f$. It is then assumed that the local floating potential and the local plasma potential are related by the usual sheath relation, chapter 2. Thus for a hydrogenic plasma:

$$V_p \approx V_f + 3kT_e/e \tag{8.2}$$

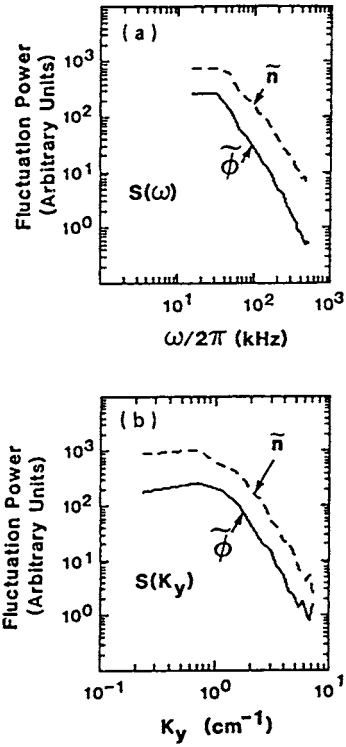

Figure 8.1. Pretext tokamak: examples of integrated fluctuation spectra. Note the power law trend for the asymptotic portion of the spectra. $\phi \equiv V_p$ here [8.7].

Again, in the simplest interpretation, any fluctuations of T_e are ignored and so it is assumed that:

$$\tilde{V}_p \approx \tilde{V}_f. \tag{8.3}$$

In order to obtain a value of $\tilde{E}_\theta$ from values of $\tilde{V}_p$ it is necessary to employ a *spatial array* of probes, so as to measure the *poloidal wavelength* λ_θ of the fluctuations or the *poloidal wave number* $k_\theta \equiv 2\pi/\lambda_\theta$, giving:

$$\tilde{E}_\theta = k_\theta \tilde{V}_p. \tag{8.4}$$

The fluctuations are found to span a range of frequencies, with most of the power in the 10–100 kHz, $k_\theta = 0.1$–$10\ \mathrm{cm}^{-1}$ ranges, figure 8.1. The phase angle between $\tilde{I}^+_{\mathrm{sat}}$ and $\tilde{V}_f$ is typically found to be in the range $\pi/4$–$\pi/2$ for the frequency range containing most of the power [8.5]. When measured, the phase angle between $\tilde{n}$ and $\tilde{T}_e$ is found to be close to 0. In the direction parallel to the magnetic field, the fluctuations are correlated over quite long distances, of the order of 10 m, for both $\tilde{I}^+_{\mathrm{sat}}$ and $\tilde{V}_f$. The plasma edge turbulence is therefore two

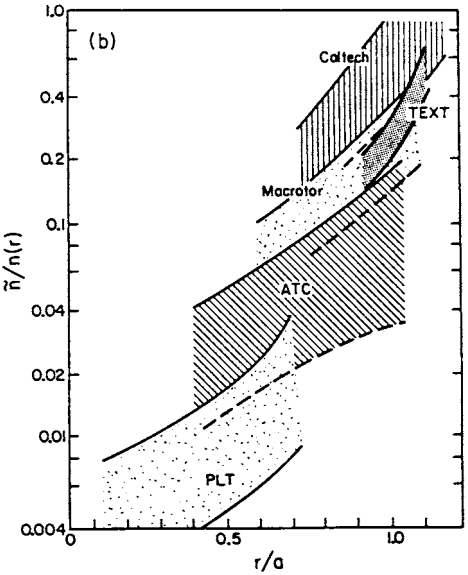

Figure 8.2. Relative fluctuation levels $\tilde{n}(r)/n(r)$ versus r/a measured in several tokamaks [8.2].

dimensional with *filaments* extending only a few cm across $\boldsymbol{B}$, but many metres long along $\boldsymbol{B}$. These filaments have been observed on high speed cine film [8.5].

Thus the total cross-field particle flux density is [8.7]

$$\Gamma_r^{\mathrm{ES}} = \frac{1}{B}\int \tilde{n}(\omega)\tilde{V}_p(\omega)k_\theta(\omega)\gamma(\omega)\sin(\alpha(\omega))\mathrm{d}\omega \tag{8.5}$$

where $\alpha(\omega)$ is the phase angle between $\tilde{n}$ and $\tilde{V}_p$ and $\gamma(\omega)$ is the degree of mutual coherence between $\tilde{n}$ and $\tilde{V}_p$. The rms values of $\tilde{n}$ and $\tilde{V}_p$ are used in equation (8.5).

The relative magnitude of fluctuations, such as $\tilde{n}/n$, generally increases strongly with radius. Figure 8.2 shows radial variation of $\tilde{n}/n$ for a variety of tokamaks. Fluctuation measurements can also be based on H_α radiation [8.8], microwave or far-infrared laser collective scattering [8.9–8.11], Li-beam measurements [8.12] and microwave interferometry and reflectometry [8.13]. Diagnostics for plasma fluctuation measurements have been reviewed by Bretz [8.14].

A net *magnetic fluctuation* flux can also occur: an *effective* radial velocity, $\tilde{v}_r$, results when the radial magnetic field fluctuates, $\tilde{B}_r \neq 0$, of magnitude:

$$\tilde{v}_r \approx v_\parallel \tilde{B}_r/B \tag{8.6}$$

where $v_\parallel$ is the parallel velocity which is very high, of the order of c_s. Thus even a relatively small $\tilde{B}_r/B$ could in principle result in rapid cross-field transport.

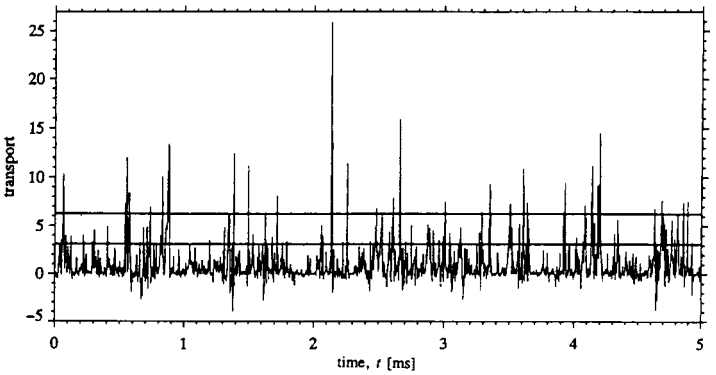

Figure 8.3. Time signal of the radial particle flux Γ_r due to radial $\tilde{E} \times B$ drift at the midplane of ASDEX (normalized to its mean value). Temperature fluctuations were neglected when calculating Γ_r from floating potential and ion saturation current fluctuations. The data were taken 1 to 2 cm outside the separatrix. The transport is directed radially outward during 75% of the time, and the integrated transport in the outward direction is larger by a factor of 15 to 20 than the integrated transport in the inward direction. Of the transport directed outward 20% (50%) is accomplished within 2.5% (10%) of the time (intervals for which Γ_r is above the upper (lower) horizontal line) [8.4].

Magnetic field fluctuations can be measured using magnetic pick-up coils. The net electromagnetic radial flux density is:

$$\boxed{\Gamma_r^{\mathrm{EM}} = \left\langle \tilde{n} v_{\parallel} \frac{\tilde{B}_r}{B} \right\rangle} \tag{8.7}$$

where, as with Γ_r^{ES}, there is only a net, time-averaged outward flux for specific correlations of $\tilde{n}$ and $\tilde{B}_r$. Measured levels are typically very small, in the range $\tilde{B}_r/B \sim 10^{-5}$ to 10^{-4} [8.2] and this type of fluctuation-driven transport appears not to be important, usually [8.5, 8.15–8.17].

There are also fluctuation-based cross-field heat flux densities—convective and conductive, electrostatic and electromagnetic:

$$\boxed{q_{\mathrm{conv}}^{\mathrm{ES}} = \tfrac{3}{2} k T \Gamma_r^{\mathrm{ES}}} \tag{8.8}$$

$$\boxed{q_{\mathrm{conv}}^{\mathrm{EM}} = \tfrac{3}{2} k T \Gamma_r^{\mathrm{EM}}} \tag{8.9}$$

$$\boxed{q_{\mathrm{cond}}^{\mathrm{ES}} = \frac{3}{2} \frac{n_e}{B} \langle k \tilde{T} \tilde{E}_{\theta} \rangle} \tag{8.10}$$

$$\boxed{q_{\mathrm{cond}}^{\mathrm{EM}} = -n_e \chi(\tilde{B}_r) \frac{\mathrm{d}T}{\mathrm{d}r}.} \tag{8.11}$$

The value of $\chi(\tilde{B}_r)$ is model dependent; Rechester and Rosenbluth [8.18], for example, give $\chi_e(\tilde{B}_r) = qRv_{te}(\tilde{B}_r/B)^2$. There is a discussion in [8.19] of whether a factor of 3/2 or of 5/2 is appropriate for equations (8.8)–(8.10).

These flux expressions can be used to calculate the associated diffusion coefficients and heat conductivities, e.g.

$$D_\perp \equiv -\Gamma_r/(\mathrm{d}n/\mathrm{d}r) \tag{8.12}$$

where $(\mathrm{d}n/\mathrm{d}r)$ is the measured (average) density radial gradient. However, this does not imply that Γ_r necessarily depends on the density gradient nor that $D_\perp$ is even positive!

It is, nevertheless, usually observed that the time-averaged fluxes *are* outward. Figure 8.3 shows a time signal of Γ_r^{ES} obtained on ASDEX, using Langmuir probes, located 1–2 cm outside the separatrix at the midplane [8.4].

As can be seen $\Gamma_r(t)$ is outward (positive) most (∼75%) of the time. The time-integrated $\Gamma_r^{\mathrm{outward}}$ is ∼15–20 times larger than the $\Gamma_r^{\mathrm{inward}}$. About 20% (50%) of the $\Gamma_r^{\mathrm{outward}}$ is accomplished within 2.5% (10%) of the time (intervals for which Γ_r is above the upper (lower) horizontal line in figure 8.3). Figures 8.4–8.6 provide information from this ASDEX study, on radial variations of both the fluctuating and mean-value quantities. Figure 8.4 shows the mean values for

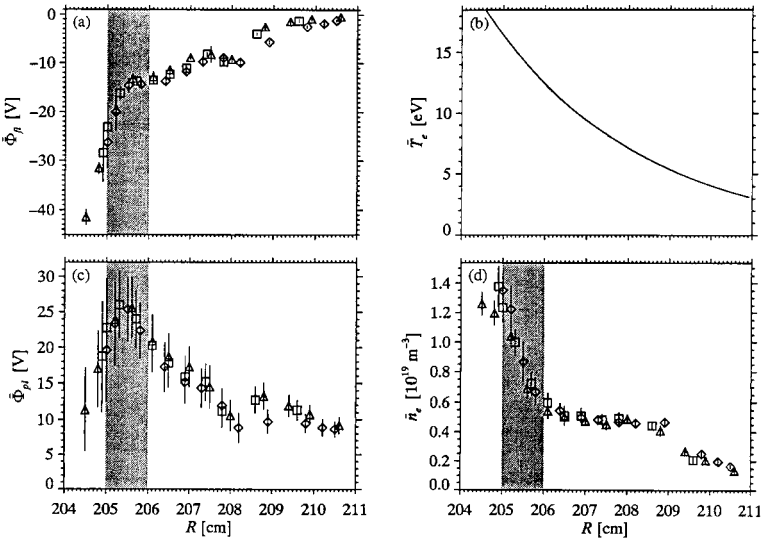

Figure 8.4. Radial profiles of floating and plasma potential, electron temperature and density (mean values). The data were taken by the fast reciprocating Langmuir probe in the midplane of ASDEX during inward and outward movement of the probe in one discharge and during inward movement in another discharge (different symbols). The grey area indicates the radial position of the separatrix which is uncertain by ∼1 cm [8.4].

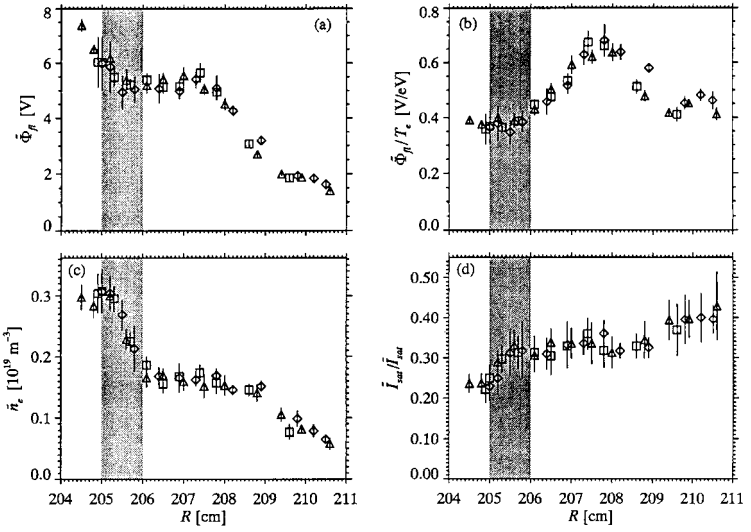

Figure 8.5. As figure 8.4. Radial profiles of density and potential fluctuation levels (absolute and relative). Discharges and symbols are the same as in figure 8.4, and the temperature profile of figure 8.4 was used to calculate $\tilde{n}$ from $\tilde{I}_{\rm sat}$, neglecting temperature fluctuations [8.4].

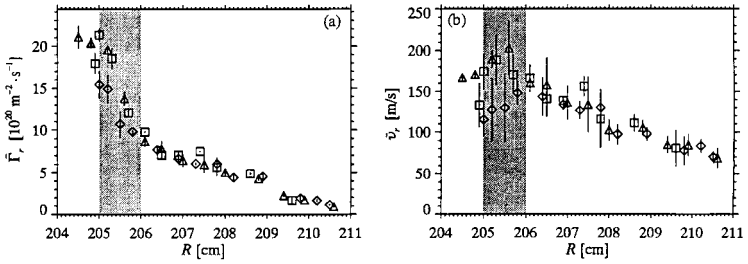

Figure 8.6. As figure 8.4. Radial profiles of the fluctuation-induced radial particle transport $\overline{\Gamma}_r$ and an equivalent radial plasma velocity $\overline{v}_r$. Temperature fluctuations were neglected when calculating these quantities [8.4].

V_f, V_p, T_e and n_e; the grey area indicates the radial position of the separatrix which is uncertain by ∼1 cm. Figure 8.5 shows the fluctuating $\tilde{V}_f$, $\tilde{V}_f/T_e$, $\tilde{n}_e$, $\tilde{I}^+_{\rm sat}/\overline{I}^+_{\rm sat}$; the latter is taken to also give $\tilde{n}/n$. There is a trend for normalized fluctuation amplitudes to increase with radius into the SOL, as seen also in figure 8.2. Figure 8.6 shows the deduced values of $\Gamma_r^{\rm ES}$ and $v_r^{\rm ES}$. One can use $\Gamma_r^{\rm ES}$, figure 8.6(a), or $v_r^{\rm ES}$, figure 8.6(b), and $\mathrm{d}n/\mathrm{d}r$, figure 8.4(d), to deduce a value of $D_\perp$ using equation (8.12): in the region of the separatrix $\lambda_n \sim 1$ cm,

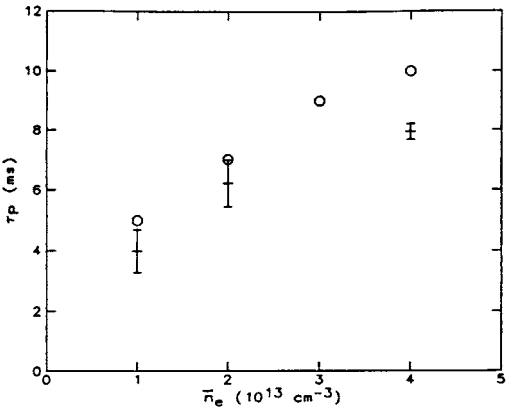

Figure 8.7. TEXT tokamak: global particle confinement (+) and particle confinement time predicted from electrostatic fluctuation measurements (O) versus chord-averaged electron density. For this scan, $B_T = 2.0$ T and $I_p = 200$ kA [8.20].

giving $D_\perp \sim \lambda_n v_r^{\mathrm{ES}} \sim 1.5\ \mathrm{m^2\ s^{-1}}$. Radially further out $n(r)$ is virtually flat, perhaps implying very large $D_\perp$, although it may be that this situation should be interpreted in terms of a *convected* radial flux rather than as a diffusive flux.

Since this value of inferred $D_\perp$ is of the same order as that which is typically measured in the SOL, section 4.3, it appears that electrostatic turbulence is the likely cause of anomalous transport in the SOL. This important matter was addressed in more detail in a study on the TEXT tokamak [8.20]. In figure 8.7 the particle confinement time measured from H_α intensities, section 3.5, is compared with the fluctuation-inferred confinement time, $\tau_p^{\mathrm{ES}} \equiv N_e / \Gamma_r^{\mathrm{ES}} A_\perp$, where N_e is the total plasma particle content and $A_\perp$ is the surface area of the plasma (the LCFS). The results show good agreement, which is particularly remarkable considering the assumption of toroidal/poloidal symmetry, also the inherent limitations of deducing τ_p from H_α measurements and the uncertainties associated with the neglect of temperature fluctuations.

The increasingly held view is that electrostatic fluctuations are the cause of anomalous cross-field particle transport, with electromagnetic fluctuations generally playing a lesser role. Similar conclusions apply to cross-field heat transport [8.5]. Evaluation of $q_{\mathrm{cond}}^{\mathrm{ES}}$, equation (8.10), requires that the temperature fluctuations $\tilde{T}$ be measured, which can be done for the electron temperature using Langmuir probes [8.5, 8.21].

Many *microinstability mechanisms* have been identified as being possible in a plasma confined by a magnetic field [8.22], and these are thought to be the source of the plasma turbulence that results in fluctuation-driven, 'anomalous' transport. (Presumably when the matter has been completely resolved the 'anomalous' characterization will be dropped.) The most basic microinstability is that

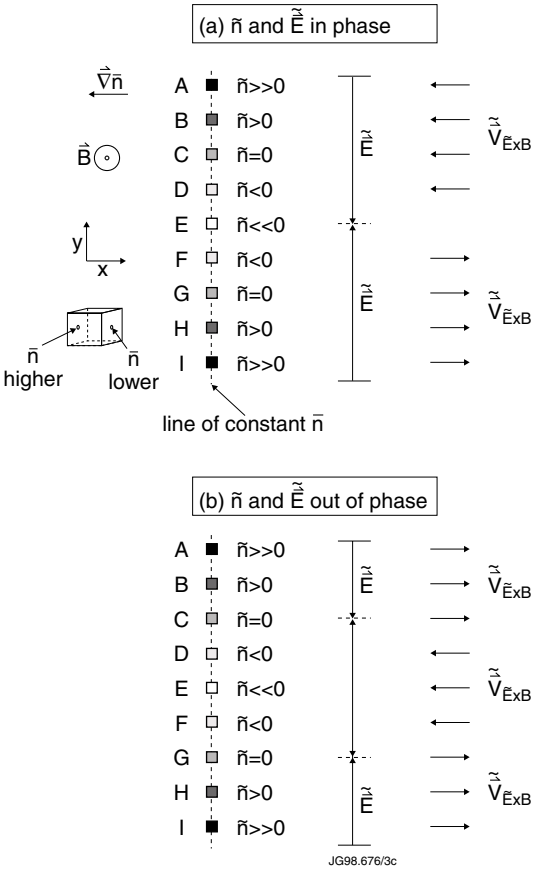

Figure 8.8. Illustration of the mechanism of the unstable drift wave microinstability which can result in 'anomalous' cross-field transport.

due to *unstable drift waves* [8.23] since this occurs even for the simplest systems: the presence of a straight $\boldsymbol{B}$-field and a density gradient ∇n perpendicular to $\boldsymbol{B}$ is sufficient, figure 8.8. This is therefore often considered to be the most basic cause of fluctuation-driven transport [8.5, 8.22].

Consider first the case of a stable drift wave, figure 8.8. Consider a line in the y-direction along which the mean density n is constant and imagine a perturbation to the density, $\tilde{n}$, such that at $t = 0$, $\tilde{n} \gg 0$ at locations A, I, etc; $\tilde{n} > 0$ at B, H, etc; $\tilde{n} = 0$ at C, G, etc; $\tilde{n} < 0$ at D, F, etc; $\tilde{n} \ll 0$ at E, etc. Under the simplest assumption, this plasma density perturbation will be in equilibrium with a perturbed electrostatic potential field $\tilde{V}$, satisfying the (linearized) Boltzmann

relation, section 1.8.2.2:

$$\frac{\tilde{n}}{n} = e\tilde{V}/kT_e. \tag{8.13}$$

As seen from figure 8.8, this results in a perturbed $\tilde{E}$-field, which then gives a perturbed, cross-field $\tilde{\boldsymbol{E}} \times \boldsymbol{B}$ *drift*, which convects plasma into the elemental volume at locations A, B, ... For location B, where $\tilde{n} > 0$ at $t = 0$, this convects lower density plasma (note ∇n is the negative x-direction) into the elemental volume at B, thus reducing $\tilde{n}$ at B, and making $\tilde{n}$ tend to go to 0, i.e. to *become* like it *was earlier* at location C at $t = 0$. At location D, where $\tilde{n} < 0$ at $t = 0$, again the cross-field convection reduces $\tilde{n}$ there, making it tend toward $\tilde{n} \ll 0$, i.e. to *become* what it *was earlier* like at E at $t = 0$. At location F, where $\tilde{n} < 0$ at $t = 0$, the convection is in the opposite direction, thus convecting higher density plasma into the region, raising $\tilde{n}$, and tending to make it approach $\tilde{n} = 0$, i.e. to *become* what it *was earlier* like at G at $t = 0$, etc. Thus the perturbation is seen to become a moving *wave* whose phase velocity is in the $+y$-direction. This is readily shown to be the electron diamagnetic drift direction, chapter 18, and indeed the magnitude of the phase velocity actually equals v_{De} [8.22, 8.23]. These waves are sometimes called *electron drift waves*.

For the simple assumptions that have been made so far this wave neither grows nor decays, however, various real effects act to shift the phase between $\tilde{V}$ and $\tilde{n}$—so as to make $\tilde{V}$ lag $\tilde{n}$ [8.24]. Consider figure 8.8(b) where the lag has become so substantial that now *high* density plasma is convected into the regions A, B, H, I which *already* had $\tilde{n} >$ or $\gg 0$, thus making the positive perturbations yet larger; at the same time, *low* density plasma is convected into regions D, E, F, where $\tilde{n}$ was already low, thus making the negative perturbations yet greater. Thus drift waves are *unstable*.

Any mechanism that restricts electron motion along $\boldsymbol{B}$ interferes with the Boltzmann Relation between $\tilde{n}$ and $\tilde{V}$, equation (8.13), being achieved, thus introducing a phase lag. Such mechanisms include classical, parallel (Spitzer) resistivity, collisions with neutrals, etc. Such processes are generally stronger at the edge region of magnetically confined plasmas. Also in the SOL the electron currents required to allow the Boltzmann relation to be satisfied are restricted by the *sheath resistance*, section 2.7, introducing further destabilization to drift waves. The role of the sheath in edge turbulence is analysed in [8.25–8.31].

References

[8.1] Wesson J 1997 *Tokamaks* 2nd edn (Oxford: Oxford University Press) p 193
[8.2] Liewer P C 1985 *Nucl. Fusion* **25** 543
[8.3] Wootton A J, Huang L K, Finkenthal M *et al* 1990 *Phys. Fluids* B **2** 2879
[8.4] Endler M, Niedermeyer H, Giannone L *et al* 1995 *Nucl. Fusion* **35** 1307
[8.5] Endler M 1999 *J. Nucl. Mater.* **266–269** 84
[8.6] Moyer R A, Lehmer R, Boedo J A *et al* 1999 *J. Nucl. Mater.* **266–269** 1145
[8.7] Levinson S J, Beall J M, Powers E J *et al* 1984 *Nucl. Fusion* **24** 527

[8.8] Zweben S J, McChesney J and Gould R W 1983 *Nucl. Fusion* **23** 825
[8.9] Mazzucato E 1976 *Phys. Rev. Lett.* **36** 792
[8.10] Equipe T F R 1983 *Phys. Plasmas* **25** 641
[8.11] Holzhauer E, Dodel G and ASDEX Team 1990 *Rev. Sci. Instrum.* **61** 2817
[8.12] Zoletnik S, Fiedler S, Kocsis G *et al* 1998 *Plasma Phys. Control. Fusion* **40** 1399
[8.13] Hartfuss H J, Geist T and Hirsch M 1997 *Plasma Phys. Control. Fusion* **39** 1693
[8.14] Bretz N 1997 *Rev. Sci. Instrum.* **68** 2927
[8.15] Ritz Ch P, Bravenac R V, Bengtson R D *et al* 1987 *J. Nucl. Mater.* **145–147** 241
[8.16] Fiksel G, Bengtson R D, Cekic M *et al* 1996 *Plasma Phys. Control. Fusion* **38** A213
[8.17] Scott B 1997 *Plasma Phys. Control. Fusion* **39** 1635
[8.18] Rechester A B and Rosenbluth M N 1978 *Phys. Rev. Lett.* **40** 38
[8.19] Ross D W 1989 *Comments Plasma Phys. Control. Fusion* **12** 155
[8.20] Rowan W L, Klepper C C, Ritz C P *et al* 1987 *Nucl. Fusion* **27** 1105
[8.21] Stangeby P C and McCracken G M 1990 *Nucl Fusion* **30** 1225 p 1350
[8.22] Wesson J 1997 *Tokamaks* 2nd edn (Oxford: Oxford University Press) p 392
[8.23] Goldston R J and Rutherford P H 1997 *Introduction to Plasma Physics* (Bristol: Institute of Physics Publishing) p 363
[8.24] Chen F F 1984 *Introduction to Plasma Physics and Controlled Fusion* 2nd edn vol 1 (New York: Plenum) p 222
[8.25] Nedospasov A V 1992 *J. Nucl. Mater.* **196–198** 90
[8.26] Berk H L, Cohen R H, Ryutov D D *et al* 1993 *Nucl. Fusion* **33** 263
[8.27] Xu X Q 1993 *Phys. Fluids* B **5** 3641
[8.28] Cohen R N 1994 *Contrib. Plasma Phys.* **34** 232
[8.29] Budaev V, Fuchs G, Ivanov R and Samm U 1993 *Plasma Phys. Control. Fusion* **35** 429
[8.30] Nedospasov A V and Tokar M 1994 *Problems of Plasma Physics* vol 18 ed B Kadomtsev (New York: Plenum)
[8.31] Nedospasov A V 1996 *Contrib. Plasma Phys.* **36** 197

PART 2

INTRODUCTION TO FLUID MODELLING OF THE BOUNDARY PLASMA

Introduction to Part II

Why do we want to model the SOL anyway? It is worth thinking carefully about this question. The answer will effect how we carry out the modelling. The SOL constitutes the interface between the astronomically hot fusion-producing plasma, and the ordinary solid-matter world of the tokamak's solid structure. The SOL is driven by strong source and sink actions. Power enters the SOL from the main plasma and exits from it to the limiter or divertor targets. In the simplest situations the plasma particle source also lies in the main plasma, feeding the SOL, with exhaust again being to the solid surfaces. Clearly if fusion reactors are to be made practical it will be essential to understand how this interface functions and how it responds to its interactions with these two very different states of matter.

Evidently the basic properties of the SOL plasma—its density and temperature—are established by this interaction. We want to know how to calculate n and T—and not just the average values in the SOL, but how they vary spatially along the SOL, since conditions may be significantly different at the interfaces than on average, and the interface values are likely to be important. How are particle and power flows reaching the solid surfaces related to n and T in the SOL? This governs the heating and erosion of edge structural components. The details of the plasma flow field and electrostatic fields are likely to govern the transport of impurity ions, released at the targets and walls—governing in part the probability that such particles will reach the confined plasma, where they can have deleterious effects. Parallel temperature gradient forces also influence impurity ion transport.

We want to know how n, T_e, T_i, $v_\parallel$, $E_\parallel$ *vary spatially in the SOL, and their connection to particle, momentum and power fluxes into and out of the SOL—including out-fluxes both to solid surfaces and to volumetric loss processes such as radiation. This is the basic reason we want to model the SOL.*

The simplest, most basic analysis tool for modelling the SOL is the *two-point model*, 2 PM, which has been considered in detail, chapter 5. As the name implies, however, the 2 PM only provides information at two points along the SOL—the 'target' and the 'upstream' ends. The 2PM is therefore sometimes called a '*0D model*'. For various purposes—such as impurity transport analysis, chapter 6—we need to have further information, in particular n, T_e, T_i, $v_\parallel$, $E_\parallel$ as functions of distance $s_\parallel$ along the SOL (along $\boldsymbol{B}$). Since *parallel* plasma transport is classical, i.e. is largely understood, it is therefore appropriate to aim at carrying out at least *1D, along-*$\boldsymbol{B}$ modelling of the SOL, based on the classical laws of conservation of particles, momentum and energy.

What should we do about the strong cross-field variations of the SOL plasma? The most basic approach is to take the cross-field SOL width from experiment, or from simple analytic estimates, sections 4.3, 4.4, 5.7; the 1D, along-$\boldsymbol{B}$ model is then taken to provide a description of the *average* conditions across the SOL. At the next level of sophistication an 'onion-skin method', OSM, model of the SOL can be constructed, chapter 12: the SOL is taken to

consist of separate, along-$\boldsymbol{B}$, flux tubes nested inside each other ('onion skins') and 1D, along-$\boldsymbol{B}$ modelling is carried out for each flux tube separately, with the cross-field terms treated more or less simply. The boundary conditions for each flux tube can be taken from measurements made across the target of T_e, etc, for example using Langmuir probes. OSM analysis therefore constitutes a method of carrying out *2D modelling* of the SOL. The 2D solution is achieved by analysing the parallel and cross-field balances *sequentially* and *iteratively*. In OSM analysis values of $D_\perp^{\mathrm{SOL}}$ and $\chi_\perp^{\mathrm{SOL}}$ are outputs rather than inputs.

At the next level of sophistication are the standard 2D edge fluid codes which employ the 2D conservation equations and which use upstream boundary conditions, typically the density on the LCFS and the power entering the SOL. The values of $D_\perp^{\mathrm{SOL}}$ and $\chi_\perp^{\mathrm{SOL}}$ are inputs. The parallel and cross-field balances are treated simultaneously. The two directions can be (a) cross-field 'radially', and (b) along $\boldsymbol{B}$ or, alternatively, the projection in the poloidal plane; see figure 6.21. In either case toroidal symmetry is assumed. When toroidal symmetry is absent then a 3D treatment is required based, for example, on the radial, poloidal and toroidal directions.

In chapters 9–11, 1D models are considered in some detail. Onion- skin method modelling is dealt with in chapter 12. Chapter 13 provides a brief introduction to standard 2D fluid SOL modelling; 3D modelling is not considered here.

Once the choice has been made as to what *dimensionality* to use—whether 0D, 1D, 2D or 3D—the next important question is: does one require a *kinetic* treatment, or will a *fluid* model be adequate?

In *kinetic* modelling one endeavours to calculate the complete velocity distribution of the ions and electrons at each point [9.1–9.6]. Even if one assumes a single spatial dimension, this still involves the formidable task of calculating $f(x, v_x, v_y, v_z)$ at each location x along the SOL.

The *fluid* approach, on the other hand, settles for just finding how certain *average* quantities, such as $n(x)$ and $v(x)$ (the average or fluid velocity of the particles), depend on x. This is usually an easier task.

From the foregoing considerations the fluid approach is indicated as possibly being adequate. Accordingly, most SOL modelling to date has adopted the fluid approximation and the focus here will be primarily on this approach.

One should not accept this assumption uncritically, however. While it is not immediately obvious, the fluid approximation is only justified—at least strictly—when collisionality of the plasma particles is strong, i.e. mean free paths, mfp, are very short compared with all characteristic lengths of the problem such as connection length L and the parallel gradient lengths. As pointed out in chapter 5, this situation is often only marginally satisfied in the SOL, or even is violated. Section 9.12 discusses the connection between self-collisionality and the trustworthiness of the fluid approach.

For moderate to long mfp situations, the strictly correct approach is that the fluid approximation has to be abandoned, and one is obliged to undertake

the more demanding kinetic analysis. Fortunately, this appears to often be an overly strict view: for reasons that are not entirely clear the fluid models can often reproduce rather closely the principal results of practical interest obtained by kinetic treatments. Unfortunately, there are not many examples where such comparisons can be made, owing to the limited availability of kinetic solutions. We consider a few such comparisons in chapter 10.

Nevertheless, ultimately SOL conditions are encountered where kinetic treatments—or at least 'kinetic corrections' to the fluid treatments—become necessary. The key question is: do significant parallel temperature gradients exist along the SOL or not? When they exist, parallel heat conductivity is important—and the finiteness of its value for the SOL plasma is controlling. This regime is termed *conduction-limited*, sections 1.9, 9.11. When parallel temperature gradients are small, parallel heat conduction is unimportant, and the heat transmission properties of the sheath control SOL behaviour, thus giving the *sheath-limited* regime, sections 1.9, 9.10.

The fluid approach can encounter certain difficulties in the conduction-limited regime, but is often adequate for the sheath-limited regime. The latter may be a surprising fact since the sheath-limited regime is characterized by weak collisionality, section 4.11; the evidence for this claim is presented in table 10.2.

The reason for the difference has to do with the *closure problem* which is always encountered in fluid modelling [9.4]. This is discussed in section 9.12, but to anticipate the conclusion: if one can ignore heat conduction—as for the sheath-limited regime—then the fluid equations can be closed in a simple way. This evidently makes the fluid approach rather reliable, as born out by detailed comparisons with the few 1D kinetic treatments available, Sections 10.6, 10.7.

Chapter 9

The 1D Fluid Equations

9.1 Introduction

The 1D fluid conservation equations for a plasma can be derived at various levels of rigour and sophistication. Zawaideh *et al* [9.1] have provided a rather complete derivation of two-fluid (electrons and ions) equations that are valid from collisional to weakly collisional limits. In the highly collisional limit their equations reduce to those of Braginskii [9.2]. Here we undertake a simpler derivation of the conservation equations, and obtain results that are essentially identical to those of ZNC and Braginskii for one dimension.

9.2 The Kinetic Equation

The steady-state, spatially one-dimensional velocity distribution, $f(x, v_x, v_y, v_z)$, of particles of mass m is given by the x-component of the *Fokker–Planck (collisional) kinetic vector equation* [9.1–9.7]:

$$\boxed{v_x \frac{\partial f}{\partial x} + \frac{eE}{m}\frac{\partial f}{\partial v_x} = \left.\frac{\partial f}{\partial t}\right|_{\text{coll}} + S(x, \boldsymbol{v}).} \tag{9.1}$$

Derivatives with respect to y and z are assumed to be zero. $f(x, v_x, v_y, v_z)\,\mathrm{d}v_x\mathrm{d}v_y\mathrm{d}v_z$ is the number of particles m^{-3} at location x with velocity in the domain v_x to $v_x+\mathrm{d}v_x$, v_y to $v_y+\mathrm{d}v_y$, v_z to $v_z+\mathrm{d}v_z$. E is the electric field, $\partial f/\partial t|_{\text{coll}}$ is the change due to collisions other than events where particles are created or destroyed and S is the difference between particle creation and destruction rates. For example, if S is due to ionization of neutrals which have a drifting Maxwellian distribution characterized by a temperature T_n and average velocity v_n, then in the kinetic equation for the ions that are created one uses:

$$S(x, \boldsymbol{v}) = S_p(x)\left(\frac{\beta_n}{\pi}\right)^{3/2} \mathrm{e}^{-\beta_n(v_x-v_n)^2}\mathrm{e}^{-\beta_n v_y^2}\mathrm{e}^{-\beta_n v_z^2} \tag{9.2}$$

where $\beta_n \equiv m_n/2kT_n$ and $S_p(x)$ gives the spatial variation of the (particle) source. The $\partial f/\partial t|_{\text{coll}}$ term includes i–e and i–n momentum-transfer collisions.

When both electric and magnetic fields are present, the full kinetic equation involves $f(\boldsymbol{x}, \boldsymbol{v})$, i.e. six independent variables, and both $\boldsymbol{B}$ and $\boldsymbol{E}$. One can average over the rapid gyro-motion in the y and z directions, however, to obtain the *Gyro-Averaged Kinetic Equation* [9.1, 9.3], which is essentially the form given here in equation (9.2). Strictly, we have also assumed $\boldsymbol{B}$ constant and that $\boldsymbol{E}$ and $\boldsymbol{B}$ are parallel; these assumptions avoid the appearance in our expressions of $\boldsymbol{E} \times \boldsymbol{B}$ drifts and ∇B and curvature drifts [9.8, 9.9]; see chapter 18 regarding the latter drifts.

As will be discussed in chapter 10, solutions of the kinetic equation have been produced for simple cases. Generally kinetic analysis is difficult, however and we now develop from the kinetic equation, a hierarchy of *fluid equations* by successively multiplying the kinetic equation by $\mathrm{d}\boldsymbol{v}$, $\mathrm{m}v_x\mathrm{d}\boldsymbol{v}$, $\frac{1}{2}m(v_x^2+v_y^2+v_z^2)\mathrm{d}\boldsymbol{v}$, etc. and integrating to obtain various *average* values of the velocity distribution [9.1, 9.6, 9.10, 9.11]. It is often found easier to solve the resulting fluid equations for the average quantities than it is to try to find $f(\boldsymbol{x}, \boldsymbol{v})$.

9.3 The Conservation of Particles Equation

We multiply equation (9.1) by $\mathrm{d}\boldsymbol{v}$ and integrate. The first term gives:

$$\int_{v_x=-\infty}^{+\infty} v_x \frac{\partial f}{\partial x}\mathrm{d}v_x \int_{v_y=-\infty}^{+\infty} \mathrm{d}v_y \int_{v_z=-\infty}^{+\infty} \mathrm{d}v_z = \frac{\partial}{\partial x}\iiint v_x f \mathrm{d}\boldsymbol{v} = \frac{\mathrm{d}}{\mathrm{d}x} nv \quad (9.3)$$

where

$$\begin{aligned} n &= \int_{-\infty}^{+\infty} f \mathrm{d}\boldsymbol{v} \\ \langle\alpha\rangle &\equiv \int_{-\infty}^{+\infty} \alpha f \mathrm{d}\boldsymbol{v}/n \\ v &= \langle v_x \rangle. \end{aligned} \quad (9.4)$$

We follow here the standard convention and use no subscript when the fluid velocity is intended. It is to be emphasized that v represents the *fluid* or *average* velocity of the entire ensemble of particles at x. Note that therefore v is *not* $(v_x^2 + v_y^2 + v_z^2)^{1/2}$ here, i.e. $|\boldsymbol{v}|$, since $\boldsymbol{v}$, v_x, v_y, v_z here refer to the *particular* velocity of a particle.

The second term involves:

$$\int_{-\infty}^{+\infty} \frac{\partial f}{\partial v_x}\mathrm{d}v_x = \int \partial f = f(v_x = +\infty) - f(v_x = -\infty). \quad (9.5)$$

It is assumed that $f(v_x = \pm\infty) = 0$.

The third term is zero since whatever is gained by one part of the distribution due to $\partial f/\partial t|_{\text{coll}}$, another part loses. The fourth term is the net particle source:

$$\int S(x, \boldsymbol{v})\mathrm{d}\boldsymbol{v} \equiv S_p(x). \tag{9.6}$$

Thus, the particle conservation equation is obtained:

$$\boxed{\frac{\mathrm{d}}{\mathrm{d}x}(nv) = S_p(x).} \tag{9.7}$$

We note that we have obtained only one equation but with two unknowns (dependent variables) $n(x)$, $v(x)$ in terms of the independent variable x. We thus have not obtained a closed set of equations. We proceed to construct further averages of the distribution function, i.e. 'higher moments of the kinetic equation' in the hope of obtaining a further relation for n and v. This will succeed, but unfortunately new terms will appear, requiring further equations. The hierarchy of fluid equations never, in fact, *closes* and one can only achieve *closure* by some postulate introduced from outside this process of generating fluid equations.

9.4 The Momentum Conservation Equation

Multiply equation (9.1) by $mv_x\mathrm{d}\boldsymbol{v}$ and integrate. The first term is

$$\int mv_x^2\frac{\partial f}{\partial x}\mathrm{d}v_x\int \partial v_y\int \mathrm{d}v_z = \frac{\partial}{\partial x}\int mv_x^2 f\,\mathrm{d}\boldsymbol{v}. \tag{9.8}$$

We define the *individual random velocity* u_x:

$$u_x \equiv v_x - v \tag{9.9}$$

and thus this term becomes:

$$\begin{aligned}\frac{\partial}{\partial x}\int mu_x^2 f\,\mathrm{d}\boldsymbol{v} + \frac{\partial}{\partial x}2v\int mu_x f\,\mathrm{d}\boldsymbol{v} + \frac{\partial}{\partial x}v^2\int mf\,\mathrm{d}\boldsymbol{v}\\ = \frac{\mathrm{d}}{\mathrm{d}x}(mn\langle u_x^2\rangle) + 0 + \frac{\mathrm{d}}{\mathrm{d}x}(mnv^2).\end{aligned} \tag{9.10}$$

The second term is zero on the assumption that f is symmetrical in the random velocity, at least to first order.

While one can now continue using $\langle u_x^2\rangle$ as one of the principal (average) fluid quantities, it is more common to define this to be the 'temperature'. Strictly one should not use the term temperature unless f is a Maxwellian, or a drifting Maxwellian. We do *not* have to assume either of the latter to establish the fluid equations, but let us suppose that f in fact is a drifting Mawellian of temperature T, average velocity v:

$$f(x, \boldsymbol{v}) = n(x)\left(\frac{\beta}{\pi}\right)^{3/2}\mathrm{e}^{-\beta(v_x-v)^2}\mathrm{e}^{-\beta v_y^2}\mathrm{e}^{-\beta v_z^2} \tag{9.11}$$

where $\beta \equiv m/2kT$. Then one can readily confirm that, indeed $\langle v_x \rangle = v$ and also show that:

$$\langle u_x^2 \rangle = kT/m. \tag{9.12}$$

Hereafter, for clarity, we will employ kT/m in place of $\langle u_x^2 \rangle$ but this should not be taken as an assumption that f is necessarily a (drifting) Maxwellian.

At this point it is worth distinguishing $T_\parallel$ from $T_\perp$ and thus also the pressures $p_\parallel$ and $p_\perp$ where $p_\parallel \equiv nkT_\parallel$, $p_\perp \equiv nkT_\perp$. The parallel direction is the x-direction here, with the perpendicular direction corresponding to the gyro-motion of the particles. As a flow accelerates, it is well known that the pressure drops, i.e. flows are driven locally by the local pressure gradient, usually. But which pressure? If self-collisionality is weak, then it will be shown shortly that the increased momentum flux, represented by the flow at velocity v, arises at the expense of a decrease in the random momentum flux in the *parallel* direction only, that is $p_\parallel$. So, acceleration of a flow tends to be accompanied by a drop in $T_\parallel$–but not in $T_\perp$, if self-collisionality is weak. It is therefore important to distinguish between $T_\perp$ and $T_\parallel$.

For illustration (only) we might consider f to be a drifting Maxwellian with different $T_\parallel$ and $T_\perp$, and drift velocity v:

$$f = n(x)\frac{\beta_\perp \beta_\parallel^{1/2}}{\pi^{3/2}} \mathrm{e}^{-\beta_\parallel (v_x - v)^2} \mathrm{e}^{-\beta_\perp (v_y^2 + v_z^2)} \tag{9.13}$$

where $\beta_\parallel \equiv m/2kT_\parallel$, $\beta_\perp \equiv m/2kT_\perp$ thus $\langle u_x^2 \rangle = kT_\parallel/m \equiv \langle u_\parallel^2 \rangle$ and $\langle v_y^2 \rangle = \langle v_z^2 \rangle = kT_\perp/m \equiv \langle v_\perp^2 \rangle$.

Strictly one should use $\langle u_x^2 \rangle$ and $\langle v_\perp^2 \rangle$ in the fluid equations, not $T_\parallel$ and $T_\perp$, but for clarity we will use the latter expressions even if f is not a (two-temperature, drifting) Maxwellian.

Thus, from the first term we have

$$\frac{\mathrm{d}}{\mathrm{d}x}(p_\parallel + mnv^2) \tag{9.14}$$

which emphasizes the point that the flow momentum, mnv^2, grows at the expense of $p_\parallel$, typically. This also emphasizes that the $\mathrm{d}p/\mathrm{d}x$ term which usually appears on the RHS of the momentum equations as $-\mathrm{d}p/\mathrm{d}x$, and is thus often thought of as part of the *force* acting on the fluid, is, in reality, part of the '*ma*' of Newton's 2nd law '$F = ma$', i.e. part of the *inertia*: it is the part of the rate of momentum change associated with random, thermal motion, while the mnv^2 is the part associated with the average or fluid motion.

We now turn to the second term, which includes a true force, that due to E. We obtain, integrating by parts and assuming $f(v_x = \pm\infty) = 0$ that:

$$\frac{eE}{m} \int m v_x \frac{\partial f}{\partial v_x} \mathrm{d}\boldsymbol{v} = -eEn. \tag{9.15}$$

While one could treat E as a quantity which is externally specified, that would be quite unsatisfactory since this field can arise spontaneously within the plasma due to the ambipolar constraint that positive and negative charges move with the same v. In other cases $v_e \neq v_i$, i.e. a net *current* exists, but nevertheless $E(x)$ is as much of an unknown that we must solve for as is $n(x)$ or $v(x)$. Fortunately E appears in both the electron and ion momentum equation as $\pm eEn$. Thus by adding these equations to obtain the *plasma* momentum equation, E drops out. For various purposes, however, we want to know $E(x)$; that can be obtained from the electron momentum equation expressed as *Ohm's law*, see section 9.5.

We turn next to the $\partial f/\partial t|_{\text{coll}}$ term. From rudimentary considerations [9.12] we obtain for the case of ion–neutral momentum-loss collisions the *collision frequency*:

$$\nu_{in} = \overline{\sigma v}_{in} n_n$$

thus:

$$\left.\frac{\partial f}{\partial t}\right|_{\text{coll}} = -m_i(v_i - v_n)\overline{\sigma v_{in}} n_n n \tag{9.16}$$

where $\overline{\sigma v_{in}}$ has to be calculated from experimentally measured cross-sections σ_{mom}, and then averaged over the relative approach velocities of the neutral and ion distributions. In practice such complex calculations are often avoided and an *approach velocity* based on some average thermal velocity of ions and neutrals is used.

Of great importance are momentum-transfer collisions between electrons and ions since they occur even in fully ionized plasmas. We will consider first the situation with no T_e-gradient. From basic plasma physics we have the *electron collision time* τ_e [9.13]:

$$\tau_e^{-1} = \nu_{ei}^{\text{mom}} = 0.917 \times 10^{-16} \ln \Lambda Z_i n_e / T_e^{3/2} \simeq 10^{-15} Z_i n_e / T_e^{3/2} \tag{9.17}$$

ν [s^{-1}], n [m^{-3}], T_e [keV]. $\ln\Lambda$ is the *Coulomb factor*, see below. Z_i is the ion charge. It may seem surprising that ν_{ei} *decreases* as T_e increases, since $\nu_{ei} \propto v_e$ and $v_e \propto T_e^{1/2}$. The cross-section $\sigma_{ei}^{\text{mom}} \propto T_e^{-2}$, however, and $\nu_{ei}^{\text{mom}} \approx n_i v_e \sigma_{ei}^{\text{mom}}$. This dependence of $\sigma_{ei}^{\text{mom}}(T_e)$ is a fundamental property of the Coulomb interaction. One can estimate σ_{ei}^{mom} by considering a 90° deflection of an electron by an (essentially stationary) ion in a single collision. The total electron momentum is lost, hence we may write

$$m_e v_e = F_{\text{effective}} \Delta t_{\text{effective}} \tag{9.18}$$

where the Coulomb force is taken to have a constant, effective value $F_{\text{effective}}$ during a finite interaction time $\Delta t_{\text{effective}}$. We may *roughly* estimate

$$F_{\text{effective}} \approx \frac{Z_i e^2}{4\pi\varepsilon_0 r_{\min}^2} \tag{9.19}$$

where $r_{\min}$ is the distance of closest approach for a *head-on*, i.e. 180°, collision. Thus also

$$\Delta t_{\text{effective}} \approx r_{\min}/v_e. \tag{9.20}$$

Intuitively, the cross-section which the ion presents to the electron must be *roughly* $\sigma_{ei}^{\text{mom}} \approx r_{\min}^2$. Using also $v_e = (kT_e/m_e)^{1/2}$ one then obtains:

$$\nu_{ei}^{\text{mom}} = \frac{n_i Z_i^2 e^4}{(4\pi\varepsilon_0)^2 m_e^{1/2}(kT_e)^{3/2}} \tag{9.21}$$

which, with $n_e = Z_i n_i$, is quite close to equation (9.17). The principal deficiency of this simple estimate is the neglect of the *cumulative effect of small angle collisions* which can be shown to be more important at transferring momentum than the relatively rare, single, large angle (90°) scattering collisions [9.14]. The final result is an enhancement of ν_{ei} by a factor of $\ln\Lambda$, the *Coulomb factor* [9.14], $\ln\Lambda \approx 17$, for typical fusion plasma conditions. All the parameter dependences of equation (9.21) still hold, nevertheless.

Thus in the momentum equation for electrons the *friction force* term arises:

$$R_u \equiv -m_e(v_e - v_i)\nu_{ei}^{\text{mom}} n \tag{9.22}$$

and the same term, of opposite sign, occurs in the ion-momentum equation. Spitzer [9.15], allowing for the distribution of electron velocities and for *e–e* collisions, found that a value of almost precisely half of that given by equation (9.17) should be used for R_u [9.16]:

$$\begin{aligned}\nu_{ei}^{\text{mom}} &= \frac{0.51\text{e}^4 \ln\Lambda Z_i n_e}{3m_e^{1/2}\varepsilon_0^2(2\pi kT_e)^{3/2}} \\ &= 0.468\times10^{-16}\ln\Lambda Z_i n_e/T_e^{3/2} \qquad \text{for } T_e[\text{keV}] \\ &= 0.795\times10^{-15} Z_i n_e/T_e^{3/2} \qquad \text{with } \ln\Lambda = 17.\end{aligned} \tag{9.23}$$

When $\mathrm{d}T_e/\mathrm{d}x \neq 0$ a second collisional force arises for the electrons [9.17]:

$$R_T \equiv -0.71n\left(\frac{\mathrm{d}kT_e}{\mathrm{d}x}\right) \tag{9.24}$$

due to the fact that the electrons which strike the ion from the colder side have a larger ν_{ei}^{mom}, equation (9.17), than do those from the hot side. Thus the electrons tend to push the ions in the direction of increasing T_e, and the same force acts oppositely on the electrons.

It is important to keep in mind that this temperature gradient force R_T is every bit as much due to collisions as is R_u, although due to a coincidental, complete cancellation of various terms, this is not apparent. This may be seen from the following simple model for estimating R_T. The electrons striking the ions (essentially stationary) at x_0 from the left side, had experienced their last

collision with another electron at $x_0 - \lambda_{ee}$, while those from the right had done so at $x_0 + \lambda_{ee}$. Thus the electrons from the left have temperature $T_0 - \lambda_{ee}\mathrm{d}T/\mathrm{d}x$, assuming that e–e temperature equilibration requires only about one collision, which is approximately the case for like-mass collisions [9.18]. Therefore the net forward force on the n ions at x_0 is approximately:

$$F_{ei} \approx m_e \overline{c}_e n[\nu_{ei}^{\mathrm{mom}}(x_0 - \lambda_{ee}) - \nu_{ei}^{\mathrm{mom}}(x_0 + \lambda_{ee})] \tag{9.25}$$

which expression, assuming $\lambda_{ee}(\mathrm{d}T/\mathrm{d}x)/T \ll 1$, can be expanded. (This latter condition is merely the physical one that the temperature gradient length not be shorter than λ_{ee}.) Thus:

$$F_{ei} \approx m_e \overline{c}_e n \overline{\nu}_{ei}^{\mathrm{mom}} 3\lambda_{ee} \frac{\mathrm{d}(kT)}{kT\,\mathrm{d}x}. \tag{9.26}$$

Noting that $\lambda_{ee} \approx \overline{c}_e/\nu_{ei}^{\mathrm{mom}}$, i.e. ignoring the same factor of two difference mentioned above, one sees that the collision frequency cancels out, giving finally

$$F_{ei} \approx n \frac{\mathrm{d}(kT)}{\mathrm{d}x} \tag{9.27}$$

i.e. close to $-R_T$, equation (9.24). Thus, while the final form of R_T does not indicate that it is due to collisions, we see that this is actually the case. It is the *electron* temperature, rather than T_i which controls R_T, due to the greater thermal velocity of the electrons (assuming T_e not to be extremely small compared with T_i). As regards T-gradient forces on *impurities*, however, there exist both T_e- and T_i-gradient forces; section 6.5.2.

The total ei collisional force is defined to be

$$R \equiv R_u + R_T$$

Finally the fourth term:

$$\int m v_x S(x, \boldsymbol{v}) \mathrm{d}\boldsymbol{v} \tag{9.28}$$

which for the example of ions created by ionization of a neutral population with a drifting Maxwellian distribution, equation (9.2), gives:

$$m_i v_n S(x, \boldsymbol{v}) \tag{9.29}$$

i.e. a momentum gain. We shall ignore electron momentum due to sources as small.

We thus have the momentum equation for ions:

$$\begin{aligned} \frac{\mathrm{d}}{\mathrm{d}x}(m_i n v^2 + p_{\|i}) - eEn = & -m_i(v_i - v_n)\overline{\sigma v}_{in} n_n n \\ & + m_e(v_e - v_i)\nu_{ei}^{\mathrm{mom}} n \\ & + 0.71 n \left(\frac{\mathrm{d}kT_e}{\mathrm{d}x}\right) \\ & + m_i v_n S_p(x). \end{aligned} \tag{9.30}$$

and for electrons:

$$\boxed{\begin{aligned}\frac{\mathrm{d}p_e}{\mathrm{d}x} + eEn = & -m_e(v_e - v_i)\nu_{ei}^{\mathrm{mom}} n \\ & - 0.71n\left(\frac{\mathrm{d}kT_e}{\mathrm{d}x}\right)\end{aligned}} \tag{9.31}$$

where we have dropped most of the terms with m_e as being small.

We have also anticipated the result that due to the (generally) strong self-collisionality of electrons, see equation (9.21), $\nu \propto m^{-1/2}$:

$$T_{\|e} = T_{\perp e} \qquad p_{\perp e} = p_{\|e} = p_e \tag{9.32}$$

It is most useful to add these two equations (9.30) and (9.31), to obtain the *plasma* momentum equation since many terms cancel:

$$\boxed{\begin{aligned}\frac{\mathrm{d}}{\mathrm{d}x}(m_i n v^2 + p_{\|i} + p_e) = & -m_i(v_i - v_n)\overline{\sigma v}_{in} n_n n \\ & + m_i v_n S_p(x).\end{aligned}} \tag{9.33}$$

The plasma momentum equation brings out the obvious point that the electric field cannot exert a force on the plasma fluid which is (quasi-) neutral. Rather, the main 'force' accelerating the flow, i.e. increasing $m_i n v^2$, is usually the plasma pressure-gradient 'force', $-(\mathrm{d}/\mathrm{d}x)(p_{\|i} + p_e)$ (negative sign when moved to the RHS of the equation, as is the custom). The ion momentum equation (9.30) brings out the fact that the electric force $+eEn$ (positive sign when moved to the RHS) truly does accelerate the ion flow, adding to the $-\mathrm{d}p_{\|i}/\mathrm{d}x$ 'force'. Similarly the electron momentum equation (9.31) shows that the $-eEn$ force (on RHS) acts to slow down the electrons, almost precisely off-setting the $-\mathrm{d}p_e/\mathrm{d}x$ 'force'.

These three equations (9.30), (9.31), (9.33) are written here in the 'conservative form'. We can now resolve the uncertainty encountered in section 1.8.2.7 where the heuristic arguments used to obtain the momentum equations left us somewhat uncertain whether a $(-m_i v S_p)$ term should appear on the RHS or not: when written in the conservative form, above, the answer is 'no'; when written in the inertial form with $m_i n v\, \mathrm{d}v/\mathrm{d}x$ on the left (by combining the particle and momentum equations), the answer is 'yes'. In both cases a $(+m_i v_n S_p)$ term appears on the RHS if the neutrals being ionized were, in fact, flowing.

Returning to the problem of closing the fluid equations, we find that we now have a second equation involving n and v, but unfortunately a new unknown has appeared, $T_{\|i}$ (or $p_{\|i} \equiv nkT_{\|i}$). The other terms involve quantities that have to be externally specified, like $S_p(x)$, $\overline{\sigma v}_{\mathrm{mom}}$, v_n, n_n. We thus proceed to a further higher moment of the kinetic equation. We are going to want to bring $T_{\perp i}$ and $p_{\perp i}$ into the analysis–so we need two energy equations, sections 9.6, 9.7. First, however, we discuss *Ohm's law*.

9.5 Ohm's Law

For various purposes we will want to know $E(x)$, for example, to compute forces acting on impurity ions. The electron-momentum equation (9.31) can be seen to be a form of *Ohm's law*, since we define the *parallel current density* $j_\parallel$:

$$j_\parallel \equiv en(v_i - v_e) \tag{9.34}$$

(assuming $Z_i = 1$) and parallel electric conductivity for a fully ionized plasma [9.19]:

$$\sigma_\parallel \equiv \frac{e^2 n}{m_e \nu_{ei}^{\text{mom}}} \tag{9.35}$$

giving:

$$\boxed{E(x) = \frac{j_\parallel}{\sigma_\parallel} - \frac{0.71}{e}\frac{\mathrm{d}kT_e}{\mathrm{d}x} - \frac{1}{en}\frac{\mathrm{d}p_e}{\mathrm{d}x}.} \tag{9.36}$$

$\sigma_\parallel$ is derived assuming balance between the E-force and e–i friction force, only:

$$neE = -m_e(v_e - v_i)\nu_{ei}^{\text{mom}} n \tag{9.37}$$

together with with the definition:

$$\sigma_\parallel \equiv j_\parallel / E. \tag{9.38}$$

Thus (9.16):

$$\sigma_\parallel [\text{ohm}^{-1}\ \text{m}^{-1}] \approx 3.6 \times 10^7\ [T_e\ [\text{keV}]]^{3/2}. \tag{9.39}$$

In the simplest cases one assumes local ambipolarity, $j_\parallel = 0$, and thus $E(x)$ is given entirely in terms of quantities already being calculated. When $j_\parallel \neq 0$ further information is required, since one has a new unknown, $j_\parallel$ (or alternatively one has the two unknowns, v_e and v_i instead of just one v). This requires that further information be provided about the current externally provided to the plasma, i.e. one then requires a *current continuity equation*, see section 17.4. One may note that the Boltzmann relation, equation (1.12), is obtained from equation (9.36) for the case of $T_e =$ constant and $j_\parallel = 0$.

9.6 The Energy Conservation Equation, $T_\parallel$

Multiply the kinetic equation by $\frac{1}{2}m_i v_x^2$ and integrate. The first term gives:

$$\begin{aligned}\frac{1}{2}m_i \int v_x^3 \frac{\partial f}{\partial x}\mathrm{d}\boldsymbol{v} &= \frac{1}{2}m_i \frac{\partial}{\partial x}\int (u_x + v)^3 f\,\mathrm{d}\boldsymbol{v} \\ &= \frac{\mathrm{d}}{\mathrm{d}x}\left[\tfrac{1}{2}m_i n v^3 + \tfrac{3}{2}m_i n v\langle u_x^2\rangle + \tfrac{1}{2}m_i n\langle u_x^3\rangle\right].\end{aligned} \tag{9.40}$$

The second term in equation (9.40) is just $3/2 p_\parallel v$, while the third term is a new and most important one. It is the *ion-conducted heat flux density*:

$$q_{\parallel i,\mathrm{cond}} \equiv \tfrac{1}{2} m_i n \langle u_x^3 \rangle. \tag{9.41}$$

Our attempt to close the equations has once again generated a new dependent variable or unknown. We can proceed to yet higher moments, but the most direct approach is to stop the hierarchy here by some method. We need some assumption or idea from *outside* this analysis process.

The simplest approach is to just set $q_{\parallel i,\mathrm{cond}}$, $\langle u_x^3 \rangle = 0$. This can be justified in certain circumstances. For example, strong (self-) collisionality force velocity distributions toward Maxwellian [9.20] (or drifting Maxwellian) for which it is easily shown that $\langle u_x^3 \rangle = 0$ due to symmetry.

Let us, however, look outside the present analysis procedure to simple *gas kinetic theory* [9.21] to try to answer the question: why would a velocity distribution have a non-zero $\langle u_x^3 \rangle$, anyway? What would make it *asymmetric* in that way? There could be many reasons, of course, but *one* obvious reason is a finite λ_s, the *mean free path for self-collisions*, together with the presence of a temperature gradient: at some location x_0, the ions moving one way have a velocity distribution characteristic of the location where they experienced their last (thermalizing) collision, say at $x_0 - \lambda_s$ where $T(x_0 - \lambda_s) \approx T(x_0) - \lambda_s \mathrm{d}T/\mathrm{d}x$. Ions moving the other way, at location x_0, have a distribution characteristic of the location $x_0 + \lambda_s$, where $T(x_0 + \lambda_s) \approx T(x_0) + \lambda_s \mathrm{d}T/\mathrm{d}x)$. Thus a velocity asymmetry arises for $f(x_0, v)$, and so $\langle u_x^3 \rangle \neq 0$. Let us employ this picture from simple gas kinetic theory to develop an approximation for $q_{\parallel\mathrm{cond}}$. It is readily shown, section 2.2, that for a Maxwellian distribution the one-way random flux density of particles is:

$$\begin{aligned} \Gamma_p^{\mathrm{Max}} &= \tfrac{1}{4} n \overline{c} \\ \overline{c} &= (8kT/\pi m)^{1/2} \end{aligned} \tag{9.42}$$

while the one-way random flux density of energy (here heat) is:

$$q_E^{\mathrm{Max}} = 2kT \Gamma_p^{\mathrm{Max}}. \tag{9.43}$$

Let us use these as approximations for the actual distribution, i.e. we assume a small perturbation from Maxwellian. The *net* heat flux due to random particle motion is

$$\begin{aligned} q_E^{\mathrm{net}} &= 2k \left(T_0 - \lambda_s \frac{\mathrm{d}T}{\mathrm{d}x} - \left(T_0 + \lambda_s \frac{\mathrm{d}T}{\mathrm{d}x} \right) \right) \frac{1}{4} n \overline{c} \\ &\equiv -K \frac{\mathrm{d}kT}{\mathrm{d}x} \end{aligned} \tag{9.44}$$

with $K \equiv n \overline{c} \lambda_s$, the heat conduction coefficient. Taking $\lambda_s = \overline{c}/\nu_s$, where ν_s is the self-collision frequency we obtain:

$$K = n \frac{kT}{m \nu_s} \tag{9.45}$$

This is the classical gas kinetic result [9.21].

For collisions between charged particles we have $\nu_s \propto m^{-1/2} n T^{-3/2}$, equation (9.23), giving:

$$\boxed{K = \kappa_0 T^{5/2}} \tag{9.46}$$

a very strong function of T. Thus, often plasma heat conductivity is so high that isothermal conditions prevail. In the low temperatures of the SOL, however, this can break down, giving rise to substantial temperature gradients along flux tubes.

One also may note that $K \propto m^{-1/2}$ and thus electron heat conductivity is much larger than ion conductivity. For ions, convection is often more important than conduction.

The foregoing provides a good first estimate for $K_{e,i}$. More detailed analysis [9.2] gives the results:

$$\begin{aligned} q_{\parallel e,\mathrm{cond}} &= -K_e \frac{\mathrm{d}T_e}{\mathrm{d}x} = -\kappa_{0e} T_e^{5/2} \frac{\mathrm{d}T_e}{\mathrm{d}x} \\ q_{\parallel i,\mathrm{cond}} &= -K_i \frac{\mathrm{d}T_i}{\mathrm{d}x} = -\kappa_{0i} T_i^{5/2} \frac{\mathrm{d}T_i}{\mathrm{d}x} \end{aligned} \tag{9.47}$$

with:

$$\boxed{\begin{aligned} \kappa_{0e} &= \frac{30692}{Z_i \ln \Lambda} \approx 2000 \\ \kappa_{0i} &= \frac{1249}{Z_i^4 m_i^{1/2} \ln \Lambda} \approx 60 \end{aligned}} \tag{9.48}$$

where T [eV], $\mathrm{d}T/\mathrm{d}x$ [eV m^{-1}], q [W m^{-2}], m_i [amu] and where the approximate values in equation (9.48) assume $Z_i = 1$, $m_i = 2$, $\ln \Lambda = 15$. Equation (9.48) assumes a single ion species, charge Z_i.

Thus, from the multiplication of equation (9.1) by $\frac{1}{2} m_i v_x^2$, the first term gives:

$$\frac{\mathrm{d}}{\mathrm{d}x}\left[\frac{1}{2} m n v^3 + \frac{3}{2} p_\parallel v + q_{\parallel\mathrm{cond}}\right]. \tag{9.49}$$

The second term from multiplying equation (9.1) by $\frac{1}{2} m_i v_x^2$ is readily shown to give $-eEnv$. When $v_e = v_i$ this is simply the energy transfer from electrons to ions as a result of the ambipolar electric field.

The third term involves collisions associated with heat transfer. Here one could include, for example, heating associated with ion–neutral collisions. For simplicity we do not include any such specific terms here, except those involving charged particle collisions as follows:

(a) For the transfer of heat due to self-collisions which couple $T_\parallel$ and $T_\perp$, $Q_{\perp\to\parallel}$, we may write:

$$Q_{\perp\to\parallel} \equiv \frac{nkT_\perp - nkT_\parallel}{\tau_{\perp\to\parallel}} = \frac{p_\perp - p_\parallel}{\tau_{\perp\to\parallel}} \tag{9.50}$$

thus defining $\tau_{\perp\to\parallel}$, the (ion) *pressure anisotropy relaxation time*. It may be noted that it is 2.5 times longer than the usual ion collision time [9.1]. Often $\tau_{\perp\to\parallel}$ is simply written as τ_i or τ_T but we wish to emphasize the specific nature of this collision time.

(b) The joule heating due to the net drift of the electrons: against the dissipative (collisional) force R. By convention R, v_e, and v_i are positive, therefore the heating due to the electron drift is $-Rv_e$ while that due to the ions is $+Rv_i$; thus this heating term is:

$$Q_R \equiv -R(v_e - v_i) \tag{9.51}$$

and goes all to the electrons, essentially, since $m_e \gg m_i$.

(c) Thermal equilibration collisions between electrons and ions gives an ion heating term [9.2]:

$$Q_{eq} = \frac{3m_e}{m_i} n\nu_{eq}(kT_e - kT_i) \tag{9.52}$$

where $\nu_{eq} \approx 2.9 \times 10^{-12} n \ln \Lambda T_e^{-3/2}$, ν [s^{-1}], n [m^{-3}], T_e [eV].

The fourth term is

$$\int S(x, \boldsymbol{v}) \tfrac{1}{2} m v_x^2 \mathrm{d}\boldsymbol{v} \equiv Q_{E\parallel} \tag{9.53}$$

which for an ionization source of Maxwellian neutrals gives:

$$Q_{E\parallel} = \tfrac{1}{2} k T_n S_p(x). \tag{9.54}$$

Thus, for ions and for $T_\parallel$ or $p_\parallel$ we have:

$$\boxed{\begin{aligned} &\frac{\mathrm{d}}{\mathrm{d}x}\left[\tfrac{1}{2} m_i n v_i^3 + \tfrac{3}{2} p_{\parallel i} v_i\right] + \frac{\mathrm{d}}{\mathrm{d}x}\left(-\kappa_{0i} T_i^{5/2} \frac{\mathrm{d}T_i}{\mathrm{d}x}\right) \\ &= env_i E + Q_{\perp\to\parallel} + Q_{eq\parallel} + Q_{E\parallel i} \end{aligned}} \tag{9.55}$$

while for electrons:

$$\boxed{\begin{aligned} &\frac{\mathrm{d}}{\mathrm{d}x}\left(\tfrac{3}{2} p_{\parallel e} v_e\right) + \frac{\mathrm{d}}{\mathrm{d}x}\left(-\kappa_{0e} T_e^{5/2} \frac{\mathrm{d}T_e}{\mathrm{d}x}\right) \\ &= -env_e E - Q_{eq\parallel} + Q_R + Q_{E\parallel e} \end{aligned}} \tag{9.56}$$

where, again, we are anticipating isotropic electrons and also dropping the m_e-terms.

As anticipated we have introduced another unknown $p_{\perp i}$ since $Q_{\perp\to\parallel} = (p_{\perp i} - p_{\parallel i})/\tau_{\perp\to\parallel}$. However, we will find an equation for that in the next section. One can use Ohm's law, equation (9.36), to substitute for $E(x)$ in equations (9.55) and (9.56). The electron power terms which are associated with ionization sources S_{E_e}, are very important and are discussed separately in section 5.5; generally there is an important and substantial power *loss* by the electrons associated with ionization.

9.7 The Energy Conservation Equation, $T_\perp$

Multiply the kinetic equation by $\frac{1}{2}m(v_y^2 + v_z^2)$ and integrate to obtain for ions:

$$\frac{\mathrm{d}}{\mathrm{d}x}(p_{\perp i} v_i) = -Q_{\perp\to\parallel} + Q_{eq\perp} + Q_{E\perp i} \tag{9.57}$$

and for electrons:

$$\frac{\mathrm{d}}{\mathrm{d}x}(p_{\perp e} v_e) = -Q_{eq\perp} + Q_{E\perp e}. \tag{9.58}$$

For ionization from Maxwellian neutrals:

$$Q_{E\perp i} = kT_n S_p(x). \tag{9.59}$$

One combines the two electron energy equations, anticipating $p_{\parallel e} = p_{\perp e}$:

$$\frac{\mathrm{d}q_{\parallel e}}{\mathrm{d}x} = -env_e E - Q_{eq} + Q_R + Q_{Ee} \tag{9.60}$$

where

$$Q_{eq} \equiv Q_{eq\perp} + Q_{eq\parallel}$$

$$\boxed{\begin{aligned} q_{\parallel e} &\equiv q_{\parallel e,\text{convection}} + q_{\parallel e,\text{conduction}} \\ q_{\parallel e,\text{convection}} &\equiv \tfrac{5}{2}kT_e n v_e \\ q_{\parallel e,\text{conduction}} &\equiv -\kappa_{0e} T_e^{5/2} \frac{\mathrm{d}T_e}{\mathrm{d}x}. \end{aligned}} \tag{9.61}$$

One now has six equations for the six unknowns n, v_e, v_i, $T_{\parallel i}$, $T_{\perp i}$, T_e as functions of x: the particle conservation equation (9.7), the electron- and ion-momentum equations (9.30) and (9.31), and the electron-energy equation (9.60). If local ambipolarity is assumed, $v_e = v_i = v$ then the plasma-momentum equation (9.33) is used in place of the separate e and i ones.

When ion self-collisionality is strong then $T_{\parallel i} = T_{\perp i} = T_i$, $p_{\parallel i} = p_{\perp i} = p_i$, and one adds the two ion-energy equations to obtain:

$$\frac{\mathrm{d}}{\mathrm{d}x} q_{\parallel i} = env_i E + Q_{eq} + Q_{Ei} \tag{9.62}$$

where:

$$\boxed{\begin{aligned} q_{\parallel i} &= q_{\parallel i,\text{convection}} + q_{\parallel i,\text{conduction}} \\ q_{\parallel i,\text{convection}} &\equiv \left(\tfrac{1}{2}m_i v_i^2 + \tfrac{5}{2}kT_i\right) n v_i \\ q_{\parallel i,\text{conduction}} &\equiv -\kappa_{0i} T_i^{5/2} \frac{\mathrm{d}T_i}{\mathrm{d}x} \end{aligned}} \tag{9.63}$$

$$q_{\parallel i,\text{convection}} \equiv \left(\tfrac{1}{2}m_i v_i^2 + \tfrac{5}{2}p_i\right) n v_i.$$

(One notes an ambiguity involved in the expressions for $q_{\parallel i,\text{conduction}}$, also Q_{eq}: which T_i is one to use when $T_{\parallel i} \neq T_{\perp i}$? This is just one of the limitations of the simple expressions used above.)

In this case one has four equations for the four unknowns, n, v, T_i, T_e, equations (9.7), (9.33), (9.60), (9.62).

If collisionality is so strong that equipartition occurs, $T_i = T_e$, section 4.11, then one adds the e and i energy equations:

$$\frac{\mathrm{d}q_\parallel}{\mathrm{d}x} = Q_R + Q_E \tag{9.64}$$

where:

$$\boxed{\begin{aligned} q_\parallel &= q_{\parallel\text{convection}} + q_{\parallel\text{conduction}} \\ q_{\parallel\text{convection}} &= \left(\tfrac{1}{2}m_i v^2 + 5kT\right)nv \\ q_{\parallel\text{conduction}} &\approx -\kappa_{0e}T_e^{5/2}\frac{\mathrm{d}T_e}{\mathrm{d}x} \end{aligned}} \tag{9.65}$$

where one has used the fact that $\kappa_{0_i} \ll \kappa_{0_e}$. One thus has the most basic set of three conservation equations—equations (9.7), (9.33), (9.64)—for the three unknowns n, v, T as functions of x.

9.8 The Parallel Viscous Stress

For very weak collisionality $\tau_{\perp\to\parallel} \to \infty$ and only the $-\mathrm{d}p_{\parallel i}/\mathrm{d}x - \mathrm{d}p_e/\mathrm{d}x$ 'forces' are available to accelerate the flow. $p_{\perp i} \neq p_{\parallel i}$ and one should—strictly speaking—use the two ion energy equations (9.55) and (9.57). When $\tau_{\perp\to\parallel}$ has intermediate values some of the parallel flow acceleration comes from $-\mathrm{d}p_{\perp i}/\mathrm{d}x$. One can still employ the two ion energy equations for $p_{\perp i}$ and $p_{\parallel i}$ but a common practice is to introduce instead the *parallel stress tensor* π:

$$\boxed{\pi \equiv \tfrac{2}{3}(p_\parallel - p_\perp)} \tag{9.66}$$

$$p \equiv (p_\parallel + 2p_\perp)/3 \tag{9.67}$$

so

$$p_\parallel = p + \pi \quad \text{and} \quad p_\perp = p - \frac{\pi}{2} \tag{9.68}$$

and then to work with p and π, rather than $p_\perp$ and $p_\parallel$.

Clearly π is directly related to the coupling of $T_\parallel$ and $T_\perp$ and will be important in the momentum equation (9.30). We must use the *energy* equation, however, in order to estimate π, since the coupling of the two pressure 'reservoirs' is really an *energy* coupling. Let us note first that π_i is indeed the term we need in the ion *momentum* equation (9.30), which using (9.68) gives:

$$\frac{\mathrm{d}}{\mathrm{d}x}(m_i n v^2 + p_i + \pi_i) = \text{RHS of equation (9.30)} \tag{9.69}$$

($-eEn$ has been moved to the RHS) and so one sees that, in moving $\mathrm{d}\pi_i/\mathrm{d}x$ to the RHS one obtains another 'force' on the flow, namely $-\mathrm{d}\pi_i/\mathrm{d}x$ in addition to the usual $-\mathrm{d}p_i/\mathrm{d}x$ 'force'. Just as for the latter, $-\mathrm{d}\pi_i/\mathrm{d}x$ is really part of the flux of momentum in the flow direction associated with random, thermal motion, i.e. part of 'ma', inertia.

We turn now to the task of estimating π_i. We are seeking an expression which will relate the power transfer rate $Q_{\perp\to\parallel}$ to the dominant term in the energy equation associated with the temperature drop which accompanies flow acceleration. To obtain a reasonably simple estimate it is necessary to make some rather strongly simplifying approximations, including the neglect of all the S-source terms in the ion fluid equations. We also drop the E-terms and $q_{\parallel i,cond}$ and ignore the electrons:

$$\frac{\mathrm{d}}{\mathrm{d}x}(nv) = 0 \tag{9.70}$$

$$\frac{\mathrm{d}}{\mathrm{d}x}(m_i n v^2 + p_i + \pi_i) = 0 \tag{9.71}$$

$$\frac{\mathrm{d}}{\mathrm{d}x}(m_i n v^3 + 3p_{\parallel i} v) = 2\frac{(p_{\perp i} - p_{\parallel i})}{\tau_{\perp\to\parallel}} = \frac{-3\pi_i}{\tau_{\perp\to\parallel}} \tag{9.72}$$

$$\frac{\mathrm{d}}{\mathrm{d}x}(p_{\perp i} v) = -\frac{(p_{\perp i} - p_{\parallel i})}{\tau_{\perp\to\parallel}} = \frac{3}{2}\frac{\pi_i}{\tau_{\perp\to\parallel}}. \tag{9.73}$$

Subtract (9.73) from (9.72):

$$\frac{\mathrm{d}}{\mathrm{d}x}\left(m_i n v^3 + \left(2p_i + \tfrac{7}{2}\pi_i\right)v\right) = -\frac{9}{2}\frac{\pi_i}{\tau_{\perp\to\parallel}}. \tag{9.74}$$

Expanding the LHS of equation (9.74), using equations (9.70) and (9.71) and dropping terms involving π_i itself as small, one obtains the final result [9.1, 9.2]:

$$\boxed{\pi_i = -\frac{4}{9}p_i\tau_{\perp\to\parallel}\frac{\mathrm{d}v}{\mathrm{d}x} \equiv -\eta_\parallel\frac{\mathrm{d}v}{\mathrm{d}x}} \tag{9.75}$$

where $\eta_\parallel$ is defined as the *parallel viscosity coefficient*.

We can thus see that the cooling effect on the flow associated with acceleration is primarily through the $p_i\mathrm{d}v/\mathrm{d}x$ term, which is balanced by $Q_{\perp\to\parallel}$, giving an expression for π_i. The latter appears not only in the energy equation, but in the momentum equation also. The change to the momentum equation is as shown, equation (9.71)—and so the two previous unknowns $p_{\parallel i}$ and $p_{\perp i}$ have been replaced by two new unknowns p_i and π_i. For the latter, however, we use the simple relation, equation (9.75)—and so we still have enough equations to match the unknowns, although we use only a single ion momentum equation, constituting a valuable simplification.

The ion energy equations are similarly combined by adding them:

$$\frac{\mathrm{d}}{\mathrm{d}x}\left[\left(\tfrac{3}{2}p_{\parallel_i} + p_{\perp i}\right)v_i\right] = \mathrm{RHS} \tag{9.76}$$

and substituting equation (9.68) gives:

$$\frac{5}{2}\frac{\mathrm{d}}{\mathrm{d}x}(p_i v_i) + \frac{\mathrm{d}}{\mathrm{d}x}(\pi_i v_i) = \mathrm{RHS} \tag{9.77}$$

where $(\mathrm{d}/\mathrm{d}x)(\pi_i v_i)$ is the heat generated by the parallel viscous stress.

We note that $\tau^e_{\perp\to\parallel}/\tau^i_{\perp\to\parallel} \approx (m_e/m_i)^{1/2}$ which is the reason for generally assuming that electron self-collisionality is strong enough to ensure electron pressure isotropy.

Although kinetic corrections are not discussed until chapter 26, it is worth noting at this point that for weakly collisional situations the foregoing approximation for π_i becomes quite unphysically large: as $\tau_{\perp\to\parallel} \to \infty$, $\pi_i \to \infty$. It is readily seen that this is unphysical since the largest (negative) value π_i can take is $-p_i$: as $\tau_{\perp\to\parallel} \to \infty$, $p_{\perp i}$ becomes completely de-coupled from $p_{\parallel i}$, which can therefore drop to very low values as v increases. The lowest values $p_{\parallel i}$ can attain is zero, of course, making $\pi_i = -p_i$, which is the largest (negative) value possible for π_i. More detailed considerations, chapter 26, indicate $\approx -0.5p_i$ as the limit. If, however, the uncorrected 'Braginskii' [9.2] viscosity, equation (9.75), is used in weakly collisional situations, an unphysically strong forward force is exerted on the flow, sometimes resulting in strange fluid behaviour, such as pressure *increasing* as the flow accelerates.

9.9 The Conservation Equations Summarized

To summarize, a widely used form of the conservation equations is the zero-current one for $j_\parallel = 0$, and $v_n = 0$ (a non-drifting neutral 'background'):

(1) *Particle conservation.*

$$\boxed{\frac{\mathrm{d}}{\mathrm{d}x}(nv) = S_p(x)} \tag{9.78}$$

from equation (9.7).

(2) *Momentum conservation.*

$$\boxed{\frac{\mathrm{d}}{\mathrm{d}x}(m_i n v^2 + p_i + p_e + \pi_i) = -m_i v \overline{\sigma v}_{in} n n_n} \tag{9.79}$$

from equations (9.33) and (9.68), with:

$$\boxed{\pi_i = -\frac{4}{9} p_i \tau_{\perp\to\parallel} \frac{\mathrm{d}v}{\mathrm{d}x}.} \tag{9.80}$$

(3) *Energy conservation.* For ions:

$$\boxed{\frac{\mathrm{d}}{\mathrm{d}x}\left[\left(\tfrac{5}{2}p_i + \tfrac{1}{2}m_i n v^2 + \pi_i\right)v - \kappa_{0i} T_i^{5/2} \frac{\mathrm{d}T_i}{\mathrm{d}x}\right] = enEv + Q_{eq} + Q_{Ei}} \tag{9.81}$$

from equations (9.62) and (9.77). For electrons:

$$\boxed{\frac{\mathrm{d}}{\mathrm{d}x}\left[\frac{5}{2}p_e v - \kappa_{0e}T_e^{5/2}\frac{\mathrm{d}T_e}{\mathrm{d}x}\right] = -envE - Q_{eq} + Q_R + Q_{Ee}} \tag{9.82}$$

from equations (9.60) and (9.61).

(4) *Ohm's law*

$$\boxed{E = -\frac{0.71}{e}\frac{\mathrm{d}kT_e}{\mathrm{d}x} - \frac{1}{en}\frac{\mathrm{d}p_e}{\mathrm{d}x}} \tag{9.83}$$

This provides six equations for the six unknowns, n, v, π_i, T_e, T_i, E as functions of x (and $p_{e,i} \equiv nkT_{e,i}$). It is also common to ignore π_i (see section 11.3 for a discussion of the justification for doing so) and to assume $T_e = T_i$, $p = p_e + p_i$, resulting in the simpler set of three equations in three unknowns n, v, T:

$$\boxed{\begin{aligned} \frac{\mathrm{d}}{\mathrm{d}x}[nv] &= S_p && (9.84)\\ \frac{\mathrm{d}}{\mathrm{d}x}[(m_i v^2 + 2kT)n] &= -m_i v\overline{\sigma v}_{in}nn_n && (9.85)\\ \frac{\mathrm{d}}{\mathrm{d}x}\left[\left(\tfrac{1}{2}m_i v^2 + 5kT\right)nv - \kappa_{0e}T_e^{5/2}\frac{\mathrm{d}T_e}{\mathrm{d}x}\right] &= Q_R + Q_E. && (9.86) \end{aligned}}$$

The above equations are essentially identical to those of Braginskii [9.2] and ZNC [9.1] for one dimension.

9.10 The Sheath-Limited Regime

Further to sections 1.9, 4.10 and 5.3 we note that there are two important situations where the plasma is approximately isothermal in the parallel direction:

(a) Parallel heat conductivity may be very high and weak temperature gradients can be enough to carry all the power which entered the flux tube. Thus, *regardless* of whether significant plasma flow—and thus parallel heat convection—exists or not, the flux tube can be nearly isothermal.

(b) Even if the heat conductivity is low, if it happens that most of the particles enter the flux tube far upstream from the target, parallel convection can carry most of the power. This also reduces parallel temperature variation: as shown in section 2.8 the heat flux density through the sheath is typically:

$$q_{sh} \approx 7kTnv. \tag{9.87}$$

Since $q_{\parallel\text{convected}} = \left(\frac{1}{2}m_i v^2 + 5kT\right)nv = 6kTnv$ (when Mach number = 1) most of the parallel power can be carried by convection in such cases—and with little change of T therefore being required along the flux tube. Indeed if the sheath transmission coefficient were slightly smaller, ~6, rather than ~7, and if the

particle source were entirely at the upstream end, then the flow would be at $M \approx 1$ throughout its length, the convected power would equal the sheath power—and all this would occur with T precisely constant. Even relaxing from this extreme still implies *a tendency for strong flows to flatten parallel temperature profiles*.

This is termed the *sheath-limited regime*, section 1.9, since the SOL is essentially isothermal along a given flux tube and it is the heat transmission properties of the sheath that are defining of SOL properties.

Ohm's law thus reduces to

$$E = -\frac{1}{en}\frac{\mathrm{d}p_e}{\mathrm{d}x} = -\frac{kT_e}{e}\frac{\mathrm{d}n}{\mathrm{d}x} \tag{9.88}$$

which integrates to give the Boltzmann relation, equation (1.12). One can then use that E in the ion energy equation (9.81) so it is not necessary to assume isothermal ions in situations where the electrons—due to their very high conductivity—may well be isothermal.

As pointed out in section 2.6, in the sheath-limited regime SOL collisionality may be too weak to *ensure* the electrons—or ions—are Maxwellian and, depending on the *source* of particles, the distributions may or may not be Maxwellians. If the electrons are non-Maxwellian one still anticipates that the distribution will remain roughly constant along the length of the system because the mean free paths for self-collisions exceed the system length.

9.11 The Conduction-Limited Regime

Here the opposite situation is assumed, convection is not strong, parallel (electron) conduction is limiting and temperature drops along the SOL are substantial. The Boltzmann relation cannot be used in this case and whenever the E-field is needed, Ohm's law is employed, equation (9.36). It is common to assume equipartition, $T_e = T_i$, and to ignore π_i, i–n friction, and Q_R. Consistent with convection not being important, it is implicitly assumed that the recycle ionization occurs very close to the solid surfaces, and so flow effects, including convection, are relegated to a thin layer immediately adjacent to the solid surfaces. This thin region is ignored except for the transition of v from 0 to the plasma sound speed, and the associated density drop.

One now needs only momentum and power equations, and the former takes an extremely simple form:

$$\boxed{\frac{\mathrm{d}}{\mathrm{d}x}[n(m_i v^2 + 2kT)] = 0} \tag{9.89}$$

with $v = 0$ over the vast majority of the SOL, i.e. $p = nkT = \text{constant} = p_{\text{upstream}}$. In the thin particle source layer, $m_i v^2$ increases from 0 to $2kT$ at the target, so $p_{\text{target}} = 1/2 p_{\text{upstream}}$.

The power equation is also simple:

$$\boxed{\frac{\mathrm{d}}{\mathrm{d}x}\left(-\kappa_{0e}T^{5/2}\frac{\mathrm{d}T}{\mathrm{d}x}\right) = Q_E(x)} \tag{9.90}$$

where $Q_E(x)$ is the net energy source density along the flux tube, including cross-field power.

9.12 Self-Collisionality and the Problem of Closing the Fluid Equations

When self-collisionality is very strong $q_{\parallel\text{conduction}} \to 0$ and so the fluid equations close naturally with an energy equation which involves only convection. (One also has $\pi_i \to 0$, which is convenient but not necessary for closure.) Self-collisions drive particle distributions toward (drifting) Maxwellian ones [9.20] for which $\langle u_x^3\rangle = 0$ and $q_{\parallel\text{conduction}} \propto \langle u_x^3\rangle$. For somewhat less collisional situations, one of two approaches is usually taken:

(a) a rough approximation for $q_{\parallel\text{conduction}}$ is obtained from simple gas kinetic theory, yielding $q_{\parallel\text{cond}} = -\kappa_0 T^{5/2}\mathrm{d}T/\mathrm{d}x$. Presumably if the collisionality is not too weak, the approximate nature of this expression will not introduce substantial error into the overall results—particularly for the lower moment quantities $n(x)$, $v(x)$. When collisionality does become very weak, this approximation becomes seriously wrong, see chapter 26.

(b) One retains $q_{\parallel,\text{cond}}$ or $\langle u_x^3\rangle$ but continues to calculate still higher moments of the Boltzmann equation, $\langle u_x^4\rangle$, etc. Presumably, if collisionality is not too weak, one can employ approximations for these higher moments to close the fluid equation hierarchy at that higher level—and, presumably, the errors then introduced for lower moments, including $q_{\parallel,\text{cond}}$, will not be too large. For very weak collisionality however, this approach should also fail—at least strictly speaking.

Fortunately, it appears that nature is more forgiving than the foregoing consideration would imply. In sections 10.6, 10.7 we compare results obtained for some simple systems which are *completely* collisionless, i.e. mean free paths are much longer than system size—comparing a fully kinetic treatment which properly allows for the collisionlessness, and simple fluid models which should, strictly speaking, not be applicable. As will be seen, the principal quantities of practical interest turn out to be about the same as calculated by the two methods. The reason for this good agreement has not been fully explained to date.

References

[9.1] Zawaideh E, Najmabadi F and Conn R W 1986 *Phys. Fluids* **29** 463
[9.2] Braginskii S I 1965 *Reviews in Plasma Physics* vol 1, ed M A Leontovich (New York: Consultants Bureau) p 205

[9.3] Goldston R J and Rutherford P H 1997 *Introduction to Plasma Physics* (Bristol: Institute of Physics) p 219
[9.4] Wesson J 1997 *Tokamaks* 2nd edn (Oxford: Oxford University Press) p 56
[9.5] Holt E H and Haskell R E 1965 *Foundations of Plasma Dynamics* (New York: Macmillan) p 134
[9.6] Scheuer J T and Emmert G A 1990 *Phys. Fluids* B **2** 445
[9.7] Bissell R C and Johnson P C 1987 *Phys. Fluids* **30** 779
[9.8] Wesson J 1997 *Tokamaks* 2nd edn (Oxford: Oxford University Press) p 44
[9.9] Goldston R J and Rutherford P H 1997 *Introduction to Plasma Physics* (Bristol: Institute of Physics) pp 21, 33
[9.10] Wesson J 1997 *Tokamaks* 2nd edn (Oxford: Oxford University Press) p 77
[9.11] Holt E H and Haskell R E 1965 *Foundations of Plasma Dynamics* (New York: Macmillan) p 156
[9.12] Goldston R J and Rutherford P H 1997 *Introduction to Plasma Physics* (Bristol: Institute of Physics) p 149
[9.13] Wesson J 1997 *Tokamaks* 2nd edn (Oxford: Oxford University Press) p 662
[9.14] Goldston R J and Rutherford P H 1997 *Introduction to Plasma Physics* (Bristol: Institute of Physics) p 165
[9.15] Spitzer L Jr 1962 *Physics of Fully Ionized Gases* 2nd edn (New York: Interscience) p 131
[9.16] Wesson J 1997 *Tokamaks* 2nd edn (Oxford: Oxford University Press) p 71
[9.17] Wesson J 1997 *Tokamaks* 2nd edn (Oxford: Oxford University Press) p 89
[9.18] Holt E H and Haskell R E 1965 *Foundations of Plasma Dynamics* (New York: Macmillan) p 99
[9.19] Goldston R J and Rutherford P H 1997 *Introduction to Plasma Physics* (Bristol: Institute of Physics) p 174
[9.20] Holt E H and Haskell R E 1965 *Foundations of Plasma Dynamics* (New York: Macmillan) pp 114–135
[9.21] Sears F W 1953 *An Introduction to Thermodynamics, The Kinetic Theory of Gases and Statistical Mechanics* (Reading, MA: Addison-Wesley)

Chapter 10

1D Models for the Sheath-Limited SOL

10.1 Introduction

The simplest 1D fluid model is the *isothermal fluid model*, where T is taken to be constant along the flow direction. It is very convenient to use this simple model when considering the sheath-limited SOL, and we are therefore interested in comparing it with other 1D models, both fluid ones—e.g., *adiabatic* fluid models—and, particularly, *kinetic* models. We are especially interested in comparisons with *collisionless* kinetic models since the sheath-limited regime is characterized by weak collisionality, section 4.10, raising questions about the validity of fluid treatments, section 9.12. In this chapter we consider these various models and compare the principal results from them. It turns out, fortunately, that the main results vary little amongst the models, and so it is often adequate to use the isothermal fluid model when analysing the sheath-limited SOL.

10.2 The 1D Isothermal Fluid Model

The two temperatures, T_e and T_i, are treated as *constant parameters* that have to be established by some constraints on, or information about, the system other than the fluid equations. The fluid energy conservation equations are thus not used. Collisions are neglected in the momentum equations. Thus from equations (9.78), (9.79) we have the two equations:

$$\frac{\mathrm{d}}{\mathrm{d}x}(nv) = S_p \tag{10.1}$$

$$\frac{\mathrm{d}}{\mathrm{d}x}(m_i n v^2 + nkT_e + nkT_i) = 0 \tag{10.2}$$

i.e. two equations in the two unknowns, $n(x)$, $v(x)$, as functions of the single independent variable x. These are the same equations as used in section 1.8.2.1, although there the momentum equation was not written in the *conservative* form

as it is above. We have also neglected π_i for simplicity, but we will see in section 10.7 that this is a good approximation.

Assuming $S_p \propto n$, as for an ionization source or a cross-field diffusive source, one has $M(x)$ from equation (1.42) where $M \equiv v/c_s$, $c_{s,\mathrm{iso}} \equiv [k(T_e + T_i)/m_i]^{1/2}$, the isothermal acoustic speed. If S_p = constant then $M(x)$ is not greatly changed:

$$\frac{x}{L} = \frac{2M}{1+M^2} \tag{10.3}$$

see figure 1.35, and therefore it can be expected that for any approximately uniformly distributed $S_p(x)$ source, $M(x)$ will have broadly the same form. For cases where $S_p(x)$ is localized, $M(x)$ will rise from $\sim$0 upstream of the source to $\sim$1 on the target side of the source.

Regardless of the form of $S_p(x)$, in general we have for the isothermal plasma:

$$\frac{n(M)}{n_0} = \frac{1}{1+M^2} \tag{10.4}$$

where n_0 is the density far upstream where $M = 0$ is assumed. The Boltzmann relation for the electrons holds, equation (1.12), and combining it with equation (10.4), one has for all $S_p(x)$ the *electrostatic potential*:

$$V(M) = -\frac{kT}{e}\ln(1+M^2). \tag{10.5}$$

One also has, for all $S_p(x)$, the *electric field*:

$$E(M) \equiv \frac{-\mathrm{d}V}{\mathrm{d}x} = \frac{2S_p kT_e}{en_0 c_s}\frac{M(1+M^2)}{(1-M^2)} \tag{10.6}$$

and if S_p = constant then:

$$E(x) = E(M(x)) = \frac{kT_e}{eL}\frac{M(1+M^2)}{(1-M^2)} \tag{10.7}$$

since $\frac{1}{2}n_0 c_s = S_p L$ in that case. L is the system length over which the constant source S_p exists.

We thus have generally, for any $S_p(x)$, the principal results related to *particle* and *momentum* balance:

(a) $n_{se} = 0.5n_0$, where '*se*' indicates the sheath edge, i.e. plasma–sheath interface.
(b) $V_{se} = -0.69kT_e/e$, the pre-sheath, i.e. potential drop in the plasma.
(c) $v_{se} = c_{s,\mathrm{iso}} = [k(T_e + T_i)/m_i]^{1/2}$.
(d) $\Gamma_{se} = \frac{1}{2}n_0 c_{s,\mathrm{iso}}$ the particle flux density exiting the plasma, striking the solid surface.

10.3 Isothermal Model. Non-Constant Source S_p

When S_p = constant, or $S_p \propto n_e$, then the solutions for $M(x)$, etc are particularly simple. It is also possible to allow for some simple but useful x-dependence of $S_p(x)$, while still achieving analytic expressions for $M(x)$, etc. It may be, for example, that the particle source is due to ionization near the surface. Although such localized particle sources are more commonly a feature of the *high recycling regime*, section 4.8, and to a situation where $T(x)$ is not isothermal, nevertheless combinations are conceivable where $T(x) \approx$ constant, yet $S_p(x)$ is not constant.

In problem 1.20 it was shown that it is useful to define a new independent variable y:

$$y \equiv \int_0^x S_p(x')\mathrm{d}x'. \tag{10.8}$$

This then leads to the general result, independent of the form of $S_p(x)$:

$$n/n_0 = (1 + M^2)^{-1} \tag{10.9}$$

and also to the general result:

$$M(\hat{y}) = \hat{y}^{-1} - (\hat{y}^{-2} - 1)^{1/2} \tag{10.10}$$

where

$$\hat{y} \equiv y/y(L) \tag{10.11}$$

and

$$y(L) = \tfrac{1}{2}c_s n_0 \tag{10.12}$$

Once the form of $S_p(x)$ has been specified, $M(x)$ is then obtained from equation (10.10), $n(x)$ from equation (10.9), $V(x)$ from equation (10.5) and $E(x)$ from equation (10.7).

10.4 The Effect of Neutral Friction on Plasma Flow Along the SOL

Neutral hydrogen present in the SOL not only contributes to the local particle balance, via ionization, but also causes drag on the parallel plasma flow through ion–neutral, i–n, collisions—i.e. *collisional drag*. The momentum equation (10.2) now becomes

$$\frac{\mathrm{d}}{\mathrm{d}x}(m_i n v^2 + nkT_e + nkT_i) = -m_i v n \nu_{in}^{\mathrm{mom}} \tag{10.13}$$

where ν_{in}^{mom} is the i–n collision frequency for momentum transfer:

$$\nu_{in}^{\mathrm{mom}} = n_n \overline{v\sigma}_{\mathrm{mom}} \tag{10.14}$$

where n_n is the neutral density (one should allow for both atomic and molecular neutrals); $\overline{v\sigma}_{\mathrm{mom}}$ is the average over the collision (approach) velocities of the ions

and neutrals; σ_{mom} includes both ordinary i–n collisions and charge-exchange ones (for the atoms). It has been assumed here that the neutrals have no average velocity in the plasma flow direction x.

Consider a simple 1D system, figure 10.1, where the neutrals recycled from the target penetrate through a cool non-ionizing region before reaching a hotter, ionization region further upstream [10.1]. We define an ionization front to exist at $x = 0$, with the target at $x = L$. The region [0, L] has no ionization but only momentum collisions. Thus the conservation of ions is simply:

$$nv = n_f v_f = n_t c_s \tag{10.15}$$

where $n_f v_f$ is the ion flux density toward the target at the front and $n_t c_s$ is the ion flux entering the target sheath, assumed to occur at sonic speed. For simplicity we again assume isothermal conditions. Defining as before the Mach number as $M = v/c_s$, we have the plasma density ratio across the collisional region:

$$n_t/n_f = M_f. \tag{10.16}$$

We will show that the effect of momentum collisions is to drive M_f down from unity (for no collisions) toward zero (strong collisionality). Combining the particle and momentum equations (10.13) and (10.15) gives:

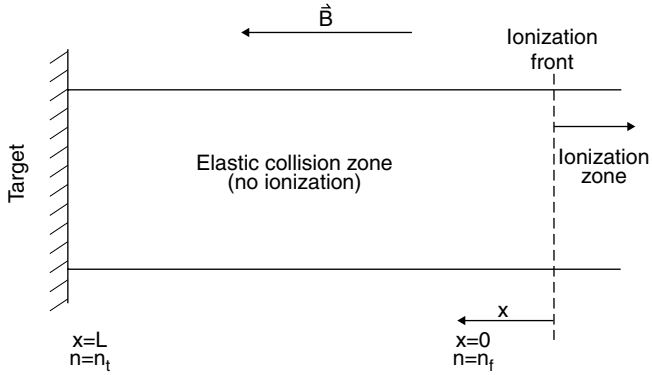

Figure 10.1. Schematic of a cool recycling region where neutrals recycling from the target pass first through a region too cold to ionize them, but where they cause frictional drag to the plasma flow to the target—a 'neutral cushion'. Further upstream T_e is high enough to ionize the neutrals, creating the plasma flow into the 'cushion'.

$$(M^2 - 1)\frac{\mathrm{d}M}{\mathrm{d}x} = -M^2 \nu_{in}^{\text{mom}}/c_s \tag{10.17}$$

which is solved for boundary conditions $M = M_f$ at $x = 0$ (note: we are trying to *find* the value of M_f) and $M = 1$ at $x = L$. $M(x)$ is given by the solution of:

$$M + M^{-1} = M_f + M_f^{-1} - \nu_{in}^{\text{mom}} x/c_s \tag{10.18}$$

where M_f is given by the solution of:

$$M_f + M_f^{-1} - 2 = \nu_{in}^{\text{mom}} L/c_s. \tag{10.19}$$

From equation (10.15) one also has $n(x)$ from:

$$n(x)/n_f = M_f/M(x). \tag{10.20}$$

For strong collisionality M_f^{-1} dominates, giving:

$$n_t/n_f = M_f \approx c_s/L\nu_{in}^{\text{mom}}. \tag{10.21}$$

Estimating the i–n momentum transfer mean free path $\lambda_{in}^{\text{mom}}$ as:

$$\lambda_{in}^{\text{mom}} \approx c_s/\nu_{in}^{\text{mom}} \tag{10.22}$$

gives:

$$\boxed{n_t/n_f = M_f \approx \lambda_{in}^{\text{mom}}/L.} \tag{10.23}$$

Thus, when many i–n momentum collisions occur in the cool region, i.e. $\lambda_{in}^{\text{mom}}/L \ll 1$, the plasma density drop across the collisional region is very large, $n_t/n_f \ll 1$. Since the plasma flux density to the target is simply proportional to n_t, $\Gamma_t = n_t c_s$, the major effect of i–n momentum collisions is to reduce the particle flux to the targets—i.e. the intensity of recycle—for given upstream plasma conditions, i.e n_f. That is, the effect of collisional drag is to *increase the particle confinement time*—since the plasma content is essentially proportional to n_f. Qualitatively this is an obvious result: anything which impedes outflow from a system, increases the confinement of the system. The confinement time of water in a bathtub, for example, is increased by any solid matter clogging the drain.

This reduction in particle outflow to the targets is evidently involved in the phenomenon of divertor detachment, chapter 16.

Unless neutral collisions are extremely frequent, the electrons continue to satisfy the Boltzmann relation throughout and so we have for the potential drop, across the collisional zone:

$$e\Delta V/kT_e \approx -\ln(L/\lambda_{in}^{\text{mom}}) \tag{10.24}$$

which can be much larger in magnitude than the pre-sheath voltage drop for $\nu_{in}^{\text{mom}} = 0$ of $\sim -1/2$, section 1.8.2.9. The extra potential drop is required to accelerate the ions to the sound speed in the presence of i–n momentum loss.

10.5 Other 1D Models for the Sheath-Limited SOL

As discussed in sections 9.1, 9.10, 9.11, the most important distinction to make in SOL modelling is between the *sheath-limited regime*, where electron parallel

heat conduction is strong enough that T is approximately constant along each flux tube in the SOL—and the *conduction-limited regime* where parallel T-gradients are significant. We will slightly extend the definition of the sheath-limited regime to include the possibility of significant *ion* temperature gradients, related to the flow acceleration, and the fact that parallel ion heat conductivity is weaker than for electrons by $\sim(m_e/m_i)^{1/2}$, section 9.6. For all the models considered in this chapter, however, the *isothermal electron* assumption—and thus the Boltzmann relation, equation (1.12)—are assumed to hold. The latter is the most basic and common characteristic of sheath-limited models.

In the following we consider a number of 1D plasma models which are relevant to the sheath-limited regime of the SOL. These models were developed starting from the 1920s with the application in mind of low temperature, non-magnetic gas discharges, but they are equally applicable to the 1D analysis of the SOL. A principal conclusion drawn from comparing the results of the different models is that none of them result in significant differences, for the quantities of most practical consequence, from the results obtained using the simplest model—i.e. the 1D isothermal model, section 10.2. Since the latter model is analytic, convenient and transparent it is fortunate that it is also so reliable.

10.6 The Kinetic 1D Model of Tonks and Langmuir. Cold Ions

In the history of plasma–surface interactions one of the most important modelling results is that by Irving Langmuir and Lewi Tonks in 1929 [10.2], who analysed the classical gas discharge problem. They provide results for both the free-fall regime where $(\lambda_{en}, \lambda_{in} \gg a)$; $\lambda_{en}, (\lambda_{in}) \equiv$ mfp; for electron– (ion–) neutral momentum-loss collisions, and a is the system scale length (the radius of a cylindrical tube, or the separation of the two planes for planar geometry, or the radius of a spherical plasma). They also give results for the neutral-collision-dominated radial diffusion regime $(\lambda_{en}, \lambda_{in} \ll a)$. We consider here their planar, free-fall result where they assumed $T_e \gg T_i$, as is typically the case for non-magnetic, low pressure (free-fall) gas discharges [10.3] and presented a complete *kinetic* analysis. That is, they calculated the actual velocity distribution of the ions at each radial location x, $0 \leq x \leq a$.

Consider the planar, long mean free-path case. The freely falling ions at x came, in part, from the particle source at x'. The increment to the ion particle flux at x due to the source at x' is given by:

$$\delta\Gamma_i(x) = v_i(x, x')\delta n_i(x) = S_p(x')\mathrm{d}x' \tag{10.25}$$

where $v_i(x, x')$ is the velocity gained by ions in falling, without collisions, in the ambipolar E-field:

$$\tfrac{1}{2}m_i\,[v_i(x, x')]^2 = -e(V(x) - V(x')). \tag{10.26}$$

Thus we have for $n_i(x)$:

$$n_i(x) = \int_0^x \frac{S_p(x')\mathrm{d}x'}{[-(2e/m_i)(V(x) - V(x'))]^{1/2}}. \tag{10.27}$$

For the electrons the Boltzmann relation is assumed, equation (1.12):

$$n_e(x) = n_0 \exp\ [eV/kT_e] = n_0 \mathrm{e}^{-\eta} \tag{10.28}$$

with

$$\eta \equiv -eV/kT_e. \tag{10.29}$$

Assume $S_p \propto n_e$, as for impact ionization of electrons, or a cross-field diffusive source (if $n_e = n_i$):

$$S_p(x') = An_0 \mathrm{e}^{-\eta(x')} \tag{10.30}$$

where A is a constant. Thus

$$n_i(x) = An_0(m_i/2kT_e)^{1/2} \int_0^x \mathrm{e}^{-\eta(x')}(\eta(x) - \eta(x'))^{-1/2}\mathrm{d}x'. \tag{10.31}$$

One may now insert n_e and n_i into the *Poisson equation*:

$$\frac{\mathrm{d}^2V}{\mathrm{d}x^2} = -e(n_i - n_e)/\varepsilon_0 \tag{10.32}$$

to obtain the *plasma-sheath* equation, valid for both plasma and sheath:

$$\left(\frac{\varepsilon_0 kT_e}{e^2 n_0}\right)\frac{\mathrm{d}^2\eta}{\mathrm{d}x^2} + \mathrm{e}^{-\eta} - A\left(\frac{m_i}{2kT_e}\right)^{-1/2} \int_0^x \mathrm{e}^{-\eta'}(\eta - \eta')^{-1/2}\mathrm{d}x' = 0. \tag{10.33}$$

One notes the appearance of the *Debye length*:

$$\lambda_{\mathrm{Debye}} = (\varepsilon_0 kT_e/e^2 n_0)^{1/2} \tag{10.34}$$

demonstrating again that the natural scale length in the sheath (where the first term is not negligible since $n_e \neq n_i$) is the Debye length. In order to solve the *plasma* equation, where $n_e = n_i$ is assumed, the first term is dropped. Defining:

$$\alpha \equiv A(m_i/2\,kT_e)^{1/2}, \quad s \equiv \alpha x \tag{10.35}$$

then

$$\mathrm{e}^{-\eta(s)} - \int_0^s \mathrm{e}^{-\eta(s')}(\eta(s) - \eta(s'))^{-1/2}\mathrm{d}s' = 0. \tag{10.36}$$

Tonks and Langmuir found a series solution for $\eta(s)$; actually, it turned out to be more convenient to obtain the inverse function $s(\eta)$, and the first few terms of their solution are given by:

$$s = \frac{2}{\pi}\eta^{1/2}\left(1 - \frac{\eta}{3} - \frac{\eta^2}{30}\cdots\right). \tag{10.37}$$

We may readily confirm from equation (10.37) that at $x = 0$, midway between the two ion-absorbing surfaces, $\eta = 0$, $\mathrm{d}s/\mathrm{d}\eta = \infty$, $\mathrm{d}\eta/\mathrm{d}s = 0$, i.e. the electric field is zero. We have for the normalized electric field:

$$\frac{\mathrm{d}\eta}{\mathrm{d}s} = \left[\frac{2}{\pi}\left(\tfrac{1}{2}\eta^{-1/2} - \tfrac{1}{2}\eta^{1/2} - \tfrac{1}{12}\eta^{3/2}\cdots\right)\right]^{-1} \tag{10.38}$$

and at some value $\eta = \eta_0$, one finds that the field goes to infinity—the *plasma-sheath edge* is encountered. Retaining just the first two terms in the expansion, one finds $\eta_0 = 1$. Retaining more terms one finds $\eta_0 = 0.854$. That is the *pre-sheath* potential drop is $-0.854kT_e/e$, and so $n_{se}/n_0 = \mathrm{e}^{-0.854} = 0.426$. Inserting $\eta_0 = 1$ into equation (10.37) and retaining just the first two terms, one finds that the plasma–sheath interface occurs at $s = s_0 = 4/3\pi = 0.424$; retaining more terms gives $s_0 = 0.405$. We note further that this must correspond (to within the normally thin and negligible width of the sheath) to the actual space available for the plasma to exist, i.e. x_0, the actual (half) separation (in metres, say) of the two solid plane walls, that is:

$$s_0 = 0.405 = \alpha x_0. \tag{10.39}$$

We thus see again, section 1.8.2.6, that a *constraint* exists on the source strength S_p in order that the plasma fit into the space available:

$$A(m_i/2kT_e)^{1/2}x_0 = 0.405. \tag{10.40}$$

For an ionization source we have:

$$A = n_n\overline{\sigma v_{iz}}(T_e) \tag{10.41}$$

and so this result is seen again, section 1.8.2.6, to constrain T_e to have some specific value, dependent on the product $n_n x_0$, if a steady-state, self-sustained plasma is to exist.

The ion particle flux density at the sheath edge:

$$\begin{aligned}\Gamma_{se} &= \int_0^{x_0} S_p(x')\mathrm{d}x' = \int_0^{x_0} An_0\mathrm{e}^{-\eta(x')}\mathrm{d}x' \\ &= \frac{An_0s_0}{\alpha}\int_0^1 \mathrm{e}^{-\eta}\mathrm{d}(s'/s_0)\end{aligned} \tag{10.42}$$

and the integral is a pure number defined to be h_0 and found from the series expansion to be $h_0 = 0.851$. Thus:

$$\Gamma_{se} = \sqrt{2}n_0h_0s_0(kT_e/m_i)^{1/2}. \tag{10.43}$$

We may define the sheath edge velocity v_{se} by:

$$\Gamma_{se} \equiv n_{se}v_{se} = n_0\mathrm{e}^{-\eta_0}v_{se} \tag{10.44}$$

Table 10.1. Comparison of isothermal fluid model and the Tonks–Langmuir kinetic model ($T_i = 0$) [10.2].

	Quantity	Normalization factor	Model: Isothermal fluid	Model: Tonks & Langmuir
1.	Plasma density at the sheath edge, n_{se}	n_0	0.5	0.425
2.	Plasma flow velocity at sheath edge, v_{se}	$(kT_e/m_i)^{1/2}$	1	1.144
3.	Plasma potential at sheath edge, V_{se}	kT_e/e	−0.69	−0.854
4.	(Floating) wall potential, V_{wall}	kT_e/e	−3.53	−3.56
5.	Particle outflux density, Γ_{se}	$n_0(kT_e/m_i)^{1/2}$	0.5	0.487
6.	Ion energy outflux density, $q_{i,se}$	$n_0kT_e(kT_e/m_i)^{1/2}$	0.25	0.34
7.	Electron energy outflux density, $q_{e,se}$	$n_0kT_e(kT_e/m_i)^{1/2}$	2.42	2.29
8.	Total energy outflux density, q_{se}	$n_0kT_e(kT_e/m_i)^{1/2}$	2.67	2.63
9.	Electron cooling rate, $q_{e,\text{cooling}}$	$n_0kT_e(kT_e/m_i)^{1/2}$	2.67	2.63
10.	Sheath heat transmission coefficient, $\gamma_{sh} = q_{se}/kT_e\Gamma_{se}$	—	5.34	5.40

thus

$$\begin{aligned} v_{se} &= \sqrt{2}\mathrm{e}^{\eta_0}h_0s_0c_{s,\text{iso}} \\ &= 1.144c_{s,\text{iso}} \end{aligned} \tag{10.45}$$

which is essentially the Bohm criterion result obtained by David Bohm in the 1940s, from analysis of the *sheath* equation, section 2.3. $c_{s,\text{iso}}$ = isothermal sound speed = $(kT_e/m_i)^{1/2}$ when $T_i = 0$. The results for the principal quantities of interest are given in table 10.1. These results are independent of the specific form of $S_p(x)$ [10.4]. (There is an error in the original results of [10.2].)

Tonks and Langmuir were the first to establish two critically important features of the plasma–sheath interface:

(a) the electric field at the sheath edge $E_{se} \to \infty$;
(b) the velocity of the sheath edge $v_{se} \approx (kT_e/m_i)^{1/2}$.

Before Langmuir's work it was thought that the ions must leave the plasma with a speed of order $(kT_i/m_i)^{1/2}$, and since it was understood that $T_e \gg T_i$ in a low pressure gas discharge (due to ohmic heat going to the electrons, while it could be argued that the ions and neutrals would have temperatures about equal to the wall), it was not understood why the ion velocity was found experimentally to be so much higher. Langmuir had thus established the essence of the Bohm criterion, a few decades before Bohm did.

It may be noted from table 10.1 that the differences for these quantities, which are the ones of greatest practical interest, is slight between the isothermal fluid model and the kinetic results of Tonks and Langmuir. In the light of the fact that the kinetic modelling assumed *complete* collisionlessness it is remarkable that a fluid model can do so well in matching the kinetic results.

10.7 Kinetic Models for $T_i \neq 0$

For non-magnetic, low pressure discharges $T_e \gg T_{i,n}$, typically, but for tokamak SOLs—where both electrons and ions receive heat input from the confined plasma—one is more interested in the case of $T_i \approx T_e$. In particular we are interested to establish the effect of *ion acceleration cooling*, which can occur even if the electrons are isothermal. Completely collisionless, kinetic treatments are particularly valuable since they describe the one extreme. Two such solutions have been published: (a) Emmert *et al.* [10.5], hereafter referred to as EWMD, (b) Bissell and Johnson [10.6, 10.7], hereafter referred to as BJ. The principal differences of the two treatments is the assumption about the ion sources:

$$S(x, v_x)_{\mathrm{EWMD}} = S_p(x)(m_i|v_x|/2kT_s)\exp(-m_i v_x^2/2kT_s) \tag{10.46}$$

$$S(x, v_x)_{\mathrm{BJ}} = S_p(x)(m_i/2\pi kT_s)\exp(-m_i v_x^2/2kT_s) \tag{10.47}$$

where T_s is a (specified) 'source temperature'. These two sources are clearly quite similar, but differing in that the BJ source is that which would result from electron, or photon, etc (i.e. neutral velocity-independent) ionization of a one-dimensional Maxwellian distribution of neutrals with $T_n = T_s$. Perhaps surprisingly, such a source does *not* result in a Maxwellian distribution of ions [10.6, 10.7]—even assuming no E-field or other ion forces—since the source must provide forward-going particles at a high rate in order to sustain Maxwellian *fluxes*. The EWMD source, on the other hand, does result in a Maxwellian ion distribution (if $E = 0$).

The ion sources are then inserted into an equation equivalent to that for the analysis of Tonks and Langmuir, equation (10.33), and the Boltzmann relation is again used for the electrons. It is readily shown that the energy sources are slightly different for the two source assumptions:

$$S_{E,\mathrm{EWMD}} = 2kT_s \quad S_{E,\mathrm{BJ}} = \tfrac{3}{2}kT_s \tag{10.48}$$

where in each case $2 \times \frac{1}{2}kT_s$ is due to averaging $\frac{1}{2}m_i(v_y^2 + v_z^2)$ while for EWMD (BJ) one obtains 1 (1/2) kT_s due to averaging $\frac{1}{2}mv_x^2$. Thus it is seen that, indeed, EWMD gives a Maxwellian flux of ion energy, see equation (2.30).

The quantities of practical interest, calculated from EWMD and BJ, were given in table 1.2 for the assumption of $T_i = T_e$, where they are compared with the results for the isothermal fluid model, section 10.2. The flow acceleration causes $T_{\|i,se} < T_{\|i}(x = 0)$; for example for BJ $T_{\|i,se}/T_e = 0.16$ (for the case of $T_{\|i}(0) = T_{\perp i}(0) = T_e$). Nevertheless, as can be seen from table 1.2, the agreement with the isothermal fluid model is quite close for these quantities of practical importance (considering $T_{\|i}$ not to be in the latter category).

The approximation for heat conductivity obtained from simple gas kinetic theory, section 9.6, would imply $q_{\mathrm{cond}} \to \infty$ for very long mean free paths, since $K \propto \lambda_s$. Clearly this is unphysical and *kinetic corrections* are needed when $\lambda_s/L \to \infty$, or $\lambda_s/\ell_T \to \infty$, where $\ell_T \equiv [\mathrm{d}T/\mathrm{d}x)/T]^{-1}$ is the parallel

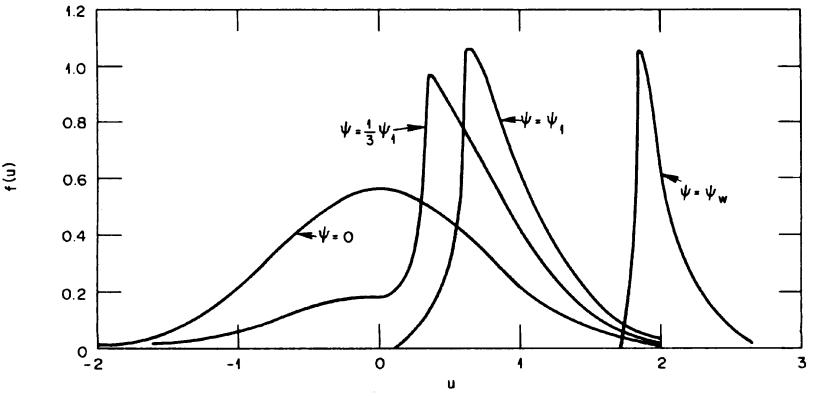

Figure 10.2. The ion distribution against $u \equiv v_x/(2kT_i/m_i)^{1/2}$ at the mid-point of the 1D system ($\psi = 0$), at a location part way to the sheath edge ($\psi = \psi_1/3$), at the sheath edge ($\psi = \psi_1$) and at the wall ($\psi = \psi_w$) [10.5]. Note how non-Maxwellian and asymmetric the ion velocity distribution is, except at the mid-point. Note also the absence of back-going ions at the sheath edge.

temperature characteristic length, chapter 26. It was also noted in section 9.6 that often ion heat conductivity is, in any case, neglected compared with ion heat convection. These collisionless ($\lambda_s/L = \infty$) kinetic solutions provide an opportunity to assess just how important (as it turns out, *unimportant*) ion heat conduction is, in a situation where it is the strongest it can possibly be. Here the ion velocity distribution is extremely unsymmetrical, see figure 10.2, implying, one would think, a large $\langle u_x^3 \rangle$, i.e. large $q_{i,\text{conduction}}$. It turns out, however, that $|q_{i,\text{conduction}}|/(q_{i,\text{convection}})$ is neverthless quite small, see figure 10.3 [10.8]. Surprisingly $q_{i,\text{conduction}}$ is actually weakly *negative*, carrying heat in the *upstream* direction, but its small magnitude makes this of no practical importance.

This example should *not*, however, be taken to prove that $q_{i,\text{conduction}}$ is *never* important. In the *high recycling regime* of divertor operation, section 4.8, there is no plasma flow far upstream from the target, and so $q_{i,\text{convection}} \to 0$ (assuming also that there is no *flow reversal*, chapter 15, or *drift effects*, chapter 18); in such situations $q_{i,\text{conduction}}$ can become important and then *kinetic corrections* may be required, chapter 26. In these present collisionless cases, however, a spatially uniform source was used, $S_p(x) = \text{constant}$, and so v and $q_{i,\text{convection}}$ are substantial at all locations.

Consider also the ion parallel viscous stress, π_i, which, in the absence of any kinetic correction would go to $-\infty$ for these completely collisionless cases, $\tau_{\perp\to\parallel} \to \infty$, $\pi \to -\infty$, section 9.8. From the computed $T_{\parallel i}$ it is possible to calculate π_i at each location, since $\pi_i = \frac{2}{3}(p_{\parallel i} - p_{\perp i}) = \frac{2}{3}nk(T_{\parallel i} - T_{\perp i})$, section 9.8, and $T_{\perp i}(x) = T_{\perp i}(0) = T_{\parallel i}(0)$, constant. One thus finds $\pi_i(0) = 0$

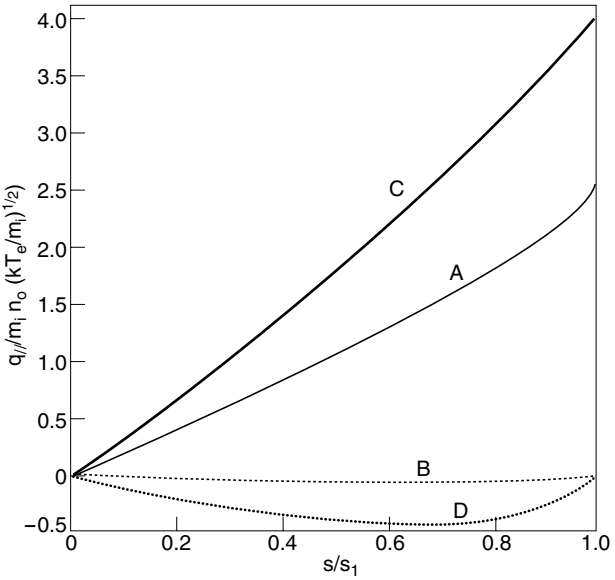

Figure 10.3. Completely collisionless case. Contribution of the normalized conducted heat flux density to the total heat flux density as a function of distance calculated from a full kinetic analysis [10.7]: (A) total for the BJ source, (B) conducted for BJ source, (C) total for EWMD source, (D) conducted for EWMD source. Spatially constant particle sources, $S_p(x)$. Clearly, parallel heat conduction is not important here even though the plasmas are completely collisionless.

and at the sheath edge one obtains the following results for the EWMD source:

$\frac{n_{se}}{n_0}$	$\frac{T_{\parallel i,se}}{T_0}$	$\frac{T_{\perp i,se}}{T_0}$	$\frac{p_{\parallel i,se}}{p_0}$	$\frac{p_{\perp i,se}}{p_0}$	$\frac{p_{i,se}}{p_0}$	$\frac{\pi_{i,se}}{p_0}$	$\frac{\pi_{i,se}}{p_{i,se}}$
0.677	0.254	1	0.169	1	0.501	−0.33	−0.66

where $T_{\perp i}(0) = T_{\parallel i}(0) = T_e \equiv T_0$, $p_0 \equiv n_0 k T_0$. In chapter 26 kinetic corrections are considered; one analysis [10.9] estimates that π_i should be limited to $-(4/7)p_i$, which is close to the result above at the *se* for this extreme of complete collisionlessness. One can also see that—for this extreme case—about as much of the 'push' on the flow comes from the viscous stress as comes from the pressure drop: $\Delta p_i \equiv 0.499 p_0$, $\Delta \pi_i \equiv 0.33 p_0$. This should not mislead us from noting, however, that *all* of the 'push' actually comes from the '$p_\parallel$-reservoir', $\Delta p_{\parallel i} = 0.83 p_0$, since none of the '$p_\perp$-pressure reservoir' is available to accelerate the flow when there are no self-collisions.

10.8 Adiabatic, Collisionless Fluid Models

We now turn to fluid models, and allow $T_{\|i}(x)$ to be non-constant (due to flow-acceleration cooling). In this section all collisions are neglected, including $Q_{\perp\to\|}$ and Q_{eq}, and only the equation for $T_{\|i}$, i.e. $p_{\|i}$, is used, equation (9.72). Also ion conduction is neglected as the method of closing the set of fluid equations; although that is strictly not justified for weak/no collisions, we have seen, figure 10.3, that the error involved can be quite small. Thus the three fluid equations are, see chapter 9:

$$\frac{\mathrm{d}}{\mathrm{d}x}(nv) = S_p(x) \tag{10.49}$$

$$\frac{\mathrm{d}}{\mathrm{d}x}(m_i n v^2 + p_{\|i} + p_e) = 0 \tag{10.50}$$

$$\frac{\mathrm{d}}{\mathrm{d}x}\left(\tfrac{1}{2}m_i n v^3 + \tfrac{3}{2}p_{\|i}v\right) = -v\frac{\mathrm{d}p_e}{\mathrm{d}x} + S_{E\|i} \tag{10.51}$$

together with $T_e =$ constant, $T_{\perp i} =$ constant; $S_{E\|i}$ is given by:

$$S_{E\|i}^{\mathrm{BJ}} = \tfrac{1}{2}kT_s S_p(x) \tag{10.52}$$

$$S_{E\|i}^{\mathrm{EWMD}} = kT_s S_p(x) \tag{10.53}$$

The Boltzmann relation is assumed for the electrons.

One notes that while the flow is termed '*adiabatic*' there is in fact the energy addition associated with the particle addition, $\frac{1}{2}kT_s$ (BJ), kT_s (EWMD). The flow is truly only adiabatic in the sense that no *additional* heat input occurs, such as perpendicular heat conduction. Because $Q_{\perp\to\|} = 0$ there is no 'help' from the $p_{\perp i}$-pressure reservoir and all the 'push' comes from $p_{\|i}$ and p_e. Because one does not need to consider $p_{\perp i}$ or $T_{\perp i}$, only the $T_\|$–energy equation is needed and one does not introduce viscous stress π_i.

Various assumptions have been made by different authors at this point:

(1) Bissell *et al* [10.7] solved the equations for $S_p^{\mathrm{BJ}}(x) =$ constant and assumed the 'source temperature' $T_s = 3T_0$, also setting $T_e = T_0$. The reason for this odd-looking assumption for T_s is that, as can be noted from examining equation (10.51), as $x \to 0$, where $v \to 0$ is assumed to hold, the amount of heat carried per ion is $\frac{3}{2}kT_{\|i}(0)$, but the BJ source only provides $\frac{1}{2}kT_s$ per ion. Therefore, if one wants to have the convenient, upstream boundary condition that $T_e = T_{\|i}(0)$ then one is obliged to specify $T_s = 3T_0$ for the 'source temperature'. $T_{\perp i}$ can be freely assigned and so one chooses here $T_e = T_{\|i}(0) = T_{\perp i}(0) = T_0$. The arbitrariness of assuming a particular value of T_s may seem surprising, but it should be noted that the 'source temperature', T_s, is not generally a physically measurable quantity or even a physically *meaningful* quantity. For the specific case of electron-impact

ionization of Maxwellian neutrals at temperature T_n, it is true that one should use the BJ source, equation (10.47), and set $T_s = T_n$, where T_n is indeed a measurable, physical quantity. However, cross-field diffusive sources are common in the edge, in which case one asks what meaning T_s has, for either the BJ or EWMD source, equations (10.46), (10.47)? The answer is that one should simply consider it to be a purely *mathematical* parameter which one is free to adjust, for example to achieve $T_e = T_i$ far upstream from the target—or some other ratio, if one has experimental information about the upstream temperature ratio. It is precisely this freedom which has been exploited here.

$T_{\|i}(x)$ drops considerably along the flow, reaching $T_{\|i,se}/T_{\|i}(0) = 0.18$, which is quite close to the kinetic result of the last section, namely 0.16.

(2) Scheuer and Emmert [10.8] used $S_p^{\mathrm{EWMD}}(x) =$ constant, also $S_p^{\mathrm{BJ}}(x) =$ constant, but with $T_s = T_e \equiv T_0$ assumed. Thus for BJ they had $T_{\|i}(0)/T_0 = \frac{1}{3}$ and for EWMD, $T_{\|i}(0)/T_0 = \frac{2}{3}$. The principal results are given in table 10.2. While it would almost never be the case that the upstream temperature ratio would just happen to have these particular values, since the principal purpose here is to demonstrate how slight the differences are with the isothermal fluid mode, we simply make comparison with the latter for the same upstream temperature assumption, see table 10.2 which contains the comparisons. For BJ, $T_{\|i,se}/T_0 = 0.162$; for EWMD, $T_{\|i,se}/T_0 = 0.282$. By straightforward algebraic manipulation, one can rearrange equations (10.49)–(10.51) to produce three equations of the form:

$$\frac{\mathrm{d}n}{\mathrm{d}x} = f(n, v, T_{\|i}, S_p, T_s, T_e)/\left(v^2 - \frac{3kT_{\|i}}{m_i} - kT_e/m_i\right) \quad (10.54)$$

$$\frac{\mathrm{d}v}{\mathrm{d}x} = g(n, v, T_{\|i}, S_p, T_s, T_e)/\left(v^2 - \frac{3kT_{\|i}}{m_i} - kT_e/m_i\right) \quad (10.55)$$

$$\frac{\mathrm{d}T_{\|i}}{\mathrm{d}x} = h(n, v, T_{\|i}, S_p, T_s, T_e)/\left(v^2 - \frac{3kT_{\|i}}{m_i} - kT_e/m_i\right) \quad (10.56)$$

with f, g, h some (not particularly interesting) functions. One notes the appearance of the common factor in the denominator:

$$v^2 - \frac{3kT_{\|i}}{m_i} - kT_e/m_i. \quad (10.57)$$

When this quantity reaches zero the solutions 'blow up', all the derivatives go to zero, i.e. a singularity is encountered, precisely in the same way that occurred with the isothermal fluid model, section 1.8.2.5. As before, we interpret this as indicating the location of the *plasma–sheath interface*, the *sheath-edge*. At this point the flow is *sonic*, when based on the local *collisionless*, 'adiabatic' sound speed:

$$\boxed{c_{s,ad}^{\mathrm{collisionless}} = [(3kT_{\|i} + kT_e/m_i)]^{1/2}.} \quad (10.58)$$

Table 10.2. Comparison of 'adiabatic' fluid models with isothermal model [10.7].

Quantity	Normalization factor	No. 1 ad. model/ isothermal	No. 2 ad. model/ isothermal	No. 3 ad. model/ isothermal	No. 4 ad. model/ isothermal
Plasma density at sheath edge, n_{se}	n_0	0.486/0.5	0.497/0.5	0.496/0.5	0.499/0.5
Plasma flow velocity at sheath edge, v_{se}	$(kT_0/m_i)^{1/2}$	1.22/1.16	1.36/1.29	1.30/1.26	1.38/1.34
Plasma potential at sheath edge, V_{se}	kT_0/e	−0.72/−0.69	−0.70/−0.69	−0.70/−0.69	−0.69/−0.69
Floating wall potential, V_w	kT_0/e	−3.33/−3.39	−3.22/−3.28	−3.27/−3.30	−3.21/−3.24
Particle outflux density, Γ_{se}	$n_0(kT_0/m_i)^{1/2}$	0.59/0.58	0.68/0.65	0.65/0.63	0.69/0.67
Ion heat outflux density, q^i_{se}	$n_0kT_0(kT_0/m_i)^{1/2}$	1.18/0.87	1.59/1.62	1.22/1.45	1.60/1.95
Electron heat outflux density, q^e_{se}	$n_0kT_0(kT_0/m_i)^{1/2}$	3.16/3.11	3.53/3.41	3.40/3.35	3.60/3.52
Total heat outflux density, q_{se}	$n_0kT_0(kT_0/m_i)^{1/2}$	4.34/4.36	5.12/5.02	4.61/4.80	5.20/5.46

Model No. 1: adiabatic, collisionless, 1D fluid model with $S^{\mathrm{BJ}}(v)$ and $T_{\|,i}(0)/T_e = 1/3$
Model No. 2: adiabatic, collisionless, 1D fluid model with $S^{\mathrm{EWMD}}(v)$ and $T_{\|,i}(0)/T_e = 2/3$
Model No. 3: adiabatic, collisional, 1D fluid model with $S^{\mathrm{BJ}}(v)$ and $T_i(0)/T_e = 3/5$
Model No. 4: adiabatic, collisional, 1D fluid model with $S^{\mathrm{EWMD}}(v)$ and $T_i(0)/T_e = 4/5$.

In each case the isothermal model, shown for comparison, assumed for the collisionless cases the adiabatic model value for $T_{\|i}(0)$; and for the collisional cases the adiabatic model value for $T_i(0)$.
Example No 1 ad. model:

$$v_{se} = (3 \times 0.162 + 1)^{1/2}(kT_0/m_i)^{1/2} = 1.22(kT_0/m_i)^{1/2}$$
$$q^i_{se} = \left(\tfrac{3}{2} \times 0.162 + \tfrac{1}{2} + \tfrac{1}{2} + \tfrac{1}{2}(1.22)^2\right) \times 0.59 n_0 kT_0 (kT_0/m_i)^{1/2}$$
$$= 1.18 n_0 kT_0 (kT_0/m_i)^{1/2}$$

Example No 2 isothermal model:

$$v_{se} = (1/3 + 1)^{1/2}(kT_0/m_i)^{1/2} = 1.16(kT_0/m_i)^{1/2}$$
$$q^i_{se} = \left(\tfrac{5}{2} \times \tfrac{1}{3} + \tfrac{1}{2} \times \tfrac{4}{3}\right) \times 0.58 n_0 kT_0 (kT_0/m_i)^{1/2} = 0.87 n_0 kT_0 (kT_0/m_i)^{1/2}$$

Insertion of the above values of $T_{\|i,se}$ confirms the tabulated values of v_{se}, table 10.2, at which the singularity was encountered.

10.9 Adiabatic, Strongly Collisional Fluid Models

Scheuer and Emmert [10.8] considered the opposite extreme to that of the last section, assuming now $\tau_{\perp\to\|} \to 0$, i.e. $T_{\|i} = T_{\perp i} = T_i$. This would correspond to strong (self-) collisionality and $\pi_i \to 0$ The fluid equations are now:

$$\frac{\mathrm{d}}{\mathrm{d}x}(nv) = S_p(x) \tag{10.59}$$

$$\frac{\mathrm{d}}{\mathrm{d}x}(m_i n v^2 + p_i + p_e) = 0 \tag{10.60}$$

$$\frac{\mathrm{d}}{\mathrm{d}x}\left(\tfrac{1}{2}m_i n v^2 + \tfrac{5}{2}p_i v\right) = -v\frac{\mathrm{d}p_e}{\mathrm{d}x} + S_E \tag{10.61}$$

plus the Boltzmann relation for the electrons. They used $S_p^{\mathrm{BJ}}(x) =$ constant, also $S_p^{\mathrm{EWMD}}(x) =$ constant.

$$S_{Ei}^{\mathrm{BJ}} = \tfrac{3}{2}kT_s S_p(x) \tag{10.62}$$

$$S_{Ei}^{\mathrm{EWMD}} = 2kT_s S_p(x). \tag{10.63}$$

Assuming $T_s = T_e \equiv T_0$ gives the result that for BJ, $T_i(0)/T_s = 3/5$; for EWMD, $T_i(0)/T_s = 4/5$. As in the last section, singularities are now encountered when v reaches the local *collisional* 'adiabatic' sound speed:

$$c_{s,ad}^{\mathrm{collisional}} = \left[\left(\tfrac{5}{3}kT_i + kT_e\right)/m_i\right]^{1/2} \tag{10.64}$$

i.e. the familiar adiabatic sound speed for a monatomic gas. The principal results are given in table 10.2. For BJ, $T_{i,se}/T_0 = 0.418$; for EWMD, $T_{i,se}/T_0 = 0.547$. The ion temperature and pressure drops are less, in bringing the flow up to sonic speed, when the full pressure reservoir is available, i.e. for strongly collisional conditions.

10.10 Adiabatic, Intermediate Collisional Fluid Models

Examination of table 10.2 shows little difference for the principal results of practical interest between the two extremes of zero (self-) collisionality, and infinitely strong (self-) collisionality. For conditions of intermediate collisionality, the fluid formulation is more complex than the models used in the last two sections, since π_i is now involved, with its complex dependence on n, T and $\mathrm{d}v/\mathrm{d}x$. In light of the small differences found for the two extremes of collisionality, it may not be considered to be worth introducing such complexity. The inclusion of the parallel

viscous stress will usually not result in much effect, although some special cases can disobey this generalization [10.10].

Complexity is also introduced by inclusion of intermediate collisionality as regards *equipartition* although the formulations are relatively simple for the two extremes of $T_e = T_i$ and, on the other hand, complete de-coupling of the electron and ion energy equation. It is evident that, in the sheath-limited regime, i.e. where heat conductivity is not limiting, that the degree of equipartition will make little difference. We have just considered the extreme of T_e and T_i fully de-coupled and $T_e(x) =$ constant. Consider the opposite case of $T_e(x) = T_i(x)$; if collisionality is strong enough to force $T_e = T_i$ it is certainly strong enough to force $T_{\perp i} = T_{\parallel i}$, so consider the results of section 10.9 where we found that T_i only dropped about 30% as the flow accelerated to sonic. With the electron pressure reservoir now also available to drive the flow, the T-drop will be still less. The local sound speed is now:

$$c_s = \left(\tfrac{8}{3}kT/m_i\right)^{1/2} \tag{10.65}$$

which, with $T_{se} \lesssim T_0$, gives a value of $v_{se} \lesssim 1.63(kT_0/m_i)^{1/2}$, which is not greatly different than for the other models, table 10.2. The other results of practical interest will also be little changed.

10.11 Comparing 1D Collisionless Kinetic and Collisionless Fluid Models

The adiabatic collisionless fluid model of section 10.8, which is essentially the same as the double adiabatic collisionless fluid model of Chew *et al*, CGL [10.11, 10.10], cannot, of course, be expected to give precisely the same results as a collisionless *kinetic* treatment, such as that of EWMD and BJ, section 10.7. It is remarkable, however, how close the results from these very different treatments can be—at least for the simple cases where they have been compared [10.8]. Some of the results of this comparison were given in table 1.2, compare models 3, 4, 5 there. See Scheuer and Emmert [10.8] for further details of these comparisons. This confirms that the assumptions used in closing the fluid equation hierarchy for the adiabatic collisionless fluid model—namely (a) to neglect $q_{\parallel}^{\text{conduction}}$ and (b) to treat $p_\perp$ and $T_\perp$ as constants—are evidently good ones to make. Considering how strongly non-Maxwellian the ion distributions are for collisionless conditions, figure 10.2, it seems surprising that the agreement can be so good. Figure 10.4 compares the $n(s)$ profiles for the two collisionless kinetic models of EWMD and BJ with the collisionless fluid model of Scheuer and Emmert (i.e., essentially CGL); a spatially constant source was assumed [10.8]. The agreement is indeed quite good all across the plasma. Figure 10.5 is similar, but for the parallel heat flux density. As might be anticipated, the agreement is not quite as good for this higher moment, but it is nevertheless quite close. Evidently, *so long as particles, momentum and energy are conserved, one usually will not go too far*

wrong in using an appropriate (collisionless) fluid model, rather than a full kinetic analysis—even in the extreme case of no collisions at all.

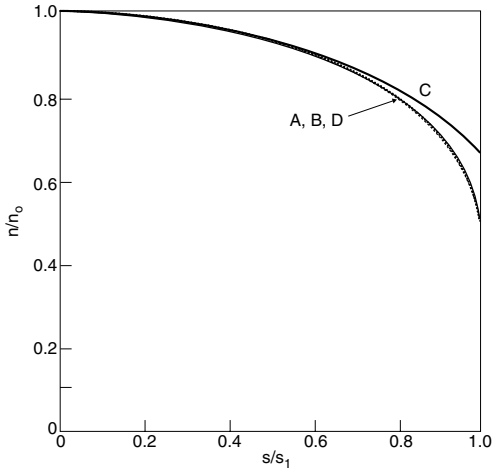

Figure 10.4. Completely collisionless case. Normalized density profile for a spatially constant source [10.8]: (A) from kinetic analysis using BJ source, (B) collisionless fluid model using BJ source, (C) from kinetic analysis using EWMD source, (D) collisionless fluid model using EWMD source. Here $T_e = T_s = T_0$. There are small differences between curves A and B near $s/s_1 = 1$, which are not obvious here.

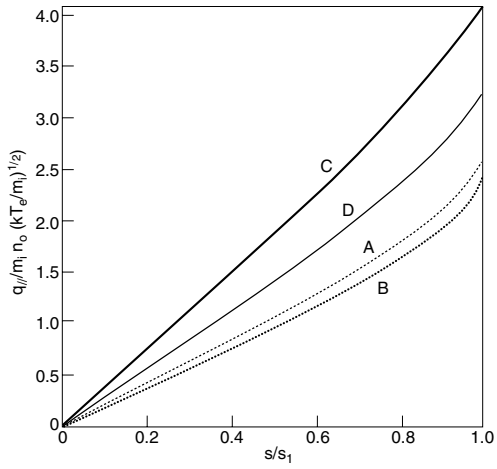

Figure 10.5. As figure 10.4 but for normalized energy flux density.

References

[10.1] Stangeby P C 1695 *Nucl. Fusion* **33** 1993
[10.2] Tonks L and Langmuir I 1929 *Phys. Rev.* **34** 876
[10.3] von Engel A 1965 *Ionized Gases* 2nd edn (Oxford: Oxford University Press) p 265
[10.4] Harrison E R and Thompson W B 1959 *Proc. R. Soc.* **72** 2145
[10.5] Emmert G A, Wieland R M, Mense A T *et al* 1980 *Phys. Fluids* **23** 803
[10.6] Bissell R C and Johnson P C 1987 *Phys. Fluids* **30** 779
[10.7] Bissell R C, Johnson P C and Stangeby P C 1989 *Phys. Fluids* B **1** 1133
[10.8] Scheuer J T and Emmert G A 1990 *Phys. Fluids* B **2** 445
[10.9] Radford G J 1992 *Contrib. Plasma Phys.* **32** 297
[10.10] Zawaideh E, Najmabadi F and Conn R W 1986 *Phys. Fluids* **29** 463
[10.11] Chew G G, Goldberger M L and Low F E 1956 *Proc. R. Soc.* A **236** 112

Chapter 11

1D Modelling of the Conduction-Limited SOL

11.1 Introduction

Modelling of the sheath-limited SOL, using say the isothermal fluid model, requires very little attention to the question of *boundary conditions*: one can specify either the 'upstream' density, n_u, or the target density, n_t. For $|M_t| = 1$ these are simply related, $n_u = 2n_t$. One usually makes no explicit assumption about power input, but rather the spatially constant temperature is specified as a SOL *parameter*. Modelling of the conduction-limited SOL, on the other hand, requires more attention to the boundary conditions, including the location chosen where they are to be imposed. Assuming that a fluid model is used based on the three conservation equations of particles, momentum and energy, it might seem that three boundary conditions would need to be specified. With regard to particles and energy one choice would be the upstream density n_u and the power entering the system, P_{in} [W]. Actually, in 1D modelling one needs to work with $q_{in}[\mathrm{W/m^2}] = P_{in}/A_{\parallel}^{\mathrm{SOL}}$, section 5.2, the power flux density parallel to $\boldsymbol{B}$ in the SOL; if one wishes to use P_{in} as the basic, specified power quantity, then one needs to also specify λ_{SOL} in order to evaluate $A_{\parallel}^{\mathrm{SOL}}$: $A_{\parallel}^{\mathrm{SOL}} \approx 4\pi R\lambda_{\mathrm{SOL}}(B_\theta/B)_m$, for example, for a single-null poloidal divertor, where λ_{SOL} and $(B_\theta/B)_m$ are specified at the midplane, section 5.6. A decision is also required as to how P_{in}, q_{in} are spatially distributed over the length of the SOL, L; fortunately, as noted already, figure 4.17, the solutions are usually rather insensitive to the spatial distribution of $P_{in}(s_\parallel)$, $q_{in}(s_\parallel)$.

With regard to the momentum equation, in some approaches $|M_t| = 1$ is *specified*. This, however, automatically rules out the possibility of supersonic solutions, or requires that, if the flow has become supersonic at some location upstream of the target, it is forced to return to sonic flow velocity at the target—which seems non-physical. As will be discussed below, it is unnecessary—and incorrect—to impose any specific value of $|M_t| \geq 1$; rather one requires (a) that

$|M_t|$ have some value ≥ 1, the Bohm criterion, chapter 2, and (b) that there be no singularities or discontinuities in n, $v_\parallel$, T, etc, at any point in the flow, see chapter 14; singularities right at the target are permitted, however, i.e., at the sheath edge. This matter of requiring *smooth* solutions does not have an analogue in two-point model analysis, and in the 2PM there is no choice but to specify the value of M_t.

If the parallel power were carried entirely by *convection*, then it would not be necessary to introduce any further boundary conditions. Consider the case of no volumetric momentum or power sources or sinks; then from chapter 9

$$p_u = 2n_t k T_t (1 + M_t^2) \tag{11.1}$$

where p_u is the upstream pressure and we assume $T_e = T_i$ for simplicity. Also:

$$q_{in} = (5kT_t + kT_t M_t^2) n_t c_{st} |M_t|. \tag{11.2}$$

Thus, if p_u and q_{in} are specified, and M_t is either specified or found by requiring that the solutions be continuous, one has enough information in these two equations to establish the values of the two unknowns, n_t and T_t. There is also enough information to establish $n(s_\parallel)$, $T(s_\parallel)$, $v(s_\parallel)$, etc.

Parallel heat conduction is usually important or dominant in the SOL, however, and since this introduces a *derivative* of T ($q_{\rm cond} = -\kappa_0 T^{5/2} {\rm d}T/{\rm d}s_\parallel$) it is then necessary to introduce more boundary condition information—specifically in the form of the sheath heat transmission coefficient γ, section 2.8. Thus, for the case of pure conduction:

$$-\kappa_0 T_t^{5/2} \frac{{\rm d}T}{{\rm d}s_\parallel}\bigg|_{s_\parallel = 0} = \gamma n_t k T_t n_t c_{st} |M_t|. \tag{11.3}$$

If $T_e \neq T_i$ then one employs two power equations with q_{in}^e and q_{in}^i being specified, also γ_e and γ_i; equipartition power transfer may be included.

An alternative choice of location to specify the boundary conditions is *entirely at the target*—rather than the *mixed-location* approach described in the foregoing. Typically experimental information is available across the target from built-in Langmuir probes, giving $T_{et}(r)$ and $I_{{\rm sat},t}^+(r)$. In the (usual) absence of information about $T_{it}(r)$ one might, for simplicity, assume $T_{it} = T_{et}$. Since $I_{{\rm sat},t}^+/e = n_t |M_t| c_{st}$, one then has enough boundary condition information to specify the problem completely—taking, as above, $\gamma_{e,i}$ to be given and M_t to be specified or found as before. *Thus, no upstream boundary condition information is used at all.* This method fits naturally with onion-skin method modelling, chapter 12. The solution of the conservation equations discussed in the next section is in the context of such *target-only* boundary conditions. Extension to treatments based on mixed-location boundary conditions is straightforward and will not be discussed here.

In 1D analysis the method of calculating the volumetric sources and sinks requires some thought. For the particle balance equation one needs to know

$S_{iz}(s_\parallel)$ [particles m^{-3} s^{-1}], the spatial distribution of the ionization rate of neutrals; for the momentum equation one needs to know the volumetric $S_{\rm mom}(s_\parallel)$ [(kg m s^{-1}) m^{-3} s^{-1}], the spatial distribution of momentum loss or gain by the plasma flow to or from the neutrals; for the energy equations one needs to know $Q_{Ee}(s_\parallel)$ and $Q_{Ei}(s_\parallel)$ [W m^{-3}], the volumetric power gain or loss associated with the hydrogenic recycling processes, including ionization, excitation, dissociation, charge exchange, etc. We note that, as for q_{in}, it is necessary to divide these source *densities* by $A_\parallel^{\rm SOL}$ for use in 1D models; here we do not employ a different symbol, and the appropriate units, and the implied division by $A_\parallel^{\rm SOL}$, are understood, as appropriate. The energy equation also requires specification of the volumetric power loss due to impurity radiation, Q_R^z [W m^{-3}]. The preferred way to find $S_{iz}(s_\parallel)$, $S_{\rm mom}(s_\parallel)$, $Q_{Ei}(s_\parallel)$, $Q_{Ee}(s_\parallel)$ is to use a Monte Carlo neutral hydrogen code such as EIRENE, NIMBUS, DEGAS, etc, section 1.8.2.4. Since neutrals are not constrained by magnetic fields, these codes have to follow the neutrals in 2D or even 3D. It is also not enough to restrict the computational zone to the simple geometry of a straightened-out SOL, as used for the *plasma* modelling itself. Since the neutrals interact with the solid walls, the entire, actual, solid structural geometry has to be provided as input to these neutral codes.

Clearly there is a problem of geometrical incompatibility between these 2D/3D neutral codes and 1D plasma modelling of the SOL. What then to do for the volumetric terms in the plasma equations? One approach is not to use the neutral codes, at least directly, but to *specify arbitrarily* the spatial distribution of the volumetric terms, perhaps using simple analytic expressions. One might, for example, specify that $S_{iz}(s_\parallel)$ fall off exponentially along $s_\parallel$ with some specified characteristic 'ionization length', and that $\int_0^L S_{iz} {\rm d}s_\parallel = |M_t| n_t c_{st}$, the flow into the sheath. One could use a neutral code for guidance in specifying the ionization length: once the 1D plasma solution is found, a 2D (poloidal plane) plasma grid, see section 6.6, can be used, to specify a 'plasma background' in the SOL part of the grid, over a specified SOL radial width $\lambda_{\rm SOL}$; plasma conditions can be specified in the main plasma part of the grid from experimental measurements; the solid surfaces, walls and targets, are included in the computational domain of the neutral code. The neutral code is then run for this specified plasma background, and from the calculated spatial distribution of $S_{iz}(s_\parallel)$ one can extract estimates for the ionization lengths to be used in the analytic prescription.

In a more sophisticated variant of this approach, the analytic prescription is dispensed with and the neutral and 1D plasma codes are directly coupled in an *iterative* mode of operation: the plasma solution from the previous iteration is used as the background for the neutral code, which calculates the neutral-related source and sink terms (averaged radially across the SOL to give 1D expressions for $S_{iz}(s_\parallel)$, etc) for the plasma equations used for the next iteration. This method has been used in the EDGE1D code [11.1] employing the NIMBUS neutral code, and with mixed-location boundary conditions.

For calculating the impurity radiation sink, Q_R^z [W m^{-3} or W m^{-2}], an

impurity Monte Carlo code such as DIVIMP [11.2] can be employed in a similar way. Alternatively a *multi-fluid* plasma model can be used, where in addition to the e and D^+ (say) fluids, additional impurity fluids, e.g., C^+, C^{2+}, etc, are included. The EDGE1D code, for example, models impurities in this way.

We consider next the cross-field or radial *span* of the 1D system. In true 1D analysis of the SOL, such as EDGE1D, the radial span is taken to be the entire width of the SOL, which can be estimated using simple analytic expressions, chapters 4, 5. In onion-skin method, OSM, modelling, chapter 12, the radial span is taken to be that of an individual flux tube within the SOL, which is taken to be composed of many such nested flux tubes. This modelling method—which is actually 2D—is described in chapter 12. Briefly, this also uses iterative coupling of 1D plasma solvers to neutral and impurity Monte Carlo codes, but now including *radial variation* across the SOL, rather than a radially averaged solution, as above. The radial variation enters naturally from the imposed boundary conditions across the SOL, taken from measurements, for example at the targets; the SOL width, λ_{SOL}, is not specified nor are there any input assumptions about cross-field transport coefficients, $D_\perp$, $\chi_\perp$, etc. The latter, in fact, can be *extracted* from the analysis, i.e., in effect from the measured radial variations, e.g., across the targets, chapter 12.

In addition to cross-field sinks and sources associated with the neutral hydrogen and with impurities, there are cross-field sources and sinks resulting from *cross-field (plasma) transport*. In section 1.8.2.4, for example, the cross-field particle source, $S_{p,c\text{-}f}$, was estimated as $D_\perp n/\lambda_{sol}^2$. Similar terms arise in the other balances. One can employ such simple approximations in 1D modelling. In the onion-skin method, opportunities arise to treat such terms in less approximate ways using iteration of the solution; see chapter 12.

11.2 1D Fluid Modelling for the Conduction-Limited SOL

The boundary conditions are taken here to be at the target, in the form of T_e, T_i and n_e at locations across the targets—ideally from experimental measurements. The application may be to limiters or divertors but here the discussion will be primarily in a divertor context.

We start where we left off in chapter 10, with the sheath-limited SOL and T_e and T_i constant. We will assume that the particle source is due to ionization occurring uniformly over some specified length L_{iz}, section 6.5.5.2 starting at the target and that the total integrated strength of the source is equal to the particle outflux density to the target, $n_t c_{st}$, where subscript t indicates the target, boundary values. We assume $|M_t| = 1$ for now. We appropriate the 1D isothermal model of section 10.2 making the change:

$$s_\parallel = L - x \tag{11.4}$$

where, as before L is the connection length, i.e. half the distance to the other

target along $\boldsymbol{B}$. Thus equation (10.1) becomes:

$$\frac{\mathrm{d}(nv)}{\mathrm{d}s_\parallel} = \begin{cases} \dfrac{n_t c_{st}}{L_{iz}} & 0 \le s_\parallel < L_{iz} \\ 0 & L_{iz} \le s_\parallel < L. \end{cases} \tag{11.5}$$

One may note that equation (11.5) ensures that there will be no *flow reversal*, chapter 15, in this case since we have arranged that the total, integrated particle source equals the outflow rate to the targets:

$$\int_0^L S_p \mathrm{d}s_\parallel = n_t c_{st}. \tag{11.6}$$

One may note that $S_p > 0$ and $v_t = -c_{st}$. Thus for S_p constant over $0 \le s_\parallel < L_{iz}$ we have:

$$S_p = -n_t c_{st}/L_{iz} \tag{11.7}$$

which was used in equation (11.5) along with $\mathrm{d}s_\parallel = -\mathrm{d}x$.

The momentum equation (10.2) gives:

$$n(s_\parallel)/n_t = \frac{2}{1+M^2}. \tag{11.8}$$

Combining equations (11.5) and (11.6) with equations (11.7) and (11.8) gives the flow Mach number $M(s_\parallel)$ as the solution of the equation:

$$\frac{s_\parallel}{L_{iz}} = 1 + \frac{2M}{1+M^2} \tag{11.9}$$

for $0 \le s_\parallel \le L_{iz}$, while for $L_{iz} \le s_\parallel \le L$, $M(s_\parallel) = 0$. Since the flow is isothermal we also have $v(s_\parallel)$ from equation (11.7) given implicitly by:

$$\frac{s_\parallel}{L_{iz}} = \frac{(c_s + v)^2}{c_s^2 + v^2} \tag{11.10}$$

for $0 \le s_\parallel \le L_{iz}$, while for $L_{iz} \le s_\parallel \le L$ we have $v(s_\parallel) = 0$. Thus one has $n(s_\parallel)$ from equation (11.8) and also the electric field from equation (10.7):

$$E(s_\parallel) = \begin{cases} \dfrac{kT_e}{eL_{iz}} \dfrac{M(1+M^2)}{(1-M^2)} & 0 \le s_\parallel \le L_{iz} \\ 0 & L_{iz} \le s_\parallel \le L. \end{cases} \tag{11.11}$$

One may note that $E(s_\parallel) \le 0$, i.e. it points toward the target.

In this simplest approach, if the boundary conditions are different at the two targets, then there will be discontinuities in $n(s_\parallel)$, etc at the mid-point location in the SOL since each half of the SOL is solved separately.

We now relax the isothermal assumption, which is unacceptable for the conduction-limited regime. One can readily replace the prescription of

constant temperature with, for example, the parallel heat conduction equations, equations (4.89), (4.90). In the most basic conduction case one assumes $T_e = T_i$ at all points and thus, since $\kappa_{0e} \gg \kappa_{0i}$, the heat is conducted essentially by electrons. Thus one obtains:

$$T(s_\parallel) = \left[T_t^{7/2} + \frac{7}{2\kappa_{0e}} q_t^{e\&i} s_\parallel \right]^{2/7} \tag{11.12}$$

where:

$$q_t^{e\&i} = \gamma n_t c_{st} k T_t \tag{11.13}$$

and γ is the sheath heat transmission coefficient, section 2.8. Equation (11.12) is based on the further assumptions that:

(a) all of the heat entered at the 'top end', at $s_\parallel = L$ (small changes are involved if it is assumed instead that the heat input, required to provide the heat flux density at the target, $q_t^{e\&i}$, entered uniformly over the length L);
(b) there are no volumetric sources or sinks of power in the flux tube.

One may note from equations (11.12) and (11.13) that the solution for $T(s_\parallel)$ for each flux tube is given completely once the target conditions are specified. One may also note that, conveniently, $T(s_\parallel)$ can be fully solved for independently of the solutions for $n(s_\parallel)$ and $v(s_\parallel)$ in this (pure conduction) case.

One then proceeds to the particle conservation equation which we now write in a more general way as:

$$\Gamma(s_\parallel) = n(s_\parallel) v(s_\parallel) = n_t c_{st} + \int_0^{s_\parallel} S_p(s'_\parallel) \mathrm{d}s'_\parallel. \tag{11.14}$$

Here $S_p(s_\parallel)$ may be specified, as earlier, to be a constant over some length—or of some more complex form, see below. One may also include a *volume recombination sink* in S_p as a negative contribution, see below. Unless one specifies the absolute magnitude of S_p to be such that equation (11.6) continues to hold then there will exist either a state of *over-ionization* on the flux tube, with $v(L) > 0$, i.e. flow reversal, chapter 15, or there will be under-ionization with $v(s_\parallel) < 0$ at all points including $v(L) < 0$. Such a situation may exist in actuality, of course, but is not compatible with the simplest assumption of a *stagnation point* existing at $s_\parallel = L$. We return to this point later.

Next we consider the momentum equation:

$$n(s_\parallel) \left[2kT(s_\parallel) + m_i (v(s_\parallel))^2 \right] = 4 n_t k T_t. \tag{11.15}$$

One may note that in all of the particle and momentum equations so far, sonic target conditions have been assumed. We note also that in writing equation (11.15), it has been assumed that there are no volumetric sources or sinks of momentum, for example ion–neutral friction or viscosity.

Since $T(s_\parallel)$ has been independently solved for, equation (11.12), we may note that we have just two coupled equations (11.14) and (11.15) for the two dependent variables (unknowns) $n(s_\parallel)$ and $v(s_\parallel)$ in terms of the one independent variable $s_\parallel$. One can therefore obtain a solution for $n(s_\parallel)$ by eliminating v to give:

$$n^2 - \frac{4n_t k T_t}{m_i c_s^2} n + \frac{\Gamma^2}{c_s^2} = 0. \tag{11.16}$$

One knows $\Gamma(s_\parallel)$ at each point from equation (11.14) and $c_s(T(s_\parallel))$ at each point from equation (11.12). Having obtained $n(s_\parallel)$ from equation (11.16), one then obtains $v(s_\parallel)$ from $v(s_\parallel) = \Gamma(s_\parallel)/n(s_\parallel)$.

Alternatively one may eliminate n to obtain for $v(s_\parallel)$ or $M(s_\parallel)$:

$$M^2 - \frac{4n_t k T_t}{m_i c_s \Gamma} M + 1 = 0, \tag{11.17}$$

which is solved to give:

$$M(s_\parallel) = \left(\frac{2n_t k T_t}{m_i c_s \Gamma}\right) + \left[\left(\frac{2n_t k T_t}{m_i c_s \Gamma}\right)^2 - 1\right]^{1/2}. \tag{11.18}$$

Equation (11.18) illustrates the problem of a supersonic transition occurring at some point upstream of the target, chapter 14. The *assumption* and thus *assignment* as boundary condition of $M_t = 1$ at $s_\parallel = 0$ can run into trouble since $|M| > 0$ is possible at some upstream point. The term $(2n_t k T_t/m_i c_s \Gamma) < 0$, since $\Gamma < 0$. For $s_\parallel \to 0$ this term $\to -1$ and so $M \to -1$ which causes no difficulty. For $s_\parallel > 0$, however, it is necessary to ensure that there is no imaginary root in the equation for $M(s_\parallel)$. This will happen, however, if $T(s_\parallel)$ (i.e. $c_s(T(s_\parallel))$ rises very rapidly while $\Gamma(s_\parallel)$ falls slowly, since this can make the term $|2n_t k T_t/m_i c_s \Gamma| < 1$. As discussed in chapter 14, if this happens then one must increase the specified $|M_t|$ to that particular value greater than unity that will give smooth solutions for $n(s_\parallel)$ and all boundary conditions must then be changed to allow for $|M_t| \neq 1$.

Turning to the electric field $E(s_\parallel)$: since $n(s_\parallel)$ and $T(s_\parallel)$ are now known, all the information is available to calculate E from Ohm's law, section 9.5, assuming no current, $j_\parallel = 0$. Thus we have, for each flux tube the values of T_e, T_i, n, M and E at each location $s_\parallel$, see figure 11.1.

Variation on this conduction model would include allowing for $T_e(s_\parallel)$ and $T_i(s_\parallel)$ to be independent:

$$T_e(s_\parallel) = \left[T_{et}^{7/2} + \frac{7}{2\kappa_{0e}} q_t^e s_\parallel\right]^{2/7} \tag{11.19}$$

$$T_i(s_\parallel) = \left[T_{it}^{7/2} + \frac{7}{2\kappa_{0i}} q_t^i s_\parallel\right]^{2/7} \tag{11.20}$$

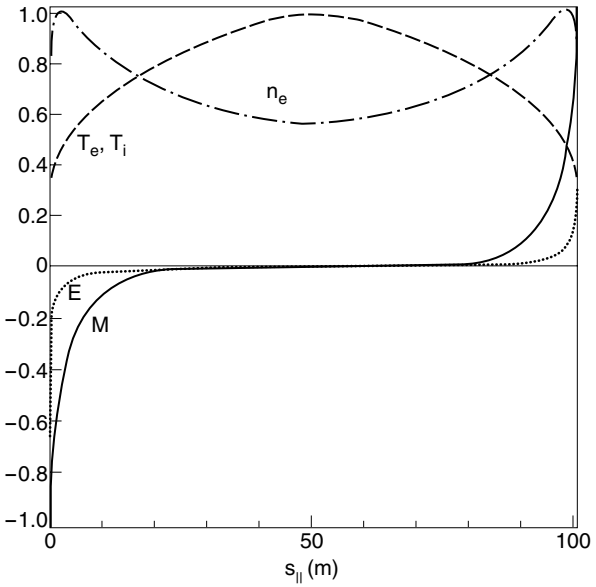

Figure 11.1. An example of 1D solutions for the simple conduction-controlled case. $T_e(s_\|) = T_i(s_\|)$. $T_t = 20$ eV, $n_t = 10^{19}$ m^{-3}. Conditions are the same at each target. Total length of the flux tube, target to target, 101 m. The ionization source is assumed to decay exponentially from the target with decay length of 5 m. All parallel power carried by electron heat conduction. Here: $T^{\max} = 57$ eV, $n^{\max} = 1.25 \times 10^{19}$ m^{-3}, $n_e^{up} = 0.70 \times 10^{19}$ m^{-3}, $M^{\max} = 1$. As $M \to 1$, $E \to \infty$, equation (11.11); however, for purposes of display the E-plot is cut off here at $E^{\max} = 49$ V m^{-1}, thus providing a scale.

where

$$q_e^t = \gamma_e k T_{et} n_t c_{st} \tag{11.21}$$

$$q_i^t = \gamma_i k T_{et} n_t c_{st}. \tag{11.22}$$

Equipartition collisions have been neglected. The momentum equation becomes:

$$n(kT_e + kT_i + m_i v^2) = 2n_t(kT_{et} + kT_{it}) \tag{11.23}$$

and the solution proceeds essentially as before.

Radiative loss is often important in the SOL. This can be included by altering equation (11.19) to give:

$$T_e(s_\|) = \left[T_{et}^{7/2} + \frac{7}{2\kappa_{0e}} \left(q_t^e s_\| - \int_0^{s_\|} \mathrm{d}s'_\| \int_0^{s'_\|} \mathrm{d}s'' Q_R(s''_\|) \right) \right]^{2/7} \tag{11.24}$$

where the electron cooling power $Q_R(s_\parallel)$ [W m^{-2}] has to be prescribed analogously to $S_p(s_\parallel)$. $Q_R(s_\parallel)$ may be given by some simple, analytic prescription or it may be more sophisticated, see below. One may note that a power *sink*, $Q_R < 0$, causes $T_e(s_\parallel)$ to *rise* faster than it would if Q_R were neglected, see equation (11.24). This occurs here, of course, because $s_\parallel$ increases in the upstream direction.

The *flow field*, $v(s_\parallel)$ is one of the most important aspects of the SOL. This controls the friction force on impurities—and if flow reversal occurs, the consequences for impurities may be quite important. The flow also controls parallel heat *convection*, which is not always negligible compared with conduction. If one uses a simple prescription for $S_p(s_\parallel)$, such as it being constant over $0 \leq s_\parallel \leq L_{iz}$, thereafter dropping to zero—as above—then one may be seriously in error regarding the calculation of the flow field and the processes it affects. An important improvement of the method is therefore to couple it iteratively to a *neutral hydrogen code*, such as EIRENE, NIMBUS, DEGAS, etc, as already discussed.

This then allows for a physically more realistic treatment of parallel heat convection which is now included. For electron power balance, from section 9.9:

$$\frac{\mathrm{d}}{\mathrm{d}s_\parallel}\left(\frac{5}{2}kT_e nv - \kappa_{0e}T_e^{5/2}\frac{\mathrm{d}T_e}{\mathrm{d}s_\parallel}\right) = -Q_{eq} + Q_R^Z + Q_{Ee} \tag{11.25}$$

where we have dropped the–enE term, but this could be included, also adding Ohm's law, equation (9.36), to the set of simultaneous equations.

The electron cooling term, Q_R, has been divided into a part due to hydrogen Q_{Ee}, and a part due to impurities, Q_R^Z. The hydrogen neutral code provides $Q_{Ee}(s_\parallel)$ for each flux tube. The values of $Q_R^Z(s_\parallel)$ can be estimated analytically or can be taken from an iteratively coupled impurity code such as DIVIMP.

One notes the presence now of parallel electron convection, the $\frac{5}{2}kT_e nv$ term in equation (11.25). One notes the presence of three dependent variables (unknowns) in equation (11.25): $T_e(s_\parallel)$, $n(s_\parallel)$, $v(s_\parallel)$. The Q_{eq} term, equation (9.52), is a function of $n(s_\parallel)$, $T_e(s_\parallel)$, $T_i(s_\parallel)$, and so all four independent variables are implicit in equation (11.25).

Power balance for ions, equation (9.81):

$$\frac{\mathrm{d}}{\mathrm{d}s_\parallel}\left[\left(\tfrac{5}{2}nkT_i + \tfrac{1}{2}m_i nv^2\right)v - \kappa_{0i}T_i^{5/2}\frac{\mathrm{d}T_i}{\mathrm{d}s_\parallel}\right] = Q_{eq} + Q_{Ei} \tag{11.26}$$

where viscosity and the enE term have been neglected. The neutral hydrogen code provides the values for $Q_{Ei}(s_\parallel)$ for each flux tube, including both ionization-related and charge-exchange gains/losses. Results shown in figure 11.2 are for the same conditions as for figure 11.1 except that now the ion and electron powers are carried separately, and also conduction and convection are now both included. The weak ion collisionality is not compensated for by the ion heat convection and as a result $T_i^{\max}$ is much larger than in figure 11.1. Since the electrons now only have to transport their own target power, $T_e^{\max}$ drops compared with figure 11.2.

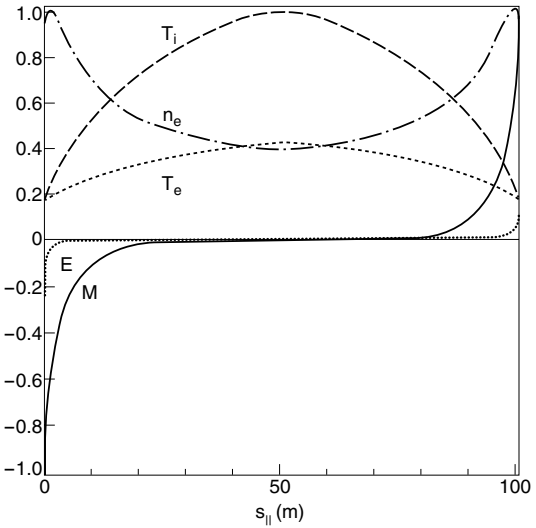

Figure 11.2. Conditions are the same as in figure 11.1 except that now the ion and electron powers are transported separately, and both conduction and convection are included. No other power terms. Here: $T_e^{\max} = 49$ eV, $T_i^{\max} = 115$ eV, $n_e^{\max} = 1.25 \times 10^{19}$ m^{-3}, $n_e^{up} = 0.49 \times 10^{19}$ m^{-3}, $M^{\max} = 1$, ($E^{\max} = 60$ V m^{-1}, for scaling).

Results shown in figure 11.3 are for the same conditions as in figure 11.2 except now the power lost by electrons in the recycle process is included, raising $T_e^{\max}$ slightly.

Results shown in figure 11.4 are the same as in figure 11.3 except that now the effect of electron cooling due to impurity radiation is included, assuming a total amount of radiation equal to twice the electron power reaching the target, distributed uniformly over the first 10 m from each target. This causes $T_e^{\max}$ to rise more substantially.

The particle conservation equation, equation (9.78):

$$\frac{\mathrm{d}}{\mathrm{d}s_\parallel}(nv) = -S_p^{\text{source}}(s_\parallel) + S_p^{\text{sink}}(s_\parallel) \tag{11.27}$$

where the signs of the terms reflect the direction of increasing $s_\parallel$. The ionization source calculated by the neutral hydrogen code gives $S_p^{\text{source}}(s_\parallel)$. The sink term is due to volume recombination, which can include two-body and three-body recombination:

$$S_p^{\text{sink}} = n_e n_i \overline{\sigma v}_{\text{rec}}. \tag{11.28}$$

The momentum equation, equation (9.79):

$$\frac{\mathrm{d}}{\mathrm{d}s_\parallel}(m_i n v^2 + nkT_e + nkT_i) = -m_i v \overline{\sigma v}_{in} n n_n \tag{11.29}$$

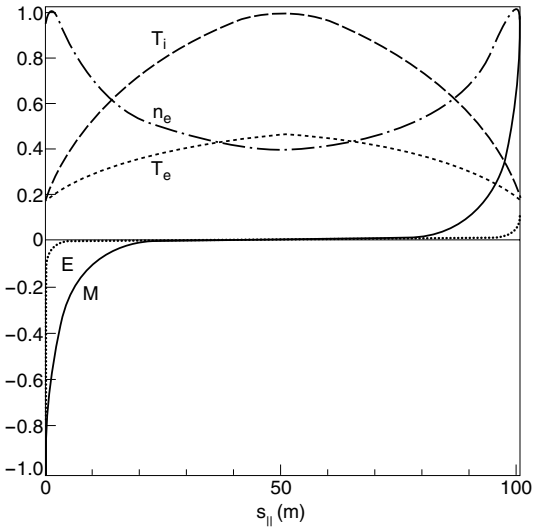

Figure 11.3. Conditions are the same as in figure 11.2 except that now the electron cooling due to hydrogen recycle is included. Here: $T_e^{\max} = 52$ eV, $T_i^{\max} = 115$ eV, $n_e^{\max} = 1.24 \times 10^{19}$ m^{-3}, $n_e^{up} = 0.47 \times 10^{19}$ m^{-3}, $M^{\max} = 1$ ($E^{\max} = 60$ V m^{-1}, for scaling).

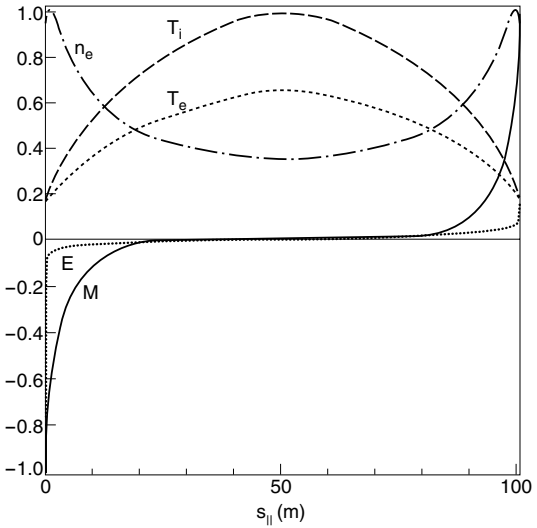

Figure 11.4. Conditions are the same as in figure 11.3 except that now impurity radiative cooling of the electrons is included, assuming a total amount of radiated power equal to twice the electron power reaching the target. Here: $T_e^{\max} = 74$ eV, $T_i^{\max} = 115$ eV, $n_e^{\max} = 1.23 \times 10^{19}$ m^{-3}, $n_e^{up} = 0.42 \times 10^{19}$ m^{-3}, $M^{\max} = 1$ ($E^{\max} = 60$ V m^{-1}, for scaling).

where viscosity has been neglected. The neutral hydrogen code provides the neutral density, $n_n(s_\parallel)$ and the ion–neutral frictional collisional rate, $\overline{\sigma v}_{in}(s_\parallel)$.

One thus has four equations, equations (11.25), (11.26), (11.27) and (11.29) for the four dependent variables n, v, T_e, T_i to be solved for as functions of the independent variable $s_\parallel$. If one includes the $\pm envE$ term in the power equations then one also needs Ohm's law, equation (9.36). Since the equations are so strongly coupled now, it is necessary to solve them using appropriate numerical methods such as:

(a) Runge–Kutta solvers which start from the target boundary conditions, for each flux tube, and calculate in the upstream direction [11.3];
(b) more sophisticated CFD (computational fluid dynamic) methods which relax the entire solution simultaneously [11.4, 11.5].

We must allow for the possibility that $|M_t| \neq 1$; the Runge–Kutta solver used in [11.3] contains an explicit algorithm which searches for the unique value of M_t which gives smooth solutions everywhere; the CFD solver used in [11.4] and [11.5] automatically evolves to smooth solutions, at the same time finding the value of $|M_t| \geq 1$. Thus for the particle conservation equation the target boundary condition is:

$$\Gamma_t = n_t v_t = M_t n_t c_{st}. \tag{11.30}$$

For the electron power one uses:

$$q_t^e = \gamma_e M_t k T_{et} n_t c_{st} \tag{11.31}$$

where one might take $|M_t| > 1$ into account when calculating the floating potential, but since the effect is not large, the standard value of $\gamma_e \approx 5$, section 2.8, may be adequate. For ion power we may note from equation (9.63) that as $s_\parallel \to 0$ then:

$$q_{\parallel i,\text{convection}} \to \left(\tfrac{5}{2} k T_{it} + \tfrac{1}{2} M_t^2 (k T_{et} + k T_{it})\right)\Gamma_t. \tag{11.32}$$

Thus, in order to avoid a situation where $q_{\parallel i,\text{convection}}$ near the target carries *more* power than q_t^i—therefore requiring that $q_{\parallel i,\text{conduction}}$ carry heat *away* from the target, making $T_i(s_\parallel)$ initially *drop* for increasing $s_\parallel$ (which one might prefer to avoid as possibly being unphysical)—one will then have to re-define the ion sheath heat transmission coefficient to be:

$$\gamma_i = \frac{\left(\tfrac{5}{2} k T_{it} + \tfrac{1}{2} M_t^2 (k T_{et} + k T_{it})\right)}{k T_{et}} \tag{11.33}$$

and

$$q_t^i = \gamma_i M_t k T_{et} n_t c_{st}. \tag{11.34}$$

Since we are not sure what the value of γ_i is precisely, even for $|M_t| = 1$, section 25.1, it may not be unreasonable to allow ourselves this freedom. For $T_{et} = T_{it}$ this gives $\gamma_i = \frac{5}{2} + M_t^2$ which together with $\gamma_e = 5$ gives the total coefficient $\gamma = 7.5 + M_t^2$, as assumed in chapter 14.

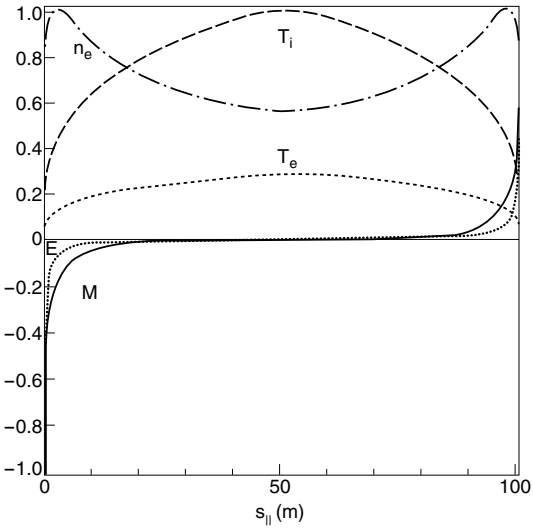

Figure 11.5. The results here assume parallel conduction (only) for each channel, no convection, no recycle or impurity radiation losses. In contrast with the results of the earlier figures, the target density has been raised to $n_t = 5{\times}10^{19}$ m^{-3}, in order to raise the parallel power sufficiently to induce a midstream sonic transition, which occurs here at about 0.6 m from the targets. Here: $T_e^{\max} = 104$ eV, $T_i^{\max} = 364$ eV, $n_e^{\max} = 7.38 \times 10^{19}$ m^{-3}, $n_e^{up} = 4.1 \times 10^{19}$ m^{-3}, $M^{\max} = 2.95$ ($E^{\max} = 123$ V m^{-1}, for scaling).

For momentum the total (static plus dynamic) pressure at the target is:

$$p_t^{\text{total}} = n_t(1 + M_t^2)(kT_{et} + kT_{it}). \tag{11.35}$$

With regard to the *input* to each flux tube, we start by considering the power. The simplest assumption is that the total power enters at the 'top end', at $s_{\|} = L$, and of a magnitude equal to the sum of the power removed at the target, q_t, plus the integral sum of the volumetric power loss. Since the latter is only known once the complete solution has been obtained, one generally has to proceed by iteration. The electron and ion power 'channels' can be treated separately. It was shown in section 4.10.1, see figure 4.17, that the spatial distribution of the power input has little effect on the shape of $T(s_{\|})$. For the (effectively) opposite assumption of the power entering uniformly over length L, the $T(s_{\|})$ profile is slightly flatter, figure 4.17. Any assumption about the spatial input of the power is readily incorporated. Since we do not know whether the anomalous $\chi_{\perp}$ is spatially constant in the SOL it is fortunate that the input power spatial distribution has so little effect on the solutions.

Results shown in figure 11.5 assume parallel conduction (only) for each channel, no convection, no recycle or impurity radiation losses. However, the target density has been raised to $n_t = 5 \times 10^{19}$ m^{-3} in order to induce a sonic

transition, which occurs here at about 0.6 m from the targets.

The integrated, net particle flux along the SOL will generally not match the particle outflux to the target since some of the neutrals will be ionized in the main plasma. In the simplest approach one just ignores this and adjusts the strength of the ionization source so that the target ion outflow equals the total ionization calculated to occur within the SOL. That is, one takes only the *spatial distribution* $S_{iz}(s_\parallel)$ from the neutral code, not the absolute magnitude. At a next level of approximation, one specifies an additional cross-field source, perhaps spatially uniform over L, and of total strength equal to the calculated total ionization rate in the main plasma. In onion-skin method modelling further refinements are possible, chapter 12.

References

[11.1] Keilhacker M, Simonini R, Taroni A and Watkins M L 1991 *Nucl. Fusion* **31** 535
[11.2] Stangeby P C and Elder J D 1995 *Nucl. Fusion* **35** 1391
[11.3] Stangeby P C, Elder J D, Fundamenski W *et al* 1997 *J. Nucl. Mater.* **241–243** 358
[11.4] Fundamenski W, Stangeby P C, Elder J D *et al* 1999 *J. Nucl. Mater.* **266–269** 1045
[11.5] Fundamenski W 1999 *PhD Thesis* University of Toronto Institute for Aerospace Studies

Chapter 12

‘Onion-Skin’ Method for Modelling the SOL

12.1 The Concept of a SOL Flux Tube

Chapters 9–11 describe a number of 1D models, as also does section 1.7 and much of chapters 4 and 5. But can their application be justified to the plasma contained within arbitrarily chosen magnetic flux bundles, i.e. *individual flux tubes* in the SOL? Can one usefully analyse the SOL in terms of ‘flux tubes’—i.e. as a set of SOL ‘onion skins’? (Here a flux tube is defined to be an elementary volume aligned with a magnetic line of force $\boldsymbol{B}$ such that a constant value of magnetic induction is contained in the flux tube, i.e. $BA_{\parallel} = \text{constant}$, where $A_{\parallel}$ is the cross-sectional area of the flux tube normal to $\boldsymbol{B}$, e.g. $A_{\parallel}^{\mathrm{SOL}}$ of section 5.6.) After all, the SOL has the thickness that it does have, λ_{SOL}, precisely because particles, momentum and heat have sufficient time to diffuse a radial distance of λ_{SOL} before being removed at the targets. This raises the question: what sense does it make to apply the parallel conservation laws to individual flux tubes in the SOL? Should pressure, for example, not be ‘smudged’ or averaged over the entire SOL, thus making invalid any concept of pressure balance, etc on an *individual* flux tube?

It might be thought that the mere fact that transport is so strongly *anisotropic* for plasmas in strong magnetic fields might justify the flux-tube concept. Anisotropic transport, however, only ensures that the SOL will be long and thin, leaving unanswered the question of the viability of analysis based on *individual flux tubes within the SOL*.

But if pressure balance along a single magnetic flux line in the SOL—which we may consider to be the thinnest of all possible flux tubes—is not satisfied, then other basic issues are raised. For example, the often-used method of identifying the location of the separatrix (for attached conditions, chapter 16) at an upstream Langmuir probe location by assuming pressure equality along $\boldsymbol{B}$, and knowing the separatrix location (‘strike point’) at the divertor target [12.1], would be invalid.

Consider also the widely used expression relating λ_n and $D_\perp$ for the simple SOL, $\lambda_n^2 \approx D_\perp L/c_s$, section 4.3. In addition to assuming $D_\perp$ is spatially constant, these derivations implicitly assume that the entire SOL can be characterized by a single value of λ_n. (Because the poloidal flux surfaces vary in their 'radial' separation for different poloidal locations, radial scale lengths automatically vary simply due to this effect of magnetic geometry, even if there are no other causes of variation. We remove this type of variation from consideration here, however, since we will *always* consider any local radial scale length as having been mapped to some reference location, e.g. the outside mid-plane.) Thus, consider for example the derivation of $\lambda_n(D_\perp)$ in section 4.3, equation (4.3): the LHS of the equation assumes that the density decay length all along the LCFS and just at the LCFS, is a constant λ_n, and also the characteristic decay length *across* the SOL *at* the target is this same λ_n. (We also assume that the *entire* simple SOL is characterized by this same value of λ_n—say across the SOL upstream—although we did not need to use that result in this particular derivation.) But are such assumptions justified? Why, if cross-field transport is capable of moving around particles and power over radial distances of order λ_n, is there *any* connection between radial profiles at different locations within the SOL?

We must address therefore the question of the *utility*—for purposes of *analysis*—of the concept of individual flux tubes (sub-layers) of the SOL, and of parallel pressure balance, etc. Unless such a picture of the SOL can be justified then most approximate SOL analysis is unsound. Also, the successful application of the 'onion-skin' method of modelling SOLs, which has been shown to be capable of quite well replicating 2D code solutions [12.2], section 12.3, would not be understandable.

The basic question then is that of the *utility* of the flux-tube approach, i.e.

(a) of choosing a control volume which is thinner than the SOL and aligned with $\boldsymbol{B}$, and then
(b) applying *one*-dimensional, along-$\boldsymbol{B}$, analysis of the conservation equations, treating the other, cross-field directions as giving rise to more or less simple 'cross-field sources and sinks' in the 1D conservation equations, then
(c) analysing the cross-field balances, *subsequently*.

The implicit assumption of such a procedure is that the along-$\boldsymbol{B}$ and cross-field analysis can be largely de-coupled and carried out *sequentially*—to a first approximation. That is, it is not necessary *simultaneously* to solve the balances in both directions. *We wish to demonstrate that it is possible to do this*.

It is important here to distinguish between the simple types of OSM modelling where the solution is *not iterated*, and types of OSM modelling which involve solving the parallel and perpendicular balances *iteratively*. The very simplest type of non-iterative OSM modelling involves the application of the two-point model, section 5.2, to individual flux tubes. The inclusion of the effects of cross-field sources/sinks is then necessarily approximated in highly simplified ways, e.g., all the entering power is assumed to enter at the

upstream end, or uniformly along L, etc, section 4.10. The necessity of justifying the OS method is therefore *essential* for such non-iterative approaches. This matter is not critical for iterative OSM approaches but the computational time required to reach a converged solution will be less if the OS method of treating perpendicular and parallel balances separately and sequentially is valid. In iterative OSM the perpendicular flux densities of particles, momentum and power can be made proportional to the local values of the second derivatives, in the perpendicular direction, of density, etc, the standard assumption of diffusive cross-field transport. In that case the OSM approach is simply an alternative numerical procedure for carrying out 2D modelling—although retaining a key advantage that boundary condition information taken from experiment *spans* the SOL radially, section 12.2, and therefore one can *extract* $\chi_{\perp}^{\mathrm{SOL}}$ from OSM analysis, chapter 20. All types of OSM modelling are actually *two* dimensional, although the simplest versions treat the cross-field transport in a rough way.

One is certainly free to choose *any* triad of orthogonal co-ordinate directions, and *any* control volume, and then to pick *any* co-ordinate as the 'preferred' one to be subject to 1D analysis, with the effects of the other directions treated as 'orthogonal-direction sources and sinks'—but generally it will *not* be possible to achieve any useful degree of de-coupling of the analysis in the three directions and one will be stuck with a complicated, multi-coordinate, coupled analysis. No simple, approximate treatment will be possible.

We will now demonstrate the general result that the flux-tube approach *does* result in a useful degree of de-coupling—or rather one should say, a useful *simplification* of the coupling—between the along-$\boldsymbol{B}$ and cross-field directions, for both the sheath-limited and conduction-limited regimes. We will also demonstrate a specific and important result of flux-tube analysis; *total pressure tends to be approximately constant along a flux tube, or, more to the point, it is not sensitive to the details of cross-field transport*.

We take flux tubes, then, as our control volumes. In that case the 1D form of the conservation equations can be used with $s_{\parallel}$ parallel to $\boldsymbol{B}$, and all cross-field terms then appear as sources/sinks in these equations, see chapter 11. We must now demonstrate that:

(a) This leads to simple boundary conditions.
(b) Pressure will (usually) be constant in a flux tube and, more to the point, *it is not much affected by cross-field terms*.
(c) As many other quantities as possible will either be constant, not affected by the cross-field terms, or will be insensitive to their spatial distribution, etc.
(d) One can *then* address cross-field balance, i.e. *subsequently, i.e., sequentially*.

As to point (a), *boundary conditions*, certainly the flux tube is a good choice of control volume since we apply the Bohm criterion and sheath heat transmission coefficients, chapter 2, at the target end. At the upstream end one can assume there

are no influxes (symmetric geometry assumed), or the analysis can be carried out from target to target.

We turn next to the key question of pressure constancy and start with the simple SOL case, T constant along the flux tube. We start with the tentative hypothesis that the first two, basic 1D conservation equations, section 9.9, will adequately describe the system:

$$\frac{\mathrm{d}}{\mathrm{d}s_\parallel}(nv) = S_p(s_\parallel) \tag{12.1}$$

$$\frac{\mathrm{d}}{\mathrm{d}s_\parallel}(mnv^2 + p_e + p_i) = 0 \tag{12.2}$$

where

$$S_p(s_\parallel) = S_{p,c\text{-}f}(s_\parallel) = D_\perp \frac{\mathrm{d}^2 n}{\mathrm{d}r^2}. \tag{12.3}$$

We have assumed cross-field transport is diffusive, see section 1.8.2.4. We could include the effects of volume recombination and i–n friction but since these are not cross-field terms they are not of interest with regard to justifying flux tubes as useful control volumes.

Equation (12.2) is just the statement of the constancy of total pressure in the flux tube:

$$p_{\text{total}} \equiv mnv^2 + p_e + p_i \tag{12.4}$$

and so we appear to be off to an excellent start: the only cross-field term present, $S_{p,c\text{-}f}(s_\parallel)$, has no effect on p_{total}!

Although we will now look more carefully at the assumption that there really are no important cross-field terms left out of equation (12.2), the final conclusion below is that this indeed is usually the case and this critically important conclusion therefore will stand.

So, we now ask: is equation (12.2) really satisfied—even for the simple SOL? After all, equation (12.2) assumes that there is no cross-field transport of *momentum* into the flux tube. The first way this assumption would be violated would be if the newly 'created' particles (from $S_{p,c\text{-}f}$) entered the flux tube, carrying some $s_\parallel$-momentum. For S_{iz}, i.e. ionization of neutrals, it may often be reasonable to assume that the new ions are created 'dead in the water' from random neutrals and so there is no momentum source or sink, S_{mom}, needed on the RHS of equation (12.2). But for $S_{p,c\text{-}f}$ is this true? The flux tube closest to the separatrix *imports* ions from the main plasma—presumably having no birth $s_\parallel$-momentum—but it *exports* ions with $s_\parallel$-momentum to the next flux tube further out. Thus, that flux-tube does indeed suffer a net momentum *loss* due to cross-field *particle* diffusion, $S_{\text{mom}} < 0$. All the flux tubes further out are net importers of both particles and momentum—and so for them $S_{\text{mom}} > 0$. Averaged over the entire SOL, $S_{\text{mom}} = 0$, for this process; however, equation (12.2) is *not* strictly valid for any *individual* flux tube.

We must therefore estimate the magnitude of this effect. We assume for a start that $\mathrm{d}v_\parallel/\mathrm{d}r = 0$ (but we will also allow for velocity shear and shear viscous stress next). Thus the momentum source density due to this process is:

$$S_{\mathrm{mom},D_\perp} = mv_\parallel S_{p,c\text{-}f} = mv_\parallel D_\perp(\mathrm{d}^2n/\mathrm{d}r^2) = mv_\parallel D_\perp n/\lambda_n^2. \tag{12.5}$$

For the whole length of a tube this gives a total:

$$\int S_{\mathrm{mom},D_\perp}\mathrm{d}s_\parallel = L\overline{nv}_\parallel D_\perp m/\lambda_n^2 \tag{12.6}$$

where $\overline{nv}_\parallel$ is the average flux density along the SOL. At this point we use one of the results that we are trying to prove here, namely that for the simple SOL n drops by a factor of only two, $n_u/n_t = 2$, along the flux tube's length (we will thus only be demonstrating *consistency*, finally). For $S_{p,c\text{-}f}(s_\parallel)$ approximately constant:

$$\overline{nv}_\parallel \approx \tfrac{1}{2}n_t c_s \simeq \tfrac{1}{4}n_u c_s. \tag{12.7}$$

Thus the total from equation (12.5) compared with the upstream pressure $p_{eu} + p_{iu} = mn_u c_s^2$ is:

$$\frac{L\overline{nv}_\parallel D_\perp m/\lambda_n^2}{mn_u c_s^2} \simeq \frac{1}{8} \tag{12.8}$$

where we have used $\lambda_n^2 = 2D_\perp L/c_s$ (again we will only demonstrate consistency here). We are justified in ignoring this small correction, equation (12.8), in our simple analysis in light of the other, cruder approximations already involved in such analysis.

There is in addition the cross-field diffusion of momentum due to *perpendicular shear stress*, at rate proportional to $\eta_\perp(\mathrm{d}v_\parallel/\mathrm{d}r)$, where $\eta_\perp$ is the (anomalous) shear viscosity coefficient.The value of $\eta_\perp^{\mathrm{SOL}}$ is poorly known but a reasonable guess may be $\eta_\perp \approx nmD_\perp$, based on analogy with classical transport [12.3]. This gives:

$$S_{\mathrm{mom},\eta_\perp} = v_\parallel \eta_\perp/\lambda_v^2 \tag{12.9}$$

where λ_v is the (parallel) velocity radial decay length. Assuming λ_v is of order λ_n and $\eta_\perp \sim nmD_\perp$, it is readily seen that this contribution is of the same order as $S_{\mathrm{mom},D_\perp}$ and therefore can also be neglected.

Although *parallel viscous stress*, section 9.8, is not a cross-field term, for completeness we mention it here. When $\eta_\parallel$ is limited by an appropriate kinetic factor, chapter 26, this effect also makes only a small contribution to pressure balance.

We are thus able to substantiate our initial proposition: for the simple SOL, the choice of flux tubes as control volumes has the most valuable simplification that cross-field transport does not greatly affect the constancy of pressure within the tube.

This then leads to other valuable simplifications, principally that $n(s_\parallel)$ only changes by a factor of 2 in this sheath-limited regime that we have been considering, as the isothermal flow accelerates to the sound speed. This in turn justifies our simple picture that its characteristic decay length λ_n applies upstream, downstream and along the LCFS boundary.

From the last point we can also conclude that the boundary condition along the cross-field boundary, i.e. the LCFS, is also simple and convenient, namely the cross-field particle flux density is approximately constant along the LCFS. This retrospectively justifies use of equation (12.7).

(One can extend the simple SOL analysis to cases where $D_\perp$ is not constant with $s_\parallel$, or where cross-field gradients vary because the separation of poloidal flux surfaces varies with $s_\parallel$ due to B_θ/B varying along a flux tube [12.4]. While the cross-field influx density across the LCFS is no longer constant with $s_\parallel$, it varies in a readily calculable way and the basic, controlling factors continue to hold, namely:

(a) $p_{\text{total}} \approx$ constant in the flux tube;
(b) $n_t/n_u \approx 1/2$.

This is still adequate justification for using flux tubes as control volumes. That is, the fact that $S_{p,c\text{-}f}(s_\parallel)$ may vary with $s_\parallel$ because of specified factors such as magnetic geometry does not compromise the utility of the flux-tube approach.)

Note we have also demonstrated that the analysis of the cross-field particle balance can be done *after* having carried out along-$\boldsymbol{B}$ analysis. That is, it is reasonable to take λ_n as constant along a field line. This was the key in establishing $\lambda_n \sim (D_\perp L/c_s)^{1/2}$ for the simple SOL.

Continuing with the question of pressure constancy, we turn next to the more interesting conduction-limited regime, adding to equations (12.1) and (12.2) the conduction equation (9.90), to give $T(s_\parallel)$. The first and most important fact is that p_{total} is still not very much influenced by cross-field terms. Indeed we show below that $S_{\text{mom},D_\perp}$ and $S_{\text{mom},\eta_\perp}$ tend to be even less important than for the simple SOL.

$T(s_\parallel)$ is, of course, influenced by the cross-field heat sources—however, as shown in section 4.10, the precise spatial distribution of the heat source $q_{in}(s_\parallel)$ has remarkably little influence on the form of $T(s_\parallel)$, thanks to the very strong dependence of classical parallel conduction on T, namely $K_\parallel \propto T^{5/2}$. Thus here also a major simplification is enjoyed for the choice of flux tube as control volume. $T(s_\parallel)$ tends to be mainly sensitive to the total *integral* heat input, $\int q_{in}(s_\parallel)\mathrm{d}s_\parallel$, and not the *details* of spatial distribution. This makes for valuable simplifications regarding the cross-field boundary (the LCFS) for heat input to the SOL.

Because the conduction-limited regime tends to correlate with the high recycling regime and with particle (ionization) source, $S_p = S_{iz}$, being localized rather near the targets, then $\Gamma(s_\parallel) \equiv nv_\parallel$ only increases very near the target, making $\overline{nv}_\parallel$ much smaller in equation (12.6) than for the simple SOL. One notes further that there will not generally be any compensating increase in $S_{c\text{-}f}$, just

because the region where $v_\parallel \neq 0$ is smaller: S_p is now largely due to S_{iz}. This makes $S_{\mathrm{mom},D_\perp}$ and $S_{\mathrm{mom},\eta_\perp}$ smaller still for the conduction-limited regime.

We thus note that—as for the sheath-limited regime—the cross-field balances, now including heat balance, can be carried out *sequentially* to the along-$\boldsymbol{B}$ analysis. In section 5.7 we obtained approximations for $\lambda_{q\parallel}$ and λ_T based on the implicit assumption that such characteristic lengths are constant all along $\boldsymbol{B}$. Thus we could use equation (5.54), for relating total power into the SOL P_{SOL} [W] and λ_T:

$$P_{\mathrm{SOL}} = n_u \chi_\perp k T_u A_p / \lambda_{T_u}. \tag{12.10}$$

Parallel heat conduction is so strong, for any reasonably high value of T_u, that $T(s_\parallel)$ tends to be nearly constant over most of the upstream end of the flux tube, figure 4.17, i.e. the region above the X-point which is in contact with the main plasma where P_{SOL} enters the SOL. It is for this reason that λ_{T_u} can be treated as being constant, to a first approximation, over the entire surface area of the plasma A_p. We note also that $n_u k T_u$, i.e. the plasma pressure, tends to be constant along a field line—which also simplifies greatly the use of equation (12.10) in formulating simple approximate expressions for λ_T, $\lambda_{q\parallel}$: everything on the RHS of equation (12.10) is constant, if $\chi_\perp$ is.

It is thus seen that an element of *propitiousness* is involved in the almost complete de-coupling of parallel and perpendicular heat balance for the conduction-limited SOL: were $K_\parallel$ independent of T, for example, there would be a more complicated coupling, making any simple analysis difficult or impossible. For $K_\parallel$ constant, for example, then $T(s_\parallel)$ would *not* be insensitive to the details of the spatial distribution of the cross-field heat flux, nor would T_u be a robust quantity. This would make flux-tube-by-flux-tube two-point modelling impossible, as well as all other *non-iterative* OSM modelling approaches. *Iterative* OSM modelling would still be viable, but the computational time required to relax to a converged solution would be increased.

Note that the foregoing only demonstrates the *consistency* of an analysis approach based on flux tubes rather than constituting a strict proof. Further, such complications as drifts, chapter 18, have not been considered here and so what has been established is a *tendency*, rather than something absolute.

Thus for both sheath-limited and conduction-limited regimes, analysis of the SOL based on individual flux tubes makes possible a simple approximate treatment because the coupling of the particle and heat balances in the parallel and perpendicular directions is so simple that these balances can be assessed separately and sequentially. It is true that the features of the SOL are powerfully influenced by cross-field transport. But major simplification *happens* to hold that is analogous to the flow of water down a mountain side which has been sculpted into a series of terraces—for example paddy-fields on sloping terrain: while gravity dominates the pattern of water run-off down such terrain, the flow pattern is from one terrace-reservoir to the next one lower down, and occurs—or could be arranged to occur if desired—as a uniform cascade all along the length

of each terrace. Water run-off down a natural hillside would usually follow far more complicated three-dimensional patterns. For the SOL, however, the analogy of a *radial series of reservoirs* is good first approximation, making it useful to develop an *'onion-skin'* method for modelling the SOL, section 12.2.

12.2 The Onion-Skin Method of Modelling the SOL

In the onion-skin method, OSM, the boundary conditions are usually taken to be at the target, in the form of T_e, T_i and n_e at locations across the targets—ideally from experimental measurements. The essential point is that boundary condition information—i.e., solution-constraining information—should be input (a) from *experiment* and (b) *across* the SOL, radially—thereby constraining each separate flux tube. Such experimental input need not be across the targets, nor be from probes, although we start from this for illustration.

OSM modelling can be carried out at a wide variety of levels of sophistication. In the earliest applications [12.5], very simple, analytic OSM models were included within the DIVIMP code, in order to generate 'plasma backgrounds' into which (Monte Carlo) particles could be launched. At that time, no actual experimental data were employed as boundary conditions, but illustrative examples only were used. At the next stage of development [12.6], experimental measurements of n_e and T_e across (JET) limiters were used as boundary conditions—while still using simple, analytic OSM models. Next, full 1D fluid models as described in chapter 11 were introduced, together with experimental boundary conditions [12.7, 12.8] and further evolution of the OS method has continued [12.2, 12.9–12.15].

One could start by considering the particularly simple case where each flux tube in the SOL is assumed to be in the sheath-limited regime with T_e and T_i constant along each flux tube, but varying radially in accord with the radial variation of the boundary values at the target. Thus one would employ the balance equations given in section 10.2, equations (11.4)–(11.11). For each flux tube this gives the values of T_e, T_i, n, v and E at each location $s_\parallel$. Since T_e, T_i and n generally vary across the targets, this OS method thus generates a *2D solution* of the SOL. It may be seen that the information needed to give the radial variations at each location along the SOL entered the solution directly from the *target boundary conditions*. In contrast with the standard 2D fluid model approach, chapter 13, this information does *not* enter via imposed cross-field transport coefficients—$D_\perp$, $\chi_\perp$, etc—which, in fact, *are not imposed in the OS method*. Indeed, these coefficients can be *extracted*, in effect from the target boundary conditions, using the OS method, chapter 20.

In the standard 2D fluid code approach the boundary conditions are imposed at *one point*, e.g., the density at the upstream separatrix location, or along a *single flux surface*, e.g., the power flow across the separatrix. By contrast, in the OS method, the boundary conditions, or solution-constraining information, are

specified *radially across the entire SOL*—making it *unnecessary to assume values for the cross-field transport coefficients*. This spatially distributed constraint input can be from probes—at targets or upstream—or from spectroscopic measurements, etc [12.14]. Input of so much experimental information as to over-constrain the solutions can be handled by employing algorithms to minimize the variance between the experimental input, in total, and the computed values [12.15].

The foregoing is the simplest OSM model based on the conservation equations (here only particle and momentum). We may apply the term 'OSM *model*' to refer to such solutions based on conservation equations. For various applications one may wish to have more freedom, namely to directly *prescribe* spatial variations of $n(s_\parallel)$, $T_{e,i}(s_\parallel)$, $v(s_\parallel)$, etc. For example, when using a Monte Carlo neutral hydrogen code such as EIRENE, or a Monte Carlo impurity code such as DIVIMP, which require a 'plasma background' into which to launch the Monte Carlo particles, one may use 'OSM models', or alternatively one may use what one might better call 'OSM *prescriptions*' in which any or all of $n(s_\parallel)$, $T_e(s_\parallel)$, $T_i(s_\parallel)$, $v(s_\parallel)$, $E(s_\parallel)$ are *arbitrarily prescribed* without considering whether these quantities satisfy the conservation equations. Such flexibility can be useful when trying to discover what sort of plasma background is implied to exist by the measured hydrogenic and impurity spectroscopic signals, see section 6.6.4. A wide range of prescribed plasma backgrounds can be generated easily, and since a Monte Carlo run is also very quick on current computers, a wide range of possibilities can be easily explored. Having discovered *what* plasma is present one can then better consider *how* such a plasma could exist, i.e., consistent with the conservation equations. That is, one can obtain guidance from such a procedure in identifying what physical processes are likely to be operating in a given situation. This can be particularly useful for complex regimes, such as divertor detachment, chapter 16, where one may not be confident about one's ability to model fully (with the conservation equations) all the critical features of the problem.

Returning to the 'OSM models', a number of important refinements are worth including: parallel heat conduction and convection, volumetric sources and sinks for particles, momentum and energy, etc, i.e., the comprehensive 1D model given in section 11.2, equations (11.12)–(11.35). The models are applied to each flux tube separately. The 1D plasma solver is used to generate 2D SOL solutions, which are iterated with a neutral hydrogen code such as EIRENE. For inclusion of impurity effects, the 1D plasma equations can be extended to a multifluid mode; alternatively a Monte Carlo impurity code such as DIVIMP can be operated iteratively with the 1D plasma solver.

The integrated, net particle source along a flux tube would only by coincidence match the particle outflow to the target for that flux tube. The particle excess or deficit is attributed to cross-field particle fluxes. *Flow reversal*, chapter 15, is therefore often present on some flux tubes. If a flux tube has a particle excess, then this excess is assigned to an *additional particle sink*, $S_{\text{sink}}^{\text{additional}}(s_\parallel)$, distributed spatially in some specified way, and of absolute magnitude such that

$\int_0^L S_{\text{sink}}^{\text{additional}}(s_\parallel)\mathrm{d}s_\parallel$ is equal to the particle excess on that flux tube. A similar procedure is used for any flux tube in particle deficit, by using an $S_{\text{source}}^{\text{additional}}(s_\parallel)$. The simplest assumption is that these additional sinks or sources are distributed uniformly along the flux tube, but they may be assigned in a weighted way, for example weighted by the local value of $\mathrm{d}^2n/\mathrm{d}r^2$, the second derivative of the radial density gradient (which is established iteratively). Such a weighting would be appropriate if $D_\perp$ were hypothesized to be spatially constant in the SOL. Indeed this method would result in the *extraction* of an essentially experimentally measured value of $D_\perp$. Since cross-field transport is anomalous, we do not know, however, if $D_\perp$ is spatially constant. Therefore, the assumption of spatially constant cross-field sources and sinks may be all that can really be justified.

Some OSM solvers [12.9, 12.15] solve the conservation equations from target to target on each flux tube. Experimental target boundary conditions are unlikely to result in equal (total) pressures at each target. It is not uncommon for the inner target plasma, of a single null poloidal divertor, to be quite cool, and volumetric pressure loss processes—principally due to ion–neutral friction—can account for much of the pressure imbalance between the two targets. Whatever pressure discrepancy remains after all such processes have been explicitly allowed for is attributed to cross-field momentum transport—both diffusive, i.e., proportional to shear viscosity $\eta_\perp$—and convective. Appropriate momentum sources or sinks are then assigned, similar to the assignment of the cross-field particle sources and sinks, to give pressure balance.

Thus, while in its simplest form, OSM modelling simply ignores particle and momentum cross-field sources and sinks, and takes all the cross-field power input to be distributed in some simple way—in more sophisticated versions, spatially distributed sinks and sources of particles, momentum and energy are included to give balances. In the most sophisticated treatments these sources and sinks are spatially distributed along each flux tube, weighted by the second (radial) derivative of the n, $v_\parallel$, $T_{e,i}$ profiles, established through iteration. For the most part inclusion of cross-field contributions, even at the crudest level, is usually found not to change the solutions very much: as noted in chapter 5, SOL solutions based on target boundary conditions are rather insensitive to most modelling assumptions.

Various OSM models and OSM prescriptions have been implemented as background plasma 'SOL options' within the DIVIMP code [12.10]. 'SOL Opt. 22', for example, gives the Runge–Kutta solution of equations (11.25)–(11.35), allowing for flow reversal, supersonic transitions, etc, and with coupling to the NIMBUS or EIRENE neutral hydrogen codes. 'SOL Opt. 23' has most of the same physics as 'SOL Opt. 22' but uses a CFD solver [12.9, 12.15] which is better able to model detachment than is 'SOL Opt. 22' and is also stable to the inclusion of the equipartition power term Q_{eq} and parallel viscosity for which 'SOL Opt. 22' can be unstable. 'SOL Opt. 21' is a hybrid model prescription for detached divertors.

12.3 Code–Code Comparisons of Onion-Skin Method Solutions with 2D Fluid Code Solution of the SOL

The intended mode of operation for the onion-skin method is to take the downstream, i.e. target, boundary conditions from *experiment*. It constitutes an important *test* of the validity of the OS assumption and method, however, if instead one takes these boundary conditions from a 2D fluid code such as B2, EDGE2D, UEDGE, etc—and then compares the 2D OSM solution that results with the 2D fluid code solution throughout the entire SOL. Results from such a code–code comparison involving the EDGE2D code [12.16] and an OS model in DIVIMP ('SOL Option 23', see last section) [12.9, 12.15], are now considered.

The EDGE2D/NIMBUS solution, shown in figure 12.1, was obtained with the following input: power flux across the separatrix of 1 MW (split equally between electrons and ions), separatrix density of 5×10^{18} m^{-3}, cross-field coefficients $D_\perp = 0.15$ m^2 s^{-1}, $\chi_\perp^e = \chi_\perp^i = 1$ m^2 s^{-1}, and boundary conditions, $\gamma_e = 5$, $\gamma_i = [2.5 + M_0^2(T_{e,0} + T_{i,0})/(2T_{e,0})]$.

Results are only displayed for the separatrix ring and the sixth ring out for the computational mesh used. (The 'rings' refer to the flux lines in the poloidal plane, see figure 13.2, i.e. to the individual flux tubes; 'knots' are the individual grid points lying along each ring.) The plasma is well attached and in the conduction-limited regime, with some asymmetry between inner and outer targets (increasing with distance away from the separatrix) and with significant radial gradients across the SOL.

The OSM/NIMBUS solutions were obtained by using the EDGE2D target values of I_{sat}^+ (particle flux density) and T_e as the boundary conditions. The OSM used NIMBUS to calculate the neutral source/sink terms, and thus included the same atomic physics as EDGE2D. The same sheath heat coefficients, γ_e, γ_i were also used. There were no impurities in either case. The parallel heat conductivity employed the same kinetic correction, see chapter 26 in the OSM and EDGE2D.

In OSM modelling the total cross-field source of particles, momentum and energy—integrated over the length of each flux tube—is set equal to the total loss for that flux tube, i.e. loss to the two targets and to volumetric processes. As noted already, the *spatial distribution* of these cross-field sources (or sinks) is, however, freely specifiable. Since the solutions are iterated it is possible to make the cross-field particle flux density, for example, proportional to $\mathrm{d}^2n/\mathrm{d}r^2$, as holds if cross-field transport is assumed to be purely diffusive and with a constant $D_\perp$. Usually the spatial distribution is not of first order importance. (This is a valuable result since we do not, in fact, know if cross-field transport is purely diffusive, nor if diffusive, how $D_\perp$ varies.) For the results shown here the cross-field source assumptions were as follows:

(a) particle flux densities were made proportional to the local density, n;
(b) momentum flux densities were made proportional to the local value of nv;
(c) the electron energy input was assumed to be uniform from X-point to

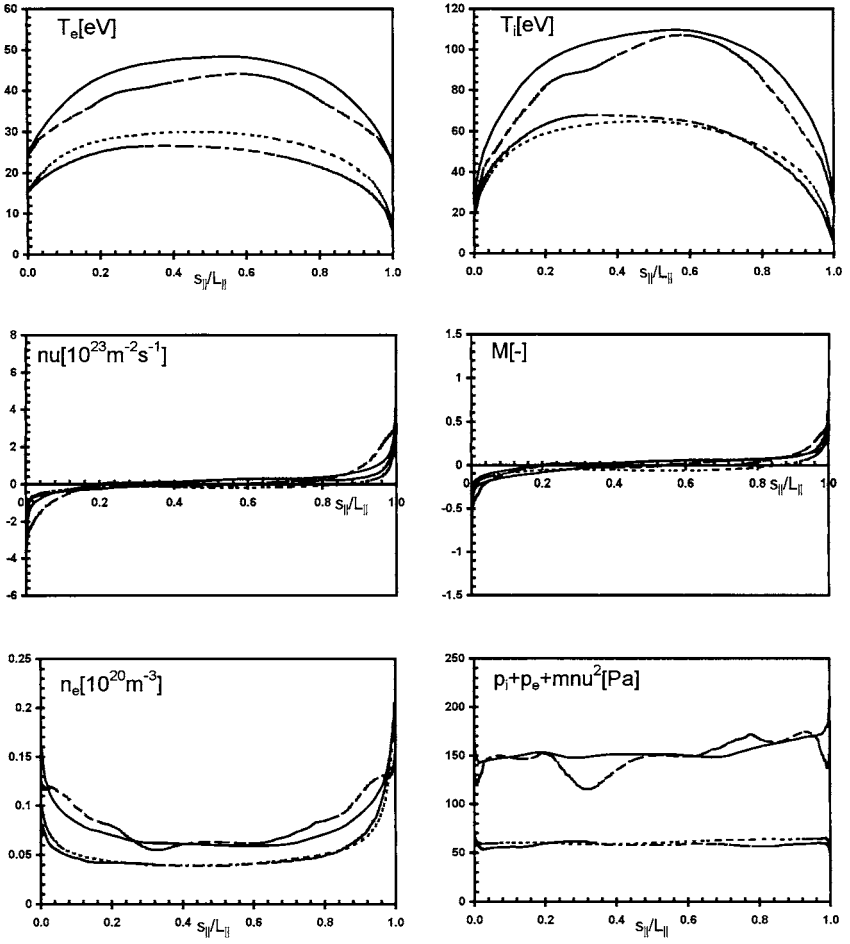

Figure 12.1. Along-***B*** plots comparing 2D fluid code (EDGE2D) results and OSM modelling results. Details of the case are given in the text. The boundary conditions for the OSM were taken from the EDGE2D target values, and therefore agreement at those points is exact. Solid line is the OSM on the separatrix ring, dashed line the EDGE2D. The dotted line is the OSM for the sixth ring out into the SOL, the dot–dashed line the EDGE2D. Agreement throughout the computational domain is typically to within ∼10%.

mid-point, with the ratio of inputs to each half of the flux tube adjusted, through iteration, to achieve matching to the required boundary conditions (T_{et}, $I_{\rm sat}^{+}$) at each target;

(d) the total ion energy input was set equal in magnitude to the total electron energy input for each flux tube and distributed spatially in the same way as

for the electrons. Since, when working from input from a 2D fluid code, boundary condition information is available for the ions, i.e. T_{it}, then the ion energy input can be handled completely separately from the electrons, and in the analogous way. Anticipating the experimental situation, however, where generally T_{it} is not measured, this alternative approach was employed here.

As can be seen from figure 12.1 the level of agreement between the 2D fluid code and the OSM results is quite good, even though the cross-field fluxes were treated in the above simple way in the OSM analysis. Other such comparisons are given in [12.2], based on the less sophisticated SOL Opt. 22 in the DIVIMP code. Similarly good agreement was reported there for a number of different plasma conditions. Typically agreement is found to be within a few tens of per cent or better. These code–code comparisons are therefore encouraging for the intended application of the OS method where the target boundary conditions are taken from experiment rather than from another code.

References

[12.1] Davies S J, Erents S K, Stangeby P C *et al* 1999 *J. Nucl. Mater.* **266–269** 1028
[12.2] Stangeby P C, Elder J D, Fundamenski W *et al* 1997 *J. Nucl. Mater.* **241–243** 358
[12.3] Hutchinson I H 1987 *Phys. Plasmas* **30** 3777
[12.4] Stangeby P C, Erents S K, De Kock L and Tagle J A 1990 *Plasma Phys. Control. Fusion* **32** 475
[12.5] Stangeby P C, Farrell C, Hoskins S and Wood L 1988 *Nucl. Fusion* **28** 1945
[12.6] Stangeby P C and Farrell C 1990 *Plasma Phys. Control. Fusion* **32** 677
[12.7] Stangeby P C and Elder J D 1992 *J. Nucl. Mater.* **196–198** 258
[12.8] Shimizu K, Itami K, Kubo H *et al* 1992 *J. Nucl. Mater.* **196–198** 476
[12.9] Fundamenski W, Stangeby P C and Elder J D 1999 *J. Nucl. Mater.* **266–269** 1045
[12.10] Stangeby P C and Elder J D 1995 *A Guide to the DIVIMP Code*
Elder J D and Stangeby P C 1996 *DIVMP Reference Manual* available from the author
[12.11] Monk R D, Horton L D, Loarte A *et al* 1995 *J. Nucl. Mater.* **220** 612
[12.12] LaBombard B, Goetz J, Kurz C *et al* 1995 *Phys. Plasmas* **2** 2242
[12.13] LaBombard B, Goetz J A, Hutchinson I *et al* 1997 *J. Nucl. Mater.* **241–243** 149
[12.14] Lisgo S *PhD Thesis* UTIAS, in preparation
[12.15] Fundamenski W 1999 *PhD Thesis* UTIAS
[12.16] Simonini R, Corrigan G, Radford G, Spence J and Taroni A 1994 *Contrib. Plasma Phys.* **34** 368

Chapter 13

An Introduction to Standard 2D Fluid Modelling of the SOL

We start by considering a basic 2D fluid edge model for the pure plasma. We will assume toroidal symmetry and thus the problem reduces to 2D. One direction is radial, cross-field, designated by coordinate r. For the second coordinate there is a choice: (a) $s_\parallel$, measured along $\boldsymbol{B}$, or (b) s_θ, the projection of the parallel direction in the poloidal plane, $s_\theta = s_\parallel(B_\theta/B)$, figure 6.21. It is perhaps conceptually easier to work with $s_\parallel$, which we will start with here. We could simply 'straighten' out the SOL, as in the simple approach of chapter 1, but since the model will have to be solved using a computer code there is little penalty in taking the actual SOL geometry into account. As a simple illustration here we will give the model equations for a *perfectly circular* SOL, of a *cylindrical tokamak* of length $2L$.

The three parallel, 1D conservation equations which are developed in chapter 9 only need minor extensions to include what are effectively 'cross-field sources'. Indeed, such sources were used even in the simplest formulation of section 1.8.2.4. We therefore write, following the equations in chapter 9, the following.

(1) *Particle balance*

$$\frac{\partial}{\partial s_\parallel}(nv_\parallel) = \frac{1}{r}\frac{\partial}{\partial r}r\left(D_\perp\frac{\partial n}{\partial r} + nv_{\text{pinch}}\right) + S_{iz}(r, s_\parallel) \qquad (13.1)$$

where $D_\perp$ and v_{pinch} are *specified anomalous* cross-field transport coefficients. $S_{iz}(r, s_\parallel)$ is the ionization source whose calculation generally requires the use of a coupled hydrogen neutral code such as DEGAS, EIRENE, NIMBUS, etc. The latter codes require as input the spatial distribution of n_e, T_e and T_i, and the code then outputs the S_{iz}, S_{mom}, Q_{Ee}, Q_{Ei} sources and sinks due to the plasma–neutral interactions. The plasma model and the neutral model must thus be solved *iteratively*.

(2) *Momentum balance*

$$\frac{\partial}{\partial s_\parallel}(p_i + p_e + m_i n v_\parallel^2 + \pi_i) = S_{\text{mom}}(r, s_\parallel) + \frac{1}{r}\frac{\partial}{\partial r} r\left[m_i v_\parallel \left(D_\perp \frac{\partial n}{\partial r} + n v_{\text{pinch}} \right) \right] + \frac{1}{r}\frac{\partial}{\partial r} r\left[\eta_\perp \frac{\partial v_\parallel}{\partial r} \right]. \tag{13.2}$$

Compare with equation (9.79). The second to last term is due to the *convection* of parallel momentum cross-field, and the last term the *diffusion* of such momentum. The divergence of these fluxes constitutes a momentum source/sink for the parallel equation (13.2). Similarly the divergence of the cross-field particle flux density

$$n v_r \equiv \Gamma_r = -D_\perp \frac{\partial n}{\partial r} - n v_{\text{pinch}} \tag{13.3}$$

gives an effective particle source in equation (13.1). The cross-field viscosity $\eta_\perp$ is generally taken to be anomalous and may be of order $\eta_\perp \approx n m_i D_\perp$ [13.1]. S_{mom} tends to be a sink due to friction with the neutrals, but includes the momentum gained if the neutrals being ionized have a non-zero average velocity in the parallel direction. Such neutral motion will, in fact, be a result of the presence of friction.

(3) *Ion energy balance*

$$\frac{\partial}{\partial s_\parallel}\left[\left(\tfrac{5}{2} p_i + \tfrac{1}{2} m_i n v_\parallel^2 + \pi_i\right) v_\parallel - \kappa_{0i} T_i^{5/2} \frac{\partial T_i}{\partial s_\parallel} \right] = +en v_\parallel E_\parallel + Q_{eq} + Q_{Ei}(r, s_\parallel) + \frac{1}{r}\frac{\partial}{\partial r} r\left[n \chi_\perp^i \frac{\partial (kT_i)}{\partial r} - \left(\tfrac{5}{2} kT_i + \tfrac{1}{2} m_i v_\parallel^2\right)\Gamma_r \right]. \tag{13.4}$$

Compare with equation (9.81). As in section 9.5, $E_\parallel$ is given by Ohm's law:

$$E_\parallel = -\frac{0.71}{e}\frac{\partial (kT_e)}{\partial s_\parallel} - \frac{1}{en}\frac{\partial p_e}{\partial s_\parallel} + \frac{j_\parallel}{\sigma_\parallel}. \tag{13.5}$$

Often $j_\parallel$ is neglected; if it is included then appropriate boundary conditions have to be included at the targets, section 17.4. It is still less common to include *cross-field* currents, section 17.5. The last term in equation (13.4) is due to the conduction and convection of energy cross-field. The cross-field heat conduction is taken to be anomalous with $\chi_\perp^i \approx D_\perp$.

(4) *Electron energy balance*

$$\frac{\partial}{\partial s_\parallel}\left[\frac{5}{2}p_e v_\parallel - \kappa_{0e}T_e^{5/2}\frac{\partial T_e}{\partial s_\parallel}\right] = -env_\parallel E_\parallel - Q_{eq} + Q_R + Q_{Ee} + \frac{1}{r}\frac{\partial}{\partial r}r\left[-\frac{5}{2}kT_e\Gamma_r + n\chi_\perp^e\frac{\partial(kT_e)}{\partial r}\right]. \quad (13.6)$$

Compare with equation (9.82).

$E \times B$ drift contributions, chapter 18, to all four balance equations can be included, but often these are neglected.

Solving these four balance equations gives the four unknowns n, $v_\parallel$, T_e, T_i, as functions of $s_\parallel$; also $p_{e,i} = nkT_{e,i}$.

With regard to boundary conditions: one notes that there are now four boundaries of the SOL, see figure 13.1: (a) the two targets, (b) the LCFS, or more typically a closed flux surface somewhat deeper in the main plasma, (c) the outside, wall side. The target boundary conditions are as before. The main plasma conditions are typically: (a) a specified density n_e mid-way between targets on the LCFS, or inner flux surface used as the boundary, (b) the total heat inflow in the electron and ion 'channels'. Various wall-side boundary conditions are used, for example: (a) $n_w = T_{ew} = T_{iw} = 0$, or (b) $\mathrm{d}n/\mathrm{d}r|_w, \mathrm{d}T_e/\mathrm{d}r|_w, \mathrm{d}T_i/\mathrm{d}r|_w = 0$, or some specified values. As pointed out in section 6.5.5, unfortunately these wall-side boundary conditions can have significant effects on the SOL solutions, and since very little is known about plasma conditions in this region, unanswered questions arise.

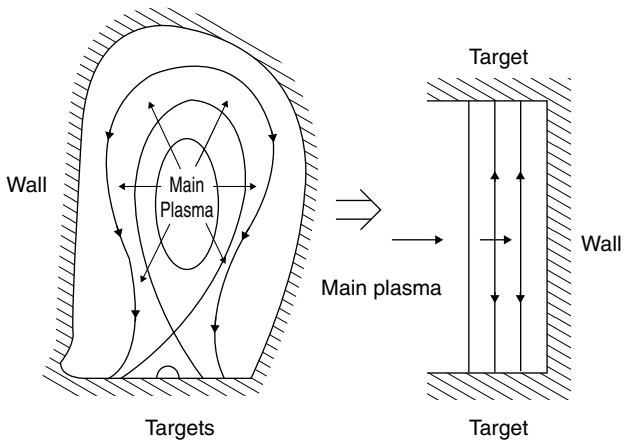

Figure 13.1. Schematic outline of the field line geometry at the plasma edge showing parallel flow to the divertor plates and perpendicular flow from the main plasma to the SOL.

Impurities can be included by adding extra 'fluids', one for each charge state of each impurity species. Thus, there will be a particle conservation equation for the electrons and for each 'ion fluid', with overall neutrality imposed, $n_e = \sum_j z_j n_j$, the sum being over all the ion fluids. Similarly, extra momentum equations are added for each impurity ion fluid. These equations are coupled through the parallel impurity forces, section 6.5.3. In order to limit the computational requirements, individual energy equations are not generally employed. Instead it is assumed that $T_i = T_z$ for all impurity species and charge states. Boundary conditions for the impurity fluids involve as yet unsolved problems with regard to the velocity entering the magnetic pre-sheath and Debye sheath. In reality, each impurity fluid will have a different $v_{\|\mathrm{BMPSE}}$, which will also differ from the $v_{\|\mathrm{BMPSE}}$ of the hydrogenic ion fluid, depending on the details of where the impurities entered the SOL, the degree of collisional coupling, etc. This, however, is very complicated and typically it is assumed that the $v_{\|\mathrm{BMPSE}}$ of the impurity fluids equals the hydrogenic $v_{\|\mathrm{BMPSE}}$ or is given by the impurity ion sound speed. In the absence of information on the matter, the specified values $D_\perp$ and v_{pinch} are usually taken to be the same as for the hydrogenic ions.

The source and sink terms in the particle balance equation for each impurity ionization stage j are given by:

$$S_p = n_e n_{j-1} \overline{\sigma v}_{iz}^{j-1} - n_e n_j \overline{\sigma v}_{iz}^{j} - n_e n_j \overline{\sigma v}_{\mathrm{eirec}}^{j} - n_H n_j \overline{\sigma v}_{\mathrm{cxrec}}^{j} + n_e n_{j+1} \overline{\sigma v}_{\mathrm{eirec}}^{j+1} + n_H n_{j+1} \overline{\sigma v}_{\mathrm{cxrec}}^{j+1} \tag{13.7}$$

where $\overline{\sigma v}_{\mathrm{eirec}}(T_e, n_e)$ is the e–i recombination rate due to two-body and three-body recombination and $\overline{\sigma v}_{\mathrm{cxrec}}(T_e, T_i, T_H, n_e)$ is the charge-exchange recombination rate. The coupled neutral code provides the calculated local value of the hydrogenic density needed for the latter process.

Examples of 2D fluid codes which are *multi-fluid*, i.e. contain impurity fluids, are B2 [13.2], EDGE2D [13.3], UEDGE [13.4], UEDA [13.5].

The entire 2D fluid code calculation—as is also the case for the Monte Carlo approach, section 6.5—is carried out on a mathematical 2D 'grid' which is generated by a separate code. For predictive work, e.g. for a future machine, the grid is calculated from the specified spatial distribution of B_ϕ and B_θ. For interpreting an experiment, the values of the magnetic field are measured by pick-up coils. The parallel direction in the grid is that of $\boldsymbol{B}$. The cross-field direction, within the poloidal plane, is orthogonal to $\boldsymbol{B}_\theta$ at each point. Thus a *curvilinear* and (primarily) *orthogonal* coordinate system is generated; figure 13.2 is such an example. Because the grid is also necessarily finite (not infinitely fine) the straight-line cell boundaries of the grid are not perfectly orthogonal and this requires attention to avoid non-conservation of particles, momentum and energy. Even in the poloidal plane, the target surface elements are usually not orthogonal to $\boldsymbol{B}_\theta$, and so the grid is distorted into a non-orthogonal shape near the targets, figure 13.2. This necessitates further attention to avoid non-conservation effects. The *grid generator* code outputs the 2D coordinate of each cell corner in tokamak

(R, z) coordinates and also the values at the cell centres of the two orthogonal coordinates s_θ and $s_\perp$. Here, s_θ indicates distance measured from outside target to inside target in the poloidal plane. (Increments of these two distances are given by the local value of B_θ/B, also output by the grid generator code.) The grid code also outputs the *metric coefficients* h_θ and $h_\perp$ for each grid cell. In a 2D orthogonal coordinate system of coordinates s_θ and $s_\perp$, the length of a line element ds is given by:

$$\mathrm{d}s^2 = h_\theta^2(\mathrm{d}s_\theta)^2 + h_\perp^2(\mathrm{d}s_\perp)^2. \tag{13.8}$$

Let the two unit vectors be $\boldsymbol{i}_\theta$, $\boldsymbol{i}_\perp$, then:

$$\nabla\phi = \frac{1}{h_\theta}\frac{\partial\phi}{\partial s_\theta}\boldsymbol{i}_\theta + \frac{1}{h_\perp}\frac{\partial\phi}{\partial s_\perp}\boldsymbol{i}_\perp \tag{13.9}$$

$$\boldsymbol{\nabla\cdot A} = \frac{1}{h_\theta h_\perp}\left[\frac{\partial}{\partial s_\theta}h_\perp A_\theta + \frac{\partial}{\partial s_\perp}(h_\theta A_\perp)\right], \tag{13.10}$$

etc (ϕ is any arbitrary scalar quantity and $\boldsymbol{A}$ any arbitrary vector quantity.) Thus, if the grid is perfectly circular then $\mathrm{d}s_\theta = r\mathrm{d}\theta$ where r is the radius of the poloidal surface and:

$$\mathrm{d}s^2 = r^2\mathrm{d}\theta^2 + \mathrm{d}r^2 \tag{13.11}$$

$$\boldsymbol{\nabla}\phi = \frac{1}{r}\frac{\partial\phi}{\partial\theta}\boldsymbol{i}_\theta + \frac{\partial\phi}{\partial r}\boldsymbol{i}_\perp \tag{13.12}$$

$$\boldsymbol{\nabla\cdot A} = \frac{1}{r}\frac{\partial A_\theta}{\partial\theta} + \frac{1}{r}\frac{\partial}{\partial r}(rA_\perp), \tag{13.13}$$

etc.

For complete derivations of the 2D fluid equations, including curvature, $\boldsymbol{E}\times\boldsymbol{B}$ and diamagnetic drifts, see the PhD thesis of M Baelmans [13.6]. A reduced form, as originally used in the B2 code originated by B J Braams [13.7] and including the time dependence is as follows.

Particles:

$$\frac{\partial}{\partial t}(n) + \frac{1}{h_r h_\theta}\frac{\partial}{\partial s_\theta}(h_r n v_\theta) + \frac{1}{h_r h_\theta}\frac{\partial}{\partial r}(h_\theta n v_r) = S_{iz}. \tag{13.14}$$

Momentum:

$$\begin{aligned}\frac{\partial}{\partial t}(\rho v_\parallel) &+ \frac{1}{h_r h_\theta}\frac{\partial}{\partial s_\theta}\left(h_r\rho v_\theta v_\parallel - \frac{h_r}{h_\theta}\eta_\theta^i\frac{\partial v_\parallel}{\partial s_\theta}\right)\\ &+ \frac{1}{h_r h_\theta}\frac{\partial}{\partial r}\left(h_\theta\rho v_r v_\parallel - \frac{h_\theta}{h_r}\eta_r^i\frac{\partial v_\parallel}{\partial r}\right)\\ &= S_{\mathrm{mom}}v_\parallel - \frac{B_\theta}{B}\frac{1}{h_\theta}\frac{\partial p}{\partial s_\theta}.\end{aligned} \tag{13.15}$$

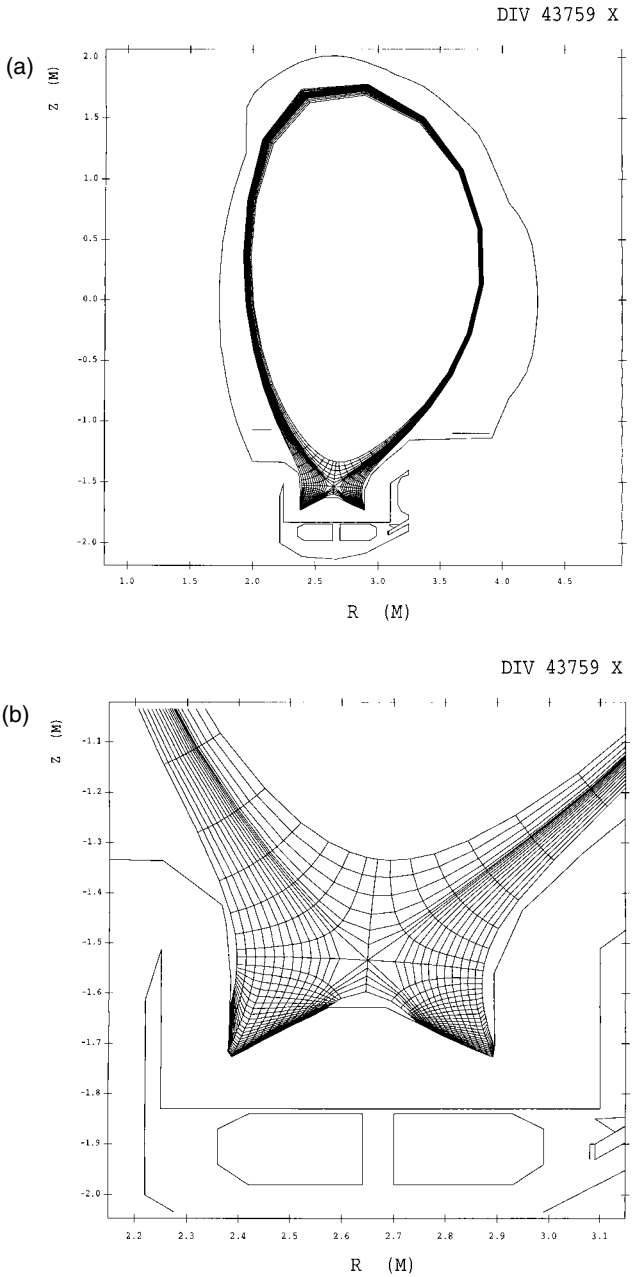

Figure 13.2. Example of a (primarily) orthogonal grid for JET: (a) overview, (b) close-up view of divertor. Note that the grid becomes non-orthogonal near the targets to accommodate the 'non-orthogonal targets'.

Electron energy:

$$\frac{\partial}{\partial t}\left(\tfrac{3}{2}nkT_e\right)+\frac{1}{h_r h_\theta}\frac{\partial}{\partial s_\theta}\left(h_r\frac{5}{2}nv_\theta kT_e-\frac{h_r}{h_\theta}\chi_\theta^e\frac{\partial kT_e}{\partial s_\theta}\right)+\frac{1}{h_r h_\theta}\frac{\partial}{\partial r}\left(h_\theta\frac{5}{2}nv_r kT_e-\frac{h_\theta}{h_r}\chi_r^e\frac{\partial kT_e}{\partial r}\right)=Q_{Ee}+Q_R-Q_{eq}+\frac{v_\theta}{h_\theta}\frac{\partial p_e}{\partial s_\theta}+\frac{v_r}{h_r}\frac{\partial p_e}{\partial r}. \tag{13.16}$$

Ion energy:

$$\frac{\partial}{\partial t}\left(\tfrac{3}{2}nkT_i+\tfrac{1}{2}\rho v_\parallel^2\right)+\frac{1}{h_r h_\theta}\frac{\partial}{\partial s_\theta}\left[h_r\left(\tfrac{5}{2}nv_\theta kT_i+\tfrac{1}{2}\rho v_\theta v_\parallel^2\right)-\frac{h_r}{h_\theta}\left(\chi_\theta^i\frac{\partial kT_i}{\partial s_\theta}+\frac{1}{2}\eta_\theta^i\frac{\partial v_\parallel^2}{\partial s_\theta}\right)\right]+\frac{1}{h_r h_\theta}\frac{\partial}{\partial r}\left[h_\theta\left(\tfrac{5}{2}nv_r kT_i+\tfrac{1}{2}\rho v_r v_\parallel^2\right)-\frac{h_\theta}{h_r}\left(\chi_r^i\frac{\partial kT_i}{\partial r}+\frac{1}{2}\eta_r^i\frac{\partial v_\parallel^2}{\partial r}\right)\right]=Q_{Ei}+Q_{eq}-\frac{v_\theta}{h_\theta}\frac{\partial p_e}{\partial s_\theta}-\frac{v_r}{h_r}\frac{\partial p_e}{\partial r} \tag{13.17}$$

where

$$\begin{aligned}S_{\mathrm{mom}\,v_\parallel}&=\text{volume sources of parallel momentum}\\ \eta_\theta^i,\ \eta_r^i&=\text{poloidal and radial ion viscosity coefficients}\\ \chi_\theta^{e,i},\ \chi_r^{e,i}&=\text{thermal conductivities}\\ v_\theta&=v_\parallel(B_\theta/B).\end{aligned}$$

Most of the terms in equations (13.14)–(13.17) can readily be related to those in equations (13.1)–(13.6). For inclusion of impurity terms and equations see, for example, [13.8].

Figure 13.3 gives an example of B2-EIRENE modelling of ITER [13.9]. The plots give the radial profiles of n_e, T_e, and total plasma pressure p at the upstream end and at the target plate. For both cases the results are 'mapped' along $\boldsymbol{B}$ to the outside mid-plane and plotted against the radial location of the $\boldsymbol{B}$-line there. For this case 200 MW enters the edge from the main plasma with 120 MW being radiated in the edge by impurities—the core-produced He, sputtered C and injected (0.2%) Ne. One notes that the e-folding lengths for n_e, T_e, p (at the outside mid-plane) are 2 cm, 2 cm, 1 cm, respectively. In the divertor there is a cold region close to the separatrix with T_e otherwise rather constant radially. There is a drop in plasma pressure near the separatrix, corresponding to'partial detachment', chapter 16. B2/EIRENE has also been used for systematic studies of operating tokamaks, C-MOD, DIII-D, JET and JT-60U, aimed at reproducing experimental measurements in order to assess code reliability [13.10].

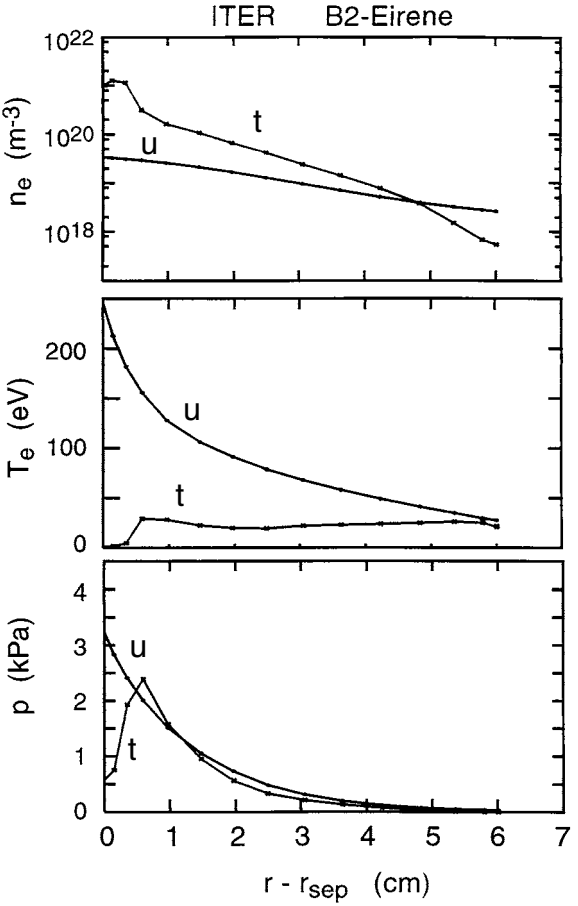

Figure 13.3. Example of B2/EIRENE code solutions for ITER [13.9]. Radial profiles of n_e, T_e and total plasma pressure p at the upstream end (u) and at the target (t) (mapped to the outside mid-plane).

References

[13.1] Hutchinson I H 1987 *Phys. of Fluids* **30** 3777
[13.2] Braams B 1987 A multi-fluid code for simulation of the edge plasma in tokamaks *NET report* EUR-FU IXII-80-87-68
[13.3] Simonini R, Taroni A, Keilhacker M *et al* 1992 *J. Nucl. Mater.* **196–198** 369
[13.4] Rognlien T D, Milovich J L, Rensink M E and Porter G D 1992 *J. Nucl. Mater.* **196–198** 347
[13.5] Ueda N, Itoh K and Itoh S I 1989 *Nucl. Fusion* **29** 173
[13.6] Baelmans M 1991 *PhD Thesis* Ecole Royale Mililtaire, Belgium, Report No 100

[13.7] Braams B 1986 *PhD Thesis* University of Utrecht
[13.8] Keilhacker M, Simonini R, Taroni A and Watkins M L 1991 *Nucl. Fusion* **31** 535
[13.9] Kukushkin A S 1999 ITER JCT Garching, private communication
[13.10] Loarte A, Kukushkin A S, Pacher H D *et al* 1999 *J. Nucl. Mater.* **266–269** 1123

PART 3

PLASMA BOUNDARY RESEARCH

Introduction to Part III

Part III of this book is a collection of essays on more-or-less active research topics in plasma edge physics. The selection of topics is inevitably arbitrary. The coverage is uneven and the topics chosen tend to reflect the personal interests of the author. The material in this part will undoubtedly date more quickly than that in parts I and II, and in any subsequent edition of the book, it is probable that some of this material would be revised, removed or replaced.

Chapter 14

Supersonic Flow along the SOL

In section 1.8.2.5 it was shown that for *isothermal* flow along the SOL, the Mach number cannot exceed unity; otherwise singularities would exist somewhere upstream of the sheath entrance. Analysis of the sheath itself, chapter 2, shows that the flow entering the sheath must be sonic or *supersonic*. It is shown in section 14.2 that smooth (non-singular) sonic transitions can occur in the flow upstream of the sheath entrance when the flow is *non-isothermal* with the flow entering the sheath at $M_t < -1$ [14.1]. In the next section we consider first the effect of supersonic flow on the SOL properties.

14.1 The Effect on the SOL of Supersonic Flow Into the Sheath

Pressure balance, section 9.4, gives:

$$n(2kT + m_i v^2) = n_t(2kT_t + m_i v_t^2) = 2n_u k T_u \equiv p_u \tag{14.1}$$

where we assume $T_e = T_i$ here. For illustration we assume that parallel heat conduction controls $T(x)$:

$$[T(x)]^{7/2} = T_t^{7/2} + \tfrac{7}{2} q_\parallel x/\kappa_0 \tag{14.2}$$

section 4.10. Assuming no volumetric power loss, then the power flux density enters the sheath and from section 2.8:

$$q_\parallel = \gamma n_t k T_t |M_t| c_{st}. \tag{14.3}$$

We will allow for the dependence of the sheath heat transmission coefficient γ on M_t. We do not attempt a complete treatment but estimate:

$$\gamma(M_t) = 7.5 + M_t^2 \tag{14.4}$$

based on the assumptions that:

(a) the ion power flux density into the sheath equals the parallel convective heat flux density at speed $M_t c_{st}$, i.e. $\left(\frac{5}{2}kT_t + \frac{1}{2}mv_t^2\right)\Gamma_t$ or $\left(\frac{5}{2} + M_t^2\right)kT_t\Gamma_t$, section 9.9;
(b) the electron heat flux density can still be approximated as $5kT_t\Gamma_t$; strictly the sheath potential drop decreases in magnitude as the flow becomes more supersonic, reducing the factor 5 somewhat, but we ignore this small correction here.

The foregoing equations can be combined to give:

$$T_t = f_{T_t}(M_t)\left[\frac{m_i}{2e}\frac{4q_\parallel^2}{\gamma_1^2 e^2 n_u^2 T_u^2}\right] \tag{14.5}$$

and since $\gamma_1 = 8.5$ is the value for $|M_t| = 1$, we can write:

$$f_{T_t}(M_t) \equiv \left[\frac{8.5(1 + M_t^2)}{2|M_t|(7.5 + M_t^2)}\right]^2 \tag{14.6}$$

which we call the *Mach number target temperature factor*. The rest of the terms on the RHS of equation (14.5) are as before for $|M_t| = 1$, equation (5.8), and thus we may write:

$$T_t = f_{T_t}(M_t)T_{t1} \tag{14.7}$$

and also:

$$n_t = f_{n_t}(M_t)n_u T_u / 2T_{t1} = f_{n_t}(M_t)n_{t1} \tag{14.8}$$

where T_{t1} and n_{t1} are the values that would have existed if $|M_t|$ had equalled unity, and where:

$$f_{n_t}(M_t) \equiv 2/[f_{T_t}(M_t)(1 + M_t^2)] \tag{14.9}$$

is the *Mach number target density factor*. The particle flux density to the target becomes:

$$\Gamma_t = f_{\Gamma_t}(M_t)n_{t1}c_{st1} \tag{14.10}$$

where:

$$f_{\Gamma_t}(M_t) \equiv |M_t| f_{n_t}(M_t)[f_{T_t}(M_t)]^{1/2} \tag{14.11}$$

is the *Mach number target flux factor*. These factors are plotted in figure 14.1. Strongly, supersonic flow can cool the plasma significantly, at the same time also rarifying it significantly. Perhaps surprisingly, however, the particle flux to the targets is not greatly affected by supersonic flow, and is still largely governed by the *upstream* parameters, equation (5.13). As $|M_t| \to \infty$, $f_{\Gamma_t} \to 4/\gamma \approx 0.47$.

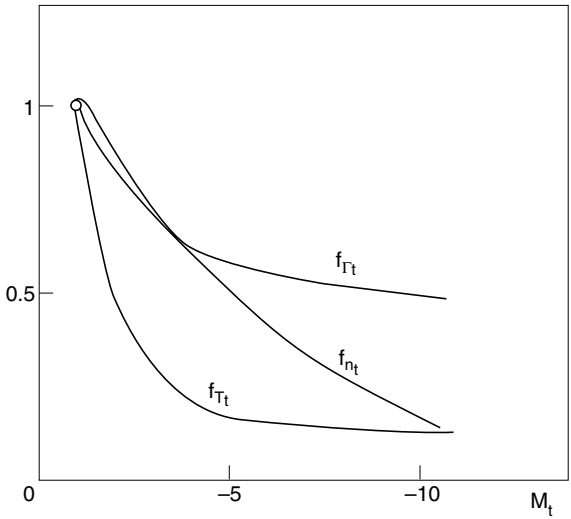

Figure 14.1. Mach number target temperature, equation (14.6), density, equation (14.9), and flux, equation (14.11), factors show that as $|M_t|$ increases, both T_t and n_t drop substantially, but the particle flux to the target only changes by a factor $\lesssim 0.5$.

14.2 The Mid-stream Sonic Transition for an Analytic Case

It might appear from the last section that M_t is a completely free parameter. Yet we saw from the two-point model, section 5.2, that the system is uniquely specified by imposing just *two* parameters, say n_u and $q_\parallel$, while it was always imposed that M_t have the specific value of unity. If M_t is now to be 'free', what in fact constrains its value? And how, generally, is a unique solution specified? We address this question in this and the next sections by considering a simple analytic case. The situation for numerical codes is briefly addressed in section 14.4.

For illustration we assume a constant particle source localized near the target:

$$\Gamma(x) = n(x)v(x) = \begin{cases} n_t v_t (1 - x/L_i) & \text{for } x \le L_i \\ 0 & \text{for } x \ge L_i \end{cases} \tag{14.12}$$

where x is measured upstream from $x = 0$ at the target and L_i is the specified length of the source region. We wish to establish the circumstances under which this source can drive the flow supersonic, $|v_t| > c_{st}$ (note: v and $v_t < 0$). The sound speed at the target:

$$c_{st} = (2kT_t/m_i)^{1/2}. \tag{14.13}$$

It is convenient to define a dimensionless speed $M(x)$:

$$M(x) \equiv v(x)/c_{st}. \tag{14.14}$$

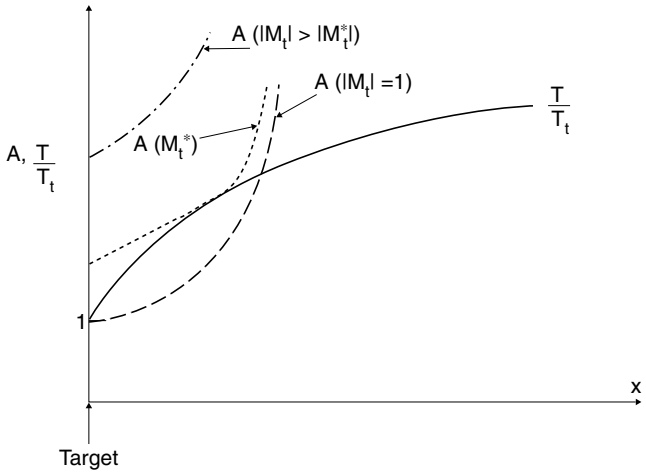

Figure 14.2. When temperature increases with distance x from the target, a mid-flow sonic transition occurs at the point x^* where the parameter $A(M_t, x)$, equation (14.15), equals the normalized temperature $T(x)/T_t$. This occurs for a unique value of M_t, namely M_t^*, such that the curve $A(M_t^*, x)$ just touches the $T(x)/T_t$ curve tangentially at x^*.

It is important to note that this is *not* the (local) Mach number, since the speed has been normalized to the sound speed at the *target*, not the *local* sound speed. (The true local Mach number depends on x due to the x-dependence of both $v(x)$ and $T(x)$, while the $M(x)$ here only depends on x through $v(x)$.)

We now combine equations (14.1), (14.12)–(14.14) to obtain:

$$M(x) = \frac{(1+M_t^2)}{2M_t(1-x/L_i)} - \left[\underbrace{\left(\frac{1+M_t^2}{2M_t(1-x/L_i)} \right)^2}_{\equiv A(x)} - \frac{T(x)}{T_t} \right]^{1/2}. \qquad (14.15)$$

No solution for $M(x)$ exists if $A(x) < T(x)/T_t$ at any point in the flow. For isothermal flow it is thus only necessary that $A(x) \geq 1$ at all points; for a given value of M_t, the smallest $A(x)$ occurs at $x = 0$, i.e. is $A(0)$, and a value of $|M_t| = 1$ is then sufficient to ensure real solutions for $M(x)$ at all points. When $T(x)$ is a rising function, e.g. due to finite heat conductivity, however, then $A(x)$ may be less than $T(x)/T_t$ in some region (dependent on the specified value of L_i). Figure 14.2 indicates the general possibilities, showing that a critical value of M_t exists, M^*: if $|M_t| < |M_t^*|$ then a region exists near the target where $A(x) < T(x)/T_t$ and no solution for $M(x)$ exists; if $|M_t| > |M_t^*|$ then there is no problem with an imaginary $M(x)$. We will show below that for the choice of $M_t = M_t^*$ precisely a smooth, mid-stream sonic transition occurs. This is therefore the actual solution and one sees that there is a unique value of M_t—and a unique solution generally—for a given set of control parameters $(L_i, p_u, q_\parallel)$.

Thus the previous boundary condition that $|M_t| = 1$ *is now replaced by the constraint that* $v(x)$*,* $n(x)$*, etc have no mid-stream discontinuities.*

Before proceeding to this demonstration, we may note that one way to view the cause of supersonic flow is as a competition between the rates of change of $\Gamma(x)$ and $T(x)$ [14.2]. If $\Gamma(x)$ drops only slowly (L_i long) compared with a rapid rise of $T(x)$, then $A(x)$ will be less than $T(x)/T_t$ *unless* $|M_t|$ *is large*. Thus we may view supersonic flow as being 'caused' by temperature-parallel scale lengths being shorter than particle-flux-parallel scale lengths. Consider the situation just at the onset of supersonic flow so that $|M_t| = 1$ and thus:

$$A(x) \approx (1 - x/L_i)^{-2}. \tag{14.16}$$

We are interested in locations very near the target where the flow will first become supersonic, thus $A(x) \approx 1 + 2x/L_i$. We may introduce a characteristic temperature scale length L_T:

$$T(x)/T_t \approx 1 + x/L_T. \tag{14.17}$$

Thus, the flow at the target will remain subsonic (no imaginary root for equation (14.15) provided:

$$L_T > L_i/2 \tag{14.18}$$

We see that the temperature scale length at the target must remain longer than half the particle-source scale length if the target conditions are to remain sonic.

We consider next the specific $T(x)$ profile given by conduction, equation (14.2):

$$T/T_t = \left(1 + \frac{7q_\parallel x}{2\kappa_0 T_t^{7/2}}\right)^{2/7}.$$

Thus:

$$T/T_t \approx 1 + \frac{q_\parallel x}{\kappa_0 T_t^{7/2}} \tag{14.19}$$

for x small. The criterion for avoiding supersonic flow now becomes a condition on the absolute value of target temperature T_t:

$$T_t > T_t^{\text{crit}} \equiv (q_\parallel L_i/2\kappa_0)^{2/7}. \tag{14.20}$$

If T_t is driven lower then supersonic flow will result. We may obtain a criterion in terms of the control parameters $q_\parallel$ and p_u by relating c_{st} (thus T_t) to $q_\parallel$ and p_u using equation (14.3). Thus by combining equations (14.1), (14.3), (14.14), (14.15):

$$p_u = \frac{2q_\parallel(1 + M_t^2)}{\gamma |M_t| c_{st}}. \tag{14.21}$$

Therefore supersonic flow will occur when:

$$p_u > p_u^{\text{crit}} = \frac{4q_\parallel(2\kappa_0/q_\parallel L_i)^{1/7}}{\gamma(2e/m_i)^{1/2}} \tag{14.22}$$

where $|M_t| = 1$ was used in equation (14.21) to obtain the onset of supersonic flow. Thus, for a given heat flux, the flow will go supersonic if it is 'pushed hard enough', i.e. if p_u is large enough. Equation (14.21) can also be re-written to give a criterion in terms of $q_\parallel$, showing that for a given upstream pressure p_u (thus a given upstream density n_u since T_u is so insensitive to all variations, section 5.2) supersonic flow will occur when:

$$q_\parallel < q_\parallel^{\text{crit}} = [(\gamma p_u (2e/m_i)^{1/2}/4]^{7/6} (L_i/2\kappa_0)^{1/6}. \tag{14.23}$$

That is 'starving the SOL for power' can drive it supersonic. One may note that raising n_u or lowering $q_\parallel$ are also ways of causing divertor detachment, chapter 16, and so a number of processes are likely to set in at the same time when low values of T_t occur—including also strong radiative power loss, section 5.5. The present criteria for the onset of supersonic flow should therefore only be taken as rough indicators.

Example: $q_\parallel = 10^8$ W m^{-2}, $L_i = 1$ m which gives $T_t^{\text{crit}} = 18$ eV from equation (14.22). This value is somewhat unrealistically high because of the assumption that $T(x)$ is controlled entirely by heat conduction, equation (14.2). In fact, for $x < L_i$ heat convection carries much of the parallel power flow, and just at the target—which is the location where the flow just goes supersonic—it carries most of the power. This effect can be allowed for by including a factor f_{cond} in equation (14.19)—multiplying $q_\parallel$, section 5.4. For $f_{\text{cond}} = (8.5\text{–}6)/8.5 = 0.294$ (see last part of section 5.2) then T_t^{crit} is reduced by $(f_{\text{cond}})^{2/7} \approx 0.7$, making $T_t^{\text{crit}} = 12.8$ eV. Also p_u^{crit}, equation (14.22), is multiplied by $(f_{\text{cond}})^{-1/7}$ while $q_\parallel^{\text{crit}}$, equation (14.23), is multiplied by $(f_{\text{cond}})^{1/6}$. For the above example and assuming also $L = 100$ m one obtains: $p_u^{\text{crit}} = 1.3 \times 10^3$ N m^{-2}, $n_t^{\text{crit}} = 1.6 \times 10^{20}$ m^{-3}, $T_u^{\text{crit}} = 117$ eV, $n_u^{\text{crit}} = 3.6 \times 10^{19}$ m^{-3}.

14.3 Supersonic Solutions for an Analytic Case

In this section we obtain expressions for the characteristics of supersonic solutions including the target Mach number M_t (which is also the true local Mach number at that location), the location of the sonic transition x^*, etc, for the simple analytic case set up in the last section.

We differentiate equation (14.15) to obtain for $x < L_i$:

$$\frac{M'}{M} = \frac{T'/T_t - (M^2 + T/T_t)^2 (M_t/M)/(L_i(1 + M_t^2))}{T/T_t - M^2} \tag{14.24}$$

The sonic transition occurs when the denominator of equation (14.24) is zero. In order for the transition to be smooth, the numerator must simultaneously go to zero [14.3]. Thus at the sonic point:

$$T/T_t = M^2 \tag{14.25}$$

$$T'/T_t = \frac{(M^2 + T/T_t)^2 (M_t/M)}{L_i(1 + M_t^2)}. \tag{14.26}$$

Note that, since $M < 0$, equation (14.25) gives:

$$(T/T_t)^{1/2} = -M. \tag{14.27}$$

From equation (14.2) we also have:

$$T/T_t = (1 + \alpha x)^{2/7} \tag{14.28}$$

where

$$\alpha \equiv \frac{7}{2}\frac{q_\parallel}{\kappa_0 T_t^{7/2}}. \tag{14.29}$$

The preferred control parameters of this problem are p_u, $q_\parallel$ and L_i; however, it is convenient to replace p_u with T_t as a control parameter. Later we will obtain an expression relating p_u and T_t, so that p_u can then be used instead.

From equation (14.28) one obtains a second expression for T' and when this is equated to equation (14.26) and equations (14.25), (14.27), (14.28) are used one obtains the principal result:

$$\frac{(1 + M_t^2)}{2M_t} = -\frac{7}{\alpha L_i}((\alpha L_i + 1)/8)^{8/7} \tag{14.30}$$

which gives M_t in terms of the control variables (α, L_i), i.e. using equation (14.29), the control variables $(q_\parallel, T_t, L_i)$. One also obtains the location of the sonic transition:

$$x^* = ((T^*/T_t)^{7/2} - 1)/\alpha \tag{14.31}$$

where T^* is the temperature at the sonic point:

$$T^*/T_t = ((\alpha L_i + 1)/8)^{2/7}. \tag{14.32}$$

One can combine equations (14.1), (14.3), (14.13) to obtain the relation between T_t and p_u:

$$p_u = \frac{2q_\parallel(1 + M_t^2)}{\gamma|M_t|c_{st}} = \frac{2q_\parallel(1 + M_t^2)}{\gamma|M_t|(2e/m_i)^{1/2}T_t^{1/2}}. \tag{14.33}$$

For the same example as above (but leaving out the f_{cond} factor) one obtains $M_t(T_t)$, figure 14.3(a) and $M_t(p_u)$, figure 14.3(b). The sonic point moves out to the limiting position $x^* = L_i/8$ as $|M_t| \to \infty$.

14.4 Supersonic Solutions in Numerical Codes

For the onion-skin model, OSM, based on Runge–Kutta, 'one-way marching' of the solution, upstream from the target, section 12.2 (e.g. 'SOL Opt. 22' in the DIVIMP code), the unique value of M_t required to give a smooth sonic transition is found by a straightforward, explicit search technique. Successively refined estimates for the specified M_t are made until the magnitude of the discontinuities at

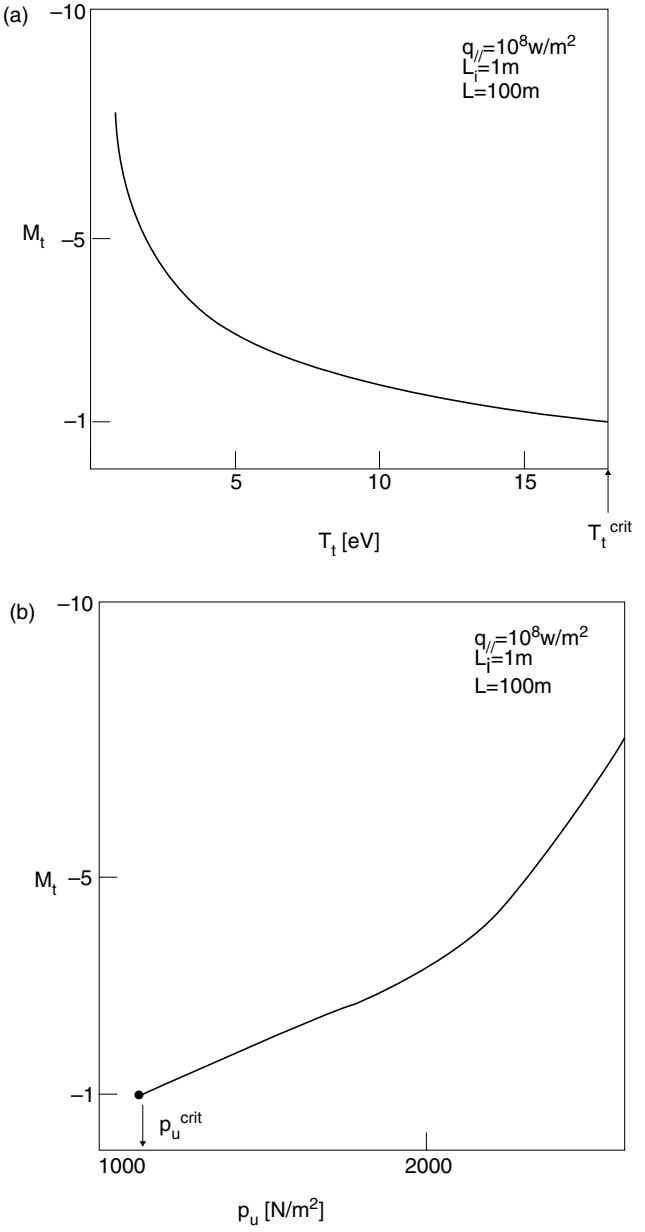

Figure 14.3. For the particular case of $q_{\|} = 10^8$ [W m^{-2}], $L = 100$ m, L_i (length of ionization region) = 1 m: (a) the target Mach number M_t and target temperature T_t are uniquely related. For $T_t \geq T_t^{\text{crit}}$ the flow at the target is sonic. (b) M_t and upstream pressure p_u are also uniquely related. For $p_u \leq p_u^{\text{crit}}$ the flow at the target is sonic.

the sonic point fall below some specified value. For more sophisticated numerical analysis based on computational fluid dynamics, CFD, techniques, e.g. the 1D OSM 'SOL Opt. 23' in DIVIMP [14.4], or in 2D edge fluid codes, the solution naturally evolves smooth sonic transitions as it iterates, since the entire flow field is 'relaxed' simultaneously. The value of $|M_t| \geq 1$ evolves without being forced to any specified value.

References

[14.1] Stangeby P C 1991 *Plasma Phys. Control. Fusion* **33** 677
[14.2] Harbour P J and Loarte A 1994 *Contrib. Plasma Phys.* **34** 312
[14.3] Chodura R *Physics of Plasma–Wall Interactions in Controlled Fusion* ed D E Post and R Behrisch (New York: Plenum) p 99
[14.4] Fundamenski W 1999 *PhD Thesis* University of Toronto

Chapter 15

Flow Reversal in the SOL

In the absence of $\boldsymbol{E} \times \boldsymbol{B}$ drifts, chapter 18, and other such complicating effects, plasma flow only occurs between particle source and particle sink regions. The particle source for limiter SOLs is often cross-field diffusion from the confined plasma and so the particle source—and the resulting parallel plasma flow—tends to be well distributed along the SOL, with the flow direction being toward the target at all points. Divertor SOLs, on the other hand, can be in the high recycling regime, section 5.3, with the recycle ionization occurring quite near the divertor targets. In the simplest, purely 1D picture this then implies stagnant plasma over most of the SOL, extending between the ends of the ionization zones at each target. Such a situation would be undesirable from the viewpoint of impurity transport: any impurities entering the stagnant part of the SOL, e.g. from wall sputtering by charge-exchange neutrals, would experience no 'flushing' action by plasma flow to the targets (sinks) and would cause unacceptable contamination of the main plasma, section 6.5. This picture would also be difficult to understand regarding the *radial* profile of $n_e(r)$ upstream: one anticipates that $n_e(r)$ will be a decreasing function of r, and indeed experimental measurements of $n_e(r)$ confirm that to be the case (which is fortunate if strong plasma–wall contact is to be avoided!). But how could such $n_e(r)$ profiles exist? If cross-field transport is due solely to diffusion (no radial 'pinch' effect) then a decaying $n_e(r)$ profile implies a *source* of particles at/near the separatix, or a flux of particles entering the SOL across the separatrix. That, however, appears to be ruled out here. In principle one could solve this puzzle by invoking a convective radial 'pinch' drift process directed inward that was just such as to balance the outward radial flux of particles, but such a solution raises questions of credibility.

A more credible explanation is that of *flow reversal* [15.1–15.8] under high recycling conditions. This is inherently a two-dimensional effect.

For illustration, consider a deep 'slot' divertor with solid walls along each side of the divertor 'plasma leg' which terminates at the target, figure 15.1. In this picture the separatrix lies along the axis of the 'slot', with the SOL on the right side, private plasma on the left. Generally $T_e(x)$ will vary with distance

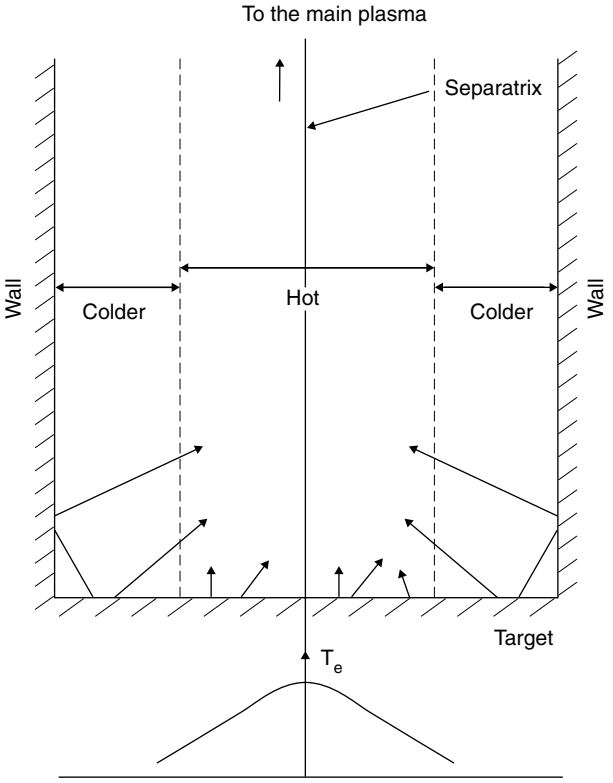

Figure 15.1. Schematic of a deep slot divertor with separatrix along the centre line. The temperature tends to peak on the separatrix due to power influx from the main plasma, which makes for more ionizing conditions there. Recycling neutrals—from all parts of the target—therefore tend to be ionized near the separatrix, resulting in 'over-ionization' on those flux tubes, and flow reversal.

r across the 'plasma leg', being highest—and thus usually most ionizing—near the separatrix. Therefore, neutrals recycling from the target near the separatrix will tend to be re-ionized within flux tubes near the separatrix—*but so will the neutrals recyling from the outer parts of the target*. Thus the flux tubes near the separatrix tend to have a *source excess* while the outer flux tubes suffer a *source deficit*. That is, in the near-separatrix flux tubes there is a stronger *source* of particles than the (target) *sink*, while for the outer flux tubes, the opposite occurs. Overall particle balance is satisfied by flow reversal in the source-excess tubes: a 'watershed' forms at some point within the ionization region in those tubes, figure 15.2. Between the 'watershed' and the target, plasma flow is toward the target. Upstream of the 'watershed' flow is away from the target. The latter is the reversed flow and would exist, in a symmetrical divertor tokamak, all the way to

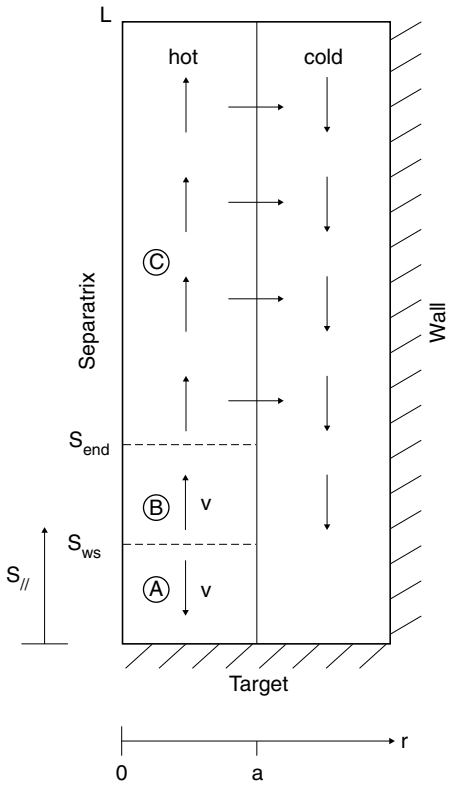

Figure 15.2. Flow reversal schematic. In the 'over-ionized' (hot) flux tubes, a 'water-shed' forms at $s_{\|} = s_{ws}$ with plasma flow in region A being toward the target and away from it in regions B and C. The ionization occurs over regions A and B. The 'under-ionized' (cold) flux tubes are fed by cross-field diffusion from the hot flux tubes. Thus a large scale convective cell, involving flow reversal, is established.

the midpoint between the two targets. The reversed flow velocity would drop to zero by the midpoint as a result of 'drainage' of particles via cross-field diffusion into the outer flux tubes. The latter acts as a distributed source for the outer tubes which are therefore characterized by parallel flow toward the target, all along their length.

An impurity 'flushing action' can thus still exist even in high recycling divertor SOLs. One also has an explanation for the existance of upstream, radially decaying $n_e(r)$ profiles without need to involve an inward pinch.

(Sometimes the term 'flow reversal' is used [15.9] to refer to what might better be called the 'backflow of impurities' [15.10] out of a divertor—due, for example, to a strong temperature-gradient force, chapter 6. Here we will restrict the term 'flow reversal' to refer to the main (hydrogenic) species.)

Since this phenomenon is dependent on the spatial details of the ionization pattern, and since the excess/deficit levels are usually small compared with the target flows [15.8], it is difficult to make any simple quantitative estimates, and the use of hydrogenic neutral codes is necessary. Experimental evidence for flow reversal has also been reported, however [15.3, 15.11–15.19].

We now outline a simple model which provides a *rough* estimate for the velocity in the flow-reversed region, and which serves to illustrate the basic physical processes involved. Consider the right-hand side part of the 'plasma leg' shown in figure 15.1. We will assume that the n and T profiles in the near-target region are given. The radial profiles are exponential:

$$n(r) = n_0 \mathrm{e}^{-r/\lambda_n} \tag{15.1}$$

$$T(r) = T_0 \mathrm{e}^{-r/\lambda_T} \tag{15.2}$$

where $n_0, T_0, \lambda_n, \lambda_T$ are given. We assume that T is constant along $\boldsymbol{B}$ on each flux tube throughout the ionization zone. We will approximate the ionization rate coefficient for hydrogen, figure 1.25, $\overline{\sigma v}_{iz}$, as being zero for $T_e < 10$ eV and constant above 10 eV and thus all the ionization of the recycling neutrals occurs in $0 \leq r \leq a$, where a is given by $T_0 \mathrm{e}^{-a/\lambda_T} = 10$ eV. We model the SOL as consisting of two flux tubes, figure 15.2: the *hot tube* $0 \leq r \leq a$, near the separatrix, with the cold *tube* outboard of it representing the rest of the SOL. There are three zones along the hot tube:

(A) from $s_\parallel = 0$ to $s_\parallel = s_{ws}$, where s_{ws} is the location of the 'watershed', the flow is toward the target;
(B) from $s_\parallel = s_{ws}$ to s_{end}, where s_{end} is the end of the ionization region; here the flow is reversed and increases from $v_\parallel = 0$ at s_{ws} to v_{end} at s_{end};
(C) from $s_\parallel = s_{\mathrm{end}}$ to the halfway point to the next target the flow is also reversed but decreases to $v_\parallel = 0$ as the excess particles are 'drained off' to the cold tube by cross-field diffusion.

We wish to estimate the value of v_{end}, the maximum reversed velocity.

The total target flow is ϕ_t:

$$\phi_t = \int_0^\infty \Gamma_0 \mathrm{e}^{-r/\lambda_\Gamma} \mathrm{d}r = \Gamma_0/\lambda_\Gamma \tag{15.3}$$

where

$$\Gamma_\parallel(r) = \Gamma_0 \mathrm{e}^{-r/\lambda_\Gamma} \tag{15.4}$$

$$\Gamma_0 = n_0 c_{s0} \tag{15.5}$$

$$\lambda_\Gamma^{-1} = \lambda_n^{-1} + (2\lambda_T)^{-1} \tag{15.6}$$

section 4.4. (ϕ_t, and also the fluxes below, should be multiplied by B_Θ/B at the target to obtain the actual *deposited* fluxes per metre toroidally around the torus.)

The total flux reaching the hot tube target is ϕ_t^{hot}:

$$\phi_t^{\text{hot}} = \int_0^a \Gamma_0 \mathrm{e}^{-r/\lambda_\Gamma} \mathrm{d}r = \frac{\Gamma_0}{\lambda_\Gamma}(1 - \mathrm{e}^{-a/\lambda_\Gamma}) \tag{15.7}$$

while the total flux to the cold target ϕ_t^{cold}:

$$\phi_t^{\text{cold}} = \int_a^\infty \Gamma_0 \mathrm{e}^{-r/\lambda_\Gamma} \mathrm{d}r = \frac{\Gamma_0}{\lambda_\Gamma} \mathrm{e}^{-a/\lambda_\Gamma}. \tag{15.8}$$

Now ϕ_t^{hot} is equal to the total ionization occurring within region A, while ϕ_t^{cold} is equal to the total ionization occurring within region B, i.e.:

$$\phi_{\text{excess}} \equiv \phi_t^{\text{cold}}. \tag{15.9}$$

Assuming isothermal conditions along the hot tube throughout regions A and B, then the plasma density increases from n_t at $s_\parallel = 0$ to $2n_t$ at $s_\parallel = s_{ws}$ (isothermal flow, section 1.8.2.7). Density then drops again to n_{end} at $s_\parallel = s_{\text{end}}$, where $M = M_{\text{end}}$, $v = v_{\text{end}}$.

From momentum balance in region B:

$$2n_t T = n_{\text{end}} T (1 + M_{\text{end}}^2). \tag{15.10}$$

One notes that in this crude model we have now replaced the radial variations of n and T within the hot tube with radially averaged values there. Thus particle balance gives for region A:

$$n_t c_s a = \phi_t^{\text{hot}} \tag{15.11}$$

and for region B:

$$n_{\text{end}} M_{\text{end}} c_s a = \phi_{\text{excess}}. \tag{15.12}$$

Combining equations (15.7)–(15.12) gives an equation for M_{end}:

$$M_{\text{end}}^2 - 2(\mathrm{e}^{a/\lambda_\Gamma} + 1) M_{\text{end}} + 1 = 0. \tag{15.13}$$

Example: say $\lambda_n = \lambda_T = a/\ln 3$, $T_0 = 30$ eV. Thus $\mathrm{e}^{a/\lambda_T} = 3$, $\mathrm{e}^{a/\lambda_\Gamma} \approx 5.2$, $\phi_t^{\text{hot}}/\phi_{\text{excess}} \approx 6.2$ and $M_{\text{end}} \approx 0.085$. Taking $T \approx 20$ eV as a radially-averaged temperature in the hot tube gives $c_s = 4.4 \times 10^4$ m s^{-1} (D^+ ions) and so $v_{\text{end}} \approx 3.7 \times 10^3$ m s^{-1}.

In Region C, $v_\parallel$ decreases and $M_\parallel$ decreases even more rapidly since $T(s_\parallel)$ increases.

This crude estimate merely serves to illustrate the processes involved and indicates that reversed flow Mach numbers may be significant.

In section 1.8.2.8 we considered the consequences of an ionization source being close to the targets, thus apparently implying $v \approx 0$ over most of the length of the SOL—and that this in turn appeared to imply that the SOL width would extend radially until plasma contact occurred at the walls. If this were actually

to happen then limiters and divertors would not, in fact, limit the radial size of the plasma, but rather the walls would—possibly an undesirable result. In fact, flow reversal means that the high recycling SOL is *not* generally characterized by $v \approx 0$ and there are *not* SOL particles with SOL dwell times $\rightarrow \infty$. Thus SOL decay lengths remain finite. The quantitative implications of flow reversal for SOL widths are considered in chapter 21.

Flow reversal velocities have been measured on a number of tokamaks, based on the Doppler shifts of various impurity lines observed in the SOL [15.11–15.15], and with Mach probes [15.16–15.19]. It is not necessarily the case, as noted earlier, that the impurity ion motion is in the same direction as the (hydrogenic) fuel ions. In some situations it can be argued that the neutral and ionic hydrogen will be so strongly coupled collisionally that they will have almost the same velocity along $\boldsymbol{B}$. In such cases, measurements of the Doppler shift of the H_β line have been used to establish the fuel ion velocity [15.9] (although in this particular case (fuel ion) flow reversal was not observed).

It should be noted that the presence of plasma flow away from the nearest target may be due to processes other than the ionization-driven flow reversal considered in this chapter. In chapter 18 it is shown that 'return' flows along $\boldsymbol{B}$ in the SOL can be driven by radial and poloidal drifts (i.e., across $\boldsymbol{B}$). The latter flows, however, can be expected to reverse direction with a change in the direction of $\boldsymbol{B}$. This might also occur for ionization-induced reversed flow, but would seem to be less likely.

References

[15.1] Nedaspasov A and Tokar M Z 1983 *Proc. XIIth EPS Conf. (Aachen, 1983)*
[15.2] Harbour P J, Johnson P C, Proudfoot G *et al* 1984 *J. Nucl. Mater.* **128–129** 359
[15.3] De Kock L *et al* 1988 *Proc XIIth IAEA Conf. (Nice, 1988)*
[15.4] Petravic M, Heifetz D, Heifetz S *et al* 1984 *J. Nucl. Mater.* **128–129** 91
[15.5] Reiter D 1992 *J. Nucl. Mater.* **196–198** 80
[15.6] Cooke P I H and Prinja A K 1987 *Nucl. Fusion* **27** 1165
[15.7] Krasheninnikov S I 1992 *Nucl. Fusion* **32** 1927
[15.8] Maddison G P, Reiter D, Stangeby P C and Prinja A K 1993 *Proc. 20th EPS Conf. (Lisbon, 1993)* pp 4–57
[15.9] Gafert J, Behringer K, Coster D *et al* 1999 *J. Nucl. Mater.* **266–269** 365
[15.10] Neuhauser J, Schneider W, Wunderlich R and Lackner K 1984 *J. Nucl. Mater.* **121** 194
[15.11] Isler R C, Brooks N H, West W P *et al* 1999 *Phys. Plasmas* **6** 541
[15.12] Gafert J, Behringer K, Coster D *et al* 1997 *Plasma Phys. Control. Fusion* **39** 1981
[15.13] Pitcher C S, Goetz J A and LaBombard B 1999 *J. Nucl. Mater.* **266–269** 1009
[15.14] Isler R C, Brooks N H, West W P *et al* 1999 *J. Nucl. Mater.* **266–269** 376
[15.15] Isler R C, Brooks N H, West W P and Porter G D 1999 *Phys. Plasmas* **6** 1837
[15.16] LaBombard B, Goetz J A, Hutchinson I *et al* 1997 *J. Nucl. Mater.* **241–243** 149
[15.17] Boedo J A, Porter G D, Schaffer M J *et al* 1998 *Phys. Plasmas* **5** 4305
[15.18] Boedo J A, Lehmer R, Moyer R A *et al* 1999 *J. Nucl. Mater.* **266–269** 783
[15.19] Tsios N, Dorn C, Kyriakakis G *et al* 1999 *J. Nucl. Mater.* **266–269** 1230

Chapter 16

Divertor Detachment

16.1 Introduction

As we have seen, sections 5.6, 5.7, a magnetic confinement arrangement that is effective enough to contain the main, fusion producing plasma is *too* good for the SOL, resulting in quite small plasma-wetted areas, and very intense plasma–solid interactions.

It appears that we can do little to reduce n and T at the *upstream* end of the SOL, i.e. adjacent to the main plasma, since the plasma conditions there are essentially set by n and T in the main plasma; those quantities have to satisfy the Lawson criterion [16.1], and density-limit criteria related to stability [16.2]. In the absence of volumetric power- and momentum-loss processes in the SOL, the plasma power flux at the target and the plasma pressure there are also fixed. We have seen, section 5.3, that the target *particle* flux is not fixed, however, and quite large fluxes occur in the high recycling regime (conduction-limited regime), sections 1.9, 5.3, 9.10, 9.11. This is a most valuable effect since it *directly* reduces the target plasma temperature by 'dilution', thus reducing physical sputtering yields. There is also an effect due to the volumetric radiative power loss associated with the ionization of each recycling neutral, section 5.5. While the latter effect is helpful in reducing the power flux density on the target, the help is limited: every recycled neutral creates an ion–electron pair which returns to the target, depositing the recombination energy there. As was shown in section 5.5, the power actually deposited on the target (thermal kinetic and potential energy) is never less than about 75% of the input power for the simple conditions assumed there.

Impurity radiation—from either intrinsic or injected impurities—could dissipate most of the power entering the SOL by volumetric loss processes, section 5.7.3. However, the contamination of the main plasma may be unacceptable. *We are therefore interested in finding a way to decrease the particle flux reaching the target, for given upstream conditions in the SOL.* Such a state has been found and is called *divertor detachment*, section 16.3. Although it is the

particle balance that we seek to control, we will see that—as was the case in achieving high particle fluxes in the high recycling regime—it is the *momentum* and *power* balances that actually have to be manipulated in order to control the particle balance. As is always the case for a (particle) *self-sustained* plasma, the particle fluxes are not *directly* constrained to exist at any particular level, but are only constrained *indirectly* by momentum and power balances. We will return to this point in section 16.4 on understanding divertor detachment. In the next section we consider some relevant background material and in section 16.3 the experimental observations of divertor detachment in tokamaks are reviewed.

16.2 Background Relevant to Divertor Detachment

The desirability of operating an ITER-like device 'in a regime similar to MARFES or detachment' was recognized at an early point [16.3]. Earlier still, Tenney and Lewin [16.4] in 1974 proposed a way to 'extinguish' a SOL plasma by terminating it in a gas box maintained at high pressure, $\sim$1 torr. Ion–neutral collisions and radiative loss from injected argon gas would drop the temperature to $\leq$ 0.1 eV where volume recombination would take over, replacing surface recombination as the particle sink. The solid surface would thus experience little particle and power load.

This 'gaseous divertor' concept was tested by Hsu *et al* [16.5] in the Princeton QED (quiet energetic dense) device, figure 16.1. QED consisted of a cylindrical vacuum vessel in which an axial magnetic field was generated by a series of external circular coils. The plasma was generated in an arc jet and flowed down the axis of the device through two limiting apertures for a total distance of about 1.2 m before striking the end collector. The parallel power density in the 1–2 cm diameter beam was $\sim$5 MW m^{-2} in the central section of the machine giving electron temperatures around 5 eV, densities around 10^{20} m^{-3} and plasma pressures $\sim$600 mtorr.

Hsu showed that stable detached plasmas could be produced by puffing gas into the 'divertor' chamber. Figure 16.1(b) shows the decrease in the axial heat flux seen on calorimeter C_A and the associated rise in the radial heat flux C_R as the neutral pressure in chamber D was raised. The QED results were modelled by Hsu assuming that the dominant process for energy and momentum removal was collisions between ions and neutrals. At sufficiently high neutral pressures the electron temperature fell to $T_e \sim 0.2$ eV and the plasma appeared to recombine.

The fact that ion–neutral friction can decrease plasma particle flow to a surface, for given 'upstream' conditions has been known since the 1920s from the gas discharge work of Schottky [16.6]. (The fact that friction decreases mass outflow for given upstream conditions was known earlier, e.g. clogged drains in bath tubs!) We replicate here the essence of Schottky's analysis (see also the closley related analysis by Tonks and Langmuir of 1929 [16.7]).

Schottky considered the classical gas discharge (no magnetic field) in a long

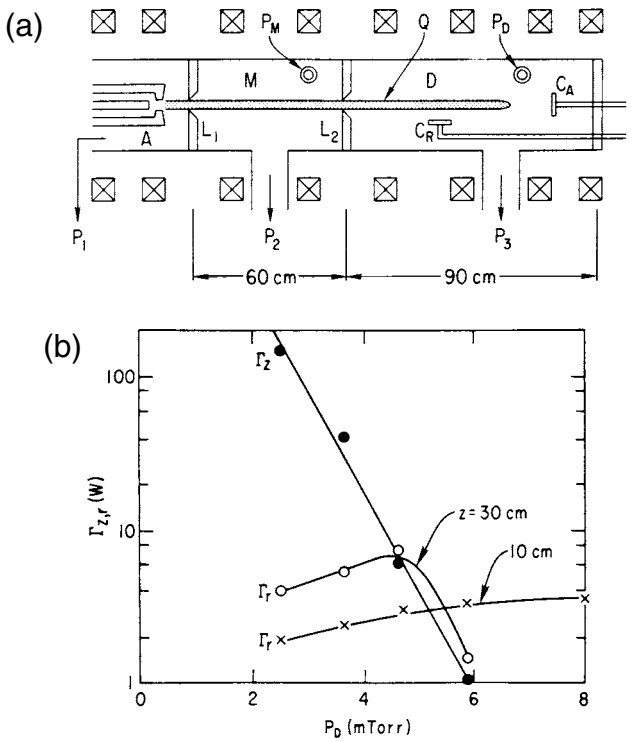

Figure 16.1. (a) Schematic of the Princeton QED used for exploring the gaseous divertor concept. C_A and C_R are calorimeters for measuring the axial and radial heat fluxes respectively. (b) Scaling of calorimeter signals with gas pressure in 'divertor' chamber D at various distances, z, from L2 [16.5]. $C_A \rightarrow \Gamma_Z$, $C_R \rightarrow \Gamma_r$.

cylinder with the ionization rate taken to be, section 1.8.2.4:

$$S_{iz} = n_g n \overline{\sigma v_{iz}}. \tag{16.1}$$

The neutral gas density n_g is considered to be a *given* quantity (we may note that this is not the case in a tokamak, section 16.4). Here we will consider slab geometry with an axis of symmetry at $x = 0$ and infinite planar walls at $x = \pm L$. The ions are impeded in their flow to the wall suffering ion–neutral collisions: $\lambda_{in} < L$, where λ_{in} is the ion–neutral mean free path for momentum loss. The outflow rate is taken to be given by *ambipolar diffusion* [16.8]:

$$\Gamma(x) = -D_{\text{amb}} \frac{\mathrm{d}n}{\mathrm{d}x} \tag{16.2}$$

where for $T_e \gg T_i \approx T_g$, as is common for low/medium pressure gas

discharges [16.9], one has:

$$D_{\text{amb}} \approx \frac{kT_e}{m_i \nu_{in}} \tag{16.3}$$

[16.8] where ν_{in} in is the ion–neutral momentum-transfer frequency:

$$\nu_{in} \approx (kT_g/m_i)^{1/2}/\lambda_{in}. \tag{16.4}$$

Particle balance gives:

$$\frac{\mathrm{d}\Gamma}{\mathrm{d}x} = S_{iz}(x). \tag{16.5}$$

Thus one obtains the differential equation for the plasma density $n(x)$:

$$\frac{\mathrm{d}^2 n}{\mathrm{d}x^2} + an = 0 \tag{16.6}$$

where

$$a \equiv n_g \overline{\sigma v}_{iz}/D_{\text{amb}} \tag{16.7}$$

is taken to be a constant.

The solution to equation (16.6) is:

$$n(x) = n_0 \cos(\sqrt{a}x) \tag{16.8}$$

with $n_0 = n(0)$, the density on axis. Schottky, also Tonks and Langmuir, took the wall to occur at the first zero of the cosine function (also the first zero of the zeroth order bessel function for cylindrical geometry). Thus, the requirement for the plasma 'to fit into the space available', section 1.8.2.6, gives the usual type of constraint, which here is:

$$\sqrt{a}L = \pi/2. \tag{16.9}$$

This becomes, as usual in gas discharge theory [16.10], a constraint giving the value of T_e required for steady state, in terms of the neutral density and the system size:

$$\overline{\sigma v}_{iz}(T_e)/kT_e = \pi^2/(4n_g L^2 m_i \nu_{in}). \tag{16.10}$$

A similar result was found in section 1.8.2.6 for collisionless plasma flow to the walls. Note that while $n \to 0$ at the wall in this model, the wall particle flux is non-zero:

$$\Gamma_{\text{wall}} = -D_{\text{amb}} \left.\frac{\mathrm{d}n}{\mathrm{d}x}\right|_{x=L} = \int_0^L S_{iz}(x)\mathrm{d}x = \pi D_{\text{amb}} n_0/2L \tag{16.11}$$

Thus:

$$\Gamma_{\text{wall}} \approx n_0 \left(\frac{\lambda_{in}}{L}\right)\left(\frac{\pi kT_e}{2m_i(kT_g/m_i)^{1/2}}\right). \tag{16.12}$$

We thus have obtained the key result of gas discharge theory relevant to divertor detachment: *for given upstream plasma conditions, n_0 and T_0, the particle flux to the surface Γ_{wall} decreases with increasing ion–neutral collisionality*:

$$\boxed{\Gamma_{\text{wall}} \propto (\lambda_{in}/L).} \tag{16.13}$$

Another way to put it is that the particle confinement time τ_p increases as *i–n* collisionality increases.

$$\tau_p = N/\Gamma_{\text{wall}} \tag{16.14}$$

$$N = \int_0^L n(x)\mathrm{d}x \tag{16.15}$$

which gives:

$$\tau_p = \frac{4L^2}{\pi^2 D_{\text{amb}}} \approx \left(\frac{L}{\lambda_{in}}\right)\left(\frac{4L(kT_g/m_g)^{1/2}}{\pi^2 kT_e}\right) \tag{16.16}$$

that is:

$$\boxed{\tau_p \propto (L/\lambda_{in}).} \tag{16.17}$$

The electrons are assumed to still satisfy the Boltzmann relation, section 1.8.2.2, giving:

$$V(x) = \frac{kT_e}{e}\ln(\cos(\sqrt{a}x)). \tag{16.18}$$

Tonks and Langmuir [16.7] reported experimental confirmation of the equivalent of this result for cylindrical geometry, figure 16.2. As can be seen, the model is found to be in good accord with experiment in this regard as indeed it has turned out to be generally; e.g. light emission from gas discharges can be reliably calculated using such models, etc. One may note from figure 16.2 that the ambipolar electric field increases for increasing ion–neutral collisionality. As we would put it today, this increased field is required to accelerate the ions to the Bohm speed, section 2.3, in the presence of friction.

In 1966 Self and Ewald [16.11] elaborated further on Schottky's collisional model, expressing $n(x)$, and Γ_{wall} in terms of the parameter $A \equiv (1 + \nu_{in}/n_g\overline{\sigma v}_{iz})^{-1}$; see figure 16.3. Their results reduce to that of Schottky for $\nu_{in} \gg \nu_{iz} = n_g\overline{\sigma v}_{iz}$, $A \to 0$ and also extend to the case of no ν_{in} collisions, $A \to 1$. In this more refined analysis the unphysical assumption of $n(L) \neq 0$ was avoided (by including ion inertia, which is neglected in diffusion models) but the key features remain the same as in Schottky's analysis of 1924, namely Γ_{wall} falls with falling A, i.e. with increasing $\nu_{in}/n_g\overline{\sigma v_{iz}}$. It is clear that this effect requires low temperatures where $\overline{\sigma v}_{iz}$ is small.

At low temperatures other processes also set in, however, including *volume recombination* which is also an important process in divertor detachment [16.12–16.18]. Figure 3.23 shows that recombination becomes more important than ionization at $T_e \leq 1.3$ eV. It is noteworthy that at $T_e = 1$ eV, however, the absolute

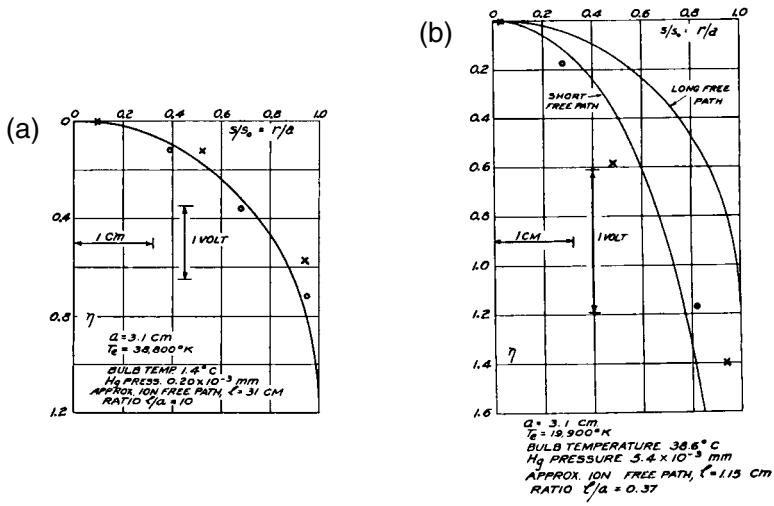

Figure 16.2. Measurements by Tonks and Langmuir [16.7] of the spatial distribution of the plasma electrostatic potential across the radius ($a = 3.1$ cm) of a cylindrical gas (Hg vapour) discharge tube. $\eta \equiv -eV/kT_e$. No magnetic field. Comparison with theory for free-fall and collisional motion (solid lines); probe measurements (points). (a) Very low pressure, $p = 2 \times 10^{-4}$ torr; thus long mean free path for ion–neutral frictional collisions, $\lambda_{in} = 31$ cm $\gg a$. (b) Higher gas pressure, $p = 5.4 \times 10^{-3}$ torr; thus short mean free path, $\lambda_{in} = 1.15$ cm $< a$. The potential drops more rapidly with radius for shorter λ_{in}/a; thus, via the Boltzmann factor, $n_e(r)$ drops more rapidly and thus also does the ion flux reaching the cylinder walls.

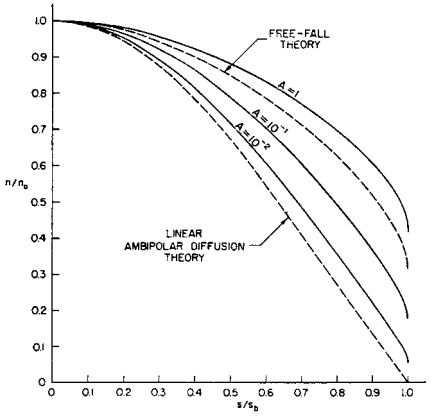

Figure 16.3. Self–Ewald theory [16.11]. Density profiles for plane-symmetric discharge, compared with those of the free-fall (Tonks and Langmuir) and linear ambipolar diffusion (Schottky) theories. $A = (1 + \overline{\sigma v}_{\rm mom}/\overline{\sigma v}_{iz})$. No magnetic field. The stronger the friction, the more n_{se} decreases, hence also the particle flux to the walls.

recombination rate is rather low, $\sim 10^{-17}$ m^3 s^{-1}, so that for $n_e = 10^{20}$ m^{-3}, for example, the recombination time, $\tau_{\rm rec} \sim 10^{-3}$ sec. This is somewhat long compared with typical SOL dwell-times and unless the parallel flow speed is slowed significantly below sonic levels, volume recombination would not have time to act as a significant sink [16.19]. A *synergistic* effect can exist, however, between i–n friction, slowing the flow, and volume recombination [16.21, 16.20].

16.3 Experimental Observations of Divertor Detachment

One of the earliest sets of measurements of T_{et}, T_{it}, n_{et} as functions of n_e for a divertor are shown in figure 16.4, from ASDEX [16.22]. For present purposes let us assume a tight coupling exists between n_u and $\overline{n}_e$, chapter 19, and that we may consider the horizontal axis of figure 16.4 to be n_u, effectively. This figure then encompasses all three divertor regimes, sections 1.9, 4.8, 5.3, 9.10, 9.11:

(a) The sheath-limited or low recycling regime at the lowest $\overline{n}_e$, where n_t increases approximately linearly with $\overline{n}_e$ and T_t is fairly high, > 10 eV.

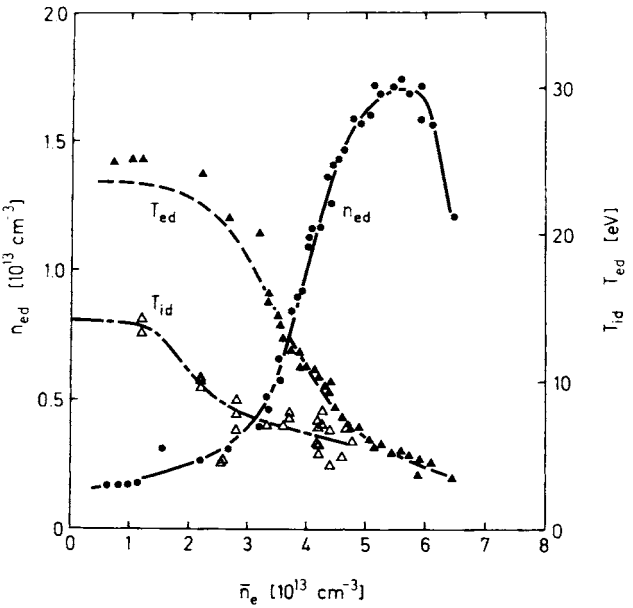

Figure 16.4. ASDEX, 1983. Scaling of the electron temperature and density measured by a Langmuir probe, and the ion temperature deduced from Doppler-broadened CIII radiation of the ASDEX divertor plasma with the main plasma density [16.22]. The decrease in $n_{ed} (\equiv n_{et})$ at the highest density would, today, be attributed to divertor detachment.

(b) The conduction-limited or high recycling regime where n_t increases rapidly, at least quadratically, with $\overline{n}_e$, section 5.2.
(c) The detached regime where n_t saturates and starts to fall.

The significance of this startling n_t-'rollover' was not fully appreciated at the time, and the concept (and term) 'divertor detachment' was not invoked until the early 1990s.

(It is worth noting that, while the feature $n_t \approx n_u$ is indeed a defining property of the sheath-limited regime, this does *not* necessarily imply $n_u \propto \overline{n}_e$: if significant ionization occurs in the main chamber, inside the LCFS, then n_u and $\overline{n}_e$ can be coupled non-linearly as is the case for limiter operation, equations (4.49), (4.69). Therefore the relationship between n_t and n_u, expected on the basis of SOL theory, does not necessarily imply the same relationship between n_t and $\overline{n}_e$.)

By the early 1990s, the detached divertor state had been observed on most divertor tokamaks; see the early review by Matthews [16.23]. See also [16.24–16.29]. Figure 16.5 [16.30], shows a typical result as observed on JET for an ohmically heated discharge using no impurity injection. Detachment in this case was achieved simply by puffing D_2, figure 16.5(b), so as to raise $\overline{n}_e$ slowly, (c), in a quasi-steady-state evolution. JET was operated with 'sweeping' of the location of the strike point in order to reduce local heating of the target. The sweep frequency of 4 Hz, caused the j_{sat}^+ signals, (d), (f), to show a 4 Hz structure as the strike point was swept over them (therefore one should focus on the *envelope* of the j_{sat}^+ plots). The characteristic, in fact the *defining*, observations of detachment are:

- 'roll-over' and decrease of the ion saturation current, j_{sat}^+, of Langmuir probes built into the inner and outer divertor targets, (d), (f), i.e. the 'n_t-rollover' seen on ASDEX, figure 16.4;
- the D_α radiation from the target regions does *not* roll over/decrease, but continues to increase with $\overline{n}_e$, (e), (g).

This *anti-correlation* of j_{sat}^+ and D_α is perhaps the most characteristic feature of detachment. It stands in contrast with the tight, positive correlation that exists in the attached regimes (sheath and conduction limited) where indeed these two methods of measuring steady-state in/out fluxes of neutrals/ions usually agree in absolute magnitude to within a factor of 2, typically [16.30]; see also figure 4.10. One may note from the $j_{sat}^+(\overline{n}_e)$ behaviour that the two divertors legs pass through the sheath-limited regime ($j_{sat}^+ \propto \overline{n}_e$) and conduction-limited regime ($j_{sat}^+ \propto (\overline{n}_e)^2$, approximately) before entering detachment, with the inner divertor leg preceding the outer one. A further feature of detachment is that it occurs when the target Langmuir probes indicate *low temperatures*, $T_e \approx$ *a few eV* or less [16.23, 16.30].

A useful concept for quantitatively assessing when detachment starts, and also the 'strength' of the detachment, is given by the *degree of detachment* DOD [16.30, 16.31], defined as:

$$\mathrm{DOD} \equiv \phi_t^{\mathrm{calculated}} / \phi_t^{\mathrm{measured}} \tag{16.19}$$

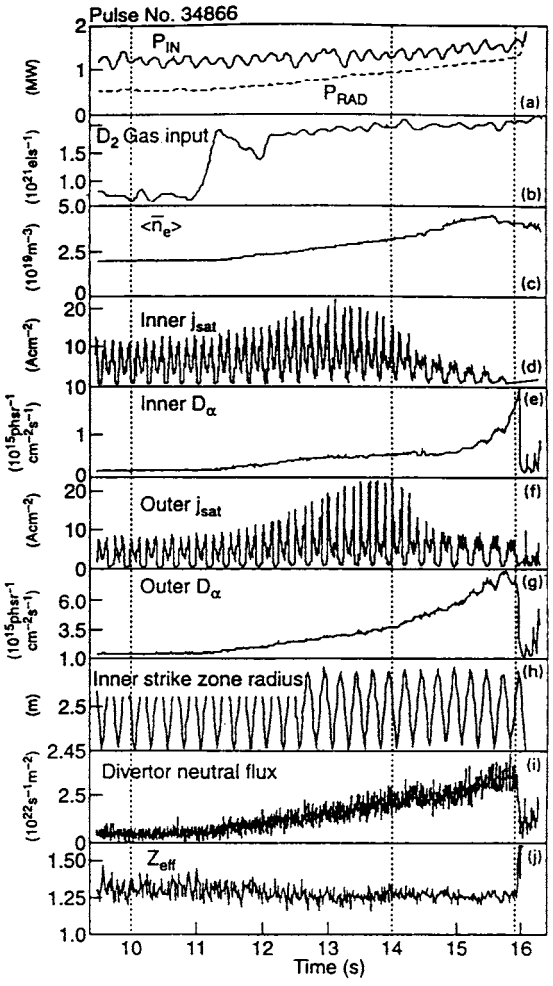

Figure 16.5. JET [16.30]. Evolution of the measured main plasma and divertor plasma parameters in an ohmic density ramp where the following are plotted from top to bottom: (a) ohmic power and radiated power, (b) D_2 gas fuelling, (c) main plasma line-averaged density, (d) inner divertor ion flux, (e) average inner divertor D_α photon flux (note the increase of D_α as the ion flux decreases, characteristic of divertor detachment), (f) outer divertor ion flux, (g) average outer divertor D_α photon flux, (h) radius of the inner strike point on the divertor target (4 Hz strike point sweeping), (i) neutral hydrogen flux in the subdivertor module at the cryopump location, (j) main plasma Z_{eff}.

where ϕ_t^{measured} is the measured flux of ions to the target, measured by built-in Langmuir probes, and:

$$\phi_t^{\text{calculated}} \equiv C(\overline{n}_e)^2 \tag{16.20}$$

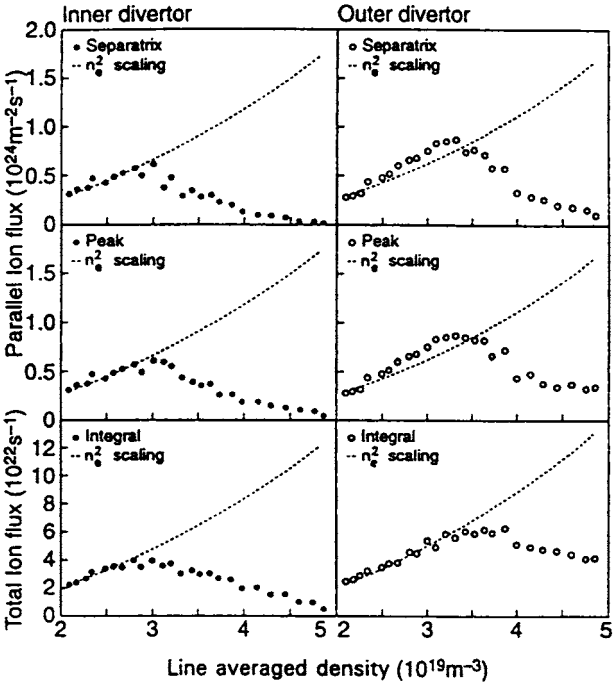

Figure 16.6. JET [16.30]. Measured and extrapolated ion fluxes to the inner and outer divertors for an ohmic density ramp. The same quadratic law is used for the separatrix ion flux, the peak ion flux to the divertor and the integral ion flux to both the inner and the outer divertor.

is the calculated, extrapolated 'attached' target ion flux. Equation (16.20) is based on the prediction of the basic two-point model, equation (5.14), that $\phi_t \propto n_u^2$ in the high recycling regime, plus the further assumption that $n_u \propto \overline{n}_e$. C is a normalization constant which is obtained experimentally from the low density phase of the discharge where $\overline{n}_e$ is ramped up, and where it is assumed that the discharge is in the high recycling regime. Figure 16.6 shows some examples for JET ohmic discharges. The DOD may be based on the ion flux to either inner or outer target; alternatively, it can also be based on the peak in the ion flux density, or on the total flux to the target. Figure 16.7 shows the variation in DOD, as variously defined, for the same JET discharges as shown in figure 16.6. One of the advantages of using the concept of DOD to quantitatively characterize detachment is that it is based exclusively on measurements made at the targets. A problem, however, is the necessity of assuming that $n_u \propto \overline{n}_e$, chapter 19.

A *substantial drop* of plasma pressure along the SOL is another key characteristic of divertor detachment. This is shown in figure 16.8 for CMOD data, employing divertor target probes and an upstream reciprocating probe [16.32].

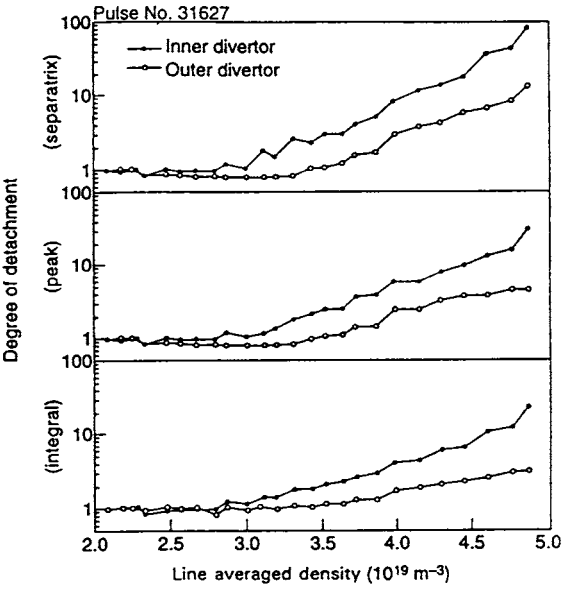

Figure 16.7. JET [16.30]. Measured degree of detachment, DOD, for the discharge of figure 16.6 for the separatrix, peak and integrated ion fluxes for both the inner and the outer divertor, versus line-averaged density. Note the large DOD reached at the inner divertor, typical of total divertor detachment.

Ideally one would consider total pressure (ions and electrons); however, measurements of T_i^{SOL} are only rarely made and here p_e is plotted as an (assumed) indicator of total pressure behaviour. Again the three regimes are evident for different values of $\overline{n}_e$:

(a) In the sheath-limited case, there is not much change in T_e along the SOL and pressure is also conserved.
(b) In the conduction-limited case substantial parallel T_e-gradients occur but pressure is still conserved on a field line.
(c) In detachment—which occurs here only near the separatrix—substantial pressure loss exists along the flux tubes. One may note that 'detachment' should not be taken to mean *total* loss of plasma contact with the target—and 'partial detachment' is a more appropriate term [16.24, 16.32, 16.33]. For one thing, the loss of pressure often only occurs near the separatrix, with the outer part of the SOL remaining attached. Even in the pressure-loss region, however, some plasma contact remains.

Further information on the loss of pressure along the SOL is shown in figure 16.9 [16.32], also from CMOD. As T_e (Langmuir probe) at the target drops below ~5 eV, the p_e^t/p_e^u ratio drops from a value of ~ unity by an order of

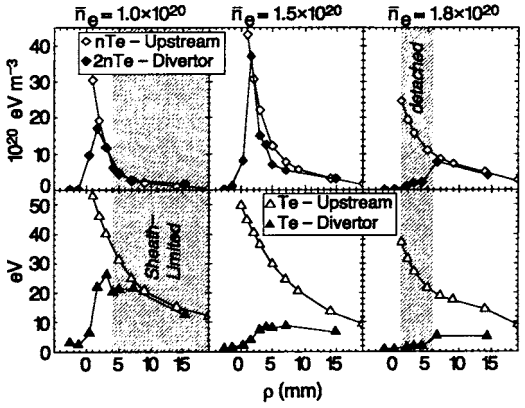

Figure 16.8. CMOD [16.32]. Comparison of the electron temperature and pressure profiles 'upstream' and at the divertor plate for three values of $\overline{n}_e$. Divertor plate pressures are multiplied by a factor of 2 to account for the dynamic pressure in the sound speed flow there.

magnitude or more. At the same time the heat flux reaching the target decreases (as calculated using sheath theory, section 2.8, together with probe measurements of T_e and $j_{\rm sat}^+$).

Pressure-drop results, such as these in figures 16.8 and 16.9, would suggest that perhaps the *defining* observations of detachment should be taken to be the loss of pressure along a SOL field line. This has the advantage of not requiring an assumption to be made of a linear variation between n_u and $\overline{n}_e$, as is explicitly required for application of the DOD concept, and is also implicit in the association of the onset of detachment with 'rollover' and a decrease of $j_{\rm sat}^+$ as $\overline{n}_e$ continues to rise. (In principle, however, a drop in $j_{\rm sat}^+$ could be attributed to a hypothetical drop in $n_u/\overline{n}_e$, since the latter ratio is often unknown.) This approach has the disadvantage, on the other hand, of requiring the availability of an upstream probe, in addition to target probes—and assumes that one can identify the flux tube location of the upstream probe with great precision. The latter, difficult problem is discussed further in chapter 19.

A further characteristic of divertor detachment often observed is a change in the ratio of certain hydrogenic emission lines from the divertor, indicative of the presence of *volume recombination*, figure 3.22 [16.24, 16.34, 16.35]. In some studies, as on JET [16.24, 16.36], the rollover of $j_{\rm sat}^+$ coincides precisely with the sudden increase in the D_γ/D_α ratio, implying that volume recombination is an essential and necessary element in divertor detachment. On ASDEX-U, however, the recombination rate is found to be too small at the point of rollover to account for the drop in particle sink/source rate [16.37]. Also in other studies, for example, on JT-60U [16.38], and for auxiliary-heated discharges in CMOD with nitrogen

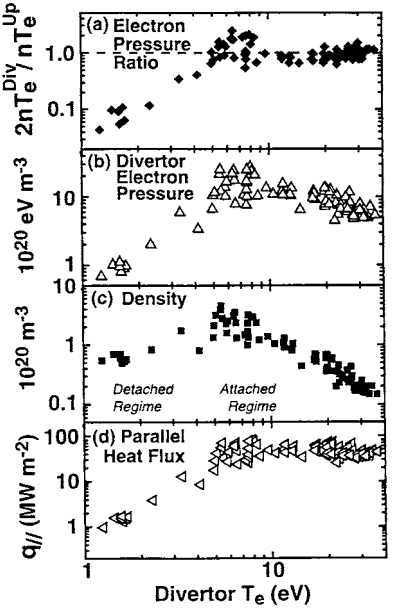

Figure 16.9. CMOD [16.32]. Outer divertor conditions on the $\rho = 2$ mm flux surface (at the outside mid-plane) versus electron temperature at the outer divertor target: (a) upstream/divertor electron pressure ratio, (b) divertor electron pressure, (c) divertor density, (d) parallel heat flux at divertor surface, inferred from sheath theory with $\gamma = 7$.

injection [16.35], recombination appears to play a secondary role in detachment and is evidently not a critical element in the detachment process [16.35, 16.39, 16.40, 16.41].

Measurement of T_{et} near detachment has been problematical. It appears that Langmuir probes are often not trustworthy in tokamaks at the very low temperatures of detachment, $\sim$ a few eV, evidently due to the presence of significant electrical resistances internal to the plasma (additional, that is, to the probe's sheath resistance) which form part of the complete electrical circuit of the probe, and also to kinetic effects, see section 2.7. Fortunately, the spectroscopic measurements of the D_γ/D_α ratio [16.24], and other spectroscopic information [16.34, 16.35] provide rather precise measurements of T_e in detached plasmas and confirm values of $T_e = 0.4$–1.5 eV [16.34, 16.35]. On DIII-D [16.21] Thompson scattering measurements provided separate confirmation of values of $T_e = 0.8$–2 eV in the target region during detachment, while Langmuir probes in the target register erroneously high values of T_e, two to three times higher [16.42]. On DIII-D the onset of detachment can coincide with an abrupt drop in the divertor T_e, accompanied

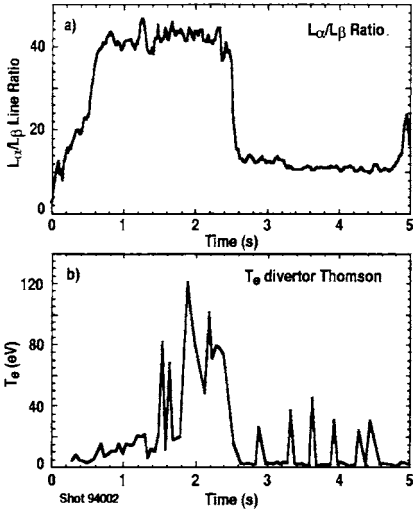

Figure 16.10. DIII-D [16.43]. (a) The ratio of L_α to L_β as measured by a vertical view of the divertor from a VUV spectrometer. The lower ratio after gas puffing indicates that plasma recombination is responsible for a significant fraction of the deuterium radiation. (b) The electron temperature of the divertor as measured by Thomson scattering. The higher-temperature points after the transition to detached operation are due to ELMs occasionally captured by the diagnostic.

by a change in the hydrogenic line ratios indicative of the change from an ionization-dominated plasma to a recombination-dominated one, figure 16.10 [16.43]. The Thompson scattering diagnostic on DIII-D provides a spatially resolved picture of n_e, T_e and p_e in a detached divertor plasma, figure 16.11 [16.44]:

(a) *near the separatrix:* the temperature remains very low, ~1 eV, over a very considerable (parallel) distance, extending from the target to near the X-point; over this region n_e and T_e rise (going upstream), implying the existence of an 'ionization front' at some distance upstream from the plate where T_e finally starts to rise and n_e is also large;
(b) *for flux tubes further out:* here the pattern of $n_e(s_\parallel)$, $T_e(s_\parallel)$, $p_e(s_\parallel)$ is more like that of attached plasmas with pressure approximately constant along $\boldsymbol{B}$, and n_e falling and T_e rising, figure 4.17.

The fact that D_α radiation tends to increase during detachment, even though j_{sat}^+ is falling, may be due less to the increased efficiency of the D_α-*emission* process at very low T_e, figure 3.29, than to the contribution of D_α from *recombination*-driven processes, figure 3.32. Overall, the most intense radiating region during the high recycling phase is near the targets, but as detachment proceeds the radiating

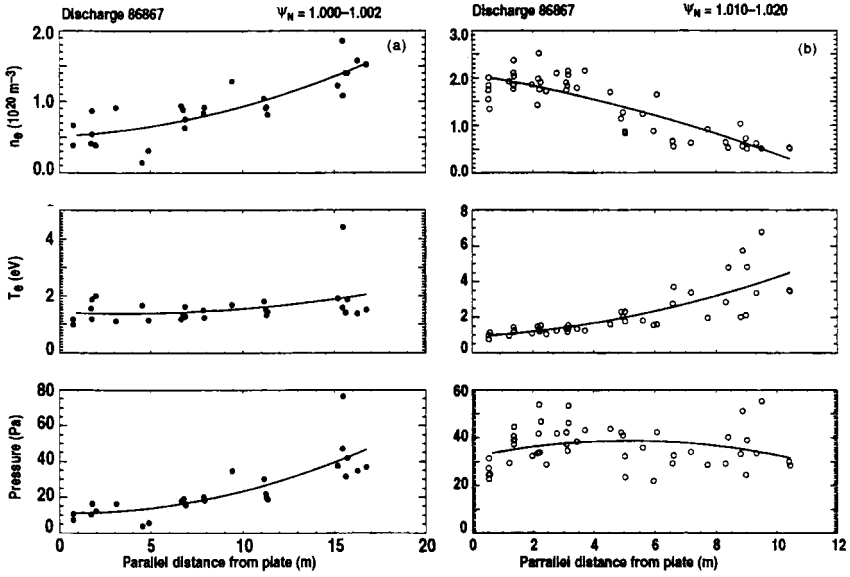

Figure 16.11. DIII-D [16.44]. Along-$\boldsymbol{B}$ profiles of electron density, temperature, and pressure for two values of ψ (flux surface identifier) during the L-mode phase of deuterium-induced radiative divertor operation: (a) near the separatrix, $\psi = 1.000$–1.002; and (b) further out in the SOL, $\psi = 1.010$–1.020. Note that near the separatrix substantial pressure drop (factor of 4–5) is observed between the X-point and the target plate. Pressure is roughly constant further out in the SOL plasma.

zone tends to move away from the targets and settles near the X-point [16.29, 16.30, 16.33, 16.35, 16.41, 16.44, 16.45] where it can form an intense, localized radiation zone like a MARFE [16.46], chapter 22. On DIII-D a tangential TV system provides 2D images of D_α, D_γ and CIII radiation in the divertor and X-point regions, from attached to (partially) detached conditions [16.47]. In detachment, recombination-dominated hydrogenic radiation is strong near the outer target, with ionization-dominated hydrogenic radiation occurring further upstream, part way to the X-point and then strong CIII radiation near the X-point. This location of these different types of radiation are as expected from atomic physics, given values of $T_e \leq 1$ eV near the target (strong hydrogenic recombination), $T_e \sim 5$ eV further upstream where hydrogenic ionization increases, and $T_e \sim$ 6–8 eV near the X-point where excitation of CIII lines is strong.

A further feature of detachment is that the neutral (D_2) pressure in regions adjacent to the divertor leg does not decrease as j_{sat}^{+} falls, but continues to increase just as the D_α emission does [16.30, 16.33]. This apparently contradictory feature is returned to in the next section. On DIII-D, D_2 puffing induced detachment and the measured (infrared camera) power received by the targets dropped

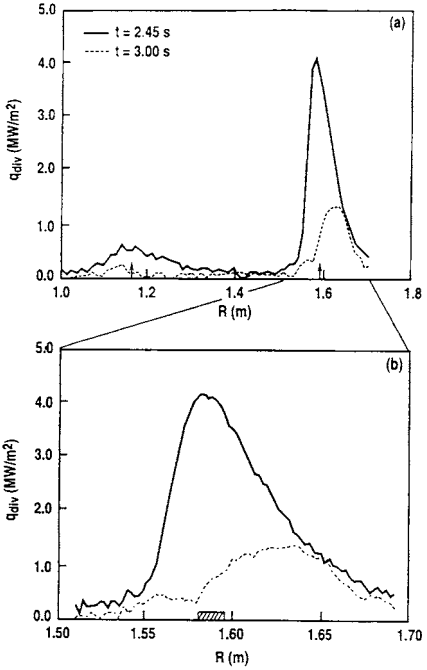

Figure 16.12. DIII-D [16.33]. (a) Heat flux across the divertor floor as a function of the major radius coordinate (R) at two time slices for shot 79 342: (i) pre-puff ($t \approx 2.45$ s) and (ii) after ≈ 0.5 s of D_2 injection ($t \approx 3.0$ s). The arrows represent the inboard and the outboard divertor separatrix strike points determined by the EFITD magnetics code. (b) An expanded view of the heat flux profile under the outboard divertor leg. A small outward shift in the outboard divertor separatrix strike point occurred during deuterium injection (shaded area).

substantially with peak heat flux densities decreasing by a factor of 3–5, figure 16.12 [16.33]; about half the power loading is radiative [16.49]. The attractive implications for reactors are evident.

In H modes, if the plasma is detached between ELMs, it tends to re-attach during the ELM [16.31, 16.48], evidently a 'burn-through' effect.

16.4 Understanding Detachment

16.4.1 Introduction

Divertor detachment clearly involves quite low temperature plasma, $T \leq$ few eV, where a rich complexity of atomic/molecular processes occurs, not otherwise encountered in fusion devices. It seems unlikely, therefore, that any simple,

universal model for detachment will be valid. It appears that ion–neutral friction may generally play an important role. Volume recombination appears always to be present, although it apparently does not necessarily play a central role. Understanding of the importance of supersonic flow, chapter 14, drift effects, chapter 18, radiation trapping, section 3.5, thermal instability [16.45, 16.50], or molecular activated recombination, MAR [16.51–16.53], etc is evolving. It seems likely that different detachment scenarios exist, each with a different combination of these basic physical effects (and possibly others not yet identified) controlling the detachment. Here we attempt to identify some of the factors and constraints which evidently play a role in explaining detachment.

16.4.2 Low Plasma Temperatures Necessary but Not Sufficient for Detachment

Experimentally it is clear that $T_t \leq$ few eV is necessary for divertor detachment to occur. The simplest way to induce detachment is to raise $\overline{n}_e$ (thus presumably n_u also, chapter 19) and from the basic two-point model, 2PM, section 5.2, i.e. simply from conservation of momentum and power along flux tubes, we obtain the result that $T_t \propto n_u^{-2}$, equation (5.10). The same basic 2PM, however, also shows that low T_t is not sufficient:

- Since $\Gamma_t = q_\parallel / \gamma e k T_t$, the particle flux density reaching the target actually *rises*, the opposite of the defining property of detachment which is that j_{sat}^+, i.e. Γ_t *falls*.
- Pressure is still conserved along each flux tube, which is not in accord with the very large drops observed.
- All of the power into the SOL still reaches the target, which is also not in accord with the observed substantial reductions.

Clearly *volumetric losses* of momentum and power are involved in detachment. We therefore consider this next in terms of the extended 2PM, section 5.4.

16.4.3 The Necessity of Volumetric Momentum and Power Losses

Since the defining characteristic of detachment is often taken to be a drop of *particle* flux to the target, the first explanation of detachment that comes to mind involves a replacement of the *surface* recombination sink by a *volume* recombination sink. Such a thought, however, is based on the implicit assumption that the particle *source* is fixed, given. This is an incorrect notion, which may originate in the uncritical assumption of a close equivalence between SOL particle and power balances. The power source for the SOL *is* essentially given, of course. In steady-state operation, however, the particle balance involves *self-sustained recycling* which is free to settle down at any level of intensity whatsoever, thereafter resulting in the situation: source gives sink, gives source, gives sink, etc. In such a situation the intensity of the recycle rate is therefore set by the constraint that the

other conservation equations—for momentum and power—have to be satisfied. Since the conservation equations are coupled, this then *indirectly* constrains the particle balance, Γ_t. This constraint does not, in any way, *rule out* volume recombination as a factor in detachment, obviously. Recombination is not, however, *logically necessary* in order to explain a decrease in particle recycling.

We may recall that the two-point model, 2PM, chapter 5, is the most basic form of the simultaneous conservation of particles, momentum and power. Let us consider the extended 2PM, section 5.4, and the two *generic* correction factors f_{mom} and f_{power}. (We distinguish here between, on the one hand, *generic* processes involving loss of momentum or power, which we have characterized by f_{mom} and f_{power}, and on the other hand, specific *physical* processes, such as collisions of ions with neutrals, volume recombination, etc. The latter physical processes may involve one or other or both of the generic processes.) First we will consider if momentum loss, i.e. a drop in f_{mom}, *on its own*, would be sufficient to explain the main observed features of detachment:

(a) The drop in Γ_t: from equation (5.29) we have that $\Gamma_t \propto f_{\text{mom}}^2$ and so, indeed, momentum loss would have a very strong effect on reducing particle flux to the target.
(b) The drop in p_t: since by definition $p_t \propto f_{\text{mom}}$, then obviously the loss of plasma pressure would also be explained. One would also have an explanation, in principle, of the observation that the *neutral* pressure near the divertor continues to increase with $\overline{n}_e$ in detachment: the momentum of the plasma is transferred to the neutrals, increasing their pressure.
(c) The drop in q_t: the power reaching the target, however, would *not* drop, equation (5.19).

Thus, momentum loss acting on its own would not be sufficient to explain the principal features of detachment.

Next we consider whether power loss, i.e. a drop in $(1 - f_{\text{power}})$, *on its own* would be sufficient:

(a) The drop in Γ_t : from equation (5.29) we have that $\Gamma_t \propto (1 - f_{\text{power}})^{-1}$ and so Γ_t would actually *rise* with increased power loss (this is essentially the same effect on Γ_t as reducing T_t).
(b) The drop in p_t: there would be no drop.
(c) The drop in q_t: since by definition $q_t \propto (1 - f_{\text{power}})$ equation (5.19), then obviously the power drop would be explained.

Thus, volumetric power loss acting on its own would not be sufficient to explain the principal features of detachment either. (While some authors have contended otherwise [16.41], i.e., for the idea that one can 'power-starve the SOL into detachment', such arguments are not based on satisfying all three balances simultaneously—particle, momentum and power—as is involved in the 2PM analysis employed above. If considerations are restricted to power balance alone, then it is readily seen that if the power reaching the recycling region is reduced,

then ionization, hence also Γ_t, must drop. The question of how that can occur consistently with momentum balance, however, is left begging.)

Evidently both volumetric power *and* momentum loss processes are required to explain detachment. We may note, however, that these two loss processes *compete* with regard to their influence on Γ_t: power loss *raises* Γ_t while momentum loss *reduces* Γ_t. The f_{mom} and f_{power} factors are generic; the actual *physical* processes causing the volumetric momentum and power losses, for example ion–neutral collisions or volume recombination, usually involve *both* types of loss. This further complicates any detailed explanation of detachment and simple generalizations will probably not be valid. The balances may be *delicate* and are likely to ultimately hang on the *details* of the basic processes, and on the specific geometry involved, etc. This means that any analytic models of detachment will be of only limited use. Computer codes will only be able to do significantly better if they incorporate correctly all the details of the basic physical processes involved; it is not clear if we currently know how to do that.

16.4.4 The Effect of Volume Recombination Acting Alone

In the last section we considered *generic* volumetric momentum and power loss. Next we consider actual physical processes which could cause such losses. In this section we consider volume recombination. In the following section we consider ion–neutral collisions. Volume recombination is clearly the first candidate to consider for explaining detachment. Experimentally its presence is directly observable through the increased D_γ/D_α line ratio, section 16.3, and it is evidently always present during detachment. Unlike ion–neutral collisions, it can *directly* reduce Γ_t by replacing the surface particle sink with a volumetric particle sink. Also, as just noted, it can also in principle, reduce Γ_t *indirectly* through volumetric loss of momentum and power (which losses would, however, have to occur in the right ratio, see equation (5.29); the latter equation does not include the *direct* effect of volume recombination in removing particles). At the same time, the loss of p_t and q_t could also be accounted for by volume recombination.

The main cause of the *power* loss is unlikely to be the volume recombination process itself. While it is true that sufficiently strong volume recombination would reduce the power actually reaching the target (as thermal, kinetic and potential energy), since volume recombination occurs at $T \leq 1$ eV, most of the SOL input power was probably lost before it reached the region of volume recombination itself. Radiative processes in the SOL, both hydrogenic and impurity—occurring further upstream where T is higher—probably removed most of the SOL input power to achieve the low temperature needed for volume recombination to be possible. One notes from equation (5.25) that $T_t \propto (1 - f_{\text{power}})^2 n_u^2$, and so power loss is as effective at reducing T_t as is raising $n_u(\overline{n}_e)$. It is true that the volume recombination process itself involves some radiative electron cooling; however: (a) much of the radiation may be trapped, section 3.5, and (b) three-body recombination, which appears to be the dominant process [16.34], retains some

of the potential energy of recombination in the electron thermal energy content of the plasma (indeed, when three-body recombination dominates, the electron temperature can even rise somewhat in the recombining region, as seen in code results [16.54]).

There is also the direct loss of the thermal energy content of the recombining ions, which goes into neutral heating; however: (a) much of this energy is recaptured by the plasma when those neutrals are re-ionized, rather than reaching the walls as true energy loss, and (b) the temperature is so low in the recombining region that there may be little thermal or kinetic content left in the plasma anyway.

The effect of volume recombination on reducing Γ_t would appear to be straightforward. We will, however, next show that the *total* of the volume plus surface recombination rate, for fixed upstream conditions, would not be expected to decrease with the onset of volume recombination unless some other mechanism also removes *momentum* from the plasma.

In section 1.8.2.3 it was shown that a volumetric particle *source*, such as ionization, drives a plasma toward sonic speed. The analysis for a volumetric particle *sink* essentially involves changing the sign of S_p in equation (1.31) (other less important changes also occur, see section 16.4.6) showing that volume recombination drives a flow *away* from sonic speed. Since detachment does not involve *complete* loss of plasma contact with the solid surface, the Bohm criterion still applies at the sheath edge and so the flow must still achieve $|M_t| \geq 1$ there. The only simple way to meet all these constraints is that in the hotter, ionizing region upstream of the volume recombination zone, the plasma must accelerate to $|M| = 1$ at the interface between the ionizing and recombining zones. In the recombining zone, the flow would then be expected to accelerate further to supersonic speeds and subsequently enter the sheath at $|M_t| \geq 1$. Thus the basic flow constraints can be satisfied that $|M|$ is driven toward unity in regions where there are particle sources, and driven away from $|M| = 1$ in regions where there are particle sinks.

Consider now the location of the interface between the volumetric source and sink regions where $|M_{\text{int}}| = 1$: so far as the plasma flow upstream of this interface 'knows', this could just as well be a sheath edge in front of a solid target. (Strictly, the power flux density across the interface would be slightly smaller than across a sonic sheath edge and so the two sonic interfaces would not appear as being perfectly identical to the flow.)

Thus the two-point model results of section 5.2 would essentially hold, but now relating the upstream conditions of p_u, $q_\parallel$, etc to the conditions at the interface. Therefore the particle flux crossing the interface would obey the usual 2PM result, equation (5.13)—and there would be no decrease of Γ_{int} but rather just a continuance of the standard high recycling result that $\Gamma_{\text{int}} \propto n_u^2$, $\Gamma_{\text{int}} \propto \overline{n}_e^2$. Γ_{int}, of course, represents the *total* source/sink. Thus the *total* recycling flux would continue to grow with $\overline{n}_e^2$, although Γ_t could decrease.

There is not, at present, a great deal of experimental information on total recycling intensities, and in some tokamak detachments it may well be the case

that the total recycling source/sink *does* in fact continue to grow with $\overline{n}_e^2$; in most cases all that is known experimentally is that j_{sat}^+, Γ_t decrease. On CMOD, however, measurements of the total intensity of source/sink have shown cases where the total drops substantially and a simple swapping of sinks is clearly not what is involved [16.35, 16.39, 16.41]. It therefore appears that volume recombination is neither necessary nor sufficient on its own to explain the basic features of divertor detachment. It is nevertheless apparently usually present during detachment and thus clearly plays a role in the process. It may be that it does this in a *synergism* with some other process, such as ion–neutral friction, see section 16.4.6. It may also be the case, of course, that for some particular cases of detachment it is, in fact, a necessary and sufficient explanation. Simple generalizations appear to be questionable regarding detachment.

To sum up the main conclusion from this 'gedanken experiment', where a scenario has been postulated involving volume recombination *alone*: the flow Mach number, M_{int}, is expected to be unity at the interface between ion source and ion sink, and thus, no significant departure is anticipated from the basic feature of the high recycling regime that source–sink rates increase rapidly with increase in n_u, $\overline{n}_e$. We are therefore motivated to look for a mechanism which can cause M_{int} to decrease below unity, so as to give a decreased source–sink rate, even in the face of increasing n_u, $\overline{n}_e$. One candidate is ion–neutral friction, which can provide such a mechanism in a divertor, next section.

16.4.5 The Effect of Ion–Neutral Friction Acting Alone

We have seen from the gas discharge theory of Schottky and others, section 10.4, that ion–neutral friction can reduce the plasma particle flow to a solid boundary surface for fixed upstream plasma conditions, i.e. can increase the particle confinement time. These studies are clearly relevant to divertor detachment, but there are also major differences which prevent any direct application of these non-tokamak findings to the detachment phenomenon in divertors. The principal difference lies in the origin and properties of the 'neutral cushion' involved. In gas discharge theory, almost always (with rare exceptions [16.55]) the gas density can be taken as a fixed, given, parameter independent of the plasma density or temperature. Thus the 'neutral cushion' is fixed and the neutral density given; it is also assumed that the neutrals have no directed velocity themselves. In QED, section 16.2, the plasma source and the 'neutral cushion' were made completely independent of one another by use of a separate, differentially pumped chamber, figure 16.1(a). By contrast, in a divertor the 'neutral cushion' is *self-sustained*: the neutrals doing the cushioning of inflowing ions will all become ionized themselves, and will then in turn be cushioned on their way out of the plasma by other recycling neutrals. Clearly the cushioning effect is constrained in a way that does not occur in discharges or QED. This raises the question whether the neutral cushioning effect can be *strong enough* actually to remove the plasma momentum. (Aside: note that the term 'self-sustained' as here applied to the cushioning effect,

refers to something different from the previous use of the term as applied to *particle* balance. A gas discharge is self-sustained in a particle balance sense, but not in a cushioning, momentum sense.)

The relation between temperature and neutral density is also different in these different systems. In QED, T_e was set by the arc jet conditions totally independent of the gas density in the cushion. In a gas discharge T_e is largely *set* by the value of the neutral density (parameter), section 1.8.2.6, section 16.2. One of the most basic objectives of gas discharge modelling is to identify this dependence which, as we have seen, derives largely from *particle* balance. In the divertor case, the relation between T_e and the neutral density is not primarily a consequence of particle balance, but rather of *momentum* and *power* balances: T_t is partly controlled by upstream pressure and power input, equation (5.9), and partly by volumetric momentum and power losses, equation (5.26). Secondly, in the first two devices T_e is either constant spatially or the spatial variations are of no importance, while in detached divertors the fact that T_e varies strongly along the field lines is important. The latter means that ionization, ion–neutral friction and volume recombination need not—and almost certainly will not—occur at the same places, nor at the same temperatures. Since the relation between temperature and neutral density is central to the processes involved in divertor detachment, it is clear that the findings from gas discharge studies, and research using plasma simulators such as QED, are only indirectly applicable to divertors.

We therefore start again and consider the case of a *neutral cushion*, *self-sustained by the neutrals recycling from a solid surface* [16.19, 16.56]. Since a description for a self-consistent gas target is sought, it is appropriate to consider the fate of an *individual* recycling neutral—and specifically the *number of elastic collisions it experiences before being ionized*—rather than the neutral density in the divertor, as the parameter that governs the model. We will also take T_e as a free parameter since it is not rigidly linked to the neutral density, as it is for gas discharges.

One is seeking an operating condition where there are copious elastic (one also includes charge-exchange collisions in a broadened definition) collisions before ionization, since a recycling neutral that is ionized immediately upon entering the plasma causes no (collisional) momentum loss to the plasma flow. One is therefore drawn to consider low plasma temperatures—which, of course, is also suggested by the low T_e measured in detachment. The controlling parameter is N, the number of elastic/charge-exchange collisions a recycling neutral experiences before ionization. For entry into an infinite plasma at constant T_e and T_i, the value of N (per recycling atom) is roughly $N = \overline{\sigma v}^{cx}_{i-n}/\overline{\sigma v}_{iz}$. A more refined estimate is given by [16.19]:

$$N = (\overline{\sigma v}_{iz} + \overline{\sigma v}_{\mathrm{dis}})^{-1}\left[\frac{1}{2}\overline{\sigma v}^{\mathrm{D_2}}_{i-n} + \overline{\sigma v}^{cx}_{i-n}\left(\frac{\overline{\sigma v}_{\mathrm{dis}}}{\overline{\sigma v}_{iz}}\right)\right] \tag{16.21}$$

where $\overline{\sigma v}_{iz}$ is the ionization rate (taken to be equal for atoms and molecules), $\overline{\sigma v}_{\mathrm{dis}}$ is the dissociation rate, $\overline{\sigma v}^{\mathrm{D_2}}_{i-n}$ is the elastic collision rate for D_2 on D^+

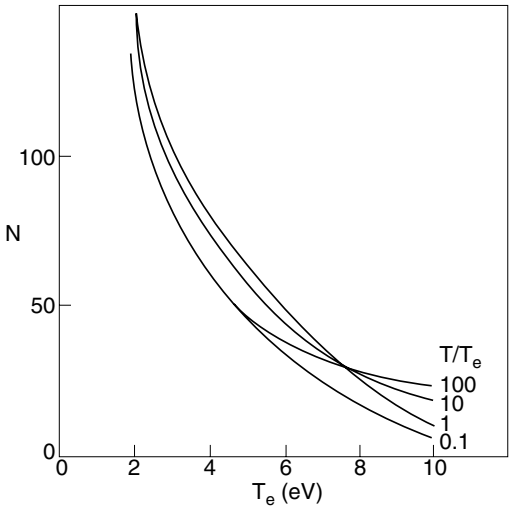

Figure 16.13. N versus T_e (eV). N is the calculated number of elastic and cx collisions before ionization for hydrogen molecules entering a uniform, infinite plasma at temperatures T_e and T_i [16.19].

and $\overline{\sigma v}^{cx}_{i-n}$ is the charge exchange rate [16.57, 16.58]. The latter two quantities are calculated assuming the velocity of the encounter is dominated by the ion temperature. Atom production from dissociation of molecular ions has been neglected. The results are shown in figure 16.13. Clearly, in a *uniform* plasma at low T_e, for example less than 3 eV, the number of collisions that each recycling neutral experiences before ionization would be quite large, even more than 100.

We should note, however, that N is an *upper limit* to the *effective* number that would actually occur: as already pointed out, the ionization is not likely to occur at low temperatures. Rather, most of the neutrals will travel through the cool cushion, to be ionized further upstream, above an *ionization* front where T_e is higher, figure 10.1.

In order for a neutral to remove an ion's momentum totally in a collision, the neutral must, on average, have no velocity in the same direction as the ion velocity. Neutrals which have not suffered an ion collision since they last had contact with a solid surface will have an approximately isotropic velocity distribution and so such neutrals will, on average, remove most of the ion's momentum when they do have their first i–n collision. After that collision, however, the neutral will be moving with approximately the plasma flow speed and any subsequent collisions of that particular neutral with ions will *not* be effective at removing ion momentum. In order for all i–n collisions to be effective at removing momentum, the neutral would have to 're-visit' the solid surfaces between each collision, thus transferring the momentum out of the system. (The latter considerations

apply when neutral–neutral collisions are infrequent; for high neutral densities the effectiveness of i–n collisions at removing plasma momentum depends on the subsequent transfer of momentum to the walls by neutral–neutral collisions, i.e. on *neutral viscosity* [16.59, 16.60].)

Thus we should only extract the basic, qualitative point from figure 16.13 that low plasma temperatures, ≤ 5 eV, are needed to cause significant ion–neutral friction.

Next we consider how plasma flow will be affected by the presence of a uniform density of neutrals, n_n—that is neutrals which have no average velocity. This is analysed in section 10.4 for the situation of present interest, namely, conditions so cold as to give no ionization in the friction (cushion) zone. The ionization source of particles is taken to exist further upstream where conditions are hotter. The two regions are separated by an 'ionization front'. The result is that Γ_t is reduced from the value it would have had in the absence of i–n collisions, $\Gamma_{t,\mathrm{ref}}$, (i.e. for fixed upstream conditions) according to equation (10.21), that is approximately:

$$\Gamma_t / \Gamma_{t,\mathrm{ref}} = c_s / L_{\mathrm{cushion}} \nu_{in}^{\mathrm{mom}} \approx \lambda_{in}^{\mathrm{mom}} / L_{\mathrm{cushion}} \tag{16.22}$$

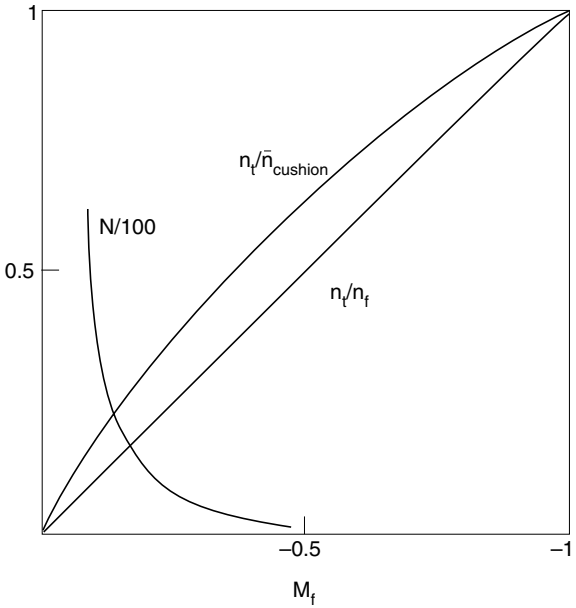

Figure 16.14. N, $n_t/\overline{n}_{\mathrm{cushion}}$ and n_t/n_f as a function of M_f for a neutral cushion [16.19]. n_t, n_f are the plasma densities at the target and ionization front, see figure 10.1. $\overline{n}_{\mathrm{cushion}}$ is the average plasma density in the cushion region and M_f is the flow Mach number at the ionization front.

where L_{cushion} is the length of the neutral cushion, figure 10.1, i.e. the region within which there is a constant neutral density, n_n causing momentum loss but no ionization. The ion–neutral momentum collision frequency ν_{in}^{mom}:

$$\nu_{in}^{\text{mom}} = n_n \overline{\sigma v}_{in}^{\text{mom}}. \tag{16.23}$$

Equation (16.22) shows that the reduction in particle flux to the target is approximately equal to the inverse of the number of mean free paths of the neutrals for ion–neutral momentum collisions within the cushion.

We now relate the collision parameter $c_s/L_{\text{cushion}}\nu_{in}^{\text{mom}}$ to N. The average dwell-time of an ion in the cushion is:

$$\tau_{\text{cushion}} = \frac{\overline{n}_{\text{cushion}} L_{\text{cushion}}}{n_t c_s} \tag{16.24}$$

where $\overline{n}_{\text{cushion}}$ is the average plasma density in the cushion, and one can calculate $n_t/\overline{n}_{\text{cushion}}$ in terms of M_f, the Mach number at the ionization front, from equation (10.20), figure 16.14. The number of collisions experienced by each ion in traversing the collisional zone is $\nu_{in}^{\text{mom}}\tau_{\text{cushion}}$, which is also the number N of collisions for each neutral, assuming complete recycling and steady state.

Thus:

$$N = (\overline{n}_{\text{cushion}}/n_t)(L_{\text{cushion}}\nu_{in}^{\text{mom}}/c_s), \tag{16.25}$$

see figure 16.14. Finally then we obtain $\Gamma_t/\Gamma_{t,\text{ref}}$ as a function of N, figure 16.15. One thus sees that at low temperature, where N is large, there can be a substantial reduction in target particle flux due to ion–neutral friction.

As noted, the question of the *effectiveness* of the i–n collisions is an important one, but, unfortunately, is not readily assessed by simple analytic modelling.

Another factor making impossible any strong generalizations about the role of i–n friction in detachment is the *competition* between momentum and power loss, as these influence Γ_t, equation (5.29). As with volume recombination, last section, most of the power loss probably occurs upstream from the cushion and will usually be due to hydrogenic and impurity radiation—with the momentum loss occurring nearer the target and being due to i–n collisions. When such different mechanisms are in competition, any simple assessment is difficult. *Experimentally* it is known that, as the divertor evolves from high recycling into detachment, the power reaching the target drops, i.e. $(1 - f_{\text{power}})$ does decrease, figure 16.12. Also it is known from experiment that large pressure losses set in, i.e. f_{mom} decreases, figure 16.9. It does indeed appear to be the case experimentally that the relative momentum loss is greater than the relative power loss. (It is to be noted that there is *already* significant power loss in the high recycling regime before detachment, but no momentum loss; it is the *changes* in these factors that are involved in explaining detachment.) In experiments, however, many effects than other i–n friction may be occurring in detachment, and it is not warranted to interpret these observed changes as conclusive evidence that i–n friction is the principal cause of the observed drop in $\Gamma_t(j_{\text{sat}}^+)$. Computer modelling can

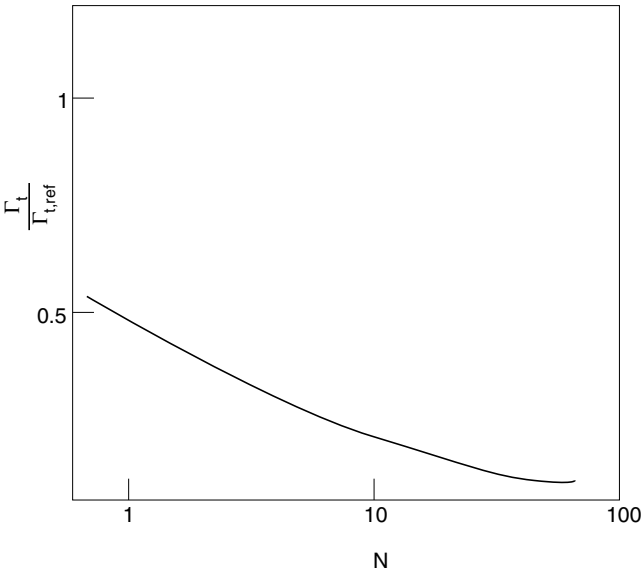

Figure 16.15. The decrease in particle flux density reaching the target as a function of N, the number of elastic collisions per ionization [16.19].

provide guidance, but since balances may be delicate and the number of important processes may be large, it is not certain that the basic physics processes are being included with adequate accuracy.

16.4.6 The Combined Effect of Ion–Neutral Friction and Volume Recombination on Detachment

When friction and volume recombination occur in the same region, we have for particle conservation:

$$\frac{\mathrm{d}}{\mathrm{d}x}(nv) = S_{\mathrm{rec}} = -n^2\overline{\sigma v}_{\mathrm{rec}} \tag{16.26}$$

while momentum conservation gives, section 10.4:

$$\frac{\mathrm{d}}{\mathrm{d}x}[n(2kT + mv^2)] = -mvS_{\mathrm{rec}} - mv(1 - v_n/v)S_{\mathrm{mom}} \tag{16.27}$$

where:

$$S_{\mathrm{mom}} = nn_n\overline{\sigma v}_{\mathrm{mom}}. \tag{16.28}$$

It may be noted that the frictional term used here [16.39] is slightly different from the one employed in section 10.4: here allowance is made for the fact that the neutrals have some average velocity v_n in the flow direction, thus reducing the

effectiveness of the ion–neutral collisions for momentum transfer by the factor $(1 - v_n/v)$. Assuming isothermal conditions and defining Mach number $M \equiv v/(2kT/m_i)^{1/2}$ as before, then gives:

$$\frac{\mathrm{d}M}{\mathrm{d}x} = -\frac{S_{\mathrm{rec}}}{(1-M^2)nc_s} + \frac{M^2(1 - M_n/M)S_{\mathrm{mom}}}{(1-M^2)nc_s}. \tag{16.29}$$

We may note a number of important facts from equation (16.29):

(a) The process of friction, acting alone, is consistent with a flow situation where the flow speed is changing *toward* sonic. Since in the ionization region, upstream of the friction region, the Mach number increases from zero, and since the Bohm criterion requires that $|M_t|$ be at least 1, the effect of friction, by itself, will be to *lower* the Mach number at the interface between the ionization region and the friction ('cushion') region. In section 10.4 it was shown, equation (10.16), that the smaller this interface Mach number is, the smaller the particle density is at the point where $|M| = 1$, thus the smaller the particle outflow is. The effect of friction, by itself, therefore is to reduce the total sink rate, and hence in steady-state recycling conditions, the source rate. This same point was made earlier.

(b) Volume recombination, acting alone, is consistent with a flow situation where the flow speed is changing *away* from sonic. A situation where $|M_t| \geq 1$ is a required boundary condition means that the Mach number at the interface between the ionization zone and the volume recombination zone must be supersonic. Since information cannot be transmitted upstream in supersonic flow the total source and sink will therefore be fixed, for fixed upstream conditions, irrespective of what occurs downstream of the sonic point. This same point was also made earlier.

Turning to the case where both friction and volume recombination are present: at least for the simplest detachment scenarios, one requires a subsonic interface between source and sink, which then requires that the 'friction be stronger than the volume recombination'; specifically:

$$\frac{S_{\mathrm{rec}}}{S_{\mathrm{mom}}M^2(1 - M_n/M)} < 1 \tag{16.30}$$

is required. This criterion is approximately:

$$\frac{S_{\mathrm{rec}}}{S_{\mathrm{mom}}(1 - M_n/M)} = \frac{\overline{\sigma v}_{\mathrm{rec}}}{(1 - M_n/M)(n_n/n)\overline{\sigma v}_{\mathrm{mom}}} < 1. \tag{16.31}$$

This ratio has been calculated [16.39] for the specific example of $T_e = T_i = 1$ eV, $n_n/n = 0.1$ and is shown in figure 16.16 against n with M_n/M treated as a parameter. As can be seen from this figure, so long as the neutrals are not actually moving at virtually the plasma speed, i.e. so long as $M_n/M \leq 0.99$, then this

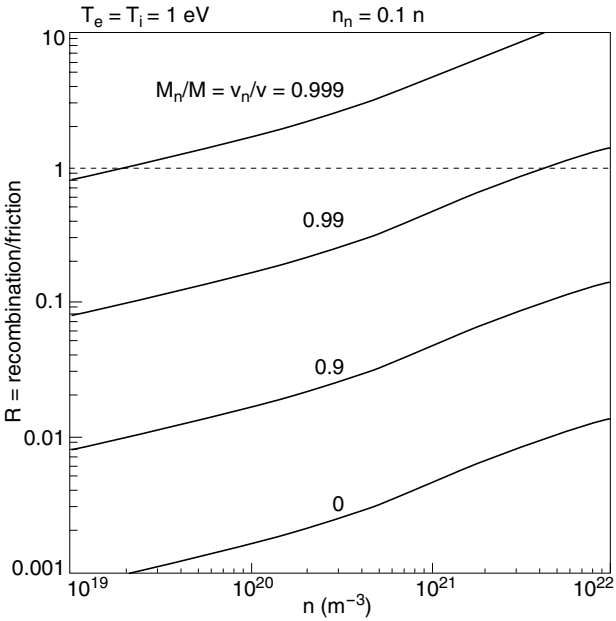

Figure 16.16. [16.39]. The ratio R of recombination rate to friction rate, equation (16.31), for various conditions. v_n is the average neutral velocity in the parallel direction. v is the plasma velocity in that direction. n is the plasma density. For the particular case of $T_e = T_i = 1$ eV and $n_n = 0.1\ n$.

criterion will be satisfied. The plasma flow will then remain subsonic up to the target sheath edge. The contribution of volume recombination to the pressure loss will be small compared with that of the *i–n* friction. As density drops, due to the cushioning and the volume recombination, the latter process 'turns itself off' rather quickly compared with friction, since three-body recombination is such a strong function of density.

It is also clear from equation (16.29) that the effect of volume recombination is to *generally* oppose the effect of *i–n* friction (we saw earlier that these two processes exert opposite influences on T_t). This means that the tendency of *i–n* friction—which is to reduce the Mach number entering the cushion, M_f, thus reducing the total source/sink (equation (10.16))—is offset to some degree, or even completely, by the effect of volume recombination. This evidently occurs in some code studies of detachment [16.20]—see also the code results of the next section. That is, compared with *i–n* friction acting alone, the additional effect of volume recombination is to *raise* M_f, i.e. to *raise* the strength of the total source/sink. Of course, just as with volume recombination acting alone in a supersonic region, section 16.4.4, there is still some degree of *replacement* or *swapping* of the surface sink for a volume sink and so $\Gamma_t(j_{\text{sat}}^+)$ could very well decrease by adding volume recombination to *i–n* friction.

16.4.7 2D Fluid Code Modelling of Divertor Detachment using the UEDGE Code

The UEDGE code is a 2D multi-fluid plasma code, chapter 13, which can be run with a variety of geometries [16.54, 16.61, 16.62]. Parallel transport is assumed to be classical with flux limits imposed to simulate kinetic effects, chapter 26, and prevent excessive parallel thermal transport in steep temperature gradient regions. For the present code runs, perpendicular transport was assumed to be anomalous with spatially constant transport coefficients: $D_\perp = 0.5\ \mathrm{m^2\ s^{-1}}$, $\chi_{\perp i} = \chi_{\perp e} = 0.7\ \mathrm{m^2\ s^{-1}}$. Neutrals which arise from recycling of the ion current to the plate were also treated as a fluid with the neutral diffusivity determined by charge exchange and elastic scattering rates. An equation for the parallel momentum of the neutral fluid was included to permit determination of momentum transfer from the ions to neutrals via charge exchange.

The UEDGE code can be run in either a steady-state or time-dependent mode. In the steady-state mode, the particle, energy and momentum balance equations are solved with the time derivative terms set to zero. The solution is said to be converged when the sum of all residuals is less than a specified constant, typically 10^{-8}. The solutions described here were obtained in the steady-state mode.

Although the UEDGE code is capable of properly handling the full geometry of a divertor tokamak, here a simple slab model was chosen to examine the effect of charge exchange friction and volume recombination on detachment. The plasma is 5 cm thick radially (the y-direction), and 1 m poloidally (the x-direction), as shown in figure 16.17. The toroidal field is assumed constant at 5.0 T, and the poloidal field is constant at 0.3 T, giving a field pitch angle of 3.43 °. The field line length is 16.67 m.

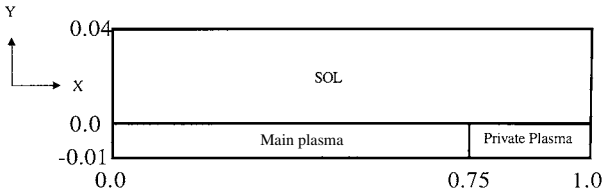

Figure 16.17. UEDGE code calculation [16.54]. Slab geometry used for the analysis. Dimensions are in metres, the toroidal field is 5.0 T, and the poloidal field 0.3 T. Total radial (y) extent = 0.05 m; total poloidal (x) length extent = 1 m.

UEDGE was run by fixing the temperature at the main plasma boundary ($y = -0.01$ and $0.0 \leq x \leq 0.75$), and the behaviour of the divertor plasma was examined as this temperature was varied. Increasing the main plasma temperature is equivalent to increasing the power flowing into the SOL. $T_e = T_i$ was assumed at the inner boundary ($y = -0.01$ m) for all runs reported here. The plasma

density at the boundary was assumed to be 0.7×10^{20} m $^{-3}$, and was held fixed for all runs. The radial temperature gradient was assumed to be zero, and the radial particle flux was likewise assumed zero, at the outer wall and the private flux wall. The plasma boundary conditions at the entrance to the sheath, i.e. the end of the calculational domain, were essentially the standard sheath conditions, section 2.8. If the plasma flow velocity upstream from the divertor plate was greater than Mach 1, then a zero gradient boundary condition ($\mathrm{d}v_\parallel/\mathrm{d}s = 0$) at the plate was assumed, rather than forcing Mach 1. (See chapter 14 on the matter of not fixing the exit Mach number, other than requiring that it be sonic/supersonic.)

In order to elucidate the roles of ion–neutral friction and volume recombination, it was arranged that the code could turn either process off/on. For fixed upstream $T_u^{\mathrm{sep}} = 25$ eV the results were as follows.

Friction	Volume recombination	I_t [A m^{-1}]	I_{ioniz} [A m^{-1}]	$I_{\mathrm{rec}}/I_{\mathrm{ioniz}}$	T_{et} [eV]
off	off	453	453	0	0.58
off	on	463	464	0.003	1.09
on	off	366	366	0	0.56
on	on	243	476	0.49	0.61

I_t is the total particle flux (multiplied by the elementary charge $e = 1.6 \times 10^{-19}$ C) to the target per metre of depth into the page of figure 16.17, i.e. per metre toroidally. I_{rec} is the total volume recombination rate and I_{ioniz} the total ionization rate. As can be seen, volume recombination by itself causes no reduction of particle flux to the target for this case (indeed, a slight increase occurs); (three-body) recombination is particularly ineffective here because of a slight heating effect on the electrons.

Friction by itself causes a drop in the target particle flux and the ionization rate, i.e. the particle confinement time rises due to the 'partly plugged drain' effect. Figure 16.18 shows the Mach number as a function of (poloidal) distance approaching the target. The effect of friction is seen to reduce the flow speed near the target from supersonic to very low subsonic—which is the plugging effect. One may also note from this figure that recombination by itself still involves supersonic flow near the target, as anticipated from the simple analysis of the last section.

The combination of friction with volume recombination causes a substantial drop in the target flux. For the conditions here, the total ionization source is *not* reduced, but even rises slightly. This is associated with a Mach number which can be seen to rise slightly, figure 16.18—the effect referred to in the last section, namely that recombination opposes the effect of friction on Mach number. Evidently, the code results presented here are not universally representative of detachment conditions, since they would not correspond to the cases observed in CMOD of a drop in the total source–sink rate [16.35] (in the latter experiment

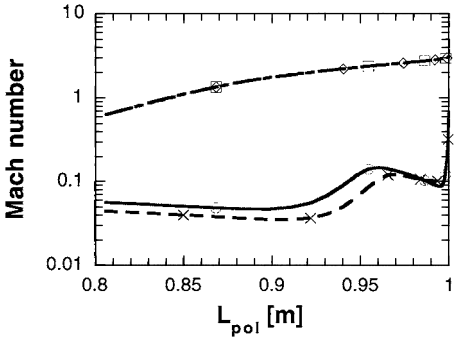

Figure 16.18. UEDGE code calculation [16.54]. Poloidal profile of Mach number for the four cases with varying assumptions of charge-exchange and recombination effects. Squares: friction and recombination off. Diamonds: friction off, recombination on. Crosses: friction on, recombination off. Circles: friction and recombination on.

the power entering the SOL decreased as detachment proceeded, which would correspond here to reducing the upstream boundary temperature—which was in fact fixed in these code runs).

It is illuminating to consider also the spatial distribution of ionization and recombination, figure 16.19, and also of T_e, figure 16.20. For the code run with both friction and recombination turned off, the ionization region ends with approximately sonic flow, followed by acceleration to supersonic conditions. $T_e(s)$ remains rather constant from the end of the ionization region to the target, figure 16.20; here most of the parallel heat flow is carried by the powerful convected heat flux characteristic of sonic/supersonic flow, and conduction contributes little, hence $\nabla_\parallel T_e \approx 0$. With both friction and volume recombination turned on, the source/sink interface occurs at $L_{\rm pol} \approx 0.97$ m, where the flow is quite subsonic, $|M| \approx 0.1$. From this point to the target the parallel heat flux is again carried virtually entirely by convection [16.42–16.44, 16.63]. One may note the contrast between these $T(s)$-profiles which are flattened by convection near the targets, and the extremely steep $T(s)$-profiles that are typical of pure conduction, figure 4.17. Upstream of the particle sources, the $T(s)$-profiles steepen into those characteristic of pure conduction.

A synergism may be noted between friction and volume recombination: the friction, in slowing the flow, gives the volume recombination process sufficient time to act that it can become a strong particle sink [16.21, 16.20, 16.64]. At supersonic speed it is readily shown that, in its short transit time through the low temperature region where the volume recombination rate is significant, the flow will experience very little recombination. On ASDEX, the plasma flow velocity has been measured near the targets, showing that when detachment occurs, the parallel velocity drops by a factor of about 3 [16.65]. Studies of detachment

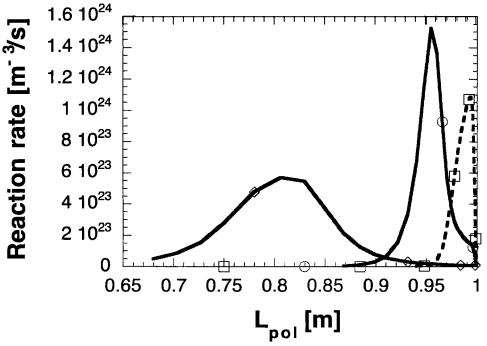

Figure 16.19. UEDGE code calculation [16.54]. Spatial distribution of ionization and recombination for various assumptions of charge-exchange and recombination effects. Circles: ionization rate with friction and recombination on. Diamonds: ionization rate with friction and recombination off. Squares: recombination rate with friction and recombination on.

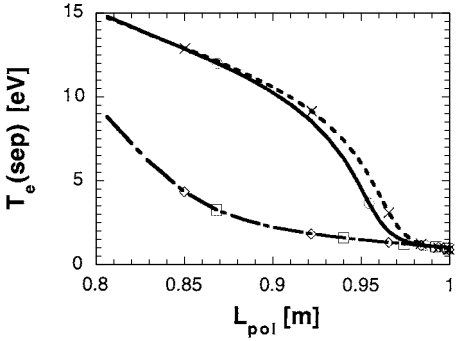

Figure 16.20. UEDGE code calculation [16.54]. As figure 16.18 but for T_e. Symbols have the same meaning as in figure 16.18.

using the EDGE2D/NIMBUS code found that strong recombination alone was not sufficient to produce complete divertor detachment, but that it had to be accompanied by strong charge-exchange momentum removal [16.66].

16.4.8 The 'Cause' versus the 'Explanation' of Detachment

One can *induce* divertor detachment simply by raising $\overline{n}_e$, e.g. by D_2 puffing. This sets in motion a train of effects which will result in the detached state. Equally one can, for a fixed $\overline{n}_e$, induce/cause detachment by puffing an impurity gas

into the tokamak. This also precipitates a number of processes whose combined consequence is detachment. Indeed, simply reducing the divertor temperature to a few eV—by any means, apparently—will precipitate detachment.

At a basic level one might take the view that detachment is caused by reducing the *power* into the divertor region ('power starving')—and certainly, as shown above, unless such loss occurs, detachment would appear not to be possible. Volumetric power loss then is a *necessary* condition for detachment. From an *operational* point of view it is also *sufficient* since it will precipitate a state of affairs in the divertor where i–n friction will become strong and so both momentum and power losses will have been induced to occur. Alternatively, one could take the view that detachment is caused by increasing i–n friction in the divertor and certainly that also seems to be a necessary condition for detachment. For momentum, in principle, there exists an operational equivalent to 'forcing the divertor into detachment by starving it of power': if, for example, it were practical to pump away all the ions reaching the target, and then to re-inject them at high velocity counter to the plasma flow direction, then presumably one could 'force the divertor into detachment by starving it of momentum'. In that case the volume *power* loss mechanisms would 'simply have to sort themselves out', just as one might have taken the view in the 'power-starvation' scenario that the *momentum* loss mechanisms 'would simply have to sort themselves out'.

In fact *both* momentum and power reduction evidently must exist for detachment to occur and any adequate *explanation* of detachment has to explain how each of the momentum and power balances can actually be satisfied. It is not sufficient—for an *explanation* at least—to leave either mechanism 'to sort itself out'.

Despite this, there is an inevitable tendency to wish to ascribe a single, simple explanation to a prominent phenomenon, such as divertor detachment. The first question that arises when it is learnt that Γ_t actually *drops* as $\overline{n}_e$ is raised beyond some critical point is: 'Where did the particles go?'. The best answer to that is probably: 'They didn't *go* anywhere. They just *stayed* longer. The particle confinement time simply went up because the drain got partly plugged'. The partial plugging is likely due to i–n friction which, since it is not a feature of the regimes preceding detachment, is therefore the 'new player' and thus, might be called the 'explanation of detachment'. While volumetric power loss must also increase in detachment, such losses were already occurring in the preceding regimes, and so it perhaps lacks the 'novelty' feature sought by some people to be viewed as an 'explanation'.

Such disputes are essentially semantic. The basic point is that all three conservation equations must have a satisfactory explanation, simultaneously.

Experimentally, volume recombination is generally a feature of detachment but it is not clear as yet whether it is an essential part of the loss of particles, momentum and power—or is incidental. There may be no single detachment scenario.

References

[16.1] Wesson J 1997 *Tokamaks* 2nd edn (Oxford: Oxford University Press) p 11
[16.2] Wesson J 1997 *Tokamaks* 2nd edn (Oxford: Oxford University Press) p 353
[16.3] Cohen S A, Werley K A, Harrison M F A *et al* 1992 *J. Nucl. Mater.* **196–198** 50
[16.4] Tenney F H and Lewin G 1974 *Princeton Plasma Physics Laboratory Report* MATT 1050 p 75
[16.5] Hsu W L, Yamada M and Barrett P J 1982 *Phys. Rev. Lett.* **49** 1001
[16.6] Schottky W 1924 *Phys. Z.* **25** 635
[16.7] Tonks L and Langmuir J 1929 *Phys. Rev.* **34** 876
[16.8] Goldston R J and Rutherford P H 1997 *Introduction to Plasma Physics* (Bristol: Institute of Physics) p 193
[16.9] von Engel A 1965 *Ionized Gases* 2nd edn (Oxford: Oxford University Press) p 264
[16.10] von Engel A 1965 *Ionized Gases* 2nd edn p 243
[16.11] Self S A and Ewald H N 1966 *Phys. Fluids* **9** 2486
[16.12] Post D E 1995 *J. Nucl. Mater.* **220–222** 143
[16.13] Krasheninnikov S I, Yu Pigarov A , Knoll D A *et al* 1997 *Phys. Plasmas* **4** 1638
[16.14] Borrass K, Coster D, Reiter D and Schneider R 1997 *J. Nucl. Mater.* **241–243** 250
[16.15] Porter G D, Allen S L, Brown M *et al* 1996 *Phys. Plasmas* **3** 1967
[16.16] Krasheninnikov S I and Soboleva T K 1996 *Phys. Plasmas* **3** 2280
[16.17] Knoll D A, McHugh P R, Krasheninnikov S I and Sigmar D J 1996 *Phys. Plasmas* **3** 293
[16.18] Napiontek B *et al* 1997 *Controlled Fusion and Plasma Phys: Proc. 24th Eur. Conf. (Berchtesgaden, 1997)* vol 21A, part IV (Geneva: European Physical Society) p 1413
[16.19] Stangeby P C 1993 *Nucl. Fusion* **33** 1695
[16.20] Porter G D 1996 23rd EPS Vol. 20C, Part II, p 699
[16.21] Isler R C, McKee G R, Brooks N H *et al* 1997 *Phys. Plasma* **4** 2989
[16.22] Shimomura Y, Keilhacker M, Lackner K *et al* 1983 *Nucl. Fusion* **23** 869
[16.23] Matthews G F 1995 *J. Nucl. Mater.* **220–222** 104
[16.24] McCracken G M, Stamp M F, Monk R D *et al* 1998 *Nucl. Fusion* **38** 619
[16.25] Pitcher C S and Stangeby P C 1997 *Plasma Phys. Control. Fusion* **39** 779
[16.26] Lipschultz B, Goetz J, LaBombard B *et al* 1995 *J. Nucl. Mater.* **220–222** 50
[16.27] Allen S, Bozek A S, Brooks N H *et al* 1995 *Plasma Phys. Control. Fusion* A **37** 191
[16.28] Neuhauser J, Alexander M, Becker G *et al* 1995 *Plasma Phys. Control. Fusion* A **37** 37
[16.29] Asakura N, Hosogane H, Tsuji-Iio S *et al* 1996 *Nucl. Fusion* **36** 795
[16.30] Loarte A, Monk R, Martin-Solis J R *et al* 1998 *Nucl. Fusion* **38** 331
[16.31] Horton L D, Vlases G C, Andrew P *et al* 1999 *Nucl. Fusion* **39** 1
[16.32] LaBombard B, Goetz J, Kurz C *et al* 1995 *Phys. Plasmas* **2** 2242 and LaBombard B, Goetz J, Hutchinson I H 1997 *J. Nucl. Mater.* **241–243** 149
[16.33] Petrie T W, Hill D N, Allen S L *et al* 1997 *Nucl. Fusion* **37** 321
[16.34] Lumma D, Terry J L, and Lipschultz B 1997 *Phys. Plasmas* **4** 2555
[16.35] Lipschultz B, Terry J L, Boswell C *et al* 1999 *J. Nucl. Mater.* **266–269** 370
[16.36] McCracken G M, Monk R D, Meigs A *et al* 1999 *J. Nucl. Mater.* **266–269** 37
[16.37] Wenzel U, Behringer K, Carlson A *et al* 1998 *Proc. 25th EPS Conf. on Controlled Fusion and Plasma Physics (Praha)* ECA vol 22C 504

[16.38] Kubo S *et al* 1998 *Proc. 25th EPS Conf. on Controlled Fusion and Plasma Physics (Prague)* vol I p 56
[16.39] Pitcher C S, Goetz J A, LaBombard B *et al* 1999 *J. Nucl. Mater.* **266–269** 1009
[16.40] Goetz J A, LaBombard B, Lipschultz B *et al* 1999 *Phys. Plasmas* **6** 1899
[16.41] Lipschultz B, Terry J L, Boswell C *et al* 1999 *Phys. Plasmas* **6** 1907
[16.42] Boedo J A, Porter G D, Schaffer M J *et al* 1998 *Phys. Plasmas* **5** 4305
[16.43] Leonard A W, Porter G D, Wood R D *et al* 1998 *Phys. Plasmas* **5** 1736
[16.44] Fenstermacher M E, Allen S L, Brooks N H *et al* 1997 *Phys. Plasmas* **4** 1761
[16.45] Krashininnikov S I, Rensink M, Rognlien T D *et al* 1999 *J. Nucl. Mater.* **266–269** 251
[16.46] Lipschultz B, LaBombard B, Marmar E S *et al* 1984 *Nucl. Fusion* **24** 977
[16.47] Fenstermacher M E, Allen S L, Hill D N *et al* 1999 *J. Nucl. Mater.* **266–269** 348
[16.48] Bosch H-S, Fuchs J C, Gafert J *et al* 1999 *Phys. Plasmas* **41** A401
[16.49] Lasnier C J, Hill D N, Allen S L *et al* 1999 *J. Nucl. Mater.* **266–269** 577
[16.50] Hutchinson I H 1994 *Nucl. Fusion* **34** 1337
[16.51] Janev R K, Post D E, Langer W D *et al* 1984 *J. Nucl. Mater.* **121** 10
[16.52] Krasheninnikov S I, Yu Pigarov A, Soboleva T K *et al* 1997 *J. Nucl. Mater.* **241–243** 283
[16.53] Reiter D, Chr. May, Baelmans M and Borner P 1997 *J. Nucl. Mater.* **241–243** 342
[16.54] Porter G D private communication
[16.55] Stangeby P C, 1970 *DPhil Thesis* Oxford
[16.56] Ghendrih P 1994 Phys. Plasmas **1** 1929
[16.57] Janev R K, Langley W D, Evans K Jr, Post D E Jr 1987 *Elementary Processes in Hydrogen–Helium Plasmas* (Berlin: Springer)
[16.58] Haas G, Bachmann P, Duchs D *et al* 1992 *J. Nucl. Mater.* **196–198** 481
[16.59] Krasheninnikov S I, Catto P J, Helander P *et al* 1995 *Phys. Plasmas* **2** 2717
[16.60] Wising F, Krasheninnikov S I, Sigmar D J *et al* 1997 *J. Nucl. Mater.* **241–243** 273
[16.61] Rognlien T, Milovich J, Rensink M, Porter G 1992 *J. Nucl. Mater.* **196–198** 347
[16.62] Rognlien T *et al* 1994 *Contrib. Plasma Physics* **34** 362
[16.63] Fenstermacher M E, Boedo J, Isler R C *et al* 1999 *Phys. Plasma Control. Fusion* A **41** 345
[16.64] Wenzel U, Behringer K, Buchl K *et al* 1999 *J. Nucl. Mater.* **266–269** 1252
[16.65] Gafert J, Behringer K, Coster D *et al* 1999 *J. Nucl. Mater.* **266–269** 365
[16.66] Maggi C F, Horton L D, Corrigan G *et al* 1999 *J. Nucl. Mater.* **266–269** 867

Chapter 17

Currents in the SOL

17.1 Introduction

The SOL plasma is a good electrical conductor. Spitzer parallel conductivity (due to e–i collisions only) at $T_e = 100$ eV is about equal to that of stainless steel, although it does drop rapidly with decreasing T_e, namely as $\sigma_{\parallel}^{\text{cond}} \propto T_e^{3/2}$ [17.1]. At the same time the SOL is characterized by substantial temperature differences along and across $\boldsymbol{B}$. One therefore anticipates the existence of *thermoelectric currents*. Two types of thermoelectric current are discussed here—driven by either radial or parallel T_e-gradients, sections 17.2, 17.4.

Since the SOL has non-negligible electrical conductivity, it responds to the tokamak transformer action. Toroidal currents—in the expected direction and of the calculated magnitude—have been measured [17.2]. These currents will not be discussed further here.

One often speaks of the plasma inboard of the LCFS as being the 'confined plasma', almost implying that the SOL plasma is not confined. The latter is only true, however, with regard to the parallel-to-$\boldsymbol{B}$ direction where the plasma essentially 'explodes': it is driven by an uncompensated pressure-gradient force, characterized by $\Delta p \approx p$, at speeds up to sonic, section 1.8.2.5. In all other directions—and although even stronger pressure-gradient forces are involved—there is a compensating force, namely the $\boldsymbol{j} \times \boldsymbol{B}$ force, and so the SOL plasma does not 'explode' in those directions, nor does it necessarily even move very quickly, i.e. it is *confined* in those directions. There must therefore also be such confinement-related currents present in the SOL. These are discussed in section 17.5.

We anticipate that $\sigma_{\parallel}^{\text{cond}} \gg \sigma_{\perp}^{\text{cond}}$, but nevertheless cross-field currents arise and we wish to know something about cross-field conductivity. These are related to the confinement currents, section 17.5. It is assumed that the parallel electrical conductivity is classical and is given by the Spitzer value plus the appropriate addition for the effect of electron–neutral collisions [17.3].

It is also important to bear in mind that currents can be driven in a medium by processes other than the force exerted by an electric field, i.e. ohmic currents, for which conductivities, such as $\sigma_{\parallel}^{\text{cond}}$ and $\sigma_{\perp}^{\text{cond}}$, are the appropriate parameters characterizing the medium. Consider, for example, the current constituted by the charge carried on the mechanically driven belt of a van de Graaf generator. This current is not driven by an E-field (and indeed it exists in the face of an *opposing* E-field). It would therefore be quite inappropriate in this case to define a conductivity by dividing the current by E (for one thing, this would give a negative conductivity!). In a plasma subject to a $\boldsymbol{B}$-field we will see that currents, for example diamagnetic currents, move across the field lines, yet no E-field need be present and no $\sigma_{\perp}^{\text{cond}}$ is to be associated with the process. We will also see that radial E-fields can exist in tokamaks while there is no radial current at all. The concept of $\sigma_{\perp}^{\text{cond}}$ may therefore seem to be rather suspect. On the other hand, an electrode such as a Langmuir probe, inserted inside the LCFS, is generally found to draw positive (negative) current when a positive (negative) potential difference is applied between the vessel walls and the electrode. It is therefore appropriate to define a *dynamic* $\sigma_{\perp}^{\text{cond}}$ based on *changes* of current and field, see section 17.5.3.

17.2 Thermoelectric Currents Driven by Cross-Field Temperature Gradients

Even for the simple SOL, chapter 4, where no parallel T-gradients exist, perpendicular T-gradients still exist. We therefore start with an analysis of the thermoelectric currents which might be driven in that case [17.4]. (Even if parallel T-gradients do exist, the picture of cross-field thermoelectric currents is essentially the same as given in the following, provided that the perpendicular T-gradients are evaluated just in front of the sheaths.)

For simplicity we will assume that $n(r)$ and $T(r)$ decay radially with the same scale length λ:

$$T(r) = T_0 \mathrm{e}^{-r/\lambda} \qquad n(r) = n_0 \mathrm{e}^{-r/\lambda}. \tag{17.1}$$

We assume $T_e = T_i$ here. We will not make any assumption about the radial variation of the electric potential of the plasma, $V_{\text{plasma}}(r)$, but will attempt in the following to deduce its shape, i.e. the radial electric field. As an aid to understanding we will consider a number of limiter (or divertor target) arrangements: the limiter may be segmented into a radial set of slices, figure 17.1, or it may be a continuous, electrical conductor. Each of the separate segments may be allowed to float electrically or they may be connected, perhaps through an external resistive load. For either the segmented limiter or for the continuous limiter we assume that the plasma contact with the outside world is exclusively with these solid surfaces. Thus the net current to the limiter, as a whole, is zero and the limiter floats electrically relative to the plasma in an average or integral sense. In practice, electrically continuous limiters/divertor targets are the norm and they are often

connected to 'machine earth'. The latter—or any other external—connection is irrelevant to the potential *difference* between the plasma and the limiter, provided that the limiter is, in fact, the only point of electrical contact between the plasma and the rest of the world. If the 'machine earth' is defined to be at reference potential $V_{\text{ref}} = 0$, then the average potential of a hydrogenic plasma in contact with the limiters will be about $+3kT_e/e$, i.e. the plasma will float *positively* relative to the limiters and to the rest of the world, so as to achieve zero net outflow of current from the plasma. Sometimes the potential of the plasma at some representative point of contact with the limiter is taken to have reference value $V_{\text{ref}} = 0$, in which case the limiters, and the rest of the world, will float at $\sim -3kT_e/e$ relative to that part of the plasma.

We now consider various cases.

17.2.1 Case A. Segmented Limiter with $j_\perp = 0$

In Case A, the limiter is assumed to be segmented very finely with each segment electrically floating. We assume that $\sigma_\perp^{\text{cond}} = 0$, or more specifically, that there are no cross-field currents. In this case each individual segment will float at $\sim -3kT_e(r)/e$ relative to the potential of the local plasma at the sheath edge, $V_{\text{plasma}}(r)$. In this case we can not infer anything about the shape of $V_{\text{plasma}}(r)$; it is unconstrained.

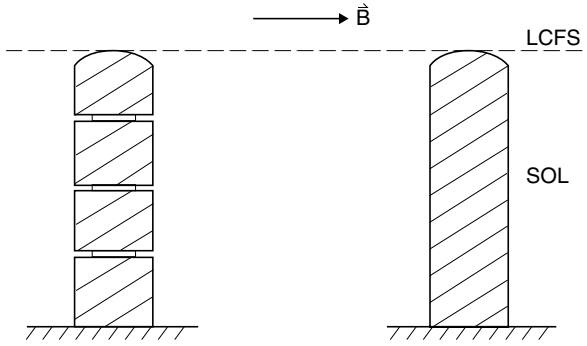

Figure 17.1. Two limiter types: on the right, the standard electrically continuous, conducting limiter; on the left a segmented limiter, with each electrically conducting segment electrically insulated from each other and from the vessel walls.

17.2.2 Case B. Continuous Limiter with $j_\perp = 0$

We continue here to assume $\sigma_\perp^{\text{cond}} = 0$ and, specifically, no cross-field currents, but now either connect all the segments directly to each other (i.e. not through resistive loads) or simply take the limiter to be a continuous conductor. Because there are no cross-field currents, each segment—or each portion of the continuous

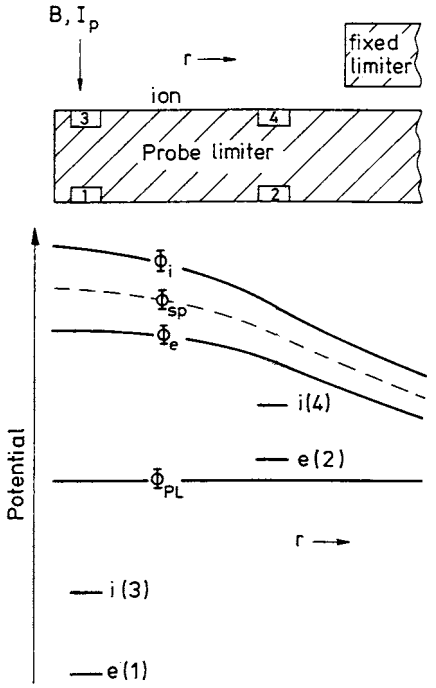

Figure 17.2. DITE tokamak [17.2]. Short lines: the relative potentials of built-in Langmuir probes when electrically floating, in a probe limiter which is deeply immersed. $\Phi_{i,e}$ is the inferred plasma space potential on the ion/electron side, see section 17.3. Φ_{sp} is the inferred plasma potential in the absence of the probe limiter. Potentials as a function of radial distance in the plasma, extending inboard and outboard of the LCFS defined by the fixed limiter. The probe limiter is movable. $\Phi = V$ here.

limiter—will continue to receive ambipolar fluxes, i.e. equal fluxes of electrons and ions, i.e. no net current. If we take the limiter potential to be $V_{\text{ref}} = 0$, then the plasma potential will vary radially as $T_e(r)$:

$$\boxed{V_{\text{plasma}}^{\text{SOL}}(r) \approx +3kT_e(r)/e.} \tag{17.2}$$

One will thus have a *radial electric field* in the SOL E_{SOL} which points radially *outward*. Just such radial electric fields are typically seen experimentally in SOLs, at least approximately, see figure 17.2. This implies that $\sigma_{\perp}^{\text{cond}}$ and cross-field currents are, as expected, not very large, but it is also clear from experiments that they are not actually zero. If they were, then it would not be possible to operate a Langmuir probe in the main plasma of a tokamak; section 2.7. Further evidence is provided by limiters with built-in single Langmuir probes which show that non-ambipolar fluxes exist to different parts of the limiter, i.e. net currents;

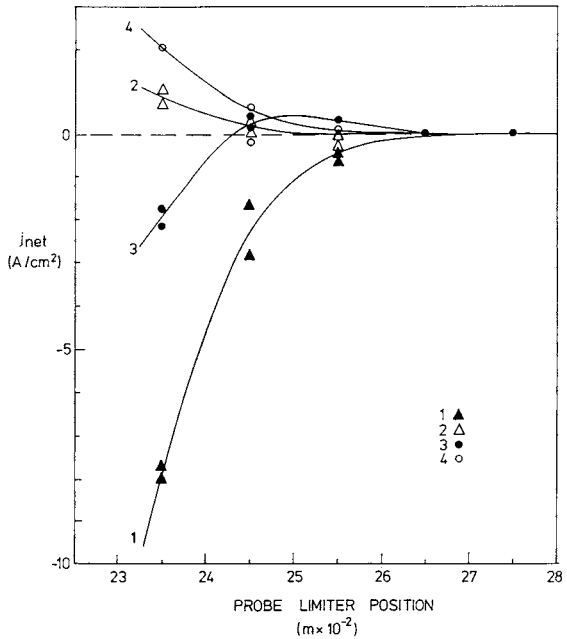

Figure 17.3. DITE tokamak [17.2]. As figure 17.2. Net current density j_{net} flowing into the probe limiter at the positions of the built-in probes as a function of the probe limiter position in a reference deuterium discharge. Probes at the same potential as the probe limiter.

an example from the DITE tokamak is shown in figure 17.3. This is seen when the probes, which are referenced to the limiter potential, are biased to the same potential as the (continuous, conducting) limiter: the probes radially furthest into the plasma typically receive net electron current in that situation while probes radially further out receive net ion currents. In this bias arrangement the probes are effectively just part of the limiter itself and therefore they indicate that net electron fluxes reach the part of the limiter which is radially furthest in, with net ion fluxes reaching the parts of the limiter which are radially furthest out. Below we consider an explanation for this particular pattern of non-ambipolar fluxes.

17.2.3 Case C. Segmented Limiter with $\sigma_{\perp}^{\text{cond}} \to \infty$

Let us now go to the opposite extreme and assume $\sigma_{\perp}^{\text{cond}} \to \infty$. Thus $V_{\text{plasma}} =$ constant and it is natural now to take the plasma potential as $V_{\text{ref}} = 0$. (We may note in passing that this assumption of $\sigma_{\perp}^{\text{cond}} \to \infty$ is clearly too extreme since measurements of $V_{\text{plasma}}^{\text{SOL}}(r)$ usually show spatial variation, approximately according to equation (17.2).) Let us assume that the limiter is finely segmented and that each segment floats. Each segment will float at $-3kT_e(r)/e$ since there

will be ambipolar fluxes to each segment.

17.2.4 Case D. Continuous Limiter with $\sigma_{\perp}^{\text{cond}} \to \infty$

As for case C, we assume $\sigma_{\perp}^{\text{cond}} \to \infty$ but now take the limiter to be electrically continuous. This approximates to most actual limiter situations, at least so far as the pattern of non-ambipolar currents is concerned. As in case C, the plasma is an equipotential which we take to be at $V_{\text{ref}} = 0$. We take the equipotential limiter to be at V_l. The plasma and limiter potentials will evolve to a steady state where V_l will attain that value which will make the *total*, i.e. *integral* net current to the limiter zero. We will now evaluate V_l. The total, integral flux of electrons to the limiter per metre poloidally, see section [2.2], also figure 17.4, is:

$$\begin{aligned}\Gamma_e^{\text{total}} &= \int_0^{\infty} \mathrm{d}r \tfrac{1}{4} n(r) \overline{c}_e(r) \exp[(eV_l/kT_0)\mathrm{e}^{r/\lambda}] \\ &= \tfrac{1}{4} n_0 \overline{c}_{e0} \lambda \int_0^{\infty} \mathrm{d}x \mathrm{e}^{-3x/2} \exp[\eta_l \mathrm{e}^x] \end{aligned} \tag{17.3}$$

where $\eta_l = eV_l/kT_0$ is the normalized limiter potential; subscript '0' indicates values at the LCFS. It is convenient to define:

$$F(\eta_l) = \int_0^{\infty} \mathrm{d}x \mathrm{e}^{-3x/2} \exp[\eta_l \mathrm{e}^x] \tag{17.4}$$

which is plotted in figure 17.5. The total integral ion current is not influenced by V_l, assuming that all parts of the limiter remain at negative (ion-attracting) potential, thus:

$$\begin{aligned}\Gamma_i^{\text{total}} &= \int_0^{\infty} \mathrm{d}r \tfrac{1}{2} n(r) c_s(r) \\ &= \tfrac{2}{3} \tfrac{1}{2} n_0 \overline{c}_{s0} \lambda \end{aligned} \tag{17.5}$$

with

$$c_{s0} \equiv (2kT_0/m_i)^{1/2}.$$

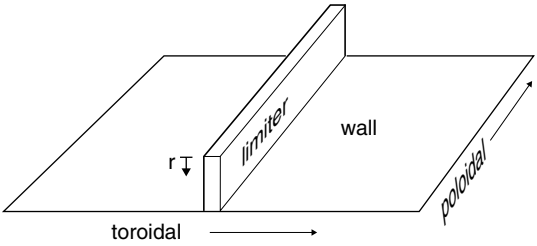

Figure 17.4. Schematic of poloidal limiter geometry for a 'straightened out' SOL.

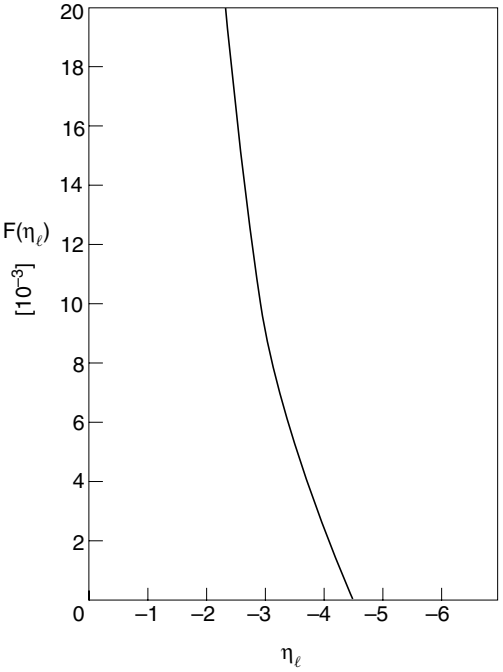

Figure 17.5. Radial current function F, defined in equation (17.4).

The condition of zero net current, $\Gamma_e^{\text{total}} = \Gamma_i^{\text{total}}$, then gives the relation for η_l:

$$F(\eta_l) = \frac{2}{3}\left(\pi \frac{m_e}{m_i}\right)^{1/2}. \tag{17.6}$$

Example: D^+ ions, then $\eta_l = -2.45$ which is to be compared with an ambipolar floating potential of: $\eta_{l,\text{amb}} = \frac{1}{2}\ln(\pi m_e/m_i) = -3.53$. Thus at the tip of the limiter, $r = 0$, $V_l = -2.45kT_e/e$, i.e. the limiter potential is less repelling of electrons than is the case for ambipolar floating conditions and thus there is net electron current to the limiter near the tip. Radially further out there is net ion current to the limiter. For example, at $r = \lambda$, $T = \exp(-1)T_0 = 0.37T_0$ and so $V_{l,\text{amb}} = -3.53 \times 0.37kT_0/e = -1.3kT_0/e$ which is to be compared with the actual value here of $V_l = -2.45kT_0/e$. Thus the limiter potential at that radial location is more repelling of electrons than is the case for ambipolar floating conditions and thus there is net ion current to the limiter there. The cross-over from net electron to net ion current occurs at $r/\lambda \approx 0.37$, i.e. rather near the tip. Figure 17.6 shows the two spatial distributions of electron flux to the surfaces.

This result evidently explains the observations described earlier; however, it has to be noted that the magnitude of the effect is over-estimated here: in reality

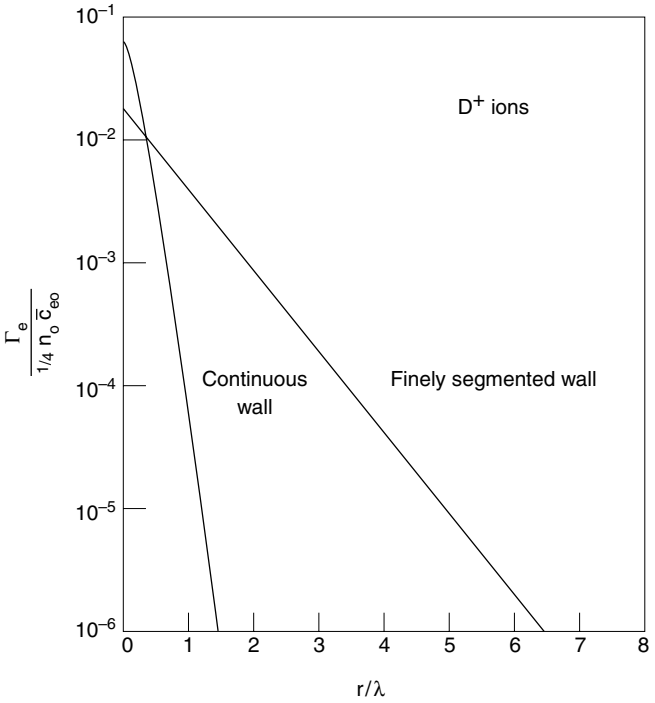

Figure 17.6. The radial distribution of the electron current density to an electrically continuous limiter, and to a finely segmented limiter, see figure 17.1 [17.4].

$\sigma_\perp^{\text{cond}}$ remains finite, indeed cross-field conductivity and currents are relatively weak and so $V_{\text{plasma}}^{\text{SOL}}(r)$ is not at all constant, but approaches that for case B with $\sigma_\perp^{\text{cond}} = 0$. Thus, in reality, $V_{\text{plasma}}^{\text{SOL}}(r)$ *approaches* the relation of equation (17.2) and therefore conditions are closer to being ambipolar at each radial location. The *tendency* remains, however, for net electron collection to occur near the tip, with net ion collection further out. We may also now quantify what we mean by 'relatively weak cross-field currents' as being ones which will not result in current densities to the solid surface which at any point are large compared with enc_s.

The existence of these thermoelectric currents has a number of implications:

(1) As shown in figure 25.12, the heat flux density to a solid surface is a function of the sheath voltage drop, being nearly a minimum for local ambipolar floating conditions. An electrically continuous limiter or divertor plate therefore extracts more heat from a given SOL plasma (given n and T) than would a segmented limiter where each segment was allowed to float individually. In particular, the tip of the limiter, which already experiences the greatest heat load, suffers the largest increase.

(2) Direct, thermoelectric power generation would be achieved using a

segmented limiter and with the segments connected through the external load [17.4]. Compared with the use of an electrically continuous limiter, this would also reduce the enhanced heat load just mentioned, since the non-ambipolar currents would be smaller.

17.3 Inferring $V_{\mathrm{plasma}}^{\mathrm{SOL}}(r)$ from Probe Measurements of $V_{\mathrm{float}}(r)$ and $T_e(r)$

Consider the case of an electrically continuous limiter or divertor plate at reference potential $V_{\mathrm{ref}} = 0$. We therefore anticipate $V_{\mathrm{plasma}}^{\mathrm{SOL}}(r) > 0$. We assume that there is a set of built-in Langmuir probes in the limiter or plate providing measurements of $V_{\mathrm{float}}(r)$ and $T_e(r)$, or that a separate movable probe provides the same radial information. It is assumed that at each radial location the probe floats at a potential relative to the local value of $V_{\mathrm{plasma}}^{\mathrm{SOL}}(r)$ which is the *theoretical* one, section [2.6], i.e. the local plasma potential $V_{\mathrm{plasma}}^{\mathrm{SOL}}(r) \approx V_{\mathrm{float}}(r) + 3kT_e(r)/e$, and thus from the measurements of $T_e(r)$ and $V_{\mathrm{float}}(r)$, the values of $V_{\mathrm{plasma}}^{\mathrm{SOL}}(r)$ are obtained. One notes, therefore, that $V_{\mathrm{plasma}}^{\mathrm{SOL}}(r)$ obtained in this way is not a purely experimentally measured quantity, but is partly inferred from theory—with the theory giving the floating sheath potential drop. Some uncertainty is therefore involved: for example, the effective secondary electron emission coefficient may not be known, which can come into the calculation of the drop. An example of $V_{\mathrm{plasma}}^{\mathrm{SOL}}(r)$ obtained in this way is shown in figure 17.2.

17.4 Thermoelectric Currents Driven By Parallel Temperature Gradients

In the complex SOL, typically a divertor but also including some operating conditions with limiters, parallel temperature gradients exist. For a divertor having in/out symmetry of the two divertor regions, there will be no thermoelectric currents, but when the two divertor plasmas have different temperatures then, as for the case of radial temperature differences examined in the previous section, (positive) current will flow *through the plasma* from the *hot region* to the *cold one*. Such currents were first reported from JET by Harbour [17.5]. Harbour also provided a theoretical analysis which is extended here.

Consider figure 17.7 with the hotter plasma at the left end, the colder at the right end. Without pre-judging that the plasma current will, in fact, flow from hot to cold, we take the convention that the positive current direction is from left to right. Note that we are analysing a current *parallel* to $\boldsymbol{B}$ in this section, $\boldsymbol{j}_{\parallel}$. We will make a number of simplifying assumptions:

(i) $T_i = T_e$;
(ii) $\sigma_{\parallel}^{\mathrm{cond}} \to \infty$;

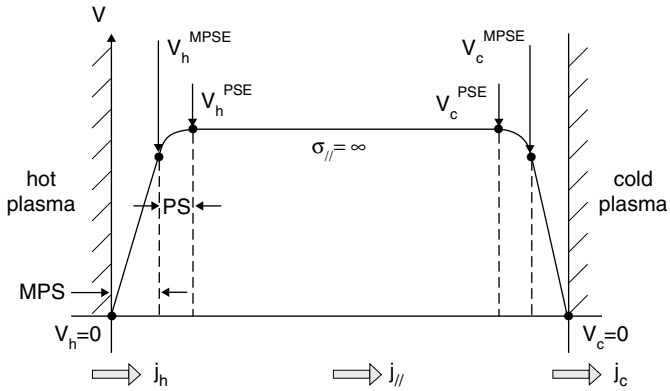

Figure 17.7. Electrothermal currents flow along the SOL. Here, the direction of positive current is simply defined to be from left to right; however, it is proven that the current direction turns out to be from hot to cold, i.e., $\boldsymbol{j}_\parallel$ is positive, figure 17.8. The voltage reference is taken to be $V_h = 0$, at the hot end.

(iii) $\sigma_\perp^{\text{cond}} = 0$, and specifically, that there are no cross-field currents, therefore 1D current transport;
(iv) no parallel pressure gradients, $\nabla_\parallel p = 0$;
(v) no applied voltage between the ends and no external load impedance. The two ends are assumed to be at the same potential, e.g. 'machine earth'.

Because of $\sigma_\parallel^{\text{cond}} \to \infty$ there is no voltage drop in the plasma between each pre-sheath entrance, figure 17.7. We will show that there is net electron current to the hot-end target and net ion current to the cold-end target. We have for the total current at the hot end:

$$\boldsymbol{j}_h = e(\boldsymbol{\Gamma}_h^i - \boldsymbol{\Gamma}_h^e) \tag{17.7}$$

where $\boldsymbol{\Gamma}_h^{i,e}$ are the (vector) particle flux densities of ions and electrons:

$$\boldsymbol{\Gamma}_h^i = -n_h c_{sh} \tag{17.8}$$

$$\boldsymbol{\Gamma}_h^e = -\tfrac{1}{4} n_h \overline{c}_{eh} \exp[-eV_h^{\text{MPSE}}/kT_h] \tag{17.9}$$

where n_h is the density at the magnetic pre-sheath entrance, MPSE, at the hot end. Similarly:

$$\boldsymbol{j}_c = e(\boldsymbol{\Gamma}_c^i - \boldsymbol{\Gamma}_c^e) \tag{17.10}$$

$$\boldsymbol{\Gamma}_c^i = n_c c_{sc} \tag{17.11}$$

$$\boldsymbol{\Gamma}_c^e = \tfrac{1}{4} n_c \overline{c}_{ec} \exp[-eV_c^{\text{MPSE}}/kT_c] \tag{17.12}$$

and

$$n_c \equiv n_c^{\text{MPSE}}.$$

We assume that, at each end, a potential drop of $kT \ln 2$ exists across the pre-sheath, where the ionization source occurs and the flow is accelerated up to the sound speed in the parallel direction at the magnetic pre-sheath entrance, section 1.8.2.8:

$$eV^{\mathrm{MPSE}} + kT \ln 2 = eV^{\mathrm{PSE}}. \tag{17.13}$$

PSE indicates pre-sheath entrance. Current continuity gives:

$$\boldsymbol{j}_h = \boldsymbol{j}_\parallel = \boldsymbol{j}_c. \tag{17.14}$$

Defining the temperature ratio:

$$r_T \equiv T_h / T_c \tag{17.15}$$

also

$$\eta_h \equiv eV_h^{\mathrm{MPSE}} / kT_h \tag{17.16}$$

and

$$\alpha \equiv \tfrac{1}{2}(m_i/\pi m_e)^{1/2} \tag{17.17}$$

we obtain a relation for the floating potential at the hot end V_h in terms of r_T and T_h:

$$-1 + \alpha \mathrm{e}^{-\eta_h} = r_T^{1/2}(1 - 2^{r_T - 1}\alpha \mathrm{e}^{-r_T \eta_h}). \tag{17.18}$$

We have also used parallel pressure balance here, $n_h/n_c = T_c/T_h$. One can also obtain the normalized current density:

$$\hat{j}_\parallel \equiv \frac{j_\parallel}{en_h c_{sh}} = -1 + \alpha \mathrm{e}^{-\eta_h}. \tag{17.19}$$

In figure 17.8, the normalized floating potential η_h and $\hat{j}_\parallel$ are shown as functions of r_T for the case of D^+ ions. As one can see, $\boldsymbol{j}_\parallel$ is in fact always in the positive direction, i.e. the net electron flow *in the plasma* is toward the *hot* end and, as $\boldsymbol{r}_T$ increases from 1, $|V_h|$ falls and $\boldsymbol{j}_\parallel$ increases. For $r_T \to \infty$, $V_h \to 0$ and $\hat{j}_\parallel \to \frac{1}{2}(m_i/\pi m_e)^{1/2} - 1$, i.e. the current *saturates*. One may note that the saturation value of $j_\parallel$ is large compared with $j_{h,\mathrm{sat}}$, i.e. $en_h c_{sh}$, but is vanishingly small compared with $j_{c,\mathrm{sat}}$, i.e. $en_c c_{sc}$. For intermediate values of r_T, $\hat{j}_\parallel \propto r_T^{1/2}$, as is evident from figure 17.8. As $r_T \to 1$, $\eta_h \to \ln \alpha = 0.5 \ln(m_i/4\pi m_e)$, which may be recognized as the normalized floating potential drop when $T_e = T_i$, section 2.6.

For the simple geometry assumed here $\boldsymbol{j}_\parallel$ is constant along $\boldsymbol{B}$. In a tokamak the cross-sectional area of flux tubes varies poloidally due to toroidal effects and it is actually the poloidal current between poloidal flux surfaces that is constant.

It can be useful to relax the simplifying assumptions made above. The parallel electrical conductivity is finite and the resistance of the flux tube may be significant. The potential profile would then be expected to look like figure 17.9, where we have also allowed that one might wish to apply an *external bias* between

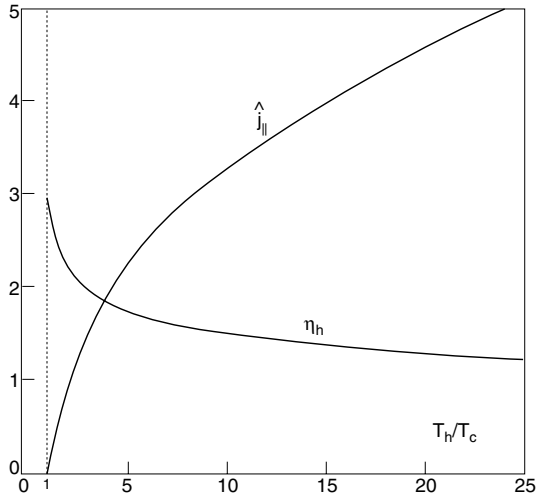

Figure 17.8. The normalized thermoelectric current density $\hat{j}_\parallel$, equation (17.19), and the normalized potential of the plasma at the hot end, η_h, equation (17.16). Note that the thermoelectric current in fact flows from hot to cold end, i.e., $\boldsymbol{j}_\parallel$ is positive, i.e., the *electron* flow is from cold end to hot end. Note the $\eta_h > 0$ here because the reference potential has been taken to be at the wall at the hot end, $V_h = 0$.

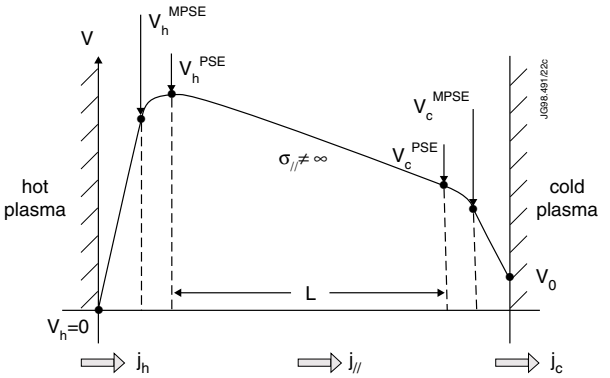

Figure 17.9. Thermoelectric currents allowing for (a) the application of a voltage difference between the two targets and (b) finite electrical resistance of the plasma.

the targets and so V_0, the potential of the cold end, is made adjustable, i.e. ΔV applied $= V_c - V_h = V_0$. We have Ohm's law for $\sigma_\parallel$ from section 9.5:

$$ej_\parallel/\sigma_\parallel = -e\frac{\mathrm{d}V}{\mathrm{d}s} + 0.71\frac{\mathrm{d}kT_e}{\mathrm{d}s_\parallel} + \frac{1}{n}\frac{\mathrm{d}p_e}{\mathrm{d}s}. \tag{17.20}$$

and we will now also allow for the existance of a parallel pressure gradient. $\sigma_\parallel$ is a function of T_e and so depends on $s_\parallel$, section 9.5:

$$\sigma_\parallel \approx 3.6 \times 10^7 \, T_e^{3/2} \tag{17.21}$$

σ [ohm^{-1} m^{-1}], T [keV].

We therefore define an average $\overline{\sigma}$:

$$\overline{\sigma}_\parallel \equiv \left[\frac{1}{L} \int_h^c \frac{\mathrm{d}s_\parallel}{\sigma_\parallel} \right]^{-1} \tag{17.22}$$

where the integral is from the hot end to the cold end.

We can then integrate equation (17.20) to obtain:

$$\hat{j}_\parallel = -\gamma \left[\frac{eV_c^{\mathrm{PSE}}}{kT_h} - \frac{eV_h^{\mathrm{PSE}}}{kT_h} - 0.71\left(\frac{T_c}{T_h} - 1\right) - \frac{1}{kT_h} \int_h^c \frac{1}{n} \frac{\mathrm{d}p_e}{\mathrm{d}s_\parallel} \mathrm{d}s_\parallel \right] \tag{17.23}$$

where

$$\gamma \equiv \frac{\overline{\sigma}_\parallel kT_h}{e^2 L n_h c_{sh}}. \tag{17.24}$$

We can eliminate V_c^{PSE} and V_h^{PSE} to obtain a relation for $\hat{j}_\parallel$ by noting that:

$$\begin{aligned} eV_h^{\mathrm{PSE}} &= eV_h^{\mathrm{MPSE}} + kT_h \ln 2 \\ eV_c^{\mathrm{PSE}} &= eV_c^{\mathrm{MPSE}} + kT_c \ln 2 \end{aligned} \tag{17.25}$$

$\hat{j}_h = -1 + \alpha \mathrm{e}^{-\eta_h}$, as before while

$$\hat{j}_c = r_n^{-1} r_T^{-1/2} (1 - \alpha \mathrm{e}^{-\mathrm{e}(V_c^{\mathrm{MPSE}} - V_0)kT_c)} \tag{17.26}$$

where

$$r_n \equiv n_h / n_c. \tag{17.27}$$

As before:

$$\hat{j}_c = \hat{j}_\parallel = \hat{j}_h. \tag{17.28}$$

Combining equations (17.23)–(17.28) gives an equation for $\hat{j}_\parallel$ as a function of n_h, T_h, r_n, r_T, V_0, $\sigma_\parallel$ and the pressure integral:

$$\begin{aligned} \hat{j}_\parallel = & -\gamma \left[\frac{eV_0}{kT_h} + \left(\frac{1}{r_T} - 1\right)(\ln 2 - 0.71 + \ln \alpha) \right. \\ & \left. + \ln\left[\frac{1 + \hat{j}_\parallel}{(1 - r_n r_T^{1/2} \hat{j}_\parallel)^{1/r_T}} \right] - \frac{1}{kT_h} \int_h^c \frac{1}{n} \frac{\mathrm{d}p_e}{\mathrm{d}s_\parallel} \mathrm{d}s_\parallel \right]. \end{aligned} \tag{17.29}$$

Since the sheath heat transmission coefficient depends on the actual potential difference between plasma and surface, section 25.5, and thus on the current density $\hat{j}_\parallel$, it is useful to consider power flows in this analysis [17.6, 17.7], including

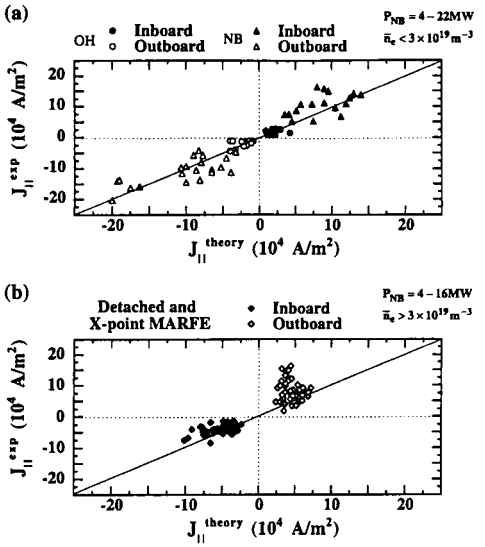

Figure 17.10. JT60-U [17.15]. Comparison of calculated J^{theory} and measured SOL currents $J_{\|}^{\text{exp}}$ at the position of peak $J_{\|}$. (a) In ohmically heated (OH) and neutral beam (NB) heated L-mode discharges under attached divertor conditions, and (b) under detached divertor conditions and during the X-point MARFE. The discharge parameters were $I_p = 1.2$ and 1.8 MA, $B_t = 2.0$ and 3.5 T and $P_{\text{NB}} = 4$–22 MW.

the possibility of a thermal instability, leading to in/out divertor asymmetry [17.8–17.10]; we do not discuss this further here. For further analysis of parallel electric currents see [17.11–17.14].

Parallel currents passing through the inner and outer targets of single-null divertor discharges in JT60-U have been measured using Langmuir probes built into the targets [17.15]. Figure 17.10 shows the experimental results for (a) attached, (b) detached conditions. For attached conditions the measured currents agree well with the theoretical thermoelectric currents—both as to direction (toward the cold, inside target) and magnitude. In detachment, the outer target plasma became the colder end and, as predicted, the current direction reversed; the magnitude of the currents in detachment, however, were found to be somewhat larger than theoretical levels.

17.5 Cross-Field Currents

17.5.1 Experimental Results

It is clear that cross-field conductivity is non-zero. Unless $\sigma_{\perp}$ is non-zero the thermoelectric currents discussed in section 17.2 could not exist, nor could Langmuir probes draw any current when located inside the LCFS—which, in fact, they do. That is, when the potential applied to a probe is varied, in general the

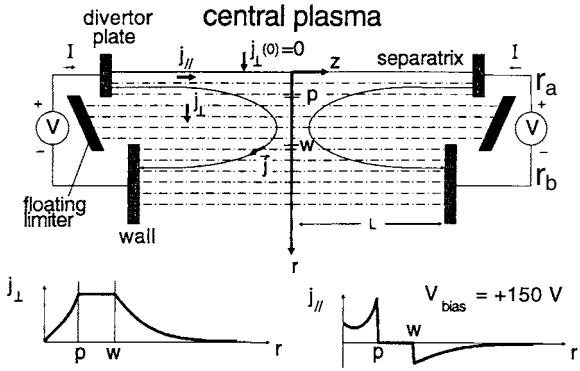

Figure 17.11. Tokamak de Varennes [17.16, 17.17]. Plasma biasing modelling geometry. The SOL field lines are presented as straight lines bounded at both extremities by three types of electrode: neutralization plates, insulated limiters and vessel walls. Typical perpendicular and parallel currents are also shown.

current reaching it varies—and this current must have crossed field lines if the probe is located inside the LCFS. We may therefore speak in some general sense of a cross-field conductivity $\sigma_\perp$, although, as mentioned at the beginning of this chapter, cross-field currents are not the result of cross-field E-fields only.

A further important body of experimental knowledge about $\sigma_\perp$ is generated by *edge-biasing experiments*, including unipolar, divertor bias experiments [17.16, 17.17]. In this biasing configuration on the Tokamak de Varennes, figure 17.11, an external voltage difference ΔV was applied between: (a) the two divertor target plates of the single null divertor, shorted together, and (b) the wall. A radial gap existed between $r_p = r_w$, containing SOL plasma, whose value of $\sigma_\perp$ or $\mu_\perp$ ($\sigma \equiv en\mu$) was established by measuring $I_\perp$ and ΔV. Ideally the region between r_p and r_w would have magnetic field lines closing on themselves, i.e. have no solid end-plates—but this is impractical. Alternatively, if the end-plates in this region were insulators, this would also make for a simple interpretation of $I_\perp$ against ΔV in terms of $\mu_\perp$. In the TdeV experiments the end-plates were actually floating conductors (graphite) which makes interpretation less certain; nevertheless, taking a simple interpretation of the measurements [17.17] gave an empirical value of $\mu_\perp \approx 10^{-2}$ m^2 V^{-1} s^{-1}; see figure 17.12. Interestingly, this value is not greatly different from that given by the classical Einstein relation:

$$D/\mu = kT/e \tag{17.30}$$

assuming $D_\perp \approx 1$ m^2 s^{-1} and $T \sim 25$ eV, typical SOL values.

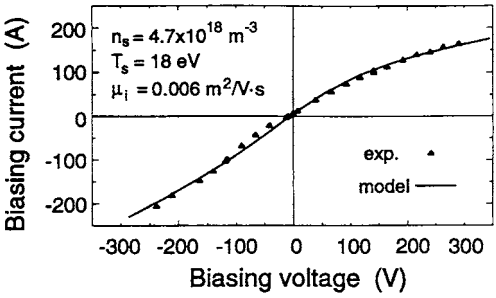

Figure 17.12. Tokamak de Varennes [17.17]. I–V characteristics of the divertor plates in a typical hydrogen TdeV discharge ($\overline{n}_e = 2.5 \times 10^{19}$ m^{-3}, $I_p = 210$ kA). T_s and n_s are, respectively, the electron temperature and the density at the separatrix. The best fit to data is obtained with a mobility of 0.006 m^2 V^{-1} s^{-1}.

17.5.2 Simple Models for $\sigma_\perp$

How to explain non-zero $\sigma_\perp$? In a fully ionized plasma, the e–i collisions result in a negligible *classical* $\sigma_\perp$ [17.18]. A first thought is that cross-field transport of current may be just as anomalous as the transport of particles, momentum and heat. Bohm [17.19], followed by others, simply took $\mu_\perp$ to be anomalous and to be related to $D_\perp$ by the Einstein relation. If the transport mechanism is indeed *completely* unknown, then this may be a reasonable starting hypothesis. It may be, however, that cross-field transport is due to electrostatic, quasineutral fluctuations, chapter 8, which have the property of being locally ambipolar, i.e. they would give no net current $j_\perp$ [17.16]. If the transport is due to magnetic fluctuations, however, then a net (non-ambipolar) $j_\perp$ can exist.

The topic of cross-field conductivity remains substantially conjectural, despite many years of study, and the following discussion should be viewed in that light.

In the SOL the neutral density is not negligible and it may be that i–n momentum-loss collisions can explain $\Gamma_\perp$ values. Consider an infinite cylinder

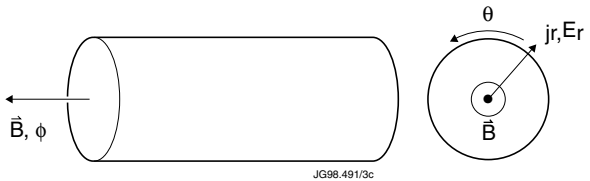

Figure 17.13. A cylindrical plasma with axis aligned to $\boldsymbol{B}$. A voltage is applied between the cylinder wall, as one electrode, and a wire lying along the axis, as the second electrode.

with $\boldsymbol{B}$ along the axis, figure 17.13. Let the cylinder wall be one electrode with a wire along the axis being the other, and let a cross-field potential be applied creating a radial electric field $E_\perp$ and drawing current density $j_\perp$. An $\boldsymbol{E} \times \boldsymbol{B}$ drift, chapter 18, is created and the electrons and ions drift poloidally with speed $v_0 = -E_\perp/B$. Collisions with neutrals cause momentum loss to this drifting plasma—essentially to the ions due to their larger mass. In steady state, this frictional forces balance with a poloidal $\boldsymbol{j} \times \boldsymbol{B}$ force, here $-j_\perp B$. Balancing this force with the frictional force of $-m_i n \nu_{in} v_0$, where ν_{in} is the ion–neutral momentum-loss frequency, $\nu_{in} = n_n \overline{\sigma v}_{in}^{\text{mom}}$, then gives:

$$j_\perp = \frac{m_i n \nu_{in}}{B^2} E_\perp \tag{17.31}$$

hence

$$\sigma_\perp = \frac{m_i n \nu_{in}}{B^2} \qquad \mu_\perp = \frac{m_i \nu_{in}}{eB^2}. \tag{17.32}$$

Shear viscous forces—anomalous or not—can lead to a similar result. Indeed all forces in the poloidal momentum equation need to be included.

We may also consider how the plasma would respond if *both* relations had to be satisfied simultaneously, i.e., an anomalous $\sigma_\perp^{an}$ was simply *required* to hold, yet at the same time, force balance had to still be satisfied, of course.

Since we will need to employ the *complete 3D momentum equation* in the next section, it is convenient to introduce it at this point. It is a generalization of the 1D result of section [9.9] [17.20]; for the steady state:

$$mn\boldsymbol{v} \cdot \nabla \boldsymbol{v} + \nabla p + \nabla \cdot \overleftrightarrow{\boldsymbol{\Pi}} \mp en(\boldsymbol{E} + \boldsymbol{v} \times \boldsymbol{B}) \pm \boldsymbol{R} = \boldsymbol{S}_{\text{mom}} \tag{17.33}$$

where the upper sign is used when applied to ions, the lower sign when applied to the electrons. The collisional force between e and i is given by:

$$\boldsymbol{R} = en\left(\frac{\boldsymbol{j}}{\sigma_\parallel} + \frac{\boldsymbol{j}_\perp}{(\sigma_\parallel/0.51)}\right) - 0.71 \ln \nabla T_e \tag{17.34}$$

(neglecting a small term). $\overleftrightarrow{\boldsymbol{\Pi}}$ is the viscous stress tensor and includes both parallel (classical) viscous stress, as discussed in chapter 9, and cross-field viscous stress, generally assumed to be anomalous. We will not deal specifically with $\overleftrightarrow{\boldsymbol{\Pi}}$ here. For ions $\boldsymbol{S}_{\text{mom}} = -m_i n \nu_{in} \boldsymbol{v}$, assuming stagnant neutrals. $\boldsymbol{S}_{\text{mom}}$ for electrons is neglected as small. Note that for electrons the inertia term, the first one on the LHS of equation (17.33), is also negligible.

If we add together equation (17.33) for e and i, ignoring $\overleftrightarrow{\boldsymbol{\Pi}}$, we obtain the plasma momentum equation and the useful relation for current density $\boldsymbol{j}$ (including $j_\perp$):

$$m_i n \boldsymbol{v}_i \cdot \nabla \boldsymbol{v}_i + \nabla p - \boldsymbol{j} \times \boldsymbol{B} = \boldsymbol{S}_{\text{mom},i}. \tag{17.35}$$

Here

$$p \equiv p_e + p_i \tag{17.36}$$

and

$$\boldsymbol{j} \equiv en(\boldsymbol{v}_i - \boldsymbol{v}_e). \tag{17.37}$$

At this point let us re-derive the earlier result for $\sigma_\perp$ based purely on i–n collisions: we apply equations (17.33) and (17.35) in cylindrical geometry. The *radial* component of the *ion* equation (17.33) gives:

$$m_i n\left(v_{ri}\frac{\partial v_{ri}}{\partial r} + \frac{v_{\theta i}\partial v_{ri}}{r\partial\theta} + v_{zi}\frac{\partial v_{ri}}{\partial z}\right) + \frac{\partial p_i}{\partial r} + en(E_r + v_{\theta i}B_z) + R_r = -m_i n\nu_{in}v_{ri}. \tag{17.38}$$

For toroidal geometry further terms appear, e.g. due to centrifugal forces.

We now need an equation for j_r which can be obtained from the *poloidal* component of the *plasma* equation (17.35):

$$m_i n\left(v_{ri}\frac{\partial v_{\theta i}}{\partial r} + \frac{v_{\theta i}}{r}\frac{\partial v_{\theta i}}{\partial\theta} + v_{zi}\frac{\partial v_{\theta i}}{\partial z}\right) + \frac{1}{r}\frac{\partial p}{\partial\theta} + j_r B_z = -m_i n\nu_{in}v_{\theta i}. \tag{17.39}$$

If we could justify dropping all the terms in equation (17.38) except the one containing E_r and B_z then we obtain the earlier result, $v_{\theta i} = -E_r/B_z$, and if we can justify dropping similar terms in equation (17.39), we also obtain the earlier relation between j_r and $v_{\theta i}$, hence also the result of equation (17.32) for $\sigma_\perp$. We now consider how to justify these deletions.

From geometry $\partial/\partial\theta = 0$ and $\partial/\partial z = 0$. We assume that v_r—even if due to anomalous transport—is very small and drop such terms. We simply *assume* (tentatively) the absence of a radial pressure gradient here. Assuming $\sigma_\parallel$ is large and $j_\perp$ small, then $R_r \approx 0$.

Now what if the relation between j_r and E_r is additionally *imposed*:

$$j_r = \sigma_\perp^{an} E_r \tag{17.40}$$

where $\sigma_\perp^{an}$ is a *specified*, anomalous value. If we drop all the above terms now then the problem will be *over-constrained*. We therefore relax the assumption that $\partial p_i/\partial r = 0$.

Thus

$$\frac{\partial p_i}{\partial r} + en(E_r + v_{\theta i}B_z) = 0 \tag{17.41}$$

$$j_r B_z = \sigma_\perp^{an} E_r B_z = -m_i n\nu_{in}v_{\theta i} \tag{17.42}$$

which give:

$$v_{\theta i} = -\frac{\sigma_\perp^{an} E_r B_z}{m_i n\nu_{in}} \tag{17.43}$$

$$\frac{\partial p_i}{\partial r} = -en\left(1 - \frac{\sigma_\perp^{an} B_z^2}{m_i n\nu_{in}}\right)E_r. \tag{17.44}$$

Thus assuming that B_z, $\sigma_\perp^{an}$, ν_{in} and n have been specified, then for an imposed E_r, one finds j_r, $v_{\theta i}$, $\partial p_i/\partial r$ from equations (17.39), (17.43), (17.44). We see

that in order for force balance to still hold in the presence of anomalous conductivity, $v_{\theta i}$ is no longer simply $-E_r/B_z$ and the radial pressure gradient cannot be ignored. The foregoing assumes a circular cross-section; for extension to toroidal geometry, $r\mathrm{d}\theta \rightarrow \mathrm{d}s_{\mathrm{pol}}$.

17.5.3 Models for $\sigma_\perp$ in a Tokamak

Consider the *plasma* momentum equation, equation (17.35), where we will leave aside the viscous and inertial terms, but retain the i–n collisional term. The effect of each of these three terms is broadly the same and for simplicity we will carry only the collisional terms, as illustrative. We use a right hand co-ordinate system (r, θ, ϕ) for the radial, poloidal and toroidal directions. Thus:

(a) Radial momentum balance:

$$\frac{\partial p}{\partial r} - j_\theta B_\phi + j_\phi B_\theta = 0. \tag{17.45}$$

We take $S_{\mathrm{mom},r} \approx 0$ since $v_r \approx 0$.

(b) Poloidal momentum balance:

$$-\frac{\partial p}{r\partial\theta} - j_r B_\phi = -S_{\mathrm{mom},\theta}. \tag{17.46}$$

(c) Toroidal momentum balance:

$$j_r B_\theta = -S_{\mathrm{mom},\phi} \tag{17.47}$$

$\partial/\partial\phi = 0$ from symmetry.

Since the SOL plasma is well confined radially, then one must have at least one *diamagnetic current* in the SOL, say the *poloidal diamagnetic current*, equation (17.45):

$$j_\theta = \frac{1}{B_\phi}\frac{\partial p}{\partial r} \tag{17.48}$$

if $j_\phi = 0$.

From equation (17.46) we have the *radial diamagnetic current* j_r:

$$j_r = -\frac{1}{rB_\phi}\frac{\partial p}{\partial\theta} + \frac{S_{\mathrm{mom},\theta}}{B_\phi}. \tag{17.49}$$

These same currents, equations (17.48), (17.49), are found by approaching the problem from the view point of *drifts*, section 18.4.

Generally magnetic confinement requires that the powerful—indeed potentially explosive—∇p force be balanced by a $\boldsymbol{j} \times \boldsymbol{B}$ force. This must occur for *all* locations in the plasma—not just in the main plasma but in the SOL also—at least for all directions *except* any direction in which the plasma *is* essentially

'exploding'. Only in the SOL and only for the parallel direction is the latter situation the case, with the plasma accelerating to the sound speed or faster. In the poloidal direction within the SOL the plasma is *not* exploding, indeed for a single-null divertor its exit speed at the targets is $\approx (B_\theta/B)_t c_s \ll c_s$. Thus, the very strong $(1/r)\partial p/\partial\theta$ poloidal pressure-gradient force must be virtually completely balanced by the $j_r B_\phi$ force at each poloidal location in the SOL.

While the pressure-gradient force is usually dominant—since fluids are usually controlled by ∇p forces—it is possible that other forces may be significant in the poloidal pressure balance, such as neutral friction. In that case the $j_r B_\phi$ force will be balanced with *all* the forces involved, as equation (17.49) indicates, not just $(1/r)/\partial p/\partial\theta$, and it would not be appropriate to then call j_r a purely 'diamagnetic current'.

Let us consider this basic case, then, where:

$$\boxed{j_r = -\frac{1}{r B_\phi}\frac{\partial p}{\partial \theta}.} \tag{17.50}$$

This current was first analysed by Gerhauser and Claassen [17.11], in toroidal geometry, and by Rozhansky and Tendler [17.21, 17.22], in cylindrical geometry. While *locally* such radial currents must exist in the SOL, it is perhaps surprising that there is no *total*, i.e. *integrated* radial current (for cylindrical geometry). This is shown in chapter 18 on drifts by considering the details of the spatial distribution of j_r. It is also readily seen from equation (17.50). The integral current through the LCFS, or through any complete flux surface within the SOL, is:

$$I_{\text{radial}} = \int_{\text{outerSE}}^{\text{innerSE}} -\frac{1}{r B_\phi}\frac{\partial p}{\partial \theta} \tag{17.51}$$

where the integral is from (Debye) sheath edge to sheath edge. For targets employing glancing angles of $\boldsymbol{B}$, which is standard, the plasma density, and thus pressure, at the se is very small, section 2.10. For a *cylindrical* tokamak (not toroidal) $r B_\phi \to a B_\phi$, constant, and so $I_{\text{radial}} = 0$ for all closed flux surfaces in the SOL. For a torus one also needs a factor of $2\pi R$ in equation (17.51), which gives the current per unit length (of cylinder); note that R can vary substantially with θ.

It is noteworthy that if it were physically justifiable to stop the integration at the magnetic pre-sheath entrances, MPSEs, then a very different result would hold: usually an inside/outside pressure asymmetry exists—for example due to $\boldsymbol{E}\times\boldsymbol{B}$ drifts, chapter 18. Thus $p_i^{\text{MPSE,inside}} \neq p_i^{\text{MPSE,outside}}$, and generally neither pressure is negligibly small. In that case, a net I_{radial} would exist. Further, one could change E_{radial} by external biasing, thus changing the poloidal $\boldsymbol{E}\times\boldsymbol{B}$ drift, and thus the in/out pressure asymmetry. One would thus be able to change I_{radial} externally by imposing some ΔV_{radial} across flux surfaces by an electrode arrangement. The cross-field electrical conductivity could then be calculated. None

of this, however, appears to be justifiable—within the basic picture as developed here—since it is not evident why Γ_r^{MPS} should be ignored, or the integral for I_{radial} stopped at the MPSE, rather than at the se. Thus in the basic picture there is no evident explanation in the foregoing for the experimental observation that a substantial I_{radial} *can* indeed be drawn by applying a $\Delta V_{\mathrm{radial}}$. A variety of explanations for this $\sigma_\perp \neq 0$ may be considered:

(1) As for the simpler analysis of section 17.5.2, it may just be that $\sigma_\perp$ is anomalous and one should simply insert $j_r = \sigma_\perp^{an} E_r$ into equation (17.46) and calculate the poloidal rotational velocity then required for momentum balance.
(2) The foregoing classical analysis of diamagnetic currents is for a *cylindrical* tokamak. When *toroidicity* is allowed for, finite I_{radial} is found [17.23], including a finite I_{radial} for $\Delta V_{\mathrm{radial}}^{\mathrm{applied}} = 0$ and a variation with $\Delta V_{\mathrm{radial}}^{\mathrm{applied}}$; thus $\sigma_\perp \neq 0$. Although the currents found are comparable to experimental ones [17.23], the variation of these currents with E_{radial}, which defines $\sigma_\perp$, is small compared with experiment.
(3) It has been suggested [17.24] that turbulence within the MPSs may block Γ_r^{MPS}, in which case various physical processes affecting $p_i^{\mathrm{MPSEinner}}/p_i^{\mathrm{MPSEouter}}$—such as poloidal $\boldsymbol{E} \times \boldsymbol{B}$ drifts (including externally applied ones), neutral friction, viscosity, etc—might explain the observed $I_{\mathrm{radial}} - \Delta V_{\mathrm{radial}}^{\mathrm{applied}}$ relations.
(4) As mentioned, usually the poloidal pressure gradient force would be expected to dominate the poloidal pressure balance; however, if friction (or viscosity) is strong enough, then, even if the $\partial p/\partial\theta$ term does integrate to zero, the other terms may give a finite I_{radial}. Such strong friction and viscous forces have been considered in [17.25]. To see how this works out for the case of i–n friction, let us assume very strong friction such that equation [17.47] for toroidal plasma pressure balance gives:

$$j_r = -S_{\mathrm{mom},\phi}/B_\theta = \frac{m_i n v_{in} v_{i\phi}}{B_\theta}. \tag{17.52}$$

We now need an equation relating to E_r and $v_{i\phi}$. Consider the *ion* momentum equation (17.33) which does contain E_r in the radial component:

$$v_{i\phi} = -\frac{1}{enB_\theta}\frac{\partial p_i}{\partial r} + \frac{E_r}{B_\theta} + v_{i\theta}\frac{B_\phi}{B_\theta}. \tag{17.53}$$

(We may note in passing that if we apply equation (17.53) to the main plasma, where E_r^{main} is *not* constrained by the same considerations as E_r^{SOL}, equation (17.2), but adjusts itself freely to satisfy ion radial momentum balance, and if also $v_{i\phi}$ and $v_{i\theta}$ are damped and small, then E_r^{main} must be in the *opposite* direction to E_r^{SOL}, i.e. pointing inward, and the ions in the main plasma are largely confined *electrostatically*. In that case one also has the interesting situation of $E_r \neq 0$ while $I_r = 0$, since there can be no net radial current across closed magnetic flux surfaces.)

It is clear that we are not going to obtain a simple relation involving only j_r and E_r, as in a usual Ohms law. Let us then define a $\mu_\perp$ and $\sigma_\perp$ based on a *differential* relation:

$$\mu_\perp \equiv \frac{1}{en}\frac{\partial j_r}{\partial E_r} \tag{17.54}$$

and thus we put the non-E_r terms in equation (17.53) aside. This then gives:

$$\sigma_\perp = \frac{m_i n \nu_{in}}{B_\theta^2}. \tag{17.55}$$

In obtaining this result we have assumed for simplicity that changing E_r will not change $v_{i\theta}$ or $\partial p_i/\partial r$, which may very well not be true. It is noteworthy that the value of $\sigma_\perp$ here—for the SOL of a toroidal magnetic confinement geometry—is larger by the factor $(B_\phi/B_\theta)^2$ than the simple expression found earlier, equation (17.32). The reason for the difference is that we are now considering a closed toroidal geometry—rather than an infinitely long cylinder—and here it is meaningful to consider the frictional damping of the *toroidal* velocity, which gives a larger $\sigma_\perp$ than the damping of poloidal velocity, which is all that could be involved in the infinite cylindrical case.

A very strong viscous stress could similarly result in a finite I_{radial} [17.21]. It should be noted that these currents are still only *local* ones, and in carrying out the integral to obtain I_{radial}, the substantial off-setting currents through the MPSs have to be included.

It is a remarkable and noteworthy fact that even without the application of any external electrical biasing to the SOL, both an E_r and a (local) j_r exist—*yet they have essentially nothing to do with each other*. As discussed in section 17.1, E_r arises largely due to the fact that $T_e(r)$ decays radially. The plasma-wetted surfaces are electrically conducting, and particle fluxes to these surfaces tend to be locally ambipolar. Completely independently, the poloidal force balance in the SOL, equation (17.50), gives rise to a non-zero (local) j_r. It would thus make no sense to take the ratio of these two unrelated quantities to define a no-bias value of $\sigma_\perp$. This also means that a definition of a with-bias $\sigma_\perp$ or $\mu_\perp$ has to be based on *changes* in E_r and I_r, equation (17.54).

In toroidal geometry other drifts are important which have not been considered here, specifically the ∇B drifts, see section 18.2. In toroidal geometry, diamagnetic drifts are not completely divergence free, due to the ∇B and centrifugal drifts primarily, see section 18.7. These have associated cross-field currents which close within the plasma by flowing along the field lines, including within the SOL and reaching the targets [17.14, 17.26]—the *Pfirsch–Schlüter* currents; see section 18.5.

Figures 17.14 and 17.15 show examples of SOL currents in JET, measured at the inner target, near the inner strike point (ISP) and the outer strike point (OSP) [17.26]; figure 17.14 is for the ion ∇B-drift towards the X-point (downwards), and figure 17.15 the reverse. The measurements are from Langmuir probes built into

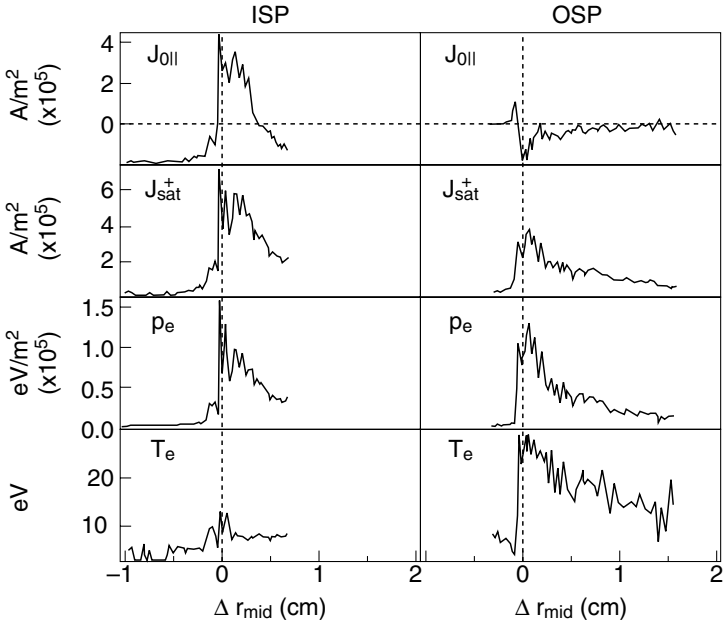

Figure 17.14. JET [17.26]. ∇B-drift *toward* X-point (down). Profiles of $j_{\|}(\equiv J_{0\|})$ for ISP (inner strike point) and OSP regions for discharge 30 589. Also shown are probe-derived profiles of ion saturation current $J_{\rm sat}^{+}$ projected onto the magnetic field, electron pressure p_e and electron temperature T_e. The profiles are mapped to the outer mid-plane and plotted as a function of $r_{\rm mid}$, the mid-plane radial distance from the nominal separatrix.

the targets. Most of the $j_{\|}$ profiles can be attributed to the thermoelectric currents due to parallel temperature gradients, section 17.4: one sees for figure 17.14, where $T_e^{\rm outer} > T_e^{\rm inner}$, that $j_{\|}$ is for the most part a positive current flowing out of the divertor target where the plasma is hotter (the outside here) and into the target where the plasma is colder (the inside here); for figure 17.15, $T_e^{\rm inner} > T_e^{\rm outer}$ and, as expected, most of the $j_{\|}$ current reverses. For these attached discharges $p_e^{\rm inside} \approx p_e^{\rm outside}$. One may note small peaks in the $j_{\|}$ profiles very close to the strike points which have opposite polarity to most of the $j_{\|}$. In [17.26] it is shown that these are due to Pfirsch–Schlüter currents in the SOL. Similar current patterns have been measured on COMPASS-D [17.27]. Such current patterns have been reproduced in code modelling [17.28].

We conclude by noting that there are many contributions to cross-field currents and it is still an open question whether $\sigma_{\perp}$ can be fully computed from classical/neo-classical considerations or whether $\sigma_{\perp}$ has a *directly* anomalous component (we allow here that anomalous cross-field viscous damping of toroidal or poloidal velocities still falls within the category of 'classical', although that makes $\sigma_{\perp}$ *indirectly* anomalous).

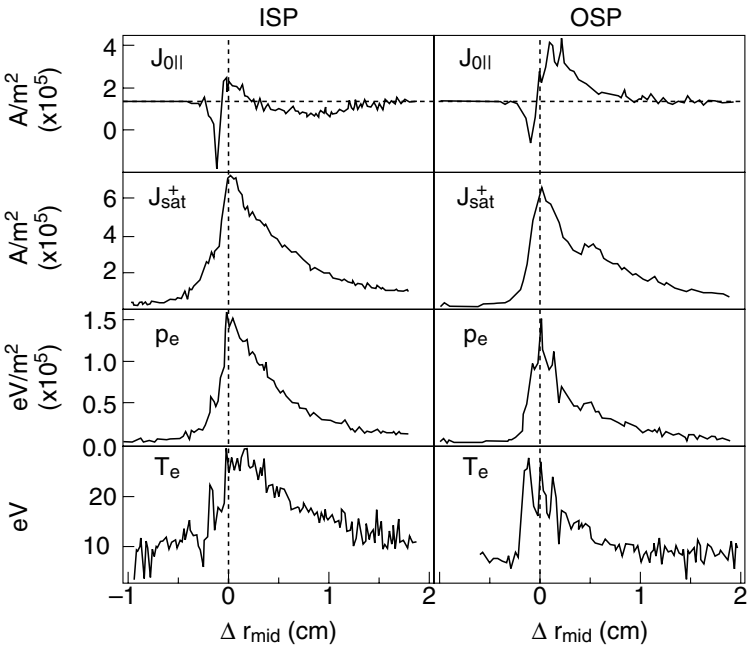

Figure 17.15. JET [17.26]. ∇B-drift *away* from X-point (up). Profiles of $j_{\|}$ for ISP and OSP regions for discharge 31 485. Otherwise as figure 17.14.

17.6 A Concluding Comment

The analysis of SOL currents in this chapter only constitutes an introduction to what is clearly a complex subject. Only the basic aspects of some of the effects have been illustrated here. Experimental reality is certain to be more complex. For a start, SOL currents and drifts, next chapter, are closely coupled. Interactions of other types are also likely and could be such as to offset the trends found on the basis of the simple analysis used here. In order to elucidate more adequately these complex effects it is necessary to employ 2D or 3D fluid codes which incorporate currents and drifts self-consistently with realistic ionization patterns, etc, and to confront the code output with experimental data. Such studies are now in progress [17.28–17.30].

References

[17.1] Goldston R J and Rutherford P H 1997 *Introduction to Plasma Physics* (Bristol: Institute of Physics Publishing) p 175
[17.2] Pitcher C S 1987 *PhD Thesis* University of Toronto Institute for Aerospace Studies

[17.3] Holt E H and Haskell R E 1965 *Foundations of Plasma Dynamics* (New York: Macmillan) pp 263–73
[17.4] Stangeby P C 1981 *Culham Laboratory DITE* Memo 294
[17.5] Harbour P J 1988 *Contrib. Plasma Phys.* **28** 417
[17.6] Staebler G M and Hinton F L 1989 *Nucl. Fusion* **29** 1820
[17.7] Stangeby P C 1990 *Nucl. Fusion* **30** 1153
[17.8] Staebler G M 1996 *Nucl. Fusion* **36** 1437
[17.9] LaBombard B, Goetz J A, Hutchinson I *et al* 1997 *J. Nucl. Mater.* **241–243** 149
[17.10] Hayashi N, Takizuka T, Hatayama A, Ogasawara M 1999 *J. Nucl. Mater.* **266–269** 526
[17.11] Gerhauser H and Claassen H A 1990 *J. Nucl. Mater.* **176–177** 721
[17.12] Gerhauser H and Claassen H A 1987 *KFA Juelich Report* JUEL-2125
[17.13] Chankin A V, Clement S, de Kock L *et al* 1992 *J. Nucl. Mater.* **196–198** 739
[17.14] Chankin A V 1997 *J. Nucl. Mater.* **241–243** 199
[17.15] Kamagai A, Asakura N, Itami K *et al* 1997 *Plasma Phys. Control. Fusion* **39** 1189
[17.16] Staebler G M 1995 *J. Nucl. Mater.* **220–222** 158
[17.17] Lachambre J L, Quirion B, Boucher C *et al* 1994 *Nucl. Fusion* **34** 1431
[17.18] Goldston R J and Rutherford P H 1997 *Introduction to Plasma Physics* (Bristol: Institute of Physics Publishing) p 196
[17.19] Bohm D 1949 *The Characteristics of Electrical Discharges in Magnetic Fields* ed A Guthrie and R K Wakerling (New York: McGraw-Hill)
[17.20] John Wesson 1997 *Tokamaks* 2nd edn (Oxford: Oxford University Press) p 89
[17.21] Rozhansky V and Tendler M 1994 *Phys. Plasmas* **1** 2711
[17.22] Roshansky V and Tendler M 1993 *Proc. 20th EPS Conf. on Controlled Fusion Plasma Physics (Lisbon)* vol 17C part 2 p 843
[17.23] Chankin A V and Stangeby P C 1996 *Plasma Phys. Control. Fusion* **38** 1879
[17.24] Rozhansky V A and Tendler M 1998 Comments *Plasma Phys. Control. Fusion* **18** 323
[17.25] Van Schoor M and Weynants R 1998 *Plasma Phys. Control. Fusion* **40** 403
Van Schoor M and Weynants R 1999 *J. Nucl. Mater.* **266–269** 1240
[17.26] Schaffer M J, Chankin A V, Guo H-Y *et al* 1997 *Nucl. Fusion* **37** 83
[17.27] Silva C G, Fielding S J, Axon K B and Booth M G 1999 *J. Nucl. Mater.* **266–269** 679
[17.28] Rognlien T D, Ryutov D D, Mattor N and Porter G D 1999 *Phys. Plasmas* **6** 1851
[17.29] Baelmans M, Reiter D, Weynants R R and Schneider R 1995 *J. Nucl. Mater.* **220–222** 982
[17.30] Chankin A V 1999 personal communication

Chapter 18

Drifts in the SOL

18.1 Experimental Observations Implying the Presence of Drifts in the SOL

In/out divertor asymmetries, observed in single-null divertor tokamaks, were discussed in section 5.9. These asymmetries are observed to change—although not necessarily completely reversing—when the direction of the toroidal field, $\boldsymbol{B}_\phi$, is changed. Figure 18.1 [18.1] shows the maximum value of T_e measured at the inside and outside targets of JET. For the 'normal' $\boldsymbol{B}_\phi$ (see next section for definitions), T_e tends to be higher on the outside, being more symmetric, or even sometimes switching to the inside when $\boldsymbol{B}_\phi$ is reversed. The direction of the toroidal current, $\boldsymbol{I}_\phi$, is less important. Figure 18.2 [18.2] shows that in/out P_{rad}, H_α and j_{sat}^+ ratios on JET exceed unity for the normal direction of $\boldsymbol{B}_\phi$, reversing (or at least diminishing significantly) when $\boldsymbol{B}_\phi$ is reversed. Similar behaviour is observed on other tokamaks [18.3], although inconsistencies exist [18.1, 18.2]. Possible explanations of these observations are ∇B and $\boldsymbol{E} \times \boldsymbol{B}$ drifts in the SOL [18.1–18.6] since the direction of such drifts depends on the direction of $\boldsymbol{B}_\phi$ (but not $\boldsymbol{I}_\phi$). The principal part of the diamagnetic drift, section 18.2, does not appear to be directly involved [18.2, 18.7].

Taking into consideration the observations, figure 5.28, that the total power entering the divertor 'legs' is often symmetrical, one is inclined to start by seeking an explanation in terms of particle drifts, rather than power drifts. Any particle drift which transported particles preferentially toward the inside target, for normal $\boldsymbol{B}_\phi$, would tend to increase the plasma density there. This increases volumetric power losses there and so temperature decreases, in accord with observation, figure 18.1. Also, as pointed out in section 5.9, a positive feedback effect would then be expected to set in, with n_e rising further, T_e dropping further, while Γ_t, H_α, P_{rad}, j_{sat}^+ would rise—also in accord with observation, figure 18.2.

We will therefore start by considering the effect of $\boldsymbol{E} \times \boldsymbol{B}$ particle drifts.

Before proceeding, it is to be noted that we will only be considering here the $\boldsymbol{E} \times \boldsymbol{B}$ and other drifts which arise *naturally* in the SOL. A number of

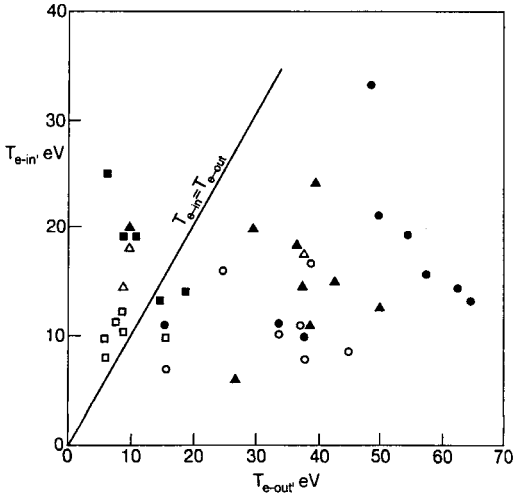

Figure 18.1. JET [18.1]. Maximum temperature at the two strike zones observed in JET discharges. Circles—normal B_ϕ and I_p, squares—reversed B_ϕ, triangles—reversed I_p plasmas. Open symbols correspond to ohmic discharges, dark symbols to NBI heated discharges.

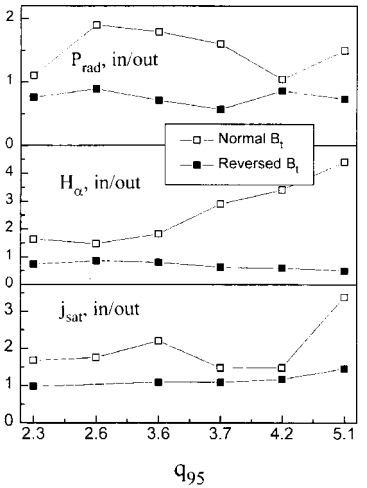

Figure 18.2. [18.2]. q-dependence of in–out asymmetries in local radiated power, H_α intensity and peak ion saturation current density for a set of dedicated L-mode discharges in JET.

important benefits can result from (active) *electrical biasing* of various edge structures relative to one another—for example increased divertor exhaust into the vacuum pumps [18.8]. We will not attempt to analyse or review here this important application of *drift manipulation*, but refer the interested reader to the references in [18.8] and the review by Staebler [18.9].

18.2 Definitions

By convention, the 'normal' direction of $\boldsymbol{B}_\phi$ is that for which the ∇B-drift of the ions is toward the bottom, i.e., toward the targets when the divertor is at the bottom. The ∇B-drift velocity [18.10, 18.11]:

$$\boldsymbol{v}_{\nabla B} = \pm \frac{v_\perp^2 m}{2eB^3} \boldsymbol{B} \times \nabla B \tag{18.1}$$

where $v_\perp$ is the gyroscopic speed and m the mass of the species. The $+$ sign is for ions, the $-$ sign for electrons. In a tokamak $B_\phi \propto 1/R$ and so ∇B points inward along the major axis. Thus, for $\boldsymbol{B}_\phi$ as shown in figure 18.3—i.e., the normal

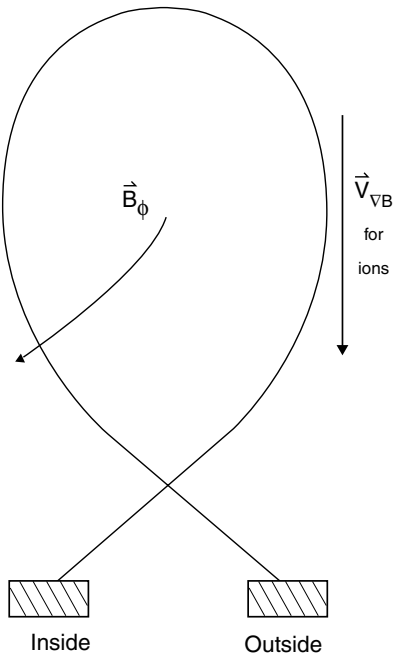

Figure 18.3. For the toroidal magnetic field in the clockwise direction (when viewed from above)—which is defined to be the 'normal' direction—the ∇B-drift of the ions is toward the bottom.

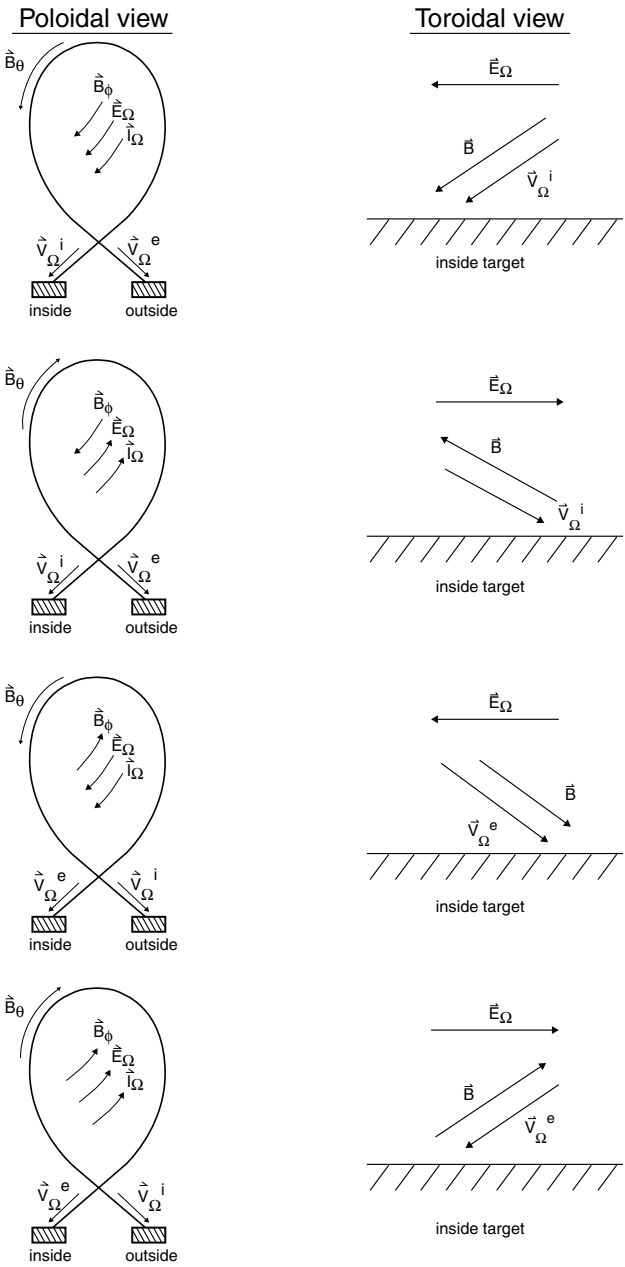

Figure 18.4. For toroidal $\boldsymbol{B}_\phi$ in the 'normal direction' the ion (ohmic) drift side is always toward the inner target, with the electron (ohmic) drift side toward the outside target, regardless of the direction of the toroidal plasma current $\boldsymbol{I}_\phi$ ($\equiv \vec{I}_\Omega$ here).

direction—$\boldsymbol{v}_{\nabla B}$ for ions is toward the targets, toward the bottom. Since the ∇B-drift is in opposite directions for opposite charges, this drift results in currents and charge separation, top/bottom of the plasma. For 'reversed' field, $\boldsymbol{v}_{\nabla B}$ for ions is away from the targets, toward the top.

Since $\boldsymbol{B} \times \nabla B$ drifts (and also the *curvature* drifts [18.11]) are up/down, they do not *directly* contribute to in/out asymmetries (although they may do so indirectly, see section 18.5), and so we will, for a start, only consider them for purposes of unambiguously defining the $\boldsymbol{B}_\phi$-direction. By contrast the $\boldsymbol{E} \times \boldsymbol{B}$ drifts are capable of directly causing in/out asymmetries, and so we start by considering them.

The transformer action of a tokamak induces a toroidal electric field $\boldsymbol{E}_\phi$ which causes the toroidal plasma current $\boldsymbol{I}_\phi$ ($\equiv \vec{I}_\Omega$) to flow. $\boldsymbol{E}_\phi$ is also present in the SOL and, although the resulting toroidal currents are smaller than exist in the main plasma due to the greater resistivity, nevertheless the SOL ions do drift to some degree in the direction parallel to $\boldsymbol{E}_\phi$ and the SOL electrons drift anti-parallel. These currents have been measured, chapter 17. One can thus speak of the 'ion drift side' and the 'electron drift side' of the targets, as the sides receiving these $\boldsymbol{E}_\phi$-drifts. (All targets, of course, also receive both ions and electrons due to the usual 'sink action', section 1.1.) As shown in figure 18.4, for $\boldsymbol{B}_\phi$ normal the ion drift side is always on the inside, with the electron drift side on the outside, regardless of the direction of $\boldsymbol{E}_\phi$, $\boldsymbol{I}_\phi$.

It is almost inevitable that radial and poloidal (parallel) gradients of electric potential—i.e., electric fields—will arise spontaneously in the SOL—even without any attempt to impose external potentials, see section 17.2. These result in $\boldsymbol{E} \times \boldsymbol{B}$ drifts [18.12, 18.13]:

$$\boldsymbol{v}_{\boldsymbol{E}\times\boldsymbol{B}} = \frac{\boldsymbol{E} \times \boldsymbol{B}}{B^2}. \tag{18.2}$$

Note that $\boldsymbol{v}_{\boldsymbol{E}\times\boldsymbol{B}}$ is independent of species, charge or mass. It therefore does not give a net current.

It is also inevitable that radial and poloidal gradients of plasma pressure will exist in the SOL. These result in diamagnetic drifts [18.14]:

$$\boldsymbol{v}_{\nabla p} = \frac{\boldsymbol{B} \times \nabla p}{enB^2}. \tag{18.3}$$

Equations (18.2) and (18.3) can be derived from the ion radial momentum equation (17.53), using the sign conventions of figure 18.5. Note that $\boldsymbol{v}_{\nabla p}$ does depend on sign of the charge and so diamagnetic currents arise. A more complete treatment of these and other drifts is discussed in [18.2], [18.7], [18.15]–[18.18]. Drift effects have now been included in 2D fluid edge codes [18.16], [18.19–18.22]; see review by Baelmans *et al* [18.23].

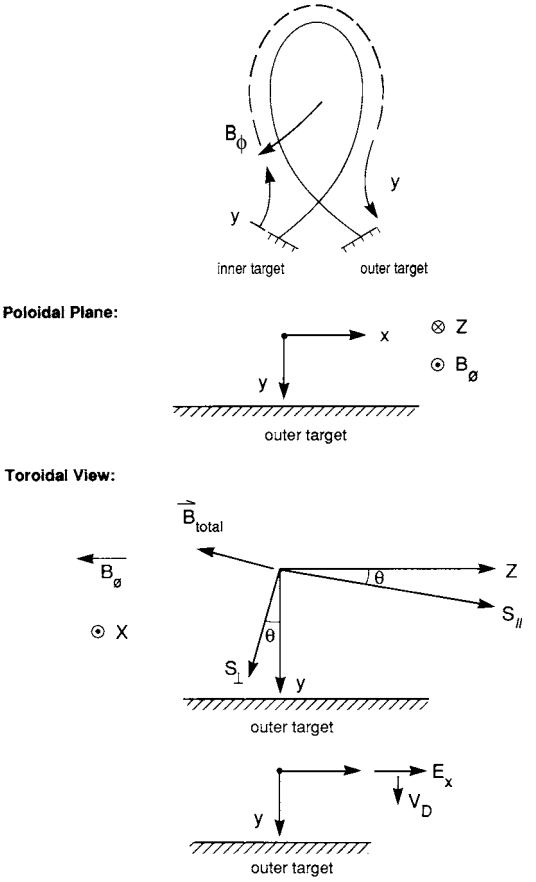

Figure 18.5. The different coordinate systems used in the analysis of $\boldsymbol{E} \times \boldsymbol{B}$ drifts.

18.3 The Consequences of $\boldsymbol{E} \times \boldsymbol{B}$ Drifts

18.3.1 The Radial and Poloidal $\boldsymbol{E} \times \boldsymbol{B}$ Drifts

There are two $\boldsymbol{E} \times \boldsymbol{B}$ drifts in the SOL:

(a) The poloidal $\boldsymbol{E} \times \boldsymbol{B}$ drift due to the radial electric field across the SOL.
(b) The radial $\boldsymbol{E} \times \boldsymbol{B}$ drift due to the poloidal electric field along the SOL.

A radial electric field can arise in the SOL for various reasons but the simplest is the one discussed in chapter 17: limiters and divertor targets are usually electrically conducting and may be used to define $V_{\text{ref}} = 0$; plasma flow to the plasma-wetted surface is usually found to be approximately locally ambipolar and so, at each radial location in the SOL, the plasma potential is $V_{\text{plasma}}(r) \sim +3kT_e(r)/e$;

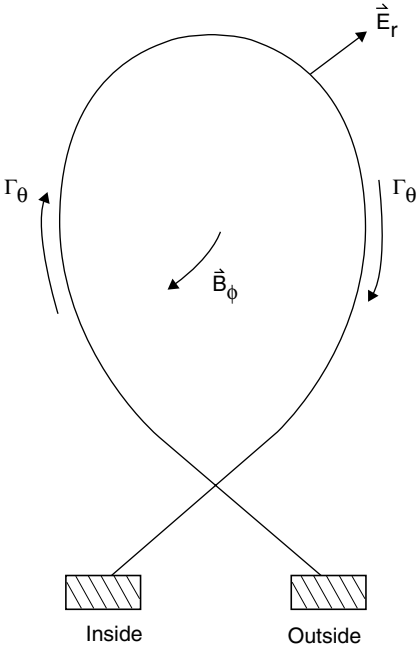

Figure 18.6. The radial electric field in the SOL is usually outward. Therefore for $\boldsymbol{B}_\phi$ in the 'normal' direction, the $\boldsymbol{E} \times \boldsymbol{B}$ poloidal drift direction is clockwise.

since $T_e(r)$ decays radially, $\partial T_e/\partial r < 0$, therefore $\partial V/\partial r < 0$ and so the radial electric field, $E_r \equiv -\partial V/\partial r$ is

$$E_r \approx \frac{3kT_e}{e\lambda_{T_e}} \tag{18.4}$$

i.e., it points radially outward in the main SOL (but oppositely in the private plasma). The resulting $\boldsymbol{E} \times \boldsymbol{B}$ drift in the main SOL is then in the poloidal direction, from inside to outside for $\boldsymbol{B}_\phi$ normal, see figure 18.6, giving poloidal flux density Γ_θ^{dr} [electrons and ions $\mathrm{m}^{-2}\ \mathrm{s}^{-1}$]:

$$\Gamma_\theta^{dr} \approx \frac{3kT_e n}{e\lambda_{T_e} B}. \tag{18.5}$$

Parallel electric fields exist in the SOL, as given by Ohm's law, section 9.5:

$$E_\parallel = \frac{j_\parallel}{\sigma_\parallel} - \frac{0.71}{e}\frac{\partial T_e}{\partial s_\parallel} - \frac{1}{en}\frac{\partial p_e}{\partial s_\parallel}. \tag{18.6}$$

In the sheath-limited regime, $\partial T_e/\partial s_\parallel \approx 0$ and taking for simplicity $j_\parallel = 0$, one obtains from the fact that p drops by $\frac{1}{2}$ along the SOL that $E_\parallel \approx -kT_e/2eL$

directed toward each target. The projection of $E_\parallel$ in the poloidal plane gives a larger value, $E_\theta \approx (B/B_\theta)kT_e/2eL$, figure 18.7. The resulting radial $\boldsymbol{E} \times \boldsymbol{B}$ particle flux density Γ_r^{dr}:

$$\Gamma_r^{dr} \approx (B/B_\theta)nkT_e/2eLB \tag{18.7}$$

is directed from the outer SOL into the main plasma (and into the private plasma below the X-point), also from the main plasma (or private plasma) into the inner SOL—for normal $\boldsymbol{B}_\phi$; see figure 18.7.

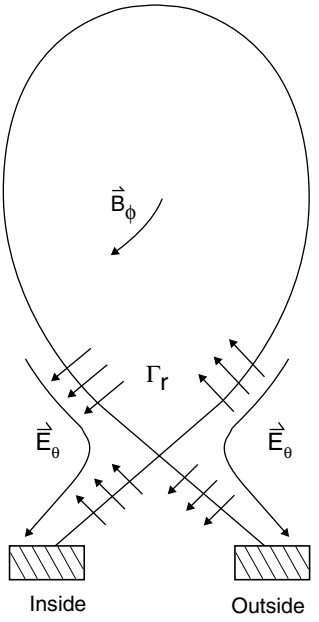

Figure 18.7. Parallel electric fields tend to be toward the targets, thus for $\boldsymbol{B}_\phi$ in the 'normal' direction the radial $\boldsymbol{E} \times \boldsymbol{B}$ drift direction is (a) for locations above the X-point: from the outside SOL into the main plasma, and out again into the inner SOL, and (b) for locations below the X-point: from the outer SOL into the private plasma and out again into the inner SOL.

For the conduction-limited regime this radial $\boldsymbol{E} \times \boldsymbol{B}$ drift is stronger since the thermoelectric term in equation (18.6) can be large. Here $E_\parallel \approx -kT_{eu}/eL$, where T_{eu} is the upstream temperature. Thus $E_\theta \approx (B/B_\theta)kT_e/eL$ and Γ_r^{dr}:

$$\Gamma_r^{dr} \approx (B/B_\theta)nkT_{eu}/eLB \tag{18.8}$$

and the directions are as for the sheath-limited regime, figure 18.7.

Next we consider how the SOL responds to these $\boldsymbol{E} \times \boldsymbol{B}$ drift flows of particles. It does so rather differently for the two drift directions. The poloidal

drift flux in the main SOL Γ_θ^{dr} is effectively in the same direction as the usual, no-drift, parallel flows to the target $\Gamma_\parallel$—i.e., the standard flows resulting from the ionization of hydrogen. It thus combines with this flow. In effect, it 'pushes the flow forward' to the outer target in the main SOL while 'working against' the flow toward the inner target—for normal $\boldsymbol{B}_\phi$. As a result, the plasma density/pressure is raised at the outer target while being reduced at the inner. This situation is analysed in more detail below.

Γ_r^{dr}, unlike Γ_θ^{dr}, does not directly 'compete' with $\Gamma_\parallel$. In the simplest picture, this radial drift forms its own closed loop of recirculating flow, figure 18.8, where we have assumed that the recycle patterns at each target are also locally closed—i.e., the 'high recycling' divertor situation (the neutrals recycling from the outer/inner target all ionize close to the outer/inner target, creating a local plasma flow back to the outer/inner target; we exclude ionization-pattern-induced flow reversal in this simplest picture). In this case, the flow pattern caused by Γ_r would consist of flow from the outer SOL, across the LCFS into the main plasma, out again across the LCFS into the inner SOL, with the circuit being completed by parallel-to-$\boldsymbol{B}$ flow along the SOL over the top side of the plasma. Clearly much more complex flow patterns could arise resulting in direct interaction (i.e., co-mingling) of the Γ_r-flow fields and those associated with the spatial distribution

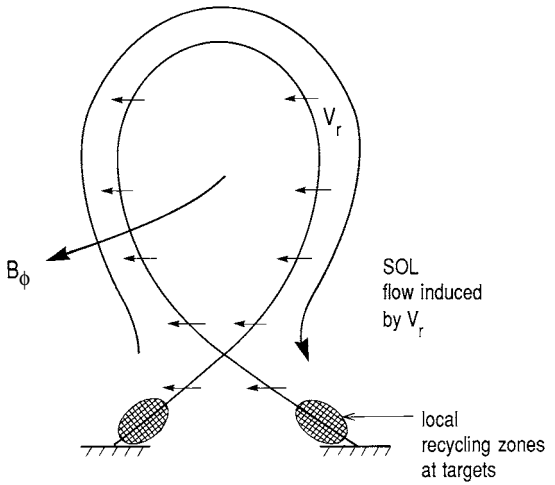

Figure 18.8. [18.5]. For the situation where the poloidal $\boldsymbol{E} \times \boldsymbol{B}$ drift can be neglected compared with the radial $\boldsymbol{E} \times \boldsymbol{B}$ drift, a return flow is induced along the SOL, from inside to outside target regions ('forward' direction of $\boldsymbol{B}$ assumed). Here, it is also assumed for simplicity that the local recycling zones at each target are very close to the target in question, and thus the two types of parallel flow ($\boldsymbol{E} \times \boldsymbol{B}$ induced, and ionization induced) do not directly interact, i.e., do not 'co-mingle'.

of ionization. Here, however, we will only consider the simplest possible case as indicated in figure 18.8. In this simplest case, if $\Gamma_r = 0$, then the entire region in the SOL, between the recycling zones localized near the two targets, would be stagnant; it is only due to $\Gamma_r \neq 0$ that there is any parallel-to-$\boldsymbol{B}$ flow in most of the SOL, for these assumptions. In the presence of dissipative forces, such as friction or shear viscosity, the parallel flow needed to close this loop, results in parallel pressure drops along the SOL, giving in/out asymmetries. This case is considered in section 18.4.

18.3.2 Comparison of Drift Fluxes with the Basic SOL Fluxes

Parallel fluxes projected onto the poloidal direction give $\Gamma_\theta^{\parallel}$:

$$\Gamma_\theta^{\parallel} \approx n c_s B_\theta / B. \tag{18.9}$$

We can compare Γ_θ^{dr}, equation (18.5), with $\Gamma_\theta^{\parallel}$:

$$\Gamma_\theta^{dr} / \Gamma_\theta^{\parallel} \approx \rho_{s\theta} / \lambda_{T_e} \tag{18.10}$$

where $\rho_{s\theta} \equiv c_s / \omega_{i\theta}$ and $\omega_{i\theta} = eB_\theta / m_i$, the ion poloidal gyro-frequency.

We can also compare Γ_r^{dr}, equation (18.8), with the cross-field anomalous particle flux density:

$$\Gamma_r^{an} \approx n D_\perp / \lambda_{\mathrm{SOL}} \tag{18.11}$$

by estimating $\lambda_{\mathrm{SOL}} \approx (D_\perp L / c_s)^{1/2}$:

$$\Gamma_r^{dr} / \Gamma_r^{an} \approx \rho_{s\theta} / \lambda_{\mathrm{SOL}} \tag{18.12}$$

i.e., essentially the same result as equation (18.10).

Example: $T = 25$ eV, $B_\theta = 0.3$ T, D^+, giving $\rho_{s\theta} \approx 3$ mm, which is not negligible compared with typical λ_{SOL} values of the order of 1 cm. One thus anticipates that while drifts would not usually dominate SOL behaviour, they may be expected to modify it noticeably. Drift effects may be anticipated to be more important for high temperature parts of the SOL since $\rho_{s\theta} / \lambda_{\mathrm{SOL}} \propto T^{3/4} D_\perp^{-1/2}$.

18.3.3 Comparison of Radial and Poloidal Drift Fluxes

Consider first the sheath-limited regime with $\nabla_\parallel T \approx 0$. We integrate Γ_θ^{dr}, equation (18.5), over 1 m toroidally and across the width of the SOL, λ_{SOL} (taken to be λ_{T_e} here) to obtain the total flow (along the main SOL):

$$\phi_\theta^{dr} \approx 3nkT_e / eB. \tag{18.13}$$

We integrate Γ_r^{dr}, equation (18.7), over 1 m toroidally and along the entire length of the LCFS from the top of the machine to the outer target, which is a length $(B_\theta / B)L$ in the poloidal plane:

$$\phi_r^{dr} \approx nkT_e / 2eB. \tag{18.14}$$

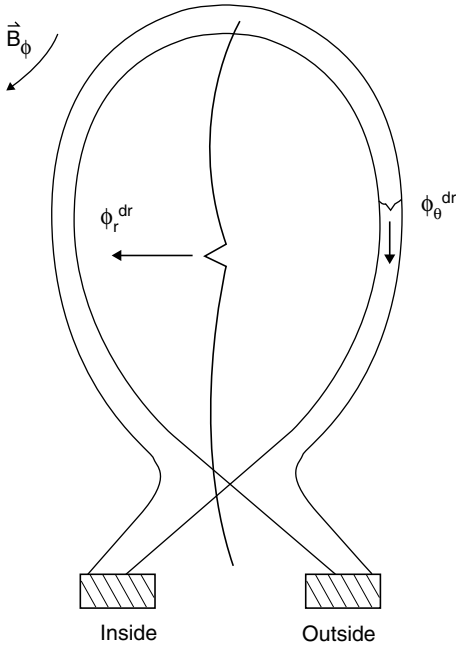

Figure 18.9. The total poloidal, ϕ_θ^{dr}, and radial, ϕ_r^{dr}, $\boldsymbol{E} \times \boldsymbol{B}$ fluxes integrated over the tokamak.

ϕ_θ^{dr}, ϕ_r^{dr} [particles/m toroidally /s] are shown schematically in figure 18.9. Clearly, in this regime, the poloidal drift dominates and, to first order, one can neglect the radial drift.

Consider next the conduction-limited regime where $\nabla_\parallel T$ is large, $T_{eu} \gg T_{et}$. From equation (18.8) we then obtain:

$$\phi_r^{dr} \approx nkT_{eu}^{\text{sep}}/eB \tag{18.15}$$

(the potential drop across the MPS, $\sim 3kT_{et}$, is ignored since $T_{et} \ll T_{eu}$) while the total poloidal flux at the top of the machine:

$$\phi_\theta^{dr} \approx n_{eu} E_{ru} \lambda_{\text{SOL}}/B. \tag{18.16}$$

E_{ru} no longer has very much to do with the variation of potential or T_e across the target in this situation, and is governed instead by the evolution of plasma potential V along the SOL. Consider figure 18.10. We assume the plasma temperatures $T_b \approx T_c \approx 0$ while $T_a \equiv T_{et}^{\text{sep}}$, $T_{\text{d}} \equiv T_{eu}^{\text{sep}}$ are the separatrix values. Taking $V_b \equiv 0$, then $V_a \approx 3kT_{et}^{\text{sep}}/e$;

$$V_c \approx V_b + 0.71(kT_c - kT_b)/e \approx 0$$
$$V_{\text{d}} \approx V_a + 0.71(kT_{\text{d}} - kT_a)/e \approx kT_{eu}^{\text{sep}}/e$$

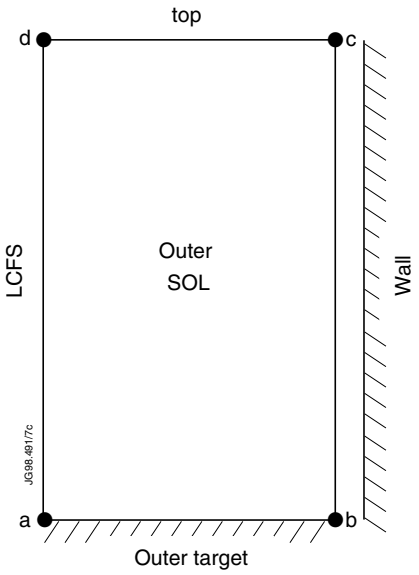

Figure 18.10. The 'straightened-out' SOL on the outside.

assuming $T_{eu}^{\text{sep}} \gg T_{et}^{\text{sep}}$. Thus $E_{ru} \approx kT_{eu}^{\text{sep}}/e\lambda_{\text{SOL}}$ and from equation (18.16):

$$\phi_\theta^{dr} \approx n_{eu} k T_{eu}^{\text{sep}}/eB. \tag{18.17}$$

At this point, it appears that ϕ_r^{dr} and ϕ_θ^{dr} are of about the same magnitude. We have not, however, allowed yet for the fact that n also varies substantially along the SOL in this regime. Thus equation (18.15) for ϕ_r^{dr} may be corrected, to first order, by replacing n with the average value of n along the LCFS from top to outer target. Since $T_u \gg T_t$, then from pressure conservation we have $n_u \ll n_t$ and so the average $\bar{n}_{\text{LCFS}} \gg n_u$. The correction for ϕ_θ^{dr} is smaller: we might replace n_{eu} in equation (18.17) with the average value across the SOL at the top, perhaps $0.5n_u$. Thus allowing for the large $\nabla_\parallel T$ and the large $\nabla_\parallel n$ in this regime, it is expected that the radial $\boldsymbol{E} \times \boldsymbol{B}$ drift fluxes are more important than the poloidal ones. The foregoing comparison of the two drifts is only to aid understanding and any serious modelling exercise should include both in order to avoid artificial sources or sinks.

18.3.4 The Effect of Poloidal $\boldsymbol{E} \times \boldsymbol{B}$ Drift on SOL Asymmetries

At this point, it is to be noted that the common practice, which we have followed here, of referring to Γ_θ^{dr} as being in the 'poloidal' direction (and thus the use of 'θ') is strictly incorrect, see figure 18.5. Strictly, this is in the direction perpendicular to $\boldsymbol{B}$. Although in practice this distinction is unimportant since $B_\theta/B \ll 1$,

it is potentially confusing. Here we will continue with the common practice of writing v_θ for $v_\perp$ and Γ_θ for $\Gamma_\perp$, etc, but will nevertheless take the correct components. Hence, the total flux in the true poloidal direction y of figure 18.5:

$$\Gamma_y = \cos\theta \Gamma_\theta^{dr} + \sin\theta \Gamma_\parallel. \tag{18.18}$$

Thus

$$\Gamma_y = n(\cos\theta v_\theta^{dr} + \sin\theta v_\parallel) \tag{18.19}$$

where v_θ^{dr} is the 'poloidal' drift velocity:

$$v_\theta^{dr} \equiv E_r/B \tag{18.20}$$

i.e., strictly one should write this as $v_\perp^{dr}$. Thus one has the particle conservation equation:

$$\frac{\mathrm{d}\Gamma_y}{\mathrm{d}y} = \frac{\mathrm{d}}{\mathrm{d}y}\left[n(\cos\theta v_\theta^{dr} + \sin\theta v_\parallel)\right] = S_p \tag{18.21}$$

where S_p is the particle source rate due to ionization or cross-field diffusion, section 1.8.2.4. Also:

$$\theta = \sin^{-1}(B_\theta/B) \approx B_\theta/B. \tag{18.22}$$

Note that one could re-write equation (18.21) as:

$$\frac{\mathrm{d}}{\mathrm{d}y}\left[n\sin\theta v_\parallel\right] = S_p + S_p^{dr} \tag{18.23}$$

where

$$S_p^{dr} \equiv -\frac{\mathrm{d}}{\mathrm{d}y}\left[n\cos\theta v_\theta^{dr}\right]. \tag{18.24}$$

That is, one has an *effective* particle source due to cross-field drift, specifically given by the negative of the divergence of the cross-field flux density, in precise analogy to the effective cross-field diffusion source, section 1.8.2.4.

This then leads naturally to a formulation of the parallel momentum equation allowing for drifts starting from the form in section 1.8.2.3:

$$mnv_\parallel \frac{\mathrm{d}v_\parallel}{\mathrm{d}s_\parallel} = -\frac{\mathrm{d}p_i}{\mathrm{d}s_\parallel} + neE_\parallel + S_m^{dr} - mv_\parallel S_p^{dr} - mv_\parallel S_p \tag{18.25}$$

where S_p^{dr} and S_m^{dr} are the particle and momentum 'source' rates, respectively, for the parallel direction due to the divergence of the drift flow at speed v_θ^{dr}.

For simplicity we take the isothermal approximation, thus the first two terms on the RHS of equation (18.25) become:

$$-c_s^2 m\frac{\mathrm{d}n}{\mathrm{d}s_\parallel} \tag{18.26}$$

where

$$c_s^2 = k(T_e + T_i)/m. \tag{18.27}$$

Defining the coordinate pair $(s_\parallel, s_\perp)$ in the (x, y)-plane, see figure 18.5, we have:

$$\mathrm{d}y = \cos\theta \mathrm{d}s_\perp, \quad \mathrm{d}x = \cos\theta \mathrm{d}s_\parallel, \quad \text{etc.} \tag{18.28}$$

Then:

$$S_m^{dr} = -\frac{\mathrm{d}}{\mathrm{d}s_\perp}(m v_\parallel n v_\theta^{dr}). \tag{18.29}$$

Therefore,

$$S_m^{dr} - m v_\parallel S_p^{dr} = -\cos\theta m n v_\theta^{dr} \frac{\mathrm{d}v_\parallel}{\mathrm{d}y}. \tag{18.30}$$

Combining expressions (18.25), (18.26), (18.28) and (18.30) gives:

$$n\frac{\mathrm{d}v_\parallel}{\mathrm{d}y}\left(\frac{v_\theta^{dr}}{\tan\theta} + v_\parallel\right) = -c_s^2\frac{\mathrm{d}n}{\mathrm{d}y} - v_\parallel\frac{S_p}{\sin\theta}. \tag{18.31}$$

If one treats v_θ^{dr} as specified, and also T_e, T_i, $S_p(y)$, $\theta(y)$, then we have two equations (18.21) and (18.31), to give the two quantities $n(y)$ and $v_\parallel(y)$. Here we assume that θ is constant along y. We combine the particle balance equation (18.21) and the momentum equation (18.31) to obtain:

$$n\frac{\mathrm{d}v_\parallel}{\mathrm{d}y}\left(\frac{v_\theta^{dr}}{\tan\theta} + v_\parallel\right) + v_\parallel\frac{\mathrm{d}}{\mathrm{d}y}\left[n\left(\frac{v_\theta^{dr}}{\tan\theta} + v_\parallel\right)\right] = -c_s^2\frac{\mathrm{d}n}{\mathrm{d}y}. \tag{18.32}$$

We define

$$v \equiv v_\parallel + \frac{v_\theta^{dr}}{\tan\theta} \tag{18.33}$$

and we can now integrate equation (18.32) to give:

$$n\left(v^2 + c_s^2 - \frac{v v_\theta^{dr}}{\tan\theta}\right) = G, \text{ a constant.} \tag{18.34}$$

At this point, the boundary conditions are needed to specify $v_\parallel$ (or v) at the entrance to the magnetic pre-sheath in front of the target plates, $v_{\parallel\mathrm{BMPSE}}$, allowing for the presence of poloidal drift. This has been evaluated in [18.24], [18.25]. To a first approximation, the 'intuitive' result is obtained:

$$M_t = 1 - 2\gamma \tag{18.35}$$

where

$$M_t \equiv v_{\parallel\mathrm{BMPSE}}/c_s \tag{18.36}$$

and

$$\gamma \equiv \frac{v_\theta^{dr}}{2c_s\tan\theta}. \tag{18.37}$$

See also [18.4], [18.26], [18.27]. The term 'intuitive' is used because one could derive this result simply by assuming that the total velocity (the vectorial sum of drift and parallel velocity) at the MPSE is the sound speed. The analysis employed in [18.25] and [18.26] is, nevertheless, from first principles and broadly follows the same line of reasoning used to establish the Bohm, sections 2.3, 2.4, and Chodura, section 2.10, boundary conditions, by considering the entrance speed required to result in a sheath and magnetic pre-sheath where the potential varies in a non-oscillatory way.

Thus one has the simple result for the boundary condition on v:

$$v_t = c_s \tag{18.38}$$

to be used with equation (18.34). From equation (18.34) we thus have the density just in front of the target:

$$n_t = \frac{G}{2c_s^2(1-\gamma)}. \tag{18.39}$$

We can thus calculate the in/out density ratio $n_t^{in}/n_t^{\text{out}}$—which, since the isothermal assumption is made here, is also the pressure asymmetry. We will assume v_θ^{dr}, $\gamma^{\text{out}} > 0$ at the outer target and $\gamma^{in} = -\gamma^{\text{out}}$ $(= \gamma)$. Thus from equation (18.39):

$$n_t^{in}/n_t^{\text{out}} = \frac{1-\gamma}{1+\gamma} \tag{18.40}$$

Figure 18.11. Thus as the poloidal drift becomes strong, i.e., $\gamma \to 1$, the density and pressure ratios go to zero, i.e., an extreme asymmetry exists.

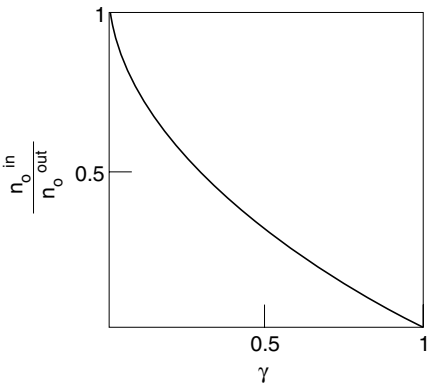

Figure 18.11. Asymmetry in density at inner and outer divertor targets due to $\boldsymbol{E} \times \boldsymbol{B}$ poloidal drift. The strength of the drift is given by $\gamma \equiv E_r/(2Bc_s \tan\theta)$. Effect shown for the main SOL.

The total out flux density to the target:

$$\Gamma_{\text{yt}} = n_t c_s \sin\theta \tag{18.41}$$

and thus the target particle fluxes are also in this ratio. Using equation (18.41), one can relate the constant G to the total integrated source, S_p, per m toroidally:

$$G = c_s(1-\gamma^2)S_p^{\text{total}}/\sin\theta. \tag{18.42}$$

It is also useful to relate n_t to $n_{\max}$, the maximum of n in the flux tube—roughly midway between the targets and thus the value that should be associated with the 'upstream' density in the SOL, i.e., the main plasma density in the simplest picture. From equation (18.34) we have $n(v)$. Differentiating we find:

$$n_{\max} = \frac{G/c_s^2}{(1-\gamma^2)}. \tag{18.43}$$

Thus:

$$\frac{n_t}{n_{\max}} = \frac{1+\gamma}{2}. \tag{18.44}$$

Thus, at the inside, for very strong drifts, $\gamma^{in} \to -1$, one would obtain complete disappearance of the plasma, i.e., complete plasma detachment. Cohen and Ryutov, however [18.27], argue that some finite density, rather than zero, will remain. The influence of the poloidal $\boldsymbol{E} \times \boldsymbol{B}$ drift on the SOL structure was first analysed by Tendler and Rozhansky [18.28]. They noted that the pressure asymmetry between the strike points causes plasma flow along the field lines, giving rise to a net toroidal velocity of order E_r/B_θ. In [18.29] they also argued that toroidal rotation in the same direction can be driven near the separatrix by anomalous radial transport in the presence of shear of the poloidal rotation.

It should not be assumed that a poloidal $\boldsymbol{E} \times \boldsymbol{B}$ drift toward, say, the outer target will necessarily involve *net* transport of plasma from the inner divertor to the outer. In the simplest situation (with no ionization-driven flow reversal, chapter 15) each divertor region is *locally self-sustained* as to particle balance, with the total ionization that occurs in each divertor equalling the particle outflow to the local target. In that case there can be no *net* transfer of plasma between the two target regions. If a poloidal $\boldsymbol{E} \times \boldsymbol{B}$ drift raises the density and pressure in the outer divertor, then the magnitude of the recycle rate there will increase—and the target flux will rise—but since that process is entirely locally sustained, there is no need for plasma to be transported into the outer divertor volume, once a steady state has become established. The $\boldsymbol{E}_r \times \boldsymbol{B}$ drift must therefore be *compensated* by a '*return flow*' of some sort. The simplest type of return flow is a parallel flow, from the outside (higher pressure) to the inside (lower pressure) (the normal direction of $\boldsymbol{B}$ assumed) at velocity $v_\parallel^{\text{return}}$. There is zero net transfer of plasma when $(B_\theta/B)v_\parallel^{\text{return}} = (B_\phi/B)E_r/B$, i.e., approximately $v_\parallel^{\text{return}} = E_r/B_\theta$. Such flows, all along the SOL, can be substantial: say $E_r \approx kT_e/e\lambda_T \approx 50$ [eV]/0.02 [m] = 2500 [V m^{-1}] and $B_\theta = 0.25$ [T], then $v_\parallel^{\text{return}} = 10^4$ m s^{-1}. A significant fraction of the $\boldsymbol{E} \times \boldsymbol{B}$ flow simply forms a natural re-circulation pattern in the edge, turning to pass along the magnetic pre-sheaths (as $\boldsymbol{E}_\theta \times \boldsymbol{B}$

flow) in front of the targets, then returning along the private plasma (as $\boldsymbol{E}_r \times \boldsymbol{B}$ flow), closing on itself, see section 18.4, point (V), and figure 18.15.

Finally, it is worth commenting on the *heuristic* treatment used here to establish the particle balance and momentum balance equations (18.21) and (18.25). In this non-rigorous approach the effects of the drifts have had to be introduced *explicitly* using expressions for $\boldsymbol{v}_{E\times B}$, equation(18.2), whose origin is not necessarily clear. Equations (18.2) for $\boldsymbol{v}_{E\times B}$ and (18.3) for $\boldsymbol{v}_{\nabla p}$ can, for example, be obtained by analysing single-particle motion to obtain these *guiding centre drifts* [18.30], section 18.7. It might therefore appear that it is necessary to 'patch' guiding centre drifts into fluid equations. This is not correct. When the complete 3D form of the momentum equation is used [18.2, 18.31]:

$$\nabla(nm\boldsymbol{v}\boldsymbol{v} + \overleftrightarrow{p}) = en(\boldsymbol{E} + \boldsymbol{v} \times \boldsymbol{B}) \tag{18.45}$$

then all drifts are automatically included—including ones involving toroidicity (finite a/R) [18.2], section 18.7. The only reason that we had to 'patch up' the momentum equation used here, equation (18.25), was that we did not use the complete 3D momentum equation, but a simplified 1D form. The same applies to the particle balance equation. For a rigorous derivation, see Baelmans [18.15].

18.3.5 The Effect of Radial $\boldsymbol{E} \times \boldsymbol{B}$ Drift on SOL Asymmetries

The postulated flow pattern induced by the radial $\boldsymbol{E} \times \boldsymbol{B}$ drift is shown in figure 18.8. The flow along the SOL required to close this flux loop is simplified to slab geometry in figure 18.12. We have a $v_\parallel^{\text{return}}$ due to this parallel return flux needed to close the loop. This is in addition to any $v_\parallel$ associated with ionization or cross-field diffusion sources. Assuming that E_θ is largest near the X-point, where the pitch angle is smallest and therefore poloidal T-gradients are often largest, then most of the influx to the SOL caused by v_r^{dr} is near the inside end of the SOL flux tube, and most of the outflux (back into the core via v_r^{dr}) is near the outside end of the SOL flux tube. In figure 18.12, we have simplified to the extreme of all influx at the inside end, all outflux at the outside end. Although $v_\parallel^{\text{return}}$ will vary along the flux tube due (a) to the very fact that n varies (i.e., the effect we are trying to extract here), and (b) to the fact that the cross-sectional area of the flux tube varies poloidally (by a factor $\approx a/R$)—we will simply take here a constant value of $v_\parallel^{\text{return}}$ as being representative of the magnitude of the induced parallel flow along the SOL.

The total out/in flux is given by:

$$\phi \approx \tfrac{1}{2} 2\pi a 2\pi R n v_r^{dr}. \tag{18.46}$$

Assume this flux is carried by a SOL flux tube of thickness λ_{SOL}, we have:

$$\phi = 2\pi R(B_\theta/B) n v_\parallel^{\text{return}} \lambda_{\text{SOL}}. \tag{18.47}$$

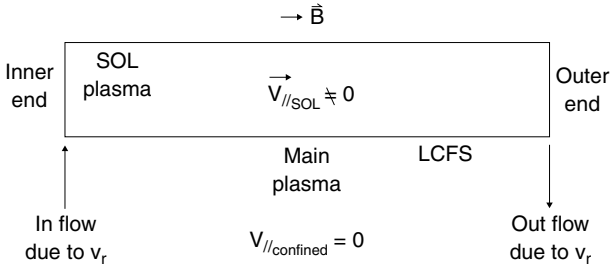

Figure 18.12. Case of radial $\boldsymbol{E} \times \boldsymbol{B}$ drift. The SOL has been straightened out. The wall is on the top side; the confined plasma is on the bottom side. The parallel return flow, $v_{\parallel \mathrm{SOL}}$, is induced by the radial $\boldsymbol{E} \times \boldsymbol{B}$ flux which, here, is taken to enter the SOL near the inner target and to exit back to the confined plasma at the outer end. This induced parallel flow generally suffers frictional loss, thus making the plasma pressure at the inner target higher than at the outer target—which is the opposite pattern of the poloidal drift.

Thus:

$$v_{\parallel}^{\mathrm{return}} \approx \frac{a\pi v_r^{dr}}{(B_\theta/B)\lambda_{\mathrm{SOL}}}. \tag{18.48}$$

Taking:

$$v_r^{dr} = \frac{E_\theta}{B} = \frac{kT}{ea\pi B} \tag{18.49}$$

gives:

$$v_{\parallel}^{\mathrm{return}} = \frac{kT}{eB_\theta \lambda_{\mathrm{SOL}}}. \tag{18.50}$$

Example: $T = 100$ eV, $c_s = 10^5$ m s^{-1}, $B_\theta = 0.5$ T, $\lambda_{\mathrm{SOL}} = 10^{-2}$ m, one finds $v_{\parallel}^{\mathrm{return}} \approx 2 \times 10^4$ m s^{-1} which is significant compared with the sound speed. We therefore can anticipate significant drag on this SOL flow caused by shear viscosity and perhaps by neutral friction. For simplicity, we assume here that the plasma just inside the LCFS is stagnant. We also assume a no-slip condition at the LCFS. The shear stress acting on the SOL flow is then:

$$\tau = \mu_\perp \left.\frac{\mathrm{d}v_{\parallel}^{\mathrm{return}}}{\mathrm{d}r}\right|_{\mathrm{LCFS}} \tag{18.51}$$

where we make the approximation:

$$\left.\frac{\mathrm{d}v_{\parallel}^{\mathrm{return}}}{\mathrm{d}r}\right|_{\mathrm{LCFS}} \approx \frac{v_{\parallel}^{\mathrm{return}}}{\delta} \tag{18.52}$$

where δ is the boundary layer shear viscosity thickness, given by the usual Reynolds expression:

$$\delta \approx \left(\frac{\mu_\perp L}{mnv_{\parallel}^{\mathrm{return}}}\right)^{1/2} \tag{18.53}$$

(which is readily derived by assuming that the shear stress acting on the flow in a layer of thickness δ, length L, removes all the flow momentum). Thus:

$$\tau \approx \frac{\mu_\perp v_\parallel^{\text{return}}}{(\mu_\perp L/mn v_\parallel^{\text{return}})^{1/2}}. \tag{18.54}$$

In order for the SOL flow to close the loop a pressure drop Δp must exist along the SOL to balance the shear force, thus:

$$\tau L \approx \Delta p \lambda_{\text{SOL}} \tag{18.55}$$

using

$$\mu_\perp = mn D_\perp \tag{18.56}$$

(by analogy with classical results); also:

$$p = 2nkT \tag{18.57}$$

$$c_s^2 = 2kT/m \tag{18.58}$$

giving:

$$\frac{\Delta p}{p} = \frac{v_\parallel^{\text{return}}}{c_s^2 \lambda_{\text{SOL}}} (v_\parallel^{\text{return}} L D_\perp)^{1/2}. \tag{18.59}$$

Example: $T = 100\,\text{eV}$, $v_\parallel^{\text{return}} = 2 \times 10^4\ \text{m s}^{-1}$, $c_s = 10^5\ \text{m s}^{-1}$, $\lambda_{\text{SOL}} = 10^{-2}\ \text{m}$, $L = 50\ \text{m}$, $D_\perp = 1\ \text{m}^2\ \text{s}^{-1}$ gives $\Delta p/p = 0.2$ from the inside to the outside.

Clearly, the foregoing is a rough estimate and all that can be concluded from it is that for reasonable assumptions about the edge parameters one finds $\Delta p = 0(p)$, i.e., there is a substantial pressure difference from inside to outside, due to flows induced by radial $\boldsymbol{E} \times \boldsymbol{B}$ drifts.

Neutral friction would contribute further to the existence of a pressure difference along the SOL—with the higher pressure existing at the inside end of the SOL for normal $\boldsymbol{B}$—in order to drive the parallel return flux to the outside end against these momentum losses.

At the inner target the increased pressure corresponds to $f_{\text{mom}} > 1$, section 5.4, which for fixed upstream conditions then reduces T_t, equation (5.26), while raising n_t, equation (5.28), and raising Γ_t, equation (5.29). This will increase volumetric power losses which generally increase with decreasing T_t and increasing n_t and Γ_t, thereby causing a positive feedback effect.

18.3.6 Comments on the Effects of Radial and Poloidal $E \times B$ Drifts

It is thus seen that:

(a) poloidal drifts tend to be more important than radial drifts in the sheath-limited regime, with the roles reversing in the conduction-limited regime;

(b) for normal $\boldsymbol{B}_\phi$, poloidal drifts in the main SOL tend to raise the pressure at the outside divertor while the radial drifts favour the inside;
(c) For normal $\boldsymbol{B}_\phi$, poloidal drifts in the private plasma are from outside to inside and tend to raise the pressure at the *inside* divertor; this can be a larger effect than the poloidal drift in the main SOL [18.32].

As discussed in section 5.9, there exists a positive feedback effect in the conduction-limited regime. Thus if the inside density is raised, either by radial $\boldsymbol{E} \times \boldsymbol{B}$ drifts or by poloidal $\boldsymbol{E} \times \boldsymbol{B}$ drifts in the private plasma, one anticipates a further enhancement of density and temperature asymmetries.

On a separate issue, it may be noted that poloidal $\boldsymbol{E} \times \boldsymbol{B}$ drifts can be quite sizeable and can be observed experimentally, for example, by spectroscopic observation of impurity 'plumes' resulting from injection of impurities into the SOL [18.33]. We may estimate:

$$v_\theta^{dr} \approx \frac{3kT_e}{e\lambda_{T_e}B}. \tag{18.60}$$

Example: $T_e = 25$ eV, $\lambda_{T_e} = 10^{-2}$ m, $B = 3$ T giving $v_\theta^{dr} \approx 2500$ m s^{-1}. This is comparable to the poloidal projection of parallel flow sonic speeds and so is quite detectable.

18.4 Diamagnetic Drifts and Currents in the SOL

There are at least two important differences between $\boldsymbol{E} \times \boldsymbol{B}$ drifts and diamagnetic ∇p-drifts:

(a) ∇p-drifts are largely divergence free [18.7] which means that the flux patterns form closed circuits within the plasma and do not constitute fluxes onto external surfaces such as targets and limiter surfaces. See section 18.7.
(b) ∇p-drifts constitute not only particle flows but currents also, since the sign of the drift velocity is charge dependent, equation (18.3).

These two properties of ∇p-drifts have a number of important consequences. We deal first with the divergence-free property. This can be demonstrated in some generality [18.2, 18.7], section 18.7. Here we consider a simple demonstration for the case of a cylindrical (not toroidal) tokamak with a 'toroidal' limiter, figure 18.13. Consider the orthogonal co-ordinates x and y with x measured radially outward from the LCFS and y measured poloidally. As with $\boldsymbol{E} \times \boldsymbol{B}$ drifts, we will take the ∇p-drifts to be in the purely radial and poloidal directions, although strictly the two directions are radial and the second direction perpendicular to $\boldsymbol{B}$. Then:

$$v_y^{\nabla p} = \frac{1}{enB}\frac{\partial p_i}{\partial x} \tag{18.61}$$

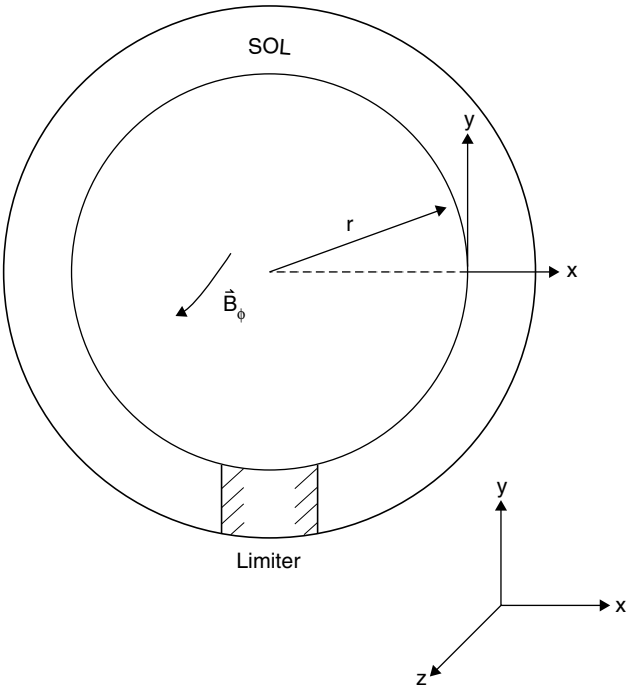

Figure 18.13. Poloidal cross-section of a cylindrical (i.e., not toroidal) tokamak with a longitudinal rail limiter (or poloidal divertor) at the bottom.

The sign in equation (18.61) is in accord with convention (for ions); however, in the SOL $\partial p_i/\partial x$ is negative and so $v_y^{\nabla p}$ is actually in the clockwise direction in figure 18.13. Also:

$$v_x^{\nabla p} = -\frac{1}{enB}\frac{\partial p_i}{\partial y} \tag{18.62}$$

where the negative sign in equation (18.62) is necessary for the choice of x direction here. Since pressure increases away from the target, i.e. $\partial p_i/\partial y > 0$ on the outside, $\partial p_i/\partial y < 0$ on the inside. Thus $v_x^{\nabla p}$ is radially inward on the outside, carrying particles from the outer SOL into the main plasma; on the inside it carries particles from the main plasma into the inner SOL.

We now consider the resulting particle fluxes at various locations to show that the flow is divergence free, see figure 18.14:

$$(1) \qquad \phi_y^{\text{top}} = \int_{\text{LCFS@top}}^{\infty} n v_y^{\nabla p} \mathrm{d}x = \int \frac{1}{eB}\frac{\partial p_i}{\partial x}\mathrm{d}x = -\frac{p_i^{\text{top,LCFS}}}{eB}. \tag{18.63}$$

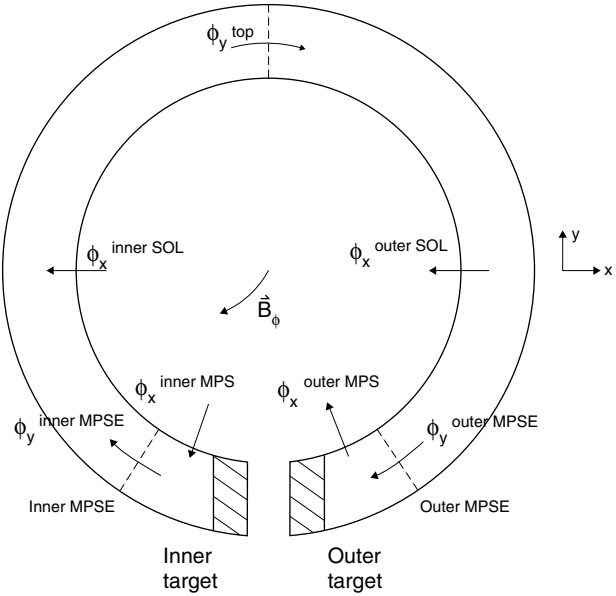

Figure 18.14. Detailed accounting of the radial and poloidal $\boldsymbol{E} \times \boldsymbol{B}$ fluxes for a cylindrical tokamak.

ϕ [ions/m poloidally /s] throughout.

(2)
$$\phi_x^{\text{outer SOL}} = \int_{\text{outer MPSE,LCFS}}^{\text{top,LCFS}} n v_x^{\nabla p} \mathrm{d}y = -\int \frac{1}{eB} \frac{\partial p_i}{\partial y} \mathrm{d}y$$
$$= -\frac{-p_i^{\text{top,LCFS}} + p_i^{\text{outer MPSE,LCFS}}}{eB}. \tag{18.64}$$

Note that this is just the radial flux crossing the LCFS between the top and the outside magnetic pre-sheath entrance, MPSE.

(3)
$$\phi_y^{\text{outer MPSE}} = \int_{\text{LCFS@outer MPSE}}^{\infty} n v_y^{\nabla p} \mathrm{d}x$$
$$= \int \frac{1}{eB} \frac{\partial p_i}{\partial x} \mathrm{d}x = \frac{-p_i^{\text{outer MPSE,LCFS}}}{eB} \tag{18.65}$$

(4)
$$\phi_x^{\text{outer MPS}} = \int_{\text{outer SE,LCFS}}^{\text{outer MPSE,LCFS}} n v_x^{\nabla p} \mathrm{d}y$$
$$= \frac{-p_i^{\text{outer MPSE,LCFS}} + p_i^{\text{outer SE}}}{eB} \tag{18.66}$$

where SE is the (Debye) sheath entrance.

$$\phi_x^{\text{inner SOL}} = \frac{p_i^{\text{top,LCFS}} - p_i^{\text{inner MPSE,LCFS}}}{eB} \tag{5}$$ (18.67)

$$\phi_y^{\text{inner MPSE}} = \frac{-p_i^{\text{inner MPSE,LCFS}}}{eB} \tag{6}$$ (18.68)

$$\phi_x^{\text{inner MPS}} = \frac{p_i^{\text{inner MPSE,LCFS}} - p_i^{\text{inner SE,LCFS}}}{eB} \tag{7}$$ (18.69)

We are now in a position to demonstrate a number of important results. First we may simplify equations (18.66), (18.69) by dropping p_i^{SE} as small since, for the usual glancing angle targets, the potential drop in the MPS + Debye sheath occurs almost all in the MPS and, from the Boltzmann equation for the electrons, then $n^{\text{SE}} \ll n^{\text{MPSE}}$, thus $p^{\text{SE}} \ll p^{\text{MPSE}}$, section 2.10. Thus we may note the following results:

(I) $\phi_y^{\text{outer MPSE}} = \phi_x^{\text{outer MPS}}$, i.e. the poloidal diamagnetic flux entering the outside MPS is entirely deflected away from the outside target and enters the main plasma. This flux therefore leaves the plasma and does not reach the target. A similar deflection occurs on the inside and the poloidal flux entering the inner SOL from the MPS is entirely provided by the radial inflow into the inside MPS from the main plasma. Because no fluxes leave the system by this mechanism, the diamagnetic drifts are not expected to influence the Bohm–Chodura criterion, which remains as in its basic form (or if $\boldsymbol{E} \times \boldsymbol{B}$ drifts are important, then as given by equation (18.35), see [18.24], [18.25]).

(II) In general, the flux patterns close internally:

$$|\phi_y^{\text{top}}| = |\phi_x^{\text{inner SOL}}| + |\phi_y^{\text{inner MPSE}}| = |\phi_x^{\text{outer SOL}}| + |\phi_y^{\text{outer MPSE}}|, \quad \text{etc.}$$

For a single-null divertor configuration, the patterns are slightly more complex, since the private plasma is involved; however, an analysis along the foregoing lines gives the pattern shown in figure 18.15. Again, the poloidal diamagnetic flows are deflected in the MPSs and do not reach the solid surfaces, closing internally.

(III) With regard to the diamagnetic *currents* involved: all the foregoing applies to the electrons, but in reverse directions; hence, positive currents flow is in the same directions as the ion particle flows. Although the foregoing considerations focused on the LCFS, any flux surface in the SOL gives a similar result. One may thus consider the implications for *diamagnetic radial currents*:

$$j_x = e(\Gamma_x^i - \Gamma_x^e) \tag{18.70}$$

j [amps m^{-2}]. For $T_e = T_i$:

$$j_x = 2e\Gamma_x^i. \tag{18.71}$$

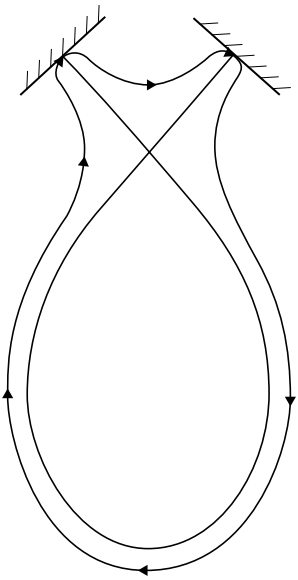

Figure 18.15. The diamagnetic drift fluxes form closed loops which pass along the magnetic pre-sheaths at each target, not actually reaching the targets. The $\boldsymbol{E} \times \boldsymbol{B}$ drift fluxes form similar patterns, but with some of the flux reaching the solid surfaces, typically.

While such currents can certainly exist *locally*, there is no *total, i.e. integrated*, radial current. This may be seen by adding the various contributions in figure 18.14, but is also simply the result of integrating $\Gamma_x^{\nabla p}$ from the SE of one target to the sheath edge of the other, as shown in section 17.5.3.

(IV) *Poloidal diamagnetic currents* are given by the poloidal particle fluxes:

$$j_y = e(\Gamma_y^i - \Gamma_y^e) \approx 2e\Gamma_y^i. \tag{18.72}$$

Combining with equation (18.61):

$$j_y B = \boldsymbol{j} \times \boldsymbol{B}|_x = \frac{2\partial p_i}{\partial x} = \frac{\partial p}{\partial x} \tag{18.73}$$

Which gives the *radial magnetic confinement force balance*, section 17.5.3. Since the SOL plasma is certainly not exploding radially, it must be in force balance—and the foregoing is the main part of this balance. These currents are not insignificant:

$$j_y \equiv j_{\text{poloidal}} \approx \frac{2nkT}{B\lambda_{\text{SOL}}}. \tag{18.74}$$

Example: $n = 10^{19}$ m^3, $T = 25$ eV, $B = 3$ T, $\lambda_{\text{SOL}} = 10^{-2}$ m, which gives $j_{\text{pol}} \approx 3000$ A m^{-2}, and is the equivalent of a value of $j_\parallel$ which is perhaps

ten times larger. This can be comparable to typical j_{sat}^{+} values; however, the comparison is not very meaningful since these diamagnetic currents do not reach the solid surfaces, but close via internal loops within the plasma. One should also note that j_{pol} is a net current while fluxes to solid surfaces tend to be ambipolar—i.e. no net current—and one can only draw a net ion current, j_{sat}^{+}, to an element of surface by biasing it so as to repel the electrons.

(V) Turning to $\boldsymbol{E} \times \boldsymbol{B}$ *flows* in contrast with the diamagnetic flows, which are divergence free (in cylindrical geometry, at least), the $\boldsymbol{E} \times \boldsymbol{B}$ flows are not divergence-free (even in cylindrical geometry). The $\boldsymbol{E} \times \boldsymbol{B}$ flows would be divergence free if n were either a constant or depended solely on electrostatic potential V. Thus, if we start by ignoring density variations then we may anticipate that a flow pattern similar to the closed diamagnetic flow pattern of figure 18.15 will exist [18.7]. Such flow patterns, involving closure by poloidal $\boldsymbol{E} \times \boldsymbol{B}$ flows along the private plasma, have been deduced from probe measurements in the private plasma of DIII-D [18.34]. Taking density variations into account modifies this picture somewhat, such that some of the poloidal $\boldsymbol{E} \times \boldsymbol{B}$ flow reaches the solid surface.

18.5 Pfirsch–Schlüter flows

In toroidal geometry there exist almost vertical ∇B and centrifugal (individual particle) drifts of electrons toward the top of the torus and ions toward the bottom, for the normal direction of $\boldsymbol{B}$, reversing with reversal of field direction. For $p_{\parallel} = p_{\perp}$ the total vertical drift velocity is readily estimated to be:

$$v_{dr} \approx \pm 2p/enBR \tag{18.75}$$

where the signs are different for ions and electrons. The resulting charge separation drives parallel currents called Pfirsch–Schlüter, P–S, currents and the corresponding parallel particle flows are called Pfirsch–Schlüter, P–S, flows. These drifts can also directly influence the plasma density in the divertor. The density is mainly determined by the transport of ions as the heavier, less mobile component. One should then expect a larger density in the divertor (at the bottom) for normal $\boldsymbol{B}_{\phi}$ than for reversed $\boldsymbol{B}_{\phi}$.

In [18.2], see also section 18.7, it is shown that the ∇B and centrifugal (individual particle) drift fluxes are almost exactly equal to the non-divergence-free part of the diamagnetic (fluid) drift flux, equation (18.3). It is only the latter part that results in the effective source of ions and electrons that drives the P–S currents and flows. Although $\boldsymbol{E} \times \boldsymbol{B}$ drifts do not generate currents they do constitute particle flows and a contribution to the P–S ion flow is due to the non-divergence-free part of the poloidal $\boldsymbol{E} \times \boldsymbol{B}$ drift, equation (18.2). We therefore start our analysis of P–S flows by considering the sum of these two vertical fluid

drifts, see figure 18.5:

$$\boldsymbol{v}_\perp = \left(\boldsymbol{E}_r - \frac{\boldsymbol{\nabla}_r p}{en} \right) \times \frac{\boldsymbol{B}}{B^2}. \tag{18.76}$$

The drift flux density $n\boldsymbol{v}_\perp$ is not divergence free because of the R-dependence of the magnetic field, $B \propto 1/R$, which also causes a second effect through geometry. Let us start with the latter effect. The cross-sectional area of a magnetic flux tube, say for power, $A_{q\parallel}^{\mathrm{SOL}}$, chapter 5, varies inversely with magnetic field, $A_\parallel^{\mathrm{SOL}} \propto 1/B$. In chapter 5 we neglected this variation but we will take it into account here. Since $B \propto 1/R$ in toroidal geometry, $A_\parallel^{\mathrm{SOL}} \propto R$. The 1D particle conservation equation is readily adapted to allow for variable $A_\parallel^{\mathrm{SOL}}$, giving for example:

$$\frac{\partial (A_\parallel^{\mathrm{SOL}} n v_\perp)}{\partial \theta} = \frac{\partial (R n v_\perp)}{\partial \theta} = 0 \tag{18.77}$$

if $v_\perp$ is divergence free; see for example [18.35]. Therefore for a divergence-free $v_\perp$ one has $Rnv_\perp =$ constant and $nv_\perp \propto 1/R$—even before taking into account the *specific* dependences of $v_\perp$ on B. From equation (18.76) we see that the latter introduces a further B-dependence so that overall we may write:

$$n v_\perp^{d\text{-}f} = n v_\perp (B/B_0)^2 \tag{18.78}$$

where 'd-f' indicates the 'divergence-free poloidal drift velocity', which is the form of equation (18.76) that would hold for cylindrical geometry, i.e. evaluated for $B = B_0$; also:

$$B = B_0 R_0 / R \tag{18.79}$$

and

$$R = R_0 + r \cos\theta. \tag{18.80}$$

See figure 18.16. We may thus define a 'non-divergence-free poloidal drift velocity', $v_\perp^{n\text{-}d\text{-}f}$, by:

$$v_\perp^{n\text{-}d\text{-}f} \equiv v_\perp - v_\perp^{d\text{-}f}. \tag{18.81}$$

It is then readily shown, by taking the approximations $(1 + (r/R_0)\cos\theta)^2 - 1 \approx (2r\cos\theta)/R_0$ and $(1 + (r/R_0)\cos\theta)^{-1} \approx 1$, that:

$$v_\perp^{n\text{-}d\text{-}f} = v_\perp^{d\text{-}f} \frac{2r}{R_0} \cos\theta. \tag{18.82}$$

The $\boldsymbol{E} \times \boldsymbol{B}$ drift is always non-divergence-free, even in cylindrical geometry, since it is proportional to $n_e E_r$, which cannot be written as a gradient, so strictly speaking we mean here that we are including in $v_\perp^{n\text{-}d\text{-}f}$ that part of the $\boldsymbol{E} \times \boldsymbol{B}$ drift which is due to $B \propto 1/R$.

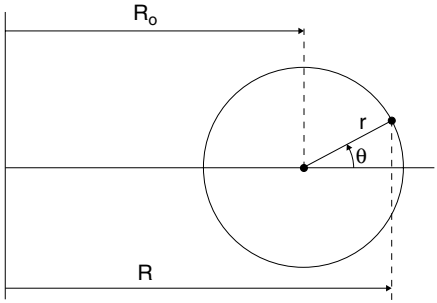

Figure 18.16. Toroidal tokamak geometry. Poloidal cross-section.

Let us assume, for simplicity, that there is no parallel flow due to ionization or other causes, and the only parallel flux density $nv_\parallel$ that exists is that required to compensate for $nv_\perp^{n\text{-}d\text{-}f}$; then:

$$nv_\perp^{n\text{-}d\text{-}f}(B_\phi/B) = nv_\parallel(B_\theta/B) \tag{18.83}$$

where the components in the true poloidal direction y have been taken, figure 18.5. One thus obtains:

$$v_\parallel = v_\perp^{d\text{-}f} q\cos\theta \tag{18.84}$$

where $q \equiv rB_\phi/R_0B_\theta$ has been used. For simplicity we have also assumed n, p, etc constant along the SOL.

The same result is obtained by employing more systematic analysis than the foregoing [18.36, 18.37], to give finally the Pfirsch–Schlüter velocity:

$$\boldsymbol{v}_\parallel^{\mathrm{PS}} = 2q\cos\theta\left(\boldsymbol{E}_r\frac{-\nabla_r p}{en}\right)\times\frac{\boldsymbol{B}_0}{B_0^2} \tag{18.85}$$

Thus, in the simplest situation, $\boldsymbol{v}_\parallel^{\mathrm{PS}}$ is maximum at the outside of the tokamak, zero at top and bottom, and a negative minimum at the inside. Its direction changes when the field direction is changed. Probe measurements in the SOL of JT-60U [18.38] and on JET [18.39] indicate parallel flows roughly consistent with the magnitude and direction given by equation (18.85), although the spatial variation has not been fully established and a return flow due to $\boldsymbol{E}_r \times \boldsymbol{B}$ poloidal drift, section 18.4.3 should also be considered.

The diamagnetic portion of equation (18.85) also gives *currents*—Pfirsch–Schlüter, P–S, currents. The currents and ion flows are in the anticlockwise direction on the outside when the ∇B-ion drift is toward the bottom of the tokamak. P–S currents also exist in the main plasma, but are smaller than in the SOL for two reasons:

(a) radial gradients are larger in the SOL,
(b) $\boldsymbol{E}_r$ and $-\nabla_r p$ are usually in the same direction in the SOL, reinforcing each other, whereas in the main plasma they are in opposite directions and can even cancel (consider the radial ion pressure balance equation (17.53); if $v_{i\phi}$ and $v_{i\theta}$ are small then the ion pressure gradient is almost entirely balanced by the radial electric field, i.e. the ions in the main plasma tend to be confined electrostatically; the electron–ion ensemble, the plasma, is confined by the $\boldsymbol{j} \times \boldsymbol{B}$ force, of course, since an electric field exerts no force on the quasineutral plasma).

From equation (18.85) one may estimate the magnitude of the ion parallel return flux density at the outside midplane ($\theta = 0$):

$$\Gamma_{i\parallel}^{\text{mid}} \approx 2q \frac{nkT}{e\lambda_{\text{SOL}} B}. \tag{18.86}$$

This is $\sim q$ times larger than the poloidal drift density itself, equation (18.60). It is comparable to the parallel drift flux density driven by radial $\boldsymbol{E} \times \boldsymbol{B}$ drifts, equation (18.50)—although flowing in the opposite direction along the SOL. Flow velocities at a significant fraction of the sound speed are therefore indicated, and have been reported [18.38, 18.39].

As remarked at the beginning of this section, these non-divergence-free drifts (both diamagnetic and $\boldsymbol{E} \times \boldsymbol{B}$), for normal $\boldsymbol{B}_\phi$, tend to raise the density and pressure at the bottom (thereby driving the parallel return flows back toward the top, as just discussed). While that does not *directly* contribute to any in/out asymmetry, it can do so indirectly: assuming the divertor is located at the bottom, then an increased divertor density has a cooling effect on the target plasma—which will generally be a stronger effect on the inside than the outside since the inside already tends to be cooler and denser. As mentioned earlier, lower target T_e leads to more radiation and interaction with neutrals, which further increases n_e and reduces T_e by a positive feedback effect—similar to the effect of the basic radial $\boldsymbol{E} \times \boldsymbol{B}$ effect.

We may consider a further consequence of the P–S flows [18.40]: these parallel flows will inevitably be associated with parallel variations in plasma pressure. Poloidal variations of plasma pressure therefore also exist and, according to equation (17.50), will cause radial currents, j_r [$A\ \text{m}^{-2}$], to flow. In cylindrical geometry, owing to in/out symmetry, there will be no net, integrated radial current, but in toroidal geometry there is a net current, $I_{r,\text{net}}$ [A], because the outside is of larger area than the inside and the field is weaker there. At least such a current is able to flow in the SOL where net radial current can close through the targets; in the main plasma $I_{r,\text{net}} = 0$ even for toroidal geometry because all the field lines are closed. It can be shown [18.40] that this gives a force on the SOL ions of magnitude $\langle j_r \rangle B_\theta$ which causes an additional parallel mass flow (additional to the basic P–S flows) from the outside to the inside, for the normal field direction. This flow can result in a net parallel ion flow from the outside target region to the

inside. This force can also raise the pressure on the inside, thus offering another potential explanation of divertor in/out asymmetries, in addition to the effect of radial $\boldsymbol{E} \times \boldsymbol{B}$ flows discussed in 18.3.5.

18.6 Heat Flux Drifts in the SOL

Similar to the diamagnetic $\boldsymbol{B} \times \nabla p$ particle fluxes, there exist heat fluxes associated with ∇T [18.7]:

(a) conducted: $$\boldsymbol{q}_{\nabla T} = \frac{5}{2}\frac{p}{eB^2}\boldsymbol{B} \times \nabla T \tag{18.87}$$

(b) convected: $$\boldsymbol{q}_{\nabla p} = \frac{5}{2}\frac{kT}{eB^2}\boldsymbol{B} \times \nabla p \tag{18.88}$$

(c) total: $$\boldsymbol{q}_{\text{diam}} = \frac{5}{2}\frac{1}{eB^2}\boldsymbol{B} \times \nabla(pT). \tag{18.89}$$

These fluxes are, however, largely divergence free, closing on themselves within the plasma and not depositing heat on solid structures—in analogy with the diamagnetic particle fluxes.

The $\boldsymbol{E} \times \boldsymbol{B}$ drifts, on the other hand, can carry plasma heat flux out to solid surfaces [18.3, 18.4, 18.41]:

$$\boldsymbol{q}_{E\times B} = \frac{5}{2}\frac{p}{B^2}\boldsymbol{E} \times \boldsymbol{B}. \tag{18.90}$$

Since $\boldsymbol{E} \times \boldsymbol{B}$ drifts usually generate *return* flows along the SOL, it is necessary to allow for the heat convected by such parallel-to-$\boldsymbol{B}$ heat flows. It was noted in section 5.9 that the power reaching the outer and inner divertor fans is often relatively symmetrical (irrespective of the ion ∇B-drift direction) and thus it may be that the *net* effect of heat flux drifts—when the return heat flows along the SOL are also allowed for—may not be large. It is clear that this situation is complex, and varying behaviour is likely, perhaps explaining why power symmetry, in/out, is observed in some tokamaks, but not others, section 5.9.

18.7 Two Alternative Descriptions of Drifts

So far in this chapter we have, without explicitly noting doing so, switched back and forth between what are in fact two *alternative* ways of describing drifts—*fluid drifts* and *guiding centre drifts*. It would lead to error if one were to *add* drifts from one approach—say the guiding centre ∇B-drift, equation (18.1)—to one from the other approach—say the fluid diamagnetic drift, $v_{\nabla p}$, equation (18.3).

For a systematic treatment of these two alternative and equivalent approaches to describing drifts it is recommended that the reader refer to the text by Goldston and Rutherford, G&R [18.42]. In chapters 2 and 3 of G&R the single particle

analysis for uniform and non-uniform $\boldsymbol{B}$-fields is given—generating the *guiding centre drift* expressions. Here terms such as the ∇B-drift, equation (18.1), are obtained. As can be noted from equation (18.1), the *specific, total* velocity of the *individual* particle appears—in this case, the component of the individual ion's velocity perpendicular to $\boldsymbol{B}$, $v_\perp$. Of course one is free to average over the entire distribution of ions, which will then generate a term involving the *perpendicular pressure*, $p_\perp$, where:

$$p_\perp = nkT_\perp \quad (\text{also } p_\parallel = nkT_\parallel) \tag{18.91}$$

and

$$\langle \tfrac{1}{2} m_i v_\perp^2 \rangle \equiv kT_\perp \quad (\text{also } \langle \tfrac{1}{2} m_i v_\parallel^2 \rangle \equiv \tfrac{1}{2} kT_\parallel) \tag{18.92}$$

where '$\langle\ \rangle$' indicates the average over the distribution of particles. This gives an expression for a guiding centre drift flux density:

$$n\langle \boldsymbol{v}_{gc} \rangle = \frac{p_\perp}{eB^3} \boldsymbol{B} \times \nabla B. \tag{18.93}$$

In chapter 7 of G&R the alternative *fluid drift* analysis is presented, which starts from the standard form of the *momentum* equation, equation (17.33) (note, however, that this then gives rise to fluid *particle* drift fluxes!). From this analysis, terms such as the fluid diamagnetic drift follow, equation (18.3).

As G&R note: 'The crucial point is that, while the two approaches are very different, if they are each carried through consistently to the same order, they give the same answer for any observable quantity at that order.' They then go on to demonstrate for some simple but important examples that this is indeed the case.

Chankin [18.2] provides relatively complete expressions for the particle flux densities for these two approaches. For the *fluid* approach:

$$\begin{aligned} n\boldsymbol{v}_f (\equiv n\boldsymbol{v}) = {} & nv_\parallel \frac{\boldsymbol{B}}{B} + \frac{n}{B^2} \boldsymbol{E} \times \boldsymbol{B} + \frac{1}{eB^2} \boldsymbol{R} \times \boldsymbol{B} + \frac{1}{eB^2} \boldsymbol{B} \times \nabla p_\perp \\ & + \frac{(p_\parallel - p_\perp + nmv_\parallel^2)}{eB^3} \boldsymbol{B} \times \boldsymbol{B} \cdot \nabla \left(\frac{\boldsymbol{B}}{B} \right). \end{aligned} \tag{18.94}$$

Here we may use the subscript f to emphasize 'fluid' treatment, but since the absence of any subscript is usually taken to mean the fluid velocity, this is unnecessary and will be dropped here. The $\boldsymbol{E} \times \boldsymbol{B}$ drift term, equation (18.3), may be recognized in equation (18.94). The term involving the electron–ion friction force R we will not consider further here. The first term on the RHS is just the non-drift part of $\boldsymbol{v}$, while the last term is a higher order one.

For the average over the ion distribution Chankin gives the *average guiding centre* flux density:

$$\begin{aligned} n\langle \boldsymbol{v}_{gc} \rangle = {} & n\langle \boldsymbol{v}_{gc\parallel} \rangle \frac{\boldsymbol{B}}{B} + \frac{n}{B^2} \boldsymbol{E} \times \boldsymbol{B} + \frac{p_\perp}{eB^3} \boldsymbol{B} \times \nabla B + \frac{(p_\parallel + nmv_\parallel^2)}{eB^3} \boldsymbol{B} \\ & \times \boldsymbol{B} \cdot \nabla \left(\frac{\boldsymbol{B}}{B} \right) + \frac{p_\perp}{eB^3} \boldsymbol{B} \left(\boldsymbol{B}\ \mathrm{curl} \left(\frac{\boldsymbol{B}}{B} \right) \right). \end{aligned} \tag{18.95}$$

The ∇B drift, equation (18.1), is recognized as the third term, while the fourth term is the *curvature drift*; both are important for non-uniform $\boldsymbol{B}$-fields, as in tokamaks, and are of comparable magnitude and in the same direction, although oppositely directed for electrons and ions. Thus they create currents. One could add to equation (18.95) a term involving $\boldsymbol{R}$. The last term is a higher order one.

The diamagnetic drift is an extremely important one for magnetic confinement systems. Consider the case of a straight cylindrical plasma with a uniform axial field B_z; see figure 9.1 of G&R. The powerful pressure gradient force, -$\mathrm{d}p/\mathrm{d}r$, is balanced by a $j_\theta B_z$ force, but where does the j_θ come from? There are no ohmic currents involved in this simple system. The j_θ arises entirely spontaneously within the plasma, simply from the presence of B_z and the p-gradient. Indeed j_θ is just the familiar *diamagnetic current*: as can be seen from equation (18.3) this drift is charge dependent. The ions and electrons drift in opposite θ-directions, thus making a net current. (The $\boldsymbol{E} \times \boldsymbol{B}$ drift, which is not charge dependent, generates no currents.) So, for purposes of calculating *plasma currents* it is essential to retain the *complete* form of the fluid diamagnetic drift flux. If, on the other hand, one is only interested in modelling the particle flows, then it is useful to take advantage of an important fact: *the diamagnetic flux is almost entirely divergence free*.

The diamagnetic term can be rewritten [18.2]:

$$\frac{\boldsymbol{B} \times \nabla p_\perp}{eB^2} = -\mathrm{curl}\,[(p_\perp/eB^2)\boldsymbol{B}] + \frac{2p_\perp}{eB^3}\boldsymbol{B} \times \nabla B + \frac{p_\perp}{eB^2}\mathrm{curl}\boldsymbol{B}. \qquad (18.96)$$

For the case of a uniform $\boldsymbol{B}$, the last two terms are zero and one sees that since the diamagnetic flux can be written as the curl of a quantity, it is divergence free. If in some particular problem we are not interested in calculating currents, but just the flows themselves, their effects on pressure, their contributions to fluxes reaching solid surfaces bounding the system, etc, then we would do well to *drop the divergence-free part of the diamagnetic flux term completely*. Its retention can lead to nothing useful and, on the other hand, can create problems of accumulating errors in the numerical computational scheme. Such terms have therefore been dropped in some numerical codes [18.2, 18.20, 18.21, 18.32].

Consider next the case of the non-uniform $\boldsymbol{B}$ of a tokamak where $|\nabla B| \approx |\mathrm{curl}B| \approx B/R$, where here R is the major radius (not the ei-friction force). One thus sees that the last two terms in equation (18.96) are small compared with the diamagnetic flux (LHS) (and also to the first term on the LHS): they are $\sim\lambda_{\mathrm{SOL}}/R$ smaller. It is therefore also advisable to retain only these *non-divergence-free components of the diamagnetic drift* in numerical code work [18.20].

Equation (18.96) also provides a further important insight: with the aid of the identity:

$$\boldsymbol{B} \times \nabla B + B\mathrm{curl}\boldsymbol{B} - \boldsymbol{B}\left(\boldsymbol{B} \cdot \mathrm{curl}\left(\frac{\boldsymbol{B}}{B}\right)\right) = \boldsymbol{B} \times \boldsymbol{B} \cdot \nabla\left(\frac{\boldsymbol{B}}{B}\right) \qquad (18.97)$$

one can show that the fluid drift flux, equation (18.94), and the average guiding

centre flux density, equation (18.95), become identical—and the divergence-free part of the diamagnetic drift is dropped. We are therefore able to see that the well known effect of the (guiding centre) ∇B and curvature drifts, which is to cause top/bottom charge separation in tokamaks, resulting in force-free Pfirsch–Schlüter return currents along $\boldsymbol{B}$—is also implicit in the fluid drift treatment, although this was not at first apparent. Conversely, one also sees that the guiding centre approach does indeed encompass the effect of a pressure gradient, $\nabla p_\perp$, although that also was not immediately obvious.

18.8 A Concluding Comment

We must conclude on the same cautionary note as the previous chapter on SOL currents: the analysis of SOL drifts in this chapter only constitutes an introduction to what is clearly a complex subject. Just the basic aspects of some of the effects have been illustrated here. Experimental reality is certain to be more complex. For a start, SOL currents and drifts are closely coupled. Interactions of other types are also likely and could be such as to offset the trends found on the basis of the simple analysis used here. In order to elucidate these complex effects more adequately it is necessary to employ 2D or 3D fluid codes which incorporate currents and drifts self-consistently with realistic ionization patterns, etc, and to confront the code output with experimental data. Such studies are now appearing [18.15, 18.16, 18.20–18.22, 18.32].

References

[18.1] Chankin A V, Clement S, Erents S K *et al* 1994 *Plasma Phys. Control. Fusion* **36** 1853
[18.2] Chankin A V 1997 *J. Nucl. Mater.* **241–243** 199
[18.3] Hinton F L and Staebler G M 1989 *Nucl. Fusion* **29** 405
[18.4] Staebler G M 1991 *Nucl. Fusion* **31** 729
[18.5] Stangeby P C and Chankin A V 1996 *Nucl. Fusion* **36** 839
[18.6] Hutchinson I H, LaBombard B, Goetz J A *et al* 1995 *Plasma Phys. Control. Fusion* **37** 1389
[18.7] Chankin A V and Stangeby P C 1994 *Plasma Phys. Control. Fusion* **36** 1485
[18.8] Schaffer M J, Maingi R, Hyatt A W and Ali Mahdavi M 1996 *Nucl. Fusion* **36** 495
[18.9] Staebler G M 1995 *J. Nucl. Mater.* **220–222** 158
[18.10] Wesson J 1997 *Tokamaks* 2nd edn (Oxford: Oxford University Press) p 46
[18.11] Goldston R J and Rutherford P H 1997 *Introduction to Plasma Physics* (Bristol: Institute of Physics Publishing) p 32
[18.12] Wesson J 1997 *Tokamaks* 2nd edn (Oxford: Oxford University Press) p 44
[18.13] Goldston R J and Rutherford P H 1997 *Introduction to Plasma Physics* (Bristol: Institute of Physics Publishing) p 24
[18.14] Goldston R J and Rutherford P H 1997 *Introduction to Plasma Physics* (Bristol: Institute of Physics Publishing) p 97

[18.15] Baelmans M 1994 *PhD Thesis* Juelich Report JUEL-2891 Katholieke Universiteit Leuven
[18.16] Baelmans M, Reiter D, Weynants R R and Schneider R J 1995 *J. Nucl. Mater.* **220–222** 982
[18.17] Gerhauser H and Claassen H A 1987 *KFA Juelich Report* JUEL-2125
[18.18] Gerhauser H and Claassen H A 1990 *J. Nucl. Mater.* **176–177** 721
[18.19] Rognlien T D, Milovich J L, Rensink M E and Porter G D 1992 *J. Nucl. Mater.* **196–198** 347
[18.20] Radford G J, Chankin A V, Corrigan G *et al* 1996 *Contrib. Plasma. Phys.* **36** 187
[18.21] Chankin A V personal communication
[18.22] Rognlien T D, Ryutov D D, Mattor N and Porter G D 1999 *Phys. Plasmas* **6** 1851
[18.23] Baelmans M, Reiter D and Weynants R R 1996 *Contrib. Plasma Phys.* **36** 117
[18.24] Stangeby P C and Chankin A V 1995 *Phys. Plasmas* **2** 707
[18.25] Stangeby P C 1995 *Phys. Plasmas* **2** 702
[18.26] Hutchinson I H 1996 *Phys. Plasmas* **3** 6
[18.27] Cohen R H and Ryutov D 1993 *Comments Plasma Phys. Control. Fusion* **35** 1271
[18.28] Tendler M and Rozhansky V 1990 *Comments Plasma Physics Control. Fusion* **13** 191
[18.29] Tendler M and Rozhansky V 1992 *J. Nucl. Mater.* **196–198** 912
[18.30] Goldston R J and Rutherford P H 1997 *Introduction to Plasma Physics* (Bristol: Institute of Physics Publishing) p 19
[18.31] Goldston R J and Rutherford P H 1997 *Introduction to Plasma Physics* (Bristol: Institute of Physics Publishing) p 97
[18.32] Rognlien T D, Porter G D and Ryutov D D 1999 *J. Nucl. Mater.* **266–269** 654
[18.33] Jablonski D, La Bombard B, McCracken G M *et al* 1997 *J. Nucl. Mater.* **241–243** 782
[18.34] Boedo J A, Schaffer M J, Maingi R *et al* 1999 *Proc. 26th EPS Int. Conf. on Plasma Physics and Controlled Fusion (Maastricht, 1999)*
[18.35] Chankin A V and Stangeby P C 1996 *Plasma Phys. Control. Fusion* **38** 1879
[18.36] Hugill J 1992 *J. Nucl. Mater.* **196–198** 918
[18.37] Wesson J 1997 Tokamaks 2nd edn (Oxford: Oxford University Press) p 152
[18.38] Asakura N, Sakurai S, Hosogane N *et al* 1998 IAEA
[18.39] Erents S K, Chankin A V, Davies S J *et al* 1999 *Proc. 26th EPS Int. Conf. on Plasma Phys. and Controlled Fusion (Maastricht, 1999)*
[18.40] Chankin A V and Stangeby P C 1999 to be published
[18.41] Hutchinson I H, Goetz J A, Jablonski D F *et al* 1996 *Plasma Phys. Control. Fusion* A **38** 301
[18.42] Goldston R J and Rutherford P H 1997 *Introduction to Plasma Physics* (Bristol: Institute of Physics Publishing)

Chapter 19

The Relation Between SOL and Main Plasma Density for Divertors

The divertor two-point model, sections 5.2, 5.7, shows that the 'upstream' density, n_u—and specifically the value of n_u on the separatrix, n_u^{sep}—is the most influential of all the SOL 'control parameters'. Unfortunately n_u^{sep} is not measured on a regular basis on most tokamaks—and its measurement, directly or by inference from other measurements, is problematical. The value of $\overline{n}_e$, on the other hand, is invariably measured on tokamaks. We are therefore interested in establishing—at least experimentally—the ratio of $n_u^{\text{sep}}/\overline{n}_e$, using such data as are available for n_u^{sep}. One might then assume that this ratio holds generally and could use it to establish n_u^{sep}—as needed for modelling the SOL using two-point models, onion-skin models, or 2D edge fluid codes.

The 'upstream' location is most commonly taken to be at the outside mid-plane, rather than at the mid-point between targets along the SOL. (For concreteness the present discussion assumes a single-null poloidal divertor at the bottom of the vessel.) Since—at least theoretically—plasma conditions vary little between these two locations, this should be inconsequential. In any case, when SOL radial profiles of $n_e(r)$, $T_e(r)$ are measured somewhere in the region above the X-points—i.e. the 'main SOL', as distinct from the 'divertor SOL' between X-points and targets—then the usual practice is to map the profiles to the outside mid-plane by taking into account the flux expansion between the actual measurement location and the outside mid-plane. Thus, the characteristic radial decay lengths, ℓ, at the two locations are related by:

$$\frac{\ell_{\text{meas}}}{\ell_{\text{mid}}} = \frac{(B_\theta/B)_{\text{mid}}}{(B_\theta/B)_{\text{meas}}} \tag{19.1}$$

see section 5.6.

Radial profiles of upstream $n_e(r)$ and $T_e(r)$ are made using movable Langmuir probes on some tokamaks. In order to avoid over-heating the probe, it must be rapidly moved—usually involving reciprocation—if it is used to reach

the separatrix or further in. On some tokamaks these profiles are obtained by non-probe techniques such as Li beams or laser Thompson scattering.

A major difficulty arises in attempting to extract the separatrix values from such data, $n_{eu}^{\rm sep}$, $T_{eu}^{\rm sep}$. At the divertor *targets*, the location of the separatrix is often apparent from the radial measurements of $T_{et}(r)$ and $I_{{\rm sat},t}^{+}(r)$ themselves: often these quantities have peaks which can often—although not always—be taken to indicate the location of the separatrix. By contrast the upstream radial profiles usually vary smoothly through the location where the separatrix is thought to be, providing no direct indication of its location.

The locations of all magnetic surfaces within the plasma—including the separatrix—are mathematically constructed from measurements by magnetic pick-up coils located *outside* the plasma. The accuracy of this construction is therefore only moderate, and the uncertainty in the location of the separatrix at the outside midplane can be a centimetre or more. Since upstream radial characteristic lengths are also of this order, large uncertainty in identifying $T_{eu}^{\rm sep}$ and $n_{eu}^{\rm sep}$ from the profiles can arise. Various methods of dealing with this problem have been used [19.1–19.5]. One approach is to identify the location of the separatrix at the target by taking the peaks in the $T_{et}(r)$ or $I_{{\rm sat},t}^{+}(r)$-profiles to give the location there. Then, for discharges far from detachment, where it is believed that total pressure (electron plus ion, static plus dynamic) is constant along $\boldsymbol{B}$, the upstream location of the separatrix is identified as the location where the total pressure is the same as at the target, separatrix. In some cases, the required shift in the location of the upstream separatrix obtained this way—relative to that deduced from the magnetic pick-up coils—is quite small, only $\sim$1 mm for CMOD [19.3], but it is usually larger, of order $\sim$1 cm. For detached conditions it then has to be assumed that the location of the separatrix remains fixed.

An alternative approach to establishing values of $n_{eu}^{\rm sep}$ and $T_{eu}^{\rm sep}$ is to employ target measurements as the exclusive experimental input, together with onion-skin modelling, OSM, chapter 12. Briefly, in OSM the target data are used as boundary conditions for 1D, along-$\boldsymbol{B}$ modelling of the SOL, based on the conservation equations for particles, momentum and energy—thus giving a complete 2D plasma solution for the SOL, including calculated values of $n_{eu}^{\rm sep}$, $T_{eu}^{\rm sep}$, etc.

On JET the onion-skin method approach has been used to analyse ohmic, L-mode and H-mode discharges. Figure 19.1 shows a sample of results for ohmic and L-mode shots, obtained with JET operating with the so-called gasbox divertor [19.5]. These OSM-calculated values of $n_{eu}^{\rm sep}$ are in good agreement with values measured using a fast reciprocating probe at the top of the torus—provided the probe's profiles are shifted to give a pressure match with the OSM-calculated pressure at the probe—i.e. momentum conservation is assumed to hold between the target and upstream probe.

OSM analysis was also applied to H-mode discharges (between ELMs) [19.4]. The principal correlation was found to be with ELM frequency, but also with dependence on the shape of the main plasma (its triangularity) and target configuration (horizontal versus vertical divertor targets). Figure 19.2

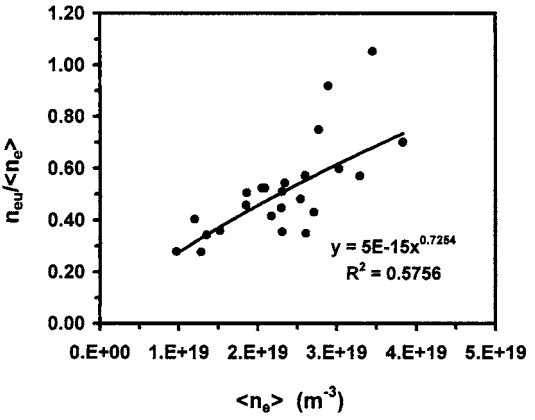

Figure 19.1. Ratio of separatrix to volume average density against separatrix density. For a set of JET ohmic and L-mode discharges. JET operated with the gasbox divertor [19.5].

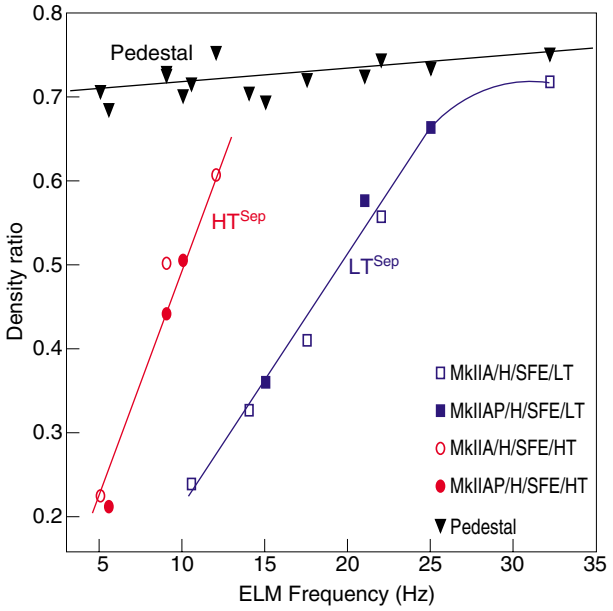

Figure 19.2. Variations of $n_{eu}^{sep}/\overline{n}_e$ as a function of ELM frequency for JET horizontal target operation. MkII divertor [19.4]. Low triangularity (LT^{sep}) and high triangularity (HT^{sep}) discharges. Also shown is $n_e^{ped}/\overline{n}_e$, where n_e^{ped} is the 'pedestal density'.

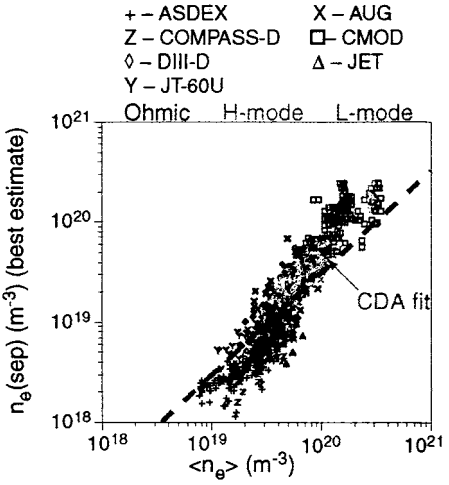

Figure 19.3. The dependence of the separatrix density on the line-averaged core density for a number of tokamaks [19.1].

shows $n_{eu}^{\rm sep}/\overline{n}_e$ against ELM frequency for horizontal targets, for high and low triangularity. Also shown in figure 19.2 is the 'pedestal density' ratio, $n_e^{\rm ped}/\overline{n}_e$, where $n_e^{\rm ped}$ is the density measured a short distance inside the separatrix at the top of the sharp density rise—i.e. pedestal—that characterizes H-modes, chapter 7. It is very valuable when measurements of $n_e^{\rm ped}$ are available as this makes it possible to remove from consideration the various transport processes that occur in most of the main plasma—i.e. inboard of the 'transport barrier' (pedestal region) that exists just at the edge of the main plasma in H-modes.

One may note from figure 19.2 that $n_{eu}^{\rm sep} \rightarrow n_e^{\rm ped}$ as ELM frequency increases. It is not presently clear what this indicates about the nature of the H-mode transport barrier.

Figure 19.3 gives an extensive collection from a number of tokamaks of $n_{eu}^{\rm sep}$ against $\overline{n}_e$ [19.1], largely obtained from direct measurements upstream. As can be seen, at low $\overline{n}_e$, $n_{eu}^{\rm sep} \ll \overline{n}_e$, but with rising $\overline{n}_e$, $n_{eu}^{\rm sep} \rightarrow\sim \overline{n}_e$, i.e. the same trend as seen in the JET data, figure 19.1. This tendency is the one expected from the Engelhardt model, section 4.6: as density increases, the fraction of the neutrals ionized inside the separatrix increases. This leads to $n_{eu}^{\rm sep} \rightarrow \overline{n}_e$ and a flat $n_e(r)$ profile in the main plasma—assuming that radial transport is purely diffusive and there is a steady state with no pinch, etc. This has not actually been proven by detailed analysis and it may be that this faster-than-linear rise of $n_{eu}^{\rm sep}$ with $\overline{n}_e$ could be an indication of a B-dependence, the basic nature of which has also not been identified: the high $\overline{n}_e$ data in figure 19.1 are largely from CMOD, which has high B. If one assumes that $n_{eu}^{\rm sep}$ depends on $\overline{n}_e$, only then does a best fit to

the data of figure 19.3 give:

$$n_{eu}^{\text{sep}} \propto \overline{n}_e^{1.6}. \tag{19.2}$$

A best fit that also allows for dependences on elongation κ, and toroidal field strength B_ϕ, gives a more linear dependence on $\overline{n}_e$ (for ohmic and L-mode shots) [19.1]:

$$n_{eu}^{\text{sep}} = 0.002\,36 \overline{n}_e^{1.08} \kappa^{1.11} B_\phi^{0.78}. \tag{19.3}$$

The physical basis for either (19.1) or (19.3) is not clear as yet. In any case, an earlier assumption/prescription that $n_{eu}^{\text{sep}}/\overline{n}_e = 0.3$ turns out, according to this extensive compilation, to be pessimistic for an ITER-like tokamak where for $\overline{n}_e = 10^{20}$ m^{-3} one obtains $n_{eu}^{\text{sep}} \approx 0.6 \times 10^{20}$ m^{-3}. Such an increase of a factor of 2 in n_{eu}^{sep} has large—and very positive—implications for divertor operation, since, from two-point modelling one predicts that $T_t \sim n_u^{-3}$ and $n_t \sim n_u^4$, section 5.7—and thus physical sputtering will be greatly reduced, while radiative power exhaust (which increases with increasing n_t and decreasing T_t) will be raised.

In conclusion, while much work remains to be done in order to explain the relation between the principal SOL 'control parameter' n_{eu}^{sep}, and the main plasma density, $\overline{n}_e$, a substantial, empirical database has now been established which allows one to carry out SOL analysis based on the actual control parameter, $\overline{n}_e$—a quantity which is regularly measured for tokamak discharges.

References

[19.1] Porter G D, Davies S, LaBombard B *et al* 1999 *J. Nucl. Mater.* **266–269** 917
[19.2] Porter G D, Moller J, Brown M and Lasnier C 1998 *Phys. Plasmas* **5** 1410
[19.3] LaBombard B, Goetz J A, Hutchinson I *et al* 1997 *J. Nucl. Mater.* **241–243** 149
[19.4] Davies S J, Erents S K, Stangeby P C *et al* 1999 *J. Nucl. Mater.* **266–269** 1028
[19.5] Erents S K, Stangeby P C, LaBombard B *et al Nucl. Fusion* to be published

Chapter 20

Extracting $\chi_{\perp}^{\mathrm{SOL}}(r)$ From Target Plasma Data Using the Onion-Skin Method

20.1 The General Method

The power to the divertor targets of tokamaks must not exceed the critical values where melting or sublimation will occur. A key parameter in this respect is the power decay width of the scrape-off layer, SOL, which is controlled by the cross-field heat thermal diffusivity, $\chi_{\perp}^{\mathrm{SOL}}$. In common with other cross-field transport coefficients this cannot yet be derived theoretically from first principles, but is anomalous and must be extracted from experimental data.

One approach to inferring $\chi_{\perp}^{\mathrm{SOL}}$ is to employ 2D fluid code calculation of the SOL, section 6.6.3, where $\chi_{\perp}^{\mathrm{SOL}}$ is one of the input assumptions—along with the power into the SOL, P_{in}, and the 'upstream' plasma density, i.e. the density at the edge of the core, n_u. If one has experimental data on n and T at some locations in the SOL, then one can vary the input assumptions in the 2D code—including $\chi_{\perp}^{\mathrm{SOL}}$—to try to match the measurements of density, n, and temperature, T. When a match is achieved one could conclude that the value of $\chi_{\perp}^{\mathrm{SOL}}$ has been established.

A different approach is based on onion-skin method, OSM, analysis, chapter 12. In this approach one does not need to input $\chi_{\perp}^{\mathrm{SOL}}$, but rather $\chi_{\perp}^{\mathrm{SOL}}$ can be extracted from the 2D plasma solution generated by the OSM. In other words, the experimental data input for the target—and specifically the *radial* variations of n and T across the target—implicitly contain the information about $\chi_{\perp}^{\mathrm{SOL}}$.

Movable Langmuir probes—or fast reciprocating probes, FRPs—are used on some tokamaks to measure SOL plasma radial profiles in the upstream regions. This can, in principle, give a measurement of T_u, n_u, but only provided the location of the separatrix at the FRP is known very reliably. The separatrix location calculated from magnetic pick-up signals is sometimes not reliably known to within a centimetre or more—which is comparable to the characteristic radial

decay lengths of the SOL upstream. Thus FRP measurements of T_u, n_u can be somewhat uncertain.

By contrast, Langmuir probes built into the divertor targets sometimes show clear maxima in measured T_e and/or the ion saturation current, I_{sat}^{+}, which one can identify with the separatrix at the target. That is, it may be easier to identify the location of the separatrix at the target than upstream.

This then allows the approach where one works entirely from the target data using the OSM and calculates the upstream conditions, T_u, n_u. For Langmuir probe measurements, it is actually the particle flux density to the target, as given by I_{sat}^{+}, and the target electron temperature, T_{et}, that are measured; in the (usual) absence of direct measurements of the target ion temperature T_{it}, it is necessary to assume or infer some value for T_{it} as well as a value for the plasma flow Mach number, M_t, at the target in order to infer the value of plasma density n_{et}, and to complete the set of needed boundary conditions. Since one has generated a complete 2D edge solution using the OSM, the calculated values for the radial gradients of n and T are available at every point, and one can perform particle and power balances to extract $D_{\perp}^{\mathrm{SOL}}$ and $\chi_{\perp}^{\mathrm{SOL}}$. One has expressions for the local value of particle flux density, $\Gamma_{\perp}$, and heat flux density, $q_{\perp}$ (for ions and electrons separately, if required; we treat the combined situation here):

$$\Gamma_{\perp} = D_{\perp} n/\lambda_n \tag{20.1}$$

$$q_{\perp} = \chi_{\perp} nkT/\lambda_T + \tfrac{5}{2} D_{\perp} nkT/\lambda_n \tag{20.2}$$

where λ_n, $\lambda_{\perp}$ are the local radial scale lengths as calculated by the OSM, which also provides calculated values for the local n and T, leaving just $D_{\perp}^{\mathrm{SOL}}$ and $\chi_{\perp}^{\mathrm{SOL}}$ as unknowns. It is to be noted that $\lambda_n = -((1/n)\mathrm{d}n/\mathrm{d}r)^{-1}$ and $\lambda_T = -((1/T)\mathrm{d}T/dr)^{-1}$ are the *local* radial scale lengths at radial location r and one should not assume $\lambda_n(r)$ and $\lambda_T(r)$ constant with radius. Factor 5/2 or 3/2 in equation (20.2), chapter 8. Consider a closed volume of the edge, say that bounded by the separatrix ring, the outermost ring in the grid and the two divertor targets, figure 20.1. Then global particle and power balances give:

$$\Phi_{\perp} = \Sigma \Gamma_{\perp} \delta A_{\perp} = -\Sigma S_{iz} + \Sigma S_{\mathrm{recomb}} + \Sigma \Gamma_{\parallel t} \delta A_t \tag{20.3}$$

$$Q_{\perp} \equiv \Sigma q_{\perp} \delta A_{\perp} = \Sigma P_{\mathrm{vol}} + \Sigma q_{\parallel t} \delta A_t \tag{20.4}$$

where:

- $\delta A_{\perp}$ are the elemental areas along the separatrix flux surface and along the outermost flux surface, and flows can be locally either into or out of the closed volume.
- ΣS_{iz} is the total hydrogenic ionization occurring within the closed volume, as calculated by the neutral hydrogen code, e.g. EIRENE.
- $\Sigma S_{\mathrm{recomb}}$ is the total hydrogenic two- and three-body recombination in the closed volume, calculated in the OSM.

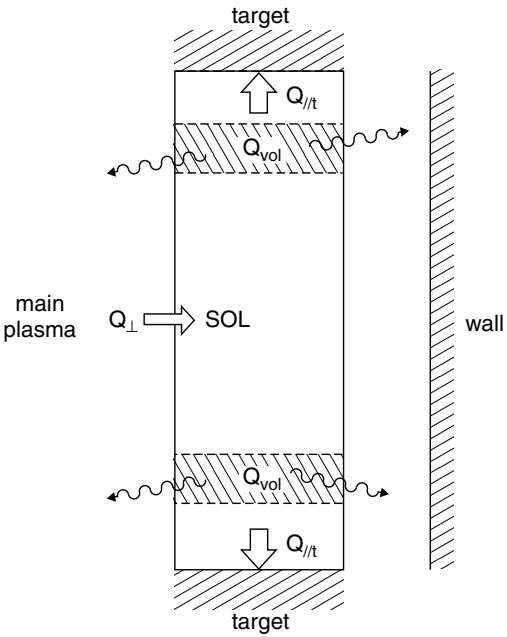

Figure 20.1. The SOL 'straightened out'. A power balance analysis can be used to extract $\chi_\perp^{\mathrm{SOL}}$ from the 2D plasma solutions produced by OSM. A similar particle balance analysis can be used to extract $D_\perp^{\mathrm{SOL}}$.

- $\Gamma_{\|t}$ and $q_{\|t}$ are the target flux density of particles and heat, which are known from the *boundary conditions. Note that this is the experimental input which contains the principal information giving* $D_\perp^{\mathrm{SOL}}$, $\chi_\perp^{\mathrm{SOL}}$.
- $\Sigma\Gamma_{\|t}\delta A_t$ and $\Sigma q_{\|t}\delta A_t$ are the sums over the two targets, with δA_t being the elements of divertor target area, multiplied by the cosine of the angle between $\boldsymbol{B}$ and the target normal vector.
- $\Sigma P_{\mathrm{vol}} \equiv Q_{\mathrm{vol}}$ is the total volumetric power loss/gain by the ions and electrons due to (a) hydrogenic processes such as charge exchange (ions), excitation, ionization, etc (electrons)—as calculated by the neutral hydrogen code; (b) radiated power (electron cooling) which could be taken, e.g., from DIVIMP or could be estimated from measurements of P_{rad} and (c) electron–ion equipartition power, if one treats the electron and ion power balances separately.

One thus has two equations for the two unknowns $D_\perp^{\mathrm{SOL}}$ and $\chi_\perp^{\mathrm{SOL}}$, and so finds their average value along the separatrix (strictly the outermost ring is also involved but its contribution may be small). One can then define a new closed volume by using the next flux surface out into the SOL and repeat the exercise, etc. Thus one can, in principle, establish the *radial* profiles of $D_\perp^{\mathrm{SOL}}(r)$ and $\chi_\perp^{\mathrm{SOL}}(r)$.

It is evident from equations (20.3) and (20.4) that for reliable extractions of $D_\perp^{\mathrm{SOL}}$ and $\chi_\perp^{\mathrm{SOL}}$ one requires that the terms which contain these quantities not be too small compared with the other terms—otherwise errors and uncertainties will make the extracted values unreliable. For $\chi_\perp^{\mathrm{SOL}}$ and the power balance this is not a problem since the source of energy for the SOL is always the main plasma, and the cross-field power terms must always be at least comparable to the other terms.

For $D_\perp^{\mathrm{SOL}}$ and the particle balance, however, it may well be the case that most of the ionization occurs in the SOL, making the term involving $D_\perp^{\mathrm{SOL}}$ small. Then $D_\perp^{\mathrm{SOL}}$ cannot be reliably extracted. In the light of this one can proceed by just using the power balance and dropping cross-field convection, thus $D_\perp^{\mathrm{SOL}}$, thereby obtaining an *effective* $\chi_\perp^{\mathrm{SOL}}$. Alternatively, there is the option of *specifying* some assumed ratio of $D_\perp^{\mathrm{SOL}}/\chi_\perp^{\mathrm{SOL}}$, for example 0.4 [20.1], and including perpendicular convection in the power balance, without needing to solve the particle balance.

In section 4.10.1, figure 4.17, it was shown that upstream temperatures depend very little on the assumed spatial distribution of the cross-field power source. Indeed T_u is seen to be rather insensitive to variations in *all* input assumptions—thus n_u is also. In short, upstream plasma conditions are quite robust to variations in all inputs and assumptions and so, if the plasma conditions have been matched downstream—as input boundary conditions—then a good match overall is more or less assured. This is the principal reason why OSM solutions can match 2D fluid code solutions rather well—at least when working from downstream boundary conditions. When calculating in the downstream direction from upstream boundary conditions, n_u and P_{in}, the opposite situation is encountered with calculated downstream conditions then being very sensitive to most inputs.

With regard to the $\chi_\perp^{\mathrm{SOL}}$ extraction: the calculated cross-field temperature gradient will only differ by a factor of $2^{2/7} \approx 1.2$ for the two rather opposite assumptions about the spatial distribution of the cross-field power source (i.e. of P_{in} all at $s_\parallel = L$ versus uniformly over L). Furthermore, even that small variation is cancelled out when extracting $\chi_\perp^{\mathrm{SOL}}$, since the cross-field conduction coefficient is given by $K_\perp = n\chi_\perp^{\mathrm{SOL}}$, and due to pressure balance the upstream density changes just inversely to T. It is assumed, however, that the divertor plasma has not detached, which results in loss of parallel pressure balance, chapter 16.

All this can be brought out in another way: one extracts $\chi_\perp^{\mathrm{SOL}}$ from analysis of the expression, simplified from equation (20.4).

$$\Sigma q_\parallel \delta A_{\parallel t} = \Sigma \delta A_\perp (nkT)\chi_\perp/\lambda_T. \tag{20.5}$$

Assuming pressure conservation, the factor nkT is not dependent on the assumption made in the OSM of how the cross-field power source was distributed—the same point as already made above. For high recycling assumptions, as made here, $\lambda_T = \frac{7}{2}\lambda_q$, i.e. λ_T is given by the input plasma conditions at the targets, and so that factor is also independent of the assumption about power input distribution. This indicates again why the OSM-extraction procedure is not dependent

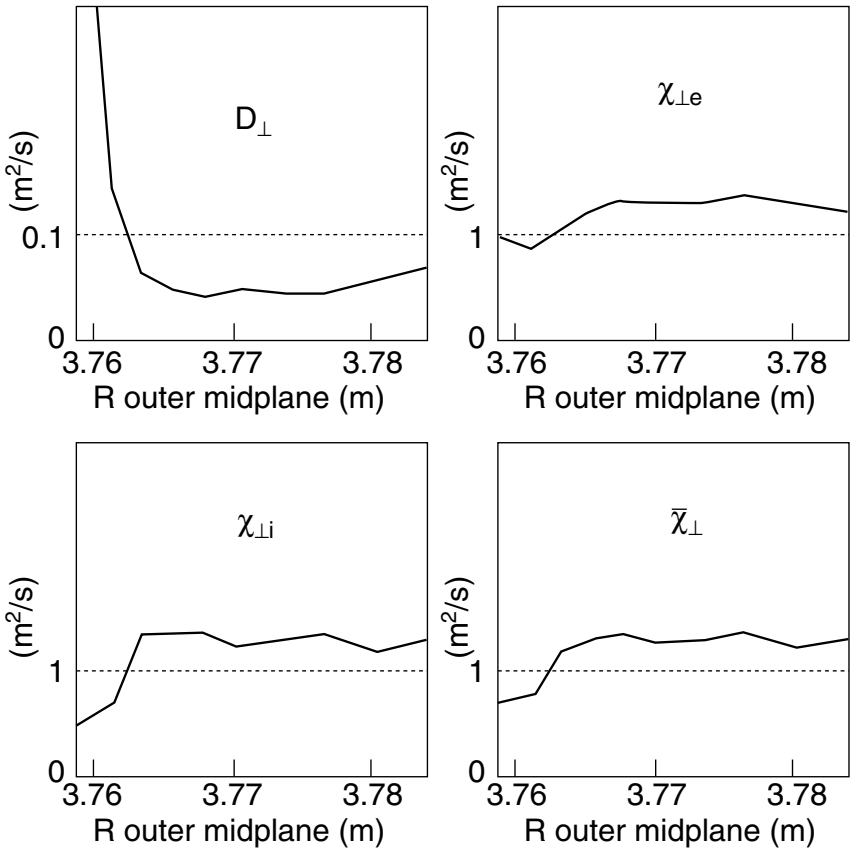

Figure 20.2. Extracted $D_\perp$, $\chi_\perp$ for a 'moderate recycling' JET case. Transport coefficients from the 2D onion-skin model solutions as a function of ring location at the outside mid-plane. EDGE2-D input values, dashed [20.2].

on the assumption used in the OSM as to how the cross-field source was spatially distributed—at least for the 'classical' high recycling case considered here.

When volumetric momentum and power sinks/sources are present, the analysis obviously becomes more complex, and no simple consideration along the lines of the foregoing demonstration of robustness appears to be possible. The OSM-extraction procedure contained in the DIVIMP code allows for these effects, at least those due to the hydrogen recycling, by employing the NIMBUS code to calculate the volumetric terms, iterating with the OSM plasma solver. Impurity-related terms, calculated by DIVIMP, could be used or an analytic expression for $P_{\mathrm{rad}}(s_\parallel)$, with the magnitude taken from experimental measurement. For such cases one can only show that, in fact, the extraction can still be reliable—as shown in [20.2] for a moderately high recycling case based on an EDGE2-D solution

where the *input* $\chi_\perp^{SOL}$ was known and the OSM-extracted value of $\chi_\perp^{SOL}$ was found to be in good agreement with it.

Results are shown in figure 20.2 for this 'moderately conduction-limited' case. The extraction procedure gives values of $D_\perp(r)$, $\chi_\perp^{e,i}(r)$ as functions of radius. Here the input coefficients used in the EDGE2-D code were, in fact, spatially constant with: $D_\perp = 0.1\ \mathrm{m^2\ s^{-1}}$, $\chi_\perp^{e,i} = 1\ \mathrm{m^2\ s^{-1}}$. The extraction procedure has worked satisfactorily over most of the radial span of the SOL, with the extracted values matching the input values, usually to within a few tens of per cent. By extracting $D_\perp^{SOL}$ first, cross-field convection could be included in the power balance to then extract $\chi_\perp^{SOL}$. The $D_\perp^{SOL}$ values extracted in this case would be expected to be roughly reliable since the NIMBUS calculations showed that about 10% of the neutrals were ionized inside the separatrix, thereby providing a reasonably strong cross-field particle flow.

These tests of the onion-skin method, i.e. of successfully extracting the input $\chi_\perp$-values, are demanding since the extraction procedure uses the entire 2D density and temperature fields. A particularly demanding aspect is that the OSM solution must successfully generate the *radial* variation of n, T_e, T_i—in fact, the second derivatives of these quantities in the radial direction. Most applications of OSM solutions do not demand such fidelity—for example, calculating the upstream separatrix density from target data, chapter 19.

Inclusion of the NIMBUS-calculated hydrogenic ionization pattern makes it possible to calculate the 2D plasma parallel flow field and hence the parallel heat *convection*. As noted earlier, ion parallel heat convection can be important and the difference between the upstream conditions calculated by the DIVIMP/NIMBUS OSM and the simple two-point model, next section—which necessarily neglects parallel convection—are largely due to this.

20.2 A Simple Two-Point Model for Estimating $\chi_\perp^{SOL}$ and n_u

A problem with the use of complex codes is that conceptual transparency is lost and the analysis tool appears to be just a 'black box'. In the present case the use of the complicated OSM to generate the 2D plasma solution and then the use of a similarly complicated '$\chi_\perp^{SOL}$-extractor' code can leave one with little feeling for what is *essentially* responsible for the extracted $\chi_\perp^{SOL}(r)$ pattern—which tends to be due to the fact that $\chi_\perp^{SOL}$ increases with radius, often [20.1, 20.3, 20.4]. To address this problem, in this section we develop a much simpler and cruder analysis procedure based on the standard divertor two-point model, 2PM, section 5.2. This approach is more transparent and makes it clear that the radial dependence of $\chi_\perp^{SOL}(r)$ is almost directly implied by the observed tendency for $\lambda_T(r)$ to be an increasing function of radius. One would hope that this cruder extraction procedure would replicate the trends of $\chi_\perp^{SOL}(r)$ and be reasonably close in absolute magnitude—compared with the more complete treatment. This will be seen to be the case.

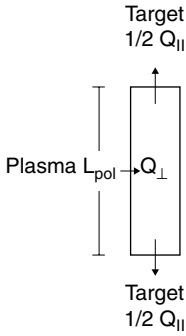

Figure 20.3. A crude $\chi_{\perp}^{\mathrm{SOL}}$-extractor using the simple 2PM, two-point model.

Although the simple two-point model neglects many processes included in the full approach—principally heat convection and volumetric sources/sinks—it turns out that these factors are not controlling for this particular problem. The two analysis procedures complement each other: one is reluctant to trust a crude estimate on its own because of what is neglected, while a complicated approach raises 'black box' concerns.

The principal deficiency of the simple 2PM is its neglect of parallel ion heat convection, and so upstream T_{iu} can differ sometimes by a factor $\gtrsim 2$. By contrast, n_u and T_{eu} do not usually differ greatly between 2PM and the OSM.

One can use the simple 2PM to construct a simple $\chi_{\perp}^{\mathrm{SOL}}$-extractor procedure along the following lines: consider the SOL in the poloidal plane representation, figure 20.3. The volume considered extends 1 m toroidally (into the page of the figure). One has total cross-field power $Q_{\perp}$:

$$Q_{\perp} = L_{\mathrm{pol}} n_{eu} k T_{eu} \chi_{\perp}^{\mathrm{SOL}} / \lambda_{T_{eu}} \tag{20.6}$$

where L_{pol} is the target-to-target length in the poloidal plane. The total power (per m toroidally) along the SOL and entering the target (we ignore volumetric losses), $Q_{\parallel}$:

$$Q_{\parallel} = 2\gamma n_t k T_t c_{st} \lambda_{qt} (B_{\theta}/B_{\phi})_t \tag{20.7}$$

where $(B_{\theta}/B_{\phi})_t$ = cosine of angle between $\boldsymbol{B}$ and normal-to-target surface; λ_{qt} = power width of SOL at the target.

The factor of 2 in equation (20.7) assumes the same plasma at inner and outer targets. Assuming $Q_{\parallel} = Q_{\perp}$ and pressure balance, gives the estimate for $\chi_{\perp}^{\mathrm{SOL}}$:

$$\chi_{\perp}^{\mathrm{SOL}} \approx \left(\frac{\gamma (B_{\theta}/B_{\phi})_t}{L_{pol}} \right) c_{st} \lambda_{T_{eu}} \lambda_{q_t}. \tag{20.8}$$

When one has both target and upstream probe data, then experimental values for all the quantities on the RHS of equation (20.8) are available, and one has a

quick, convenient estimate for $\chi_\perp^{\mathrm{SOL}}$, and a quick check on the value extracted by the more involved DIVIMP/NIMBUS OSM $\chi_\perp^{\mathrm{SOL}}$-extractor. Also, often $(\gamma(B_\theta/B_\phi)_t/L_{\mathrm{pol}}) \approx$ constant and one can readily check to see whether the radial variation of $\chi_\perp^{\mathrm{SOL}}(r)$ is directly apparent from the experimental data, since then:

$$\chi_\perp^{\mathrm{SOL}} \propto T_{et}^{1/2}\lambda_{T_{eu}}\lambda_{q_t}. \tag{20.9}$$

If one has only target probe data then one can use the fact that, for the conduction-limited regime:

$$\lambda_{T_{eu}} \approx \tfrac{7}{2}\lambda_{q_\parallel} \tag{20.10}$$

together with the magnetic flux-expansion relation, section 5.6:

$$\Delta_u(B_\theta/B_\phi)_u = \Delta_t(B_\theta/B_\phi)_t \tag{20.11}$$

where Δ is the radial separation of two flux surfaces.

Hence:

$$\lambda_{q_u}(B_\theta/B_\phi)_u = \lambda_{q_t}(B_\theta/B_\phi)_t \tag{20.12}$$

and

$$\chi_\perp^{\mathrm{SOL}} \approx \left(\frac{7}{2}\frac{(B_\theta/B_\phi)_t^2}{L_{\mathrm{pol}}(B_\theta/B_\phi)_u}\right)c_{st}\lambda_{q_t}^2 \tag{20.13}$$

$$\propto T_{et}^{1/2}\lambda_{q_t}^2. \tag{20.14}$$

It is often observed that cross-field decay lengths λ increase moving away from the separatrix into the SOL and, since $T_{et}^{1/2}$ has relatively weaker radial variation, this implies $\chi_\perp^{\mathrm{SOL}}(r)$ increasing radially in the SOL.

20.3 Examples from JET

The DIVIMP/NIMBUS OS method was applied to divertor target probe measurements of $T_e(r)$ and $I_{\mathrm{sat}}^+(r)$ for a number of discharges [20.4]. The discharges spanned a wide range of parameters—I_p, B, P_{in} and confinement type (ohmic, L-mode, H-mode). Convection was allowed for in the $\chi_\perp$-extraction by assuming $D_\perp^{\mathrm{SOL}} = 0.4\chi_\perp^{\mathrm{SOL}}$; it was not attempted to extract $D_\perp^{\mathrm{SOL}}$ separately. $T_{it} = T_{et}$ was assumed. The range of conditions covered by this data set is best summarized by figure 20.4 where the ratio of density and electron temperature at the mid-plane to that at the target n_u/n_t, T_{eu}/T_{et}, are plotted as a function of ν_{SOL}^*, section 4.10.2, for separatrix values of T_{eu} and n_u from the complete dataset. Densities and temperatures at the target and upstream are seen to be similar for discharges with low collisionality, but T_{eu}/T_{et} can increase by a factor of up to 5 for discharges with high collisionality.

Clearly the larger the value of n_u, i.e. high ν_{SOL}^*, the further the SOL is into the high recycling, conduction-limited regime where T_{eu}/T_{et} is large. The data

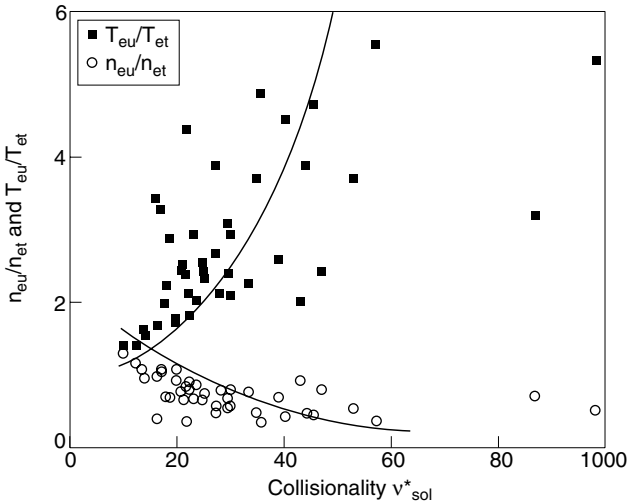

Figure 20.4. Results from OSM analysis of a large number of JET shots [20.4]. Upstream-to-target ratios of n_e and T_e against upstream collisionality parameter ν^*_{SOL}. Solid lines from simple 2PM theory, section 4.10.2.

set extends down to low levels of collisionality where the sheath-limited regime is approached.

One can compare the $f_n \equiv n_u/T_u$ and $f_{Te} \equiv T_{eu}/T_{et}$ ratios in figure 20.4 with what is predicted in section 4.10.2 using the basic 2PM. Since only the electrons are involved we use $\gamma_e = 5$ in evaluating C_2, equation (4.101). The results shown in figure 20.4 used a factor 6/7 in equation (4.101), i.e. mid-way between assuming all the power input at the 'top' (the 4/7 factor in equation (4.101)), or uniformly over the flux-tube length (the 8/7 factor in equation (4.101)). Clearly the basic 2PM matches the OSM results for f_n and f_{T_e} not badly, even though neglecting the convection and volumetric losses included in the OSM.

Density and temperature scale lengths $\lambda_{n_{eu}}$, $\lambda_{T_{eu}}$ are often assumed constant across the SOL, and are often used in models together with separatrix densities and temperatures for estimation of the total power to divertor targets, for example. The common expectation that $\lambda(r) =$ constant may stem from probe measurements in the shadow of limiters, where $n_{eu}(r)$ and $T_{eu}(r)$ radial profiles were often found to be exponential over two or three decades in the limiter SOL [20.5]. In divertor plasmas, SOL scale lengths on JET are not constant with radius and $\lambda_{T_{eu}}$ can vary by as much as a factor of 5 over a mid-plane distance of 15 mm. Density SOL scale lengths do not change as much with increasing radius, but still show an increase. Examples of this behaviour are shown in figure 21.3 for $\lambda_{T_{eu}}(r)$ and in figure 21.4 for $\lambda_{n_{eu}}(r)$, derived from gradients between each 'skin' in the OSM.

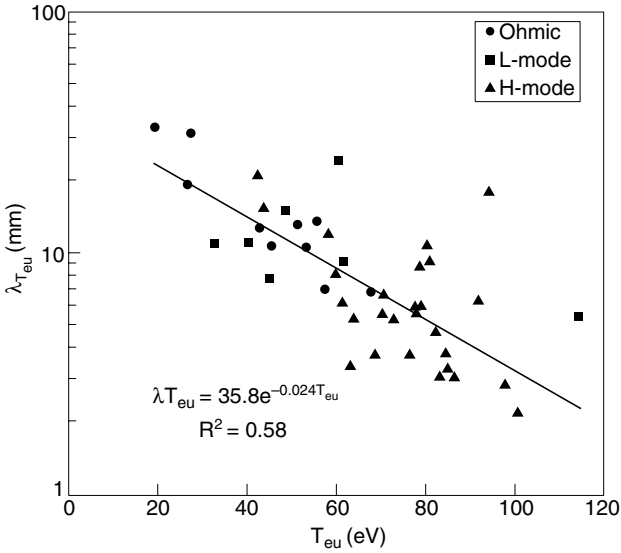

Figure 20.5. Radial decay length of upstream T_e, from OSM analysis of a number of JET discharges [20.4], shows a significant correlation with upstream T_e.

There did not appear to be a strong correlation of λ-value with any main plasma parameter, but $\lambda_{T_{eu}}$ did show a correlation with local parameters, in particular T_{eu}. This is shown in figure 20.5. The clear fall in SOL thickness with increasing separatrix temperature mirrors the increasing SOL scale length with radius as the temperature falls across the SOL for each discharge. The best fit to this data is an exponential fall in $\lambda_{T_{eu}}$ with T_{eu}, shown as the solid line in figure 20.5. A selection of $\chi_{\perp}^{SOL}(r)$ profiles is shown in figure 20.6 for JET ohmic, L-mode and H-mode discharges. Most radial profiles show $\chi_{\perp}^{SOL}$ increasing with radius, also reported on JT60 [20.3] and CMOD [20.1].

The increase $\chi_{\perp}^{SOL}$ with radius is not what would be expected from a Bohm type of behaviour, equation (4.8), and is chiefly a consequence of the experimentally observed increasing $\lambda_{T_{eu}}$ with radius, equation (20.9). A comparison of $\chi_{\perp}^{SOL}$ close to the separatrix deduced from the OSM and that calculated from the simple model formulated in section 20.2, equation (20.8), is shown in figure 20.7. There is generally reasonable agreement between the simple model extractor and the OSM extractor. While the OSM extractor is required in order to obtain the more trustworthy value—since more terms are included in the power balance—the advantage of the simple extractor is its transparency and direct connection with the input data. The good agreement between the two methods as to trend, and approximately as to magnitude, shown in figure 20.7 constitutes a useful check on the more complete procedure of the OSM and $\chi_{\perp}$-extractor.

No clear scaling of $\chi_{\perp}^{SOL}$ with main plasma parameters (I_p, B_ϕ, $\langle n_e \rangle$) was

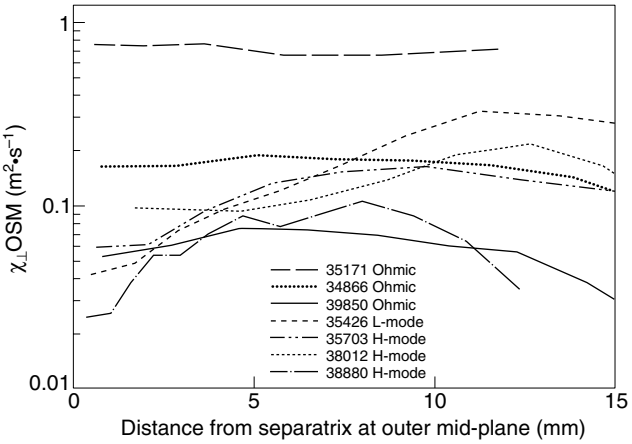

Figure 20.6. JET. Radial variation of $\chi_{\perp}^{\mathrm{SOL}}(r)$ extracted using OSM analysis for a number of JET discharges [20.4]. The general trend is for $\chi_{\perp}^{\mathrm{SOL}}(r)$ to rise with r or be constant.

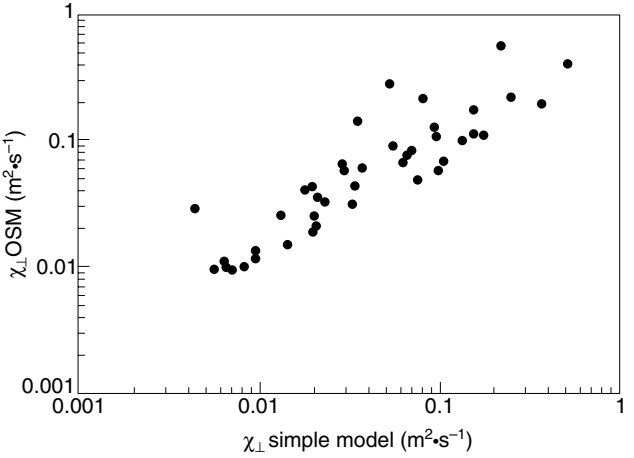

Figure 20.7. JET. As for figures 20.5, 20.6, comparison of $\chi_{\perp}^{\mathrm{SOL}}$ extracted from OSM analysis and a simple 2PM analysis showing reasonable agreement [20.4].

found and indeed there seems to be no clear scaling with local plasma parameters with the exception of upstream temperature, T_{eu}, derived using the OSM. The scaling of $\chi_{\perp}^{\mathrm{SOL}}$ with T_{eu} is shown in figure 20.8 for $\chi_{\perp}^{\mathrm{SOL}}$ (i.e. the value close to the separatrix) taken from the complete database. Also shown in figure 20.8 is the best fit to the data, which is approximately $\chi_{\perp}^{\mathrm{SOL}} \propto T_{eu}^{-2}$. Clearly both $\chi_{\perp}^{\mathrm{SOL}}(r)$ and $\chi_{\perp}^{\mathrm{sep}}$ fall with increasing T_{eu}, although there is considerable scatter in the data.

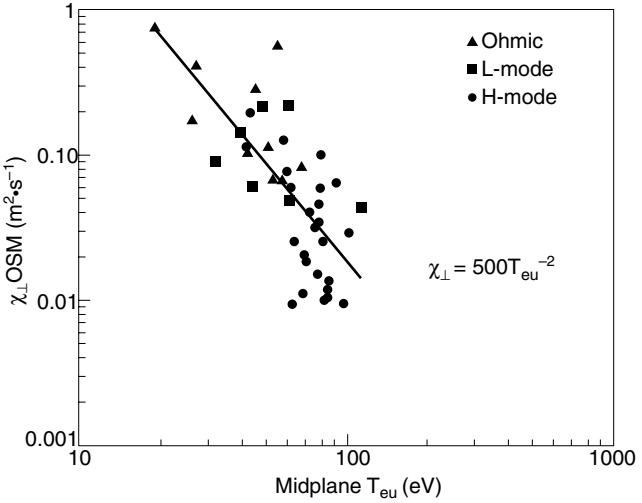

Figure 20.8. JET. As for figures 20.5–20.7. Extracted $\chi_{\perp}^{\mathrm{SOL}}$ (near separatrix) values show a significant correlation with upstream T_e [20.4].

The OS method of extracting $\chi_{\perp}^{\mathrm{SOL}}$, as applied in the foregoing, is subject to at least two errors and uncertainties:

(a) The target heat flux q_t is not actually measured, but is inferred from the Langmuir probe measurements of $T_{et}(r)$, $I_{\mathrm{sat},t}^{+}(r)$—plus *theoretical* values for the sheath heat transmission coefficient γ, chapter 2. The latter assumed $T_{et} = T_{it}$ and other simplifications such as no (effective) secondary electron emission from the target, etc. Thus γ was taken to be constant across the target. As seen from equation (20.8), the extracted $\chi_{\perp}^{\mathrm{SOL}}$ will be directly and linearly affected by any changes in γ—including any radial variations of $\gamma(r)$.

(b) Often overall power accounting in a tokamak is imperfect and 'missing power' is unaccounted for. Such was the case for many of the JET shots. Since the extraction procedure is based on a power balance analysis, uncertainty is implied.

Uncertainties will be reduced for this method when the experimental input data is supplemented by measurements of T_{it} (also T_{iu}) and by infra-red thermographical measurements of the target heat deposition [20.6].

References

[20.1] LaBombard B, Goetz J A, Hutchinson I H *et al* 1997 *J. Nucl. Mater.* **241–243** 149
[20.2] Stangeby P C, Elder J D, Fundamenski W *et al* 1997 *J. Nucl. Mater.* **241–243** 358

[20.3] Shimizu K, Itami K, Kubo H *et al* 1992 *J. Nucl. Mater.* **196–198** 476
[20.4] Erents S K and Stangeby P C 1998 *Nucl. Fusion* **38** 1637
[20.5] Erents S K, Tagle J A, McCracken G M *et al* 1988 *Nucl. Fusion* **28** 1209
[20.6] Lasnier C J, Hill D N, Petrie T W *et al* 1998 *Nucl. Fusion* **38** 1225

Chapter 21

Measurements of $D_{\perp}^{\mathrm{SOL}}$, $\chi_{\perp}^{\mathrm{SOL}}$ and the Decay Lengths for Divertor SOLs

The power scrape-off length, $\lambda_{q\parallel}$, is one of the most important practical quantities of the SOL since it controls the amount of solid surface involved in plasma power exhaust—and thus it governs the problems of target heat removal, melting, etc. The principal unknown involved in $\lambda_{q\parallel}$ is $\chi_{\perp}^{\mathrm{SOL}}$, the anomalous cross-field heat diffusivity in the SOL. For the conduction-limited regime the two-point model predicts $\lambda_{q\parallel} \propto (\chi_{\perp}^{\mathrm{SOL}})^{7/9}$, section 5.7. We are therefore interested in measurements of $\lambda_{q\parallel}$ and/or $\chi_{\perp}^{\mathrm{SOL}}$.

One may consider the temperature decay lengths, λ_{T_e}, λ_{T_i}, and the density decay length, λ_n, to be the fundamental lengths, with the others—for power particle and momentum fluxes, etc—then being expressed in terms of these basic ones. For example, for the conduction-limited regime one has the particularly simple relation: $\lambda_{q\parallel} = \frac{2}{7}\lambda_T$, section 5.7.

One's first thought is that λ_n should be related to $D_{\perp}^{\mathrm{SOL}}$, and one might be inclined to use the relation for the simple SOL, $\lambda_n = (2D_{\perp}^{\mathrm{SOL}}L/c_s)^{1/2}$, equation (4.7). For divertors, typically operating in the high recycling, conduction-limited regime, with most of the ionization occurring outside the separatrix, the SOL is therefore not simple and there is no obvious reason for this expression to be valid.

The λ_n and λ_T are also important because they control the penetration into the plasma of recycling hydrogen neutrals—and also of edge-produced impurity neutrals—i.e. they control 'edge screening'.

An edge database of tokamak divertor scrape-off lengths has been established [21.1]. An example is shown in figure 21.1, where λ_{T_e} and λ_n have been plotted against T_{eu}^{sep}. The common practice of quoting characteristic radial lengths at the outside mid-plane is used throughout this section. For the conduction-limited regime we may calculate from equations (5.77) and (5.80) the expected

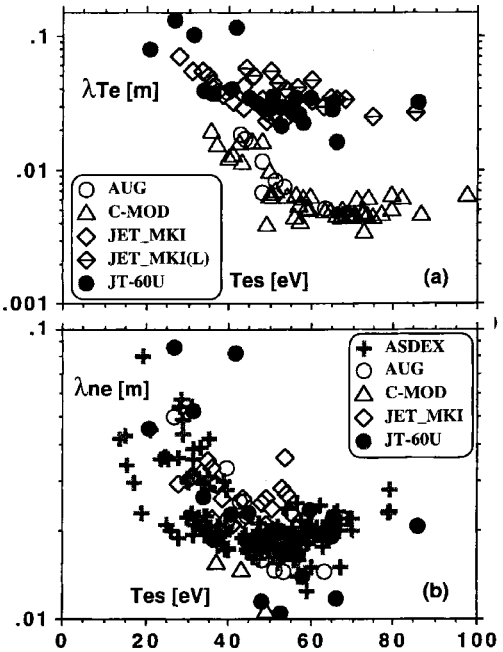

Figure 21.1. Value of upstream radial decay lengths of T_e for a number of tokamaks plotted against upstream T_e [21.1].

relation between $\lambda_{q\parallel}$ or λ_{T_u} and T_u:

$$\lambda_{T_u} \propto T_u^{-5/4}(n_u \chi_\perp^{\mathrm{SOL}})^{1/2} q R. \tag{21.1}$$

The tendency for λ_{T_e} to decrease with increasing T_{eu}^{sep} seen in figure 21.1 may thus be explained. One may also note the tendency for λ_{T_u} to be longer for larger machines—apparently a reflection of the R-dependence of equation (21.1). Note however, that n_u is not a constant and probably $\chi_\perp^{\mathrm{SOL}}$ is not either. It is necessary to know the dependence of $\chi_\perp^{\mathrm{SOL}}$ on T_u, n_u, q, R, B, etc if one is to fully test theoretical predictions of $\lambda_{q\parallel}$, λ_T, etc.

Complicating the situation is the common observation that the radial profiles of n and T are often not representable by single exponentials, i.e. by a single decay length λ_n or λ_T. Often the characteristic radial decay lengths ℓ_n and ℓ_T:

$$\ell_n(r) = -\left[\frac{1}{n}\frac{\mathrm{d}n}{\mathrm{d}r}\right]^{-1} \qquad \ell_T(r) = -\left[\frac{1}{T}\frac{\mathrm{d}T}{\mathrm{d}r}\right]^{-1} \tag{21.2}$$

are functions of radial distance into the SOL, typically increasing with r. The database for the CMOD tokamak is particularly extensive [21.2] since a fast

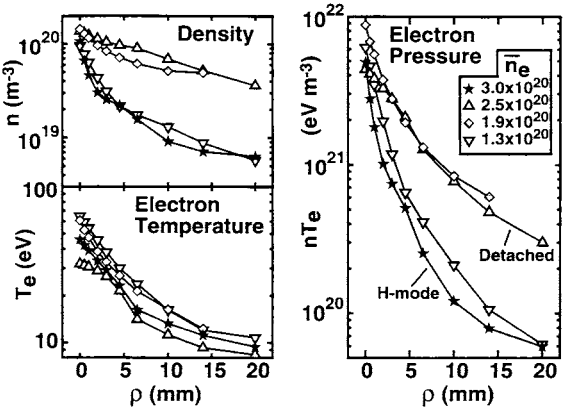

Figure 21.2. CMOD. [21.2]. Cross-field density, electron temperature and electron pressure profiles at an upstream fast-scanning probe location. The cross-field coordinate, ρ, labels the local flux surface according to its distance outside the LCFS at the plasma mid-plane.

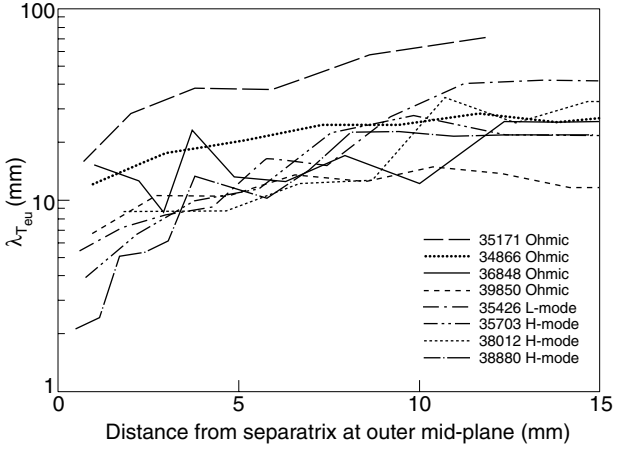

Figure 21.3. Radial variations of the radial decay length of upstream T_e, $\ell_{T_{eu}}$, for a number of JET shots, from OSM analysis [21.3]. The general trend is for the $\ell_{T_{eu}}(r)$ to increase with r.

scanning (Langmuir) probe, FSP, scans through the upstream SOL on almost all discharges. Figure 21.2 shows exponential plots of $n_e(r)$, $T_e(r)$ and electron pressure, $n_e(r)T_e(r)$ for a range of CMOD conditions, indicating this common pattern of ℓ_n and ℓ_T increasing with r. A similar pattern is seen in the collection of JET ohmic, L-mode and H-mode shots shown in figure 21.3, $\ell_{T_{eu}}$, and figure 21.4,

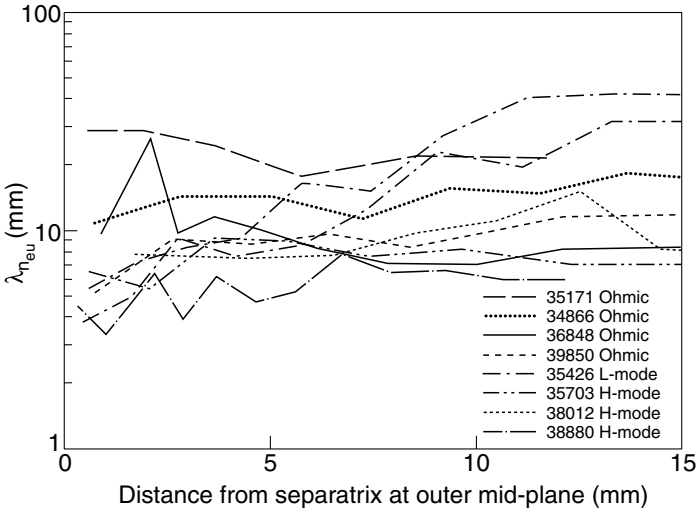

Figure 21.4. As for figure 21.3 but for upstream n_e.

$\ell_{n_{eu}}$ [21.3]. These JET data were calculated from measured plasma conditions across the outer target, $T_{et}(r)$ and $I^{+}_{\mathrm{sat},t}(r)$, and using the onion-skin method, chapter 12, to calculate the upstream profiles of $n_{eu}(r)$ and $T_{eu}(r)$. The tendency for the lengths to increase radially is more pronounced in these JET data for $\ell_{T_{eu}}(r)$ than for $\ell_{n_{eu}}(r)$. One may note a rather complicated variation amongst the three different confinement regimes, and with variation of n_e, I_p, q, B. The basic properties of these dependences has not been established.

A larger collection of CMOD data are given in figure 21.5 for $\ell_{n_{eu}}$, $\ell_{T_{eu}}$ and $\ell_{p_{eu}}$ (electron pressure), plotted against T_{eu}—for a variety of operating conditions—high recycling, low recycling, detached and 'death ray' (a state sometimes seen in association with detachment)—with individual points representing specific radial locations across the SOL [21.2]. Substantial scatter may be noted, presumably indicating other dependences of these lengths than on T_{eu}. Neverthless, a clear trend with T_{eu} is apparent: all three lengths show an inverse dependence on T_{eu}. A curve for $T_{eu}^{-5/4}$ is overlain on the $\ell_{p_{eu}}$ plot; the rough match may be a reflection of the dependence of ℓ_{T_u} on T_u predicted for the conduction-limited regime, equation (21.1). As can be seen from figures 21.3–21.5, $\ell_{T_{eu}}$ and $\ell_{n_{eu}}$ are of comparable magnitude, within large scatter. One notes that ℓ_n and ℓ_T can be rather small, less than 1 cm, indicating $\lambda_{q\parallel}$ of only a few mm. While these are the *outside mid-plane* values, the power width at the divertor is still likely to be only ~1 cm for any likely flux expansion.

The *deposited* power width on the divertor targets can be directly measured using infra-red thermography or indirectly using target Langmuir probes, and a database has been assembled [21.4]. Since the deposited power profile may not be

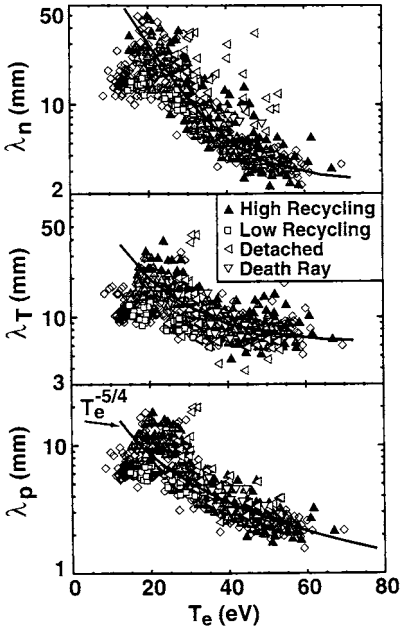

Figure 21.5. CMOD [21.2]. Local cross-field gradient scale length density ($\ell_{n_{eu}}$), electron temperature ($\ell_{T_{eu}}$) and electron pressure ($\ell_{p_{eu}}$), versus local electron temperature (T_e) at the scanning probe location.

characterized by a single decay length, it is convenient to define an effective width as being that which when multiplied by the measured *peak* flux density equals the measured *integrated* flux deposited on the target. As noted above, the basic unknown in calculating $\lambda_{q\parallel}$—and thus for a given flux expansion and given target geometry, $\lambda_q^{\mathrm{deposited}}$—is $\chi_\perp^{\mathrm{SOL}}$. If cross-field *convection* is also important, then the unknown $D_\perp^{\mathrm{SOL}}$ is also involved. Assuming for simplicity that cross-field heat flux is dominated by conduction and, generally, that all of the other assumptions of the basic two-point model of section 5.7 hold—including the dominance of conduction in the parallel heat transport, $T_u/T_t \gg 1$, etc—then we may again appropriate the analytic results of section 5.7, equation (5.77), to relate λ_q to $\chi_\perp^{\mathrm{SOL}}$ (hereafter we will not distinguish between $\lambda_{q\parallel}$ and $\lambda_q^{\mathrm{deposited}}$, assuming that they have a constant ratio for all machines and operating conditions, which is not true in reality, of course). None of this will get us anywhere so long as $\chi_\perp^{\mathrm{SOL}}$ is completely unknown. One may therefore *hypothesize* that perhaps $\chi_\perp^{\mathrm{SOL}}$ depends on various quantities as a product of powers, say [21.4]:

$$\chi_\perp^{\mathrm{SOL}} \propto T_{eu}^{\alpha} n_{eu}^{\beta} q^{\gamma} B_\phi^{\delta} R^{\varepsilon} Z_{\mathrm{eff}}^{\eta} \tag{21.3}$$

where $\alpha, \beta, \gamma, \delta, \varepsilon, \eta$ are constant coefficients which have to be found. There is no

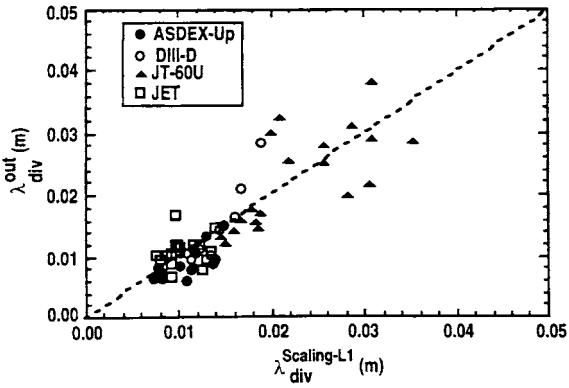

Figure 21.6. Measured outer divertor power width for ohmic and L-modes versus scaling law, equation (21.5), for the ITER power deposition database [21.4].

physical basis for this hypothesis, but it is convenient and may be as good as any other hypothesis about this *anomalous*, i.e. unknown, quantity. Such hypotheses are often made concerning such quantities as the energy confinement time, τ_E, characterizing the main plasma [21.5]. Obvious problems with such hypotheses are: (a) other parameters may also be important, (b) the dependence may not be as a product of powers of the parameters, but rather sums or differences may be involved, as well as off-sets. One can readily show that combining equations (5.77), (5.80) and (21.3) gives:

$$\lambda_q \propto P_{\mathrm{SOL}}^{(2\alpha-5)/(9+2\alpha)} n_u^{(7\beta+7)/(9+2\alpha)} q^{(4\alpha+7\gamma+4)/(9+2\alpha)} \times B_{\phi}^{7\delta/(9+2\alpha)} R^{(7\varepsilon+14)/(9+2\alpha)} Z_{\mathrm{eff}}^{(7\eta+2\alpha+2)/(9+2\alpha)}. \tag{21.4}$$

Z_{eff} has also entered from the dependence of the parallel electron heat conductivity coefficient $\kappa_0 \propto (Z_{\mathrm{eff}})^{-1}$, equation (9.48).

Since the SOL upstream separatrix density, n_u, is often not known, it was replaced by the main plasma density $\overline{n}_e$, on the assumption that $n_u \propto \overline{n}_e$. We have seen, chapter 19, that the ratio $n_u/\overline{n}_e$ is not in fact constant and this will therefore introduce some error. The measured power deposited on the outer target, $P_{\mathrm{dep,out}}$, was used in place of P_{SOL}, since this was more readily available in the study, although that meant that volumetric power losses in the SOL were not allowed for.

Measurements of $\lambda_q^{\mathrm{dep,out}}$ for a number of tokamaks, for ohmic and L-mode discharges, were then fitted by equation (21.4), with the choice of the power coefficients being adjusted for best fit, figure 21.6, [21.4]. This gave the fitting:

$$\lambda_q^{\mathrm{dep,out}} = (6.6) \times 10^{-4} R^{1.21} P_{\mathrm{dep,out}}^{-0.19} q^{0.59} n_e^{0.54} Z_{\mathrm{eff}}^{0.61}. \tag{21.5}$$

λ, R[m], P [MW], $n[10^{19}\mathrm{m}^{-3}]$. The corresponding best fit for $\chi_\perp^{\rm SOL}$ was:

$$\chi_\perp^{\rm SOL} \propto \overline{n}_e^{-0.02} T_{eu}^{1.17} q^{-0.29} R^{-0.01} Z_{\rm eff}^{0.41}. \tag{21.6}$$

One may note the absence of any correlation with the magnetic field, and so Bohm diffusion is not indicated ($\chi_\perp^{\rm Bohm} \propto T/B$), although the T-dependence is Bohm-like. One may also note the substantial discrepancy with the dependence $\chi_\perp \propto T_{eu}^{-2}$ extracted using the onion-skin method analysis on JET data, chapter 20. As discussed, the errors and assumptions involved in these methods of extracting $\chi_\perp^{\rm SOL}$ remain substantial, and such discrepancies are likely to persist until these techniques are better refined.

Another database for $\chi_\perp^{\rm SOL}$ has been produced based on the total power entering the SOL, $P_{\rm SOL}$, and equation (20.3), see [21.6, 21.7]:

$$\frac{P_{\rm SOL}}{A_\perp} = 2\chi_\perp^{\rm SOL} n_u k T_u / \lambda_{T_u} + \tfrac{5}{2} D_\perp^{\rm SOL} n_u k T_u / \lambda_{n_u} \tag{21.7}$$

where $A_\perp$ is the area of the separatrix surrounding the confined plasma, $A_\perp \approx 2\pi R 2\pi a$; the factor of 2 assumes $T_e = T_i$ and $\chi_e = \chi_i$. It was assumed that $D_\perp^{\rm SOL}/\chi_\perp^{\rm SOL} = 0.24$, and so just the one unknown was involved in equation (21.7). $P_{\rm SOL}$ was taken to be the difference between the tokamak input power and the power radiated in the main plasma, both measured quantities. The plasma quantities n_u, T_u, λ_{T_u} and λ_{n_u} were taken from upstream measurements from, for example, a reciprocating Langmuir probe. As already discussed in chapter 19, a major difficulty in using upstream measurements is identifying the location of the separatrix—particularly in H-modes where the radial decay lengths may be only millimetres, while the uncertainty in the location of the separatrix—as calculated from the magnetic pick-up coils—is of order ~1 cm. Various methods were employed to try to correct for this uncertainty [21.6], including the technique described in chapter 19 of re-adjusting the upstream separatrix location in order to obtain electron pressure equality with measurements made at the target, where the separatrix may be more reliably located. Results for $\chi_\perp^{\rm SOL}$ are given i
for ohmic, L-mode and H-mode discharges, plotted against $P_{\rm SOL}/A_\perp$. The very large scatter is attributed to uncertainties in the location of the separatrix. The H-mode diffusivities are smaller than the ohmic and L-mode values.

Three $\chi_\perp^{\rm SOL}$-extraction methods are summarized and compared in table 21.1:

(a) the onion-skin method, chapter 20;
(b) the $\lambda_q^{\rm deposited}$ method described in this section;
(c) the upstream data method described in this section.

In addition, 2D fluid codes are used to model individual shots and the input values of $D_\perp^{\rm SOL}$, $\chi_{\perp e,i}^{\rm SOL}$ are adjusted until a best fit is achieved to all the available measurements for that shot—both upstream and target profiles of plasma parameters, also spatial distributions of hydrogenic line intensities such as D_α, etc. In this way databases can be produced for $\chi_\perp^{\rm SOL}$ and its functional dependence on T_u, n_u,

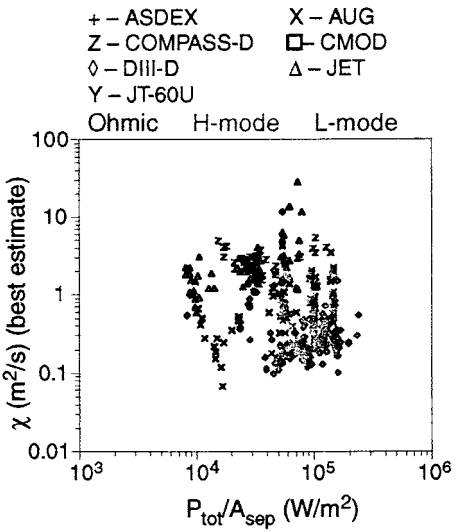

Figure 21.7. Variation of the radial thermal diffusivity at the separatrix with the surface radial power density. Data from a number of tokamaks. $\chi_\perp$ extracted using the 'upstream data method', see text [21.6, 21.7].

Table 21.1. $\chi_\perp^{SOL}$-extraction methods.

		The onion-skin method chapter 20	The $\lambda_q^{deposited}$ method	The upstream data method
1.	Principal experimental input	$T_{et}(r)$ $I^+_{sat,t}(r)$	$q_t^{deposited}(r)$	$P_{in} - P_{rad}^{main}$ n_u T_u λ_{n_u} λ_{T_u}
2.	Model used	OSM	Basic 2PM	—
3.	Constraints on $\chi_\perp^{SOL}$	none	$\chi_\perp^{SOL} \propto T_u^\alpha n_u^\beta \ldots$ with $\alpha, \beta \ldots$ adjustable	none
4.	Other critical assumptions	• any missing power does not reach target • γ known	• $n_u/\bar{n}_e$ constant • P_t^{dep}/P_{SOL} constant	• location of separatrix is reliably known • $D_\perp^{SOL}/\chi_\perp^{SOL}$ known • $\chi_{\perp e}^{SOL} = \chi_{\perp i}^{SOL}$
5.	Radial information?	yes	no	no

B_ϕ, etc can be established in the form of equation (21.3), or otherwise. A simple approximation to this method has also been developed [21.8] using a model which assumes that perpendicular and parallel heat fluxes are purely conductive, neglects volumetric power losses and uses both target and upstream probe data as input.

A number of theories have been developed to *predict from basic principles* how $\chi_\perp^{\rm SOL}$ should depend on T, n, B, etc. These have been incorporated into the general relations between λ_q and $\chi_\perp^{\rm SOL}$, equations (5.77)–(5.79), and comparisons made with experimental databases [21.9–21.11].

We turn next to the upstream *density* profile and λ_{n_u}. While $\lambda_{q\parallel}$, $\lambda_q^{\rm dep}$ and λ_{T_u} may be more or less simply related to $\chi_\perp^{\rm SOL}$ as given by the two-point model, section 5.7, it is not immediately clear what λ_n depends on for the high recycling, conduction-limited regime where it is assumed that all of the ionization occurs within the SOL plasma immediately in front of the divertor targets. The general tendency that is expected when ionization of the recycling hydrogen occurs in the SOL, rather than the main plasma, is for λ_n to broaden, section 4.9. Let us imagine a SOL where the neutrals are also confined by $\boldsymbol{B}$, and so the recycling neutrals that are created by the ionic outflux to the target for one particular flux tube are all re-ionized within the same flux tube. Since each flux tube is *self-sustained* in a particle-balance sense, it would seem that there is no reason for $n(r)$ to vary radially at all, i.e. $\lambda_n \to \infty$. This picture runs into two difficulties (over and above the idea of neutrals being confined by $\boldsymbol{B}$!):

(a) $\lambda_T(r)$ will still decay radially since the power input occurs in the main plasma. Thus at some radial depth into the SOL, T_e will become too cold to cause ionization. The flux tubes further out could not be sustained in this hypothetical scenario, and so $n_e(r)$ would be approximately a step function, dropping to zero where T_e became small compared with ionization potential I_{iz}, figure 4.6.

(b) Unless $D_\perp = 0$, there could not be any radial variation of $n_e(r)$ at all, in fact—not even near the radius where $T_e \sim I_{iz}$—since that would result in cross-field particle fluxes, according to $\Gamma_\perp = -D_\perp {\rm d}n/{\rm d}r$. That would be inconsistent with the flux-tube-by-flux-tube particle balance hypothesized.

Next we consider the realistic situation where recycling neutrals are not constrained by $\boldsymbol{B}$. Since the conditions are highly ionizing, i.e. with short mean free paths of the neutrals to be ionized, the situation is not very much different from the first scenario: each flux tube is *nearly* in individual local particle balance with most of the neutrals being ionized within a specific flux tube having originated from ions exiting that flux tube onto the target. Therefore we appear to still be obliged to contemplate a scenario where the ionization on each flux tube occurs just in front of the target, and the total ionization source on each flux tube equals the target out-flux for that flux tube. That then implies a *stagnant* region extending over most of the SOL, i.e. the entire region upstream of the ionization region.

This picture, however, is incompatible with non-zero $D_\perp$ and observed upstream radially decaying $n_e(r)$ profiles, where $\lambda_{n_u} \approx \lambda_{T_u}$, figures 21.3, 21.4: no

upstream source of particles exists in this picture to support the cross-field fluxes implied by $D_\perp \neq 0$ and $\lambda_{n_u} \neq \infty$.

One resolution of this problem lies in *flow reversal*, chapter 15: the flux-tube-by-flux-tube particle balance is not, in fact, perfect, and a large scale *convection cell* arises within the SOL. This picture is obviously a complex one and we cannot expect to find simple analytic models for λ_{n_u} as was the case for λ_{T_u}, section 5.7. We can, however, extract some rough idea of what to expect theoretically for λ_{n_u} from this flow reversal picture.

With regard to the flow-reversed region, the dwell time of particles within the SOL is still *roughly* $\tau_{\rm SOL} \approx L/c_{su}$ since the parallel plasma velocity is still of order c_{su}, albeit somewhat smaller, chapter 15, perhaps $0.1c_{su}$, and the distance involved between source and sink is still $\approx L$. Thus, particles will diffuse cross-field a distance of order $(D_\perp^{\rm SOL}\tau_{\rm SOL})^{1/2}$, just as for the simple SOL, chapter 4, i.e. one still anticipates that λ_{n_u} will be of order $(D_\perp^{\rm SOL}L/c_s)^{1/2}$, a little larger perhaps. *Drift effects*, chapter 18, involving large scale flows along the SOL, would lead to broadly similar conclusions.

This estimate for λ_{n_u} may be compared with the rough estimate of λ_{T_u} obtained from equations (5.55), (5.72):

$$\lambda_{T_u} \approx \left(\frac{49}{4}\frac{en_u\chi_\perp^{\rm SOL}L^2}{\kappa_0 T_u^{5/2}}\right)^{1/2} \tag{21.8}$$

giving an estimate for the ratio:

$$\lambda_{n_u}/\lambda_{T_u} \approx \left(\frac{4}{49}\frac{10^{-16}D_\perp^{\rm SOL}\kappa_0}{e\chi_\perp^{\rm SOL}v_{\rm SOL}^* c_{s0}}\right)^{1/2} \tag{21.9}$$

where the collisionality parameter $v_{\rm SOL}^* = 10^{-16}n_u L/T_u^2$, equation (4.105), $c_{s0} = 9788$ m s^{-1} (the speed for D^+ plasma at $T = 1$ eV). Using $\kappa_0 = 2000$, $e = 1.6 \times 10^{-19}$ and assuming $D_\perp^{\rm SOL} = \chi_\perp^{\rm SOL}$ and $v_{\rm SOL}^* = 50$, as a representative value for the conduction-limited regime, section 5.8, we find:

$$\lambda_{n_u}/\lambda_{T_u} \approx 1. \tag{21.10}$$

Thus, one anticipates that the upstream decay lengths for density and temperature—based on a picture of the high recycling regime which involves flow reversal—to be roughly comparable. This is sometimes observed experimentally, figures 21.3, 21.4.

Figures 21.8, 21.9, [21.12], show larger collections of measurements $\lambda_{n_u}/\lambda_{T_{eu}}$ for JET shots in the conduction-limited regime, figure 21.8, and similarly for CMOD, figure 21.9. The $\lambda_{n_u}/\lambda_{T_{eu}}$ ratios have been plotted against T_{et} as a rough indicator of operating regime: for very low T_{et} the transition to detachment is occurring while for high T_{et} the transition to the sheath-limited regime sets in. The JET data span from the C-L regime up toward the S-L

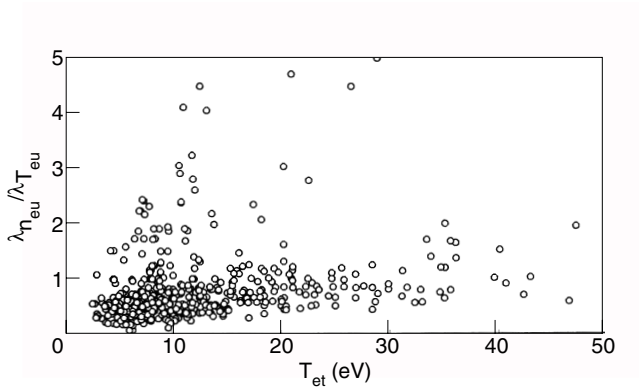

Figure 21.8. Ratio of upstream radial decay lengths of n_e and T_e, from OSM analysis, of a number of JET discharges, and for various locations across the SOL [21.12]. Plotted versus target electron temperature. Attached discharges.

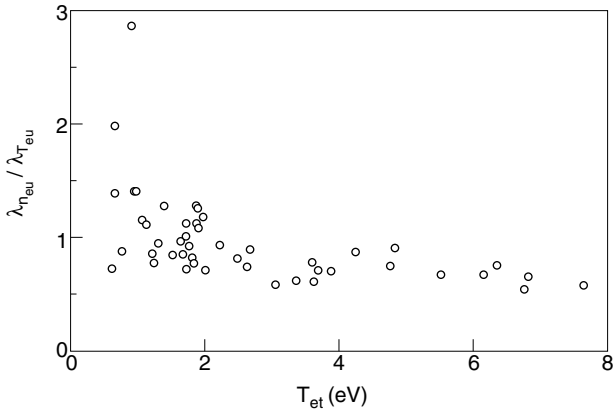

Figure 21.9. Ratio of upstream radial decay lengths of n_e and T_e measured using an upstream reciprocating probe on CMOD [21.2] versus target electron temperature. At the lowest values of T_{et}, detachment is starting to occur.

regime. While the data scatter is substantial, there does appear to be a tendency for this ratio to be $\sim\frac{1}{2}$ in the C-L regime, increasing somewhat perhaps as the transition to the S-L regime is approached. The CMOD data spans from the C-L regime down toward/into detachment. The ratio again appears to be $\sim\frac{1}{2}$ in the C-L regime, increasing as detachment is approached. The SOL widens, in a particle sense, as detachment sets in. Similar results have been reported from JT-60U [21.13, 21.14]. This picture is not, however, a universal one. On AUG, λ_{n_u} tends to be significantly larger than $\lambda_{T_{eu}}$ [21.15]. The reason for these

inconsistencies remains unresolved at this time.

We may arrive at roughly the same theoretical expectation for $\lambda_{n_u}/\lambda_{T_u}$ from a different consideration of the conduction-limited SOL: in section 5.8 it was shown that in the C-L regime one expects that the upstream density and temperature are related, roughly, according to:

$$T_u \propto (n_u L)^{1/2}. \tag{5.116}$$

If the SOL stays at approximately the same collisionality across its radial extent, $\nu^*_{\rm SOL} \propto n_u L/T_u^2$, i.e. equation (5.116) holds across the SOL, then this means that:

$$\lambda_{n_u} \sim \tfrac{1}{2}\lambda_{T_u}. \tag{21.11}$$

That is, we again anticipate that the two scale lengths will be roughly equal.

The foregoing, however, begs the question: but why should collisionality remain constant across the SOL? It may very well be the case that *on the separatrix*, equation (5.116) holds for cases in the conduction-limited regime—and so, if in the first place one *chooses* the cases to be in this regime on the separatrix—as was done for the JET data shown in Figure 5.27, for example—then it is perhaps not too surprising that $n_u^{\rm sep}$, $T_u^{\rm sep}$ and $L^{\rm sep}$ should be related. The data in figure 5.27, however, are for flux tubes at *various locations* across the SOL, and not just the separatrix. It appears that there exists a tendency for the SOL to remain, roughly at constant collisionality across the SOL width.

We may turn to the basic two-point model of section 5.2, and its extensions, section 5.4, for insight on this matter. Equations (5.4), (5.6), (5.7) may be combined to give:

$$T_u = \left(\frac{49}{32}\frac{e^3\gamma^2}{m_i\kappa_0^2}\right)^{1/5} T_t^{1/5}(n_u L)^{2/5}. \tag{21.12}$$

Now, *if* it can be argued that $T_t(r)$ is not expected to vary greatly across the target—or at least that $T_t^{1/5}$ is not expected to vary greatly—then the theoretical relation of equation (21.12) matches rather closely to the experimental observations of figure 5.27. Even the absolute magnitude matches reasonably well: taking $T_t = 10$ eV, constant, as representative, and $\gamma = 7$, m_D^+, $\kappa_0 = 2000$ gives:

$$T_u = 1.7 \times 10^{-7}(n_u L)^{0.4} \tag{21.13}$$

T [eV], n [m^{-3}], L [m]. Equation (21.13) is shown as the dashed line in figure 5.27. We thus have an explanation of the tendency for the collisionality to remain constant across the SOL—with all the implications already shown of that state of affairs—*provided we can explain the tendency for* $[T_r(r)]^{1/5}$ *to not vary greatly across the target*. It might be thought that, since such a small exponent (1/5) is involved, this is essentially guaranteed. This, however, is not the case since the target conditions—n_t, T_t, Γ_t—are strong functions of upstream conditions, i.e., they are 'volatile', not robust, quantities; see discussion in section 5.2.

Indeed, it is readily shown that the foregoing argument is actually *circular*: precisely to the degree that the collisionality is constant across the SOL—to that degree, and *only* to that degree, is $[T_t(r)]^{1/5}$ constant. (This should not be surprising: after all equation (21.12) was obtained directly from the basic relations of the two-point model, just as the expressions of section 5.8 were. The only additional assumption needed in section 5.8 in order to obtain equations (5.112) and (5.114) were that the values of collisionality be approximately constant. In this section, on the other hand, the only additional assumption is that $[T_t(r)]^{1/5} \sim$ constant. Thus the two assumptions are equivalent, even if that is not immediately obvious.) In order to close this argument, therefore, we require a completely *separate reason* why $T_t(r)$ should *tend* not to vary *too* greatly.

An explanation is that *parallel heat convection* tends to be important in the outer part of the SOL—even when parallel conduction dominates the regions closer to the separatrix—and this prevents $T_t(r)$ from dropping as rapidly from its separatrix value as it would if conduction dominated everywhere.

It is evident that if the parallel plasma flow is significant over much of the length of a flux tube, then parallel heat convection will be important, the conduction will carry less of the power and so the parallel temperature drop will decrease. One can bring this out in an approximate and quantitative way by including the factor f_{cond}—the fraction of the parallel power carried by conduction—in the extended two-point model, sections 5.4, 5.7. In the table in section 5.7 we see that $T_t \propto f_{\mathrm{cond}}^{-4/7}$ (without $\lambda_{q\parallel}$-variation) or $\propto f_{\mathrm{cond}}^{-8/9}$ (with $\lambda_{q\parallel}$-variation). Also $T_u/T_t \propto f_{\mathrm{cond}}^{6/7}$ or $\propto f_{\mathrm{cond}}^{10/9}$.

The tendency for the conduction-limited regime to result in flow reversal, with target-directed flow occurring in the outer part of the SOL, would make parallel heat convection more important in the outer part of the SOL, where conduction is also weaker due to lower T_e—and may explain the tendency for $T_t(r)$ not to drop as rapidly with r as would be the case were conduction alone involved.

This and other speculations as to the cause of $T_t(r)$ tending not to vary strongly, or for λ_{n_u} to tend to be of order λ_{T_u}, or for collisionality to tend to be constant across the SOL—all of which have been seen to be equivalent—are discussed in [21.12].

It is clear from figures 21.8 and 21.9 that, at most, the relation $\lambda_{n_u}/\lambda_{T_u} \sim 1$ is merely a *tendency* of the conduction-limited regime. Much scatter and many exceptions are thus to be expected. It seems likely that the modelling for λ_{n_u} will always be more difficult than the modelling for λ_{T_u} and λ_q; particle balance in the C-L regime is inherently more complicated than power balance.

Turning finally to a target variable, the particle flux density Γ_t, or equivalently the ion saturation current density $I_{\mathrm{sat},t}^+ \equiv e\Gamma_t$: the basic equations of the two-point model, equations (5.4), (5.6) and (5.7), can also be combined to give:

$$\Gamma_t = I_{\mathrm{sat},t}^+/e = \left(\frac{e}{2m_i}\right)^{7/10}\left(\frac{7\gamma e L}{4\kappa_0}\right)^{4/10} T_t^{-3/10} n_u^{14/10}. \tag{21.14}$$

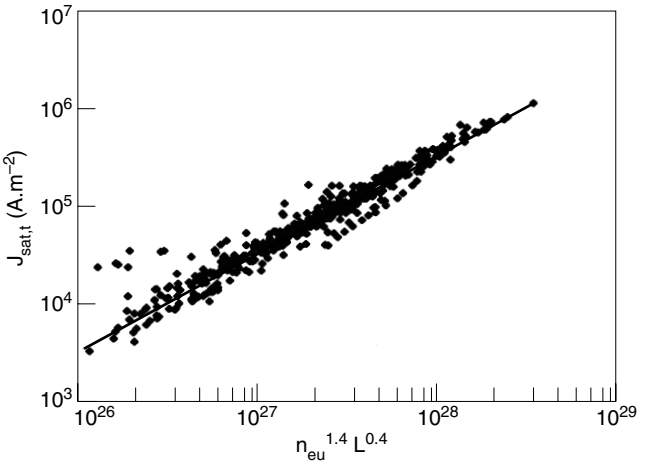

Figure 21.10. Measured values of the Langmuir probe ion saturation currents for a number of JET discharges plotted against $n_{eu}^{1.4}L^{0.4}$. The straight line is from theory, equation (21.14) [21.12]. L is the connection length. n_{eu} is the upstream density for each flux tube.

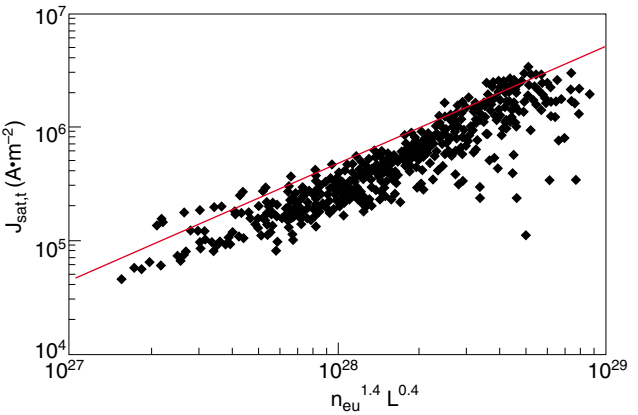

Figure 21.11. As figure 21.10 but for CMOD [21.12].

Thus, again, if one can argue that T_t—or at least $T_t^{-0.3}$—should not vary greatly across the SOL, then one expects the simple correlation $I_{\mathrm{sat},t}^{+} \propto\sim n_u^{1.4}$ to hold. Equation (21.14), evaluated for m_D^{+}, $\gamma = 7$, $T_t = 10$ eV constant, $\kappa_0 = 2000$ gives the solid lines in figure 21.10, compared with JET data, and figure 21.11,

compared with CMOD data; the variation of L has also been allowed for. Within substantial scatter the theoretical relation matches experiment reasonably well. It is often stated that $I_{\mathrm{sat},t}^{+} \propto\sim n_u^2$ is characteristic of the C-L regime, equation (5.14), but that is the theoretical prediction when $q_{\parallel}$ is fixed—which is not assumed in equation (21.14).

One thus also anticipates the *tendency* for the relation to hold:

$$\lambda_{\Gamma t} \equiv \lambda_{I_{\mathrm{sat},t}^{+}} \approx 1.4\lambda_{n_u} \tag{21.15}$$

a relation also reported from comparisons of the two-point model with 2D code results [21.16, 21.17]. Thus in the C-L regime the relations between the radial scale lengths are anticipated to have a *rough tendency* toward:

$$\lambda_{q\parallel} \approx \tfrac{2}{7}\lambda_{T_u} \tag{21.16}$$

$$\lambda_{q\parallel t} \approx \lambda_{q\parallel u} \tag{21.17}$$

$$\lambda_{T_t} \approx \infty \tag{21.18}$$

$$\lambda_{\Gamma_t} \approx \lambda_{q\parallel} \tag{21.19}$$

$$\lambda_{n_u} \approx \tfrac{2}{5}\lambda_{T_u} \tag{21.20}$$

$$\lambda_{n_u} \approx \tfrac{5}{7}\lambda_{q\parallel} \tag{21.21}$$

$$\lambda_{\Gamma_t} \approx \tfrac{7}{5}\lambda_{n_u}. \tag{21.22}$$

The caveats mentioned in connection with the ratio $\lambda_{n_u}/\lambda_{T_u}$ apply to all of these relations: only a rough tendency is likely to exist and numerous exceptions can be anticipated.

References

[21.1] McCormick K, Asakura N, Bosch S *et al* 1999 *J. Nucl. Mater.* **266–269** 99
[21.2] LaBombard B, Goetz J A, Hutchinson I H *et al* 1997 *J. Nucl. Mater.* **241–243** 149
[21.3] Erents S K and Stangeby P C 1998 *Nucl. Fusion* **38** 1209
[21.4] Loarte A, Bosch S, Chankin A *et al* 1999 *J. Nucl. Mater.* **266–269** 587
[21.5] Wesson J 1997 Tokamaks 2nd edn (Oxford: Oxford University Press) p 175
[21.6] Porter G D, Davies S, LaBombard B *et al* 1999 *J. Nucl. Mater.* **266–269** 917
[21.7] Porter G D and the DIII-D Team 1998 *Phys. of Plasmas* **5** 4311
[21.8] Umansky M V and LaBombard B 1999 *J. Nucl. Mater.* **266–269** 721
[21.9] Itoh S I and Itoh K 1994 *Plasma Phys. Control. Fusion* **36** 1845
[21.10] Connor J W, Counsell G, Erents S K *et al* 1999 *Nucl. Fusion* **39** 169
[21.11] Counsell G F, Connor J W, Erents S K *et al* 1999 *J. Nucl. Mater.* **266–269** 91
[21.12] Erents S K, Stangeby P C, LaBombard B *et al Nucl. Fusion* at press
[21.13] Asakura N, Koide Y, Itami K *et al* 1997 *J. Nucl. Mater.* **241–243** 559
[21.14] Sakurai S, Asakura N, Hosogane N *et al* 1999 *J. Nucl. Mater.* **266–269** 1191
[21.15] Schweinzer J, Sandmann W, Haas G *et al* 1999 *J. Nucl. Mater.* **266–269** 934
[21.16] Maddison G P, Stangeby P C, Pitcher C S 1996 *Int. Workshop on Theory of Fusion Plasmas (Varenna)*
[21.17] Maddison G P and Stangeby P C to be published

Chapter 22

MARFEs

22.1 Experimental Observations

A tokamak *density limit* associated with a *disruption* of the plasma current (or, if an H-mode is involved, transition back to L-mode), occurs when $\overline{n}_e$ is raised above a critical level, $\overline{n}_{\mathrm{DL}}$ [22.1]. Measurements of $\overline{n}_{\mathrm{DL}}$ from a number of tokamaks have been found to be well described by the empirical *Hugill diagram* and the *Greenwald Limit* [22.2]:

$$\rho_{\mathrm{DL}}^{\mathrm{GW}} \approx 1 \tag{22.1}$$

where

$$\rho \equiv \frac{\overline{n}_e}{I_p/\pi a^2} \tag{22.2}$$

with $\overline{n}_e$ [10^{20} m^{-3}], I_p [MA], a [m]. The physical basis for the density limit is not entirely understood, and quite different density-limiting processes appear to be controlling, depending on operating conditions—auxiliary heating, pumping, safety factor, pellet fuelling, etc [22.3, 22.4]. Some of these processes are essentially edge phenomena [22.5], while others primarily involve the main plasma, e.g., the effect of impurity radiation on power balance, leading to a contraction of the current channel due to thermal collapse radially [22.1]. We do not consider further here this very important, but complex, matter.

At somewhat lower values of ρ, MARFEs often form. The density threshold for MARFE formation is found to be in the range [22.6]:

$$\rho_{\mathrm{MARFE}} \approx 0.4\text{–}0.9. \tag{22.3}$$

A MARFE is a toroidally symmetric belt of intense radiation typically appearing near the inside wall of a tokamak, figure 22.1. 'MARFE' is an acronym for multifaceted asymmetric radiation from the edge. It is asymmetric *poloidally* and is usually quite localized. It is thus distinct from the poloidally uniform *radiating mantle*, chapter 23. It is also localized *radially*, existing in the SOL and just inside the LCFS. The MARFE is cold, $T_e \approx$ a few eV, and dense, $n_e \geq \overline{n}_e$, and

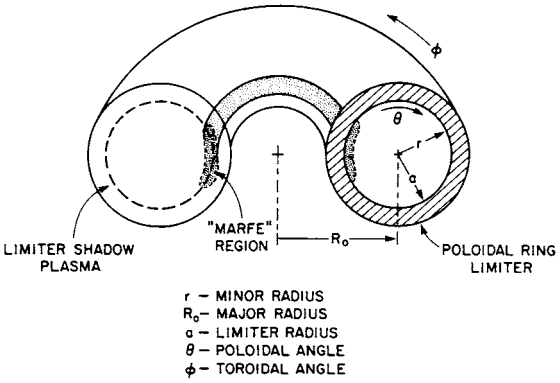

Figure 22.1. Illustration of the toroidal nature of the MARFE. The poloidal ring limiter radial extent is indicated by the cross-hatched area [22.6].

Table 22.1. Conditions for occurrence of MARFEs and disruptions on various tokamaks [22.6].

Machine	R (m)	A (m)	B_ϕ (T)	κ	$\rho = \frac{\pi a^2 \bar{n}_e}{I_p}$ (10^{20} MA^{-1} m^{-1}) MARFE	Disruption	Comment[a]
ALC-C	0.64	0.165	6–10	1	0.5 ± 0.05	1	1
	0.577	0.1	8	1	0.5 ± 0.05		1
	0.705	0.1	8	1	0.5 ± 0.05		1
	0.64	0.165	8	1	0.5 ± 0.05		1
	0.64	0.165	8	1	0.75 ± 0.05	1	1,2
ASDEX	1.65	0.4	2.2	1	0.7 ± 0.05	1	1,3
	1.65	0.4	2.2	1	0.85 ± 0.05	1.5	1,3,4
D-III	1.4	0.4	2	1	0.45	0.75	1
	1.4	0.4	2	1.4	0.32		1
DITE	1.17	0.26	2.7	1	0.55	0.6	1
	1.17	0.26	2.7	1	0.55	1	1
FT	0.83	0.2	6–8	1	0.75 ± 0.05	1	5
JET	2.96	1.25	2.5–3.4	1.2–1.6	0.55–0.3	0.7–0.5	1,5
TFTR	2.5	0.82	4	1	0.4 ± 0.05	0.7	1
	2.5	0.82	4	1	0.8 ± 0.05	1.0	1

[a] Comments: 1—constant plasma current; 2—pellets; 3—diverted; 4—neutral beam injection; 5—falling plasma current.

can radiate a significant fraction of the power reaching the edge. The MARFE appears often to be a precursor to the density limit disruption. When the cold, radiating region penetrates sufficiently far into the main plasma to reach the $q = 2$ surface it may precipitate MHD instability and disruption.

The radiation for the MARFE is typically hydrogenic and from low—but

not the lowest—impurity charge states, e.g. CIII, thus confirming that T_e is low in the MARFE. The radiation is generally from low Z elements, C typically, which radiate most strongly at low T_e, figure 3.21.

MARFE thresholds for several tokamaks are given in table 22.1 [22.6]. While the scaling of $\overline{n}_e^{\text{MARFE}}$ goes primarily as $I_p/\pi a^2$, the threshold is raised somewhat with pellet injection and with neutral beam heating. The threshold density is also lowered somewhat by injection of impurities [22.7].

22.2 Modelling MARFEs

The basic cause of MARFEs is thought to be *radiation thermal instability*. The radiative power loss rate coefficient $L_z(T_e)$ is a strong function of T_e, see figure 3.21; $L_z \equiv P_{\text{rad}}/n_e n_z$. One may also note that for low Z elements, radiation power increases with decreasing T_e, at the low values of T_e at the edge, i.e. $\mathrm{d}L_z/\mathrm{d}T_e < 0$. For carbon, for example, the 'coronal' values of L_z increase by several orders of magnitude when T_e decreases from ~30 eV to ~10 eV; 'non-coronal' effects reduce this temperature sensitivity, figure 3.20. If for any reason the temperature decreases in some region, then P_{rad} will increase, thus tending to cause a further decline in T_e. At the same time the heat transport into the radiating zone will increase and, if the transport is strong enough, the drop in T_e will stabilize at a slightly lower value. At low temperatures, as is characteristic of the edge plasma, the electron parallel heat conduction is weak, $K_\parallel \propto T^{5/2}$, and assuming conduction is the primary heat transport mechanism, a thermal collapse to quite low temperatures will occur.

The collapse is contributed to further because of parallel pressure conservation: as T drops in the radiation zone, the plasma density n_e rises, thus further increasing P_{rad}. If we assume a constant impurity fraction $\alpha_z \equiv n_z/n_e$, then P_{rad} will increase still faster with decreasing T. This effect—a MARFE—is more generally termed a *radiative condensation*.

If $L_z(T_e)$ does not increase indefinitely as T_e decreases, the temperature in the MARFE will finally stabilize at a quite low value, a few eV, possibly low enough for volume recombination also to occur. Since recombination rates are a strongly increasing function of density, the high density in a MARFE increases the likelihood of this process. The enhanced recycling that results adds to radiative power loss.

We may gain some further insight into MARFE behaviour by considering a quite idealized situation where only parallel electron heat conduction occurs and the impurity fraction α_z is a constant. We will ignore hydrogenic radiation. Consider a flux tube of length L which may be inside or outside the LCFS. We assume the heat enters the flux tube uniformly over its length L and is entirely radiated in a MARFE extending over a length L_m, at one end of the flux tube, figure 22.2. We assume for simplicity that L_m scales with L, i.e. $L_m/L \equiv f_m$, a constant. We will characterize the plasma conditions in the flux tube by the

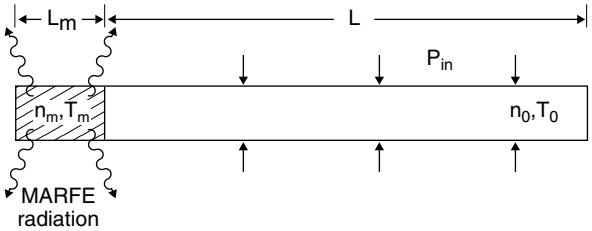

Figure 22.2. A simple model of a MARFE. A flux tube of length L is hot at one end, temperature T_0, and cold at the other end, $T_m \ll T_0$, with $n_m \gg n_0$ due to pressure balance. The conditions at the cold end are such as to result in strong hydrogenic and impurity radiation which, together with the finite parallel heat conductivity, sustains the strong T-variation.

density, n_0, and temperature, T_0, at the opposite end from the MARFE. We take $T_e = T_i = T$. If the flux tube is inside the LCFS then L is half the total circumference of the tube; in the SOL, L is approximately the connection length. T_m is the temperature in the MARFE. Thus, from section 4.10.1 power balance gives:

$$\tfrac{4}{7}\kappa_0(T_0^{7/2} - T_m^{7/2})/L = \alpha_z n_m^2 L_z(T_m) L_m. \tag{22.4}$$

We will also assume here that there is no particle flow along the flux tube, no recombination, no friction, etc, and that pressure balance gives:

$$n_m T_m = n_0 T_0. \tag{22.5}$$

One can combine equations (22.4) and (22.5) to find $T_m(n_0)$ and $n_m(n_0)$, with L, T_0, α_z, f_m and the radiating species being specified as control parameters. There are three solutions in general. As can be seen from figure 3.20, for $T_e \geq 30$ eV, L_z is very small (for coronal equilibrium radiation). Therefore, providing $T_0 \geq 30$ eV, and provided $\alpha_z f_m L^2 n_m^2$ is not extremely large, then one solution is the *weak radiation* i.e. non-MARFE, solution with $T_m \approx T_0$ and $n_m \approx n_0$.

We turn then to the more interesting cases where $T_m \ll T_0$, which permits neglect of the $T_m^{7/2}$ term in equation (22.4), and in combination with equation (22.5) gives:

$$\frac{L_z(T_m)}{T_m^2} = \frac{4\kappa_0}{7\alpha_z f_m}\frac{T_0^{3/2}}{L^2 n_0^2}. \tag{22.6}$$

$L_z(T_m)/T_m^2$ is plotted in figure 22.3, using L_z for carbon for coronal equilibrium, figure 3.20. As can be seen, L_z/T_m^2 has a maximum which occurs at $T \approx 4$ eV. Therefore, the RHS of equation (22.6) must not exceed a certain threshold if a *strongly radiating* solution, i.e. a MARFE, is to be possible. For a specified L and T_0 this means that a MARFE can only exist for values of n_0 greater than a critical value given by equation (22.6) and by the maximum value of L_z/T_m^2,

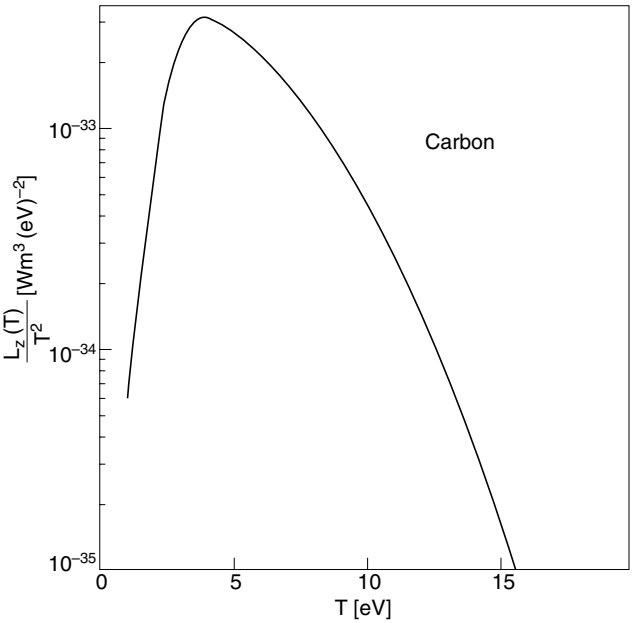

Figure 22.3. Plot of $L_z(T)/T^2$ against T, where L_z is the electron radiative cooling function for carbon, section 3.5. $L_z \equiv P_{\text{rad}}/n_e n_z$.

which for coronal C is $\approx 3 \times 10^{-33}$ [W m^3 (eV)$^{-2}$]. This finding would therefore broadly accord with the experimental observation of the existence of a MARFE density threshold. For n_0 exceeding the threshold, there are two solutions: one with $T_m \geq 4$ eV, and one with $T_m \leq 4$ eV. We will show below that the higher temperature solution is usually unstable to temperature collapse.

For illustration, figures 22.4 and 22.5 give $T_m(n_0)$ and $n_m(n_0)$ for the specific example of $T_0 = 50$ eV, $L = 50$ m, $\alpha_z = 0.03$ and $f_m = 0.01$. For completeness the weakly radiating solutions are also shown. The calculated values of P_{rad} are of order 10^7 W m^{-3}, which are approximately as observed in experiment [22.7]. For these parameters the critical value of n_0, n_0^{crit}, is $\approx 1.3 \times 10^{19}$ m^{-3}. For $n_0 < n_0^{\text{crit}}$, only the weakly radiating solution is possible. For $n_0 > n_0^{\text{crit}}$ there are two *equilibrium* solutions which are strongly radiating. We next consider the *stability* of these two solutions.

Consider a negative perturbation to T_m. For the colder solution, this causes P_{rad} to decrease and at the same time the heat conducted into the MARFE increases. Therefore T_m rises and this solution is seen to be stable. For the hotter, strongly radiating, solution a decrease in T_m causes both P_{rad} and the conducted heat flux to increase. This solution will be stable if the heat conduction increases faster than P_{rad}, otherwise it is unstable. Introduce a small perturbation δT_m to

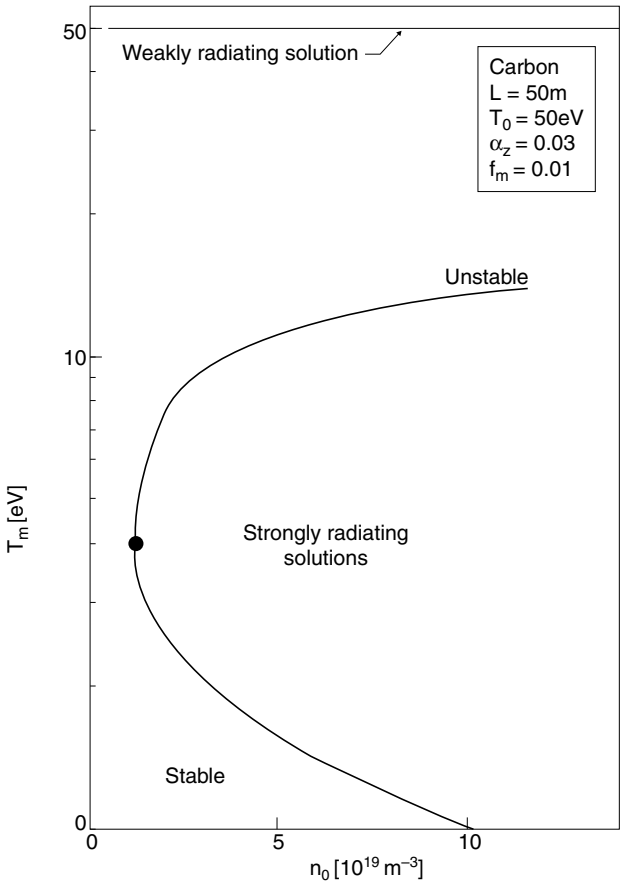

Figure 22.4. Results of the simple MARFE model of section 22.2 giving the temperature in the MARFE, T_m, against the density in the flux tube far from the MARFE, n_0. For the particular parameters shown. There are two stable solutions and one unstable one. The coldest, strongly radiating solution is stable—the MARFE solution.

equation (22.4). Instability occurs when:

$$\alpha_z f_m n_m^2 L^2 [L_z(T_m - \delta T_m) - L_z(T_m)] > \tfrac{4}{7}\kappa_0 [T_0^{7/2} - (T_m - \delta T_m)^{7/2}] - \tfrac{4}{7}\kappa_0 [T_0^{7/2} - T_m^{7/2}]. \tag{22.7}$$

This gives:

$$\frac{\mathrm{d}L_z(T_m)}{\mathrm{d}T_m} < -\frac{2\kappa_0 T_m^{5/2}}{e\alpha_z f_m n_m^2 L^2} \tag{22.8}$$

L_z [W m^3], T [eV], n [m^{-3}], L [m]. Again we see that the colder solution, where $\mathrm{d}L_z/\mathrm{d}T > 0$, is stable. The hotter, strongly radiating, solution is also stable if α_z

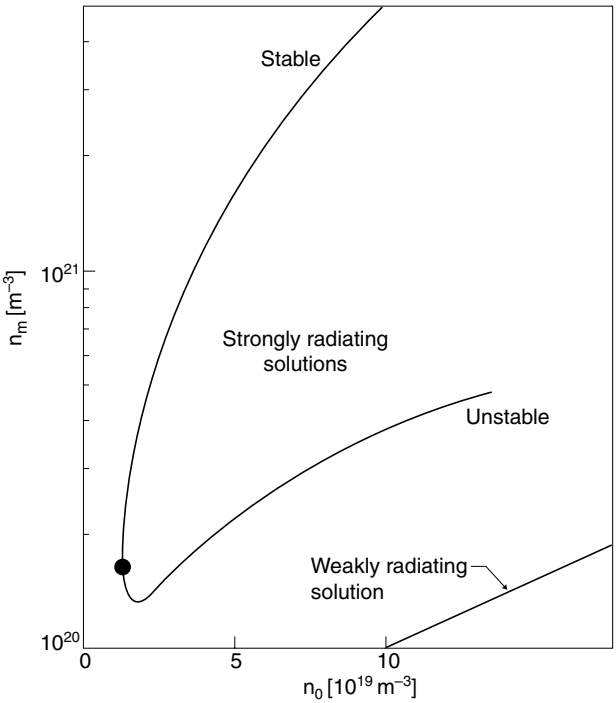

Figure 22.5. Results of a simple MARFE model of section 22.2 giving the plasma density in the MARFE, n_m, against the density in the flux tube far from the MARFE, n_0. There are two stable solutions and one unstable solution. The highest density, most strongly radiating solution is stable—the MARFE solution.

is very small or L extremely short, etc—but typically this solution is not stable. It is readily shown for the foregoing example that the inequality (22.8) is satisfied by a large margin for all T_m values of interest, $T_m \leq 20$ eV, i.e. for cases that are actually strongly radiating.

We may calculate n_0^{crit} from equation (22.6) using $[L_z(T_m)/T_m^2]_{\max} \approx 3 \times 10^{-33}$ [W m^3 (eV)$^{-2}$] $\approx 1.2 \times 10^5$ [m^3 J^{-1}]:

$$n_0^{\text{crit}} = \left[\frac{4\kappa_0 T_0^{3/2}}{7e^2\alpha_z f_m L^2 [L_z(T_m)/T_m^2]_{\max}}\right]^{1/2} \tag{22.9}$$

for n [m^{-3}], T [eV], L [m], L_z/T^2 [m^3 J^{-1}]. We may replace L with plasma current I_p by using $L = \pi Rq$, $q = aB_\phi/RB_\theta$ and $B_\theta = \mu_0 I_p/2\pi a$, section 1.3, to obtain:

$$n_0^{\text{crit}} = \frac{I_p}{\pi a^2}\frac{1}{B_\phi}\left[\frac{\mu_0\kappa_0 T_0^{3/2}}{7\pi^2 e^2\alpha_z f_m [L_z/T^2]_{\max}}\right]^{1/2} \tag{22.10}$$

I [A], B [T], all else as before. We may note that *some* of the experimental observations concerning the MARFE threshold are in accord with this very simple model, namely:

(a) $n_0^{\text{crit}} \propto I_p/\pi a^2$;
(b) n_0^{crit} is somewhat reduced by the addition of extra impurities; equation (22.10) gives $n_0^{\text{crit}} \propto \alpha_z^{-1/2}$.

It is also evident, however, that this model must be too simple since it predicts the dependence $n_0^{\text{crit}} \propto B_\phi^{-1}$ which is not observed. We do not have to look far to identify neglected effects and unjustified assumptions:

(a) perpendicular heat conduction has been neglected;
(b) perpendicular and parallel heat convection have been neglected. At the low temperature of the MARFE, neglect of convection is particularly serious;
(c) equation (22.10) has no predictive capability so long as T_0 is a free parameter. All we can extract from the present analysis is that T_0 cannot be much greater than ~100 eV, for values of n_0 and L of interest, if MARFE formation is to be possible. Thus one only expects to find MARFEs near the edge;
(d) the assumption that α_z and f_m are constants is unjustified;
(e) the value of n_0^{crit} relates to a density near the edge, which is not generally identical to $\overline{n}_e$, chapter 19;
(f) hydrogenic radiation has been neglected, although it can be a major contributer to measured P_{rad} from MARFEs [22.8]; power consumption due to strong, localized hydrogenic recycling at the MARFE may play an important role [22.5];
(g) pressure balance along the MARFE's flux tube could be substantially affected by volume recombination and ion–neutral friction, etc.

The foregoing model is therefore presented merely for illustration of the principles that are involved in MARFE analysis. Nevertheless, if we use the foregoing example values of α_z, etc, equation (22.10) gives:

$$n_0^{\text{crit}} \approx 1.3 \frac{I_p}{\pi a^2} \frac{1}{B_\phi} \tag{22.11}$$

n [10^{20} m^{-3}], I [MA], a [m], B [T]. For B_ϕ of a few T, equation (22.11) is seen to be in reasonable agreement with the measured values of ρ_{MARFE}, section 22.1.

A satisfactory model to explain ρ_{MARFE}—and ρ_{DL} also—remains outstanding. Strong temperature-gradient forces (parallel to the magnetic field) exist at the MARFE, resulting in strong forces on the impurity ions acting in the direction away from the MARFE, section 6.4. It is therefore not immediately obvious how the MARFE remains intact. A convincing picture of the particle, momentum and energy balances of a MARFE emerges from a B2 multifluid (D ions plus C ions) code analysis carried out for ASDEX-U single-null divertor geometry [22.9], figure 22.6. The high plasma density at the MARFE, associated with the low

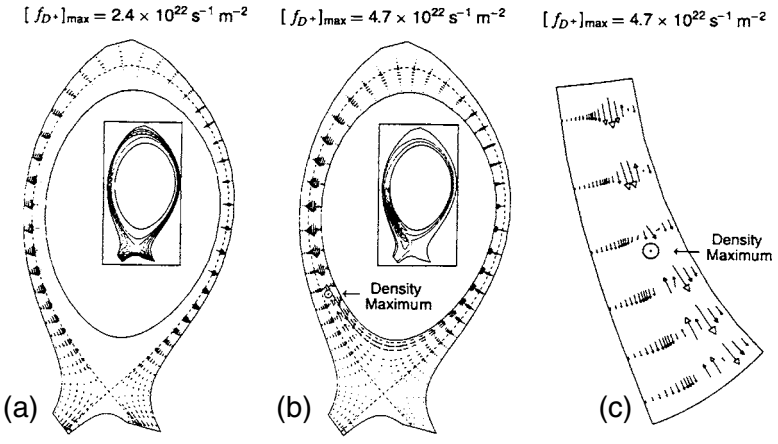

Figure 22.6. [22.9]. Flow patterns in the boundary of AUG as predicted by the B2 code for: (a) a normal high recycling discharge; (b) a high density MARFE discharge. A close-up in the vicinity of the MARFE is provided in (c).

temperature there, causes strong cross-field particle loss to the adjacent flux tubes. This cross-field flow of D^+ ions induces parallel inflows of plasma, into the MARFE. This parallel flow provides the frictional force on the impurity ions required to balance the parallel temperature-gradient force which, by itself, would act to expel the impurity ions from the MARFE.

The code analysis (22.9) allowed for volume recombination, but in fact the computed temperatures never fell low enough, $\leq$1 eV, for this to be an important effect. Experimental measurements on CMOD [22.8], however, found $T_e = 0.7$–1.0 eV and $n_e = (2\text{–}3) \times 10^{21}\ m^{-3}$ in MARFEs, together with direct spectroscopic evidence for strong hydrogenic recombination radiation. Recombination in MARFEs has also been observed in TEXTOR [22.10]. When volume recombination in a MARFE is strong then the flow recirculation pattern shown in figure 22.6 would be enhanced by *neutral* cross-field flows out of the MARFE. While the simple model developed above gives a MARFE with, for example $T_m = 1$ eV and $n_m = 5 \times 10^{21}\ m^{-3}$, this must be somewhat fortuitous since recombination radiation and all hydrogenic radiation were neglected.

Note that the MARFE shown in figure 22.6 is the 'classical' type, appearing near the inside wall and inside the LCFS.

The tendency for MARFE formation to favour the inner—rather than outer—edge region is presumably due to the fact that heat outflow from the central plasma is strongest on the outside of a tokamak, section 5.9. The latter fact is most evident from studies of double-null divertor configurations, e.g. ASDEX, where the inner and outer SOLs were completely separated. In single-null divertors, the total power transported along the SOL into the inner and outer divertor 'legs' is ap-

proximately equal, due to the strong parallel heat conductivity—but nevertheless, any region near the inside edge—whether inside or outside the LCFS—is more susceptible to radiative condensation and MARFE formation, since the (parallel) connection length to the effective source location at the outside is greater. Since an instability is involved in a MARFE, it may not require very much asymmetry between inside and outside to trigger a MARFE at the inside.

In summary, the defining characteristics of MARFEs are:

(a) a toroidally symmetric, poloidally localized, strongly radiating region;
(b) n_e is high, T_e low in the MARFE;
(c) a thermal instability, a radiation condensation, is involved.

22.3 Divertor MARFEs

Much of the analysis in the last section carries over to the modelling of a strongly radiating divertor, i.e. where the targets provide additional power sinks. The same tendency to radiative condensation occurs, although the general practice is not to call the strongly radiating regions immediately in front of ('anchored to') the targets 'MARFEs', but to reserve that term for situations where the radiation zone is 'floating away' from solid surfaces. The tendency for divertor radiation to be stronger at the inside than the outside, section 5.9, appears to be due to the same reason as MARFE formation favouring the inside. As $\overline{n}_e$ is raised, the divertor configuration would seem to be a natural one for 'spawning' MARFEs: once the radiating region constitutes a stronger energy sink than the target, the 'anchor' to the target is weakened or lost, and the radiative condensation region might now be expected to 'float off' as a MARFE. Such conjectures are broadly in accord with observation. The general evolution is that, as density is raised, the divertor first detaches—usually at the inside—and then with further increase of density a MARFE forms [22.11–22.13].

Figure 22.7 gives the line-integrated radiated power in the JT-60 tokamak looking at the divertor from above for various values of $\overline{n}_e$ and ~11 MW of neutral beam injection, NBI, heating [22.11]. At low $\overline{n}_e$ (earliest times in these shots), two identifiable radiation peaks appear corresponding approximately to the two strike points (separatrices) on the graphite targets. For high $\overline{n}_e$ (later time in the shots) the two radiation peaks coalesce to form a single peak in the vicinity of the X-point. Measurements from other views confirm that the radiation region slips vertically away from the plates as $\overline{n}_e$ is raised and moves towards the X-point, or above it, where the radiation stabilizes. Similar results have been reported from DIII-D [22.12, 22.13], and other divertor tokamaks [22.14]. It is found that essentially 100% of the power that flows into the SOL can be radiated at or near the divertor at the highest $\overline{n}_e$; figure 22.8 [22.15] shows this for the CMOD tokamak. These regions are referred to as 'X-point MARFEs', or as 'divertor MARFEs' (appearing between the X-point and the outer strike point). Whether such regions are truly 'MARFEs' might be questioned; it is not clear that thermal

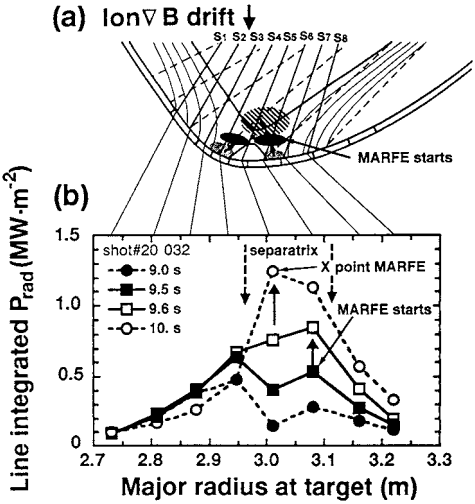

Figure 22.7. [22.11]. The horizontal chord-averaged radiation distribution in JT-60U at four densities as viewed from above. Density increases with time. An X-point MARFE has clearly formed at 10 s.

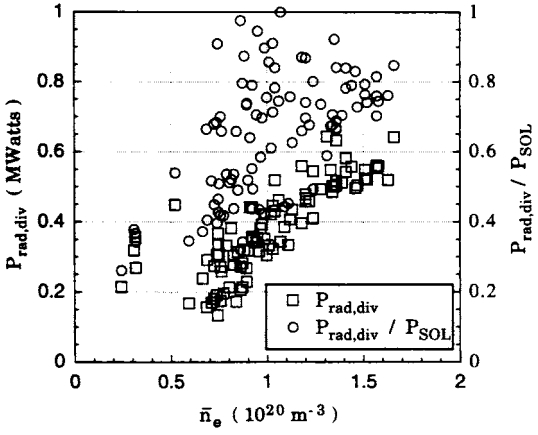

Figure 22.8. CMOD [22.15]. Radiated power in the divertor region (□) is plotted versus $\overline{n}_e$: $P_{\mathrm{RAD,div}}/P_{\mathrm{SOL}}$, the fraction of the power flowing in the SOL which is radiated, is plotted as well (○).

instability is involved in the same way as for 'classical' MARFEs. Modelling indicates that chemical sputtering of carbon is central to the formation of this type of MARFE [22.16–22.18].

It has thus been demonstrated that a *radiating divertor solution* can be achieved—although the fact that much of the radiation power does not occur within the divertor 'legs' themselves raises an important issue about the divertor design: does one need long divertor legs, which have large volumes, in order to radiate away the power reaching the edge? Such divertor designs are very expensive since they use up valuable space inside the magnetic field coils which could otherwise be used to contain more hot, fusion-producing plasma. Some divertor designs call for such configurations, but, if it turns out that the radiation zone will always coalesce into a compact MARFE at or near the X-point, a large divertor volume may not be needed or justified.

It is also a concern that the MARFE often ends up inside the confined plasma, where its cooling effect may MHD-destabilize the confined plasma and be a contributing factor in the density limit process.

References

[22.1] Wesson J 1997 *Tokamaks* 2nd edn (Oxford: Oxford University Press) p 353
[22.2] Wesson J 1997 *Tokamaks* 2nd edn (Oxford: Oxford University Press) p 631
[22.3] Maingi R, Mahdavi M A, Jernigan T C *et al* 1997 *Phys. Plasmas* **4** 1752
[22.4] Maingi R, Mahdavi M A, Petrie T W *et al* 1999 *J. Nucl. Mater.* **266–269** 598
[22.5] Borrass K, Schneider R and Farengo R 1997 *Nucl. Fusion* **37** 523
[22.6] Lipschultz B 1987 *J. Nucl. Mater.* **145–147** 15
[22.7] Lipschultz B, LaBombard B, Marmar E S *et al* 1984 *Nucl. Fusion* **24** 977
[22.8] Lipschultz B, Terry J L, Boswell C *et al* 1998 *Phys. Rev. Lett.* **81** 1007
[22.9] Kastelewicz H, Schneider R and Neuhauser J 1995 *Plasma Phys. Control. Fusion* **37** 723
[22.10] Samm U, Brix M, Durodie F *et al* 1999 *J. Nucl. Mater.* **266–269** 666
[22.11] Asakura N, Hosogane H, Tsuji-iio S *et al* 1996 *Nucl. Fusion* **36** 795
[22.12] Petrie T W, Hill D N, Allen S L *et al* 1997 *Nucl. Fusion* **37** 321
[22.13] Petrie T W, Maingi R, Allen S L *et al* 1997 *Nucl. Fusion* **37** 643
[22.14] Pitcher C S and Stangeby P C 1997 *Plasma Phys. Control. Fusion* **39** 779 p 815
[22.15] Lipschultz B, Goetz J, LaBombard B *et al* 1995 *J. Nucl. Mater.* **220–222** 50
[22.16] Shimizu K, Hosogane N, Takizuka T *et al* 1994 *15th IAEA* 431
[22.17] Shimizu K, Takizuka T and Sakasai A 1997 *J. Nucl. Mater.* **241–243** 167
[22.18] Fenstermacher M E, Allen S L and Brooks N H 1997 *Phys. Plasmas* **4** 1761

Chapter 23

The Radiating Plasma Mantle

High Z impurities retain some of the orbital electrons even at the highest temperatures in the centre of fusion plasmas, and therefore strongly radiate in such conditions, cooling the plasma and reducing fusion reactivity. Low Z impurities only radiate significantly at the lower temperatures near the edge. They may therefore be compatible with an attractive power removal option—the *radiating cold plasma mantle*—[23.1]. In this regime, the energy confinement across most of the radius of the main plasma would still be achieved by the effect of a magnetic field in reducing convection and conduction. Therefore the overall energy confinement time would be the same, regardless of how the power reaching the edge was finally dissipated. By dispersing this exhaust power via a poloidally and toroidally thin radiation layer near the LCFS, however, considerable advantages could be realized compared with exhaust through plasma-wetted surfaces: (a) the plasma contacting the solid surfaces could be made quite cold, reducing or eliminating sputtering, (b) the power could be deposited approximately uniformly over the entire wall area of the containment vessel—perhaps of the order of 10^3 m^2 for a reactor—rather than in small plasma-wetted areas, thereby greatly easing the practical problems of power transfer to coolants without melting damage.

These same benefits can, in principle, attend power removal by a strong MARFE, chapter 22; however: (a) the radiation power is then less uniformly distributed over the walls, (b) the MARFE may be more destabilizing than a uniform radiative edge—although the latter can also be de-stabilizing, and has been associated with the density limit disruption [23.2].

An early demonstration of the cold radiating mantle was reported for the ISX-B tokamak with neon puffing and neutral beam heating [23.3]. An unanticipated *improvement* in energy confinement time τ_E was found in these so-called *Z-mode discharges*. In the absence of auxiliary heating, experiments on the JET [23.4], TFTR [23.5], DITE [23.6] and TEXTOR [23.7] tokamaks showed that by increasing $\overline{n}_e$, a cold radiating mantle could be produced even without injection of extrinsic impurities. This was accompanied by a state termed *limiter detachment* where the plasma density and temperature at the LCFS—and also

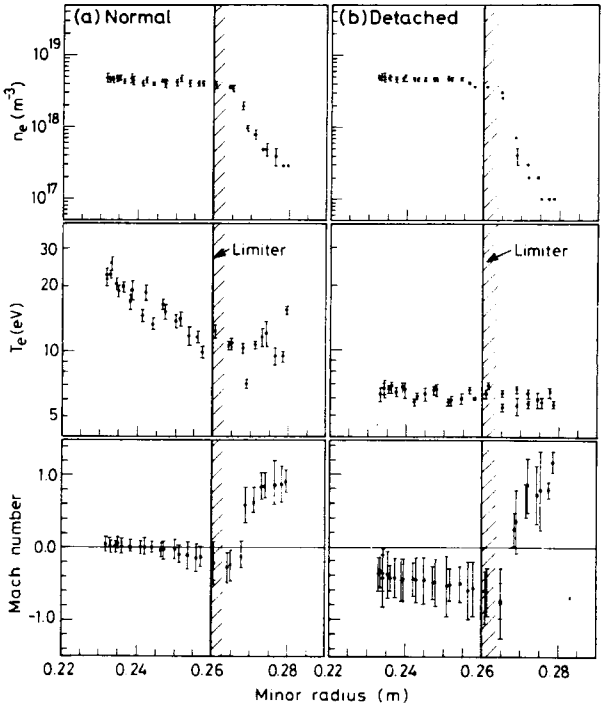

Figure 23.1. DITE tokamak [23.6]. Plasma edge profiles for normal and detached discharges (discharge (a), 100 kA and discharge (b), 130 kA). Measurements made at 450 ms at the top of the torus.

extending some distance inside the LCFS—remained at quite low levels. That is, plasma contact with the solid surfaces of the limiter was greatly reduced—analogously to the state of divertor detachment, chapter 16 [23.8]. Figure 23.1 shows radial profiles of $n_e(r)$ and $T_e(r)$ for such a detachment limiter state on DITE. While the reduction in limiter sputtering is a benefit of limiter detachment, it is not clear that this is a reactor-relevant mode of operation, since the weak limiter contact could make helium pumping inefficient.

The most extensive experimental investigation of the radiating plasma mantle was carried out on TEXTOR during the 1990s [23.9–23.12]—and using auxiliary heating and gas injection, typically of neon. The plasma temperature at the (limiter) LCFS remains fairly high, figure 23.2, even as the radiated fraction $\gamma \equiv P_{\text{rad}}/P_{\text{heat}}$ reaches as high as 95%. These limiter discharges are therefore not considered to be detached. Again, as with the ISX-B Z-mode, the energy confinement actually improves with γ, figure 23.3. Remarkably, the density limit is raised at the same time, with densities in the main plasma exceeding the

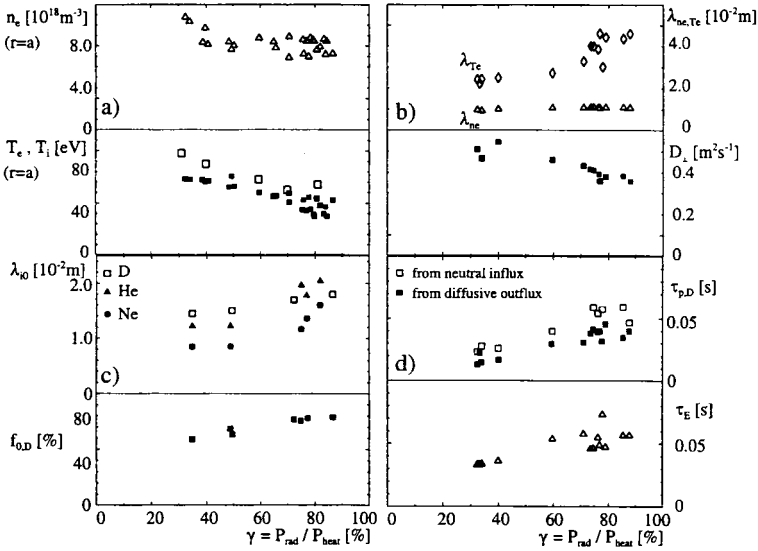

Figure 23.2. TEXTOR [23.9–23.12]. (a) Electron density n_e, electron temperature T_e and ion temperature T_i at the last closed flux surface plotted against radiation level γ ($I_p = 400$ kA, $\overline{n}_e = 0.9$–$1.0\ n_{GW}$, $P_{tot} = 2.2$–2.7 MW); (b) decay length λ of electron density and temperature in the scrape-off layer and diffusion coefficient $D_\perp$ at the LCFS plotted against radiation level γ; (c) penetration depth λ_{i0} of deuterium, helium and neon atoms into the confined plasma and fraction of ionization inside the LCFS f_0, D against radiation level γ; (d) particle confinement time of deuterium $\tau_{p,D}$ and energy confinement τ_E time against radiation level γ.

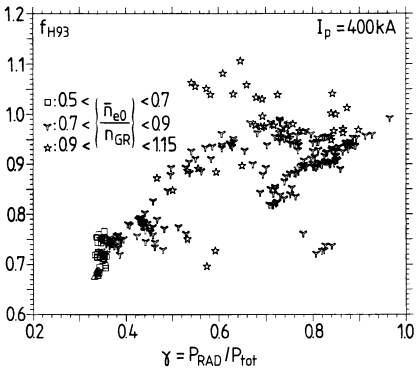

Figure 23.3. TEXTOR [23.9–23.12]. Values for the energy enhancement factor f_{H93} as a function of the radiated power fraction γ at a plasma current $I_p = 400$ kA. The corresponding values for the normalized density $\overline{n}_{e0}/\overline{n}_{e0,GR}$ are indicated, where $\overline{n}_{e0,GR}$ is the Greenwald density, equation (22.1).

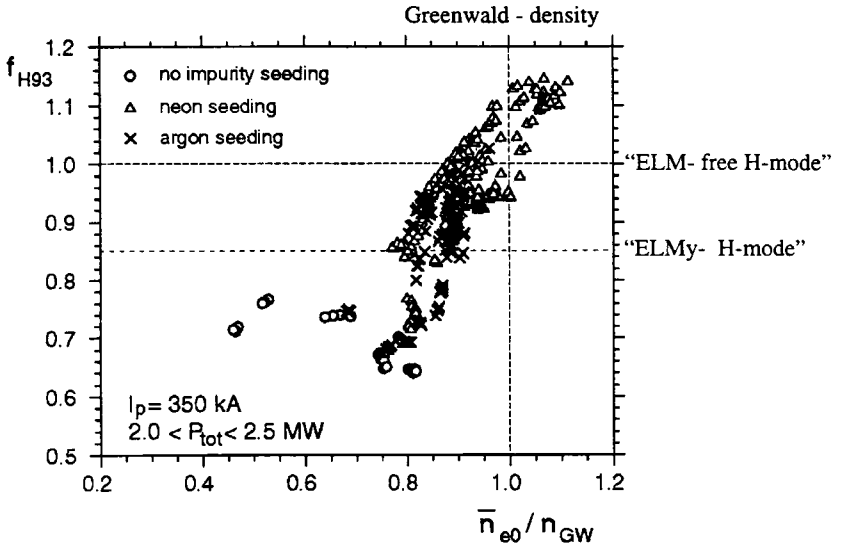

Figure 23.4. TEXTOR [23.9–23.12]. Enhancement factor f_{H93} with respect to the ITER93H-P scaling plotted against Greenwald number $\overline{n}_{e0}/\overline{n}_{\mathrm{GW}}$ at a plasma current of $I_p = 350$ kA for discharges with neon (open triangles)/argon (crosses) seeding and without additional impurity seeding (open circles).

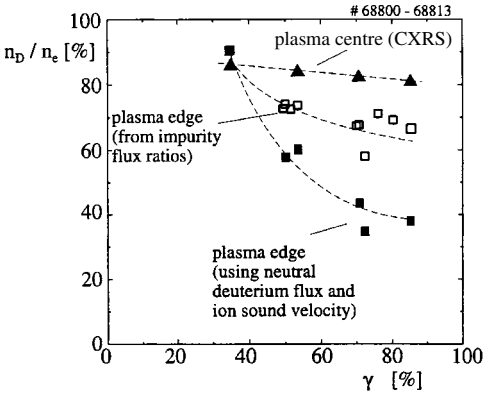

Figure 23.5. TEXTOR [23.9–23.12]. Deuterium concentration n_D/n_e in the plasma centre and at the plasma edge plotted against radiation level γ.

Greenwald limit, chapter 22, figure 23.4. It is also remarkable that the dilution caused by the injected impurities, while substantial at the edge—at the radiating mantle—is not substantial in the centre of the main plasma, figure 23.5. That is,

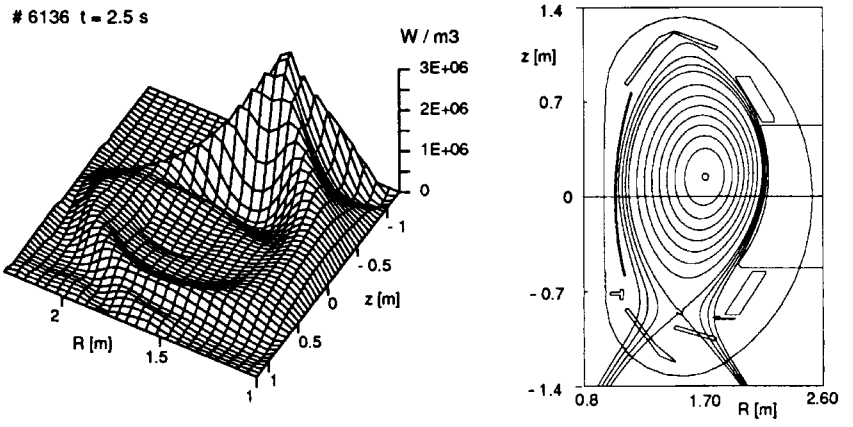

Figure 23.6. Distribution of the radiation emissivity obtained from bolometry (left) over the poloidal cross-section of ASDEX-Upgrade (right). Most of the radiation is concentrated near the separatrix and there is an absolute maximum close to the X-point (shot 6136, $t = 2.5$ s) [23.16].

the impurity level is high where it is wanted, in the mantle, but not where it would do harm, in the hot core of the main plasma. This promising mode of operation has been tested on other tokamaks such as DIII-D [23.13] and ASDEX-U [23.14–23.16], in both limiter and divertor configurations. See the review of multi-machine results in [23.17].

On ASDEX-U, operating with a divertor, this mode is called CDH-mode—for 'completely detached high confinement mode'. Neon and deuterium are puffed with careful feedback control into auxiliary heated discharges so as to achieve a rather precise radiation profile, see figure 23.6: about half the input power is radiated in an approximately uniform mantle inside the separatrix, while about the same fraction is radiated in the SOL and divertor. Very little power reaches the targets. It is necessary to keep the main plasma radiation level just below that where the H-mode will be lost ($H \rightarrow L$ transition), chapter 7. This not only achieves the standard H-mode good energy confinement, but the ELMs are the relatively harmless type-III ELMs, characteristic of operation just above the L–H transition rather than the damaging, high-power type-I ELMs, chapter 7. At the same time, since $P_{\mathrm{rad}}^{\mathrm{total}} \approx P_{in}$, the target power load is reduced to technically feasible values—the usual benefit of detachment, chapter 16. Figure 23.7 shows a schematic of the operating window for the CDH mode.

The benefits of these attractive regimes, based on substantial mantle radiation, have yet to be reproduced on large tokamaks, perhaps because the atomic physics scale lengths that are involved do not scale with machine size. Reactor relevance is therefore an issue.

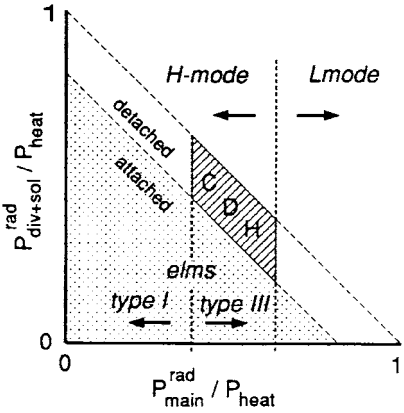

Figure 23.7. ASDEX-U. Schematic representation of the CDH regime in terms of radiated power inside the separatrix and power loss in the scrape-off layer plus divertor. The CDH mode requires a high total radiated power fraction to minimize the target load (divertor detachment), and radiation inside the separatrix adjusted such that the remaining power outflow is slightly above the H–L threshold (in order to obtain the type-III ELM regime) [23.16].

References

[23.1] Gibson A and Watkins M L 1977 *CF & PP, Proc. 8th EPS (Prague, 1977)* vol 1, 31
[23.2] Wesson J 1997 *Tokamaks* 2nd edn (Oxford: Oxford University Press) p 353
[23.3] Lazarus E A, Bell J D, Bush C E *et al* 1985 *Nucl. Fusion* **25** 135
[23.4] O'Rourke J, Campbell D, Denne B *et al* 1985 *Proc. 12th EPS Conf (Budapest, 1985)* vol 1 155
[23.5] Strachan J D, Moody F P, Bush C E *et al* 1985 *Proc. 12th EPS Conf (Budapest, 1985)* vol 1 339
[23.6] McCracken G M, Allen J, Axon K *et al* 1987 *J. Nucl. Mater.* **145–147** 181
[23.7] Samm U *et al* 1987 *KFA Juel Report* 2123
[23.8] Matthews G F 1995 *J. Nucl. Mater.* **220–222** 104
[23.9] Messiaen A M, Ongena J, Unterberg B *et al* 1997 *Phys. Plasmas* **4** 1690
[23.10] Unterberg B, Messiaen A M, Ongena J *et al* 1997 *Plasma Phys. Control. Fusion* B **39** 189
[23.11] Unterberg B, Brix M, Jaspers R *et al* 1999 *J. Nucl. Mater.* **266–269** 75
[23.12] Tokar M Z, Rapp J, Reiser D *et al* 1999 *J. Nucl. Mater.* **266–269** 958
[23.13] Jackson G L, Murakami M, Staebler G M *et al* 1999 *J. Nucl. Mater.* **266–269** 380
[23.14] Gruber O, Kallenbach A, Kaufmann M *et al* 1995 *Phys. Rev. Lett.* **74** 4217
[23.15] Kallenbach A, Dux R, Mertens V *et al* 1995 *Nucl. Fusion* **35** 1231
[23.16] Neuhauser J, Alexander M, Becker G *et al* 1995 *Plasma Phys. Control. Fusion* A **37** 37
[23.17] Ongena J, Messiaen A M, Unterberg B *et al* 1999 *Plasma Phys. Control. Fusion* A **41** 379

Chapter 24

Z_{eff}, P_{rad} and the Relation Between Them

With regard to the role of impurities in magnetically confined devices, the two 'bottom line' quantities of the greatest importance are the Z_{eff} in the core plasma and the radiated power, P_{rad}, which is usually dominated by impurities. These two quantities are therefore the best documented impurity quantities for confinement devices. We do not attempt a comprehensive survey of these data here, but instead review the results for a specific machine, JET, the most reactor-relevant device operated to date. The focus will also be on the *intrinsic* impurities, as being more fundamental than injected ones. As yet there are no significant data on the intrinsic He ash impurity (but only for injected He) and so it is the role of impurities produced from the edge structures that is considered here.

The fundamental questions are:

(a) Are there discernible correlations between Z_{eff} and P_{rad}, on the one hand, and the machine control parameters $\overline{n}_e$ and P_{in}, on the other?
(b) If so, can we understand and explain such correlations?
(c) Is there at least a correlation between Z_{eff} and P_{rad}?
(d) If so, can we understand and explain it?

Unfortunately, the answer to most of these questions may be 'no'.

Often it is found that the data scatter for Z_{eff} and P_{rad} is so large that it can be hard to discern correlations. In order to help to identify any patterns it can be useful to select data for very restricted sets of operating conditions. Figure 24.1(a) shows an example of Z_{eff} measurements made on JET for ELMy H-modes, Chapter 7, with P_{in} restricted to the range 10–14 MW, and with no wave-heating, I_p restricted to 2.4–2.7 MA and a restricted set of plasma shapes ('triangularity' $<$ 0.25) [24.1]. Two different divertor configurations were involved, Mk I and Mk II, and with either C or Be targets for the Mk I. Despite the tight restriction of control parameters the Z_{eff} values still show such a wide scatter as a function of $\overline{n}_e$ that it is difficult to discern trends. One trend which is just discernible is for Z_{eff} to decrease for the highest $\overline{n}_e$, a trend that has been widely seen in tokamaks [24.2], and is sometimes much clearer than here, see e.g. results for CMOD [24.3]. The

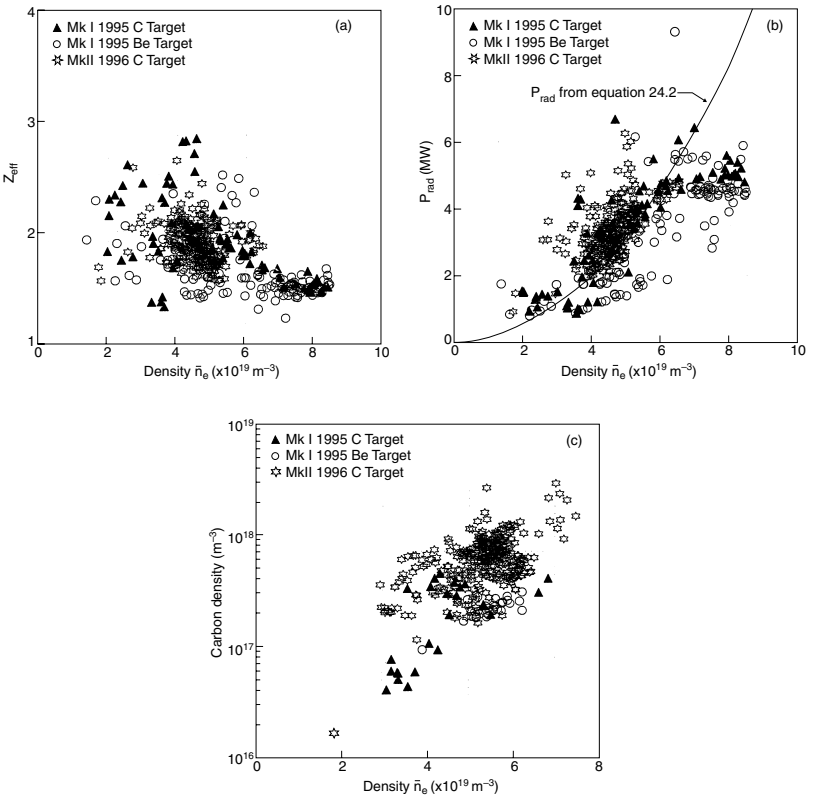

Figure 24.1. JET [24.1]. (a) Z_{eff} for different divertors, Mk IC, Mk IBe and Mk II, during ELMy H-mode campaigns, against core plasma density. Total input power P_T in the range 10–14 MW, with $2.4 < I_p < 2.7$ MA, triangularity $\delta < 0.25$ and no ICRH or LH heating. The target temperature in the Mk I divertor was ∼400 K and in the Mk II divertor it was 600 K. (b) P_{rad} dependence on core plasma density, $\overline{n}_e$. The solid curve represents the $\overline{n}_e$ result of equation (24.2). (c) Carbon density versus $\overline{n}_e$.

plot of P_{rad} against $\overline{n}_e$ for the same JET shots shows the same substantial scatter, figure 24.1(b). It was found on JET that even for Be divertor targets, C constitutes the main contributor to Z_{eff} and P_{rad}, perhaps indicating that the divertor targets are not the most important impurity source for the main plasma—although the Be targets had become contaminated with C. It is also not uncommon to find that C dominates Z_{eff} and P_{rad}, even in tokamaks which contain no graphite components; in CMOD, employing Mo plasma-facing components, before boronization, C was the largest contributor to Z_{eff} [24.3], presumably arising from C impurities in the Mo. Measurements of the central C density in JET for the same shots also show great scatter, figure 24.1(c).

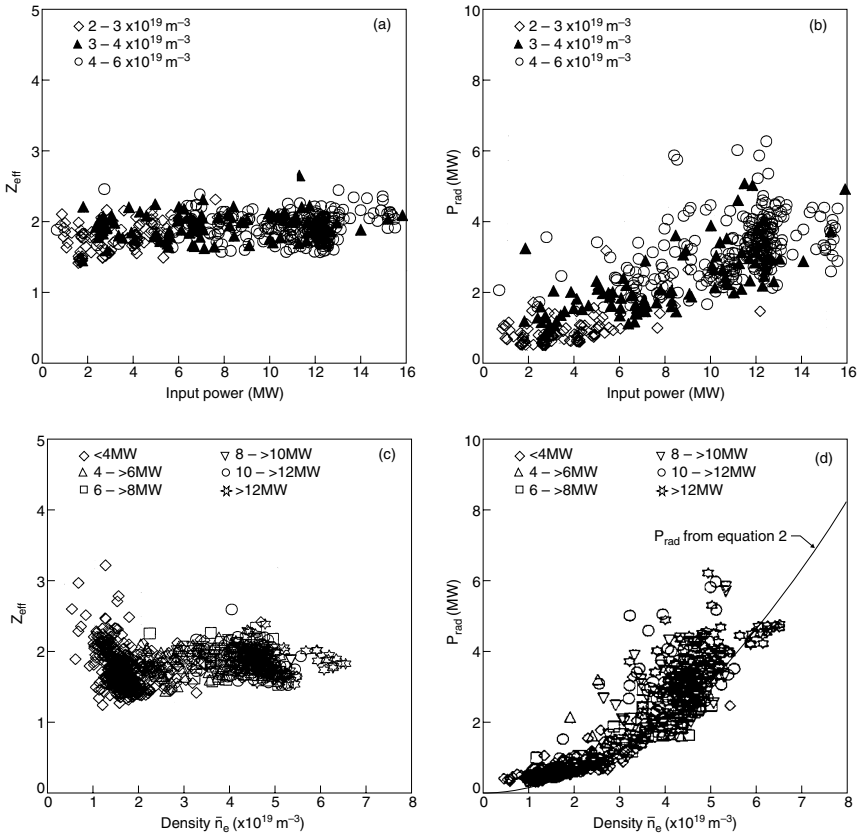

Figure 24.2. JET [24.1]. Parametric dependence of Z_{eff} and P_{rad} on total input power and core plasma density in JET Mk II diverted discharges, ELMy H-modes, with $2.4 < I_p < 2.7$ MA, ohmic and neutral beam heating only and triangularity $\delta < 0.25$: (a) dependence of Z_{eff} on input power for various densities, (b) dependence of P_{rad} on input power for various densities, (c) dependence of Z_{eff} on density $\overline{n}_e$ for various input powers, (d) dependence of P_{rad} on density $\overline{n}_e$ for various input powers. The solid curve is a fit from equation (24.2).

Figure 24.2 focuses on the JET Mk II shots and looks to possible correlations of Z_{eff} and P_{rad} with P_{in} as well as $\overline{n}_e$. For the most part trends are again hard to discern. It might be hoped that L-mode operation (thus no ELMs) might show more discernible trends, and this can be the case. Figure 24.3, [24.4] shows a comparison of Z_{eff} against $\overline{n}_e$ for JET L-mode discharges for three different variants of the JET Mk II divertor: (a) with plasma contact on the horizontal targets, (b) on the vertical targets, (c) for the 'gas box' variant. See [24.4] for further details; here we merely note that the divertor is progressively more 'closed' to recycling

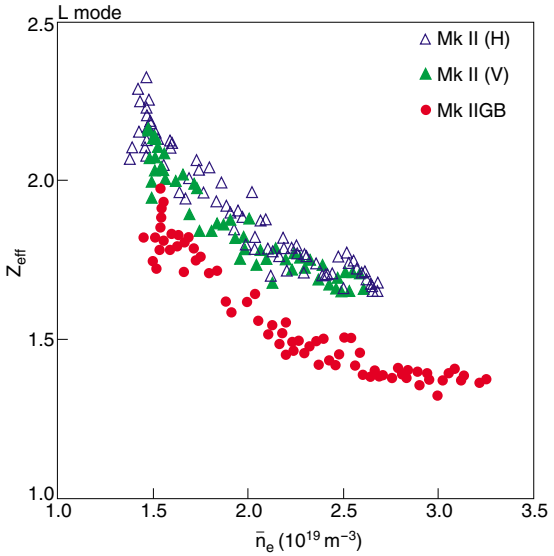

Figure 24.3. JET [24.4]. Z_{eff} in L-mode plasmas appears to decrease with divertor closure to recycling neutrals going from Mk II horizontal target → vertical → Mk IIGB. This may not be obvious in H-modes due to strong impurity sources produced by ELMs depositing power outside the divertor.

hydrogenic neutrals, going from (a) to (b) to (c), i.e. there is less leakage of hydrogen neutrals out of the divertor. Figure 24.3 shows a clear trend to decreased Z_{eff} as the divertor closure is increased—perhaps indicating the importance of sputtering of the main chamber walls by energetic neutrals.

Even if the correlations between these 'bottom line' impurity quantities and the machine control parameters, $\overline{n}_e$ and P_{in}, can often be hard to discern, we might hope that correlations would be more evident for quantities that are directly related to the *impurity production rate*. Unfortunately, it can be equally hard to discern trends in these data. Figure 24.4 gives plots of central C density as functions of the intensity of C^{2+} (CIII) light released when C is sputtered into the plasma at (a) the inner wall, (b) the inner target, (c) the outer target. The large scatter in these plots may indicate that the variability has largely to do with *transport*, rather than *production* of impurities. The reasonable success achieved at modelling the low charge state spectroscopic lines, which are released very near the production site, e.g. figure 6.20, using local probe measurements of n_e and T_e, also encourages the hope that we may have not too deficient an understanding of production—at least when it is due to physical sputtering.

We may attempt to identify some of the reasons why our understanding of the factors controlling Z_{eff} and P_{rad} remains weak:

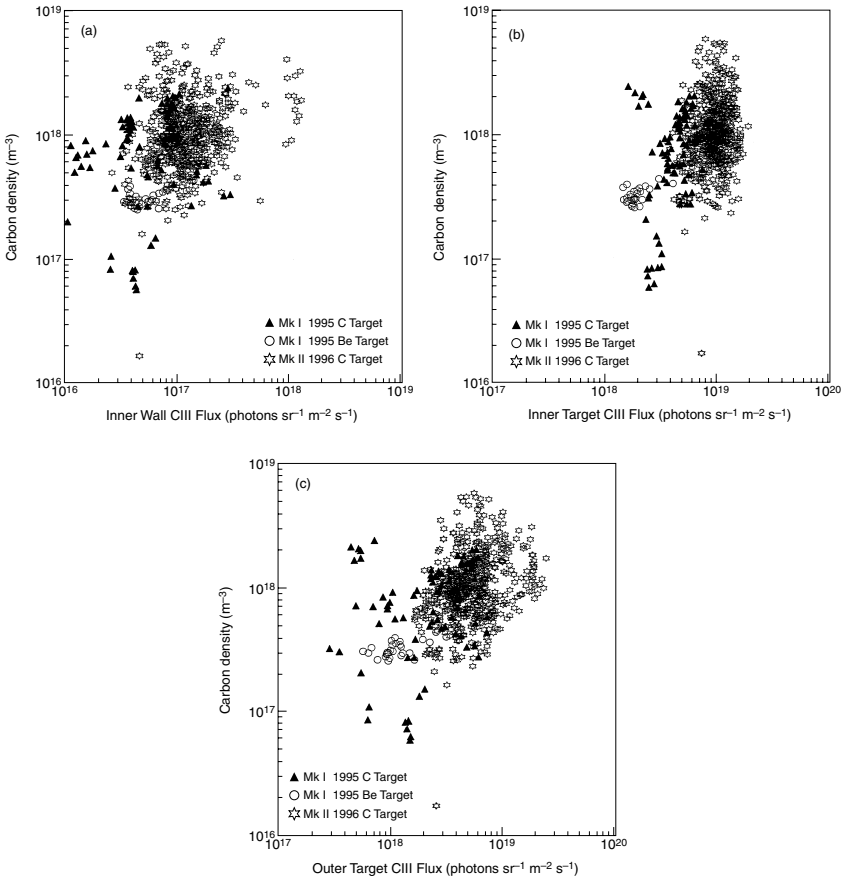

Figure 24.4. JET [24.1]. Comparison of the photon fluxes from CIII (465.0 nm) in the three campaigns for different divertors, Mk IC, Mk IBe and Mk II, with the core carbon density measured by charge exchange at $r/a = 0.2$. ELMy H-modes. Operating conditions: total input power P_T in the range 10–14 MW with $2.4 < I_p < 2.7$ MA, triangularity $\delta < 0.25$. No ICRH or LH heating. (a) Horizontal midplane CIII photon flux, (b) inner target CIII photon flux, (c) outer target CIII photon flux.

(1) There is uncertainty about the location of the most important sources. The entire plasma-facing structure can release impurities. It is not enough to identify the strongest source since the efficiency of contaminating the main plasma probably varies greatly with location. A relatively weak source may be controlling. Wall sources are particularly a concern and may be due, not only to neutral hydrogenic bombardment, but also to (unplanned for) plasma contact [24.5].
(2) The 'bottom line' quantities, Z_{eff}, P_{rad}, $n_z(0)$ are the result of a long chain of

processes, with substantial uncertainties characterizing each individual link in the chain.

(3) It appears that changes in $\overline{n}_e$ may influence production and transport oppositely, similarly for P_{in}—which would tend to obscure trends.

(4) Carbon appears to usually be the most important contaminant in plasma devices. This is unfortunate since this is one of the most difficult elements to understand with regard to plasma–surface interactions:

   (i) Both chemical and physical sputtering occur, section 3.3. RES, radiation-enhanced sublimation, section 3.3.4, may also occur. Not just methane, but also higher hydrocarbons are produced in quantity by chemical sputtering. Carbon has unity sputtering yield for atomic and ionic oxygen impact. Carbon forms a variety of hydrogenated re-deposition solids, with varying sputtering properties. Carbon, of course, is the basis of life and reacts in highly diverse, complex ways with the rest of the elements in the periodic table. It is unfortunate, but perhaps inevitable, that we are obliged to struggle with this versatile actor.

   (ii) The dependence of chemical sputtering on bombarding flux density and metal contaminants is uncertain.

   (iii) The break-up kinetics of CH_4 and the higher hydrocarbons is not well known and lack of knowledge about the probability of sticking to solid surfaces of the molecular fragments, arising by electron impact in the plasma, adds further uncertainty.

   (iv) Carbon tends to be ubiquitous in vacuum systems and is not readily removed through the vacuum pumps. It migrates from graphite components to the surfaces of non-C components. It is present as a significant impurity in many metals. It is left on surfaces by human contact.

   (v) Carbon is transported inside the containment vessel in both volatile and non-volatile forms.

What is required in order to move forward on this clearly difficult problem? Since there has been some success in modelling production, it would seem that the best procedure is to try to extend modelling and understanding to the next stages—the intermediate charge states, which are still located in the edge, but at some distance from the source. By moving up the chain of charge states it may eventually be possible to piece the entire transport picture together and to succeed in relating the 'bottom line' quantities to machine control variables.

Against this rather sobering back-drop, a surprising and encouraging discovery has been made: surveying results from a large number of tokamaks, for both divertor and limiter operation, Matthews has shown that a simple correlation exists *between* Z_{eff} and P_{rad} [24.6, 24.7]. Behringer found a similar result earlier for JET limiter operation [24.8]. Although this correlation is also not understood, it is most valuable information. The level of P_{rad} required to achieve adequate radiative cooling for reactor operation can be estimated and at the same time the

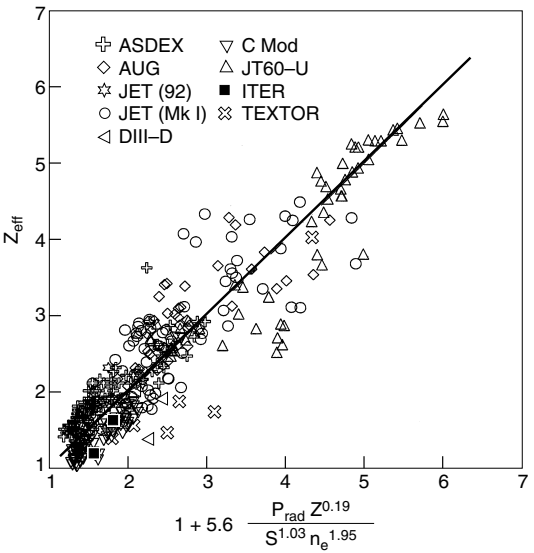

Figure 24.5. (24.6), (24.7). Matthews' law. Z_{eff} versus a scaling law close to that of equation (24.2) for experimental data from CMOD, ASDEX, AUG, DIII-D, JT60-U, TEXTOR and JET. The desired ITER operating points are also indicated.

permitted level of Z_{eff} (for tolerable fuel dilution) is known. Therefore information on the connection between these two quantities is invaluable.

Provided that radiation occurs near the edge of the main plasma, or outside the LCFS, the ratio $Z_{\text{eff}}/P_{\text{rad}}$ constitutes a *figure of merit*: the lower this ratio, the better. It is understood here that Z_{eff} is the value in the centre of the main plasma, and therefore Z_{eff} is closely related to the central *dilution factor*, n_D/n_e:

$$n_D/n_e = \frac{Z - Z_{\text{eff}}}{Z - 1} \tag{24.1}$$

for a single impurity species of charge Z. Assuming a density limit restricts n_e, then fusion power is proportional to $(n_D/n_e)^2$, and thus it is important to have Z_{eff} be as low as possible. Example: for C^{6+} and $Z_{\text{eff}} = 2.5$ one finds $n_D/n_e = 0.7$ and the fusion power is reduced by half.

A high value of (edge) P_{rad} is desirable as a means of dispersing the exhaust power over the large wall area.

A survey of a large group of tokamaks has revealed a remarkably robust relationship to exist between measured values of Z_{eff} and P_{rad} [24.6, 24.7], figure 24.5. The data are fitted reasonably well by:

$$Z_{\text{eff}} = 1 + \frac{7P_{\text{rad}}}{(S_\perp \overline{n}_e^2)} \tag{24.2}$$

$P_{\rm rad}$ [MW], $\overline{n}_e$ [10^{20} m^{-3}], and $S_\perp$, the surface area of the main plasma, $\approx 2\pi a\kappa^{1/2}2\pi R$ [m^2]. The robustness of this empirical 'Matthews law' is important as it implies that extrapolation to reactors may be reasonably reliable. In figure 24.5 are shown points for the desired operation of an ITER-like device, which is seen to fall near this scaling relation. The solid lines in figures 24.1(b) and 24.2(d) are essentially equation (24.2).

Although this scaling is also found in computer code analysis, the robustness of the relationship is still not fully understood. Let us assume that the radiated power comes from a uniform shell of thickness $\Delta_{\rm rad}$, then the radiating volume is $V_{\rm rad} = S_\perp \Delta_{\rm rad}$. Let us define 'compression' factors $C_n \equiv n_{e,{\rm rad}}/\overline{n}_e$ and $C_z \equiv n_{z,{\rm rad}}/\overline{n}_z$, where $n_{e,{\rm rad}}$ and $n_{z,{\rm rad}}$ are the average values of electron and impurity density within the radiating volume, and $\overline{n}_z$ is the average impurity density in the main plasma. We have, section 3.5:

$$P_{\rm rad}[W] = V_{\rm rad} n_{e,{\rm rad}} n_{z,{\rm rad}} L_z \tag{24.3}$$

and hence, defining the average impurity ion concentration $f_z \equiv \overline{n}_z/\overline{n}_e$, we obtain

$$f_z = P_{\rm rad}/(S_\perp \Delta_{\rm rad} C_n C_z \overline{n}_e^2 L_z) \tag{24.4}$$

thus also:

$$Z_{\rm eff} \approx 1 + Z(Z-1) f_z = 1 + \frac{Z(Z-1)P_{\rm rad}}{S_\perp \Delta_{\rm rad} C_n C_z \overline{n}_e^2 L_z}. \tag{24.5}$$

Comparing equations (24.2) and (24.5) we see that *if* $Z(Z-1)/\Delta_{\rm rad} C_n C_z L_z \approx$ constant, then the simple, observed relation of equation (24.2) would be explained. It is not evident, however, why this parameter grouping should be constant, although it is found to be so for a wide range of computer code cases analysed using the DIVIMP code, section 6.6; while each of the individual factors $\Delta_{\rm rad}$, C_n, C_z, L_z, averaged over the radiating zone was found to vary by an order of magnitude or more, the parameter group remained constant within a factor of 2. Only if extreme and unphysical plasma conditions were imposed, e.g. a cold, < 50 eV plasma everywhere including the main plasma, was the robust relation broken in the code analysis. This finding remains unexplained.

References

[24.1] McCracken G M, Barnsley R and Guo H Y 1999 *Nucl. Fusion* **39** 41
[24.2] Stangeby P C and McCracken G M 1990 *Nucl. Fusion* **30** 1225
[24.3] Lipschultz B, Goetz J, LaBombard B *et al* 1995 *J. Nucl. Mater.* **220–222** 967
[24.4] Guo H Y 1999 private communication
[24.5] Umansky M V, Krasheninnikov S I, LaBombard B and Terry J L 1998 *Phys. Plasmas* **5** 3373
[24.6] Matthews G F, Allen S, Asakura N *et al* 1997 *J. Nucl. Mater.* **241–243** 450
[24.7] Matthews G F, Balet B, Cordey J G *et al* 1999 *Nucl. Fusion* **39** 19
[24.8] Behringer K *et al* 1986 *Proc. 11th Int. Conf. on Plasma Physics and Controlled Nuclear Fusion Research (Kyoto, 1986)* IAEA-CN-47/A-IV-1

Chapter 25

Further Aspects of the Sheath

25.1 The Ion Velocity Distribution at the Sheath Edge

It is important to know the velocity distribution of the ions at the sheath edge, *se*, for at least two reasons:

(a) to establish the ion heat outflux and the ion sheath heat transmission coefficient;
(b) to be able to calculate ion sputtering rates. Note that the task is to calculate the v_x-velocity distribution, where x is the parallel direction, i.e. into the sheath edge; generally it is taken that the two perpendicular directions are characterized by Maxwellian distributions.

The crudest approximation is to assume a drifting Maxwellian at the *se*, equation (2.15), with drift velocity equal to the sound speed. This is, however, unphysical since at the *se* there are no backward-going ions, which a drifting Maxwellian contains. The ion heat flux convected into the *se* by a drifting Maxwellian is unphysically high.

When the sputtering yield is not a strong function of impact energy, then it is acceptable to calculate the sputtering rate for an ion impact energy $E_{\text{impact}} \approx 2kT_i + 3kT_e$, where the $2kT_i$ is *roughly* the thermal energy of the ions at the *se*, and the $3kT_e$ represents the energy gained in the sheath potential drop (hydrogenic plasma assumed). For low temperature plasmas, the average ion energy estimated in this way can be near, or below, the threshold for physical sputtering, section 3.3.1. Near threshold, yields vary extremely rapidly with impact energy and so in such cases it is necessary to take the actual velocity or energy distribution of the ions into account. The task is to calculate this distribution at the *se*, allowing for the further acceleration through the sheath is straightforward.

The *electron* velocity distribution at the *se* can be known precisely, see figure 2.5; it is a truncated Maxwellian, cut off at the energy corresponding to the potential drop in the sheath. Unfortunately, *there is no unique ion velocity distribution at the sheath edge*. This distribution depends on the details of the physical processes occurring in the pre-sheath, including the degree of collisionality and on

the velocity distribution of the ions when they were created. Strictly, a full kinetic analysis (wherein the complete velocity distributions are calculated at each point in space) is required for each case of interest. Such analysis are, however, rarely available. We will consider examples of a complete kinetic analysis for the case where the ions are accelerated *collisionlessly* from their source points to the *se* which, it may be hoped, are indicative of the more general case where ion–ion (self) and ion–neutral collisions occur.

The only constraint that exists on the ion velocity distribution at the *se* is the generalized Bohm criterion [25.1–25.5]; section 2.4:

$$\boxed{\int_0^\infty \frac{f_i^{se}(v_x)\mathrm{d}v_x}{v_x^2} \leq \frac{m_i}{kT_e}.} \tag{25.1}$$

This constraint, in fact, permits a rather wide latitude for the ion velocity distribution $f_i^{se}(v_x)$. We note first that expression (25.1) is not even an equality. Supersonic flow into *se*, the chapter 14, corresponds to the '<' in (25.1). No kinetic analysis for a pre-sheath giving rise to supersonic flow into the *se* has been produced as yet, and we will not deal with this case further here. In chapter 14 we made the rough estimate that the sheath heat transmission coefficient is $\gamma(M_t) = 7.5 + M_t^2$. Hereafter we will consider cases where the equality holds in (25.1) corresponding to the more common case of sonic flow into the *se* [25.6].

Relation (25.1) is still not very constraining as will now be seen. Tonks and Langmuir solved the fully collisionless, $T_i = 0$ case, section 10.6. Subsequently it was shown [25.1] that the $f_i^{se}(v_x)$ calculated by Tonks and Langumir does satisfy the equality form of (25.1). This distribution is shown in figure 25.1. One may note the sharp cut-off at the high velocity end, corresponding to ions which have fallen all the way from the symmetry plane between the two absorbing walls (planar geometry). Note also the low energy cut-off at $v_x = 0$, since there are no backward-going ions at the *se*.

Riemann has produced one of the few kinetic solutions which include collisions in the pre-sheath [25.3]. It is, however, only for $T_i = 0$ and the collisions are ion–neutral charge-exchange ones, which are rather different in their effect on $f_i(v_x)$ from ion–ion (self-) collisions, which are often more important for fusion applications. Riemann's solution for $f_i^{se}(v_x)$ is also given in figure 25.1; it also satisfies the equality form of (25.1). One notes that again there are no backward-going ions; there is now no upper velocity cut-off.

For fusion applications we are likely to be more interested in the case $T_e \approx T_i$. Two kinetic analysis are available for $T_i \neq 0$, both of them collisionless: the Bissell and Johnson, BJ, and the Emmert *et al*, EWMD, solutions, introduced in section 10.7. The $f_i^{se}(v_x)$ for these two analyses are shown in figure 25.2 for the case of $T_i = T_e$. Both satisfy the equality form of (25.1). For comparison, a drifting Maxwellian, drift velocity equal to $(2kT/m_i)^{1/2}$, is also shown in figure 25.1. It is evident that the ion heat flux associated with the latter distribution will be significantly higher than for the kinetic analysis results, owing to the more

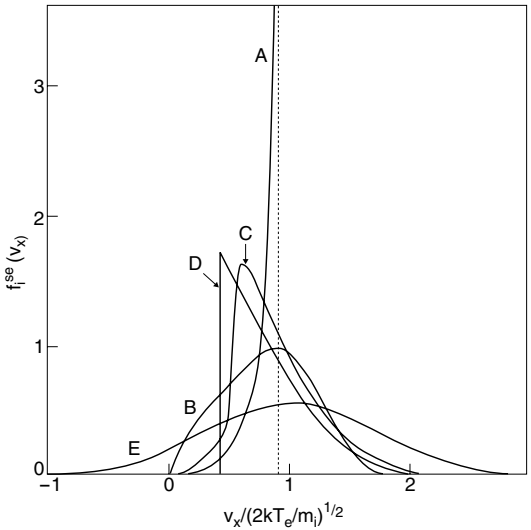

Figure 25.1. Various ion velocity distributions at the plasma/sheath interface. Only the distribution in the direction toward the surface is shown. All distributions normalized, $\int_{-\infty}^{\infty} f(u)\mathrm{d}u = 1$. (A) Tonks and Langmuir; collisionless ions, the $T_i = 0$. (B) Riemann; collisional ions, $T_i = 0$. (C) Emmert *et al*; collisionless ions, only the $T_e = T_i$ case is shown. (D) Chekmarev *et al*; collisional ions, only the $T_e = T_i$ case is shown. (E) A drifting Maxwellian, with drift velocity $v_x = c_s$, i.e., $f(u) \propto \exp[(-u-1)^2]$. See [25.33] for further details and references.

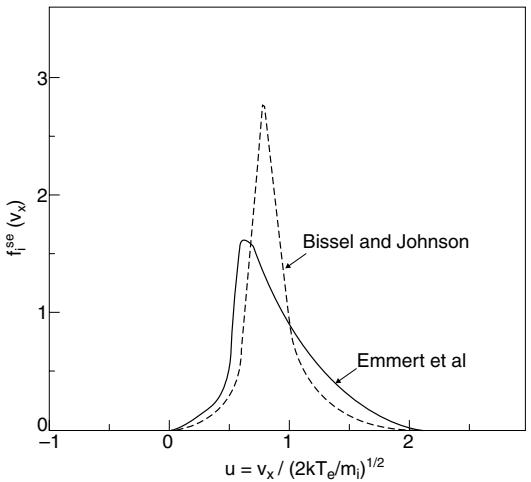

Figure 25.2. The normalized ion velocity distribution at the sheath edge, $f_i^{se}(v_x)$ from collisionless kinetic analysis for two source assumptions, that of Bissell and Johnson, and that of Emmert *et al.* See section 10.7.

extended high energy tail. The backward-going ions are also unphysical. The drifting Maxwellian contains more high energy ions than the kinetic distributions, which could result in substantial over-estimates of physical sputtering when the average impact energy is near or below the threshold for sputtering.

Figure 10.2 shows $f_i^{\mathrm{EWMD}}(v_x)$ at various locations: (a) the symmetry point; (b) the *se*; (c) the wall. It may be noted that $f_i^{\mathrm{EWMD}}(v_x)$ is a Maxwellian at the symmetry point, which could be viewed as a satisfactory 'upstream' boundary condition. This, however, can be disputed. As pointed out in section 10.7 the BJ source—which does *not* give a Maxwellian $f_i(v_x)$ at the symmetry point—is the one that would be appropriate if the ions were produced by electron-impact ionization of a Maxwellian distribution of neutrals, with temperature T_s, where T_s is the 'source temperature' characterizing the BJ or EWMD sources, equations (10.46), (10.47). This apparent paradox may be resolved by noting that in order to produce a Maxwellian distribution of *ions*, one must produce the higher velocity ions at a faster rate than the lower velocity ions—i.e. one must achieve Maxwellian *fluxes*—but that does not occur for electron-impact (or photon-) ionization of a Maxwellian distribution of *neutrals*, since the ionization rate is independent of the neutral velocity (assuming the neutral velocity is not extremely high).

It has to be noted that a 'source temperature' is not a physically measurable quantity. Rather, it is a purely *mathematical* parameter characterizing these sources. One is free to choose values of T_s to achieve whatever 'upstream' velocity distribution one wants—or strictly, whatever average ion thermal energy ('temperature') one wants. There is no general answer to the question: 'Which of these sources is more physical?' Possibly neither is entirely representative of any particular situation. Nevertheless, we will assume that either of the sources is roughly representative of the case where 'upstream $T_e = T_i$' when we set T_s equal to T_e. Fortunately, as can be seen from figure 25.2, the $f_i^{se}(v_x)$ are not too different for these two sources. Of course other sources could also be employed which might cause greater variation.

We now proceed to calculate the ion sheath heat transmission coefficients for these sources. We first define two different ion heat flux densities at the *se*:

(1) $q^i_{se,\mathrm{total}}$ is the ion heat flux density resulting from both the energy input from the ion source, as well as the energy gained from the electrons in the presheath q^{ei}_{ps}, *roughly* $0.5kT_e$ per ion, section 1.8.2.9.

(2) $q^i_{se,\mathrm{cooling}} \equiv q^i_{se,\mathrm{total}} - q^{ei}_{ps}$. For purposes of modelling the heat-sink effect of the sheath on the ion population of the SOL one uses $q^i_{se,\mathrm{cooling}}$. For purposes of calculating the heat load on the solid surface one would use $q^i_{se,\mathrm{total}}$ adding to it the energy gained in the sheath potential drop, plus the potential energy of recombination.

Likewise one defines for the electrons $q^e_{se,\mathrm{total}}$ and $q^e_{se,\mathrm{cooling}} = q^e_{se,\mathrm{total}} + q^{ei}_{ps}$.

Table 25.1. Predictions of the principal quantities of interest by four models for the case of $T_e = T_\perp^i(0) = T_\parallel^i(0) = T_0$, temperature at the symmetry point; n_0 = density at symmetry point; H^+ ions [25.7].

			Iso.	Ad.	EWMD	B&J	Ave
(1)	Plasma density at sheath edge n_{se}	n_0	0.50	0.49	0.66	0.52	0.54
(2)	Plasma flow speed at sheath edge v_{se}	$(kT_0/m_i)^{1/2}$	1.41	1.60	1.35	1.27	1.41
(3)	Plasma potential at sheath edge V_{se}	kT_0/e	−0.69	−0.72	−0.41	−0.65	−0.62
(4)	Potential of electrically floating solid V_w	kT_0/e	−3.19	−3.08	−2.91	−3.26	−3.13
(5)	Particle outflux density Γ_{se}	$n_0(kT_0/m_i)^{1/2}$	0.71	0.78	0.89	0.66	0.76
(6)	Ion heat outflux density q_{se}^i	$n_0kT_0(kT_0/m_i)^{1/2}$	2.49	2.40	2.08	1.33	2.08
(7)	Electron heat outflux density q_{se}^e	$n_0kT_0(kT_0/m_i)^{1/2}$	3.20	3.40	4.00	3.04	3.41
(8)	Total heat outflux density q_{se}	$n_0kT_0(kT_0/m_i)^{1/2}$	5.69	5.80	6.08	4.37	5.49
(9)	Ion cooling rate q_c^i	$n_0kT_0(kT_0/m_i)^{1/2}$	2.08	1.95	1.78	0.99	1.70
(10)	Electron cooling rate q_c^e	$n_0kT_0(kT_0/m_i)^{1/2}$	3.60	3.85	4.30	3.38	3.78
(11)	Ion heat transmission coefficient γ_i		2.93	2.50	2.00	1.50	2.23
(12)	Electron heat transmission coefficient γ_e		5.07	4.96	4.83	5.12	5.00
(13)	Total heat transmission coefficient γ		8.0	7.46	6.83	6.62	7.23

The sheath heat transmission coefficients are defined based on $q_{se,\text{cooling}}$. Results are shown in table 25.1 [25.7] where comparison is made with the isothermal (Iso.) and adiabatic (Ad.) model result. For the isothermal model one has that $q^i_{se,\text{total}} = \frac{7}{2}kT\Gamma_{se}$ for $T_e = T_i$, equation (2.92). In chapter 2 we therefore took our first estimate for γ_i as 3.5, based on this. We now see, however, that for a start this is an over-estimate because we should use $q^i_{se,\text{cooling}}$ which would drop γ_i down by ~0.5 (actually down to $\gamma_i = 2.93$, table 25.1). It is still further on the high side due to the fact that a drifting Maxwellian is implied in a fluid model. We therefore should not use the γ_i from any fluid model of the pre-sheath, isothermal or other.

As can be seen from table 25.1, γ_i for the two kinetic analyses are significantly smaller, as anticipated, just 1.75 when averaging the two results.

It is to be noted that these two kinetic analysis of the pre-sheath are completely collisionless. For some situations this may be a good approximation to reality. Consider the case of a high recycling divertor with the ionization source of neutrals located near the targets in the SOL. Equation (6.89) provides an estimate of the scale length of the particle source (measured along $\boldsymbol{B}$). For $n_{et} = 10^{19} m^{-3}$, a length of 1 m is representative. The self-collisional length is $\lambda_{ii} \approx 10^{16} T_i^2 / n_e$ which can exceed this source length for $T_{it} \geq 40$ eV. Ion–neutral collision lengths may also be longer. For other cases, however, ion–ion collisions will occur over the length of the SOL where the ions are 'created' by cross-field transport or ionization—i.e. in the pre-sheath—and these collisionless kinetic analyses will not be strictly valid. The ions are also probably not Maxwellian upstream, usually, making these analyses still less valid.

The effect of ion–ion collisions will be to broaden $f^i_{se}(v_x)$, i.e. increasing the high energy population, thus raising γ_i. This effect was seen for the $T_i = 0$ case, figure 25.1, where the effect of collisions is rather strong. The effect of collisions for $T_i \neq 0$ will be less dramatic since $f^i_{se}(v_x)$ extends to $v_x \to \infty$ even without collisions.

Although no generally valid value for γ_i can be specified, it may be reasonable to increase the value obtained from these collisionless kinetic solutions somewhat, to allow for the (likely) presence of collisions, to give:

$$\boxed{\gamma_i \approx 2.5} \tag{25.2}$$

as a recommended value.

For purposes of calculating sputtering yields at a detailed level, in the absence of a kinetic solution for the specific case being treated it may be reasonable to use the $f^i_{\text{wall}}(v_x)$ of Emmert *et al*, figure 10.2. This is only part of the refinement that can be introduced when detailed sputtering calculations are attempted: the foregoing only gives the distribution of the velocity in the forward direction, v_x. One can calculate the distribution of impact angles and total impact energies by assuming Maxwellian velocity distributions for v_y and v_z. Laboratory measurements of sputtering yields, section 3.3, have been made as a function of impact energy and impact angle. It is questionable, however, that much refinement of this sort is sensible since, in practice, solid surfaces are quite roughened by plasma exposure. It is also to be noted that, to this point, we are still only considering the case of $\boldsymbol{B}$ perpendicular to the solid surface.

25.2 The Case of $\boldsymbol{B}$ Parallel to the Solid Surface

The Chodura analysis of the *oblique sheath*, section 2.10, cannot be applied to $\psi = 0$, i.e. $\boldsymbol{B}$ perfectly parallel to the solid surface. It is not clear how

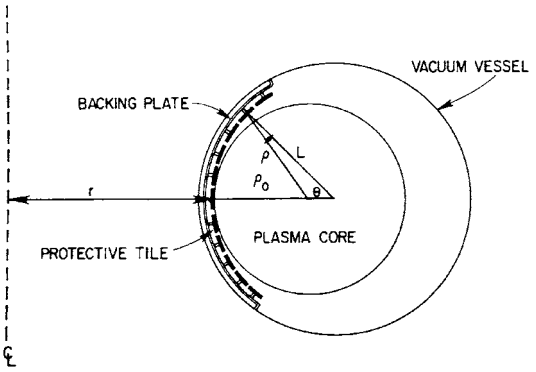

Figure 25.3. Vertical section through the TFTR vacuum vessel showing the plasma core and the first wall limiter. The minor radius of the limiter is L and the minor radius of the plasma core is ρ_0. (25.9).

charged particles reach a solid surface in this situation. It is known experimentally, however, that fluxes of particles and heat to solid surfaces parallel to $\boldsymbol{B}$ can be surprisingly high. Matthews *et al* [25.8] carried out a Langmuir probe study on the DITE tokamak using a 6 cm diameter probe head whose angle to $\boldsymbol{B}$ could be changed with the probe *in situ*. Langmuir collecting elements were flush mounted in the end of this tilt probe which could be positioned from $\psi = 45°$ to 100°. It was found that the ion saturation current to the collector elements followed the expected cos ψ dependence for ψ not too close to 90°; for ψ within a few degrees of 90° the flux did not decrease further, but instead remained constant at a level equal to about 5–10% of the normal incidence ($\psi = 0$) level.

Several tokamaks such as JET, TFTR and TORE SUPRA have been operated using the inner wall as a large area limiter—the 'wall-limiter', figure 5.5. The poloidal plane geometry of the plasma surface contact is approximately that of two circles in contact at the inner mid-plane with the wall curvature somewhat larger than the plasma radius of curvature; figure 25.3 illustrates for TFTR [25.9]. According to the standard cosine ψ model of deposition there should be a null in deposited flux densities to the inner wall at the midplane since $\psi = 90°$ there, figure 25.4 [25.9]. At locations above or below the mid-plane, the deposited flux densities would be expected to increase. With increasing distance from the mid-plane, the gap between LCFS and wall increases introducing a partially off-setting effect, assuming parallel flux densities decrease with radial distance outside the LCFS—which here is the magnetic surface that touches the inner wall at the mid-plane. The predicted result is readily shown to be a double-peaked poloidal distribution of deposited particle and heat flux densities, figure 25.4, with a null at the mid-plane [25.9].

The inner wall on TFTR was viewed with CCD cameras employing filters which provided poloidal and toroidal profiles of D_α, CII, etc. light [25.10].

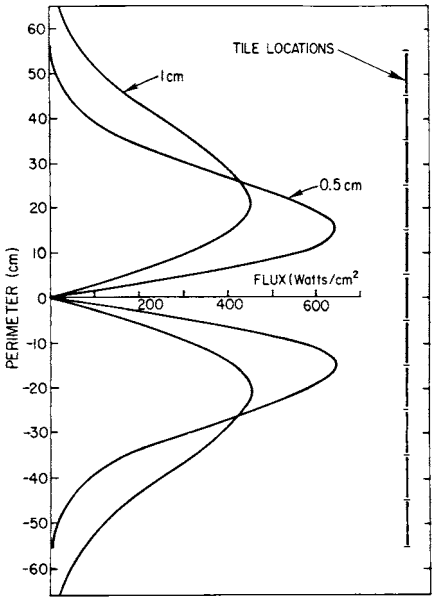

Figure 25.4. The poloidal distribution of the flux scraped off at distance L_θ from the midplane plotted for two values of scrape-off length λ [25.9].

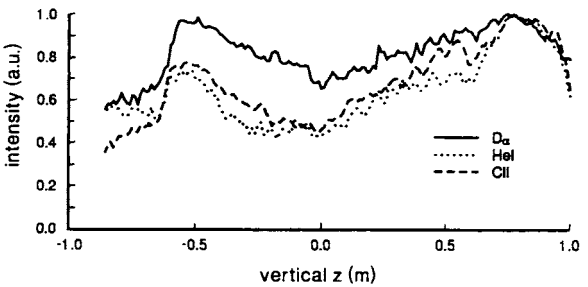

Figure 25.5. Experimentally measured poloidal profiles at the TFTR inner wall for D_α, HeI and CII radiation. Supershot discharges with $I_p = 0.8$ MA, $B_T = 3.5$ T, $P_{\mathrm{NBI}} \approx \mathrm{M}W$, $\overline{n}_e \approx 1.9 \times 10^{19}$ m^{-3} [25.10, 25.11]. One may note the absence of any mid-plane null; compare figure 25.4.

Typically, the mid-plane null is not observed; a relative minimum at the mid-plane was sometimes found, but at a level not much different from the upper and lower poloidal peaks; in some cases there was no minimum at all; figure 25.5 [25.10,25.11]; see also [25.12]. On TORE-SUPRA [25.13,25.14] similar mid-plane deposition has been observed. On TEXTOR, operated with a

pumped limiter whose front face is parallel to $\boldsymbol{B}$ over an extended region, about 0.15 m poloidally, substantial recycling fluxes were observed (D_α light) along the front face [25.15].

Clearly then, substantial fluxes can reach solid surfaces even at $\psi = 90°$. On the other hand, experimental evidence superficially at variance with the above results was reported by Matthews *et al* for the DIII-D divertor plate tiles [25.16]. Because of alignment variations, each divertor tile had a slightly different ψ, although all within $88° < \psi < 90°$. The deposited heat flux measured for individual tiles was found, however, to follow approximately the standard $\cos\psi$ values up to $= 89.5°$. It is thus evident that some subtlety characterizes this situation.

Theoretical understanding of the $\psi = 90°$ case is still evolving. Since the ion Larmor radius, ρ_i, is larger than the electron Larmor radius, ρ_e, it would seem plausible that the solid surface would charge up *positively*, i.e. opposite to the standard $\psi \neq 90°$ situation. An analysis based on such a picture, and for the specific case of $\rho_i \approx \lambda_{\text{Debye}}$, showed that plasma instabilities gave rise to turbulent, cross-field transport to the solid surface [25.17]. In practice it is likely that, while some of the plasma-wetted surfaces may have $\psi = 90°$, that there will be other plasma-wetted surfaces in the same device with $\psi \neq 90°$, and that all of the solid surfaces will be connected together, i.e. be at the same potential. Thus, even the solid surface at $\psi = 90°$ may be charged negatively relative to the local plasma, as usual. An analysis has been reported for this situation, assuming $\rho_i \gg \lambda_{\text{Debye}}$, and taking the cross-field diffusion to be due to charge-exchange collisions with cold neutrals [25.18].

There does not yet appear to be any general and complete analysis of the $\psi = 90°$ situation. We therefore do not know the equivalent of the Bohm criterion for perpendicular plasma velocity to a solid surface, $v_{\perp S}$. The lack of this critical boundary condition prevents definitive conclusions, although as will now be shown, provided $v_{\perp S}$ is not too small, we may still arrive at some useful findings.

Consider again the Engelhardt model, sections 4.6, 6.4, but now with the LCFS coinciding *at all points* with the solid surface. Let us suppose that we *did*, in fact, have the prescription for $v_{\perp S}$. We would then write as before, equation (4.61):

$$\Gamma_\perp^{\text{neutral}} = \Gamma_\perp^{\text{ion}} = D_\perp(\overline{n}_e - n_{\text{LCFS}})/\lambda_{iz} \tag{4.61}$$

but now instead of equation (4.62):

$$\Gamma_\perp^{\text{ion}} = D_\perp n_{\text{LCFS}}/\lambda_n^{\text{SOL}} \tag{4.62}$$

where λ_n^{SOL} characterizes the sink action, we would use:

$$\Gamma_\perp^{\text{ion}} = n_{\text{LCFS}} v_{\perp S} \tag{25.3}$$

where $v_{\perp S}$ now characterizes the sink action. Combining equations (4.61) and (25.3) then provides the complete solution giving:

$$\overline{n}_e = \frac{\Gamma_\perp^{\text{neutral}}}{D_\perp}\left(1 + \frac{D_\perp}{\lambda_{iz} v_{\perp S}}\right). \tag{25.4}$$

We do not, however, know the value of $v_{\perp S}$ and so this solution is not immediately useful.

We may recall from equation (4.66) for the SOL-sink case, however, that, provided λ_n^{SOL} can be neglected relative to λ_{iz}, the solution becomes independent of the value of λ_n^{SOL}, i.e. of the strength of the SOL sink. That is, if the limiting part of the transport occurs inside the LCFS, then the precise value of the SOL-sink strength parameter drops out of the solution. An analogous situation exists here with regard to equation (25.4): provided $v_{\perp S}$ is large compared with the *effective diffusion speed*:

$$v_{\mathrm{diff}} \equiv D_\perp/\lambda_{iz} \tag{25.5}$$

then $v_{\perp S}$ drops out of the solution. That is, one goes over to the 'hard' boundary condition where $n_{\mathrm{LCFS}} \ll \overline{n}_e$, i.e. we may take $n_{\mathrm{LCFS}} \approx 0$.

Since, at the present time, we are only in a position to be able to work usefully with the hard boundary condition case, let us explore the implications of this case. We should not, however, forget that this boundary condition may not be valid for a specific case of interest. Any findings here are therefore tentative.

Let us see if this boundary condition can be used to explain the experimentally observed fluxes to $\psi = 90°$ surfaces [25.19]. Consider the 2D probelike case of a limiter shown in figure 25.6. Cross-field motion of particles directly onto the front face of the limiter constitutes a local sink, causing a depression of the plasma density in front of the limiter. Assuming the hard BC we postulate that for flux surfaces close enough to the LCFS, this density depression is strong, i.e. n drops by a factor of more than $\frac{1}{2}$ from the distant value, and is thus sufficiently strong to induce sonic plasma flow along $\boldsymbol{B}$ in the flux tubes just inside the limiter face, extending inward over some radial distance λ_f. We now evaluate λ_f. The particle flux density onto the front face is:

$$\Gamma_\perp \approx D_\perp n/\lambda_f \tag{25.6}$$

and particle balance gives:

$$\Gamma_\perp 2L_f = (2)\left(\tfrac{1}{2}nc_s\right)\lambda_f \tag{25.7}$$

where $2L_f$ is the length of the front face. The factor of 2 on the RHS is due to the collection from both sides, while the factor $\frac{1}{2}$ is due to the density drop at sonic conditions, section 1.8.2.7; n is the distant, unperturbed density. Equating (12.6) and (25.7) gives:

$$\lambda_f = (2L_f D_\perp/c_s)^{1/2} \tag{25.8}$$

as the characteristic length of radial decay of density just in front of the front face of the limiter. For the 'soft' BC, $v_{\perp S}$ would also appear in the expression for λ_f, thus complicating matters.

The flux density to the limiter *sides* is:

$$\Gamma_\parallel = \tfrac{1}{2}nc_s. \tag{25.9}$$

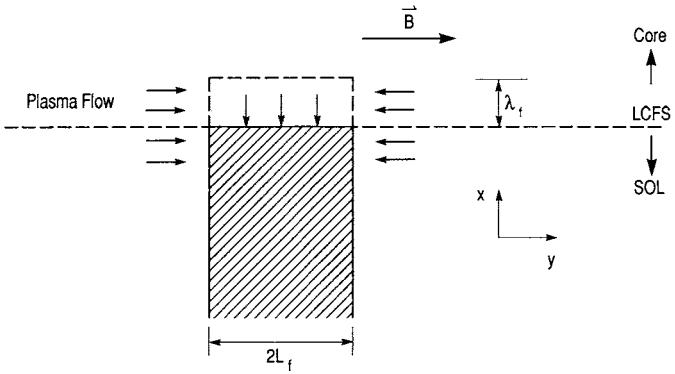

Figure 25.6. Schematic of a blunt-nosed limiter or probe with the front face, of length $2L_f$, parallel to $\boldsymbol{B}$. Because of cross-field loss directly onto the front face, the density is depressed there, causing transport along $\boldsymbol{B}$ inside the LCFS. Owing to this 'funnelling' effect, more loss occurs at the front face than would happen if parallel motion inside the LCFS could not occur [25.19].

The total flux to the front surface is:

$$\phi_\perp = 2L_f D_\perp n/\lambda_f \tag{25.10}$$

and the flux to the two side surfaces is:

$$\phi_\parallel = (2)\left(\tfrac{1}{2}nc_s\right)\lambda_s \tag{25.11}$$

where

$$\lambda_s = (2LD_\perp/c_s)^{1/2} \tag{4.7}$$

equation (4.7), is the SOL density decay length, with $2L$ being the distance between limiters. One thus obtains:

$$\Gamma_\perp/\Gamma_\parallel = (2D_\perp/L_f c_s)^{1/2} \tag{25.12}$$

$$\phi_\perp/\phi_\parallel = (L_f/L)^{1/2}. \tag{25.13}$$

Applying this to the experiment with the $\psi = 90°$ tilt-probe case [25.8]: $L_f \approx 0.03$ m, $D_\perp \approx 0.5$ m^2 s^{-1}, $T \approx 15$ eV, $c_s \approx 4\times10^4$ m s^{-1}, giving $\Gamma_\perp/\Gamma \approx 0.03$, which is of the same order of magnitude as the experimental result, ~0.05–0.1. Such a simple model should not be expected to provide better agreement; we may also note:

(a) The above picture describes a 2D *funnelling effect* since the front face captures more than 'its fair share' of outgoing particle flow thanks to *parallel* motion inboard of the LCFS. The tilt probe actually involves a 3D funnelling effect, which would be stronger than the 2D one analysed above.

(b) The value of λ_f for this particular case is so short, ~1 mm, that in reality complications related to finite ρ_i would be involved.

It can be noted from equation (25.13), for the total fluxes, that this substantial diversion—or 'funnelling'—of outflux directly onto the limiter by 2D motion can only be expected when L_f is a substantial fraction of L. This can occur in the case of inner wall limiters as on TFTR. Such limiters do not involve surfaces perfectly parallel to $\boldsymbol{B}$. One can estimate the equivalent value of L_f as being that of the plasma-wetted extent, i.e. that within distance λ_s of the LCFS. For TFTR that was of the order of $L_f \approx 0.5$ m (in the poloidal plane) while $L = \pi a$ (also in the poloidal plane) ≈ 2.5 m. Thus, from equation (25.13), $\phi_\perp/\phi_\parallel \approx (0.2)^{1/2} \approx \frac{1}{2}$, and it can be expected that a substantial fraction of the total outflux would go directly onto the TFTR wall limiter by cross-field motion and the 'funnel effect'. This is hypothesized to explain the substantial infilling of the conventionally expected mid-plane dip in deposited fluxes, figure 25.5 [25.19].

It can be noted from equation (25.13) that there exists an actual diversion of outflux onto the front surface, raising the $\phi_\perp/\phi_\parallel$ ratio beyond that which would be expected on the basis of geometry alone, which would be $\phi_\perp/\phi_\parallel \approx L_f/L$—thus the description 'funnel effect'. It should be noted that the funnelling action occurs in the confined plasma, inboard of the LCFS, in a situation where a solid surface is adjacent to the confined plasma—over a portion of the LCFS; this geometry has no direct equivalent in the divertor configuration, presumably explaining Matthews' observation that the standard cosine law was found to hold at the DIII-D divertor targets [25.16].

Nevertheless, cross-field transport within the divertor plasma itself will cause deposition on surfaces tangential to $\boldsymbol{B}$, $\psi = 90°$. Consider figure 25.7, which shows several divertor tiles, each of length L_t toroidally; two are properly aligned so that $\psi < 90°$, while one tile is out of alignment such that $\psi = 90°$ happens to hold for that tile. Within the distributed region of height λ_t in figure 25.7 (shaded), ions are lost to both the $\psi = 90°$ surface and to the exposed end of the aligned tile, while this region is supplied by a nearly sonic flow of flux density nc_s along $\boldsymbol{B}$. Adopting the 'hard' BC again, and thus the picture that the density in the shaded region drops from the undistributed value n at a distance λ_t above the $\psi = 90°$ tile surface to a small value at the tile surface then a total flux $\sim\frac{1}{2}nc_s\lambda_t L_p$ goes to the $\psi = 90°$ tile where L_p is the poloidal width of the plasma 'footprint' on the tile. Flux balance to the $\psi = 90°$ surface gives:

$$\tfrac{1}{2}\lambda_t n c_s = D_\perp n L_t/\lambda_t \tag{25.14}$$

so that:

$$\lambda_t = (2D_\perp L_t/c_s)^{1/2}. \tag{25.15}$$

The cross-field flux density onto the $\psi = 90°$ surface is therefore:

$$\Gamma_\perp = 0.5\lambda_t n c_s/L_t = (D_\perp/2L_t c_s)^{1/2} n c_s \tag{25.16}$$

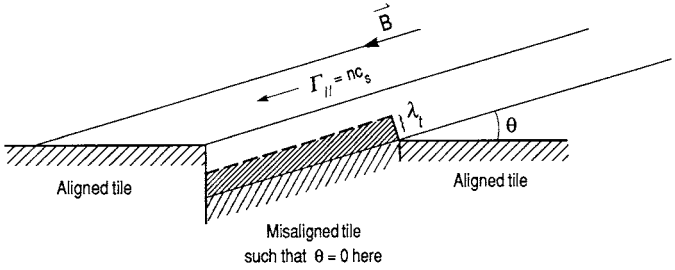

Figure 25.7. Schematic of two divertor tiles showing one misaligned tile such that its surface is precisely tangential to ***B***. Within the shaded region, direct cross-field transport onto the misaligned tile removes about half the particles travelling along ***B***, with about half continuing on to the exposed end of the adjacent, aligned tile. Thus the tile surface tangential to ***B*** does receive some deposition, whereas in the standard model it would not [25.19].

which is independent of ψ (although the foregoing implicitly assumed that $\lambda_t < L_t \cos\psi$). The flux density onto the $\psi = 90°$ surface is therefore reduced from the parallel flux density, nc_s, by the factor $(D_\perp/2L_t c_s)^{1/2}$, rather than the factor $\cos\psi$.

For the DIII-D divertor tiles [25.16], $L_t = 0.13$ m. The plasma temperature and the $D_\perp$ value in the divertor were not given, but for $T = 10$ eV and $D_\perp = 0.25\ \mathrm{m^2\ s^{-1}}$, the reduction factor is 6×10^{-3}. The DIII-D study reported that heat flux densities onto the tiles with $\psi = 90°$ were $\leq 5 \times 10^{-3}$ of the parallel value. These observations may thus be explained, although further tests using different tile lengths, L_t, are needed. It is also to be noted that the DIII-D measurements were of heat, rather than particle, flux density.

Returning to limiter geometry, the B2 code was modified to study the funnelling effect for a large area limiter, approximating the ALT-II limiter in the TEXTOR tokamak [25.21]. A toroidal limiter extended poloidally from $\theta_1 = -26.5°$ to $\theta_2 = -63.5°$, with the front face lying on the circle of minor radius $a = 0.45$ m, giving $L_f = \pi a((\theta_1 - \theta_2)/360) = 0.15$ m. It is readily shown that for this geometry the simple model is modified to include the effect of the magnetic pitch angle, θ_{pitch}, equation (1.3):

$$\lambda_f = (2D_\perp L_f/\theta_{\mathrm{pitch}} c_s)^{1/2} \tag{25.17}$$

$$\Gamma_\perp = n_\infty v_{\perp S}^{\mathrm{ref}} \text{ where } v_{\perp S}^{\mathrm{ref}} \equiv (\theta_{\mathrm{pitch}} c_s D_\perp/2L_f)^{1/2} \tag{25.18}$$

$$\phi_\perp/\phi_\parallel = (L_f/a\pi)^{1/2}. \tag{25.19}$$

The subscript ∞ is used to emphasize that this is for the density far from the limiter on the same flux surface as the front face, rather than the local density along the front face. The code runs used $\theta_{\mathrm{pitch}} = 0.086$, constant. In the grid cells lying along the front face, the B2 code was modified to include perpendicular

fluxes onto the front face at flux density $\Gamma_\perp = nv_{\perp S}$, where n is the local density in the cell calculated by the code and $v_{\perp S}$ is assigned specific, constant values that were varied from code run to code run.

The first test was to see if $\Gamma_\perp$ saturated as $v_{\perp S}$ was assigned values large compared with $v_{\perp S}^{\text{ref}}$. For the specific plasma conditions employed in the runs, $T \approx 40$ eV, thus $c_s \approx 6.3 \times 10^4$ m s^{-1}. A value of $D_\perp = 1$ m^2 s^{-1} was used for all runs. Thus, $v_{\perp S}^{\text{ref}} \approx 130$ m s^{-1}. Figure 25.8 shows $\Gamma_\perp$ for the cells across the front face, numbered 9 to 18. As can be seen, $\Gamma_\perp$ does, in fact, saturate for $v_{\perp S} >\sim 1300$ m s^{-1}, i.e. $\gg v_{\perp S}^{\text{ref}}$, over most of the front face. The flux densities are higher at the edges, which may be an artifact associated with inadequate grid resolution near the sharp corners of the limiter used for the code calculations.

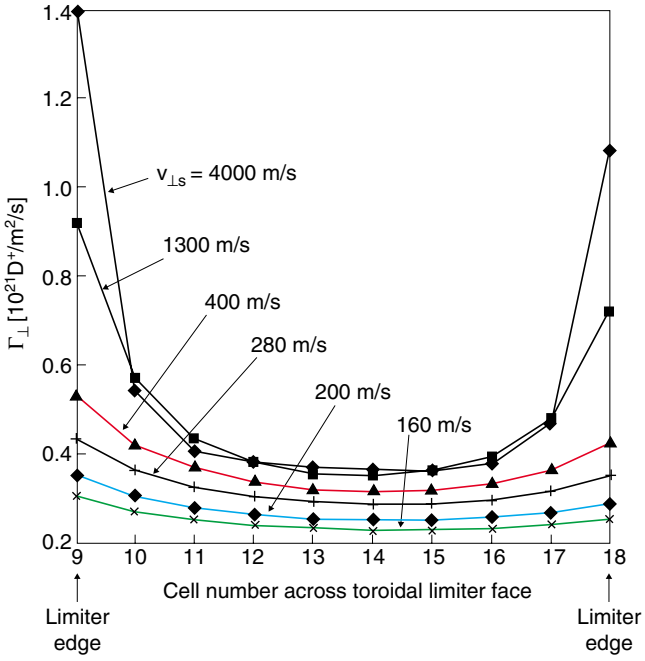

Figure 25.8. B2 code modelling of flues onto a surface parallel to ***B*** [25.21]. See text.

The absolute magnitude of the average saturated value of $\Gamma_\perp$ calculated by the code, $\sim 5 \times 10^{20}$ [D$^+$ m^{-2} s^{-1}], was also roughly in agreement with equation (25.18), evaluated for the value of $n_\infty \approx 7 \times 10^{18}$ m^{-3} on the same flux surface as the front face, at the poloidally opposite side of the tokamak: $n_\infty v_{\perp S}^{\text{ref}} \approx 9 \times 10^{20}$ [D$^+$ m^{-2} s^{-1}]. The fluxes onto the front surface, $\phi_\perp$, are approximately in accord with equation (25.19), and are thus substantial compared with the total parallel fluxes to the sides of the limiter—broadly in accord with what has been observed on TEXTOR [25.15].

The code gave the Mach number and n_e profiles along the front face flux tube, figure 25.9, shows the anticipated decrease of n_e to values small compared with n_∞, and $|M| \rightarrow 1$ at the edges of the flux tube that passes the front face. The value of λ_f extracted from the code results, ~6 mm, was close to that given by equation (25.17), 7.4 mm.

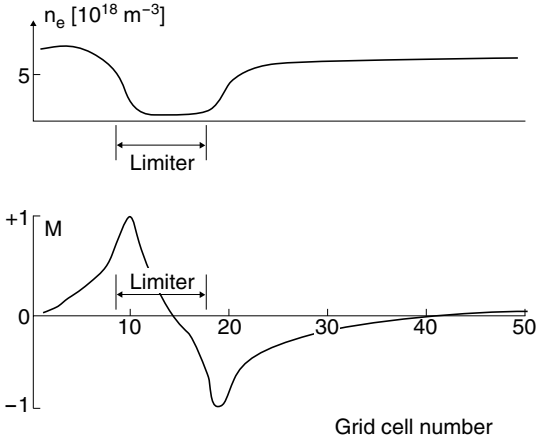

Figure 25.9. B2 code modelling of flues onto a surface parallel to ***B*** [25.21]. See text.

So long as a general theory of the $\psi = 90°$ case is lacking, and thus the equivalent to the Bohm criterion for $v_{\perp S}$ is missing, the above findings must be tentative. It is nevertheless an encouraging—and experimental—fact that the plasma-wetted area of wall limiters is even larger than is already indicated by simple geometry. Whether or not this is actually due to the 'funnelling effect' described above, remains to be seen.

25.3 The Bohm–Chodura Boundary Conditions and the Density Gradient at the Entrance to the Sheaths

At the entrance to the Debye sheath, the ion flow velocity into the sheath must be at least equal to the acoustic speed, i.e. the Bohm criterion, chapter 2. Within the sheath we may consider the densities n_e and n_i to be functions of the spatial variable $s_\parallel$ in the flow direction, with $s_\parallel = 0$ at the sheath entrance where $n_e = n_i \equiv n_0$—or of the potential V, where $V = 0$ at $s_\parallel = 0$ and V necessarily decreases going into the Debye sheath, if that is to be a region of net positive space charge density, section 2.3. Unless the Bohm criterion is satisfied, the rate of decrease of n_i—with respect to either $s_\parallel$ or V—will be greater than the rate of change of n_e, section 2.3. That will result in the contradiction of the Debye sheath having a net positive charge density. This is readily demonstrated by assuming for

the electron density the Boltzmann relation (and T_e = constant), equation (1.12):

$$n_e = n_0 \exp(eV/kT_e) \tag{1.12}$$

while for the ions one has the conservation of particles and momentum, chapter 9:

$$\frac{\mathrm{d}}{\mathrm{d}s_\parallel}(n_i v) = 0 \tag{25.20}$$

$$m_i n_i v \frac{\mathrm{d}v}{\mathrm{d}s_\parallel} = -\frac{\mathrm{d}p_i}{\mathrm{d}s_\parallel} + en_i E \tag{25.21}$$

where we assume no volume sources, or sinks, or friction, and no change of cross-sectional area of the flux tube, etc. From (1.12) we find, using $E \equiv -\mathrm{d}V/\mathrm{d}s$, and assuming the Bohm criterion in the *marginal* form—where n_e and n_i decrease exactly together to give quasi-neutrality as the flow enters the Debye sheath—that:

$$(v_0^2 - c_s^2)\frac{\mathrm{d}n}{\mathrm{d}s_\parallel}\bigg|_{s_\parallel=0} = 0 \tag{25.22}$$

where $v_0 \equiv v(0)$ at the sheath edge, $c_s \equiv [k(T_e + T_i)/m_i]^{1/2}$ and we have assumed isothermal ions. Clearly the only value of v_0 that will permit the plasma density to decrease entering the sheath edge, $\mathrm{d}n/\mathrm{d}s_\parallel|_{s_\parallel=0} \neq 0$ is $v_0 = c_s$, i.e. the Bohm criterion. We may note that *if* we could assume $E = 0$ in equation (25.21) then we would appear to obtain the false result that at all points $v = c_s$; this is incorrect because if $E = 0$ then n = constant, equation (1.12), i.e. $\mathrm{d}n/\mathrm{d}s_\parallel = 0$, and so one does *not* conclude that $v(s_\parallel) = c_s$ is necessary in that case; it is only when the presence of an electric field is required, as in the sheath, and thus n cannot be constant, equation (1.12), that equation (25.22) results and $v_0 = c_s$ is required to hold.

The case of $\mathrm{d}n_i/\mathrm{d}s_\parallel|_{s_\parallel=0}$ may be termed the 'gentle entry' into the sheath, giving the Bohm criterion in its marginal form. For $|\mathrm{d}n_e/\mathrm{d}s_\parallel| > |\mathrm{d}n_i/\mathrm{d}s_\parallel|$ at the *se* one has supersonic flow at the sheath edge, $|v_0| > c_s$.

When $\boldsymbol{B}$ is at an angle $\psi > 0°$ to the solid surface, Chodura has shown that, in addition to the Debye sheath with its strong electric field, there arises a magnetic pre-sheath, MPS, where a significant electric field also exists, section 2.10; see also Riemann's separate proof [25.20]. This field is needed to accelerate the ions in the MPS to reach the acoustic speed perpendicular to the solid surface at the Debye sheath edge.

The Chodura–Riemann criterion gives that the flow velocity of the ions *along* $\boldsymbol{B}$ as the flow *enters* the MPS is also c_s. The demonstration of this is the same as the above—although now, since the MPS is quasi-neutral, with $n_e \approx n_i$ throughout, the requirement is that n_e and n_i decrease together; it might appear that this would require that $v_{\parallel \mathrm{BMPSE}} = c_s$ *precisely*, precluding the possibility of supersonic flow at the MPSE; however, it can be shown that when the effect of ion inertia in the $\boldsymbol{E} \times \boldsymbol{B}$ direction within the MPS is taken into account, then $|v_{\parallel \mathrm{BMPSE}}| > c_s$ is also possible [25.22].

25.4 The Sheath Boundary Conditions in the Presence of $\boldsymbol{E} \times \boldsymbol{B}$ and Diamagnetic Drifts

In chapter 18 the sheath boundary condition, in the presence of $\boldsymbol{E} \times \boldsymbol{B}$ drifts, was found to be the 'intuitive BC':

$$v_{\parallel \mathrm{BMPSE}}/c_s = 1 - \frac{v_\theta^{dr}}{c_s \tan\theta}. \tag{25.23}$$

One says 'intuitive' since one's first thought, perhaps, is that at the MPSE:

$$v_y = \sin\theta v_{\parallel 0} + \cos\theta \frac{E_x}{|B|} - \frac{\cos\theta}{en|B|}\frac{\partial p_i}{\partial x} = \sin\theta c_s. \tag{25.24}$$

See chapter 18 for definitions. Equation (25.24) is based on the assumption that the total parallel-to-$\boldsymbol{B}$ velocity at the MPSE is the vector sum of the parallel velocity, the $\boldsymbol{E} \times \boldsymbol{B}$ drift and the diamagnetic drift, and equals the sound speed. We should neglect the diamagnetic term in equation (25.24) since it is almost entirely divergence free, section 18.4, that is, while the component of particle flux density $\boldsymbol{\Gamma}_{\nabla pi}$ in the y-direction does decrease with $s_\parallel$ or V, this decrease is just compensated by the increase in the x-component of $\boldsymbol{\Gamma}_{\nabla pi}$, i.e. along the surface. Thus for the ∇B ion drift toward the bottom targets, thus $\boldsymbol{B}_z$ and $\boldsymbol{B}_{\mathrm{tor}}$ in the negative z- direction, then $v_\theta^{dr} = -E_x/|B|$, and equation (25.24) gives equation (25.23).

This thinking is not really justifiable, however, since it is not derived from the fundamental physical requirement that the n_e and n_i decrease together at the MPSE. Consider equations (18.21) and (18.31) from section 18.3.4 on poloidal $\boldsymbol{E} \times \boldsymbol{B}$ drifts—the drifts involved here. Neglecting particle source S_p and assuming v_θ^{dr} constant along $s_\parallel$ or y, then these equations can be combined to give:

$$\left[\left(v_{\parallel 0} + \frac{v_\theta^{dr}}{\tan\theta}\right)^2 - c_s^2\right]\frac{\mathrm{d}n}{\mathrm{d}y}\bigg|_{\mathrm{MPSE}} = 0. \tag{25.25}$$

Thus, by the same arguments used in section 25.3, we now have proven that the 'intuitive BC', equation (25.23) is, in fact, valid [25.23]. A separate, elegant proof has been given by Hutchinson [25.24]. This BC is also used by Cohen and Ryutov [25.25].

The 'intuitive BC' is, however, only a first approximation. For example, v_θ^{dr} is not constant with $s_\parallel$ or y since E_x varies at the MPSE. This and other factors have been taken into account in a more general formulation of the sheath boundary condition in the presence of $\boldsymbol{E} \times \boldsymbol{B}$ drifts [25.23].

Cohen and Ryutov [25.26] have derived the sheath boundary conditions as applied to *currents* entering the sheath, allowing for $\boldsymbol{E} \times \boldsymbol{B}$ drifts—and also diamagnetic drifts which, unlike mass flow, influence currents, section 18.7. They also assess the effects of structural irregularities on the solid surface [25.27,25.28].

25.5 Expressions for the Floating Potential, Particle and Heat Flux Densities Through the Sheath

In this section we seek to establish expressions for *nine* key sheath quantities, namely: the potential drop across the sheath and the electron (and ion) particle (and energy) flux densities to floating (and biased) surfaces. The derivations here are an extension of those given in sections 2.6, 2.7.

We seek to relate these nine quantities to the plasma density and temperatures (ion, electron), and in the case of the biased surface, to the bias voltage.

The Bohm criterion, section 2.3, is the starting point in this undertaking since it provides a value for the ion particle flux density from a plasma to a surface (thus also the electron particle flux density if the surface is floating). The ion current density entering the sheath and reaching the solid surface is:

$$j^+ = en_{se}c_s = en_{se}(k(T_e + T_i)/m_i)^{1/2}. \tag{25.26}$$

If in flowing through the plasma the ions do not suffer momentum loss due to collisions with other particles, and if T_e and T_i are spatially constant, then we can also relate j^+ to conditions far from the surface, namely:

$$j^+ \simeq 1/2en_0c_s(T_e, T_i). \tag{25.27}$$

In more complex plasmas the relation between n_0 and n_{se} can be quite different and temperature variations in the flow direction can also occur. In such cases detailed modelling of the plasma (pre-sheath) is required in order to relate n, T_e and T_i at the sheath edge to values far away. Such modelling is the subject of chapters 9–11 and will not be dealt with further here. Equation (25.26) is generally true, however; that is one can express the particle flux to the surface in terms of the *local* plasma density and temperature.

We are now in a position to deduce a value for the floating voltage V_f, the potential at which a solid surface floats to receive zero net current. We wish to allow for secondary electron emission from the surface, arising from electron impact, since this is significant even at rather modest energies, $T_e \geq 30$ eV (by contrast, ion-induced secondary electron emission is usually only important for ion impact energies of $\geq$1 keV), section 3.1. We thus have that the secondary electron current density is:

$$j^-_{\mathrm{SEC}} = \delta_e j^-_{\mathrm{TOT}} = \delta_e(j^-_{\mathrm{NET}} + j^-_{\mathrm{SEC}}) \tag{25.28}$$

where: δ_e = secondary electron emission coefficient (includes both true s.e.e. and electron back-scatter, section 3.1), j^-_{TOT} = total electron current density striking the surface, $j^-_{\mathrm{NET}} \equiv j^-_{\mathrm{TOT}} - j^-_{\mathrm{SEC}} = (1 - \delta_e)j^-_{\mathrm{TOT}}$.

We thus have that:

$$j^-_{\mathrm{NET}} = 1/4en_{se}\bar{c}_e(1 - \delta_e)\exp(eV_f kT_e). \tag{25.29}$$

For floating conditions we have that:

$$j^-_{\mathrm{NET}} = j^+ \tag{25.30}$$

hence equating equations (25.26) and (25.29) one has

$$\boxed{\frac{eV_f}{kT_e} = 0.5 \ln\left[\left(2\pi \frac{m_e}{m_i}\right)\left(1 + \frac{T_i}{T_e}\right)(1-\delta_e)^{-2}\right].} \tag{25.31}$$

Equation (25.31) does not include the pre-sheath voltage drop and one may add $\sim\frac{1}{2}kT_e/e$ to find the potential difference between the surface and the plasma far from the surface, section 1.8.2.8. The value of V_f equation (25.31), is shown in figure 2.8. As can be seen, V_f is reduced by increasing T_i/T_e or by increasing secondary electron emission. The often-quoted statement that 'the floating voltage is about $-3kT_e/e$ can thus be in error. It is also quite different for heavy ion plasmas, being about $-6kT_e/e$ for Hg vapour plasma, for example. The Bohm criterion, which is implicit in equation (25.26), is dependent on δ_e [25.4,25.29], but unless $\delta_e \to 1$, the effect is small and is generally ignored.

We consider next the *energy transmission* of the sheath. As indicated in section 2.6, the electron distribution at the sheath solid interface can still be Maxwellian, at least in the forward direction. We may therefore use the fact that for a Maxwellian distribution the energy flux in the x-direction is just $2kT$ times the particle flux in the x-direction, equation (2.30).

If we wish to calculate the power removal rate from the plasma electron population, then we must note that these escaping electrons actually possessed a higher kinetic energy as they were removed from the plasma, namely, one higher by the amount $|eV_f|$. Thus the electron power flux density *removed from the plasma* is:

$$q_e = (2kT_e - eV_f)\frac{j^-_{\mathrm{TOT}}}{e} + eV_f\frac{j^-_{\mathrm{SEC}}}{e}. \tag{25.32}$$

(Note that V_f is negative.)

The last term in equation (25.32) represents the energy re-injected *into* the plasma by secondary electrons accelerated to energy $-eV_f$. We neglect the thermal energy of the secondary electrons since it is only a few electron volts. Thus we can write for the electron energy crossing the *se*:

$$q_{e,se} = \left(\frac{2kT_e}{1-\delta_e} - eV_f\right)\frac{j^+}{e}. \tag{25.33}$$

For purposes of modelling the energy balance of the SOL electron population, it is useful to define $q_{e,\mathrm{cooling}}$, the energy flux density of *cooling* the plasma electron population, i.e.

$$q_{e,\mathrm{cooling}} \equiv q_{e,se} + q^{ei}_{ps} \tag{25.34}$$

where q^{ei}_{ps} is the power transferred form the electrons to the ions in the pre-sheath to accelerate the ions up to sound speed. Now $q^{ei}_{ps}/(j^+/e)$ is less than

the total pre-sheath potential drop since not all of the ions fall through the entire pre-sheath. Approximately, $q_{ps}^{ei} \approx 0.5kT_e j^+/e$ but the specific value will vary somewhat depending on precisely what model assumptions are made about the pre-sheath. This aspect of the result is therefore not just a property of the sheath itself. Fortunately this is a relatively small contribution. We thus take:

$$q_{e,\text{cooling}} \simeq q_{e,se} + (\sim)0.5kT_e(j^+/e). \tag{25.35}$$

We consider next the ion energy flux crossing the *se*. To calculate this we need to know the actual ion velocity distribution at the *se*, which is a rather unusual one, having no back-going ions in the distribution since the sheath is 100% absorbing of ions, see section 25.1. Here, for a first estimate we will use the expression for $q_{\|i,\text{convection}}$, equation (9.65) and assume isotropic ions:

$$q_{\|i,\text{convection}} = \left(\tfrac{5}{2}kT_i + \tfrac{1}{2}m_i v^2\right)nv. \tag{25.36}$$

Thus, taking $v = c_s$ and $n = n_{se}$:

$$q_{i,se} = 3.5kT_i n_{se} c_s = 3.5kT_i \frac{j^+}{e}. \tag{25.37}$$

Assuming that this corresponds to a drifting Maxwellian (which does, in fact, have back-going ions), then this result is in some error—on the high side, see section 25.1, and the factor 3.5 should be replaced by 2.5, equation (25.2).

We also have the ion cooling rate due to sheath loss:

$$q_{i,\text{cooling}} \simeq q_{i,se} - 0.5kT_e(j^+/e). \tag{25.38}$$

The electric field in the sheath serves to transfer energy from the electrons to the ions. Thus the electron heat flux density actually received by the solid surface is:

$$q_{e,\text{surface}} = \frac{2kT_e}{1-\delta_e}\frac{j^+}{e} \tag{25.39}$$

while the ion thermal plus (directed) kinetic energy flux density actually received by the solid surface is:

$$q_{i,\text{surface}} = (2.5kT_i - eV_f)\frac{j^+}{e}. \tag{25.40}$$

To this total flux, $q_{\text{surface}} \equiv q_{e,\text{surface}} + q_{i,\text{surface}}$, should be added the *potential* energy associated with e–i and molecular recombination, if the actual heating effect *on* the solid surface is required, equation (25.55), below.

It is useful to define the electron ion and total energy *sheath transmission coefficients*, γ_e, γ_i, γ:

$$\gamma_e \equiv q_{e,\text{cooling}}/(kT_e j^+/e) \tag{25.41}$$

$$\gamma_i \equiv q_{i,\text{cooling}}/(kT_e j^+/e) \tag{25.42}$$

$$\gamma \equiv (q_{e,\text{cooling}} + q_{i,\text{cooling}})/(kT_e j^+/e) \tag{25.43}$$

and so:

$$\gamma_e \approx \frac{2}{1-\delta_e} - 0.5\ln\left[\left(2\pi\frac{m_e}{m_i}\right)\left(1+\frac{T_i}{T_e}\right)(1-\delta_e)^{-2}\right] + \sim 0.5 \qquad (25.44)$$

while for the ions:

$$\gamma_i \approx 2.5\frac{T_i}{T_e} - \sim 0.5. \qquad (25.45)$$

The total energy transmission factor:

$$\boxed{\gamma \approx \frac{2.5T_i}{T_e} + \frac{2}{1-\delta_e} - 0.5\ln\left[\left(2\pi\frac{m_e}{m_i}\right)\left(1+\frac{T_i}{T_e}\right)(1-\delta_e)^{-2}\right].} \qquad (25.46)$$

Relation (25.46) is shown in figure 25.10 for D^+ ions.

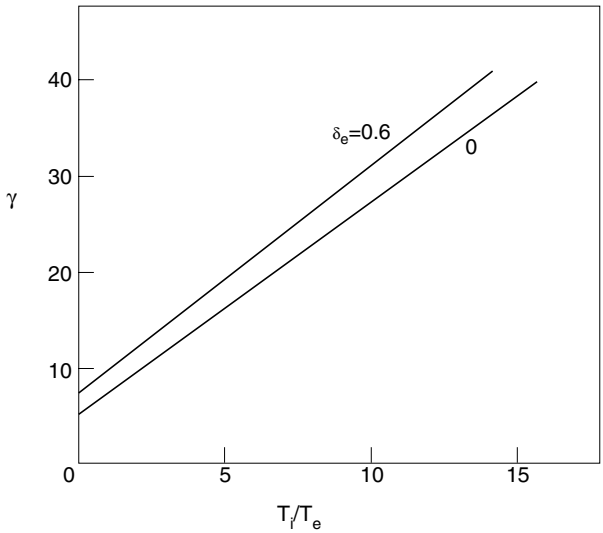

Figure 25.10. The sheath heat transmission coefficient γ, equation (25.46), as a function of T_i/T_e and secondary emission coefficient, δ_e [25.34]. D^+ ions.

Note: when $\delta_e = 1 - [(2\pi m_e/m_i)(1+T_i/T_e)]^{1/2}$ then $V_f = 0$; for example for $T_i = 10T_e$ and H^+ ions this occurs for $\delta_e \approx 0.8$. Then the electrons reach the surface unimpeded by any sheath, so $q_{e,\text{surface}} = 1/4n\bar{c}_e 2kT_e$ and the surface heating rate can be extremely high.

The inclusion of the effect of secondary electron emission in the calculation of eV_f (thus also of γ) warrants further discussion. In their pioneering work on this problem, Hobbs and Wesson [25.29] fully accounted for the existence of secondary electrons by allowing for the presence of injected secondary electron in the plasma far from the sheath (thus reducing the density of primary electrons

there below the ion density). It turns out that this has a negligible influence on V_f, provided $\delta_e \neq 1$, and the Hobbs–Wesson value for V_f is the same as that given in equation (25.31) (taking $T_i = 0$, their assumed value). These authors also found the (electron) heat flux density through the sheath to be:

$$q_{e,se} = 1/4 n_0 \bar{c}_e 2kT_e F(\delta_e) \tag{25.47}$$

where they define

$$F(\delta_e) \equiv \left(\frac{\pi m_e}{8m_i}\right)^{1/2}\left[\ln\left(\frac{(1-\delta_e^2)}{2\pi m_e/m_i}\right) + \frac{5-\delta_e}{1-\delta_e}\right]. \tag{25.48}$$

For $T_i = 0$ equation (25.33) gives the same value for $q_{e,se}$ as obtained by Hobbs and Wesson except that:

(a) These authors (incorrectly) take $j^+ = en_0 c_s$, neglecting the pre-sheath density drop; thus the n_0 in equation (25.47) should read n_{se}.
(b) Hobbs and Wesson include a pre-sheath energy contribution, $\frac{1}{2}kT_e$ in equation (25.47).

Clearly neither equations (25.46) nor (25.47) can be applied for strong secondary electron emission, $\delta_e \geq 1$ since a singularity occurs at $\delta_e = 1$. Hobbs and Wesson, in fact, showed that for $\delta_e \gtrsim 0.8$, an electron space charge layer will occur at the surface inhibiting any further secondary emission. Thus these equations do not apply for strong secondary electron emission, which can set in at $T_e \gtrsim 100$ eV, section 3.1.

We should, in principle, also include secondary electron emission due to ion, photon, metastable atom impact, etc. Usually ions will not create significant amounts of secondary electrons for fusion edge conditions since the required energy, $\gtrsim$1 keV, normally implies intolerable levels of sputtering and surface heating. Photon fluxes are only $\sim$1 W cm^{-2} *on average* in the edge region (contrasted with the tens to thousands of W cm^{-2} of charged particle power flux along the magnetic field lines to surfaces) and so usually one can neglect this process compared with electron impact s.e.e.; however, near probes, limiters, etc high gas levels are often present (due to the release of hydrogen initially deposited in the solid as ions), and so strong local sources of radiation can exist arising from electron impact with this gas. These photons may increase s.e.e. locally to substantial levels.

Equations (25.28) to (25.31) can be generalized to allow for these additional s.e.e. processes by simply replacing δ_e with δ where

$$\delta \equiv (\delta_e + \delta_i + j)/(1 + \delta_i + j) \tag{25.49}$$

and $\delta_i \equiv$ ion s.e.e. coefficient, $j \equiv j_{\text{photon}}/n_{se}c_s$, $j_{\text{photon}} \equiv$ s.e.e. flux density due to photons, metastable atoms, etc.

Now that we have dealt with the particle and energy flow to an electrically *floating* surface, let us examine the case of an *electrically biased* surface. We

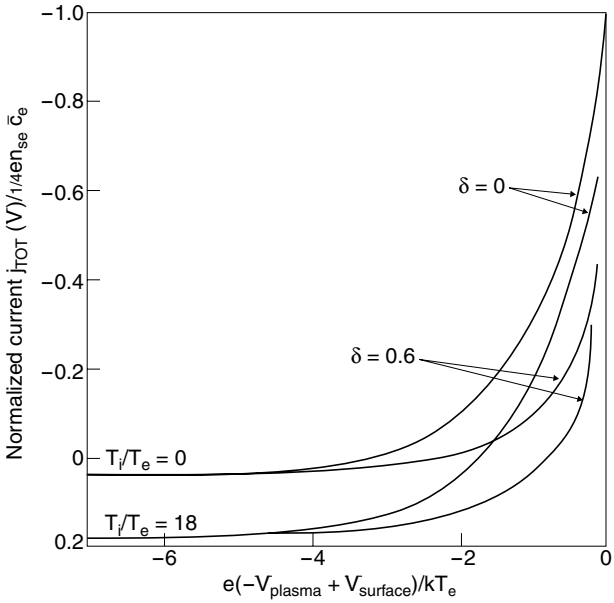

Figure 25.11. The normalized current as a function of the applied potential to a surface, i.e., the Langmuir I–V characteristic, equation (25.51) [25.34]. $V \equiv V_{\text{surface}} - V_{\text{plasma}}$. D^+ ions.

will restrict out attention to the case of surfaces which are biased negatively with respect to the plasma. As we shall see, as the surface potential approaches the plasma potential, the heat flux can reach extremely high values.

So long as the surface is negative with respect to the plasma, a sheath still exists, although its thickness varies. We thus have that the ion current is still given by $j^+ = en_{se}c_s$. The net electron current is:

$$j_{\text{NET}}^- = (1/4)n_{se}\bar{c}_e e(1-\delta)\exp(eV/kT_e) \tag{25.50}$$

where V is the negative potential applied to the surface relative to plasma potential. The net total current density can therefore be written

$$\boxed{\frac{j_{\text{TOT}}(V)}{(1/4)en_{se}\bar{c}_e} = \left[\left(1+\frac{T_i}{T_e}\right)\left(\frac{2\pi m_e}{m_i}\right)\right]^{1/2} - (1-\delta)\exp\left(\frac{eV}{kT_e}\right).} \tag{25.51}$$

Relation (25.51) is shown in figure 25.11. The net total current reaches the 'saturation ion current' j_{sat}^+, which is just the j^+ of equation (25.26), at sufficiently negative potentials. Increasing the potential above the floating potential causes an exponential increase in the electron current. In the simplest model, the electron current attains the saturation value $j_{\text{sat}}^+ = (1/4)n_{se}\bar{c}_e e$ at $V = 0$ and this then

remains constant for all $V > 0$. Often a true saturation electron current is not observed but the current continues to rise with V; however, the increase is slower than exponential. The solid–plasma interaction is difficult to model for $V > 0$ since no sheath is present and the applied electric field penetrates far into the plasma causing a significant perturbation.

Next consider the power flux density to an electrically biased surface. The ion power is

$$q_{i,\text{surface}}(V) \approx j^{+}(2.5kT_i - eV) \tag{25.52}$$

while for the electrons

$$q_{e,\text{surface}}(V) = 2kT_e j^{-}_{\text{TOT}}. \tag{25.53}$$

(We neglect q^{ei}_{ps} as small here.) Note that we use j^{-}_{TOT} in the last expression rather than j^{-}_{NET} since every electron striking the surface deposits, on average, $2kT_e$ there. Again, we neglect the thermal energy of the emitted secondaries. Thus we may write the total power flux density reaching the surface in the form of a transmission coefficient

$$\frac{q_{\text{surface}}(V)}{kT_e(j^{+}/e)} \equiv \gamma(V) = -\frac{eV}{kT_e} + \frac{2.5T_i}{T_e} + 2\left[\left(1 + \frac{T_i}{T_e}\right)\left(\frac{2\pi m_e}{m_i}\right)\right]^{-1/2} \exp\left(\frac{eV}{kT_e}\right). \tag{25.54}$$

Note that δ does not appear in this last expression. Relation (25.54) is shown in figure 25.12. The power removed from the plasma as a function of V is $q_{se}(V) = q_{\text{surface}}(V) - j_{\text{TOT}}(V)|V|$. It is important to distinguish between the power to biased and floating surfaces, i.e. equation (25.54) versus equation (25.46), [25.30, 25.31].

Note that the heat flux is nearly a minimum at the floating potential [25.32]. At potentials below floating, the power flux increases slightly due to the increasing impact energy of the ions. For potentials above floating, the electron particle, and thus energy, flux increases exponentially fast. Operation at potentials near or above the plasma potential is often hazardous due to this strong heating.

The foregoing analysis applies to the case of no magnetic field. Provided ion motion is along $\boldsymbol{B}$-field lines, this theory should also apply when $\boldsymbol{B} \neq 0$. For ion motion oblique to magnetic field lines, as occurs when the plane of the collecting surface is not parallel to the $\boldsymbol{B}$-field, further analysis is required, section 2.10.

Further requirements that can be added to the q_{surface}—values already calculated include:

(a) Ion back-scatter. The impacting ions tend to be reflected from the surface (usually as neutrals), depositing only a fraction R_{iE} of their impact energy there, section 3.2.
(b) The e–i recombination energy χ_i should be added.

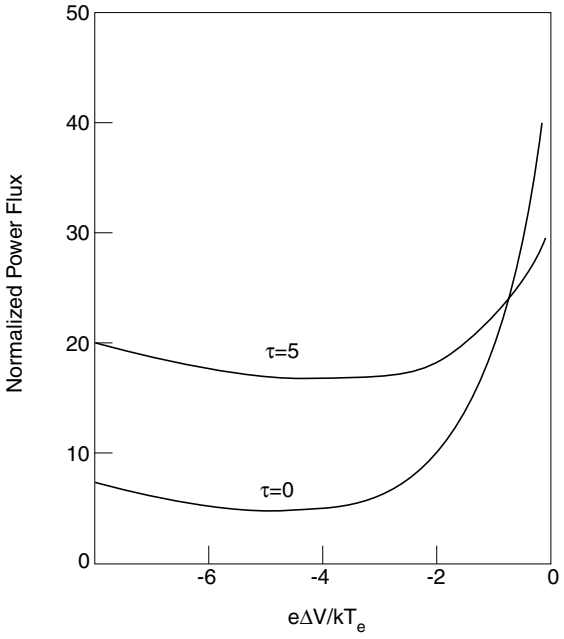

Figure 25.12. The (normalized) heat flux to a surface as a function of its potential relative to the plasma (electrically bias surface), and of $\tau \equiv T_i/T_e$ [25.34]. $\Delta V \equiv V$ here. D^+ ions.

(c) Atom–atom recombination energy χ_r should be added (if molecular formation ensues). Here also an ion particle reflection coefficient R_{iN}, should be allowed for.

(d) Electron back-scatter, section 3.1. For purposes of computing *particle* fluxes (hence floating potential) it is not necessary to distinguish between electron-induced secondary electron emission and electron back-scatter. For purposes of calculating *heat* flux and γ_e, however, the distinction can be worth making since a secondary electron only removes a few eV from the solid, while the back-scattered electron can return a sizeable fraction of $2kT_e$ to the plasma, section 3.1.

(e) Pre-sheath contributions. As indicated above, pre-sheath contributions can also be added. In the simplest case this introduces $(\sim)\frac{1}{2}kT_e$ to γ_e, but for more complex pre-sheaths, other values may be appropriate, see section 25.1.

Including these latter refinements one may rewrite

$$\frac{q_{\text{surface}}}{j^+/e} \approx \left[2.5T_i - eV_f\left(\frac{m_e}{m_i}, \frac{T_i}{T_e}\right)\right](1 - R_{iE}) + \frac{2kT_e}{1-\delta}(1 - R_{eE}) + \varepsilon_{\text{pre.sh.}} + \chi_i + \chi_r(1 - R_{iN}). \tag{25.55}$$

Example:

$$H^+ \text{ on W}, T_i = 20 \text{ eV}, \quad T_e = 10 \text{ eV}. \text{ Then } \chi_i = 13.6 \text{ eV}, \quad \chi_r = 2.2 \text{ eV},$$
$$\delta \approx 0.3, R_{iN} \approx 0.5, \quad R_{iE} \approx 0.3, \quad R_{eE} \approx 0.15, \quad eV_f = -2.1kT_e$$

and thus

$$\frac{q_{\text{surface}}}{j^+/e} = 49.7 + 24.3 + (\sim 5) + 13.5 + 1.1 \approx 94 \text{ eV}$$

hence

$$\frac{q_{\text{surface}}}{kT_e j^+/e} \approx 9.4 = \gamma.$$

Ideally one should employ values of R_{iE}, R_{eE}, R_{iN} and δ which are appropriate for the actual incident angle of the particles. In practice, surface roughness implies that one should probably use average values. The effect on heat flux and γ of terms, which are independent of T_e and T_i, such as χ_i, is only significant when T_e and T_i are rather small, i.e., generally smaller than χ_i. For many edge plasma conditions, e.g., the foregoing example, the T-independent contributions to γ are not great and can be ignored, to first order. In some divertor devices, however, very low temperature (and high density) plasmas have been achieved near the surface, with $T \leq 1$ eV (detachment, chapter 16). In such cases one should include further T-independent contributions to γ, for example, the energy removed from the solid for each secondary electron emitted, a few eV. For a non-floating surface the solid will also gain (lose) the electron work function energy corresponding to the net gain (loss) of an electron from the plasma. For the case of a high density edge, plasma neutrals emitted from the solid into the plasma will be dissociated (into Franck–Condon atoms of a few eV energy), electronically and vibrationally excited and ionized all quite close to the surface. One should then include in the calculation of heat flux to the actual surface, contributions due to Franck–Condon atoms, photons, excited neutrals, etc impacting on the surface. Clearly the calculation of heat flux to a surface for high density, low temperature edge plasmas requires special treatment, and this will not be dealt with further here.

As noted in section 2.4, when electron self-collisionality is extremely weak throughout the entire plasma, then even the forward-going, high energy tail of the electron velocity distribution may be missing since there is no collisional 'replenishment' of the Maxwellian distribution. This situation is a complex one since the actual distribution will then depend on assumptions about the electron source, however, the general tendency will be for $|V_f|$ to decrease, since the electrons reaching the solid surface are, of necessity, average ones, rather than high energy ones [25.33]. The sheath heat transmission coefficient therefore also decreases.

References

[25.1] Harrison E R and Thompson W B 1959 *Proc. Phys. Soc.* **72** 2145
[25.2] Allen J E 1976 *J. Phys. D: Appl. Phys.* **9** 2331
[25.3] Riemann K-U 1981 *Phys. Fluids* **24** 2163
[25.4] Riemann K-U 1991 *J. Phys. D: Appl. Phys.* **24** 493
[25.5] Riemann K-U 1996 *Contrib. Plasma Phys.* **36** S19
[25.6] Stangeby P C and Allen J E 1970 *J. Phys. A: Math. Gen.* **3** 304
[25.7] Bissell R C, Johnson P C and Stangeby P C 1989 *Phys. Fluids* B **1** 1133
[25.8] Matthews G F, Fielding S J, McCracken G M *et al* 1990 *Plasma Phys. Control. Fusion* **32** 1301
[25.9] Budny R V 1980 *J. Vac. Sci. Technol.* **17** 298
[25.10] Budny R V and the TFTR Group 1990 *J. Nucl. Mater.* **176–177** 427
[25.11] Pitcher C S, Stangeby P C, Bell M G *et al* 1992 *J. Nucl. Mater.* **196–198** 241
[25.12] Skinner C H, Hogan J T, Brooks J N *et al* 1999 *J. Nucl. Mater.* **266–269** 940
[25.13] Seigneur A, Guilhem D, Hogan J *et al* 1993 *20th EPS (Lisbon)* vol 2, p 603
[25.14] Guilhem D, Hogan J, Aniel T *et al* 1999 *J. Nucl. Mater.* **266–269** 272
[25.15] Gray D S, Baelmans M, Boedo J A *et al* 1999 *Phys Plasmas* **6** 2816
[25.16] Matthews G F, Hill D N and Ali Mahdavi M 1991 *Nucl. Fusion* **31** 1383
[25.17] Theilhaber K and Birdsall C K 1989 *Phys. Fluids* B **1** 2260
Theilhaber K and Birdsall C K 1989 *Phys. Fluids* B **1** 2244
[25.18] Daube Th, Riemann K-U and Schmitz H 1998 *Phys. Plasmas* **5** 117
[25.19] Stangeby P C, Pitcher C S and Elder J D 1992 *Nucl. Fusion* **32** 2079
[25.20] Riemann K-U 1994 *Phys. Plasmas* **1** 552
[25.21] Reiter D 1999 private communication
[25.22] Stangeby P C 1995 *Phys. Plasmas* **2** 702
[25.23] Stangeby P C and Chankin A V 1995 *Phys. Plasmas* **2** 707
[25.24] Hutchinson I H 1996 *Phys. Plasmas* **3** 6
[25.25] Cohen R H and Ryutov D D 1995 *Comments Plasma Phys. Control. Fusion* **16** 255
[25.26] Cohen R H and Ryutov D D 1999 *Phys. Plasmas* **6** 1995
[25.27] Cohen R H and Ryutov D 1998 *Phys. Plasmas* **5** 2194
[25.28] Cohen R H, Cid R E, Hooper E B *et al* 1999 *J. Nucl. Mater.* **266–269** 258
[25.29] Hobbs G D and Wesson J A 1966 *Culham Laboratory Report* CLM-R61
Hobbs G D and Wesson J A 1967 *Plasma Phys.* **9** 85
[25.30] Staebler G M and Hinton F L 1989 *Nucl. Fusion* **29** 1820
[25.31] Stangeby P C 1990 *Nucl. Fusion* **30** 1153
[25.32] Kimura H, Maeda H, Ueda N *et al* 1978 *Nucl. Fusion* **18** 1195
[25.33] Wang W X, Okamoto M, Nakajima N *et al* 1997 *Nucl. Fusion* **37** 1445
[25.34] Stangeby P C 1986 *Physics of Plasma–Wall Interactions in Controlled Fusion* ed D E Post and R Behrisch (New York: Plenum) p 41

Chapter 26

Kinetic Effects and Corrections to Collisional Expressions

26.1 Introduction

Parallel transport coefficients are explicitly or implicitly functions of the collision mean free path. The conducted parallel electron heat flux density, section 9.6:

$$q_{\parallel \mathrm{cond}} = -K_{\parallel e}\frac{\mathrm{d}T}{\mathrm{d}s_{\parallel}} \tag{26.1}$$

q [W m^{-2}], T [eV], s [m], with

$$K_{\parallel e} \approx e n_e v_{\mathrm{te}} \lambda_{\mathrm{te}} \approx 2000 T_e^{5/2} \tag{26.2}$$

$e = 1.6 \times 10^{-19}$, n [m^{-3}], v [m s^{-1}], λ [m], where v_{te} is the *typical* thermal velocity of the electrons:

$$v_{\mathrm{te}} \equiv (kT_e/m_e)^{1/2} \tag{26.3}$$

and λ_{te} is the electron collisional mean free path for the *typical* electrons for (collisions with charge particles only):

$$\lambda_{\mathrm{te}} \equiv v_{\mathrm{te}}/\nu_{\mathrm{te}} \tag{26.4}$$

where ν_{te} [s^{-1}] is the electron collision frequency.

We may recall that the introduction of such transport coefficients as $K_{\parallel}$ and the parallel viscosity coefficient $\eta_{\parallel}$, section 9.8, are *approximations* introduced to close the set of fluid equations in a reasonably simple way. It is appropriate therefore to consider when these approximations will involve significant errors and what corrections can then be included to try to extend the utility of the convenient *fluid* modelling approach. These corrections are termed *kinetic corrections* since a fully kinetic analysis—in contrast with a fluid analysis—does not require such corrections. Kinetic analysis is often prohibitively difficult, however, and therefore the incentive is strong to retain a fluid approach as far as is possible.

The development of the estimate for $K_\parallel$ given in section 9.6 makes it clear that an implicit assumption was involved in equation (9.44) that the temperature scale length L_T is much longer than λ_{te}. It is also implicit that λ_{te} is shorter than the length of the system L. Generally, the approximations underlying all parallel transport coefficients implicitly assume *short collisional lengths*, i.e. strong collisionality:

$$\lambda \ll L_{\text{scale}}, L_{\text{system}} \tag{26.5}$$

where L_{scale} is the appropriate parallel gradient scale length, e.g. L_T, in the SOL; L_{system} is the length to the nearest solid surface, thus $L_{\text{system}} \leq L$.

Various prescriptions for *kinetic correctors* for fluid transport coefficients have been reported, and in some cases, comparisons have been made with kinetic analysis to test the prescriptions and to provide guidance for the specification of what would otherwise be arbitrary adjustment factors in the kinetic correctors. It is unlikely that any single kinetic corrector prescription will be useful in all circumstances. There is inevitably an *ad hoc* spirit to this approach. One cannot expect complete consistency. Indeed, the approach has been subject to criticism [26.1, 26.2] in this regard. Since complete kinetic treatments are not generally possible, however, there seems to be little alternative to 'patching up' the fluid transport coefficients as best as possible [26.3].

26.2 Kinetic Correction for Parallel Heat Conductivity

As $\lambda_{\text{te}} \to \infty$, the classical (Braginskii [26.4], Spitzer–Härms [26.5]) parallel electron heat conduction coefficient $K_{\parallel e} \to \infty$, equation (26.2). This can lead to unphysical results since even a slight temperature gradient would result in unlimited heat fluxes. The one-way Maxwellian heat flux density, equation (9.43):

$$\phi_E^{\text{Max}} = 2kT\tfrac{1}{4}n\bar{c} \tag{26.6}$$

presumably provides some indication of a *limit* on the actual heat flux density for $\lambda_{\text{te}} \to \infty$. Thus we might assume the existence of a *limited heat-flux* density:

$$q_{e,\text{limit}} = \alpha_e n v_{\text{te}} k T_e \tag{26.7}$$

where α_e is some numerical factor of order unity.

From the detailed Braginskii–Spitzer–Härms analysis for $K_{\parallel e}$, it can be shown [26.6] that most of the heat is carried by electrons in the high velocity tail of the distribution:

$$q_{\text{Spitzer}} = -en_e\, v_{\text{te}}\, \lambda_{\text{te}} \frac{\mathrm{d}T_e}{\mathrm{d}s_\parallel} \int_0^\infty g(v/v_{\text{te}})\mathrm{d}(v/v_{te}) \approx -2.9 \times 10^{-19} n_e v_{\text{te}} \lambda_{te} \frac{\mathrm{d}T_e}{\mathrm{d}s_\parallel}. \tag{26.8}$$

The distribution g, figure 26.1, shows that most of the contribution to the heat flux comes from hot electrons with velocities:

$$v_{\text{he}} \approx 3\text{–}5 v_{\text{te}}. \tag{26.9}$$

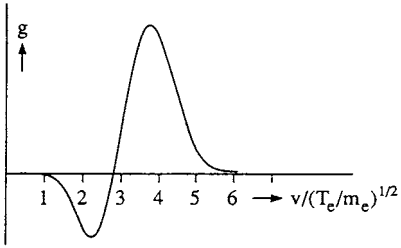

Figure 26.1. Contribution of electrons with different velocities v to the heat flux q_e [26.6].

In section 9.4 we saw that collision frequency $\nu_e \propto v_e^{-3}$, hence the mean free path, $\lambda_e \approx \nu_e/v_e \propto v_e^4$. That is, hotter electrons are *much* less collisional that the typical electrons. For the situation to be collisional, so far as heat transport is considered, is therefore much more demanding than simply satisfying $\lambda_{\text{te}} < L_{\text{scale}}, L_{\text{system}}$. It is necessary that $\lambda_{\text{he}} \lesssim L_{\text{scale}}, L_{\text{system}}$, thus [26.6]:

$$\lambda_{\text{te}} \lesssim 0.01 L_{\text{scale}}, L_{\text{system}} \tag{26.10}$$

has to be satisfied.

If we take $L_{\text{scale}} = L_T$ as being the relevant length for comparison then, combining equations (26.2) and (26.9) gives [26.6]:

$$q_{\parallel e} \leq q^*_{\parallel e} \equiv 0.03 e n_e v_{\text{te}} T_e \tag{26.11}$$

for T [eV]. For the case of no volumetric power sinks in the SOL we may take the target electron power flux density to be indicative of SOL fluxes:

$$q_{\text{te}} = \gamma_e k T_{\text{et}} n_t c_{\text{st}} \tag{26.12}$$

with $\gamma_e \approx 5$, chapter 2. Thus at the target:

$$\frac{q_{\text{te}}}{q^*_{\parallel e}} = \frac{5}{0.03}\left(\frac{2m_e}{m_i}\right)^{1/2} \sim 4 \tag{26.13}$$

for D^+ and $T_e \approx T_i$. Thus, the classical conductivity is marginally invalid near the sheath edge. This should only be taken as an indication that the situation is marginal since heat convection—which is generally strong near the sheath, reducing the flux that has to be carried by conduction—has been neglected, as have volumetric power sinks/sources, etc.

When $\lambda_{\text{he}} > L_T$, where L_T is characteristic of the typical electrons, then the fast, heat-carrying electrons penetrate into the cold region. Thus the *actual* temperature scale length which governs the heat flux is not as short as L_T, but is longer and is of order λ_{he}. Therefore, the effective coefficient $K_{\parallel e}$ is reduced when calculating $q_{\parallel e}$ based on equation (26.1) with T_e the average electron energy. That

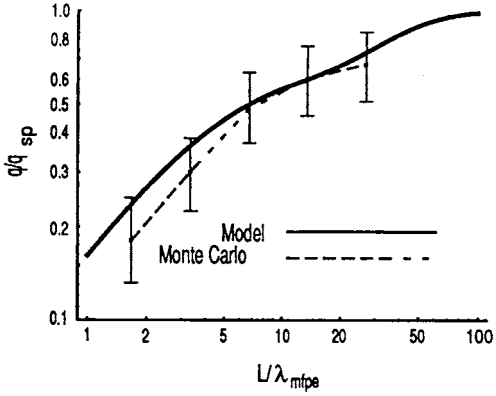

Figure 26.2. Heat flux normalized to Spitzer value as a function of the ratio of the field-line length to the mean free path. The model used $\alpha_e = 0.15$, equation (26.16) [26.3].

is, the actual $q_{\|e}$ will be less than $-K_{\|e}(\mathrm{d}T_e/\mathrm{d}s_\|)$ based on the classical value of $K_{\|e}$, equation (26.2). The magnitude of this reduction can be gauged from a selection of cases which have been analysed using a full kinetic treatment [26.3, 26.6]. Figure 26.2 shows $q_{\|e}^{\text{kinetic}}/[-K_{\|e}(\mathrm{d}T_e/\mathrm{d}s_\|)]$ as a function of L_T/λ_{te} [26.3].

One thus anticipates that in a situation such as the SOL where $q_{\|e}$ is essentially *given*, imposed by P_{SOL}, the power flow into the SOL—then as collisionality is weakened the temperature gradient will have to increase in order to carry the same power. That is, L_T will become still shorter. This situation could be induced to occur by reducing the plasma density. Figure 26.3 shows an example of such *steepening* of the parallel temperature profile $T_e(s_\|)$ for a kinetic analysis, compared with the profile that would be calculated for the kinetically calculated $q_{\|e}$ and using the classical $K_{\|e}$ [26.6].

It may seem surprising that the allowance for kinetic, i.e. long λ, effects results in a *steepening* of the $T_e(s_\|)$ profile. After all, when λ_{te} is *extremely* long compared with L_{system}, we know that *isothermal* conditions will set in, i.e. $T_e(s_\|) \approx$ constant. It has to be noted, however, that this steepening effect is characteristic of *intermediate* collisionality. For very strong collisionality, $\lambda_{\text{he}} \ll L_{\text{scale}}, L_{\text{system}}$, no kinetic corrections are needed, of course, while for very weak collisionality, $\lambda_{\text{he}} \gg L_{\text{system}}$, one obtains approximately the same answer whether one uses a kinetic or a fluid treatment, namely $T(s_\|) \approx$ constant: as was shown in section 4.10.2—where all derivations were based on classical $K_{\|e}$—when collisionality is weak, i.e. when $\nu^*_{\text{SOL}} \equiv L/\lambda_{te} < 10$, then $T(s_\|)$ approaches constancy. In a kinetic treatment, as the mean free path becomes longer, the weakly collisional tail of the distribution becomes more depleted as these electrons can become lost in one transit through the system. For this case, the particle and energy loss rates are determined by velocity-space scattering into

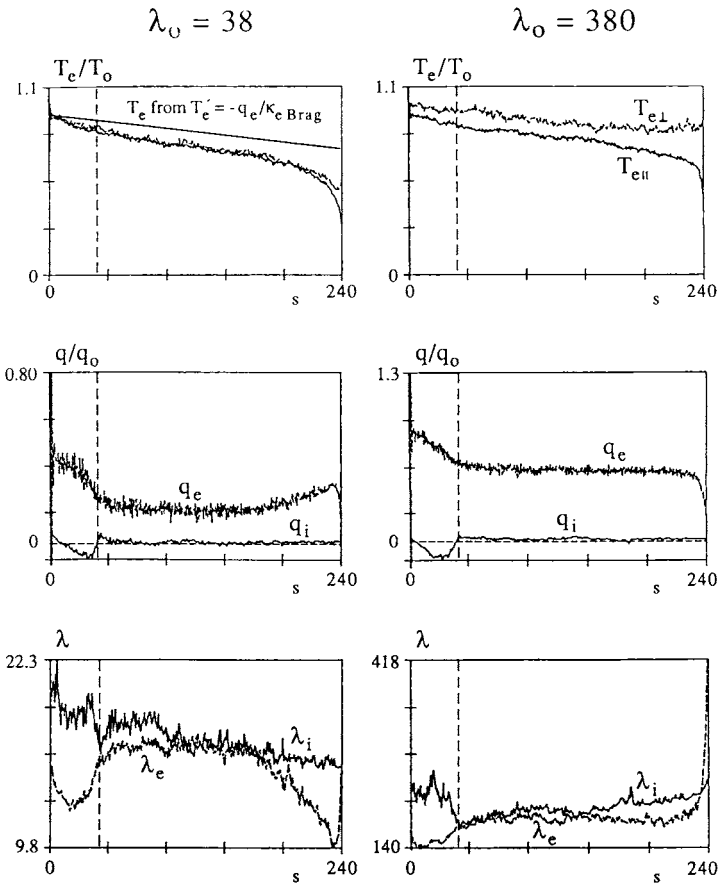

Figure 26.3. Electron temperature and heat flux for a case where the collisional mean free path is somewhat shorter than the system length (left) and a case where it is comparable (right) [26.6].

the tail region [26.3] and 'temperature' is spatially constant.

A simple *kinetic correction prescription* is often used to reproduce approximately this effect that at intermediate levels of collisionality the $T(s_\parallel)$ profile steepens: equation (26.1) is replaced by:

$$\frac{1}{q_\parallel} = \frac{1}{q_{e,\text{limit}}} + \frac{1}{q_{\text{Spitzer}}} \tag{26.14}$$

where $q_\parallel$ is the (given) total heat flux density, $q_{e,\text{limit}}$ is the limited heat flux

density given by equation (26.7) and $q_\parallel$ is given by equation (26.8). Thus:

$$\frac{\mathrm{d}T}{\mathrm{d}s_\parallel} = -(\kappa_0 T^{5/2}(q_\parallel^{-1} - q_{e,\mathrm{limit}}^{-1}))^{-1}. \tag{26.15}$$

Since necessarily $q_\parallel < q_{e,\mathrm{limit}}$ then it is seen that the inclusion of the heat limiter $q_{e,\mathrm{limit}}$ is always to increase the steepness of the $T(s_\parallel)$ profile, similar to the effect seen in figure 26.3 of [26.6].

An estimate for the value of α_e can be obtained by fitting the relation of equation (26.14) to the sample kinetic results of figure 26.2, using equation (26.8):

$$\frac{q_\parallel}{q_{\mathrm{Spitzer}}} \approx \frac{1}{1 + (1/\alpha_e)\lambda_{\mathrm{te}}/L_T}. \tag{26.16}$$

This is compared with the sample kinetic results in figure 26.2 for the choice of $\alpha_e = 0.15$, which is seen to give a reasonably good fit.

The effect of including $q_{e,\mathrm{limit}}$ may be illustrated by considering the simple example of $q_\parallel$ =constant, i.e. all the power enters at the upstream end, at $x = 0$, and exits through the sheath at $x = L$. Thus the analysis is the correction to that of section 4.10.2. The upstream conditions, n_u, T_u, are again taken to be the *control parameters* of the problem—along with L, and now α_e. Also, as before, the lumped *collisionality parameter* $\nu^*_{\mathrm{SOL}} (= L/\lambda_{\mathrm{te}} \approx 10^{-16} n_u L/T_u^2)$ is largely controlling. The target temperature T_t, given in equation (4.109) in terms of $f_T \equiv T_u/T_t$, is now given by the implicit equation:

$$\frac{\nu^*_{\mathrm{SOL}}}{10.4} = \frac{C_4}{\alpha_e}(f_T^{-3} - 1) + (f_T^{1/2})(1 - f_T^{-7/2}) \tag{26.17}$$

where

$$C_4 \equiv \frac{7\gamma c_{s0}}{12 v_{\mathrm{te0}}} \tag{26.18}$$

and $c_{s0} \equiv (2kT/m_i)^{1/2}$, $v_{\mathrm{te0}} \equiv (8kT/\pi m_e)^{1/2}$ for $T = 1$ eV. For D^+ and $\gamma = 7$, $c_{s0} = 9.79 \times 10^3$ m s^{-1}, $v_{\mathrm{te0}} = 6.7 \times 10^5$ m s^{-1} and $C_4 = 0.060$.

The complete $T(x)$ profile is then obtained:

$$\frac{x}{L}\frac{\nu^*_{\mathrm{SOL}}}{10.4} = \frac{C_4}{\alpha_e}\left[\left(\frac{T}{T_u}\right)^3 - 1\right] + f_T^{1/2}\left[1 - \left(\frac{T}{T_u}\right)^{7/2}\right]. \tag{26.19}$$

The relation $T_t(\nu^*_{\mathrm{SOL}})$ is shown in figure 26.4 for the value of $\alpha_e = 0.15$. As can be seen, the effect of the heat limiter is not very large, for this simple case, for any value of collisionality ν^*_{SOL}, but the effect is largest at intermediate collisionality, and is in the direction of *increasing* the T-gradient, as anticipated. This is seen in further detail from example $T(x)$ profiles, figure 26.5. Even for this simple case, the effect of the heat limiter is not insignificant with respect to the value of L_T near the target: for intermediate collisionality, $\nu^*_{\mathrm{SOL}} \approx 10$, the value of L_T

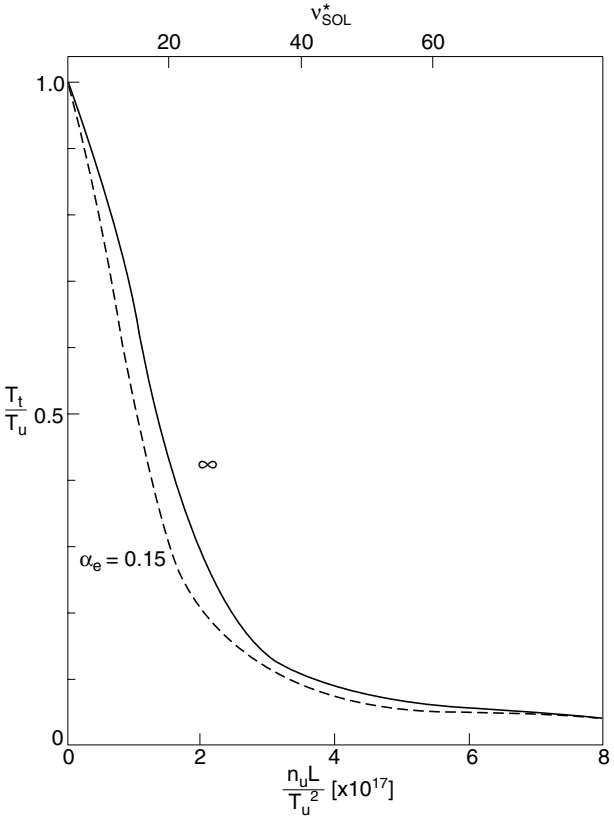

Figure 26.4. The target temperature, normalized to the upstream temperature, T_t/T_u, as a function of the (upstream) collisionality parameter $\nu^*_{\rm SOL}$ for a value of the heat-limiter parameter $\alpha_e = 0.15$, and for no heat limiter, $\alpha_e = \infty$; equation (26.19). The effect of including this heat limiter is not great, and manifests itself primarily for intermediate collisionality, making the T-gradient somewhat steeper.

is reduced by a factor of $\sim$5. This would significantly increase the T-gradient force on impurities, section 6.5, significantly; however, the coefficient for the T-gradient force *also* requires kinetic correction, section 26.4. It could well be that for less simple cases—with localized power loss due to radiation—that heat-limiter corrections could be yet more important. On the other hand, parallel heat *convection* has been neglected in the foregoing, an effect which reduces the fraction of the power carried by conduction, and thus also the importance of any conductive heat limiter.

A full kinetic analysis carried out numerically via a Fokker–Planck approach [26.7] shows in detail the modest increases in temperature drop for

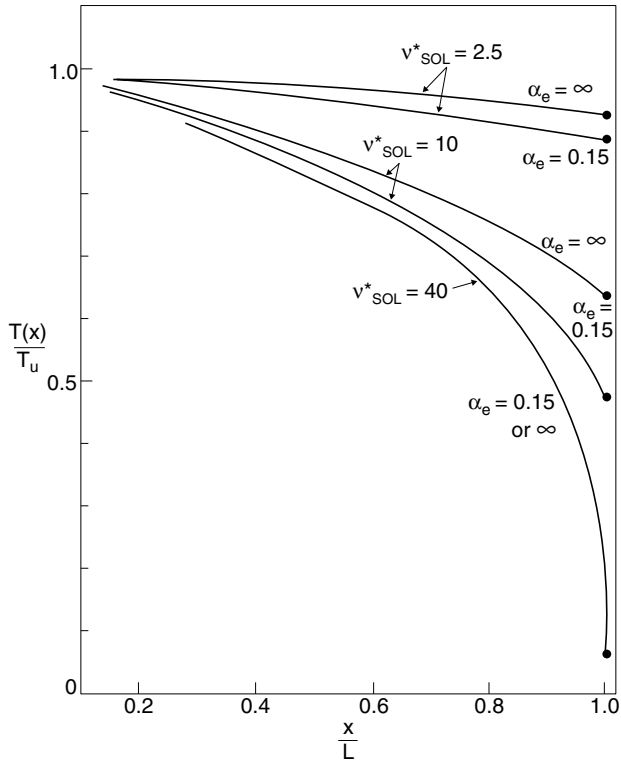

Figure 26.5. Temperature profiles for different levels of collisionality, with and without a heat limiter. As with figure 26.4 it is clear that the effect of this heat limiter is greatest for intermediate collisionality.

intermediate levels of collisionality, $\nu^*_{\mathrm{SOL}} \approx 5$–$20$, compared with the classical result.

As already noted, the simple heat limiter used above does not encompass the transition to very weak collisionality where one knows that T-gradients must *diminish*, and isothermal conditions must be approached. In order to allow for such a transition, more complex heat-limiter prescriptions have been developed [26.3].

The simple heat limiter used above has also been criticized [26.2] for leading to unphysical results for some parameter ranges. It is readily shown, for example, that equation (26.19) gives non-monotonic $T(x)$, for all values of ν^*_{SOL}, whenever:

$$\alpha_e < \frac{\gamma c_{s0}}{2 v_{\mathrm{te0}}} \tag{26.20}$$

for example, for $\alpha_e \leq 0.05$ if $\gamma = 7$, $c_{s0} = 9.79 \times 10^3$ m s^{-1} and $v_{\mathrm{te0}} = 6.7 \times 10^5$ m s^{-1}. This is a concern since (a) the appropriate value to use for α_e

is uncertain and may be less than 0.15 for some circumstances, and (b) the value of γ can be larger than 7, section 25.5. When relation (26.20) is satisfied, the simple heat-limiter prescription gives unphysical results for all collisionality—for this simple case of constant parallel power flux density $q_\parallel$. There is thus some concern for the use of such a prescription, generally.

Such kinetic correctors to fluid models as heat-flux limiters are invariably *ad hoc*. They are not likely to be completely consistent, or capable of addressing all aspects of any particular problem. Unphysical results may also occur for some cases. Nevertheless, for the foreseeable future there appears to be no practical alternative to their use for most problems.

26.3 Kinetic Correction for Parallel Viscosity

As pointed out in section 9.8, as collisionality is reduced, the classical, Bragniskii parallel viscous stress $\pi_i \to -\infty$ and the viscosity coefficient $\eta_\parallel \to \infty$, typically resulting in a very strong, unphysical forward force on the plasma flow. From equation (9.68), however, it is seen that under no circumstances can π_i be smaller than $-p_i$.

By extending the fluid approximation to include more moments (21), Radford [26.8] showed that, in fact, π_i could never become more negative than $-\frac{4}{7}p_i$. This corresponds closely to the results given in section 10.7 for a completely collisionless case where it was possible to calculate π_i precisely using kinetic modelling. This case corresponds to the strongest possible viscous stress. As reported in section 10.7, π_i at the sheath edge reached $-0.33p_i$, for p_i taken to be the upstream ion pressure, and $-0.66p_i$, for p_i taken to be the pressure at the sheath edge.

It is thus appropriate to employ a *viscous-stress limiter* analogous to the heat-flux limiter, which prevents $|\pi_i|$ from exceeding $\sim 0.5p_i$, regardless of how steep the parallel velocity gradient becomes. When this is done, it is usually found that the parallel viscous stress plays a relatively small role in the parallel pressure balance.

26.4 Kinetic Correction for the Parallel Temperature Gradient Force Coefficients

The expression for the frictional force exerted by the 'background' plasma fluid on the impurity fluid, equation (6.34), contains the collision time τ_s explicitly, thus emphasizing that the friction force is directly dependent on the degree of collisionality. Since the expressions for the temperature-gradient force coefficients, equations (6.27) and (6.28), do not explicitly contain τ_s, it may seem that these forces are not the result of collisions. This is incorrect, as the simple estimate of section 9.4, equation (9.26), makes clear: the collision time τ_s enters in two ways, which in the high collisionality limit happen to cancel exactly. For less collisional

conditions, complete cancellation does not occur and so a kinetic correction is needed.

A prescription used in the UEDGE code [26.9] is to multiply the classical T-gradient coefficients by a factor:

$$f_{\nabla T} \equiv (1 + \alpha_F(\lambda/L_{\text{grad}})^2)^{-1} \tag{26.21}$$

where α_F is an adjustable numerical factor of order unity,

$$\lambda \equiv \lambda_{\text{ti}} + \lambda_{\text{te}} \tag{26.22}$$

where

$$\begin{aligned} \lambda_{\text{ti}} &\approx 10^{16} T_i^2/n_i \\ \lambda_{\text{te}} &\approx 10^{16} T_e^2/n_i \end{aligned} \tag{26.23}$$

and L_{grad} is taken to be the smallest of the T_e, T_i, n_e, or pressure parallel scale lengths. Thus when collisionality is weak, $\lambda \gg L_{\text{grad}}$ and $f_{\nabla T} \to 0$, i.e. the T-gradient forces disappear, just as the frictional forces do.

In the Garching applications of the B2 code [26.10], a different type of kinetic corrector is sometimes used. The value of the T-gradient that is actually used to compute the forces on impurities, $(\mathrm{d}T/\mathrm{d}s_\parallel)_{\text{used}}$, is taken to be the smaller of the code-calculated (classical) value, $(\mathrm{d}T/\mathrm{d}s_\parallel)_{\text{code}}$, and $0.3T/(\alpha_F\lambda)$, where α_F is an adjustable numerical factor of the order of unity.

In the DIVIMP code, a further corrector is sometimes included: the T-gradient forces on impurities are set to zero within distance λ of the target. As noted in section 6.6.4, when using Monte Carlo modelling of impurities, it is not necessary to employ *ad hoc* kinetic correctors for the T_i-gradient force if the complete expressions are used for the collision terms [26.11].

Although the electric field force on impurities does not directly involve collisions at all, the parallel electric field itself is calculated from Ohm's law, section 9.5, which requires kinetic correction for weak collisionality. A simple prescription sometimes used in DIVIMP is to replace the fluid-model-calculated value of $E_\parallel$ with $\sim kT/2eL$ (the collisionless pre-sheath value, section 1.8.1.9), whenever $\lambda > L$, where L is the connection length.

References

[26.1] Prasad M K and Kershaw D S 1989 *Phys. Fluids* B **1** 2430
[26.2] Day M, Merriman B, Najmabadi F and Conn R W 1996 *Contrib. Plasma Phys.* **36** 419
[26.3] Cohen R H and Rognlien T D 1994 *Contrib. Plasma Phys.* **34** 198
[26.4] Braginskii S I 1965 *Reviews in Plasma Physics* vol 1, ed M A Leontovich (New York: Consultants Bureau) p. 205
[26.5] Spitzer L and Härm R 1953 *Phys. Rev.* **89** 977

[26.6] Chodura R 1992 *Contrib. Plasma Phys.* **32** 219
[26.7] Kupfer K, Harvey R W, Sauter O *et al* 1996 *Phys. Plasmas* **3** 3644
[26.8] Radford G, 1992 *Contrib. Plasma Phys.* **32** 297
[26.9] Rognlien T D 1997 private communication
[26.10] Schneider R 1997 private communication
[26.11] Reiser R, Reiter D and Tokar M Z 1998 *Nucl. Fusion* **38** 165

Chapter 27

Impurity Injection Experiments

For some time studies have been carried out of transport in the main plasma by the injection of non-recycling impurities, e.g. by laser blow-off. Although the impurity neutrals may become ionized in the edge plasma, in these main plasma studies no attempt is made to follow the low ionization stages which can, in principle, provide information on edge transport (in the SOL, divertor, pumps, etc).

Here we discuss the situation where the behaviour in the edge of the injected impurities is the principal objective.

The *recycling* and *non-recycling* cases are sufficiently different that they are discussed separately here: section 27.1, recycling case; section 27.2, non-recycling case.

For a non-recycler the specific injection location can strongly influence the level of impurity in the main plasma, i.e. the impurity confinement time. Thus one may have an opportunity to study the *local* forces acting on the impurities near the injection point. Non-recyclers constitute *local edge probes*, potentially.

For a recycler the initial injection location tends not to matter. One, however, has an opportunity to investigate the compression or retention of impurities in the divertor and any pumping which may exist.

One therefore tends to investigate somewhat different aspects of impurity behaviour in the edge with recyclers versus non-recyclers.

27.1 Injection of Recycling Impurities

Impurity injection experiments involving recycling gases such as neon have been carried out on various tokamaks. The interpretation methods used, however, are phenomenological and are not adequate for extraction of well defined values of *divertor retention* and *pumping*. The importance of impurity injection to achieve radiative divertor operation justifies increased effort to interpret these experiments. In section 27.1.3 a possible method is described for a more ambitious interpretative approach, based on the measurement of at least two calibrated spectroscopic signals—one in the divertor, one in the main plasma—together with use of an interpretive impurity code such as DIVIMP, section 6.6.

It is important to be clear as to what it is we want to understand and measure when injecting recyclers. There are at least three different basic types of information potentially of interest here:

(a) *Divertor retention or compression* of the impurity, i.e. the ratio of the total impurity content of the divertor region (neutral plus ion) to the total impurity content inside the separatrix. This is one of the main things one is interested in when puffing radiators like Ne, Ar, etc.
(b) *Pumping*. For He one is not directly interested in divertor retention and compression, but in *removing* (pumping) the impurity and in the divertor exhaust gas impurity *enrichment*. Conversely, for Ne, Ar, etc one is less interested in pumping away these gases; one would just as soon they did not pump (except perhaps to permit feed-back control); the presence of pumping just complicates the analysis and understanding of what is going on; nevertheless it is a complication one has to deal with since one of the ways to achieve good divertor compression may be to puff and pump the fuel gas, e.g. D_2, [27.1–27.10], in which case the impurity will probably also get pumped whether one wants that or not.
(c) '*Fuelling efficiency*', i.e. for a recycler like Ne, the total Ne particle content of the plasma divided by the number of Ne atoms injected into the torus. Although this is a readily measured quantity, it is generally not of primary interest: it may be largely indicative of the recycling coefficient of partially saturated surfaces far from the principal plasma-wetted surfaces; such coefficients probably vary greatly from machine to machine, or even for a given machine, with conditioning, etc. It is not obvious what one would do with such information.

The simplest model is the *single-reservoir model*, section 27.1.1. This is adequate to provide basic understanding of such things as:

(i) pumping;
(ii) how it is possible that decay time can be infinite, $\tau^* \approx \infty$, yet 'fuelling efficiency' may be $\ll 1$.

The single-reservoir model is not, however, adequate for modelling divertor *retention* and *compression*. For that one needs at least a *two-reservoir model*, section 27.1.2, ideally with at least two unknown (fitting) time constants τ_{pump} and τ_D, the latter being the characteristic time for transfer of particles from the divertor reservoir to the main plasma reservoir. With these two characteristic times one can obtain rough estimates of (a) pumping, (b) retention.

Even the two-reservoir model with an extension to include full (radial) modelling of the main plasma, as used by Roth, Krieger and Fussmann [27.11] and Dux *et al* [27.12], is not adequate for getting at the true divertor retention. An approach which might achieve this, based on (i) calibrated spectroscopic signals from the divertor, and (ii) an impurity code such as DIVIMP, is discussed in section 27.1.3.

27.1.1 Single-Reservoir Model

We follow the picture of McCracken *et al* [27.13]. The single population N here is just that of the impurities inside the plasma (the main plasma, SOL and divertor); the gas content inside the vacuum vessel is ignored. Let there be a single value of the *global recycling coefficient* R, which can include the effect of an active pump. Then:

$$\dot{N} = \phi_{in} - \frac{N}{\tau_p} + \frac{RN}{\tau_p} \equiv \phi_{in} - \frac{N}{\tau_p^*} \tag{27.1}$$

where ϕ_{in} [particles s^{-1}] is the actual gas puffing rate in this simplest case, τ_p is the *particle confinement time*, i.e., the replacement time, and $\tau_p^* \equiv \tau_p/(1-R)$ is the *decay time*.

Thus, for *start-up*, and assuming ϕ_{in} = constant and $N(0) = 0$ one obtains

$$N(t) = \tau_p^* \phi_{in}(1 - e^{t/\tau_p^*}). \tag{27.2}$$

Note that from a measurement of the initial slope of $N(t)$ one can deduce or confirm the value of ϕ_{in} since $\dot{N}(0) = \phi_{in}$.

Note: $N_\infty = \tau_p^* \phi_{in}$, thus one can extract τ_p^* either from a measurement of N_∞ or from the measured rise time of $N(t)$. Thus one obtains, for example, a measure of *pumping*: one obtains a *single* and *simple* indicator—albeit *phenomenological*—of how the pumping changes, e.g. with puff and pump of D_2, or with $\overline{n}_e$, or with P_{in}, etc. Such an indicator is of great value even if one also carries out detailed code modelling of $N(t)$ to identify the *physical details* of the pumping. Clearly it will always be useful to have such a simple, *global* indicator of pumping.

Note: in practice one cannot very easily use the start-up phase to find τ_p^* since ϕ_{in} is not constant in time, as the valve often gives a 'dribbling' inflow. A more fundamental problem is that the *radial equilibration 'settling down' time* of the main plasma, $\tau_{\text{main}} \approx a^2/D_\perp$ can be comparable to τ_p^*, preventing interpretation based on such a simple equation as equation (27.2).

For *decay*, with the gas inflow turned off, $\phi_{in} = 0$, one has:

$$N = N(0)e^{-t/\tau_p^*} \tag{27.3}$$

and so, in principle, one can also extract τ_p^*, including the effect of pumping. One still has the problem, however, that τ_p^* and τ_{main} may be comparable, in which case equation (27.3) does not apply.

It seems likely that the 'fuelling efficiency' effect often has to do with (possibly) low values of 'R_{far}', i.e. the value of wall/target reflection (perhaps also including the effect of any active pump) at remote locations where the fuel particles initially enter and where surfaces may not be saturated. Suppose that each particle recycles n times characterized by a value R_{far} before entering the region where the 'principal' value of R applies, e.g. the intensely bombarded strike point

regions where surfaces may be saturated (and so the 'principal' R may be $\approx$ unity). The *effective* gas fuelling rate is then:

$$\phi_{in}^{\text{eff}} = \phi_{in}(R_{\text{far}})^n \tag{27.4}$$

which may be much smaller than ϕ_{in}. It would be difficult/impossible to model R_{far} or n reliably, and it is not obvious that anything very useful would result even if one could. It may be worth noting, however, that this effect only changes the results for this single-reservoir model slightly:

(i) the initial slope is now $N(0) = \phi_{in}^{\text{eff}}$, which, aside from the problems with valve 'dribble' and τ_{main}, would provide a measure of ϕ_{in}^{eff} and thus a check on the measured 'fuelling efficiency', since $N_\infty = \phi_{in}^{\text{eff}}\tau_p^*$;
(ii) the characteristic growth and decay times are still τ_p^*, unchanged (although there remain the problems re 'dribble' and τ_{main}).

Note: the τ_p used here is the *true* particle confinement or replacement time, i.e. in steady state

$$\tau_p = N/\phi_{\text{total}} \tag{27.5}$$

where ϕ_{total} is the total number of impurity particles being ionized per second (both from any puff, ϕ_{in}, plus the recycling source(s)), at any location in the plasma, and N is the total impurity content of the plasma (main plasma, SOL, divertor). Unfortunately τ_{main} is sometimes, incorrectly, called the 'confinement time' and written as τ_p [27.11]. It is important to distinguish between these two times. In this single-reservoir model, τ_{main} does not appear and so one cannot allow for the fact that the observed decay time, τ_p^*, might have largely to do with transport in the main plasma, i.e. the time required for the main plasma to equilibrate radially. In order to allow for that effect one must employ a two-reservoir model at least, with one of the reservoirs taken to be the main plasma, i.e. the region inside the separatrix, next section.

27.1.2 The Garching Two-Chamber Model

Starting in the mid-1980s Garching researchers have pioneered these studies beginning with the paper of Fussmann *et al* at the *Symposium on Energy Removal and Particle Control in Fusion Devices (Princeton, NJ, 1984)* [27.14] and the 1986 *Nuclear Fusion* paper of Janeschitz, Fussmann *et al* [27.15]; see [27.11]–[27.31]. The analysis procedure commends it and has evolved over this period and the most complete description is given by Roth, Krieger and Fussmann [27.11].

The total impurity *ion* content in the main plasma (the first reservoir) is N_{main}. The total impurity *neutral* content of the divertor (the second reservoir) is N_{div} (there is, presumably, also an impurity *ion* content of the divertor, but this is not explicitly referred to; this will be seen to be one of the deficiencies of this analysis procedure, below).

The most *physically* satisfactory way to describe particle transfers is in terms of fluxes ϕ [particles s^{-1}]. This, however, does not lead to a *convenient, simple*

formulation of the problem where one would like to be able to characterize the various processes by a single *phenomenological* parameter. The latter is best achieved by defining *characteristic times* for the various transfer processes in terms of a 'reservoir content' and an associated flux ϕ. There is a price paid for this convenience: usually the 'reservoir content' is not well defined physically—but only phenomenologically. Thus, one tends to extract only *trends* from such an analysis procedure. Nevertheless, the relative simplicity of this approach commends it and has resulted in its widespread use. It is also a good place to start in the understanding and analysis of the problem.

One has for N_{div}:

$$\dot{N}_{\text{div}} = \phi_+ - \gamma\phi_D - \phi_{\text{pump}} + \phi_{\text{ext}}^{\text{div}} \tag{27.6}$$

where

(a) ϕ_+ is the ionic outflow across the separatrix into the SOL/divertor. In order to introduce the finite equilibration time of the main plasma, this model assumes that $\phi_+ = N_{\text{main}}/\tau_{\text{main}}$ (Roth *et al* call τ_{main} the 'plasma confinement time' and write it as τ_p; this will be avoided here, but the relation to Roth's symbols should be kept in mind). Again it is to be emphasized that the first chamber/reservoir in this model is the main plasma itself.

(b) ϕ_D is the fuelling rate of the main plasma from the divertor. Conceptually, the simplest case is when the main plasma is *neutral* fuelled, i.e. neutrals escape from the divertor at rate ϕ_D then 'attack' the main plasma radially, becoming ionized in a symmetrical shell either inside or outside the separatrix, see figure 27.1. It is assumed that $\phi_D \propto N_{\text{div}}$, the total neutral content of the divertor, and then ϕ_D is replaced by N_{div}/τ_D, where τ_D is a 'divertor retention time' of some sort. The precise physical meaning of τ_D is not clear and it is best to consider it to be a phenomenological quantity. In any case it is unknown and is found by fitting the model to measured $N_{\text{main}}(t)$ (or some related main plasma quantity) as discussed below. The main plasma may, however, be *ion* fuelled, i.e. the neutrals are ionized within the divertor and cross into the main plasma as ions. N_{div}/τ_D is still used to represent ϕ_D, but then the physical meaning of N_{div} and τ_D is even less clear and, again, they should be thought of as phenomenological quantities. Presumably, for ion fuelling, $\phi_D \propto N_+^{\text{div}}$, the *ion* content of the divertor, but perhaps we may assume that $N_+^{\text{div}} \propto N_{\text{div}}$; thus, for ion fuelling, the value of τ_D is assumed to 'soak up' this relation. We know that the neutral density must vary greatly throughout the divertor volume, and these variations themselves will vary with plasma conditions; thus the value of τ_D must indeed be particularly phenomenological, and it should be established experimentally for each different plasma condition. The γ-factor is explained below.

(c) ϕ_{pump} is also taken to be proportional to N_{div} (although one might ask if this 'N_{div}' is really the same 'N_{div}' as used in $\phi_D = N_{\text{div}}/\tau_D$; presumably these '$N_{\text{div}}$s' are at least proportional to each other so, again, the τs have to 'soak

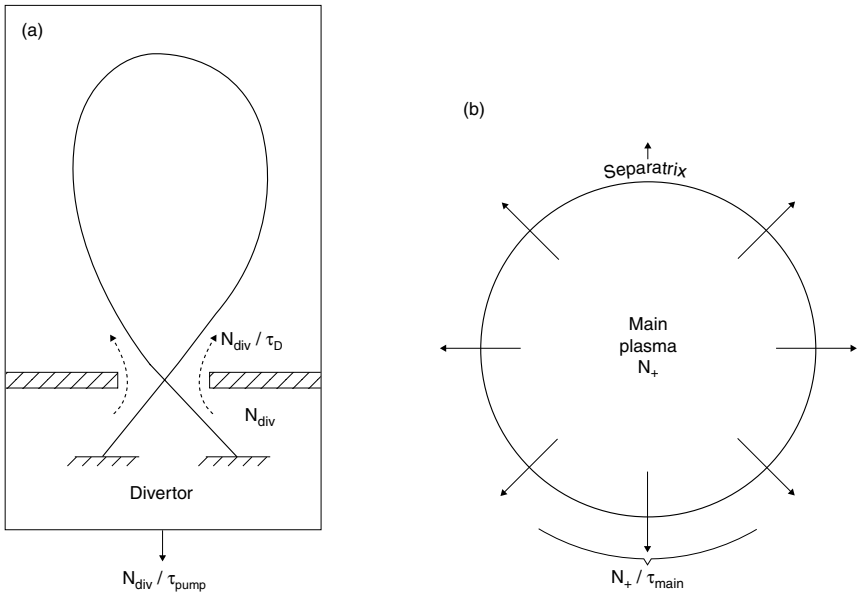

Figure 27.1. (a) In the simplest picture of the two-reservoir model one imagines a divertor gas box (the first reservoir) of neutral content $N_{\rm div}^0$ (divertor ion content is ignored) which leaks neutrals at a rate $\phi_D \equiv N_{\rm div}/\tau_D$ into the vacuum region surrounding the confined plasma. Neutrals may also be removed by a pump at rate $N_{\rm div}/\tau_{\rm pump}$. (b) The second reservoir is the confined plasma inside the separatrix of content N_+ (neutrals ignored) which loses ions at rate $N_+/\tau_{\rm main}$ (where $\tau_{\rm main} = a^2/D_\perp^{\rm main}$, say) into the SOL, which immediately transfers these ions into the divertor, i.e., the SOL is not itself a reservoir here but merely a conduit of particles. (c) Although a flux $N_{\rm div}/\tau_D$ exits the divertor as neutrals, the effective ionic fuelling across the separatrix is only $\gamma N_{\rm div}/\tau_D (\gamma < 1)$, where γ depends on the radial location of ionization and thus on the assumed values of E_0, $n_e(r)$, $T_e(r)$. Thus the effective transfer rate from divertor reservoir to core reservoir is only $\gamma N_{\rm div}/\tau_D$. One finds γ by setting $N_+^{\rm ss}/\tau_{\rm main} = \gamma\phi_D$ ('ss' for steady state) and knowing $\tau_{\rm main}$ (e.g., $a^2/D_\perp^{\rm main}$) and the ratio $N_+^{\rm ss}/\phi_D$ (e.g., from the Engelhardt model). (d) The resulting particle flow balance for the analytic version of the two-reservoir model. (e) When using the ZEDIFF radial code one does not use the γ factor. Instead the full influx $\phi_D = N_{\rm div}/\tau_D$ from the divertor is considered to enter radially and uniformly with given energy E_0 into a given $n_e(r)$, $T_e(r)$ plasma (SOL and main plasma), thus ionizing in some specific radial pattern. ZEDIFF uses this source, together with assumed values of $D_\perp$, $v_{\rm pinch}$, $\tau_\parallel^{\rm SOL}$, to calculate $n_z(r,t)$ for all charge states. ZEDIFF also then calculates the loss rate ϕ_+ from the main plasma back to the divertor, as shown. The main plasma should no longer be spoken of as a 'reservoir' since its contents are now analysed in radial detail; one might speak instead of a 'population', which would now be the entire content of SOL and main plasma—usually dominated by the main plasma (except at start-up). The divertor reservoir remains as before, bottom of (d), except now ϕ_+ replaces $N_+/\tau_{\rm main}$ and $N_{\rm div}/\tau_D$ replaces $\gamma N_{\rm div}/\tau_D$.

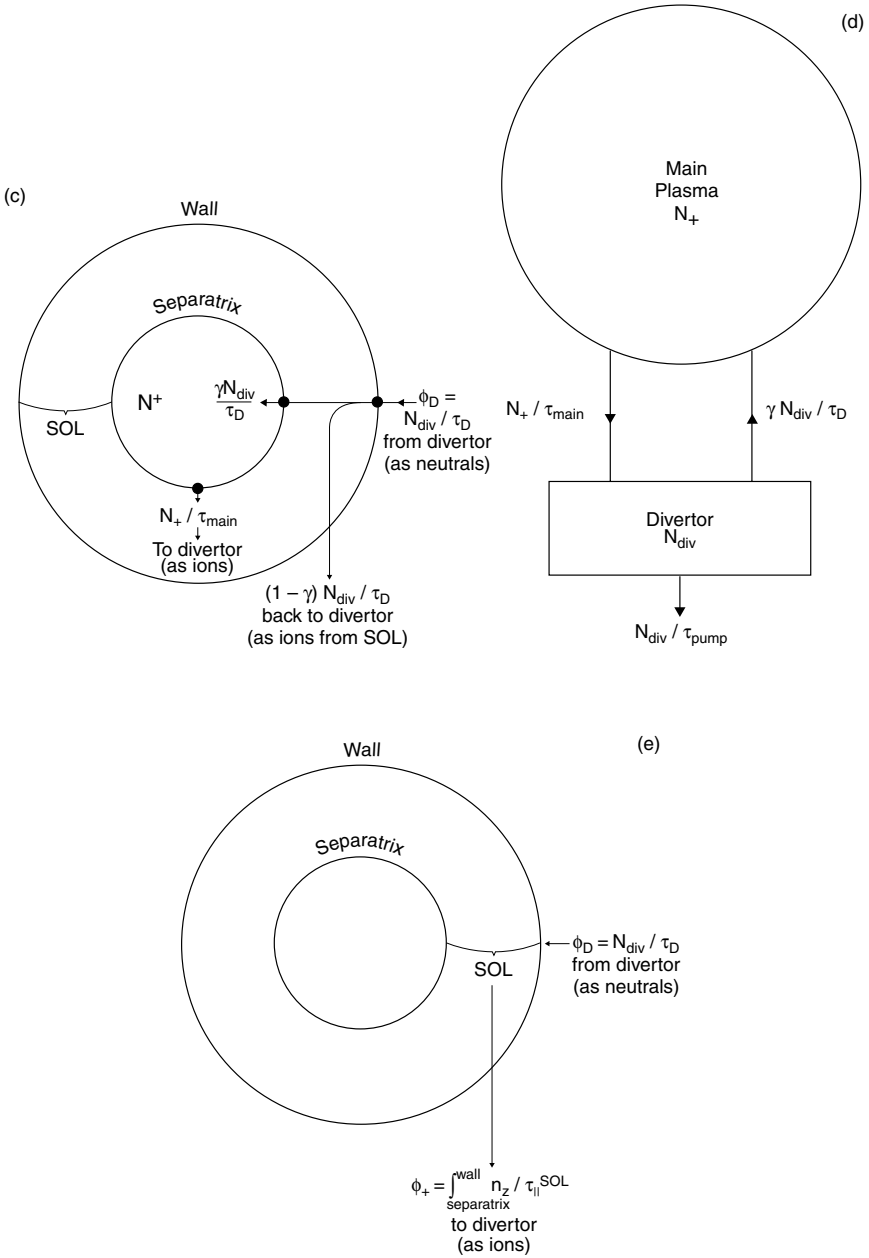

Figure 27.1. Continued.

up' unknown—and probably varying—relations). Thus one writes $\phi_{\text{pump}} = N_{\text{div}}/\tau_{\text{pump}}$ with τ_{pump} a second, unknown phenomenological quantity which is also to be extracted by fitting model results for $N_{\text{main}}(t)$ to the measured $N_{\text{main}}(t)$ for each plasma condition. That is a *two*-parameter fitting exercise is required.

(d) $\phi_{\text{ext}}^{\text{div}}$ is a prescribed, external injection rate into the divertor which can be time dependent. One might choose to replace it with an effective value, as per equation (27.4).

Thus the two reservoirs are fully described by:

$$\dot{N}_{\text{main}} = -\frac{N_{\text{main}}}{\tau_{\text{main}}} + \frac{\gamma N_{\text{div}}}{\tau_D} + \phi_{\text{ext}}^{\text{main}} \tag{27.7}$$

$$\dot{N}_{\text{div}} = \frac{N_{\text{main}}}{\tau_{\text{main}}} - \frac{\gamma N_{\text{div}}}{\tau_D} - \frac{N_{\text{div}}}{\tau_{\text{pump}}} + \phi_{\text{ext}}^{\text{div}} \tag{27.8}$$

where $\phi_{\text{ext}}^{\text{main}}$ and/or $\phi_{\text{ext}}^{\text{div}}$ may be zero, and are, in any case, *given*.

Note: one has two equations for the two unknowns, $N_{\text{main}}(t)$, $N_{\text{div}}(t)$ in terms of (the assumed known) τ_{main} and the two unknown parameters τ_D, τ_{pump}. The latter two quantities have to be extracted from the measured $N_{\text{main}}(t)$ decay in a *two-parameter fitting*.

One also notes the presence of a shielding factor γ, discussed next.

The simplest case to consider is *neutral* fuelling of the main SOL by neutrals which leak out of the divertor at a rate N_{div}/τ_D. These neutrals are imagined to distribute themselves uniformly around the edge of the main plasma, and then to penetrate radially in some distance where they are ionized. See figure 27.1(c). For simplicity assume all the neutrals are ionized at some distance from the separatrix, λ_{iz} ($\lambda_{iz} > / < 0$ for ionization inside/outside LCFS). Note: one needs to specify a radial neutral energy E_0 in this model in order to be able to calculate λ_{iz}.

Now in steady state, and for $\phi_{\text{ext}}^{\text{main}} = 0$, and no pumping, we must have:

$$\frac{N_{\text{main}}^{\text{SS}}}{\tau_{\text{main}}} = \gamma\phi_D = \gamma\frac{N_{\text{div}}^{\text{SS}}}{\tau_D} \tag{27.9}$$

(SS for steady state) which now indicates why a shielding factor is required when one assumes $\phi_+ = N_{\text{main}}/\tau_{\text{main}}$, which we do here: the ratio N_{main}/ϕ_D will depend on the value of E_0, i.e. λ_{iz}. Equation (27.9) also indicates how γ is to be calculated. We can illustrate using the Engelhardt model, section 4.6, for slab geometry, wall plates separated by distance $2a$; the impurity ion density in the main plasma, assuming only diffusion and no pinch, is given by:

$$n_{\text{main}} = \begin{cases} \Gamma_D(\lambda_{iz} + \lambda_{\text{SOL}})/D_\perp^{\text{main}} & \text{for} \quad \lambda_{iz} \geq 0 \\ \Gamma_D\lambda_{\text{SOL}}\mathrm{e}^{\lambda_{iz}/\lambda_{\text{SOL}}}/D_\perp^{\text{SOL}} & \text{for} \quad \lambda_{iz} \leq 0 \end{cases} \tag{27.10}$$

with

$$\lambda_{\text{SOL}} = (D_\perp^{\text{SOL}}\tau_\parallel^{\text{SOL}})^{\frac{1}{2}} \tag{27.11}$$

where Γ_D is in units [particles m^{-2} s^{-1}]. One relates $\Gamma$to ϕ using $\phi/\Gamma = A_s$, surface area of the plasma.

One has:

$$N_{\text{main}}^{\text{SS}} \approx a n_{\text{main}} [\text{ions m}^{-2}]. \tag{27.12}$$

Suppose

$$\tau_{\text{main}} = a^2/D_\perp. \tag{27.13}$$

It is then readily shown, starting with equations (4.72), (4.73) that:

$$\gamma = \begin{cases} \dfrac{D_\perp^{\text{main}}}{D_\perp^{\text{SOL}}}\left(\dfrac{\lambda_{iz} + \lambda_{\text{SOL}}}{a}\right) & \lambda_{iz} > 0 \\ \lambda_{\text{SOL}} \dfrac{e^{\lambda_{iz}/\lambda_{\text{SOL}}}}{a} & \lambda_{iz} < 0. \end{cases} \tag{27.14}$$

Typically $\gamma \ll 1$; Roth *et al* give sample values of $\gamma \approx 0.25$ and 0.08 for He and Ar for a specific plasma example. One finds λ_{iz} using E_0 and *given* radial profiles of $n_e(r)$, $T_e(r)$.

Note: at this point a problem must be pointed out. One recognizes, of course, that τ_D reflects all the unknown, complex physics of impurity transport in the edge; the whole point of this analysis procedure is to 'push' all those unknown phenomena into τ_D, and to then extract τ_D from the experimental $N_{\text{main}}(t)$ decay profile. So that is alright. Unfortunately, *precisely* the same unknown physics governs $\tau_\parallel^{\text{SOL}}$, thus λ_{SOL}, and thus γ. In the procedure here this is ignored and values of $\tau_\parallel^{\text{SOL}}$ are simply *assumed*, typically a ms, or so. This is a logical flaw in this analysis method. We will have to keep track of its consequences in the following. To sum up: γ is treated in this method as if it can be known *a priori*, a *given*—although, in reality, it is not and probably varies as much as does τ_D, i.e. with variations in $\overline{n}_e$, P_{in}, etc.

Now, as noted already, the main plasma may not actually be refuelled by *neutrals* leaking out of the divertor region, which enter the main SOL but rather may be *ion* fuelled by particles which were ionized in the divertor plasma and then were transported as ions to the main plasma. In this case the calculation of γ needs separate consideration, as discussed below.

Note: the shielding factor γ is not a shielding factor as one thinks of normally, i.e. one that depends only on the conditions in the plasma edge, i.e. on λ_{iz} and λ_{SOL}: one notes that τ_{main}, $D_\perp^{\text{main}}$ (and any $v_{\text{pinch}}^{\text{main}}$) are also involved, owing to the specific way that γ is introduced here, equation (27.9).

In steady state one obtains from equations (27.7) and (27.8) the steady state content ratio, i.e. the *divertor retention* that we are looking for:

$$\frac{N_{\text{main}}^{\text{SS}}}{N_{\text{div}}^{\text{SS}}} = \tau_{\text{main}}\left(\frac{1}{\tau_{\text{pump}}} + \frac{1}{\tau_D/\gamma}\right) \tag{27.15}$$

where one has used the fact that, in steady state:

$$\phi_{\text{ext}} = N_{\text{div}}^{\text{SS}}/\tau_{\text{pump}}. \tag{27.16}$$

Suppose $\tau_{\text{pump}} \gg \tau_D/\gamma$ then

$$\frac{N_{\text{main}}^{\text{SS}}}{N_{\text{div}}^{\text{SS}}} = \frac{\tau_{\text{main}}}{\tau_D/\gamma} \tag{27.17}$$

which clearly illustrates two important points:

(a) One improves divertor retention either by reducing divertor leakage (a long τ_D) or by better shielding by the boundary plasma surrounding the main plasma SOL (a small γ).
(b) Only the ratio τ_D/γ matters for divertor retention, $N_{\text{main}}^{\text{SS}}/N_{\text{div}}^{\text{SS}}$, not τ_D or γ separately. It will turn out, as discussed below, that it is τ_D/γ that is extracted from the measured $N_{\text{main}}(t)$ decay—and thus the uncertainties concerning γ do not affect the calculation of the divertor retention ratio.

In the case of an *ion*-fuelled main plasma what do we mean exactly by 'leakage from the divertor'; after all, no *neutrals* leak at all, they are *all* ionized in the divertor. Thus one would perhaps start by assuming that one should use $\phi_D = \phi_{\text{rec}}$, the total recycling source at the targets (also adding in any external ϕ_{ext}). Then, provided one *knew* all the, possibly complicated, physics governing impurity transport in the edge, one could use a code like DIVIMP to find the ratio between $N_{\text{main}}^{\text{SS}}$ and ϕ_D, for the particular 2D ionization distribution calculated for the recycling source and taking the neutral energy to be known, etc. One would then insert that computed $N_{\text{main}}^{\text{SS}}/\phi_D$ into equation (27.9) and find γ. Clearly, however, this is assuming the very thing that we are acknowledging from the outset that we do *not* know, i.e. the edge impurity transport physics—i.e. precisely the same problem as was encountered with neutral fuelling. This has to be avoided, clearly. Proceeding anyway, let us imagine that, effectively, the ion-fuelling case amounts to neutrals being ionized along the separatrix of the main plasma. Then one knows the effective γ^{eff} from equation (27.14):

$$\gamma^{\text{eff}} = \frac{D_{\perp}^{\text{main}}}{D_{\perp}^{\text{SOL}}} \frac{\lambda_{\text{SOL}}}{a} \tag{27.18}$$

which should then be used together with an *effective* τ_D^{eff}. So one would have, for example:

$$\gamma^{\text{eff}} \frac{N_{\text{div}}^{\text{SS}}}{\tau_D^{\text{eff}}} = \frac{N_{\text{main}}^{\text{SS}}}{\tau_{\text{main}}} \tag{27.19}$$

whereas, in fact, it should be:

$$\gamma^{\text{actual}} \frac{N_{\text{div}}^{\text{SS}}}{\tau_D^{\text{actual}}} = \frac{N_{\text{main}}^{\text{SS}}}{\tau_{\text{main}}}. \tag{27.20}$$

We may note, however, that:

$$\gamma^{\text{actual}}/\tau_D^{\text{actual}} = \gamma^{\text{eff}}/\tau_D^{\text{eff}} \tag{27.21}$$

and since it is only the τ_D/γ ratio that comes into the expression for the divertor retention, i.e. $N^{SS}_{main}/N^{SS}_{div}$, it makes no difference to use $\gamma^{eff}/\tau^{eff}_D$—which, we will then simply call γ/τ_D.

Note: however, there is still a fly in the ointment. While it is perfectly obvious that we do not want to attempt to calculate γ^{actual} *a priori*—it is not actually any easier to calculate γ^{eff} since λ_{SOL}, thus $\tau^{SOL}_{\|}$, is involved. While the latter expression may look innocent, all the complicated edge impurity transport physics that govern τ_D or γ^{actual} also govern γ^{eff}. Happily, it is only the ratio τ_D/γ that comes into the divertor retention ratio, equation (27.15), so that aspect is no problem. As with the case of neutral fuelling, however, one cannot reliably extract the value of τ_D itself from this analysis procedure (although publications using this method usually do, unfortunately).

To re-capitulate: equation (27.15) provides us the answer to our principal question, namely, what is the divertor retention? It does so in terms of two unknowns, τ_{pump}, τ_D. How are we to evaluate these quantities? In this analysis procedure it is done by measuring a *single* quantity—the temporal decay of $N_{main}(t)$ or some related main plasma quantity such as the ArXVI intensity; see figure 27.2 as an example from the paper of Roth *et al*. It should be emphasized that in this analysis procedure *these are the only impurity input data*. Neither $N_{div}(t)$ nor any related *divertor* impurity signal is used. (One does however, also need information about $D^{main}_{\perp}$, v^{main}_{pinch}, e.g. from laser blow-off injection studies; in any case, the transport in the main plasma is assumed to be *known*, i.e. τ_{main}.)

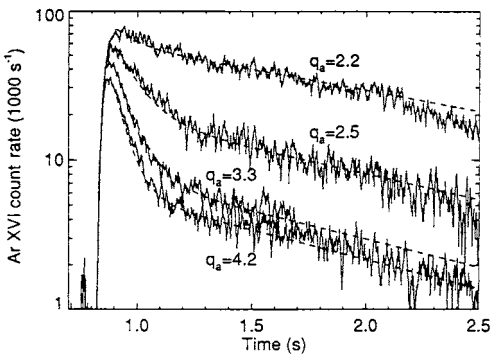

Figure 27.2. ASDEX [27.11]. Temporal decay of the ArXVI line measured in the main plasma after Ar injection in ohmic discharges.

Roth *et al* [27.11] give the analytic solution to equations (27.7) and (27.8) for decay, i.e. after ϕ^{main}_{ext}, ϕ^{div}_{ext}, are set to zero:

$$N_{main}(t) = A\exp(-t/\tau_{short}) + B\exp(-t/\tau_{long}) \tag{27.22}$$

where the two *observable* decay times involved, τ_{long} and τ_{short}, are related to the

unknown system time constants by:

$$\tau_{\text{pump}} = \frac{\tau_{\text{short}}\tau_{\text{long}}}{\tau_{\text{main}}} \tag{27.23}$$

$$\tau_D/\gamma = \frac{\tau_{\text{short}}\tau_{\text{long}}\tau_{\text{pump}}}{(\tau_{\text{main}} - \tau_{\text{short}})(\tau_{\text{long}} - \tau_{\text{pump}})}. \tag{27.24}$$

Thus, provided that one can actually discern a τ_{short} and a τ_{long} in the decaying $N_{\text{main}}(t)$ signal—as is the case for the examples of Roth *et al* in figure 27.2—then one can find the two basic unknowns, τ_{pump} and τ_D/γ. Note that it is the combination τ_D/γ that is extracted, which is fortunate, since this combination appears in the expression for divertor retention, equation (27.15).

Inverting equations (27.23), (27.24) one obtains:

$$1/\tau_{\text{short(long)}} = (2\tau)^{-1}(1 + (-)[1 - 4\tau^2/\tau_{\text{main}}\tau_{\text{pump}}]^{1/2}) \tag{27.25}$$

where

$$\tau^{-1} \equiv \tau_{\text{main}}^{-1} + (\tau_D/\gamma)^{-1} + (\tau_{\text{pump}})^{-1}. \tag{27.26}$$

For the case of not too strong pumping, i.e. $\tau_{\text{pump}} \gg \tau_D/\gamma$, τ_{main}, one has a conveniently simple regime: one can show from equations (27.25), (27.26) that:

$$\tau_{\text{decay}} \approx \tau_{\text{long}} \approx \tau_{\text{pump}}\left(1 + \frac{\tau_{\text{main}}}{\tau_D/\gamma}\right) \tag{27.27}$$

also

$$\frac{N_{\text{main}}^{\text{SS}}}{N_{\text{div}}^{\text{SS}}} \approx \tau_{\text{main}}/(\tau_D/\gamma). \tag{27.28}$$

So:

$$\tau_{\text{decay}} \approx \tau_{\text{pump}}\left(1 + \frac{N_{\text{main}}^{\text{SS}}}{N_{\text{div}}^{\text{SS}}}\right) \tag{27.29}$$

i.e.

$$\frac{N_{\text{main}}^{\text{SS}} + N_{\text{div}}^{\text{SS}}}{\tau_{\text{decay}}} = \frac{N_{\text{div}}^{\text{SS}}}{\tau_{\text{pump}}} \tag{27.30}$$

which just corresponds to the two reservoirs decaying, while staying in steady-state equilibrium with each other. This is the situation referred to in [27.30], [27.31]. Thus, from a knowledge of τ_{pump}—perhaps using some estimate based on known pumping speeds and volumes in the system (although proceeding that way confuses the important distinction between *phenomenological* and *physical* pumping time constants)—and a measured τ_{decay}—one directly obtains the divertor retention $N_{\text{main}}^{\text{SS}}/N_{\text{div}}^{\text{SS}}$ from equation (27.29). This is the simplest version of the two-chamber model.

In ASDEX, the divertor retention was investigated extensively for inert gases [27.11]. Short gas puffs were applied in the main chamber and the decay of the

impurity line radiation in the main plasma was monitored. Figure 27.2 shows the temporal decay of the ArXVI line after Ar injection into the ohmic phase of discharges with various values of the safety factor q. Two exponential decay times can be discerned, as expected for a two-chamber model. The fast decay largely results from the outflux from the main plasma into the divertor, eventually reaching equilibrium. The slow decay is largely the result of Ar pumping of the divertor chamber by the external pumps.

In fact, Roth *et al* [27.11] did not use the analytic analysis procedure above. This procedure is simply for insight and illustration. $\tau_{\text{long}} - \tau_{\text{pump}}$, equation (27.24), can be small, causing uncertainties. The value of τ_{main} is subject to uncertainties. Also, one may be able to measure a *number* of charge states in the main plasma, and by fitting all of these to the model, the extractions of τ_D and τ_{pump} should be more reliable. Furthermore, the use of τ_{main} only very approximately deals with the effects of transport in the main plasma: for times short compared with τ_{main}, different charge states will have different time behaviour in the main plasma. Also, a time-dependent ϕ_{ext} is usually involved, making analytical modelling difficult. Accordingly Roth *et al* used a fully time-dependent 1D (radial) impurity transport code, ZEDIFF [27.11], to model the main plasma. Dux *et al* [27.12] used the similar STRAHL code.

ZEDIFF and STRAHL give as output $n_z(r, t)$, the impurity density in the main plasma of each charge state at each radius, at each time—thus a computed $N_{\text{main}}(t)$ and all other main plasma quantities. (Thus, it is not really a 'two-reservoir model': there is one 'reservoir', that of the neutral content of the divertor, N_{div}—while the second *population*, the ion content of the main plasma, is modelled in 1D spatial detail, and so should not be referred to merely as a 'reservoir'.) ZEDIFF and STRAHL require as input:

(i) *specified* radial $n_e(r)$, $T_e(r)$ in the main plasma and the SOL;
(ii) *assigned* values of cross-field transport, $D_{\perp}^{\text{main}}$, $v_{\text{pinch}}^{\text{main}}$;
(iii) an *assigned* sink action strength in the SOL, $n_z/\tau_{\parallel}^{\text{SOL}}$, where $\tau_{\parallel}^{\text{SOL}}$ has an *assigned* value, e.g. $\sim$1 ms;
(iv) *assumptions* about where the neutrals are ionized; the total strength of the ionization source is again simply set to equal N_{div}/τ_D, which is the fuelling rate of the confined plasma by the divertor; the spatial distribution of the ionization source, however, is also of importance; if one thinks that the confined plasma is actually fuelled by neutrals entering around the edge of the main plasma, then, taking some *assigned* value of the neutral energy E_0, and *given* $n_e(r)$, $T_e(r)$, one calculates the radial distribution of ionization (assuming the neutrals enter radially from a wall, rather than from divertor targets, however); if estimates of neutral penetration indicate that most neutrals are ionized in the divertor, and thus that the confined plasma is *ion* fuelled, i.e. by ionic diffusion across the separatrix from the SOL, then the ionization source is simply taken to be at the separatrix, as in the analytic approach.

This then gives a closed set of equations for N_{main} and N_{div}. Input parameters

and data, to repeat, are: $n_e(r)$, $T_e(r)$, $D_\perp^{\text{main}}$, $v_{\text{pinch}}^{\text{main}}$, $\tau_\parallel^{\text{SOL}}$, E_0. One also has, as before, the two unknown, phenomenological quantities τ_D and τ_{pump} which one finds by adjusting them in the modelling of $N_{\text{main}}(t)$ until the latter fits the measurements, e.g. of ArXVI intensity in the main plasma or any other measured quantity in the main plasma.

One final aspect is needed to close the equations: the value of ϕ_+ needed in equation (27.6) is calculated from the ZEDIFF output:

$$\phi_+ = \int_{\text{separatrix}}^{\text{wall}} n_z/\tau_\parallel^{\text{SOL}} \mathrm{d}V \tag{27.31}$$

i.e. an integral over the volume of the SOL.

At the end of this analysis procedure one also has, from the model, calculated $N_{\text{div}}(t)$ and $N_{\text{main}}(t)$. The 'divertor retention' can then be taken to be $N_{\text{div}}^{\text{SS}}/(N_{\text{div}}^{\text{SS}}+N_{\text{main}}^{\text{SS}})$, say—although, since N_{div} does not include N_+^{div}, and since, in fact, its exact physical meaning is not entirely clear, this measure of 'divertor retention' only gives *trends*—for example as tokamak heating is increased—rather than absolute quantities.

It is thus seen that the ZEDIFF-based approach is not fundamentally different from the analytically based one:

(a) In both cases one has to assume that $n_e(r)$, $T_e(r)$ $D_\perp^{\text{main}}$, $v_{\text{pinch}}^{\text{main}}$, $\tau_\parallel^{\text{SOL}}$, E_0 are given, thus τ_{main} also. One has to assume the same simple geometrical patterns of fuelling the main plasma.

(b) In both cases τ_{pump} and τ_D are unknowns which have to be extracted by matching a model result to an observed decay signal of an impurity quantity in the main plasma. In the analytic approach τ_D/γ always appears as this combination, although one can calculate γ separately—albeit with major and questionable assumptions. In the ZEDIFF-based approach the parameter τ_D appears by itself, although the same questionable assumptions that were involved in explicitly calculating γ in the analytic approach are still implicitly present in the analysis.

For both methods it can be said that

The great strength of this approach is that one does not need to measure any quantity in the divertor. One just measures $N_{\text{main}}(t)$, or some main plasma quantity such as ArXVI.

In fact, even if one had a measurement of some divertor quantity, e.g. the impurity recycle influx at the targets, one would not know how to incorporate that information into this analysis procedure. The reason is that N_{div} is really a phenomenological quantity, rather than an actual neutral particle count. If one measured the total impurity recycle flux at the target, or the total ArII intensity or the Ar^+ density in the divertor, etc, one would not know how to relate that to N_{div}.

The information that is obtained, then, from this procedure, is the *trend* of τ_D with, for example, changes in auxiliary heating of the tokamak, or changes in $\overline{n}_e$, etc. Clearly, *higher τ_D simply means better divertor retention*.

The actual impurity *ion* content of the divertor—which may represent a significant part of the impurity content of the divertor—is assumed to be proportional to $N_{\rm div}$, and so the effectiveness of *divertor retention* will be indicated, as to *trend*, by the ratio of $N_{\rm div}/N_{\rm main}$, which this procedure calculates. One cannot go further with this method, and calculate the *actual* ratio of impurity particle content of the divertor to that of the main plasma.

Dux *et al* [27.12] have employed a variant of the Garching method. It can be the case that $N_{\rm main}(t)$ does not clearly show two distinct decay times, which makes a two-parameter extraction problematical. For this situation Dux *et al* calculated $\tau_{\rm pump}$ from first principles, i.e. the known speed of the ASDEX-U turbo pump and the volume of the divertor (3 m^3). As previously discussed, however, $\tau_{\rm pump}$ in this analysis method is strictly a *phenomenological* quantity which really should be extracted from the experimental data for each plasma condition—by *fitting* to $N_{\rm main}(t)$.

Dux *et al* also make the point that, while $\tau_{\parallel}^{\rm SOL}$ may well not be known, the divertor $N_{\rm div}(t)/N_{\rm main}(t)$ retention is found to depend on the ratio of $\tau_{\parallel}^{\rm SOL}/\tau_D$—and the (extracted) value of τ_D is found to increase together with the (assumed) value of $\tau_{\parallel}^{\rm SOL}$. This relates to the same point made earlier, namely that (a) it is the ratio τ_D/γ that governs divertor retention and (b) that it is this ratio which is actually extracted from the analysis of the $N_{\rm main}(t)$ decay; further, (c) one can see from equation (27.14) that indeed γ does increase with $\tau_{\parallel}^{\rm SOL}$ (although not linearly).

To summarize: the two-chamber model is an advance over the one-reservoir model since (a) it allows for radial transport in the main plasma, and (b) it permits extraction of a characteristic divertor retention time τ_D (both models can yield extracted values of $\tau_{\rm pump}$). Thus divertor retention, $N_{\rm div}^{\rm SS}/N_{\rm main}^{\rm SS}$, can be estimated.

The only impurity data input is for the main plasma, specifically temporal decay of the main plasma content or a specified spectroscopic line in the main plasma. No divertor signals are used.

The divertor content is defined in a phenomenological way, thus rendering τ_D and $\tau_{\rm pump}$ phenomenological also. Thus only the *approximate trends* of divertor retention can be estimated.

Major and questionable assumptions have to be made regarding (a) the loss time from the SOL to the divertor, $\tau_{\parallel}^{\rm SOL}$, (b) the spatial distribution of the refuelling of the main plasma due to 'leakage' from the divertor.

The great strength of the approach is that a *single* main plasma signal is sufficient input. However, it is probably too much to expect that quantities which primarily have to do with processes at the edge—$\tau_{\rm pump}$ and τ_D—could be extracted with great reliability from such restricted input data.

Nevertheless, the Garching two-reservoir model is the most sophisticated tool employed to date to extract information on impurity pumping and divertor retention. It is the place to start in order to understand and analyse recycling impurity experiments. We will see in the next section why it will not be easy to

improve on this analysis procedure. It is also reassuring that calculations using the full edge code B2/EIRENE replicate the trends found using the Garching reservoir model [27.32].

27.1.3 Modelling which Uses an Edge Impurity Code and Both Divertor and Main Plasma Spectroscopic Signals

Putting aside the uncertainties in the definitions and measurements of τ_D, τ_{pump} and divertor retention, $N_{\text{div}}^{\text{SS}}/N_{\text{main}}^{\text{SS}}$—suppose that we had, in fact, extracted valid numbers for these quantities, and knew how they varied with $\overline{n}_e$, P_{in}, the magnitude of puff and pump of D_2, q, machine size, etc. Then, even without any modelling or understanding of the processes underlying the impurity transport in the edge (and this phenomenological analysis procedure does not, of course, involve any consideration of such matters), we would still know something extremely valuable, namely something that is the equivalent of knowing how energy confinement τ_E scales with $\overline{n}_e$, P_{in}, etc. With a sufficiently extensive database we would be able to *scale* to a reactor, for example, and would know what the divertor retention and pumping would be—and all without considering the details of parallel force balances on impurities in the SOL, etc.

That, then, would be a first—and highly useful—level of analysis of the data.

We could go further, nevertheless—to a second level of analysis, as one might propose along the lines described in this section. There are two reasons for attempting this. First, as discussed above, the phenomenological analysis procedures do not even give fully satisfactory extractions of τ_D, τ_{pump} and divertor retention. Secondly, we want to be able to relate these *global, phenomenological* quantities to the underlying *edge physics processes*. We would like, for example, to understand how and why changes in the plasma flow along the SOL (say due to puffing D_2) or changes in the parallel temperature gradients (say due to changes in P_{in}), and the associated impurity forces, affect divertor retention and pumping.

This second level of analysis requires the use of a model/code of the edge and main plasma. A way of proceeding to do this is described in the following.

Impurity codes like DIVIMP calculate all the quantities needed to evaluate the *actual* divertor retention: the ionic and neutral impurity particle content at all points through the main plasma, SOL and divertor regions. The problem, of course, is to be sure that the calculations are credible. The best way to do that is to compare as many other code-calculated quantities as possible with experiment—particularly impurity line intensities of as many charge states, at as many locations, as possible. If the code matches those signals then the credibility of the other code calculations, such as divertor retention, is increased. At a minimum one should measure a low charge state in the divertor and a high one in the main plasma. Credibility is increased, however, the more data are matched.

The simplest experimental situation to interpret in order to extract divertor retention is the *steady-state* one (in contrast with the one- and two-reservoir model approaches where one is *obliged* to work with time-varying signals) where impurity and plasma are constant in time everywhere. For a non-recycler this

requires a constant ϕ_{ext} ('bleed'). For a recycler with pump off, a brief puff is adequate—while with pump on, a steady 'bleed' is needed. Since the codes operate most naturally in calculating steady-state conditions, this is the easiest situation to interpret.

All the usual code input information is needed, e.g. for DIVIMP, the plasma conditions across the target. One also needs to make input assumptions about $D_{\perp}^{\text{SOL}}$, $v_{\text{pinch}}^{\text{SOL}}$, $D_{\perp}^{\text{main}}$, $v_{\text{pinch}}^{\text{main}}$, and $n_e(r)$, $T_e(r)$ in the main plasma. The 'plasma background' throughout the SOL has to be calculated—using an onion-skin model, chapter 12, or an edge fluid code, chapter 13. One does *not* of course, introduce parameters $\tau_{\parallel}^{\text{SOL}}$ and τ_D; these are, in effect, *calculated* by the code.

In order to match the spectroscopic signals it is necessary to know the *photon efficiencies* for the lines used. Unfortunately, the database is often weak for the low charge states—which are important in the divertor.

The pumping/removal would be handled as follows when using DIVIMP:

(a) For a non-recycler, every neutral and ion which strikes any solid surface is removed. The primary source location has to be specified.
(b) For a recycler with pump off: neutrals and ions are recycled from every solid surface with unit probability (actually a value slightly less than 1 is used so that the calculation will terminate). The primary source location has to be specified in the code, but has no effect on the final result, since the recycle source dominates.
(c) For a recycler with pump on: DIVIMP can achieve pumping by specifying the reflection coefficients < 1 for specified segments of wall and/or target for neutrals and/or ions.

It may well be the case that the calculated steady-state divertor and spectroscopic signals in the main plasma will not be particularly sensitive to the details of the pumping—nor perhaps even to whether the pump is on/off in the code. While analysis of the steady state may be the best way for deducing divertor retention, it may not be adequate for reliably deducing the pumping. For the latter one will probably have to use temporal decay experiments.

27.2 Injecting of Non-Recycling Impurities

Consideration of the injection of non-recyclers turns out to be an appropriate occasion for reviewing some basic facts about our understanding of edge plasmas.

Generally: we still know very little about edge impurity transport. Little is known about cross-field transport coefficients for impurities in the edge. Theories about impurity parallel transport are still largely unconfirmed experimentally.

Specifically: we do not know if the theoretically anticipated accumulation of impurities upstream from the target, due to the parallel temperature-gradient force, is really a problem or not. Do long range plasma flows exist in the SOL—perhaps due to flow reversal, or $\boldsymbol{E} \times \boldsymbol{B}$ drifts, etc—which overcome this 'SOL impurity trap' effect, section 6.5? Will extra, externally induced SOL plasma

flows have to be induced by 'puff and pump' of D_2, in order to flush out the SOL, compressing the impurities into the divertor and/or enhancing their removal into the pumps? If so, how much puffing is needed? We know little about the far periphery of the SOL, which may be collisionless, and thus may provide an impurity sink action back to the divertor targets—even when the friction and T-gradient force balance in the main part of the SOL is such as to cause a 'SOL impurity trap' to exist there; or is transport out to the walls a rapid process in the far periphery? Does the far periphery, in fact, constitute an important sink action of the SOL?

Despite much effort on studying the problem of edge impurity transport, our level of understanding remains partial. The reason is largely due to the fact that there is a problem within a problem: even if we knew the SOL/divertor plasma background perfectly—i.e. n_e, T_e, T_i, $E_\parallel$, $v_\parallel$ in complete 2D detail—we would then still have to sort out how the perpendicular and parallel transport of impurities behaved in that given plasma background. Establishing the plasma background is thus the first step.

Unfortunately we have incomplete information on the plasma background. Nor can we have a high level of confidence in our edge models/codes—particularly regarding, $v_\parallel$. On CMOD, substantial $v_\parallel$ has been measured at both inside and outside SOLs near the midplane (by a Mach probe and by modelling the 'plume' from impurity puffing [27.33]), where codes and models often show rather stagnant conditions. Such flows presumably arise from more complicated recycling patterns than we currently understand—or are due to $\boldsymbol{E} \times \boldsymbol{B}$ drifts, that we also understand imperfectly. Since friction and the ion-temperature-gradient force are the most important forces on impurities in the edge, this is a major concern. Adding to this concern is our very limited knowledge about T_i which enters even more strongly than $v_\parallel$ into the expression for the friction force—and also governs the T_i-gradient force.

In order to sort out edge impurity transport we will require more information on the edge plasma background—-particularly on T_i and $v_\parallel$.

The injection of non-recyclers provides valuable opportunities to address these problems.

It is surprising that impurity injection has not been used more for edge probing than it has, considering its potential to tackle the problem at both levels, i.e. measurements of the edge plasma background plus direct monitoring of the impurity transport itself. Injection of recyclers can provide a valuable diagnostic, e.g. He injection [27.34]; however, non-recyclers provide the greatest scope for edge probing since there is no 'competition' between the primary injection and any recycling source.

Injection of CH_4 and N_2 into the edge of CMOD has provided measurements of the local plasma conditions at the injection location, including both parallel and poloidal drift velocities [27.33]. This requires spatially resolved measurements of the lower charge state distribution, e.g. by CCD cameras, near the injection point. Recyclers could also be used for such measurements, provided there is no local recycling surface—and provided the injection is not so prolonged as to cause a

large build-up of background.

The use of a non-recycler makes it possible to get almost directly at the question of whether a 'SOL impurity trap' exists and whether (and how much) puff and pump of D_2 is needed to overcome such a trap: the amount of the impurity reaching the main plasma can be measured, e.g. by CX spectroscopy; one knows the (quite localized) impurity source and its strength since recycle sources are absent; thus one can infer the 'SOL screening' or 'penetration efficiency' or 'local SOL sink strength', etc—*for that injection location*. One can then vary the injection location, thus carrying out a *localised probing* of the 'SOL sink strength', etc. This cannot be done using a recycler.

Such studies have been carried out on CMOD using N_2 and CH_4 [27.35], with the main plasma impurity content N_{main} being measured by emission spectroscopy together with the MIST 1D (radial) code. A steady-state 'bleed' ϕ_{ext} (rather than a brief 'puff') of impurity was used and the 'penetration factor' was defined:

$$PF \equiv N_{\text{main}}/\phi_{\text{ext}} \quad [\text{s}] \tag{27.32}$$

which is simply the particle confinement time, τ_p, of course. It is preferable to use the term 'confinement time' rather than 'penetration factor' since the latter can be misleading: suppose $D_\perp$ is increased, all else held fixed; then τ_p is reduced and the content is reduced—yet, because of the higher $D_\perp$, it is clear that an individual particle can 'penetrate' the plasma more deeply (also leaving more quickly).

Note that one does not have the problem here that one has for a recycler, equation (27.4), where uncertainties about the partial nature of the recycling at the less exposed surfaces renders a measurement of PF, τ_p unusable for a 'recycler'. Here the impurities only have 'one go' at contaminating the main plasma—i.e. from the initial ionization source—and recycling uncertainties do not arise.

The measurement of PF, τ_p, then, is the experimental input to the model or code which one seeks in order to establish the 'SOL sink strength' (*which requires definition*, see below), as a function of injection location, $\overline{n}_e$, P_{in}, amount of puff and pump of D_2, etc. This sought-for 'SOL sink-action' parameter is the principal output of the analysis, just as divertor retention and τ_{pump} were for the analysis of recycler injection.

In the next section we consider some simple analytic models to illustrate the procedure. In section 27.2.2 a procedure based on the use of an interpretive code like DIVIMP is outlined.

27.2.1 Simple Analytic Models for the Penetration Factor (Confinement Time) Based on a 'SOL Sink Strength' Parameter

In reality, the injection of a non-recycler results in a highly localized ionization source. We will start by considering the simpler case of a toroidally/poloidially uniform source. Later we will show that, so far as the modelling of PF, τ_p is concerned, the localized nature of the source does not matter (this important fact also applies to the code-based analysis).

For illustration we will consider three analytic cases here:

(a) A 'standard' Engelhardt model case where the sink action is parallel, along the SOL to the divertors.
(b) A modified Engelhardt case with both parallel sink action and perpendicular sink action, as to a wall surrounding the edge of the SOL
(c) A case without parallel sink action in the main part of the SOL, but with a parametrized sink action in a 'far peripheral' region, i.e. an outer SOL (where the loss is parallel and/or perpendicular).

The general result for the Engelhardt model for the case of ionization occurring within the SOL is given by [27.36, 27.37]:

$$n_{\text{main}} = \frac{\Gamma_0}{D_\perp^{\text{SOL}}} \lambda_{\text{SOL}} \sinh\left[\frac{a_w - a_i}{\lambda_{\text{SOL}}}\right] \Big/ \cosh\left[\frac{a_w - a_s}{\lambda_{\text{SOL}}}\right] \tag{27.33}$$

for slab geometry with Γ_0 particle influx density [neutrals $\text{m}^{-2}\ \text{s}^{-1}$]; $\lambda_{\text{SOL}} \equiv (\tau_{\text{SOL}} D_\perp^{\text{SOL}})^{1/2}$, where τ_{SOL} is the parallel loss-time to the divertor; radial locations are measured outward from the main plasma with $r = a_s$ being the location of the separatrix, a_i the location within the SOL where all neutrals are assumed to ionize, and a_w the wall location. A 'hard' boundary condition is assumed at the wall, $n(a_w) = 0$, and so there can also exist significant (perpendicular) loss to the walls.

One can show that the Engelhardt result already quoted for this case, equation (27.10), also equation (4.67), can be derived from the more general equation (27.33) assuming $(a_w - a_i) \gg (a_i - a_s)$, i.e. a distant wall, i.e. neglecting perpendicular sink action. We define $\lambda_{iz} \equiv (a_s - a_i)$, i.e. negative here. For $\lambda_{iz} > 0$ there is a general form equivalent to equation (27.33), see (27.36), but we will simply use the approximation of equation (27.10a) here.

Note: the parameter τ_{SOL} is the simple, single parameter we need to describe the 'SOL sink-action strength' or 'SOL screening effectiveness', etc. We would like to be able to infer this quantity from experiments and establish its dependence on $\overline{n}_e$, P_{in}, puff rate, etc.

(a) *'Standard' Engelhardt model (purely parallel sink action).* For this case we use equation (27.10). For slab geometry $N_{\text{total}} = a_s n_{\text{main}}$[ions m^{-2}] with Γ_0 in [neutrals $\text{m}^{-2}\ \text{s}^{-1}$] giving:

$$\tau_p = PF = \frac{a_s n_{\text{main}}}{\Gamma_0} = \begin{cases} (\lambda_{iz} + \lambda_{\text{SOL}}) a_s / D_\perp^{\text{main}} & \lambda_{iz} \geq 0 \\ \lambda_{\text{SOL}} \text{e}^{\lambda_{iz}/\lambda_{\text{SOL}}} a_s / D_\perp^{\text{SOL}} & \lambda_{iz} \leq 0. \end{cases} \tag{27.34}$$

One can easily show that PF, τ_p increases with τ_{SOL}, i.e. with weakening of the SOL sink action strength, as intuitively expected.

Note: from a measured value of PF, τ_p one can thus extract τ_{SOL} from equation (27.34)—*provided* one knows $D_\perp$ and can reliably calculate λ_{iz}. We will return to this critical point.

(b) *Ionization within the SOL and with both parallel and perpendicular sink action*. For this case we use equation (27.33) and, for simplicity also assume $|\lambda_{iz}|/\lambda_{\rm SOL} \ll 1$, i.e. ionization rather near the wall, i.e. shallow penetration of neutrals, giving:

$$n_{\rm main} = \frac{\Gamma_0}{D_\perp^{\rm SOL}} \frac{\lambda_{iz}}{2} {\rm e}^{-\Delta/\lambda_{\rm SOL}} \tag{27.35}$$

where $\Delta \equiv (a_w - a_s)$, the total width of the SOL. As with case (a), PF, $\tau_p = a_s n_{\rm main}/\Gamma_0$ and so again, from a measurement of PF, τ_p one can extract $\tau_{\rm SOL}$—provided $D_\perp$, Δ and λ_{iz} are known.

(c) *No parallel loss. Only 'far peripheral' loss*. Assume no parallel loss in the SOL itself. This might be due to the existence of a temperature-gradient 'SOL impurity trap', in the absence of plasma flow (or only weak flow). We also assume that impurity ions are somehow lost in a 'far peripheral' region outside the main part of the SOL. Such loss might be due to collisionless parallel loss to the targets (assuming no T-gradient trap existing there due to the collisionlessness), or due to perpendicular loss to walls—or perhaps due to a combination of parallel and perpendicular losses to various solid structures existing in the far edge. We characterize any/all such loss by a 'far peripheral loss time', $\tau^{\rm FP}$, which is thus now the single-sink-parameter equivalent of $\tau^{\rm SOL}$. It is probably best to consider $\tau^{\rm FP}$ to be phenomenological since it may not be feasible to calculate it and it may be due to a number of unidentified processes. For this case we have, as a variation of equation (27.10):

$$n_{\rm main} = (\lambda_{iz} + \lambda^{\rm FP})\Gamma_0/D_\perp^{\rm FP} \tag{27.36}$$

with

$$\lambda^{\rm FP} \equiv (D_\perp^{\rm FP}\tau^{\rm FP})^{1/2} \tag{27.37}$$

and $\lambda_{iz}(> 0)$ is here measured inward from the outer edge of the SOL itself, i.e. the interface between the SOL and the 'far peripheral' region. As before PF, $\tau_p = a_s n_{\rm main}/\Gamma_0$ and so, again, from a measurement of PF, τ_p one can extract the sink strength parameter, here $\tau^{\rm FP}$. One needs to know λ_{iz}, Δ, $D_\perp^{\rm FP}$ to do this.

The foregoing shows how, *in principle*, one can extract the sink action strength parameter, $\tau^{\rm SOL}$ or $\tau^{\rm FP}$, from a measurement of PF, τ_p. It is clear, however, that unless one has some further experimental input this will be problematical since one has to also know λ_{iz} and $D_\perp$. How can one obtain information on the latter? Probably the best prospects are to supplement the PF, τ_p measurements with spatially resolved spectroscopic/CCD camera measurements of the low and medium charge states in the vicinity of the injection point. This, however, really requires the use of an edge interpretive code like DIVIMP, and is thus beyond the scope of the simple analytical interpretations described in this section. Such procedures are discussed in the next section.

In conclusion, then, given only a measurement of PF, τ_p for a non-recycling, injected impurity—it is possible to extract the value of an (essentially) phenomenological 'SOL sink-action strength parameter', τ^{SOL} or τ^{FP}—although only approximately since one will only have estimates for λ_{iz} and $D_\perp$. (One must also assume the applicability of simple, symmetrical models for PF, $\tau_p(\tau^{\mathrm{SOL}}, \lambda_{iz}, D_\perp)$, equations (27.34)–(27.37).) It is all too likely that changes in $\overline{n}_e$, P_{in}, puff rate, etc will alter λ_{iz} and/or $D_\perp$, just as much as τ^{SOL}—and the concern is that without more measured information than just PF, τ_p values one may not be correctly relating changes in $\overline{n}_e$, etc—to changes in 'SOL sink-action strength'. One presumably has Langmuir probe measurements for different $\overline{n}_e$, etc—and so it should be possible to roughly *estimate* λ_{iz} (and perhaps $D_\perp^{\mathrm{SOL}}$) and their changes. Nevertheless, it is clear that such procedures—based solely on PF, τ_p values, essentially—should be viewed as just an initial approach to analysing such experiments.

Before leaving this section, we turn to the unfinished matter that, in reality, the impurity injection is not toroidally/poloidially symmetrical, but is highly localized.

Let the complete peripheral area of the confined plasma be $A_\perp$ ($\approx 2\pi R 2\pi a_s$), and the effective area over which the injected particles enter the confined plasma be some fraction f of this. Let the injection rate be ϕ_0 [neutrals s^{-1}]. Then, had this influx actually been symmetrical, one would have uniform influx density $\Gamma_0^{\mathrm{uni}} = \phi_0/A_\perp$, e.g. to be inserted in equations (27.33)–(27.36). In reality, the localized influx density is $\Gamma_0^{\mathrm{loc}} = \phi_0/fA_\perp$—which, if this had actually occurred over the entire surface area of the plasma, would result in a value of n_{main} larger by a factor f^{-1} than Γ_0^{uni} would give. However, the localized injection is *diluted* by this very same factor f^{-1} before the particles have traversed very much radial distance inside the separatrix, owing to the rapidity of parallel transport. Thus, the main plasma content, hence PF, τ_p, is virtually the same whether the injection is local or symmetrical.

Note that this only holds for ionization in the *main plasma*. The distribution of impurities in the SOL is, of course, quite non-symmetrical and any modelling of that aspect should take the full three dimensionality of the problem into account [27.33], see next section.

27.2.2 Interpretation Using a Code Such as DIVIMP

When using an interpretive code like DIVIMP to model PF, τ_p one does not use an adjustable input parameter such as τ^{SOL}. Rather the parallel forces on the impurity are specified, related to the background plasma properties—n_e, T_e, T_i, $v_\parallel$, $E_\parallel$, also the perpendicular transport is followed based on assumed values of $D_\perp$ and/or v_{pinch}. τ_{SOL} is calculated as an incidental *output* of the code. The code calculates PF, τ_p and many other aspects of the impurity behaviour. By adjusting various 'knobs' in the code—corresponding to the various unknowns such as $D_\perp^{\mathrm{SOL}}$—one can, in principle, match the experimental PF, τ_p values. Since there are numerous knobs/unknowns one should have as many experimental

constraints, i.e. additional measurements, as possible. Ideally one would have measurements of: (a) the 2D or 3D spatial distributions of line intensities for each charge state from the neutral state up; and (b) Doppler-measured ion temperatures and drift velocities for each charge state. One would, ideally, also have non-impurity data with as much spatial detail as possible, including D_α, Langmuir probe measurements, etc.

If one can match all of the experimental data simultaneously then one can be reasonably confident that $D_\perp^{\mathrm{SOL}}$, λ_{iz}, etc have been correctly found. The code does not assume single values of λ_{iz}, of course, but computes the actual 2D or 3D spatial distribution of ionization; the point remains as before, however, that one needs to account for changes in $D_\perp$ and ionization spatial distribution—associated with changes in operating parameters such as $\overline{n}_e$, P_{in}, puff rate, etc—to be sure that any changes in PF are actually due to changes in the parallel/perpendicular impurity ion transport in the SOL—i.e. the 'SOL sink-action strength'.

What then, finally, is extracted from such a procedure? The following, ideally:

(a) One would know if a 'SOL impurity trap' exists and what the nature and magnitudes of the forces causing it were.
(b) The effect of puff and pump of D_2—as to magnitude and location—would be understood in terms of the changes this causes to the parallel force balance for impurities, $D_\perp$, the spatial ionization pattern, etc.
(c) One would find $D_\perp^{\mathrm{SOL}}$, also spatially resolved $v_\parallel$, T_i.
(d) It is useful to have a single, simple parameter indicative of the 'SOL sink-action strength'; that would be available as the code-calculated value of τ^{SOL}.
(e) A modelling of $P_{\mathrm{rad}}/Z_{\mathrm{eff}}$ would have been achieved—which would be useful for understanding, but perhaps more useful as part of the effort to develop radiative divertor solutions for reactors. One would have established the level of *divertor retention*, just as for the recycling case.
(f) Various detailed outputs would be available which should, in principle, guide efforts in maximizing $P_{\mathrm{rad}}/Z_{\mathrm{eff}}^{\mathrm{main}}$. For example, the impurity particle confinement time would be established *for each grid location* where neutrals are ionized; it may, sometimes, be the case that a small fraction of the total ionization source is responsible for most of $Z_{\mathrm{eff}}^{\mathrm{main}}$; in that case, identifying the 'culprit' could assist in finding ways to maximize $P_{\mathrm{rad}}/Z_{\mathrm{eff}}^{\mathrm{main}}$, e.g. by manipulation of edge baffles, etc.

References

[27.1] Wade M R, Hogan J T, Allen S L *et al* 1998 *Nucl. Fusion* **38** 1839
[27.2] Bosch H-S, Coster D, Dux R *et al* 1997 *Plasma Phys. Control. Fusion* **39** 1771
[27.3] Horton C D, Vlases G C, Andrew P *et al* 1999 *Nucl. Fusion* **39** 1
[27.4] Higashijima S, Kubo H, Sugie T *et al* 1999 *J. Nucl. Mater.* **266–269** 1078
[27.5] Itami K, Hosogane N, Konoshima S *et al* 1999 *J. Nucl. Mater.* **266–269** 1097

[27.6] Bosch H-S, Dux R, Haas G *et al* 1996 *Phys. Rev. Lett.* **76** 2499
[27.7] Schaffer M J, Wade M R, Maingi R *et al* 1995 *J. Nucl. Mater.* **241–243** 585
[27.8] Schaffer M J, Whyte D G, Brooks N H *et al* 1995 *Nucl. Fusion* **35** 1000
[27.9] Wade M R, West W P, Wood R D *et al* 1999 *J. Nucl. Mater.* **266–269** 44
[27.10] Bosch H-S, Ullrich W, Bard A *et al* 1999 *J. Nucl. Mater.* **266–269** 462
[27.11] Roth J, Krieger K and Fussmann G 1992 *Nucl. Fusion* **32** 1835
[27.12] Dux R, Kallenbach A, Bessenrodt-Weberpals M *et al* 1996 *Plasma Phys. Control. Fusion* **38** 989
[27.13] McCracken G M, Samm U, Stangeby P C *et al* 1993 *Nucl. Fusion* **33** 1409
[27.14] Fussmann G, Poschenrieder W, Bernhardi K *et al* 1984 *J. Nucl. Mater.* **121** 164
[27.15] Janeschitz G, Fussmann G, Kotze P B *et al* 1986 *Nucl. Fusion* **26** 1725
[27.16] Neuhauser J, Aratari R, Bessenrodt-Weberpals M *et al* 1991 *Plasma Physics and Controlled Nuclear Fusion Research 1990, Proc. 13th Int. Conf. (Washington, DC, 1990)* vol. 1 (Vienna: IAEA) p 365
[27.17] Janeschitz G, Gianella R, Jaeckel H J *et al* 1990 *Controlled Fusion and Plasma Heating, Proc. 17th Eur. Conf. (Amsterdam, 1990)* vol. 14B, part III (European Physical Society) 1365
[27.18] Janeschitz G, Gottardi N, Jaeckel H *et al* 1991 *Controlled Fusion and Plasma Physics, Proc. 18th Eur. Conf. (Berlin, 1991)* vol. 15C, part III (European Physical Society) p 97
[27.19] Lippmann S, Mahadavi A, Roth J, Krieger K, Fussmann G and Janeschitz G 1991 *Controlled Fusion Plasma Physics, Proc. 18th Eur. Conf. (Berlin, 1991)* vol. 15C, part III (European Physical Society) p 201
[27.20] Hillis D L, Finken K H, Hogan J T *et al* 1990 *Phys. Rev. Lett.* **65** 2382
[27.21] Finken K H, Hillis D L, Dippel K H *et al* 1990 *J. Nucl. Mater.* **176–177** 816
[27.22] McCracken G M, Samm U, Bertschinger B *et al* 1992 *J. Nucl. Mater.* **196–198** 199
[27.23] McCracken G M, Bombarda F, Graf M *et al* 1995 *J. Nucl. Mater.* **220–222** 264
[27.24] Harbour P J, Barnsley R, Campbell D *et al* 1995 *Proc. 22nd EPS Conf. on Controlled Fusion and Plasma Physics (Bournemouth)*
[27.25] Schaffer M J, Whyte D G, Brooks N H *et al* 1995 *Nucl. Fusion Lett.* **35** 1000
[27.26] McCracken G M, Lipschultz B, LaBombard B 1995 *et al Proc. 22nd EPS Conf. Controlled Fusion and Plasma Physics (Bournemouth)*
[27.27] Hillis D L, Hogan J T, Finken K H *et al* 1992 *J. Nucl. Mater.* **196–198** 35
[27.28] Wade M R, Hogan J T, Hillis D L *et al* 1995 *J. Nucl. Mater.* **220–222** 178
[27.29] Janeschitz G, Ran L B, Fussmann G, Krieger K, Steuer K H and ASDEX Team 1990 *Max-Planck-Institut für Plasmaphysik, Garching Report* IPP III/147
[27.30] Kallenbach A, Dux R, Mertens V *et al* 1995 *Nucl. Fusion* **35** 1231
[27.31] Richard N, Terreault B, Haddad E *et al* 1997 *J. Nucl. Mater.* **241–243** 760
[27.32] Coster D P, Schneider R, Neuhauser J *et al* 1997 *J. Nucl. Mater.* **241–243** 690
[27.33] Jablonski D, La Bombard B, McCracken G M *et al* 1997 *J. Nucl. Mater.* **241–243** 782
[27.34] Davies S J, Morgan P D, Ul'Haq Y *et al* 1997 *J. Nucl. Mater.* **241–243** 426
[27.35] McCracken G M, Granetz R S and Lipschultz B 1997 *J. Nucl. Mater.* **241–243** 777
[27.36] Fussmann G 1986 *Nucl. Fusion* **26** 983
[27.37] Post D E and Lackner K 1986 *Physics of Plasma–Wall Interactions in Controlled Fusion* ed D E Post and R Behrisch (New York: Plenum) P. 627

Appendix A

Solutions to Problems

This appendix was co-written with Peter Schwanke.

Chapter 1

1.1. $q(a) = 3.75$, $\theta_{\text{pitch}}(a) = 0.13$ radians.

1.3. (a) For $I_p(a) = I_p(-a)$ the X-point is at $(x, y) = (0, 0)$. For $I_p(a) = 2I_p(-a)$ the X-point is at $(-a/3, 0)$, i.e. closer to the weaker current.

(b)
$$\begin{aligned}\mathbf{B}_\theta &= (B_{\theta x}, B_{\theta y}) \\ &= \frac{\mu_0 I_p}{2\pi}\left(\frac{-y}{(a-x)^2+y^2} - \frac{y}{(a+x)^2+y^2},\right. \\ &\quad \left.\frac{(a+x)}{(a+x)^2+y^2} - \frac{(a-x)}{(a-x)^2+y^2}\right).\end{aligned}$$

(c) The expression for $s_\parallel$ is only valid to the halfway point, then the sign of dx has to be changed.

(f) Simple estimate from $B_\theta(a) \approx \mu_0 I_p/2\pi a = 0.5$ T and $L \approx \pi R q$ with $q(a) \approx aB_\varphi/RB_\theta$, thus $L \approx 38$ m. Or, using the fact that the separatrix is roughly a circle of diameter $2^{1/2}a$ in the poloidal plane gives $L \approx 27$ m. Numerical integration gives $L \approx 21$ m for $K = 1.1$. As $K \to 1$, $s_\parallel^{\max} \to \infty$ because $B_\theta \to 0$ at the origin (X-point).

1.4. (a) (i) $L = 0.70$ m, (ii) 10.7 m.

(b) (i) $\tau_{\text{SOL}} = 16\ \mu s$, (ii) 240 μs. For both $\tau_{\text{main}} \approx 97$ ms.

(c) (i) $\tau_{ii}^{\text{SOL}} = 1\ \mu$s. Collisional.

(d) (i) $\lambda_{\text{SOL}} = 2.83$ mm, $V_{\text{SOL}} = 0.016$ m^3.
(ii) $\lambda_{\text{SOL}} = 11$ mm, $V_{\text{SOL}} = 0.062$ m^3. $V_{\text{main}} = 0.64$ m^3.

(e) (i) $A_{\text{wet}} = 0.023$ m^2, (ii) 0.094 m^2. $A_{\text{wall}} = 7.14$ m^2. With bevelling A_{wet} increases by a factor 1/sin 10° = 5.76, so for (i) $A_{\text{wet}} = 0.13$ m^2.

(f) $A_{\text{wet}} = 0.47$ m^2.

1.5. (a) $\lambda_{\text{Debye}} = 3.7\ \mu$m.

(b) (i) $E_\parallel \approx 20$ V m^{-1}, (ii) $E_\parallel \approx 1.3$ V m^{-1}.
(c) $n = 0.47 n_0$.
(d) ~ -14 volts.
(e) (i) 2.3 aN, (ii) 0.15 aN. For ions, force is toward sheath, for electrons away.
(f) 128 N m^{-2}.

1.6. $\dfrac{\partial n}{\partial t} + \dfrac{\partial (nv)}{\partial x} = S_p$.

1.7. A term *nmg* appears on the RHS.

1.8. Retain the term on the LHS of equation (1.24), use $E \approx kT/eL$, to obtain $n \approx n_0 \exp[(eV/kT_e)(1 + 2m_e/m_i)]$. Thus for D^+, factor is $\exp[1 + 1/1836] \approx 1.0005$.

1.10. The approximation is good for $T_e = 100$, 1000 eV but is useless for 10 eV where ionization is due to the high energy electrons in the tail of the distribution, not the average ones.

1.11. (a) For $T = 8$ eV:

$$\nu^{iz}_{\text{coll}} = 3 \times 10^4 \text{ s}^{-1},\ \tau^{iz}_{\text{coll}} = 33\ \mu\text{s},\ \lambda^{iz}_{\text{coll}} = 1 \text{ m}$$
$$\nu^{\text{cx}}_{\text{coll}} = 13 \times 10^4 \text{ s}^{-1},\ \tau^{cx}_{\text{coll}} = 7.7\ \mu\text{s},\ \lambda^{cx}_{\text{coll}} = 0.24 \text{ m}$$

for $T = 80$ eV:

$$\nu^{iz}_{\text{coll}} = 30 \times 10^4 \text{ s}^{-1},\ \tau^{iz}_{\text{coll}} = 3.3\ \mu\text{s},\ \lambda^{iz}_{\text{coll}} = 0.1 \text{ m}$$
$$\nu^{cx}_{\text{coll}} = 50 \times 10^4 \text{ s}^{-1},\ \tau^{cx}_{\text{coll}} = 2\ \mu\text{s},\ \lambda^{cx}_{\text{coll}} = 0.062 \text{ m}.$$

(b)

Process	$\nu_{\text{coll}}[\text{s}^{-1}]$	λ_{coll} [m]
$e + H_2 \rightarrow H_2^+ + 2e$	$3 \times 10^4/40 \times 10^4$	0.10/0.008
$e + H_2 \rightarrow 2H^0 + e$	$7 \times 10^4/3 \times 10^4$	0.043/0.10
$e + H_2 \rightarrow H_0 + H^+ + 2e$	$\sim 0/2 \times 10^4$	long/0.16

Values are shown in the table above for $T = 8/80$ eV.

1.12. Ionization times:

	$T = 10$ eV	100 eV
C^0	5 μs	1 μs
C^+	50 μs	3 μs
C^{2+}	1.4 ms	20 μs
C^{3+}	long	100 μs
C^{4+}	long	long

Thus if the dwell time is 1 ms then C^{2+} is the typical state at 10 eV, C^{4+} at 100 eV.

1.13. At $r = 0$, $S_{p,c-f} = 3n_0a^2D_\perp = 9 \times 10^{22}$ m^{-3} s^{-1} and $S_{p,iz} = 2 \times 10^{23}$ m^{-3} s^{-1}.
At $r = 1/a = 0.01$ m, $S_{p,c-f} = 2e^{-1}n_0a^2D_\perp = 2.2 \times 10^{22}$ m^{-3} s^{-1} and $S_{p,iz} = 0$.

1.14. (a) $2\tan^{-1}(1) - 1 - 2\tan^{-1}\left(\frac{1}{2}\right) + \frac{1}{2} = CL/c_s$, i.e. $0.144 = CL/c_s$, instead of $0.571 = CL/c_s$.
(b) $\lambda_{\rm SOL} = (D_\perp L/(0.144c_s))^{1/2} = 2.64(D_\perp L/c_s)^{1/2}$ compared with $(D_\perp L/(0.571c_s))^{1/2} = 1.32(D_\perp L/c_s)^{1/2}$. Thus $\lambda_{\rm SOL}$ approximately doubles.
(c) The numerical value of the LHS of equation (1.44) drops from 0.571 to 0.144 to 0 as $M(0)$ increases to 1. Thus $\lambda_{\rm SOL} \to \infty$. Then all of the particles are provided by ionization and there is no need for any cross-field source.

1.17. For $M(0) = \frac{1}{2}$, $n_1 = \frac{5}{8}n_0$, $\Gamma_{se} = \frac{5}{8}n_0c_s$; for $M(0) \to 1$, $n_1 \to n_0$ since there is no longer the need for a p-gradient force to drive the flow up to sound speed at the sheath edge.

1.18. $\Delta V_{\rm plasma} \approx 0.69kT_e \approx 14$ volts, thus sheath drop is ~86 volts. $L_{\rm sheath} \sim \lambda_{\rm Debye} \sim 10^{-5}$ m. Thus $E_{\rm sheath} \sim 10^7$ V m^{-1} while $E_{\rm plasma} \sim 10$ V m^{-1}. It is as if E has a singularity at the sheath edge.

1.20. (b) Constant is $n_0c_s^2$.
(e) $y(1) = \frac{1}{2}n_0c_s$.
(f) For $a = 1/3$ the source is near the 'upstream' end and most of the increase of M occurs there, while for $a = 3$ the source is near the sheath end and M only rises from low values to reach unity near the sheath.

Chapter 2

2.1. The right surface receives $[1]en_{se}c_s$ of positive ions plus $[0.538]en_{se}c_s$ of electrons, and thus receives a positive current of $[0.462]en_{se}c_s$. The left surface receives $[1]en_{se}c_s$ of positive ions, but also $[1.462]en_{se}c_s$ of electrons for a net *received* current of $[-0.462]en_{se}c_s$ (i.e. a net *injected* current of $[0.462]en_{se}c_s$.

2.2. Not a bad approximation when $T_i \geq T_e$. For $T_i = 0$ no ions reach the floating surface, and to prevent any electrons reaching the surface requires $V_{sf} \to -\infty$.

2.6. Require $n^{1/3}/T_e < \varepsilon_0/e$ for n [m^{-3}], T [eV], thus $n^{1/3}/T_e < 5 \times 10^7$. Satisfied by fusion and interstellar plasmas.

2.8. (a) $\sim 10^{-8}$.
(d) $\lambda_D \sim 2 \times 10^{-5}$ m, $\Delta V_{\rm sh} \sim 2800$ volts from the Child–Langmuir law.

2.9. Unless n_e decreases with x at least as fast as n_i there will not be net positive space charge in the (monotonic) sheath, to balance the net negative charge

on the solid surface to give shielding.

2.11. (c) $g(v') = n(m_e/2\pi kT_e)^{1/2} \exp[-m(v')^2/2kT_e] \exp[eV/kT_e]$.

2.12. Require $\alpha > 1$. The number of slow electrons must not be too great or the ion density will be too susceptible to the 'acceleration–rarefaction' effect and n_i will drop too rapidly upon entering the sheath.

2.14. (a) $I^+_{\rm sat} = 21$ A.

(b) $kT_e = -e\Big(2\dfrac{\mathrm{d}(I/I^+_{\rm sat})}{\mathrm{d}V_{\rm applied}}\Big|_{V_{\rm applied}=0}\Big)^{-1}$.

2.16. $I^+_{\rm sat} = 21$ A, as for problem 2.14(a), but here

$$kT_e = -e\Big(\frac{\mathrm{d}(I/I^+_{\rm sat})}{\mathrm{d}V_{\rm applied}}\Big|_{V_{\rm applied}=0}\Big)^{-1},$$

i.e. no factor of 2.

2.17. (a) $\Gamma_{se} = 3.79 \times 10^{23}$ m^{-2} s^{-1}.

(b) $V_{sf} = -26.4$ volts.

(c) $q^e_{ss} = 1.21$ MW m^{-2}.

(d) $q^e_{sa} = 2.81$ MW m^{-2}.

(e) $q^i_{ss} \approx 4.03$ MW m^{-2}.

(f) $q^i_{se} \approx 2.43$ MW m^{-2}.

(g) $\gamma = 8.6$.

(h) At the point where $V = \frac{1}{3}V_{sf}$, $q^e = (2kT_e + \frac{2}{3}|eV_{sf}|)\Gamma_{se}$ and $q^i = (2kT_e + \frac{1}{3}|eV_{sf}|)\Gamma_{se}$.

2.18. There is no pre-sheath density drop. $q^e_{ss} = 34$ MW m^{-2}, $q^i_{ss} = 1.6$ MW m^{-2}. Thus total power to the surface is reduced by the presence of the sheath (for given plasma conditions).

2.19. (a) $\Gamma_{\|\rm B\ MPSE} = 1.9 \times 10^{23}$ m^2 s^{-1}.

(e) $V_{\rm surface} = -26.4$ volts.

(i) The heat fluxes are just double those in problem 2.17 since in the latter n_e at the sheath edge is 10^{19} m^{-3}, while here that is the upstream density.

(b) (c), (d), (f), (g), (h), (i):

ψ	$\Gamma_{\rm DSE}$	$\Gamma_{\rm received}$	$\frac{eV_{\rm MPS}}{kT_e}$	$L_{\rm MPS}$	$E_{\rm MPS}$	$E_{\rm DS}$	$q^{\rm total}_{\rm received}$
[°]	[10^{23} m^{-2} s^{-1}]			[10^{-4} m]	[V m^{-1}]	[V m^{-1}]	[MW m^{-2}]
10	1.9	1.9	−0.15	1.1	∼1300	$\sim 4.0 \times 10^6$	5.2
50	1.2	1.2	−0.44	5.0	∼8900	$\sim 3.4 \times 10^6$	3.4
85	0.17	0.17	−2.44	6.4	∼38 000	$\sim 7.5 \times 10^5$	0.46

Chapter 3

3.1. Agreement is sometimes no better than a factor of ∼2.

3.2. Electrons escape if $v_\parallel/v_\perp > (2/3\pi)\tan\psi$.

3.4. The first M_2 particle tends to transfer all its energy to the second one and so has no energy with which to escape.

3.5. $E_{th} = E_B/\gamma(1-\gamma)$ gives $E_{th} = 30$ eV (C), 37 eV (Fe), 216 eV (W).

3.6. Sometimes the agreement is no better than a factor of ~ 2.

3.7. $\Gamma_{se} = 2.57 \times 10^{23}$ m^{-2} s^{-1}, $V_{sf} = -87$ volts, $E_0 \approx 140$ eV. Take $Y \approx 0.01$. Thus $\Gamma_C \approx 2.6 \times 10^{21}$ C m^{-2} s^{-1}, and for a solid carbon density of $\sim 2 \times 10^3$ kg m^{-3}, $\Gamma_C \approx 5 \times 10^{-5}$ kg m^{-2} s^{-1}. Thus the *gross* erosion rate $\approx 2.6 \times 10^{-8}$ m s^{-1} ≈ 0.8 m/year. Such a loss would be unacceptable as a *net* loss; however, *re-deposition* has to be allowed for.

3.8. For $E_0 \approx 140$ eV, $Y \sim 0$. For $E_0 \approx 1400$ eV, $\Gamma \approx 8.1 \times 10^{23}$ m^{-2} s^{-1}, and at $T = 300$ K, $Y \approx 0.007$. Thus $\Gamma_W \approx 6 \times 10^{21}$ W m^{-2} s^{-1} and for W solid density of $\approx 2 \times 10^4$ kg m^{-3}, the erosion rate is $\approx 1.7 \times 10^{-3}$ kg m^{-2} s^{-1}. Thus the gross erosion rate is $\approx 9 \times 10^{-8}$ m s^{-1} ≈ 2.5 m/year. For given plasma conditions (and not too hot) W has an apparently enormous advantage over C, since there is no W sputtering at all. (In reality this picture is modified since: (i) the impacting D^+ have an energy distribution and some of the high energy D^+ will sputter, (ii) low Z impurities such as C are probably unavoidable and they may have sufficient energy to sputter, (iii) therefore self-sputtering will also occur.) Even at extremely high edge temperatures—and quite beyond anything seriously contemplated—the W erosion rate is not much more than the C rate at much lower temperatures. Such W rates, however, would cause completely unacceptable contamination of the core plasma, see figure 6.2.

3.9. Using the total chemical sputtering yields of figure 3.8, at 300 K, physical + chemical sputtering rate $\approx (5 \times 10^{-5} + 4 \times 10^{-5})$ kg m^{-2} s^{-1}; at 700 K: $\approx (5 \times 10^{-5} + 3 \times 10^{-4})$ kg m^{-2} s^{-1}.

3.10. $E_0 \approx 10$ eV, giving a chemical sputtering rate $\approx 7 \times 10^{-5}$ kg m^{-2} s^{-1}. While the physical sputtering may be negligible here, the chemical sputtering is about the same as in problem 3.9.

3.11. (a) Normalization factor $A = 2Y_0E_B$.

(c) ∞, i.e. the integral used to calculate $\overline{E}$ diverges. Therefore the cut-off is important if one wants to find the average penetration of the sputtered neutrals into the plasma before ionizing, or the power carried away by the sputtered particles, etc.

3.12. (a) Normalization factor $A = Y_0[E_B^{-1} - (E_B + E_{\max})^{-1} + E_B/(2(E_B + E_{\max})^2) - E_B/(2E_B^2)]^{-1}$.

(b) $E_B/2$ is still the most probable energy of the sputtered neutrals provided $E_{\max} \geq E_B/2$, which is the case here.

(c) $\overline{E} = A[\ln(1+E_{\max}/E_B) + 2E_B/(E_B+E_{\max}) - E_B^2/(2(E_B+E_{\max})^2 - 3/2]$.

3.13. For 100 eV D^+ on W, $E_{\max}$ is calculated to be negative, i.e. there is no sputtering since $E_0 = 100$ eV is below the sputtering threshold. For 300 eV D^+ on W:

(a) $E_{max} = 3.5$ eV, normalization factor $A = 220$ eV.
(b) Now $E_{max} < E_B/2$, and since $Y(E)$ is an increasing function for $E < E_B/2$, therefore the most probable energy is E_{max}.
(c) $\overline{E} = 2.2$ eV.

The sputtered C neutrals, problem 3.12, will penetrate the plasma much more deeply than the W neutrals, since (i) their average energy is higher, (ii) their velocity is higher still, because of the lighter mass, (iii) ionization rates are not greatly different.

3.14. (a) $E_{max} = E_0 = 100$ eV. Normalization factor $A = 17$ eV.
(b) Most probable energy is $E_B/2 = 3.7$ eV.
(c) $\overline{E} = 22$ eV.
Thus neutral particles from self-sputtering are more energetic than ones from D^+-sputtering, and will penetrate the plasma more deeply before becoming ionized.

3.15. (a) $n_e n_j \overline{\sigma v}_{iz}^{j} + n_e n_j \overline{\sigma v}_{\text{rec}}^{j} = n_e n_{j-1} \overline{\sigma v}_{iz}^{j-1} + n_e n_{j+1} \overline{\sigma v}_{\text{rec}}^{j+1}$. The $\overline{\sigma v}$ depend (primarily) on T_e.
(b) 7.
(d) Ionization becomes strong even for values of T_e well below I_{iz} due to the high energy electrons in the tail of the distribution.

3.16. $P_{\text{rad}} \approx 10^5, 10^3, 2 \times 10^2$ W m^{-3} at $T = 5, 50, 5000$ eV. Low Z impurities are useful for radiatively dissipating the power that reaches the plasma edge, where T is low, but do not cool the hot plasma core significantly.

3.17. Consider as an example $T = 10^4$ eV where $P_{\text{rad,loss}}/n_e n_u \approx 10^{-32}$ W m^3, figure 3.19(a), and $P_{\text{cool}}/n_e n_u \approx 4 \times 10^{-32}$ W m^3, figure 3.19(b). P_{cool} contains the ionization power, $\overline{\sigma v}_{iz}{}^{4+} I_{iz}$ which P_{rad} does not. From figure 1.26, $\overline{\sigma v}_{iz}{}^{4+} \approx 4 \times 10^{-16}$ m^{-3} s^{-1} and from problem 3.15(d), $I_{iz} = 392$ eV, which then gives $\overline{\sigma v}_{iz}{}^{4+} I_{iz} \approx 3 \times 10^{-32}$ W m^3, i.e. approximately the difference.

3.18. The shorter τ is, the less time there is to ionize to higher states; similarly the smaller n_e is. The larger n_0 is, the more charge exchange recombination occurs, which reduces $\langle Z \rangle$.

3.19. For $n_e \tau = 10^{19} \times 10^{-2} = 10^{-17}$ s m^{-3}, $P_{\text{rad}} \approx 10^5, 500, 300$ W m^{-3} for $T = 5, 50, 500$ eV, figure 3.20. For $n_e \tau = 10^{19} \times 10^{-4} = 10^{-15}$ s m^{-3}, $P_{\text{rad}} \approx 6 \times 10^4, 10^5, 6 \times 10^4$ W m^{-3} for $T = 5, 50, 500$ eV. Thus for $T = 50, 500$ eV, for shorter dwell times the radiated power is much larger (although the radiated *energy* is not so different). For 5 eV the radiated power is not affected very much since the temperature is nearly the most efficient for coronal radiation already, figure 3.17.

3.20. (a) $E_0 \approx 105$ eV, $Y \approx 0.008$.
(b) $\Gamma_{\parallel}^{D^+} = 2.5 \times 10^{23} D^+$ m^{-2} s^{-1}, $\Gamma_{\text{dep}}^{D^+} = 2.1 \times 10^{22} D^+$ m^{-2} s^{-1}, $\Gamma^{C^0} \approx 2 \times 10^{20}$ C m^{-2} s^{-1}.
(e) $n_c \approx 3.4 \times 10^{16}$ C m^{-3}, $P_{\text{rad}} \approx 7 \times 10^4$ W, $E_{\text{rad,pot},z} \approx 2500$ eV.

3.21.

Element	$P_{\text{rad}}^{\text{main}}$[MW]	$P_{\text{rad}}^{\text{SOL}}$[MW]
Be	1	0.04
B	1.5	20
C	3	20
Ne	10	0.4
Ar	25	5

The low Z elements tend to be powerful radiators at the low temperatures characteristic of the edge plasma (although Be requires particularly low T_e to radiate strongly), while the high Z elements radiate strongly at the high temperatures characteristic of the main plasma.

3.22. (a) $\approx 6 \times 10^{21}$ H_α s^{-1}.
(b) $\approx 2 \times 10^{19}$ recombinations s^{-1}.
(c) $\tau_{iz} \approx 8\ \mu s^{-1}$, $\tau_{\text{loss}} \approx 4\ \mu s^{-1}$, and only half the H_α radiation is released. Therefore, in order to interpret easily a measured H_α intensity as an H^0-influx rate, one must be sure that the H^0 stayed in the plasma long enough to be ionized.

3.23. H_α radiation will be almost constant for 20 eV $< T_e <$ 300 eV. At 300 eV recombination is negligible. At 2 eV the H_α-rate increases to $\approx 3 \times 10^{22}$ H_α s^{-1}; recombination increases to $\approx 5 \times 10^{21}$ recombinations s^{-1}, which is still negligible (consider however what happens at 1 eV). In all cases if the loss time of H^0 is cut in half then the H_α rate is also. In reality, at low T, however, the H^0 will have a greater chance of escaping the plasma before being ionized and the H_α rate could fall below that for higher temperatures. In order to interpret H_α measurements as particle influxes therefore requires detailed modelling of the neutral transport.

3.24. (a) $\approx 5 \times 10^{21}$ photons s^{-1} of 514 nm radiation, $\approx 10^{21}$ photons s^{-1} of 464 nm radiation.

3.25. For $n_e = 10^{19}$ m^{-3}, $P_{\text{rad}} \approx 10^2$ W, with/wo re-absorption of Lyman lines. For 10^{20} m^{-3}, $P_{\text{rad}} \approx 10^6$ W without re-absorption, and $\approx 10^5$ W with. For 10^{21} m^{-3}, $P_{\text{rad}} \approx 10^8$ W without re-absorption, and $\approx 5 \times 10^6$ W with. For $n_e = 10^{21}$ m^{-3}: total ionization rate $\approx 5 \times 10^{27}$ s^{-1} and the total H_α rate is thus $\approx 10^{25}$ H_α s^{-1}, figure 3.29, which for 1.9 eV per H_α photon, gives a power of ≈ 3 MW. Thus the H_α radiated power is a small fraction of the total if Lyman radiation is not re-absorbed, but is a major part of the total if the Lyman is re-absorbed.

3.26. The ionization mean free path for 2 eV H^0 in this plasma is a few cm. Thus a slab geometry with a gap of a few cm, and a large area, would approximate the situation.

(a) $\tau_{iz} \approx 2\ \mu s$.
(b) $\phi_0 \approx 6 \times 10^{25}$ s^{-1}.

(c) (i) and (ii) $\approx 10^{24} \mathrm{H}_\alpha\ \mathrm{s}^{-1}$.

(d) It must be the same as τ_{iz} . One can check to see if such a loss time is likely for this geometry: say the gap is 4 cm, area 25 m^2: $\frac{1}{2} n_e c_s \approx 2 \times 10^{24} \mathrm{H}^+\ \mathrm{m}^{-2}\ \mathrm{s}^{-1}$; thus for a total area of 50 m^2 for ion loss, the loss rate is $\approx 10^{26} \mathrm{H}^+\ \mathrm{s}^{-1}$, i.e. roughly ϕ_0, thus OK.

3.27. A state with $R_{iz} = R_{\mathrm{rec}}$ is achieved at $T_e \approx 1.2$ eV, figure 3.23. From figure 3.31 one finds that the H_α rate is $\approx 2 \times 10^{21} \mathrm{H}_\alpha\ \mathrm{s}^{-1}$ from each of the excitation and recombination processes. Power input is still required to provide the radiation losses.

Chapter 4

4.18. No.

4.19. (a) $\lambda_p/\lambda_{q\|} = (1 + 3\lambda_n/2\lambda_T)/(1 + \lambda_n/\lambda_T)$.

(b) The same.

4.20. (b) $\lambda_n/\lambda_T = 0.6$.

(c) λ_n here is 1.14 times larger than the value from equation (4.7).

(d) $D_\perp = 0.06\ \mathrm{m}^2\ \mathrm{s}^{-1}$, $\lambda_T = 1.67$ cm.

(e) $D_\perp = 0.066\ \mathrm{m}^2\ \mathrm{s}^{-1}$, $\chi_\perp = 0.32\ \mathrm{m}^2\ \mathrm{s}^{-1}$.

4.21. (b) $V_{\mathrm{loop}} = 0.25$ volts, which is smaller than the assumed loop voltage in part (a). Note, however, that the *effective* radius of the current channel, a_{eff}, is smaller than a, the radius of the LCFS, since the conductivity peaks on axis. This smaller a_{eff} raises the resistivity and the loop voltage.

(e) $L = 47$ m.

(f) $q_{\mathrm{dep}} \approx 5\ \mathrm{MW\ m}^{-2}$. Bevel the limiter.

(g) $V_{fs} \approx 600$ volts, $E_0 \approx 10^3$ eV, thus sputtering yield is of order $Y \approx 10^{-2}$, $\Gamma_\| \approx 10^{23}\ \mathrm{m}^{-2}\ \mathrm{s}^{-1}$, $\Gamma_{\mathrm{dep}} \approx 2 \times 10^{22}\ \mathrm{m}^{-2}\ \mathrm{s}^{-1}$, $\Gamma_C \approx 2 \times 10^{20}\ \mathrm{C\ m}^{-2}\mathrm{s}^{-1} \approx 4 \times 10^{-6}\ \mathrm{kg\ m}^{-2}\ \mathrm{s}^{-1} \approx 2 \times 10^{-9}\ \mathrm{m\ s}^{-1}$. Thus 1 cm is eroded in $\approx 5 \times 10^6$ s ≈ 50 days. This may be acceptable for a *start-up* limiter since its total exposure time to plasma may be brief (before the plasma is transferred to, say, divertor targets for the majority of the exposure time in each discharge).

4.22. If $T_u > 1.9 T_t$ then the error in either expression is $< 3\%$ compared with the complete expressions.

4.23.

$$T(s_\|) = \begin{cases} \left[T_u^{7/2} - \dfrac{7 P_{\mathrm{SOL}} s_\|^2}{4 A_{q\|} \kappa_0 L_x}\right]^{2/7} & 0 \le s_\| \le L_x \\ \left[T_u^{7/2} - \dfrac{7 P_{\mathrm{SOL}} (s_\| - (L_x/2))}{2 A_{q\|} \kappa_0}\right]^{2/7} & L_x \le s_\| \le L. \end{cases}$$

4.24.

$$T(s_\parallel)=\begin{cases}\left[T_u^{7/2}-\dfrac{7P_{\rm SOL}s_\parallel^2}{4A_{q\parallel}\kappa_0 L_x}\right]^{2/7} & 0\le s_\parallel\le L_x\\ \left[T_u^{7/2}+\dfrac{(0.15)7P_{\rm SOL}(s_\parallel^2-L_x^2)}{4A_{q\parallel}\kappa_0(L-L_x)}-\dfrac{7P_{\rm SOL}(s_\parallel+L_x)}{2A_{q\parallel}\kappa_0}\right]^{2/7} & L_x\le s_\parallel\le L.\end{cases}$$

4.35. $\overline{n}_e = 1.45\times10^{20}$ m^{-3}, $\tau_p^{\rm main\ iz} = 0.05$ s, $\tau_p^{\rm SOL\ iz} = 0.0045$ s. Contributions from main ionization is $N^{\rm main} = 5\times10^{19}$ m^{-2}, and from SOL ionization, $N^{\rm SOL} = 2.25\times10^{19}$ m^{-2}, so ionization within the main plasma is more important in this case.

Chapter 5

5.20.

Case	n_t [10^{19} m^{-3}]	Γ_t [10^{24} m^{-2} s^{-1}]	$E_{\rm imp}$ [eV]	$\phi_{\rm rec}$ [10^{24} s^{-1}]	τ_p [ms]
1	92	9.0	~5	2.7	11
2	6.5	3.3	~140	0.49	30
3	1.6	2.8	~1600	0.84	36
4	3.7	2.3	~200	0.69	43

Case	$Y_{\rm phys}$	$Y_{\rm chem}$	$\phi_{\rm sput}$ [10^{22} s^{-1}]	τ_z [ms]
1	~0	~0.006	~1.6	~19
2	~0.007	~0.015	~2.2	~14
3	~0.006	~0.02	~2.2	~14
4	~0.008	~0.02	~1.9	~16

5.21. For $T_t = 20$ eV, $E_{\rm impact} \approx 100$ eV, and so W sputtering would be slight. This gives $n_u = 8.2\times10^{19}$ m^{-3}.

5.22.

n_u [10^{19} m^{-3}]	T_t [eV]	n_t [10^{19} m^{-3}]	$\phi_{\rm rec}$ [10^{22} s^{-1}]	J–H factor	H_α [10^{20} s^{-1}]	τ_p [s]
1	150	0.13	0.59	~13	~4.5	0.17
2	94	1.1	0.94	~20	~4.7	0.21
4	22	8.6	4	~60	~6.7	0.20
8	5.6	69	16	~160	~10	0.10

For $n_u < 2 \times 10^{19}$ m^{-3} the sheath-limited expressions apply here, and for $n_u > 2 \times 10^{19}$ m^{-3} the conduction-limited ones. For the latter regime, $\tau_p = 8 \times 10^{18}/n_u$, which is in approximately in agreement with the JET results of figure 4.11.

5.27.

n_u [10^{19} m^{-3}]	f_{power}	f_{mom}	Relative ϕ_{rec}
4	0.35	1	25
5	0.45	1	46
6	0.65	0.2	4

Relative $\phi_{\text{rec}} \equiv (n_u/10^{19})^2 f_{\text{mom}}^2/(1 - f_{\text{power}})$.

5.28.

n_u [10^{19} m^{-3}]	T_t [eV]	F_u [eV]	n_t [10^{20} m^{-3}]	Γ_t [10^{24} m^{-2} s^{-1}]	q_t [MW m^{-2}]
1.5	42	51	0.19	1.7	92
2	20	29	0.54	3.3	83
2.5	8.3	18	1.6	6.3	67
2.67	4.0	16	35	9.8	50

$F_u^{\min} = 16$, $T_t^{\min} = 4$ eV, $n_u^{\max} = 2.7 \times 10^{19}$ m^{-3}, $q_{\text{rad}}^{\max} = q_\parallel/4$.

5.29. $A_{\text{wet}} = 15$ m^2, $\cos\psi = (B_\theta/B)_t \cos\beta$, $\psi = 89.1°$.

5.31. (a) $\lambda_{q\parallel} = 5.6$ mm.
(b) $A_{q\parallel} = 0.063$ m^2, $q_\parallel = 31$ MW m^{-2}.
(c) $T_u = 69$ eV.
(d) $q_{\text{dep}} = 0.7$ MW m^{-2}.
(f) $T_t = 7.5$ eV, $n_t = 1.4 \times 10^{20}$ m^{-3}, $\Gamma_t = 3.7 \times 10^{24}$ m^{-2} s^{-1}.
(g) $f_{\text{power}} = 0.27$, $P_{\text{rad}}^{\text{SOL}} = 1.46$ MW.

Chapter 6

6.12. For $n_e = 10^{19}$ m^{-3}, and using figure 1.26, and $\ln\Lambda = 15$: for $T_e = 10$ eV:

State	τ_{iz} [μs]	τ_s [μs]	τ_T [μs]
C^+	50	22	12
C^{2+}	2 000	5.7	3.1
C^{3+}	50 000	2.5	1.4
C^{4+}	long	1.4	0.77
C^{5+}	long	0.81	0.49
C^{6+}	long	0.56	0.34

for $T_e = 100$ eV:

State	τ_{iz} [μs]	τ_s [μs]	τ_T [μs]
C^+	5	696	390
C^{2+}	14	174	97
C^{3+}	70	77	43
C^{4+}	33 000	43	24
C^{5+}	long	28	16
C^{6+}	long	19	11

At $T_e = 10$ eV all charge states are collisional with the D^+ and one anticipates that all C ions will tend to have the same temperature and (fluid) velocity as the D^+. At 100 eV the C^+ and C^{2+} are only weakly collisional and so will tend not to move with the D^+ fluid velocity and will tend to be colder (assuming the C started as cold neutral atoms). The C^{3+} is marginally collisional while the higher states are collisional.

6.13. (a) $\tau_{iz} = 330\ \mu$s.

(b) $\lambda_{\rm mom} = 0.7$ m, 80 μs, yes.

(c) 45 μs. $T_z(t) = T_i - (T_i - T_{z0})e^{-t/\tau_T}$. $T_z(\tau_T) = 65$ eV, $T_z(2\tau_T) = 87$ eV, $T_z(3\tau_T) = 95$ eV.
$\overline{T}_z = \tau_{iz}^{-1} \int_0^{\tau_{iz}} T_z(t)dt = T_i + (T_i - T_{z0})(\tau_T/\tau_{iz})(e^{-\tau_{iz}/\tau_T} - 1)$, so here $\overline{T}_z = 87$ eV.

(d) $\tau_\parallel = 69\ \mu$s, $D_\parallel = 9.6 \times 10^4$ m^2 s^{-1}, $\Delta s_\parallel^{\rm diff} \approx (2D_\parallel \tau_{iz})^{1/2} \approx 8$ m. v_{th} at 100 eV is 4×10^4 m s^{-1}, $v_{th}\tau_{iz} = 13$ m, v_{th} at 5 eV is 0.89×10^4 m s^{-1}, $v_{th}\tau_{iz} = 3$ m. The ion is collisional and so one is not surprised that $\lambda_{\rm mom}$ is shorter than $v_{th}\tau_{iz}$. On the other hand it may perhaps be surprising that, as a result of the chaotic, thermal motion of diffusive collisions, the C^{3+} 'cloud' can spread out (in both directions) by an amount much greater than $\lambda_{\rm mom}$.

(e) v_{th} at 87 eV is 3.7×10^4 m s^{-1}, $\Delta s_\parallel^{th} \equiv v_{th}\tau_{iz} = 12$ m $> \Delta s_\parallel^{\rm diff}$. One notes that $\Delta s_\parallel^{th}/\Delta s_\parallel^{\rm diff} = (\tau_{iz}/2\tau_\parallel)^{1/2}$ so in general this is not a good estimate.

(f) $\Delta s_\perp \approx (2D_\perp \tau_{iz})^{1/2} \approx 0.02$ m. Cross-field diffusive transport is enormously slower than parallel diffusive transport, thus from an initial point source the ion 'cloud' will become very long and thin.

6.16. (a) $2\tan^{-1} M - M = (\pi/2 - 1)(x/L)$. For $M = \frac{1}{2}$, $x/L = 0.748$, thus $s/L = 0.252$. $c_s = 7.9 \times 10^4$ m s^{-1}, $v_i = -4 \times 10^4$ m s^{-1} (toward the target).

(c) $s_0 = 25.2$ m. For $v_0 > 0$, $s(\tau_{iz}) = 15.8$ m. For $v_0 < 0$, $s(\tau_{iz}) = 14.4$ m. The effect of friction is much greater than the effect of E. For

$v_i = -4 \times 10^4$ m s^{-1}, the ions would be at $s = 13.2$ m if they moved with the D^+, i.e. they would have moved further from the starting point s_0 .

(d) Estimate of 'cloud' centre: $s = (15.8 + 14.4)/2 = 15.1$ m, with spread $\approx \pm\Delta s^{\text{diff}} = \pm 8$ m, thus spanning ~ 7 m $< s <\sim 23$ m.

6.20. (a) See figure A1.

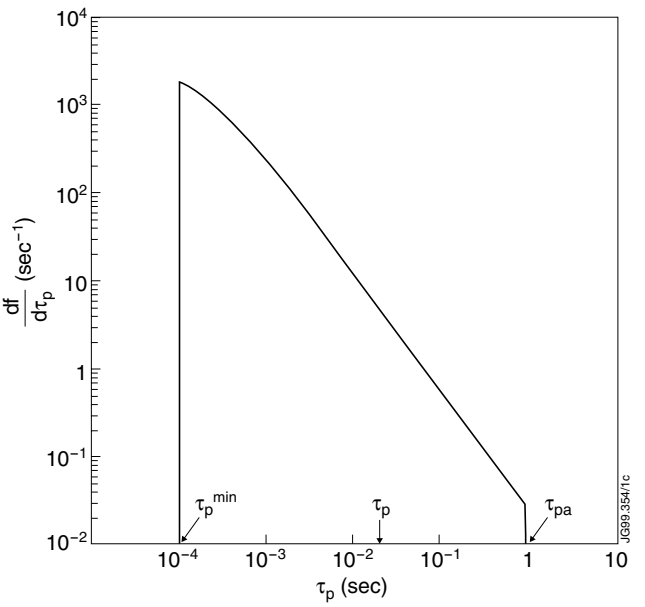

Figure A.1.

(c) $\tau_p^{\min}$ is given by $2(2D_\perp \tau_p^{\min})^{1/2} = \lambda_{iz}$. $\overline{\tau}_p = 0.02$ s. There is no maximum τ_p but $\mathrm{d}f/\mathrm{d}\tau_p$, which is already a rapidly decreasing function of τ_p for $\tau_p < \tau_{pa}$, where τ_{pa} is given by $2(2D_\perp \tau_{pa})^{1/2} + \lambda_{iz} = 2a$, decreases even faster for $\tau_p > \tau_{pa}$. Thus we may take τ_{pa} as an estimate for $\tau_p^{\max}$. Here $\tau_{pa} = 1$ s. We may cut the distribution off abruptly at $\tau_p = 1$ s, ignoring the small error this introduces to the normalization, $\int_{\tau_p^{\min}}^{\infty} \frac{\mathrm{d}f}{\mathrm{d}\tau_p}\mathrm{d}\tau_p \approx \int_{\tau_p^{\min}}^{\tau_{pa}} \frac{\mathrm{d}f}{\mathrm{d}\tau_p}\mathrm{d}\tau_p \approx 1$. The fraction of particles with $\tau_p > \overline{\tau}_p$ is $\sim$20%.

6.26. $D_\parallel = 4200$ m^2 s^{-1}.

6.27. (a) v_C changes by $\Delta v_C \approx \pm 4100$ m s^{-1}, $1/2m_C(\Delta v_C)^2 = 1.1$ eV. $\Delta T_C^f = 1.8$ eV, a comparable change.

(b) Δv_C is the same as in (a). $\Delta T_C^f = 0.47$ eV.

(c) These are essentially the same processes and when T_z is significantly less than T_i then $1/2m_z(\Delta v_z)^2 \approx \Delta T_z^f$.

6.28. (a) $v_{th} = 8900\ \mathrm{m\ s^{-1}}$, $v_{th}\tau_s \approx 0.01\ \mathrm{m} \ll s_{\mathrm{inj}}$.
(b) $v_{\mathrm{diff}} = 872\ \mathrm{m\ s^{-1}}$, $v_E = -45\ \mathrm{m\ s^{-1}}$, $v_{T_i} = 495\ \mathrm{m\ s^{-1}}$, $v_{T_e} = 176\ \mathrm{m\ s^{-1}}$, $v_{\text{prompt-loss}} = 246\ \mathrm{m\ s^{-1}} - v_B$.
(c) $n_p = 1.73 \times 10^{23}/(246 - v_B)$, which for $v_B = -1000\ \mathrm{m\ s^{-1}}$ gives $n_p = 1.4 \times 10^{20}\ \mathrm{m^{-3}}$.

6.30. $M_i = -0.026$, $\lambda_{ii} = 0.1$ m, $\lambda_T = 7.25$ m, $\lambda_{ii}/\lambda_T = 0.014$, hence the Neuhauser criterion is satisfied. Leakage is expected for $M_i = -0.014$, $v_B = -430\ \mathrm{m\ s^{-1}}$. From problem 6.28 $v_{T_i} = 495\ \mathrm{m\ s^{-1}}$ and so one expects leakage to occur for $|v_B| < 495\ \mathrm{m\ s^{-1}}$, allowing only for FF and FiG, i.e. approximately the same result.

6.31. $q_{\|i}^{\mathrm{cond}} \approx 2.6 \times 10^4\ \mathrm{W\ m^{-2}}$, $q_{\|i}^{\mathrm{conv}} \approx 3.2 \times 10^4\ \mathrm{W\ m^{-2}}$ and so the Krashininnikov criterion is satisfied. Leakage onset is expected when $|v_B| = 650\ \mathrm{m\ s^{-1}}$, roughly as before.